VDI-Buch

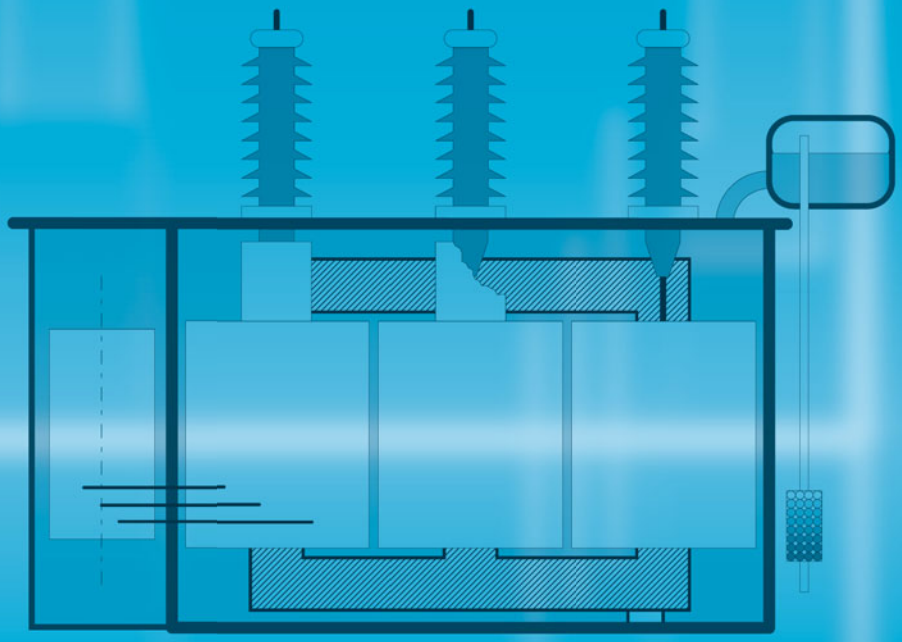

Andreas Küchler

High Voltage Engineering

Fundamentals · Technology · Applications

VDI

Springer Vieweg

VDI-Buch

Andreas Küchler

High Voltage Engineering

Fundamentals – Technology – Applications

Springer Vieweg

Andreas Küchler
Schweinfurt, Germany

VDI-Buch
ISBN 978-3-642-11992-7 ISBN 978-3-642-11993-4 (eBook)
DOI 10.1007/978-3-642-11993-4

Library of Congress Control Number: 2017941508

Springer Vieweg

Original german edition published with title: Hochspannungstechnik

Printed on acid-free paper

This Springer Vieweg imprint is published by Springer Nature
The registered company is Springer-Verlag GmbH Germany
The registered company address is: Heidelberger Platz 3, 14197 Berlin, Germany

Preface

The main task of **high voltage engineering** is to gain *technological control of high electrical field strengths and voltages.* Their effects can impressively be observed in nature (or in a high voltage laboratory) as “lightning and thunder phenomena” if the “insulation system consisting of air” is failing. Formerly, historical authorities such as Zeus, Jupiter or Wotan have been responsible for these natural forces and their risks. But now, the high voltage engineers guarantee for the safe and reliable function of all electrical insulation systems. Only in this way, all the other technical applications of electricity are made available. In consequence, high voltage technology is both a *key technology* for a wide spectrum of technical applications that are indispensable for the modern society and a *cross-sectional technology* integrating different scientific disciplines. High voltage engineering is a fascinating, challenging, interdisciplinary and multifaceted field of activity that will always be a prerequisite and essential support for the technical progress.

High voltages enable the *generation*, *transmission* and *distribution* of electrical energy at relatively low currents and ohmic losses. The minimization of power loss preserves resources and reduces emissions and it is therefore a prerequisite for secure, economical and eco-friendly electricity supply. Furthermore, high voltage and ultra-high voltage AC and DC networks are prerequisites for the development of remote energy sources, for the large-area load balancing and for a transnational energy market. Additionally, high voltage technology has wide-ranging *industrial applications*, such as for example X-ray devices, lasers, high efficiency light sources, lithotripters, shock wave generators, fragmentation devices, accelerators, transmitter tubes, copiers, electrostatic precipitator or coating and enameling devices. Problems of high voltage engineering must also be tackled in power electronics and for the electromobility, in the area of electromagnetic compatibility, in physical and technological research, or in the field of high-temperature superconductivity. For all applications it is common to choose **high electrical field strengths** on the one hand in order to ensure that the dimensions, weight, material usage, costs, losses and environmental pollution remain as low as possible. On the other hand,

the **electric field stress** must *always* be *lower* than
the **dielectric strength** of the insulating materials

so that discharges and a destructive breakdown can definitely be excluded. Between these poles, the tasks of engineers are largely to implement economical and technically optimal system solutions. For that purpose, high voltage engineers should be primarily wide ranging and practice oriented and should have a theoretically sound overview.

The **concept of the book** consists of a systematic, coherent and comprehensive presentation of

fundamentals, technologies and *applications***.**

For this purpose, high voltage engineering is classified into six main topics:

- **Electrical stresses** by fields and waves (Chapter 2)
- **Dielectric strength** of gases, liquids and solids (Chapter 3)
- **Dielectric system characteristics** of insulating materials (Chapter 4)
- **Insulating materials** and their technology (Chapter 5)
- **Testing, measurement and diagnosis** (Chapter 6)
- **Typical insulation systems** for different types of stresses (Chapter 7).

Already the basic Chapters 2, 3 and 4 include practical examples, applications, notes and exercises. Also the description of technologies and applications in the Chapters 5, 6 and 7 is always related to the fundamentals. Special emphasis is laid on the presentation of scientific and practical contexts as well as on *clarity in words and illustrations*. A comprehensive *keyword index* and an extensive *bibliography* shall facilitate access to special issues and to further sources for the reader.

The book is therefore suitable both for the initial training of high voltage engineering in class-room studies or private studies and for the deeper guidance to specific areas and to specialist technical literature. It is intended to be useful as a *workbook in academia and in the professional work*.

This edition of "High Voltage Engineering" is equivalent to the fourth edition of the German reference book "Hochspannungstechnik", and for the first time it is also published in English language. For more than 20 years, the **previous German editions** are widely used by undergraduate and postgraduate students, engineers, scientists, universities, manufacturers, service companies and utilities. In 1996 the first edition was initially developed from the author's lectures at the University of Applied Sciences Würzburg-Schweinfurt. The new editions in 2004, 2009 and 2017 were always stimulated by strong interests of the readership. In each case, comprehensive revisions, adaptions to the state of the art, stronger involvements of application subjects and inclusions of new and innovative topics were made.

Therefore, the **English edition** includes numerous improvements in details and many extensions and new features being related to the great *actual challenges* in high voltage engineering. For example, ultra-high voltage AC and DC transmission with voltages of more than 1,000 kV, DC cable runs with more than 500 kV, switchgear with alternative insulating gases and transformers with alternative insulating liquids are built. That's why the sections about insulation systems for *high voltagc DC transmission* in Chapter 7 were fundamentally revised and much expanded, regarding stresses, dielectric strength and design for DC voltages and with regard to transformers, bushings, cables and fittings for HVDC. This is supplemented in Chapter 3 and 6 by sections about the generation and evaluation of *partial discharges* at DC voltage. Additional current topics are the introduction of so-called *"alternative" climate-friendly insulating gases* instead of SF_6 and the use of so-called *"alternative" eco-friendly insulating liquids* instead of mineral oil. Revisions have also been made in the sections about the *conduction behavior* and the *dielectric behavior* of solid and liquid dielectrics (Chapter 4), about the *oscillating behavior* during impulse voltage tests (Chapter 6) and about *transformer testing* (Chapter 7). On the suggestion of renowned expert colleagues, it is finally proposed in Chapter 3 that the term "*electronegativity*", which is commonly used in high voltage engineering, should be replaced by the term "*electron affinity*".

At various places in the text, references to new *technical regulations* and *standards* are also made. This is, however, possible only in extracts or examples, according to the current but impermanent status of standardization. The reader must finally consult the appropriate valid and updated regulations and standards directly. The limited space of the book naturally necessitates also intense abridgement of many contents and a very subjective compromise between *completeness* and *depth*. I therefore request all experts to be lenient towards the author if they find their special subject to be inadequately dealt with. I hand over this book to the reader, with a request for comments and suggestions which are always welcome. Please contact Andreas.Kuechler@fhws.de.

Now, my personal recommendation would be "*to read with a pen*", that is, to understand the examples, exercises and field plots through own calculations and to delve into interesting topics through

written side notes and extracts. Useful supplements for this could be a mathematical formulary and textbooks on experimental physics, basic electromagnetic theory or material sciences.

Many **expert colleagues and friends** have supported me during the creation of the first three German editions. As I could already express my gratitude for their help in these preceding editions, I now want to thank all direct and indirect supporters who were the prerequisite for the fourth German edition and for the first Englisch edition of "High Voltage Engineering" in the present form.

With many colleagues from universities I could conduct an intensive scientific discourse, for which I would like to give my thanks to the professors Dr. *R. Bärsch*, Dr. *F. Berger*, Dr. *G. Chen*, Dr. *Ch. Frank*, Dr. *S. Grossmann*, Dr. *S. Gubanski*, Dr. *V. Hinrichsen*, Dr. *F. Jenau*, Dr. *M. Koch*, Dr. *J. Kindersberger*, Dr. *M. Liebschner*, Dr. *H. Okubo*, Dr. *R. Patsch*, Dr. *R. Plath*, Dr. *K. Rethmeier*, Dr. *M. Rossner*, Dr. *S. Tenbohlen*, Dr. *W. S. Zaengl* (†) and Dr. *M.H. Zink*.

Furthermore, my sincere thanks go to Dr. *I. Atanasova-Höhlein*, Dr. *K. Backhaus*, *S. Bhumiwat*, *M. Chmielewski*, Dr. *W. Exner*, *S. Eyring*, Dr. *J. Fabian*, Dr. *R. Färber*, *R. Fritsche*, Dr. *J. Fuhr*, Dr. *W. Hauschild*, *A. Hopf*, *M. Hörmann*, Dr. *Ch. Hurm*, Dr. *S. Jaufer*, Dr. *U. Kaltenborn*, *Ch. Krause*, Dr. *M. Krüger*, *N. Kurda*, *A. Langens*, Dr. *C. Leu*, *L. Lundgaard*, *M. Pegelau*, Dr. *R. Pietsch*, Dr. *U. Piovan*, *B. Preidecker*, Dr. *U. Prucker*, *K. Rädlinger*, *M. Rösner*, *J. Roßmann*, Dr. *J. Schiessling*, *B. Schlittler*, *Ph. Schmitt*, *T. Schnitzer*, *J. Seiler*, *B. Spatta*, Dr. *J. Speck*, *Th. Steiner*, *J. Titze* and *E. Zerr* for many expert discussions and suggestions. I am also grateful to the companies that contributed to the preparation of the editions by photographic material and professional exchange.

The University of Applied Sciences Würzburg-Schweinfurt (FHWS) and the Faculty of Electrical Engineering provided a sound scientific basis for this publication by the implementation of high voltage engineering in teaching and research. And of course, my students have been a great help owing to their questions, contributions and theses. Important scientific and professional support was also given by our current and former staff members *M. Fell*, *S. Harrer*, *B. Hochbrückner*, *F. Hüllmandel*, *F. Klauer*, *H.-P. Öftering*, *A. Reumann*, Dr. *F. Schober*, *S. Sturm*, *F. Swobodnik* and *I. Wirth*. I am also very grateful for that.

Furthermore, *Omicron Electronics GmbH* and *B. Walker* deserve very high recognition and reward for the great assistance in translating from German to English.

Finally, special thanks go to Ms. *S. Bromby*, to Mr. *Th. Lehnert* and to *Springer-Verlag GmbH* for editing the book, for great patience and understanding and for very good cooperation.

Last but not least, these thanks also include my family. My sons *Florian* and *Sebastian* could provide valuable tips from the students' perspective. Also my parents *Ursula* and *Johannes* contributed significantly to the development of the work because of their continuous encouragement and permanent support. Nevertheless, the realization of the edition was primarily achieved due to the great understanding, the strong backing and the enormous patience of my wife *Christiane*.

Schweinfurt and Hammelburg, March 2017

Andreas Küchler

Contents

Symbols and Abbreviations

Variable scalar quantities are written in italics, *vectorial* quantities are represented in bold and italics, e.g. $v(t)$ and $\boldsymbol{E}(\boldsymbol{x},t)$.

For *time-dependent* currents, voltages and charges, small letters, such as i, v and q are used, for time-dependent field quantities, capital letters such as $E(t)$ are used.

Peak values are characterized by umbrella hat or caret on the letter, for example, $\hat{E}$ and $\hat{V}$. *Constant quantities and r.m.s. values* are symbolized by capital letters, such as E, I, V and Q.

Symbols with underlining signify *complex quantities*, for example $\underline{z}$, $\underline{i}$ and $\underline{v}$.

The applied *units* generally correspond to the International System of Units (SI units). Only for the units of pressure, temperature and time, also the traditional and descriptive units of bar (1 bar = 10^5 Pa), degrees Celsius (°C) and the usual time units are resorted to.

Symbols

In the following section, the most important symbols are explained. They are arranged according to small letters, capital letters and Greek letters. The meanings of different *indices* result from the text. Unfortunately, using the same symbols for totally different quantities cannot be completely avoided because of the overlapping of different science disciplines in the fields of high voltage engineering. The reader is therefore requested to infer the applicable meaning from the context of the text.

a	Distance, width, coefficient, exponent
b	Regression coefficient, constant
c	Constant
d	Distance, flashover distance
e	Elementary charge, unit charge
e	e = 2.718281..., , Euler number, base of the natural logarithm
f	Frequency, impulse factor, shape factor
$f(...)$	Function of ...
g	Acceleration due to gravity
$g(...)$	Function of ...
h	Height, frequency or empirical distribution function (statistics), absolute air humidity
i	Current, counting index
j	Imaginary unit, counting index
k	Constant, counting index, lifetime exponent
k	Boltzmann constant
l	Length, counting index
m	Mass, counting index
n	Number (quantity), counting index, optical refractive index
p	Geometry factor, potential coefficient, pressure, power loss density, p-factor, probability
q	Charge
r	Radius, distance, divider ratio, relative air humidity
s	Distance, Laplace operator, steepness, empirical standard deviation
$\boldsymbol{s}$	Spatial vector
t	Time

$\tan\delta$	Dissipation factor
u	Velocity, coordinate ($\underline{w}$-plane), measurement uncertainty
v	Voltage, coordinate ($\underline{w}$-plane), empirical variation coefficient
w	Energy density, water content (relative or absolute)
$\underline{w}$	Complex number
x	Space coordinate, length
$\boldsymbol{x}$	Spatial vector
x	Definite value of a random variable
y	Space coordinate
z	Space coordinate, axial length
$\underline{z}$	Complex number
$\boldsymbol{A}, A$	Area (vector and magnitude)
A	Voltage-time area, Constant (Paschen's law),
Al	Aluminium (chemical symbol)
Ar	Argon (chemical symbol)
$\boldsymbol{B}, B$	Magnetic flux density
B	Constant (Paschen's law)
B	Boron (chemical symbol)
C	Capacitance
C	Carbon (chemical symbol)
Ca	Calcium (chemical symbol)
Cl	Chlorine (chemical symbol)
Cu	Copper (chemical symbol)
$\boldsymbol{D}, D$	Dielectric displacement density
$\underline{D}$	Complex r.m.s. phasor for the dielectric displacement density
D	Distance, diameter, theoretical density function (statistics)
$\boldsymbol{E}, E$	Electric field strength / intensity / stress (vector and magnitude)
$\underline{E}$	Complex r.m.s. phasor for the electric field strength
$\boldsymbol{F}, F$	Force (vector and magnitude)
F	Theoretical distribution function, probability (statistics)
F	Fluorine (chemical symbol)
Fe	Iron (chemical symbol)
G	Conductance, shear modulus
$\boldsymbol{H}, H$	Magnetic field intensity (... strength)
H	Hydrogen (chemical symbol)
He	Helium (chemical symbol)

$I, \underline{I}$	Current, complex r.m.s. phasor
$\boldsymbol{J}, J$	Conduction current density
$\underline{J}$	Complex r.m.s. phasor for the conduction current density
J	Iodine (chemical symbol)
K	Capacitance coefficient, constant, Kerr constant
K	Potassium (chemical symbol)
L	Inductance, length
M	Mutual inductance
Mg	Magnesium (chemical symbol)
N	Number
N	Nitrogen (chemical symbol)
Ne	Neon (chemical symbol)
O	Oxygen (chemical symbol)
$\boldsymbol{P}, P$	Electrical polarization
P	Real power, power loss
P	Phosphorous (chemical symbol),
Q	Charge, reactive power
R	Resistance, radius, range (statistics)
R	General chemical group
$\underline{S}, S$	Complex power, apparent power
S	Sulfur (chemical symbol)
Si	Silicon (chemical symbol)
T	Time, period, temperature
V	Volume, variation coefficient
$V, \underline{V}$	Voltage, complex r.m.s. phasor
W	Energy, Probability (statistics)
X	Reactance, random variable
Y	Random variable
$\underline{Y}$	Admittance (complex conductance)
Z	Characteristic line impedance, intrinsic impedance
$\underline{Z}$	Impedance, complex phasor
α	Angle, ionization coefficient
β	Ionization coefficient
γ	Surface ionization coefficient
δ	Loss angle, relative air density,

	Weibull exponent
$\tan \delta$	Dissipation factor
ε	Permittivity
η	Field efficiency factor, space charge density, attachment coefficient, capacitive voltage overshoot, voltage efficiency (impulse circuit)
ϑ	Temperature
κ	Electrical conductivity
λ	free path length, thermal conductivity
μ	Permeability, ion mobility, expectation value
ν	Optical frequency, continuous index
ρ	Resistivity, reflection, refraction or transmission coefficient (traveling waves)
σ	Surface charge density, force per area, standard deviation
$\sigma(t)$	Step function
τ	Time constant, propagation time (traveling waves)
φ	Potential
ω	Angular frequency
Θ	Contact angle

Abbreviations

AC	Alternating Current (amplitude current)
AC	Prefix characterizing alternating electric quantities
ACLD	AC long duration test (outdated)
ACSD	AC short duration test (outdated)
AMF	Axial magnetic field contacts
ASTM	American Society for Testing and Materials
AV	Applied voltage test
BEM	Boundary element method
BNC	Benzyl neocaprate
CCA	Charging current analysis
CD	Coupling device
CIGRÉ	Conseil International des Grands Réseaux Electriques
CISPR	Comité International Special Des Perturbations Radiophoniques
CO	Carbon monoxide
CO2	Carbon dioxide
CSM	Charge simulation method
CTI	Comparative tracking index
D	Discharge
DAC	Damped AC voltage
DBT	Dibenzyl toluene
DC	Direct current
DC	Prefix characterizing time-independent electric quantities
DCA	Discharge current analysis
DEC	Dielectric equivalent circuit
DFT	Discrete fourier transform
DIL	Design insulation level
DKD	German calibration service
DP	Mean degree of polymerization
DSP	Digital signal processor
DTE	Ditolylether
DVA	Discharge voltage analysis
EMC	Electromagnetic compatibility
EN	European standard
EP	Epoxy resin
EPR	Ethylene-propylene rubber
EPS	Equipotential surface
Eq.	Equation
ESD	Electrostatic discharge
FCL	Fault current limiter
FDA	Frequency domain analysis
FDM	Method of finite differences
FDS	Frequency domain spectroscopy
FEM	Finite element method
FeO	Iron oxide
FFT	Fast Fourier transform
FID	Flame ionization detector
FT	Fast transients
FW	Filament winding
G1, 2	Spark gap 1, 2
GC	Gas chromatograph
GIL	Gas-insulated line

GIS Gas-Insulated Switchgear
GRP Glass-fiber reinforced plastic
GWP Global warming potential
HDPE High-density polyethylene
HEMP High altitude electromagnetic pulse
HPLC High Pressure/Performance Liquid Chromatography
HTSC High-temperature superconductivity
HTV High-temperature vulcanization (silicone)
HV High voltage
HVAC High voltage alternating current
HVDC High voltage direct current

IEC International Electrotechnical Commission
IEEE The Institute of Electrical and Electronic Engineers
IEM Integral equation methods
IR Infrared light
IRC Isothermal relaxation current
IVPD Induced voltage test with PD measurement
IVW Induced voltage withstand test

KFT Karl Fischer titration

LCC Line-commutated converter
LDPE Low-density polyethylene
LFH Low-frequency heating
LHe Liquefied helium
LI Lightning impulse
LIC Chopped lightning impulse
LN2 Liquefied nitrogen
LSI Liquid Silicone
LSF6 Liquefied Sulfur hexafluoride
LTS, LTSC Low-temperature superconductivity
LV Low voltage
LV Arc-performance index

MBT Monobenzyl toluene
MCM Monte Carlo method
MIPB Mono-isopropyl-biphenyl
MOM Method of moments
MP Metallized paper

NEMP Nuclear electromagnetic pulse

OFC Oxygen-free copper
OIP Oil-impregnated paper
OLI Oscillating lightning impulse voltage
OLTC On-load tap changer
OSI Oscillating switching impulse voltage

PA Polyamide
PAI Polyamidimide
PC Polycarbonate
PCB Polychlorinated biphenyl
PD, pd Partial discharge
PDC Polarization / Depolarization current
PDE Partial discharge extinction
PDI Partial discharge inception
PDM Partial discharge measuring device
PE Polyethylene
PES Polyethersulfone
PF Phenolic resin (phenol formaldehyde resin)
PFL Pulse forming line
PI Polyimide
PMMA Polymethylmethacrylate
PP Polypropylene
PR Polarity reversal
PSU Polysulfone
PTB Physikalisch-technische Bundesanstalt (Federal Institute of Metrology)
PTFE Polytetrafluoroethylene
PTI Proof tracking index
PU Polyurethane
PVC Polyvinylchloride
PVDF Polyvinylidenfluoride
PXE Phenyl-xylyl-ethane

RBP Resin-bonded paper
RIP Resin-impregnated paper
RIS Resin-impregnated synthetics
RIV Radio interference voltage
RMF Radial magnetic field contact
r.m.s. Root-mean-square
RTV Room-temperature vulcanization silicone
RVA Recovery voltage analysis
RVM Recovery voltage method
RW Regulating winding

SCSM Surface charge simulation method
SF6 Sulfur hexafluoride
SI Switching impulse voltage

SiC Silicon carbide
SIR Silicone rubber
SMES Superconductive magnetic energy storage
SSB Superconductive Current Limiter

T Thermal defect
TCD Thermal conductivity detector
TEM Transverse electromagnetic (wave)
TF Transfer function
TP Triple point
TP Thermal fault with paper decomposition

UHF Ultra high frequency
UHV Ultra high voltage
UV Ultraviolet light

VDE Verband der Elektrotechnik Elektronik Informationstechnik (Association for Electrical, Electronic and Information Technology)
VLF Very low frequency
VPI Vacuum-pressure impregnation
VSC Voltage source converter

XLPE Cross-linked polyethylene

ZnO Zinc oxide

1 INTRODUCTION

1.1 The Function of High Voltage Technology

The main task of high voltage technology and engineering is to *keep high electric field strengths under control*. They do not only occur in apparatus operated or tested at high voltages, they can also be found in apparatus at comparatively low voltages and with small insulation, e.g. in thin capacitor insulations made of polymer films.

The *electric field strength,* and not the voltage, is the relevant quantity for the electric strength ("breakdown strength") of insulating materials. Nevertheless, our discipline is usually called "high voltage technology" and "high voltage engineering", which is not strictly correct.

Basically, high voltage engineering has to guarantee that the **electric stress**, given by the **electric field strength** E, is significantly smaller than the **electric strength** (breakdown strength) E_d *always*, i.e. under all possible circumstances:

"Stress" E	<<	E_d "Strength"	(1.1-1)
(Field strength)		(Electric strength)	

This principle, which is easy to formulate, but difficult to achieve, is discussed in Chapter 2 (Electric Fields) and Chapter 3 (Electric Strength).

Note: Theoretically, an even simpler condition $E < E_d$ should be sufficient, but in reality E_d cannot be determined exactly. Therefore it is always necessary to consider a sufficient safety margin $E << E_d$.

Note: The terms *"electric field intensity"*, *"electric field strength"* and *"electric field stress"* often are used synonymously. In order to avoid confusion with the **"electric strength"** (which refers to the breakdown strength of the *insulating material*) the term **"electric field intensity"** (which clearly refers to the intensity or strength of the *field*) would be the best choice. Nevertheless, the terms **"electric field strength"** or **"electrical field stress"** are used in high voltage engineering.

> Therefore the reader is faced with the challenge always to distinguish clearly between the *strength* (intensity, stress) *of a* **field** and the *breakdown strength, electrical strength or dielectiric strength of a* **material.**

The following Chapters 4 (Dielectric System Properties), 5 (Insulating Materials), 6 (Testing, Measuring, Diagnosis) and 7 (Applications) describe the indispensable technological tools and important applications.

1.2 Applications of High Voltage Technology

The most important applications of high voltage technology are in the field of equipment and systems for the **transmission** and **distribution of electrical energy**.

Common rated voltages for three-phase AC systems in Germany are 12 kV, 24 kV, 123 kV, 245 kV and 420 kV. Higher transmission voltages are used in countries with very long transmission distances between power plants and metropolitan areas (e.g. in North America, Asia, South America, Southern Africa, Eastern Europe, Russia). Meanwhile, voltages in the range of 1 MV are used for extreme transmission applications (e.g. in China and India).

More and more often, three-phase, high-voltage AC (HVAC) transmission reaches technological and economical limits which can be overcome by means of high-voltage DC (HVDC) transmission. Voltages of more than 1000 kV are used today.

Note: If *DC transmission* is used, problems with transmission line inductances (for very long distances) or with cable capacitances (e.g. for submarine cables) can be avoided. It is possible to connect non-synchronous

A. Küchler, *High Voltage Engineering*, VDI-Buch,
DOI 10.1007/978-3-642-11993-4_1

electric systems and systems with different power frequencies. Furthermore, there is an effective controllability of power flow, reactive power is not transmitted. Therefore HVDC transmission can be used for limitation of short-circuit currents and for stabilization of large electric systems.

High-voltage engineering has to provide safe, reliable and economic insulation systems for power apparatus and systems, e.g. for generators, transformers, switchgear, cables, transmission lines etc. (*Chapter 7*).

High voltages are *necessary for power transmission* because of the quadratic dependence of transmission-line losses P_L from current I. These losses are given for a line-to-ground voltage (phase voltage) V_{Ph} by

$$P_L = 3\,R\,I^2 \quad \text{and} \quad S = 3\,V_{Ph}\,I \qquad (1.2\text{-}1)$$

If a high apparent power S has to be transmitted, losses can most effectively be reduced by reduction of the current I, i.e. by increasing the voltage V_{Ph}.

An economic and environment-friendly power transmission with low losses can only be achieved using higher voltages.

There are upper voltage limits, because insulation costs increase with voltage. If the standard voltage levels are considered, often it is economical to choose a rated voltage in kV close to the transmission distance in km. In metropolitan areas with high transmission power, voltages are significantly higher in order to reduce currents and line losses to a tolerable degree.

Other applications of high voltage engineering can be found in many fields of technology (Chapter 7.4), e.g.

- in *telecommunications* (high power transmitters),
- in *X-ray technology* (acceleration of electrons by high voltages),
- in *laser* technology (electric gas discharges for stimulation of atoms),
- in *medical* engineering (e.g. lithotripters for fragmentation of kidney stones by electro-acoustic shock waves),
- in *research* applications (generators for acceleration of particle beams),
- in *production technology* (electrostatic lacquering and coating, material treatment and high-speed formation by shock waves),
- in testing of *electromagnetic compatibility* (by high voltages),
- in protection against lightning and overvoltages,
- in *environmental protection* (electrostatic filters),
- in *recycling* technology (fragmentation and separation of materials by electro-acoustic shock waves),
- in the electroporation of biological cells (sugar beets, fruits, wine),
- in *electronic components* (e.g. capacitors),
- in electronic tubes and copiers
- or in *ignition devices* (e.g. spark plugs in motor vehicles).

1.3 Perspectives of High Voltage Engineering

Obviously high voltage technology is a key technology for reliable, economic, efficient and environment-friendly power supply systems. Additionally it is an indispensable requirement for many technological innovations, and it is faced with new challenges continuously.

High voltage technologies are also required for the further development of power engineering. Especially for the use of combined heat and electricity production and for the use of renewable energy sources it is necessary to have strong transmission and distribution grids at one's disposal. The demands for heat and electricity are not synchronous and wind and solar energy are supplied with particularly high fluctuations. Because of the lack of storage possibilities, it is necessary to compensate

for these fluctuations by means of peak power plants via high-voltage transmission grids.

New challenges for high voltage engineering arise from the wish to reduce CO_2 emissions by the use of the global potential of hydro power. Transmission distances of more than 1000 km and high power ratings can only be realized by means of high voltage direct current (HVDC) technology [1].

Note: Alternatively to electricity transmission it is often proposed to use solar energy from desert regions for the production of *hydrogen* gas by electrolysis, to transport the gas via *pipelines* and to generate electricity again, e.g. in *fuel cells*. Unfortunately, the efficiency of such a system is significantly lower than for a comparable fully electrical system.

Generally high temperature superconductivity can be used for the reduction of current losses and for the reduction of transmission voltages, but it will not be possible to transmit electrical energy without high voltages. New high-voltage apparatus for existing transmission systems and for new functions will be developed [203], Chapters 7.5 and 5.4.6.

1.4 Overview

The contents of this book relate to the problems encountered by high voltage engineers. They shall be explained exemplarily by means of a typical insulation system in power engineering. Thereby a first insight is given into the ideas, concepts and methods of high-voltage engineering:

For this purpose, a *wall bushing* is chosen as an *example* for a typical insulation system, Figure 1-1. The function of a wall bushing is to feed a conductor on high voltage potential through a grounded wall, with an insulation-core diameter as small as possible and without electric discharges on the surfaces and at the electrodes. For this purpose, the conductor is fed through the main insulation body containing conductive grading layers (e.g. through an oil-impregnated paper core containing metallic foils with different lengths). The insulation core is assembled in a housing that consists of an outdoor porcelain component, a flange, an

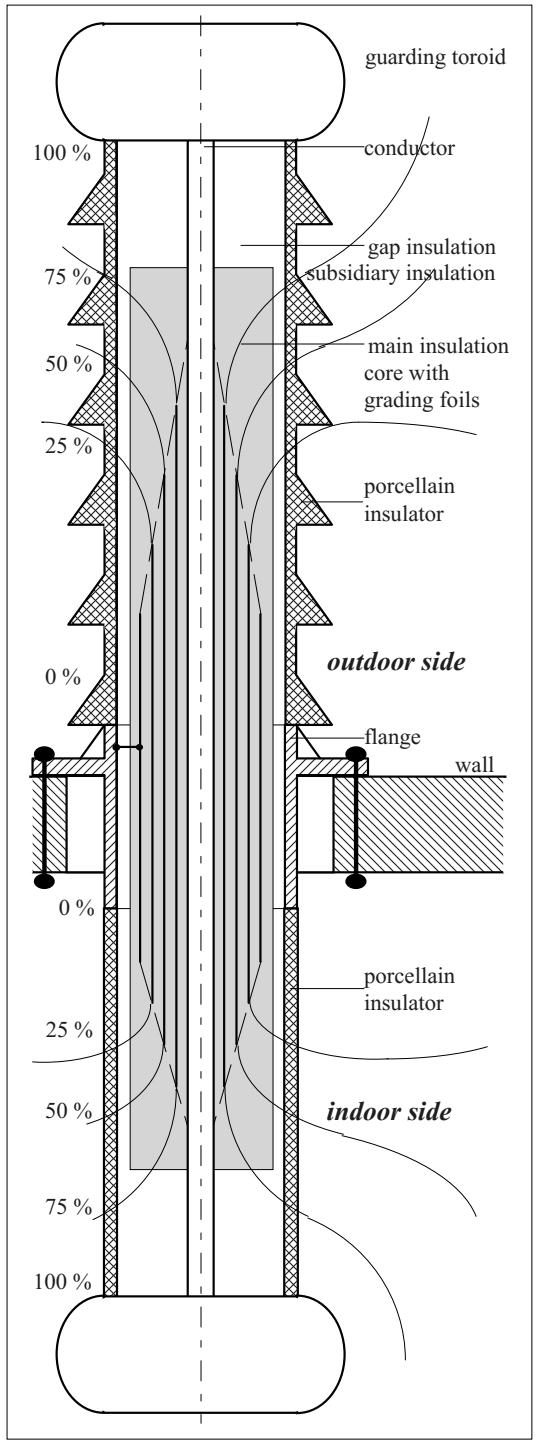

Figure 1-1: Wall bushing, example for a typical insulation system in high voltage engineering (schematic).

indoor porcelain and screening toroids. The gaps are filled with an additional insulating material (e.g. with mineral oil) and form a subsidiary insulation.

For a given design, it is necessary at first to determine the **electrical stress**, i.e. the *electric field strength*, in order to evaluate the stresses on the insulating materials. First order estimations can often be performed by analytical calculations and estimates, but complex insulation systems normally require numerical calculations in order to get accurate results in different dielectrics. Field calculation methods are described in *Chapter 2*. Figure 1-1 shows equipotential lines schematically in steps of 25 %.

Calculated field strengths have to be compared with the very different **electric strengths** of the insulating materials. The lowest strength is provided by the ambient air (external strength). The highest strength is required for the highly stressed main insulation (internal strength). Special attention has to be paid to the electric strengths of interfaces and contaminated surfaces which can be improved by shed profiles. The electric strength of dielectrics, interfaces, surfaces and insulation systems is discussed in *Chapter 3*.

Properties, **technology** and treatment of **different insulating materials** are described in *Chapter 5*. Every insulating material has a particular characteristic profile and specific processing characteristics. Therefore the possible applications are very different. For example, porcelain is insensitive against ambient influences; therefore, it is a very good housing material. Oil has very good properties for the impregnation of cellulose and other fibers and for the filling of gaps and holes. These materials and applications are examples only; there are alternatives, of course.

If the field strengths are too high or electric strengths too low, a redesign and an improvement of the *high voltage design* is necessary. Very often this is an iterative process of optimization. The most important tools are the methods of potential grading (field grading), e.g. by grading layers, insulation system geometries (e.g. lengths, diameters) and electrode contours. Additionally, an appropriate selection of dielectric materials has to be performed, considering technological, economic and ecological aspects. Furthermore the questions of manufacturing, quality control and testing have to be considered.

After manufacturing, the quality of a product has to be proved by high voltage tests, normally with AC, impulse and DC voltages. **Test and measuring techniques** are described in *Chapter 6*. They have to fulfill strict requirements according to ISO 9000 ff and other international standards.

Furthermore, operating times of high voltage apparatus exceed the nominal lifetimes in many cases. Therefore **diagnostic methods** are very important for the condition assessment of aged and defective equipment. Consequently, onsite measurements and continuous monitoring ("online monitoring") of power apparatus are of high interest, additionally to laboratory measurements. Many decisions have to be made about re-investments these days, i.e. the estimation of residual lifetime is very important for economic and safe energy systems.

Typical insulation systems for AC, DC and impulse voltages in the field of power engineering and for many other applications are discussed in *Chapter 7*.

Note: In terms of high voltage engineering, an "**insulation**" or "insulation system" is the entirety of dielectric materials and devices which are combined to a technical system in order to provide a galvanic separation of electrically conducting parts. The term "**isolation**" is sometimes used synonymously, but it means separating properties or separation functions in a more general sense. "Insulation" refers to the dielectric materials, parts and systems.

2 ELECTRIC STRESSES

Electric stresses must always be considered if electric field strengths are in the range of the electric strengths of the insulating materials, i.e. calculation of electric field intensities is of fundamental importance.

The most important equations for the description of electric fields in high voltage engineering are summarized in *Section 2.1* [2], [3]. *Section 2.2* describes how different stresses (e.g. by AC, DC and impulse voltages) result in the development of different fields. Basic arrangements can be treated by analytical calculations (*Section 2.3* and *2.4*), but complex insulation systems normally require numerical calculation [4] (Section 2.5). Traveling waves need special consideration because of their character as fast changing electromagnetic processes [5] (*Section 2.6*).

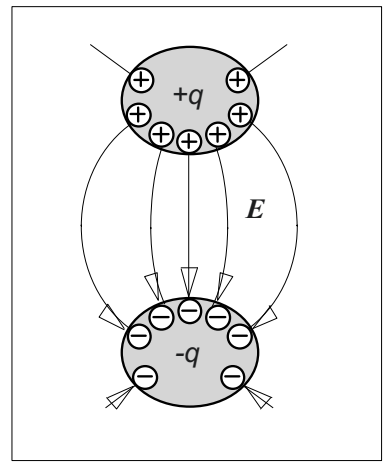

Figure 2.1-1: Electric source field (irrotational electrostatic field with charges as sources and sinks of the field).

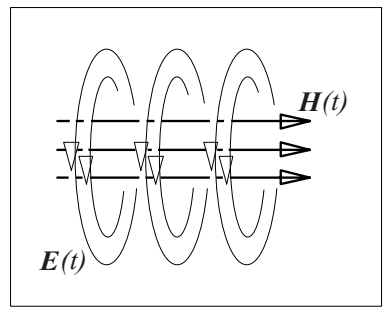

Figure 2.1-2: Electric curl field (induced electric field, electromagnetic field).

2.1 Basic Field Theory

Electric fields cannot be sensed by human beings directly. Fields can only be noticed indirectly by their physical effects. *The electric field describes a physical condition of space.* The electric field strength is defined by its mechanical *force* on electric charges (or charged test bodies).

There are two sources of electric fields:

- Positive and negative electric *charges* are sources and sinks (i.e. starting and ending points) of the field ("*electrostatic field*"), Figure 2.1-1.
- Furthermore, there are electric fields which are induced by *time-varying magnetic fields.* Magnetic field lines can be regarded as *curl lines* of closed field line loops ("*curl field*"), Figure 2.1-2.

Electric charges cannot be divided infinitely. The smallest quantity of charge is the *elementary charge* $e = 1.6022 \cdot 10^{-19}$ As.

Charges can be distributed differently,

- as a *single charge* or *point charge* (e.g. electrons with the charge q = -e or protons with q = +e),
- as a *line charge* (e.g. on a wire with a negligibly small diameter),
- as a *surface charge* (e.g. on the surface of a conductive electrode, Figure 2.1-1) and
- as a space charge (e.g. as a "space charge cloud" in a gas discharge).

Point charges and line charges are idealizations which are useful for field calculations.

The quantities *potential*, *voltage*, *current* and *capacitance* are integral quantities, which have to be derived from the actual field quantities (Section 2.1.2). Although these integral quantities are used very often, it must not be forgotten that they only reflect partial aspects of the field properties. Therefore, exact knowledge and calculation of the electric field is very important for high voltage engineering.

A. Küchler, *High Voltage Engineering*, VDI-Buch,
DOI 10.1007/978-3-642-11993-4_2

2.1.1 Field Quantities

The **electric field strength** $\boldsymbol{E}$ is defined by means of the mechanical force $\boldsymbol{F}$ on a positive test charge q^+, Figure 2.1-3:

$$\boldsymbol{E} = \boldsymbol{F}/q^+$$

or

$$\boldsymbol{F} = q^+ \cdot \boldsymbol{E} \qquad (2.1\text{-}1)$$

Electric field strength $\boldsymbol{E}$ and force $\boldsymbol{F}$ are *vector quantities*, which are printed here in ***bold and italic*** letters. The direction of the field vector $\boldsymbol{E}$ is identical with the direction of force $\boldsymbol{F}$ on a positive test charge. These directions are visualized by **field lines** in a field plot. In the case of a negative test charge, the directions of field and force vectors are anti-parallel.

According to Eq. (2.1-1) the magnitude $E = F/q^+$ of the field strength $\boldsymbol{E}$ is calculated from the magnitude F of force $\boldsymbol{F}$. The density of field lines corresponds to the field strength.

Analogy to the gravitation field: The force on charges in the electric field is analogous to the force on masses in the gravity field $\boldsymbol{g}$. In the field of the Earth's acceleration $\boldsymbol{g}$, the force on a test body of mass m is $\boldsymbol{F} = m \cdot \boldsymbol{g}$, parallel to the direction of the gravity field.

In an electrostatic field positive and negative charges are the origin (source) of the electric field. Therefore a field quantity $\boldsymbol{D}$ is defined which is directly related to the field-generating charges: The **dielectric displacement density** *(electric flux density)* $\boldsymbol{D}$ is proportional to the electric field strength:

$$\boldsymbol{D} = \varepsilon_0 \varepsilon_r \boldsymbol{E} \qquad (2.1\text{-}2)$$

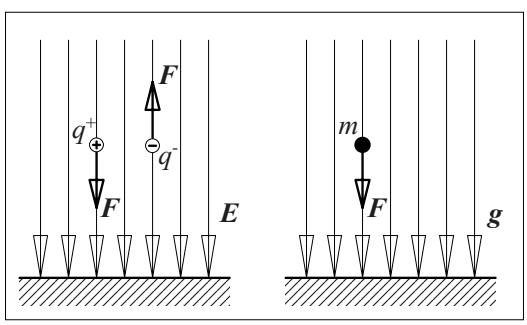

Figure 2.1-3: Forces on test bodies in the electric field (left) and in the gravity field (right).

The magnitude of $\boldsymbol{D}$ corresponds to the surface charge density σ on an ideal conductive electrode, see also Figure 2.1-1:

$$D = \sigma = \mathrm{d}q/\mathrm{d}A \qquad (2.1\text{-}3)$$

Therefore the dimension of D is the dimension of a charge divided by the area, i.e. $[D] = \mathrm{As/m^2} = \mathrm{C/m^2}$.

According to Eq. (2.1-2) the relation between $\boldsymbol{D}$ and $\boldsymbol{E}$ is given by a fundamental physical constant, the **electric constant**, i.e. the (absolute) **permittivity of vacuum**,

$$\varepsilon_0 = 8.8542 \text{ pF/m}.$$

Additionally, Eq. (2.1-2) contains the **relative permittivity** ε_r, which has no dimension and which depends on the properties of the dielectric material.

The relative permittivity ε_r is always greater than 1 because the electric field polarizes available charges within the dielectric material and thereby generates a reverse field. This means that the field strength E for a given charge density (or for a given electric flux density D) is lower than in vacuum with $\varepsilon_r = 1$. This effect of *polarization* is described by a factor $\varepsilon_r > 1$, Section 4.2.

Technical insulating materials always have a small (residual) **conductivity** κ. The forces of the electric field can therefore accelerate mobile charge carriers, and a drift current proportional to the field strength arises. The **current density** is

$$\boldsymbol{J} = \kappa \cdot \boldsymbol{E} \ . \qquad (2.1\text{-}4)$$

The field of the current density $\boldsymbol{J}$ is called an **electrical conduction field**; in high voltage engineering it is especially important for DC stresses. The field of the electric flux density $\boldsymbol{D}$, the so called **dielectric displacement field** is usually dominant in case of AC stresses and always dominant in case of impulse voltages. For relatively slowly changing (quasi-static) processes, induced field components can often be neglected. Rapidly changing fields, e.g. in the case of the skin effect, eddy currents and electromagnetic wave propagation, must be described as **curl fields** or **electromagnetic fields**.

2.1.2 Equipotential Lines, Potential, Voltage and Capacitance

A charge q, which is moved against the force $\boldsymbol{F}$ of the electric field $\boldsymbol{E}$, has a potential energy W_{pot}, analogous to the potential energy of a mass m in the gravitation field $\boldsymbol{g}$, Figure 2.1-4. We refer to potential φ based on the value of the charge:

$$\varphi = W_{pot}/q \qquad (2.1\text{-}5)$$

A surface of equal potential or equal potential energy is described as an **equipotential surface** (or an *equipotential line* in a two-dimensional sectional view. Both are *orthogonal* to the field lines, i.e. a movement of charges on the equipotential plane (*orthogonal* to the field direction) is possible without any force or energy.

Note: The *equipotential surface* is not the surface of a body or the interface between different materials. Here the term *surface* is used in a general *mathematical* sense in order to describe an area.

Electric field plots in high voltage engineering are very often *visualized* by means of equipotential lines. Their course can be approximated analytically in some simple cases. Numerical solutions also normally consist of potential values which are used for the interpolation of equipotential lines.

Potential and potential energy must always be related to a surface area with $W_{pot} = 0$ and $\varphi = 0$. This *reference surface* can be chosen freely. Therefore potential is not an absolute quantity; only potential differences $\Delta\varphi$ and differences of potential energy ΔW_{pot} can be defined. A potential difference is very often referred to as a **voltage** V or *voltage difference* ΔV:

$$\Delta\varphi_{21} = V_{21} = \Delta V_{21} \qquad (2.1\text{-}6)$$

For a given electric field $\boldsymbol{E}$ the voltage or the potential difference between point 2 and 1 can be calculated by integration. Thereby the difference of the potential energies is described as a line integral of the field force along the integration path. According to Eq. (2.1-1) $\boldsymbol{F}$ is replaced by $q \cdot \boldsymbol{E}$:

$$\begin{aligned} V_{21} = \Delta\varphi_{21} = \varphi_2 - \varphi_1 &= \frac{1}{q}\,\Delta W_{21} \\ &= \frac{1}{q}\int_2^1 \boldsymbol{F}\,\mathrm{d}\boldsymbol{x} \\ &= \frac{1}{q}\int_2^1 q\boldsymbol{E}\,\mathrm{d}\boldsymbol{x} \end{aligned}$$

$$\boxed{V_{21} = \Delta\varphi_{21} = \varphi_2 - \varphi_1 = \int_2^1 \boldsymbol{E}\,\mathrm{d}\boldsymbol{x}} \qquad (2.1\text{-}7)$$

Thus, the voltage or the potential difference between two points 2 and 1 is given by the line integral of the electric field strength $\boldsymbol{E}$ along the path $\boldsymbol{x}$.

In an *electrostatic field* the result of the integration is independent of the integration path. If different paths are chosen, the result is always the same; it depends only on the potential difference between the starting and

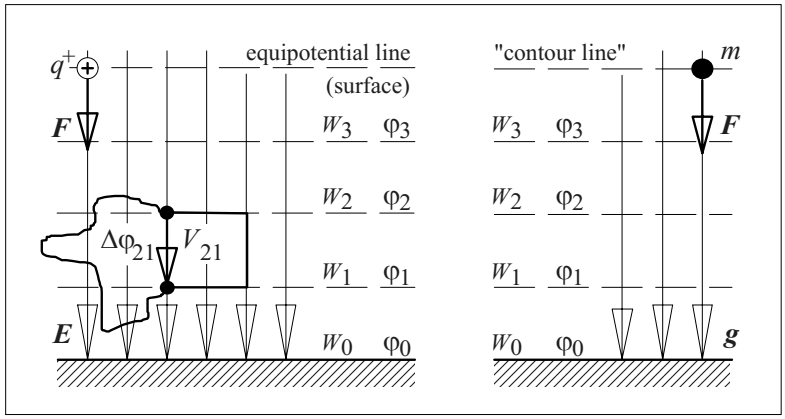

Figure 2.1-4: Potential energy, potential and voltage in the electric field (left) and in the gravitation field (right).

end points, Figure 2.1-4. Therefore it is also referred to as a so-called *potential field*. According to Eq. (2.1-7) and (2.1-8) the field strength is the negative gradient of the potential $\boldsymbol{E} = -\,\mathrm{grad}\,\varphi$, it is therefore referred to as a *gradient field*. Sometimes the field is called *irrotational*, because there are *no* time-varying magnetic field lines which can be regarded as curl lines of an induced electric field.

For a *curl field* or an *electromagnetic field*, which is not irrotational, the result of the integration according to Eq. (2.1-7) would depend on the definition of the integration path. For example, the integration along a field line in Figure 2.1-2 would give a finite value, different from zero, even if starting and end point were identical. The definition of a *scalar potential* φ, a potential difference $\Delta\varphi$ and a voltage is **no longer possible** for the curl field or the electromagnetic field. The definition of a *vector potential* shall not be considered further here [2], [3].

If the spatial distribution of a static electric field $\boldsymbol{E}(\boldsymbol{x}) = \boldsymbol{E}(x,y,z)$ is known, the potential distribution $\varphi(x,y,z)$ can be determined from Eq. (2.1-7). Conversely, if the potential distribution is given (*scalar field)*, the *electric field strength* can be determined by forming the *gradient*, i.e. by differentiation

$$\boldsymbol{E} = -\,\mathrm{grad}\,\varphi. \qquad (2.1\text{-}8)$$

For Cartesian coordinates *x, y, z* we find

$$\begin{aligned}\boldsymbol{E}(x,y,z) &= \{E_x,\ E_y,\ E_z\} \qquad (2.1\text{-}8a)\\ &= -\,\mathrm{grad}\,\varphi\\ &= -\,\{\partial\varphi/\partial x,\ \partial\varphi/\partial y,\ \partial\varphi/\partial z\}.\end{aligned}$$

For *cylindrical coordinates r, α, z*, the field strength vector $\boldsymbol{E}$ can be described as

$$\begin{aligned}\boldsymbol{E}(r,\alpha,z) &= \{E_r,\ E_\alpha,\ E_z\} \qquad (2.1\text{-}8b)\\ &= -\,\mathrm{grad}\,\varphi\\ &= -\,\{\partial\varphi/\partial r,\ r^{-1}\cdot\partial\varphi/\partial\alpha,\ \partial\varphi/\partial z\}.\end{aligned}$$

For spherical coordinates *r, α, ϑ* we find

$$\begin{aligned}\boldsymbol{E}(r,\alpha,\vartheta) &= \{E_r,\ E_\alpha,\ E_\vartheta\} \qquad (2.1\text{-}8c)\\ &= -\,\mathrm{grad}\,\varphi\\ &= -\,\{\partial\varphi/\partial r,\ (r\cdot\sin\vartheta)^{-1}\cdot\partial\varphi/\partial\alpha,\\ &\qquad r^{-1}\cdot\partial\varphi/\partial\vartheta\}.\end{aligned}$$

By specifying a voltage (or a potential difference) the energy that is accumulated during *acceleration* of a charged particle *in the electric field* can be directly calculated. This is important for the description of ionization and discharge processes. The kinetic energy results from the difference of potential energies according to Eq. (2.1-5):

$$\begin{aligned}W_{kin} &= W_{pot2} - W_{pot1}\\ &= q\,(\varphi_2 - \varphi_1) \;=\; q\,\Delta\varphi_{21}\\ &= q\,V_{21}. \qquad (2.1\text{-}9)\end{aligned}$$

The electrostatic field is caused by charges on the electrode surfaces in accordance with Figure 2.1-1, i.e. the electrode configuration stores a distinct amount of charge at a given potential difference (voltage). The charge storage capacity is defined by the quotient of the charge and the voltage, which is called "**capacitance**" *C*:

$$C = q\,/\,V = q\,/\,\Delta\varphi \qquad (2.1\text{-}10)$$

In many cases a wide-ranging field configuration can be replaced by a lumped circuit element (i.e. by a capacitance *C*), Figure 2.1-5.

The use of lumped capacitances as equivalent circuits of distributed fields enables their inclusion in network calculations. This is especially important for the estimation of (parasitic) *stray capacitances* (*air capacitances*) in high voltage measuring circuits or in complex insulation systems.

Furthermore, the whole *capacitively stored energy W* in the field volume can be calculated as a function of the voltage by means of the capacitance *C*:

$$W = \tfrac{1}{2}\,C\,V^2 \qquad (2.1\text{-}11)$$

This relation can be understood from the example of a *parallel-plate capacitor* (see Figure 2.1-5 right). For a surface area *A*, an electrode distance *x* and a homogeneous electric field strength $E = V/x$, the capacitance is

$$\begin{aligned}C &= q\,/\,V\\ &= (D\cdot A)\,/\,(E\cdot x)\\ &= (\varepsilon_0\varepsilon_r E\cdot A)\,/\,(E\cdot x)\end{aligned}$$

$$C = \varepsilon_0 \varepsilon_r \cdot A / x.$$

I.e.

$$C = \varepsilon \cdot A / x \qquad (2.1\text{-}12)$$

The *stored energy W* is calculated, if the build-up of field strength *E* is described by the transport of infinitesimal amounts of charge d*q* against the field force d*F* = *E* d*q*. The energy d*W* = *x* d*F* = *x E* d*q* = *V* d*q,* which is necessary for that purpose, is stored in the electric field (as *potential energy* of the charge d*q*). The integration of all charges gives the total amount of energy:

$$W = \int dW = \int V(q)\, dq$$

$$= \int_0^q (q/C)\, dq$$

$$= \tfrac{1}{2}\, q^2/C$$

$$= \tfrac{1}{2}\, C\, V^2 \qquad \text{q.e.d.}$$

The *volume density of the energy w* in the homogeneous (uniform) field of the parallel-plate capacitor is derived by the division of energy *W* by the volume *v* = *A*·*x*. For the homogeneous field *w* is independent of the position:

$$w = W/v$$

$$= [\tfrac{1}{2}\, (E\, x)^2\, \varepsilon\, A/x] / (A\, x)$$

$$= \tfrac{1}{2}\, \varepsilon_0 \varepsilon_r\, E^2$$

Within an infinitesimal small volume element ΔV the field can be regarded as homogeneous for any field configuration. Therefore the **volume density of energy** is always given by

$$w = \partial W/\partial V$$

$$= \tfrac{1}{2}\, \varepsilon_0 \varepsilon_r\, E^2$$

$$= \tfrac{1}{2}\, E\, D. \qquad (2.1\text{-}13)$$

This means that the energy density increases quadratically with the field strength. Therefore, *E* has to be as high as possible in *energy storage capacitors*, and the maximum volume density of energy is essentially determined by the electrical breakdown strength of the dielectric material.

2.1.3 Maxwell's Equations

Classic problems of high voltage engineering are mostly limited to static, stationary and quasi-stationary electric fields, e.g. for DC, power frequency AC and impulse stresses.

Nevertheless, high electrical stresses can occur for all kinds of fields, as described in Chapter 1, and high voltage engineering has to deal not only with conventional DC, AC and impulse fields, but also with very rapidly changing fields.

Therefore, the **Maxwell's Equations** for *stationary* (not moving) *bodies* are the starting point of this description, from which the respective valid simplifications are deduced. For clarity, this description is limited to the *integral form* of the field equations, Figures 2.1-6 ff.

Maxwell's Equations are subdivided into three categories,

- the main **Field Equations** (the first and second circular law, i.e. Ampere's and Faraday's law resp.), which describe the relation between time-varying electric and magnetic field quantities (Figure 2.1-6),
- the **Continuity Equations**, which describe the sources or the lack of sources of the field quantities (i.e. the continuity of magnetic flux and current, Figure 2.1-7) and

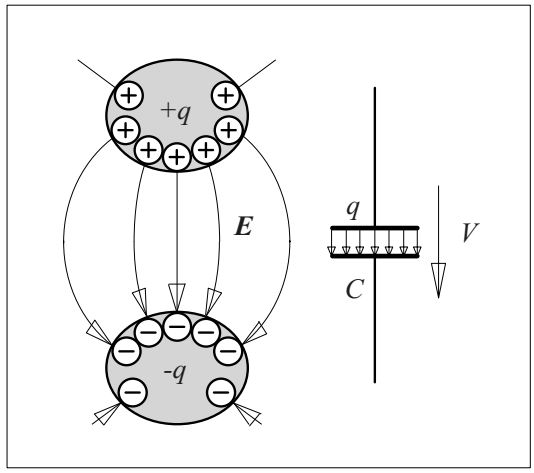

Figure 2.1-5: Allocation of an ideal capacitance to the electrostatic field between two electrodes.

- the **Material Equations** (constitutive relations), which describe the relation between field quantities under the influence of different material properties (Figure 2.1-8).

These equations can be evaluated analytically for defined special cases. For this purpose, it is necessary to find simplifications, which result from spatial symmetries (e.g. fields with plane, cylindrical or spherical symmetry) and particular time dependencies (e.g. static DC fields or harmonic fields with sinusoidal time dependence).

2.1.3.1 Maxwell's Main Field Equations

The *physical meaning* of the main field equations consists in the insight that a time-varying magnetic flux $\iint \boldsymbol{B}\,\mathrm{d}\boldsymbol{A}$ induces an electric curl field $\boldsymbol{E}$ (**law of induction, Faraday's law, second circular law**), Eq. (2.1-14). The induced voltage (electromotive force) is the integral of $\boldsymbol{E}$ around a closed loop. It is equivalent to the derivate of the magnetic flux (through the loop) with respect to time. Furthermore, a magnetic curl field $\boldsymbol{H}$ is caused by an electric current, i.e. by a "flux of a current density" (**law of the magnetomotive force, Ampere's law, first circular law**), Eq. (2.1-15). The current or the magnetomotive force is calculated both from the conduction current density $\boldsymbol{J}$ (moving charge carriers) and/or from the displacement current density $\partial\boldsymbol{D}/\partial t$ (time-varying electric field).

Finally, Maxwell's Main Field Equations describe the generation of an electric (or magnetic) curl field from a time-varying magnetic (or electric). field This mutual interdependence is the reason for the propagation of electromagnetic waves, which occur, for example, as line-bound waves on transmission lines or measuring cables in high voltage engineering.

2.1.3.2 Maxwell's Continuity Equations

The *physical content* of the Continuity Equations consists of a statement about the continuity and the sources of magnetic and electric fields, Figure 2.1-7.

Magnetic fields are solenoidal, i.e. free of sources. If a closed surface area A is considered, there are no sources or sinks of magnetic field lines within the enclosed volume, i.e. the magnetic flux $\iint \boldsymbol{B}\,\mathrm{d}\boldsymbol{A}$, which enters the volume on one side, must leave it on the other side, Figure 2.1-7 (left). A mathematical description of the solenoidal character of the magnetic field is given, if the closed surface integral $\oiint \boldsymbol{B}\,\mathrm{d}\boldsymbol{A}$ is set equal to zero, because of the compensation of incoming and outgoing magnetic fluxes, Eq. (2.1-16).

The continuity equation for the **field of the displacement density** Eq. (2.1-17a) states that the displacement density field $\boldsymbol{D}$ is free of sources, if there are no charges within an closed surface A ($Q = 0$). These charges would act as sources and drains of the field and the closed-surface integral would give a magnitude different from zero. Calculating the dielectric displacement flux $\iint \boldsymbol{D}\,\mathrm{d}\boldsymbol{A}$ over a closed surface A, the encolosed charge Q must be introduced a term which is different from zero.

Additionally, the **electric current density** is free of sources, if the sum of conduction current density $\boldsymbol{J}$ and displacement current density $\partial\boldsymbol{D}/\partial t$ is considered, Eq. (2.1-17b). This equation can directly derived from Eq. (2.1-15).

Note: A relation between Eq. (2.1-17b) and (2.1-17a) can be established in the following way: A time-varying conduction current $i(t) = \iint \boldsymbol{J}\,\mathrm{d}\boldsymbol{A}$, which is flowing via a conductor towards an electrode, will be continued as a displacement current $\iint \partial\boldsymbol{D}/\partial t\,\mathrm{d}\boldsymbol{A}$ within the non-conductive dielectric material adjacent to the electrode, Figure 2.1-7 (right). The conduction current is associated with a displacement and an accumulation of charge carriers close to the surface of the electrode, i.e. at the interface between conductive and insulating materials.

The integration of Eq. (2.1-17b) over time provides a relation between the displacement density $\boldsymbol{D}$ and the charge, which is enclosed by the closed surface A if it is assumed that there is no charge on the electrode at the beginning of the integration process:

$$\oiint_A \left(\boldsymbol{J} + \frac{\partial \boldsymbol{D}}{\partial t} \right) \mathrm{d}\boldsymbol{A} \quad = \quad 0$$

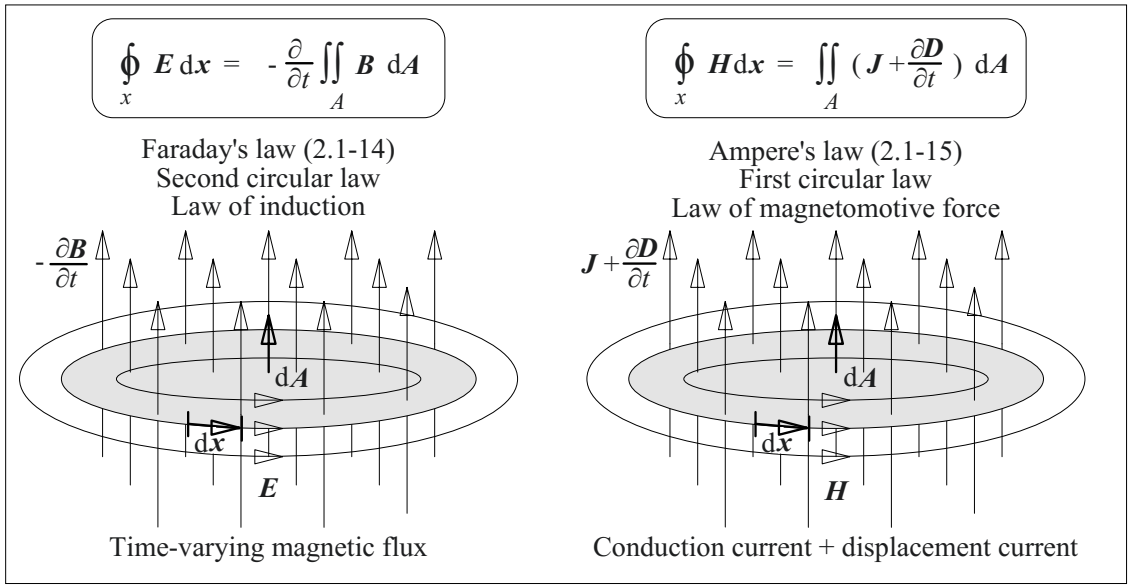

Figure 2.1-6: Integral form of Maxwell's main field equations for stationary (not moving) bodies. Coupling of electric and magnetic field quantities by means of Faraday's law of induction (left) and by Ampere's law of magnetomotive force (right).

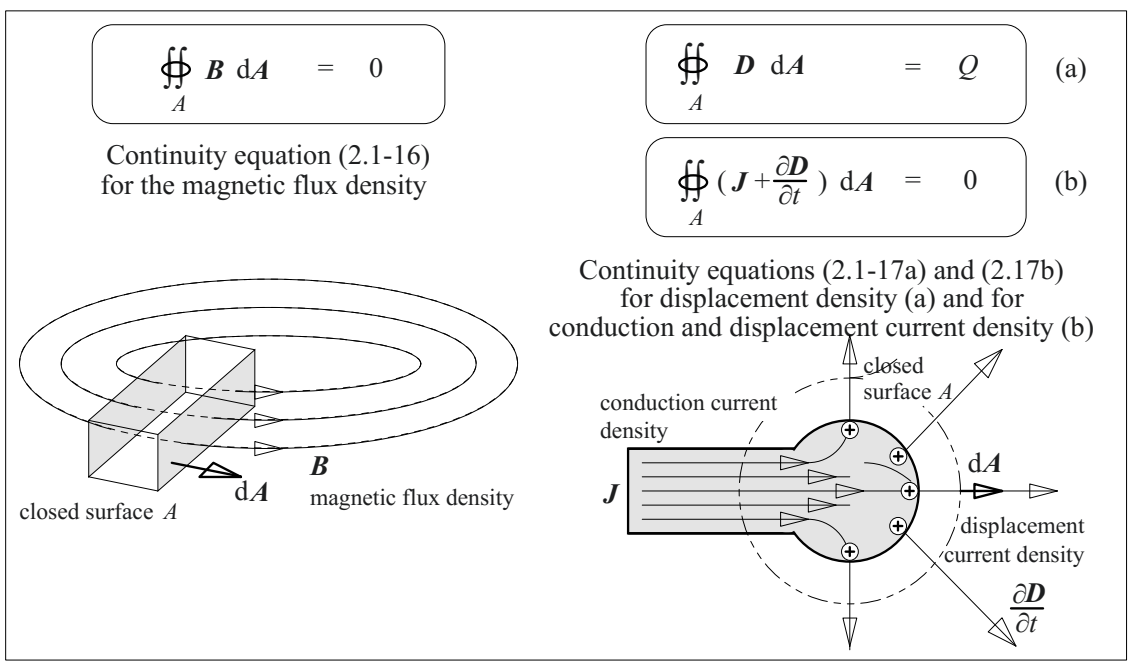

Figure 2.1-7: Integral form of Maxwell's continuity equations for the magnetic flux density (left, spatial view of a closed surface area A) and for conduction and displacement current density (right, sectional view).

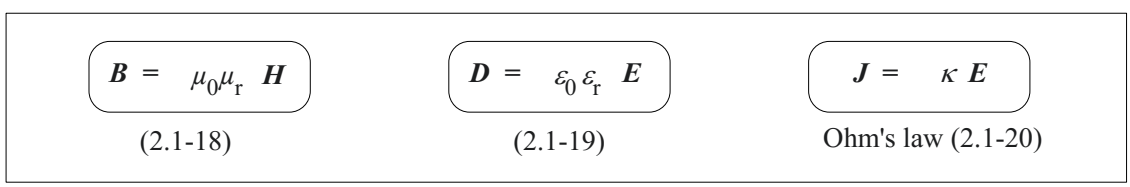

Figure 2.1-8: Material equations (constitutive relations) for the magnetic and electric field quantities.

$$\oint\!\!\oint_A \frac{\partial \boldsymbol{D}}{\partial t}\,\mathrm{d}\boldsymbol{A} = -\oint\!\!\oint_A \boldsymbol{J}\,\mathrm{d}\boldsymbol{A} = i(t)$$

The integration over the time gives Eq. (2.1-17a):

$$\oint\!\!\oint_A \boldsymbol{D}\,\mathrm{d}\boldsymbol{A} = \int i(t)\,\mathrm{d}t = Q\,.$$

Nevertheless, it must be noted that this derivation required additional assumptions. Therefore the two equations are not equivalent.

Eq. (2.1-17a) plays an important role for field calculation purposes:

$$\oint\!\!\oint_A \boldsymbol{D}\,\mathrm{d}\boldsymbol{A} = Q \qquad (2.1\text{-}21)$$

The charge can also be seen as the integral of the space charge density η over the volume V, which is enclosed by the closed surface area A:

$$\oint\!\!\oint_A \boldsymbol{D}\,\mathrm{d}\boldsymbol{A} = \iiint_V \eta\,\mathrm{d}V \qquad (2.1\text{-}22)$$

Eq. (2.1-21) or (2.1-22) is called **"Gauss's law"**. It states that the integral of the flux density $\boldsymbol{D}$ over any closed surface equals the charge enclosed [481]. It allows the analytical calculation of electrostatic fields in some important cases, Figure 2.1-9.

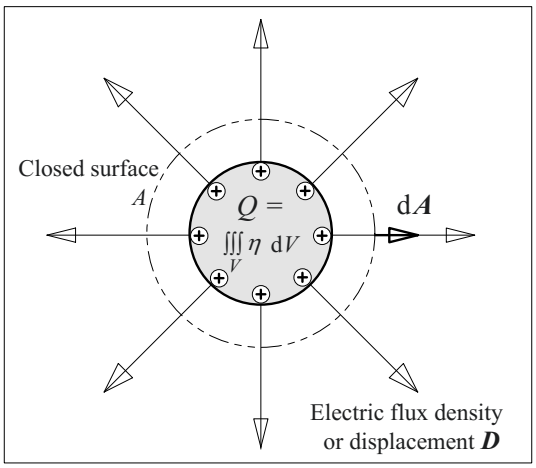

Figure 2.1-9: Charges as sources of the electric flux desity (displacement D), i.e. as reason of the static electric field ("Gauss's law").

2.1.3.3 Material Equations

The material equations describe the interaction of electric and magnetic fields with materials, Figure 2.1-8. They constitute the relations between $\boldsymbol{E}$ and $\boldsymbol{D}$, $\boldsymbol{B}$ and $\boldsymbol{H}$, and $\boldsymbol{E}$ and $\boldsymbol{J}$, therefore they are also called **constitutive relations**.

A magnetic field $\boldsymbol{B}$ can cause an orientation of magnetic dipoles ("elementary magnets") within a material. This effect of *magnetic polarization* causes an additional field, which enhances or reduces the resulting field strength. Eq. (2.1-18) accounts for the magnetic polarization by the factor μ_r (relative permeability).

An electric field $\boldsymbol{E}$ can cause a displacement of charges or an orientation of electric dipoles within a material. This effect of this *electric polarization* causes an additional field, see Section 4.2. If the amount of charge on the electrodes is constant, the resulting electric field strength is reduced. If the field strength is imposed by an impressed voltage or field strength, additional charges are accumulated on the electrodes by the polarization effect. Eq. (2.1-19) accounts for the increase in electric displacement density (proportional to the charge) via the dielectric polarization by the factor ε_r (relative permittivity). ε_r is always greater than 1, because each type of matter can be polarized to a greater or lesser extent, e.g. by displacement of lattice atoms, by orientation of polar molecules or molecule groups, or by displacement of atomic nuclei relative to their electron shells.

Electric polarization is of high importance for high voltage engineering, since it determines *relative permittivities* and *capacitances*. Additionally there are *polarization losses* (*dissipation losses*) depending on temperature and frequency.

Eq. (2.1-19) is the basis of all high voltage field calculations for insulating systems which consist of more than one insulating material

and which are stressed with *time-varying electric fields*.

Moreover, an electric field $\boldsymbol{E}$ can accelerate free and mobile charge carriers within a material. Because of collision processes there is a mean drift velocity of the charge carriers in the direction of the electric field, described by a current density $\boldsymbol{J}$ proportional to the electric field strength $\boldsymbol{E}$. Eq. (2.1-20) correlates the electric current density with the electric field strength by the factor κ (electric conductivity); it is equivalent to Ohm's law.

Eq. (2.1-20) is the basis of all high voltage field calculations for insulating systems, which are stressed with *direct voltage (DC voltage)*.

2.1.4 Classification of Fields

Depending on the gradient of field changes $\partial../\partial t$ (i.e. the time rate of change), Maxwell's Equations can be simplified. Three categories have proved to be useful [394]:

1. **Static and stationary (steady-state) fields** (Section 2.1.4.1): For **static fields** there are no changes of the field quantities $\boldsymbol{E}$, $\boldsymbol{H}$ and $\boldsymbol{J}$, i.e. the derivatives with respect to time are zero, $\partial../\partial t = 0$.

Concerning the time rate of change, field quantities are time-invariant, constant or **"static"**, i.e. they do not change in time. There is absolutely no coupling of magnetic and electric field quantities by Faraday's law of induction (2.1-14) or by Ampere's law (2.1-15) regarding the displacement current density $\partial\boldsymbol{D}/\partial t$. Consequently there is no propagation of electromagnetic waves. *Concerning the propagation of waves*, static fields are **"stationary"**, i.e. they are fixed to a location and do not propagate.

Note: Traditionally the time-invariant $\boldsymbol{E}$- and $\boldsymbol{H}$-fields are referred to as **electrostatic** and **magnetostatic fields**. The time-invariant electrical conduction field $\boldsymbol{J}$ is mostly referred to as a **steady-state (stationary) conduction field**. This is motivated by the conduction current, which is related to energy transport, the *power* as derivate of the energy with respect to time is therefore not equal to zero [395]. The field of the conduction current density $\boldsymbol{J}$ is caused by the *motion* of charges, and it is no longer *static* in terms of being *immobile*. Furthermore, there is coupling of $\boldsymbol{J}$ with the magnetic field $\boldsymbol{H}$ as described in Ampere's law of electromotive force (2.1-15).

Nevertheless, *concerning the field quantities*, all three kinds of fields ($\boldsymbol{E}$, $\boldsymbol{H}$ and $\boldsymbol{J}$) are both time-invariant (*static*) and fixed to a location (*stationary*) [394]. Usually the terms "**static fields**" and "**steady-state conditions**" are used.

2. **Quasi-static (quasi-stationary) fields** (Section 2.1.4.2 and 2.1.4.3): For **quasi-static** (quasi-stationary) fields there are (slowly) time-varying field quantities, but their coupling is so weak that the *electric curl field induced by the magnetic field of the displacement current* and the **wave character** of the fields can be **neglected**.

Note: If this is interpreted in the **time domain**, it means that the *wave propagation time* τ within a field volume with the dimension x has to be small in comparison with the rise time T_r of the time-varying field, see Eq. (2.1-36ff): $\tau << T_r$. In a *limited volume* with dimension x the change of field strength with time has almost no influence on field distribution; the field can therefore be regarded as "**quasi-static**" (similar to the static field distribution).

In the **frequency domain** the *dimension* x of the field volume must be small in comparison with a *quarter-wavelength* $\lambda/4$, see Eq. (2.1-36) and (-37): $x << \lambda/4$. In a *limited volume* with dimension x the change of field strength with time does not result in remarkable wave propagation effects, field changes can be regarded as quasi-simultaneous and the field can therefore be regarded as "**quasi-stationary**" (approx. fixed to the location).

Typically, quasi-static (quasi-stationary) fields are **slowly changing fields** (or low frequency fields) (Section 2.1.4.2 and 3)

- either *in conductors*, where the displacement current is negligible in comparison with a conduction current (*inductive field*),
- or *in insulating materials*, where the induced curl field is negligible in comparison with an electrostatic field (*capacitive field*).

Additionally, there are fast **changing quasi-stationary fields in conductors**, if $x << \lambda/4$. As long as the displacement current is negligible, the electromagnetic wave propagation orthogonal to the conductor surface is negligible because of extreme damping. Nevertheless, these fields are characterized by the superposition of the impressed electric conduction field and an induced electric curl field. This results in *eddy currents* that are superimposed to the impressed conduction current. Thereby they cause *current displacement* (*skin effect*, *Heaviside effect*).

3. **Non-stationary fields** (Electromagnetic Waves, Section 2.1.4.4): Generally, for rapidly varying fields the mutual coupling of electric and magnetic fields must not be neglected, because of a high *rate of change* and/or the *dimensions* of the field volume. Then the characteristics of **electromagnetic wave propagation**, the spatial dimensions and propagation time effects must be considered.

2.1.4.1 Static and Stationary Fields

a) Electrostatic and magnetostatic fields

For static fields the right side of Eq. (2.1-14) and (2.1-15) is equal to zero, since there is neither a time-varying magnetic flux nor a displacement current, nor a conduction current. Thus, there is no coupling between electric and magnetic field quantities.

Strictly speaking, static fields only exist as *magnetic* fields of permanent magnets. Static *electric* fields are a *theoretical fiction*, assuming that immobile charges are sources of a static electric field without causing conduction current, charge transport or energy transport. This would only be possible for a *perfect* dielectric ($\kappa = 0$) that does not exist in reality.

Nevertheless, a **static electric field** is often assumed in order to approximate the field and to *simplify field calculations*: A static field is only dependent on the permittivities of dielectric materials. It should be noted that the calculation results are not valid for static electric fields and stationary conduction fields, for which the conductivities would be significant, but only for quasi-static (quasi-stationary) cases, Section 2.1.4.3.

b) Stationary (steady-state) conduction fields

Conduction currents are accompanied by energy transport and by a stationary (steady-state) power flow different from zero, Eq. 2.1-24. In comparison with electrostatic and magnetostatic fields, **steady-state conduction fields** are characterized by a time-invariant conduction current density $\boldsymbol{J}$ and a proportional time-invariant electric field strength $\boldsymbol{E}$, Figure 2.1-10.

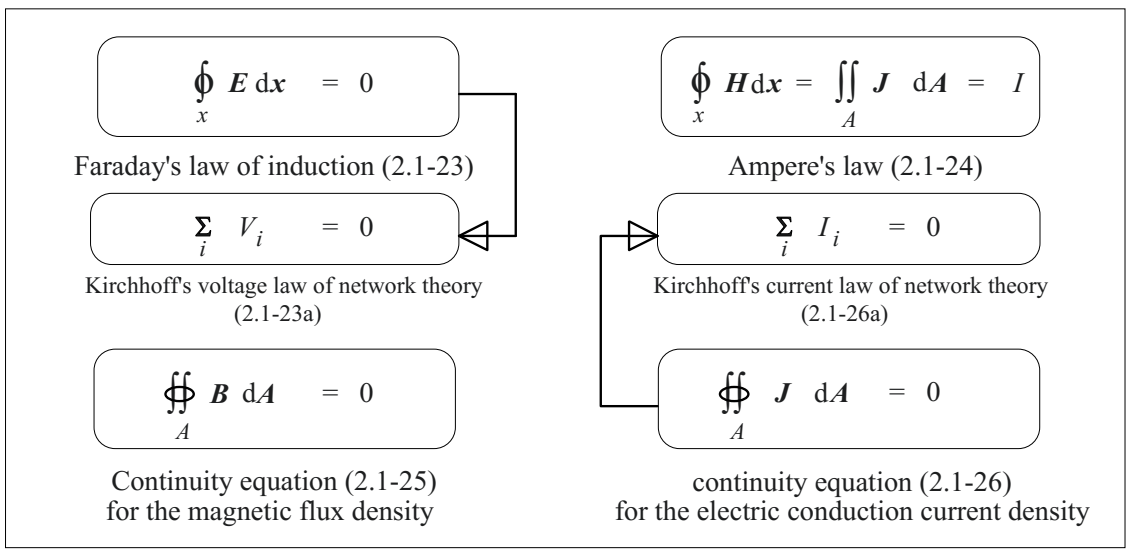

Figure 2.1-10: Simplification of Maxwell's equations for stationary fields (all derivates of field quantities with respect to time are equal to zero).

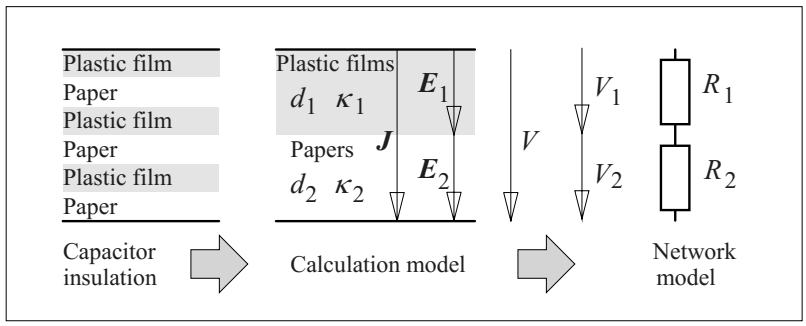

Figure 2.1-11:

Stationary (steady-state) conduction field in a capacitor insulation stressed with constant DC voltage.

According to Eq. (2.1-23) the ring integral of $\boldsymbol{E}$ dx around a closed loop and the sum of the voltages V_i in a closed loop are zero, therefore it is an irrotational field. This means that the calculation of voltages and potential differences between two points with Eq. (2.1-7) is independent of the integration path, Figure 2.1-4. Therefore, it is a so called "*potential field*" with unequivocally defined voltages and potential differences.

The electric field under electrical stress with constant **direct voltage** (DC voltage) is always a *stationary (steady-state) conduction field*. The field distribution does not change with time, but owing to the (residual) *conductivity* κ according to Eq. (2.1-20) there is a conduction current $\boldsymbol{J} = \kappa \cdot \boldsymbol{E}$, which determines the field distribution. The *permittivities* and Eq. (2.1-19) do *not* have *any significance* for the formation of a steady conduction field.

Example: Capacitor dielectric

A constant DC voltage (U = 3 kV) is applied to the dielectric of a capacitor for a very long time. The insulation is arranged in layers of polymeric films (d_1 = 30 µm, $\kappa_1 = 10^{-16}$ S/m) and oil-impregnated paper (d_2 = 30 µm, $\kappa_2 = 10^{-14}$ S/m). The field stress, i.e. the field strength, shall be calculated for the materials, Figure 2.1-11.

In a calculation model, two equivalent layers replace all films and papers. The total voltage is calculated with Eq. (2.1-7) from the sum of the two partial voltages on the polymeric films and the impregnated papers:

$$V = d_1 E_1 + d_2 E_2.$$

Furthermore, the current density is equal in both materials according to the Continuity Equation (2.1-26):

$$J = \kappa_1 E_1 = \kappa_2 E_2$$

Field strengths are calculated as

$$E_1 = V/(d_1 + d_2 \cdot \kappa_1/\kappa_2) = 99 \text{ kV/mm}$$

and

$$E_2 = E_1 \cdot \kappa_1/\kappa_2 = 1 \text{ kV/mm}.$$

Result: E_1 = 99 kV/mm (polymeric films)

E_2 = 1 kV/mm (papers)

In spite of the same thickness, the papers are stressed with $V_2 = E_2 \cdot d_2$ = 0.03 kV only, i.e. with approx. 1 % of the total voltage. Because of their low conductivity (their high specific resistance $\rho = 1/\kappa$) the polymeric films are stressed with 99 % of the total voltage.

Note: Paper layers in capacitor dielectrics are used in order to impregnate the gaps between the films with insulating oil, i.e. the paper acts as wick for the impregnation. The insulation strength must be guaranteed by the polymeric films, which normally have a significantly higher breakdown strength than oil-impregnated paper.

2.1.4.2 Quasi-stationary (Inductive) Fields in Conductors

In materials with **high conductivities** (*conductors*), it is possible to neglect displacement current density $\partial \boldsymbol{D}/\partial t$ in comparison to conduction current density $\boldsymbol{J}$ up to the GHz range. Therefore, the field can be regarded as **quasi-stationary** and the electromagnetic wave character is negligible, Eq. (2.1-29) and (-31), Figure 2.1-12. The condition is

$$\partial \mathrm{D}/\partial t = \varepsilon_0 \varepsilon_\mathrm{r} \, \partial \mathrm{E}/\partial t \ll J = \kappa \cdot E \,. \quad (2.1\text{-}27)$$

The *spatial and temporal limits* for the quasi-stationary regime, which are defined in Eq. (2.1-36) and (-37), are also valid here.

$$\oint_x \boldsymbol{E}\,\mathrm{d}\boldsymbol{x} = -\frac{\partial}{\partial t}\iint_A \boldsymbol{B}\,\mathrm{d}\boldsymbol{A}$$

Faraday's law of induction (2.1-28)

$$\oint_x \boldsymbol{H}\,\mathrm{d}\boldsymbol{x} \cong \iint_A \boldsymbol{J}\,\mathrm{d}\boldsymbol{A} = I$$

Ampere's law (2.1-29)

$$\oiint_A \boldsymbol{B}\,\mathrm{d}\boldsymbol{A} = 0$$

Continuity equation (2.1-30) for the magnetic flux density

$$\oiint_A \boldsymbol{J}\,\mathrm{d}\boldsymbol{A} \cong 0$$

Continuity equation (2.1-31) for the conduction current density

Figure 2.1-12: Maxwell's equations for quasi-stationary inductive fields in conductors (Displacement current density in conductors is neglected).

Owing to the high electric conductivity κ, even low electric field strengths $\boldsymbol{E}$ cause high current densities $\boldsymbol{J}$. Therefore, even low induced field strengths according to Eq. (2.1-28) must be considered. This means that there is a coupling between the electric conduction current field and the magnetic field by Faraday's law of induction.

The electric field is no longer irrotational, i.e. an unequivocal *definition of scalar potentials or voltage differences* according to Eq. (2.1-7) is *not possible*, the line integral $\int \boldsymbol{E}\cdot\mathrm{d}\boldsymbol{x}$ would depend on the integration path.

Example: Eddy currents and current displacement

The effect of "current displacement" and "eddy currents" in conductors can be explained by the electric curl field $\boldsymbol{E}(t)$, which is induced by the time-varying magnetic field, causing time-varying current density $\boldsymbol{J}(t)$. The induced field $\boldsymbol{E}(t)$ causes an eddy current density $\boldsymbol{J}_e(t) = \kappa\cdot\boldsymbol{E}(t)$, which enhances the current density at the conductor's surface and reduces it within the conductor (current displacement, skin effect).

Even for AC at power frequency 50 or 60 Hz, current displacement causes an increase in resistance in the range of a few percent for common conductor materials. In the magnetic cores of electrical machines and transformers, there are so-called eddy current losses, which are reduced by thin, mutually insulated core laminations. Since these subjects are not directly related to high voltage engineering, we refer you to more information given in the literature [2].

Even for very **fast changing currents in conductors**, the fields are **quasi-stationary** in the direction orthogonal to the conductor's surface. The displacement current can be neglected in comparison with the conduction current and there is almost no or an extremely strongly damped and spatially limited electromagnetic wave propagation orthogonal to the conductor's surface.

The quasi-stationary inductive field is important for high voltage engineering only in *materials with high conductivities*, e.g. in conducting electrodes, conducting connection lines and transformer windings. In *dielectric materials with low conductivities*, the displacement current density must normally not be neglected in comparison with the very small conduction current density, even at slowly changing fields, Section 2.1.4.3.

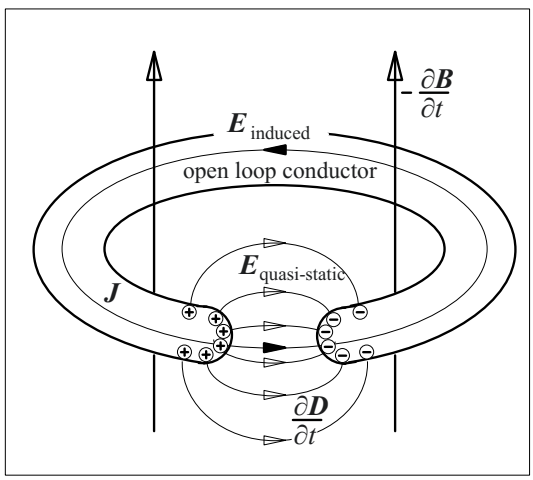

Figure 2.1-13: Quasi-stationary fields within and outside the conductor material (inductive and capacitive fields).

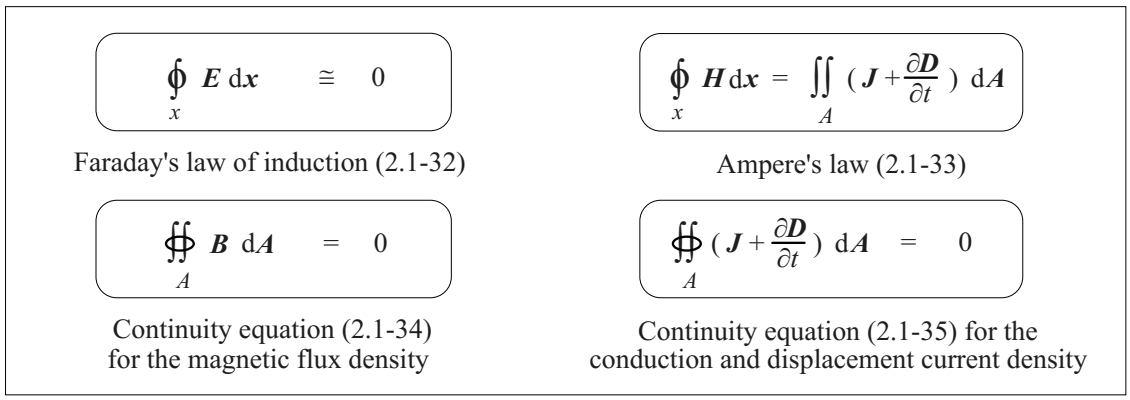

Figure 2.1-14: Maxwell's equations for quasi-stationary/ quasi-static (capacitive) displacement fields in insulating materials (Induction of electric curl fields by magnetic fields is neglected).

Example: Transformer winding

The fields in a transformer winding are determined by the time-varying magnetic field, which induces an electric curl field *within the conductor*. Thereby charges are displaced to the conductor's surface, Figure 2.1-13. The conduction current is much greater than the displacement current, therefore it is a **quasi-stationary inductive field**.

On the *outside of the conductor*, the conduction current is continued in the dielectric (mainly) as a displacement current. The surface charges cause a quasi-static electric field. *Within the dielectric*, the source field is much stronger than the (induced) curl field, which is normally negligible. Then it is a **quasi-static** (quasi-stationary) **capacitive field**.

2.1.4.3 Quasi-stationary/ Quasi-static (Capacitive) Displacement Fields in Dielectrics

High voltage engineering predominantly considers electric fields in *dielectrics*, i.e. in *insulating materials* (so-called "non-conductors") with a comparatively low (residual) conductivity κ. Eq. (2.1-27) is not fulfilled and displacement currents normally exceed small conduction currents, even at low frequencies. In Ampere's law (2.1-33) and in the Continuity Equation (2.1-35) both current components must be considered, Figure 2.1-14.

The electric field is a source field and exceeds the induced electric field strength if the rate of change of the magnetic field remains low, e.g. see Figure 2.1-13. Then *potential and voltage differences* can *approximately* be defined according to Eq. (2.1-7) because the induced curl field is neglected relative to the source field, see Eq. (2.1-32). This means that the electromagnetic wave character is neglected and the field is both a **quasi-stationary** and a **quasi-static** field. Sometimes it is referred to (imprecisely) as a **"static electric field"** or an **"electrostatic field"** only.

Power frequency (AC) voltage, **switching impulse (SI)** voltage and **lightning impulse (LI)** voltage are the most important voltage stresses of high voltage insulating materials. In most cases, they can be described as quasi-static (quasi-stationary) capacitive fields.

Within a field volume under consideration, a quasi-static (quasi-stationary) description is allowed, if all changes of the fields are *nearly synchronous*, i.e. without any significant delay. This means that traveling wave processes, which have to be considered for fast changing fields, can be neglected. Thereby **limits for the validity of the quasi-static description** are defined **in space and time** as follows:

The *propagation time* $\tau = x/u$ of an electromagnetic wave through the volume under consideration (length x, traveling wave velocity u) must be *negligibly small* in comparison with the time over which the field changes.

This means for *sinusoidally* changing fields with the period T and the frequency f:

$$\tau = x/u \quad << T/4 = (4f)^{-1} \qquad (2.1\text{-}36a)$$

and with the wavelength $\lambda = T \cdot u$

$$x \quad << \lambda/4. \qquad (2.1\text{-}36b)$$

For a *transient* process with a rise time T_r we find accordingly

$$\tau = x/u \quad << T_r \qquad (2.1\text{-}37)$$

With a limit of 0.5 % for the voltage error, the length x of long lines should be

$$x \quad < \lambda/60\,. \qquad (2.1\text{-}38)$$

For overhead lines with air insulation, which shall be regarded as quasi-static (quasi-stationary), at $f = 50$ Hz (60 Hz) x must remain < 100 km (< 80 km). For cables with a reduced traveling wave velocity, this limit is further reduced. For a lightning impulse voltage with $T_r \cong 1$ µs, the length in air is only $x < 22$ m, if the rise with T_r is approximated by a quarter-period of an AC voltage with $T = 4$ µs.

In the common insulating materials displacement currents normally exceed conduction currents for impulse and AC voltages:

$$\partial D/\partial t = \varepsilon_0 \varepsilon_r \, \partial E/\partial t >> J = \kappa \cdot E \qquad (2.1\text{-}39)$$

This is the case of the quasi-static (quasi-stationary) "dielectric **displacement field**", which is often called "electrostatic field". Field distributions are determined by the relative permittivities ε_r of the different materials, Figure 2.1-15 (top). Simple geometries can be described by a network model with capacitances.

In case of predominant conduction current, the field is a (quasi-stationary) electrical **conduction field**. Field distributions are determined by the conductivities κ, Figure 2.1-15 (bottom). Simple geometries can be described by a network model with resistances.

Example: Capacitor dielectric (continued)

A power frequency AC voltage ($f = 50$ Hz, root-mean-square/ r.m.s. voltage $V = 3$ kV) is applied to a capacitor insulation according to Figure 2.1-11 ($d_1 = d_2 = 30$ µm, $\varepsilon_{r1} = 2.2$, $\varepsilon_{r2} = 4.4$). The electric field strength in the different materials shall be determined, Figure 2.1-15.

The total voltage is calculated from the sum of the two partial voltages on the polymeric films and the impregnated papers according to Eq. (2.1-7):

$$v(t) = d_1 E_1(t) + d_2 E_2(t)$$

From this, the r.m.s. values for V and D follow:

$$V = d_1 E_1 + d_2 E_2.$$

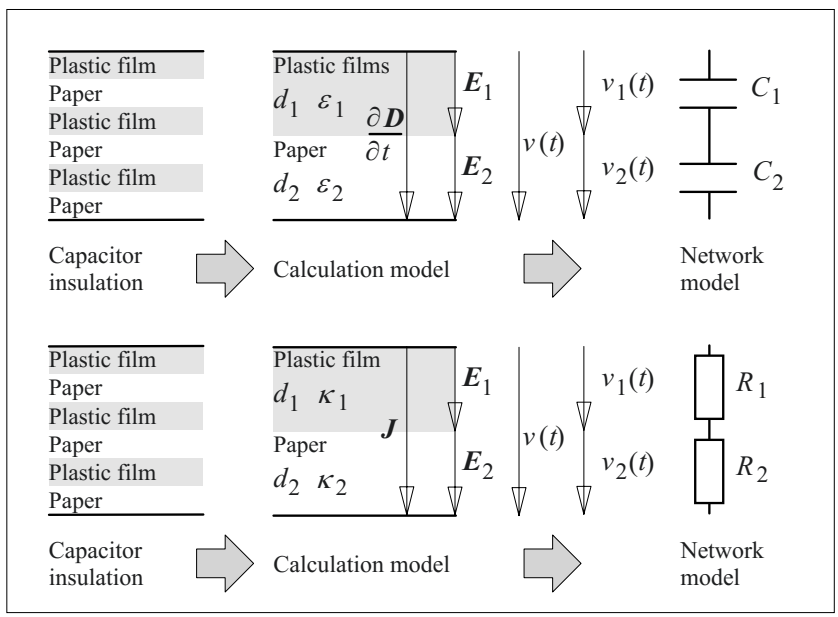

Figure 2.1-15:

Quasi-static (quasi-stationary) fields in a capacitor insulation stressed with a time-varying voltage v(t).

Top: Displacement current dominates (dielectric displacement field, often denominated as "electrostatic field" or "capacitive field").

$\partial D/\partial t >> J$

Bottom: Conduction current dominates (Electrical conduction field).

$J >> \partial D/\partial t$

Moreover, the displacement current density according to Eq. (2.1-35) is equal in both materials:

$$\partial D/\partial t = \varepsilon_1 \cdot \partial E_1/\partial t = \varepsilon_2 \cdot \partial E_2/\partial t$$

The conduction current density J is neglected. The time integral gives the r.m.s. values

$$D = \varepsilon_1 \cdot E_1 = \varepsilon_2 \cdot E_2.$$

From this, field strengths are calculated from the equation for the r.m.s voltage V,

$$E_1 = V/(d_1 + d_2 \cdot \varepsilon_1/\varepsilon_2) \quad = 67 \text{ kV/mm}$$

and

$$E_2 = E_1 \cdot \varepsilon_1/\varepsilon_2 \quad = 33 \text{ kV/mm}.$$

Note: Obviously the plastic dielectric with the lower permittivity $\varepsilon_{r1} = 2.2$ is stressed with $E_1 = 67$ kV/mm, i.e. twice as strongly as the oil-impregnated papers, the field is displaced into the material with the lower permittivity. This effect of **"field displacement"** is of high importance for high voltage engineering: In the given case, the material with the lower breakdown strength (the paper) is fortunately stressed with the lower field strength. However, very often there are cases where the electric field is "displaced" into the dielectric with the lower strength (e.g. in air bubbles with $\varepsilon_r = 1$).

The question, whether a slowly changing field must be regarded as an electrostatic field or as an electrical conduction field, can be answered by considering the **transition process** between the initial displacement field and the stationary conduction field, Figure 2.1-16 gives an example. If the time, which is relevant for field variations, is significantly shorter than a time constant τ describing the transient behavior of the insulation system, an **electrostatic field** (dielectric **displacement field**) can be assumed:

$$\begin{aligned} &\text{AC quarter-period} \quad T/4 \ll \tau \\ &\text{or rise time} \quad T_r \ll \tau \end{aligned} \qquad (2.1\text{-}40)$$

Fields, which vary very slowly in comparison with the transition time constant τ of the dielectric system, can be regarded as **electrical conduction fields**, which are determined by conductivities:

$$\begin{aligned} &\text{AC quarter-period} \quad T/4 \gg \tau \\ &\text{or rise time} \quad T_r \gg \tau \end{aligned} \qquad (2.1\text{-}41)$$

Example: Capacitor dielectric (continued)

Following the application of a DC voltage, the system needs several hours to approach a steady-state condition, i.e. to charge the capacitance C_1 of the highly resistive polymeric films via the insulating resistance R_2 of the comparatively conductive oil-impregnated papers.

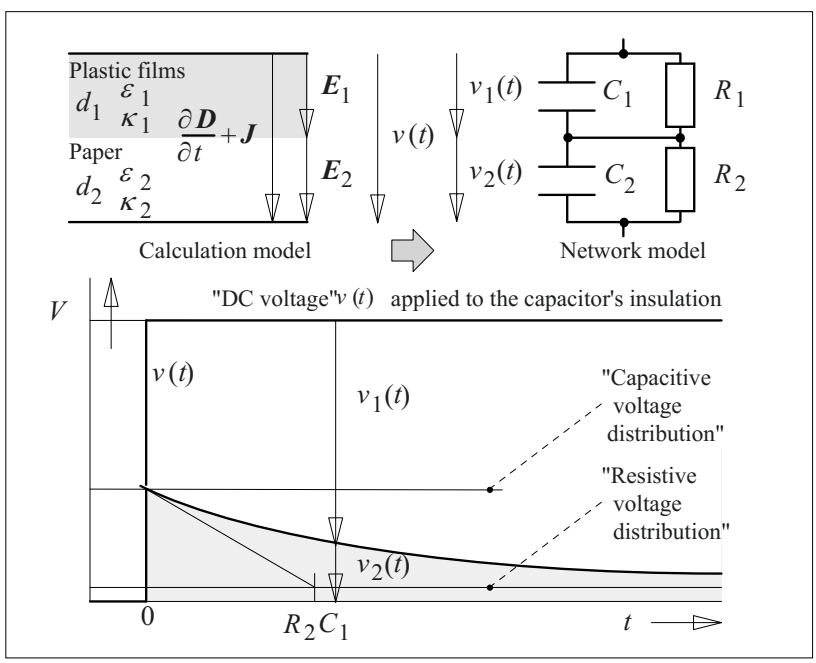

Figure 2.1-16:

Transition from the displacement field (electrostatic field, quasi-static field) with a "capacitive voltage distribution" to a stationary (steady-state) conduction field with a "resistive voltage distribution" during the application of a so-called "DC voltage" v(t).

The relevant time-constant is approximately $R_2C_1 \cong 0.5$ h, Figure 2.1-16. This time-constant is significantly longer than $T/4 = 5$ ms for an AC voltage at $f = 50$ Hz. Therefore, the assumption of an electrostatic field (dielectric displacement field) in the above-mentioned example was justified. Immediately after the application of the DC voltage, a "*capacitive voltage distribution*" is caused, according to the electrostatic field (displacement field). It marks the beginning of a **transition process**, approaching a "*resistive voltage distribution*", according to the electrical conduction field.

Example: Self-discharging of a Dielectric

The self-discharging of a capacitor or a homogeneous dielectric is also an exponential transition process. The time-constant $\tau_d = R \cdot C = \varepsilon/\kappa$ results from a calculation in a network model, which describes the exponential discharging of a capacitance C via the parallel insulating resistance R. The geometric quantities cancel each other out, so that the time constant is $\tau_d = \varepsilon/\kappa$.

If field theory is considered, the result is the same: In a self-discharging dielectric material the conduction current $J \cdot dA$ is fed from the change of the electric field, i.e. the "electric circuit" is closed by the anti-parallel displacement current $-\partial D/\partial t \cdot dA$, which is equal in magnitude. By means of the constitutive (material) Equations (2.1-19) and (-20) a differential equation for the decrease of the electric field strength $E(t)$ is derived:

$$\kappa \cdot E(t) = -\varepsilon \cdot \partial E/\partial t$$

The solution is an exponentially decreasing field strength with the time constant $\tau_d = \varepsilon/\kappa$, see Eq. (2.4-3).

In the previously discussed example of a capacitor dielectric, the time constants for the self-discharging of the polymeric films are $\tau_{d1} = \varepsilon_1/\kappa_1 = \varepsilon_0\varepsilon_{r1}/\kappa_1 \cong 50$ h and for the oil-impregnated papers $\tau_{d2} = \varepsilon_2/\kappa_2 = \varepsilon_0\varepsilon_{r2}/\kappa_2 \cong 1$ h.

Transition processes in complex insulation systems have to be determined by network analysis. Especially for **DC** and **polarity reversal (PR) stresses** it is necessary to base the analysis on the actually given field distribution (e.g. on a given steady-state conduction field). According to the field changes (application or polarity reversal of a "direct voltage") a displacement field (electrostatic, quasi-static or AC field resp.) must be superimposed. During a more or less complex *transition* process, a new steady-state condition in the form of a (stationary) conduction field is approached. Thereby it is possible that the insulating system is stressed for a short time completely differently from as one would assume from a pure AC or DC voltage distribution at the beginning and at the end of the transition [7].

2.1.4.4 Non-stationary, Time-varying Fields (Electromagnetic Waves)

Fast changing fields, which no longer fulfill the conditions for a quasi-static (quasi-stationary) description (eq. (2.1-36 to (-38)), have to be described by *Maxwell's Equations* (2.1-14) to (-17) in their universal form. Therefore, the mutual coupling between electric and magnetic field quantities must especially be considered. This results in **electromagnetic waves** with finite phase velocity u.

Maxwell's Main Field Equations (2.1-14) and (-15), i.e. Faraday's and Ampere's law, transferred into their differential form, can be differentiated with respect to time and can be mutually inserted into each other. The results are two independent partial differential equations for the electric and magnetic field quantities $\boldsymbol{E}(\boldsymbol{x},t)$ and $\boldsymbol{H}(\boldsymbol{x},t)$. It can be shown that the solution approaches

$$f(z - ut) \quad \text{and} \quad g(z + ut)$$

both satisfy the differential equations. They can be interpreted as wave processes that are propagating in the $+z$- and $-z$-directions. Boundary conditions and material properties determine the particular distribution of the electromagnetic wave-fields $\boldsymbol{E}(\boldsymbol{x},t)$ and $\boldsymbol{H}(\boldsymbol{x},t)$.

Example: Uniform plane wave

For example, a uniform plane wave in $+z$-direction within a non-conductive insulating material ($\kappa = 0$) shall be considered: From Maxwell's Main Field Equations, i.e. from Faraday's and Ampere's law it is concluded that the field vectors $\boldsymbol{E}$ and $\boldsymbol{H}$ are orthogonal to the direction of propagation and orthogonal to each other, Figure 2.1-6. Such a field is called *transverse electric and magnetic field*, *transverse electromagnetic wave* or *TEM wave*, Figure 2.1-17.

The so-called *phase front* is spanned by the vectors $\boldsymbol{E}$ and $\boldsymbol{H}$ orthogonally relative to the direction of propagation. It is a surface or plane of constant phase (e.g. the

wavefront), and it propagates with the *phase velocity u* in +*z*-direction, Figure 2.1-17 with Eq. (2.1-42). The magnitudes of the related vectors ***E*** and ***H*** have a constant ratio $E/H = Z$, the so called *wave impedance*, Figure 2.1-17 with Eq. (2.1-43).

The *phase velocity* in vacuum and in gases is equal to the *speed of light*

$$u = u_0 = 300 \cdot 10^6 \text{ m/s}, \qquad (2.1\text{-}44)$$

the *wave impedance* is equal to the *intrinsic impedance of the free space*

$$Z = Z_0 = 377\ \Omega. \qquad (2.1\text{-}45)$$

In *insulating materials* with $\mu_r \cong 1$ the quantities u_0 and Z_0 are to be divided by the square root of ε_r:

$$\begin{aligned} u &= u_0 / \sqrt{\varepsilon_r} \\ Z &= Z_0 / \sqrt{\varepsilon_r} \end{aligned} \qquad (2.1\text{-}46)$$

High voltage engineering must always consider the traveling wave character of the fields, if the quasi-static description causes significant errors. According to Eq. (2.1-36) to (-38), this limit is reached for materials with $\varepsilon_r = 1$ (e.g. for air)

- for a length of approx. *100 km (80 km)* in the case of *AC voltage f* = 50 Hz (60 Hz),
- for a length of approx. *5 km* in the case of *switching impulse (SI) voltage* (time to crest $T_{cr} = 250$ µs),
- for a length of approx. *25 m* in the case of *lightning impulse (LI) voltage* (front time $T_1 = 1.2$ µs) and
- for lengths of *less than 0.2 m* in the case of *"fast transients"* (rise time $T_r < 10$ ns) in gas insulated switchgear (GIS) or gas insulated lines (GIL).

For AC and SI voltages we can assume *quasi-static (quasi-stationary) conditions* in many cases, for LI voltages these conditions can be assumed if the circuit dimensions are limited to a few tens of meters. Overvoltages with rise times in the µs range are *always* to be regarded as *traveling waves* in the distributed systems of energy or data transmission. The same applies to the very steep fast transients, which excite significant traveling waves even in systems with lengths of a few meters only. It is concluded that high voltage engineering mostly has to deal with *guided traveling waves* on transmission lines, see Section 2.6. Important practical examples are

- lightning strikes into an overhead transmission line,
- „fast transients" (FT) in pressurized gas-insulated switchgear (GIS),
- impulse generators for the so-called "pulsed power technology" and
- measurement signals on long measuring cables.

2.2 Electrical Stresses in High Voltage Engineering

Insulating systems in high voltage engineering are based on insulating materials, which have to satisfy very different requirements. Of course, the *electric strength* plays a dominant role, but it is only a single property among

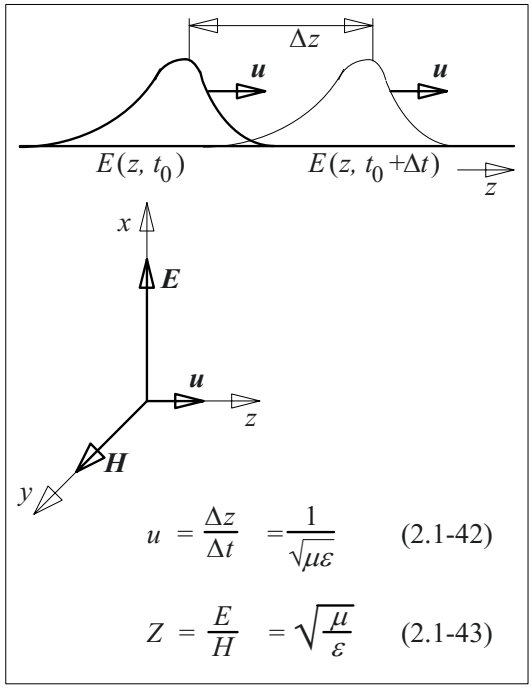

$$u = \frac{\Delta z}{\Delta t} = \frac{1}{\sqrt{\mu\varepsilon}} \qquad (2.1\text{-}42)$$

$$Z = \frac{E}{H} = \sqrt{\frac{\mu}{\varepsilon}} \qquad (2.1\text{-}43)$$

Figure 2.1-17: Uniform plane wave with transverse E- and H-field vectors.

many others. Each insulating material has a specific *profile* of properties that determines whether the material is suitable for a special application or not. In the following some important elements of such profiles are summarized:

1. Electric strength (dielectric strength),
e.g. short term strengths and life-time characteristics for AC, DC and impulse voltage stresses, also under the influence of pollution.

2. Dielectric properties,
e.g. permittivity, dissipation factor, conductivity and surface resistance.

3. Thermal properties,
e.g. permissible holding and maximum temperatures, thermal conductivity, coefficient of thermal expansion, thermal capacitance, flammability, tracking resistance, temperature dependences of material parameters.

4. Mechanical properties,
e.g. tensile and flexural strength, modulus of elasticity, degree of hardness.

5. Resistance to environmental influences,
e.g. weather-resistance, resistance to ultraviolet rays and resistance against chemical impacts.

6. Processing possibilities,
e.g. casting, extruding, welding, bonding and mechanical machining.

7. Availability and costs,
for procurement and processing.

8. Possibilities for recycling and disposal.

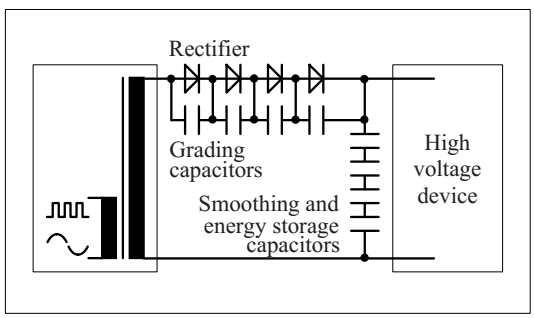

Figure 2.2-1: Half-wave high-voltage rectifier circuit with grading and smoothing capacitors.

The design of an insulating system has must ensure that the property profiles of the dielectric materials satisfy all test and service stresses. These stresses can be of an electrical, thermal, mechanical and chemical/physical nature.

In the following, only the various **electrical stresses** will be discussed, such as DC voltages (Section 2.2.1), AC voltages (Section 2.2.2), switching and lightning impulse voltages (Sections 2.2.3 and 2.2.4), fast rising impulses (e.g. fast transients, Section 2.2.5) and mixed stresses (Section 2.2.6). During the calculation of electric field strengths, it is necessary to consider the different characters of the electric fields. Figure 2.2-4 gives an overview at the end of this chapter.

The wide range of *non-electric stresses* in high voltage engineering will be addressed together with the description of special insulating material properties (Chapter 5) and the different technical applications (Chapter 7).

2.2.1 DC Voltage Stress

Many technical applications are associated with high DC voltage stresses:

1.) In devices for the DC supply of X-ray tubes, in monitors, charging devices, copiers, impulse circuits, lacquering and coating devices and in test equipment there are high electric DC fields, especially in the barrier junction of the rectifier components and in the dielectrics of smoothing and energy storage capacitors, Figure 2.2-1.

These stresses are *frequently* not a matter of *pure steady-state DC voltage*, often there are *mixed voltage stresses*: Grading capacitors and rectifier components are additionally stressed by a superimposed AC voltage. The voltage of smoothing capacitors contains a certain “ripple” and energy storage capacitors (“surge capacitors”) are discharged abruptly. Furthermore, in many cases the DC voltage is not applied long enough for the formation of a steady-state (stationary) conduction field, Fig-

ure 2.1-16. The individual voltage stress of single components is derived only from the analysis of voltages in a given circuit. Different circuits for the generation of high DC voltages are described in Section 6.2.

2.) In high-voltage direct-current (HVDC) transmission systems AC-transformers feed converter circuits, which are arranged in series on the DC side, Figure 2.2-2. Thereby, there are *mixed AC and DC* stresses on the insulation.

The insulation also has to withstand *transient processes* occurring after switching on and off or polarity reversal of the DC voltage. Therefore, special DC test procedures with polarity reversals and voltage profiles determine the DC insulation design, see Figure 2.2-4.

For the *calculation* of electric field strengths after voltage changes or reversals it is necessary to superimpose a dielectric *displacement field* (quasi-static field), which describes the amplitude of the voltage change, and the initially given *stationary conduction field* (initial steady-state condition), Section 2.1.4.4.

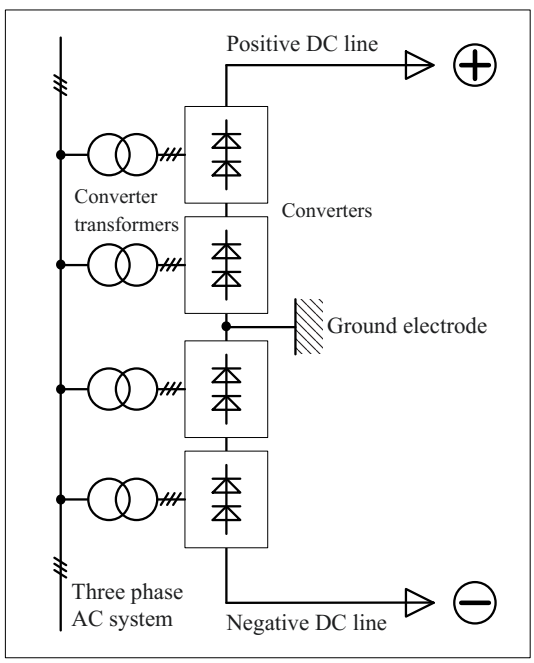

Figure 2.2-2: Converter station of a high-voltage direct-current (HVDC) transmission system.

During steady-state DC voltage application, there are problems with very high line-to-ground voltages (approx. above 500 kV). Pollution and wetting of insulator surfaces cause unpredictable distortions of the electric fields because of comparatively high and non-uniform conductivities of the wetted deposits on the surfaces [7] ... [10].

2.2.2 AC Voltage Stress

Energy transmission with three phase AC systems requires the application of high voltages in order to limit the losses. Therefore insulation systems are stressed by high AC voltages with frequencies of $f = 50$ Hz or $f = 60$ Hz According to the considerations of Sections 2.1.4.3 and 2.1.4.4 *quasi-static* (quasi-stationary) *displacement fields* can normally be assumed in the insulation of power apparatus. This means that the *permittivities* determine the distribution of the electric fields for the common insulating materials with low conductivities.

The transmission voltage of a three-phase AC system is defined by the *"highest voltage for equipment"* V_m, which must not be exceeded in any part of the electrical grid [11]. This voltage is the highest r.m.s. value of the phase-to-phase voltage for which the equipment and its insulation is designed. Standardized values are

in the **"medium voltage (MV) range"**
($1\ \text{kV} < V_m < 52\ \text{kV}$)

$V_m =$ 3.6 kV,
7.2 kV,
12 kV (common in Germany),
17.5 kV,
24 kV (common in Germany),
36 kV,

in the **"high voltage (HV) range"**
($52\ \text{kV} \leq V_m < 300\ \text{kV}$)

$V_m =$ 52 kV,
72.5 kV,

123 kV (common in Germany),
145 kV,
170 kV,
245 kV (common in Germany),

and in the **"extra high voltage (EHV) range"** ($V_m \geq 300$ kV)

$V_m =$ 300 kV,
362 kV,
420 kV (common in Germany),
525 kV,
765 kV.

Note: In a very general sense, "*high voltage*" is any voltage level above *low voltage* (1 kV). The boundaries between *medium and high voltage* depend on local circumstances, history or common usage. Nevertheless, the band 30 kV to 100 kV frequently contains the accepted boundary. The above-mentioned classification is used in German transmission and distribution systems for instance.

Note: Sometimes in Germany the standardized voltage levels V_m = 12, 24, 123, 245 and 420 kV are still denominated with the old "nominal voltages" 10, 20, 110, 220 and 380 kV (400 kV).

Insulation breakdown is normally determined by the highest occurring value of the AC voltage, i.e. by the **peak value**. For sinusoidal voltages and under normal service conditions, the insulation between phases (line-to-line, index "LL") is stressed with the peak value

$$\hat{V}_{LL} = \sqrt{2} \cdot V_m \qquad (2.2\text{-}1)$$

and between phase and ground (line-to-ground, index "LG") with the peak value

$$\hat{V}_{LG} = \sqrt{2} \cdot V_m / \sqrt{3} \,. \qquad (2.2\text{-}2)$$

Electrical equipment is designed and rated to withstand this *continuous voltage stress* for many decades.

For a short time, power-frequency *overvoltages* can occur, e.g. during a sudden load reduction. In grids up to V_m = 123 kV the neutral point (star point) does not always have a solid grounding. In the case of a single phase-to-ground fault, the neutral-point potential is therefore shifted and the insulations between the unaffected phases and ground are stressed with the phase-to-phase voltage according to Eq. (2.2-1). Resonant overvoltages at power frequency should be excluded by the grid topology, but they can occur together with harmonics.

The strength of insulation against power-frequency overvoltages has to be proven by means of a specified AC voltage withstand test with a duration of 1 minute (*"rated short-duration power-frequency withstand voltage test"*). The r.m.s. value of the test voltage is always specified in relation to the highest voltage for equipment V_m [11]. This reference of test voltages to the maximum voltage stresses in service is called *"insulation coordination"*, Section 6.1.4.

The test voltage value is nearly $3 \cdot V_m$ for the lower voltage levels and approx. between $2 \cdot V_m$ to $1.5 \cdot V_m$ for the higher levels. This short-duration test voltage is an important design parameter for insulation systems.

For the higher voltage levels a successful AC voltage withstand test is not sufficient. Depending on the kind of equipment, *insulation quality* must be guaranteed by the proof of *partial discharge* (PD) intensity limits at different AC test voltage levels (see Section 3.6, 6.4.2 and Chapter 7).

AC voltage tests on **cables** with high capacitances are performed with *very low frequency* (VLF) f = 0.1 Hz in order to reduce the capacitive reactive power. Alternatively, tests with higher frequencies can be performed with *resonance test circuits instead of the less meaningful DC tests*, Figure 2.2-4, Section 6.2.1.

Transformers must be tested with *increased frequencies* (e.g. with f = 100 Hz for 50 Hz transformers and f = 120 Hz for 60 Hz transformers) in order to avoid saturation of the magnetic core after exceeding the design voltage and at the start of the test voltage. If the

frequency is doubled, the induced voltage $V_i \sim \partial B/\partial t \sim \omega \cdot B$ is also increased by a factor of two without any increase in magnetic flux density B, Figure 2.2-4.

Significantly higher frequencies occur if the line voltage contains *harmonics*. This can result in a distortion of the voltage curve, so that peak values differ significantly from the peak values of a sinusoidal voltage with the same r.m.s. value. Furthermore, harmonics can cause enhanced capacitive currents and enhanced dielectric *losses*. Lossy and thick insulation systems (e.g. in old power factor correction capacitors with oil-impregnated paper insulation) are subject to higher thermal stresses.

2.2.3 Switching Impulse Voltage Stress ("Internal Overvoltages")

Pulse-shaped overvoltages can be caused by switching operations in the electrical grid, e.g. by interruption of a currents during the opening of inductive circuits. As the origin is in the grid itself, the *switching impulses* (SI) are called *"internal overvoltages"*.

For equipment with $V_m > 300$ kV the electric strength against SI overvoltages is normally proven during a type test. The peak value of the standardized *"rated switching impulse withstand voltage"* V_{rS} is defined in relation to V_m as part of the insulation coordination [11], Section 6.2.3.1. Normally the peak time T_p (time to crest) is 250 µs and the time to half-value (tail time) is 2500 µs.

During the calculation of electric fields in common insulating systems, *quasi-static* (*quasi-stationary*) conditions in the form of *dielectric displacement fields* can be assumed, which are determined by *permittivities*, cf. Section 2.1.4.4. The errors of a quasi-stationary analysis are negligible up to lengths of approx. 5 km, if T_p = 250 µs, Eq. (2.1-37), Figure 2.2-4.

2.2.4 Lightning Impulse Voltage Stress ("External Overvoltages")

Direct lightning strikes into **power apparatus** cause travelling waves in the widely distributed overhead lines and cables. These waves lead to very high short-duration overvoltages. Also lightning strikes into line towers, overhead ground wires or into other structures nearby can lead to rapidly changing fields and traveling wave processes being coupled in. As the surges are generated atmospherically, i.e. they are caused by external lightning impulses (LI), we refer to *"external overvoltages"*.

Amplitudes and time responses of external overvoltages are subject to strong variations. Nevertheless, characteristic properties are a fast rising voltage in the µs range and a significantly slower decline of the overvoltage impulse (Section 6.2.4). For of electrical power equipment a standardized lightning impulse voltage with a so-called front time T_1 = 1.2 µs and a time to half-value (tail time) T_2 = 50 µs is defined. As part of the insulation coordination, the different service voltage levels V_m are each associated with a peak value of the *"rated lightning impulse withstand voltage"* V_{rL} [11]. They are more than twice the so-called short-duration AC withstand voltage.

For the calculation of electric fields, q*uasi-static* (quasi-stationary) conditions and *dielectric displacement fields* can be assumed in relatively small systems only, i.e. for dimensions limited to approx. 25 m, Figure 2.2-4. In systems with distributed parameters (distributed systems), e.g. in cables and overhead lines, the *wave-character* of the fields must be considered. This is especially the case if the trailing part of the impulse voltage is chopped. Depending on the inductance of the circuit, chopping times far below 100 ns can occur. In circuits with low losses (e.g. if a non-damped capacitive voltage-divider is used), the chopping can be an excitation of significant transient traveling wave oscillations.

Another example for pulsed electric stresses is the *discharging of energy storage capacitors*, which are often referred to as impulse capacitors, Figure 2.2-4. Typically the discharge periods or the time-constants of the discharge processes are in the µs range. Therefore in smaller systems quasi-static fields can be assumed.

(Impulse) discharge circuits of high power pulse technology (pulsed power) are used in many technical applications, Section 7.4.2:

- In *medical engineering* acoustic shockwaves are generated by igniting a spark gap in water or by an electroacoustic transducer. The energy is supplied by the discharging of a high voltage capacitor. For example, in a *lithotripter* the resulting shock wave is focused on a kidney stone (nephrolith) or a gallstone in order to pound it to tiny pieces.
- In production technology focused acoustic shock waves can be used for *high-speed forming* of metallic materials.
- Shock waves are used for *electrodynamic fragmentation*, i.e. for the fragmentation and grinding of inhomogeneous or composite materials, e.g. for *recycling* applications [12].
- *Electroporation* can be applied for the opening and disruption of biological cells at room temperatures with low energy consumption.
- High energy impulses can be used to generate very fast temperature rises for the production of *nanometric particles* by melting and condensing.
- Pulse discharge circuits are necessary for the power supply of *impulse lasers* and for other *impulse* (*flash) light sources*.

2.2.5 Fast-rising Impulse Stresses ("Fast Transients")

There are many examples of fast rising impulses in different technical applications:

1.) In **gas-insulated switchgear** (GIS) discharge processes are caused for example by flashovers or by switching of disconnectors.

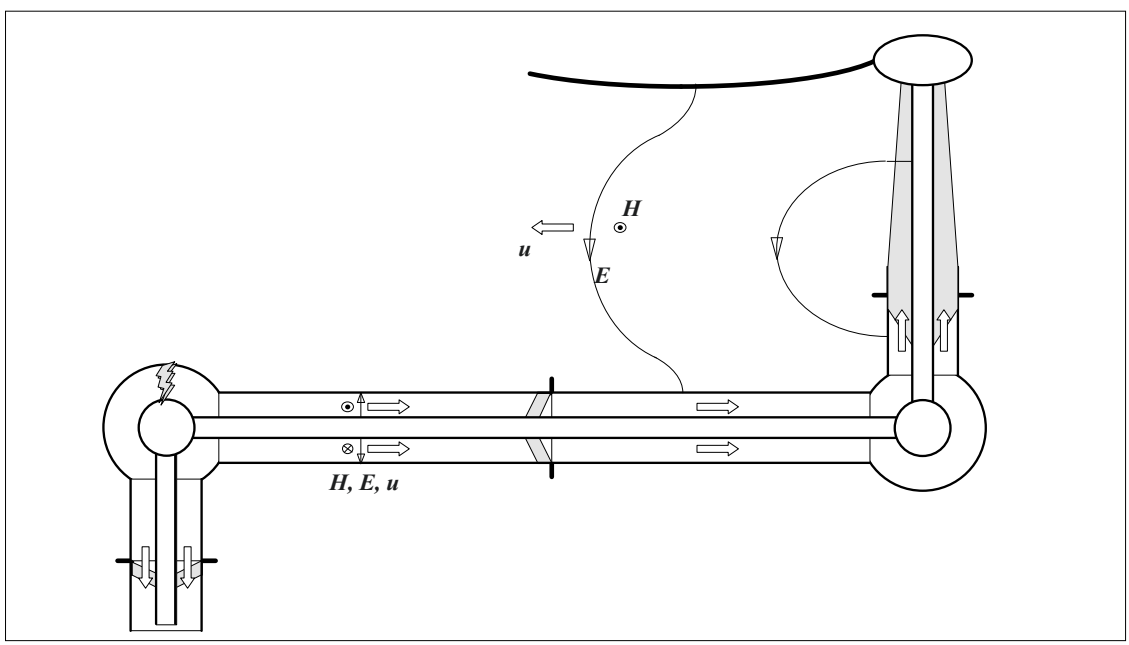

Figure 2.2-3: Propagation of traveling waves within and on the outside of a gas-insulated switchgear (GIS) after a breakdown in gas (schematic illustration without respect to reflections).

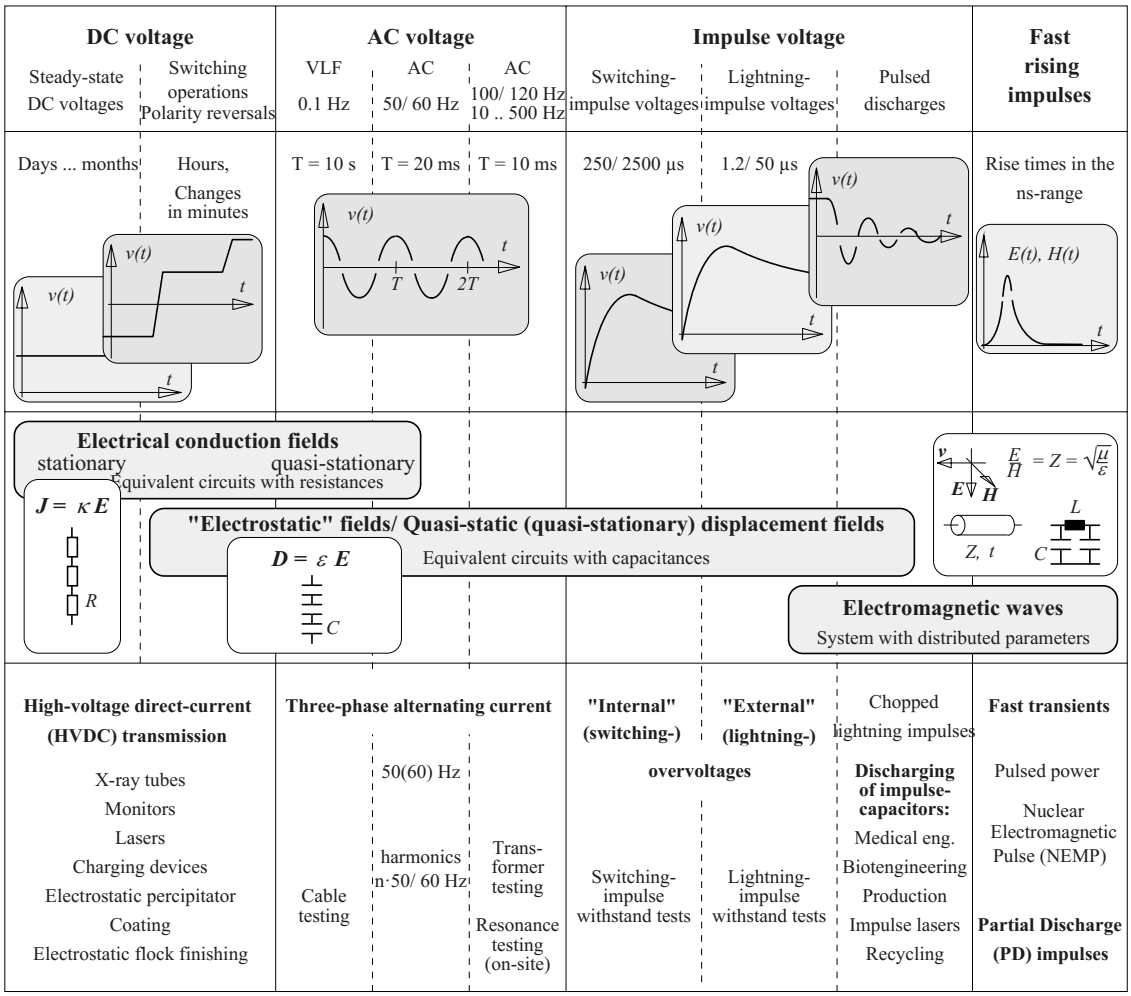

Figure 2.2-4: Overview of important technical voltage stresses in high voltage engineering: Typical time curves (top), kinds of fields and equivalent circuits (middle) and typical applications (bottom).

Because of the high gas pressures and the low insulation distances, discharges have *rise times* in the ns range, therefore they can excite traveling waves. Owing to the length (frequently many meters) of the coaxial tubular conductors and shielding, *traveling waves* can often propagate without significant damping. At discontinuities of the line impedance *reflections* occur, and different waves are superimposed. Normally they propagate within the tubular shielding, but via the bushings they can also propagate outside, Figure 2.2-3 and -4 [13].

Therefore, highly stressed insulations (e.g. in transformers and bushings) are endangered by *significant transient overvoltages*. In unfavorable situations, the excitation of *self-resonances* (e.g. in the transformer windings) can result in further voltage overshoots. Wave propagation on the *outside* of the shielding can cause unwanted electromagnetic interferences in the *secondary systems* of the plant. Specific measures have to be taken in order to guarantee *"electromagnetic compatibility"* (EMC).

2.) **Testing of power equipment** with respect to very fast voltage transients is normally performed together with a lightning impulse test by a fast *"chopping"* of the voltage by means of a chopping spark gap. The time to chopping is 4 to 6 µs (chopped lightning impulse, chopped-wave lightning impulse).

For the calculation of fast transients, the fast-changing character of the processes must be considered. Mostly the transients can be described as guided TEM-waves on coaxial lines (*traveling waves*, Section 2.6). On a surface with constant phase (wavefront) the closed-loop integral about $\boldsymbol{E}\cdot\mathrm{d}\boldsymbol{x}$ is zero (the vectors $\boldsymbol{H}$ and $\boldsymbol{B}$ do not penetrate the wavefronts!), therefore voltages between the inner and the outer conductor can be defined according to Eq. (2.1-7). *Attention*: The definition of voltages with components parallel to the direction of wave propagation is **no longer** possible!

3.) Other *examples* for very fast rising high-voltage impulses can be found in **pulsed-power technology** for the generation of extremely short impulses with extremely high power ratings. These pulses are generated by means of traveling-wave lines and they are used to feed particle-beam accelerators in science for the investigation of materials in extreme conditions and for the ignition of controled nuclear fusion processes. The rise times and the half-value widths of these impulses are in the range of some ns and some 10 ns resp., peak power and peak voltage reach the TW and the MV range [14], [15].

4.) In the case of a nuclear explosion in the space outside of the Earth's atmosphere, it is expected that the action of the resulting radiation in the atmosphere will separate positive and negative charge carriers in the vertical direction. Separation and recombination of charges will cause a pulsed electromagnetic field, the so-called **nuclear electromagnetic pulse** (NEMP). It is expected that high overvoltages will be induced in the widely distributed systems of telecommunications, information technology and energy transmission and distribution.

5.) If a high AC field strength is applied to an insulation defect, **partial-discharge (PD) impulses** occur, normally without causing an immediate breakdown. These impulses also have very short rise times in the ns range. For a single partial discharge the dissipation of energy and the charge magnitude are very small. Nevertheless, the discharge impulses are a dangerous phenomenon of AC voltage stress, owing to their erosive effects in sensitive, mainly organic insulating materials. The fast changing electromagnetic field of partial discharges is important for partial discharge measurements.

6.) The transmission characteristics of **high-voltage measuring systems** are determined by means of step-generators providing rectangular pulses with rise times in the ns range. Because of the large spatial dimensions, traveling wave oscillations on measuring cables and direct coupling of free electromagnetic waves must be considered [18], [19].

2.2.6 Mixed-field Stresses

In many cases electric stresses are a combination of the cases described above. Then it is often difficult to determine the electric field strengths and the relevant electric strengths. Important examples:

1. Superposition of DC and AC voltages in the converter transformers of HVDC systems.

2. DC voltage and polarity reversal tests: A stationary conduction field and a quasi-stationary displacement field are superimposed, if the amplitude or the polarity of the voltage is changed. Depending on conductivity κ and self-discharge time-constant ε/κ, it takes a very long time to approach a new steady-state condition. During such a transient process, significant stresses can occur on materials in a layered insulation, which are much less highly stressed initially and in the steady state.

3. Rectifier and converter circuits: Many electronic devices are stressed with a superposition of DC, AC and impulse voltages.

4. Energy-storage and impulse capacitors: During the charging process, the dielectrics are stressed with an increasing voltage. Depending on the time of storage, the field after voltage application approaches a steady-state conduc-

tion field. During the discharging process there is a pulsed stress, often in the form of a damped oscillation.

5. Fast transients: Rapidly changing traveling waves are superimposed on the actual field condition given by the quasi-static power frequency state. Thereby high overvoltages can occur, for which the equipment is not insulated sufficiently.

In *field calculations* for the determination of electrical stresses, the different kinds of fields are normally calculated separately and *superimposed linearly* into *mixed stresses*. In contrast to magnetic materials with non-linear magnetization curves, solid insulating materials behave more or less linearly, as long as discharges do not occur. Liquid dielectrics can have *non-linear conductivities,* however, Section 4.2.2.2.

In situations with mixed stresses, it is often difficult to *evaluate* calculated field strengths. For the example of impulse capacitors, the steady-state DC voltage is absolutely noncritical in comparison with the fast changing stress during the discharging process, although the amplitudes are identical in both cases.

For practical design purposes, *breakdown* and *lifetime tests* are necessary, with conditions close to the *real service conditions*.

2.3 Conduction and Displacement Fields in Homogeneous Dielectrics

For static, stationary and slowly changing (quasi-static, quasi-stationary) fields in insulating materials, the electric field can be regarded as irrotational, i.e. as an electrostatic field. An induced electric curl field does not occur or can be neglected. Therefore, the definition of potential differences and voltages is acceptable.

If the whole field volume that is to be considered consists of a **single homogeneous** (uniform) **insulating material** (dielectric), the field distribution is not determined by material properties (permittivity ε, conductivity κ) and the electric field calculations are based on the same relationships. Therefore, the field calculation methods, which are described in the following, can be applied for most of the.

First of all, the *direct analytic evaluation of the field equations* is performed (Section 2.3.1 and 2.3.2). It allows the calculation of basic field configurations with homogeneous, spherically symmetric and cylindrically symmetric fields. Some important high voltage field configurations can be approximated from this.

A *graphical method* (Section 2.3.3) allows a qualitative or semi-quantitative field sketch to be determined using some simple drafting rules. Often this is very valuable for a first qualitative estimation of field conditions.

The *method of conformal mapping* (Section 2.3.4) allows the calculation of some special cases, e.g. the field stress enhancement at the edges of a parallel-plate capacitor (edge field).

By means of the fields of *equivalent charges* (Section 2.3.5) it is also possible to calculate important field configurations, e.g. sphere against sphere or cylinder against plane.

In many cases, only the *maximum field strength* is of interest. For many field configurations, it can be derived from already calculated cases by *similarity relationships and geometry factors* (Schwaiger's field efficiency factor, Section 2.3.6).

Before numerical field calculation methods were available, the only possibility for the determination of field strengths in systems with arbitrarily shaped electrodes was the *measurement* of electrical *conduction fields* in a semi-conductive liquid (*electrolytic tank)* or on a semi-conductive paper (*field plotter*), Section 2.3.7).

2.3.1 Analytic Evaluation of the Continuity Equation (Gauss's Law)

2.3.1.1 General Calculation Method

If Eq. (2.1-17), i.e. the Continuity Equation for conduction and displacement current

$$\oiint_A \left(\boldsymbol{J} + \frac{\partial \boldsymbol{D}}{\partial t} \right) \mathrm{d}\boldsymbol{A} = 0 ,$$

is integrated over the time, it results in "Gauss's law", Eq. (2.1-21) and (2.3-1). It states that the integral of the flux density $\boldsymbol{D}$ over any closed surface, i.e. the total displacement flux $\iint \boldsymbol{D} \cdot \mathrm{d}\boldsymbol{A}$, equals the charge Q enclosed.

$$\boxed{\oiint_A \boldsymbol{D}\ \mathrm{d}\boldsymbol{A} = Q} \qquad (2.3\text{-}1)$$

With Eq. (2.3-1), field calculations can be performed for some basic configurations in four steps:

Step 1:
For configurations with symmetrical fields, Eq. (2.3-1) is solved for the magnitude D of displacement vector $\boldsymbol{D}$, in order to get a relationship between field-generating *charge* Q and the *electric field strength* $E = D/\varepsilon$.

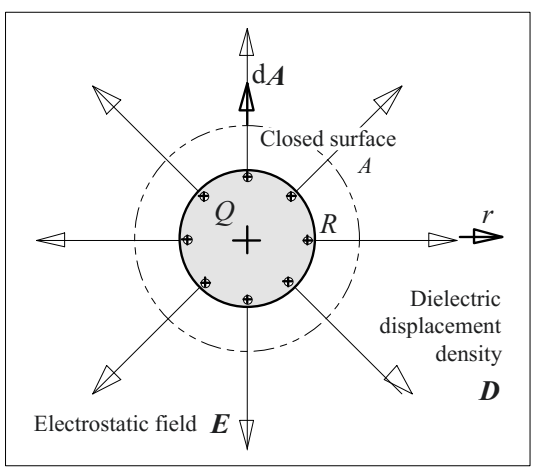

Figure 2.3-1: Spherically symmetrical electrode in free space (Gauss's law).

Example: **Spherical electrode in free space**

The magnitude of the electric field strength E shall be calculated as function of voltage V and radius r for the spherically symmetric arrangement according to Figure 2.3-1. The counter-electrode with the negative counter-charges is assumed to be infinitely far away.

Step 1:
The surface of a sphere with the radius r is chosen as the closed surface for integration. Thereby the symmetry of the configuration is utilized, because the displacement density has a constant magnitude $\boldsymbol{D}(r)$ over the entire chosen surface. Furthermore, the vectors $\boldsymbol{D}$ and $\mathrm{d}\boldsymbol{A}$ are parallel to each other, over the entire closed surface. The scalar product $\boldsymbol{D} \cdot \mathrm{d}\boldsymbol{A}$ equals the product of the magnitudes $D \cdot \mathrm{d}A$. The displacement density is constant all over the surface of integration, and it can be brought out from under the integral sign in Eq. (2.3-1):

$$\oiint_A \boldsymbol{D}\ \mathrm{d}\boldsymbol{A} = D(r) \oiint_A \mathrm{d}A = Q$$

The remaining integral over the closed surface gives the surface area $A(r) = 4\pi r^2$ itself:

$$D(r) \cdot A(r) = D(r) \cdot 4\pi r^2 = Q$$

This gives

$$D(r) = Q/(4\pi r^2) \quad \text{and}$$
$$E(r) = Q/(4\pi\varepsilon r^2) . \qquad (2.3\text{-}2)$$

The magnitude of the electric field strength decreases proportionally to $1/r^2$, i.e. quadratically with the radius.

Step 2:
In high voltage engineering the electric field strength E normally has to be given as a function of the applied *voltage* V. This is possible, if the field strength, which is derived from Gauss's law according to Eq. (2.3-1), is integrated according to Eq. (2.1-7):

$$\boxed{V_{21} = \Delta\varphi_{21} = \varphi_2 - \varphi_1 = \int_2^1 \boldsymbol{E}\ \mathrm{d}\boldsymbol{x}} \qquad (2.3\text{-}3)$$

Thereby a relationship between Q and V is determined, i.e. $Q = f(V)$.

Step 3:
According to Eq. (2.1-10) the ratio of Q and V defines the **capacitance** C of the field configuration:

$$C = Q / V \qquad (2.3\text{-}4)$$

Step 4:
The desired relationship between **field strength** E and *voltage* V

$$E = f(V)$$

is derived from the first step with $E = f(Q)$ and from the second step with $Q = f(V)$.

Step 5:
In an additional step, maximum values of field strength can be determined and optimization problems can be solved, e.g. the minimization of maximum field strength.

Example: Spherical electrode (continued)

Step 2:
Continuing with the former example, the voltage between the electrode surface with radius $r = R$ and the counter-electrode (carrying the negative counter-charges) with the radius $r \to \infty$ is given by

$$V_{R\infty} = \int_R^\infty E(r)\,\mathrm{d}r = \frac{Q}{4\pi\varepsilon}\int_R^\infty \frac{1}{r^2}\,\mathrm{d}r$$

$$= \frac{Q}{4\pi\varepsilon}\left[\frac{-1}{r}\right]_R^\infty$$

$$= Q/(4\pi\varepsilon R),$$

if the integration is performed radially, i.e. in parallel with the electric field E. Therefore it gives

$$Q = 4\pi\varepsilon R\, V. \qquad (2.3\text{-}5)$$

Step 3:
From that, the capacitance is derived:

$$C = Q/V = 4\pi\varepsilon R. \qquad (2.3\text{-}6)$$

Step 4:
According to Eq. (2.3-2) and (2.3-5) from steps 1 and 2, the electric field strength is

$$E(r) = V\, R/r^2. \qquad (2.3\text{-}7)$$

Step 5:
Maximum field-strength is found on the electrode surface for the smallest possible radius $r \to R$, i.e.

$$E_{\max} = E(R) = V/R. \qquad (2.3\text{-}8)$$

2.3.1.2 Spherically Symmetric Fields

The electric field of a *"conducting sphere in free space"* was calculated in the former example, see Figure 2.3-1 and Equations (2.3-6) to (2.3-8). Maximum field strength occurs at the electrode surface.

Note: The field of the conducting sphere in free space with a vanishingly small radius $R \to 0$ approaches the field of a *point charge*. This theoretical case is important for field calculations with the equivalent-charge simulation method, Section 2.3.5.

The smaller the radius of curvature R of an electrode, the higher the electric edge-field strength will be, Eq. (2.3-8).

> Generally, **sharp edges** (with small radii R) **must therefore be avoided in high voltage engineering**, in order to avoid electrical overstressing of the adjacent insulating material.

Example: Sharp-edged point electrode

The field in the vicinity of a metallic point electrode shall be calculated approximately as a spherically symmetric field with R = 1 mm. What is the expected peak voltage $\hat{V}$ for the inception of discharges in air ($\hat{E}_\mathrm{i}$ = 5 kV/mm)?

From Eq. (2.3-8) we conclude that $\hat{V} = \hat{E}_{\max} \cdot R$ = 5 kV.

Note: High field strengths at sharp-edged point electrodes do only occur in a small volume close to the point. The inception field strength is therefore significantly higher than the commonly used peak value $\hat{E}_\mathrm{i}$ = 3 kV/mm = 30 kV/mm which is valid for air gaps in the centimeter range, Figure 3.2-15. Discharge inception cannot be described exactly by specifying a constant inception field strength, see Chapter 3.

In high voltage engineering, field stress enhancements at sharp edges are reduced by sufficient radii of curvature. In many cases, sharp-edged parts have to be protected by *shielding electrodes* (e.g. spheres or toroids). The field strengths on the surface can be estimated by approximation from Eq. (2.3-8) if approximately spherically symmetric conditions are assumed with a counter-electrode very far away:

$$E_{\max} = V/R \qquad (2.3\text{-}8)$$

The capacitance in air can be approximately described according to Eq. (2.3-6) using the rule of thumb

$$C/\mathrm{pF} \approx R/\mathrm{cm} \ . \qquad (2.3\text{-}9)$$

Note: If the counter-electrode (e.g. the grounded wall, ceiling or floor) is located at a finite distance, higher capacitances and field strengths occur. Numerical field calculation methods achieve a significantly better accuracy than the analytic estimation, Section 2.3.5.

Example: Shielding electrodes

The *diameters of shielding electrodes* for use in air ($\hat{E}_{bd}$ = 30 kV/cm, ε_r = 1) and insulating oil ($\hat{E}_{bd}$ = 150 kV/cm, ε_r = 2.2) shall be sized for the voltage amplitudes $\hat{V}$ = 10 kV, 100 kV and 1 MV so that the field strengths do not exceed 2/3 of the breakdown field strength.

The diameters are derived from Eq. (2.3-8):

$$D = 2R = 2\hat{V} / (2/3 \cdot \hat{E}_D) \ .$$

Peak voltage $\hat{V}$		**10 kV**	**100 kV**	**1 MV**
Air:	*D*	**1 cm**	**10 cm**	**1 m**
	C	0.5 pF	5 pF	50 pF
Insulating Oil:	*D*	**2 mm**	**2 cm**	**20 cm**
	C	0.2 pF	2 pF	22 pF

Note: The results show that *high voltage laboratories* need shielding electrodes with diameters in the meter range.

Much *more compact high voltage equipment* can be designed by means of electrically stronger insulating materials (e.g. insulating oil or sulfur hexafluoride SF_6). It has to be considered that E_{bd} of insulating oil is not a constant value, but inter alia is dependent on the width of the oil ducts ("volume effect", "distance effect" or "size effect", see Chapters 3 and 5).

A so-called *spherical capacitor* consists of an inner sphere with the radius R_1 and a counter electrode consisting of a concentric outer sphere with the finite radius R_2, Figure 2.3-2a.

The *calculation of field strength* is performed in five steps, analogous with the calculation steps for the spherical electrode in free space:

The use of Gauss's law (eq. (2.3-1), Step 1) on the spherically symmetrical configuration according to Figure 2.3-2a gives the same equation (2.3-2) again because of the similar field conditions. *E* decreases with the radius *r* proportional to $1/r^2$ (*step 1*).

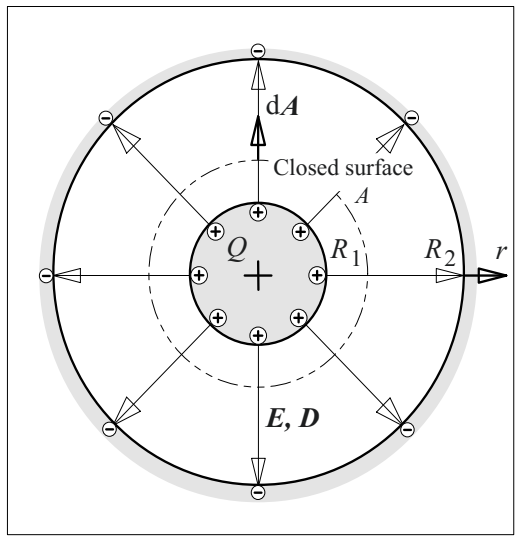

Figure 2.3-2a: Spherical capacitor (or cylindrical capacitor resp.).

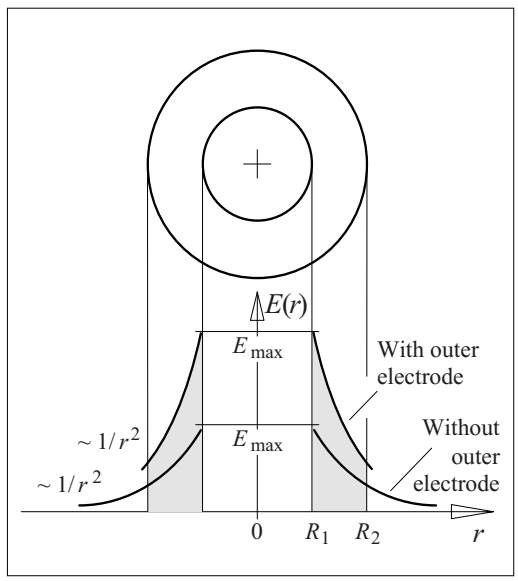

Figure 2.3-2b: Field strength curves E(r) for the spherical capacitor.

The integration of the field strength according to Eq. (2.3-2) (*Step 2*) must not be performed from radius *R* to infinity, because the field is limited to the space between the inner and outer electrodes, i.e. integration has to be performed between the radii R_1 and R_2. Inserting the new integration limits and $V_{12} = V$, we obtain

$$V = \frac{Q}{4\pi\varepsilon}\left(\frac{1}{R_1} - \frac{1}{R_2}\right) \qquad (2.3\text{-}10)$$

and

$$Q = \frac{4\pi\varepsilon}{\frac{1}{R_1} - \frac{1}{R_2}}\, V. \qquad (2.3\text{-}11)$$

The *capacitance* of a spherical capacitor is given by $C = Q/V$ (*Step 3*):

$$C = \frac{4\pi\varepsilon}{\frac{1}{R_1} - \frac{1}{R_2}} \qquad (2.3\text{-}12)$$

The field strength curve between inner and outer electrodes is derived from Eq. (2.3-2) and (2.3-11) *(Step 4)*:

$$E(r) = \frac{1}{\left(\frac{1}{R_1} - \frac{1}{R_2}\right) r^2}\, V \qquad (2.3\text{-}13)$$

For the extreme value $R_2 >> R_1$ Eq. (2.3-12) and (2.3-13) approach Eq. (2.3-6) and (2.3-7).

The maximum field strength at the inner sphere with $r = R_1$ *(Step 5)* is higher in comparison with the sphere in free space, Figure 2.3-2b. The areas under the field strength curves correspond to the integral of the function $E(r)$, i.e. to the applied voltage V.

We obtain the *maximum field strength* from Eq. (2.3-13) for the radius $r = R_1$ on the surface of the inner sphere (*surface* or *edge field strength*):

$$E_{max} = E_1 = \frac{R_2}{R_1 R_2 - R_1^2}\, V \qquad (2.3\text{-}14)$$

From the calculated field strengths *optimization problems* can be solved by means of *extreme value determination*:

For a given outer radius R_2 the inner radius R_1 shall be chosen so that the *maximum field strength* (*surface/edge field strength*) E_1 will be minimal.

In the extreme cases $R_1 \to 0$ and $R_1 \to R_2$, there are infinitely high surface/edge field strengths E_1. The *optimum inner radius* R_1 for a minimum surface field strength E_1 is between 0 and R_2 therefore, and it is determined, if the derivate of E_1 with respect to the variable R_1 is set to zero, see Eq. (2.3-14):

$$\frac{\partial E_1}{\partial R_1} = -\frac{R_2 - 2R_1}{(R_1 R_2 - R_1^2)^2}\, R_2 V \stackrel{!}{=} 0$$

We obtain for R_1 and E_{1min}:

$$R_1 = R_2/2 \quad \text{and} \quad E_{1min} = 4\,V/R_2 \qquad (2.3\text{-}15)$$

Another example for optimization problems is the *maximization* of the *capacitively stored energy* $W = \frac{1}{2} C V^2$ by variation of the inner radius R_1 for a given outer radius R_2 and an permissible field strength E_{bd}. This is particularly important for capacitors in which the greatest quantity of energy is to be stored for given dimensions.

The capacitively stored energy is calculated according to Eq. (2.3-12) and (2.3-14)

$$W = \tfrac{1}{2}\, C\, V^2$$

$$W = \tfrac{1}{2}\left[4\pi\varepsilon R_1 R_2 (R_2 - R_1)^{-1}\right]\left[E_{bd}\,(R_2 - R_1)\,R_1/R_2\right]^2$$

$$W = E_{bd}^2\, 2\pi\varepsilon\,(R_2 - R_1)\,R_1^3/R_2$$

$$W = E_{bd}^2\, 2\pi\varepsilon\,(R_2 R_1^3 - R_1^4)/R_2$$

In the extreme cases $R_1 \to 0$ and $R_1 \to R_2$ the field energy is minimal, i.e. $W \to 0$. The radius R_1 for *maximum field energy* is determined, if the derivate of W with respect to the variable R_1 is set to zero:

$$\partial W/\partial R_1 = E_{bd}^2\, 2\pi\varepsilon\,(R_2\, 3R_1^2 - 4R_1^3)/R_2 = 0$$

The result for R_1 is

$$R_1 = R_2\, 3/4. \qquad (2.3\text{-}16)$$

For many applications in high voltage engineering the electric field can be regarded as spherically symmetric, either by approximation or in limited field regions, Figure 2.3-3.

2.3.1.3 Cylindrically Symmetric Fields

The so called *"cylindrical capacitor"* consists of concentric (coaxial) cylinders with the radii R_1 and R_2, Figure 2.3-4. To begin with, field

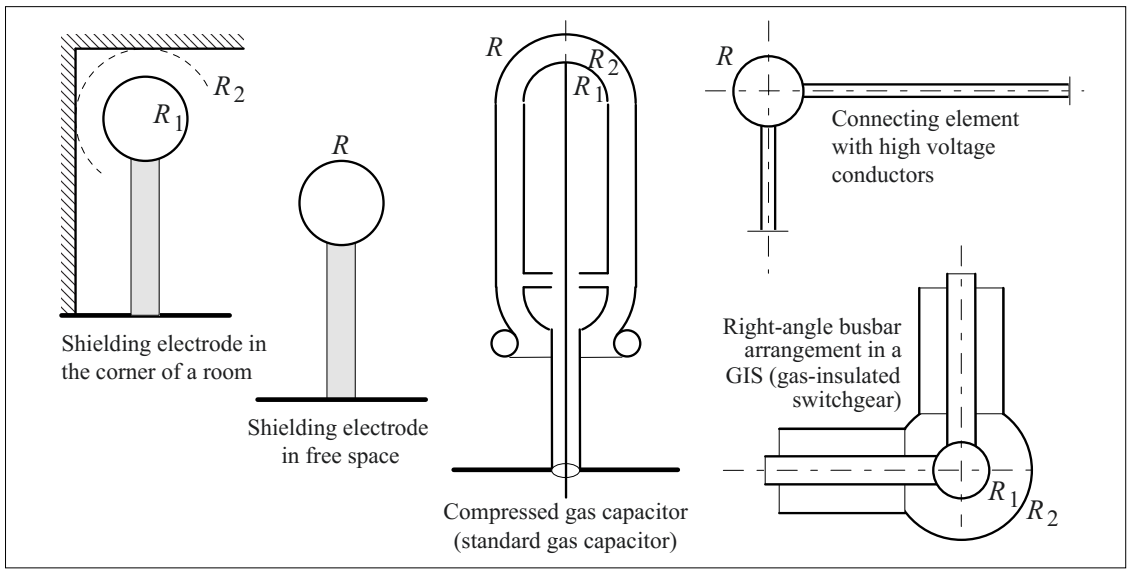

Figure 2.3-3: Examples for spherically and cylindrically symmetric fields in HV engineering (approximations).

distortions at the edges of the cylinders are neglected, i.e. it is assumed that there is a two-dimensional field, which does not change along the axis of the cylinders.

Calculation of *field strengths* is performed in *five steps*, as in the case of the spherically symmetric field:

For the application of Gauss's law, Eq. (2.3-1), *Step 1*, a closed surface is defined, completely enclosing the inner cylinder. It consists of a cylindrical lateral surface with the radius r and the cylinder length z, and two plane end areas, Figure 2.3-4.

The lines of dielectric displacement density $\boldsymbol{D}$ are nearly orthogonal to the vectors of the area elements $\mathrm{d}\boldsymbol{A}$ of the end areas. For the integration over the total closed surface, the contribution of the end areas can therefore be neglected. On the lateral surface $\boldsymbol{D}$ and $\mathrm{d}\boldsymbol{A}$ are in

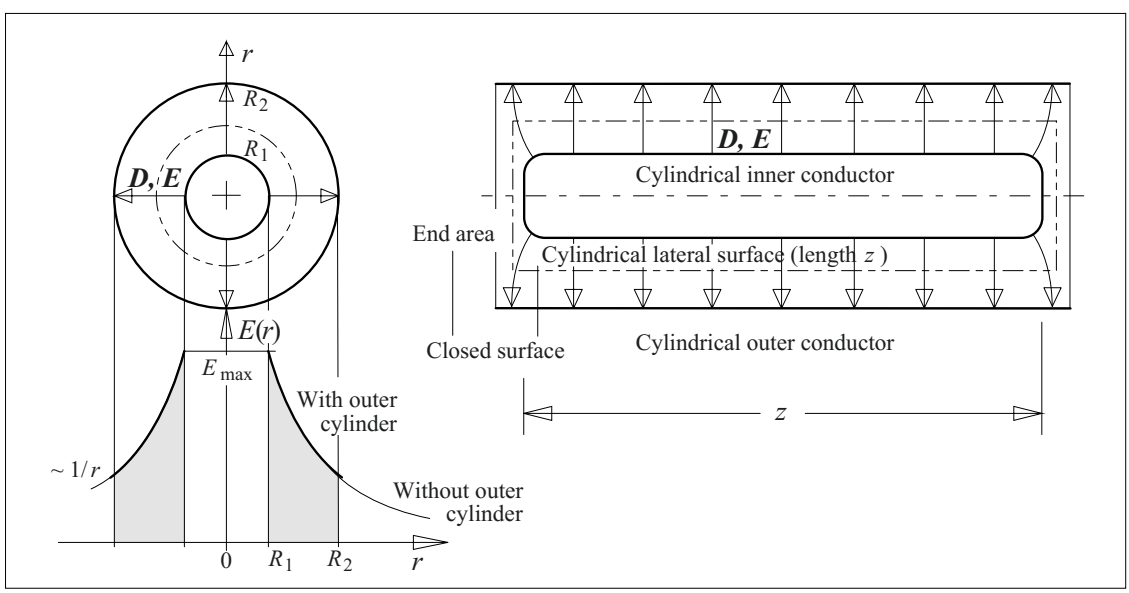

Figure 2.3-4: Cylindrically symmetric electrode configuration (top) with field strength profile (bottom).

parallel, so the vector product can be replaced by the scalar product of the magnitudes. $D(r)$ is nearly constant on the lateral surface and can be brought out from under the integral sign. The remaining integration of $\mathrm{d}\boldsymbol{A}$ over the lateral surface gives the surface area value $A = 2\pi r\, z$

$$Q = D(r) \iint \mathrm{d}A = D(r)\, A = \varepsilon E(r)\, 2\pi r\, z$$

The magnitude of the electric field strength decreases with the radius r proportional to $1/r$:

$$E(r) = Q / (2\pi\varepsilon\, z\, r) \qquad (2.3\text{-}17)$$

The integration of field strength $E(r)$ from the inner to the outer cylinder according to *Step 2* and Eq. (2.3-3) with $V_{12} = V$ gives

$$V = \frac{Q}{2\pi\varepsilon\, z} \ln \frac{R_2}{R_1}\,, \qquad (2.3\text{-}18)$$

i.e.

$$Q = \frac{2\pi\varepsilon\, z}{\ln \dfrac{R_2}{R_1}}\, V\,. \qquad (2.3\text{-}19)$$

The *capacitance* of the cylindrical capacitor is $C = Q/U$ *(Step 3)*:

$$C = \frac{2\pi\varepsilon\, z}{\ln \dfrac{R_2}{R_1}} \qquad (2.3\text{-}20)$$

In *Step 4* the *field strength profile* between inner and outer cylinders is evaluated from Eq. (2.3-17) and (2.3-19):

$$E(r) = \frac{V}{r \ln \dfrac{R_2}{R_1}} \qquad (2.3\text{-}21)$$

The area under the field strength curve equals the voltage (potential difference) between the cylinders, which is the integral of $E(r)$ in radial direction, Figure 2.3-4.

In *step 5* the *maximum field strength* is derived from Eq. (2.3-21) for the radius $r = R_1$:

$$E_{\max} = E_1 = \frac{V}{R_1 \ln \dfrac{R_2}{R_1}} \qquad (2.3\text{-}22)$$

Also for cylindrically symmetric fields we find: the smaller the radius of curvature R_1 of the inner cylinder the higher the electric field strength at the inner cylinder will be, Eq. (2.3-22). However, the increase of field strength is smaller than in the spherically symmetric field. **Small radii are also to be avoided in cylindrically symmetric fields** in order to stay below the breakdown strength of the adjacent dielectric materials.

Eq. (2.3-22) gives the maximum field strength for the ideal cylindrically symmetric field and not the field strength at the *edges of the cylinders.* Significant *field stress enhancements* and *high local fields* can occur there depending on the electrode profiles at the electrode edges.

Note: It is natural to look at a *"cylindrical conductor in free space"*, as was done for the "sphere in free space", i.e. the extreme case with the counter-electrode with the negative counter-charges is assumed to be infinitely far away, i.e. $R_2 \to \infty$. If the field strength is integrated according to Eq. (2.3-17), the result is an infinite voltage (potential difference), which can directly be seen from Eq. (2.3-18). For a finite potential difference and $R_2 \to \infty$ the field strength will be zero, see Eq. (2.3-21).

Therefore it is always necessary to consider an *outer cylinder with a finite radius* $R_2 < \infty$ in a cylindrically symmetrical field.

The field between two cylinders approaches the field of an ideal *"line charge"* for the extreme case $R_1 \to 0$ and $R_2 \to \infty$. This theoretical extreme case is important for field calculations with the equivalent charge method together as with "point charges" and other equivalent charges (Section 2.3.5). Nevertheless, the counter-charges are not located infinitely far away, but are also line charges at finite distances.

From the calculated field strengths *optimization problems* can be solved by means of *extreme value determination*:

For a given outer radius R_2 the inner radius R_1 shall be chosen so that the *maximum field strength* (*surface/edge field strength*) E_1 will be minimal.

In the extreme cases $R_1 \to 0$ and $R_1 \to R_2$, there are infinitely high surface/edge field strengths E_1. The *optimum inner radius* R_1 for

minimum surface field strength E_1 is between 0 and R_2 therefore, and it is determined from Eq. (2.3-22), if the derivate of E_1 with respect to the variable R_1 is set to zero.

During the differentiation, the rules for derivate of a fraction have to be applied to the whole fraction at first. Additionally, the rules for the derivate of a product have to be applied for the differentiation of the denominator [6].

$$\frac{\partial E_{\max}}{\partial R_1} = V \frac{0 - [\ln\frac{R_2}{R_1} + R_1 \frac{R_1}{R_2} \frac{-R_2}{R_1^2}]}{(R_1 \ln\frac{R_2}{R_1})^2}$$

$$\frac{\partial E_{\max}}{\partial R_1} = V \frac{-[\ln\frac{R_2}{R_1} - 1]}{(R_1 \ln\frac{R_2}{R_1})^2} \stackrel{!}{=} 0$$

R_1 and $E_{1\min}$ are derived from Eq. (2.3-22):

$$R_1 = R_2/\mathrm{e} \quad \text{and} \quad E_{1\min} = \mathrm{e}\, V/R_2 \tag{2.3-23}$$

Note: The irrational number e = 2.71828... is the *base of the natural logarithm* and it is occasionally called *"Euler number"* or *"Napier's constant"*.

Another example for optimization problems is the *maximization* of the *capacitively stored energy* $W = \frac{1}{2} C V^2$ by variation of the inner radius R_1 for a given outer radius R_2 and a permissible field strength E_{bd}. This is particularly important for capacitors in which the greatest possible quantity of energy is to be stored for given dimensions.

The maximum stored energy is calculated according to Eq. (2.3-20) and (2.3-22)

$$W = \frac{1}{2} C V^2$$

$$W = \frac{1}{2} [2\pi\varepsilon z / \ln(R_2/R_1)] [E_{\mathrm{bd}} R_1 \ln(R_2/R_1)]^2$$

$$W = E_{\mathrm{bd}}^2 \pi\varepsilon z R_1^2 \ln(R_2/R_1).$$

In the extreme cases $R_1 \to 0$ and $R_1 \to R_2$ the field energy is minimal, i.e. $W \to 0$. The radius R_1 for *maximum field energy* is determined, if the derivate of W with respect to the variable R_1 is set to zero:

$$\begin{aligned} \partial W/\partial R_1 &= E_{\mathrm{bd}}^2 \pi\varepsilon z \\ &\quad \cdot[2R_1 \ln(R_2/R_1) + R_1^2 (R_1/R_2)(-R_2/R_1^2)] \\ &= E_{\mathrm{bd}}^2 \pi\varepsilon z R_1 [2 \ln(R_2/R_1) - 1] \\ &= 0 \end{aligned}$$

The result for R_1 is

$$R_1 = R_2 / \mathrm{e}^{1/2}. \tag{2.3-24}$$

For many *applications* in high voltage engineering the electric field can be regarded as cylindrically symmetric, either by approximation or in limited field regions. Some examples are already shown in Figure 2.3-3. Cylindrically symmetric fields also occur in high-voltage cables, in gas insulated switchgears, in bushings and close to cylindrical conductors.

Example: Thin wire

The field in the vicinity of a thin wire shall be approximated by a cylindrically symmetric field with R_1 = 1 mm and R_2 = 1 m. What is the expected peak voltage $\hat{V}$ for the inception of electrical discharges in air ($\hat{E}_{\mathrm{i}}$ = 4 kV/mm)?

From Eq. (2.3-22) it is concluded that

$$\hat{V} = \hat{E}_{\max} R_1 \ln(R_2/R_1) \quad = 27.6 \text{ kV}$$

Note: High field strengths at thin conductors with very small radii only occur in a small volume close to the conductor. Inception field strength is therefore significantly higher than the commonly used value $\hat{E}_{\mathrm{i}}$ = 3 kV/mm = 30 kV/cm which is valid for air in the centimeter range, Figure 3.2-15. Discharge inception cannot be described exactly by a constant inception field strength, Chapter 3.

Example: Tubular conductor and cable

The *diameters of high-voltage conductors* with *coaxial outer conductors* shall be sized for use in **air**-insulated tubular conductors ($\hat{E}_{\mathrm{bd}}$ = 30 kV/cm, ε_{r} = 1), in **oil**-insulated tubular conductors ($\hat{E}_{\mathrm{bd}}$ = 150 kV/cm, ε_{r} = 2.2) and in **thermoplastic**-insulated cables (polyethylene, $\hat{E}_{\mathrm{bd}}$ = 450 kV/cm, ε_{r} = 2.2). Peak voltages shall be $\hat{V}$ = 10 kV/ 100 kV/ 1 MV; 2/3 of the breakdown strength must not be exceeded and the outer diameter shall be as small as possible.

The smallest outer diameters are achieved, if the ratio of the radii R_2/R_1 = e is chosen such that the maximum field strength E_1 is minimal. With $\hat{E}_{1\min} = 0.67\, \hat{E}_{\mathrm{bd}}$ we get

$$D_2 = 2\,R_2 = 2\,\mathrm{e}\,\hat{U}/(0.67\,\hat{E}_{\mathrm{bd}}) \quad \text{and}$$

$$D_1 = 2\,R_1 = 2\,\hat{U}/(0.67\,\hat{E}_{\mathrm{bd}}).$$

Note: The same result is obtained by extreme value determination, i.e. if Eq. (2.3-22) is solved for R_2, and if the derivate of R_2 with respect to R_1 is set to zero in order to determine the minimum.

Voltage	$\hat{V}$	**10 kV**	**100 kV**	**1 MV**
Air:	D_2	**2.7 cm**	**27 cm**	**2.7 m**
	D_1	1 cm	10 cm	1 m
	C'	56 pF/m	56 pF/m	56 pF/m
Insulating Oil:	D_2	**5.4 mm**	**5.4 cm**	**54cm**
	D_1	2 mm	2 cm	20 cm
	C'	122 pF/m	122 pF/m	122 pF/m
Poly-ethylene:	D_2	**1.8 mm**	**1.8 cm**	**18 cm**
	D_1	0.7 mm	0.7 cm	7 cm
	C'	122 pF/m	122 pF/m	122 pF/m

Note: The result shows that the application of electrically strong insulating materials (insulating oil, SF_6, polyethylene) allows very *compact designs* in comparison with air. The assumption of a constant value for $\hat{E}_{\mathrm{bd}}$ neglects that the electric strength of insulating oil and polyethylene decreases with increasing insulation thickness (*"volume effect"*, *"size effect"*). The mentioned voltages and field strengths are short-term strengths, as may be used for designs with respect to *short-term voltage tests*. Permissible *service voltages and field strengths* are significantly lower, especially for oil and polyethylene (Section 2.2.2 to 2.2.4). The *capacitance* per unit length C' only depends on the permittivity ε_r, because the ratio of radii is the same in all cases.

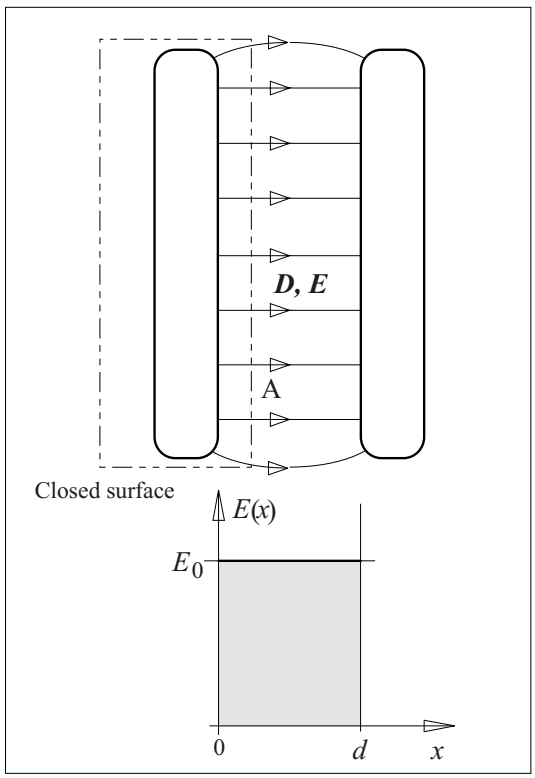

Figure 2.3-5: Uniform electric field in a parallel-plate capacitor (approximation without consideration of field distortions at the electrode edges.

2.3.1.4 Uniform (Homogeneous) Fields

Between two parallel plane electrodes at a distance d there is a uniform electric field with the constant field strength $E = V/d$ (*"parallel-plate capacitor"*). In the first instance, field distortions at the electrode edges shall be neglected. Even in this simple case, the calculation of field strength is performed *in the five steps* mentioned above, just in order to illustrate the method:

For the application of Gauss's law (eq. (2.3-1), *Step 1*) a closed surface is defined, enclosing one of the electrodes completely. It consists of a surface A between the plane parts of the electrodes and of additional faces in the outer parts of the field volume, which extend surface A to form a closed surface, Figure 2.3-5.

The outer faces are only penetrated by a small displacement flux $\iint \boldsymbol{D}\,\mathrm{d}\boldsymbol{A}$; its contribution to the total flux over the closed surface is therefore neglected.

Between the electrodes, $\boldsymbol{D}$ and $\mathrm{d}\boldsymbol{A}$ are in parallel, so the product of the vectors can be replaced by the scalar product of the magnitudes. D is nearly constant on the surface A and can be brought out from under the integral sign. The remaining integration of $\mathrm{d}A$ over the surface A gives the area of the surface A itself:

$$Q = D \iint \mathrm{d}A = D\,A = \varepsilon\,E\,A$$

Therefore, the magnitude of the electric field strength E is constant for all values of x between the electrodes:

$$E(x) = Q/(\varepsilon\,A) = E_0 = \text{const.} \qquad (2.3\text{-}25)$$

The integration of field strength $E(x)$ according to Eq. (2.3-3) (*Step 2*) from one electrode to the other gives

$$V = E_0\, d = Q\, d/(\varepsilon A)\,.$$

This means

$$Q = \varepsilon\, A\, V/d\,. \qquad (2.3\text{-}26)$$

The *capacitance* of the parallel-plate capacitor follows from $C = Q/V$ (*Step 3*):

$$C = \varepsilon A\,/d \qquad (2.3\text{-}27)$$

The *field strength curve* between the electrodes is calculated from Eq. (2.3-25) and (2.3-26), *Step 4*:

$$E(x) = E_0 = V/d = \text{const.} \qquad (2.3\text{-}28)$$

The area under the field strength curve equals the voltage (potential difference) between the electrodes which is the integral of $E(x)$ in the x-direction, Figure 2.3-5.

The indication of *maximum field strength* (*Step 5*) is unnecessary for the uniform field. Nevertheless, field stress enhancements can occur at strongly curved edges of the electrodes (see also Figure 2.3-8 and 2.3-9).

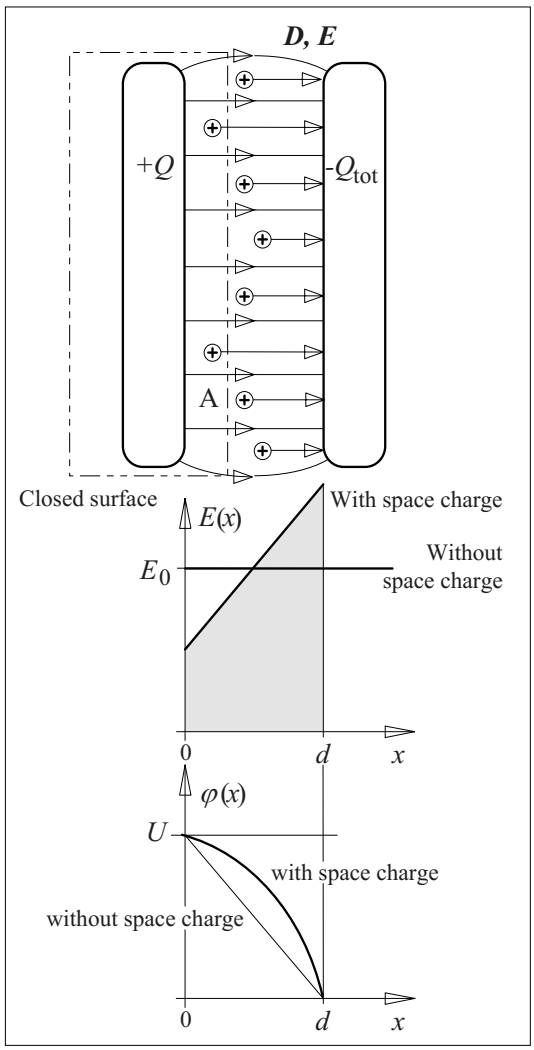

Figure 2.3-6: Space charges in the dielectric of a parallel plate capacitor (see fig. 2.3-5).

2.3.1.5 Field Distortions by Space Charges

Electric discharges in gaseous dielectrics can generate "*space charge clouds"* which strongly modify („distort") the local electric field. Space charges can also be generated in liquid and solid insulating materials under the influence of electrical stresses.

Example: Space charge in a parallel-plate capacitor

The influence of space charges and the basic calculation method are explained for the example of a uniform field with constant and positive space charge density η. (volume density of charge). The counter-charges are assumed to be on the negative electrode, Figure 2.3-6:

During the application of Gauss's law (eq. (2.3-1), *Step 1*) it has to be considered that the total enclosed charge within the closed surface is dependent on the actual position of the surface between the electrodes. The total charge consists of the sum of the charges on the enclosed electrode and the (space) charges within the enclosed insulating volume:

$$\begin{aligned} Q(x) &= Q + \iiint \eta\, \mathrm{d}V \\ &= Q + \eta\, A\, x \\ &\overset{!}{=} D \iint \mathrm{d}A \qquad = D\, A \;= \varepsilon\, E\, A. \end{aligned}$$

This means that the magnitude of the *electric field strength E* between the electrodes is *no longer constant*; it increases linearly with x and it becomes maximal at the counter-electrode at $x = d$, Figure 2.3-6:

$$E(x) = Q(x)/(\varepsilon A) = Q/(\varepsilon A) + x\, \eta/\varepsilon \qquad (2.3\text{-}29)$$

The further calculation can be performed in analogy to the steps described above, but it is to be considered that the total stored charge Q_{tot} consists of the positive

charge Q *on the electrode* and the positive charge $\iiint \eta \, dV = d\,A\,\eta$ stored *in the dielectric.*

$$Q_{tot} = Q + d \cdot A \cdot \eta$$

Thereby the *capacitance* $C = Q_{tot}/V$ is increased. The *potential* no longer decreases linearly with x, but is described by a second order polynomial, which can be derived by the integration of Eq. (2.3-29), Figure 2.3-6.

In **non-uniform fields**, e.g. in spherically or cylindrically symmetric fields, space charges can *increase or decrease the (geometric) inhomogeneity* (non-uniformity) of the field, depending on polarity. Thereby the discharge behavior in non-uniform fields is strongly influenced (*"polarity effect"*, Section 3.2.5.2).

Note: Especially in the *insulation of a capacitor* consisting of layers with different materials (Section 2.4), the space charges stored in the material and the surface charges at the interfaces can cause a dangerous *"recharging"* of the electrodes and a *"recovery voltage"*, even after a temporary short circuit of the electrodes (Section 2.4.4.3). Therefore, capacitors must be **short-circuited** *permanently*.

2.3.2 Analytic Solution of Poisson's Equation

The continuity of the displacement density is described by Eq. (2.3-1) in *integral* form. The equivalent in differential form is

$$\text{div}\, \boldsymbol{D} = \eta. \qquad (2.3\text{-}30)$$

According to Eq. (2.1-8) the field strength is

$$\boldsymbol{E} = -\,\text{grad}\,\varphi$$

and **Poisson's Equation** can be derived. It can be used for **electrostatic (irrotational) fields**:

$$\text{div grad}\,\varphi = \nabla^2\,\varphi = \Delta\,\varphi = -\,\eta/\varepsilon \qquad (2.3\text{-}31)$$

Note: Poisson's Equation is called **Laplace's Equation** for $\eta = 0$.

The *differential operators* div (divergence), grad (gradient), ∇ (nabla, Hamilton's operator, del operator) and Δ (delta, Laplace's operator) are expressed differently depending on the *coordinate system* (Cartesian, cylindrical and spherical coordinates) [2], [3], [6]. Poisson's Equation is written

in *Cartesian coordinates* (x, y, z)

$$\Delta\varphi = \frac{\partial^2\varphi}{\partial x^2} + \frac{\partial^2\varphi}{\partial y^2} + \frac{\partial^2\varphi}{\partial z^2} = -\,\eta/\varepsilon\,, \qquad (2.3\text{-}32)$$

in *cylindrical coordinates* (r, α, z)

$$\Delta\varphi = \frac{1}{r}\,\frac{\partial}{\partial r}\left(r\,\frac{\partial\varphi}{\partial r}\right) + \frac{1}{r^2}\,\frac{\partial^2\varphi}{\partial\alpha^2} + \frac{\partial^2\varphi}{\partial z^2}$$

$$= -\,\eta/\varepsilon \qquad (2.3\text{-}33)$$

and in *spherical coordinates* (r, α, ϑ)

$$\Delta\varphi = \frac{1}{r^2}\,\frac{\partial}{\partial r}\left(r^2\,\frac{\partial\varphi}{\partial r}\right) + \frac{1}{r^2\sin\vartheta}\,\frac{\partial}{\partial\vartheta}\left(\sin\vartheta\,\frac{\partial\varphi}{\partial\vartheta}\right) + \frac{1}{r^2\sin^2\vartheta}\,\frac{\partial^2\varphi}{\partial\alpha^2}$$

$$= -\,\eta/\varepsilon \qquad (2.3\text{-}34)$$

Note: The derivation of Eq. (2.3-32) to (-34) is omitted and referred to the literature [2], [3], [6].

The *application of Poisson's Equation* shall be exemplified for the uniform field of a parallel-plate capacitor without space charges, Figure 2.3-5. Nevertheless, all the other cases in Section 2.3.1 can be calculated.

Example: Uniform field without space charges

Step 1: At first, *Poisson's Equation* is *simplified* to *Laplace's Equation* ($\eta = 0$) which is only dependent on the variable x. Naturally, Cartesian coordinates are used here, with $\varphi(x,y,z) = \varphi(x)$. Now Eq. (2.3-32) is

$$\Delta\varphi = \partial^2\varphi/\partial x^2 = -\,\eta/\varepsilon = 0\,.$$

Step 2: The simplified *differential equation is solved in general form*, by two integrations in this case:

$$\partial\varphi/\partial x = k_1 \quad \text{und} \quad \varphi(x) = k_1\,x + k_2\,.$$

Step 3: The integration constants k_1 and k_2 are determined from the *boundary conditions*. From

$\varphi(x=0) = V$ we obtain $V = 0 + k_2$ and from

$\varphi(x=d) = 0$ we obtain $0 = k_1 d + k_2$.

With the solutions $k_2 = V$ and $k_1 = -V/d$ the potential is

$$\varphi(x) = V\,(1 - x/d)$$

Step 4: For a given potential distribution, the electric field is defined unequivocally. The vector of the electric field strength $\boldsymbol{E}$ can be obtained by the *calculation of the gradient* according to Eq. (2.1-8). In a uniform field with Cartesian (x, y, z)-coordinates the result

$$\boldsymbol{E} = \text{-grad}\ \varphi = \{-\partial\varphi/\partial x, 0, 0\} = \{U/d, 0, 0\}\ .$$

gives a constant magnitude of the field strength

$$E = V/d = E_0 = \text{const.} \qquad \text{q.e.d.}$$

Note: If Poisson's Equation is evaluated in *cylindrical or spherical coordinates*, the calculation of the gradient (the field vector resp.) must also be performed in cylindrical or spherical coordinates, Eq. (2.1-8), [2], [3], [6]. According to the steps described above, the symmetries of the configuration should be used for the *simplification* of Poisson's Equation. The *general solution of the differential equation* gives a general expression for the *potential* distribution and the constants of integration have to be determined by means of the *boundary conditions*. The electrostatic field strength is derived from the potential distribution by calculation of the *gradient*.

2.3.3 Graphical Field Mapping (for Plane Fields)

Normally, technical field configurations in high voltage engineering differ more or less from the basic configurations discussed in the former chapters. Therefore it is helpful to draw qualitative distributions of *field lines and equipotential lines* graphically, i.e. free-hand, just by approximation and without any complicated calculations.

If some *drawing rules* are regarded, a **field map or field pattern** for a *plane (two-dimensional) configuration* can be created. It gives a qualitative impression of the electrical stress, but with appropriate care it is often also possible to roughly determine field strengths and capacitances.

Graphical field mapping gives a good impression of the distribution of field lines and equipotential lines. Therefore, it can be used to support basic physical understanding and to perform plausibility checks of numerically calculated field distributions, i.e. to exclude coarse calculation mistakes.

The **value of the graphical mapping** lies in the *rapid creation of a qualitative overview map,* which cannot replace a numerical calculation, but which can prepare for and supplement it. Furthermore, graphical mapping requires a thorough analysis of the field geometry. Thereby *a valuable and deep understanding* of the physical character of the electrical stress is created.

The **drawing rules** are deduced from the properties of field lines and equipotential lines. (Frequently just referred to as "potential lines"). At first, a *plane, two-dimensional field* is discussed, which does not change in the third dimension and can be drawn in the drawing plane, Figure 2.3-7:

1.) Field lines and equipotential lines are **orthogonal** (**rectangular** to each other).

2.) **Electrode surfaces** are equipotential surfaces (normally reference and high voltage potentials are 0 % and 100 %).

3.) Field lines and electrode surfaces are orthogonal (deduced from 1. and 2.).

4.) The distance a between two equipotential lines is always related to the same potential difference ΔV. The distance b between two field lines (or displacement lines) is always related to the same charge ΔQ on the electrodes, i.e. to the same displacement flux. From this it follows that the element capacitance $\Delta C = \Delta Q/\Delta V$, which is related to every "box" or element with a length z, is equal for all "boxes" (elements) on the field map:

$$\Delta C = \Delta Q/\Delta V = \varepsilon\, z\, b/a = \text{const.} \qquad (2.3\text{-}35)$$

This means that the **aspect ratio** b/a is equal for all elements:

$$b/a = \text{const.} \qquad (2.3\text{-}36)$$

The best way for field mapping is to draw *square elements*, i.e. if $b/a = 1$ is chosen. The aspect ratio is correct, if the four sides

of the square element touch an **inscribed circle**, Figure 2.3-7.

Traditional tools of graphic field mapping are *blank paper, pencil and eraser (rubber)*; also good choices are simple graphics programs which make it easier to improve the map iteratively.

It is advisable to *begin* with the drawing in an area where the *potential distribution is known*. The *electrode* contours give an orientation for the distribution of the *equipotential* lines.

As a first approximation, *field lines* are drawn orthogonally to the equipotential lines and the electrode contours. The aspect ratios of the resulting boxes have to be constant according to Eq. (2.3-36). *Irregularities* with respect to the *drawing rules* (1. to 4.) indicate how the actual map has to be *improved* by repositioning of field lines and equipotential lines.

In practice there will often need to be a greater number of *iteration steps* in order to achieve a satisfactory result.

The graphical method of field mapping shall be explained for the practically important example of the fields at the edges of a parallel-plate capacitor, Figure 2.3-8 and 2.3-9:

Example: Edge field of a parallel-plate capacitor

Step 1 (Figure 2.3-8a): At first, the known *potential distribution* in the uniform or known part of the field is drawn (1). The further course of the *equipotential lines* is approximately orientated with the given electrode contours (2).

Note: It is advisable, to start with a small number of equipotential lines only (e.g. lines for 0 %, 25 %, 50 % 75 % and 100 %). The completed map can be further refined by interpolation if necessary.

Step 2 (Figure 2.3-8a): The map is supplemented by *field lines* rectangular to the equipotential lines, with the aspect ratio $b/a = 1$. It is advisable to proceed along an electrode contour (e.g. on the high voltage side).

The *inscription of circles* shows whether the aspect ratios of the boxes differ significantly from the desired value 1 in cases (3).

Step 3 (Figure 2.3-8b): Now the *initial map is improved*. In this example the distance between the 25 %-line and the lower electrode is increased (4). The 75 %-line is shifted closer to the upper electrode (inner side and edge), the distance to the outer side is increased considerably (5). It must be taken in to account that the field strength in the electrode edge region must decrease from the upper electrode towards the lower electrode, i.e. the distance of the equipotential lines increases.

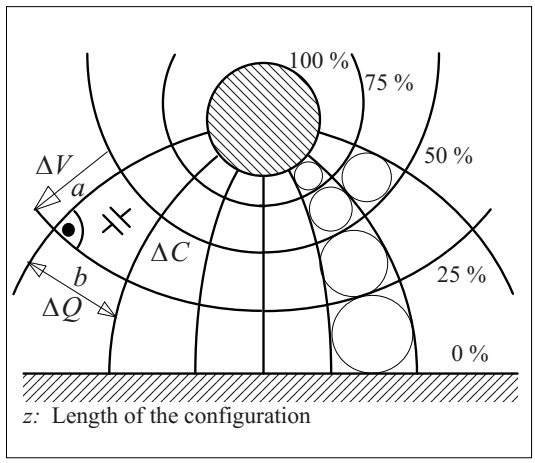

Figure 2.3-7: Graphic mapping of field lines and equipotential lines for two-dimensional fields.

A *check* of the aspect ratios and the angles shows that the field map still needs to be improved.

Step 4 (Figure 2.3-8c): The final field pattern is obtained by *iterative approximations* with respect to the drawing rules.

In the given example it is advisable to start with the inscribing of circles in the region with the uniform field and to proceed towards the regions with non-uniform fields (6). Position and direction of the equipotential lines and the field lines and the diameters of the inscribed circles have to be adjusted iteratively and *step-by-step*.

The *evaluation* of a completed field pattern provides approximate information about the *location and magnitude of maximum field strength*, the field strength *profiles* along contours and the *capacitance* to be assigned to the electric field.

The field strength for any element of the field pattern is

$$E \approx \Delta V/a \,. \qquad (2.3\text{-}37)$$

ΔV is the potential difference and a is the distance between two equipotential lines for the considered element ("box"). E is the medium field strength in the element ("box"), its accuracy depends on the accuracy of the drawing.

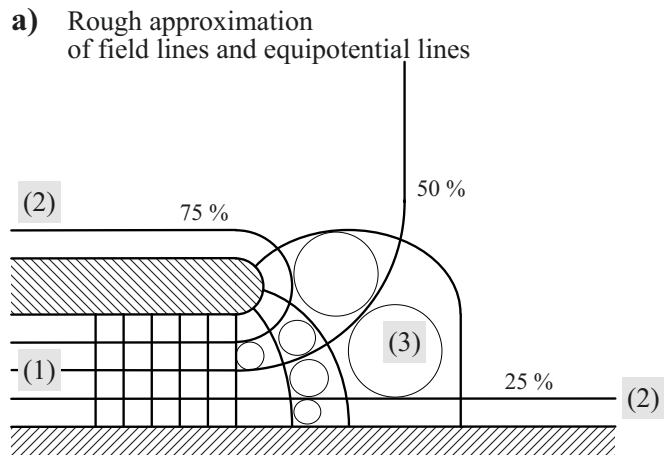

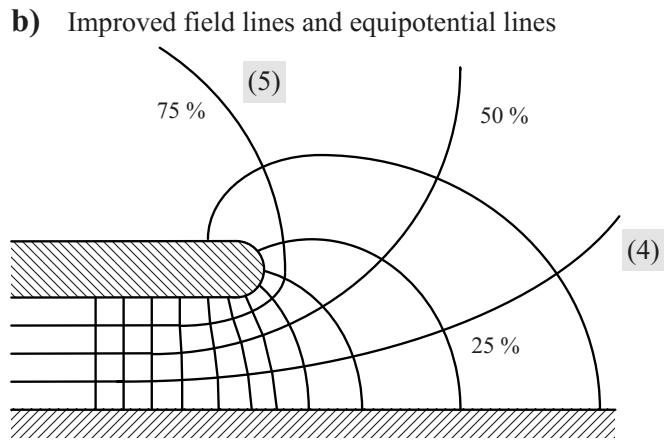

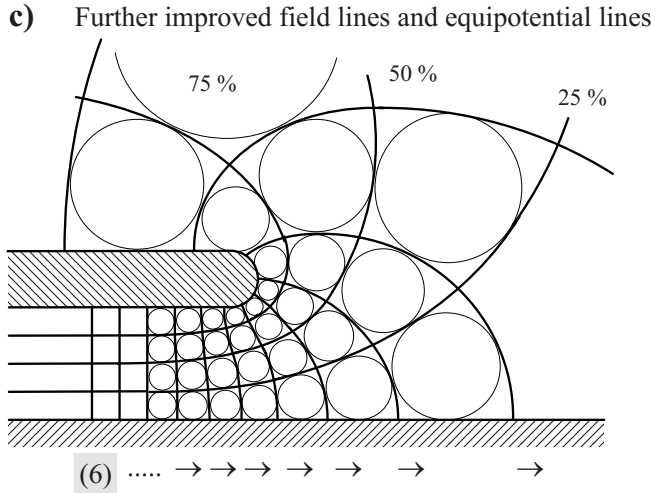

Figure 2.3-8:

Graphical mapping of field lines and equipotential lines for the two-dimensional (plane) edge field of a parallel-plate capacitor in different stages of iteration:

a) A first rough approximation which does not match the drawing rules in many items.

b) Improved map according to the mismatch in a former step.

c) Further improved map generally matching the drawing rules.

For qualitative conclusions, iteration c) is often sufficient.

Field strengths, which are taken from graphic field patterns, have to be *handled with care*. In general, accurate quantitative values require a numerical or an analytical analysis if possible.

The whole field volume can be regarded as a series and parallel connection of equal element capacitances ΔC, Figure 2.3-7. The number of parallel branches n_p and the number of series connections n_s can be counted from the field map. According to Eq. (2.3-35) and with b/a = 1 the total capacitance is

$$C_{tot} = \Delta C\, n_p/n_s = \varepsilon z\, n_p/n_s \qquad (2.3\text{-}38)$$

Often the determination of capacitance is possible with less inaccuracy. Capacitance is an integral quantity and Graphical inaccuracies compensate each other as a result of the integral view of the entire field space.

Example: Edge field of a parallel-plate capacitor (continued)

Step 5 (Figure 2.3-8c and 2.3-9): The point of maximum field strength is at the inner side of the electrode curvature. The magnitude of maximum field strength is

$$E_{max} \approx \Delta V/a_{min} = 0.25\, V/a_{min}.$$

The minimum distance a_{min} between the 100 % and the 75 % equipotential line is nearly half that in the uniform region of the field. Therefore, the field stress enhancement factor is approximately 2. Indeed, the real maximum field strength will be somewhat higher because the field strength is not constant within the smallest square element, and the measurement according to Eq. (2.3-37) gives a *medium value* for the element only. A field strength profile along the 100 % electrode contour can be determined from the field pattern with Eq. (2.3-37), Figure 2.3-9.

The capacitance of the ideal parallel-plate capacitor $C_0 = \varepsilon A/d$ has to be increased by an additional edge-field capacitance C_{edge}: $C_{tot} = C_0 + C_{edge}$. C_{edge} is calculated with Eq. (2.3-38) for z = 1 m in air and for the region which is displayed in Figure 2.3-8c (i.e. just the region with the "circles", but only at the curvature and at the outer side):

$$C_{edge} \approx \Delta C\, n_p/n_r = \varepsilon z\, n_p/n_r = \varepsilon z\, 5/4 \approx 11 \text{ pF}.$$

The described graphical method can be used for plane two-dimensional fields. Nevertheless, it can also be applied to **rotationally symmetric fields**, which are two-dimensional as well. For the example in Figure 2.3-7, it is now assumed that there is a horizontal axis of rotation at the lower line in the Figure. Thereby the rod-shaped elements ΔC with the length z are transformed into circular, ring-shaped elements with the circumference $2\pi r$:

$$\Delta C = \varepsilon\, 2\pi r\, b/a$$

Because of $\Delta C = \Delta Q/\Delta V$ = const., the aspect ratio of the elements is

$$b/a = \text{const.}/r\,. \qquad (2.3\text{-}39)$$

Therefore, the aspect ratio b/a has to be adjusted *depending on* r, proportional to $1/r$. Thus, the accurate drawing of a field image is much more difficult.

Graphical field mapping can also be applied to **configurations with several dielectrics** (Section 2.4). Additionally to the drawing rules described above, it is necessary to consider the *"refraction laws"* for field lines and equipotential lines at the interfaces between insulating materials, Figure 2.4-10 and 2.4-25.

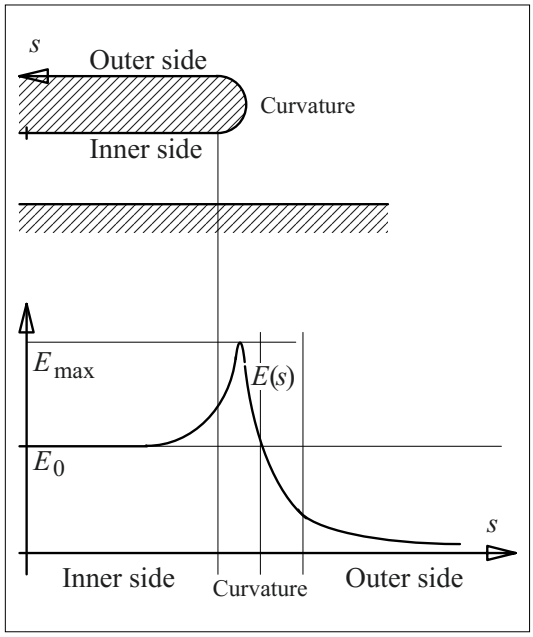

Figure 2.3-9: Qualitative profile of field strength magnitude along the 100 % electrode contour (coordinate s).

For **three-dimensional fields** only rough qualitative drawings are possible without any quantitative information. In general three-dimensional field lines do not lie in a drawing plane, they penetrate it normally. Therefore it is not possible to draw the field lines in a plane. A *two-dimensional field map* has to be restricted to the *equipotential lines*, which are the intersecting lines between the equipotential surface and the drawing plane. Meaningful field patterns can only be calculated with numerical field calculations (Section 2.5).

Nevertheless, *rough sketches* are valuable to support the engineer's imagination and physical understanding, but they must not be overestimated.

2.3.4 Conformal Mapping (for Plane Fields)

Conformal mapping is a method for the *analytic* calculation of some important t*wo-dimensional high-voltage fields*.

Note: Conformal mapping was of high importance before numerical field calculation methods were available. Today it is of *historical* interest mainly: There are only a few important field configurations still based on conformal mapping.

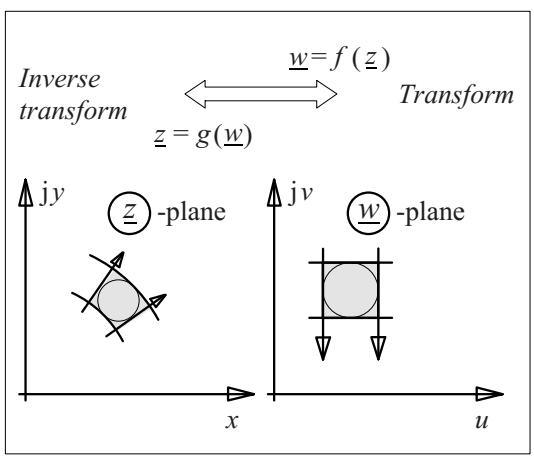

Figure 2.3-10: Conformal mapping of field lines and equipotential lines from the complex z-plane into the w-plane.

The basic idea of conformal mapping is to *transform* the *x,y*-plane (together with a given complicated electrode configuration) into a *u,v*-plane, where the electrode configuration can be *calculated easily*. Afterwards the solution is transformed inversely, back into the *x,y*-plane, Figure 2.3-10.

For this purpose, the geometric *x,y*-plane is regarded as a complex $\underline{z}$-plane ($\underline{z} = x + \mathrm{j}y$) and the geometric *u,v*-plane as a complex $\underline{w}$-plane ($\underline{w} = u + \mathrm{j}v$). Thereby, the two geometric axes are replaced by a real and an imaginary axis. The so called **conformal mapping** is performed by a complex function

$$\underline{w} = f(\underline{z})$$

or

$$u + \mathrm{j}v = f(x + \mathrm{j}y).$$

It maps the points from the $\underline{z}$-plane onto the $\underline{w}$-plane. The complex function has two important properties [2], [3], [6], Figure 2.3-10:

- Figures of *finite size* may be subject to deformations by conformal mapping, but the **angles** between curves, and hence the orthogonality of field lines and equipotential lines is preserved, i.e. confomal mapping is **isogonal**.
- **Figures** of sufficiently *small size* **preserve their shape**, and infinitesimal elements described by field lines and equipotential lines preserve their aspect ratio during the transformation.

Note: These statements are not valid for the *origin*, which is a *singularity (pole).*

This means that *potential fields*, which are calculated in the $\underline{z}$-plane, preserve their potential field character during the *transformation* onto the $\underline{w}$-plane and vice versa, Figure 2.3-10. Nevertheless, the macroscopic field pattern may be deformed.

Note: Mathematically, every regular function of a complex quantity $f(\underline{z}) = f(x+\mathrm{j}y)$ fulfills Laplace's Equation (2.3-22) for the two-dimensional case, i.e. if the space charge η is zero:

$$\partial^2 f/\partial x^2 + \partial^2 f/\partial y^2 =$$

$$f''(\underline{z})\,(\partial \underline{z}/\partial x)^2 + f''(\underline{z})\,(\partial \underline{z}/\partial y)^2 =$$

$$f''(\underline{z})\;1^2 + f''(\underline{z})\;\mathrm{j}^2 =$$

$$f''(\underline{z}) - f''(\underline{z}) = 0$$

q.e.d.

From

$$f(x+\mathrm{j}y) = \underline{w} = \mathrm{u}(x,y) + \mathrm{j}\,\mathrm{v}(x,y)$$

it is further concluded that

$$\partial^2 f/\partial x^2 + \partial^2 f/\partial y^2 =$$

$$(\partial^2 u/\partial x^2 + \mathrm{j}\,\partial^2 v/\partial x^2) + (\partial^2 u/\partial y^2 + \mathrm{j}\,\partial^2 v/\partial y^2) =$$

$$(\partial^2 u/\partial x^2 + \partial^2 u/\partial y^2) + \mathrm{j}\,(\partial^2 v/\partial x^2 + \partial^2 v/\partial y^2) \overset{!}{=} 0.$$

This equation can only be fulfilled, if real and imaginary parts are both zero. This means that the functions $u(x,y)$ and $v(x,y)$ are both *solutions of Laplace's Equation*.

If the curves in the $\underline{w}$-plane, which are defined by v = const. ~ φ, are regarded as *equipotential lines* (Figure 2.3-10 right), the function $\varphi(x,y) \sim v(x,y)$ = const. defines the potential distribution in the x,y-plane. The orthogonal curves with u = const. can then be regarded as *field lines*, Figure 2.3-10.

Example: The function $\underline{w} = \underline{z}^2$

The function $\underline{w} = \underline{z}^2 = (z\cdot e^{\mathrm{j}\alpha})^2 = z^2\cdot e^{\mathrm{j}2\alpha}$ doubles the angles α of all complex vectors $\underline{z}$ emanating from the null point. The function can therefore be used to transform an **electrode consisting of two orthogonal walls** in the x,y-plane (α = 90°) into a plane electrode in the u,v-plane (2α = 180°), Figure 2.3-11.

In the u,v-plane, the field above a plane electrode is a *uniform field* and the potential increases linearly with voltage V and with the distance v (k is a constant):

$$\varphi = v\,V\,k$$

This is the equation for equipotential lines in the w-plane. The relation between w- and z-plane is given by

$$\underline{w} = \underline{z}^2 = (x + \mathrm{j}\,y)^2$$

and

$$u + \mathrm{j}\,v = (x^2 - y^2) + \mathrm{j}\,x\,y\,.$$

Therefore, the equipotential lines (v = const.) are *hyperbolas* in the x,y-plane, symmetric with respect to the bisecting line between x- and y-axis.:

$$\varphi \sim v = x\,y = \text{const.}$$

For the field lines (u = const.) there are hyperbolas symmetric with respect to x- and y-axis.:

$$u = x^2 - y^2 = \text{const.}$$

The potential distribution in the x,y-plane is

$$\varphi = v\,V\,k = x\,y\;V\,k\,.$$

In the x,y-plane, the potential of the rectangular electrodes is set to zero (reference electrode). The equipotential line with the diagonal distance a from the origin is selected as a counter-electrode with the potential $\varphi = V$. The constant $k = 2/a^2$ is determined with the boundary condition $\varphi = V$ for $x = y = a/2^{1/2}$:

$$\varphi = x\,y\;V\,2/a^2$$

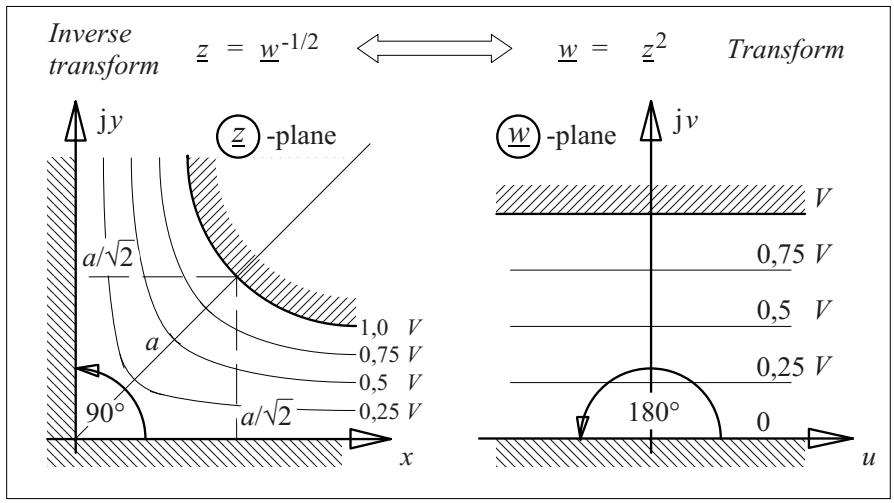

Figure 2.3-11: Conformal mapping of field lines and equipotential lines for a rectangular electrode: $\underline{w} = \underline{z}^2$

The electric field strength $\boldsymbol{E}$ is the gradient of φ:

$$\boldsymbol{E} = -\operatorname{grad}\varphi = -\{\partial\varphi/\partial x, \partial\varphi/\partial y, \partial\varphi/\partial z\}$$

$$\boldsymbol{E} = -V\,2/a^2\ \{y,\ x,\ 0\}$$

The magnitude is

$$E = 2V\,(\sqrt{x^2+y^2})/a^2 \quad .$$

In the *inner corner* of the reference electrode ($x \to 0$, $y \to 0$) there is no longer any field strength, i.e. $E \to 0$.

At the surface of the *hyperbolic high voltage electrode* in the axis of symmetry ($x = y = a/2^{1/2}$) the field strength is $E = 2\,V/a$, i.e. twice as high as in a uniform field with the same electrode distance a. However, field strengths increase further outside the axis of symmetry.

The situation close to the axis of symmetry is comparable with a curved conductor (e.g. a tubular conductor) in the corner of a building.

Generally it is difficult to find a function which transforms a *given configuration* into a calculable basic configuration. Therefore a different technique is used: starting from *given functions* $\underline{w} = f(\underline{z})$, one investigates field configurations that arise in the x, y plane.

In this way a large number of technically relevant configurations could be calculated analytically. Meanwhile, any field configuration can be directly calculated numerically (Section 2.5). Therefore, it is not necessary to discuss all of the many special cases that are more or less suitable for conformal mapping; they can be found in the literature [2], [3], [4], [16], [17].

Figure 2.3-12 shows some calculable configurations and the related transforms. Some are discussed in the following.

<u>Example:</u> Conductor bundle

In order to reduce the field strengths at the surfaces of conductors of high voltage overhead lines (for the voltage levels $V_m = 245$ kV and above), single conductors are normally replaced by conductor bundles.

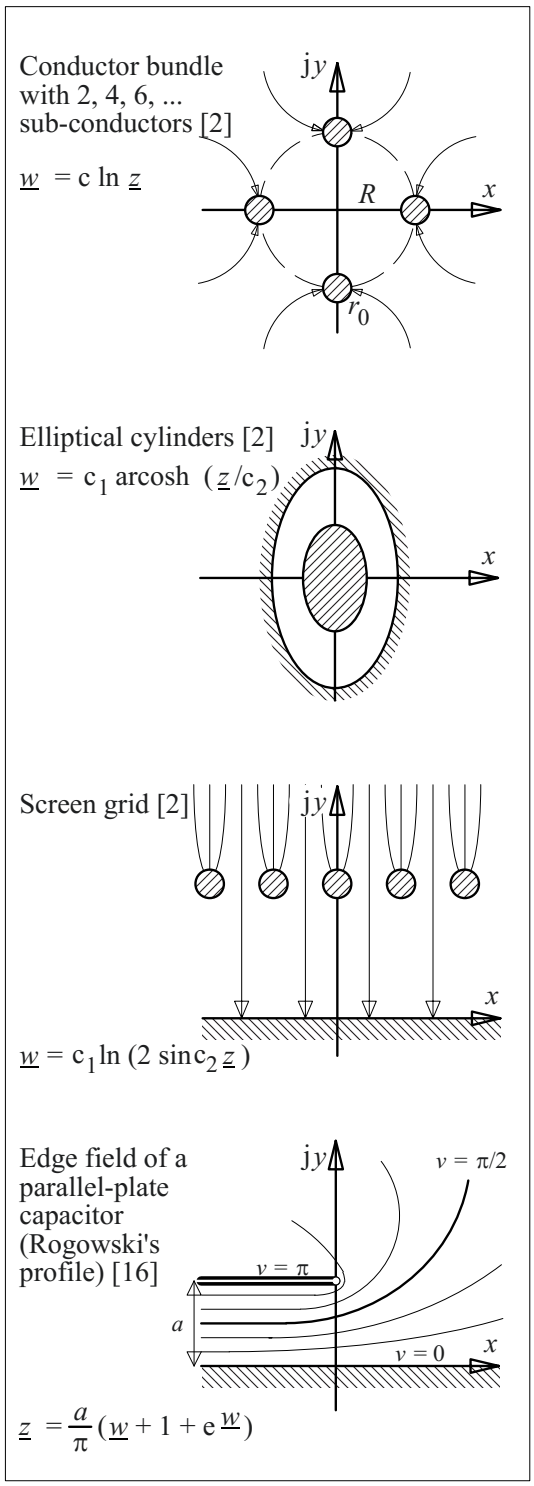

Figure 2.3-12: Examples for two-dimensional fields, which can be calculated by conformal mapping. (see the literature).

A conductor bundle consists of n parallel sub-conductors with the radius r_0. They are uniformly distributed on a circle with the radius R, and they have the same potential, Figure 2.3-12 top. An *equivalent radius* R' for a single cylindrical conductor with the *same capacitance* against a distant counter-electrode is calculated by means of the function $\underline{w} = \ln \underline{z}$ for small sub-conductor radii $r_0 << R$ [2]:

$$R' = R\,(n\,r_0/R)^{1/n} \qquad (2.3\text{-}40)$$

If two identical conductor bundles are led in parallel with the distance a, the charge can be determined from the capacitance calculations according to Section 2.3.5.3. The maximum field strength at the conductor surface is deduced from this [2]:

$$E = V / \{2\,r_0\,n\,\ln(a/R')\} \qquad (2.3\text{-}41)$$

The reduction ratio of field strength E to field strength E_0 at the surface of a single conductor with the radius r_0 is

$$E/E_0 = \ln(a/r_0) / \{n\,\ln(a/R')\}. \qquad (2.3\text{-}42)$$

These equations are also valid for conductor bundles which are led at a distance h above a conducting plane (ground), if a and V are replaced by $a = 2h$ and $V = 2\,\Delta V_{L/G}$. This plane is then regarded as a plane of symmetry in a configuration with two parallel conductor bundles, see also Section 2.3.5.3.

Example:
Edge field of a parallel-plate capacitor

The *field at the edge of a parallel-plate capacitor* is especially important for high voltage engineering, Figure 2.3-12 bottom. During the transformation into the $\underline{w}$-plane a uniform field is achieved by a clockwise rotation of the upper electrode surface by 180° about an axis laying in the edge of the electrode. The equipotential lines in the uniform field of the $\underline{w}$-plane are defined by the equation v = const. .

In the $\underline{z}$-plane there are equipotential lines, which are bent around the edge of the *upper electrode*. Close to the edge the field strength is strongly enhanced; it approaches an infinite magnitude at the edge itself. At the *lower electrode* the field strength decreases in the outward direction.

The volume between the electrodes is divided into two parts by the equipotential surface that is represented by the line $v = \pi/2$, the so called **Rogowski profile**: In the *upper volume* the equipotential lines curve around the upper electrode and field strengths along these lines reach local maxima $E > E_0 = V/a$. In the *lower volume* the field strength never exceeds the value of the uniform field $E \leq E_0 = V/a$. Electrodes which are shaped according to the Rogowski's profile (**Rogowski electrodes**) are of high importance in high voltage engineering, because field stress enhancements at the electrode edges can be avoided with them. An important application is the testing of the *breakdown strength* of materials.

Along Rogowski's profile, the field strength continuously decreases in the outward direction. Therefore the curvature of the electrode could be increased further in order to achieve a more compact construction. This is required for higher voltages with very large electrodes. The smallest dimensions are achieved if the field strength is kept constant along the curved electrode: $E = E_0$. The corresponding contour is referred to as **"Borda's profile"**, which can also be determined by conformal mapping or by iterative numerical optimization. The **Borda's profile** is a spiral contour with a continuously decreasing radius of curvature. An important application is *field grading in cable entrance fittings and cable joints*, Figure 2.4-36, 7.1.1-4 and -5.

Note: Electrodes with a contour shaped according to *Borda's* profile are frequently but *imprecisely* referred to as *Rogowski* electrodes.

In many practical cases it is often sufficient to use a cylindrical electrode edge with a *constant* **radius of curvature** R greater than the electrode distance d:

$$R > d \qquad (2.3\text{-}43)$$

The distance d is the distance between two identical rounded plate electrodes, see Figure 2.3-5. Therefore, the distance in the Figures 2.3-8 and 2.3-9 is $d/2$.

Note: The **field stress enhancement** is estimated for this case, if a cylindrically symmetric field with $R_1 = R$, $R_2 = R + d/2$ and $R = d$ is assumed according to Eq. (2.3-22) and (2.3-28). The result $E_1/E_0 = 2.47$ strongly overestimates the field stress enhancement, which is significantly lower. A better result is achieved, if an increased "effective outer radius" $R_2 = 2R + d/2$ is assumed at the edge of the electrode, Figure 2.3-8c). The result $E_1/E_0 = 1.1$ is consistent with the real field stress enhancement which can also be estimated by *Schwaiger's field efficiency factor* , Section 2.3-6 [22].

These estimations show that results are strongly dependent on the simplifying assumptions. *Estimations* cannot generally replace exact analytical or accurate numerical calculations. Similar to the graphical field mapping (Section 2.3.3), however, field strength estimations are a good tool to get a feeling for the orders of magnitude.

2.3.5 Charge Simulation Method

The Charge Simulation Method (CSM) is another traditional tool for the analytical calculation of specific high voltage engineering field configurations. It can also be used for the numerical calculation of any electrostatic field (Section 2.5).

The Charge Simulation Method is directly based on the physics of electrostatic fields, whereby source fields are generated by **superposition of the fields of many single charges**. However, these *equivalent charges* are not positioned on the electrode surfaces where they should be in reality. Instead, one proceeds from simplified charge distributions (point charges, line charges, ring charges etc.) and selects the *electrode contours* from the resulting equipotential surfaces afterwards. Therefore, the method is sometimes called the **"indirect method"** [67]. The charges represent only a limited number of *equivalent* charges, giving the same electrostatic field between the electrodes as an infinite number of *real* charges. In English the term **„charge simulation method "**(CSM) is common, but the method is also called **"equivalent charge method"**.

In the following chapters important high voltage engineering fields are discussed, i.e. fields in the vicinity of two point charges (Section 2.3.5.1), between two conducting spheres (Section 2.3.5.2), in the vicinity of two line charges in parallel (Section 2.3.5.3) and between conducting cylinders (Section 2.3.5.4). Because of their symmetries, these cases also include the fields between spheres or cylinders and conducting planes [2].

This allows some important field configurations to be calculated analytically, e.g. spherical screening electrodes beside flat walls, spherical spark gaps (measuring spark gaps), cylindrical conductors beside flat walls and overhead lines.

2.3.5.1 Conducting Spheres (Point Charges)

The fields in the vicinity of conducting spheres result from the *superposition of the fields or potentials* of point charges.

The potential in the vicinity of a **single point charge** Q is derived from the electric field strength according to Eq. (2.3-2) by integration from r to ∞:

$$\varphi(r) = \frac{Q}{4\pi\varepsilon} \cdot \frac{1}{r} \qquad (2.3\text{-}44)$$

The reference potential is $\varphi(\infty) = 0$. The counter charge $-Q$ is assumed for $r = \infty$. The field of **two point charges** Q_1 and Q_2 results from the superposition of the potentials; r_1 and r_2 are the distances from the point charges Q_1 and Q_2 to a reference point P at which the potential φ is formed by superimposing the potentials $\varphi_1 + \varphi_2 = \varphi$, Figure 2.3-13:

$$\varphi(r) = \frac{1}{4\pi\varepsilon}\left(\frac{Q_1}{r_1} + \frac{Q_2}{r_2}\right) \qquad (2.3\text{-}45)$$

Example: "Image charges" with equal magnitude and opposite polarity

If the charges $Q_1 = Q$ and $Q_2 = -Q_1 = -Q$ have the same magnitude but opposite polarity, the condition for equipotential surfaces is

$$\varphi(r) = \frac{Q}{4\pi\varepsilon}\left(\frac{1}{r_1}-\frac{1}{r_2}\right) = \text{const.} \qquad (2.3\text{-}46)$$

The counter-charges $-Q_1 = -Q$ and $-Q_2 = +Q$ are infinitely far away and compensate each other in this case. Because of the mirror-symmetrical position of the charges $Q_1 = +Q$ and $Q_2 = -Q$ with respect to the plane equipotential surface $\varphi = 0$, the terms *"image charges"* and *"surface of reflection"* can be used.

According to Eq. (2.3-46) the potential $\varphi = 0$ results for infinite radii r_1 and r_2 and for finite radii if $r_1 = r_2$, i.e. for the plane of symmetry orthogonal to the connecting line between the two charges, Figure 2.3-14.

For the actual positions of the charges the potentials theoretically approach infinite positive and negative values ($r_1 = 0$ or $r_2 = 0$). This is the extreme case of the so called *point charge*.

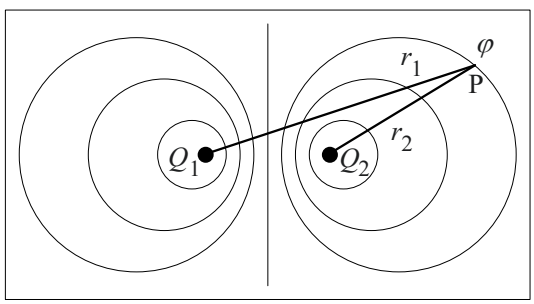

Figure 2.3-13: Superposition of electrostatic fields, which are generated by two point charges.

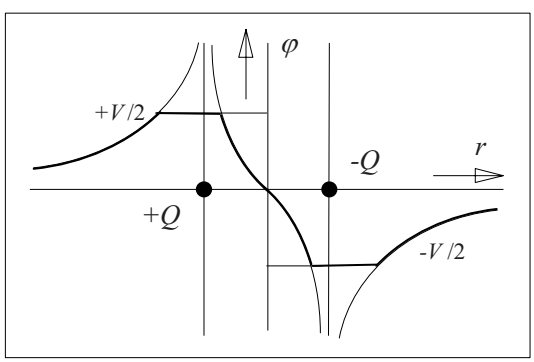

Figure 2.3-14: Potential profile on the connecting line between two point charges +Q and -Q (see also fig. 2.3-13). +V/2 and -V/2 are the potentials of two equipotential surfaces, which were selected as electrode contours (potential difference V).

For the calculation of practical electrode configurations two equipotential surfaces (e.g. with $\varphi = +V/2$ and $\varphi = -V/2$) have to be selected, which serve as electrode surfaces. In the given example, however, these surfaces are *not* spherical.

For two charges Q_1 and Q_2 with opposite polarity and *different* charge amounts the equipotential surface $\varphi = 0$ shall be determined. Obviously, this will not be the geometric plane of symmetry (as in the former example). Nevertheless, in a more general sense Q_1 and Q_2 are referred to as *"image charges"* and the surface $\varphi = 0$ as *"surface of reflection"*.

With Eq. (2.3-45) the condition for the surface of reflection $\varphi = 0$ is

$$Q_1/r_1 + Q_2/r_2 = 0$$

and

$$r_1/r_2 = Q_1/(-Q_2) = k\,. \qquad (2.3\text{-}47)$$

In the case of opposite polarities the ratio of the charges $k = Q_1/(-Q_2)$ is a positive quantity and Eq. (2.3-47) describes a *circle equation*. This will be shown in the following, Figure 2.3-15. The center point (midpoint) M of the circle is chosen as the origin of a Cartesian *x,y*-coordinate system.

From Eq. (2.3-47) and Figure 2.3-15 we find

$$k^2 = \frac{r_1^2}{r_2^2} = \frac{(a+b+x)^2+y^2}{(b+x)^2+y^2}$$

This equation is rearranged in order to constitute the circle equation in the *x,y*-coordinate system:

$$k^2(b+x)^2 + k^2y^2 = a^2 + 2a(b+x) + (b+x)^2 + y^2$$

$$(k^2\text{-}1)\,[(b+x)^2 + y^2] = a^2 + 2ab + 2ax$$

$$(k^2\text{-}1)\,[x^2 + y^2] = a^2 + 2ab + 2ax - (k^2\text{-}1)\,[b^2 + 2bx]$$

$$x^2 + y^2 = \frac{a^2 + 2ab}{k^2 - 1} - b^2 + \frac{2a \cdot x}{k^2 - 1} - 2b \cdot x$$

This expression describes a *circle* around the coordinate origin M, if the term containing x (on the right side of the equation) is zero. The first term, which is independent of x and y, is then equal to the square of the radius r_0:

$$x^2 + y^2 = r_0^2 + 0$$

Two equations for the *position b of the equivalent charge* Q_2 and for the *radius* r_0 *of the equipotential line* are defined from this. Then b is derived from the second term containing x, and this term is set to zero:

$$b = \frac{a}{k^2 \quad 1} \qquad (2.3\text{-}48)$$

The first term provides r_0 by inserting b from Eq. (2.3-48):

$$r_0^2 = \frac{a^2 + 2ab}{k^2 - 1} - b^2$$

According to Eq. (2.3-48) b is inserted:

$$r_0^2 = \frac{a^2\left(k^2 - 1\right) + 2a\,a}{\left(k^2 - 1\right)^2} - \frac{a^2}{\left(k^2 - 1\right)^2}$$

$$= \frac{a^2 k^2}{\left(k^2 - 1\right)^2}$$

With $k > 1$ we find for the radius r_0 of the equipotential line $\varphi = 0$ the relation

$$r_0 = \frac{a\,k}{k^2 - 1} \,. \qquad (2.3\text{-}49)$$

Note: It was shown that the condition $\varphi = 0$ in the *x,y*-plane corresponds to a *circle* equation according to Figure 2.3-15. This is valid for all planes containing the connecting line between the charges Q_1 and Q_2. Such planes result from a rotation of the *drawing plane* under consideration about the connecting line (i.e. the *x*-axis). The *circular equipotential line* $\varphi = 0$ is thereby transformed into a *spherical equipotential surface*; the configuration under consideration is spherically symmetric.

The surface of the sphere remains an equipotential surface, if *another charge* Q_3 is inserted at the origin M, Figure 2.3-16. The potential at any point P is given by the superposition of the potentials, which are attributed to the three *equivalent charges* Q_1, Q_2 and Q_3:

$$\varphi_P = \varphi_1 + \varphi_2 + \varphi_3 \qquad (2.3\text{-}50)$$

With Eq. (2.3-44) and $\varphi_1 + \varphi_2 = 0$ we get for all points S on the surface of the sphere

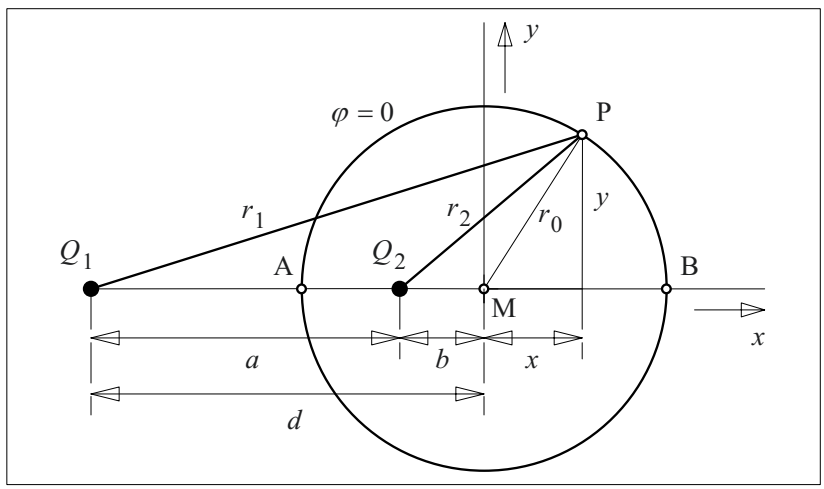

Figure 2.3-15: Geometric description of the equipotential surface $\varphi = 0$ as circular equation or as spherical surface.

$$\varphi_S = \varphi_3 = \frac{Q_3}{4\pi\varepsilon\, r_0}\,. \qquad (2.3\text{-}51)$$

Example: Metallic sphere without charge

An uncharged metallic sphere (radius r_0) is exposed to the field of a point charge Q_1. The distance d between Q_1 and the center point M of the sphere is given. The following quantities shall be determined:

(1) Magnitude and position of the equivalent charge,
(2) Potential of the sphere's surface,
(3) Potential distribution in the field volume and
(4) Maximum field strength.

Note: The metallic sphere without charge in an electric field can be regarded as a model of a conducting particle or as an electrode at free potential.

(1) Equivalent charges

A configuration with a spherical equipotential surface can be described by three equivalent charges Q_1, Q_2 and Q_3 according to Figure 2.3-16. The specification of an uncharged sphere means that the charges Q_2 and Q_3 must be equal in magnitude and opposite in polarity:

$$Q_3 = -Q_2 \qquad (2.3\text{-}52)$$

Q_2 can be determined with Eqs. (2.3-47) to (-49) from the given quantities Q_1, r_0 and d:

$$\begin{aligned} d &= a + b \\ &\overset{(48)}{=} a + a/(k^2 - 1) \\ &= a\,k^2/(k^2 - 1) \\ &\overset{(49)}{=} r_0\,k \\ &\overset{(47)}{=} r_0\,(-Q_1/Q_2) \end{aligned}$$

The *magnitude of the equivalent charge* Q_2 is

$$Q_2 = -Q_1\,r_0/d. \qquad (2.3\text{-}53)$$

The division of Eq. (2.3-48) by Eq. (2.3-49) gives

$$b/r_0 = 1/k = -Q_2/Q_1\,. \qquad (2.3\text{-}54)$$

The *position b of the equivalent charge* Q_2 is calculated with Eq. (2.4-53):

$$b = r_0^{\,2}/d \qquad (2.3\text{-}55)$$

Therefore, the magnitude Q_2 and the position b of the equivalent charge are expressed by the given quantities Q_1, r_0 and d. Q_2 is the so called "image charge" with respect to Q_1, the "surface of reflection" is the surface of the sphere in this case. According to Eq. (2.3-52),

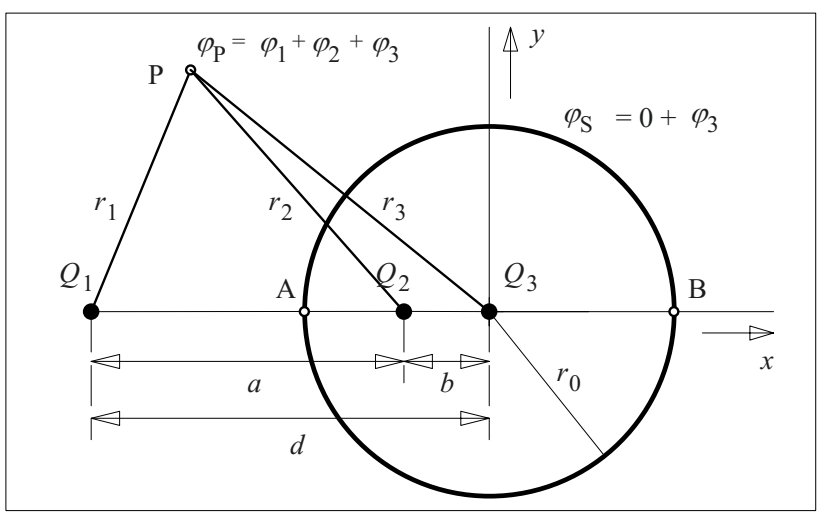

Figure 2.3-16: Conducting sphere with the potential φ_S, described by three equivalent charges.

the equivalent charges Q_3 and Q_2, have the same magnitude, but opposite polarity.

Note: The considered charges Q_1, Q_2 and Q_3 cause the *correct field distribution on the outside* of the conducting sphere, but they do not represent the *real charge distribution* on the electrode, therefore they are called **equivalent charges**. On a conducting electrode, real charges are distributed continuously over the surface because of the electrostatic forces. The area charge density equals the local dielectric displacement density, Eq. (2.1-3) and Figure 2.3-17. Only the total charge magnitudes are identical with the equivalent charges.

(2) Potential of the sphere's surface

Prior to the insertion of the charge Q_3 the surface of the sphere has the potential $\varphi = 0$ because of the image charges Q_1 and Q_2, Figure 2.3-15. With Q_3 and Eqs. (2.3-51) to (-53) the potential is

$$\begin{aligned} \varphi_S &= 0 + \varphi_3 \\ &= Q_3 / (4\pi\varepsilon r_0) \\ &\overset{(52)}{=} - Q_2 / (4\pi\varepsilon r_0) \\ &\overset{(53)}{=} (Q_1 r_0/d) / (4\pi\varepsilon r_0) \\ \varphi_S &= Q_1 / (4\pi\varepsilon d) \,. \end{aligned} \qquad (2.3\text{-}56)$$

Therefore, the *potential of the sphere's surface* is *identical* with the potential of the center point M in the field of the point charge Q_1 *prior to the insertion of the sphere*. This is also valid for any field configuration, which always can be generated from the superposition of single equivalent charges, Figure 2.3-17.

(3) Potential distribution in the field volume

In the field volume on the outside of the conducting sphere, the potential is given by the

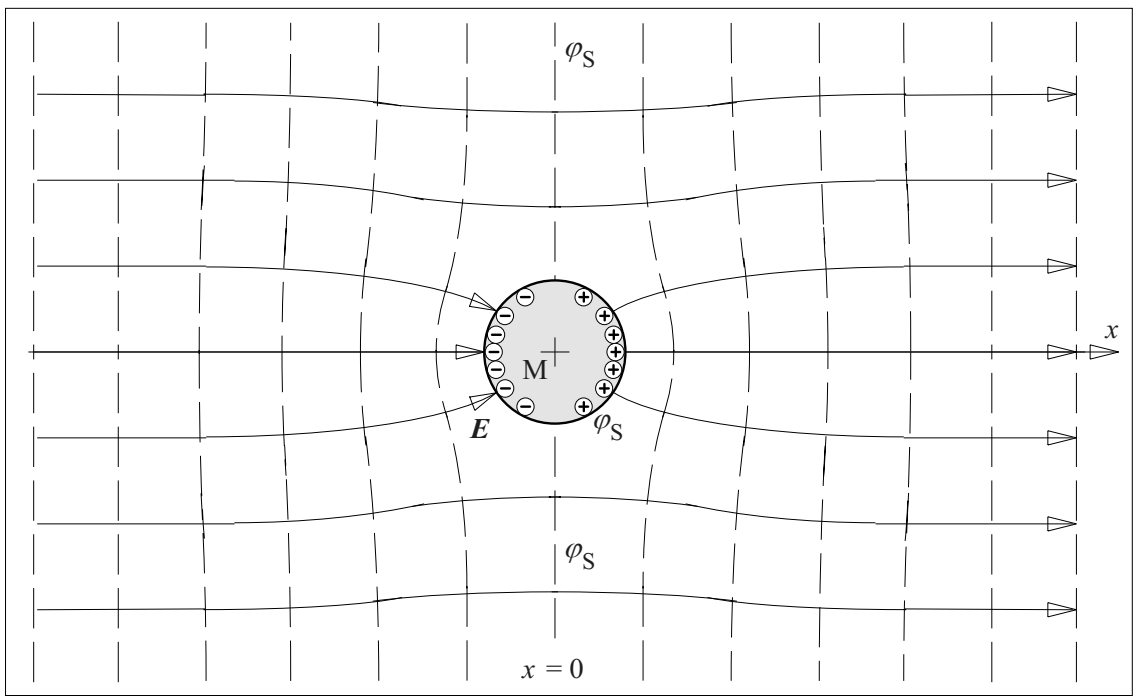

Figure 2.3-17: "Distortion" of a uniform electrostatic field by a conducting sphere without any net charge. The potential of the sphere is equal to the potential of the center point M prior to the insertion of the sphere. The charge distribution in this picture refers to real charge carriers which are distributed continuously over the surface of the sphere. In contrast to this, calculations are performed with a few "equivalent charges", which are located on the x-axis, see fig. 2.3-16.

superposition of the potentials, assigned to the three charges:

$$\varphi_P = \varphi_1 + \varphi_2 + \varphi_3$$

With Eq. (2.3-44) and Figure 2.3-16 we find

$$\varphi_P = \frac{1}{4\pi\varepsilon}\left(\frac{Q_1}{r_1}+\frac{Q_2}{r_2}+\frac{Q_3}{r_3}\right).$$

Q_2 and Q_3 can be replaced by Q_1 according to Eq. (2.3-53) and (-52):

$$\varphi_P = \frac{Q_1}{4\pi\varepsilon}\left(\frac{1}{r_1}-\frac{r_0}{d\,r_2}+\frac{r_0}{d\,r_3}\right) \qquad (2.3\text{-}57)$$

In this equation, the distances r_1, r_2 and r_3 between P and the equivalent charges Q_1, Q_2 and Q_3 have to be replaced by the coordinates of point P, Figure 2.3-16. Field strengths are calculated from the gradient of the potential according to Eq. (2.1-8).

(4) Maximum field strengths

The maximum field strength occurs on the x-axis for $x = -r_0$ at point A on the surface of the sphere. The electric field on the x-axis has an x-component only; according to Eq. (2.1-8a) it can be determined by the derivate of the potential φ with respect to x.

In the interval $-d < x \leq -r_0$ the potential $\varphi(x)$ is calculated along the x-axis from Eq. (2.3-57) with $r_1 = d + x$, $r_2 = -(b + x)$ and $r_3 = -x$.

The distances r_1, r_2 and r_3 between P and the equivalent charges are positive quantities (magnitudes) and therefore have to be inserted in the considered interval $-d < x \leq -r_0$ on the negative x-axis according to the preceding definition; x defines the position of the considered point P on the x-axis, Figure 2.3-16:

$$\varphi(x) = \frac{Q_1}{4\pi\varepsilon}\left(\frac{1}{d+x} + \frac{r_0}{d}\cdot\frac{1}{b+x} - \frac{r_0}{d}\cdot\frac{1}{x}\right)$$

for $-d < x \leq -r_0$

The x-component of the electric field strength E_x is calculated from the gradient of the potential φ:

$$E_x = -\partial\varphi/\partial x$$

$$= \frac{-Q_1}{4\pi\varepsilon}\left(\frac{-1}{(d+x)^2} - \frac{r_0}{d\,(b+x)^2} + \frac{r_0}{d\,x^2}\right) \qquad (2.3\text{-}58)$$

for $-d < x \leq -r_0$

The maximum field strength E is found at $x = -r_0$ at point A. It is equal to the x-component of the field strength E_x at this point:

$$E = E_x = \ldots\ldots$$

$$= \frac{-Q_1}{4\pi\varepsilon}\left(\frac{-1}{(d-r_0)^2} - \frac{r_0}{d\,(r_0^2/d - r_0)^2} + \frac{r_0}{d\,r_0^2}\right)$$

$$= \frac{-Q_1}{4\pi\varepsilon}\left(\frac{-1}{(d-r_0)^2} - \frac{d}{r_0\,(r_0 - d)^2} + \frac{1}{d\,r_0}\right)$$

$$= \frac{-Q_1}{4\pi\varepsilon}\;\frac{-d\,r_0 - d^2 + \left(d^2 - 2\,d\,r_0 + r_0^2\right)}{d\,r_0\,(d - r_0)^2}$$

$$= \frac{Q_1}{4\pi\varepsilon}\;\frac{3\,d\,r_0 - r_0^2}{d\,r_0\,(d - r_0)^2}$$

After canceling of r_0, the maximum field strength at point A at $x = -r_0$ is

$$E = E_x = \frac{Q_1}{4\pi\varepsilon}\;\frac{3d - r_0}{d\,(d - r_0)^2}\,. \qquad (2.3\text{-}59)$$

This equation allows one to calculate the *field stress enhancement* caused by the sphere. Prior to the insertion of the sphere, the charge Q1 causes the electric field strength

$$E_1 = E_{1x} = \frac{Q_1}{4\pi\varepsilon}\;\frac{1}{(d - r_0)^2}\,. \qquad (2.3\text{-}60)$$

at point A according to Eq. (2.3-2). With the Eqs. (2.3-59) and (-60), the ratio of the enhanced and the original field strength is

$$\frac{E}{E_1} = 3 - \frac{r_0}{d} \qquad (2.3\text{-}61)$$

For a nearly *uniform field* E_0 the distance d is $d >> r_0$ and the field strength is enhanced by a **factor of 3**, Figure 2.3-18:

$$E = 3\,E_0 \qquad (2.3\text{-}62)$$

Note: This result shows that *conductive particles* can cause dangerous field stress enhancements in insulations. Very often real particles differ more or less from the ideal spherical shape and therefore cause *significantly higher field stress enhancements*. Clean processing of insulating materials for the *prevention of conducting impurities* is a basic requirement of high voltage technology manufacturing!

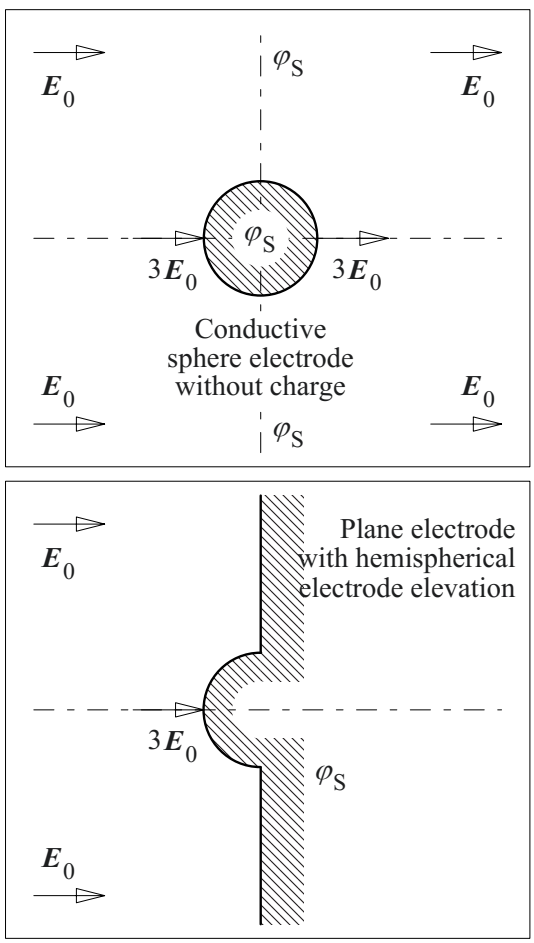

Figure 2.3-18: Field enhancement by a conductive sphere without charge (top) and by a hemispherical electrode elevation on a plane electrode (bottom) in the originally uniform field.

In the special case of a uniform field ($d >> r_0$) the configuration is symmetric with respect to the equipotential plane φ_S, Figure 2.3-17. This plane can then be seen as a plane electrode with a *hemispherical electrode elevation*, Figure 2.3-18. The maximum field strength is three times as high as in the undisturbed uniform field.

The field stress enhancement caused by a conducting hemisphere on a *plane* electrode can also be regarded as a model for the field stress enhancement on an *uneven electrode surface*. The unevenness of electrode surfaces is responsible for early discharge inception on electrodes at voltages with macroscopic field strengths significantly below anticipated inception field strengths (in air $\hat{E}_D$ is approx. 30 kV/cm).

2.3.5.2 Field between Two Conducting Spheres (Sphere-to-sphere Gap)

The charge simulation method also allows one to calculate the field between two spherical electrodes (**sphere-to-sphere arrangement**) and between a spherical electrode and a plane of symmetry (**sphere-to-plane arrangement**). Important practical applications are *sphere gaps* or *spherical high voltage shielding electrodes* close to a flat wall. Therefore, the comparatively laborious iterative calculation is explained here, Figure 2.3-19:

Two conducting spheres are specified with the radius r_0, the center point's distance d and the potential difference $\Delta\varphi = V$. The calculation is performed in two steps:

(1) By positioning *equivalent charges*, the specified spherical surfaces are approximated by the calculated equipotential surfaces.

(2) *Field strengths* are determined from the superposition of equivalent charge fields after the positioning of the charges.

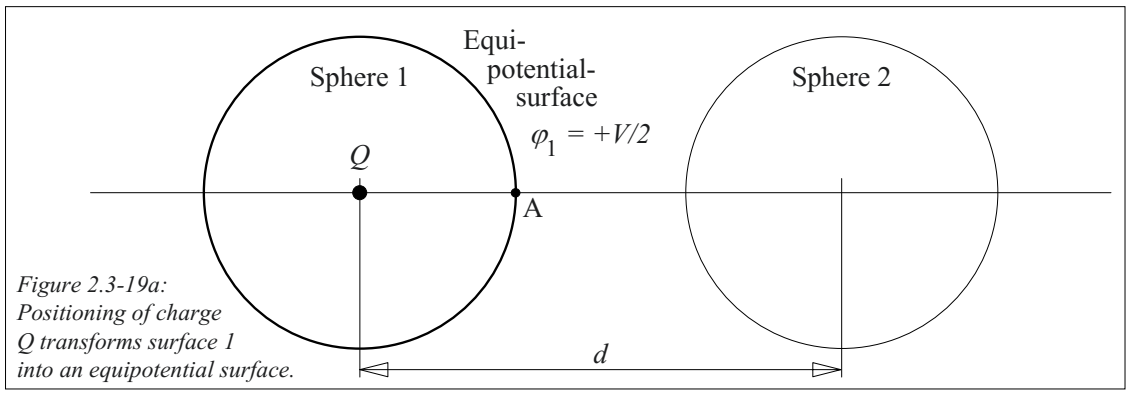

Figure 2.3-19a:
Positioning of charge
Q transforms surface 1
into an equipotential surface.

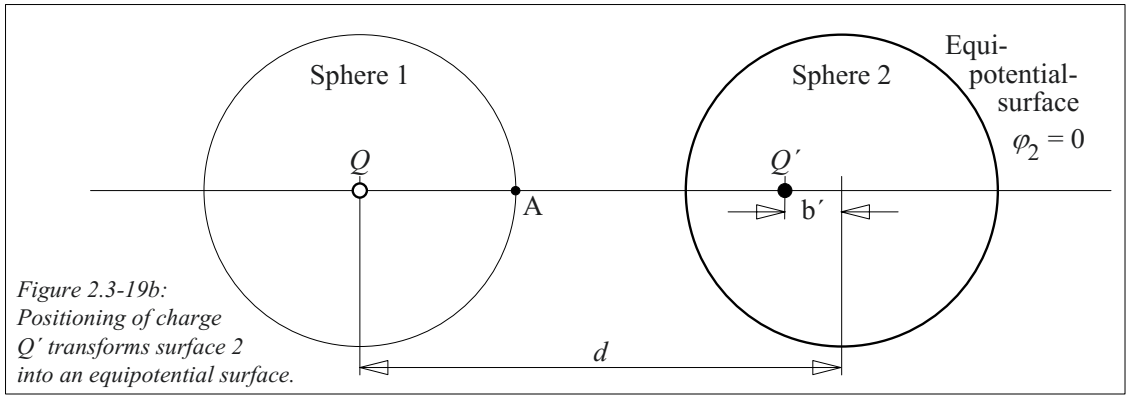

Figure 2.3-19b:
Positioning of charge
Q′ transforms surface 2
into an equipotential surface.

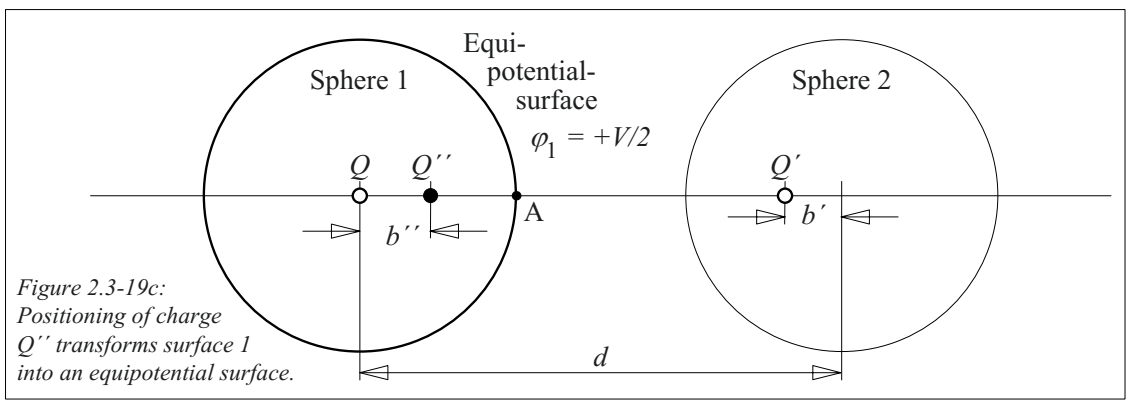

Figure 2.3-19c:
Positioning of charge
Q′′ transforms surface 1
into an equipotential surface.

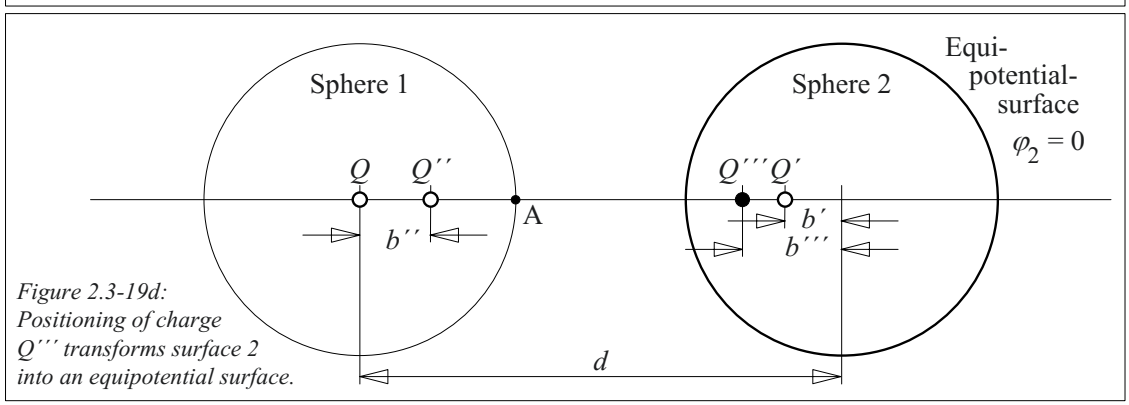

Figure 2.3-19d:
Positioning of charge
Q′′′ transforms surface 2
into an equipotential surface.

(1) Equivalent charges

(a) At first, an equivalent charge Q is positioned at the center point of a virtual sphere 1. Because of the spherically symmetric field the spherical surface 1 is an equipotential surface. The potential $\varphi_1 = V/2$ is determined by choosing the magnitude of Q. Now the spherical surface 2 is <u>not</u> an equipotential surface, because of the radially symmetric field of the charge Q in the center point of sphere 1, Figure 2.3-19a.

(b) The spherical surface 2 can be transformed into an equipotential surface with the potential $\varphi_2 = 0$ by positioning an *image charge* Q' at a distance b' from its center point, Figure 2.3-19b. The charges Q and Q' are comparable to the charges Q_1 and Q_2 in Figure 2.3-15. After the positioning of Q', the sphere 1 is <u>no longer</u> an equipotential surface.

(c) Sphere 1 becomes an equipotential surface again by positioning an equivalent charge Q'' as an image charge with respect to Q', Figure 2.3-19c. The charge Q in the center point 1 causes a spherically symmetric field with concentric equipotential surfaces. The potential is the sum of the potentials related to the charge Q and the charge couple (Q', Q''):

$$\varphi_1 = \varphi_1(Q) + \varphi_1(Q', Q'') = V/2 + 0 = V/2$$

Now sphere 2 is <u>no longer</u> an equipotential surface.

(d) Sphere 2 becomes an equipotential surface again if Q''' is positioned as an image charge with respect to Q'', Figure 2.3-19d. The potential of sphere 2 is zero again:

$$\varphi_2 = \varphi_2(Q, Q') + \varphi_2(Q'', Q''') = 0 + 0 = 0$$

Now sphere 1 is <u>no longer</u> an equipotential surface.

(e) If further image charges are placed alternately, the state of two spherical equipotential surfaces with the potentials $\varphi_1 = V/2$ and $\varphi_2 = 0$ can be further *iteratively* approximated.

If a second analogous **row of charges** of opposite polarity (starting with the equivalent charge -Q at the center point of sphere 2) is formed, the potentials of the two spheres 1 and 2 are approximated by the potentials $\varphi_1 = 0$ and $\varphi_2 = -V/2$. After the superposition of the two rows of charges the intended potential difference between the two spheres $\Delta\varphi = V/2 - (-V/2) = V$ is obtained.

In the following, the **equations**, which are necessary for the calculation of magnitude and position of the equivalent charges, are compiled. The listing refers to the *steps (a) to (e)* that were described above:

(a) Q causes the equipotential surface 1 ($\varphi_1 = V/2$) according to Eq. (2.3-44):

$$\begin{aligned} b &= 0 \\ Q &= 0.5\, V\, 4\pi\varepsilon r_0 \end{aligned} \qquad (2.3\text{-}63a)$$

(b) Q' and Q cause the equipotential surface 2 ($\varphi_2 = 0$) according to Eq. (2.3-55) and (-53):

$$\begin{aligned} b' &= r_0^2/d \\ Q' &= -Q\, r_0/d \end{aligned} \qquad (2.3\text{-}63b)$$

(c) Q'' and Q', together with Q, cause the equipotential surface 1 ($\varphi_1 = 0 + V/2 = V/2$). The distance d to the counter charge must be reduced by the distance b':

$$\begin{aligned} b'' &= r_0^2/(d - b') \\ Q'' &= -Q'\, r_0/(d - b') \end{aligned} \qquad (2.3\text{-}63c)$$

(d) Q''' and Q'', together with Q' and Q, cause the equipotential surface 2 ($\varphi_2 = 0 + 0 = 0$). The distance d to the counter charge must be reduced by the distance b'':

$$\begin{aligned} b''' &= r_0^2/(d - b'') \\ Q''' &= -Q''\, r_0/(d - b'') \end{aligned} \qquad (2.3\text{-}63d)$$

(e) and so on .....

Note: Because of the *recursive character*, these equations are well-suited to producing a simple numerical iteration program. This example illustrates the basic idea of *numerical field calculation* with the charge simulation method, which iteratively approximates the given electrode contours by placing equivalent charges.

Example: Sphere gap with $r_0 = 0.2\ d$

A sphere gap shall be calculated for the special case with $r_0 = 0.2\ d$. For this purpose the Equations (2.3-63..) are evaluated numerically, Figure 2.3-20. The first charge row (*white background*) causes the potential $\varphi_1 = V/2$ on sphere 1, the second charge row (*grey background*) causes the potential $\varphi_2 = -V/2$ on sphere 2. Row no. 1 starts with the equivalent charge +Q at the center point of sphere 1, alignment no. 2 with the equivalent charge -Q in the center point of sphere 2. It should be noted that each row contains charges on both spheres alternately. All of the positive charges are aligned within sphere 1, all negative charges within sphere 2. With increasing number of iteration steps the magnitude of the charges and the distances to the adjacent charges are reduced drastically.

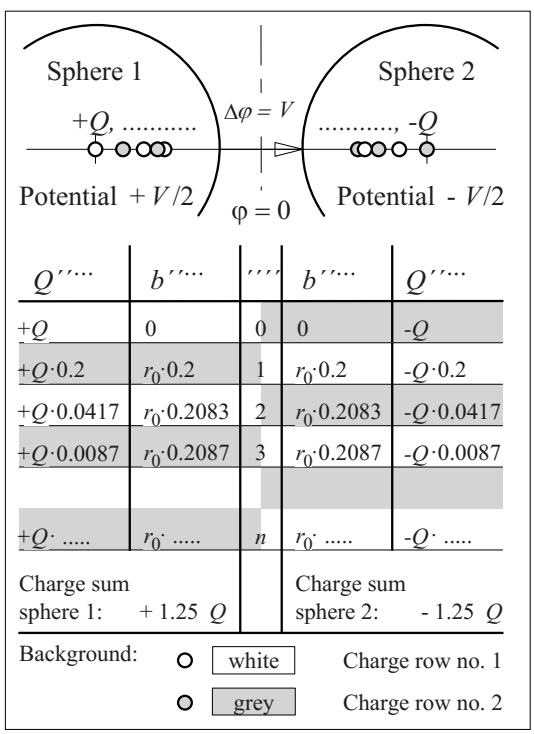

$Q'''\cdots$	$b'''\cdots$	$''''$	$b'''\cdots$	$Q'''\cdots$
$+Q$	0	0	0	$-Q$
$+Q\cdot 0.2$	$r_0\cdot 0.2$	1	$r_0\cdot 0.2$	$-Q\cdot 0.2$
$+Q\cdot 0.0417$	$r_0\cdot 0.2083$	2	$r_0\cdot 0.2083$	$-Q\cdot 0.0417$
$+Q\cdot 0.0087$	$r_0\cdot 0.2087$	3	$r_0\cdot 0.2087$	$-Q\cdot 0.0087$
$+Q\cdot$	$r_0\cdot$	n	$r_0\cdot$	$-Q\cdot$ .....
Charge sum sphere 1:	+ 1.25 Q		Charge sum sphere 2:	- 1.25 Q

Background: white — Charge row no. 1; grey — Charge row no. 2

Figure 2.3-20: Position and magnitude of the equivalent charges for the calculation of a sphere gap with $r_0 = 0.2\ d$.

The *capacitance of the sphere gap* can be calculated with Eq. (2.1-10) and (2.3-63a) from the charge sums in the spheres:

$$C = Q_{sum}/V = 1.25\ Q/V = 2.5\ \pi\varepsilon\ r_0 \qquad (2.3\text{-}64)$$

Surprisingly, this capacitance is smaller than the capacitance

$$C = 4\ \pi\varepsilon\ r_0$$

between a sphere with the same size and a concentric counter electrode infinitely far away, Eq. (2.3-6).

The plane of symmetry between the spheres is an equipotential plane with the potential $\varphi = 0$. The calculated arrangement also covers the case of a *spherical electrode against a plane electrode* (sphere-to-plane arrangement). In comparison with Eq. (2.3-74) the capacitance is doubled:

$$C = 5\ \pi\varepsilon\ r_0 \qquad (2.3\text{-}65)$$

(2) Maximum field strengths

The potentials assigned to the equivalent charges can be superimposed, as in the above Section 2.3.5.1. The field distribution is derived from the potential distribution using gradient generation.

For the determination of *maximum field strength* on the connecting line of the spheres' center points at the spheres' surfaces (point A, Figure 2.3-19) it is possible to *sum the magnitudes of the field vectors directly* because all field vectors related to the equivalent charges are in parallel at this point.

According to Eq. (2.3-2) the field component of a single charge is

$$E_i = Q_i / (4\pi\varepsilon\, r_i^2)\ .$$

The index "*i*" is the number of a single equivalent charge, r_i it the distance between equivalent charge Q_i and field point A, Figure 2.3-19.

At point A both the positive charges in sphere 1 and the negative charges in sphere 2 cause field vectors in the same direction. Therefore, the summation of all field components E_i has to be performed with the *same* positive sign.

According to the alternating polarity of the charges, the signs in Eq. (2.3-66) alternate as well:

$$E_{\max} = \frac{1}{4\pi\varepsilon}\left[\frac{+Q}{r_0^2} + \frac{-Q'}{(r_0 - b')^2} + \frac{+Q''}{(r_0 - b'')^2} + \ldots - \frac{-Q}{(d - r_0)^2} - \frac{+Q'}{(d - r_0 - b')^2} - \frac{-Q''}{(d - r_0 - b'')^2} - \ldots\right] \quad (2.3\text{-}66)$$

Note: The correct field magnitude at point A is also achieved, if all *charges* are inserted as *magnitudes* and all *summands* are superimposed with *positive sign*.

The charges belong alternately to the first charge row (started in sphere 1 with $+Q$) and to the second row (started in sphere 2 with $-Q$).

The *first line of the equation* contains the summation of all contributions from the positive charges in sphere 1. The distance between $+Q$ and point A is equal to the sphere's radius r_0, the following distances are each reduced by b', b'', b''', …

The *second line of the equation* contains the summation of all contributions from the negative charges in sphere 2. Now the distance between $-Q$ and point A is equal to $(d - r_0)$, the following distances are also each reduced by b', b'', b''', ...

It no longer makes sense to insert Eq. (2.3-63) into Eq. (2.3-66). In fact, the numerical values for the equivalent charges and their positions are used.

Example: **Sphere gap** (continued)

In the former example a sphere gap with $r_0 = 0.2\ d$ was concerned and the equivalent charges Q, Q', Q'', Q''' and their positions b, b', b'', b''' were determined. By inserting the numerical values in Eq. (2.3-66) we find with

$$Q = 0.5\ V\, 4\pi\varepsilon\, r_0$$

according to Eq. (2.3-63a):

$$E_{\max} = 0.736\ V/r_0 = 3.68\ V/d = 2.21\ V/s$$

The radius of the spheres is $r_0 = 0.2\ d$, the distance between the center points of the spheres is d and the "sparking distance" between the spheres is $s = 0.6\ d$.

The results can be compared with the field strength in a *parallel-plate capacitor*

$$E = 1 \cdot V/s,$$

with the field strength at the surface of a *single sphere*

$$E = 1 \cdot V/r_0$$

and the maximum field strength in a sphere gap *with a very large gap* ($d >> r_0$)

$$E = 0.5 \cdot V/r_0\ .$$

2.3.5.3 Parallel Line Charges

Some important configurations in high voltage engineering can be calculated by means of *line charges* with a uniformly distributed charge Q along the line length L. In the following, the electric field in the vicinity of two parallel line charges with equal magnitude but opposite polarity is discussed, Figure 2.3-21.

The potential distribution in the field volume is determined by the superposition of the two potentials assigned to the two line charges. It is a two-dimensional field so that consideration of a plane orthogonal to the line charges is sufficient, Figure 2.3-22. The counter-charges and the reference potential $\varphi_B = 0$ cannot be considered to be at an infinite distance as for the spherically symmetric field. Here, infinite potential difference would occur, see Section 2.3.1.3. For calculation purposes finite radii r_{B1} and r_{B2} are introduced in order to specify the distances between the charges and the coaxial counter-charges. They can be eliminated later on, if counter charges at large distances are assumed, Figure 2.3-22. The calculation is performed with the assumption and superposition of two cylindrically symmetric fields around the two line charges.

The superposition of the potentials φ_1 and φ_2, which are assigned to the charges $+Q$ and $-Q$, is performed at point P. With Eq. (2.3-18) we find

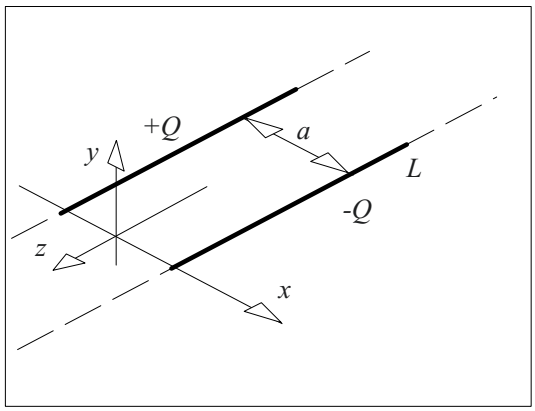

Figure 2.3-21: Infinitely long line charges in parallel (three-dimensional view).

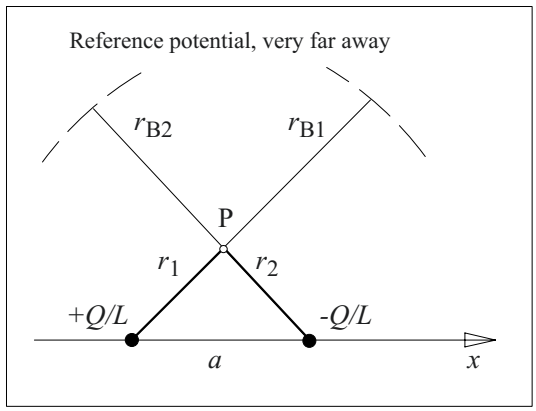

Figure 2.3-22: Infinitely long line charges in parallel (sectional view).

$$\varphi = \varphi_1 + \varphi_2$$

$$= \frac{Q/L}{2\pi\varepsilon} \ln\frac{r_{B1}}{r_1} - \frac{Q/L}{2\pi\varepsilon} \ln\frac{r_{B2}}{r_2}$$

$$= \frac{Q/L}{2\pi\varepsilon} \ln\left(\frac{r_{B1}}{r_1} \cdot \frac{r_2}{r_{B2}}\right) .$$

If the reference potential is assumed to be far away, i.e. if

$$r_1, r_2, a \ll r_{B1} \approx r_{B2}$$

and

$$r_{B1}/r_{B2} \approx 1 ,$$

the distances *to the reference potential* r_{B1} and r_{B2} can be reduced:

$$\varphi = \frac{Q/L}{2\pi\varepsilon} \ln\frac{r_2}{r_1} \qquad (2.3\text{-}67)$$

According to Eq. (2.3-67) *equipotential surfaces* φ = const. are described by the condition

$$r_2/r_1 = k = \text{const.}. \qquad (2.3\text{-}68)$$

During the discussion of point charges in Section 2.3.5.1, it was already shown that such a condition is a *circle equation* for the drawing plane under consideration, see Eq. (2.3-47) ff. Therefore, all of the *equipotential surfaces are cylindrical surfaces* in the two-dimensional field under consideration of the parallel line charges.

It can be shown that the *field lines are circles* too. They all pass through the intersections of the line charge axes +*Q* and -*Q* with the plotting plane [2]. This results in a *graphical plotting method* for a field and equipotential line plot, Figure 2.3-23:

- At first, a circle with the radius $r = a/2$ is plotted through the charge-axis points +*Q* and -*Q*. The two semicircles describe two field lines.
- At any point P_1, P_2, ... the "field-line circle" and the "equipotential-line circle" intersect orthogonally.
- Owing to symmetry, all center points M_1, M_2, ... of the equipotential-line circles are located on the *x*-axis. Furthermore, the radii M_1P_1, M_2P_2, ... touch the field-line circle tangentially, and the center points are determined from the intersections of the tangents at P_1, P_2, ... with the *x*-axis.
- Additional field lines are plotted as circles with center points on the *y*-axis.

The potential of the points P_1, P_2, ... and of the associated equipotential surfaces is given by Eq. (2.3-67). The plane of symmetry between the charges +*Q* and -*Q* is an equipotential surface with the reference potential $\varphi = 0$. Field lines and equipotential lines on both sides are given by reflection in the plane of symmetry.

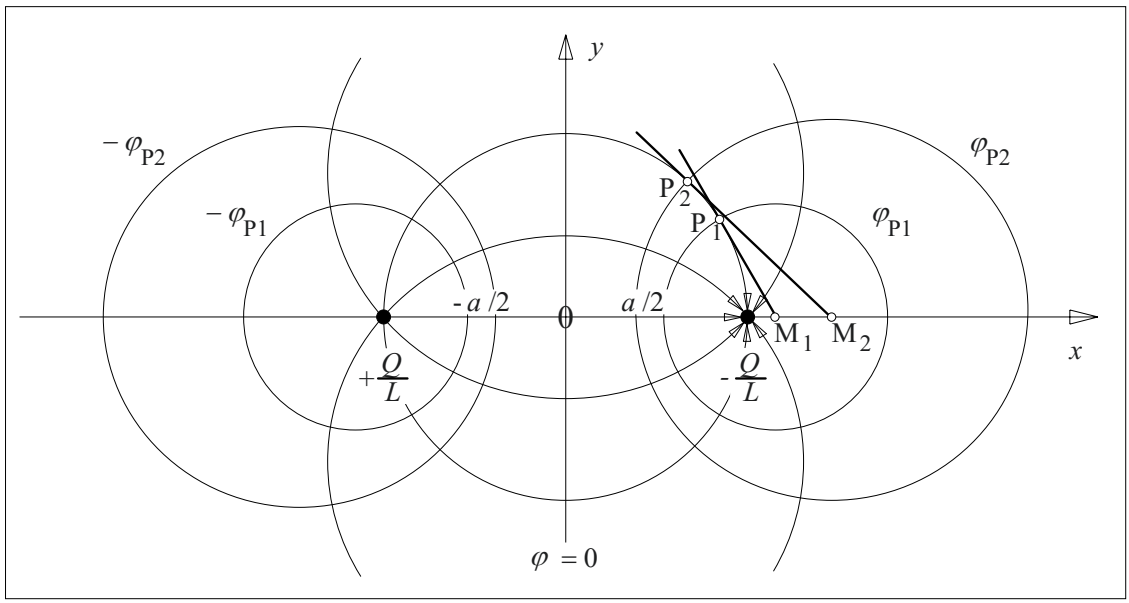

Figure 2.3-23: Graphical design of a pattern with field lines and equipotential lines for parallel line charges.

Potential values have opposite polarities on both sides, Figure 2.3-23.

Any equipotential surfaces caused by the equivalent line charges can be interpreted as electrode contours for field calculations with the charge simulation method. The field of the parallel line charges contains some important high-voltage electrode arrangements that are discussed as *examples* in Section 2.3.5.4. They include parallel cylinders, cylindrical conductors beside plane electrodes, eccentric tubular conductors and overhead line conductors, Figure 2.3-23.

2.3.5.4 Fields in the Vicinity of Cylindrical Conductors

Example 1: Parallel Cylinder Conductors (Cylinder-to-Cylinder, "Two-conductor Line")

If two cylindrical conductors with the radius r_0 and the distance d of the center points is given, the distance a of the equivalent line charges is unknown, i.e. the position b of the equivalent charges has to be determined, Figure 2.3-24.

The geometric relations were already considered in the case of the field between two point charges. In both cases, the relation $r_2/r_1 = k =$ const. describes a circle with a radius r_0 and a distance b between the circle's center point and the position of the equivalent charge, Eq. (2.3-47) and (-68).

Note: In the case of point charges, the factor k both has a geometric meaning and describes a ratio of charges. This means that k is given for given charges, and that there is only one circular equipotential line (spherical equipotential surface resp.). In the case of parallel line charges, there is *no* relation between k and the charge magnitudes. Therefore, there can be any number of circular equipotential lines (or cylindrical equipotential surfaces).

The geometric relations Eq. (2.3-48) and (-49) can therefore be taken from Section 2.3.5.1:

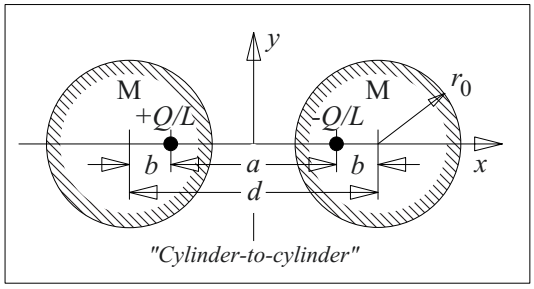

Figure 2.3-24: Parallel cylindrical conductors, calculation with equivalent line charges.

$$b = a / (k^2 - 1)$$
$$r_0 = a\,k / (k^2 - 1) \qquad (2.3\text{-}69)$$

The unknown *position b* (or *a*) *of the equivalent charges* shall now be expressed by the given quantities r_0 and *d*. the factor *k* is to be eliminated in the process. With

$$d = a + 2b$$
$$= a + 2a / (k^2 - 1)$$
$$= a\,(k^2 + 1) / (k^2 - 1)$$

we form

$$(d/2)^2 - r_0^2$$
$$= \frac{a^2}{4} \cdot \frac{k^4 + 2k^2 + 1}{(k^2 - 1)^2} - \frac{a^2}{4} \cdot \frac{4k^2}{(k^2 - 1)^2}$$
$$= \frac{a^2}{4} \cdot \frac{k^4 - 2k^2 + 1}{k^4 - 2k^2 + 1} = \frac{a^2}{4} .$$

The distance between the equivalent charges is

$$a = 2\sqrt{(d/2)^2 - r_0^2} .$$

If the conductor's radius r_0 is replaced by the diameter $d_0 = 2r_0$, we get

$$a = \sqrt{d^2 - d_0^2} . \qquad (2.3\text{-}70)$$

According to Figure 2.3-24 the distance $b = (d - a)/2$ between the conductor's axis and the line charge is determined from this.

The *potential distribution* along the *x*-axis, where the highest electric field strengths occur, is derived from Eq. (2.3-67):

$$\varphi(\mathrm{x}) = \frac{Q/L}{2\pi\varepsilon} \ln \frac{r_2(x)}{r_1(x)}$$

The distances $r_1(x)$ and $r_2(x)$ have to be defined in intervals, so that the distances are positive. In the interval of interest $-a/2 < \mathrm{x} < +a/2$ (between the line charges) the potential is

$$\varphi(\mathrm{x}) = \frac{Q/L}{2\pi\varepsilon} \ln \frac{a/2 - x}{a/2 + x} . \qquad (2.3\text{-}71)$$

The *field strength profile* $E(x) = E_x(x)$ along the *x*-axis is derived from Eq. (2.3-71):

$$E(x) = -\partial\varphi/\partial x$$
$$= -\frac{Q/L}{2\pi\varepsilon} \cdot \frac{\partial}{\partial x}\left[\ln(a/2 - x) - \ln(a/2 + x)\right]$$
$$= -\frac{Q/L}{2\pi\varepsilon} \left[\frac{-1}{(a/2 - x)} - \frac{1}{(a/2 + x)}\right]$$
$$= \frac{Q/L}{2\pi\varepsilon} \left[\frac{1}{(a/2 - x)} + \frac{1}{(a/2 + x)}\right] \qquad (2.3\text{-}72)$$

The same result is obtained by direct *superposition of the field strengths, Eq*. (2.3-17).

Figure 2.3-25 shows the profiles of potential and field strength along the *x*-axis between the conductors according to Eqs. (2.3-71), (-72).

Within the conductors themselves, the equations of the charge simulation method give false results. The potential within an ideal conductor is constant, the electric field strength tends towards zero.

Outside of the conductors, for $x > d/2 + r_0$ and for $x < -d/2 - r_0$, potential and field strength magnitudes decrease in the outward direction. The field strengths at the outside of the conductors are significantly lower than the field strengths at the inner sides where the conductors are facing each other.

For the calculation of *capacitance C*, the potential difference *V* is determined as a function of the equivalent charge *Q* from Eq. (2.3-71):

$$V = \varphi(x = -d/2 + r_0) - \varphi(x = d/2 - r_0)$$
$$= \frac{Q/L}{2\pi\varepsilon} \ln \left[\frac{a/2 + d/2 - r_0}{a/2 - d/2 + r_0} \frac{a/2 + d/2 - r_0}{a/2 - d/2 + r_0}\right]$$

$$= \frac{Q/L}{\pi\varepsilon} \ln \frac{a/2 + d/2 - r_0}{a/2 - d/2 + r_0}$$

The capacitance is equal to the ratio $C = Q/U$:

$$C = \frac{\pi\varepsilon\, L}{\ln \dfrac{a/2 + (d/2 - r_0)}{a/2 - (d/2 - r_0)}} \qquad (2.3\text{-}73)$$

With the distance a between the charges according to Eq. (2.3-70), the capacitance can be written as function of the geometric quantities d and r_0:

$$C = \frac{\pi\varepsilon\, L}{\ln\left[\dfrac{d}{2r_0} + \sqrt{\left(\dfrac{d}{2r_0}\right)^2 - 1}\right]} \qquad (2.3\text{-}74)$$

Note: The deviation of Eq. (2.3-74) from Eq. (2-3-73) requires some intermediate steps. Thereby it is reasonable to cancel the expression $(d/2 - r_0)^{-1/2}$ out in the argument of the logarithm, and to make the denominator rational by expanding the fraction.

For large distances d and accordingly for small radii r_0, i.e. for $d >> r_0$, Eq. (2.3-74) is simplified:

$$C \approx \frac{\pi\varepsilon\, L}{\ln \dfrac{d}{r_0}} \qquad (2.3\text{-}75)$$

Note: This approximation can also be derived directly from Eq. (2.3-73), if the distance a between the charges is assumed to be equal to the distance d between the conductors for large distances d, Eq. (2.3-70). Therefore, we find for the numerator in the argument of the logarithm

$$a/2 + d/2 - r_0 \approx d - r_0 \approx d.$$

The denominator is

$$a/2 - d/2 + r_0 = -b + r_0 \approx r_0,$$

as the distance b between line charge and conductor axis is small in comparison with the conductor's radius r_0.

The validity limits of the approximation Eq. (2.3-75) result from an *error estimation* for different ratios d/r_0:

d/r_0	2.5	5	10	20
C_{approx}/C	0.757	0.973	0.996	0.9992
Error in %	24.3	2.7	0.4	0.08

I.e. for many electrode arrangements in high voltage engineering, the simplified Eq. (2.3-75) can be used, if the distance d of the conductors is much greater than the radius r_0.

Maximum field strength results from Eq. (2.3-72) at the conductor surface at $x = d/2 - r_0$.

In order to get an exact solution, Q is replaced by $Q = C \cdot V$ with C according to Eq. (2.3-74):

$$E_{max} = \frac{V \cdot \sqrt{\left(\dfrac{d}{2r_0}\right)^2 - 1}}{(d - 2r_0) \cdot \ln\left[\dfrac{d}{2r_0} + \sqrt{\left(\dfrac{d}{2r_0}\right)^2 - 1}\right]} \qquad (2.3\text{-}76)$$

For $d >> r_0$, i.e. for large distances d or small conductor radii r_0, Eq. (2.3-76) is simplified:

$$E_{max} \approx \frac{V}{2\, r_0 \cdot \ln \dfrac{d}{r_0}} \qquad (2.3\text{-}77)$$

For thin wires, the *inception voltage for corona discharges* can be derived, if the inception field strength E_i for discharges is known:

$$V_i \approx E_i \cdot 2\, r_0 \cdot \ln(d/r_0) \qquad (2.3\text{-}78)$$

The validity limits of Eq. (2.3-77) and (2.3-78) result from an *error estimation* for different ratios d/r_0:

d/r_0	5	10	20	40
E_{approx}/E	0.637	0.813	0.904	0.951
Error in %	36.3	18.7	9.6	4.9

Thus, the approximate Eqs. (2.3-77) and (2.3-78) for the maximum field strength and for the corona inception voltage are only accurate enough for large ratios d/r_0. Therefore, in general the exact solution from Eq. (2.3-76) must be used.

Example 2: Cylinder-to-Plane

A common high voltage electrode arrangement is a cylindrical conductor, which is led at a height h above or beside a conducting plane. This case can be reduced to the former example of parallel cylinders, if the conducting plane is regarded as a plane of symmetry or an equipotential surface with the potential $\varphi = 0$ and if the arrangement is complemented symmetrically with a second cylinder (image conductor), Figure 2.3-26. The *capacitance* C of the arrangement is twice the capacitance C' of the associated parallel cylinders. With Eq.

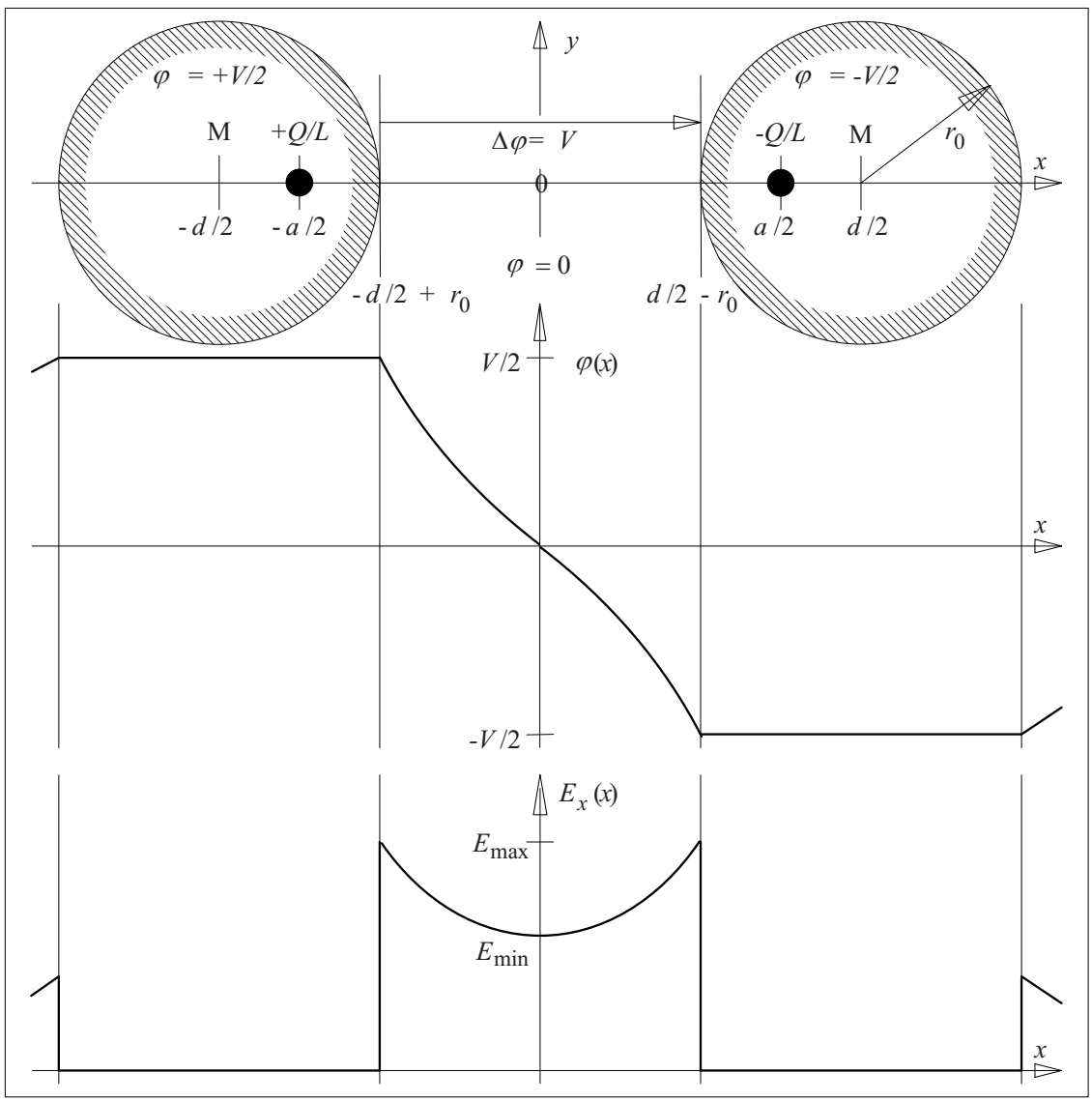

Figure 2.3-25: Parallel cylindric conductors: Potential and field strength profiles along the connecting line of the conductor centre points (x-axis) in the x,y-plane. The profiles within the conductors can not be determined from the equivalent charges.

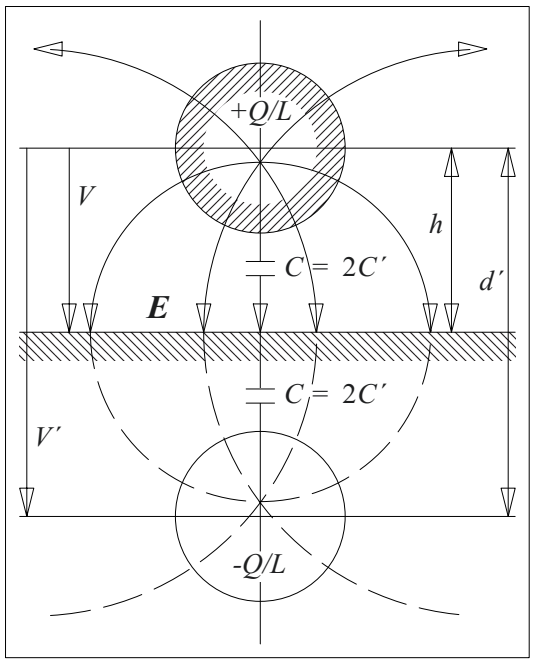

Figure 2.3-26: Cylindric conductor above a conducting plane. Field calculation by means of a symmetric image charge.

(2.3-75) and $d' = 2h >> r_0$ the capacitance is

$$C \approx \frac{2\pi\varepsilon L}{\ln \frac{2h}{r_0}} \quad . \qquad (2.3\text{-}79)$$

The *maximum field strength* is obtained from Eq. (2.3-76) or (-77), if the voltage V and distance d are replaced by $V' = 2\ V$ and $d' = 2\ h >> r_0$:

$$E_{max} \approx \frac{V}{r_0 \cdot \ln \frac{2h}{r_0}} \quad . \qquad (2.3\text{-}80)$$

For the *corona inception voltage* of a thin wire above a conducting plane we find

$$V_i \approx E_i \cdot r_0 \cdot \ln (2h/r_0) \, . \qquad (2.3\text{-}81)$$

Example 2a: Cylinder-to-Plane (numerical example)

The diameters and distances of cylindrical conductors above conducting planes shall be dimensioned for application in air ($\hat{E}$ = 30 kV/cm, $\varepsilon_r = 1$) and in insulating oil ($\hat{E}$ = 150 kV/cm, $\varepsilon_r = 2.2$) for the peak voltages $\hat{V}$ = 10 kV, 100 kV and 1 MV without the field intensities exceeding $^2/_3$ of the breakdown voltages. Furthermore, the capacitance per unit length of the configuration shall be calculated. In all cases the ratio $h/r_0 = 10$ shall be assumed to be equal.

Solution: Because of the ratio $d/r_0 = 20$, approximate Eq. (2.3-80) for the *maximum field strength* will provide an error of approx. 10 % (see above estimate). Therefore, the exact Eq. (2.3-76) is evaluated: If $2r_0$ is factored out in the denominator, the equation can be solved for r_0. For d and V the terms $2h$ and $V' = 2V$ have to be inserted:

$$r_0 = \frac{\frac{2\hat{V}}{0.67\hat{E}_D}\sqrt{10^2-1}}{2(10-1)\ln\left[10+\sqrt{10^2-1}\right]}$$

$$= 0.5540 \cdot \hat{V}/\hat{E}_D$$

The capacitance can be estimated from Eq. (2.3-79) with a small error.

Voltage $\hat{V}$:		**10 kV**	**100 kV**	**1 MV**
Air:	r_0	**2 mm**	**1.9 cm**	**18.5 cm**
	h	2 cm	19 cm	1.85 m
	C/L	18.5 pF/m	18.5 pF/m	18.5 pF/m
Oil:	r_0	**0.4 mm**	**3.7 mm**	**3.7 cm**
	h	3.7 mm	3.7 cm	37 cm
	C/L	40.8 pF/m	40.8 pF/m	40.8 pF/m

Note: As shown in all the examples with the spherical electrode (Section 2.3.1.2), with the cylindrically symmetrical tubular conductor (Section 2.3.1.3) and with the cylinder-to-plane arrangement (in the current example) it is also shown here that air-insulated equipment for the MV-range needs insulation distances and radii of curvature of the order of meters.

Much more compact *dimensions* are possible with electrically strong materials (e.g. insulating oil or sulfur hexafluoride gas SF_6).

Attention: The *electric strengths* assumed to be constant in these examples for simplicity, are not constant in reality. They depend, for example, on the type and duration of the electric field stress, on the insulating material thickness, on the insulating volume, on the electrode surface, on the inhomogeneity of the field or on environmental influences (pressure, temperature, water content, ...) for instance.

The *capacitance per unit length* does not change with the dimensions h and r_0 because of the assumption of a constant ratio h/r_0, which determines the capacitance, in this example.

Example 3: Overhead ground wire
(Shielding effect and field stress enhancement)

Grounded wires above overhead lines are used to protect the phases against direct lightning strikes. Here, it shall be investigated, to what extent the vertical electrostatic field in the atmosphere (i.e. in the air) is influenced by a grounded wire (radius r_0, height h above ground), Figure 2.3-27.

The original *field in the air* $\boldsymbol{E}_0$ is assumed to be uniform; it is directed in the negative x-direction. The potential is

$$\varphi_1 = E_0 \cdot x \, .$$

In the ground wire a charge Q is influenced whose field $\boldsymbol{E}_S$ is superimposed on the original field $\boldsymbol{E}_0$. The *additional field of the charges in the wire* against the grounded plane can be calculated from the superposition of the fields associated with Q and with an image charge $-Q$ on the x-axis at $x = -h$. According to Eq. (2.3-67), the potential is

$$\varphi_2 = \frac{Q}{2\pi\varepsilon L} \ln \frac{r_2}{r_1} \, .$$

At the *surface of the grounded wire* (and in the plane of symmetry, i.e. on the ground surface), the sum of the potentials must be zero. This condition can be used to calculate the magnitude of the influenced charge Q:

$$\varphi = \varphi_1 + \varphi_2 = 0$$

$$\varphi = E_0 \cdot x + \frac{Q}{2\pi\varepsilon L} \ln \frac{r_2}{r_1} = 0$$

For all points on the wire surface, the distances to the equivalent charges $+Q$ and $-Q$ are $r_1 \approx r_0$ and $r_2 \approx 2h$ approximately. Because of the large height $h >> r_0$, the equivalent charges are close to the axes of the wire and its image. With $x \approx h$ the charge is

$$Q = -2\pi\varepsilon L \frac{E_0 \cdot h}{\ln \frac{2h}{r_0}} \, . \qquad (2.3\text{-}82)$$

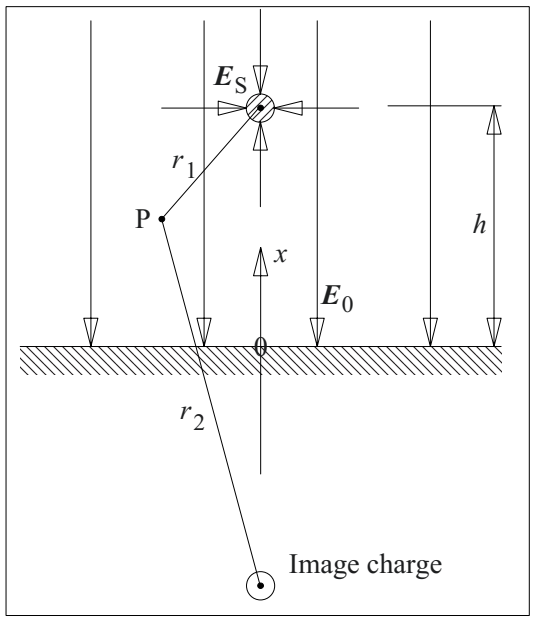

Figure 2.3-27: Distortion of the electric field in air by a conducting overhead ground wire.

The *field strength* on the x-axis is the derivate of the potential with respect to x according to Eq. (2.3-72) or it is the superposition of the field strengths according to Eq. (2.3-17). Q is inserted from (2.3-82):

$$E_x(x) = E_0 + E_{+Q} + E_{-Q}$$

$$\overset{(17)}{=} E_0 + \frac{Q}{2\pi\varepsilon L}\left(\frac{1}{h-x} + \frac{1}{h+x}\right)$$

$$\overset{(82)}{=} E_0 - \frac{E_0 \cdot h}{\ln \frac{2h}{r_0}}\left(\frac{1}{h-x} + \frac{1}{h+x}\right) \qquad (2.3\text{-}83)$$

Note: The discussion of the signs shows that the original field E_0 and the additional field of the charges have opposite directions underneath the ground wire ($0 < x < h$). Above the ground wire ($x > h$), the field E_0 in the air and the field contribution of the upper equivalent charge $+Q$ are superimposed with the same sign; the field contribution of the image charge $-Q$ is in the opposite direction, Figure 2.3-27.

The field strength at the *ground surface* ($x = 0$) is

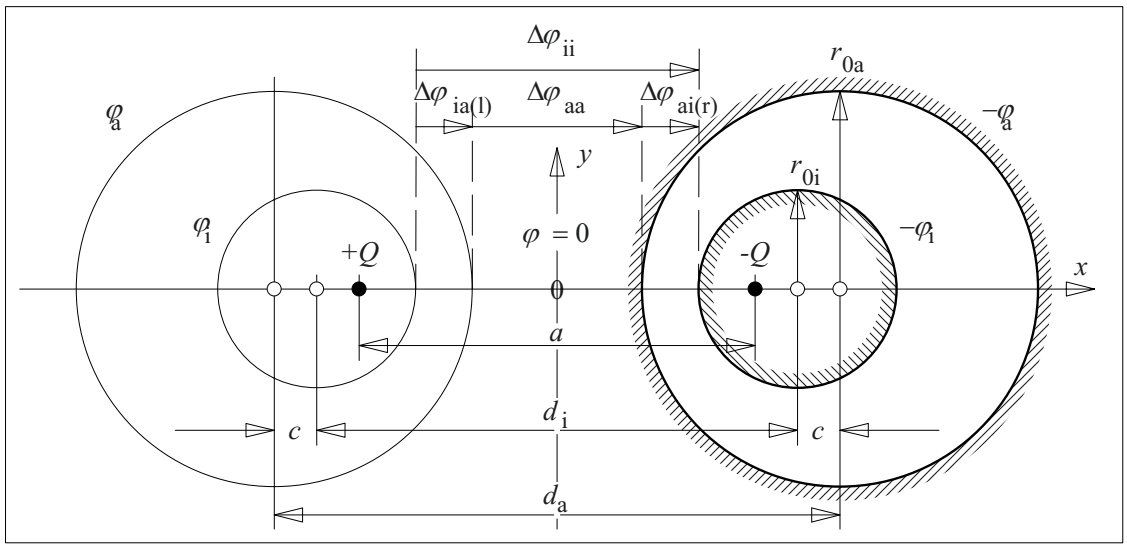

Figure 2.3-28: Calculation of eccentric conductors with equivalent line charges in parallel.

$$E_x(0) = E_0\left(1 - \frac{2}{\ln\frac{2h}{r_0}}\right). \qquad (2.3\text{-}84)$$

Note: For a ratio $h/r_0 = 1000$ the field strength is $E_x(0) = 0.74\ E_0$, i.e. there is only a weak shielding of the original field at the ground surface. Improved shielding efficiency is achieved by a *screen grid*, e.g. by an arrangement of parallel grounded wires at small intervals.

At the *upper side of the wire*, the contribution associated with upper equivalent charge Q predominates according to Eq. (2.3-82). The contribution caused by the distant image charge $-Q$ and the original field E_0 can be neglected. With the conditions $x = h + r_0$ and $2h/r_0 >> 1$ Eq. (2.3-83) provides

$$E_x(h + r_0) \approx E_0\,\frac{h/r_0}{\ln\frac{2h}{r_0}}. \qquad (2.3\text{-}85)$$

Note: For a ratio $h/r_0 = 1000$ there is a field stress enhancement of $E/E_0 = 132$. In cases of very high field strengths E_0, discharges are possible at sharp edges of grounded conductors. Especially during a lightning discharge, a discharge channel propagates from the cloud towards the ground and causes a very high increase of the local electric field strength in a limited field region. This can be regarded as an increase of the primary field E_0 which initiate *upward discharges* starting from overhead line wires, lightning conductors or other grounded structures. The discharges propagate upwards, meet the downward discharge within a limited range and cause a conducting path to the ground.

Example 4: Eccentric tubular conductor

The electric field between eccentric tubular conductors (cylinders) can be calculated with parallel line charges, if the outer and the inner conductor are interpreted as equipotential surfaces in the field of two mirror-symmetric line charges, Figure 2.3-23 and 2.3-28.

The cylinder radii r_{0i} and r_{0a} and the lateral offset of the cylinder axes c (eccentricity) are given. The distance a of the equivalent charges and distances d_i and d_a of the center points are unknown. Therefore, the Equations (2.3-70) ff cannot be applied directly.

The solution can be based on the fact that the charge distance a is equal for both the arrangement with the large cylinders (r_{0a}, d_a) and for the arrangement with the small cylin-

ders (r_{0i}, d_i). With Eq. (2.3-70) and Figure 2.3-28 we get the following solution

$$a^2 = d_i^2 - 4r_{0i}^2 = d_a^2 - 4r_{0a}^2$$

I.e.:

$$d_a^2 - d_i^2 = 4r_{0a}^2 - 4r_{0i}^2$$

$$(d_i + 2c)^2 - d_i^2 = 4r_{0a}^2 - 4r_{0i}^2$$

$$d_i = (r_{0a}^2 - r_{0i}^2 - c^2)/c \qquad (2.3\text{-}86)$$

From this all unknown geometric quantities in Figure 2.3-28 are determined. The charge distance a is determined from Eq. (2.3-70), the distance d_a is $d_a = d_i + 2c$.

Instead of a difficult general calculation, a *numerical evaluation* with specific numerical values is recommended here.

Numerical example:

It shall be investigated how much capacitance and maximum field strength are changed for an arrangement with eccentric tubular conductors (r_{0i} = 5 cm, $r_{0a} = e \cdot r_{0i}$ = 13.59 cm, c = 1 cm) in comparison with coaxial configurations.

From Eq. (2.3-86) we get d_i = 158.73 cm. From this d_a = 160.73 cm and a = 158.41 cm are derived. The *maximum field strength* at the surface of the inner cylinder can be determined from Eq. (2.3-76) with $d = d_i$ and $r_0 = r_{0i}$, if the voltage V is interpreted as potential difference $\Delta\varphi_{ii}$ between the two inner cylinders.

$$E_{max} = \Delta\varphi_{ii} / 32.45 \text{ cm} \qquad (*)$$

The potential difference $\Delta\varphi_{ii}$ has to be related to the potential difference $\Delta\varphi_{ai(r)}$ between the outer and inner cylinders on the right side: The x-axis intersects the inner cylinders at $x_i = \pm(d_i/2 - r_{0i}) = \pm 74.37$ cm and the outer cylinders at $x_a = \pm(d_a/2 - r_{0a}) = \pm 66.78$ cm. For points x_i and x_a on the negative x-axis the potentials can be calculated with Eq. (2.3-71):

$$\varphi_i = 3.458 \cdot Q/(2\pi\varepsilon L)$$

$$\varphi_a = 2.464 \cdot Q/(2\pi\varepsilon L)$$

From this, the potential differences are given:

$$\Delta\varphi_{ii} = (3.458 + 3.458) \cdot Q/(2\pi\varepsilon L)$$

$$= 6.916 \cdot Q/(2\pi\varepsilon L)$$

$$\Delta\varphi_{ai(r)} = (-2.464 + 3.458) \cdot Q/(2\pi\varepsilon L)$$

$$= 0.994 \cdot Q/(2\pi\varepsilon L)$$

The ratio of the potential differences is

$$\Delta\varphi_{ii}/\Delta\varphi_{ai} = 6.958 .$$

The *maximum field strength* is calculated from Eq. (*):

$$E_{max} = \Delta\varphi_{ai}\ 6.958 / 32.45 \text{ cm}$$

$$= \Delta\varphi_{ai} / 4.664 \text{ cm} .$$

In the cylindrically symmetric case, maximum field strength according to Eq. (2.3-22) is

$$E_{(cyl)max} = \Delta\varphi_{ai} / 5 \text{ cm} .$$

The *field stress enhancement* caused by the eccentricity c = 1 cm is 7.2 %:

$$E_{max}/E_{(cyl)max} = 1.072$$

Note: The *capacitance* C_{ai} between the inner and the outer cylinder can be calculated, if the capacitances C_{ii} and C_{aa} between the cylinders of the same size are calculated with Eq. (2.3-74). C_{ii} can then be regarded as a series circuit consisting of C_{ia}, C_{aa} and C_{ai}, Figure 2.3-28.

From this the *magnitude of the equivalent charge* $Q = C_{ai} \cdot \Delta\varphi_{ai}$ is also determined. Eq. (2.3-71) and (-72) then allow one to calculate *potential and field strength profiles* along the x-axis.

<u>Example 5:</u> Three-phase overhead line
("Working capacitance")

A three-phase overhead line is a so called *multi-phase system*, consisting of a number of parallel cylindrical conductors with different potentials and insulated against each other. The calculation of multi-phase systems is possible by means of equivalent line charges and their image charges. For a detailed analysis the basic literature can be consulted [2], [4].

As an example, a *three-phase overhead line* connected to a three-phase AC voltage system shall be considered (complex r.m.s. values of the phase voltages: $\underline{V}_{10}$, $\underline{V}_{20}$, $\underline{V}_{30}$). Perfect *symmetry* of the voltages, the conductor properties (line parameters per unit length) and the currents ($\underline{I}_1$, $\underline{I}_2$, $\underline{I}_3$) is assumed.

During the calculation of three-phase systems, lines and cables are described by line impedances determined by series resistances, series inductances, parallel capacitances and parallel conductances.

The charge simulation method allows the **calculation of a so-called "working capacitance"** of a three-phase system. This is *not* the capacitance between oppositely charged conductors, such an arrangement does *not* exist in a three-phase system.

The working capacitance C_b is defined by the single-phase capacitive charging current $\underline{I}_{C1}$ in a symmetric three-phase overhead line without load. In the positive-sequence network (i.e. in a transformed single-phase equivalent circuit) the following relationship is established:

$$\underline{I}_{C1} = \mathrm{j}\omega C_b \cdot \underline{V}_{10} \qquad (2.3\text{-}87)$$

Physically, the charging current $\underline{I}_{C1}$ is not only fed from the displacement field that is associated with the phase-to-ground voltage $\underline{V}_{10}$. The fields between the considered phase L1 and the other phases L2 and L3 cause additional displacement currents to be coupled in, i.e. there are additional influences of the phase-to-phase voltages $\underline{V}_{12}$ and $\underline{V}_{31}$, Figure 2.3-29. In order to calculate with the simple Eq. (2.3-87) despite this, it is necessary to define a *working capacitance C_b whose magnitude takes into account the influence of all interferences*.

Note: The simple assumption of a single-phase equivalent circuit, consisting solely of the so-called positive-sequence network, and considering capacitive couplings by the magnitude of the working capacitance, is only valid in the case of *perfect symmetry*. This means that the three-phase system has to be built symmetrically *and* that it has to be operated symmetrically too.

From the physical viewpoint, the single-phase equivalent circuit (the so-called positive-sequence network) is *not* identical with the phase L1 alone. Capacitive and magnetic couplings to the neighboring phases are taken into account by the magnitudes of the working capacitances and working inductances.

In the case of *asymmetric* three-phase systems, the three coupled circuits L1, L2 and L3 are transformed into three *decoupled* circuits (positive-sequence network, negative-sequence network and zero-sequence network) in order to allow a simpler and clearer calculation (*method of symmetrical components* [20]). A working capacitance can no longer be specified because the condition of symmetrical voltages and fields is no longer fulfilled.

In the special case of *perfect symmetry*, the single-phase equivalent circuit is identical with the positive-sequence network. According to Eq. (2.3-87) $1/(\mathrm{j}\omega C_b) = \underline{V}_{10}/\underline{I}_{C1}$ is the "positive-sequence impedance" of the unloaded line (resistive and inductive components are neglected).

The working capacitance C_b shall be calculated from the ratio of the charge q_1 on line L1 to the phase voltage v_{10}. The quantities q_1 and v_{10} are the instantaneous values of the time variant quantities. The charging current $i_{C1}(t)$ or $\underline{I}_{C1}$ has to carry the charge q_1 to and from the conductor. The influence of the ground is taken into account by image charges, Figure 2.3-29.

The voltage v_{10} is equal to the potential φ_1, which is established by the superposition of the contributions from all equivalent charge pairs:

$$\varphi_1 = \varphi_1(q_1,-q_1) + \varphi_1(q_2,-q_2) + \varphi_1(q_3,-q_3)$$

For overhead lines, the charge distances a_{12}, a_{13}, D_{12}, D_{13} and $D_{11} \approx 2h$ are very large in comparison to the conductor radius r_{01}. The potential at the surface of conductor L1 is determined with Eq. (2.3-67):

$$\varphi_1 = \frac{q_1}{2\pi\varepsilon L}\ln\frac{2h_1}{r_{01}} + \frac{q_2}{2\pi\varepsilon L}\ln\frac{D_{12}}{a_{12}} + \frac{q_3}{2\pi\varepsilon L}\ln\frac{D_{13}}{a_{13}}$$

The distance from any charge (with the exception of q_1) to the surface of conductor L1 is approximately equal to the charge distance to the charge q_1. The distance from q_1 to the conductor's surface is approximately equal to r_{01}.

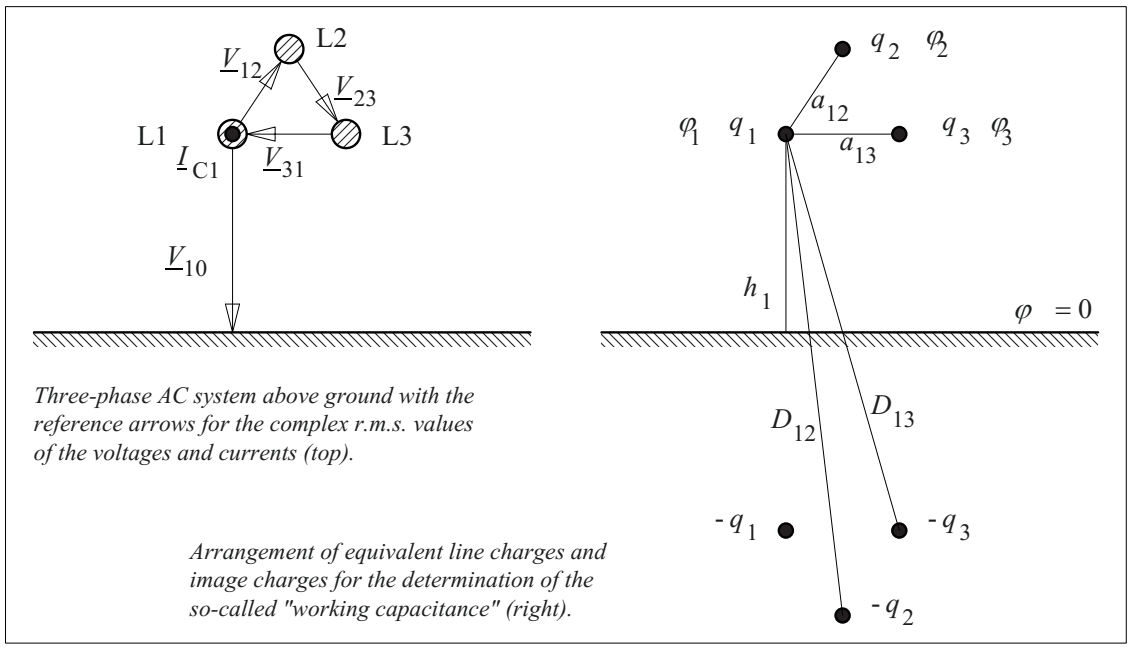

Three-phase AC system above ground with the reference arrows for the complex r.m.s. values of the voltages and currents (top).

Arrangement of equivalent line charges and image charges for the determination of the so-called "working capacitance" (right).

Figure 2.3-29: Calculation of the "working capacitance" for a symmetric three-phase system with the charge simulation method. The influence of the ground is taken into account by image charges.

In a geometrically perfectly symmetric system, the equivalent distances are equal to each other. In practice, cyclic exchanging of the phase positions compensates for the asymmetries:

$$h_1 = h_2 = h_3 = h$$

$$r_{01} = r_{02} = r_{03} = r_0$$

$$D_{12} = D_{23} = D_{31} = D = 2h$$

$$a_{12} = a_{23} = a_{31} = a$$

With this the expression for the potential of conductor L1 is simplified:

$$\varphi_1 = \frac{1}{2\pi\varepsilon L}\left[q_1 \ln\frac{D}{r_0} + (q_2 + q_3)\ln\frac{D}{a}\right]$$

In a symmetric three-phase system the sum of the charges is zero:

$$q_1 + q_2 + q_3 = 0$$

This gives the condition

$$q_2 + q_3 = -q_1 .$$

For the potential φ_1 it follows that

$$\varphi_1 = \frac{q_1}{2\pi\varepsilon L}\left[\ln\frac{D}{r_0} - \ln\frac{D}{a}\right]$$

$$\varphi_1 = \frac{q_1}{2\pi\varepsilon L}\ln\frac{a}{r_0} .$$

From this the working capacitance is derived:

$$C_b = \frac{q_1}{\varphi_1} = \frac{2\pi\varepsilon L}{\ln\dfrac{a}{r_0}} \qquad (2.3\text{-}88)$$

It is worth noting that the working capacitance, which could possibly (but misleadingly) be understood as capacitance between conductor L1 and ground, does *not* depend on the distance h between conductor and ground. The working capacitance is exclusively dependent on the distance *a between conductors* and on the conductor radius r_0.

For overhead lines with *conductor bundles*, the radius r_0 is to be replaced by the much larger equivalent radius R' according to Eq. (2.3-40), i.e. it gives a greater working capacitance than

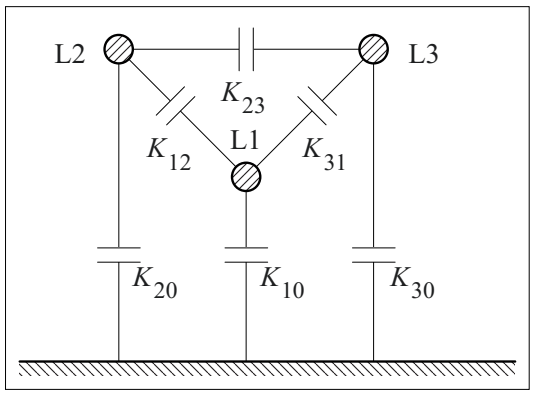

Figure 2.3-30: Coupling and ground capacitances (capacitance coefficients) of a three-phase system.

for single conductors. It can be calculated from Eq. (2.3-88).

If *several three-phase AC systems* are operated in close proximity to each other, e.g. on the same tower, the working capacitance is influenced. The former calculation for φ_1 has to be complemented with further terms associated with the additional AC conductors. Owing to the relatively large distances, they are generally of minor importance.

Generally, the charge simulation method also allows one to calculate the working capacitance of a *three-phase cable* or a *three-phase gas-insulated line*, for which the distances between the conductors are comparable with the conductor's radii [2]. In practice, values measured and specified by manufacturers are used, but they are only valid for a specific product. *High and very high voltage cables* are designed as single-phase cables with cylindrically symmetric fields, so that the working capacitance corresponds to the line-to-ground capacitance according to Eq. (2.3-20).

The *typical magnitude* of the working capacitance per unit length is approximately $C_b/L \approx$ 10 nF/km for overhead lines and $C_b/L \approx 120$ nF/km for single-phase polymer cables (with $\varepsilon_r = 2.2$ and $R_a/R_i = e$, Eq. (2.3-20)). For oil-impregnated paper cables and for cables with a smaller radius ratio R_a/R_i (e.g. medium voltage cables with a large conductor cross-section), significantly higher values can occur.

Note: Because of the high capacitive reactive power, *economic AC power transmission with cables* is normally limited to lengths of a few 10s of km.

The **measurement of the working capacitance** C_b is performed via partial capacitances, Figure 2.3-30. The charging current $\underline{I}_{C1}$ is constituted from the superposition of all displacement currents that are coupled into L1 and which are calculated from the capacitance coefficients K_{1j} and the associated potential differences $\underline{V}_{1j}$:

$$\underline{I}_{C1} = j\omega[K_{10}\underline{V}_{10} + K_{12}\underline{V}_{12} + K_{31}(-\underline{V}_{31})]$$

Because of the symmetry, $K_{12} = K_{31}$:

$$\underline{I}_{C1} = j\omega[K_{10}\underline{V}_{10} + K_{12}(\underline{V}_{12} - \underline{V}_{31})]$$

By means of a vector diagram it can be shown that $\underline{V}_{12} - \underline{V}_{31} = 3\ \underline{V}_{10}$ in a symmetric three-phase system. Thereby we get

$$\underline{I}_{C1} = j\omega\ [K_{10} + 3\cdot K_{12}]\ \underline{V}_{10}\ .$$

The comparison with Eq. (2.3-87) gives the working capacitance:

$$C_b = K_{10} + 3\cdot K_{12} \qquad (2.3\text{-}89)$$

The capacitance to ground K_{10} and the coupling capacitance K_{12} are determined from two measurements:

During the *first measurement*, L2 and L3 are grounded, i.e. K_{20} and K_{30} are short-circuited. The measured capacitance C^* between L1 and ground is

$$C^* = K_{10} + K_{12} + K_{31} = K_{10} + 2\cdot K_{12}\ .$$

During the *second measurement* the conductors L1, L2 and L3 are connected to each other. The measured capacitance C^{**} between L1-L2-L3 and the ground is now

$$C^{**} = K_{10} + K_{20} + K_{30} = 3\cdot K_{10}\ .$$

For the partial capacitances we find

$$K_{10} = C^{**}/3 \quad \text{and} \quad K_{12} = C^*/2 - C^{**}/6\ .$$

From this the working capacitance can be expressed as a function of the measured values C^* and C^{**}:

$$C_b = 3 \cdot C^*/2 - C^{**}/6 \qquad (2.3\text{-}90)$$

For the *calculation of field strengths*, the magnitude of the equivalent charges can be determined with Eq. (2.3-88). The calculation is performed *at a specific point in time* that is characterized by specific instantaneous values of the potentials (or phase-to-ground voltages) φ_1, φ_2, φ_3 and by the instantaneous values of the associated equivalent charges q_1, q_2, q_3, Figure 2.3-31. Nevertheless, the analytic calculation of field strengths from the gradient of the resulting potential (or from the vectorial superposition of the different field components) is very complex. Furthermore, the result is only valid for the considered instant. For other points in time, other field distributions, i.e. other locations, directions and magnitudes of the maximum field strength, are produced.

Note: The maximum voltage difference between the phases L1 and L2 is given for a sinusoidal voltage $v_{10}(t)$ = sin ωt at the time point $\omega t = 60^\circ$ with magnitude $\sqrt{3} \cdot \sqrt{2} \cdot V_{ph}$. The potential of phase L3 is zero at this time. If the conductors are arranged in a triangular configuration (i.e. in an equilateral triangle) and if ground-influences are neglected, the maximum field strength is located at the conductor surfaces of L1 and L2 close to the connecting line between these two phases, Figure 2.3-31. Because of

$$q_3(60^\circ) = 0$$

and

$$q_1(60^\circ) = -q_2(60^\circ) = C_b \cdot \Delta\varphi/2$$

L1 and L2 can be approximated as parallel cylindrical conductors, Figure 2.3-25.

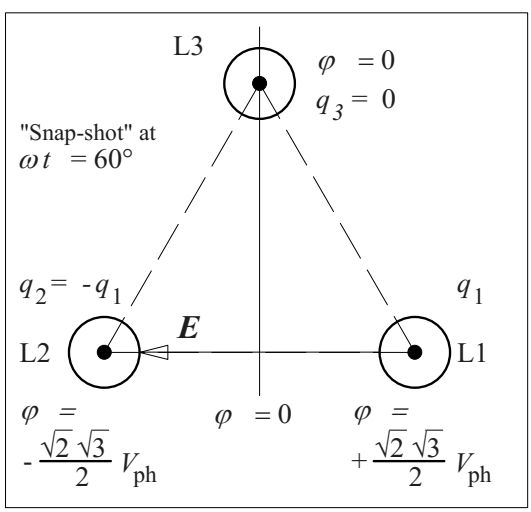

Figure 2.3-31: "Snap-shot" for the instant of maximum field strength at the surfaces of L1 and L2 (influence of the ground is neglected).

2.3.6 Similarity Relations, Field Efficiency Factor (Schwaiger's Utilization Factor)

In the above sections, the common analytical methods for the calculation of electrostatic (and quasi-static) fields were described. Of course, the high voltage problems and examples discussed are not complete, they are more exemplary in character, in order to introduce the methods and the ways of thinking.

It is clear that there is no standard procedure that always gives the desired result. It is often necessary to have a good deal of intuition, training and experience in order to find the best calculation methods and appropriate simplifications.

It is a substantial improvement for a quick and practical solution if one can avoid doing one's own complex calculation, i.e. if *already available results can be used*.

Such calculation results are given in the basic literature on electrical engineering theory, e.g. for capacitances of different electrode configurations [2].

In high voltage engineering, the *central* question has also to be answered:

> "What is the *maximum field strength* in the given insulation arrangement?"

The result can be specified independently of the applied voltage, if the maximum field strength E_{max} is given as a multiple of the mean field strength E_0 between the electrodes.

E_0 is equal to the uniform field strength in a parallel-plate capacitor with the same electrode distance s:

$$E_{\max} = \frac{1}{\eta} E_0 \qquad (2.3\text{-}91)$$

E_0 can also be regarded as the mean field strength between the electrodes:

$$E_{\text{mean}} = \frac{1}{s}\int_{P1}^{P2} \boldsymbol{E}\, \mathrm{d}\boldsymbol{x} = \frac{V}{s} = E_0$$

The maximum field strength for a given voltage V is determined from Eq. (2.3-91) by inserting $E_0 = V/s$.

The factor $\eta = E_0/E_{\max}$ is the field *efficiency factor* or *utilization factor* according to Schwaiger [21], it describes the "degree of uniformity" of the field. The inverse quantity $1/\eta$ is referred to as the *degree of non-uniformity*. In a uniform field $E_{\max} = E_0$ and the field efficiency factor is $\eta = 1$. In a very strongly non-uniform field $E_{\max} >> E_0$ and the field efficiency factor or utilization factor is $\eta << 1$.

Example: Hemispherical electrode

The maximum field strength at the surface of a hemispherical electrode on a conducting plane was calculated in Section 2.3.5.1, Figure 2.3-18. The result is $E_{\max} = 3\ E_0$, i.e. Schwaiger's field efficiency factor or the utilization factor is $\eta = 0.333 = 33.3\ \%$.

Field efficiency factors are available in catalogue-like tables from literature for a very large number of electrode arrangements [4], [22], [23]. The determination of η is performed in three steps:

1. At first, the *type of electrode arrangement* is selected from the tables, e.g. cylinder-to-plane, sphere-to-sphere, toroid-to-plane, disk-to-disk, ...

2. For each of the electrode types a specific *geometry factor p* is given as a function of geometric parameters. It is mainly to be determined from the electrode distance s and the relevant radius of curvature r:

$$p = f(\textit{geometry}) = f(s, r) \qquad (2.3\text{-}92)$$

   If additional radii R, heights h, or distances d are necessary for the description of the electrode arrangement, additional *parameters* have to be determined. Mostly they are related to r, e.g. R/r, h/r or d/r.

3. For every electrode type a *curve* is given, which shows the field efficiency factor η as a function of the geometry factor p:

$$\eta = f(p) \qquad (2.3\text{-}93)$$

   If the definition of a further parameter is required, a single curve is not sufficient. A *set of curves* for different values of the additional parameter has to be used.

Example:
Cylindrical and spherical capacitors

In the geometry catalogue, cylindrical and spherical capacitors are described with the same geometry factor $p = (r + s)/r$, because of their identical sectional view, Figure 2.3-32. Nevertheless, there are different curves for the fields with two-dimensional geometry (coaxial cylinders) and for the fields with rotational symmetry (concentric spheres).

Analytical expressions for the field efficiency factors, which are graphically represented in Figure 2.3-33, can be derived from the equations (2.3-22) and (2.3-14) for the maximum field strengths, if the radii R_1 and R_2 are replaced by r and $(r + s)$, the voltages V are replaced by $E_0 \cdot s$ and the geometry factor is introduced with $p = (r + s)/r$:

$$\eta_{\text{cyl.}} = \frac{1}{p-1}\ln p \quad \text{and} \quad \eta_{\text{spher.}} = \frac{1}{p} \qquad (2.3\text{-}94)$$

For practical applications, these equations are given as *tables of values* or as *graphs*. The geometry factor p is calculated from the given geometry and η is taken from the associated diagram, Figure 2.3-33.

Numerical example: For a coaxial, air-insulated tubular conductor with $D_a = 30$ cm and $D_i = 10$ cm the maxi-

mum possible voltage $\hat{V}$ shall be determined, if $\hat{E}_{max}$ = 15 kV/cm is accepted.

From the diameters r = 5 cm, s = 10 cm and p = 3 is calculated. The field efficiency factor $\eta \approx 0.55$ can be taken from Figure 2.3-33. With Eq. (2.3-91) we find

$$\hat{E}_0 = \eta \cdot \hat{E}_{max} = 8.25 \text{ kV/cm} \quad \text{and}$$

$$\hat{U} = \hat{E}_0 \cdot s = 82.5 \text{ kV}.$$

Note: If a considered electrode arrangement can be related to an already filed and evaluated arrangement, the determination of field efficiency factors is very advantageous for a *quick approximation* of numerical values, especially for electrode arrangements, which cannot be treated analytically or are difficult to treat analytically.

The *limited accuracy* of the method is particularly a disadvantage. In very non-uniform fields the numerical values of the field efficiency factor η are very small and can be read from a diagram (as Figure 2.3-33 for instance) only with very low accuracy. An analytical solution is therefore preferable, and furthermore it is suitable for *optimization* processes (see Section 2.3.1.2 and 2.3.1.3).

Type of electrode (sectional view)	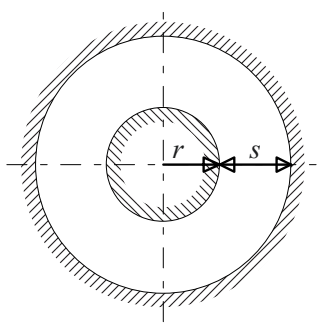
Geometry factor	$p = \frac{r + s}{r}$
Plane field arrangement	*Coaxial cylinders* Fig. 2.3-33, curve (1)
rotationally symmetric field arrangement	*concentric spheres* Fig. 2.3-33, curve (2)

Figure 2.3-32: Electrode configuration and geometry factors with reference to the curves for the determination of the field efficiency factors (example).

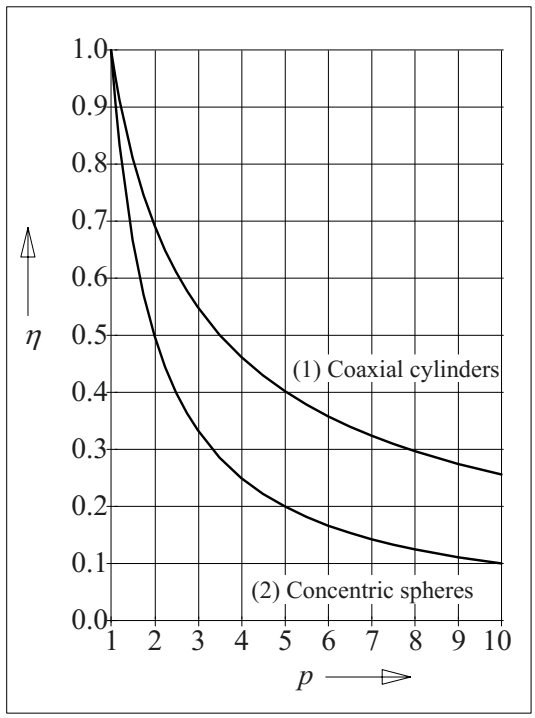

Figure 2.3-33: Field efficiency factor as a function of the geometry factor for arrangements with coaxial cylinders (1) and concentric spheres (2).

Figure 2.3-33 illustrates an interesting *relation between plane and rotationally symmetric arrangements* with identical sectional views: because of the additional curvature, the field efficient factor of the spherical arrangement decreases drastically in comparison with the cylindrical configuration. In the analytical expressions for η, the factor p can be eliminated and the relation

$$\eta_{cyl.} = -\frac{\eta_{spher.}}{1-\eta_{spher.}} \ln \eta_{spher.} \qquad (2.3\text{-}95)$$

between spherical and cylindrical arrangements is derived, Figure 2.3-34.

According to [22] this is also a useful approximation for the *general relation* between the field efficiency factors of plane field configurations and the equivalent rotationally symmetric configurations for $\eta_{plane} > 0.6$ (or $\eta_{cyl.} > 0.6$). For stronger non-uniform fields

with smaller field efficiency factors, Figure 2.3-34 can only be used for rough approximations.

Example: **Sphere gap**

The maximum field strength in a *sphere gap* with $r_0 = 0.2\ d$ shall be estimated (see Section 2.3.5.2, example "sphere gap").

At first, the field efficiency factor of an *equivalent plane configuration* with the same sectional view shall be determined. It is an arrangement of two parallel cylindrical conductors with $r = r_0$ and with the electrode distance (flashover distance) $s = 0.6\ d = 3\ r$.

From the charge simulation method we obtain with Eq. (2.3-76)

$$E_{\max(\text{plane})} = 1.462\ V/(d - 2r_0)$$

$$= 1.462\ E_0\ s/(3\ r_0)$$

$$= 1.462\ E_0\ .$$

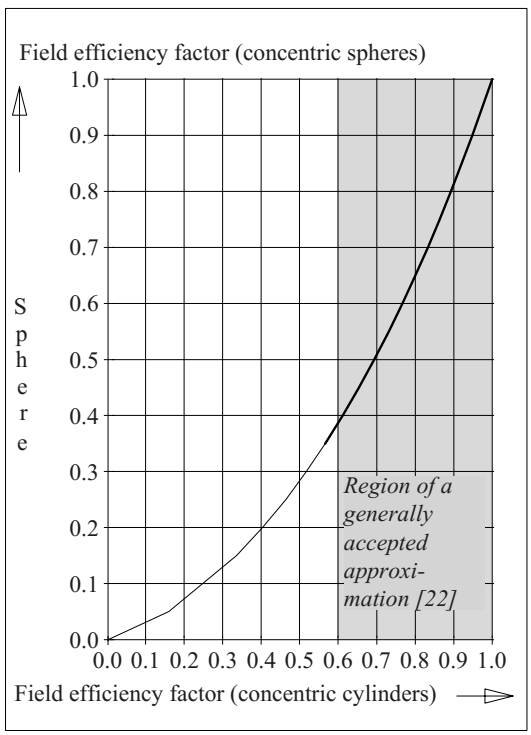

Figure 2.3-34: Comparison of the field efficiency factors of plane and rotationally symmetric electrode arrangements for the example of f cylindrical and spherical capacitors.

Thus

$$\eta_{\text{plane}} = 1/1.462 = 0.684\ .$$

From Figure 2.3-34 the field efficiency factor for the equivalent arrangement with rotational symmetry

$$\eta_{\text{rot}} \approx 0.48$$

is taken. As expected, the arrangement is significantly less uniform. The maximum field strength

$$E_{\max(\text{rot})} \approx V/(s \cdot 0.48) = 2.1 \cdot V/s\ ,$$

is in good agreement with $E_{\max} = 2.21 \cdot V/s$, calculated with the charge simulation method in Section 2.3.5.2 (sphere gap example).

It can be seen from the above numerical example that Figure 2.3-34 and Eq. (2.3-95) can be useful tools for the calculation of rotationally symmetric arrangements, if the field efficiency factor of the equivalent plane arrangement can be determined easily. Nevertheless, the method is only an approximation.

2.3.7 Measurement of Stationary Conduction Fields

Normally, the electric fields to be determined cannot be measured directly, or there are no suitable measuring methods (see Chapter 6). Therefore, we are dependent on the indirect determination of stresses by calculation.

In addition to the described analytic methods, procedures were established for the point-by-point *measurement of static conduction fields*, in order to determine complex potential distributions. In practical applications, these methods are nowadays largely replaced by more flexible and more accurate numerical field calculation methods.

Nevertheless, the analogy between steady-state conduction fields (at DC voltage) and quasi-static (slowly vaying) displacement fields (at AC voltage) is of basic importance and of great educational value.

2.3.7.1 Analogy between Dielectric Displacement Field and Static Conduction Field

The determination of *potential fields* by the measurement of static conduction fields is based on the analogy with the slowly changing dielectric displacement fields, see also Section 2.1.4. This means that permittivity ε and displacement density $\boldsymbol{D}$ have to be replaced by the conductivity κ and the conduction current density $\boldsymbol{J}$, Eq. (2.1-19) and (-20):

$$\boldsymbol{D} = \varepsilon \cdot \boldsymbol{E} \quad \text{is equivalent to} \quad \boldsymbol{J} = \kappa \cdot \boldsymbol{E} \tag{2.3-96}$$

For both kinds of fields, the electric field strength $\boldsymbol{E}$ is determined from formally identical equations. Instead of the charge Q as the source of the field, the current I is injected into the arrangement:

$$Q = \iint \boldsymbol{D}\, \mathrm{d}\boldsymbol{A} \quad \text{is equivalent to} \quad I = \iint \boldsymbol{J}\, \mathrm{d}\boldsymbol{A} \tag{2.3-97}$$

The electric field strength $\boldsymbol{E}$ and the derived quantities, potential φ and voltage V, are equivalent for the two different kinds of fields. In particular, Laplace's Equation (2.3-31) ff without space charges and current sources in the insulating volume

$$\Delta\varphi = 0 \tag{2.3-98}$$

is equally valid in both cases.

This means that the described field calculations for the electrostatic fields caused by charges are also valid for static conduction fields. Conversely, potential distributions that were measured in static conduction fields are valid for quasi-static displacement fields generated by charges.

Note: The fields, which are calculated with fixed (static) charges, are often referred to as "*static electric fields*". However, this is an auxiliary picture only, since the static case cannot exist in a real insulating material because of its (residual) conductivity. A *stationary conduction field* will inevitably develop.

Nevertheless, the electrostatic field caused by charges is a good approximation for slowly changing displacement fields in insulating materials with very low (residual) conductivity, if the conduction current density $\boldsymbol{J}$ can be neglected in comparison with the displacement current density $\partial\boldsymbol{D}/\partial t$, see also Section 2.1.4.4.

Basically, there are two methods of interest for the measurement of conduction fields, two-dimensional measurement on semi-conductive paper and three-dimensional measurement in semi-conductive liquids.

2.3.7.2 Measurements on Semi-conductive Paper ("Resistive Paper")

Two-dimensional conduction fields can be generated with the aid of semi-conductive paper by means of conductive electrodes, which are pressed onto the paper or which are painted with conductive varnish. The edge of the paper must be far away from the field region of interest in order to avoid field distortions by the artificial boundaries.

After the application of a DC voltage to the electrodes, the measurement of potential magnitudes is performed for all points of interest by means of a metal probe, which is put on the paper, point after point.

Normally, the measurement is performed in a *bridge circuit* with a null indicator in order to achieve a measurement without any reaction.

During the measurement it is useful to adjust the bridge to a distinct potential value so as to enable following the associated equipotential line on the surface of the paper by means of the probe. By suitably marking the points, an equipotential plot is generated.

Measurements on semi-conductive paper allow us to consider different conductivities κ (and different permittivities ε) by stacking papers in different numbers. However, good contact between the sheets is required.

2.3.7.3 Measurements in Semi-conductive Liquids ("Electrolytic Tank")

Any *three-dimensional* field arrangement can be measured (*field plotter*) point-by-point by lowering the electrode arrangement into a semi-conductive liquid (e.g. in a water-based electrolyte). In principle the original electrode itself can be investigated, if an electrolytic tank of sufficient size is available.

The field limitations at the basin walls must not have any influence on the field in the region of interest. Therefore, basin dimensions have to be large in many cases.

The simulation of different permittivities with liquids of different conductivities, which must be in contact at their interfaces without any mixing, is not readily achievable.

A three-dimensional field pattern requires a large quantity of data to be measured. Therefore an automatic measurement process with positioning of the measurement probe ("field plotter") is recommended.

Of course, the probe that is immersed inserted in the liquid must be insulated against the liquid, with the exception of actual measurement tip.

2.4 Conduction and Displacement Fields in Inhomogeneous Dielectrics

Matter in the electric field has a significant influence on the formation of the field and potential distribution:

- Additional fields are caused by polarization, i.e. by displacement of charge carriers (ions, charged atoms, molecules and molecule groups) or by orientation of existing dipoles in the electric field. This is described by the *permittivity* ε of the insulating material.
- The movement of charge carriers in the electric field causes a so-called conduction field. This is described by the so-called *(residual) conductivity* κ of the insulating material.

In Section 2.3, the fields in *homogeneous dielectrics* were calculated with constant permittivities ε and constant conductivities κ, i.e. it was assumed either that there was a perfectly homogeneous dielectric in the field volume, or that there was absolutely no matter (perfect vacuum). Dependences on environmental parameters (e.g. temperature), field dependences (non-linearities) and dependences on direction (isotropy) are not considered.

Under these conditions, there is absolutely no influence of the material parameters ε and κ on the potential distribution and on the magnitude and direction of the electric field $\boldsymbol{E}$.

Nevertheless, in reality the field quantities $\boldsymbol{D}$ and $\boldsymbol{J}$ depend on material properties. Thereby the capacitance C of the electrode arrangement

$$C = \frac{Q}{U} = \frac{\oiint \boldsymbol{D}\,\mathrm{d}\boldsymbol{A}}{U} = \varepsilon \frac{\oiint \boldsymbol{E}\,\mathrm{d}\boldsymbol{A}}{U} \qquad (2.4\text{-}1)$$

is also dependent on the permittivity ε. In addition, the volume resistance R and the conductance G of the electrode arrangement is a function of the conductivity κ:

$$G = \frac{1}{R} = \frac{I}{U} = \frac{\oiint \boldsymbol{J}\,\mathrm{d}\boldsymbol{A}}{U} = \kappa \frac{\oiint \boldsymbol{E}\,\mathrm{d}\boldsymbol{A}}{U} \qquad (2.4\text{-}2)$$

Note: From these equations the "self-discharging time constant" of the insulating material is derived as

$$\tau_\mathrm{d} = RC = \varepsilon/\kappa \qquad (2.4\text{-}3)$$

(see also Section 2.1.4.3, example of the self-discharging of a dielectric). I.e. for a given capacitance C the resistance R can be calculated directly, if τ_d is known.

Homogeneous insulating materials can only be found in some areas in a high voltage engi-

neering insulation system, e.g. as air insulation in overhead lines, as pressurized gas insulation in enclosed switchgear (GIS) or as cable insulation in coaxial cables. **Insulation systems** in service always need *further insulation components*, e.g. string insulators (overhead lines), post insulators (enclosed switchgear) or cable terminations (cables).

Generally, it is not sufficient to regard the homogeneous insulation parts only, also the parts with *different insulating materials* must be considered. Complex insulation systems (e.g. in transformers, bushings, cable fittings) always consist of a number of components with different insulating materials (e.g. oil, impregnated paper, impregnated pressboard, polymeric films, porcelain, epoxy resin, silicone or air).

Field and potential distributions in arrangements with a number of insulating materials can differ significantly from field and potential distributions in homogeneous arrangements. Especially at the interfaces, there are refractions of field vectors, refractions of equipotential lines and discontinuities of field quantities.

In the following the physical reason and the mathematical description of *polarization* and *conductivity* in insulating materials is discussed (Section 2.4.1). This allows one to calculate the *basic insulation structures* with interfaces orthogonal, parallel and inclined to the field direction (Section 2.4.2).

The use of *analytical field calculation methods* for insulating systems (Section 2.4.3) allows the calculation of some important *special cases*, e.g. for layered capacitor insulations, coated electrode surfaces, barrier systems, ruptures and slots, bubbles and voids, and for triple-points and interstices at the electrode surfaces.

At first, the discussion refers to the quasi-static *dielectric displacement field* (for an AC voltage) and to materials with different permittivities ε. Because of the analogies described in Section 2.3.7.1 the results can be transferred to the stationary *conduction field* (for a DC voltage) and to materials with different conductivities κ (Section 2.4.4).

2.4.1 Conductivity and Polarization

In most cases, the atomic structure of matter, i.e. the presence of charged protons and electrons, cannot be detected directly because of a statistically uniform distribution of the charges. They are either mobile (free) or immobile (fixed).

2.4.1.1 Conductivity

The forces of the electric field accelerate *mobile charges* and impacts slow them down. Statistically averaged, there is constant *drift velocity* $\boldsymbol{v}$ and a constant *current density* $\boldsymbol{J}$, which are proportional to the electric field strength $\boldsymbol{E}$ [24], [25]. The Material Equation (2.1-20) describes this relation with the proportionality coefficient κ (*conductivity*):

$$\boldsymbol{J} = \kappa \cdot \boldsymbol{E} \qquad (2.4\text{-}4)$$

Note: In gases, the linear relation is no longer valid for high field strengths. At first, there are saturation effects and then, the current increases again because of the production of further charge carriers by impacts. (see Chapter 3).

In liquid and solid insulating materials, Eq. (2.4-4) can often be used as a good approximation. Depending on the type of the mobile charge carriers, *ion conductivity* and *electron conductivity* are distinguished.

Conductivities of insulating materials strongly depend on the materials used, impurities, manufacturing processes and service conditions (e.g. on temperature, sometimes also on stress duration and field strength). For example, conductivities often increase exponentially with the temperature. The differences between different insulating materials can be many orders of magnitude. A more accurate assessment follows in Chapter 4.

The reliability of a field calculation for a stationary conduction field (i.e. for a steady-state DC voltage) depends very strongly on the reliability of the conductivity values used. For practical applications, special attention must be given to the determination of *relevant* conductivity values.

2.4.1.2 Polarization

The forces of the electric field can displace *immobile* positive and negative charge carriers against each other, and polarization of the insulating material is caused, Figure 2.4-1. There are a number of different polarization mechanisms [24], [25]:

- The displacement of the negative electron shell relative to the positive nucleus deforms the atom. It is called *electron polarization* or *polarization by deformation*.
- The displacement of atoms carrying different charges deforms molecules. It is called *atom polarization* or *polarization by deformation* as well.
- The displacement of differently charged lattice elements in a crystal lattice causes the *lattice polarization*.
- The orientation of polar molecule groups, molecules or particles (so-called electric dipoles) is called *molecular polarization* or *orientation polarization*.
- Furthermore, the accumulation of charge carriers at macroscopic or microscopic interfaces between materials with different conductivities causes polarization of the dielectric, i.e, the so-called *interfacial polarization.*

The influence of different polarization processes is always the same: From the superposition of many dipole fields, an additional electric field $\boldsymbol{E}_{\mathrm{Dip}}$ is generated, which is superimposed on the original field $\boldsymbol{E}_0$ of the same arrangement without insulating material ("vacuum field"), Figure 2.4-2b:

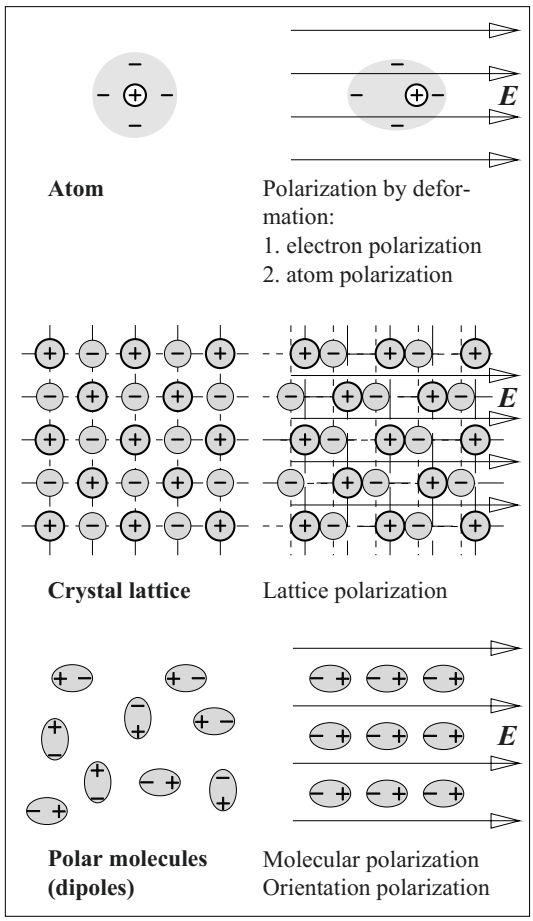

Figure 2.4-1: Polarization of insulating materials by the forces of an electric field (right).

$$\boldsymbol{E} = \boldsymbol{E}_0 + \boldsymbol{E}_{\mathrm{Dip}} \qquad (2.4\text{-}5)$$

The dipole field, generated by the displaced charges, is oppositely directed to the original vacuum field. Therefore the magnitude of the resulting field is

$$E = E_0 - E_{\mathrm{Dip}}\,. \qquad (2.4\text{-}6)$$

The physical relations shall be explained by means of a thought experiment:

An insulating material is inserted into a capacitor with the charge Q, Figure 2.4-2a and -2b. Thereby the charge Q on the electrodes is not changed, if the capacitor is not connected to an external voltage source, i.e. *constant*

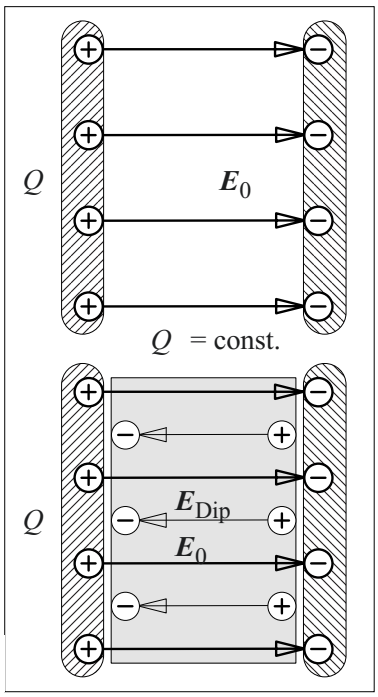

Figure 2.4-2a: Electrostatic field in vacuum.

Figure 2.4-2b: Additional electric field caused by the polarization of a dielectric for a given constant charge Q.

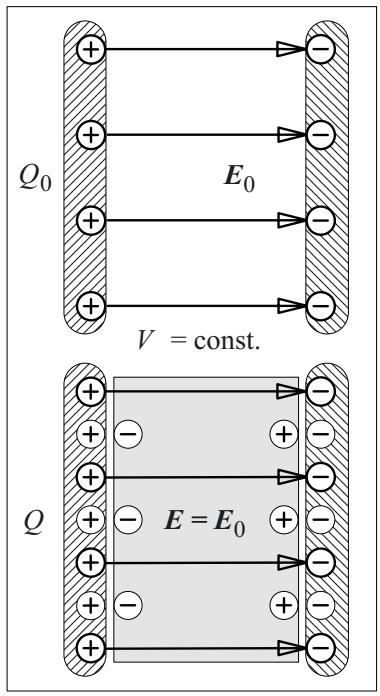

Figure 2.4-3a: Electrostatic field in vacuum.

Figure 2.4-3b: Binding of additional charges on the electrodes by polarization of a dielectric at constant voltage.

charge $Q = D \cdot A$ and constant dielectric displacement density

$$D = \varepsilon_0 \cdot E_0 = \text{const.}$$

are assumed. With Eq. (2.4-6) D is

$$D = \varepsilon_0 \cdot (E + E_{Dip})$$
$$= \varepsilon_0 \cdot E + P.$$

The term $P = \varepsilon_0 \cdot E_{Dip}$ is referred to as *(di)electric polarization*. It has the same dimension as the electric displacement density D. The vector $\boldsymbol{P} = -\varepsilon_0 \cdot \boldsymbol{E}_{Dip}$ can be seen as the fraction of the displacement density $\boldsymbol{D}$, for which the electric field is compensated by the polarized charges. Generally the displacement density is

$$\boldsymbol{D} = \varepsilon_0 \cdot \boldsymbol{E} + \boldsymbol{P}. \qquad (2.4\text{-}7)$$

The fraction $\varepsilon_0 \cdot \boldsymbol{E}$ is associated with those charges on the electrode, which are *not* compensated by the polarized charges in the insulating material. Accordingly, they generate an electric field $\boldsymbol{E}$ which is reduced in comparison with $\boldsymbol{E}_0$, see also Eq. (2.4-5) and (-6).

Usually, the influence of the polarization, i.e. the influence of the insulating material, is described by a factor ε_r , the so-called relative permittivity (relative dielectric constant). Thus, the general *Material Equation* or the Constitutive Relation (2.1-2) and (-19) is defined:

$$\boldsymbol{D} = \varepsilon_0 \cdot \varepsilon_r \cdot \boldsymbol{E} \qquad (2.4\text{-}8)$$

The absolute permittivity of vacuum ε_0 (electric constant) and the relative permittivity ε_r are often combined as permittivity ε (dielectric coefficient/ constant):

$$\varepsilon = \varepsilon_0 \cdot \varepsilon_r \qquad (2.4\text{-}9)$$

From the equality of the Equations (2.4-7) and (-8) the polarization $\boldsymbol{P}$ is derived:

$$\boldsymbol{P} = \varepsilon_0 \cdot (\varepsilon_r - 1) \cdot \boldsymbol{E} \qquad (2.4\text{-}10)$$

In vacuum there is no polarization, i.e. $\boldsymbol{P} = 0$ and $\varepsilon_r = 1$. In the presence of matter we always find $\varepsilon_r > 1$.

According to Eq. (2.4-1), the insertion of a dielectric material causes an *increase of capacitance*:

$$C = \varepsilon_r \cdot C_0 \qquad (2.4\text{-}11)$$

Note: Up to now it was assumed that a capacitor both without and with a dielectric material carries a defined *constant charge Q*. In this case, the insertion of the dielectric is associated with a polarization that reduces the field strength $\boldsymbol{E} = \boldsymbol{E}_0/\varepsilon_r$ and the capacitor voltage V, Figure 2.4-2.

Similar reasoning can also be performed for a capacitor with a *constant voltage V* and a constant field strength $\boldsymbol{E}$, both sustained by an external voltage source. In this case, the insertion of a dielectric is associated with a polarization that binds additional charges on the electrodes in addition to the existing electrode charge Q_0, Figure 2.4-3. The additional charges must be supplied by a current from the connected source. The increase of the charge Q on the electrodes corresponds to the increase of the displacement density

$$\boldsymbol{D} = \varepsilon_0 \cdot \varepsilon_r \cdot \boldsymbol{E} = \varepsilon_r \cdot \boldsymbol{D}_0 \,. \qquad (2.4\text{-}12)$$

Then the polarization $\boldsymbol{P}$ in Eq. (2.4-7) can be interpreted as the displacement density, which is associated with the additional charges that are bound on the electrodes.

The values of the relative permittivities depend strongly on the relevant *polarization mechanisms*, Fig 2.4-4. In the following some typical values (for room temperature and power frequency f = 50/ 60 Hz) are discussed:

- In a perfect *vacuum*, there is no polarizable matter. Therefore the permittivity is $\varepsilon_r = 1$.
- In *gases*, there is little matter in comparison with liquids and solids, and the atoms or molecules do not have a polar character. Because of electron polarization there is a small, often negligible increase of the relative permittivity. For *ambient air* we find $\varepsilon_r = 1.0006$.
- Materials with *symmetric, non-polar molecules* have comparatively small permittivities, caused by electron, atom or lattice polarization. For *mineral oil* and for *polyethylene (PE)* the relative permittivity is approximately $\varepsilon_r = 2.2$ to 2.3.
- *Asymmetric and more complex molecules* often have high dipole moments. Because of molecular polarization (orientation polarization) there are higher relative permittivities. Some values are $\varepsilon_r = 3.5$ for *polyvinyl chlorid*e (PVC), $\varepsilon_r = 3.5$ ... 4 for *epoxy resin (EP)*, $\varepsilon_r = 5$ for *castor oil* and up to $\varepsilon_r = 7$ for *cellulose fibers*.
- Liquids with *polar molecules* of *high mobility* have very high permittivities because of molecular polarization (orientation polarization). We find $\varepsilon_r = 40$ approximately for *glycerin* and $\varepsilon_r = 81$ for *water*.

  Note: Both water and glycerin, have a comparatively high ionic conductivity. Therefore, they can be used as dielectrics for very short impulse stresses only.
- Extreme relative permittivities $\varepsilon_r > 1000$ can be observed in so-called *ferroelectrics*. Close to the transformation temperature of a crystal structure the binding conditions can change so as to cause a so-called "polarization catastrophe", i.e. an extreme increase of the permittivity, under the influence of the electric field [25]. This effect is strongly dependent on temperature and field strength; it occurs only in the direction of certain crystal axes. For *barium titanate* $\varepsilon_r = 3000$ ... 7000 approximately.

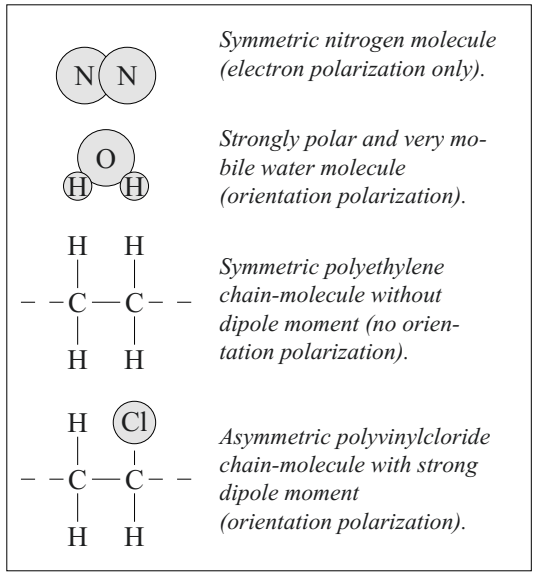

Figure 2.4-4: Examples for polarization mechanisms in insulating materials.

Permittivities are not constant quantities; they vary mainly with *temperature T* and *frequency f* of the electric field, see Figure 2.4-5 and Section 4.2.

With increasing *temperature* the mobility of given dipoles increases on the one hand, and on the other hand the Brownian motion and thermal agitation cause an increasing destruction of dipole orientation by collisions. Therefore, an increasing temperature can be associated with an increasing relative permittivity ε_r at first, because of the increasing mobility of the dipoles formerly "frozen" at lower temperatures. This is often accompanied by a structural change of the insulating material. Further increasing temperatures then result in decreasing relative permittivities, Figure 2.4-5 (top) and Figure 4.2-13.

With increasing *frequency*, the polarization is influenced by the mass inertia and interaction of the dipoles, which is maximal for the orientation of larger dipoles and minimal for the electron polarization. With increasing frequency, the dipoles cannot follow the field changes without delay, because of their mass inertia. Therefore, the relative permittivity is strongly dependent on frequency (dispersion): Generally ε_r decreases with increasing frequency in steps, which are associated with the stepwise drop-out of different polarization processes, Figure 2.4-5 (bottom), 4.2-3 and 4.2-13.

Note: Similar to the resistive losses in a conduction field (current losses), *polarization losses* (*dissipation*, *dielectric losses*) occur during the polarization process. These losses are caused by collisions and energy dissipation during the repetitive re-orientation of the dipoles with the frequency of the applied field. At low frequencies, the polarization losses are small, because of the low repetition rate. At high frequencies, there is no polarization any more and no dissipation consequently. Maximum losses are produced in the range of the transition frequency, Figure 2.4-5 bottom, see Chapter 4.

For sinusoidal AC fields the dielectric displacement current and a fictitious loss current (describing the losses both by conduction current and by polarization) can be described in frequency domain by a *complex relative permittivity*. The real part equals ε_r and the imaginary part describes the losses, see Section 4.2.4.

2.4.2 Multi-dielectric Arrangements

For multi-dielectric arrangements, special boundary conditions for field quantities of slowly changing fields at dielectric interfaces can be derived from Maxwell's Equations (Section 2.4.2.1). Multi-dielectric arrangements with interfaces orthogonal, parallel and inclined to the field direction are discussed for the dielectric displacement field, which is normally assumed for alternating fields in insulating materials (Section 2.4.2.2 to 2.4.2.4). The stationary conduction field at DC voltages is discussed analogously in Section 2.4.4.

2.4.2.1 Boundary Conditions at Interfaces

The interface between two different insulating materials is considered, Figure 2.4-6.

From the integration of the electric field strength $\boldsymbol{E}$ along a very small closed path P_1-P_2-P_3-P_4-P_1 on both sides of the interface, Faraday's law gives according to Eq. (2.1-32)

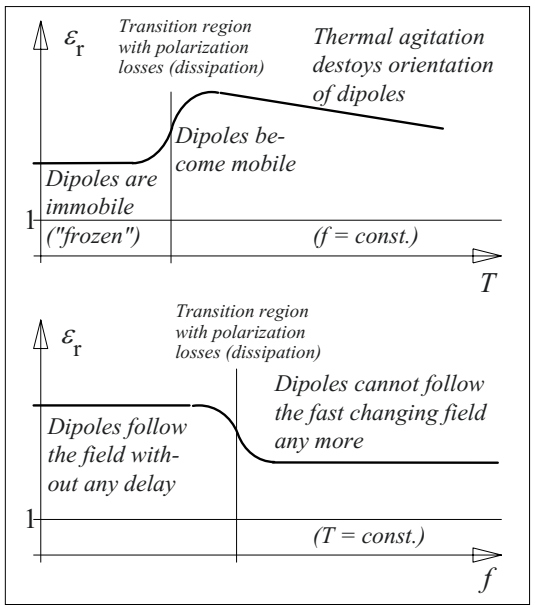

Figure 2.4-5: General dependence of the relative permittivity on the parameters temperature T and frequency f for a dielectric with orientation/ molecular polarization (schematic), cf. Figure 4.2-13.

$$\oint \boldsymbol{E}\,\mathrm{d}\boldsymbol{s} \;=\; E_{1t}\cdot s \;+\; (-E_{2t})\cdot s \;=\; 0.$$

Therefore, the *tangential components* of the *electric field strength* are equal on both sides of the interface:

$$E_{1t} \;=\; E_{2t} \qquad (2.4\text{-}13)$$

If the line P_1-P_2-P_3-P_4-P_1 is regarded as contour of a closed surface, it can be concluded from Gauss's law/ continuity Eq. (2.1-35) that all the current entering the enclosed volume on one side of the interface has to leave it on the other side. This condition is expressed by the continuity of the *normal components* of *current densities* (both conduction *and* displacement current density):

$$J_{1n} + \partial D_{1n}/\partial t \;=\; J_{2n} + \partial D_{2n}/\partial t \qquad (2.4\text{-}14)$$

In many cases, it is possible to confine oneself to the *special cases* of the stationary conduction field (without displacement current) and the dielectric displacement field (without conduction current).

Therefore, in the case of the **stationary conduction field** (at DC voltage), the *normal component of the conduction current density* ***J*** continuously passes through the interface:

$$J_{1n} \;=\; J_{2n} \qquad (2.4\text{-}15)$$

For the **dielectric displacement field** (at AC voltage, if the conduction current can be neglected) the *normal component of the displacement density* ***D*** continuously passes through the interface:

$$D_{1n} \;=\; D_{2n} \qquad (2.4\text{-}16)$$

In the following, the d*ielectric displacement field* alone is discussed. It can normally be assumed in insulating materials for alternating fields at power frequency and above.

Because of the analogy of the Equations (2.4-15) and (-16), the results can be transferred to the stationary conduction field for DC fields (Section 2.4.4). For this purpose, in particular the ratio of the permittivities $\varepsilon_1/\varepsilon_2$ must be replaced by the ratio of the conductivities κ_1/κ_2.

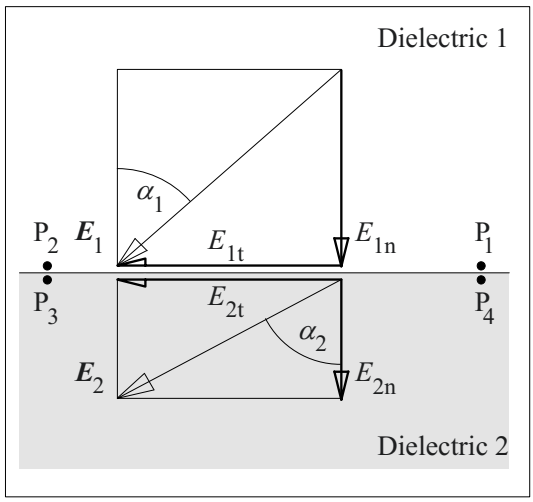

Figure 2.4-6: Vectors of the electric field strength at an interface between two dielectrics.

2.4.2.2 Interface Orthogonal (Normal) to the Field („Field Displacement")

For "sandwiched" dielectrics, if the interface between two dielectric layers (with permittivities $\varepsilon_1 = \varepsilon_0\cdot\varepsilon_{r1}$ and $\varepsilon_2 = \varepsilon_0\cdot\varepsilon_{r2}$) is orthogonal to the electric field, the displacement density continuously passes through the interface, Figure 2.4-7. The magnitudes of the field quantities D and E are identical with the magnitudes of the normal components. According to Eq. (2.4-16) the displacement densities $D_1 = D_2$ are equal, i.e.

$$\frac{E_1}{E_2} \;=\; \frac{\varepsilon_2}{\varepsilon_1} \;. \qquad (2.4\text{-}17)$$

The magnitudes of the field strengths and the permittivities are inversely rated to each other.

> The dielectric with the <u>*lower* permittivity</u> is stressed with a <u>*higher* field strength</u> than the material with the higher permittivity. This effect is called **"field displacement"** into the dielectric with lower permittivity.

Note: The *field displacement* is of fundamental importance in high voltage engineering. For instance air or gas-filled insulating layers, which have a comparatively low electric strength, are stressed with strongly enhanced field strengths because of the field displacement effect. Gas-filled *gaps*, *cracks*, *cavities*, *shrink holes* and *voids* are some of the most frequent/common reasons for defective insulations and partial discharges, Figure 2.4-8. *Partial discharges* (PD) mostly cause a slowly progressing *erosion* of the insulating material, finally leading to breakdown.

In non-uniform fields, the field displacement effect can be used to reduce the stress on regions with high field stresses and to displace some of the stress into regions with lower field strengths.

For the partially uniform field of the parallel-plate capacitor according to Figure 2.4-7, the voltage is

$$V = V_1 + V_2 = E_1 \cdot d_1 + E_2 \cdot d_2 \,.$$

With Eq. (2.4-17) the field strengths are

$$E_1 = \frac{V}{d_1 + d_2 \dfrac{\varepsilon_{r1}}{\varepsilon_{r2}}} \qquad (2.4\text{-}18)$$

and

$$E_2 = \frac{V}{d_1 \dfrac{\varepsilon_{r2}}{\varepsilon_{r1}} + d_2} \,. \qquad (2.4\text{-}19)$$

<u>Example:</u> Epoxy resin plate in an oil-insulated parallel-plate capacitor

An epoxy resin plate (d_2 = 12 mm, ε_{r2} = 4.4) is inserted into an oil-insulated parallel-plate capacitor (d = 20 mm, ε_{r1} = 2.2). The field changes shall be calculated for $\hat{V}$ = 80 kV AC.

Prior to the insertion of the plate, the field strength is $\hat{E}_0 = \hat{V}/d$ = 4 kV/mm. After the insertion of the plate, the field strengths for the oil gap and for the epoxy resin plate are $\hat{E}_1$ = 5.71 kV/mm = 1.43·$\hat{E}_0$ and $\hat{E}_2$ = 2.86 kV/mm = 0.71 $\hat{E}_0$, calculated with Eq. (2.4-18) and (-19) and with d_1 = 8 mm. The field strength in the oil is increased by 43 % through the insertion of the plate.

Note: The *highest* field displacement occurs for a very thin oil gap. With $d_1 << d_2 \cong d$ the field strength is $\hat{E}_1 \cong \hat{V}/(0 + d\ \varepsilon_{r1}/\varepsilon_{r2}) = \hat{E}_0 \cdot \varepsilon_{r2}/\varepsilon_{r1} = 2 \cdot \hat{E}_0$.

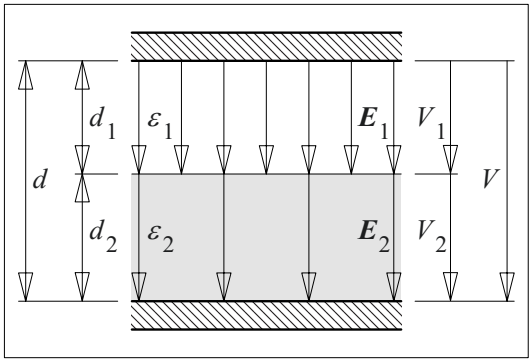

Figure 2.4-7: Two dielectrics in a parallel-plate capacitor with an interface orthogonal to the the electical field ("field displacement").

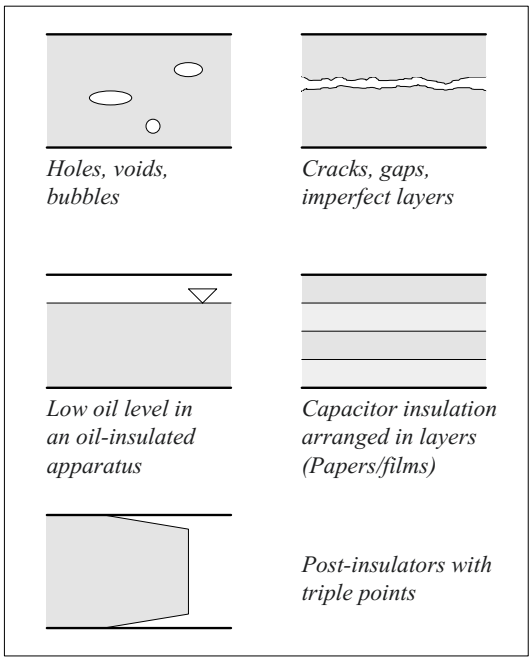

Figure 2.4-8: Examples of field displacement effects in high voltage engineering.

Example: Insulating barrier in an air-insulated parallel-plate capacitor

An insulating barrier (d_2 = 4 cm, ε_{r2} = 5) shall be introduced into an air-insulated parallel-plate capacitor (d = 5 cm). The (macroscopic) partial discharge inception field strength E_{pd} is 15 kV/mm. The partial discharge inception voltages V_{pd} shall be calculated, in order to investigate whether the electric strength can be increased by the insertion of the barrier.

Without a barrier, V_{pd} is 75 kV. In a uniform field, the inception of discharges is directly accompanied by a breakdown. With a barrier, V_{pd} is 27 kV according to Eq. (2.4-18). At this voltage the air gap breaks down (partial breakdown), but the barrier prevents a total breakdown at first. After some time, the permanent discharge activity in the air gap will erode most of the insulating barriers (made of organic materials). Thus, the insulating barrier *deteriorates* the quality of the insulation!

Note: In high voltage insulations, the effect of electric strength deterioration because of field displacement effects is countered by a complete *impregnation* of all voids and gaps with an electrically strong insulating oil.

2.4.2.3 Interface Parallel to the Field (Tangential Interface)

If the interface between two dielectrics and the electric field are in parallel (tangential), the field strength is equal on both sides. $\boldsymbol{E}$ is tangential to the interface and it is continuous according to Eq. (2.3-13), Figure 2.4-9:

$$E_1 = E_2 = E_0 = V/d \qquad (2.4\text{-}20a)$$

According to the material Eq. (2.4-8), the displacement densities on both sides of the interface are determined by

$$D_1/\varepsilon_1 = D_2/\varepsilon_2 \,. \qquad (2.4\text{-}20b)$$

Therefore, the displacement densities in the two dielectrics are different because of different polarizations. Consequently, there is more charge on the electrode surface areas adjacent to the material with the higher permittivity than on the electrode surface areas adjacent to the material with the lower permittivity.

Because of the equal field strengths in both materials, it could be supposed that an interface in parallel to the electric field should be a good insulation arrangement. Nevertheless, it can often be observed that the **electric strength** of a tangential interface is *lower* than the strength of the two adjacent materials.

This seemingly paradoxical interfacial problem can have different causes depending on the type of interface:

- Material properties close to the surface often are different from the properties of the bulk material. Often, electrons are only *weakly bound* in impurity traps. Therefore, additional charge carriers are available for the generation of *surface avalanches and discharges*.
- Additionally, deposits of *foreign conductive and semi-conductive layers* can cause potential shifts and field stress enhancements at the surface. A flashover triggered as a result of this is referred to as *"pollution flashover"*.

Note: *DC stresses* are especially critical because the semi-conductive pollution layers can have a very high conductivity in comparison with the insulating material.

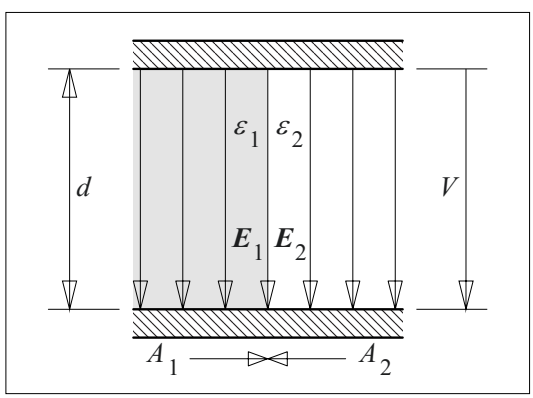

Fig. 2.4-9: Two dielectrics in a parallel-plate capacitor with an interface parallel to the field ("tangential interface").

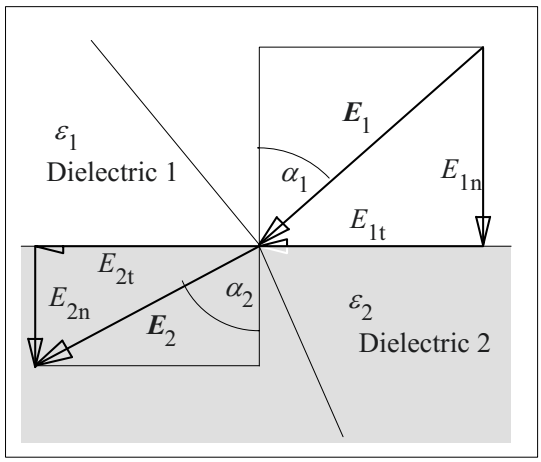

Figure 2.4-10: Vectors of the electric field strength, inclined to the interface between two dielectrics.

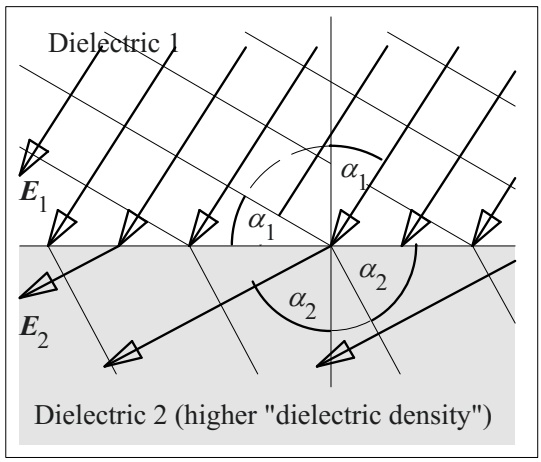

Figure 2.4-11: "Refraction" of field and equipotential lines at the interface between two dielectrics.

Also in the case of *AC stresses,* heavy pollution of insulator surfaces together with humidity can cause field distortions and flashovers. Insulators are therefore equipped with *shed profiles* , which guarantee relatively clean and dry zones, see also Figure 1-1 for example. In extreme cases *hydrophobic (water-repellent) materials* are used, e.g. silicone elastomers.

- Insulator surfaces are never totally smooth and parallel to the field. Because of the microscopic *surface roughness*, there are microscopically tiny areas with interfaces orthogonal to the field, so that *local field stress enhancements* can occur through field displacements.

2.4.2.4 Interface Inclined (at an Angle) to the Field (“Refraction Law”)

If the vector of the electric field strength $\boldsymbol{E}$ and the area vector $\boldsymbol{A}$ (orthogonal to the interface) enclose an angle α between 0° and 90°, the electric field is *“inclined to the interface”*, Figure 2.4-10. There are different angles α_1 and α_2 on both sides of the interface, i.e. field lines and equipotential lines are subject to *refraction* at the interface.

The so-called “refraction law” for the dielectric displacement field is derived from Eq. (2.4-13) and (-16). As the normal components of the displacement density $\boldsymbol{D}$ are continuous at the interface, this gives

$$D_{1n} = D_{2n}$$

and

$$\varepsilon_{r1} \cdot E_{1n} = \varepsilon_{r2} \cdot E_{2n} .$$

Furthermore, the tangential component of the electric field strength is continuous, i.e.

$$E_{1t} = E_{2t} .$$

The division of the two continuity conditions gives

$$E_{1t}/(E_{1n} \cdot \varepsilon_{r1}) = E_{2t}/(E_{2n} \cdot \varepsilon_{r2}) .$$

The quotient of tangential and normal components is equal to the tangent of the angle α_1 or α_2, Figure 2.4-10:

$$\frac{\tan \alpha_1}{\tan \alpha_2} = \frac{\varepsilon_{r1}}{\varepsilon_{r2}} \qquad (2.4\text{-}21)$$

Eq. (2.4-21) is called “refraction law” for the electric field lines and for the orthogonal equipotential lines.

It states that the angle α between field vector $\boldsymbol{E}$ and the surface normal vector d$\boldsymbol{A}$ decreases or increases with the permittivity ε. In the material with the higher permittivity (higher “dielectric density”), the field lines are refracted

away from the surface normal. In the material with the lower permittivity (lower "dielectric density") the field lines are refracted towards the surface normal. If the *permittivities* are *very different*, the field lines emerge from the material with the much higher permittivity nearly *normal to the surface*.

Equipotential lines are perpendicular to field lines. In the material with the higher permittivity they are refracted towards the surface normal, and in the material with the lower permittivity they are refracted away from the surface normal resp., Figure 2.4-11. Therefore, the angles α_1 and α_2 can also be regarded as angles between the equipotential lines and the surface contour itself. The angles in Figure 2.4-11 represent a ratio of approximately $\varepsilon_{r1}/\varepsilon_{r2} = 1/3$.

In the case of two-dimensional plane fields, the methods of **graphical field mapping** can be applied. According to Eq. (2.3-35), the concept of *equal partial capacitances*, for the rectangular cross sections defined by field and equipotential lines, would result in the condition

$$\varepsilon_r \cdot b/a = \text{const.} \qquad (2.4\text{-}22a)$$

Therefore, the aspect ratio of the rectangles would be changed in proportion to the permittivities.

For the practical mapping, however, it is more convenient to assume *equal rectangles* (e.g. quadratic boxes) in the whole field volume:

$$b/a = \text{const.} \qquad (2.4\text{-}22b)$$

Thereby, the distance of field lines is proportional to the distance of the equipotential lines and gives a graphic impression of the *electric field strength magnitude*, Figure 2.4-11.

For *capacitance estimation*, the different partial capacitances must be calculated in the different regions according to Eq. (2.3-35), and then they are combined in an equivalent network. Alternatively, elements with the same partial capacitance can be marked off in a field/equipotential-line plot, Figure 2.4-12 (bold field and potential lines).

2.4.3 Analytical Calculation of Multilayer Dielectric Arrangements

Generally, multilayer dielectric arrangements are calculated with the methods described in Section 2.3. Additionally, the boundary conditions according to Eq. (2.4-13) and (-16) must also be fulfilled.

Some important multilayer dielectric arrangements are discussed below:

Section 2.4.3.1 describes plane, cylindrically symmetric and spherically symmetric multilayer insulations. The field vectors shall be orthogonal to the interfaces (transverse multilayer dielectrics).

Weak links or defects in insulations often occur as multi-layer arrangements, e.g. as gaps and cracks (Section 2.4.3.2), as interstices and triple-points (Section 2.4.3.3) or as holes, voids and inclusions (Section 2.4.3.4). The interfaces are subject to electric field forces (Section 2.4.3.5).

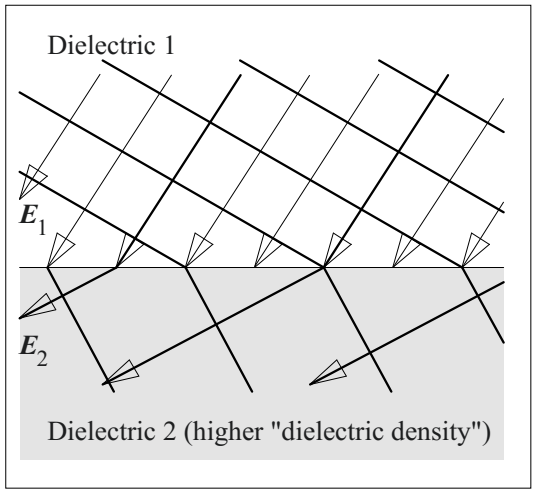

Figure 2.4-12: Outline of elements with equal partial capacitances (bold lines), for capacitance estimation in a two-dimensional arrangement.

2.4.3.1 Plane, Cylindrically Symmetric and Spherically Symmetric Multi-layer Arrangements

Very often, insulations are designed as multi-layer arrangements, which are stressed as nearly normally to the interfaces as possible in order to avoid tangential stresses along weak interfaces.

Examples:

1. **Capacitor dielectrics** consist of a number of layers of thin papers or polymer films. Voids and gaps are completely filled with an impregnating fluid. The dielectric can mostly be regarded as a plane multi-layer arrangement.

2. High voltage conductors between the windings of a transformer and the bushings are led through the insulating oil and they are wrapped with a paper layer to improve the insulation. At very high voltages a subdivision of the oil gap by cylindrical pressboard barriers may be necessary in order to guarantee sufficient electric strength.

3. **High voltage bushings** are cylindrically symmetric multi-layer arrangements, consisting of a main insulation body (core), subsidiary insulation gaps, housing insulators and ambient media, see Figure 1-1. Nevertheless, the direction of the electric field can approximately be assumed to be radial in certain regions (between the grading layers).

In the following, the analytical calculation of *basic multi-layer insulations* in plane, cylindrically symmetric and spherically symmetric arrangements is discussed, Figure 2.4-13. The *dielectrics* are always layered *transversely* to the electric field, i.e. $\boldsymbol{E}$ and the displacement density $\boldsymbol{D}$ are always normal (orthogonal) to the interfaces (parallel to the area vector $\boldsymbol{A}$). Consequently, the interfaces are regarded as equipotential surfaces.

Because of the continuity of the displacement density,

$$D_k(x_k) = D_{k+1}(x_k) \qquad (2.4\text{-}23)$$

applies for any interface at $x = x_k$ (or $r = r_k$), and the electric field strength changes abruptly at the *interface*, with the reverse ratio of the permittivities:

$$E_{k+1}/E_k = \varepsilon_k/\varepsilon_{k+1} \qquad (2.4\text{-}24)$$

In Figure 2.4-13 a gradation of the permittivity ratios was chosen according to 6 : 4 : 2 : 1, both in x- and in r-direction respectively. For all three arrangements, the electric field strength increases by 50 % at the first interface (at x_1 and at r_1) and by 100 % at the two following interfaces, Figure 2.4-13 (middle).

In a *plane arrangement* there is a uniform field within a single dielectric layer, i.e. E is constant section by section. Because of the field displacement, the field strength E_N in the dielectric N is 600 % of the field strength E_1 in the dielectric 1.

In a *cylindrically symmetric arrangement* of length z

$$E_k(r) = \frac{Q/z}{2\pi\varepsilon_0\varepsilon_{rk}} \cdot \frac{1}{r} \qquad (2.4\text{-}25)$$

generally applies for any dielectric layer k, according to Eq. (2.3-17).

The field strength profile in Figure 2.4-13 is a result of decreasing field strengths $E_k(r) \sim 1/r$ in the considered dielectrics and abrupt field strength changes at the interfaces. In comparison with the plane arrangement there is a homogenization of the stress, i.e. on the outer side there is a decrease and on the inner side there is an increase of the electric field stress.

According to Eq. (2.3-2),

$$E_k(r) = \frac{Q}{4\pi\varepsilon_0\varepsilon_{rk}} \cdot \frac{1}{r^2} \qquad (2.4\text{-}26)$$

generally applies for *spherically symmetric arrangements.* The field strength profile in Figure 2.1-13 is a result of decreasing field strengths $E_k(r) \sim 1/r^2$ in the considered dielectrics and abrupt field strength changes at the interfaces. In comparison with the plane and cylindrical arrangements, there is a strong decrease at the outer side. Dielectric no. 1, which is weakly stressed in the other arrangements, is exposed to the highest stress here.

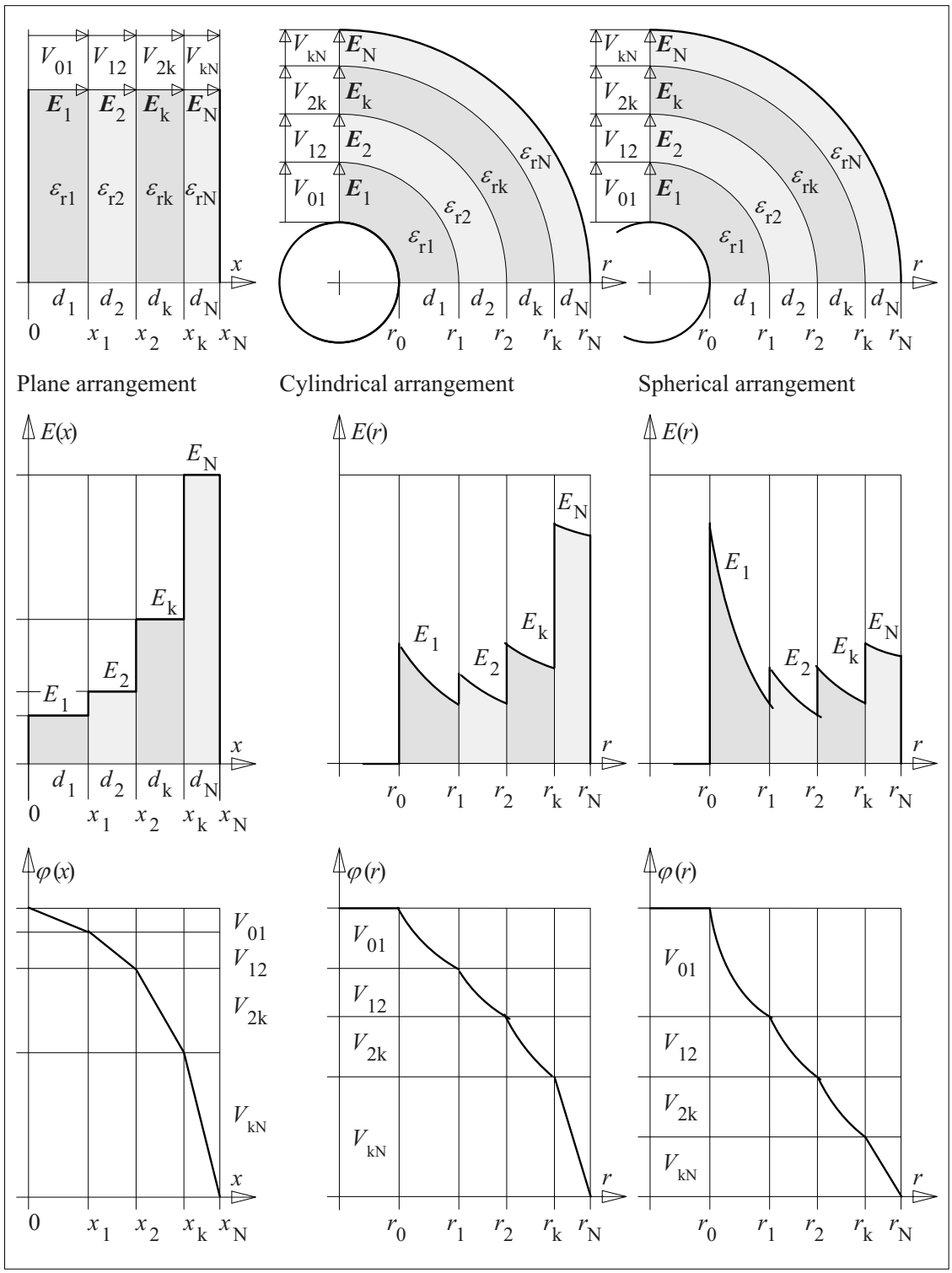

Figure 2.4-13: Plane, cylindrical and spherical multi-layer insulation arrangement (top) with the related field strength profiles (middle) and the potential profiles (bottom). The profiles in the figure are in accordance with a permittivity ratio of approximately 6 : 4 : 2 : 1 in x- or in r-direction resp..

Note: Theoretically, *constant field strengths* can also be achieved in cylindrically and spherically symmetric arrangements, if the relative permittivities according to Eq. (2.4-25) and (-26) are assumed to decrease continuously with

$$\varepsilon_r(r) \sim 1/r \qquad \text{and} \qquad \varepsilon_r(r) \sim 1/r^2$$

(refractive potential grading). Unfortunately, there is no technically practical solution for this. The approximation of the perfect permittivity profiles by discrete layers with appropriate permittivities will normally not be possible: In practice, the choice of insulating materials is very much limited because of many constraints (e.g. mechanical, thermal or chemical stresses, costs etc.). Optimizations problems often have to be solved by application of certain materials with given properties.

Example: Coated spherical electrode

For the spherically symmetric multi-layer arrangement according to Figure 2.4-13 (right) there is a high stress on the inner dielectric 1 (e.g. epoxy resin coating with $\varepsilon_{r1} = 6$) and a significantly lower stress on the outer dielectric N (e.g. air gap with $\varepsilon_{rN} = 1$). Because of the much higher electric strength of the epoxy resin, it would not make sense to seek to homogenize the field strength profile. Multi-layer insulations should be designed in such a way that the materials with the *higher electric strength* are *carrying a higher dielectric stress* than the electrically weaker materials.

For the **calculation of the plane arrangement** a constant displacement density can be assumed, Figure 2.4-13 (left):

$$D = Q/A = \text{const.}$$

The field strengths in the different layers are

$$E_k = Q/(A\,\varepsilon_k)\,.$$

With the total voltage

$$V = \sum_{i=1}^{N} E_i\, d_i = \frac{Q}{A} \cdot \sum_{i=1}^{N} \frac{d_i}{\varepsilon_i}\,,$$

the charge density

$$\frac{Q}{A} = V \Big/ \sum_{i=1}^{N} \frac{d_i}{\varepsilon_i}$$

and the *field strength* E_k in any layer k

$$E_k = \frac{V}{\varepsilon_k \sum_{i=1}^{N} \frac{d_i}{\varepsilon_i}} = \frac{V}{\varepsilon_k \left(\frac{d_1}{\varepsilon_1} + \frac{d_2}{\varepsilon_2} + \ldots + \frac{d_N}{\varepsilon_N} \right)} \qquad (2.4\text{-}27)$$

is calculated. The *potential distribution* results from the sectional integration of the electric field strengths, Figure 2.4-13 (bottom left).

The *capacitance* of the plane arrangement is determined from the series connection of the partial capacitances

$$C_k = \varepsilon_k\, A / d_k$$

or from the above-mentioned relation between Q and V with $\varepsilon_k = \varepsilon_0 \varepsilon_{rk}$:

$$C = \frac{\varepsilon_0 \cdot A}{\sum_{i=1}^{N} \frac{d_i}{\varepsilon_{ri}}} = \frac{\varepsilon_0 \cdot A}{\frac{d_1}{\varepsilon_{r1}} + \frac{d_2}{\varepsilon_{r2}} + \ldots + \frac{d_N}{\varepsilon_{rN}}} \qquad (2.4\text{-}28)$$

For the **calculation of the cylindrically symmetric arrangement,** the dependence of the displacement density on the radius r must be considered, Figure 2.4-13 (middle). Eq. (2.4-25) for the field strength $E_k(r)$ in any layer k results from

$$D = Q / A(r) = Q / (2\pi r \cdot z).$$

The length of the arrangement is z. The integration of $E_k(r)$ in the radial direction provides the partial voltage

$$V_{(k\text{-}1)k} = [Q / (2\pi\varepsilon_k \cdot z)] \cdot \ln (r_k / r_{k\text{-}1})\,.$$

The summation of the partial voltages gives the total voltage V. After that, Q can be expressed as a function of V and can be eliminated in Eq. (2.4-25):

$$E_k(r) = \frac{V}{r \cdot \varepsilon_k \sum_{i=1}^{N} \left\{ \frac{1}{\varepsilon_i} \cdot \ln \frac{r_i}{r_{i-1}} \right\}} \qquad (2.4\text{-}29)$$

This expression is valid in any layer k, i.e. for $r_{k\text{-}1} < r < r_k$.

The *potential distribution* results from the sectional integration of the electric field strengths, Figure 2.4-13 (bottom middle).

The *capacitance* of the cylindrical arrangement is determined from the series connection of the partial capacitances according to Eq. (2.3-20)

$$C_k = 2\pi\varepsilon_k z / \ln(r_k/r_{k-1})$$

or from the relation $C = Q/V$ with $\varepsilon_k = \varepsilon_0\varepsilon_{rk}$:

$$C = \frac{2\pi\varepsilon_0 z}{\sum_{i=1}^{N} \{\frac{1}{\varepsilon_{ri}} \cdot \ln\frac{r_i}{r_{i-1}}\}} \qquad (2.4\text{-}30)$$

Also for the **calculation of the <u>spherical</u> arrangement,** it has to be regarded that the displacement density depends on the radius r, Figure 2.4-13 (right). Eq. (2.4-26) for the field strength $E_k(r)$ in any layer k results from

$$D = Q / A(r) = Q / (4\pi r^2)$$

The integration of $E_k(r)$ in radial direction provides the partial voltage

$$V_{(k-1)k} = (1/r_{k-1} - 1/r_k) \cdot Q / (4\pi\varepsilon_k) .$$

The summation of the partial voltages gives the total voltage V. After that, Q can be expressed as a function of V and can be eliminated in Eq. (2.4-26):

$$E_k(r) = \frac{V}{r^2 \cdot \varepsilon_k \sum_{i=1}^{N} \{\frac{1}{\varepsilon_i}(\frac{1}{r_{i-1}} - \frac{1}{r_i})\}} \qquad (2.4\text{-}31)$$

This expression is valid in any layer k, i.e. between $r_{k-1} < r < r_k$.

The *potential distribution* results from the sectional integration of the electric field strengths, Figure 2.4-13 (bottom right).

The *capacitance* of the spherical arrangement can be determined from the series connection of the spherically symmetric partial capacitances according to Eq. (2.3-12)

$$C_k = 4\pi\varepsilon_k / (1/r_{k-1} - 1/r_k)$$

or from the relation $C = Q/V$ with $\varepsilon_k = \varepsilon_0\varepsilon_{rk}$:

$$C = \frac{4\pi\varepsilon_0}{\sum_{i=1}^{N} \{\frac{1}{\varepsilon_{ri}}(\frac{1}{r_{i-1}} - \frac{1}{r_i})\}} \qquad (2.4\text{-}32)$$

<u>Example:</u> Coated cylindrical conductor

For a cylindrical high voltage conductor (r_0 = 2 cm) the thickness or the **radius** r_1 of a cast-resin coating (ε_{r1} = 5) shall be determined in such a way that the maximum field strength in the surrounding gas becomes minimal. The conductor is led in a coaxial air-filled ground conductor (r_2 = 10 cm), Figure 2.4-14 (top). The peak value of the applied AC voltage shall be $\hat{V}$ = 100 kV.

The maximum field strength in the gas occurs

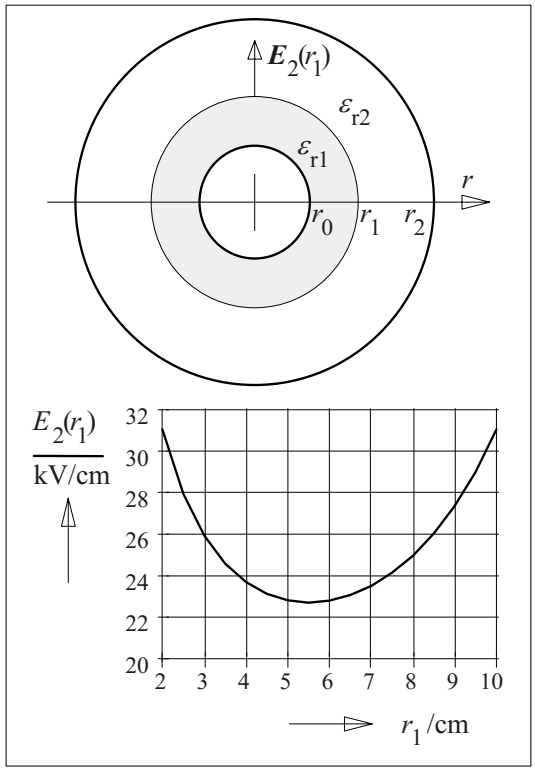

Figure 2.4-14: Cast-resin coated conductor in a gas-filled tubular ground conductor (top) and maximum field strength in the gas as a function of the coating-thickness/ radius (bottom).

at the surface of the cast-resin coating at $r = r_1$. The calculation of $E_{Gas(max)} = E_2(r_1)$ is performed according to Eq. (2.4-29). The dimensioning of the cast-resin coating (radius r_1) for minimum field strength at $r = r_1$ can generally be performed as extreme value determination by differentiation, see Chapter 2.3.1.2. For clarity, however, a numerical solution is preferred in this case, Figure 2.4-14 (bottom).

As a solution we have a coating thickness of 3.5 cm, i.e. at $r_1 = 5.5$ cm there is a field-strength minimum $\hat{E}_2(r_1) = 23$ kV/cm, which is below the breakdown strength of air at standard atmospheric conditions ($\hat{E}_D = 30$ kV/cm). For $r_1 \to r_0 = 2$ cm and for $r_1 \to r_2 = 10$ cm there are field strengths above $\hat{E}_D$. The diagram shows that a coating with a thickness of 1 cm already gives 60 % of the maximum possible field-strength reduction.

The application of SF_6 would increase the electric strength by a factor of approximately three and it would be possible to apply voltages approximately three-times higher.

Note: Similar conductor configurations can be found with conductors that are located under oil and wrapped with oil-impregnated paper.

<u>Example:</u> Coated high-voltage electrode

A spherical high voltage electrode with the radius $r_1 = 3$ cm shall be compared with a smaller electrode with the radius r_0. By means of a cast-resin coating with $\varepsilon_{r1} = 5$, the radius is increased to $r_1 = 3$ cm. The counter-electrode is assumed to be far away, $r_2 >> r_1$, Figure 2.4-15.

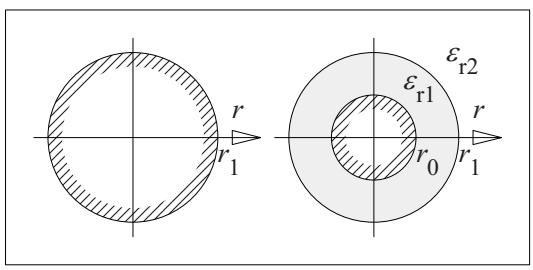

Figure 2.4-15: Spherical metallic electrode (left) and coated electrode (right) with the same external radii.

The **admissible voltages**, which can be applied to the two electrodes, shall be determined for a maximum admissible field strength $\hat{E}_{Resin}$ = 200 kV/cm in the cast-resin coating and $\hat{E}_{Air}$ = 20 kV/cm in the ambient air.

1.) According to Eq. (2.3-8), the voltage at the **metallic spherical electrode** must not exceed

$$\hat{V} = \hat{E}_L \cdot r_1 = 60 \text{ kV}$$

2.) The **coated electrode** has to be dimensioned in such a way that the field strength *at the conductor's surface* at $r = r_0$ is precisely $E_1(r_0) = \hat{E}_{Resin} = 200$ kV/cm, and that the field strength *at the coating's surface* at $r = r_1$ is precisely $E_2(r_1) = \hat{E}_{Air} = 20$ kV/cm. With Eq. (2.4-31) and $r_2 \to \infty$ two conditions are derived:

$$\hat{E}_1(r_0) = \hat{E}_{Resin} = \frac{\hat{V}}{r_0^2 \{\frac{1}{r_0} + (\frac{\varepsilon_1}{\varepsilon_2} - 1)\frac{1}{r_1}\}}$$

and

$$\hat{E}_2(r_1) = \hat{E}_{Air} = \frac{\hat{V}}{r_1^2 \frac{\varepsilon_2}{\varepsilon_1}\{\frac{1}{r_0} + (\frac{\varepsilon_1}{\varepsilon_2} - 1)\frac{1}{r_1}\}}$$

If the ratio of the two field strengths is calculated, the voltage and the bracket in the denominator are eliminated:

$$\hat{E}_{Resin} / \hat{E}_{Air} = (r_1^2 \cdot \varepsilon_2) / (r_0^2 \cdot \varepsilon_1)$$

The solution for r_0 is $r_0 = 0.42$ cm. With this value, the maximum voltage $\hat{V}$ can then be calculated from one of the two conditions mentioned above:

$$\hat{V} = 132 \text{ kV}$$

Thus, the admissible voltage at the coated electrode is twice as high as the admissible voltage at the metallic electrode. Nevertheless, on larger electrodes it is difficult to produce thick coatings, which are free from defects and which are able to carry the major fraction of the voltage. For practical applications, large metallic electrodes and toroids are used, if there is enough space in the ambient air.

2.4.3.2 Gaps and Cracks

Gaps and cracks in highly stressed insulations are defects, which must always be avoided. Gas-filled gaps remain between insulation layers for example, if the impregnation of the residual interstices is incomplete. Cracks often are caused by material ageing after long periods, and they mostly originate from mechanical and thermal stresses. Cracks can also originate from shrinkage stress during the curing of cast-resin insulation bodies.

Gaps and cracks **parallel to the electric field** are particularly critical because they bridge a major part of the insulation distance (up to the whole insulation distance) with an *interface* of very *low electric strength* and with *tangential stress*. Normally, the macroscopic field distribution is not influenced very much, but within the gap and at the interfaces there are microscopic field stress enhancements and significantly reduced electric strengths, see Section 2.4.2.3 (Parallel/ tangential multilayer dielectric).

Example: **Glass-fiber reinforced plastics** (GRP) have an extraordinarily enhanced mechanical strength because of glass fibers, which are embedded in the polymer matrix. Rods and tubes made of reinforced epoxy resin are used as mechanically and electrically stressed parts of suspension insulators, post insulators and housing insulators. These applications require a durable chemical bonding of the resin and the glass surfaces, free of any voids and defects. The bonding can be achieved by the application of a facing (primer) on the glass surface (*silane glass primer*). Incomplete or defective priming results in detachment of the fibers from the resin. In the very long cracks and cavities that arise humidity can be accumulated, which results in a significant decrease of the dielectric strength.

Gaps and cracks **orthogonal to the electric field** can approximately be regarded as multilayer arrangements with interfaces normal to the electric field, Section 2.4.2.2. The field strength E_i in a gas-filled crack or gap ($\varepsilon_{ri} = 1$) is enhanced by the factor $\varepsilon_r/\varepsilon_{ri} = \varepsilon_r$ in comparison with the original field strength, because of the field displacement effect according to Eq. (2.4-17):

$$E_i = \varepsilon_r \cdot E \qquad (2.4\text{-}33)$$

Because of the low electric strength of air-filled gaps, the inception voltage of *partial discharges* is very low. The discharges can erode insulating materials and they can eventually cause breakdown (*breakdown by erosion*).

Example: **Detachment of a dielectric**

The epoxy casting resin in a cylindrical capacitor (R_2 = 5 cm, $R_1 = R_2/e$, $\varepsilon_r = 4$) shrinks during curing onto the inner conductor, and it is partially detached from the outer conductor, leaving a circumferential gap with the width d_i between 0 and 1 mm, Figure 2.4-16. The r.m.s. value of the applied voltage V_{pdi}, for which inception of partial discharges is expected, shall be calculated.

The electric strength of air under standard atmospheric conditions is approximately $\hat{E}$ = 30 kV/cm = 3 kV/mm; it decreases with increasing distances, see Figure 3.2-15. Thus, the strength of the air gap is lowest for the highest gap width d_i = 1 mm. For this distance, the strength $\hat{E}$(1 mm) $\geq$ 4 kV/mm. If a constant field strength is assumed in the circumferential gap, discharge inception is expected to be at d_i = 1 mm.

The inception voltage V_{pdi} is calculated from Eq. (2.3-21) for the field strength at the outer radius $r = R_2$ and from Eq. (2.4-33) for the field stress enhancement in the gap:

$$V_{pdi} = E \cdot R_2 \cdot \ln(R_2/R_1) = (E_i/\varepsilon_r) \cdot R_2 \cdot \ln(R_2/R_1)$$

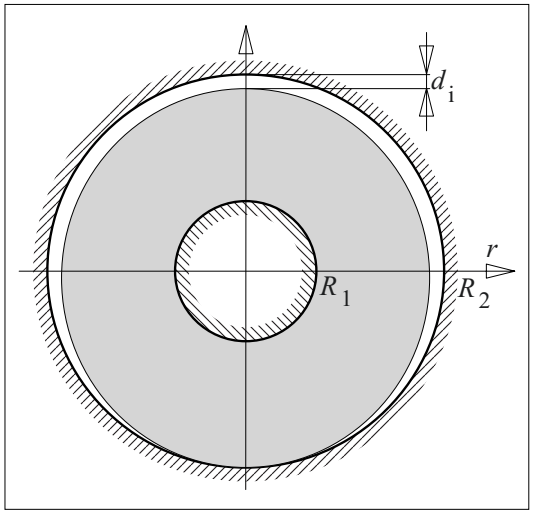

Figure 2.4-16: Detachment of a dielectric from the outer cylindrical conductor during the shrinking onto the inner cylindrical conductor.

With the partial-discharge inception field strength $\hat{E}_i \geq 4$ kV/mm, the *partial-discharge inception voltage* is $\hat{V}_{pdi} \geq 5$ kV (peak value) or $V_{pdi} \geq 3.5$ kV (r.m.s. value).

Note: The discharge inception at $V = 3.5$ kV represents practically an extreme *loss of electric strength*. Without the formation of a gap, the highest relevant field strength would occur at $r = R_1$. If the admissible field strength in the epoxy resin is $\hat{E}_{max} = 40$ kV/mm, the admissible maximum voltage would be $\hat{V}_{max} = 74$ kV (peak value) or $V_{max} = 52$ kV (r.m.s. value) according to Eq. (2.3-22).

Note: Resin-bonded paper bushing

Formerly used RBP bushing cores are "solid" insulation bodies ("hard paper") wrapped with Kraft paper and bonded or laminated with phenolic resin without being fully impregnated (RBP, *resin-bonded paper*). The bushing cores could not be fully impregnated without residual air volumes in order to avoid high mechanical stresses and cracks during the curing process. Therefore, partial discharges could occur already at the service voltage both orthogonal and parallel to the paper layers, but the phenolic resin has a durability that is sufficient in many cases. Nevertheless, according to modern criteria, permanent partial discharges and erosion are a significant quality defect because surface discharges parallel to the paper layers, partial breakdowns and full breakdowns cannot be excluded.

Nowadays, cavity-free and discharge-free **RIP insulating bodies** are used (RIP, *resin-impregnated paper*) as bushing cores. They are wrapped with crepe-paper, dried, impregnated completely with liquid epoxy resin under vacuum and cured.

Example: Capacitor dielectric of polymeric films

A capacitor dielectric is wound on from polypropylene film (thickness 12 µm, $\varepsilon_r = 2.2$). Between adjacent layers, there are non-impregnable air-filled gaps with a maximum thickness of 7 µm. The admissible voltage for four-layer insulation shall be estimated.

As the electric strength decreases with increasing gap width, discharge inception is expected for the maximum width $d_i = 4$ µm. According to Paschen's law for air, the approximate electric strength of the gap is $\hat{V}_i \geq 360$ V or $\hat{E}_i \geq 90$ V/µm, see Section 3.2.2.4.

According to Eq. (2.4-33), the field strength in the polymeric dielectric is approximately $\hat{E} = \hat{E}_i/\varepsilon_r \geq 41$ V/µm. Therefore, the whole dielectric with a thickness $d = 4 \cdot 12$ µm = 48 µm can be stressed with a voltage in the range of $\hat{V} \geq 48$ µm $\cdot$ 41 V/µm = 2 kV. This is a rough estimation of the partial discharge inception voltage only, a more accurate calculation of the multi-layer insulation according to Eq. (2.4-27) would not be very useful.

Note 1: Higher voltages are possible, if the maximum *air-gap width* can be reduced. Then it has to be ensured that the field strength in the polymeric films does not exceed the respective electric strength.

Note 2: The partial discharge behavior in capacitor dielectrics made of films or papers is essentially determined from the *edges of the metal foils,* which are wrapped as electrodes together with the dielectric layers. At the edges, there are strong field distortions, field stress enhancements and interstices without films or papers. Therefore, the *impregnation* of high-voltage capacitors is always necessary.

2.4.3.3 Interstices (Triple-Points)

Tangentially stressed interfaces are particular weak points of an insulation arrangement, Figure 2.4-17 (left). Therefore, this "*support-type arrangement*" is avoided where possible and the interface is arranged orthogonal to the electric field forming a "*creepage surface*", Figure 2.4-17 (right). Thus, tangential stresses are significantly reduced, and they decrease outwards to negligible small values. Because of the proximity of three materials, the considered microscopic region is called "*triple point*" or interstice between electrode and dielectric plate.

Unfortunately, there is an increased *normal electric field stress* in the interstice between insulating plate and bent electrode because of the field displacement effect. If the material in the interstice (e.g. air) has only a weak electric strength, the *partial discharge* inception volt-

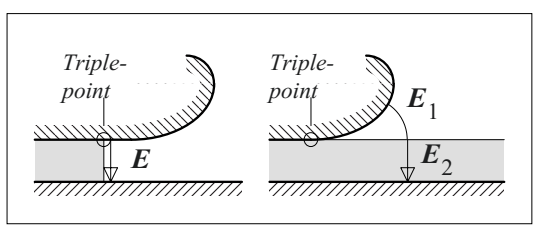

Figure 2.4-17: Insulating plate between electrodes: "Support-type arrangement" with tangential stress of the interface (left) and "creepage surface" with normal stress of the air-filled interstice (right).

age can be very low. At (significantly) higher voltages, the discharges can grow into *creeping/ surface discharges* and result in *surface flashover*. Therefore, the insulation arrangement is called a **"creepage surface"**.

Note: The creepage surface is a *basic problem* of high-voltage engineering, which cannot be avoided in many technical arrangements. Many technological measures are taken therefore, in order to prevent discharge inception in the interstices close to triple-points and to prevent the inception of surface discharges [26].

For a rough estimation of the *partial discharge inception voltage* V_{pdi}, it is simply assumed that there are small sections with regionally uniform field, Figure 2.4-18. The interface is orthogonal to the field, being uniform but different on both sides of the interface. The gap width d_1 in the interstice increases with the distance x from the triple-point. A section Δx is considered with approximately uniform field regions 1 (interstice) and 2 (insulating plate). According to Eq. (2.4-18), the field strength in the interstice is

$$E_1(d_1) = \frac{V}{d_1 + d_2 \dfrac{\varepsilon_{r1}}{\varepsilon_{r2}}} . \qquad (2.4\text{-}34)$$

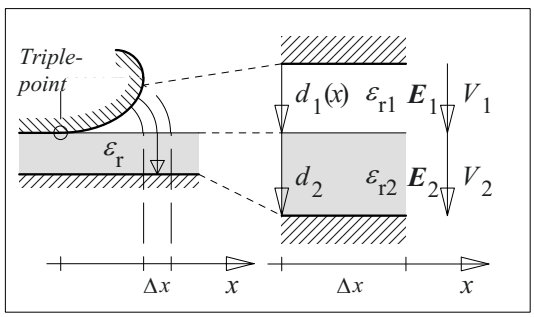

Figure 2.4-18: "Creepage surface" with highly stressed interstice (left) and an equivalent model of a small section for an approximate calculation (right).

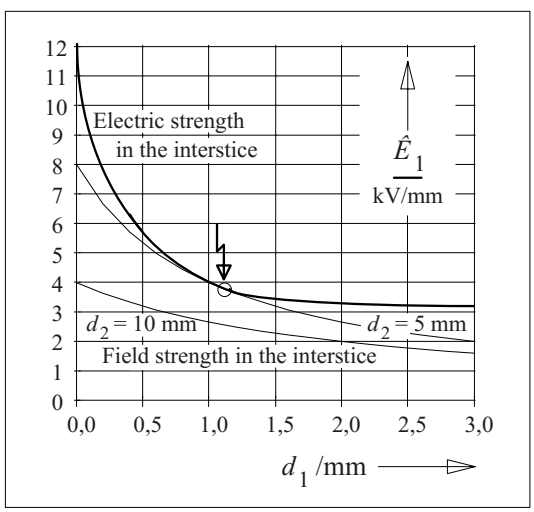

Figure 2.4-19: Field strength in an interstice as function of air-gap width at 8 kV (peak value) for insulating plates with a thickness of 5 mm and 10 mm (bottom) compared with the electric strength (top). The permittivity ratio is assumed as 1:5.

Example:
Electrode edge on an insulating plate

An electrode edge on an insulating plate according to Figure 2.4-18, is discussed. Figure 2.4-19 shows the numerical analysis of Eq. (2.4-34) for a total voltage $\hat{V}$ = 8 kV (V = 5.7 kV r.m.s.), for the insulation thicknesses d_2 = 5 and 10 mm and for the permittivity ratio $\varepsilon_{r1}/\varepsilon_{r2}$ = 1/5.

There is a *decreasing field strength in the interstice* with increasing gap width d_1. If the insulating thickness d_2 is doubled from 5 mm to 10 mm, the field strength at d_1 = 0 is reduced to half the magnitude, but a further decrease across d_1 is slower.

Figure 2.4-19 also shows a curve of the *electric strength in the interstice*. The increase of strength with decreasing air-gap width d_1 is typical for many insulating materials, e.g. for air, SF_6 and insulating oil. The curve in the picture is approximately valid for *air* at atmospheric pressure and room temperature.

For an insulating plate with thickness d_2 = 5 mm, the field strength in the gap reaches the electric strength of the gap at approximately d_1 = 1.2 mm, and partial discharges occur. Obviously, the voltage $\hat{V}$ = 8 kV (V = 5.7 kV r.m.s. value) is the *partial discharge inception volt-*

age $\hat{V}_{\mathrm{pdi}}$ (V_{pdi} r.m.s.). Normally, r.m.s. values are given.

If the insulation thickness is doubled (i.e. d_2 = 10 mm), there are no discharges at $\hat{V}$ = 8 kV (V = 5.7 kV). Nevertheless, Figure 2.4-19 shows that the curve of the electric strength is reached if the voltage (i.e. the field strength) is only increased by about 40 %.

Note: Obviously, there is *no linear relation* between the *insulation thickness* d_2 and the peak value of the *partial discharge inception voltage* $\hat{V}_{\mathrm{pdi}}$:

$$\hat{V}_{\mathrm{pdi}} \sim d_2^{\,0.5}$$

According to Eq. (2.4-34), the field strength in the interstice depends on the product $d_2 \cdot \varepsilon_{\mathrm{r1}}/\varepsilon_{\mathrm{r2}}$. In accordance with the described **model**, the peak value of the partial discharge inception voltage for **surface discharges** is

$$\frac{\hat{V}_{\mathrm{pdi}}}{\mathrm{kV}} = \sqrt{2}\,K \left(\frac{d_2}{\mathrm{cm}} \cdot \frac{\varepsilon_{r1}}{\varepsilon_{r2}} \right)^{a}. \quad (2.4\text{-}35)$$

A theoretical proportionality factor K = 18 (for air) could be determined from Figure 2.4-19. Unfortunately, **experiments** show that the factor can be significantly smaller. Probably, the theoretical model (with regionally uniform fields according to Figure 2.4-18) is too simple. Furthermore, surface effects and different electrode shapes are not taken into account. Nevertheless, the general dependences of Eq. (2.4-35) are in good agreement with experiments for the exponent a = 0.44 ... 0.5 [22], [23].

At *sharp electrode edges* the factors are approximately K = 8 for *air* and K = 21 for SF_6 [23]. For *insulating oil* a factor K = 20 can be derived from [23].

Note: For different electrode edges under *oil*, factors between 21.6 (paper wrapped conductor on paper insulation) and 15.6 (for sharp electrode edges on paper insulation) are reported without particularly taking into account the ratio $\varepsilon_{\mathrm{r1}}/\varepsilon_{\mathrm{r2}} \simeq 1/2$, which is already included in these factors [22].

Example: Edges of metal foil electrodes in capacitor insulations

For wound capacitors the metal foil electrodes and the insulating films or papers are wound together; remaining gaps and voids are filled completely with an impregnating medium, Figure 2.4-20. The electrical connection of the foils, which are displaced to left and right relative to each other, is either made at the ends with metallic tabs or made by large-area end contacts via all protruding foil edges, Figure 2.4-20 (top).

Very high field strengths occur in the interstices between the dielectric layers at the edges of the metallic foils. The critical point is not the normal (radial) field stress in the impregnating medium at the bent electrodes (as in the former example). In this case, the *tangential* (axial) *stress on the dielectric interfaces* is mainly problematic, which arises because of extreme field stress enhancements at the strongly curved electrode edges, Figure 2.4-20 (bottom).

An approximate calculation is performed for an equivalent cylindrically symmetric arrangement with $R_1 = d_{\mathrm{M}}/2$ and $R_2 = d_{\mathrm{M}}/2 + d_{\mathrm{I}}$. The curved electrode edge with a very small *radius of curvature* $R_1 = d_{\mathrm{M}}/2$ is regarded as the "inner conductor"; the adjacent metallic foils are regarded as the "outer conductor" and they are replaced by an *auxiliary cylinder* with the radius $R_2 = d_{\mathrm{M}}/2 + d_{\mathrm{I}}$. To a first approximation, the multi-layer arrangement of the dielectrics has no influence on the maximum magnitude of the electric field strength in the impregnating medium because of the tangential direction of the field $\boldsymbol{E}_{\mathrm{edge}}$ at the electrode edge, Figure 2.4-20 (bottom). This means that the field is parallel (tangential) to the surface of the films or papers, see Figure 2.4-9.

With Eq. (2.3-22), the field strength at the edge of the foil (edge field strength) is given by

$$E_{\mathrm{Rand}} = \frac{U}{R_1 \ln \frac{R_2}{R_1}} = \frac{E_0\, d_\mathrm{I}}{\frac{d_\mathrm{M}}{2} \ln\left(1+\frac{2d_\mathrm{I}}{d_\mathrm{M}}\right)},$$

and the field strength enhancement is the reciprocal of the field efficiency factor η

$$\frac{E_{\mathrm{Rand}}}{E_0} = \frac{1}{\eta} = \frac{\frac{2d_\mathrm{I}}{d_\mathrm{M}}}{\ln\left(1+\frac{2d_\mathrm{I}}{d_\mathrm{M}}\right)}. \qquad (2.4\text{-}36)$$

The numerical analysis of Eq. (2.4-36) shows that significant field stress enhancements can occur, even for round edges, Figure 2.4-21 (lower curve). If further enhancements by imperfections of the surface are considered, a factor of 3 is realistic according to Eq. (2.3-62), and field stress enhancements are even more extreme, Figure 2.4-21 (upper curve).

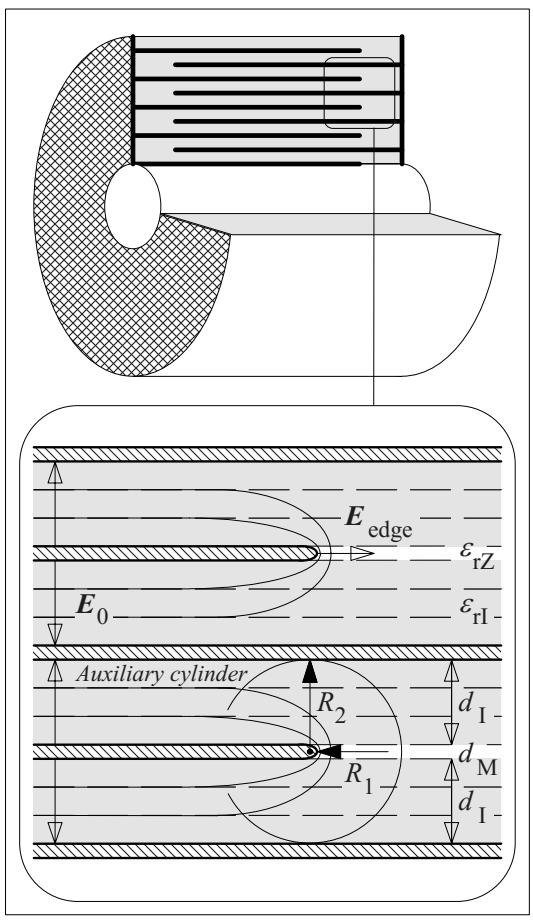

Figure 2.4-20: Roll-type capacitor with large-area end contacts of the axially shifted metal foils (top) and sectional view for the right-hand edge of the foils with equipotential lines (bottom).

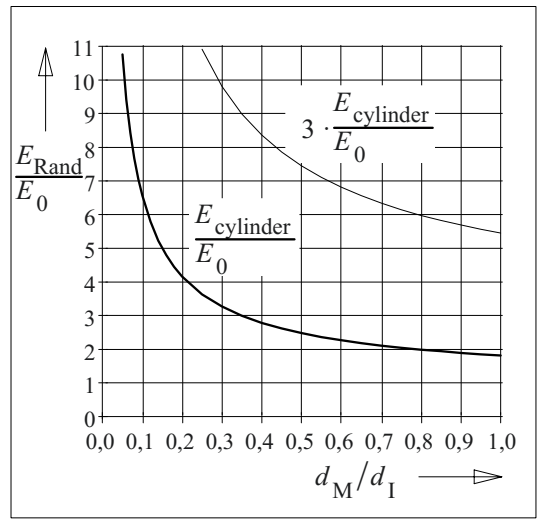

Figure 2.4-21: Field enhancement in a roll-type capacitor element at the edges of a metallic foil electrode. Lower curve: Calculation with the assumption of a cylindrically symmetric field. Upper curve: Taking into consideration additional field enhancement by imperfections of the surface.

Numerical example:
A capacitor consists of paper insulated windings with an insulation thickness d_I = 50 µm, which are impregnated with mineral oil. The edges of the 6 µm thick aluminum foils are folded, in order to guarantee a smooth curvature at the edges. Partial discharge inception was measured at a r.m.s. AC-voltage of 3 kV. The field stresses between the foils and at the edges of the foils shall be calculated.

The field strength between the foils *within the papers* is E_0 = 3 kV / 50 µm = 60 kV/mm for the uniform field region. Because of field displacement, there is a higher stress *in the impregnating oil-filled gaps*, $E_{0\text{-oil}} = \varepsilon_{\text{r-paper}}/\varepsilon_{\text{r-oil}} \cdot E_0 \simeq 120$ kV/mm. *At the edges* a field stress enhancement $E_{\mathrm{edge}}/E_0 = 3.7$ is calculated from Eq. (2.4-36) or Figure 2.4-21 with $d_\mathrm{M} = 2 \cdot 6$ µm = 12 µm (thickness is doubled at the folded edges) and $d_\mathrm{M}/d_\mathrm{I} = 0.24$. This gives the edge field strength as 220 kV/mm. Such an electric strength can be expected from oil gap widths in a range of a few µm [27]. However, the estimated very high field strength only occurs very close to the strongly curved edge. The field strength decreases very strongly with increasing distance ~1/r, i.e. at a distance of 6 µm (r = 12 µm) it is 110 kV/mm and at a distance of 18 µm (r = 24 µm) it is just 55 kV/mm.

Note: Normally, the calculation of edge field strengths and partial discharge (PD) inception voltages is not possible for practical applications, because of many unknown parameters. Therefore, *experiments with different insulation designs* are necessary, in order to determine the acceptable stress. For sharp-edged cut aluminum foils, the PD inception voltage would decrease from 3 kV to 2.5 kV (E_0 = 50 kV/mm) in the above-mentioned example. On the other hand, a significant increase of PD inception field strength could be achieved by means of special synthetic insulating liquids.

Theoretically, the **volume** of a capacitor can be minimized by choosing an optimal thickness d_M for the metal foils:

For $d_M \rightarrow 0$ the field stress enhancement factor becomes infinite, i.e. the admissible field strength and the energy density approach zero. For $d_M >> d_I$ the dead volume of the foil v_M is very much greater than the energy storage volume of the dielectric v_I and the energy density approaches zero. In-between there must be a *maximum of overall energy density*.

$$w = 0.5\, \varepsilon E_0^{\,2}\, v_I/(v_I + v_M) \qquad (2.4\text{-}37)$$

This equation can be used for the determination of the maximum energy density w, if the admissible edge field strength is given and if the equations for the volumes and Eq. (2.4-36) for E_0 are used:

The derivate of w with respect to the ratio d_I/d_M is set equal to zero. The resulting transcendental equation is solved iteratively with $d_I/d_M = 0.24$. This means that the metallic foil should theoretically be about four times as thick as the insulation.

In practice, the optimum can be assumed for *much thinner foils*: The admissible edge field strength is *not constant*. It increases significantly with decreasing radius of curvature. The best insulation design has to be determined experimentally, as mentioned above.

2.4.3.4 Dielectric Cavities and Spheres

Completely closed *cavities* in a medium with higher permittivity are defects, they can be observed e.g. as *bubbles* in insulating liquids, as *shrink holes* in epoxy resin bodies or as *voids* in porcelain insulators, Figure 2.4-22.

Dielectric spheres in a material with lower permittivity can also be defects, e.g. *non-conductive particles* in oil or in gas.

The basic effect of field displacement was already discussed for gaps and cracks in Section 2.4.3.2. For spherical defects bounded on all sides, the field distortion is less pronounced.

In solving Poisson's/ Laplace's Equation (2.3-34) for the spherically symmetric arrangement, Figure 2.4-22, it has to be considered as a boundary condition that there is a uniform field E_0 at infinite distance. Furthermore, the boundary conditions of Eq. (2.4-13) and (-16) have to be fulfilled at the sphere's surface. The solution is a **uniform field** *within the sphere* [2]:

$$E_1 = E_0 \cdot 3\, \varepsilon_2/(\varepsilon_1 + 2\, \varepsilon_2) \qquad (2.4\text{-}38)$$

Outside of the sphere, at the sphere's surface on the x-axis (which is determined by the field vector $\boldsymbol{E}_0$), the solution is

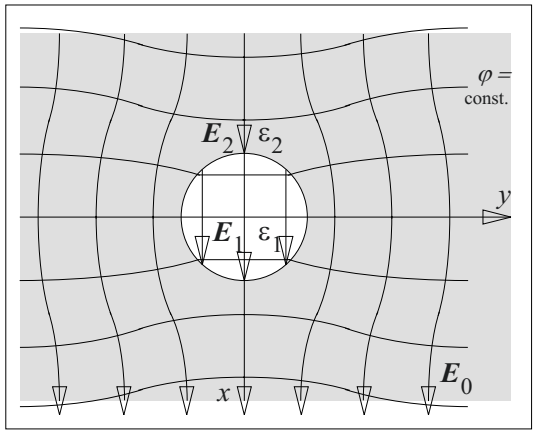

Figure 2.4-22: "Dielectric sphere" as a model of a cavity in an insulating material or as a model of a dielectric particle.

$$E_2 = E_0 \cdot 3\,\varepsilon_1/(\varepsilon_1 + 2\,\varepsilon_2)\,. \quad (2.4\text{-}39)$$

The comparison of Eq. (2.4-38) and (-39) shows that the magnitude ratio of the field vectors *normal* to the interface is the reciprocal of the permittivity ratio, see Eq. (2.4-17), transversely layered dielectric. The continuity of the *tangential* components $E_1 = E_2$ applies on the *y*-axis at the sphere's surface.

In the case of a **dielectric cavity** with a lower permittivity $\varepsilon_1 < \varepsilon_2$ the field strength E_1 in the cavity is enhanced in comparison with E_0. The maximum value is $E_1 = 1.5 \cdot E_0$ for $\varepsilon_1 << \varepsilon_2$, according to Eq. (2.4-38), i.e. in a spherical cavity there is a *limited field stress enhancement only*. It is more serious that the gas-filled cavity normally has *weak electric strength* in comparison with a highly stressed surrounding dielectric. Therefore partial discharge inception voltages are significantly lower than for a solid or liquid insulating material without any defects.

In the case of a **dielectric particle**, with a permittivity ε_1 bigger than the permittivity ε_2 of the surrounding material, the field strength E_2 outside of the sphere is higher than within the sphere. The maximum value is $E_2 = 3 \cdot E_0$ on the *x*-axis at the sphere's surface for $\varepsilon_1 >> \varepsilon_2$, according to Eq. (2.4-39). Therefore, dielectric particles can cause significant field strength enhancements in liquid and in gaseous media, and they can reduce the electric strength, especially in liquids.

2.4.3.5 Electric Forces at Interfaces

Often it is particularly troublesome that particles can follow the **electric field forces** and accumulate in the region of highest field strength.

The mechanical tensile stress exerted by an electric field **orthogonal to an interface** is [2]

$$\sigma = \partial F/\partial A = \tfrac{1}{2} \cdot E_1^{\,2}(\varepsilon_2 - \varepsilon_1)\,\varepsilon_1/\varepsilon_2. \quad (2.4\text{-}40)$$

The force acts from the higher towards the lower permittivity parallel to the field (*longitudinal* tensile stress).

In a *non-uniform field,* the forces on opposite sides of a dielectric body are no longer equal. The resulting force pulls the body towards increasing field strength.

Example:

In **insulating oil,** fibrous impurities are aligned parallel with the field lines, especially in the non-uniform regions of the field. This reduces the electric strength of long oil gaps significantly (*fiber-bridge breakdown*, *suspended solid particle mechanism*).

Also in **gas-insulated switchgear,** the electric strength is reduced by the presence of dielectric (and conductive) particles [28].

Also, the field component E_t **tangential to an interface** exerts a force orthogonal to the interface and towards the lower permittivity. The so-called *lateral pressure* is

$$\sigma = \partial F/\partial A = \tfrac{1}{2} \cdot E_t^{\,2}(\varepsilon_2 - \varepsilon_1)\,. \quad (2.4\text{-}41)$$

The tensile stress on **metallic electrode surfaces**

$$\sigma = \partial F/\partial A = \tfrac{1}{2} \cdot E_n^{\,2}\,\varepsilon \quad (2.4\text{-}42)$$

results from the field that is always acting orthogonally to the surface and parallel to the field.

Note: Eqs. (2.4-40) to (-42) can each be *deduced from an energy balance for an imaginary displacement of the interface by* an infinitesimal shift Δx by the desired force *F*. This results in a change of electric field energy, which is equal to the exerted mechanical work $F \cdot \Delta x$. The mechanical pressure σ or the tensile stress σ is determined if the force *F* is divided by the area *A* [2].

2.4.4 Direct Voltage and Transients

There is a perfect *analogy* between the stationary conduction field at a pure DC voltage and the formerly discussed dielectric displacement field.

From this analogy, the *principles of the conduction field* are deduced (Section 2.4.4.1). They can be used for calculation of some typical *examples* of insulation systems stressed with DC voltage (Section 2.4.4.2). In many cases, there are no stationary conditions: If a DC voltage is switched on, reversed in polarity or changed in magnitude, a displacement field is generated. Then, a transient process takes place, approaching a new stationary condition (Section 2.4.4.3).

2.4.4.1 Analogies to the Dielectric Displacement Field

The basic Material Equations (2.1-19) and (2.1-20) contain a perfect analogy between the fields of the dielectric displacement density $\boldsymbol{D}$ and the conduction current density $\boldsymbol{J}$.

The corresponding equations and boundary conditions are compared against each other below for the displacement field (left) and the conduction field (right):

$$\boldsymbol{D} = \varepsilon \cdot \boldsymbol{E} \qquad \boldsymbol{J} = \kappa \cdot \boldsymbol{E} \qquad (2.4\text{-}43)$$

The continuity of the normal components for the field quantities $\boldsymbol{D}$ and $\boldsymbol{J}$ is given with Eq. (2.4-15) and (2.4-16):

$$D_{1n} = D_{2n} \qquad J_{1n} = J_{2n} \qquad (2.4\text{-}44)$$

According to Eq. (2.4-13) the tangential component of the electric field strength $\boldsymbol{E}$ is also continuous at interfaces, both for the displacement field and for the conduction field:

$$E_{1t} = E_{2t} \qquad E_{1t} = E_{2t} \qquad (2.4\text{-}45)$$

Instead of a capacitance C in the displacement field, there is a conductance $G = 1/R$ (reciprocal of the resistance) in the conduction field. The following equations describe a parallel-plate capacitor e.g.:

$$C = \varepsilon \cdot A/d \qquad G = 1/R = \kappa \cdot A/d \,. \qquad (2.4\text{-}46)$$

The comparison shows that all relationships for the dielectric displacement field are also valid for the stationary conduction field, if the permittivity ε is replaced by the conductivity κ, the displacement density $\boldsymbol{D}$ by the conduction current density $\boldsymbol{J}$ and the capacitance C by the conductance G. This is also valid for the deduced Eqs. (2.4-17) to (2.4-32), which are related to interfaces orthogonal, parallel and inclined to the electric field direction.

For the **interface <u>orthogonal</u> to the electric field**, the continuity of the conduction current density $\boldsymbol{J}_1 = \boldsymbol{J}_2 = \boldsymbol{J}$ orthogonal to the interface is valid. By analogy with Eq. (2.4-17), it is concluded that

$$\frac{E_1}{E_2} = \frac{\kappa_2}{\kappa_1} \,. \qquad (2.4\text{-}47)$$

The *field strength* magnitudes and the *conductivities* are in *inverse ratio* to each other. Analogously with the dielectric field displacement, the material with the lower conductivity is stressed with a higher field strength than the material with the higher conductivity.

Note: Conductivities often differ by several orders of magnitude. Thus, the material with the higher conductivity is almost completely without stress, but the material with the lower conductivity is stressed with nearly the whole voltage. This is an almost *complete field displacement*. Figure 2.4-23 shows field and potential distribution for the conductivity ratio $\kappa_1 : \kappa_2 = 1 : 10$.

The normal components of the conduction current density J_n are certainly continuous at the interface, but the normal components of the displacement density D_n are not continu-

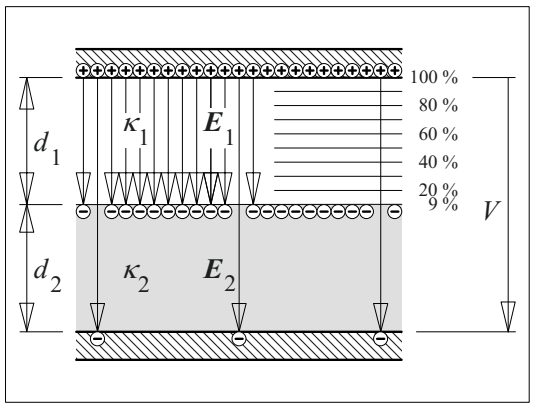

Figure 2.4-23: Field and potential distribution in two dielectrics with an interface orthogonal to the electric DC field (coductivity ratio 1 : 10).

ous. The difference between the displacement densities D_{1n} and D_{2n} is equal to a *surface charge density* σ at the interface. This effect is called *interfacial polarization*, Figure 2.4-23:

$$\begin{aligned} \sigma &= D_{2n} - D_{1n} \\ &= \varepsilon_2 E_2 - \varepsilon_1 E_1 \\ &= E_1 \cdot (\varepsilon_2 \cdot \kappa_1 / \kappa_2 - \varepsilon_1) \end{aligned} \qquad (2.4\text{-}48)$$

In the case of a short circuit at the electrodes, the surface charge (interfacial polarization) does not disappear immediately, it decreases with the time constant R_2C_1, which is determined by the geometries and by the material properties κ_2 and ε_1, see also Figure 2.1-16. If the short circuit is opened too early, an *unexpected and therefore dangerous re-charging of the electrodes* (a so-called "*recovery voltage*"), can occur (see Section 2.4.4.3).

Example: Capacitor with mixed dielectric

In capacitor dielectrics, made of oil-impregnated paper layers and high-resistive polymeric films, there is an almost complete field displacement into the polymeric films. A numerical example was already discussed in Section 2.1.4.2. The example shows that the polymeric films almost entirely produce the insulation. The paper layers are mainly used as impregnation wicks.

For an **interface parallel to the electric field**, the tangential field $\boldsymbol{E}$ is theoretically not influenced by the adjacent materials, i.e. $\boldsymbol{E}_1 = \boldsymbol{E}_2 = \boldsymbol{E}$ according to Eq. (2.4-45). The current densities are different on both sides of the interface because of the different conductivities: $\boldsymbol{J}_1 = \kappa_1 \boldsymbol{E}$ and $\boldsymbol{J}_2 = \kappa_2 \boldsymbol{E}$. According to Eq. (2.4-46) there are different area-related conductances and resistances on both sides of the interface.

It should be noted that for DC voltage stress, the interface parallel to a DC field is especially critical: *Conductive deposits and pollution layers* (e.g. caused by contaminations, impurities or wetting) can cause field distortions and extreme field stress enhancements if there are only slight non-uniformities in the layer, Figure 2.4-24.

For an **interface inclined to the electric field**, the different conductivities cause a refraction of the DC field lines and DC equipotential lines in the stationary conduction field (refraction law) by analogy with Eq. (2.4-21):

$$\frac{\tan \alpha_1}{\tan \alpha_2} = \frac{\kappa_1}{\kappa_2} \qquad (2.4\text{-}49)$$

α_1 and α_2 are the angles between the area vector $\boldsymbol{A}$ (orthogonal to the interface) and the field vectors $\boldsymbol{E}_1$ and $\boldsymbol{E}_2$, Figure 2.4-25.

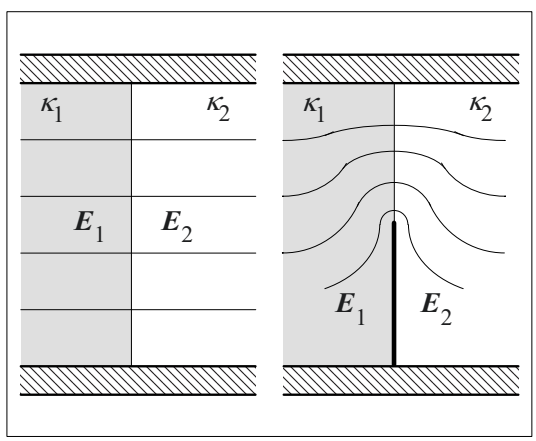

Figure 2.4-24: Interface parallel to a DC field.
Left: Ideal potential distribution.
Right: Potential distribution with a non-uniform conductive pollution layer causing extreme local field enhancements.

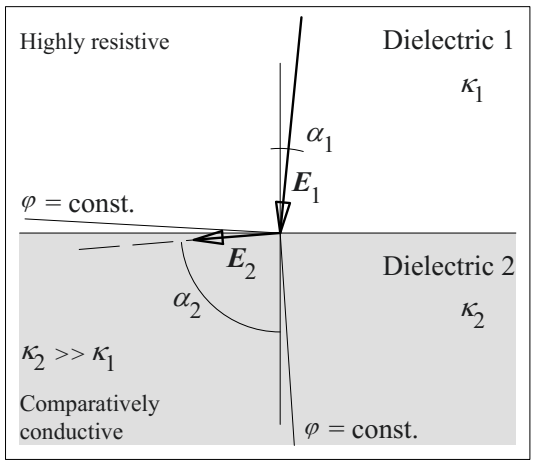

Figure 2.4-26: Refraction of field lines and potential lines in a stationary conduction field at the interface between insulating materials with very different conductivity.

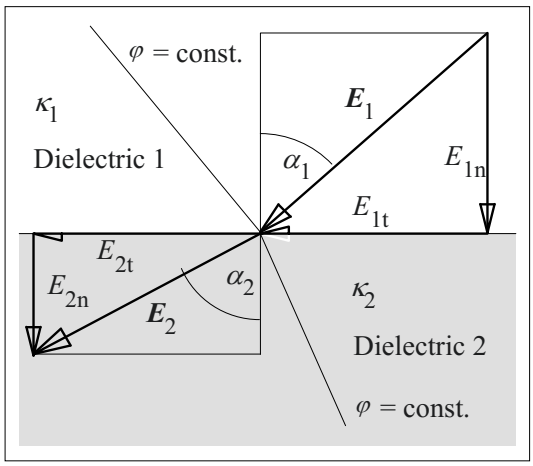

Figure 2.4-25: Vectors of the electric field strength and potential lines at an interface inclined to the electric field for two dielectrics with different conductivities ("Refraction" of field lines and potential lines at an inclined interface for a stationary conduction field).

In many practical applications, *conductivities* on both sides of the interface are *very different*. For $\kappa_2 >> \kappa_1$, the angle α_2 approaches 90°, even for very small angles α_1. In the *more conductive material 2*, the field lines are almost parallel and the potential lines are nearly orthogonal to the interface, Figure 2.4-26 (bottom). In the *more resistive material 1*, the field lines are almost orthogonal and the equipotential lines are nearly parallel to the interface, Figure 2.4-26 (top).

Note: This circumstance can clearly be explained by the fact that a *current* can only flow nearly parallel to the interface in the comparatively conductive material. Therefore, field lines must orient themselves almost parallel and equipotential lines almost orthogonal to the interface. In the highly resistive material, the field lines are almost orthogonal to the interface, which is similar to the situation close to a *conductive electrode*.

Example: In **oil-insulated equipment for high DC voltages**, the potential distribution in oil can be controlled by forming a uniform *oil duct* of higher conductivity between highly resistive *pressboard barriers* and other highly resistive insulating components (e.g. for bushings) [7].

For inclined layererd dielectrics there is also a *surface charge* at the interface. It can also be calculated from the difference of the *normal components* of the displacement density $\boldsymbol{D}$.

The *calculation* of DC voltage fields is not only complicated by the possibility of large differences of the conductivities. Furthermore, it is often difficult to get *reliable numerical values, since* conductivity is dependent on the exact material composition, on manufacturing process technology and very strongly on the temperature. Some examples are described below:

- Different porcelain mixtures have different conductivities.
- The conductivity of oil-impregnated paper increases with the water content.
- The conductivity ratio in an oil-pressboard insulation may be 100 : 1 at 20 °C (test temperature). At 90° C (service temperature) the ratio is just 10 : 1.

It was already mentioned in Section 2.4.1.1 that in practice it is very important to determine reliable and applicable conductivity values. Because of the high degree of possible variations, a field calculation with wrong conductivity values can lead to completely wrong results.

2.4.4.2 Typical DC fields

Some examples for typical DC fields shall be discussed below. Because of high conductivity differences, strong temperature dependences and the sensitivity to pollution layers, there are field distributions which are completely different from a comparable AC field.

Example 1:
Capacitor with mixed dielectric

The example of a *DC capacitor* with a mixed dielectric, made of *polymeric films* and *oil-impregnated paper with a hundredfold greater conductivity*, has already been discussed several times (Sections 2.1.4.2 and 2.4.4.1). It was shown that nearly all the voltage has to be insulated by the electrically strong polymeric films. The paper layers are relieved of the electrical stress to a large extent because of their significantly higher conductivity.

It is disadvantageous that the paper volume does not contribute to the capacitive storage volume. Therefore, it is desirable for weight reasons to design the insulation without any paper, which is only used as "impregnating wick". Then, good impregnation has to be guaranteed by adequate surface texture of the films.

Note: For *AC voltage*, the papers are stressed with a field strength, which is half as high as in the polymeric films because of the field displacement, see Eq. (2.4-17) with $\varepsilon_2/\varepsilon_1 = 2$. Nevertheless, the field strength in the paper can be the critical quantity that limits the voltage, because of the very high electric strength of polymeric films. Thus, the design does not make full use of the excellent electric strength of the polymeric films, and it is desirable therefore to replace the paper by polymeric films (*all-film dielectric*).

Example 2: **HVDC cable**

In a high voltage DC cable with a homogeneous dielectric there is a cylindrically symmetric field. According to Eq. (2.3-21), the field strength decreases proportional to $1/r$ between the inner and outer conductors, Figure 2.4-27 (curve 1). During service operation, the inner conductor is heated by the ohmic losses due to the current. As a result, there is a *temperature gradient* $T(r)$ from the inside to the outside. Because of the strong temperature dependence of the conductivity, a *conductivity gradient* is also caused. This results in a continuous field displacement from inside to outside. Depending on the conductor's temperature and the insulating material, the *field profile* is more or less *equalized*, Figure 2.4-27 (curves 2 and 3).

Nevertheless, the designer of the cable has to take into account that the cable has to withstand the voltage not only in the warmed-up service operation, but also in the *cold starting condition*.

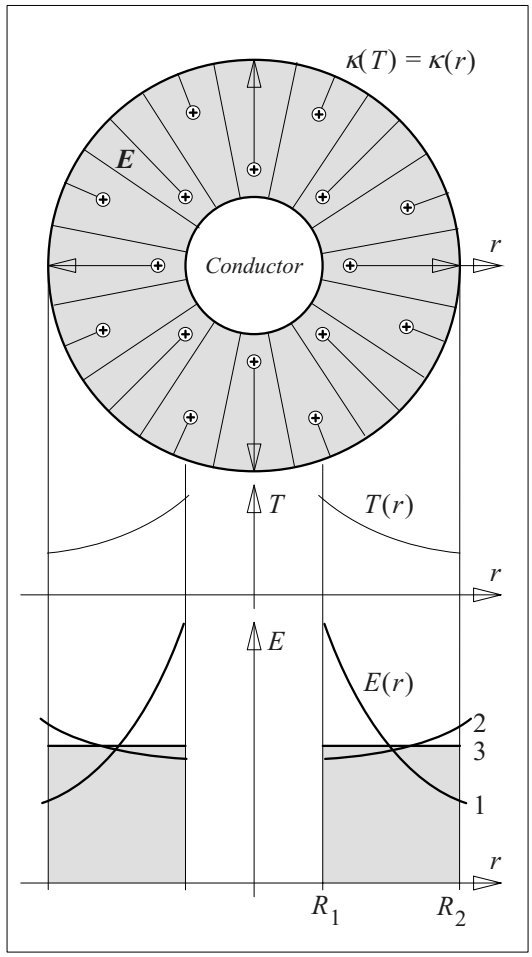

Figure 2.4-27: DC cable with a conductivity gradient caused by a temperature gradient and modification of the initial field distribution (curve 1) due to the space charge accumulation (curves 2 and 3).

The continuous variation of conductivity is accompanied by the accumulation of charge in the insulating material. In contrast to multilayer dielectrics, the charge is not accumulated at the interfaces, here it is distributed as *space charge* over the entirety of the *inhomogeneous insulating material*. This leads finally to the deviation of the field stress profile from the initial profile ~1/*r*.

The space charge is of high importance for the operation of the cable because the remaining charge can cause very high *field stress enhancements* after a *polarity reversal*. Furthermore, space charge can cause a dangerous *recharging* of the cable, if a short circuit between inner and outer conductor is opened again. Because of the high capacitance of long cables, even relatively low "*recovery voltages*" can accumulate significant and dangerous amounts of charge.

Example 3:
HVDC Bushing

A high voltage electrode in oil shall be connected via a capacitively graded bushing, both for AC and DC, Figure 2.4-28. At *AC voltage*, the capacitive grading layers have approximately the intended potentials, because of their mutual capacitances. In this way the tangential stress at the bushing surface is significantly reduced, Figure 2.4-28 (top).

Also at *DC voltage*, the intended potential distribution is approximately achieved *within* the bushing core, because of the mutual resistances of the grading layers, i.e. the grading is now resistive and no longer capacitive. *Outside* the bushing, there is a completely different potential distribution within the oil, Figure 2.4-28 (middle). The distribution is mainly determined by the electrode geometry, and the highly resistive bushing acts as a highly resistive boundary of the comparatively conductive oil volume. In this way, a very high *tangential stress* of the bushing surface can occur.

This field concentration can be avoided by a very large electrode diameter in very large oil tanks (cylinder). However, this is not generally an economic solution.

In the case of the given narrow installation conditions, the tangential field strength can also be reduced by a system of highly resistive

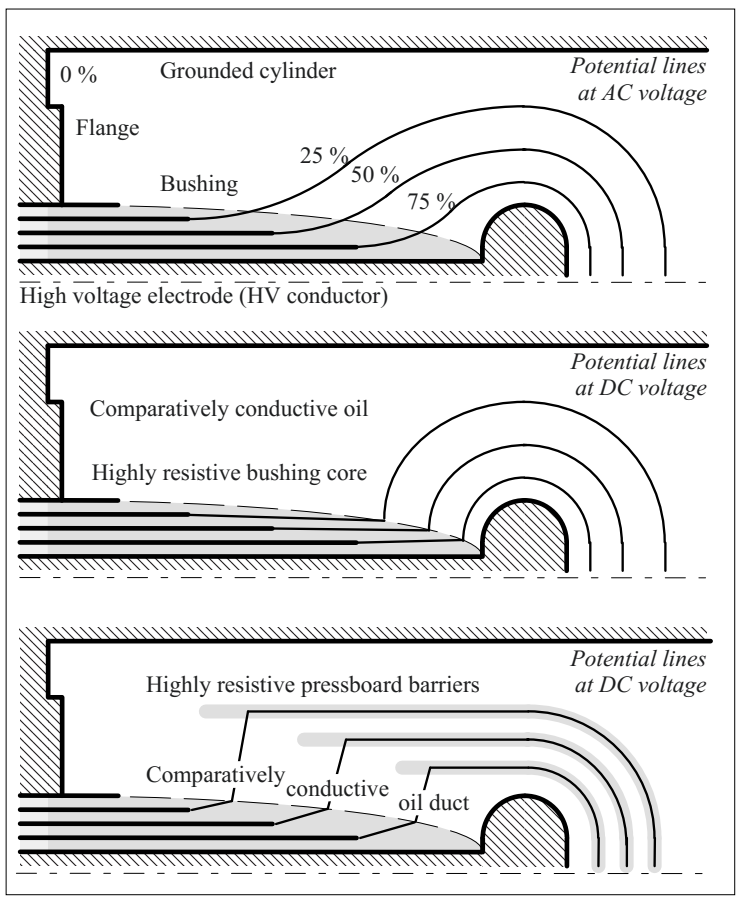

Figure 2.4-28: Connection of a HV electrode in oil via a capacitvely graded bushing at AC voltage (top) and DC voltage (middle and bottom). Improved potential distribution at DC voltage by highly resistive pressboard barriers (bottom) [7].

cylindrical *pressboard barriers* with different lengths (pressboard barrier system), Figure 2.4-28 (bottom). In this way a *uniform oil duct* shall be formed, with a current flow between high voltage and ground and with an almost uniform potential distribution.

The grading capability of the barriers at DC voltage is based on the *external potential grading* in the oil duct, which is adjusted to the *internal grading* of the bushing's grading layers. The internal bushing itself cannot influence the stationary conduction field outside the bushing [7], [10].

At *elevated temperature*, the conductivity differences between the materials and the grading capability of the barriers are reduced. A calculation with sufficient accuracy can only be achieved by *numerical field calculations* (see Section 2.5) with correct conductivity values.

According to the refraction law Eq. (2.4-49), it is concluded that the potential lines *in the oil* duct emanate from the highly resistive materials (bushing and barriers) almost orthogonally, see Figure 2.4-26. *Around the electrode*, the interfaces are orthogonal to the field (and parallel to the equipotential lines). Here, the field is displaced from the comparatively conductive oil gaps into the highly resistive barriers. Therefore, the thickness and number of the barriers must be such that the barriers can withstand the whole DC voltage.

Note: The barriers have an important function also at *AC voltage*: Although the influence of thin barriers on the AC field strength in the oil gaps is small, the electric strength of these gaps is significantly improved by a *subdivision into smaller gaps*.

Example 4: HVDC wall bushing

On the outdoor insulators of wall bushings, *pollution layers* develop by deposition of dust and dirt. The exposure to *water* by rain or by moisture condensation causes a comparatively high *surface conductivity,* Figure 2.4-29.

At *AC voltage*, the field distortion by conduction currents on the surface (creepage currents) is normally negligible, because of the comparatively high capacitive displacement currents.

At *DC voltage*, wet pollution layers, which have a significantly higher conductivity than the bushing insulator, cause very strong field distortions, especially if the pollution layer does not cover the surface completely and uniformly.

In *HVDC installations* for outdoor sites, the *non-uniform rain* on bushing insulators (e.g. in the lee side of a building) is especially critical at higher voltages, Figure 2.4-29. The high voltage potential can be shifted along the surface for long distances down to the transition zone between the dry and the wet surface. This is comparable with a sharp electrode on a

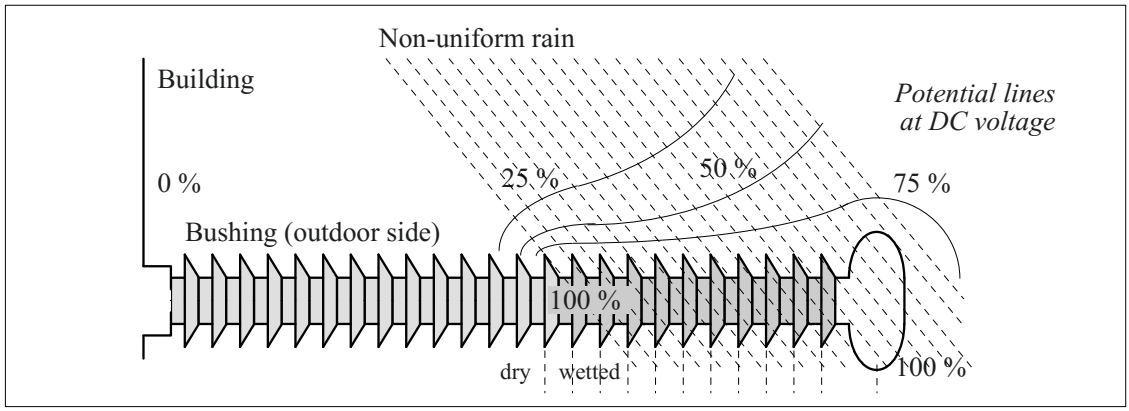

Figure 2.4-29: Air-side of an HVDC wall bushing with the formation of a wet and conductive surface layer. Because of the non-uniform rain only a part of the surface is bridged at DC voltage, see figs. 2.4-1 and -2.

creepage surface (Figures 2.4-17, -18 and -24) with extreme tangential and radial field stress enhancements, which can cause a flashover (comparatively best-case) or a radial breakdown of the bushing (worst-case).

Therefore, it is very often necessary, to apply *hydrophobic* (*water-repellent*) silicone paste on the insulator surface, in order to avoid the formation of conductive liquid films on the easily wettable porcelain surface. The application and regular renewal of the silicone paste can be avoided, if the porcelain insulator is replaced by a **composite insulator** made of a glass-fiber-reinforced plastic (GRP) tube (i.e. reinforced epoxy resin tube) with *elastomeric silicone rubber* (SIR) sheds [7], [8], [9], [10], see Section 5.3.4 with Figure 5.3-18.

Example 5: Energy storage capacitor

Energy storage capacitors are charged with *DC voltage*, and they are in general discharged by *electric pulses* or damped *high-frequency oscillations*.

During the charged condition, i.e. during a *steady-state DC stress*, the potential distribution close to the edge of a foil is significantly different from the AC distribution shown in Figure 2.4-20, see Figure 2.4-30. The impregnating gap that ends at the interstice at the edge of the foil, is filled with oil and normally has a higher conductivity κ_Z than the adjacent insulating films with κ_I. Thereby, a comparatively uniform gap is formed, where a conduction current can flow through the oil and grade the potential, Figure 2.4-30 (bottom). Thereby, the *stress at the edges* of the foil is significantly *reduced*.

Therefore, the *DC strength* of a capacitor dielectric is in practice significantly higher than the AC strength. A factor of about three can often be assumed.

The critical stress in an energy storage capacitor does not arise during the steady state DC stress, but during the fast *discharge* impulse or the *discharge* oscillation. The associated time-variant displacement field is more like Figure 2.4-30 (top). Furthermore, *space charges* accumulate at the interfaces of the polymeric films during the preceding steady-state DC phase. During an oscillating discharge, there are multiple *polarity reversals*, and a time-varying displacement field is superimposed to the steady-state space charge field. Thus, the electric field stress at the edges of the foils is much higher than for a pure DC or AC stress alone, see Section 7.3.3.

The *lifetime* of an energy storage capacitor or an impulse capacitor is therefore given by the number of possible discharges depending on the charging voltage, the frequency of the discharge oscillations and the relative magnitude of the first amplitude with reversed polarity (back-swing ratio) [29].

2.4.4.3 Transient Processes

The above-mentioned DC voltage stress assumes a steady-state condition, which requires very long times between hours and days for highly resistive insulating materials. According to Eq. (2.1-41), times should be much

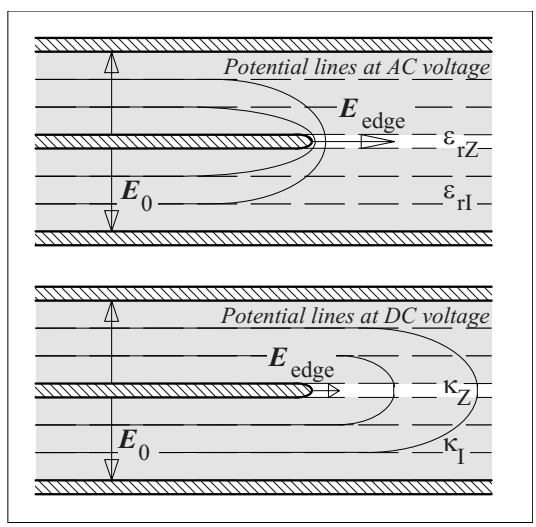

Figure 2.4-30: Electric field stress at the edges of the metallic foils in a capacitor dielectric at AC voltage (top) and reduced field stress at DC voltage (bottom) due to a comaratively high conductivity in the oil-filled interstice between the plastic films.

longer than the self-discharging time constants of the relevant materials:

$$t \quad >> \quad \tau_d = \varepsilon/\kappa \qquad (2.4\text{-}50)$$

For the **application of a DC voltage**, the following phases must be distinguished (see Figure 2.1-16):

a) If the DC voltage is applied as a *step* within a very short time (in comparison with the relevant time constants of the dielectric system) a *dielectric displacement field* can be assumed at first. It is determined by the *permittivities* ε. Geometrically simple configurations can be described by equivalent networks consisting of *capacitances* only.

b) Then, a *transient process* takes place, which consists of charging and discharging processes among the different dielectrics. A mathematical description requires the Material (Constitutive) Equations $\boldsymbol{D} = \varepsilon \boldsymbol{E}$ and $\boldsymbol{J} = \kappa \boldsymbol{E}$ together with the Continuity Equation (2.1-35) in their general form. Both conduction current density $\boldsymbol{J}$ *and* displacement current density $\partial \boldsymbol{D}/\partial t$ have to be considered.

Geometrically simple arrangements can often be described by equivalent networks consisting of *capacitances C* (for the description of the displacement current) and *resistances R* (for the description of the conduction current). Voltages and currents are then calculated with the methods of *network analysis.* The *Laplace transform* is very useful for this purpose [2], [30], [31].

Note: The description of a material by a single permittivity (capacitance) and a single conductivity (resistance) neglects that the **polarization process** of the material takes time and can continue for comparatively long times until the steady state is reached. Polarization processes are therefore described by a more complex equivalent circuit, which contains *RC* elements with different time constants for describing the different polarization mechanisms, see Section 4.3.

c) After the decay of the transient process, a *steady state* is reached, which depends on the *conductivities* (or resistivities) of the insulating materials only (Section 2.4.4.1 and 2.4.4.2). Geometrically simple arrangements can be described by an equivalent network consisting of *resistances* only.

In DC applications it often happens that a **given state** is changed **into another state** by a transient process. Examples are the transients after a *polarity reversal* (e.g. during an HVDC voltage test), after an *increase* or *decrease* of the DC voltage magnitude, after a *short circuit*, after a *discharging process* or during the development of a *recovery voltage*.

A **calculation** of the mentioned transitions can be performed in the following steps:

a) At first, the *initial state* has to be calculated. In the easiest case, this is the steady state. In an *equivalent network*, the initial state is given by the initial charge state of the equivalent capacitances. The initial state of a *complex arrangement*, which cannot be described by an equivalent network any more, has normally to be described by a numerically calculated *field pattern* or an *equipotential line plot*.

b) The *subsequent voltage step* can be described by a voltage source in an equivalent network. In more complex arrangements, which are described by field or equipotential plots, the *dielectric displacement field* associated with the voltage step can be superimposed on the initial field distribution in the form of a field plot. This gives the dielectric stress directly after the voltage step [7], [10].

c) The *transient process* can be determined by a transient network analysis in an equivalent circuit. For geometrically complex arrangements numerical field calculations have to be based on transient field theory. For practical applications it is often sufficient to calculate the *steady end state*.

Hereafter, some practical examples are discussed:

Example 1 deals with the application of a DC voltage to a multi-layer capacitor dielectric. The recovery voltage after the short circuit of a capacitor is considered in *example 2*. *Example 3* shows that there can be stress enhancements in some dielectric layers during a transient process. *Example 4* discusses the complex field conditions in a barrier system during a polarity reversal of a DC voltage.

Example 1: Application of a DC voltage

Steady-state and quasi-static capacitive fields in a two-layer capacitor dielectric were already discussed in Section 2.1.4.2 and 2.1.4.4. The two-layer dielectric is made of polymeric films and oil-impregnated papers with $d_1 = d_2 = 30$ µm, $\varepsilon_{r1} = 2.2$, $\varepsilon_{r2} = 4.4$, $\kappa_1 = 10^{-16}$ S/m and $\kappa_2 = 10^{-14}$ S/m, Figure 2.1-11, -15 and -16. The transient process shall be discussed.

As the interfaces between the materials are also equipotential surfaces, the transient process can be described with an *equivalent network* containing capacitances C_1 and C_2 together with the parallel resistances R_1 and R_2:

Immediately after the *application of the DC voltage* the dielectric displacement field causes a "*capacitive voltage distribution*", i.e. the polymeric films are stressed with 2/3 and the papers with 1/3 of the voltage.

In an *approximately exponential transient process*, the capacitance C_1 of the high resistive polymeric films is charged over the resistance R_2 of the comparatively conductive oil-impregnated papers (time constant $\tau = R_2C_1$) until the *steady-state ("ohmic") voltage distribution* is reached. This can take many hours to complete.

The polymeric films always have to withstand the whole DC voltage, the papers are stressed with only 1 % of the total voltage.

Example 2: Recovery voltage

For the capacitor in the above-mentioned example, the *steady-state* voltage at the equiva-

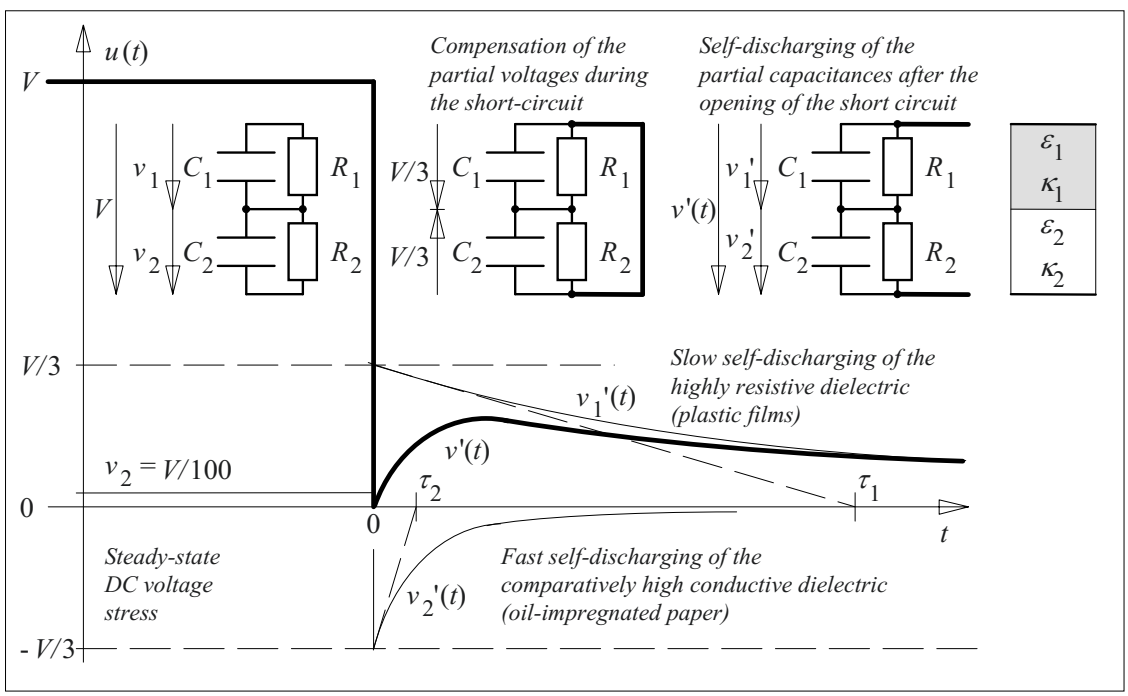

Figure 2.4-31: DC voltage stress and recovery voltage at a dielectric consisting of plastic films and oil-impregnated paper with a hundred times the conductivity (more explanations see in the text).

lent capacitance C_1 (polymeric films) is nearly the whole voltage (approx. $0.99 \cdot V$), whereas C_2 (papers) is only charged to $0.01 \cdot V$, Figure 2.4-31 (left).

During a *short circuit* of the capacitor at the external terminations, the charge $Q_1 \approx C_1 \cdot V$ is distributed among the two parallel partial capacitances C_1 and C_2, which have the same voltage, but with opposite polarity. The voltage between the outer terminations is thus zero. Theoretically, the voltages are $v_1' = -v_2' = (1/3) \cdot (C_1 \cdot V)/C_1 = V/3$ for $C_2 = 2\ C_1$, if $Q_2 = C_2 \cdot 0.01 \cdot V$ is neglected, Figure 2.4-31 (middle). The difference of the capacitively stored energies, before and after the short circuit, is dissipated as ohmic loss in the resistance of the short circuit. If the short circuit is not opened again, the parallel capacitances C_1 and C_2 are exponentially discharged via $R_2 << R_1$ with the time constant $\tau = (C_1 + C_2) \cdot R_2$.

If the *short circuit is opened again*, immediately after the connection of the terminals, however, the partial capacitances, which are charged to $v_1' = V/3$ and $v_2' = -V/3$, can only be discharged by self-discharging via the associated equivalent resistances with the self-discharging constants $\tau_1 = R_1 C_1 = \varepsilon_1/\kappa_1$ and $\tau_2 = R_2 C_2 = \varepsilon_2/\kappa_2$. In the given example, the exponential discharging of C_2 would be fifty times faster than the exponential discharging of C_1, so that the resulting voltage at the open terminals is $v'(t) = v_1'(t) + v_2'(t)$, which is called "*recovery voltage*", Figure 2.4-31 (right).

Note: This explanation of the recovery voltage is based on charges that are stored at the interfaces in the dielectric and on charge reversals between *different materials*. A similar recharging takes place, if there are *space charges stored* in the dielectric (see the example about HVDC cables in Section 2.4.4.2) or if charge is stored by means of *polarization effects*, Section 4.3.2.1.

Note: Charged capacitors and recovery voltages are some of the **main dangers for experimental work with high voltages**. Equipment with high capacitances (e.g. capacitors, cables) must therefore have a *permanent short circuit*. Also in a *series-connection* of capacitors all the single units must have an *individual* short circuit: A short circuit at the end terminals only would not prevent the individual capacitors to be (oppositely) charged. For safety reasons, it should not be assumed that the individual capacitors are identical (if only because of temperature gradients could cause differences) and that they are charged and discharged simultaneously.

Note: There are attempts to use parameters of recovery voltages for *dielectric diagnosis*, e.g. for transformers and cables [32], [33], see Section 6.4.7.5.

Example 3:
Transient enhancements of field strength in multi-layer dielectrics

After the application of a DC voltage to a multi-layer dielectric, the transition from the initial capacitive to the final ohmic potential distribution can be accompanied by *temporarily enhanced and unexpected stresses* which cannot be recognized from the initial and final states.

We discuss a three-layer dielectric consisting of a plastic barrier separating two oil-gaps with different oil qualities (aged and new oil), Fig 2.4-32. It is assumed that the *self-discharging time constants* of the aged oil, the plastic barrier and the new oil have the relation 1 : 100 : 10. The relation of the *equivalent capacitances* shall be assumed to be 1 : 2 : 2. With $\tau = RC$, the relation of the *equivalent resistances* is 1 : 50 : 5.

After the application of the DC voltage, a *capacitive voltage distribution* occurs at first, because of the dielectric displacement field, Figure 2.4-33. Dielectric 1 is stressed with half the voltage, dielectrics 2 and 3 each carry a quarter of the voltage V.

Because of the short self-discharging time constant τ_1 of dielectric 1, C_1 is *discharged quickly* and $v_1(t)$ decreases very rapidly. Thus,

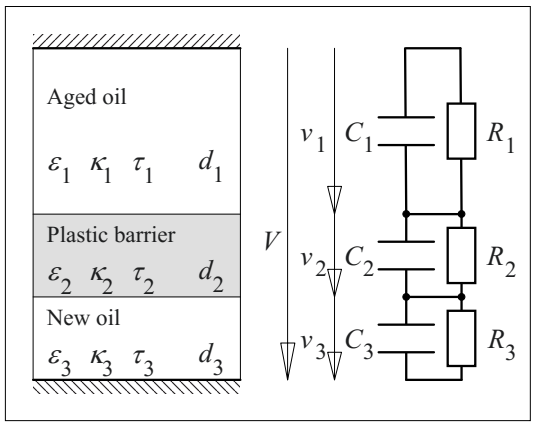

Figure 2.4-32: Three-layer dielectric with different self-discharging time constants (e.g. with the ratios 1 : 100 :10), see fig. 2.4-33 with the corresponding voltage curves after the application of a DC voltage V.

the other dielectrics 2 and 3 have to carry an additional fraction of the total voltage V. The equivalent capacitances C_2 and C_3 are recharged via R_1 at first. Therefore the voltages v_2(t) and v_3(t) increase simultaneously at first, Figure 2.4-33.

Then, the lower self-discharging time constant of dielectric 3 becomes apparent by a further discharging of C_3 together with a further recharging of C_2 via R_3 to even higher voltages.

The voltage $v_3(t)$ is increasing at first and decreasing in the long term. In between there is a distinct *maximum*.

This maximum is significantly higher than the initial voltage at this material, and it is many times higher than the final steady-state voltage. Therefore, we have a possible *overstress* of dielectric 3 *in the course of transient process*, *which is often ignored*.

In the *steady-state condition* the voltage is distributed according to the equivalent resistances, i.e. dielectric 1 is stressed with 2 %, dielectric 2 with 89 % and dielectric 3 with 9 % of the total voltage V.

Note: Compared to oil, the high stress on the plastic barrier may still be tolerable because solid materials can normally be stressed with much higher field strength than liquids.

The exact level of the overstress in dielectric 3, which is qualitatively described here, can be calculated by means of a *network analysis*. The result depends very strongly on the nature of the observed multilayer dielectric. Especially *critical* arrangements can often be found, if the initial and the final distribution are very different.

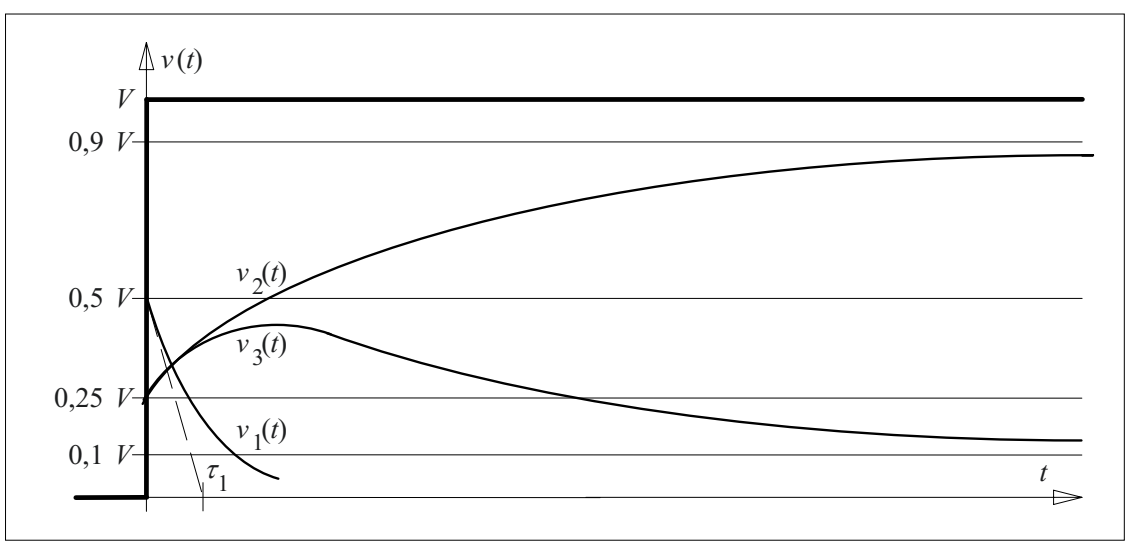

Figure 2.4-33: Voltage curves for a three-layer dielectric according to fig. 2.4-32, with a temporary voltage enhancement at dielectric 3 after the application of a DC voltage.

Example 4:
Polarity reversal of a DC voltage

Very complex field distributions, field migrations and significant field stress enhancements can occur in connection with the *polarity reversal* (PR) of a DC voltage in an oil-board barrier system, as used in HVDC insulation, e.g. in *converter transformers* or *smoothing reactors*. Normally, these fields can no longer be described by equivalent circuits, and it is necessary to perform numerical field calculations, Section 2.5.

A plane arrangement with two high-resistive barriers between two plane electrodes in comparatively conductive oil is discussed, in order to give a qualitative explanation of the conditions when reversing the voltage, Figure 2.4-34. The insulation arrangement can be regarded as a very simplified *model of a barrier system* according to Figure 2.4-28.

If a *negative DC voltage is applied* to the upper electrode, a *steady-state conduction field* in the oil develops parallel to the interfaces between oil and barriers, Figure 2.4-34a. It can be related to a conduction current from the lower to the upper electrode, conducted between the highly resistive barriers. Within the oil duct, the distance between the equipotential lines is great and the field strength is low, if the oil duct is long enough. Thus, the barrier system can grade the field in the oil duct. The barriers are stressed with nearly the whole DC voltage, in the regions where they do not overlap. The barriers have to be designed accordingly, e.g. by multi-layer design with sufficient thickness.

The *polarity reversal* can be described by the superposition of a *positive voltage step with twice the amplitude* of the DC voltage. It causes a strong dielectric *displacement field*, which is superimposed on the initial conduction field [7], Figure 2.3-34b. To a first order approximation, the field displacement from the barriers into the oil is neglected.

The *superposition* results in a *very high stress in the oil duct*, Figure 2.4-34c. Only a minor part of the stress is taken off from the barriers. Interestingly, there are “islands” with a potential higher than 100 % and lower than 0 % of the applied DC voltage. These islands are caused by positive and negative *surface charges* that were accumulated on the surfaces of the barriers during the preceding steady state, see also Figure 2.4-23.

After the polarity reversal, a *transition process* takes place, during which the capacitances of the barriers are essentially recharged via the series resistance of the oil ducts. Finally, a new stationary field distribution is formed for a positive DC voltage that is equal and opposite to the original, Figure 2.4-34d.

Note: Experience with DC voltage tests of oil-insulated equipment with barrier systems shows that the *minutes after the polarity reversal* are often critical. During this time partial discharges can occur, which disappear later on. This is an indication of high and decreasing field strengths directly after the polarity reversal, see Figure 2.4-34c.

2.4.5 Field Grading at Interfaces

Insulation arrangements with interfaces tangential to strong electric fields are especially critical in high voltage engineering for any kind of voltages, AC, DC and impulse stresses. Most of the problems arise at the interfaces to the electrically weak air, i.e. at the so-called surfaces.

Electrical discharges can be triggered, both by the normal field in the air-filled interstice at a triple point (see Section 2.4.3.3) and by the tangential field at the edge of an electrode (see Section 3.2.6), Figure 2.4-35 top (right and left). Inception voltages are comparable for both cases, Eq. (2.4-35) and (3.2-72). If a discharge is triggered by an AC voltage, strong tangential field components cause powerful surface discharges, because of high stray lateral capacitances and high capacitive AC currents in the discharge channel. Thus, insulating materials can severely be damaged by erosion at the surface, Section 3.2.6.

Arrangements with high tangential field strengths and with high lateral capacitance (i.e. with small insulation thicknesses) are susceptible to surface discharges. They can be found in many insulation arrangements, and they are called “creepage surfaces”, Figure 2.4-35 (bottom). Some common cases are given e.g.

- in arrangements with rotational symmetry (e.g. for cables, Section 7.1.1 or for bushings, Section 7.1.2),
- in plane arrangements (e.g. at the edges of a parallel-plate capacitor, or for thin insulating foils, Figure 2.4-20)
- and for the insulation surface of insulated rectangular conductors (e.g. for insulated busbars or stator winding insulations, Figure 7.1.6-4).

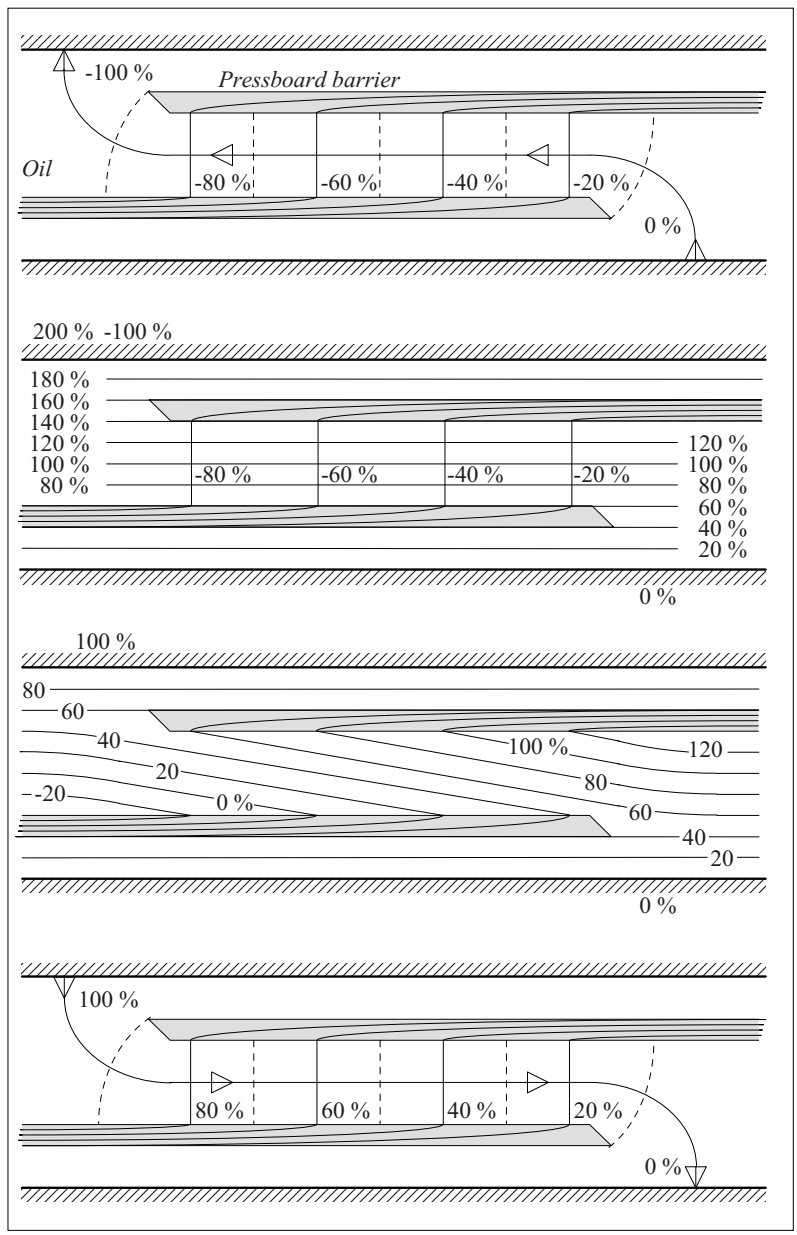

Figure 2.4-34a: Steady-state conduction field with a negative DC voltage at the upper electrode.

Figure 2.4-34b: Superposition of a dielectric displacement field with opposite polarity and twice the amplitude at polarity reversal. The field displacement at the barriers is neglected.

Figure 2.4-34c: Resulting field directly after the polarity reversal. Because of the surface charges at the interfaces, there are "islands" with potentials higher than 100 % and lower than 0 %.

Figure 2.4-34d: Steady-state conduction field after polarity reveral and after the decay of the transient process, i.e. after the re-charging of the barrier capacitances via the resistances of the oil ducts.

It is a basic task of high voltage engineering, to keep tangential electrical stresses at surfaces low. This can be achieved with different technologies for **field grading** or **potential grading**, which are explained for the example of cable entrance fittings [464], Figure 2.4-36:

(1) For g**eometric field grading**, the ground potential of the cable shield is guided outwards by the geometric contour of the *conductive deflector*, Figure 2.4-36 (1). Its funnel-shaped curvature guarantees that the field strength decreases significantly along the contour from the cable surface outwards, similar to a Rogowski profile. For *cable entrance fittings*, (Section 7.1.1.4) the deflector is located in a conical body made of an elastomeric material (grading cone). The field strengths at the surfaces have to be reduced so much that there is no danger. For the edges of parallel-plate capacitors, the electrodes are often bent (Rogowski and Borda profiles, curvature according to Eq. 2.3-43). The geometric field grading requires huge volumes, therefore leading to designs with large dimensions and diameters.

(2) A **capacitive field grading** is achieved by conductive *grading layers* between ground and high voltage potential, Figure 2.4-36 (2). The capacitances between these layers guarantee the desired potential distribution. The shift of the layers in axial direction imposes the potential of the layers on the surface of the insulation arrangement. Capacitive grading is most effective, i.e. a completely linear distribution in the axial direction can be achieved, together with very small diameters and insulation thicknesses. Capacitive grading is therefore used for high voltage *bushings* up to the highest voltages, Section 7.1.2.

Note: For HV and MV *cable entrance fittings* and *cable joints geometric grading* is mostly applied nowadays, because of production and assembly reasons. Refractive, resistive and non-linear grading are also used for medium voltage applications.

(3) **Refractive field grading** can be performed by a tube made of a *high-permittivity material*,

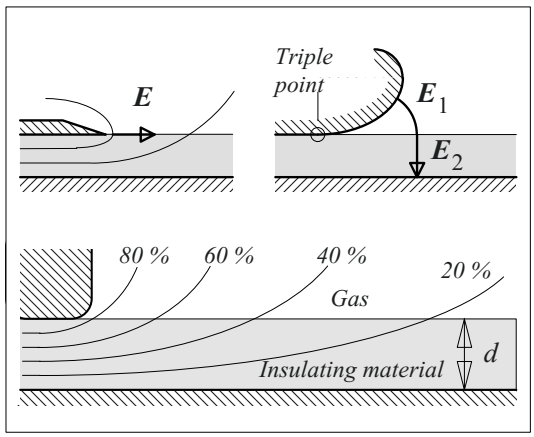

Figure 2.4-35: Triggering of surface discharges by tangential and normal field components (top left and right). Creepage surface with high tangential stress and thin insulation material (bottom, the refraction of equipotential lines is neglected).

which is shrunken or mounted onto the surface of the cable insulation and connected to the end of the cable shield, Figure 2.4-36 (3). By means of field refraction and field displacement, the field lines are displaced away from the edge of the cable shield. Thus the field is equalized and maximum field strength at the edge of cable shield is reduced.

(4) For **resistive field grading**, a *semi-conductive (i.e. semi-resistive) coating* is applied to the surface of the cable insulation, Figure 2.4-36 (4). The axial resistances and the radial capacitances relative to the inner conductor form a *RC* lattice network, which grades the potential along the coated insulation in the case of an AC stress.

(5) A **non-linear field grading** makes use of materials that have high insulating resistances at low field strengths and significantly increasing conductivities with increasing field strengths, Figure 2.4-36 (5). Thereby, locally enhanced conductivities displace the electric field and reduce the field magnitude at points with highest field strengths. *Non-linear materials* like zinc oxide (ZnO), silicon carbide (SiC) and iron oxide (FeO) are embedded in a polymeric matrix material and act as so-called *microvaristors*.

Stator winding insulation in *generators* and in big *motors* is the traditional application of resistive and non-linear field grading, Figure 7.1.6-4. The coatings are very thin and can therefore be applied to the insulated conductors, which are in close proximity to each other in winding heads.

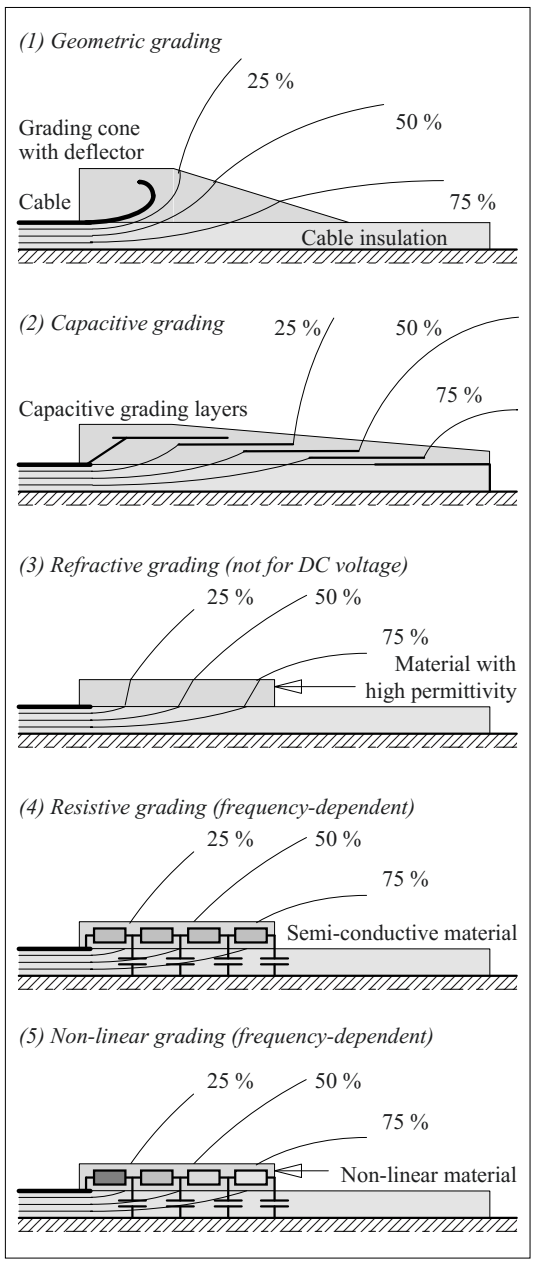

Figure 2.4-36: Technologies for field and potential grading on typical creepage surfaces, rotationally symmetric surfaces of cable insulation (example).

Refractive field grading can only be used for time-varying voltages (*AC or impulse*). **Resistive** and **non-linear gradings** are strongly *dependent on the frequency* of the applied voltage (frequency sensitivity).

All the field and potential grading methods have in common that they reduce the tangential field strengths at **interfaces and surfaces**. Nevertheless, these interfaces and surfaces are still normally *highly stressed* and have to be *treated with* particular *care*. This means that contaminations, pollutions, deposits, access of water, air-inclusions, voids and other defects have to be precluded with high reliability during the production process and service operation.

2.5 Numerical Field Calculation

Numerical field calculation is one of the most important tools for high voltage engineers in design, development and research. Sufficiently accurate field strength magnitudes for complex insulation arrangements can only be determined by numerical calculation.

Nevertheless, numerical calculations must not replace the intellectual analysis of the given kind of stress. Both a thorough preparation of the calculation and a thorough analysis/ discussion of the results are necessary, in order to avoid mistakes or wrong and too far-reaching conclusions.

It is recommended therefore, always to make a qualitative *visualization* by *field mapping* (Section 2.3.3) and to try an *analytical estimation* for a simplified insulation model. Based on these approximations, numerical results can be checked for plausibility.

2.5.1 Overview

For this introduction, the discussion is limited to electric **potential fields**, i.e to *static, quasi-static and steady-state* (capacitive) displace-

ment and conduction fields, which can be described by means of Poisson's or Laplace's Differential Equation (2.3-31), i.e. as so-called **Poissonian** or **Laplacian fields** .

Note: Considering the **vector potential**, fast changing and non-stationary fields, i.e. fields with *eddy currents* and *electromagnetic waves* can also be calculated [394].

The calculation of potential fields can be performed with different numeric methods. Three basically different solution approaches can be distinguished [34]:

a) Integral Equation Methods (IEM) superimpose field or potential quantities that are related to charges, currents and dipole moments, by means of summation or integration of the relevant contributions. If both vector and scalar potentials are defined [2], [3], the fast changing electromagnetic field can also be calculated.

The traditional method for the calculation of slowly changing fields is the *Charge Simulation Method* (CSM), which was already used for analytical calculations in Section 2.3.5. The charge simulation method can be extended to surface charges (SCSM: *Surface Charge Simulation Method*, BEM: *Boundary Element Method*). Fast changing fields can be treated with the *Method of Moments* (MOM).

It is an *advantage* of integral equation methods that spatially unlimited three-dimensional arrangements can be treated with a limited number of elements (charges, etc.). In high voltage engineering it is also advantageous that the influence of *space charges* can easily be considered. On the other hand, it is difficult to calculate fields in arrangements with many *different materials*, since the influence of interfaces has to be taken into account by many additional elements (charges, etc.)

b) The **Finite Difference Method** (FDM) and **the Finite Element Method** (FEM) discretize the whole field volume and set up differential equation systems based on the discretized Poisson's Equation (FDM) or on the extreme value determination of a specific energy-functional (FEM). The treatment of non-stationary fast changing fields is possible with the FEM.

The *advantage* of these methods is a very simple treatment of many different *materials and interfaces*. Therefore, insulation systems with a complex multi-layer arrangement and with *non-linear materials* can also be calculated. The method of finite elements has therefore prevailed in the calculation of magnetic fields because (non-linear) ferromagnetic materials have to be considered there.

It is a *disadvantage* that the *whole field volume* has to be discretized. A huge number of elements is thereby created, especially for three-dimensional arrangements. The method of finite elements allows one to adapt the fineness of the discretization to the different field regions, whereby the number of elements is further reduced.

Note: In other fields of engineering, the **Finite Element Method** has already been established for a long time, it provides mathematically analogous calculations of *mechanical, thermal and magnetic fields*. Therefore the method is very popular in many *industrial applications* because development and design of technical apparatus normally include thermal and mechanical stresses. Modern field calculation programs take the geometric data directly from CAD programs and they can calculate **combined stresses** of a mechanical, thermal, magnetic and electric nature (*multi-physics*).

c) The **Monte Carlo Method** (MCM) is based on the mean value theorem of the potential theory. It states that the potential $\varphi(P)$ at the center point P of a sphere equals the average potential on the surface of the sphere. From a point under consideration, random walks are started, which reach the electrodes of given potential with a specific frequency. In this way, a mean value is determined from the hit electrode potentials. It is a statistical estimate of the potential $\varphi(P)$, whose quality can be determined from the statistical dispersion [16].

The Monte Carlo Method is considered to be an adequate method for the calculation of single potential values in a part of the field volume which is of minor interest [34].

Hereafter, the Charge Simulation Method (Section 2.5.2), the Finite Difference Method (Section 2.5.3) and the Finite Element Method (Section 2.5.4) are discussed in more detail.

2.5.2 Charge Simulation Method

For the Charge Simulation Method, the fields of individual *equivalent charges* are superimposed at a reference point A_k by a *summation* of their individual contributions to the resulting *potential* φ_k, Figure 2.5.1:

$$\varphi_k = \varphi_{k1} + \varphi_{k2} + \varphi_{k3} + ... + \varphi_{kn} \qquad (2.5\text{-}1)$$

This idea was already used for the analytical field calculation in Section 2.3.5, Eq. (2.3-45).

Point charges (Q_1), *straight line charges* (Q_2) and *toroidal line (ring) charges* (Q_3) are successfully used as equivalent charges. The contributions φ_{kj} of the individual charges Q_j to the potential φ_k are described by *potential coefficients* p_{kj}:

$$\varphi_{kj} = p_{kj} \cdot Q_j \qquad (2.5\text{-}2)$$

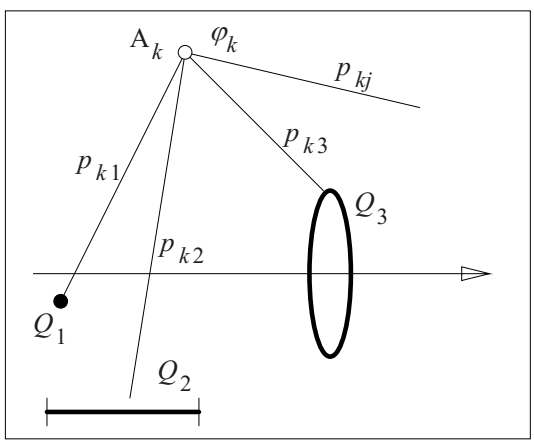

Figure 2.5-1: Point charge, line charge and toroidal line (ring) charge as basic equivalent charges of the Charge Simulation Method; contribution of a number of charges to the potential in reference point k.

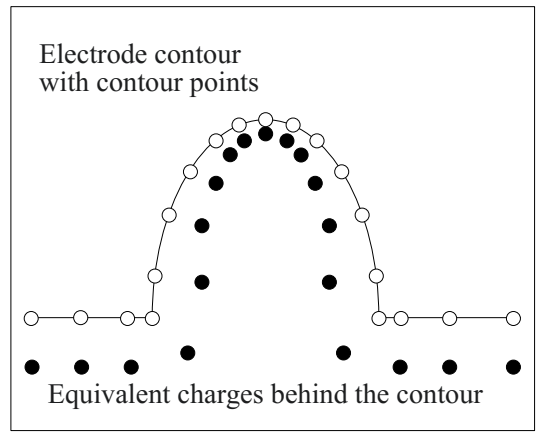

Figure 2.5-2: Setting of equivalent charges and contour points following the given contour of an electrode.

In the case of *point charges*, the potential coefficient according to Eq. (2.3-44) is given as $p_{kj} = 1/(4\pi\varepsilon \cdot r_{kj})$, i.e. as a function of the distances r_{kj}.

Equivalent relations can also be given for the straight and toroidal line charges [16].

The electrode surfaces are approximated by *equipotential surfaces*. This means that discrete equivalent charges have to be set *behind* the desired electrode contour, in order to get finite potential values on the contour. The potential at the location of the equivalent charge itself is infinite.

In a *first* step, *n equivalent charges* of unknown magnitude *are set*, based on the given electrode contour, Figure 2.5-2.

In a *second* step, an equal number of *n contour points* are chosen on the electrode contour, with the given electrode potentials φ_{E1} till φ_{En}.

In a *third* step, a system of equations can be formed using the *potential coefficients*. It gives the known potentials φ_{Ek} of the contour points as a function of the unknown *equivalent charges* Q_j. These *magnitudes of the equivalent charges* can be determined by solving the system of equations:

$$\begin{bmatrix} p_{11} & p_{12} & \cdots & p_{1n} \\ p_{21} & p_{22} & \cdots & p_{2n} \\ \cdots & \cdots & \cdots & \cdots \\ p_{n1} & p_{n2} & \cdots & p_{nn} \end{bmatrix} \cdot \begin{bmatrix} Q_1 \\ Q_2 \\ \cdots \\ Q_n \end{bmatrix} = \begin{bmatrix} \varphi_{E1} \\ \varphi_{E2} \\ \cdots \\ \varphi_{En} \end{bmatrix} \quad (2.5\text{-}3)$$

Now the equivalent charges are known, and the *potential of any point* in the field volume can be calculated according to Eq. (2.5-1) and (2.5-2).

In a *fourth* step, the quality of the equivalent charge positioning is first tested. Additional *test points* are chosen on the given contour, and the given potentials are compared with the calculated values. If the differences cannot be tolerated, the positioning of the equivalent charges has to be improved.

The contour of the calculated equipotential surface will never be identical with the given electrode surface. Both surfaces touch each other at the contour points according to the initial condition. For the test points in between, the deviation of the calculated potential on the electrode surface is determined.

There are some proven rules for the *positioning of equivalent charges*, Figure 2.5-2:

- An equivalent charge and a contour point shall be set as a pair with a close spatial relationship.
- The distance between charge and contour point shall be comparable to the distance to the adjacent charges.
- Depending on the curvature of the electrode contour, the charges shall be set closer or further apart.
- Variations of charge and contour point distances shall be performed gradually, without major variations of the adjacent distances.

The *simulation quality* is increased with the number and density of the equivalent charges. Nevertheless, the number of charges must not be too great, in order to avoid numerical problems during the solving of the system of Equations (2.5-3).

The influence of *dielectric interfaces* can be taken into account by surface charges or by equivalent charges on both sides of the interfaces [16]. In arrangements with many different materials, a significant additional effort is required; therefore, another calculation method might often then be better.

An electrode at *free potential* can be simulated, if equivalent charges are set behind the electrode with the charge-sum zero: $\Sigma Q_i = 0$.

Additional equations are thereby defined, which are necessary for the determination of the electrode potential [16].

A further development of the Charge Simulation Method makes use of *surface charges*, which approximate the physical charge distribution on the electrode surfaces and the interfaces (Surface Charge Simulation Method, Boundary Element Method).

Note: The *Charge Simulation Method* has a close relation to the *physical origin of electrostatic fields*. Therefore the CSM can easily be understood and it is one of the first numerical simulation methods used in HV engineering. Nevertheless, the position and distribution of the equivalent charges are not identical with the position and distribution of the physical charges, but the magnitudes are equal.

2.5.3 Finite Difference Method

For field calculation with the Finite Difference Method, the field volume is discretized with a grid of regular meshes, Figure 2.5-3. The potential φ_0 on a node "0" can then be given as a function of the potentials φ_1, φ_2, φ_3, ... on the adjacent nodes, if the potential $\varphi(x,y,z)$ in the directions x, y and z is approximated by a Taylor series.

In Cartesian coordinates, a variation either in x-, y- or z- direction, without any variation in the other two directions, is

$$\varphi(x) = \varphi_0 + \Delta x \cdot \partial\varphi/\partial x + (\Delta x^2/2) \cdot \partial^2\varphi/\partial x^2 + ...,$$

$$\varphi(y) = \varphi_0 + \Delta y \cdot \partial\varphi/\partial y + (\Delta y^2/2) \cdot \partial^2\varphi/\partial y^2 + ...,$$

$$\varphi(z) = \varphi_0 + \Delta z \cdot \partial\varphi/\partial z + (\Delta z^2/2) \cdot \partial^2\varphi/\partial z^2 + ...$$

For a plane **two-dimensional** arrangement according to Figure 2.5-3, the neighbor potentials of φ_0 are estimated from the Taylor series that is cut off after the second order term:

$$\varphi_1 \approx \varphi_0 + h \cdot \partial\varphi/\partial x + (h^2/2) \cdot \partial^2\varphi/\partial x^2$$

$$\varphi_3 \approx \varphi_0 - h \cdot \partial\varphi/\partial x + (h^2/2) \cdot \partial^2\varphi/\partial x^2$$

$$\varphi_2 \approx \varphi_0 + h \cdot \partial\varphi/\partial y + (h^2/2) \cdot \partial^2\varphi/\partial y^2$$

$$\varphi_4 \approx \varphi_0 - h \cdot \partial\varphi/\partial y + (h^2/2) \cdot \partial^2\varphi/\partial y^2$$

The cut off of the series after the second-order term means that the step width h, i.e. the mesh width h, must be chosen small enough, so that the potential variation can be described by a second order polynomial with sufficient accuracy. In very non-uniform fields, very small mesh elements and a very large number of nodes is required.

If the sum of the four neighbor potentials is calculated, the first order terms compensate each other because of opposite signs. According to Laplace's Equation (2.3-32) for the case without space charge, the sum of the second-order terms is also zero:

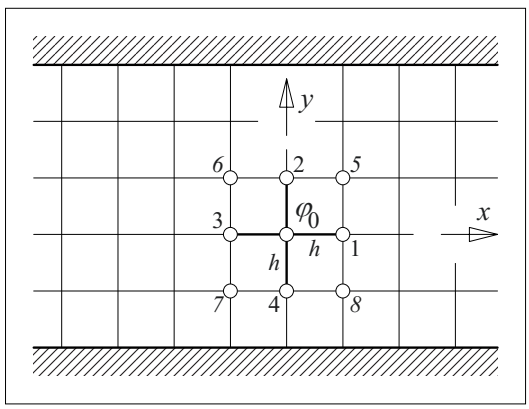

Figure 2.5-3: Discretization of a 2D field region by means of a grid with square meshes for the field calculation with the Finite Difference Method.

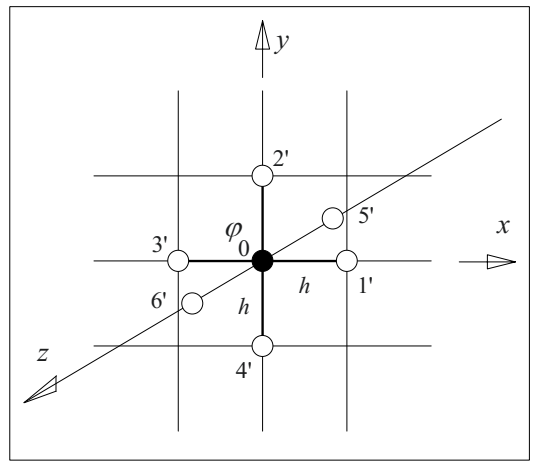

Figure 2.5-4: Discretization of the field volume for the three-dimensional field calculation with the Finite Difference Method.

$$\varphi_1 + \varphi_2 + \varphi_3 + \varphi_4 = 4 \cdot \varphi_0 . \qquad (2.5\text{-}4)$$

Therefore, the potential φ_0 is the average of the four neighbor potentials ("square algorithm"):

$$\varphi_0 = (\varphi_1 + \varphi_2 + \varphi_3 + \varphi_4)/4 \qquad (2.5\text{-}5)$$

In the same way, φ_0 can be calculated from the potentials in the diagonally adjacent nodes ("diagonal algorithm")

$$\varphi_0 = (\varphi_5 + \varphi_6 + \varphi_7 + \varphi_8)/4 \qquad (2.5\text{-}6)$$

Analogously, the equivalent equations for **three-dimensional** fields are determined. Then φ_0 is calculated from the potentials of six adjacent nodes ("cube-algorithm"), Figure 2.5-4:

$$\varphi_0 = (\varphi_{1'} + \varphi_{2'} + \varphi_{3'} + \varphi_{4'} + \varphi_{5'} + \varphi_{6'})/6 \qquad (2.5\text{-}7)$$

The finite difference method also allows one to calculate **multi-dielectrics insulation systems.** Within the materials, the above-mentioned equations are valid. For points on an interface, there are adjacent points on both sides of the interface, Figure 2.5-5. The summation of the potentials comparable to Eq. (2.5-4) has to consider that the boundary con-

ditions Eq. (2.4-13) to (-16) are satisfied. Therefore, the different potentials have to be weighted differently. Then the potential φ_0 on the interface is given by a new "square algorithm" comparable to Eq. (2.5-5) [16]:

$$\varphi_0 = \frac{1}{4}\{\varphi_1 + \varphi_3 + 2 \cdot \frac{\varepsilon_{r1}\varphi_2 + \varepsilon_{r2}\varphi_4}{\varepsilon_{r1} + \varepsilon_{r2}}\} \tag{2.5-8}$$

If the above-mentioned equations are applied to all points of the grid, a *system of linear equations* results. In order to solve the equations, *knowledge of the boundary potentials* is required.

Programming the finite difference algorithms, e.g. for iterative solution of the system of equations, *requires little effort*. The FDM was one of the first numerical methods in practically use [4].

Example: Foil edge in a capacitor dielectric

The potential distribution in a capacitor dielectric close to the edge of a metallic foil shall be calculated by means of the Finite Difference Method. Figure 2.5-6 shows a cross section through the plane insulation arrangement (compare to Figure 2.4-30). In order to get a clear and comprehensible calculation, a rather large mesh width of the grid is chosen.

For the calculation, knowledge of *all* boundary potentials is necessary. The electrode potentials are therefore set to $\varphi/V = 1$ and $\varphi/V = 0$. As the arrangement is open on the left and right hand sides, there are additional boundary points, whose potentials also have to be defined. Because of the uniformity of the field in the outer regions, the boundary potentials are set to $\varphi/V = 0$ (left) and $\varphi/V = 0.5$ (right).

Because of the symmetry of the arrangement, the calculation is limited to the potentials φ_1 to φ_6 in the lower (or upper) half of the arrangement. The equation solution based on the "square algorithm" Eq. (2.5-5) is performed by iteration and starts with assumed initial values $\varphi_i = 0$.

The iterative re-calculation of the potentials according to Eq. (2.5-5) progresses from φ_6 (right) to φ_1 (left). In the next iteration step, the direction of the iteration is reversed. In this way a fast convergence is achieved.

In the following, the iteration results are given:

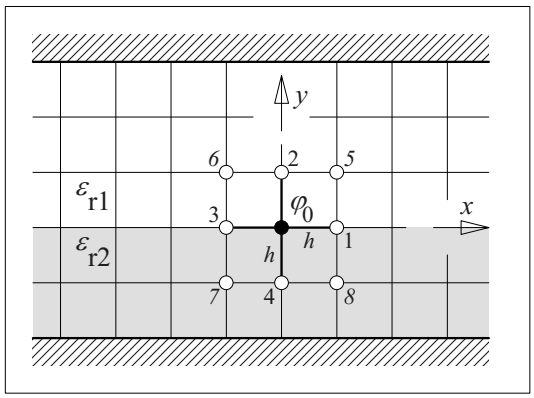

Figure 2.5-5: Calculation of multi-layer dielectrics with the Finite Difference Method.

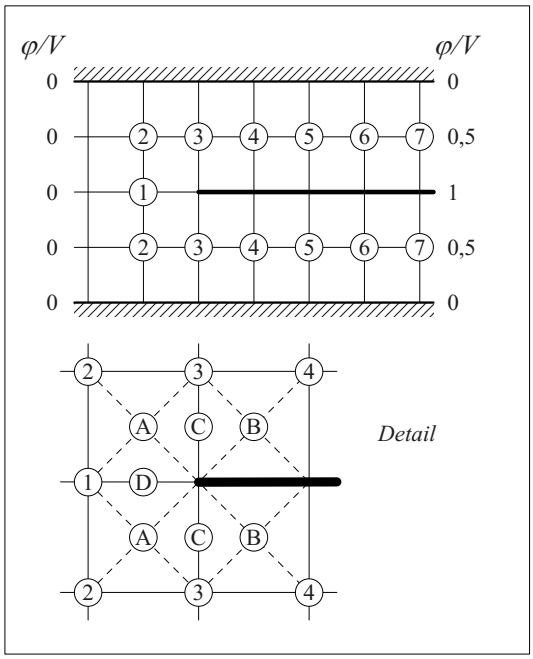

Figure 2.5-6: Calculation of a capacitor dielectric with the help of the Finite Difference Method.

(Direction)	φ_1/V	φ_2/V	φ_3/V	φ_4/V	φ_5/V	φ_6/V	φ_7/V (Boundary)
Start:	**0**	**0**	**0**	**0**	**0**	**0**	**0.5**
←	0.292	0.084	0.334	0.336	0.344	0.375	**0.5**
→		0.156	0.373	0.429	0.451	0.488	**0.5**
←	0.337	0.147	0.405	0.463	0.479	0.488	**0.5**
→		0.186	0.412	0.473	0.490	0.498	**0.5**
←	0.344	0.188	0.416	0.476	0.493	0.498	**0.5**
→		0.190	0.417	0.477	0.494	0.499	**0.5**
←	**0.345**	**0.190**	**0.417**	**0.478**	**0.494**	**0.499**	**0.5**

The iteration is finished, if the potential values only change within a predefined limit from iteration step to iteration step (here $\Delta\varphi/V < 0.001$).

By means of the "diagonal algorithm" Eq. (2.5-6), potentials at intermediate points can be calculated by *interpolation*, e.g. at A, B, C and D, Figure 2.5-6 (detail):

$$\varphi_A = 0.25\cdot(\varphi_1 + \varphi_2 + \varphi_3 + V) = 0.488\ V$$

$$\varphi_B = 0.25\cdot(\varphi_3 + \varphi_4 + V + V) = 0.724\ V$$

$$\varphi_C = 0.25\cdot(\varphi_3 + \varphi_A + \varphi_B + V) = 0.658\ V$$

$$\varphi_D = 0.25\cdot(\varphi_1 + \varphi_A + \varphi_A + V) = 0.580\ V$$

For the drawing of *field or equipotential patterns*, equipotential lines have to be determined by interpolation between the calculated potentials of the fixed nodes in the net. For this purpose, the grid in the given example is far too coarse.

Nevertheless, the result shows clearly that there is a *concentration of field and equipotential lines* close to the edge of the metallic foil. However, the calculated values are not very accurate, because of the coarse grids and the sharp edge of the metallic foil.

The Finite Difference Method has some **disadvantages**, and other methods are better suited in many cases:

1. The fixed regular grid cannot describe *curved electrodes and interface contours* with sufficient accuracy. The Charge Simulation Method and Finite Element Method are much more flexible.

Note: Sometimes the approximation of electrode and interface contours can be improved to a certain extent by a local distortion of the grid. In this case, Eqs. (2.5-4) to (-8) have to be modified.

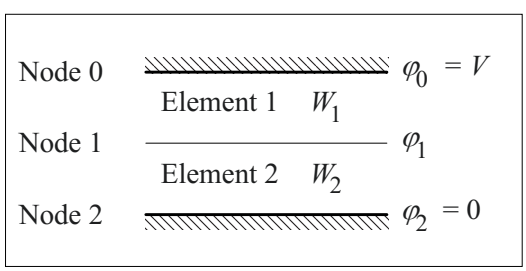

Figure 2.5-7: Calculation of potentials in a parallel-plate capacitor by minimizing the field energy (normally triangular elements are chosen).

2. The regular grid cannot be adapted to the non-uniformity of the field. A *finer discretization* in the non-uniform regions of the field would unequivocally be extended to the whole field volume. Therefore, unreasonable computing resources and times would be required. This is especially serious for three-dimensional fields. Often, the Charge Simulation Method is the simpler method.

2.5.4 Finite Element Method

The Finite Element Method (FEM) is based on the discretization of the field volume by a grid of triangles. For the calculation of **Laplacian fields**, the potentials of the *nodes* in the grid are determined in such a way that the whole *field energy is minimized*.

This principle of minimizing an *energy function* has been known in other fields of engineering and science for a long time [16], [36], [37], [38]. It is a great advantage of the Finite Element Method that common program systems can calculate *mechanical, thermal, magnetic and electric fields* at the same time (*multi-physics*). Especially for industrial applications, high voltage apparatus must be designed with respect to many different stresses.

Note: This approach can also be applied to **linearly superimposed fields** (e.g. conduction and displacement fields) and to **time-harmonic** or **transient fields**. In these cases, *different contributions to the energy* have to be summed, and their variation with time has to be considered by an additional discretization in time and by a calculation in consecutive time steps [282].

Note: With the idea of minimizing the energy, **non-stationary fields** and *electromagnetic waves* can also be treated, if *all energy contributions* are considered in the volume under consideration. This includes the stored electric energy, the stored magnetic energy, the energy fed and dissipated by conduction currents, the energy of a space charge density, the eddy current loss energy and an additional term allowing the so-called *Coulomb gauge* of the vector potential [394].

The basic calculation method for the potential determination by minimizing the field energy shall be explained for the example of a parallel-plate capacitor, Figure 2.5-7.

Example:
Minimum field energy in a parallel-plate capacitor

In the uniform field of a parallel-plate capacitor, the potential midway between the two electrodes shall be determined numerically.

The electrodes are treated as "nodes" with the given potentials $\varphi_0 = V$ and $\varphi_2 = 0$. The equipotential surface midway in-between is considered as "node" 1 with the unknown potential φ_1. Figure 2.5-7.

With Eq. (2.1-11), the field energies of the elements 1 and 2 between the nodes are

$$W_1 = \tfrac{1}{2}\cdot C_1\cdot(V - \varphi_1)^2$$
and (2.5-9)
$$W_2 = \tfrac{1}{2}\cdot C_2\cdot(\varphi_1 - 0)^2.$$

Now, the total field energy

$$W = \Sigma\, W_i = W_1 + W_2 \qquad (2.5\text{-}10)$$

is to be minimized by variation φ_1. As φ_1 is the only variable potential, the *minimum field energy* is determined from the condition

$$\partial W/\partial\varphi = \partial W_1/\partial\varphi_1 + \partial W_2/\partial\varphi_1 = 0.$$

With Eq. (2.5-9) we get

$$\tfrac{1}{2}\cdot C_1\cdot 2\cdot(V - \varphi_1)\cdot(-1) + \tfrac{1}{2}\cdot C_2\cdot 2\cdot(\varphi_1 - 0) = 0$$

and

$$\varphi_1 = V\cdot C_1/(C_1 + C_2)\,. \qquad (2.5\text{-}11)$$

For $C_1 = C_2$, the *expected solution* is

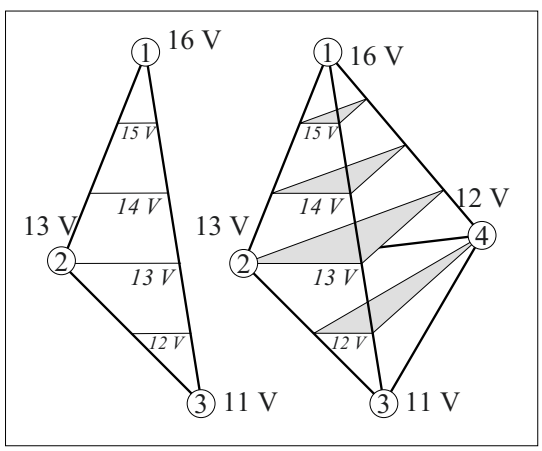

Figure 2.5-8: Triangles and tetrahedrons as (finite) elements for two- and three-dimensional fields with linear interpolation of the potential.

$$\varphi_1 = V/2 \qquad (2.5\text{-}12)$$

Note: It can easily be shown that the calculated extreme value gives a *minimum of energy*. For the other extreme values $\varphi_1 = V$ and $\varphi_1 = 0$, there is a maximum of energy in each case.

By means of that example it can also be shown how easily *field regions with different materials* can be treated. The field energies of the considered elements are just calculated with different permittivities:

Example:
Minimum field energy in a multi-layer dielectric

If in the arrangement according to Figure 2.5-7 different permittivities $\varepsilon_{r1} = 1$ and $\varepsilon_{r2} = 2$ are assumed, the capacitances are $C_2 = 2\cdot C_1$ at equal distances. The expected solution follows directly from Eq. (2.5-11):

$$\varphi_1 = V/3 \qquad (2.5\text{-}13)$$

For a realistic field calculation, the field volume has to be *discretized* by a mesh without regard to the usually unknown shape of the equipotential surfaces. Therefore, two-dimensional (plane or rotationally symmetric) problems are mostly calculated with *triangular* and three-dimensional problems with *tetrahedral elements*, Figure 2.5-8. The *corners* of these elements are the nodes of the mesh.

It is necessary to determine the field or the *potential distribution* throughout an element in order to calculate its field energy. This distribution can be *interpolated from the node potentials*. In Figure 2.5-8 a linear interpolation of the potential between the calculated or given node potentials is shown. In such a case, the field strength is assumed to be constant throughout the considered element.

The **discretization** of the whole field volume with triangular or tetrahedral elements has a significant *advantage* in comparison to the Finite Difference Method: The elements can be adjusted to the *shape of electrodes and interfaces*, and field regions of minor importance can be represented with a coarse mesh. In this way, despite high resolution in the regions of

interest, the *number of nodes and elements* is limited, Figure 2.5-9.

Electrodes with given potentials, e.g. grading layers of bushings, can be included by defining fixed node potentials. If the potentials are completely unknown, they can be simulated by regions of extremely enhanced permittivity. Then the field is displaced into the adjacent materials, and the field emanates approximately perpendicularly from the interface (comparable to a metallic electrode).

Normally, the mesh is generated by an automatic *mesh generator*, which follows the given contours. Afterwards it is often possible to optimize the mesh manually, i.e. by displacing, deleting and setting of nodes. It is very important to ensure that the dimensions of the elements are small enough for the assumption of uniform field strength within the considered element (for linear interpolation only).

For **minimizing the field energy**, the energy of the individual elements (1, 2, 3, ..., k, ..., n) is to be determined by volume integration of the field energy density:

$$W_k = \int_{V_k} \frac{1}{2} \varepsilon E^2 \, dV \qquad (2.5\text{-}14)$$

Attention: V is the *volume* here and <u>*not*</u> the voltage!

The energy of an individual element can be expressed as a function of the respective three (or four) node potentials and node coordinates:

$$W_k = f(\varphi_p, \varphi_q, \varphi_r, \varphi_s; \boldsymbol{x}_p, \boldsymbol{x}_q, \boldsymbol{x}_r, \boldsymbol{x}_s) \qquad (2.5\text{-}15)$$

The total energy is the sum of the energies of all elements:

$$W = \sum_{k=1}^{n} W_k \qquad (2.5\text{-}16)$$

The minimum energy is determined if the partial derivatives with respect to all node potentials (φ_1 to φ_m) are set equal to zero, thus resulting in a **system of equations**:

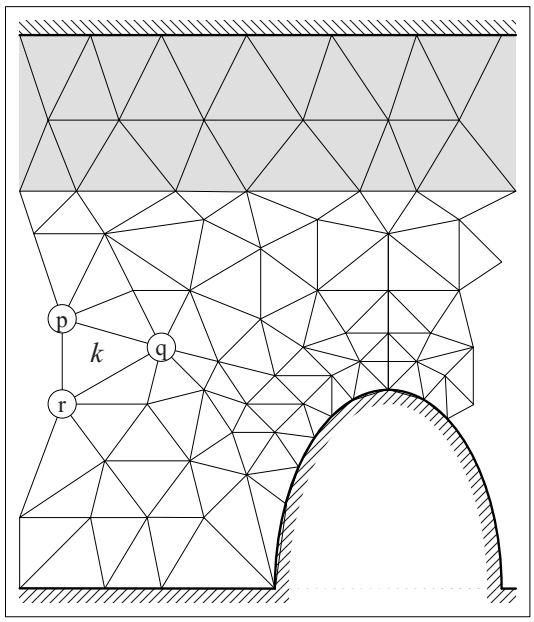

Figure 2.5-9: Discretization of a two dimensional field region with finite elements, which can be adapted to the electrode contours, to the interfaces and to the degree of field homogeneity (detail).

$$\begin{aligned} \partial W/\partial\varphi_1 &= 0 \\ \partial W/\partial\varphi_2 &= 0 \\ \ldots\ldots\ldots & \\ \partial W/\partial\varphi_j &= 0 \\ \ldots\ldots\ldots & \\ \partial W/\partial\varphi_m &= 0 \end{aligned} \qquad (2.5\text{-}17)$$

The node potentials φ_1 to φ_m are given by the *solution of the System of Equations* (2.5-17). Instead of a direct solution, an *iterative approach* is frequently chosen, which can also solve non-linear cases (e.g. in magnetic circuits or at very high electric field strengths).

Generally, the knowledge of **boundary potentials** at the borders of the field volume is necessary (i.e. on the electrodes). *Border lines* with unknown potentials (e.g. between electrodes) are regarded as field lines rectangular to the equipotential surfaces. This must be taken into account during the selection of the field volume for calculation. If necessary, the area to be calculated is to extend well beyond the region of interest in order to keep the influence of field distortions at the borders low.

Another source of inaccuracy is the *interpolation* of the potential within the individual elements if the elements are so large that the potential distribution is no longer described accurately enough by an interpolation or approximation function. The inaccuracy can be especially high for the linear interpolation, see Figure 2.5-8. Therefore, **polynomials of higher order** are used, which allow steady transitions of gradients and curvatures of the equipotential lines at the boundaries of the elements. Both the *accuracy* and the *computational time* together with the danger of *numerical instabilities* increase significantly with the order of the interpolation polynomials.

Example: Comparison between analytical and numerical solution

Similar to the example in Figure 2.5-7, the field of a cylindrical capacitor ($R_i = r_0 = 2$ cm, $R_a = r_4 = 10$ cm) shall be determined by numerical iteration for $V = 20$ kV and compared with an exact analytical solution, Figure 2.5-10.

The equipotential surfaces at $r_0 = 2$ cm ($\varphi_0 = V = 20$ kV), $r_1 = 4$ cm (φ_1), $r_2 = 6$ cm (φ_2), $r_3 = 8$ cm (φ_3) and $r_4 = 10$ cm ($\varphi_4 = 0$) are chosen as "nodes". By analogy with Eq. (2.5-9) and (-10) and by means of the capacitances C_{01}, C_{12}, C_{23} and C_{34}, the field energy can be expressed as a function of the unknown potentials φ_1, φ_2 and φ_3. With the condition for extreme values according to Eq. (2.5-17) a *system of equations* is established for the unknown potentials by setting the partial derivatives to zero:

$$\varphi_1(C_{01}+C_{12}) + \varphi_2(-C_{12}) = C_{01}V$$

$$\varphi_1(-C_{12}) + \varphi_2(C_{12}+C_{23}) + \varphi_3(-C_{23}) = 0$$

$$+\varphi_2(-C_{23}) + \varphi_3(C_{23}+C_{34}) = 0$$

For a cylinder length of 1 m, the capacitances are $C_{01} = 80.2$ pF, $C_{12} = 137.1$ pF, $C_{23} = 193.3$ pF and $C_{34} = 249.2$ pF according to Eq. (2.3-20). The *potential*s are determined as

$$\varphi_1 = 11.38 \text{ kV}, \varphi_2 = 6.34 \text{ kV} \text{ and } \varphi_3 = 2.77 \text{ kV}$$

by iteratively or directly solving the equation system. A linear approach is chosen for determination of the *field strengths*:

$$E_{01} = (\varphi_0 - \varphi_1)/(r_1 - r_0) = 4.3 \text{ kV/cm}$$

$$E_{12} = (\varphi_1 - \varphi_2)/(r_2 - r_1) = 2.5 \text{ kV/cm}$$

$$E_{23} = (\varphi_2 - \varphi_3)/(r_3 - r_2) = 1.8 \text{ kV/cm}$$

$$E_{34} = (\varphi_3 - \varphi_4)/(r_4 - r_3) = 1.4 \text{ kV/cm}$$

The *comparison* with an *analytical* solution according to Section 2.3.1.3 shows that the node potentials were calculated correctly. This can be explained by the capacitance values, which were exact values and not numerical approximations. Nevertheless, field strengths are determined with substantial errors when using linear interpolation. The analytical calculation gives considerable differences, especially in the non-uniform region of the field:

$$E_0 = 6.2 \text{ kV/cm}$$

$$E_1 = 3.1 \text{ kV/cm}$$

$$E_2 = 2.1 \text{ kV/cm}$$

$$E_3 = 1.5 \text{ kV/cm}$$

$$E_4 = 1.2 \text{ kV/cm}$$

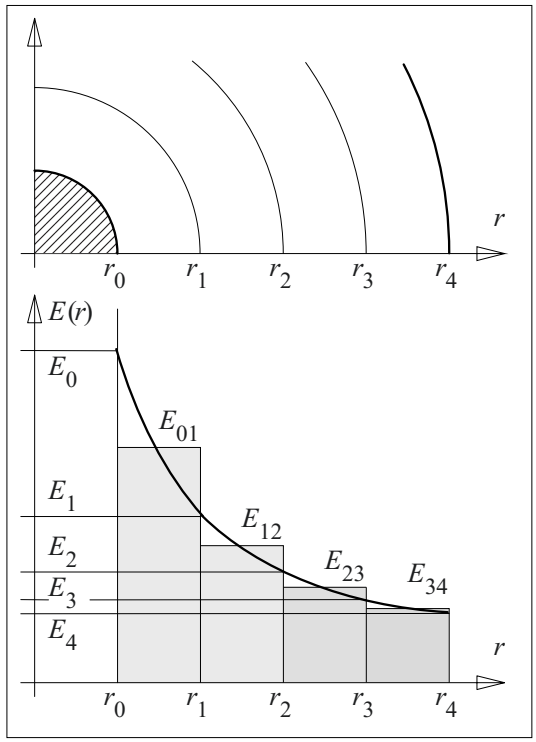

Figure 2.5-10: Comparison between analytical and numerical solution for the example of a cylindrical capacitor.

The numerically calculated field strengths can be considered as *mean field strengths* within the elements, Figure 2.5-10. Maximum values are higher, minimum values are lower. These deviations can be significantly reduced by selecting smaller elements and interpolation polynomials of higher order.

Program systems for field calculations with the Finite Element Method have user interfaces that guide the **user** through the calculation process and perform many steps automatically, Fig, 2.5-11. For this the user has particularly to learn program-specific features, which, depending on the complexity and degree of development of the program system, can involve quite considerable effort. The physical problem, understanding the problem and the basic calculation processes are often dangerously neglected by the user.

Normally, a **numerical field calculation** consists of a number of steps:

1. The user has to enter the *geometric data* of the electrode contours and areas to be calculated, either directly or by means of CAD data sets. An **adequate simplification of the geometry** is the most important preparation that determines the quality of the calculation: On the one hand, the uncritical import of *all* design details causes extremely high computational effort. On the other hand, simplifications must not be *too coarse*, in order to avoid wrong conclusions.

This is a question of *engineering feeling*, which requires high analytical abilities and a sophisticated *physical understanding of field geometries*, especially in times of complex and "user friendly" program systems.

Therefore, a *qualitative feeling* for the expected result should already exist before a calculation is started.

2. The **discretization** of the geometry is performed by an automatic *mesh generator*. The user has to give parameters defining the size and the quality of the generated mesh as a function of geometry data (e.g. radii of curvature). This can be done, for example, by de-

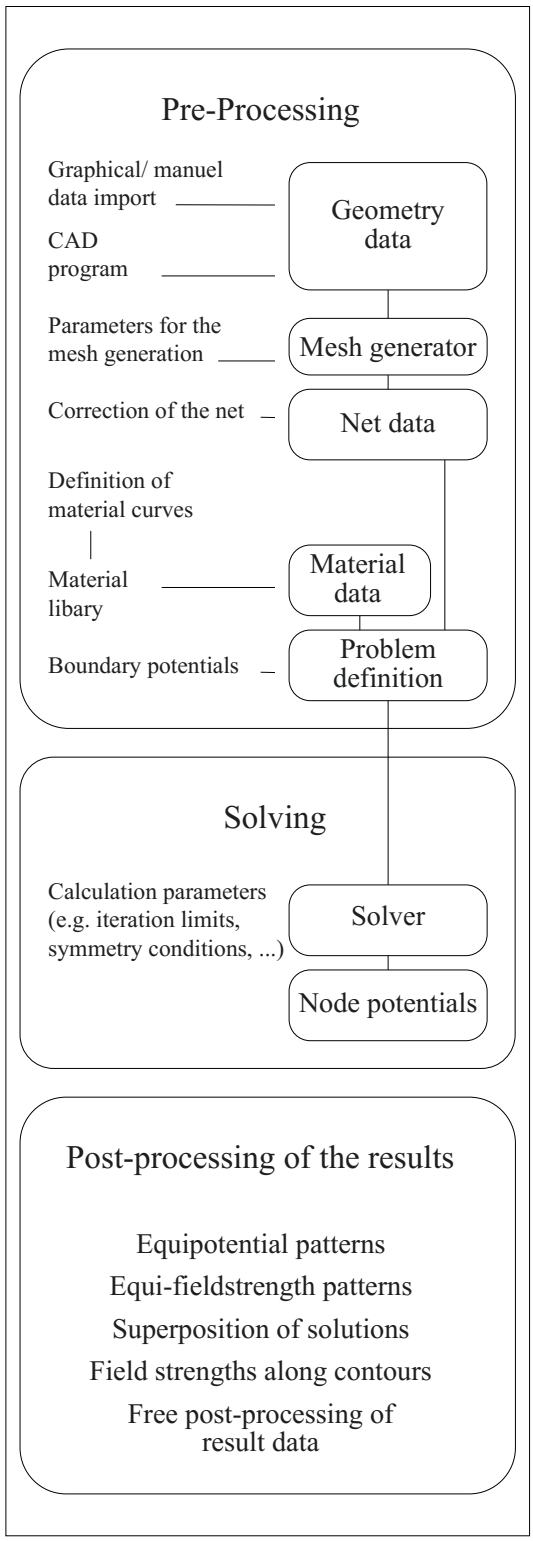

Figure 2.5-11: Structure of a Finite Element Program system for numerical field calculations.

fining node positions on the electrodes or along contours. Normally, the automatically generated mesh can be checked and manually *refined* afterwards, e.g. in order to achieve finer discretization for important field regions, or to subdivide triangles with unfavorable aspect ratios.

Again, these tasks require a qualitative feel for the expected results, as mentioned above.

3. Then, *material values* (or non-linear *material curves*) have to be allocated to the generated network elements and *potential values* have to be allocated to the electrodes and edge contours. For such a **definition of a calculation problem**, pre-defined materials can often be taken from a *material library*.

4. After this pre-processing, the **system of equations** is solved with an appropriate mathematical *solver*. Again, the user can define iteration limits, step widths and the order of the interpolation polynomials. He has to find a good compromise between accuracy of the calculation, computational time and numerical stability. The *result* is given as a list of *node potentials*. Potentials in the field volume are derived from interpolation and approximation polynomials.

Note: The solution is often performed *in a number of steps,* in which the discretization is improved based on a preceding result for the following iteration.

Note: Additionally, routines can be programmed sometimes, allowing the variation of geometry characteristics as a function of calculation results. In this way, electrode contours can be *optimized iteratively* in a number of calculation steps in order to avoid field strength increases.

5. Subsequent to the calculation, a **post-processing of the solution** or *the data* can be performed by any kind of mathematical operations.

Equipotential patterns or patterns with lines of equal field strengths are generated for visualization of the results. They can also contain field vectors in order to visualize the direction and magnitude of the field strength. Normally, equipotential patterns are *colored* in order to visualize the *magnitude of the field strength*.

Complex processes can be calculated by *superposition* of different solutions. For example, the field after the polarity reversal of a DC voltage is given by the superposition of the initial steady-state conduction field and the dielectric displacement field associated with the voltage step during the polarity reversal [7], [10].

For the evaluation of electrical stresses it is often necessary to show the magnitudes of field strengths along given *contours*. Normally, field strength magnitudes, tangential components and normal components can be distinguished.

6. Finally, the user has the important task of **checking the plausibility of the results**. Unfortunately, the complexity of modern field calculation systems leads to input data errors remaining undiscovered and often only able to be detected from a non-plausible field pattern. Such an evaluation requires a very good physical understanding and imagination as mentioned above. In addition, for example, numerically calculated field strength values can be analytically recalculated in sub-regions with simple field geometry.

2.6 Rapidly Changing Fields and Traveling Waves

For the slowly varying fields that have been discussed previously it was assumed that propagation time effects can be neglected within the observed spatial dimensions. Field changes are so slow that they can approximately be considered as simultaneous in the relevant field volume. This condition was already formulated with Eqs. (2.1-36) to (-38) in Section 2.1.4.4.

If the conditions of the quasi-static field approximation are no longer fulfilled, Maxwell's Equations have to be used in their complete form for the description of the non-stationary

electromagnetic wave field, see Section 2.1.4.4.

In relation to lightning impulse voltages and fast transients, there are a number of rapidly changing stresses in high voltage engineering. Basically, they can be described as *guided traveling waves,* see Section 2.2.4 and 2.2.5.

Note: Electromagnetic waves that propagate in free space, i.e. that do not propagate in a transmission line, do not belong to the typical stresses of high voltage engineering. Only in the hopefully hypothetical case of a nuclear explosion outside the atmosphere, it is feared that the nuclear electromagnetic pulse (NEMP) will endanger electric power systems.

Nevertheless, free electromagnetic waves can couple into measuring systems and affect the *measuring signals* in impulse and partial discharge measuring circuits [5], [18], [19]. Moreover, the electromagnetic radiation field can purposefully be used for *diagnostics*, especially for partial discharge detection.

In the following, guided traveling waves (Section 2.6.1), reflections (Section 2.6.2) and examples (Section 2.6.3) are discussed.

2.6.1 Guided TEM Wave

A rapidly increasing electric field strength between the conductors of a line is associated with a displacement current between the conductors, Figure 2.6-1. It continues as an axial conduction current in the conductor's surface. The magnetic field lines associated with the current, are closed lines around the upper conductor.

In the wave front, the *electromagnetic wave* has orthogonal vectors $\boldsymbol{E}$ (electric field strength), $\boldsymbol{H}$ (magnetic field strength) and $\boldsymbol{u}$ (phase velocity). The time-varying field quantities s $\boldsymbol{E}$ and $\boldsymbol{H}$ are mutually dependent according to Faraday's and Ampere's law, see also Figure 2.1-17. As both electric and magnetic field vectors are transverse (orthogonal) to the direction of wave propagation, the propagation mode is called TEM mode (or TEM wave).

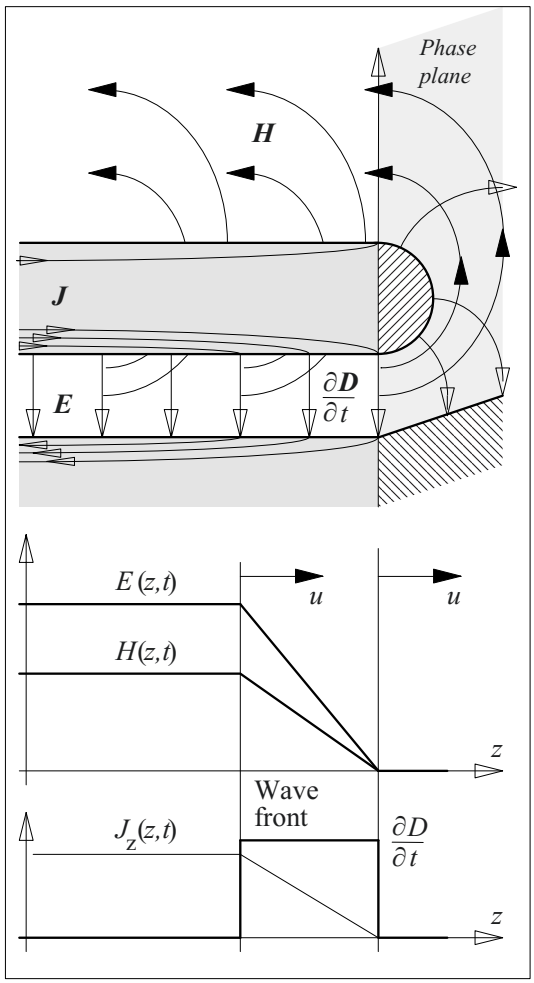

Figure 2.6-1: Propagation of a guided traveling wave on a transmission line, TEM wave with linearly rising electric and magnetic field strengths.

Note: Apart from this basic propagation mode, there are further modes which can propagate between the two conductors, but they are of minor importance for the electrical stress.

A significant simplification of the analysis is achieved, if *infinitesimal small line sections* Δz with *quasi-static field conditions* are considered, Figure 2.6-2. Instead of the field quantities $\boldsymbol{E}$ and $\boldsymbol{H}$, it is possible to perform calculations with the **integral quantities voltage** v and **current** i.

At first, a **lossless line** with $R' = 0$ and $G' = 0$ shall be considered. According to the equiva-

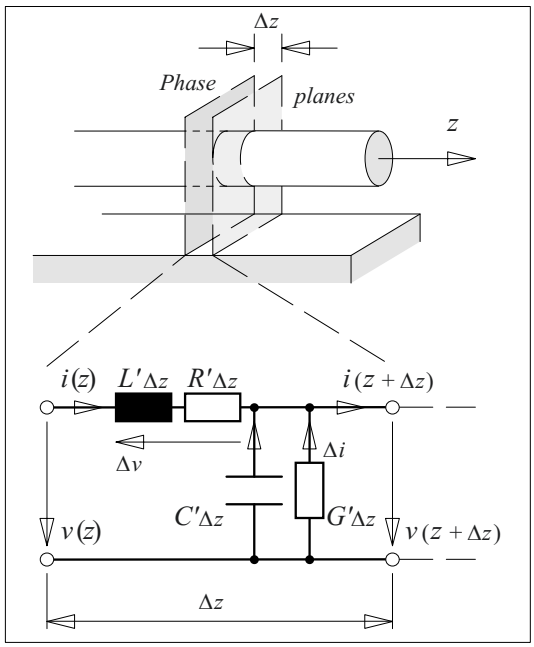

Figure 2.6-2: Description of a short line segment by an "electrically short" equivalent circuit.

lent circuit, the difference of the voltages at the positions z and $z+\Delta z$ (Kirchhoff's voltage law) is

$$v(z+\Delta z) - v(z) \quad = \Delta v \quad = - L'\Delta z \cdot \partial i/\partial t$$

and the difference of the currents (Kirchhoff's current law) is

$$i(z+\Delta z) \; - i(z) \quad = \Delta i \quad = - C'\Delta z \cdot \partial v/\partial t \; .$$

By the transition to infinitesimal small sections $\Delta z \rightarrow 0$, two partial differential equations are established for the dependence of the quantities $v(z,t)$ and $i(z,t)$ on time t and position z:

$$\partial v/\partial z \quad = - L' \cdot \partial i/\partial t \qquad (2.6\text{-}1)$$

and

$$\partial i/\partial z \quad = - C' \cdot \partial v/\partial t \qquad (2.6\text{-}2)$$

In order to insert these equations into each other, the first equation is differentiated with respect to the path z and the second equation with respect to time t:

$$\partial^2 v/\partial z^2 \quad = - L' \cdot \partial^2 i/(\partial t \partial z) \qquad (2.6\text{-}3)$$

$$\partial^2 i/(\partial z \partial t) \quad = - C' \cdot \partial^2 v/\partial t^2 \qquad (2.6\text{-}4)$$

By insertion of Eq. (2.6-4) into Eq. (2.6-3), the differential equation for the voltage is established:

$$\partial^2 v/\partial z^2 = L'C' \cdot \partial^2 v/\partial t^2 \qquad (2.6\text{-}5)$$

The analog differential equation for the current is derived, if Eq. (2.6-1) is differentiated with respect to t and Eq. (2.6-2) with respect to z:

$$\partial^2 i/\partial z^2 = L'C' \cdot \partial^2 i/\partial t^2 \qquad (2.6\text{-}6)$$

The differential Equations (2.6-5) and (-6) are called **transmission line wave equations**. The general solution for the voltage is

$$v(z,t) \quad = V \cdot \{ f(z\text{-}ut) + g(z+ut) \} \; . \qquad (2.6\text{-}7)$$

After differentiating it twice with respect to z and t, and by insertion, it can be shown that the solution satisfies the differential equation, if $u^2 = 1/(L'C')$. Thus, the **phase velocity** u is a function of the transmission line parameters L' and C':

$$u \quad = \frac{1}{\sqrt{L' \cdot C'}} \quad . \qquad (2.6\text{-}8)$$

Eq. (2.6.7) describes a traveling voltage-wave consisting of two components. The first term $f(z\text{-}ut)$ corresponds to a traveling wave in $+z$-direction, because its argument doesn't change if z increases to the same extent as ut. The second term $g(z+ut)$ correspondingly describes a traveling wave in $-z$-direction, Figure 2.6-3.

Note: The *expression "voltage"* must only be used with great care in relation to rapidly changing processes: The definition of a voltage (scalar potential) is only possible if integration of the electric field strength along a path gives a value that is *independent* of the chosen path, the ring integral of $\boldsymbol{E}\mathrm{d}\boldsymbol{x}$ must be zero. This means a closed integration path must not enclose any magnetic flux that varies with time. For the given TEM wave, this condition is only fulfilled in the so-called *phase planes* orthogonal to the line direction z. These planes are not penetrated by the magnetic field, Figure 2.6-1 and -2. The specification of

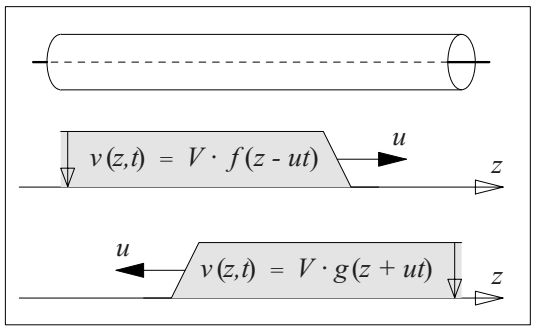

Figure 2.6-3: Traveling voltage waves in +z- and -z-direction as solutions of the transmission line wave equations.

a voltage thus only describes the electric field in a phase plane. The specification of a voltage between points that do not have the same z-coordinate is no longer allowed.

The traveling voltage-waves are accompanied by *related traveling current-waves*, which can be derived from the above-mentioned solution for the voltage waves: Eq. (2.6-7) is differentiated with respect to time and inserted into Eq. (2.6-2), which then can be used to determine the desired currents by integration. With

$$\partial v/\partial t = V\cdot\{(-u)\cdot f'(z\text{-}ut) + v\cdot g'(z\text{+}ut)\}$$

Eq. (2.6-2) is

$$\partial i/\partial z = V\cdot u\cdot C'\cdot\{f'(z\text{-}ut) - g'(z\text{+}ut)\}\ .$$

The current is determined by integration along the coordinate z:

$$i(z,t) = V\cdot u\cdot C'\cdot\{f(z\text{-}ut) - g(z\text{+}ut)\} \qquad (2.6\text{-}9)$$

Again, there are traveling current-waves in $+z$- and $-z$-directions. The two traveling current waves have opposite polarities. This means that the current direction is reversed together with the wave propagation direction, if the voltage between the conductors does not change, Figure 2.6-4.

Traveling voltage and current waves with the same propagation direction always *belong together*. They are two different mathematical representations of the same physical process: This means that voltage and current are de-

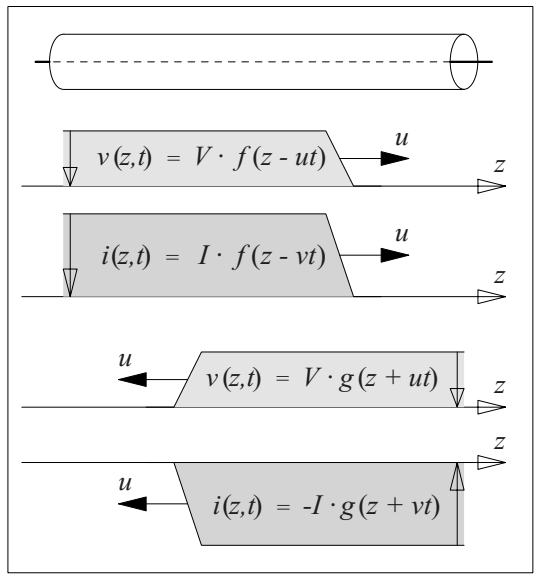

Figure 2.6-4: Related voltage and current waves in +z- and -z-direction (traveling waves).

rived from the electric and the magnetic field of the *same* traveling wave.

According to Eq. (2.6-9), the amplitudes of the related voltage and current waves have a constant ratio, the **characteristic (line) impedance** Z_L:

$$Z_L = v/i = 1/(uC')$$

For the lossless line it follows from Eq. (2.6-8) that

$$Z_L = \frac{v}{i} = \sqrt{\frac{L'}{C'}}\ . \qquad (2.6\text{-}10)$$

The line parameters L' and C' (inductance and capacitance per unit length) and the characteristic line impedance Z_L depend on the kind of the line and on the geometric dimensions, Figure 2.6-5. Generally, it can be stated that the characteristic impedance increases with increasing distance between the conductors and that it decreases with increasing conductor area.

Characteristic impedances of *overhead transmission lines* ($C' \approx 10$ nF/km, $L' \approx 1$ mH/km) are somewhere in the region above 300 Ω. For

a *gas-insulated coaxial line* with tubular conductors and the radius ratio e:1, the characteristic impedance is Z_L = 60 Ω. A *high voltage cable* with ε_r = 2.2 and r_a/r_i = e has Z_L = 40 Ω. Even lower values are given for *medium voltage cables* with large inner conductor cross sections. Coaxial *signal cables* have a characteristic line impedance Z_L = 50 Ω normally. For *transformer windings* characteristic impedances are in the range of 10^2 Ω to 10^4 Ω, because of the high inductances [45]. These values increase with the rated voltage and decrease with the rated power.

For the basic arrangements in Figure 2.6-5, the *phase velocity u* is independent from the geometric dimensions. In vacuum and (by approximation also) in gases, *u* is equal to the *speed of light* u_0 = 300,000 km/s = $3 \cdot 10^8$ m/s = 0.3 m/ns. In dielectrics with higher permittivity, the phase velocity is reduced by the factor $\varepsilon_r^{-0.5}$, see Eq. (2.6-8).

Example:
Lightning strike into an overhead line

During a lightning strike an impulse current $\hat{I}$ = 10 kA is fed into the phase conductor of an overhead line. The magnitude of the overvoltage shall be estimated.

The lightning stroke current is split up into two current waves that propagate in both directions from the point of the strike. With Z_L = 300 Ω, a peak voltage $\hat{V}$ = 300 Ω · 5 kA = 1.5 MV is calculated from Eq. (2.6-10).

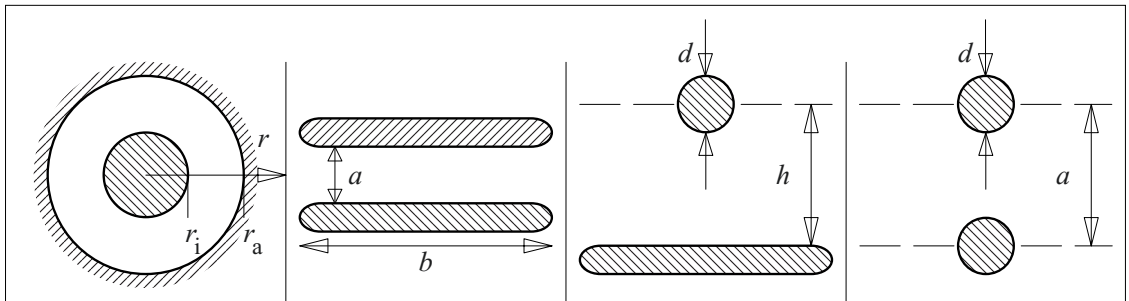

Coaxial line	Strip line (Parallel plate line)	Cylinder above plane	Two-wire line

Capacitances per unit lenth according to eq. 2.3-20, -37, -89 and -85:

$C' = \dfrac{2\pi\varepsilon}{\ln \frac{r_a}{r_i}}$	$C' = \varepsilon \dfrac{b}{a}$	$C' = \dfrac{2\pi\varepsilon}{\ln \frac{4h}{d}}$	$C' = \dfrac{\pi\varepsilon}{\ln \frac{2a}{d}}$

External inductances per unit length [2] (the internal inductances are neglected here):

$L' = \dfrac{\mu}{2\pi} \ln \dfrac{r_a}{r_i}$	$L' = \mu \dfrac{a}{b}$	$L' = \dfrac{\mu}{2\pi} \ln \dfrac{4h}{d}$	$L' = \dfrac{\mu}{\pi} \ln \dfrac{2a}{d}$

Characteristic impedances according to eq. 2.6-10:

$Z_L = \dfrac{1}{2\pi}\sqrt{\dfrac{\mu}{\varepsilon}} \ln \dfrac{r_a}{r_i}$	$Z_L = \sqrt{\dfrac{\mu}{\varepsilon}} \dfrac{a}{b}$	$Z_L = \dfrac{1}{2\pi}\sqrt{\dfrac{\mu}{\varepsilon}} \ln \dfrac{4h}{d}$	$Z_L = \dfrac{1}{\pi}\sqrt{\dfrac{\mu}{\varepsilon}} \ln \dfrac{2a}{d}$

Phase velocities according to eq. 2.6-8:

$u = \dfrac{1}{\sqrt{\varepsilon\,\mu}}$	$u = \dfrac{1}{\sqrt{\varepsilon\,\mu}}$	$u = \dfrac{1}{\sqrt{\varepsilon\,\mu}}$	$u = \dfrac{1}{\sqrt{\varepsilon\,\mu}}$

Figure 2.6-5: Line parameters, characteristic impedances and phase velocities for basic line arrangements.

Amplitude, shape and direction of a traveling wave are *not yet determined* by the transmission line wave equations or by their general solutions Eq. (2.6-7) and (-8). Furthermore, they depend on the *boundary conditions*, i.e. on the currents and voltages at both ends of the transmission line, see Section 2.6.2.

Analogous considerations also apply to the **field quantities** ***E*** and ***H*** in *dielectric media*. Based on Maxwell's Main Equations (2.1-14) and (-15), the relationships shown in Section 2.1.4.4 for the **intrinsic impedance** (*wave impedance*) *Z,* Eq. (2.1-43), and for the phase velocity*, Eq*. (2.1-42), are derived:

$$u = \frac{1}{\sqrt{\varepsilon\,\mu}} \qquad (2.6\text{-}11)$$

$$Z = \frac{E}{H} = \sqrt{\frac{\mu}{\varepsilon}}\ . \qquad (2.6\text{-}12)$$

In vacuum and (by approximation also) in gases, the phase velocity is the *speed of light* and the intrinsic impedance is the *intrinsic impedance of free space which is given by*

$$Z_0 = \frac{E}{H} = \sqrt{\frac{\mu_0}{\varepsilon_0}} = 377\ \Omega\,. \qquad (2.6\text{-}13)$$

Note: The Equations (2.6-11) to (-13) are not only valid for the field quantities of a conducted traveling wave on a line, but also for the field quantities of a *free electromagnetic TEM wave*, see Section 2.1.4.4.

Example: Field quantities in a strip line

The *characteristic (line) impedance* is $Z_L = v/i$. If voltage and current are expressed by the field quantities E and H, then because of the approximately uniform wave field between the electrodes, the characteristic impedance is

$$Z_L = \frac{v}{i} = \frac{\int \boldsymbol{E}\ \mathrm{d}\boldsymbol{s}}{\oint \boldsymbol{H}\ \mathrm{d}\boldsymbol{s}} = \frac{E{\cdot}a}{H{\cdot}b}\ .$$

The comparison with the equations in Figure 2.6-5 shows that the ratio of the field quantities E and H gives the *intrinsic impedance Z*:

$$\frac{E}{H} = \sqrt{\frac{\mu}{\varepsilon}} = Z$$

The above considerations also apply to *lossless lines* (or *perfect dielectrics*), i.e. the line parameters R' and G' in Figure 2.6-2 are neglected. The **consideration of losses** owing to constant parameters R' and G' results in traveling wave amplitudes that are *decreasing exponentially* along the propagation path (*damped line or non-ideal dielectrics*).

If special conditions cannot be assumed (e.g. "distortion-free line"), the *shape of the traveling wave* also changes. This generally means that fast impulse fronts are *flattened* and traveling wave pulses are rounded. This can be explained by the *frequency dependence* of line parameters; especially R' increases strongly with frequency because of the skin effect, and high-frequency wave components are damped accordingly.

At very high voltages and field strengths, e.g. which can occur during a lightning strike into an overhead line, *corona discharges* can also occur. They must be accounted for by a voltage-dependent *leakage* (conductance) per unit length G'. This non-linear effect causes higher damping and distortion of the traveling wave.

Often, the damping of traveling waves is not considered because the *undamped wave* normally causes the highest stresses (*"worst case"*).

2.6.2 Reflection Processes

2.6.2.1 Basics

Voltage and current at the end of a transmission line are determined by the termination, which can be a single circuit element, a network or another line.

If the ratios of voltage and current on the line and at the termination do not coincide, a *reflection* occurs, i.e. a wave traveling back, Figure 2.6-6.

Because of Kirchhoff's current and voltage laws, the superpositions of voltages and currents of the incident and the reflected waves (indices "i" and "r") give the voltage and the current at the termination. If the termination is another line, a *transmitted* or *refracted* traveling wave (index "t") propagates within it:

$$v_i + v_r = v_t \qquad (2.6\text{-}14)$$

$$i_i + i_r = i_t \qquad (2.6\text{-}15)$$

This idea can also be applied to a lumped termination, which absorbs the "transmitted" wave.

In the case of an **open circuit** ($Z_2 >> Z_1$), there can be *no resulting current* at the reflection point, i.e. the currents of the transmitted and reflected waves are $i_t = 0$ and $i_r = - i_i$. According to the Eqs. (2.6-8) to (-10), the traveling current waves are accompanied by traveling voltage waves, which satisfy the condition $v_r = + v_i$ and $v_t = 2v_i$. Therefore, the *voltage is doubled* by the reflection, Figure 2.6-7 (left), and significant overvoltages can occur in the insulating systems.

In the case of a **short circuit** ($Z_2 << Z_1$), there can be *no resulting voltage* at the reflection point, i.e. the voltages of the transmitted and the reflected waves are $v_t = 0$ and $v_r = - v_i$. The traveling voltage waves are accompanied by traveling current waves with $i_r = + i_i$ and $i_t = 2i_i$. Therefore, the *current is doubled* by the reflection, Figure 2.6-7 (middle).

If the line is terminated by an ohmic resistance Z_2, which is equal to the characteristic impedance Z_L of the line, voltages and currents are not changed when a traveling wave transits from the line to the terminating resistance. The energy of the incident traveling wave is absorbed by the terminating resistance without any reflection. This case is called **"impedance matching"**, Figure 2.6-7 (right).

In the **general case**, the reflection coefficients and the transmission (refraction) coefficients have to be determined from Eq. (2.6-14) and

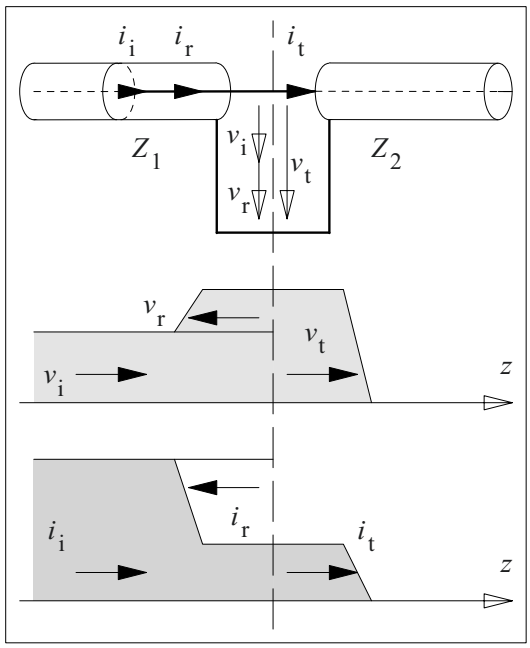

Figure 2.6-6: Reflection and transmission (refraction) of an incident traveling wave at a discontinuity of the characteristic line impedance.

(-15). By inserting $v_i = i_i Z_1$, $v_r = -i_r Z_1$ and $v_t = i_t Z_2$, Eq. (2.6-14) gives

$$i_i Z_1 - i_r Z_1 = i_t Z_2$$

and

$$i_i - i_r = i_t Z_2 / Z_1 \, .$$

With Eq. (2.6-15) we derive

$$2 \cdot i_i = i_t (1 + Z_2/Z_1) \, .$$

Then, the *transmission (refraction) coefficient for the current* is

$$\rho_i = \frac{i_t}{i_i} = \frac{2 \cdot Z_1}{Z_1 + Z_2} \, . \qquad (2.6\text{-}16)$$

With $v_t = i_t Z_2$ and $v_i = i_i Z_1$ the *transmission (refraction) coefficient for the voltage* is given by

$$\rho_v = \frac{v_t}{v_i} = \frac{2 \cdot Z_2}{Z_1 + Z_2} \, . \qquad (2.6\text{-}17)$$

From these equations, the *reflection coefficients for current and voltage* are determined by insertion of Eq. (2.6-14) and (-15):

$$r_i = \frac{i_r}{i_i} = \frac{Z_1 - Z_2}{Z_1 + Z_2} \qquad (2.6\text{-}18a)$$

$$r_v = \frac{v_r}{v_i} = \frac{Z_2 - Z_1}{Z_1 + Z_2} \qquad (2.6\text{-}18b)$$

The relationship of transmission (refraction) and reflection coefficient is in general

$$R_{v,i} = \rho_{u,i} - 1 \; . \qquad (2.6\text{-}19)$$

Figure 2.6-7 presents the coefficients according to the Equations (2.6-16) to (-19) for some special cases.

2.6.2.2 Equivalent transmission-line circuit

According to Eq. (2.6-17), the voltage at a junction between two lines or at a line with termination resistance Z_2 is given by

$$v_t = 2 \cdot v_i \cdot Z_2/(Z_1 + Z_2) \; .$$

Obviously, the voltage v_t can be described by an equivalent circuit, the so-called **transmission-line circuit**, Figure 2.6-8. This means that the source voltage $2 \cdot v_i$ is divided downwards to v_t by a *voltage divider* consisting of

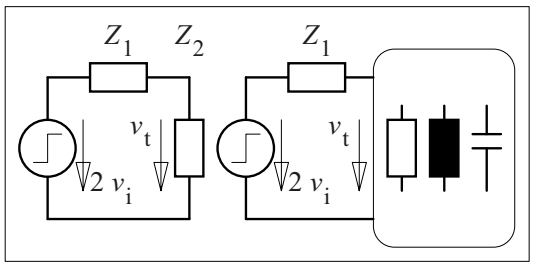

Figure 2.6-8: Transmission-line circuit with ohmic termination (left) and with a general R,L,C termination (right). The incident traveling and the line is described by the voltage source and the internal impedance.

the characteristic impedance Z_1 and the termination impedance Z_2. The same circuit is derived, if line 1 is considered as a source with the *open-circuit voltage* $2 \cdot v_i$ and the *short-circuit current* $2 \cdot i_i$. This can be described by an *equivalent source* with the source voltage $2 \cdot v_i$ and the internal impedance $Z_i = (2 \cdot v_i)/(2 \cdot i_i) = Z_1$.

The significance of the *transmission-line circuit* is the ability to handle *any kind of line terminations* consisting of *R, L, C*-circuits [2]: By means of the time-dependent voltage $v_i(t,z_1)$ at the line discontinuity $z = z_1$, the time-depend-

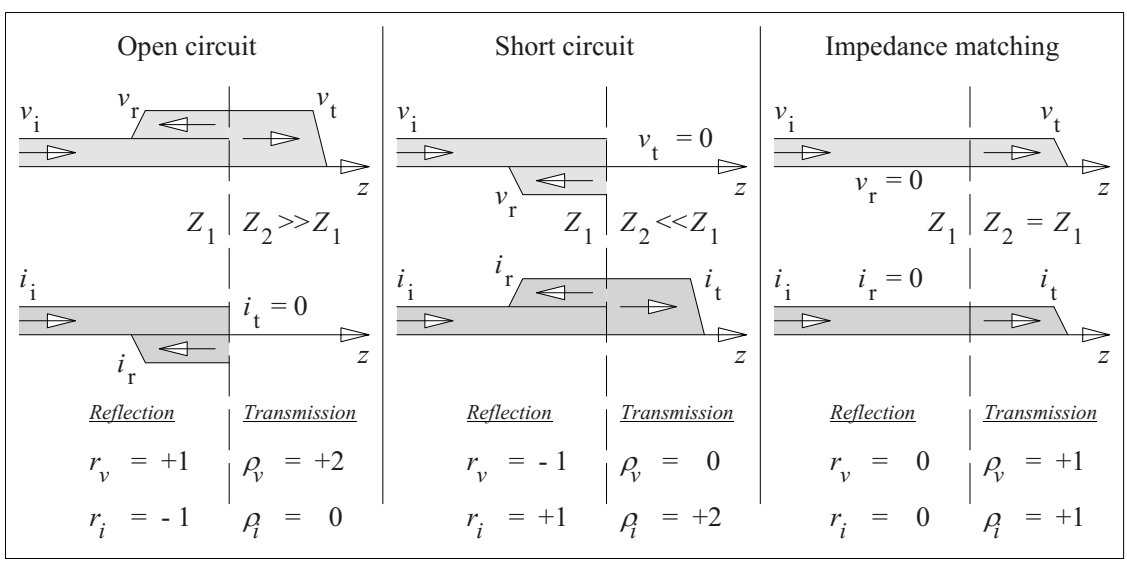

Figure 2.6-7: Reflection and transmission (refraction) of an icident traveling wave at a discontinuity of the characteristic line impedance for the special cases of open circuit, short circuit and matching impedance.

ence of $v_t(t,z_1)$ is calculated. Then, the time-dependence of $v_r(t,z_1)$ is calculated from Eq. (2.6-14) as the difference of $v_t(t,z_1)$ and $v_i(t,z_1)$:

$$v_r(t,z_1) = v_t(t,z_1) - v_i(t,z_1) \qquad (2.6\text{-}20)$$

The transmission-line circuit describes a *single reflection* only; it is *no* longer valid for multiple reflections.

Example: Reflection at a capacitance

A steep-fronted traveling wave with a step voltage amplitude V on a line with the characteristic impedance Z is reflected at a capacitance C, Figure 2.6-9.

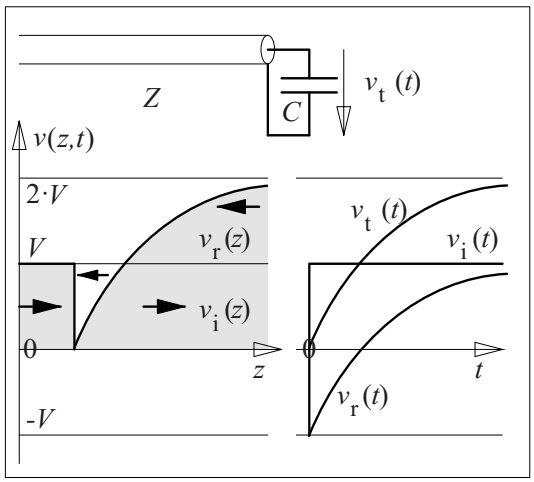

Figure 2.6-9: Reflection of a steep-fronted traveling wave at a capcitance.

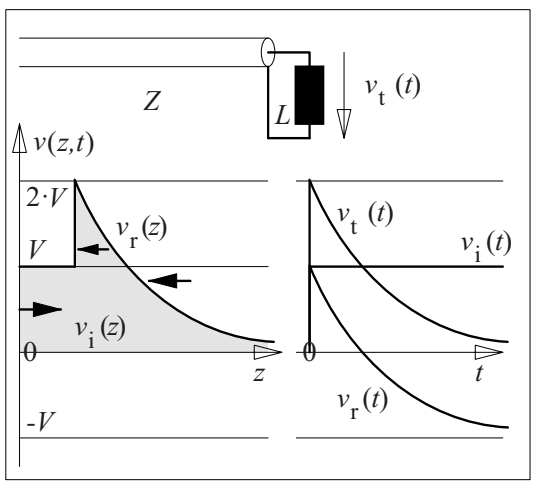

Figure 2.6-10: Reflection of a steep-fronted traveling wave at an inductance.

With respect to the transmission-line circuit, the voltage v_t increases exponentially from 0 to $2\cdot V$ with the time constant ZC. According to Eq. (2.6-20), the voltage

$$v_r(t) = V\cdot\{2\cdot[1 - e^{-t/(ZC)}] - 1\}$$

increases from $-V$ to $+V$. This means that the capacitive termination looks like a short circuit at first, i.e. while the capacitance is uncharged, and when the capacitance has been charged it looks like an open circuit. The reflected traveling wave is superimposed on the incident wave in such a way that the voltage in the wave front is compensated to zero at first and subsequently increases exponentially to $2\cdot V$, Figure 2.6-9 (left).

Example: Reflection at an inductance

A steep-fronted wave with the step voltage amplitude V on a line with the characteristic impedance Z is reflected at an inductance L, Figure 2.6-10.

With respect to the transmission-line circuit, the voltage v_t decreases exponentially from $2\cdot V$ to 0 with the time constant L/Z. According to Eq. (2.6-20), the voltage

$$v_r(t) = V\cdot\{2\cdot e^{-t/(L/Z)} - 1\}$$

decreases from $+V$ to $-V$. This means that the inductive termination looks like an *open-circuit* at first, i.e. as long as there is no significant current through the inductance. If the current is increased the inductance looks like a *short circuit*. The reflected traveling wave is superimposed on the incident wave in such a way that the voltage in the wave front increases to $2\cdot V$ at first and subsequently decreases to zero, Figure 2.6-10 (left).

2.6.2.3 Multiple Reflections

In systems with distributed parameters, normally there are not only single but also **multiple reflections**. This means that a reflected traveling wave can be reflected again and again at other discontinuities of the line and are superimposed on the original wave. Even with a few reflection points there are very complicated conditions for the spatiotemporal development of the resulting wave field.

Therefore, it is advisable to systematically visualize the propagation of the traveling waves by means of a **"traveling-wave road map"** *(Bewley lattice diagram* [39]). The propagation of the individual waves is depicted by so-called *z,t* propagation lines for every considered transmission line, Fig 2.6-11.

Wave components, which are fed in and which are reflected at the terminations, are depicted by their individual propagation lines. The magnitudes of the waves to be superimposed are calculated from the reflection and transmission coefficients.

The instantaneous value of the incident wave is regarded as the *incoming supply*. A clear description requires a *discretization* of the incident wave, i.e. only *selected wave points* are considered. Their propagation is traced by their individual propagation lines. In the case of a transition through a line discontinuity between line j and line k, the instantaneous value is multiplied by the transmission (refraction) coefficient ρ_{jk}. In the case of a reflection on line j at the junction to line k, the instantaneous value is multiplied by the reflection coefficient r_{jk}.

Example: Transmission line between two cables

In Figure 2.6-11 numerical values are given for two cables 1 and 3 with $Z_1 = Z_3 = 40\ \Omega$ and for an overhead transmission line 2 between them with $Z_2 = 360\ \Omega$. The incident traveling wave with the amplitude V at $t = \tau$ was discretized in such a way that the propagation of four wave points with the magnitudes $v_i(t=0) = 0$, $v_i(t=\tau) = V$, $v_i(t=2\tau) = 0.5 \cdot V$ and $v_i(t=3\tau) = 0$ is traced by propagation lines.

The voltage magnitudes at the two discontinuities $z = z_a$

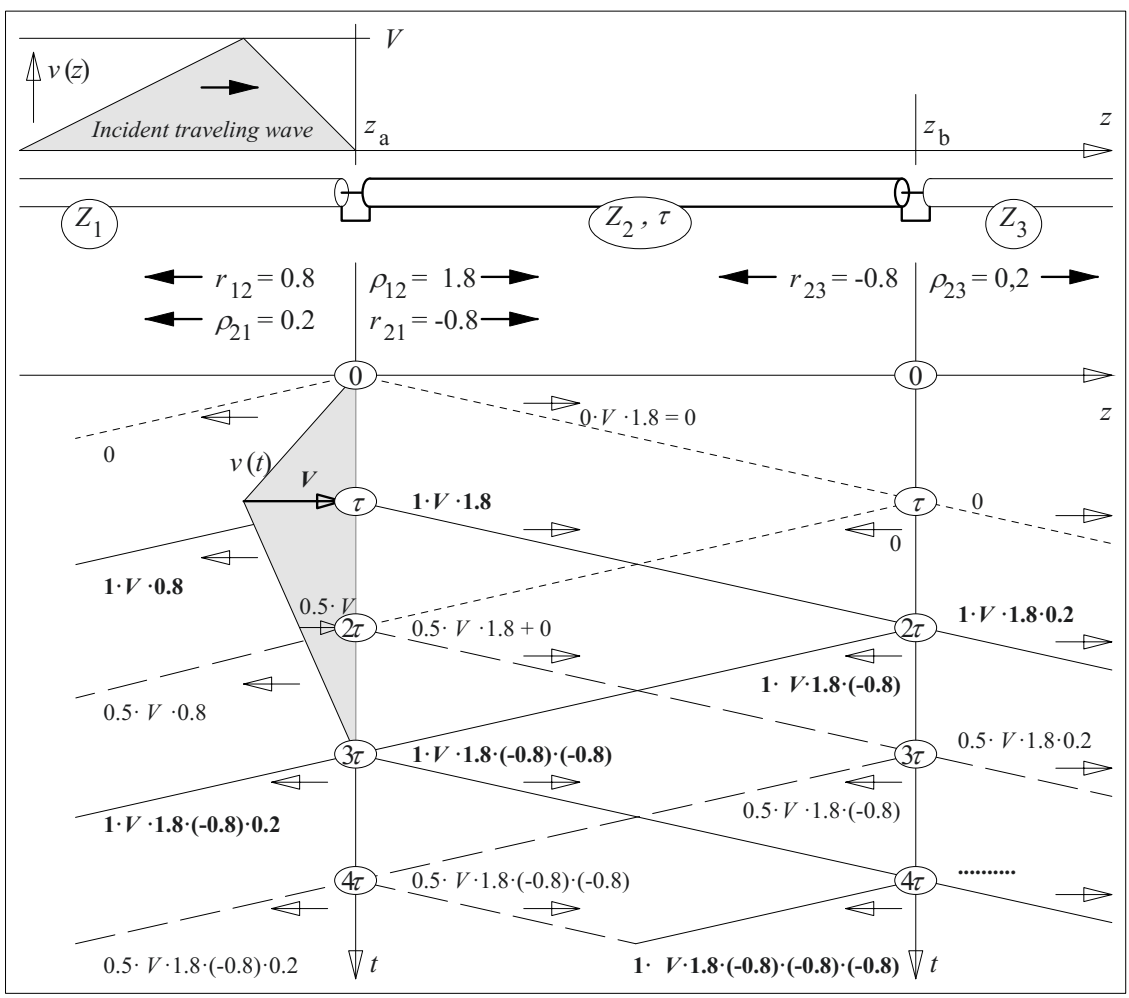

Figure 2.6-11: Description of the propagation, reflection and transmission (refraction) of traveling waves by means of a traveling-wave road map (Bewley lattice diagram) for an example.

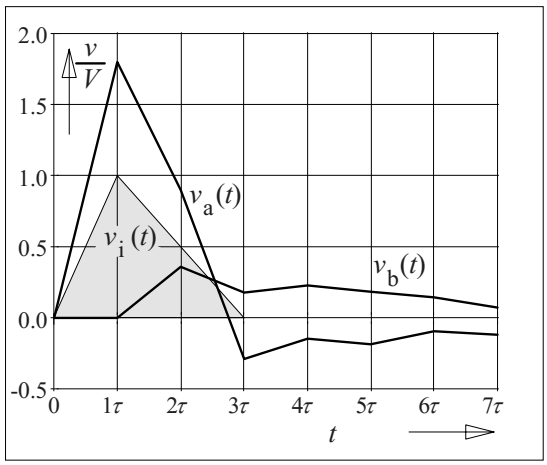

Figure 2.6-12: Voltage curves at the beginning (a) and at the end (b) of an overehead transmission line, determined with Bewley's lattice diagram, fig. 2.6-11.

and $z = z_b$ are given by transmission (refraction), reflection and superposition. They are determined by superposition of all back and forth traveling waves on one side of the discontinuity for the considered instant, Figure 2.6-12:

$T = 0$	$v(z_a) =$ 0 V	$v(z_b) =$ 0 V
τ	1.800 V	0 V
$2\,\tau$	0.900 V	0.360 V
$3\,\tau$	- 0.288 V	0.180 V
$4\,\tau$	- 0.144 V	0.230 V
$5\,\tau$	- 0.184 V	0.185 V
$6\,\tau$	- 0.092 V	0.147 V
$7\,\tau$	- 0.118 V	0.074 V

At the *beginning* of the line 2 ($z = z_a$), the voltage $v_a(t)$ follows the voltage $v_i(t)$ of the incident traveling wave. Only after twice the propagation time for $t > 2\,\tau$, there are deviations because of reflections coming from the other end of line 2.

At the *end* of line 2 ($z = z_b$), the traveling wave does not arrive before the single propagation time $t = \tau$, and the voltage $v_b(t)$ follows the incident wave $v_i(t\text{-}\tau)$ with a time-shift τ for two further propagation times.

Note: This example shows that a traveling wave propagating from a cable to an overhead transmission line can cause *significant overvoltages* by reflections. This also applies to *fast transients* in *gas-insulated switchgear* (GIS) at the bushings, which are connected to the overhead lines. For a transition from a high characteristic impedance (overhead line) to a low characteristic impedance (cable, GIS), the overvoltage is reduced by reflections.

The **Bergeron method** is another graphical method for the description of multiple reflections [39]: The voltages at the beginning (a) and at the end (b) of a transmission line are described by *resistance lines* in a *v,i*-diagram, Figure 2.6-13. The gradients are determined by the termination resistances R_1 and R_2.

Furthermore, it can be shown by addition and subtraction of Eqs. (2.6-7) and (-9) that the propagation in the $+z$ and $-z$-direction is equivalent to lines with different gradients. For a given wave point with a constant argument, we find for the propagation

in $+z$-direction $\quad 2\cdot f(z\text{-}ut) = v + i\cdot Z = \text{const.}$

and

in $-z$-direction $\quad 2\cdot g(z+ut) = v - i\cdot Z = \text{const.}$. (2.6-21)

The propagation of the traveling wave from one end of the line to the other is equivalent to

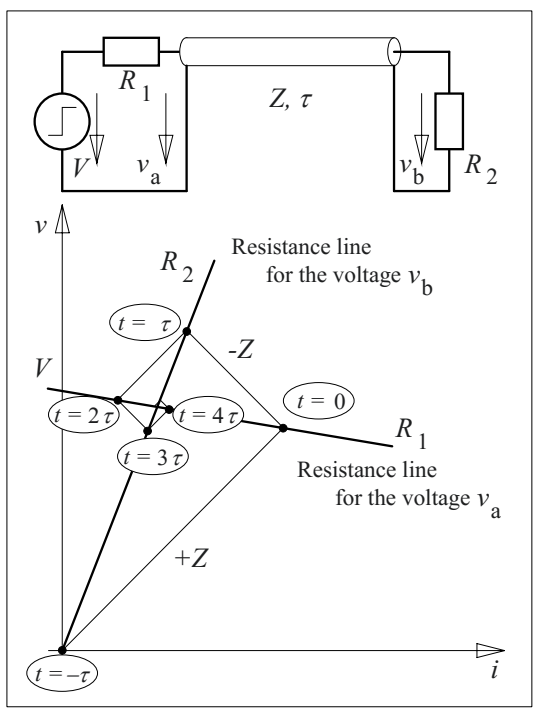

Figure 2.6-13: Description of the traveling wave propagation with Bergeron's method.

the transition from one resistance line to the other along the lines according to Eq. (2.6-21), i.e. along the "*Bergeron lines*" (thin lines in Figure 2.6-13). The gradient of the Bergeron line is dv/di = Z or dv/di = -Z. It is advisable to choose the scales for v and i in such a way that the Bergeron lines lie at an angle of 45° to the axes and are thus mutually perpendicular. We start at a time instant $t = -\tau$ at the line end (b) with the voltage $v_b = 0$ and we reach the start of the line (a) at the time instant $t = 0$ with the starting voltage v_a, which is caused by the voltage step V. The voltages for multiples of the propagation time τ are found on the respective resistance line.

Graphical methods are often unsuitable for solving complex traveling-wave problems. In particular, problems with damped lines, non-ohmic terminations, frequency dependences and non-linearities can only be solved with *network-analysis programs*. Thereby, a number of electrically short equivalent line-elements can approximate long lines according to Figure 2.6-2. Another possibility is approximation with controlled voltage sources with delayed voltages [40].

2.6.3 Examples

Traveling-wave phenomena play a role in many high voltage applications. In the following, three examples are discussed, the disconnector circuits in gas-insulated switchgear (Section 2.6.3.1), the protection zone of a lightning arrester (Section 2.6.3.2) and impulse generation by traveling-wave generators (Section 2.6.3.3).

2.6.3.1 Gas-Insulated Switchgear ("Fast Transients")

If a *disconnector* between a de-energized overhead line and an energized busbar in a **gas-insulated switchgear** (GIS) is closed, there is a breakdown of the remaining clearance between the approaching contacts shortly before the contacts touch each other, Figure 2.6-14. Then, a very fast rising traveling wave is propagating on the coaxial line of the switchgear bay (1), and it is reflected at the bushing capacitance (4). These waves are the so-called *fast transients*, already mentioned in Section 2.2.5. They can propagate in the coaxial lines of a GIS with very low damping.

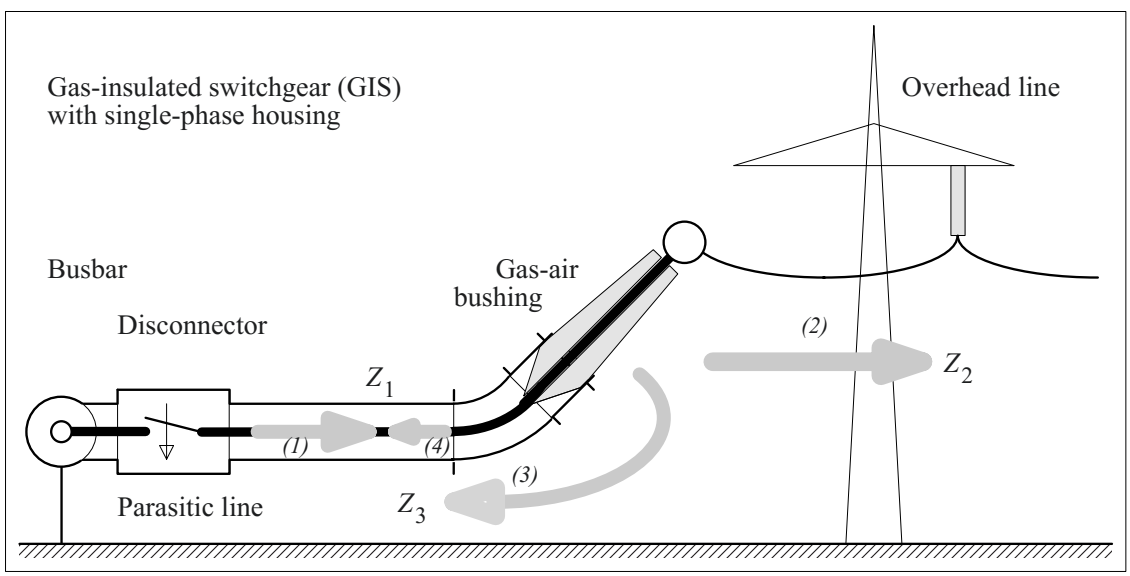

Figure 2.6-14: Generation of a traveling wave 1 by connection of a de-energized overhead line to an energized busbar. Wave 1 is reflected at the gas-air bushing (wave 4) and transmitted or refracted resp. (waves 2 and 3). The transmitted (refracted) waves propagate along the overhead line (wave 2) and along the parasitic line between GIS housing and conducting grounded structures of the building (wave 3).

The transmitted (refracted) wave is split into two waves that propagate along the overhead line and along a *parasitic line* between the enclosure of the GIS and the conducting parts of the GIS building (waves 2 and 3).

The amplitudes of the different traveling waves are determined by the characteristic (line) impedances Z_1, Z_2 and Z_3. Furthermore, the capacitance C of the bushing has to be considered in the first moment, because it must first be charged from the incident wave. See Figure 2.6-9.

According to the equivalent transmission-line circuit Figure 2.6-8, the voltage amplitude of the incident wave can be determined by two factors, i.e. by the *voltage difference* between the energized and de-energized lines at the instant of the clearance breakdown between the approaching contacts and by the characteristic (line) impedances of the adjacent lines on both sides of the disconnector. Because of the reflection at the relatively high characteristic impedance of the overhead line (Z_2), a significant *voltage enhancement* can occur, which stresses the insulation of the bushing, the switchgear and the overhead line.

The traveling wave (3) occurring between the GIS enclosure and other conducting structures is especially critical. Because of the low characteristic (line) impedance Z_3, the voltage amplitude is low. Nevertheless, this wave can cause significant damage in insufficiently protected *secondary equipment* (measurement systems, control equipment etc.) [41]. For instance, a momentary rise of the enclosure potential above ground potential can cause *back flashovers* into low-voltage circuits, e.g. into information technology circuits. Generally, rapidly changing electric and magnetic fields leaving the GIS can cause strong interference with neighboring circuits and systems. Therefore, ensuring electromagnetic compatibility (EMC) is of particular value in system design in order to avoid malfunction and damage.
Note: During the *closing of the disconnector*, the described breakdown with the subsequent transients is not the only process. After the equalization of the potential on both sides of the disconnector, there is no longer any current and the discharge expires. Because of the sinusoidal voltage on the busbar, a voltage difference is re-established and the insulating gap between the still moving contacts breaks down again. Furthermore, a *higher number of re-ignitions* occur until the contacts are fully closed. Very steep voltage and current gradients are generated thereby.

Similar processes occur if the *disconnector is opened*. With increasing distance of the contacts, the breakdown voltage increases and results in increasing amplitudes of the traveling voltage waves. The voltage enhancements caused by re-ignitions are superimposed onto voltage enhancements caused by slow switching-transients.

Note: In *large-scale gas-insulated switchgear*, reflection processes occur which are difficult to understand and yet still depend on the switching state of the substation. Insulation stresses caused by fast transients are often determined by measurements and by complex numerical simulations. For example, the direct connection of *transformers* to a gas-insulated switchgear requires a very careful analysis of the transients: Because of the high characteristic impedances of *transformer windings*, high voltage enhancements caused by reflections can be expected. Additionally, particularly in bigger installations, voltage enhancements can be caused by resonances and slower transients.

Note: Fast transients can cause stresses in insulation regions, which are without any stress in a static or quasi-static case. An example is given by a *bushing core*, Figure 2.6-15. At first, the incident wave is split up in relation to the characteristic impedances of the coaxial lines, which are formed by the concentric grading layers. Therefore, waves can also propagate in *parasitic lines* between the grounded flange and the outermost grading-foil and between the high-voltage conductor and the innermost grading-foil.

2.6.3.2 Protection Zone of a Lightning Arrester

Lightning arresters are non-linear components (resistors), which *limit overvoltages* and which carry a very small leakage current only at operating voltage. Principles and designs are discussed in Section 6.1.4.3.

For a *metal-oxide arrester*, the current increases very strongly if the voltage exceeds the rated voltage V_r, Figure 2.6-16. During a lightning impulse stress, the voltage-current characteristic of the arrester and the lightning current (which can be calculated in an equivalent transmission-line circuit according to Figure 2.6-8) determine the value of the so-called *residual voltage* V_{res}, which defines the lightning impulse **protection level** V_{pl}.

Note: For a lightning arrester consisting of a non-linear resistor *in series with a spark gap*, the protection level is defined by the *spark-over voltage* of the gap.

An arrester in the course of an overhead transmission line is now discussed, its location is point 1, Figure 2.6-17 (top). As long as the amplitude of the *incident traveling wave* is below the protection level V_{pl}, it is assumed for simplicity that the arrester remains highly resistive and that there are no reflections, Figure 2.6-17 (middle). If the amplitude of the traveling voltage wave exceeds the protection level, the arrester becomes low-resistive; there are *reflected and transmitted wave components* that reduce the voltage amplitudes before and after the arrester, Figure 2.6-17 (bottom). The resulting voltage distribution is depicted for two different time points by bold lines.

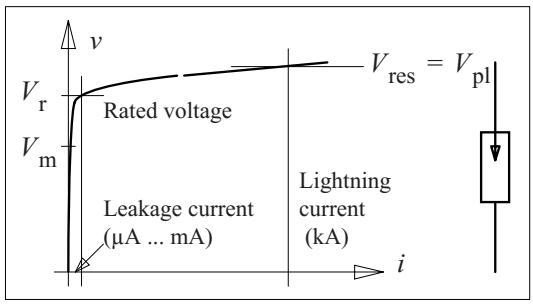

Figure 2.6-16: Ideal v,i-characteristic of a metal-oxide lightning arrester.

The voltage drop Δv at the arrester causes two traveling waves with amplitudes $-\Delta v$, which are propagating in the opposite $+z$ and $-z$ directions. In the propagation direction of the incident wave ($+z$ direction), the voltage is limited to the protection level V_{pl} throughout the line. Furthermore, in front of the arrester there is a so-called **protection zone** L_p, where a given maximum voltage V_{max} is not exceeded. It can be seen from the two time points depicted in Figure 2.6-17 that the voltage limit V_{max} at point 2 is valid for any time point. This means that the increasing voltage of the incident wave is always compensated by the increasing voltage of the reflected wave within the protection zone L_p.

The incident voltage wave (highlighted in grey) is drawn for a time point at which the

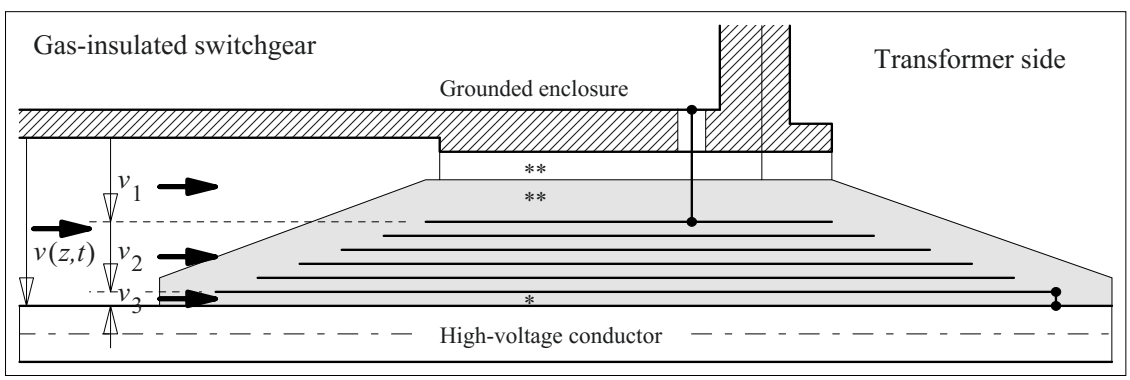

Figure 2.6-15: Transient field stresses in a bushing core above and beneath the grading layers at ground and high-voltage potential, i.e. in regions, which are without any field stress in a static or quasi-static case, (*) and (**).

permitted voltage V_{max} is reached at point 2. After that time point, the reflected wave limits the voltage magnitude to V_{max}. The length of the protection zone L_p shall be derived from Figure 2.6-17. The (spatial) gradient of the wave front is

$$\Delta v/L_p = \partial v/\partial z = (\partial v/\partial t)\cdot(\partial z/\partial t)^{-1}$$
$$= (\partial v/\partial t)\cdot u^{-1}.$$

With $2\cdot\Delta v = V_{max} - V_{pl}$ the protection zone is

$$L_p = ½\cdot(V_{max} - V_{pl})\cdot u / (\partial v/\partial t). \quad (2.6\text{-}22)$$

Numerical example: A lightning arrester with V_{pl} = 150 kV shall limit a traveling wave rising on a three-phase line with a front gradient $\partial v/\partial t$ = 500 kV/µs, so that, within the protection zone $L_{p,}$ only 80 % of the lightning impulse voltage for the 123 kV voltage level shall be reached (this means that V_{max} = 0.8 ·550 kV = 440 kV). The phase velocity is v = 300 m/µs. According to Eq. (2.6-22) the relevant protection zone is L_p = 87 m.

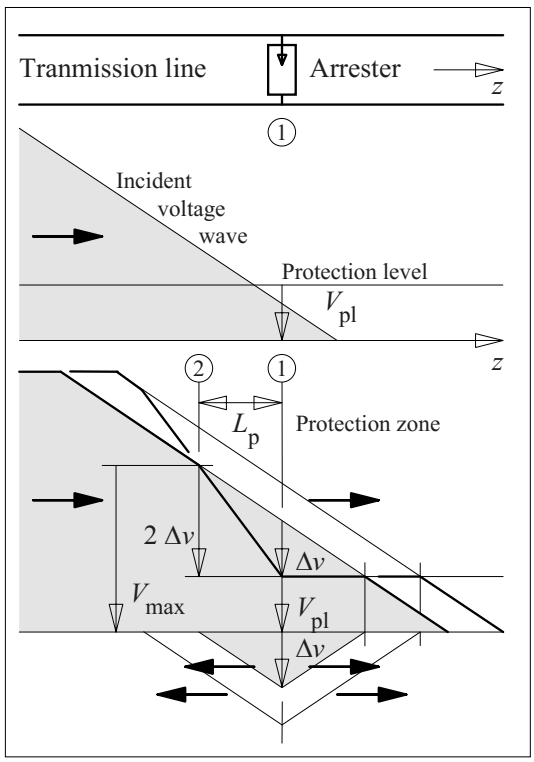

Figure 2.6-17: Protection zone of a lightning arrester with interference (i.e. compensation) of oppositely traveling voltage waves after the ignition of the lightning arrester (bottom).

Note: For the protection zone of a lightning arrester also

$$L_p/\,\mathrm{m} \approx V_m/\,\mathrm{kV} \quad (2.6\text{-}23)$$

is given as a rough guide in [22]. V_m is the maximum voltage for equipment (Section 6.1.4). More accurate calculation methods, which consider statistical error rates and acceptable error probabilities, normally give shorter protection zones [124].

Note: The calculation of a protection zone according to Eq. (2.6-22) is also valid for arrangements with an open-circuit or a high impedance at the end of the line (e.g. a *transformer winding*) [39]. The distance between arrester and line end or termination must not exceed L_p. The lightning arrester can be at the end of the line.

2.6.3.3 Traveling-Wave Generators (Transmission-Line Generators)

According to the principle of a so-called **cable generator**, the capacitively stored energy on a *charged transmission line* is converted by discharging into a very fast rising impulse in a matching impedance, Figure 2.6-18.

After the breakdown of the *switching spark gap*, a traveling wave with a voltage amplitude $V/2$ is propagated on the output line and is absorbed in a load impedance $R = Z$, which is matched with the characteristic impedance of the line. On the charged line (charging voltage V), a traveling wave with the voltage amplitude $-V/2$ is traveling in the $-z$ direction. After the reflection at the open-circuit line end, the reflected wave propagates with $-V/2$ in +z direction and discharges the line completely. A *square-wave pulse* is thereby generated in the load with a voltage $V/2$ and a half-value width $t_H = 2\cdot\tau_L$, which corresponds to twice the propagation time on the charged line.

Note: In practice, the (parasitic) inductance of the switching spark gap reduces the output voltage gradient $\partial v/\partial t$. Furthermore, mismatches and line damping cause impulse distortions.

Another principle is the discharging of two parallel lines in the so-called **Blumlein gen-**

erator, Figure 2.6-19. Both lines with the characteristic impedance Z are connected to their high-voltage conductors. The load $R = 2Z$ is connected to the two grounded conductors via an output line with the characteristic impedance $2Z$.

After the charging of the lines to the voltage V, the load is without any voltage, Figure 2.6-19 (top). After the ignition of the switching spark gap, the upper line is discharged by a traveling wave with the amplitude $-V$, see *no. 1* in Figure 2.6-19 (middle). At the output end of the line, the characteristic impedance changes from Z to $2Z+Z = 3Z$. The reflection and transmission coefficients according to Eq. (2.6-19) and (-17) are $r_v = 1/2$ and $\rho_v = 3/2$. This means that the reflected wave travels backwards with the amplitude $-V/2$, see *no. 2*. The transmitted (refracted) wave with the amplitude $-3V/2$ is divided in the ratio of the characteristic impedances onto the output line to the load ($-V$) and onto the lower pulse-forming line ($-V/2$).. The counting direction for the associated voltages is shown by reference arrows in the figure. At the load $R = 2Z$, which is matched with the output line, there is a voltage step $v_R(t) = V$ after the wave-front arrives.

The backwards traveling waves on the lines are reflected at the short-circuited spark gap (SC) on the upper line and at the open-circuit (OC) on the lower line, with and without polarity reversal, see *no. 3*. The reflected waves, which are transmitted into the output line, have the *same* polarity and (analogously to refraction *no. 2*) the amplitude $V/2$ both, see *no. 4*. Therefore, the field of the first wave, which was transmitted to the load, is completely compensated with a delay of $2 \cdot \tau_L$. The voltage

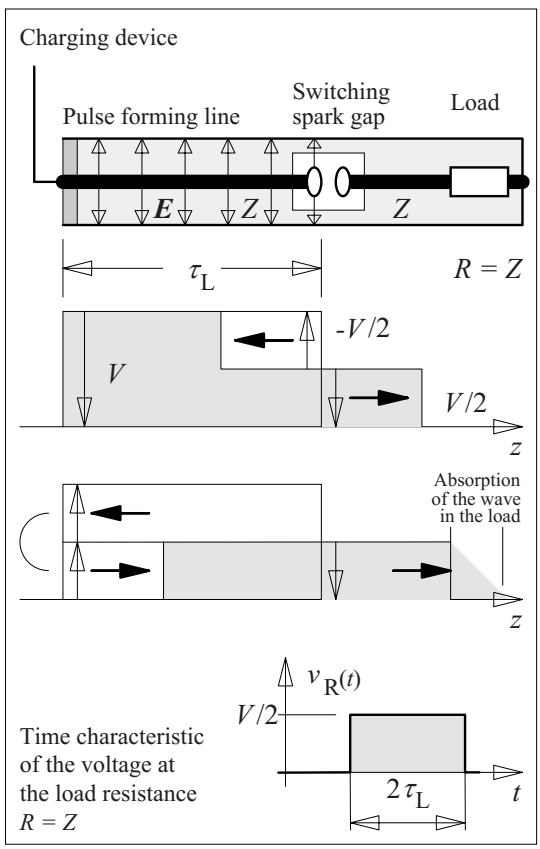

Figure 2.6-18: Generation of square-wave pulses by discharging of a pulse-forming line (traveling-wave generator).

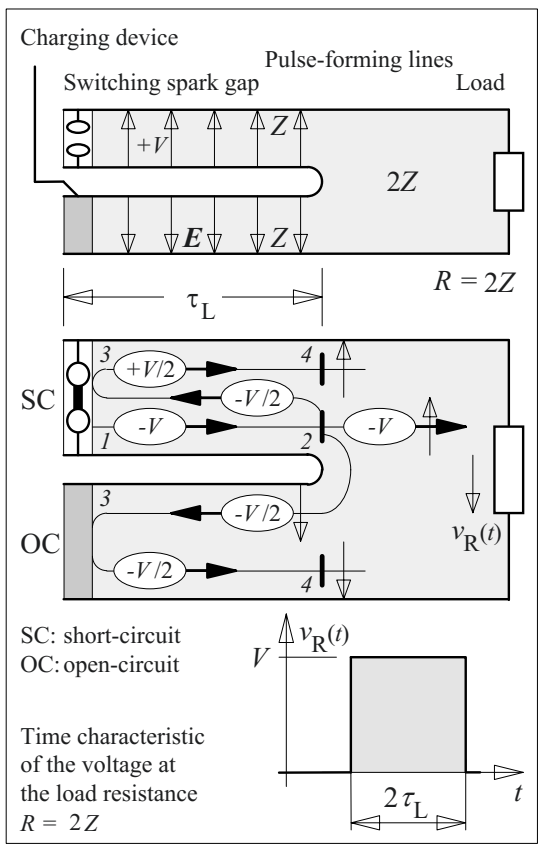

Figure 2.6-19: Generation of square-wave pulses by discharging of parallel pulse-forming lines (Blumlein generator).

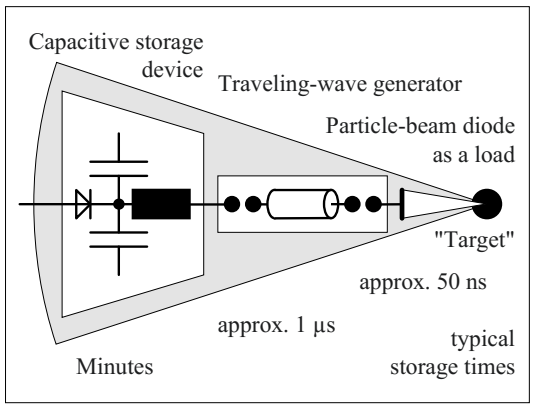

Figure 2.6-20: Module of a pulsed-power generator with spatial and temporal compression of the stored energy (schematic).

at the load decreases from V to zero. Further waves, which travel backwards into the line, compensate each other.

An important **application** of transmission-line generators is the generation of square-wave impulses for *step-response measurements* on measuring systems. Cable generators are mainly used for this purpose.

Another application is the **pulsed power technology** for the *spatial and temporal compression* of electromagnetic energy in an extremely powerful impulse [42]. For the generation of *extreme energy densities*, a number of generators are *circularly arranged around the target* as modules that are triggered simultaneously [14]. The traveling-wave generator arrangement can be a driver circuit for the acceleration of particles in basic research applications in physics, Figure 2.6-20. For example, matter could be brought into extreme conditions in order to ignite nuclear fusion reactions.

The principles of the *cable generator* or the *Blumlein generator* are chosen depending on voltage and load impedance. The generators are designed as coaxial lines or as parallel-plate lines [15]. Voltage enhancements can be achieved by multiple reflections at additional switching spark gaps, i.e. by so-called *double-bounce switching* [43]. *Water* is used as an insulating medium because of its very high relative permittivity $\varepsilon_r = 81$ and because of its high dielectric breakdown strength. Thereby high amounts of energy can be stored for short times. Furthermore, the phase velocity is reduced to $u = u_0/9 = 3$ cm/ns and the length of a line can be reduced by a factor of 9 in comparison with air, see Eq. (2.6-8). Because of the comparatively high conductivity of water, the energy can only be stored for a short time in a range of microseconds (µs). Therefore, it is necessary to charge the water-insulated line very rapidly from a conventional capacitor bank with approximately the same capacitance (see impulse generators, Section 6.2.3). The capacitor bank can store the energy for longer times, and rapid charge transfer is performed by oscillation. At the voltage maximum, the switching spark gap is ignited before significant *self-discharging* of the water-insulated capacitance can occur, Figure 2.6-20. The synchronous triggering of the switching spark gaps for the *parallel operation* of a number of modules places extreme demands on the triggering devices.

Example: Water-insulated impulse generator

A water-insulated traveling-wave generator according to Figure 2.6-18 shall be designed with coaxial lines for the generation of impulses with energies as high as possible. The peak-value of the voltage shall be $\hat{V} = 500$ kV and the half-value width $t_H = 50$ ns. The maximum permissible field strength in water is $\hat{E}_{max} = 100$ kV/cm.

According to Eq. (2.3-24) the maximum field energy of a coaxial line is given for $R_2/R_1 = e^{0.5} = 1.65$. With the charging voltage $V = 2\hat{V} = 1$ MV the radii $R_1 = 20$ cm and $R_2 = 33$ cm are calculated from Eq. (2.3-22). The length of the line is determined by the propagation time $\tau_L = t_H/2 = 25$ ns with $L = \tau_L \cdot v_0/\varepsilon_r^{0.5} = 83$ cm.

From the Equations in Figure 2.6-5, the capacitance $C = 7.5$ nF and the characteristic impedance $Z = 3.3\ \Omega$ is derived. The current amplitude of the output impulse is $\hat{I} = \hat{V}/Z = 150$ kA and the power is $P = 75$ GW.

The capacitively stored energy $W = ½\ C \cdot V^2 = 3{,}75$ kJ is ideally completely transferred into impulse energy $W = \hat{V} \cdot \hat{I} \cdot t_H = 3{,}75$ kJ. In practice, losses must of course be considered.

Other impulse circuits and many **applications** of **high-voltage impulse-technologies** are described in Section 7.3.2 and 7.4.2 [482].

3 ELECTRIC STRENGTH

It is a basic task of high voltage engineering to keep the *electric stresses* lower than the *electric strengths* of the materials under all possible circumstances. Unfortunately, the electric strength is a quantity that is subject to significant statistical variations, Figure 3.1-1. In the following, an introduction to statistics is given at first (Section 3.1). If the electric strength is insufficient, the insulation fails and discharges occur. They depend on the type of insulating material. Discharges in gases (Section 3.2) differ significantly from discharges in other dielectrics (Section 3.3). Special attention is paid to liquids (Section 3.4), solids (Section 3.5) and vacuum (Section 3.7). Discharges that do not lead directly to breakdown are known as partial discharges (Section 3.6). They are especially important for diagnostic measurements and for ageing processes.

3.1 Introduction to Statistics

The failure of the electric strength, i.e. electric discharges, can no longer be described *deterministically* because of a high number of different physical parameters. Furthermore, a high statistical variance of inception voltages for discharges, of breakdown voltages and of discharge times can be observed, Figure 3.1-1. Therefore, it seems natural to describe these quantities as *random variables* and to determine the characteristics of discharges by statistical methods. In the following, basic principles of *statistical methods* are described. Comprehensive discussions can be found in the literature [44].

3.1.1 Statistical Descriptions of Discharge Processes

3.1.1.1 Random Variables

For example, the breakdown voltage of a spark gap is determined by an applied AC voltage that is increased until the breakdown occurs. If the test is repeated several times, it can be noted that an "*exact* breakdown voltage" does not exist, and the breakdowns occur at different voltages, Figure 3.1-1a.

Note: Voltage rise tests can also be performed with *DC voltage*. In the case of *impulse voltages*, the continuously increasing voltage must be replaced by consecutive impulses with stepwise increasing peak values.

By means of a very high (infinite) number of tests, the voltage $\hat{V}_{bd50}$ with a breakdown probability of 50 % could be determined, as well as a *certain withstand voltage* (breakdown probability 0 %) and a *certain breakdown voltage* (breakdown probability 100 %).

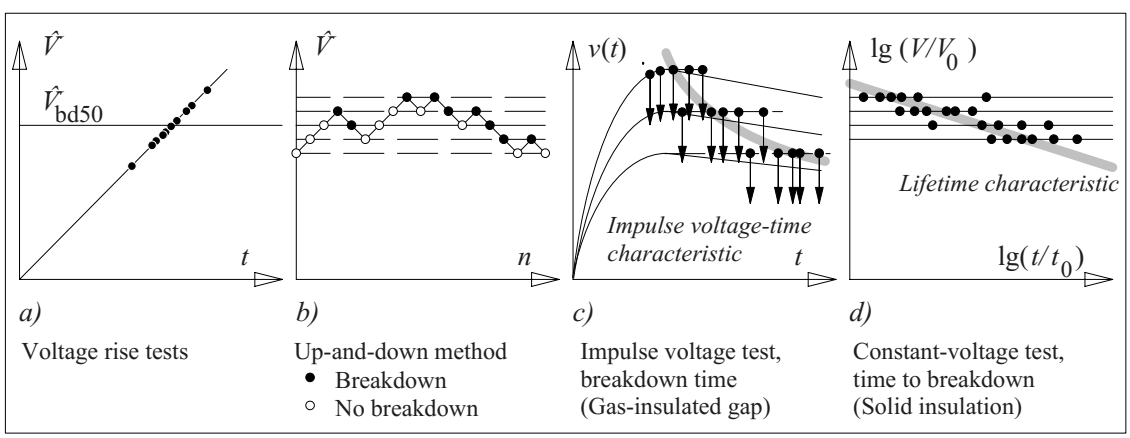

Figure 3.1-1: Examples for the stochastic character of discharge processes.

A. Küchler, *High Voltage Engineering*, VDI-Buch,
DOI 10.1007/978-3-642-11993-4_3

In practice, the *number of tests* is always *limited*. The characteristic values of a discharge have to be estimated from a limited number of measured values. The accuracy of the **estimate** is increased with the number of equivalent tests.

Example: Up-and-down method

The up-and-down method is a procedure by which to estimate the 50 % breakdown voltage, Figure 3.1-1b. It can be applied for the estimation of the impulse strength of gas-insulated spark gaps.

The test is started with a voltage where no breakdown is expected, and the voltage is increased in steps of Δv. As soon as a breakdown occurs, the voltage is decreased by Δv. For the consecutive steps, the voltage is increased if a breakdown does not occur, and it is decreased if the breakdown happens. Thereby, the voltages swing stepwise up and down around the 50 % breakdown voltage $\hat{V}_{\mathrm{bd50}}$. It can be estimated as the *arithmetic mean value* of a predefined number of voltage-values. The counting starts with the first breakdown. The exact statistical analysis is described in the literature [44].

During a statistical analysis it is assumed that a **random sample** is taken from an (unknown) **basic population**. In the case of breakdown tests on a given insulation arrangement, a limited number of breakdowns is taken at random from the theoretically infinite number of all possible breakdown tests on such an arrangement, Figure 3.1-2.

A statistical analysis has to estimate the **distribution** of the infinite basic population as accurately as possible, based on as low a finite number of tests as possible (i.e. on a sample size as small as possible).

The infinite basic population is a theoretical fiction and will remain unknown forever; every statistical statement is therefore an estimate. Nevertheless, it becomes better and better as the number of tests is increased.

Instead of the breakdown voltage, other quantities can also be considered as *random variables*. Examples are breakdown field strength, partial discharge inception voltage, inception field strength or time to breakdown, Figure 3.1-1c and d. Generally, a *random variable* is described by capital letters X and their *definite values obtained by random sampling* are given by small letters x.

Note: Often, these strict distinctions are not considered in practice: For example, it is often said that a "determination" of a 50 % breakdown voltage V_{bd50} is performed, but in reality only an estimate v_{bd50} is calculated. It is not possible to determine parameters of the (always unknown) basic population, but we can only determine *empirical parameters*, which are used as *estimates* of the *population parameters*.

Note: Here, capital and lower case letters do not describe magnitudes and time-varying functions as usual, but they represent random variables and their definite values obtained by random sampling.

3.1.1.2 Cumulative Distribution Functions

The procedure of a statistical analysis shall be explained for the example of a breakdown test with the voltage rise test according to Figure 3.1-1a, Figure 3.1-2.

Ten breakdown voltages are a **random sample** taken from a fictitious basic population. Arranged in the order of the tests, they are a **master database** (master list), which must not have any trend, i.e. any systematical dependence of the values. They must be *stochastically independent*, which can be tested graphically or by special mathematical test algorithms [44], [396].

The *distribution list with sorted values* is plotted as a **cumulative frequency polygon** or a *cumulative frequency curve* (**empirical distribution function**) $h(x)$ with $x = v_{\mathrm{bd}}$, Figure 3.1-2. For the example of ten test values, every single value represents a rate of occurrence of $\Delta h = 10$ %.

The empirical distribution function is only an *imperfect estimate* for the cumulative distribution function of the total population. A safe insulation design requires statements about

very low breakdown probabilities (e.g. 1 % breakdown voltage), which cannot be determined directly if the number of breakdown values is small.

For this purpose, a mathematical or theoretical **distribution function** $F(x)$ is sought, which approximates the empirical distribution function $h(x)$ as well as possible, and which can be extrapolated down to very low probabilities, Figure 3.1-2. The most important cumulative distribution functions are the *Gaussian normal distribution* (Section 3.1.2.2) and the *Weibull (extreme value) distribution* (Section 3.1.2.3).

Note: By analogy with the cumulative frequency polygon, the theoretical **distribution function** is often known as the **cumulative distribution function**, it is the integral of the *(probability) density function*, Figure 3.1-5.

Note: By means of graphical and arithmetical tests, it can be investigated, which *type of function* gives the best approximation of the measured values (**statistical distribution test**) [44], [396].

After the selection of the *distribution type*, the mathematical distribution curve has to be described *numerically by parameters*, which are estimated from the measured values. These parameters are different depending on the type of the distribution function, Section 3.1.2.2 and 3.1.2.3.

This type of **parameter estimation** is known as a *point estimate*. It gives mean values or variances, which can be used to describe a Gaussian normal distribution for instance. The **point estimate** is further explained in the following sections.

A mathematical distribution function is only an estimate for the (always unknown) cumulative distribution function of the total population of all possible values. By means of an

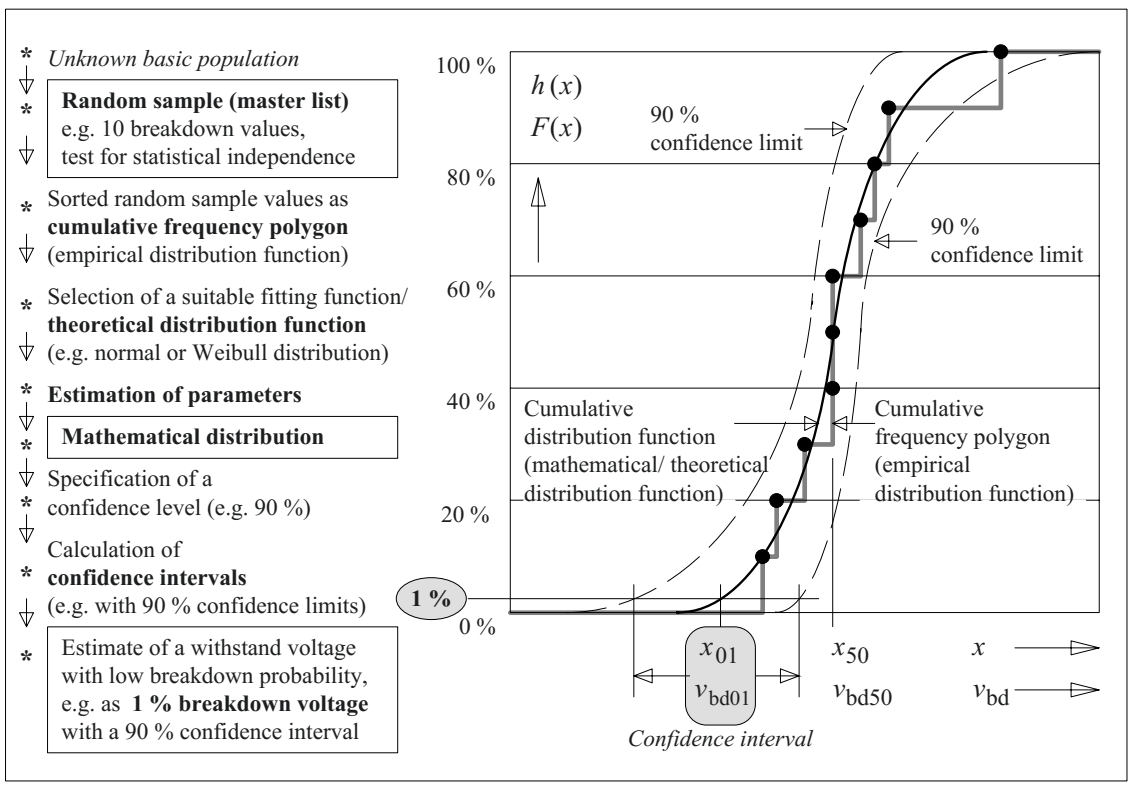

Figure 3.1-2: Statistical analysis of breakdown values from a voltage rise test according to fig. 3.1-1a.

interval estimation, *confidence intervals* are determined containing the distribution function of the total population with a specified probability (e.g. 90 %), Figure 3.1-2. For a small sample size, confidence intervals are broad and the estimate is very *uncertain*. With increasing sample size, confidence intervals decrease and the certainty of probability statements increases. Calculation of confidence intervals is described in the literature [44], [396].

The *practical importance* of the mathematical distribution function and the associated confidence interval is the determination of voltages with very *low breakdown probabilities* (so-called **withstand voltages**). According to Figure 3.1-2, the *estimate* $x_{01} = v_{bd01}$ for the 1 % breakdown voltage (more generally for the **1 % quantile** of a probability distribution) can be determined from the mathematical distribution curve. Furthermore, it can be said that the 1 % breakdown voltage can be found within the 90 % **confidence interval** (limited by the confidence limits) with a probability of 90 %, Figure 3.1-2.

Note: Unfortunately, these *confidence intervals* are *very broad* at low breakdown probabilities for many dielectrics, especially for liquid and solid insulating materials. Therefore, statements about low breakdown probabilities are only possible with **high uncertainties**. In engineering design, a withstand voltage therefore needs an additional **safety margin**.

3.1.1.3 Parameter Estimation

In the following, the **point estimate** of parameters is described, which are *generally valid*, i.e. which are not related to any special distribution function (**empirical parameters**). Sometimes they can also be used in mathematical distribution functions, e.g. in the Gaussian normal distribution. We distinguish *measures of mean values* and *measures of statistical dispersion*. The (fictitious) parameters of the basic population are discussed together with these (empirical) parameters, which are calculated from a limited number of measured values.

a) Measures of mean values

For the **basic population** consisting of all possible values, the *mean value* or the (mathematical) *expectation value* is defined as the value μ or $E(X)$, which is expected for the random variable X. Formally it is given as the (infinite) sum of *all* single values x_i, weighted with their individual probability p_i:

$$\mu = E(X) = \sum_{i=1}^{\infty} p_i \cdot x_i \qquad (3.1\text{-}1)$$

Another measure of mean values is the *median*, the *central value* or the *50 % quantile* (the 50 % value) $q_{50} = x_{50}$, which is the central value of all single values x_i. Half of the values x_i is below and half of the values x_i is above the median.

In reality, only an **empirical distribution** of a limited number n of discrete measured values x_i can be determined. If all values x_i exist only once, i.e. if the rate of occurrence is $h_i = 1/n$, the *empirical estimate* of the expectation value μ is the *arithmetic mean value* by analogy with Eq. (3.1-1):

$$x_m = \bar{x} = \sum_{i=1}^{n} h_i x_i = \frac{1}{n} \sum_{i=1}^{n} x_i \approx \mu . \qquad (3.1\text{-}2)$$

The *empirical central value* or the *empirical median* $\hat{q}_{50} = \hat{x}_{50}$ is either the value that is situated in the middle of the sorted values (for an uneven number of measured values) or the mean value of the two values in the middle (for an even number of measured values). Half of the measured values are below and half of the values are above the central value. The median is often used as an estimate for the arithmetic mean value.

Note: In statistics, *empirical quantiles* are often characterized by a "^". In order to avoid confusion with *peak values*, which are very important in high voltage engineering, this characterization is not used below.

Note: The 50 % breakdown voltage $\hat{v}_{bd50}$ is the empirical median (central value) of the random variable "breakdown voltage" $\hat{V}_{bd}$. In the latter case, the meaning is again *peak values*!

b) Measures of statistical dispersion

The statistical dispersion of the **basic population** is described by the *variance* σ^2, which is the mean-square deviation of the random variable X (i.e. of all individual values x_i) from the expectation value μ. Formally, σ^2 is given as the square of the deviation $(x_i - \mu)$, weighted with the individual probabilities p_i:

$$\sigma^2 = E(X-\mu)^2 = \sum_{i=1}^{\infty} p_i (x_i - \mu)^2 \qquad (3.1\text{-}3a)$$

The quantities

$$\sigma = \sqrt{\sigma^2}$$

and (3.1-3b)

$$V(X) = \sigma/\mu$$

are the *standard deviation* σ and the *variation coefficient* V.

Empirical measures of statistical dispersion for a finite number n of discrete measured values x_i are the *mean-square deviation*

$$s_n^2 = \frac{1}{n} \cdot \sum_{i=1}^{n} (x_i - x_m)^2 \qquad (3.1\text{-}4)$$

and the *empirical variance*

$$s^2 = \frac{1}{n-1} \sum_{i=1}^{n} (x_i - x_m)^2 \approx \sigma^2 \qquad (3.1\text{-}5a)$$

The quantities

$$s = \sqrt{s^2} \approx \sigma$$

and (3.1-5b)

$$v = s / x_m \approx V$$

are the *empirical standard deviation* s (*root-mean-square deviation*, r.m.s.d.) and the *empirical variation coefficient* v, which are used as estimates for the standard deviation σ and the variation coefficient V.

Note: Unfortunately, v and V have to be introduced as general *statistical quantities* here. Nevertheless, the characters v and V are mostly used for *voltages* in this book. Please consider the relevant context.

Note: The *empirical variance* s^2 and the *empirical standard deviation* s (r.m.s.d.) are not calculated with the relative rate of occurrence $1/n$ (as could be expected from Eq. 3.1-3 for the variance σ^2 and the standard deviation σ), but with the factor $1/(n\text{-}1)$. This is necessary for reliability purposes, as in Eq. (3.1-4) and (-5a) only the estimate $x_m = \bar{x}$ can be used instead of the expectation value μ.

For a theoretical case with $n = 1$, the *mean-square deviation* according to Eq. (3.1-4) would always give the value $s_n^2 = 0$ as the values x_i and $x_m = \bar{x}$ are identical. Nevertheless, a higher dispersion could exist and could be calculated with a larger random sample. Therefore, the weighting with $1/n$ is too optimistic.

The *empirical variance* according to Eq. (3.1-5a) with the weighting $1/(n\text{-}1)$ would give an *indeterminate* expression "zero/zero" for $n = 1$. Form this it is clear that it is not possible to give any statements about statistical dispersions with a *single* measured value only.

For small random sample sizes n, enhanced values of the empirical variance s^2 and for the empirical standard deviation s result from weighting with the factor $1/(n\text{-}1)$. For large sample sizes n, the difference between weighting with $1/(n\text{-}1)$ and $1/n$ disappears, and s^2 or s can be considered as good estimates for σ^2 or σ.

Note: Another empirical measure of statistical dispersion is the *range* R:

$$R = x_{max} - x_{min} \qquad (3.1\text{-}6)$$

3.1.1.4 Example: Series of Measurements

Empirical distribution of breakdown voltages: In a voltage rise test 19 breakdown voltages are determined (*master database, master list*):

v_{bdi}/kV = 102; 100; 107; 98; 95; 100; 104; 99; 92; 102;

103; 99; 97; 95; 101; 104; 98; 94; 100.

In a *distribution table*, the values are sorted and the rates of occurrence are calculated:

Voltage in kV	Rate of occurrence absolute	relative	Cumulative frequency absolute	relative
92	1	0.05	1	0.05
93	0	0	1	0.05
94	1	0.05	2	0.1
95	2	0.1	4	0.2
96	0	0	4	0.2
97	1	0.05	5	0.25
98	2	0.1	7	0.35
99	2	0.1	9	0.45
100	3	0.15	12	0.6
101	1	0.05	13	0.65
102	2	0.1	15	0.75
103	1	0.05	16	0.8
104	2	0.1	18	0.9
105	0	0	18	0.9
106	0	0	18	0.9
107	1	0.05	19	0.95
108	0	0	19	0.95
109	0	0	19	0.95

If the distribution list is lightly populated only, it is often advisable to sort the values into *classes*. In the given example a class interval $d = 3$ kV is chosen (start at 91.5 kV), see the horizontal lines in the distribution list:

Class in kV	Rate of occurrence absolute	relative	related to d	Relative cumulative frequency
> 91.5 - 94.5	2	0.1	0.033 /kV	0.1
> 94.5 - 97.5	3	0.15	0.050 /kV	0.25
> 97.5 - 100.5	7	0.35	0.117 /kV	0.6
>100.5 - 103.5	4	0.2	0.067 /kV	0.8
>104.5 - 106.5	2	0.1	0.033 /kV	0.9
>106.5 - 109.5	1	0.05	0.017 /kV	0.95

The curve of the relative cumulative frequency h_Σ describes the *empirical distribution function*, Figure 3.1-3a. The arbitrarily chosen division into classes determines the curve of the staircase function, which differs somewhat from the cumulative frequency polygon with the single values. *Estimates for the probability of a breakdown* at different voltages can be taken from the empirical distribution function. At 94 kV, the breakdown probability is approximately 10 % (v_{bd10}, 10 % quantile) for example. For voltages above 104 kV, a breakdown can be expected in more than 90 % of the test cases (v_{bd90}, 90 % quantile).

The curve of the relative (breakdown) density h related to the class interval $d = 3$ kV is a *density function* h/d that can be used to read off *estimates for the probability density*, Figure 3.1-3b.

Note: The probability density can be approximated by a **density function**, which is also known as a **probability density function**. It is the derivative of the *(cumulative) distribution function*, see Figure 3.1-5.

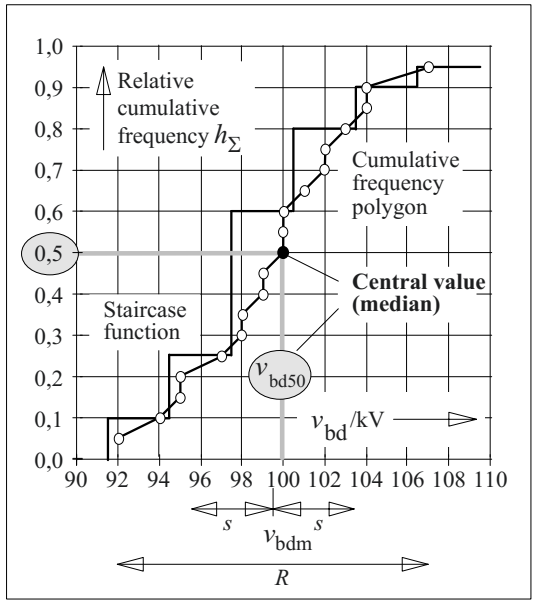

Figure 3.1-3a: Relative cumulative frequency (rate of occurrence) of measured values as empirical distribution function with and without division into classes.

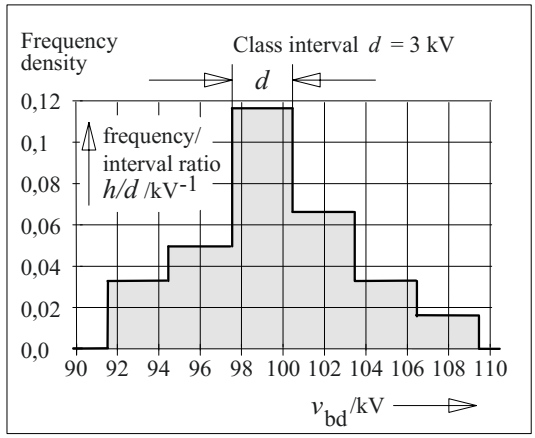

Figure 3.1-3b: Relative (breakdown) frequency related to the different classes as estimates of the probability density (probability density function).

Numerical example: The following parameters are calculated from the values of the previous example, Figure 3.1-3a:

- Arithmetic mean value, Eq. (3.1-2)
  $x_m = v_{bdm} = 99.47$ kV
- Central value (median) (from Figure 3.1-3a)
  $x_{50} = v_{bd50} = 100$ kV
- Range, Eq. (3.1-6)
  $R = 15$ kV
- Empirical standard deviation, Eq. (3.1-5a)
  $s = 3.82$ kV
- Variation coefficient, Gl. (3.1-5b)
  $v = 3.84$ %

3.1.2 Description of Discharge Processes by Distribution Functions

For the mathematical description of an empirical distribution function, the measured values are approximated by a theoretical mathematical function, which best fits the measured values. Then, the mathematical function allows statistical parameters, probabilities and confidence intervals to be calculated.

Note: The mathematical distribution function is just a *formal and arbitrary approximation* of measured values *without direct respect to the* underlying *physics*.

In the following, the Gaussian normal distribution and the Weibull distribution are discussed. Many other distributions are described in the literature [44], [396].

3.1.2.1 Comparison of Empirical and Theoretical Distribution Functions

At first, the *type of cumulative distribution function* must be selected for the best fit of the measured values. A practical test procedure is the use of a so-called *"probability paper plot"* (probability grid) with axis-divisions that give *straight lines* for the tested distribution type, Figure 3.1-4. The figure indicates how the non-linear division of the vertical ordinate is made for a linear division of the horizontal abscissa: The percentage values of the distribution curve $F(x)$ in the upper figure are transferred to the straight line in the lower figure. Mathematically, this is a transformation of the linearly divided ordinate by means of the inverse function $F^{-1}(x)$.

After a series of measurements is taken, the master database is sorted and a distribution table is built. Then, a *hypothesis* about the type of the distribution is established and the *cumulative frequency distribution* is drawn in the corresponding probability paper plot. This allows us to compare the shape of the empirical distribution function with the straight line of the theoretical distribution (**test of the distribution type**), fig, 3.1-4. In case of doubt,

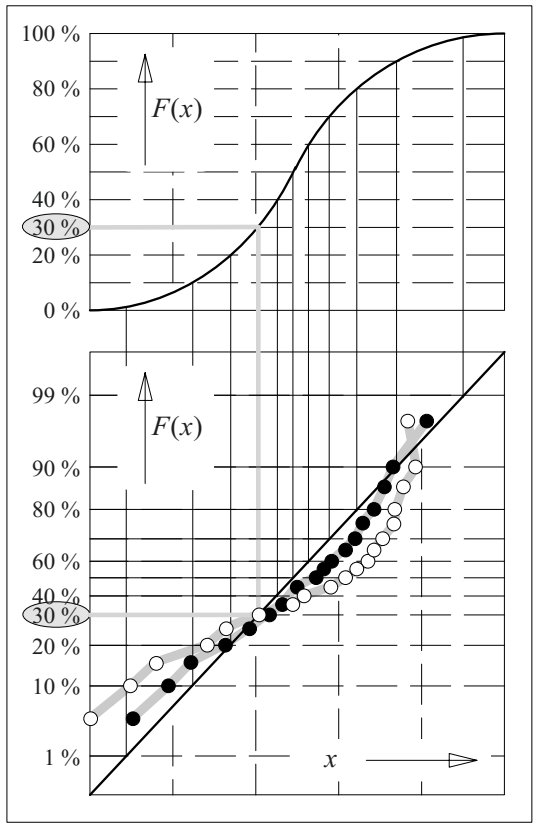

Figure 3.1-4: Curve of a mathematical distribution function (top), which is a straight line in a corresponding "probability paper plot" (bottom), compared with the empirical distributions of two different series of measurements.

the comparison has to be performed with different probability grids corresponding to different distribution types.

Note: The comparison between empirical and theoretical distribution function can also be performed mathematically. Nevertheless, trends in the range of very low and very high probabilities can often be estimated better by the graphic method [44].

After the approximation of the empirical distribution curve as a straight line in a probability paper plot, the *characteristic values of the corresponding distribution* can be taken from the graph. Then, the probability for the occurrence of an incident (e.g. breakdown at a given voltage) is normally calculated from the mathematical distribution function. Especially for very low and very high probabilities (e.g. for calculating certain withstand and certain breakdown voltages), significant *errors* can occur if the *hypothesis* deviates from the real distribution.

Note: The estimation of a distribution parameter (e.g. mean value or standard deviation) from a limited number of measured values is the so-called **point estimation**. The point estimate lies within a statistical *confidence interval*, which can be determined by means of an **interval estimation** (*confidence estimation*). The confidence interval is the region where the point estimate (e.g. the mean value) lies with a given probability (e.g. of 90 % or 95 %). The larger the sample size that is chosen, the smaller the confidence interval that can be assumed. Therefore, the higher the number of measured values that is determined, the higher the accuracy of the point estimate [44], [396].

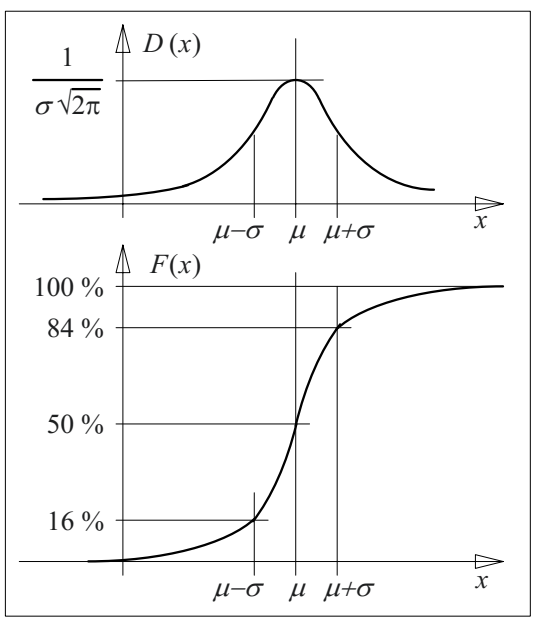

Figure 3.1-5: Gaussian normal distribution with probability density function D(x) and cumulative distribution function F(x).

Today, the statistical analysis of measured values can be performed automatically with **numerical programs**. Thereby, the measured values undergo a test for *stochastical independence*, a determination of *the distribution type*, *point estimations* for the parameters to be determined, and *interval estimations* for the confidence intervals.

3.1.2.2 Gaussian Normal Distribution

The Gaussian normal distribution describes random variables, which can be considered as a sum of many independent and arbitrarily distributed random variables, each of which only contributes to the sum to a minor extent. Therefore, the normal distribution can be applied to many processes in nature, science and technology, e.g. to stochastic noise or statistical measuring errors.

The normal distribution is *symmetric* to the expectation value μ, and it is of *infinite* width, i.e. from $x = -\infty$ to $x = +\infty$.

Note: In contrast to this, **discharge processes** are characterized by a *lower* and an *upper limit*, i.e. by a *definite withstand voltage* and a *definite breakdown voltage*. Nevertheless, the normal distribution is used for approximation in many cases, but it will not always be possible to approximate a given empirical distribution by a normal distribution satisfactorily. In many cases, the *Weibull distribution* allows a better fit.

The *probability density function*

$$D(x) = \frac{1}{\sigma\sqrt{2\pi}}\, e^{-\frac{(x-\mu)^2}{2\sigma^2}} \qquad (3.1\text{-}7)$$

is described by the *expectation value* μ (approximated by the *arithmetic mean value* x_m according to Eq. (3.1-2)) and the *standard deviation* σ, which is estimated by analogy with Eq. (3.1-5a), Figure 3.1-5:

$$\sigma^2 \approx s^2 = \frac{1}{n-1}\sum_{i=1}^{n}(x_i - x_\mathrm{m})^2 \qquad (3.1\text{-}8)$$

The *cumulative distribution function* $F(x)$ is given by integration of the probability density function Eq. (3.1-7):

$$F(x) = \int_{-\infty}^{x} D(x)\,\mathrm{d}\,x \qquad (3.1\text{-}9)$$

With the probability density function according to Eq. (3.1-7), this integral cannot be expressed by an analytical function. Therefore, the probability density function $D(x)$ is expanded into a power series (Taylor's series), which can be integrated in parts [39]. Then, the cumulative distribution function $F(x)$ is given as a series expansion, which cannot be represented by an analytical function, but from which numerical values can be calculated. In practice, these values are taken from tables [6]. An extract is given in the following:

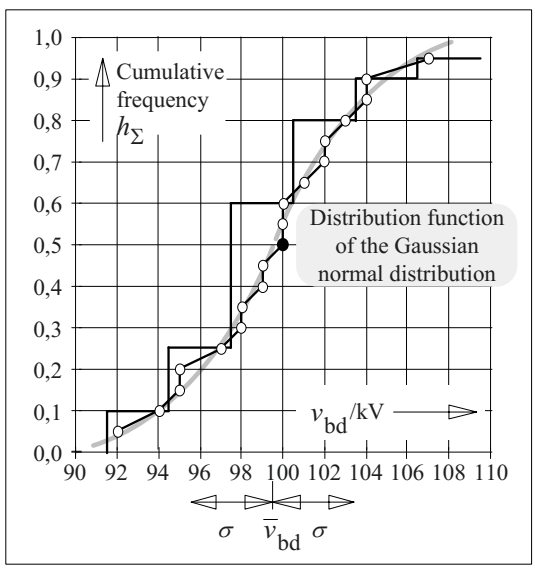

Figure 3.1-6: Comparison of an empirical distribution (cumulative frequency polygon) with a theoretical distribution function (Gaussian normal distribution).

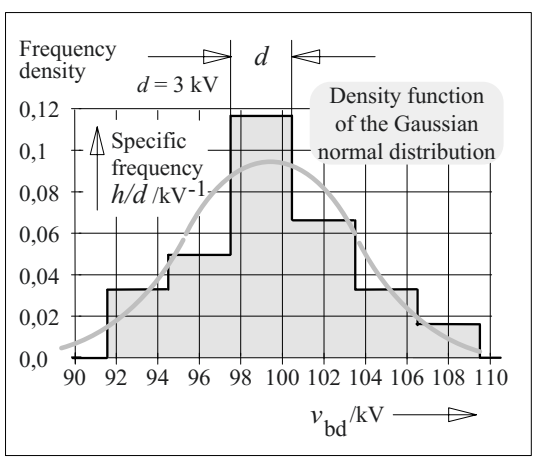

Figure 3.1-7: Comparison of the empirical density function (frequency density) with a theoretical density function (Gaussian normal distribution).

	x	$D(x)$	$F(x)$
x =	μ - 4.0·σ	0.0001/σ	0.00003
	μ - 3.5·σ	0.0009/σ	0.00023
	μ - 3.0·σ	0.0044/σ	0.00135
	μ - 2.5·σ	0.0175/σ	0.00621
	μ - 2.0·σ	0.0540/σ	0.0228
	μ - 1.5·σ	0.1295/σ	0.0668
	μ - 1.0·σ	0.2420/σ	0.1587
	μ - 0.5·σ	0.3521/σ	0.3085
x =	μ	0.3989/σ	0.5
x =	μ + 0.5·σ	0.3521/σ	0.6915
	μ + 1.0·σ	0.2420/σ	0.8413
	μ + 1.5·σ	0.1295/σ	0.9332
	μ + 2.0·σ	0.0540/σ	0.9772
	μ + 2.5·σ	0.0175/σ	0.99379
	μ + 3.0·σ	0.0044/σ	0.99865
	μ + 3.5·σ	0.0009/σ	0.99977
	μ + 4.0·σ	0.0001/σ	0.99997

By means of *parameter estimation* for μ and σ, the *theoretical normal distribution* is *fitted* to the empirical cumulative frequency polygon.

Example: Series of measurements
(continued from Section 3.1.1.4)

For the example treated in Section 3.1.1.4, the estimate for the expectation value is $\mu \approx x_\mathrm{m}$ = 99.47 kV and the estimate for the standard deviation is $\sigma \approx s$ = 3.82 kV. The corresponding distribution and density functions of the Gaussian normal distribution are compared with the empirical distribution and density functions, Figure 3.1-6 and -7.

If there is a sufficient *correspondence* (as in the case of the example) *between hypothesis and measurement*, i.e. between the Gaussian normal distribution and the cumulative frequency polygon, it is justified to calculate

probabilities by means of the theoretical distribution function.

In the case of $x = \mu - 3\sigma = 87.0$ kV for example, there is only a negligible breakdown probability of 0.13 %, i.e. this value can be considered as an estimate for the *withstand voltage* v_{bd0}. For $x = \mu + 3\sigma = 110.9$ kV, the breakdown probability is 99.87 %, therefore this value can be considered as a *definite breakdown voltage* v_{bd100}.

In a similar way, the question is answered, at which voltage a certain and given breakdown probability can be expected. An interpolation between given values (or percentages) of the cumulative distribution function in tables may have to be performed for this purpose.

Note: *Probability density functions* are derivatives of cumulative distribution functions. Therefore, they are more sensitive to variations, and they are less appropriate for a comparison between empirical and theoretical functions, Figure 3.1-7.

3.1.2.3 Weibull Distribution

The Weibull distribution is an *extreme value distribution* that is limited at the lower end. It is especially suitable for the description of breakdown processes, as it is normally assumed that there is a minimum breakdown voltage v_{bd0} (withstand voltage), i.e. a location parameter x_0 (lower extreme value, initial value), Figure 3.1-8.

The idea that a considered event (e.g. the breakdown of an arrangement with many parallel insulation gaps) occurs as the extreme value of all possible events (e.g. in the weakest insulation gap) gives an analytical expression for the *cumulative distribution function* [44]. It is valid for all values x that are higher than the initial value x_0 (e.g. the withstand voltage):

$$F(x) = 1 - e^{-\left\{\frac{x - x_0}{x_{63} - x_0}\right\}^{\delta}} \qquad (3.1\text{-}10)$$

With $x \le x_0$ we obtain $F(x) = 0$. The *probability density function* $D(x)$ is the derivative of the distribution function $F(x)$, Figure 3.1-8 (top).

Some special values of the *cumulative distribution function* $F(x)$ are calculated from Eq. (3.1-10):

Initial value (e.g. withstand voltage)	$x = x_0$	$F(x) = 0$
63 % quantile	$x = x_{63}$	$F(x) = 0.63$
End value (e.g. certain breakdown voltage)	$x = \infty$	$F(x) = 1$

The Weibull distribution can be described by the **three parameters** x_0 (*location parameter, initial value, lower extreme value*), x_{63} (*63 % quantile*) and δ (*Weibull exponent, shape parameter* or *slope*). Sometimes the difference $z_{63} = x_{63} - x_0$ is called the *scale parameter*. By means of the location, shape and scale parameters, the **three-parameter Weibull distribution** usually gives a good approximation of the cumulative frequency polygon for a se-

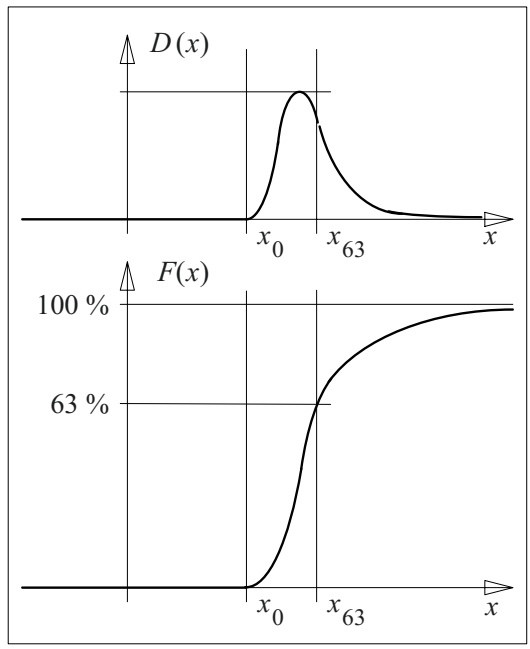

Figure 3.1-8: Weibull distribution with density function D(x) and distribution function F(x).

ries of measurements, see Figure 3.1-2 for example. Normally, the Weibull approximation is better than the approximation by the unlimited Gaussian normal distribution with two parameters.

An estimate for the *63 % quantile* can be taken directly from the cumulative frequency polygon. For example, from Figure 3.1-2 we obtain $x_{63} = v_{bd63} = 100.6$ kV by interpolation between the 0.6 and 0.65 values.

It would be an oversimplification to take the lowest value of the cumulative frequency polygon as an estimate for the *initial value* x_0 (e.g. $x_0 = 90$ kV from Figure 3.1-2). In practice, there is a very high *uncertainty* regarding such an estimation, especially for small sample sizes. In order to avoid incorrect conclusions, e.g. if a withstand voltage is to be determined, a smaller value must be chosen for x_0, which cannot be estimated accurately in most cases. Therefore, x_0 is very often set to zero ($x_0 = 0$). Thereby the cumulative distribution function is simplified to the **two-parameter Weibull distribution**, which cannot be adapted to empirical distributions as well as before.

The *Weibull exponent* δ can be estimated as the slope of a straight line in a log-log diagram. From Eq. (3.1-10) we obtain

$$-\left\{\frac{x - x_0}{x_{63} - x_0}\right\}^{\delta} = \ln\{1 - F(x)\} \ .$$

For the graphical representation in a *probability paper plot*, the common logarithm is calculated on both sides:

$$\delta \cdot \lg\left\{\frac{x - x_0}{x_{63} - x_0}\right\} = \lg\{-\ln[1 - F(x)]\}$$

With the transformations

$$\begin{aligned} z &= x - x_0 \\ z_{63} &= x_{63} - x_0 \ , \end{aligned} \qquad \text{(3.1-11)}$$

and

we obtain

$$\delta \cdot \lg\frac{z}{z_{63}} = \lg\left\{\ln\frac{1}{1 - F(x)}\right\} \ . \qquad \text{(3.1-12)}$$

Eq. (3.1-12) is the *equation of a straight line*, if the common logarithm on the right hand side is the ordinate value, the logarithm on the left hand side is the abscissa value and the Weibull exponent δ is the *gradient*.

In order to *establish a probability paper plot*, both logarithms are evaluated numerically, and this gives a probability grid for the Weibull distribution with logarithmically-subdivided axes, Figure 3.1-9:

Abscissa and		**ordinate subdivision**	
z/z_{63}	$\lg\{z/z_{63}\}$	$F(z)$	$\lg\{-\ln[1 - F(z)]\}$
0.1	- 1	0.01	- 1.998
0.2	- 0.699	0.02	- 1.695
0.3	- 0.523	0.05	- 1.290
0.4	- 0.398	0.1	- 0.977
0.5	- 0.301	0.2	- 0.651
0.6	- 0.222	0.3	- 0.448
0.7	- 0.155	0.4	- 0.292
0.8	- 0.097	0.5	- 0.159
0.9	- 0.046	0.6	- 0.038
1	0	0.7	0.081
2	0.301	0.8	0.207
3	0.477	0.9	0.362
4	0.602	0.99	0.663
5	0.699		
6	0.778		
7	0.845		
8	0.903		
9	0.954		
10	1		

Example: **Series of measurements** (continued)

The *cumulative frequency polygon* in Figure 3.1-2 and 3.1-6 shall be approximated by a *Weibull distribution function*.

For the *63 % value* (*quantile*), $x_{63} = v_{bd63} = 100.6$ kV is directly taken from Figure 3.1-9. An estimate must be found for the *initial value* x_0. For example, the withstand voltage $x_0 = 87.4$ kV, which was estimated by means of a Gaussian normal distribution, is taken for this purpose. Thereby we obtain

$$z = x - x_0 = x - 87.4 \text{ kV}$$

and

$$z_{63} = x_{63} - x_0 = 13.2 \text{ kV}.$$

Now the abscissa in Figure 3.1-9 can also be subdivided into voltage magnitudes:

x/kV	92	93	94	95	96	97	98
z/z_{63}	0.348	0.424	0.500	0.576	0.652	0.727	0.803
	99	100	101	102	103	104	105
	0.879	0.955	1.030	1.106	1.182	1.258	1.333
	106	107	108				
	1.409	1.485	1.561				

With the values from Figure 3.1-2, a cumulative frequency polygon is established, which can be approximated by a *best fit straight line*, Figure 3.1-9.

The *Weibull exponent* δ can be estimated from the straight-line gradient of an empirically determined distribution curve. For that purpose, the coordinates z_1 and z_2 for two points

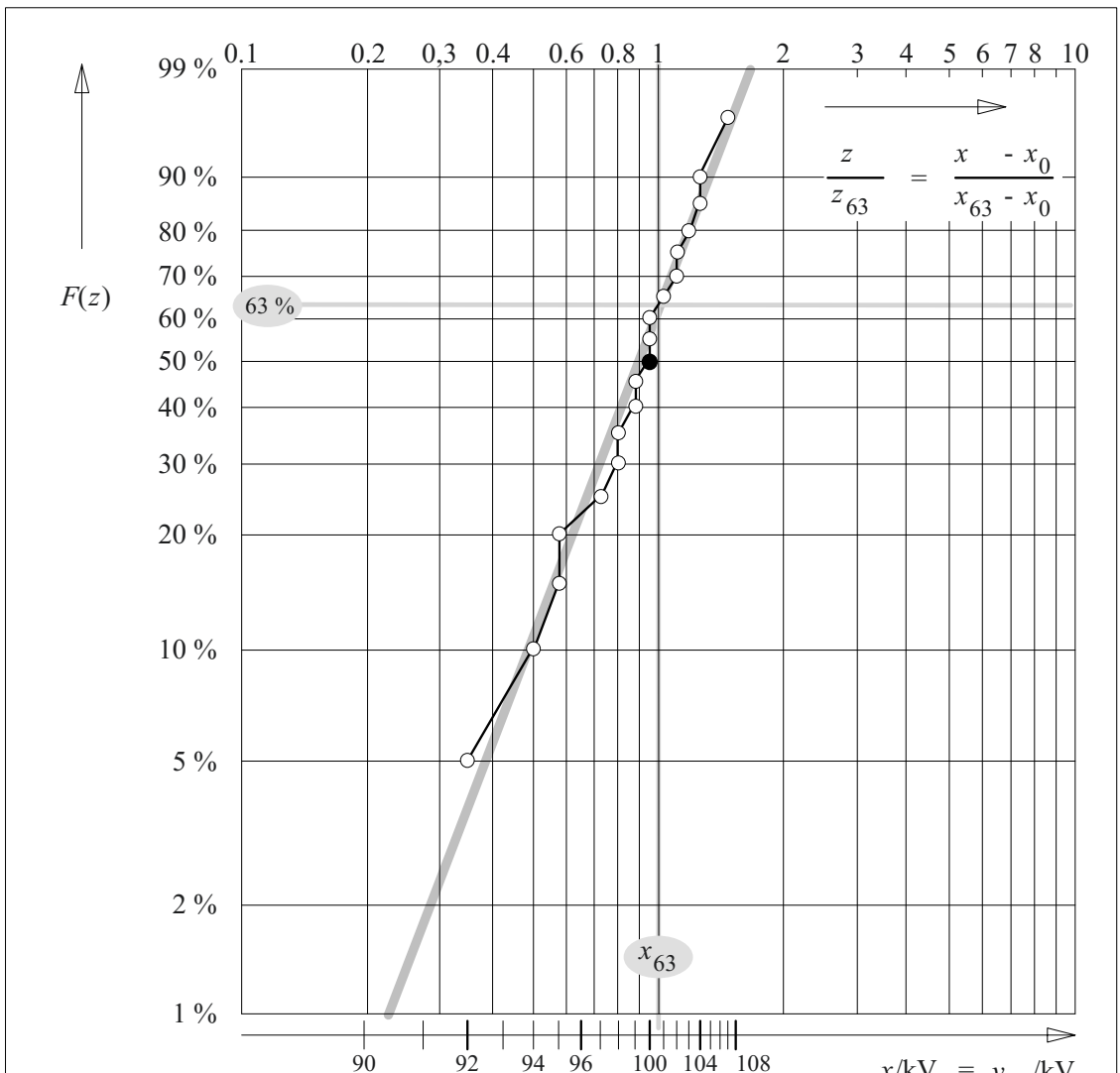

The abscissa with voltages is related to the example in the text only, it has to be calculated individually for every analysis. It is determined by the individual values for x_0 *and* x_{63}.

Figure 3.1-9: Probability paper plot for the Weibull distribution with logarithmic axes in a normalized representation (ordinate and upper abscissa).

Cumulative frequency polygon for the example in fig. Bild 3.1-2 together with an abscissa subdivided into voltage units that are related to the example (lower abscissa). Approximation of the empirical distribution in fig. 3.1-2 by a best fit straight line.

on the straight line are inserted into Eq. (3.1-12). From the difference of the two equations

$$\delta \cdot [\, \lg\frac{z_1}{z_{63}} - \lg\frac{z_2}{z_{63}} \,] = \lg \{ \ln \frac{1}{1 - F(z_1)} \} - \lg \{ \ln \frac{1}{1 - F(z_2)} \}$$

the exponent is calculated as:

$$\delta = \frac{\lg \{ \frac{\ln[1-F(z_1)]}{\ln[1-F(z_2)]} \}}{\lg \frac{z_1}{z_2}} \qquad (3.1\text{-}13)$$

For the **series of measurements** in the described **example** according to Figure 3.1-3 and -9, the function value at $z_1/z_{63} = 0.29$ is $F(z_1) = 2\ \% = 0.02$, and the function value at $z_2/z_{63} = 1$ is $F(z_2) = 63\ \% = 0.63$. With Eq. (3.1-13) the exponent is calculated:

$$\delta = 3.15$$

With this, *all parameters* of the Weibull distribution (x_0, x_{63} and δ) are estimated for the given example.

Note: From Eq. (3.1-11) and (-12) it can be seen that the magnitude of the exponent δ is strongly dependent on the definition of the initial value x_0. If x_0 is changed, a new determination of δ has to be performed.

3.1.2.4 Parameter Estimation

The Weibull distribution and the Gaussian normal distribution are extraordinarily important in high voltage engineering. Nevertheless, they are only discussed as examples. There are a number of other distributions which are used in high voltage engineering (e.g. lognormal distribution, double-exponential distribution, Wohlmuth's two-limit distribution, gamma distribution, χ^2- /chi-squared distribution, *F*- /Fisher distribution, *t*- /Student distribution, and mixed distributions). Deeper discussions can be found in the literature [44], [396].

The parameters for the description of the different cumulative distribution functions have to be estimated from measured values. Examples are given in Section 3.1.1.3 and in the two preceding sections. In these cases, parameters were determined by graphical approximation of straight lines for example. Furthermore, there are a number of **statistical estimation techniques** that will be at least briefly mentioned here:

(1) Parameters can be estimated by **graphical approximation -** see above for examples.

(2) Parameters can be estimated by calculation of **empirical moments** as estimates for theoretical moments (method of moments). In this context, the measures of mean values according to Eq. (3.1-2) are *moments of first order and* the measures of statistical dispersion according to Eq. (3.1-4) and (-5) are *moments of second order*.

(3) Parameters can be estimated with the **maximum likelihood method** in such a way that the probability of the statistical sample is maximal.

(4) The **least square method** provides parameters with the minimal root-mean-square deviation.

These methods and the methods of **interval estimation** require thorough analyses of the mathematical fundamentals of statistics, which cannot be given here [44], [396].

3.1.3 Statistical Size Effects

It is a problem of high voltage engineering that breakdown voltages, breakdown strengths and lifetimes are normally determined with *small* laboratory test samples, with a small number of test objects, or during only short test durations. Then, these results have to be transferred to insulations of *large size*, to a *large number* of objects or to very *long stress durations*.

According to **experience**, electric strengths (e.g. the 50 % breakdown voltage) decrease if the size of the arrangements, the number of test objects, or the stress duration is "enlarged" (*law of enlargement*), for example:

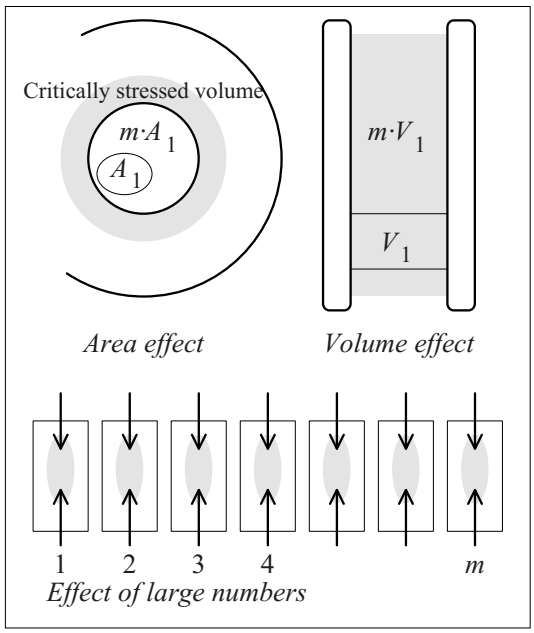

Figure 3.1-10: Size effects for the examples of area effect, volume effect and large-number effect, with grey-colored critically stressed insulation volumes.

- with increasing insulation volume, area, distance or length (*volume, area, distance or length effects*),
- with increasing number of equal test objects (*Large-number effect*) and
- with increasing stress duration (*time effect, lifetime characteristic*).

For a statistical explanation of these strength reductions, the insulation arrangement must be *subdivided into smaller parts*, which can be subject to breakdowns *independently from each other*, and which have a known cumulative distribution function (e.g. from experiments).

The condition of stochastical independence is not always fulfilled, e.g. for the *time effect*. Insulations that break down after different stress durations are *not equal* in terms of statistics. They are differently aged by time-dependent chemical and physical processes. For most of the solid and liquid dielectrics, there is a *functional dependence* of the electric strength on the stress duration, additional to the statistical dispersion. Only in the range of very short stress durations does the accidental presence of a free start electron influence the magnitude of the breakdown voltage (or field strength).

Statistical volume, area, distance and length effects are based on the fact that a breakdown needs a *highly stressed insulation volume*.

In *strongly non-uniform fields*, a critically stressed volume can only be found in a thin layer close to the curved electrode, Figure 3-1-10. If the arrangement is enlarged, primarily the enlargement of the *electrode surface area* adjacent to the high-field volume has to be considered (area effect). Insulation defects reduce the electric strength only if they are close to the electrode surface.

In *uniform* and *weakly non-uniform fields*, the whole (critically stressed) *insulation volume* has to be considered, if the arrangement is enlarged (volume effect), Figure 3.1-10. Insulation defects reduce the electric strength throughout the dielectric volume.

Highly stressed areas, volumes and parallel test objects shall each be considered as "parallel connections" of *m equal and independent elements* (area elements, volume elements or test objects), Figure 3.1-11. It will be assumed

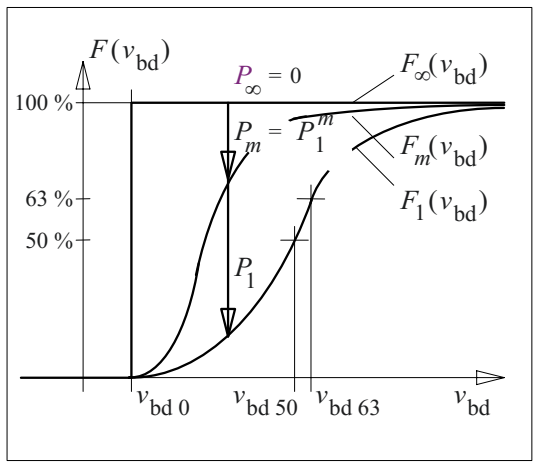

Figure 3.1-11: Statistical size effect for the parallel operation of m equal and independent elements described by a distribution function with a lower limit (e.g. Weibull distribution).

that the cumulative distribution function $F_1(v_{bd})$ for the breakdown voltage of a single element (index 1) is known (**breakdown probability**). The cumulative distribution function $F_m(v_{bd})$ for the breakdown voltage of m parallel elements (index m) will be calculated.

The **withstand probability** P_1 for a single element 1 (probability that a breakdown *does not occur*) is considered:

$$P_1(v_{bd}) = 1 - F_1(v_{bd}) \qquad (3.1\text{-}14)$$

If a number of equal elements are equally stressed, the withstand probability P_m decreases. It can be calculated by *multiplication of the individual probabilities* of the elements:

$$\begin{aligned} P_m &= P_1 \cdot P_1 \cdot P_1 \cdot P_1 \cdot \ldots\ldots \cdot P_1 \\ &= [1 - F_1(v_{bd})] \cdot [1 - F_1(v_{bd})] \cdot \ldots\ldots \\ &\qquad \ldots\ldots \cdot [1 - F_1(v_{bd})] \\ &= [1 - F_1(v_{bd})]^m \qquad (3.1\text{-}15) \end{aligned}$$

Note: For $m \to \infty$, the withstand probability P_m approaches zero, i.e. the breakdown becomes certain, but only if the voltage is above the initial value v_{bd0}, Figure 3.1-11. Below this value, a breakdown cannot occur ("single-point distribution"). Therefore, a correct determination of the *initial value* v_{bd0} is highly desirable, especially in the range of low breakdown probabilities.

In the *range of low breakdown probabilities* $F_1(v_{bd}) << 1$, Eq. (3.1-15) can be expanded into a series, which is cut off after the first-order summand:

$$P_m(v_{bd}) \approx 1 - m \cdot F_1(v_{bd}) \qquad (3.1\text{-}16)$$

With this the breakdown probability of m parallel elements is

$$\begin{aligned} F_m(v_{bd}) &= 1 - P_m(v_{bd}) \\ &\approx m \cdot F_1(v_{bd}) \,. \qquad (3.1\text{-}17) \end{aligned}$$

Example: Capacitor bank

A capacitor bank is made of 40 capacitors with an individual breakdown probability $F_1(10\ \text{kV}) = 0.1\ \%$ at the charging voltage $V = 10$ kV. For a parallel operation of the capacitors, a breakdown probability $F_{40}(10\ \text{kV}) \approx 40 \cdot 0.1\ \% = 4\ \%$ is to be expected. This is an unacceptably high value for equipment which is destroyed during a breakdown. Therefore, the charging voltage must not be raised above a safe withstand voltage V_{bd0}.

Statistical size effects mainly result in a *reduction* of the 50 % and the 63 % **breakdown voltages**, fig, 3.1-11. This reduction can be calculated for the Weibull distribution according to Eq. (3.1-10). With Eq. (3.1-15) the withstand probability is

$$\begin{aligned} P_m(v_d) &= \left[e^{-\left\{ \frac{v_{bd} - v_{bd\,0}}{v_{bd\,63} - v_{bd\,0}} \right\}^{\delta}} \right]^m \\ &= e^{-m \cdot \left\{ \frac{v_{bd} - v_{bd\,0}}{v_{bd\,63} - v_{bd\,0}} \right\}^{\delta}} \,. \qquad (3.1\text{-}18) \end{aligned}$$

The further discussion is especially clear if a *two-parameter Weibull distribution* with $v_{bd0} = 0$ is taken as an approximation. If there is an error for small probabilities, it has no importance in the range of mean probabilities.

For the *changes of a breakdown voltage* (e.g. v_{bd50} or v_{bd63}) from $v_{bd(1)}$ (one element) to $v_{bd(m)}$ (m elements) the associated withstand probabilities are equal:

$$P_1(v_{bd(1)}) = P_m(v_{bd(m)})$$

This condition can only be fulfilled if the exponents according to Eq. (3.1-18) are equal. With $v_{bd0} = 0$ we find

$$\left\{ \frac{v_{bd\,(1)}}{v_{bd\,63}} \right\}^{\delta} = m \cdot \left\{ \frac{v_{bd\,(m)}}{v_{bd\,63}} \right\}^{\delta}$$

and

$$\frac{1}{m} = \left\{ \frac{v_{bd\,(m)}}{v_{bd\,(1)}} \right\}^{\delta} .$$

Now, the *statistical size effect* for m parallel elements can be described:

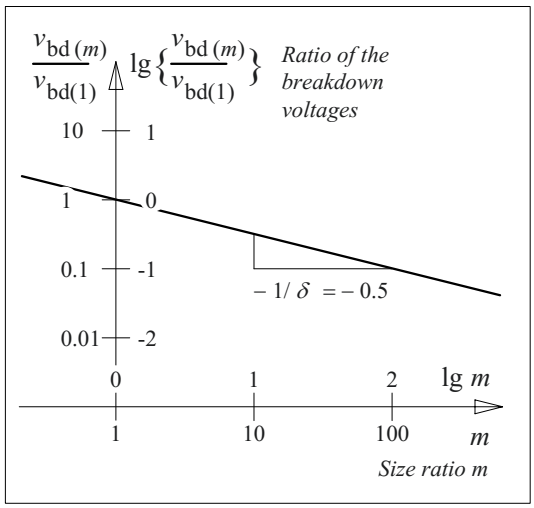

Figure 3.1-12: Statistical size effects in a log-log diagram. The gradient of the straight line is an example here.

$$\frac{v_{bd(m)}}{v_{bd(1)}} = \left\{\frac{1}{m}\right\}^{\frac{1}{\delta}} \qquad (3.1\text{-}19)$$

In a log-log diagram, $1/\delta$ can be considered as the gradient of a falling straight line, Figure 3.1-12:

$$\lg\left\{\frac{v_{bd(m)}}{v_{bd(1)}}\right\} = -\frac{1}{\delta}\cdot\lg\{m\} \qquad (3.1\text{-}20)$$

In the case of *parallel elements*, m is the number. In the case of the *volume effect*, m is the ratio of the considered volumes:

$$m = V_m/V_1 \qquad (3.1\text{-}20a)$$

In the case of the *area effect*, m is the ratio of the areas

$$m = A_m/A_1 \qquad (3.1\text{-}20b)$$

Example: Series of measurements (continued)

The *statistical size effect* shall be determined for the arrangement described by the cumulative frequency polygon according to Figure 3.1-3a.

At first, the Weibull exponent δ for a two-parameter distribution with $v_{bd0} = 0$ has to be determined from the measured values by means of Eq. (3.1-13). For the two function points $F(z_1)$ and $F(z_2)$, the function values $F(100.6\text{ kV}) = 63\ \%$ and $F(94\text{ kV}) = 10\ \%$ are selected from the cumulative frequency polygon in Figure 3.1-3a. According to Eq. (3.1-11), the abscissa values z to be used are identical with the breakdown voltages v_{bd} because of the condition $x_0 = v_{bd0} = 0$. Then, Eq. (3.1-13) gives the *exponent*

$$\delta = 33.$$

It differs significantly from the exponent determined for a three-parameter distribution (see example according to Eq. (3.1-13)). The *gradient of the straight line* in a log-log diagram according to fig, 3.1-12 is given by

$$-1/\delta = -0.03.$$

For a size ratio $m = 100$ a *strength reduction* down to 87 % is calculated from Eq. (3.1-19). This means that v_{bd63} would be reduced from 100.6 kV to 87.6 kV. For v_{bd50}, a reduction from 99.3 kV to approximately 86.5 kV would occur.

The example clearly shows that *significant strength reductions* sometimes have to be taken into account during the transfer of test results from the laboratory-test scale to *much bigger real insulations*.

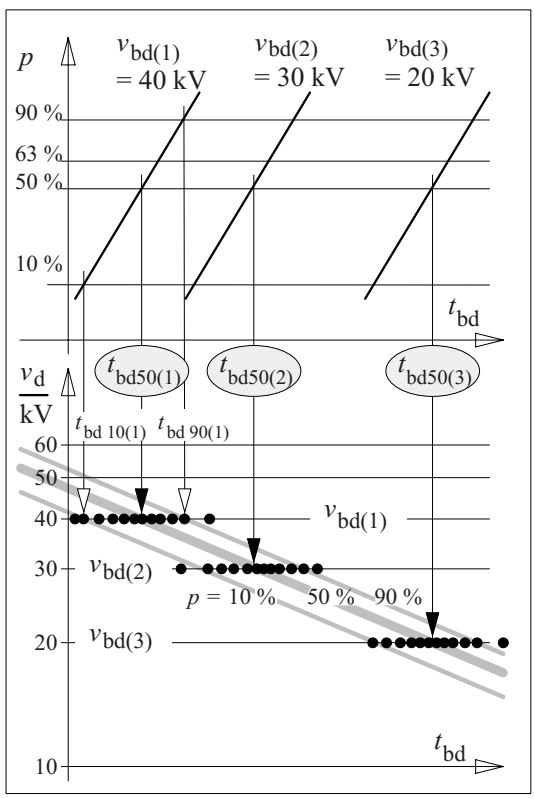

Figure 3.1-13: Constant-voltage tests with randomly distributed breakdown times (top) for the determination of a lifetime stress relationship in a log-log diagram (bottom).

Note: More accurate values for the Weibull exponent can be derived from the gradient of the straight line in a *probability graph paper*, Figure 3.1-9. The *mean straight line* averages between all given points and avoids the error which results from the deviation of the chosen points from the theoretical distribution function.

Example: Cable run

The *50 % breakdown voltage* of a 1 km long *cable run* shall be estimated. In laboratory tests on short cable lengths (10 cm and 3 m), v_{bd50} was determined (92 kV and 83 kV).

If a two-parameter Weibull distribution with $v_0 = 0$ is assumed, the statistical size effects can be described by Eq. (3.1-20). The size ratio m can either be calculated from the inner conductor surface or from the insulation volume. In both cases, it is equal to the ratio of the lengths. With m = 3 m/0.1 m = 30 and with the voltage ratio 83 kV/92 kV = 0.902, the gradient is $1/\delta = 0.0303$ or $\delta = 33$ respectively.

According to Eq. (3.1-19), the **extrapolation** for the cable length of 1 km (m = 1000 m/3 m = 333) gives the voltage ratio 0.839. Therefore, the 50 % breakdown voltage is

$$v_{bd50} = 0.839 \cdot 83 \text{ kV} = 69.6 \text{ kV}.$$

3.1.4 Correlation and Regression, Lifetime-stress Relationship

It was already mentioned in Section 3.1.3 that both *statistical dispersion* and *functional dependences* can influence measured values at the same time.

Example: Lifetime-stress relationship

The times to breakdown are determined by constant-voltage tests, Figure 3.1-1d. In addition to the statistical dispersion, there is a distinct change of the time to breakdown as a function of the voltage magnitude in solids (lifetime stress relationship/ characteristic).

Example: Impulse voltage-time characteristic

Another example is the determination of impulse voltage-time curves for gas discharge gaps, Figure 3.1-1c). Also in this case, there is a functional dependence between the peak value of the impulse voltage and the time to breakdown.

The simplest method of testing for a *functional relationship* of two random variables X and Y (e.g. of peak voltage and time to breakdown) is a *graphical representation*. It is often possible to draw a *best-fit curve* or a mean straight line (**regression curve**) by eye through the measured points (x_i, y_i) or (u_i, t_i), Figure 3.1-1c) and d). Thereby, the *central value* (*median*) is shown, i.e. the 50 % time to breakdown t_{bd50} for the examples mentioned above.

By this method, all kinds of measured values can be tested for a functional relationship. Often, the question has to be answered, if a quantity depends on a *parameter*, e.g. the time to breakdown on the peak voltage, the breakdown voltage on the gas pressure and so on. It can also be investigated, for example, whether different electric test methods give comparable results, i.e. it could be investigated whether there is a relationship between partial discharge inception voltages and impulse breakdown voltages for a given type of test objects.

A *more objective method* consists in the determination of the distribution function of the random variable (e.g. of the time to breakdown t_{bd}) for different values of a parameter (e.g. for different voltage stresses v_{bd}). From the determined points for a given breakdown probability (e.g. 10 %, 50 % and 90 % quantiles), the related best-fit curves can be calculated as approximations for the corresponding breakdown probabilities. The method shall be explained for a lifetime stress relationship, Figure 3.1-13:

Example:
Lifetime stress relationship, ageing

The properties of solid insulating polymers can change with time under the influence of electric stress. Normally, the *electric strength decreases* with the stress duration. According to experience, the *lifetime stress relationship* can be approximated by the proportionality

$$v_{bd}/v_0 \sim (t_{bd}/t_0)^{-1/k}, \qquad (3.1\text{-}21)$$

if the physicochemical process of ageing does not change during the considered time. The quantities v_0 and t_0 are reference constants and k is the *"lifetime exponent"*. In a log-log dia-

gram, Eq. (3.1-21) is a straight line (*life characteristic*) with the gradient -1/*k*:

$$\lg (v_{bd}/v_0) = (-1/k)\cdot\lg (t_{bd}/t_0) + K \quad (3.1\text{-}22)$$

The experimental determination of a lifetime stress curve is performed by constant-voltage tests, Figure 3.1-13. For each of the voltage levels $v_{bd(1)}$, $v_{bd(2)}$, $v_{bd(3)}$, ..., a larger number of test objects is stressed by the constant voltage until the breakdowns occur. Thereby a distribution of the *time to breakdown* t_{bd} is related to a voltage level. The distribution is described either by the (empirical) cumulative frequency polygon or by the deduced (theoretical) cumulative distribution function, Figure 3.1-3 (top). Very often, the two-parameter Weibull distribution gives a good fit.

The graphical representation of the 50 % time to breakdown in a voltage time diagram gives the lifetime stress curve for a breakdown probability of 50 %. The curves for other breakdown probabilities (e.g. for 10 % and 90 %, see Figure 3.1-13) can be determined in similar fashion.

Note: Typical values for the **lifetime exponent** k are of the order of $k \approx 9$ (for polyethylene) and $k \approx 13$ (for filled epoxy resin), and k is mainly dependent on the material [44]. The other quantities in the lifetime equation (3.1-22) are also strongly influenced by the test arrangement.

Note: Very often, insulations have to be designed for a lifetime of decades with very low breakdown probabilities. Generally, *lifetime stress relationships for very low breakdown probabilities* (e.g. 0.1 %) can be calculated by means of theoretical distribution functions according to Figure 3.1-13. Nevertheless, there is a significant danger of misleading conclusions:

- In the case of a small sample size, the *type of the distribution function* and the magnitude of their parameters are very often not known with sufficient accuracy.
- In the course of time, the ageing processes can change which will result in a different magnitude of the *lifetime exponent k*. This means that the gradient of the lifetime curve can change.
- Results obtained on *small test objects* within short times and under well-defined conditions can only be transferred to *large and permanently stressed insulations* with a high degree of uncertainty.

For practical applications, very large “safety margins” have to be considered with respect to the lifetime stress curve. ‘This means that the design stresses are chosen far below the stresses which seem possible according to the lifetime stress curve.

In the case of high statistical dispersion of the measured values and in the case of weak functional relationships, it is often *no longer sufficient* to recognize relationships **“by visual evidence”** only and to draw a best-fit curve. Therefore, mathematical **correlation analysis** is used in order to determine a functional relationship between the random variables X and Y (e.g. breakdown voltage and time to breakdown) from the given pairs of measured values (x_i, y_i). From the given values x_i and y_i, empirical variances, standard deviations s_x and s_y according to Eq. (3.1-5) and an empirical **covariance**

$$s_{xy} = \frac{1}{n-1}\cdot\sum_{i=1}^{n}(x_i - x_m)\cdot(y_i - y_m) \quad (3.1\text{-}23)$$

are calculated. The combination of these quantities gives the empirical *correlation coefficient*

$$r = s_{xy}/(s_x s_y)\,, \quad (3.1\text{-}24)$$

which is a measure of the intensity of the correlation. If $r = 0$ it is concluded that there is no correlation *and* $r = \pm 1$ indicates complete correlation.

The description of the functional relationship is performed by **regression analysis**. In the

simplest case of a linear coupling (linear regression), the coefficients of a *regression line*

$$y = a_{yx} + b_{yx}x \quad \text{or} \quad x = a_{xy} + b_{xy}y \tag{3.1-25}$$

are determined in such a way that the sum of

vertical y- or horizontal x-

deviations are minimal.

y and x or x and y

are *the dependent* and *the independent variables*. The *regression coefficient b* is

$$b_{yx} = r \cdot s_y/s_x \quad \text{or} \quad b_{xy} = r \cdot s_x/s_y \tag{3.1-26}$$

and the *location coefficient a* is given by

$$a_{yx} = y_m - b_{yx}x_m \quad \text{or} \quad a_{xy} = x_m - b_{xy}y_m. \tag{3.1-27}$$

The two cases with x or y as the independent parameter provide different straight lines. They are orthogonal to each other if the variables are not correlated ($r = 0$). In the case of complete correlation ($r = \pm 1$) the two straight lines are identical [6], [44].

3.2 Gas Discharges

At low field strengths and in comparison with other insulating materials, gases are *very good dielectrics* with low *losses*, low *conductivity* and a nearly frequency-independent relative *permittivity* $\varepsilon_r \approx 1$. Therefore, gases are the "natural" insulating material, especially if the ambient air is considered. Liquid and solid materials are necessary if the electric strength of the gas is not sufficient.

Unfortunately, gases generally have a significantly *lower electric strength* than solids and liquids. Under specific stress conditions, characteristic discharge processes (gas discharges) occur. This means that the relationship between current and voltage becomes non-linear (gas discharge characteristic, Section 3.2.1).

In comparison with solid and liquid dielectrics, gases have very well defined physical properties. Therefore, it is possible to develop a physical model for the mathematical description of the breakdown voltage in the case of a homogeneous and almost space-charge-free field (Paschen's law, Section 3.2.2).

Furthermore, space-charge-dominated discharges (streamer discharges, Section 3.2.3), impulse voltage-time curves (Section 3.2.4), discharges in non-uniform fields (Section 3.2.5), surface discharges (Section 3.2.6) and high-current discharges (Section 3.2.7) are of special interest.

3.2.1 Gas Discharge Characteristics

3.2.1.1 Non-self-sustained and Self-sustaining Discharge

At low electric field strengths, the current across the gap is proportional to the applied voltage ("ohmic region"), Figure 3.2-1. Free charge carriers in the gas, i.e. negative electrons and positive ions, are generated by radiation (*photoionization*, e.g. by cosmic radiation or UV light) and by collisions because of the thermal motion of the gas molecules or atoms (*thermal ionization*). Negative ions can be generated by the attachment of electrons to molecules or atoms. The number of free charge carriers is determined by the equilibrium between *generation* and *recombination* [25]. The current through the gas is very small and *does not* generate additional charge carriers. The discharge is therefore called **non-self-sustained**.

With increasing field strength, the current increases and reaches a saturation value, when all generated charge carriers are extracted by the electric field before they can recombine. The *saturation current density* is negligibly small [25] and it is approximately

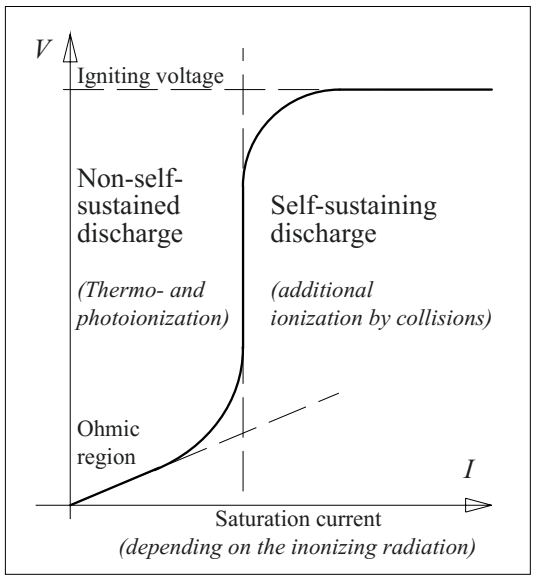

Figure 3.2-1: Gas discharge characteristic in the transition region between non-self sustained and self-sustaining discharge (schematic).

$$J_{sat} \approx 10^{-18}\ \mathrm{A/cm^2} \qquad (3.2\text{-}1)$$

But it can be increased by many orders of magnitude by ionizing radiation, see Section 4.2.2.1.

With further increasing voltages and field strengths, the charge carriers are accelerated by the electric field, and they can gather enough kinetic energy within a free path length to generate a significant number of charge carriers by collisions (*ionization by collisions, collision ionization* or *impact ionization*). Thus, the charge carriers are generated by the discharge itself, and this is known as **self-sustaining**, Figure 3.2-1.

3.2.1.2 Gas Discharge Characteristic, Operating Points

The additional charge carriers, which are generated by collision ionization, cause an increase of the current at a nearly constant voltage. This voltage is known as the *ignition voltage*.

If the ignition voltage is reached in a *uniform field* and in a *low-resistance circuit*, then the current increases very significantly and the voltage breaks down. In this case, the *breakdown voltage* V_{bd} equals the *ignition voltage* V_z.

In a circuit with *current limiting* (by a resistance or by the weak-field region of a strongly non-uniform field) there are stable discharges if the ignition voltage is reached, but the voltage does not break down. Owing to the glowing light emission, these *pre-discharges* or *partial discharges* are known as *glow discharges* or *corona discharges*. In this case, the *inception voltage* V_i for pre-discharges or partial discharges equals the *ignition voltage* V_z.

The highly non-linear functional relationship of current and voltage in a gas discharge gap is described by the so-called **gas discharge characteristic** for a *quasi-uniform field*. As the currents and voltages vary over many orders of magnitude, a log-log diagram is chosen, Figure 3.2-2.

If a rising voltage reaches the ignition voltage , collision ionization causes significantly increasing currents without any further increase of the voltage. In the beginning, the generated space charges are weak and do not yet influence the electric field strength in a uniform field. This *space-charge-free* situation is known as a *Townsend discharge*.

A strong increase of the current causes space charges that cause strong field distortions (*space-charge-dominated discharge*). Thereby, there is a further increase of the current, even for a decreasing voltage. In this region, the emission of light related to collision and recombination processes becomes so intense that it is visible for the human eyes as a glowing light phenomenon (*glow discharge*, *corona discharge*).

For very high currents, the generation of charge carriers is determined by the ohmic losses (Joule heat) in the discharge gap. This

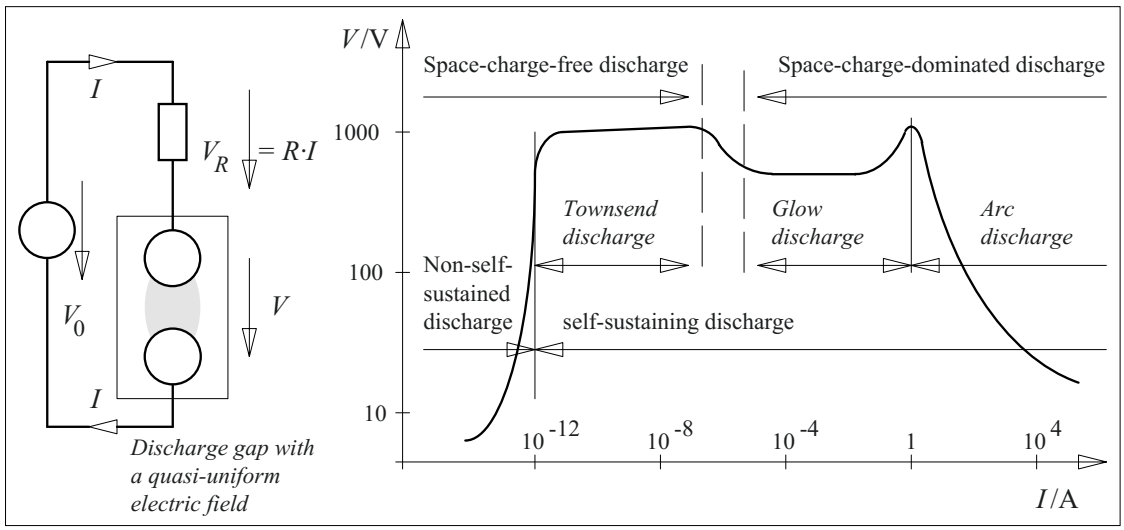

Figure 3.2-2: V,I gas discharge characteristic in a log-log diagram for one example (schematic).

means that *thermal ionization* causes the generation of many charge carriers and a very conductive gas plasma is generated. Thus, a small voltage is sufficient to drive a high discharge current. This situation is known as an *arc discharge*, which is characterized by intense light emission and (sometimes) by a curved and fluttering shape of the *"electric arc"*. The exact *V,I*-characteristic is derived from the thermal equilibrium between the generated Joule heat $P_{gen} = V \cdot I$ and the heat transfer P_{trans} to the environment by convection, radiation and heat conduction:

$$V \cdot I = P_{trans} \qquad (3.2\text{-}2)$$

The type **of discharge** depends on the *source voltage* and on the *resistance* of the whole circuit. The *working point* on the gas discharge characteristic can be determined by means of resistance lines, Figure 3.2-3a. For three working points (1, 2 and 3), the voltage drop at the resistance $V_R = R \cdot I$ and the voltage required by the discharge gap V is covered by the source voltage V_0, Figure 3.2-2 (left) and 3.2-3a.

If the *sum* of the two voltages is smaller or greater than the source voltage, there is an increase or decrease of the current I because of the voltage difference. This shows that a shift away from working points 1 and 3 causes a current change, which leads the system back to the former working point. It is therefore *stable*. A shift away from working point 2 causes a current change leading away further and further. Therefore, working point 2 is *unstable*.

Different working points on the gas discharge characteristic can be set by a variation of the source voltage V_0, Figure 3.2-3b. The related *shifting* of the resistance line determines the working points.

The saturation current is flowing during the *increase of the source voltage* V_0 and below the ignition voltage (WP 1). If the ignition voltage is reached a stable glow discharge develops (WP 2). The discharge intensity increases with increasing source voltage (WP 3). Finally, there is the transition to the arc discharge with a very high current and a small arc voltage (WP 4). Most of the source voltage drop occurs across the external series resistance R.

The marked working points are passed in the order 4, 5, 6 and 7 while *the source voltage* V_0 *is decreasing*.

Note: Different working points can also be set at constant source voltage by *varying the series resistance R*. This variation can be illus-

trated in Figure 3.2-3a/b by resistance lines with different gradients.

Note: The drawing of resistance *lines* in Figure 3.2-3a and -3b assumes that the current and voltage axes are linearly scaled. Then, the initial processes on the gas discharge curve are "compressed" at very low current values. This is not shown here in order to preserve the clarity of Figures 2.2-3a and -3b, which are *schematic sketches* only and *without any quantitative scale*.

3.2.1.3 Manifestations of Gas Discharges

Basically, gas discharges are subdivided into **pre-discharges** that do not directly cause a breakdown and **breakdowns** or **flashovers** that bridge the entire insulation gap with a conductive channel, resulting in a "break down" of the voltage, Figure 3.2-4.

In a **uniform** or a **weakly non-uniform field**, the breakdown of the voltage takes place immediately after the ignition voltage is reached, see Section 3.2.2. Pre-discharges do not occur, Figure 3.2-4.

A stable *glow discharge* (instead of an arc or spark discharge) can only be achieved if the discharge current is limited by a sufficiently high series resistance (see gas discharge characteristic, Figure 3.2-3a, Section 3.2.1.2).

Note: The manifestations of such a **glow discharge** depend on many parameters (type of gas, pressure, impurities, vessel dimensions, electrode material, voltage, and series resistance). At low pressures and at low currents, there are different zones with characteristic *luminous effects*, Figure 3.2-5 (right). The discharge conditions are discussed between cathode and anode: Directly at the cathode there is the *Aston dark space*, followed by the *cathode glow,* caused by the recombination of incident ions and electrons emitted from the cathode. Then there is the *cathode dark space* (*Hittorf / Crookes dark space*), where the electrons are not yet accelerated enough for collision ionization processes. These ionization processes occur after a longer distance from the cathode and cause the *negative glow*. The generated electrons are quickly removed by the field, and inertial ions remain as positive space charges. This causes a high field strength and a steep potential gradient near the cathode (*cathode fall*, Figure 3.2-5 left). The following discharge volume has a low field strength, and it is close to the positive anode potential (*positive column*). Therefore, the ionization probability is low (*Faraday dark space*). The electrons have to accumulate energy for collision ionizations along long paths, which can sometimes be identified by a regular structure of the luminous effects. Close to the anode, electrons can ionize attached gas molecules (*anode glow*). Attached electrons cause a minor negative space

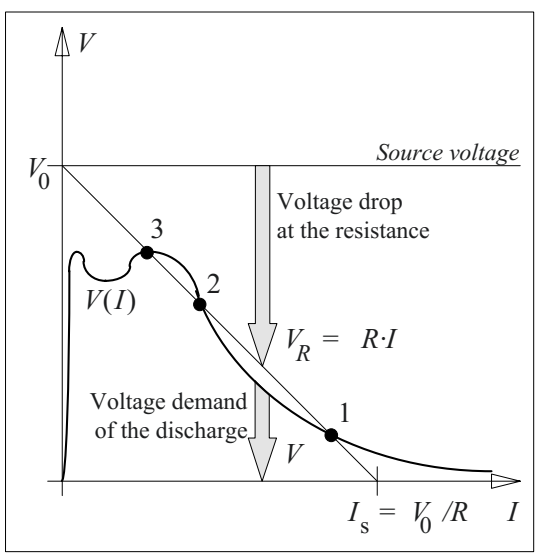

Figure 3.2-3a: Possible working points in the points of intersection between gas discharge characteristic and resistance line (linear diagram, schematic):

(1) stable, (2) instable and (3) stable working point.

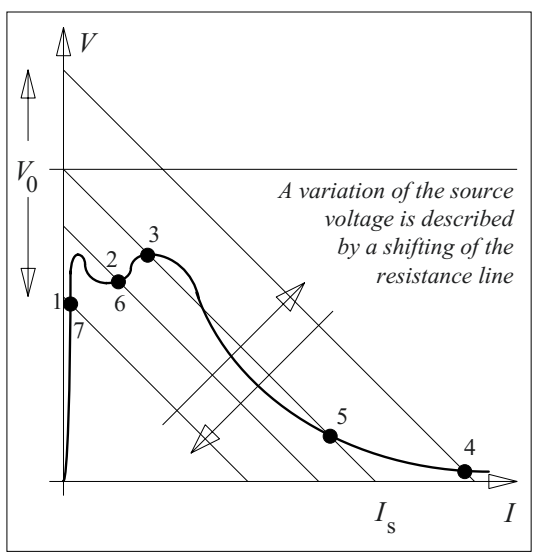

Figure 3.2-3b: Shifting of the working points along the gas discharge characterisic during the increasing of the source voltage (1,2,3 and 4) and during the decreasing of the source voltage (4, 5, 6 and 7) by the shifting of the resistance line.

charge, which is accompanied by a slightly enhanced voltage drop (*anode fall*).

Note: If the distance of the electrodes is reduced to a gap width smaller than the cathode dark space, a gas discharge is no longer possible, i.e. the electrons cannot accumulate enough energy for collision ionization. In terms of high voltage engineering, this is the region of *vacuum insulation*, where a gas discharge is no longer possible according to gas breakdown theory (*Paschen's law*, Figure 3.2-13). Then, so-called *vacuum breakdowns* occur in a *metal vapour plasma*, Section 3.7.

Note: The described luminous effects are more important for *lighting technology* than for high voltage technology, in which one normally seeks to avoid discharges completely [25].

High-current discharges at low operating voltages are known as *arc discharges* if the source provides a constant power and if there is a stationary thermal equilibrium. If the energy content of the source is limited (e.g. in the case of a charged capacitor, or in the case of the so-called *"electrostatic discharges"*) we refer to as *spark discharge*, which is characterized by a transient current impulse. *Atmospheric discharges* (*lightning*) can be considered as a special case of very long sparks (see Section 3.2.7).

In a strongly **non-uniform field**, the ignition condition for gas discharges is reached (during the rise of the test voltage) in a very small and highly stressed field volume at first, directly adjacent to the acutely curved electrode contour, fig 3.2-4. Therefore, these early discharges cannot propagate over the whole gap width as in a uniform field. *Pre-discharges* or

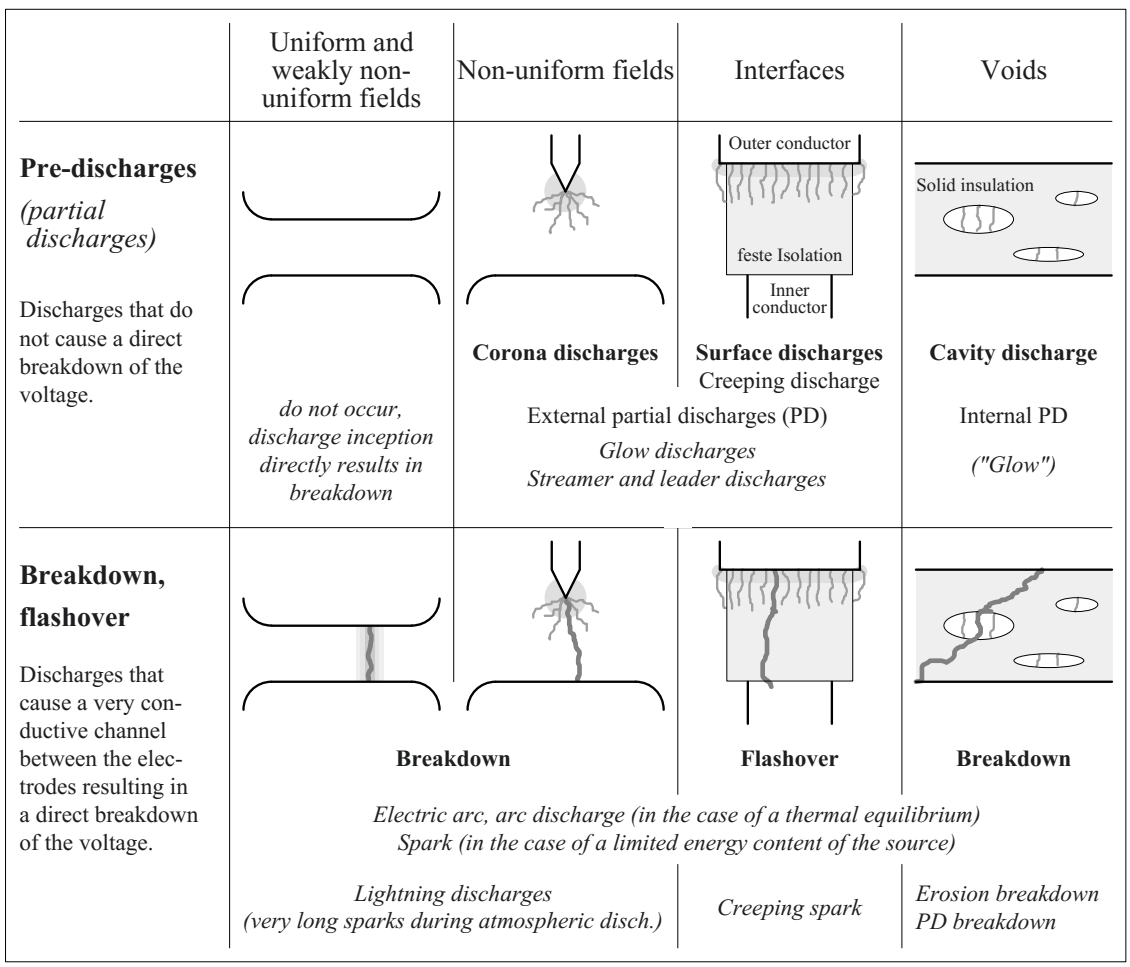

Figure 3.2-4: Important manifestations of gas discharges: Overview and the use terms.

corona discharges occur. Tips, edges and conductors with small radii are surrounded by visible luminous effects ("corona").

Visible *corona discharges* start with a uniform *glow discharge* (Townsend mechanism). Further increasing voltages cause the inception and growth of *streamers and leaders*.

Finally, the *breakdown* of the whole insulation gap takes place and an arc or a spark discharge occurs.

Also in arrangements with **interfaces** between gas and solid insulation, there can be pre-discharges, if the electric field strength is not constant along the interface, Figure 3.2-4. Such arrangements arise for cable terminations with stripped end insulation, for an insulated conductor fed through a grounded wall or for an electrode placed on the surface of an insulating plate. In these cases, the electrically strong insulating material prevents a direct breakdown between the conductors. Instead, the discharge is forced to develop as a *guided gas discharge* along the surface of the dielectric. Therefore, the arrangement is known as a *creepage surface* or *creepage configuration*, and the discharges are *creeping discharges* or *surface discharges* respectively. Normally, they start as glow discharges at a highly stressed electrode edge or in a highly stressed gas-filled interstice (see Figure 2.4-18) and they develop as *guided gas discharges* along the dielectric surface, often in the form of intense streamer and leader discharges. The breakdown process is a so-called *flashover* in this case.

Note: The breakdown is also known as a *flashover* if it takes place close to and parallel to the surface of an insulating material. For example, the "flashover" of a suspension insulator is actually a gas breakdown between the metallic fittings at the insulator ends.

Gas discharges also occur in **gas-filled cavities** in solid and liquid dielectrics. They are known as *internal partial discharges*, and they contain valuable diagnostic information for the condition assessment of the insulation quality. The breakdown is not a gas breakdown. It occurs through the failure of the solid or liquid insulation, e.g. during an increase of the applied voltage. In the case of a long-duration stress, internal partial discharges can erode solid insulation (*erosion breakdown* or *partial-discharge breakdown*) or they can generate *cracked gases* (*failure gases*).

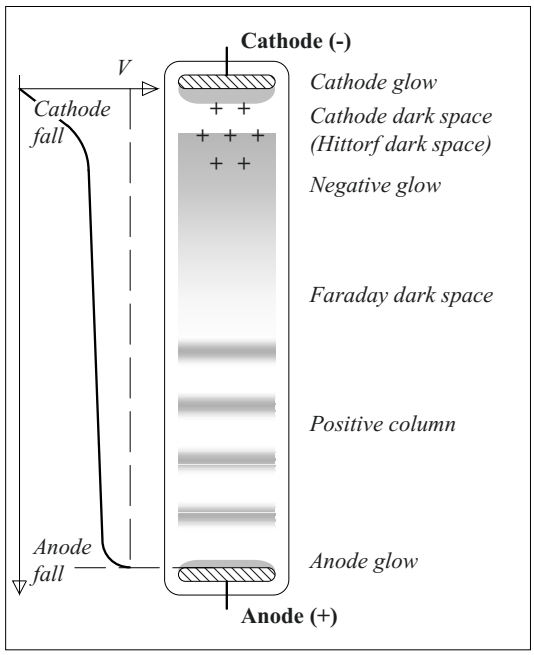

Figure 3.2-5: Luminous effects in a glow discharge at DC voltage for a gas at very low pressure (negative colours, schematic). The glow discharge is stabilized by a high series resistance.

3.2.2 Space-charge-free Discharge in a Uniform Field

(Townsend and Paschen)

Because of the constant, reproducible and physically describable properties of gases, it is possible to develop a physical/ mathematical model and an *ignition condition* for the inception of discharges (Townsend's ignition condition, Section 3.2.2.1). Furthermore, the dependence of the *breakdown voltage* upon distance, pressure and temperature can be described analytically (Paschen's law, Section 3.2.2.2 and 3.2.2.4). The discussion is re-

stricted to a (nearly) *uniform field* and the influence of *space charges* is *neglected* ("Townsend discharge").

Note: In the case of *vacuum*, other physical effects become dominant, and another approach is necessary, see Section 3.7.

3.2.2.1 Townsend's Ignition Condition (Avalanche generations, Townsend Mechanism)

The free *primary electron* (or a few primary electrons) for the *initiation of an electron avalanche* can be released from the negative electrode (cathode) if sufficient energy is supplied. The required energy W_a (work function)

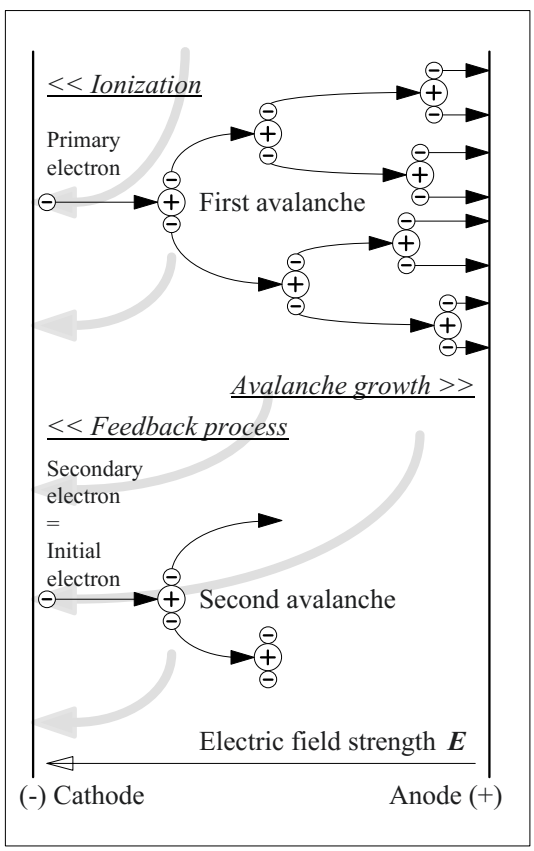

Figure 3.2-6: Physical model for the description of subsequent avalanche generations (Townsend mechanism) used for the derivation of the Townsend ignition condition and for the derivation of Paschen's law.

differs for the electrode materials and is in the range of 3 to 5 eV. There are several ways in which the energy can be supplied and in which the electrons can be released [480], e.g. by *photoelectric emission* (UV light, cosmic radiation), *by ion impacts* (in an electric field), by *thermionic emission* (at high temperatures) and by *field emission* (at very high local field strengths), Figure 3.2-6.

At first, the released primary electron is subject to arbitrary thermal movements. Collisions with molecules and gases do not ionize, as long as the kinetic energy is smaller than the ionization energy. Between the collisions, the electron is accelerated by the electric field and it accumulates kinetic energy. This causes an *electron drift* into the electric field direction. Because of the *conservation of momentum*, the lightweight electron does not lose significant energy during the collisions with the heavier gas molecules (elastic collision). Therefore, energy is accumulated until the required ionization energy is reached and an ionizing collision can occur [46], [25], [2].

Collision ionization generates additional electrons, which are also accelerated by the field and which generate more and more electrons by collisions. Thus, an *electron avalanche* develops with an increasing number of charge carriers from the cathode to the anode.

During collision ionization processes both *electrons* and less mobile *positive ions* are generated. The ions drift towards the cathode where secondary electrons are emitted. Together with the collision ionization processes there are recombination processes that are accompanied by the emission of light quanta (*photons*). These photons can also release secondary electrons from the cathode by photoionization. This means that there are different *feedback processes* providing secondary electrons at the cathode, which act as new primary electrons for the *next avalanche*, Figure 3.2-6 (bottom)

Based on these concepts, the **ignition condition** can be formulated as follows:

A single primary electron that was released from the cathode (e.g. by an external ionization source) has to generate *at least one secondary electron* at the cathode by *avalanche growth* and *feedback process*, in order to provide at least one new primary electron for the next avalanche. This means that every avalanche causes at least one *subsequent avalanche*. In this way a conductive discharge channel is generated and the voltage across the electrodes *breaks down*.

If the number of secondary (= new primary) electrons at the cathode is smaller, the process dies down, there is no development of a conductive channel and the voltage across the electrodes does *not* break down.

For the mathematical description of the ignition condition, an *ionization coefficient* α is defined (*Townsend's first ionization coefficient*). It describes the number of electrons that are generated per unit length by a single electron (collision ionization).

In an avalanche, the *increase* $\mathrm{d}N$ of the number of electrons N along the distance $\mathrm{d}x$ is

$$\mathrm{d}N = N \cdot \alpha \cdot \mathrm{d}x \,. \qquad (3.2\text{-}3a)$$

With N_1 primary electrons and with α = const. in a uniform field, we find by integration

$$\ln (N/N_1) = \alpha \cdot x \,.$$

Therefore, we get an *exponentially growing electron avalanche*:

$$N = N_1 \cdot \mathrm{e}^{\alpha \cdot x} \qquad (3.2\text{-}3b)$$

Note: The *ionization coefficient* α has to be reduced to an *effective ionization coefficient*

$$\alpha_{\mathrm{eff}} = \alpha - \eta \qquad (3.2\text{-}4a)$$

by subtraction of the *attachment coefficient* η [16]. By analogy to Eq. (3.2-3a), η describes the *decrease* of the number of free electrons per unit length by attachment of electrons to the less mobile gas molecules. Especially for *gases with a high electron affinity* (e.g. sulfur hexafluoride SF_6), the attachment of electrons greatly increases the breakdown strength.

Note: The number of electrons per unit length that are generated *by a positive ion* is described by the *ionization coefficient* β. It is much smaller than the ionization coefficient α. Therefore, it can be neglected for a first order description of the avalanche growth and the Townsend discharge mechanism:

$$\beta << \alpha \qquad (3.2\text{-}4b)$$

Owing to their large mass, *ions* lose so much energy during elastic collisions that an accumulation of energy does not occur. Therefore, the ionization energy has to be reached during a single acceleration along a single *free length of path*. Additionally, the free path for ions is shorter than the free path for electrons because of the larger *collision cross sections* of ions.

The feedback from the ions to the cathode is described by the *surface ionization coefficient* γ. It describes the number of secondary (= new primary electrons) that are generated by a single positive charge unit (positive elementary charge). γ is also known as the *feedback coefficient* or *Townsend's second ionization coefficient*.

Note: The feedback process, i.e. the generation of secondary electrons at the cathode, is not only achieved by the *kinetic energy* of the incident ions, but also by radiation (*photons*). Nevertheless, the most important effect for the release of free electrons is the direct *energetic interaction* of the ions with the surface atoms of the cathode. Therefore, the feedback coefficient γ has to take into account a number of different effects [25].

Starting with a single primary electron $N_1 = 1$, the *first avalanche* grows exponentially between $x = 0$ (cathode) and $x = d$ (anode) from a single electron up to $\mathrm{e}^{\alpha d}$ electrons, Figure 3.2-7. Simultaneously, $(\mathrm{e}^{\alpha d} - 1)$ positive elementary charges (ion charges) are generated. By means of a multiplication with the surface ionization coefficient γ, the number of secondary electrons $N_2 = \gamma (\mathrm{e}^{\alpha d} - 1)$ is calculated. These electrons are available at the cathode as new primary electrons for the *second avalanche*. Then, the growth of the electron number is determined by multiplication with the avalanche factor $\mathrm{e}^{\alpha d}$. The number of new ion charges is calculated by subtracting the number of initial primary electrons. After multiplication with the surface ionization coefficient γ,

No. of avalanche n	Number of initial electrons N_n	Number of electrons in the avalanche	Number of the positive charges additionally generated in the avalanche (positive ion elementary charges)
1	**1**	$e^{\alpha d}$	$e^{\alpha d} - 1$
2	$\gamma\,(e^{\alpha d} - 1)$	$\gamma\,(e^{\alpha d} - 1)\,e^{\alpha d}$	$\gamma\,(e^{\alpha d} - 1)\,e^{\alpha d} - \gamma\,(e^{\alpha d} - 1) = \gamma\,(e^{\alpha d} - 1)^2$
3	$\gamma^2(e^{\alpha d} - 1)^2$	$\gamma^2(e^{\alpha d} - 1)^2 e^{\alpha d}$	$\gamma^2(e^{\alpha d} - 1)^2 e^{\alpha d} - \gamma^2(e^{\alpha d} - 1)^2 = \gamma^2(e^{\alpha d} - 1)^3$
4	$\gamma^3(e^{\alpha d} - 1)^3$	$\gamma^3(e^{\alpha d} - 1)^3 e^{\alpha d}$	$\gamma^3(e^{\alpha d} - 1)^3 e^{\alpha d} - \gamma^3(e^{\alpha d} - 1)^3 = \gamma^3(e^{\alpha d} - 1)^4$
n	etc.	etc.	etc.

Figure 3.2-7: Mathematical description of the subsequent electron avalanche generations caused by a single primary electron (Townsend mechanism, avalanche-generation mechanism).

the initial number of electrons for the *third avalanche* is given by $N_3 = \gamma^2 \cdot (e^{\alpha d} - 1)^2$, Figure 3.2-7. In general, the initial number of electrons for *avalanche no. n* is

$$N_n = \gamma^{n-1} \cdot (e^{\alpha d} - 1)^{n-1} . \qquad (3.2\text{-}5)$$

Obviously, the initial numbers of electrons in consecutive avalanches are described by a *geometric series*. In the case of mathematical *convergence*, the sum of all initial electrons at the cathode is given by an analytical term:

$$N_c = N_1 + N_2 + N_3 + ... + N_n + ... = \sum_{n=1}^{\infty} [\gamma^{n-1} \cdot (e^{\alpha d} - 1)^{n-1}] = \frac{1}{1 - \gamma \cdot (e^{\alpha d} - 1)}$$

Then, the total number of electrons reaching the anode is large by a factor of $e^{\alpha d}$:

$$= \frac{e^{\alpha d}}{1 - \gamma \cdot (e^{\alpha d} - 1)} \qquad (3.2\text{-}6)$$

The *convergence condition* for the geometric series is

$$\gamma (e^{\alpha d} - 1) < 1 . \qquad (3.2\text{-}7)$$

In the case of *convergence*, Eq. (3.2-6) describes a finite sum of charges, i.e. there is *no* breakdown. Nevertheless, the number of charge carriers is increased by collision ionization and avalanche growth. There is a transient current increase, i.e. a current impulse, which is known as "*current amplification*".

Note: This effect is used, for example, in the **Geiger-Müller counter** for detection of *radioactive radiation*.

A *divergent geometric series* is obtained for

$$\gamma (e^{\alpha d} - 1) \geq 1 . \qquad (3.2\text{-}8)$$

This means that the number of initial electrons becomes infinite, a conductive channel is formed between the electrodes and the voltage

breaks down. Evidently, Eq. (3.2-8) is the **ignition condition** we are seeking for the Townsend mechanism.

The ignition condition according to Eq. (3.2-8) can *directly be explained* as follows: A single primary electron generates ($e^{\alpha d} - 1$) ion elementary charges by avalanche growth. Multiplication with the "feedback coefficient" γ gives the number $\gamma(e^{\alpha d} - 1)$ for the secondary electrons that are released from the cathode. In accordance with Eq. (3.2-8), this number has to be *bigger than or equal to one* in order to trigger at least one consecutive avalanche. This means that every initial electron has to "regenerate" itself by the avalanche growth and feedback process, Figure 3.2-7.

The ignition condition according to Eq. (3.2-8) can be solved for the term αd [2]:

$$\alpha d \quad \geq \quad \ln(1 + 1/\gamma) = k\,. \qquad (3.2\text{-}9a)$$

In general, the product αd must be replaced by the integration along a field line, see Eq. (3.2-2) and (-3):

$$\int_{x=0}^{d} \alpha \cdot \mathrm{d}x \quad \geq \quad \ln(1 + 1/\gamma) = k \qquad (3.2\text{-}9b)$$

Then, Eq. (3.2-9b) is also valid for the *non-uniform field*. Nevertheless, it must be considered that α is not constant. Because of a strong dependence on field strength, α is also *dependent on position*:

$$\alpha = \alpha(E(x)) \qquad (3.2\text{-}10)$$

Note: The quantity k depends on the material properties of the gas and the cathode. For air at atmospheric pressure and for metallic electrodes, the empirical value k = 7 is given as an example [2]. This means that approximately e^7 = 1100 electrons and positive elementary charges. have to be generated in order to release a secondary electron from the cathode. According to Eq. (3.2-9), k = 7 is approximately equivalent to a surface ionization coefficient $\gamma = 10^{-3}$. In the literature, values are given in the range of 10^{-5} [16] to 10^{-1} [25]. According to Eq. (3.2-9) this is equivalent to values $k = \alpha d$ between 11 and 3.

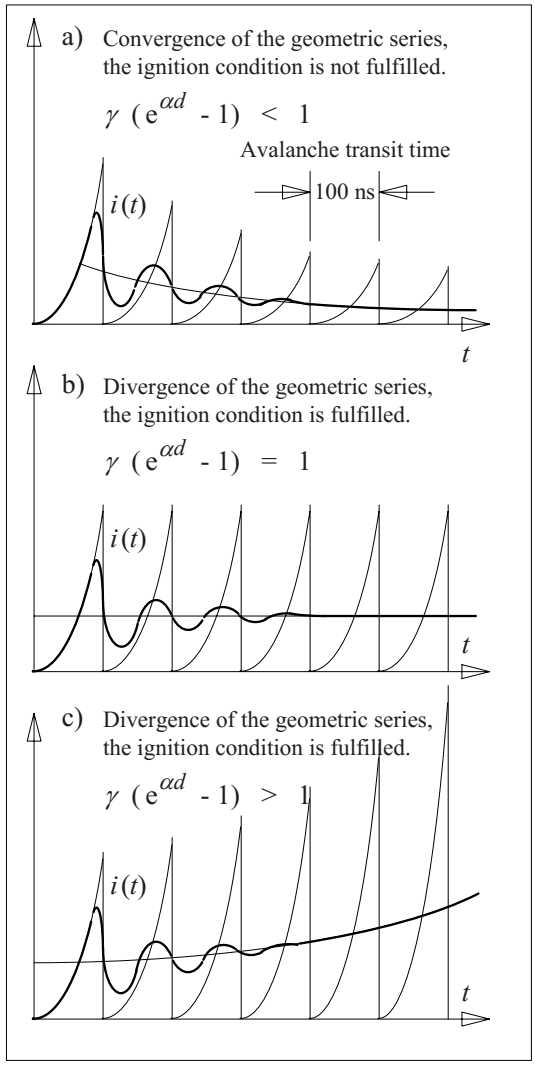

Figure 3.2-8: Development of electron avalanches for the Townsend mechanism (subsequent generations of avalanches), if the subsequent avalances are triggered by photoionization without delay: Theoretical and real current curves (schematic) [25].

The mathematical description of the ignition condition as the divergence of a geometric series (3.2-6) can clearly be explained as the *increase of consecutive avalanche currents*, Figure 3.2-8c. In the extreme case $\gamma(e^{\alpha d} - 1) = 1$, the magnitude of the consecutive avalanches is constant, Figure 3.2-8b. In the case of convergence, the magnitude of consecutive avalanches decreases, but there is a current amplification and a current impulse because of

collision ionization. A breakdown does not occur, Figure 3.2-8a. It is assumed that the first avalanche starts with a higher number N_1 of primary electrons, in order to show that the number of initial electrons for the consecutive avalanches decreases. In Figure 3.2-8, it is assumed that the consecutive avalanches are triggered by *photoionization* with practically no time-delay. For $d = 1$ cm and air under atmospheric conditions, the avalanches follow at regular intervals of approximately $\tau_- = 100$ ns, which is equal to the avalanche transit time.

In *real current curves*, the individual avalanches cannot be distinguished very clearly. The reason is a shifting of the starting points of the avalanches, which results in an equalizing of the currents.

If the consecutive avalanches are triggered by the backwards drifting *positive ions*, the avalanches start after the transit time of the positive ion cloud, which is concentrated close to the electrode and which has to travel back to the cathode, Figure 3.2-9. The starting time for consecutive avalanches can differ significantly, resulting in irregular time intervals between the avalanches. The transit time of the ions is approximately $\tau_+ = 10$ µs for $d = 1$ cm in air under atmospheric standard conditions. The total current is the superposition of electron current $i_-(t)$ during the avalanche transit time and ion current $i_+(t)$ during the transit time of the ion cloud towards the cathode. Both currents have the same (technical) direction, but they are very different in magnitude.

Note: The validity of this model with a discharge development by consecutive generation of avalanches (*Townsend mechanism*) is limited to the space-charge-free case. This means that avalanche growth is limited to cases without significant distortion of the initial field. For air, the limit is given approximately at $k = \alpha d = 20$, which is equivalent to an avalanche of $e^{20} = 5 \cdot 10^8$ electrons. The validity is restricted to small *electrode distances d* or *low pressures* (with a low ionization coefficient α). Above this limit, the discharges are described by the model of the streamer discharge, see Section 3.2.3.

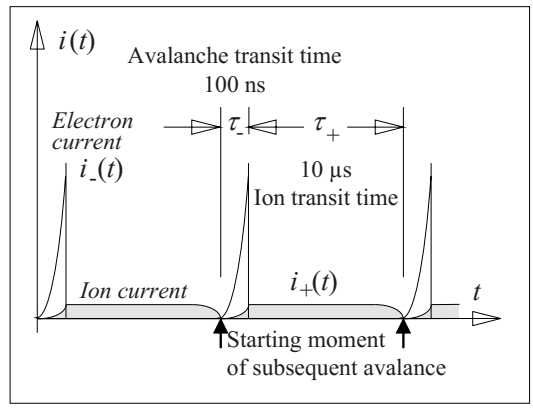

Figure 3.2-9: Electron and ion currents for the Townsend mechanism (subsequent generations of avalances), if the subsequent avalances are triggered by the backwards drifting ions (schematic) [25].

3.2.2.2 Ionization and Attachment

The ignition condition according to Eq. (3.2-8) allows us to derive an analytical expression for the *breakdown voltage* V_{bd} (Section 3.2.2.4). For this purpose, the ionization coefficients α and γ have to be expressed as functions of the electric field strength E and gas density.

α is the number of the ionizing collisions per unit length, and $1/\alpha$ is the path length per ionizing collision. On the average, an electron has to pass the distance $1/\alpha$ in the field direction, until an ionizing collision takes place, Figure 3.2-10. During this, a number of *elastic* (non-ionizing) collisions can occur, which do not transfer significant energy from the light-weight electron to heavy gas molecules (conservation of momentum). This means that the energy which is gathered during the drift in the field direction is *accumulated* until the ionization energy is reached [25], dissipation by non-elastic excitations is neglected here. Thus, the electron passes z-times the mean free path length λ_m:

$$1/\alpha = z \cdot \lambda_m \qquad (3.2\text{-}11)$$

The higher the energy

$$\Delta W = e \cdot \Delta U = e \cdot E \cdot \lambda_m$$

is, which can be gathered by an electron (charge q = e) along a free path length λ_m, the smaller is the number z of subsequent accumulation steps. Therefore, we have the functional relation

$$1/\alpha = \lambda_m / f(E \cdot \lambda_m) . \qquad (3.2\text{-}12)$$

The mean free path length λ_m is proportional to the reciprocal of the *gas density*, i.e. to the reciprocal of the *pressure p* if the temperature is kept constant. From Eq. (3.2-12) a *general relation* for the **ionization coefficient** is derived:

$$\alpha = p \cdot f(E/p) \qquad (3.2\text{-}13)$$

Normally, the relation $\alpha/p = f(E/p)$ is given as an empirical function [25], [16], [45], [46], [47], but for a qualitative consideration according to Townsend, an *analytical approximation* can be determined [46]. In this case, the accumulation of kinetic energy is neglected, i.e. it is assumed that the required ionization energy W_i is reached within a single acceleration path λ. Then, the required path length is

$$\lambda_i = W_i/(e \cdot E) . \qquad (3.2\text{-}14)$$

The probability that the available free acceleration path λ is equal to or longer than λ_i can be expressed by means of the mean free path length λ_m. For this purpose, the probability dF for the collision of an electron within a path element dx is assumed to be

$$dF = dx/\lambda_m , \qquad (3.2\text{-}15)$$

see Figure 3.2-11 and [16]. The number $N(x)$ of electrons that have not yet had a collision is diminished by collisions within the path element dx by the number

$$dN = -N(x) \cdot dF$$
$$= -N(x) \cdot dx/\lambda_m . \qquad (3.2\text{-}16)$$

If it is assumed that all considered electrons have started at x = 0, the number of the remaining electrons without collisions is calculated by integration of the relationship

$$dN/N = -dx/\lambda_m$$

from x = 0 with $N(0)$ to x with $N(x)$:

$$N(x) = N(0) \cdot \exp(-x/\lambda_m) \qquad (3.2\text{-}17)$$

This equation is known as the *Clausius law* of the path length [16]. It allows us to describe the probability $F(x)$ for $x = \lambda_i$ that an electron can be accelerated without collision along the path length $x = \lambda_i$, which is necessary for the acceleration up to the ionization energy:

$$F(\lambda_i) = \frac{N(\lambda_i)}{N(0)} = e^{-\frac{\lambda_i}{\lambda_m}} \qquad (3.2\text{-}18)$$

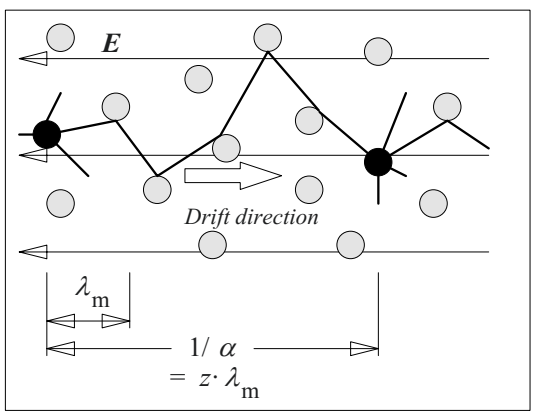

Figure 3.2-10: Two-dimensional visualization of the mean drift path of electrons between two ionizing collisions with a number of elastic collisions.

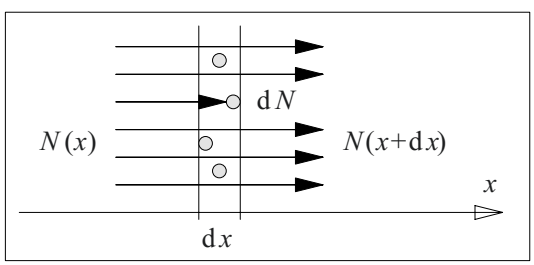

Figure 3.2-11: The Clausius law concerning path lengths.

This equation gives the *ionization probability*, if there is a collision of an electron with a gas molecule. The *probability of a collision per unit length* is, according to Eq. (3.2-15)

$$dF_S/dx = 1/\lambda_m. \qquad (3.2\text{-}19)$$

The product of the collision probability according to Eq. (3.2-19) with the ionization probability according to Eq. (3.2-18) gives the ionization coefficient α, i.e. the number of ionizing collisions per unit length:

$$\alpha = \frac{1}{\lambda_m} e^{-\frac{\lambda_i}{\lambda_m}} \qquad (3.2\text{-}20)$$

According to Eq. (3.2-14) we assume $\lambda_i \sim 1/E$. Furthermore, the mean free path length λ_m is proportional to $1/p$, if the temperature is constant. From Eq. (3.2-20) and with the constants A and B we find

$$\alpha = A\ p\ e^{-\frac{B}{(E/p)}}. \qquad (3.2\text{-}21)$$

Eq. (3.2-21) is an *approximation* for the **ionization coefficient** α that fulfills the general equation (3.2-13). For the visualization of this relationship, the ratio α/p is drawn as a function of the ratio E/p, Figure 3.2-12.

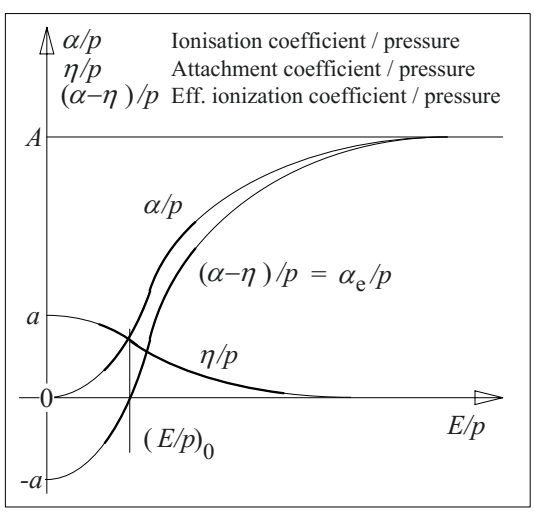

Figure 3.2-12: Ionisation coefficient, attachment coefficient and effective ionisation coefficient, all derived from physical models (thin lines) with experimentally confirmed intervals (thick lines).

By an appropriate choice of the constants A and B, a good fit of experimental ionization coefficients can be achieved, although the derivation of Eq. (3.2-21) was based on substantial simplifications [46].

Depending on the type of gas, different values are valid for the gas constants A and B at standard temperature T = 293 K = 20 °C, see table 3.2-1.

Table 3.2-1: Experimental values for the gas constants A and B in Eq. 3.2-21 [16], [21. For more values see [438] for example.

Gas	A	B	Range E/p
	1/(mm bar)	kV/(mm bar)	kV/(mm bar)
Air	1130	27.4	11 to 45
N_2	977	25.5	8 to 45
H_2	376	9.8	11 to 30
He	210	2.6	2 to 11
Ar	1020	13.5	8 to 45
CO_2	1500	34.9	37 to 75

Note: The *constants A* and *B* are also part of the equations for the breakdown voltage (Paschen's law, Section 3.2.2.4) and they can be determined from measurements of the breakdown voltage. Sometimes the values from different sources are different. Values for many gases and a discussion of different sources can be found in the literature [438].

For *gases with high electron affinity* (cf. Section 3.2.2.3), e.g. for *sulfur hexafluoride* SF_6, the attachment of electrons to gas molecules has to be taken into account using an **attachment coefficient** η, Figure 3.2-12. It describes the relative decrease of electrons per unit length, i.e. the attachment probability of an electron per unit length. It can be shown that the ratio η/p is also a function of E/p [16].

By analogy with Eq. (3.2-20), an *approximation* can also be given for η. The contact (collision) between a sufficiently slow electron and a molecule that has an electron affinity is a necessary condition for an attachment. The related probability is given by $1/\lambda_m$ according to Eq. (3.2-19). The kinetic energy or the free acceleration path λ_B must not exceed a given limit. The

probability that $x < \lambda_B$ is known as an *attachment probability*. By analogy with Eq. (3.2-18), it is given as

$$F(\lambda_B) = 1 - \exp(-\lambda_B/\lambda_m) . \quad (3.2\text{-}22)$$

The product of the collision probability $1/\lambda_m$ and the attachment probability according to Eq. (3.2-22) gives the *approximation for the attachment coefficient* with the constants *a* and *b* by analogy with Eq. (3.2.21):

$$\eta = a\ p \left\{ 1 - e^{-\frac{b}{(E/p)}} \right\} . \quad (3.2\text{-}23)$$

A qualitative curve for the illustration of this function is shown in Figure 3.2-12.

The **effective ionization coefficient** α_e is calculated as the difference of the ionization coefficient α and the attachment coefficient η:

$$\alpha_e = \alpha - \eta \quad (3.2\text{-}24)$$

According to Eq. (3.2-13), (-21) and (-23), the *effective ionization coefficient* is proportional to the pressure *p*. Furthermore, it is a function of the ratio *E*/*p*, Figure 3.2-12:

$$\alpha_e = \alpha - \eta = p \cdot f(E/p) . \quad (3.2\text{-}25)$$

Avalanche growth is only possible if the effective ionization coefficient is *greater than zero*. For air, this point is at approximately $(E/p)_0$ = 24.4 to 25 kV/(cm·bar), and for the strongly electron-affine SF_6 only at $(E/p)_0$ = 87.7 to 88.4 kV/(cm·bar). The specifications of different authors can differ as the exact experimental conditions may also be different.

For SF_6, the effective ionization coefficient $\alpha - \eta$ differs very much from the ionization coefficient α according to Eq. (3.2-21). Therefore, $\alpha - \eta$ is described by a *linear postulated solution* with constants that have to be determined empirically, Figure 3.2-12:

$$(\alpha - \eta)/p = k_i \{(E/p) - (E/p)_0\} \quad (3.2\text{-}26)$$

For SF_6, the values k_i = 27.7/kV and $(E/p)_0$ = 88.4 kV/(bar·cm) are reported at T = 293 K [39].

The feedback coefficient (*surface ionization coefficient, Townsend's second ionization coefficient*) γ has to cover a number of *very different processes* [50], [25], such as the release of electrons from the cathode by *positive ions* (γ_I), by the *photo effect* (γ_P), by *neutral atoms* (γ_N), by *field emission* (γ_F) and by *photo emission in the volume* (γ_V) as well as the *ion emission* of the anode (γ_A).

$$\gamma = \gamma_I + \gamma_P + \gamma_N + \gamma_A + \gamma_F + \gamma_V \quad (3.2\text{-}27)$$

All these effects are not only dependent on the *electrode material* and on the *type of gas*, but also (in different ways) on the *field strength* and the *pressure*, i.e. on the ratio *E*/*p*. Therefore, the relationship

$$\gamma = f(E/p) \quad (3.2\text{-}28)$$

is described by empirical curves, either with a given gas for different electrode materials or vice-versa, e.g. [25].

For small values of *E*/*p* it can be expected that the *photo effect* is dominant, because of the low ion drift velocity at high gas densities and low field strengths. At higher *E*/*p* values the *ions* play a more important role because high field strengths and low gas densities allow higher ion drift velocities [50].

Note: The *feedback processes by ions* are less dependent on field strength and pressure than avalanche growth. If a positive ion reaches the cathode, the kinetic energy W_{kin} (which is dependent on pressure and field strength) is the minor part of the released energy. The major part is contributed by the *recombination* of the *positive ion* with the negative electrons at the cathode [16], and it is equal to the ionization energy W_i during the formation of the ion. The sum of the two energies, which are released at the cathode, has to be high enough to free two electrons with the work function W_a, Eq. (3.2-28a). The first electron is necessary for the recombination with the incident positive ion and the second electron is the initial electron for the new electron avalanche.

$$2\ W_a \leq W_i + W_{kin} \approx W_i \quad (3.2\text{-}28a)$$

Numerical values for γ vary significantly depending on the *experimental conditions*. For example, coefficients that were determined in vacuum cannot be used for gas discharges because impurities and adsorption of gas molecules can significantly influence the surface properties. Typical numerical values for *short-distance/ low-pressure breakdowns* with high E/p values are given in table 3.2-2.

For the *long-distance/ high pressure breakdown* with low E/p values, the feedback coefficients are significantly lower. For *air*, SF_6 and typical electrode materials, the order of magnitude for γ is 10^{-5} (i.e. $k = 11.5$) [16]. For $p = 1$ bar and flashover distances of some cm, numerical values are $\gamma = 2 \cdot 10^{-6}$ ($k = 13$) for *air* and $\gamma = 10^{-7}$ ($k = 16$) for SF_6 [39].

During the calculation of the *breakdown voltage*, the dependence of γ on field strength and gas density is mostly neglected because of the comparatively *weak influence* of γ on the breakdown voltage (Section 3.2.2.4). For the given combination of gas and electrode material, a *constant numerical value* γ is used.

Table 3.2-2: Feedback coefficient (surface ionization coefficient) γ in vacuum for slow gas ions (10 eV) and clean electrode surfaces [51] (*) and for the short-distance/ low-pressure gas discharges [39].

	Al	*Cu*	*Fe*	*Ba*	*K*
N^+, O^+	0.035	0.025	0.020	-	0.070 (*)
Air	0.035	0.025	0.020	-	-
N^+	0.100	0.066	0.059	0.140	0.120 (*)
N_2	0.100	0.065	0.060	-	-
H_2	0.100	0.050	0.060	-	-
He^+	0.021	-	0.015	0.100	0.170 (*)
Ar^+	0.120	0.058	0.058	0.140	0.220 (*)

3.2.2.3 Electron Affinity and Electronegativity

As described before, the **attachment of electrons** to gas molecules or gas atoms plays a dominant role for the development of electron avalanges and for the *dielectric strength* of the gas.

In the case of an *electron* with low kinetic energy (e.g. caused by thermal movement or by acceleration in the electric field) that collides with a neutral gas molecule or gas atom, the electron can be attached, so that a *negative ion* in an *excited state* is created. If the electron can find a position with *lower potential energy* in the orbitals of the gas molecule or gas atom, a *stable negative ion* is formed. The **energy difference** between initial state and final state, i.e. the *energy that is released* as a photon or as kinetic energy during the described *attachment process*, is denominated as **electron affinity** [55]. Vice versa, it is equivalent to the energy that is required for the *detachment of the electron*.

Thus, gas molecules or gas atoms with a high **electron affinity** are required for a high **dielectric strength**.

For a very long time, the denomiantion **"electronegative gases"** has been established in high voltage engineering for gases with a high **electron affinity** [16], [46], [480]. Nevertheless, as it came out from an expert discussion in this case[1], this is <u>not correct</u> from a physical point of view.

Note: The term **electronegativity** that was introduced by Linus Pauling in 1932 refers to the *atomic bond* (covalent bond) between elements by means of binding electron pairs [49]. **Elements** that are comparatively close to full electron shells (e.g. the *halogens* F, Cl, Br) attract the *binding electron pairs* in the atomic bonds, and they are therefore denominated as *electronegative*. Elements that are far from full electron shells (e.g. the *alkaline metals*) provide binding electrons for this. Thereby, the positive and negative *centers of charge* in the molecule are displaced against each other and an electrical *dipole moment* is created.

Based on binding energies, a (dimensionless) **scale of electronegativity** was established for the elements with values between 4.0 (fluorine) and slightly below 1.0 (alkaline metals). The values for the individual elements are often listed in the periodic table of the elements

[1] Josef Kindersberger, Volker Hinrichsen, Isabell Hofer-Maksymiw, Johannes Seiler Andreas Hopf and Michael Rossner

[49]. The *inert noble gases* do not form atomic bonds due to their full electron shells; and they are not listed in this respect.

Electronegativity describes the contributions of the elements to the binding conditions *within a molecule*, and not at all the attachment of free electrons to molecules or atoms. In contrast, the **electron affinity** is the energy that is released during the attachment of a *free* electron (coming *from outside*) to a gas molecule or gas atom. This energy is the relevant physical quantity for the description of electron attachment to gas molecules and gas atoms and should therefore be used for the characterization of insulating-gas properties.

Note: Despite of this, there is an indirect **relation** between *electronegativity* and *electron affinity*: By means of charge displacements, electronegative elements create new *energy levels* and *orbitals* within the molecules where free electrons that come *from outside* can stably be attached with a significant release of energy. This can be seen for the most electronegative element fluorine which contributes to a high electron affinity of the SF_6 molecule or of other fluorinated molecules.

Nevertheless, the relevant parameters for the created **energy levels** are not only the *electronegativity* of the involved elements but also the *isomeric structure* of the molecule, i.e. the *spatial arrangement* of the atoms.

A strong tendency for the attraction of electrons in chemical bonds can especially be found for the *electronegative halogens fluorine* F and *chlorine* Cl, both of which can complete their outer electron shells by the inclusion of a single electron. *Oxygen* O and *sulfur* S both require two electrons for this, *nitrogen* N hardly attracts any electrons and the *inert* or *noble gases* (e.g. *neon* Ne or *helium* He) do not attract any electrons at all.

In **chemical bonds**, the resulting electron affinity determines the attachment behavior. Here, *sulfur hexafluoride* SF_6 has a strong electron affinity, especially in comparison with *air*, which has a very limited residual electron attachment capability only because of its O_2 content. Further examples of strongly electron-affine gases are the *fluorocarbons* $CBrClF_2$ and $C_2Cl_3F_3$ as well as the so-called *alternative insulating gases* that are described in Section 5.1.3.

3.2.2.4 Paschen's Law

After the above digression about ionization, attachment, electronegativity and electron affinity in the Sections 3.2.2.2 and 3.2.2.3, we now come back to **Townsend's ignition condition** in Section 3.2.2.1:

The calculation of the ignition voltage (also known as the sparking or breakdown voltage) is based on the Townsend mechanism and the related limit case of the ignition condition according to Eq. (3.2-9):

$$\alpha d = \ln(1 + 1/\gamma) \qquad (3.2\text{-}29)$$

With the effective ionization coefficient $\alpha = \alpha_e$ according to Eq. (3.2-25) we find

$$pd \cdot f(E_{bd}/p) = \ln(1 + 1/\gamma)\,. \qquad (3.2\text{-}30)$$

The feedback coefficient γ is assumed to be constant.

A general solution for the breakdown field strength E_{bd} cannot be given, but it can be seen that the ratio E/p is a function of the *product* of *pressure* and *distance* (**similarity law**):

$$E_{bd}/p = f_1(pd) \qquad (3.2\text{-}31)$$

After the expansion of the fraction E_{bd}/p by multiplying numerator and denominator by the flashover distance d, the ignition voltage $V_{bd} = E_{bd} \cdot d$ can be introduced:

$$E_{bd}/p = (E_{bd} \cdot d)/(p \cdot d) = V_{bd}/(pd) \qquad (3.2\text{-}32)$$

Then, the igniting or sparking voltage is

$$V_{bd} = pd \cdot f_1(pd) = f_2(pd)\,. \qquad (3.2\text{-}33)$$

This general relationship is known as **Paschen's law**. It means that the *ignition voltage* is a function of the *product of pressure and electrode distance pd (pressure spacing*

product, pd value), if the conditions of the Townsend mechanism are fulfilled (uniform field, negligible space charges).

Example:
Variation of flashover distance and pressure

For a flashover distance d = 2 mm in a uniform field, an ignition voltage $\hat{V}_{bd}$ = 7.5 kV is measured for air at standard atmospheric conditions (p = 1 bar, T = 293 K). For example, Paschen's law states that the ignition voltage does not change for a tenfold greater distance d = 2 cm, if the pressure is reduced to the tenth part p = 0.1 bar = 10 kPa. In both cases, the pressure spacing product pd = 2 bar mm is the same.

Note: In the equations (3.2-13) ff, the gas density was replaced by the gas pressure p at a constant temperature T. According to kinetic gas theory, the gas density of an ideal gas is proportional to p/T. If the *influence of temperature* is considered, the breakdown voltage is

$$V_{bd} = f(pd/T) . \qquad (3.2\text{-}34)$$

Very often, measurements are performed close to the standard room temperature T_0 = 293 K (i.e. 20°C) and (small) temperature and voltage deviations are taken into account by a *voltage correction factor* T_0/T. However, this is only possible in temperature ranges where proportionality exists between V_{bd} and pd/T, see Eq. (6.3.1-2).

Note: In Eq. (3.2-30), the *feedback coefficient* (*surface ionization coefficient*) γ was regarded as a constant quantity, but this is not essential: Even if γ according to Eq. (3.2-28) is regarded as a function of $E/p = V_{bd}/(pd)$, Paschen's law according to Eq. (3.2-33) remains valid.

By means of the Townsend ignition condition Eq. (3.2-9) or (-29) and the analytical approximate equation (3.2-21) for Townsend's first ionization coefficient α, an *approximate equation* for the *ignition voltage* V_{bd} can be derived in an *analytical* form:

$$\alpha d = A \cdot pd \cdot e^{-B/(E/p)} = \ln(1 + 1/\gamma)$$

Note: For *gases with low electron affinity*, α can be regarded as the effective ionization coefficient $\alpha_e = \alpha - \eta$, if α_e is described by Eq. (3.2-23) with sufficient accuracy. For the *strongly electron-affine* SF_6, Eq. (3.2-26) must be used.

Additionally, we find with Eq. (3.2-31)

$$e^{-\frac{B \cdot pd}{V_{bd}}} = \frac{\ln(1+1/\gamma)}{A \cdot pd} .$$

By solving for V_{bd}, the *approximate equation* for **Paschen's law** is given in *analytical* form:

$$V_{bd} = \frac{B \cdot pd}{\ln \frac{A \cdot pd}{\ln(1+1/\gamma)}} \qquad (3.2\text{-}35)$$

Figure 3.2-13 shows the *basic characteristic* of this function (thinner curve line). By appropriate choice of the constants A, B and γ, good agreement with *real characteristics* (thicker curve line) can be achieved.

The **range of validity** for the approximate equation (3.2-35) is limited to the space-charge-free discharge, which is described by the Townsend mechanism of consecutive avalanches. This means that the space charge generated by the avalanches must not distort the initial field too much. The *transition region* to a *space-charge-dominated streamer discharge* is given in the range of

$$\alpha d \approx 14 \ldots 18. \qquad (3.2\text{-}36)$$

According to Eq. (3.2-3), this corresponds to an avalanche growth of $e^{14} = 10^6$ to $e^{18} = 10^8$ electrons. In *air* and SF_6 at room temperature, this value is approx. reached at

$$pd_{air} \approx 13 \text{ bar mm}$$
and
$$pd_{SF6} \approx 10 \text{ bar mm}, \qquad (3.2\text{-}37)$$

according to [16]. With very low pd values the ignition voltage V_{bd} *theoretically* approaches infinitely high values, because there are no longer enough gas molecules at short distances (or low pressures) for avalanche growth by collision ionization (**short-distance/ low-pressure breakdown**).

Note: According to Eq. (3.2-35), this condition would be reached at

$$(pd)_\infty = \{\ln(1 + 1/\gamma)\}/A = k/A . \qquad (3.2\text{-}38)$$

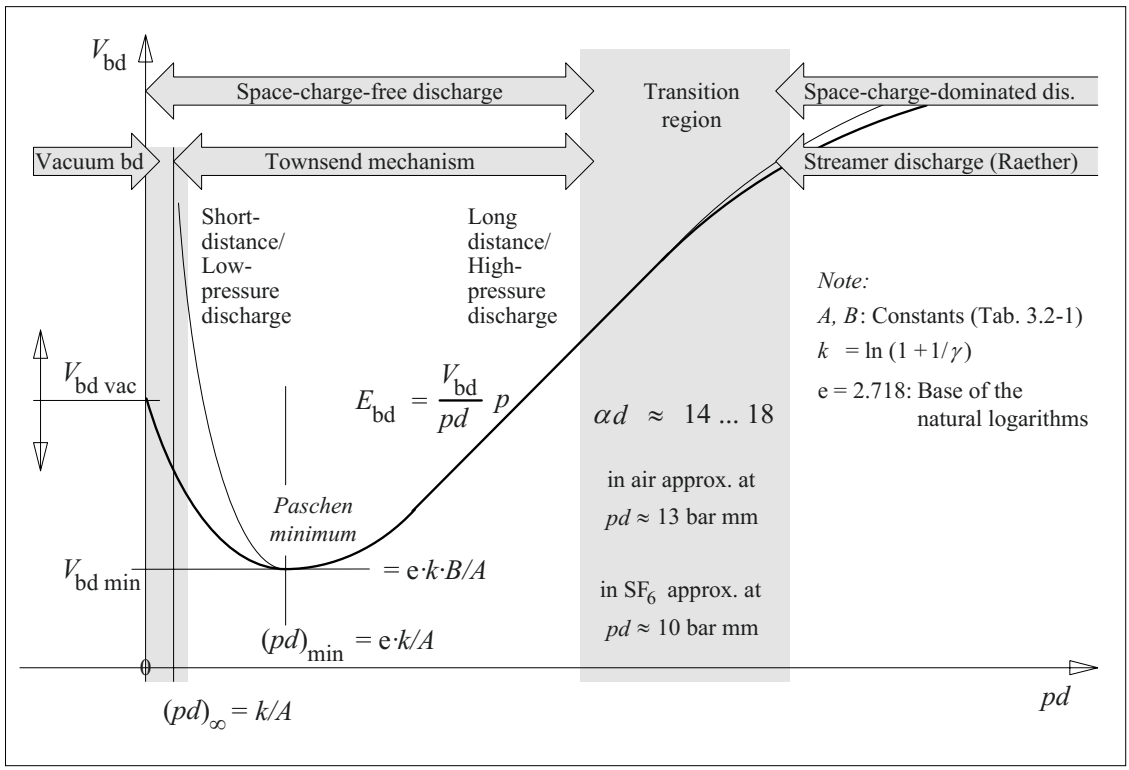

Figure 3.2-13: Paschen's law as an analytically determined approximation (thinner curve lines) and as a real curve (thicker curve lines). For the higher pd values, the diagram corresponds approximately to a log-log diagram (schematic).

For *air*, with the values from table 3.2-1 and with $\gamma = 0.025$ (see table 3.2-2) or $k = 3.7$, the value $(pd)_\infty = 3.3$ bar·µm is calculated. At atmospheric pressure, this would correspond to a flashover distance $d = 3.3$ µm.

In fact, this *theoretical case* does *not* occur because electrons are released directly from the cathode by *field emission* at short distances and high field strengths. Because of the electron impact on the anode, metal ions are released, so that a conductive *metal-vapor plasma* is generated. This process is known as a **vacuum breakdown** (Section 3.7). The model of consecutive avalanches according to the Townsend mechanism is no longer applicable. The breakdown voltage $V_{bd\,vac}$ in vacuum depends on the flashover distance (electrode spacing) d and on the electrode materials. Therefore, the *V-pd*-characteristic (Figure 3.2-13) for very low *pd* values is an example only.

The **Paschen curve** is characterized by high breakdown voltages at very low and at high *pd* values. In between, there is a *minimum*, Figure 3.2-13.

At *low pd values*, the breakdown voltage increases because the number of molecules that are available for collisions decreases (**short-distance/ low-pressure breakdown**).

High pd values are given at long distances or high pressures respectively (**long-distance/ high-pressure breakdown**). *Long distances d* corresponds to a reduction of field strength *E*. *High pressures p* reduce the free path length that is available for the acceleration of electrons. According to Eq. (3.2-21) there is a reduction of the ionization coefficient α in both cases.

The *minimum of the Paschen curve* (**Paschen minimum**), which can be derived from Eq.

(3.2-35) by extremum determination, is given as

$$(pd)_{\min} = e\cdot\{\ln(1 + 1/\gamma)\}/A$$
$$= e\cdot k/A$$
$$= e\cdot(pd)_{\infty} \qquad (3.2\text{-}39)$$

and

$$V_{\text{bd min}} = e\cdot\{\ln(1 + 1/\gamma)\}\cdot B/A$$
$$= e\cdot k\cdot B/A$$
$$= e\cdot B\cdot(pd)_{\infty}$$
$$= B\cdot(pd)_{\min}\,. \qquad (3.2\text{-}40)$$

Example: Paschen minimum for air

With the values in table 3.2-1 and with γ = 0.025 or k = 3.7. (See table 3.2-2), Eq. (3.2-39) gives the value $(pd)_{\min}$ = 9 bar·µm for air at room temperature. This is close to the *actual pd value of the minimum*. At atmospheric pressure, the minimum is expected for an electrode spacing d = 9 µm. For a distance d = 10 mm, the minimum breakdown voltage is given for a pressure p = 0.9 mbar = 90 Pa.

The *minimum breakdown voltage* for air is $V_{\text{bd min}}$ = 250 V, if B = 27.4 kV/(mm·bar) is inserted into Eq. (3.2-40). The *actual minimum breakdown voltage* is $V_{\text{bd min}}$ = 350 V according to *experiments*. This difference could be caused by a different value of the feedback coefficient γ. From $V_{\text{bd min}}$ = 350 V and from Eq. (3.2-40) it is concluded that $(pd)_{\min}$ equals 12.8 bar·µm. According to Eq. (3.2-39), this corresponds to the value k = 5.3 and the feedback coefficient (surface ionization coefficient) $\gamma = 5\cdot10^{-3}$.

Below the *minimum breakdown voltage* (ignition voltage) *gas breakdown* is *not possible*. Table 3.2-3 gives values for some gases. It can be seen that the electron-affine gases SF_6, O_2 and CO_2 have a significantly higher minimum breakdown voltage than *air*. For the *inert gases*, which are not electron-affine, the gas constants B (see table 3.2-1) and the minimum breakdown voltages are low, see Eq. (3.3-40). Additionally the values vary significantly with *electrode material*. Low minimum breakdown voltages occur for materials with low work function W_a and high corresponding surface ionization coefficient (feedback coefficient) γ.

Table 3.2-3: Paschen minima for different gases [16], [46].

Gas	$V_{\text{bd min}}$/ V	$(pd)_{\min}$/ bar·µm
SF_6	507	3.5
O_2	450	9.3
CO_2	420	6.8
Air	330 350	7.3
N_2	240 250	8.6
H_2	230 270	14
Ne	129 245	53.2
Ar	94 265	-
He	155	53.2

Example: Spark-gap lightning arresters

Because of the above-mentioned reasons, gas-filled lightning arresters are filled with *inert gases* and the arrester spark gaps are operated in the region of the Paschen minimum if low sparkover voltages are required [50]. By a special choice of electrode materials (e.g. cesium Cs or barium Ba) and inert gas mixtures (e.g. neon Ne with a small percentage of argon Ar), low sparkover voltages in the range of 100 V can be achieved [480].

Another approximation for the *breakdown voltage* (*ignition voltage*) V_{bd} can be derived if a quadratic ansatz

$$\alpha_e/p \sim \{(E/p - (E/p)_0\}^2 \qquad (3.2\text{-}41)$$

for the effective ionization coefficient α_e is inserted into the ignition condition (3.2-29), instead of the exponential ansatz according to Eq. (3.2-21). Gases with a *high electron affinity* and with significant attachment coefficients η can also be described in this manner, in contrast to the equations (3.2-21) and (-35). The solution for V_{bd} is

$$V_{\text{bd}} = (E/p)_0\cdot pd + c\cdot(pd)^{1/2}. \qquad (3.2\text{-}42)$$

with the constants according to table 3.2-4. For $pd \to 0$, V_{bd} also approaches zero. Therefore,

the short-distance/ low-pressure breakdown physics is not described correctly by this approximation, but it is restricted to higher *pd* values.

Table 3.2-4: Constants for the approximate equation (3.2-42) at room temperature.

Gas	$(E/p)_0$ see Figure 3.2-12	c	
	$\frac{\text{kV}}{\text{mm·bar}}$	$\frac{\text{kV}}{(\text{mm·bar})^{1/2}}$	
SF_6	8.80	0.27	[39]
	6.61	2.19	[45]
CO_2	3.21	5.88	[39]
Air	1.85	3.87	[39]
	2.43	2.01	[45]
	2.44	2.12	[16]
N_2	2.44	4.85	[39]
H_2	1.01	2.42	[39]

Instead of the quadratic ansatz (3.2-41), a linear ansatz according to Eq. (3.2-26) is also used for **sulfur hexafluoride** (SF_6), because of its high electron affinity:

$$\alpha_e/p = k_i\{(E/p) - (E/p)_0\}$$

In the region close to the zero crossing, this allows positive or negative values depending on whether ionizations or attachments dominate. A rapid increase of the effective ionization coefficient α_e with the related field strength E/p can also be described, Figure 3.2-12.

With $k = 14$ ($\gamma = 10^{-6}$), $k_i = 27.7$/kV and $(E/p)_0 = 8.84$ kV/(mm·bar), the ignition condition gives

$$V_{bd} = pd \cdot 8.84 \text{ kV/(mm·bar)} + 0.5 \text{ kV} . \quad (3.2\text{-}43)$$

Figures 3.2-14 and -15 show *numerically evaluated curves* related to the *approximate Eqs.* (3.2-35), (-42) and (-43). Field strengths were determined by dividing voltages by electrode spacings. The figures show that *SF_6* has a significantly higher electric strength than *air*. The electric strength of *helium* and other *inert gases* is comparatively low.

Note: Very often the *breakdown strength of atmospheric air* under standard conditions is given as $\hat{E}_{bd} = 30$ kV/cm = 3 kV/mm. According to Figure 3.2-15, this is only a guide value for distances in the range of a few centimeters.

Note: The high electric strength of SF_6 can also be used in *gas mixtures*, e.g. in mixtures with nitrogen N_2. Even a SF_6 content of 20 % is sufficient to reach 70 % of the dielectric strength of the pure SF_6 gas [22]. This also means that slight *contamination* by other gases does not significantly affect the dielectric strength of the electron-affine gas.

Eq. (3.2-35) gives the typical Paschen minimum for helium (curve 1) and air (curve 2), Figure 3.2-14. Eq. (3.2-42) no longer describes the region of the minimum correctly. Therefore, calculated curves for air (curve 3) and SF_6 (curve 4) differ significantly from reality in the region of low *pd* values. Eq. (3.2-42) must only be used for higher *pd* values. Eq. (3.2-43) gives a curve for SF_6 (curve 5) without describing the strength recovery below the Paschen minimum.

The division of breakdown voltage V_{bd} by the electrode distance d gives the *breakdown field strength* E_{bd} for a given pressure (e.g. $p = 1$ bar, Figure 3.2-15). The breakdown field strength increases with decreasing distance d because of a decreasing probability of ionizing collisions between the electrodes. The breakdown field strengths of SF_6 and air approach constant values with increasing electrode distances.

A *lower limit* results from the fact that the field strength has at least to be high enough to achieve an *effective ionization coefficient* $\alpha_e = \alpha - \eta$ that is positive, Figure 3.2-12. This means that an electron avalanche is only possible if the generation of new electrons by collisions outweighs electron attachment. The ionization coefficient α has to be bigger than the attachment coefficient η. Values for the corresponding field strength limit $(E/p)_0$ are given in table 3.2-4.

The **influence of the electrodes** has previously been accounted for by the *feedback co-*

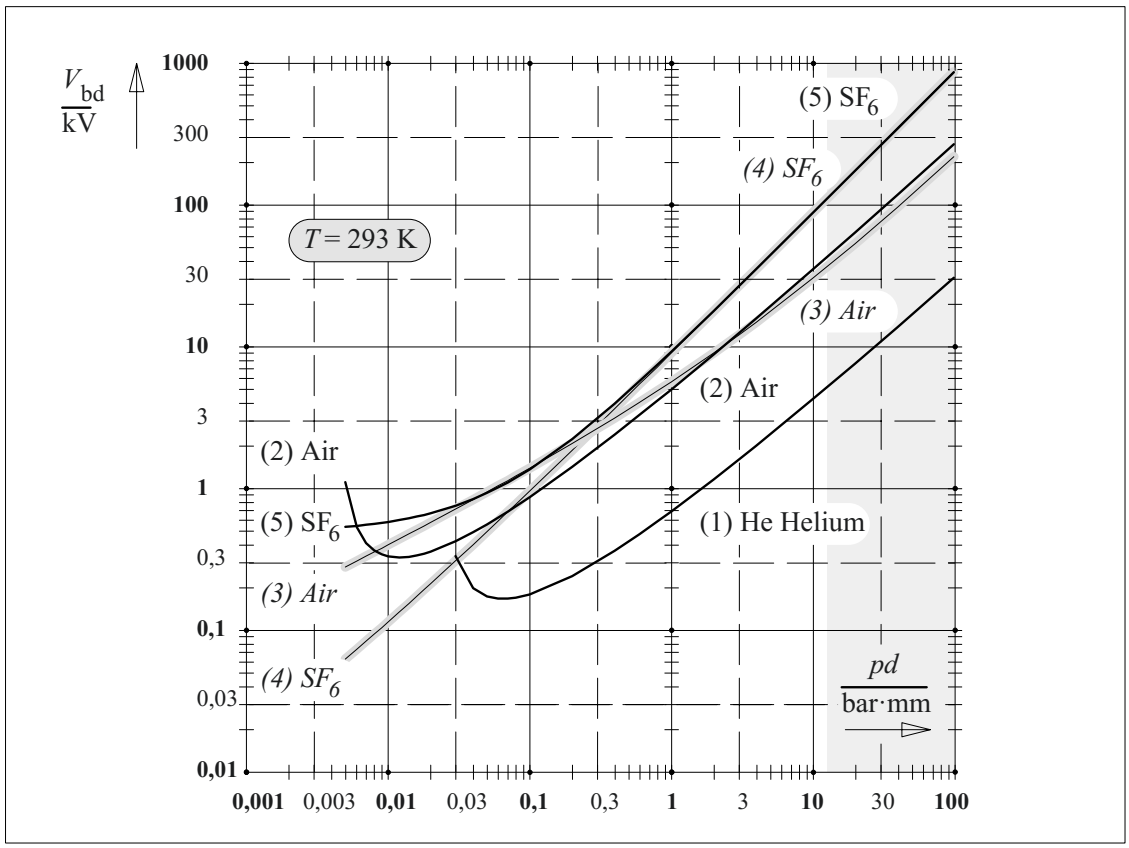

Figure 3.2-14: Calculated breakdown voltages as function of pd (Paschen curve) for diffenrent gases:
(1) Helium and (2) air according to eq. (3.2-35) and table 3.2-1 with k = 5.
(3) Air und (4) sulfur hexafluoride according to eq. (3.2-42) and table 3.2-4.
(5) Sulfur hexafluoride according to eq. (3.2-43).

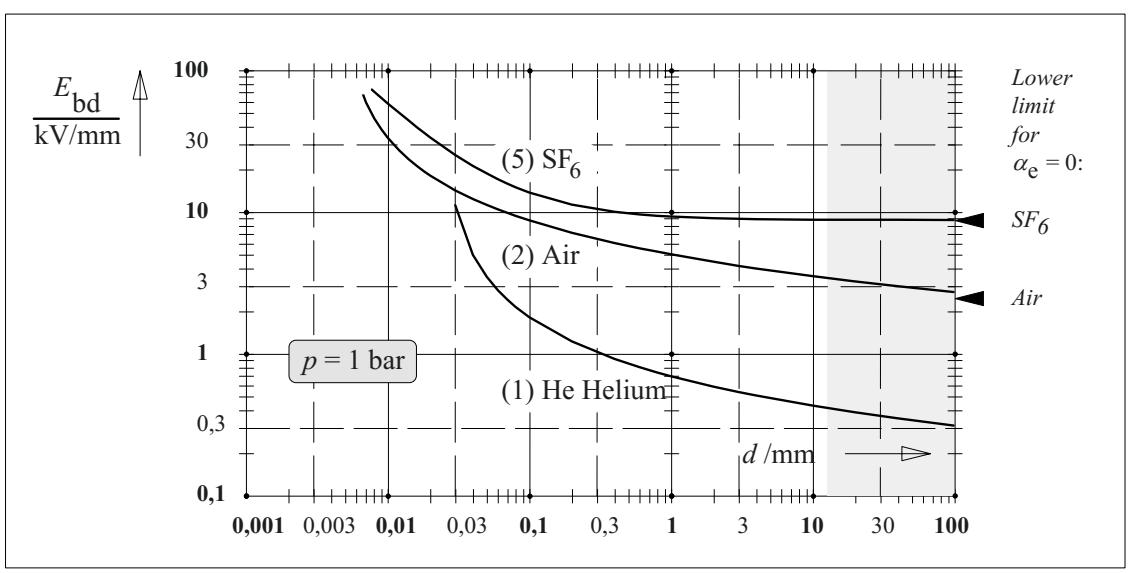

Figure 3.2-15: Calculated electrical breakdown field strengths as function of the electrode distance d for diffenent gases at normal pressure (p = 1 bar) and normal temperature (T = 293 K). Equations and legend see fig. 3.2-14.

efficient (surface ionization coefficient) γ. At higher *pd* values, the influence of γ is weak because of a twofold logarithmation in Eq. (3.2-35). Much stronger influences on breakdown voltages are exerted by the **surface roughness** of the electrodes. As was already shown in Figure 2.3-18 and Eq. (2.3-62), microscopic surface elevations (e.g. burrs, scratches, craters, tips, edges etc.) can cause *microscopic field stress enhancements* exceeding the background field several times. Nevertheless, field stress enhancement is only local and decreases quickly towards the background field strength with increasing distance from the surface. Figure 3.2-15 shows that breakdown field strengths in the region of a few 10 µm are significantly higher than in the millimeter region. According to Eq. (3.2-9b), the inception of a discharge in the *non-uniform field* close to a rough surface is determined by the integral $\int \alpha(x)\mathrm{d}x$. This means that the number of electrons $\mathrm{e}^{\int \alpha(x)\mathrm{d}x}$ in an avalanche has to reach a value corresponding to sufficient feedback to the cathode for the initiation of new avalanches.

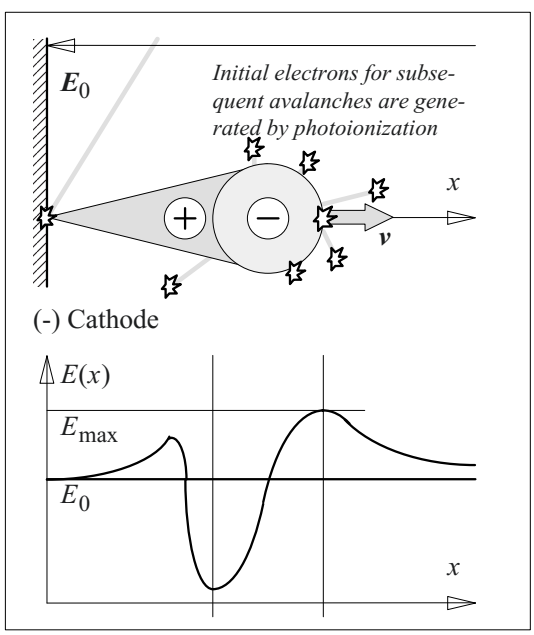

Figure 3.2-16: Distortion of the electric background field by space charges of a discharge avalanche on the axis of the avalanche. The diameter of the avalanche head increases with increasing path length because of electron diffusion.

Example: Treatment of electrode surfaces

Special requirements can be fulfilled by *polished electrodes* which must not show any damages (scratches, craters, tips etc.).

If electrode defects cannot be completely excluded, it has proved to be advantageous to *sand-blast* the surfaces in order to achieve uniform roughness and to eliminate extreme defects [50].

Under the influence of *moderate discharges*, defects like deposits or metallic tips are often burned off and a *conditioning* of the surface takes place. Nevertheless, new craters can be formed under the influence of *high-current discharges*.

In many cases, *spark gaps* have to be *conditioned* by a number of discharges in order to ensure reproducible sparkover behavior. In doing so, pre-ignitions at comparatively low voltages can frequently be observed. A simple *cleaning* of the surface is normally not sufficient because residual lint and fibers on the surface cannot be completely excluded.

3.2.3 Space-charge-dominated Discharge, Streamer Discharge

If the avalanche, which is triggered by an initial electron, grows up to 10^6 to 10^8 electrons, the electric field in the environment of the avalanche is significantly influenced by space charges, Figure 3.2-16. Comparatively immobile positive ions remain in the *avalanche tail*. Electrons that are much more mobile form a negative and approximately spherical *avalanche head*. Its diameter increases with increasing path length because of diffusion processes.

In relation to the background field $\boldsymbol{E}_0$, a large field-strength enhancement $E(x) = E_{max}$ is caused by *space charges* at the front of the avalanche head. Therefore the number of ionizing collisions and photon-emitting recombination increases.

The emitted photons cause *photoionization* in the gas volume and generate initial electrons for *consecutive avalanches* in the area around

the first avalanche's head, Figure 3.2-16. The superposition of all the avalanches quickly generates a conductive streamer, Figure 3.2-17. Therefore, the mechanism is known as a *streamer mechanism* or *streamer discharge*.

Note: The streamer need not necessarily start at the cathode. If the first avalanche starts within the gas volume, photoionizations cause the progression of both an *anode-directed* streamer and a *cathode-directed* streamer.

Photoionizations in the gas volume cause very fast bridging of long distances. A conductive path (streamer) is already formed *during the propagation time of a single avalanche*, Figure 3.2-17. Because of the high field strength and the secondary avalanches running ahead, the streamer propagates towards the anode with high velocity. In air at atmospheric pressure and in a uniform field, the streamer velocity is approximately

$$v_{st} \approx 100 \text{ cm/}\mu\text{s} . \qquad (3.2\text{-}44a)$$

Note: In strongly **non-uniform fields**, the background field is rapidly decreasing and consecutive avalanches can only start close to the avalanche's head. The velocity of streamer propagation

$$v_{st} \approx 10 \text{ cm/}\mu\text{s} \qquad (3.2\text{-}44b)$$

is therefore significantly reduced.

It is a *precondition for breakdown* that the generation of electrons by collision ionization outweighs the attachment of electrons. This means that the effective ionization coefficient $\alpha_e = \alpha - \eta$ according to Eq. (3.2-25) and Figure 3.2-12 has to be greater than zero. A breakdown is not possible below that *field strength limit* (approximate values according to [16]):

$$(E/p)_0 = 24.4 \text{ kV/(cm·bar)} \quad \textit{for air} \qquad (3.2\text{-}45)$$

$$(E/p)_0 = 87.7 \text{ kV/(cm·bar)} \quad \textit{for } SF_6 \qquad (3.2\text{-}46)$$

Note: *Surface roughness* or *particles* may cause local non-uniformities of the field and apparently lower field strength limits [16]. This effect results in different statements on field strength limits, see table 3.2-4.

Furthermore, the *number of electrons* has to reach the critical value

$$N_{crit} = 10^6 \ldots 10^8 . \qquad (3.2\text{-}47)$$

Raether's ignition condition for the *streamer mechanism* in non-uniform fields is given by analogy with Townsend's ignition condition for the avalanche-generation mechanism in uniform fields according to Eq. (3.2-9):

$$e^{\{\int_0^d (\alpha-\eta)\,dx\}} \geq N_{crit} \qquad (3.2\text{-}48)$$

$$\int_0^d (\alpha - \eta)\,dx \geq \ln\{N_{crit}\} = k_{st} = 14....18 \qquad (3.2\text{-}49)$$

This means that the *ignition condition* for the streamer mechanism formally resembles

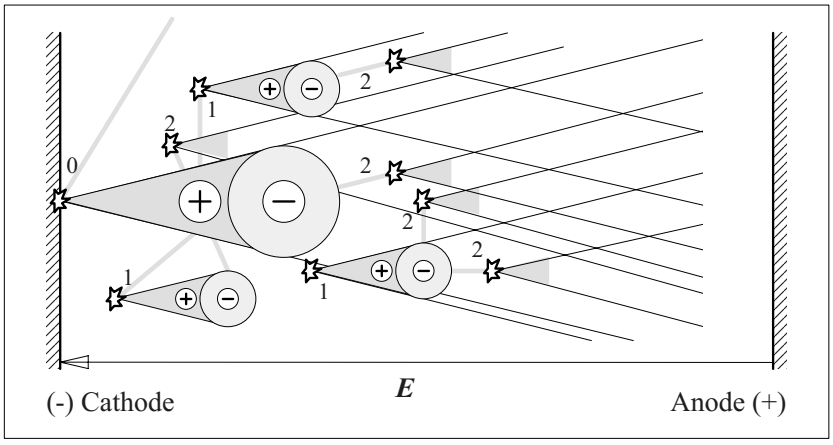

Figure 3.2-17: A physical model describing the space-charge-dominated discharge, i.e. the streamer mechanism according to Raether.

0,1,2,... Starting times for avalanches

Ignition of new avalanches by photoionization.

Townsend's ignition condition Eq. (3.2-9). Nevertheless, streamer inception is determined by the factor k_{st} which is different from factor $k = \ln(1 + 1/\gamma)$, the latter being related to the feedback coefficient γ (surface ionization coefficient).

Note: The *transition from the Townsend mechanism to the streamer mechanism* is smooth, as can be seen from the (lower) field strength limits according to Figure 3.2-15.

For *air* at *standard atmospheric conditions* and for a **uniform field**, Eq. (3.2-42) is

$$V_{bd} = d \cdot 2.44\ \text{kV/mm} + d^{-1/2} \cdot 2.12\ \text{kV/mm}^{-1/2} \qquad (3.2\text{-}50)$$

if the quadratic ansatz for α_e/p according to Eq. (3.2-41) is chosen [16].

For the description of SF_6 the linear ansatz according to Eq. (3.2-43) is more suitable. With the field strength limit $(E/p)_0$ = 8.87 kV/(mm·bar) and with k_i = 27.7/kV the ignition condition Eq. (3.2-49) results in

$$\int_0^d \{E - p \cdot (E/p)_0\}\,\mathrm{d}x \geq \frac{k_{st}}{k_i} = 0.5....0.7\ \text{kV}. \qquad (3.2\text{-}51)$$

In agreement with Eq. (3.2-43) it is found that the total voltage can exceed the voltage calculated from the field strength limit by 0.5 to 0.7 kV only [16]:

$$V_{bd} = pd \cdot 8.77\ \text{kV/(bar·mm)} + 0.7\ \text{kV} \qquad (3.2\text{-}52)$$

The ignition condition (3.2-48) and (-49) is also valid in the non-uniform field, Figure 3.2-18. In regions with *high field strength* charge carrier generation by collision ionization is predominant ($\alpha > \eta$). In regions with *low field strength* the attachment of electrons ($\alpha < \eta$) predominates.

In Eq. (3.2-48) and (-49) the integration is not to be performed until $x = d$, but it is sufficient to integrate until $x = x_0$ within the region with a positive ionization coefficient. If the *critical number of electrons* N_{crit} is reached in doing so, the avalanche has generated enough space charge for a further self-sustaining growth into the low field region. Otherwise the number of electrons decreases by attachment processes and the ignition condition is not fulfilled, fig 3.2-18 (bottom).

The *ignition condition in the non-uniform field* can also be interpreted with Eq. (3.2-51) as follows: In Figure 3.2-18 (middle), the highlighted "voltage area" above $E/p = (E/p)_0$ has

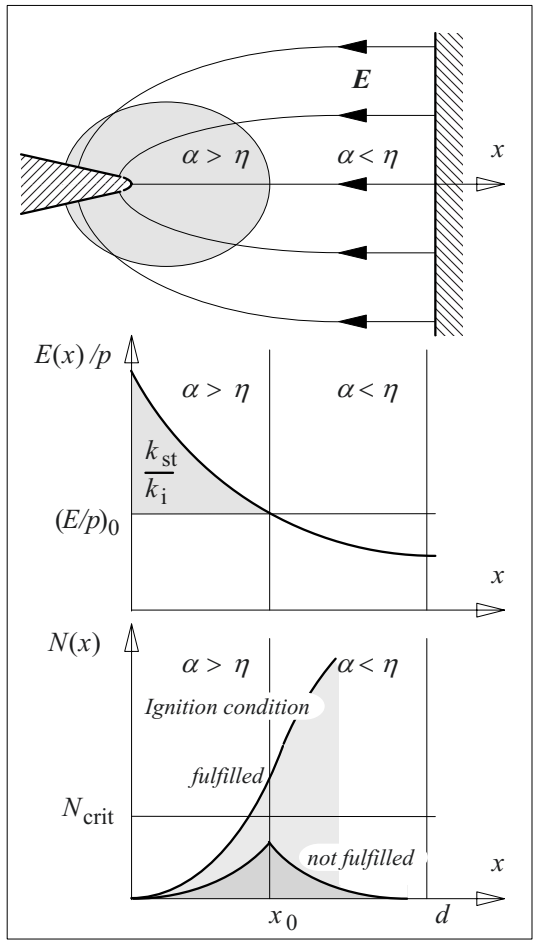

Figure 3.2-18: Development of electron avalanches in a nonuniform field close to a negative electrode tip.
Top: Regions with positive and negative effective ionization coefficients.
Middle: Field strength curve along the x-axis.
Bottom: Avalanche development with electron numbers above and below the critical number.

to exceed the value k_{st}/k_i. The value for SF_6 is approximately 0.7 kV.

Note: For non-uniform **SF_6 insulations** the critical electron number N_{krit} can be reached even for comparatively short path lengths x, in comparison with air for example. This is caused by a strong increase of the effective ionization coefficient α_e with E/p above the field strength limit $(E/p)_0$ = 8.87 kV/(bar·mm). Therefore, *very limited local field strength enhancements* by surface roughness or particles can trigger a streamer mechanism, even if the field strength limit is not yet reached in the macroscopic field.

The *sensitivity of SF_6 insulations* against *surface roughness* and contaminations by *particles* requires special care during manufacturing and assembly processes of *gas-insulated switchgear* (GIS). Therefore, they have to be tested on-site for freedom form partial discharges after the final assembly.

The former considerations are basically valid in non-uniform fields both for *negative* and *positive point electrodes*. During the integration procedure according to Eq. (3.2-48) and (-49) it has to be considered that the avalanche grows in the $+x$ direction for a negative and in the $-x$ direction for a positive point respectively.

3.2.4 Impulse and High-frequency Breakdown

3.2.4.1 Statistical and Formative Time Lag (Discharge Delay)

Only *static* breakdown voltages and field strengths have been considered previously. This means that the voltage is applied over such a long period or is increased so slowly that breakdown delay effects cannot be observed at all.

In the case of *fast rising voltages* it has to be considered that breakdown does not occur directly at $t = t_0$ when the voltage exceeds the static sparkover voltage V_0. Breakdown cannot develop before an initial electron occurs after the *statistical time lag* t_s (*ignition delay*) and before a conductive streamer has developed during the *formative time lag* t_f (*streamer formation delay*), Figure 3.2-19. The formation of a high current discharge and the final voltage collapse coincide with a comparatively short *time of voltage collapse* t_c, which is determined by the *spark resistance laws* and by the elements and properties of the *discharge circuit*. During the total time to breakdown

$$t_T = t_0 + t_s + t_f + t_c \qquad (3.2\text{-}53)$$

the stressing voltage $v(t)$ with the peak value V_{max} can significantly exceed the static breakdown voltage V_0. This means that the *impulse factor*

$$f = V_{max}/V_0 \qquad (3.2\text{-}54)$$

can be much greater than one.

Note: The sum of statistical and formative time lags

$$t_{bd} = t_s + t_f \qquad (3.2\text{-}55)$$

is also known as the *discharge time lag*. Very often, the time of voltage collapse t_c is comparatively short and can be neglected.

The **statistical time lag** t_s is caused by the stochastic character of electron generation by ionizing radiation and thermal processes. The

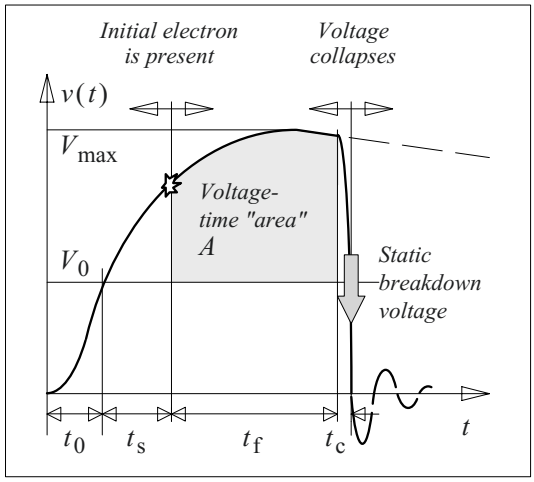

Figure 3.2-19: Discharge delay by the statistical time lag and by the formative time lag for a transient voltage stress (impulse voltage).

time lag decreases with an increasing highly stressed gas volume as the probability for the generation of an initial electron increases with an increasing critically stressed gas volume (*volume-time characteristic*).

Because of *statistical size effects* according to Section 3.1.3, the 50 % value of the ignition delay time (i.e. the statistical time lag t_{s50}) decreases with increasing number of critically stressed volume elements ΔV, Figure 3.2-20. Thereby, $W_m = 1 - F_m$ is the probability for the absence of an initial electron in m volume elements ΔV, which decreases with increasing volume. For very large volumes, t_{s50} therefore becomes very small. In a given volume, the probability $F(t_s)$ for the presence of an initial electron (initiating an avalanche) approaches 1 with increasing ignition delay time t_s.

The statistical time lag for *air* is in the region of a few 10 ns only if the electrode distances are longer than 1 mm [39]. Longer statistical time lags can be found for SF_6, because of the attachment of free electrons to gas molecules.

The statistical time lag can be practically eliminated by *irradiation of the cathode* with ionizing ultraviolet light. Furthermore, it can be reduced by a *very rough cathode surface* with local field stress enhancements causing

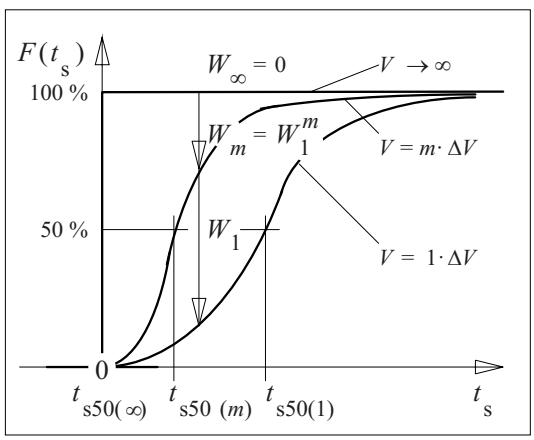

Figure 3.2-20: Statistical size effect for the decreasing the statistical time lag with the increasing critically stressed gas volume.

field emission of electrons at high overvoltages.

Note: Very high values of statistical time lags are measured in small *voids, bubbles or cavities* within dielectric materials. The probability for the presence of an initial electron is significantly reduced in small enclosed gas volumes, see Section 3.6.1.2.

The **formative time lag** t_f from the first avalanche to the formation of a conductive channel (i.e. the *spark formation time*) can have very different values.

If *Townsend's generation mechanism* is considered, many consecutive avalanche and ion transit times are required for the formation of a conductive channel. The formative time lag is of the order of 10 µs.

The Townsend mechanism can only occur for small *pd* values and for voltages close to the static breakdown voltage V_0. At high overvoltages according to Figure 3.2-19, the ionization coefficient α increases significantly. Therefore, the *transition to the streamer mechanism* occurs even for significantly smaller *pd* values, and the streamer mechanism can be assumed in most of the practical cases.

The *propagation velocity* (growth velocity) of the *streamer* channel

$$u(x, t) = \mathrm{d}x/\mathrm{d}t \qquad (3.2\text{-}56a)$$

increases with $E(x,t)$ if the reference field strength for streamer inception $E_0(x)$ is exceeded [418]. Assuming a proportionality, it can be stated that

$$u(x,t) = K \cdot \{E(x,t) - E_0(x)\}. \qquad (3.2\text{-}56b)$$

If the dependence of the field strength on the variables position x and time t is described by the functions g(x) and $v(t)$, i.e. by

$$E(x,t) = g(x) \cdot u(t), \qquad (3.2\text{-}56c)$$

it is concluded that

$$\mathrm{d}x/\mathrm{d}t = u(x,t) = K \cdot g(x) \cdot \{v(t) - V_0\}.$$

After separation of the variables x and t, two corresponding integrations from one electrode

to the other (along x from $x = 0$ to d) and from the beginning of streamer formation to the beginning of voltage breakdown (over t from $t = t_0 + t_s$ to $t_0 + t_s + t_f$) can be performed:

$$\int_0^d \frac{\mathrm{d}x}{K \cdot g(x)} = \int_{t_0+t_s}^{t_0+t_s+t_f} \{v(t) - V_0\}\,\mathrm{d}t \,. \quad (3.2\text{-}56d)$$

According to Figure 3.2-19, the right hand side of the equation describes a *voltage-time area A* below the voltage curve $v(t)$ and above the reference voltage V_0. The area is related to *streamer formation* only and can therefore be called a *formative area*.

Note: Below the reference voltage V_0, the conditions for streamer formation are not fulfilled and streamers are not possible. The reference voltage is nearly identical with the static breakdown voltage.

The voltage-time area A is also identical with the left hand side of Eq. (3.2-56d), which exclusively consists of geometric quantities and gas properties. Therefore, A is a constant quantity which is typical for a given arrangement (**Kind's voltage-time law** or **equal area criterion**) [418]:

$$\int_{t_0+t_s}^{t_0+t_s+t_f} \{v(t) - V_0\}\,\mathrm{d}t = A = \text{const.} \quad (3.2\text{-}56e)$$

If the formative area A is related to the static breakdown voltage V_0, a *characteristic time* A/V_0 is defined for the given arrangement. It can vary between 10 ns (for nearly uniform arrangements) and some 100 ns. A/V_0 is strongly dependent on the field efficiency factor η, but not so much on the flashover distance d [418].

Note: For very non-uniform arrangements, the formative area A can also be related to the flashover distance d. For air-insulated *point-to-plane arrangements*, the constants A/d = 400 kV·µs/m (negative point) and 650 kV·µs/m (positive point) are given as approximate values [16].

In *non-uniform fields* discharge delay times are longer than in *uniform fields*, because of the comparatively small gas volume with high field strength. Thereby, they show a higher scatter and the formative time lag is prolonged, because of the decreasing streamer velocity in the low-field region, Eq. (3.2-56b).

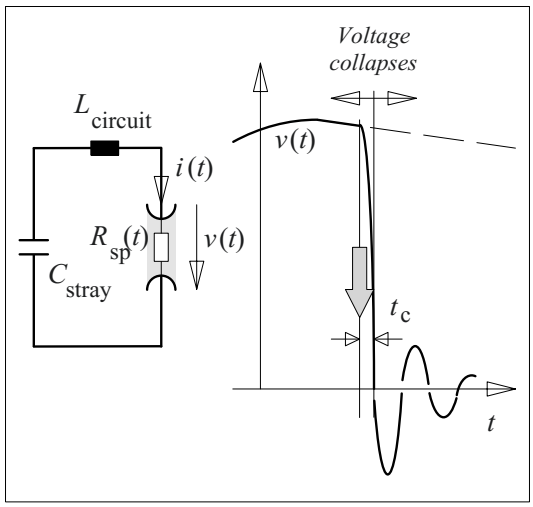

Figure 3.2-21: Ringing discharge process of a (stray) capacitance and collapse of the voltage after fomation of a conductive streamer.

The time t_c that is necessary for the final collapse of the voltage corresponds to the **spark formation time**. It depends on the parameters of the discharge circuit and the time-dependent values of the *spark resistance* $R_{sp}(t)$. In most cases, the final breakdown causes a damped ringing during the discharging of stray and circuit capacitances via the circuit inductance and $R_{sp}(t)$, Figure 3.2-21. A quarter-cycle is approximately equivalent to the time of voltage collapse t_c.

Note: Very fast voltage collapses in the region of a few ns can occur in *gas-insulated switchgear* (GIS) because of the small distances and low inductances. For example, the time constant of the current increase during discharging of a line with the characteristic line impedance Z_W = 50 Ω is $\tau = L/Z_W$ = 2 ns only, if the inductance of a ten centimeter long discharge channel is approximately L = 10 cm·1 nH/mm = 100 nH, see Figure 2.6-8. Furthermore, the voltage collapse *at enhanced pressure* can be extremely fast in *electron-affine gases*, Section 3.2.7.1 and Eq. (3.2-92). Thereby, traveling waves are excited on the weakly damped lines, causing significant overvoltages (*fast transients*, Section 2.6.3.1). Voltage collapses in *air-insulated equipment*

are significantly slower because of longer spark formation times, longer insulating distances and higher circuit inductances.

3.2.4.2 Voltage-time Characteristics

If it is assumed that the statistical time lag and the time of voltage collapse are negligible in comparison with the *formative time lag* t_f, the *impulse voltage-time characteristic* for the breakdown process can be determined from the equal area criterion (Kind's voltage-time law) according to Eq. (3.2-56e), see Figure 3.2-22:

For a given *impulse voltage curve* $v(t)$ (e.g. lightning impulse voltage 1.2/50 µs) and for a given *arrangement* with static breakdown voltage V_0 and voltage-time area A, an initial electron should be present immediately after exceeding V_0, i.e. the statistical time lag is neglected (t_s = 0). Thereby, an avalanche/ streamer starts and approaches the electrodes. Breakdown occurs as a voltage collapse when a conductive streamer is formed between the electrodes. This is assumed after the *voltage-time area A* is reached, see curves no (1) to (4) in Figure 3.2-22. If the necessary voltage-time area is not reached although V_0 is exceeded, streamer growth stops before a conductive channel between the electrodes develops and the breakdown *no longer* occurs, (curve no. 5).

The *impulse voltage-time characteristic* is determined from the correlation of breakdown times and voltage peak values of the considered voltage curve. The voltage-time characteristic *increases* towards shorter times.

It is of general importance in high voltage engineering that electrical *stress amplitudes* can be increased if *stress durations* are reduced (impulse voltage-time characteristic).

Example: Spark-gap lightning arrester

Spark-gap lightning arresters can be built with low static breakdown voltages V_0 close to 100 V if they are filled with *inert gases*. Because of their voltage-time characteristic, fast rising overvoltages can overshoot significantly up to some kV before they are chopped by a gas breakdown. Therefore, only *coarse protection* is realized, e.g. in order to divert high lightning currents. Sensitive components have to be protected additionally by an electronic *fine protection*.

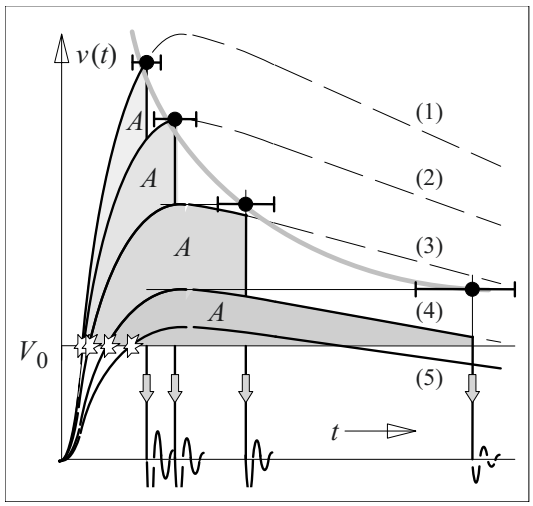

Figure 3.2-22: Determination of a voltage-time characteristic according to Kind's equal area criterion A=const. for a lightning impulse voltage 1.2/50 µs.

The voltage-time characteristic is strongly dependent on the *shape of the corresponding impulse voltage curve*. This can easily be explained by the equal area criterion. Voltage-time characteristics measured with the standard lightning impulse voltage (1.2/50 µs) cannot be directly applied to other voltage curves.

Measured breakdown times often show a large *scatter*. On one hand, the scatter results from the *statistical time lag* and from the variation of the formative time lag especially in *non-uniform fields*. On the other hand, limited variations of the area A have a significant impact on the breakdown time if the voltage curve is close to the limit case of the criterion, see Figure 3.2-22 curve (4).

Therefore, the *empirical determination* of a voltage-time characteristic gives a broad band. If enough data are available, *cumulative frequency polygons* for breakdown times can be considered and curves for breakdown probabilities of 5 % and 95 % can be calculated enclosing 90 % of the expected breakdowns.

In many cases the *Gaussian normal distribution* is applied and the breakdown band can be delimited by the threefold empirical standard deviation on both sides of the arithmetic mean value t_m. Thereby, estimates for a *certain withstand time* $t_m - 3\sigma$ and a *certain breakdown time* $t_m + 3\sigma$ are calculated according to Section 3.1.2.2.

Note: Instead of the *breakdown time* the *breakdown voltage* can also be regarded as a random variable.

Example: Chopping spark gap

During testing of high-voltage equipment (transformers, bushings etc.) tests often have to be performed with *"chopped lightning impulses"* in order to simulate the impact of very fast voltage transients. For this purpose, a chopping spark gap is connected in parallel to the test object; the gap has to spark over within a *time interval* between 4 and 6 µs [52].

If it is not possible to use a triggered spark gap which can be specifically ignited at a predefined time, preliminary tests are necessary in order to determine the *scatter of the breakdown times* at a *given test voltage* amplitude. If necessary, the electrode distance has to be adjusted so that all breakdowns occur within the specified time interval.

Note: During the testing of components for *gas-insulated switchgear* (e.g. grading capacitors) very fast voltage collapses are required in order to simulate the impact of fast transients. Very short *streamer formation times* cannot be achieved in a spatially extended impulse circuit with an air gap, therefore *"chopping under SF_6"* is often required. For this purpose, the chopping spark gap is integrated into the enclosed and SF_6 insulated test vessel in order to achieve a *very fast voltage collapse* (see Figure 3.2-21, comments above and Section 3.2.7.1).

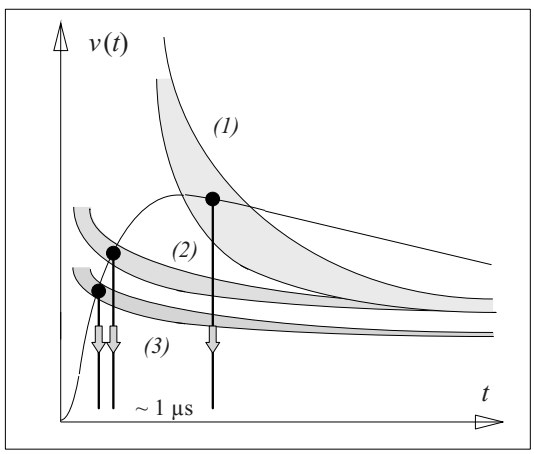

Figure 3.2-23: Voltage-time characteristics for a simple air-gap (1), an insulating gap in a GIS (2) and a lightning arrester (3).

In *uniform and weakly non-uniform fields* there are high field strengths along the entire path between the electrodes and favorable conditions to streamer propagation exist if the reference voltage V_0 is exceeded. Therefore, the streamer propagation velocity according to Eq. (3.2-44a) is high, the *formative time lag* t_f is short and the voltage-time area A is small, see Eq. (3.3-56). *Voltage-time characteristics* are comparatively *flat* down to a few 100 ns.

In strongly *non-uniform fields* the streamer propagation velocity is significantly reduced in the low-field regions, see Eq. (3.2-44b). Therefore, the *formative time lag* t_A is long and the voltage-time area A is large. *Voltage-time characteristics* show a significant *increase* towards shorter times.

Example: Insulation coordination

Outdoor installations and simple *protective air-gaps* have voltage-time characteristics with comparatively high gradients because of their non- uniform fields and long flashover distances, Figure 3.2-23. *Gas-insulated switchgear* (SF_6 insulated GIS) with more uniform fields and with shorter flashover distances have only gently sloping voltage-time characteristics. If the reference voltage V_0 is the same, a breakdown is to be expected at first in SF_6, unless the stress in the GIS is reduced by traveling wave refractions.

Valve-type/ spark-gap arresters are made of a series connection of spark gaps with a non-linear SiC resistor. The spark gaps have a *flat voltage-time characteristic* in order to fulfill their protective function, including for fast rising overvoltages, according to the principles of *insulation coordination*. Modern metal-oxide arresters no longer need spark gaps, Section 6.1.4.3.

3.2.4.3 High-frequency Breakdown

In contrast to transient impulse stresses, high-frequency stresses are long-lasting.

With increasing frequency up to 1 MHz, the breakdown strength of air at standard atmospheric conditions decreases down to 80 % of the 50 Hz strength [46]. This is caused by re-

moval of mobile electrons close to the anode and by residual positive ions which form a positive space charge cloud. After the polarity reversal, the positive space charge is in front of the cathode and increases the local field strength significantly.

The breakdown strength increases again above 3 MHz. Then, the electrons cannot follow the fast changing field without decelerating and the field distortion by residual positive ions no longer occurs. Additionally, the statistical discharge delay has a strength-increasing effect. At 100 MHz the strength is 1.5 to 1.6 times higher than at 50 Hz [46].

In *non-uniform fields*, high-frequency *pre-discharges* (both corona and surface discharges) show higher currents and higher light intensities than low-frequency pre-discharges because the low-field regions can be bridged more easily by higher displacement currents, which are proportional to frequency. This causes a *reduction of breakdown strength* because of the early inception of *leader discharges*, see Section 3.2.5.

Note: In **solids** (and sometimes also in **liquids**) there are *dielectric losses* (dissipation) that strongly increase with *frequency*. If heat transfer conditions are too unfavorable, thermal instability and the so-called *thermal breakdown* can occur at comparatively low voltages (in comparison with 50 Hz), see Section 3.5.2.

3.2.5 Discharges in Non-uniform Fields

3.2.5.1 Pre-discharges and Breakdown

Prior to the ignition of a gas discharge in a non-uniform field, space-charge-free conditions can certainly be assumed, but the field is not uniform, as was assumed for the derivation of Townsend's ignition condition, Section 3.2.2.1. For the calculation of electron avalanche growth and for the determination of an ignition condition, it is necessary to consider the variation of the *ionization coefficient* $\alpha(E)$ with the field strength $E(x)$ and with the *location* $\alpha(E(x))$ respectively, see Eq. (3.2-10). Then, the ionization coefficient has to be integrated along the electron path x according to Eq. (3.2-9b). Unfortunately, there is no universally valid result such as Paschen's law for the uniform field, but rather the result depends on the individual field geometry in this case.

In **weakly non-uniform fields,** there are favorable ionization conditions with $\alpha_e > 0$ along the whole path between the electrodes if the field strength is sufficiently high. As soon as the ignition condition for the Townsend or the streamer mechanism is fulfilled, *breakdown occurs immediately.* Pre-discharges do not occur above a *critical field efficiency factor* η_c, Figure 3.2-24. For air under standard atmospheric conditions, the critical value is $\eta_c \approx 0.2$.

In **strongly non-uniform fields**, high field strengths and favorable ionization conditions ($\alpha_e > 0$) only occur close to the curved electrode surface if the field efficiency factor η is below the critical value η_c. In the low-field region, α_e becomes negative for electron-affine gases (SF_6, oxygen and air), because of predominant electron attachment processes, Figure 3.2-18. If the *ignition condition* is fulfilled at the curved electrode, **pre-discharges** (**corona discharges**) occur without immediately causing breakdown. They begin as *glow discharges* (Townsend mechanism) at the curved electrode surface in the high-field region only. With increasing voltage, space-charge dominated *streamer discharges (bunch discharges*) start, which can propagate into the low-field region as long as the background field is strong enough. If the background field strength is too low for streamer growth, the streamer fades away. The remaining low-field gas volume between discharge head and counter-electrode is an ohmic-capacitive impedance *stabilizing* the pre-discharge, Figure 3.2-3b.

Note: The *stabilization of glow discharges* in a *strongly non-uniform field* can be explained by the following simplified model [2]: The pre-discharge at a curved electrode shall approximately be regarded as an increase of the effective electrode radius [2]. If a concentric outer

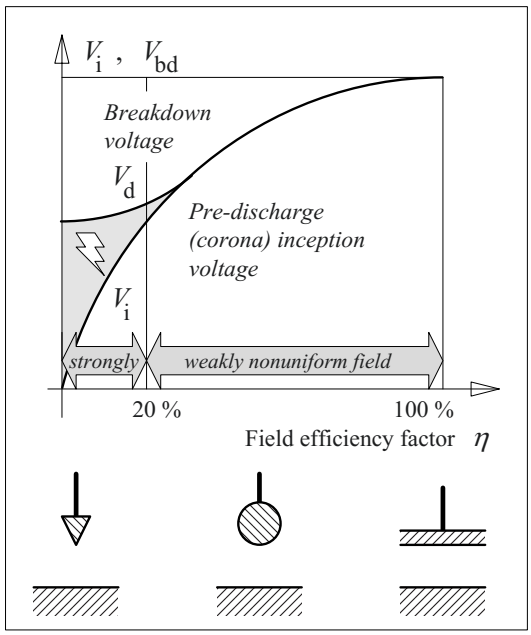

Figure 3.2-24: Pre-discharge (corona) inception and breakdown voltage in strongly and weakly non-uniform fields at constant electrode distances.

conductor with the radius R_a is assumed, there is a *minimum field strength* for a specific radius of the inner conductor, e.g. $R_{i\,min} = R_a/e$ for cylindrically symmetric arrangements, see Section 2.3.1.2 and 2.3.1.3. If the radius of the glow discharge is smaller than $R_{i\,min}$ (*strongly non-uniform field*), an increasing glow radius would cause a decreasing field strength and a stabilization of the *pre-discharge*. For radii that are greater than $R_{i\,min}$ (*weakly non-uniform field*), an increasing glow radius would cause an increasing field strength. The glow radius would no longer be stable and *breakdown* would occur immediately, which is in agreement with Figure 3.2-24.

The *inception voltage* V_i of pre-discharges (corona discharges) decreases with decreasing field efficiency factor (i.e. with increasing non-uniformity of the field), Figure 3.2-24. The *breakdown voltage* V_{bd} is stabilized at a higher level because of *space charge clouds* shielding the curved electrode ("*point electrode*"). Discharge processes are strongly influenced by the polarity of the point electrode (*polarity effect*). **Breakdown** occurs only at a higher voltage V_{bd}, if the field strength in the low-field region is sufficiently high for **streamer** growth to the counter-electrode.

For *very long flashover distances* (more than 1 m), sufficiently long stress durations and sufficiently fast voltage-time responses, the streamer growth, which is driven by collision ionization and photoionization, can be intensified by *thermal ionization*. Thereby, a high-current and bright channel is formed, which is known as a **leader** or **leader discharge**. At the head of the leader there are divergent streamer bunches supplying the leader's channel with the current that is necessary for thermal ionization. The conditions for leader discharges in *atmospheric air*, at distances of some meters and voltage amplitudes of many 100 kV are fulfilled for a *switching impulse voltage* of 250/2500 µs (positive point electrode) or a *power frequency voltage* (half-cycle with positive point electrode) due to displacement currents and current durations, but not for lightning impulses or DC voltages.

3.2.5.2 Polarity Effect

In a non-uniform field, there is a significant difference between the corona inception voltage and the breakdown voltage, which are both strongly dependent on polarity. For a *negative point electrode*, the pre-discharge inception voltage is comparatively low, but breakdown only occurs at comparatively high voltages. For a *positive point electrode*, the pre-discharge inception voltage is comparatively high, but the breakdown occurs at comparatively low voltages (*polarity effect*). The reason for this apparently inconsistent behavior is the formation of a *positive space charge* close to the point electrode. It will be explained for the example of a *point-to-plane arrangement* with a very non-uniform electric background field $\boldsymbol{E}_g$, Figure 3.2-25:

For a **positive point electrode,** avalanches have to start within the gas volume because of the very low field strength at the cathode, Figure 3.2-25 (left).

A first avalanche can start, if external radiation generates an *initial electron* within the region with positive ionization coefficient (i.e. *close*

to the point electrode). The avalanche grows into the direction of increasing field strength towards the point electrode. If the critical number of electrons N_{crit} is reached, new consecutive avalanches are permanently initiated within the gas volume by intense photoionization (streamer mechanism). Therefore, the first avalanche is followed by an abruptly increasing discharge current and a *stable glow discharge*.

The electrons are removed via the positive point electrode. A *positive space charge cloud* remains in front of the point electrode because of the comparatively immobile positive ions, Figure 3.2-25 (left middle). Thereby, the *electric field strength* is reduced in front of the point electrode, and it is enhanced in the low-field region in front of the plane electrode, Figure 3.2-15 (left bottom). Simultaneously, the *ionization boundary* $x = x_0$ with $\alpha_e = 0$ (at $E = E_0$) is shifted towards the plane electrode. The field stress enhancement in the low-field

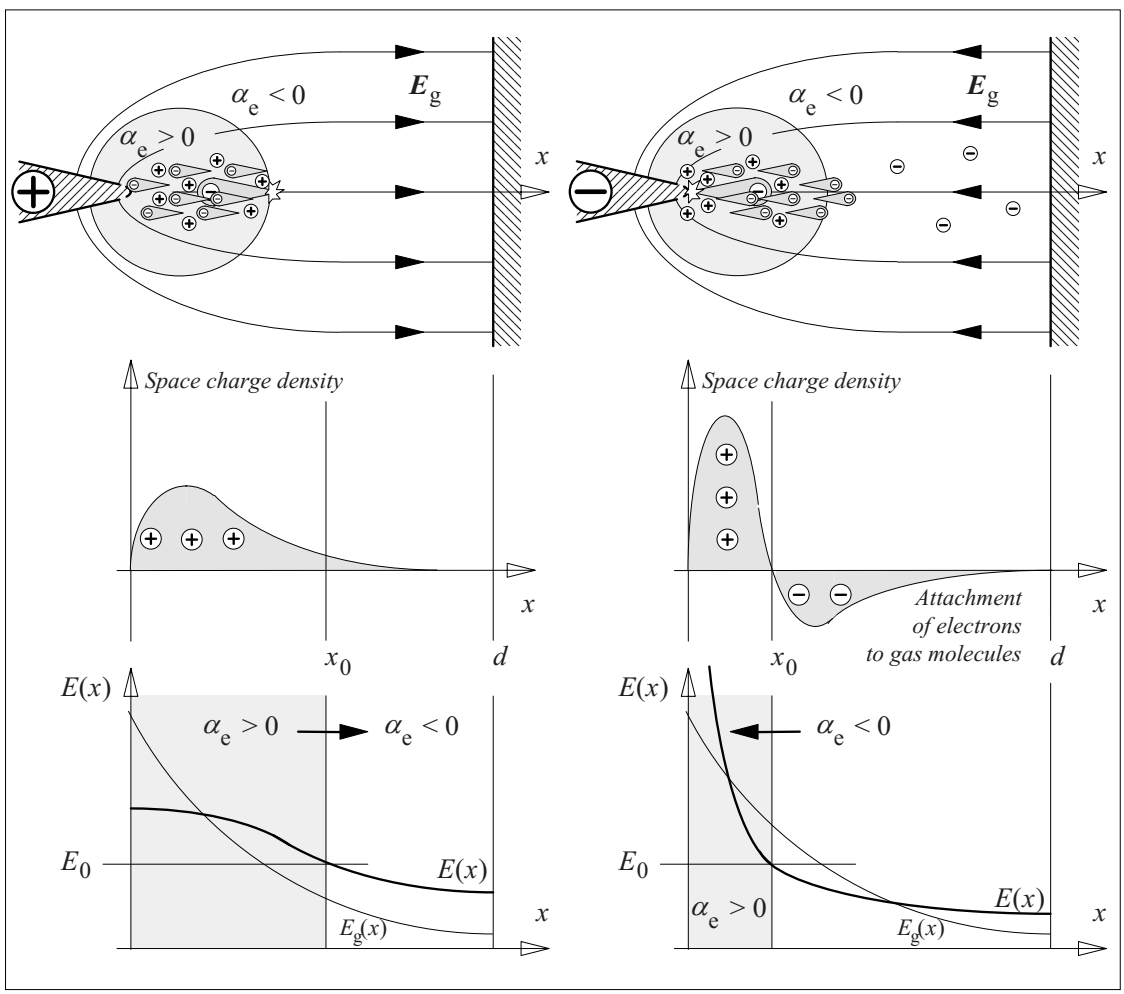

Figure 3.2-25: Polarity effect in a nonuniform field for a positive point (left) and a negative point electrode (right).

Top: Streamer propagation in high-field regions with positive effective ionization coefficient.

Middle: Formation of positve space charges by remaining positive ions in the high-field region (left and right) and formation of negative space charges by attachment of electrons in the low-field region (right).

Bottom: Field strength curve E(x) along the x-axis for the space-charge-free background field (thin lines) and for the space-charge-dominated resulting field (bold lines) with a shifting of the ionization boundaries.

region *improves* the conditions for *streamer growth* into the low-field region and for *breakdown*.

For a **negative point electrode**, an initial electron has to be provided on a very small surface on the point electrode. Therefore, a long discharge delay can be caused by the *statistical time lag* before a free electron is available, see Section 3.2.4.1. If the inception voltage is reached, a series of sporadic corona impulses occurs, which also depend on the work function of the cathode material [25].

The initiated streamers propagate into the low-field region, Figure 3.2-25 (right top). After crossing the ionization boundary $\alpha_e = 0$, the number of electrons in the avalanche is reduced by attachment to electron-affine gas molecules, and a *negative space charge* is generated in the low-field region, Figure 3.2-25 (right middle). Close to the point electrode, the avalanches leave a *positive space charge* cloud. Thereby, the electric field strength is significantly enhanced in front of the point electrode, and the field distribution is made uniform in the low-field region up to the plane counter-electrode Figure 3.2-25 (right bottom). Simultaneously, the ionization boundary $x = x_0$ with $\alpha_e = 0$ (at $E = E_0$) is shifted towards the point electrode.

Note: The increase of the negative space charge can reduce the field strength in front of the negative point electrode so that the pre-discharge is extinguished. It is ignited again after the negative ions have drifted to the anode. Thereby a continuous series of so-called *Trichel impulses* is generated. The repetition rate increases with increasing voltage because of the increasing ion drift velocity. If the drain of negative ions is equal to the regeneration, the *intermittent impulse discharge* changes over to a *continuous pre-discharge*.

For the negative point electrode, *streamer propagation* into the low-field region and *breakdown* are postponed by the equalization of the field strength profile, Figure 3.2-25 (right bottom). Therefore it can always be stated that

$$V_{\text{bd (neg. point)}} > V_{\text{bd (pos. point)}}. \qquad (3.2\text{-}57)$$

Accordingly, the breakdown at AC voltage is to be expected at the peak of a half-cycle when the point electrode is positive.

Example: Dielectric ion screen

Field distortion by ions can be shown impressively by a thin insulating screen (*dielectric ion screen*) between point and plane electrodes in air under standard atmospheric conditions, Figure 3.2-26.

Without a screen, DC breakdown voltages are very different for positive and negative point electrodes, as was stated above, Eq. (3.2-57).

If the dielectric ion screen were to be replaced by a *plane metallic electrode* at the potential of the point electrode, the field between the two planes would be uniform with breakdown voltages according to *curve (1)*. For medium distances the *dielectric ion screens* show very similar behavior for both polarities, see *curves (2)* and *(3)*.

For a positive or a negative point-electrode, positive or negative ions respectively are deposited on the screen surface. They displace the point-electrode potential onto the screen and *homogenize the field distribution* between the charged dielectric screen and the plane counter-electrode.

The screen is most effective when close *to the positive point electrode* because the drift of positive space charges into the low-field region is prevented, see Figure 3.2-25 (left). *Close to the plane counter-electrode*,

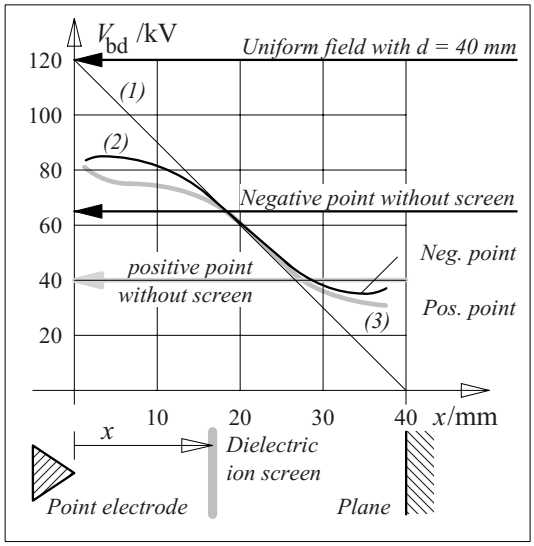

Figure 3.2-26: Impact of a dielectric ion screen on breakdown voltage in a very non-uniform d.c. field for a positive and a negative point electrode in air under standard atmospheric conditions.

the ion screen has the effect of a displaced space charge region for both polarities. This is similar to the positive point-to-plane arrangement without a screen and with a positive space charge that is responsible for the low breakdown voltages.

During **fast transient voltage stresses** (e.g. lightning impulse voltages), space charges cannot be accumulated as discussed above. In weakly non-uniform fields, even the *first* avalanche causes breakdown (streamer discharge). Therefore, the *negative point electrode* has a lower breakdown voltage than the positive point electrode because of the better avalanche starting conditions, see Section 6.3.1.1 (polarity effect for the **sphere gap**). Also for **rod-rod spark gaps**, there are other dependences because of corona discharges *on both sides*, see Section 6.3.1.2.

3.2.5.3 Corona Inception, Pre-Discharges

If the voltage is increased at a very non-uniform *point-to-plane arrangement and* different *pre-discharge phenomena* can be observed prior to breakdown, Figure 3.2-27. They depend on *voltage*, *polarity* and *flashover distance d*.

The **inception of corona discharges** takes place if the ignition condition for the streamer mechanism in the space-charge-free background field according to Eq. (3.2-49) is fulfilled. To a first-order approximation, the direction of integration and the polarity of the point electrode play a minor role. Actually, the inception behavior is also influenced by the electrode material and by the statistical time lag for the generation of initial electrons.

The *ignition condition* can be *interpreted analytically* both for concentric *cylinders* ($E \sim 1/r$) and for concentric *spheres* ($E \sim 1/r^2$) by the application of an ionization coefficient according to Eq. (3.2-21), [39]. As a result, transcendental equations are deduced. They can be solved for the inception field strength E_i if the exponential functions are approximated by second order polynomials (parabolas). The following assumptions are made: a given *radius of curvature* for the inner electrode $R_C = R_1$, a large radius of the concentric outer electrode $R_2/R_1 > 5$ and a *relative air density* δ.

$$E_i = \delta K_1 \{1 + K_2/(\delta R_C)^{1/2}\} . \qquad (3.2\text{-}58)$$

For different gases, the constants K_1 and K_2 are listed in table 3.2-5, both for cylindrical and spherical symmetry.

If the corona inception voltage is reached at first, an **intermittent corona** occurs because of the statistically scattering generation of initial electrons. At slightly higher voltages, field conditions start to change because of space charge accumulation close to the point electrode, see Section 3.2.5.2. A *stable and continuously* burning **glow discharge** is formed. In a dark room, it can be seen as a continuous weak bluish glow or a *continuous corona*, Figure 3.2-27 (right bottom).

Note: In the case of a negative point electrode, the so-called *Trichel impulses* occur at first, Section 3.2.5.2.

Table 3.2-5: Constants for the corona inception voltage according to Eq. (3.2-58).

	K_1 / kV/cm	K_2 / cm$^{1/2}$	
		Cylinder	*Sphere*
Air	30.0	0.33	0.47
N_2	44.0	0.28	0.40
SF_6	90.5	0.12	0.17

Since glow discharges in *air* need a *specific voltage per unit-length*

$$E_G = 25 \text{ kV/cm} \qquad (3.2\text{-}59)$$

(for standard atmospheric conditions), the *range* of a glow discharge is limited.

At higher voltages, isolated **streamers** grow out of the diffuse glow discharge and propagate into the low-field region because of their space-charge field. Superposition of many streamers gives bunch-like discharge phenom-

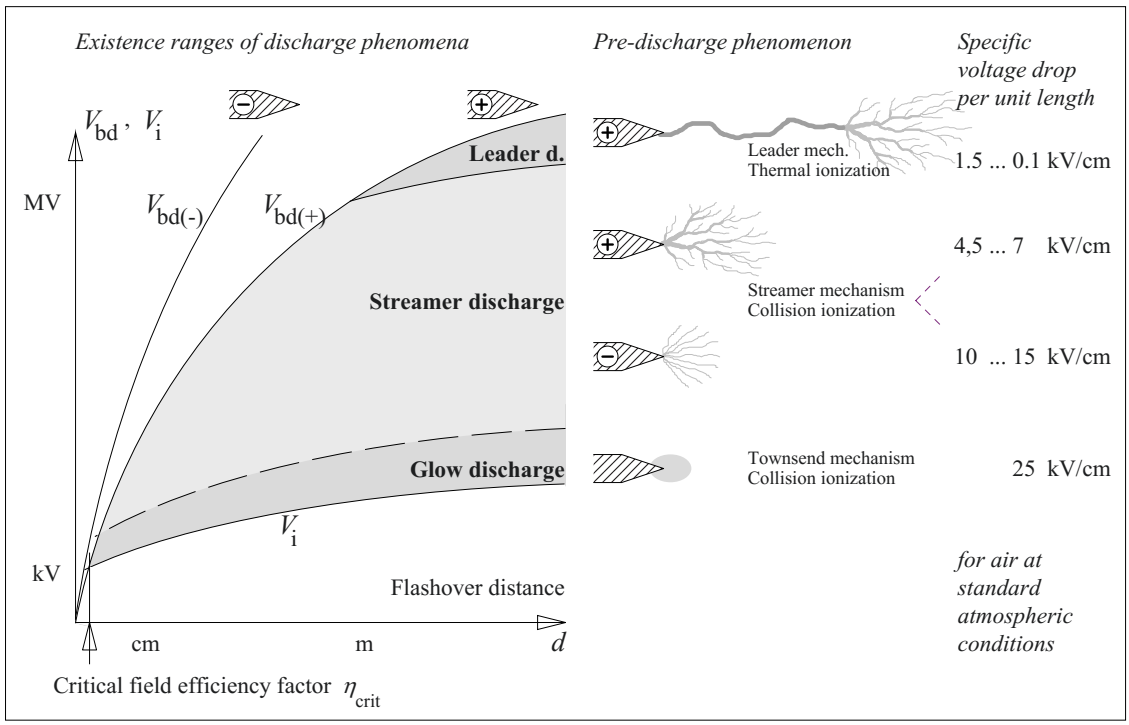

Figure 3.2-27: Existence ranges of pre-discharges in an air-insulated point-to-plane arrangement (schematic). Inception and breakdown voltages as a function of flashover distance d for positive and negative points (left). Pre-discharge phenomena and the corresponding specific voltage drop along the discharge channel (right), [22].

ena for both polarities (*streamer/ bunch discharge*), Figure 3.2-27 (middle).

A **negative streamer discharge** (coming from a negative point electrode) has to propagate through a volume with a field strength that is reduced by space charges, Figure 3.2-25 (right bottom). Therefore, the negative streamer needs a comparatively high specific voltage drop, which has to be provided by the background field (values for air at standard atmospheric conditions):

$$E_{S(-)} = 10 \ldots 15 \text{ kV/cm} \qquad (3.2\text{-}60)$$

Negative streamers start directly at the point electrode and propagate for comparatively constant lengths depending on field geometry, Figure 3.2-27 (right middle).

A so-called "**positive streamer discharge**" (coming from a positive point electrode) consists of electron avalanches propagating towards the point electrode, Figure 3.2-25 (left bottom). Nevertheless, such a discharge activity stretches out in the opposite direction with time, and it is therefore commonly known as a "*positive streamer*". It propagates through a volume with a field strength that is enhanced by space charges. Therefore, the positive streamer only needs a comparatively low voltage drop, which has to be provided by the background field):

$$E_{S(+)} = 4.5 \ldots 7 \text{ kV/cm} \qquad (3.2\text{-}61)$$

Values are valid for air at atmospheric standard conditions; the lower value applies to longer distances above 20 cm. Thus, the *range* of a positive streamer is much longer than the range of an equivalent negative streamer. This is in accordance with the lower *breakdown voltage*.

Positive streamers start randomly distributed within the critically stressed volume. Therefore, the individual streamers have different lengths. They can combine in front of the point

electrode forming channels with higher currents, Figure 3.2-27 (right middle). Consequently, positive streamers have a *more irregular and erratic appearance* than negative ones.

At *high current densities*, a bright channel of a so-called **leader discharge** exists, in which *thermal ionization* generates a large number of additional charge carriers. Since conductivity increases dramatically, the leader only needs a very low specific voltage drop, which has to be provided by the background field):

$$E_L = 0.1 \text{ ... } 1.5 \text{ kV/cm} \qquad (3.2\text{-}62)$$

Values are valid for air at standard atmospheric conditions. The higher applies to shorter distances above approximately 1 m. Thus, the *range* of a leader is very large. After the inception of a leader discharge, *very long distances* will be bridged if the *voltage* is *slightly increased*.

Leader discharge inception voltages are *only slightly below breakdown voltages* and must therefore be avoided.

At the head of the leader, there is an intense leader corona supplying the current to the leader channel. A leader always consists of a thermally ionized *high-current channel* and a *bunch-like streamer corona* at its head, Figure 3.2-27 (right top).

The conditions for the formation of a thermally ionized leader channel are

- a sufficiently *extended corona*,
- a sufficiently *long stress duration* and
- a sufficiently *fast voltage-time response* with high displacement currents.

These conditions are normally fulfilled for *long flashover distances* of more than 1 m in air and for both *switching impulse voltages* (250/2500 µs positive point electrode) and for *power frequency voltages* (point electrode at positive half-cycle), but not for lightning impulses or DC voltages.

Note: Leader discharges can also develop on the surfaces of thin insulating materials (**surface discharges**) at significantly lower voltages because there is a comparatively high capacitance between the discharge corona and the counter-electrode. Therefore, a high displacement current can be supplied to the thermally ionized discharge channel.

3.2.5.4 Breakdown Voltages

Breakdown voltages in atmospheric air can be described as follows:

Fields with a **very weak non-uniformity** (field efficiency factors between $\eta = 1$ and $\eta \approx 0.8$) can approximately be described by equations for uniform fields, Eqs. (3.2-35), (-42) and (-43). The calculated voltage values are valid for DC, AC, switching impulse and lightning impulse voltages because the ignition delay in the uniform field is short owing to the high streamer propagation velocity in a *semi-uniform field*.

In **weakly non-uniform fields** (field efficiency factors between $\eta \approx 0.8$ and $\eta_{crit} \approx 0.2$), Eq. (3.2-58) can be used to calculate *inception voltages*, which are identical with the *breakdown voltages* in this case:

$$V_{bd} = V_i = E_i \cdot \eta \cdot d \qquad (3.2\text{-}63)$$

In **strongly non-uniform fields** (field efficient factors $\eta < 0.2$), stable *pre-discharges* occur before the breakdown. Very roughly, breakdown voltages can be estimated if the *range* of a pre-discharge Δa is compared with the *flashover distance d*.

According to Figure 3.2-28, the discharge *range* of a streamer Δa_S can be calculated from the potential curve of the background field $\varphi_g(x)$ and from the specific voltage drop along the discharge channel $E_S \cdot \Delta a_S$, Eqs. (3.2-59) to (-62). The discharge grows as long as the voltage drop in the discharge can be provided by a potential difference in the background field. The breakdown voltage is

reached if the discharge range reaches the counter-electrode, i.e. if $\Delta a = d$.

For flashover distances of a few mm, *glow discharges* with E_G = 25 kV/cm can be assumed and the breakdown voltage can be estimated by

$$V_{bd\,G} \approx E_G \cdot d\,. \qquad (3.2\text{-}64)$$

For longer flashover distances, *streamer discharges* can be assumed:

$$V_{bd\,S} \approx E_S \cdot d \qquad (3.2\text{-}65)$$

Specific voltage drops per unit-length E_S are given by Eqs. (3.2-60) and (-61). Higher values are valid for *shorter distances* in centimeters and decimeters, lower values for *longer distances* in decimeters and meters.

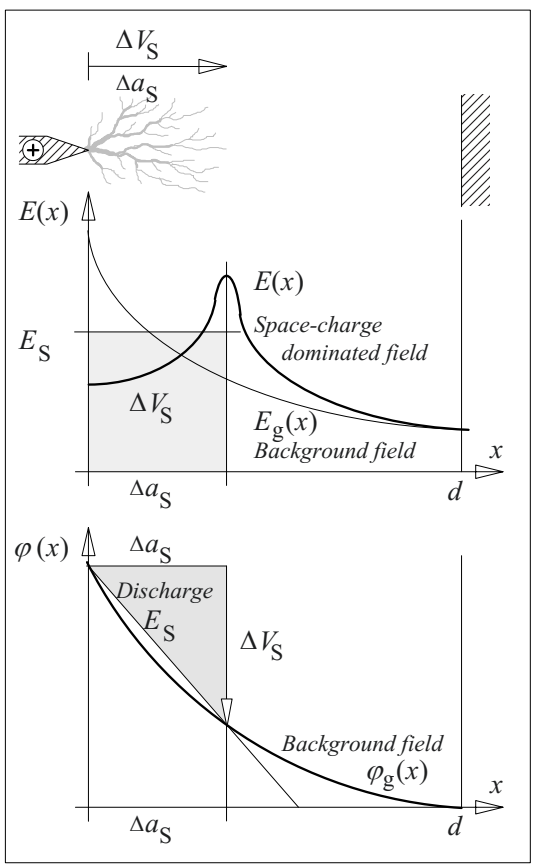

Figure 3.2-28: Estimation of a pre-discharge range from the specific voltage drop per unit-length within a discharge in comparison with the potential curve of the background field for a positive streamer [22].

For *very long flashover distances* above 1 m and AC or positive switching impulse voltages, a *leader discharge* with current-gathering streamers develops, Figure 3.2-27. In this case, the breakdown voltage is the sum of the voltage drops V_S and V_L in the streamer and in the leader

$$V_{bd\,L} = V_L + V_S \qquad (3.2\text{-}66)$$

at the moment at which the whole flashover distance is bridged:

$$d = \Delta a_L + \Delta a_S \qquad (3.2\text{-}67)$$

For very long flashover distances, the specific voltage drop per unit-length is very low and the breakdown voltage now increases only slightly with distance, Figure 3.2-29.

Note: For this reason, there are technological and economical limits for *maximum AC transmission voltage levels*.

The literature contains calculation and estimation methods for leader breakdown [16], [22].

Example: Rod-to-plane arrangement

The discharge behavior of a rod-to-plane arrangement with a flashover distance d = 1 m and a radius of curvature R_c = 1 cm at the end of the rod will be described for different voltage wave shapes.

1.) The **field efficiency factor** of the arrangement will be estimated for the model of a sphere in free space according to Eq. (2.3-8):

$$\eta = E_0/E_{max} = (V/d) / (V/R_c) = R_c/d = 0.01.$$

Obviously, the arrangement is very non-uniform. If the voltage is increased, *stable pre-discharges* will occur.

2.) **Corona inception** will occur at E_i = 44 kV/cm, Eq. (3.2-58). According to Eq. (2.3-8) or (3.2-63), this is equivalent to an inception voltage V_i = 44 kV that is nearly independent of the (very long) flashover distance d. For AC voltages, $\hat{V}_i$ = 44 kV is equivalent to the r.m.s. value $V_{i\,rms}$ = 31 kV.

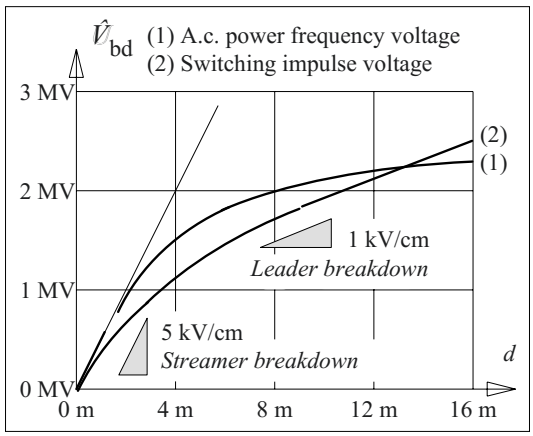

Figure 3.2-29: Peak values of the breakdown voltage for a.c. voltage (1) and positive switching impulse voltage (2) in a point-to-plane arrangement for very long flashover distances d in air [22].

3.) **Negative DC voltage**: With Eq. (3.2-65) and $E_{S(-)}$ = 10 kV/cm, a streamer breakdown is expected at $V_{bd\,S(-)}$ = 1 MV. A measured value is 900 kV [22].

4.) **Positive DC voltage**: With $E_{S(+)}$ = 5 kV/cm, a streamer breakdown is expected at $V_{bd\,S(+)}$ = 500 kV.

5.) Power frequency **AC voltage**: Breakdown is expected in the *positive peak* with $\hat{E}_{S(+)}$ = 5 kV/cm at $\hat{V}_{bd}$ = 500 kV or $V_{bd\,rms}$ = 353 kV respectively. For longer flashover distances, breakdown voltage is no longer proportional to distance because of the incipient leader mechanism, Figure 3.2-29.

6.) Negative and positive **switching impulse voltages**: Breakdown voltages are comparable with DC values. Measured values are slightly higher for negative and slightly lower for positive polarity (1.1 MV and 450 kV) owing to the incipient leader mechanism, Figure 3.2-29.

Note: At sufficiently long flashover distances, *positive switching impulses* have a lower dielectric strength than short-duration lightning impulses and slowly rising AC half-cycles because there are *optimum conditions* for the *leader mechanism*. Therefore, a *minimum strength* is given at a "*critical time to crest*" [16].

7.) Peak values for negative and positive **lightning impulse voltages** (1.1 MV and 550 kV) are slightly above the corresponding DC values. This reflects the breakdown behavior while the test voltages are increasing in steps. The first breakdowns occur in the tail of the voltage curve at a voltage that is lower than the recorded peak value, Figure 3.2-22.

Note: While the impulse voltage amplitudes are increasing, there are increasing overvoltages and shorter times to breakdown, without changing the flashover distance, see Figure 3.2-22 and Section 3.2.4.2 on *voltage-time characteristics*. In a non-uniform field, these characteristics are much steeper than in a uniform field because of the slower streamer propagation velocity, Figure 3.2-23.

3.2.5.5 Impact of Different Parameters

The discussions on non-uniform electrode arrangements in the earlier sections mostly consider *air-insulation* under *standard atmospheric conditions*. The variation of the parameters *geometry*, *pressure*, *temperature*, *gas humidity*, *type of gas* and *field distortions* has significant influences in many cases. For details, see the specialist literature [16], [22], [46], [53], [54], [55]. Only some basic dependences will be discussed here:

1.) The **geometry** of the *point-to-plane* arrangement is the extreme case of a non-uniform field with the lowest-possible field efficiency factor. Other arrangements, even the *point-to-point* arrangement, have lower field strengths at the non-uniform electrode, Figure 3.2-30. First, this causes higher *corona inception voltages*. Secondly, *breakdown voltages* are also enhanced, but they are determined primarily by the dominant discharge mechanism. The growth of the streamers and leaders is primarily dominated by the space charge field and not so much by the background field and the electrode geometry.

Note: For an ideal *point-to-point arrangement* that is completely symmetrical relative to ground, there is no *polarity effect*. There is always one side from which a positive streamer with its comparatively low specific voltage drop can start. In practice, a polarity effect cannot be avoided because one of the point electrodes is often connected to ground and the maximum field strength is reduced there by means of the grounded structures in the environment.

2.) The influence of **pressure, temperature** and *air humidity* can be described by an air-density correction factor k_1 and by an air-humidity correction factor k_2 [133]. The *real* breakdown voltage V_{bd} is deduced from the breakdown voltage $V_{bd\,0}$ under *standard atmospheric conditions*:

$$V_{bd} = V_{bd\,0} \cdot k_1 \cdot k_2 \qquad (3.2\text{-}68)$$

The *atmospheric standard conditions* are

temperature	$T = 20$ °C,
air pressure	$p = 1023$ mbar,
air humidity (absolute)	$h = 11$ g/m³,
and air humidity (relative)	$r = 60$ %.

For the **air-density correction factor**, based on the curved character of the Paschen curve we use the approximation

$$k_1 = \delta^m \qquad (3.2\text{-}69a)$$

The *relative air density* contains the parameters *pressure* (mbar) and *temperature* (°C)

$$\delta = \frac{p}{1013\,\text{mbar}} \cdot \frac{293\,\text{K}}{273\,\text{K} + T} \qquad (3.2\text{-}69b)$$

Note: If there are only small deviations from the standard atmospheric conditions in a *uniform field*, the Paschen curve Eq. (3.2-34) or (-35) can be *linearized* in the density range $0.9 < \delta < 1.1$, and an exponent $m = 1$ can then be used, see Section 6.3.1.1.

The breakdown in a strongly non-uniform field is not determined by the inception of pre-discharges, it is determined by the growth and propagation of the *streamer discharge*. Therefore, the influence of air density decreases with increasing non-uniformity of the field, and the exponent m decreases from one to zero [133]. The exponent m is tabulated as a function of a parameter g, which gives the ratio of the breakdown voltage V_{bd} and the specific voltage drop of a positive streamer discharge $V_{streamer} = 500$ kV/m · d:

$$g = \frac{V_{bd}}{(500\frac{\text{kV}}{\text{m}} \cdot d) \cdot \delta \cdot k} \qquad (3.2\text{-}69c)$$

The factors δ and k contain an air-density and an air-humidity correction respectively [133]. Under standard atmospheric conditions, both factors are equal to one. Above $g = 1$ the exponent is $m = 1$. I.e. the breakdown voltage is assumed to be proportional to air-density according to Eq. (3.2-69a) and (-68).

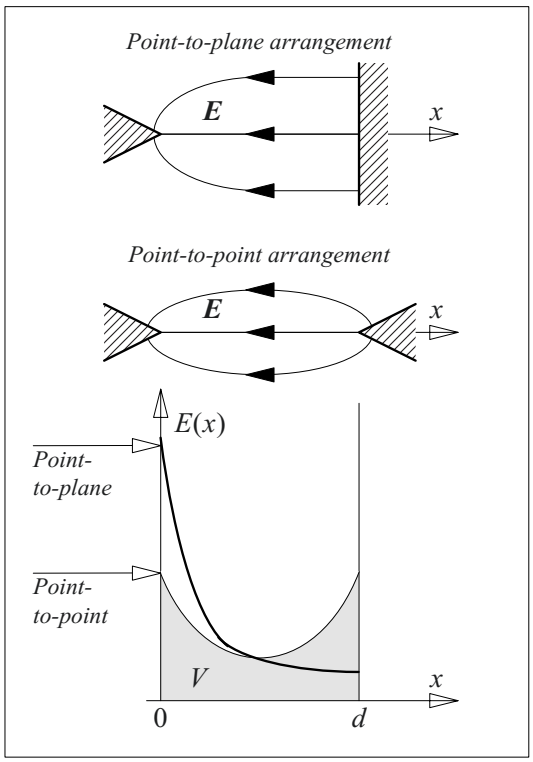

Figure 3.2-30: Field strength curves for point-to-plane and point-to-point arrangements at the same flashover distance d and at the same voltage V.

Note: Since the specific voltage drop in a negative streamer is approximately twice as great as in a positive streamer, positive streamers determine breakdown, Figure 3.2-27. Dielectric tests with impulse voltages are normally performed with positive polarity. Negative polarities are only used as an addition. Therefore, the above mentioned relationships refer to the *positive streamer*.

The influence of **air humidity** is negligible for uniform and weakly non-uniform fields and for negative streamer discharges. The breakdown voltage increases with the *absolute* (and not with the relative) air humidity only for *positive streamer discharges*. The correction for humidity is

$$k_2 = k^w . \qquad (3.2\text{-}70a)$$

The exponent w is tabulated as a function of the parameter g. It is $w = 1$ close to $g = 1$, for g

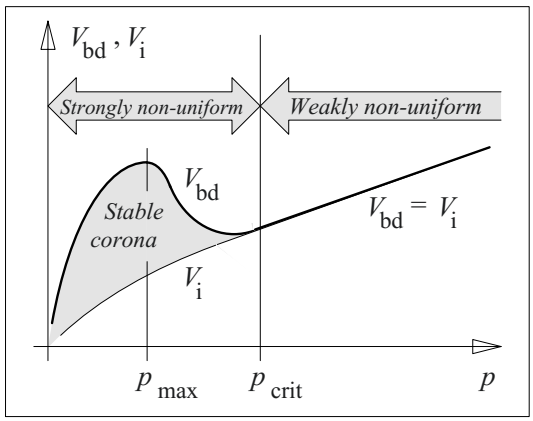

Figure 3.2-31: Effect of the variation of gas pressure on the discharge behavior of a point-to-plane arrangement [39] (schematic).

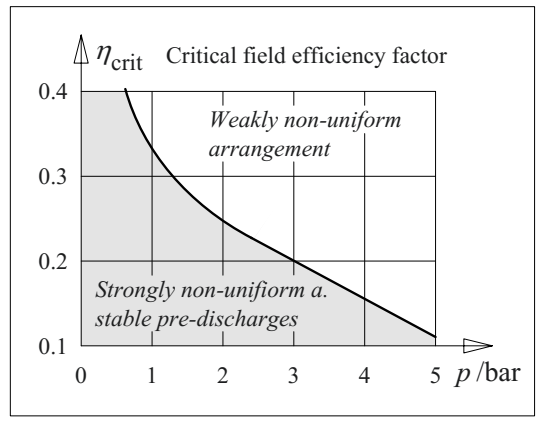

Figure 3.2-32: Variation of the critical field efficiency factor with pressure in sulphure hexafluoride SF6 [22], [55].

< 0.2 and $g > 2$ the exponent w decreases to 0, i.e. there is no longer an air-humidity correction. For AC voltages, the dependence on the *absolute air humidity h* is given by the factor

$$k = 1 + 0.012 \cdot \left(\frac{h/(\mathrm{g/m^3})}{\delta} - 11 \right). \quad \text{(3.2-70b)}$$

The range of validity and variations for DC and impulse voltages are described in the standard [133]. If a relative air humidity of 80 % is exceeded, the dielectric strength of *surfaces* can be reduced significantly because *creepage currents* can cause field distortions and *pollution flashover*.

Note: The empirical relationships for air-humidity correction are in good accordance with measurements for *long flashover distances* ($d > 1$ m) and correspondingly high voltages. For *shorter distances* ($d < 0.5$), i.e. mainly for *medium voltages* (up to approx. 200 kV), the described method is difficult to apply and can provide incorrect results [387]. In particular, surface creepage arrangements show reductions of flashover voltages in the medium voltage range even at above 50 to 60 % relative air humidity [387]. Nevertheless, this is a **surface effect** that is sensitive to *relative air humidity* and not a **gas-breakdown effect** that would be sensitive to *absolute air humidity*.

3.) For **compressed-gas insulations**, the influence of high pressure can no longer be described by the linear approach according to Eq. (3.2-68) to (-70). The *discharge behavior* in a strongly non-uniform field can change significantly during *increasing pressure*, Figure 3.2-31. At low pressure, a significant difference can exist between inception voltage V_i and breakdown voltage V_{bd}, which disappears at high pressures. Obviously, the "strongly non-uniform arrangement" has changed into a "weakly non-uniform arrangement" just by increasing the pressure above a critical value p_{crit}. This can also be interpreted as a *decrease of the critical field efficiency factor* η_{crit} with increasing pressure, Figure 3.2-32. For a given arrangement (η = const.), an increase in pressure shifts the discharge behavior from a range with pre-discharges to a range without.

The suppression of pre-discharges with increasing pressure can be *explained* by the *decreasing range of photon emission* with increasing gas density, which significantly degrades the conditions for secondary avalanches and streamers.

Example: Locally fixed defect in a GIS

Faulty production or mounting procedures in a compressed-gas insulation system can cause *locally fixed defects*, e.g. tips, edges, burrs or metal chips. Such defects cause a very non-uniform local field, and they show a pressure dependence according to Figure 3.2-31. Breakdown voltages can be stabilized at a comparatively high level by pre-discharges, but they can occur for sufficiently long lasting stresses only (DC, AC and switching impulse level). *Lightning impulse breakdown* and *pre-discharge inception* can occur at lower voltages, significantly dependent on the degree of non-uni-

formity. *Lightning impulse* and *partial-discharge* AC tests can therefore be used as *indicators for locally fixed defects* in gas-insulated switchgear (GIS).

Example: Free particles in a GIS

In a compressed-gas insulation system, *free particles* can also occur, e.g. chips, abraded matter or welding sputter. Similar to fixed defects, they also *distort the field*. Additionally, they can be electrically charged, lifted by electric field forces from the less curved electrode (*lift-off voltage*) and migrate to the counter-electrode where the field is enhanced by the charges of the particles. These particles are discharged at the electrode, reloaded, lifted again, transported to the counter-electrode and so on repetitively. *Particle movement* doesn't play a role for the short-lasting lightning impulse stress, but it causes *partial discharges* and a strong decrease of *AC and DC breakdown* voltages. Therefore, gas-insulated switchgear must also be tested with AC voltage after the final mounting, in order to test for free particles.

3.2.6 Surface Discharges

3.2.6.1 Arrangements with Surfaces

Multi-layer dielectrics containing a gaseous dielectric have interfaces that are known as "*surfaces*". Field calculations are described in Section 2.4.2 (for AC, switching impulse and lightning impulse voltages) and in Section 2.4.4 (for DC voltage).

In high-voltage engineering, surfaces are characterized by three circumstances:

- First, they occur *in very large numbers* in string and post insulators, bushings, cable terminations and insulating housings.
- Secondly, they only have a very *weak dielectric strength*
- Thirdly, *surface discharges* are comparatively strong and have a high *erosive effect*.

Therefore, surface discharges are one of the *main problems* in high-voltage design.

Surfaces occur in three different *basic types*.

1.) For an **electric field, perpendicular to a surface**, the direction of electrical gas discharges is also perpendicular to the surface. This is not a surface discharge in a narrow sense. Nevertheless, significant field stress enhancements can occur owing to *field displacement* (Section 2.4.2.2 and 2.4.4.1). *Partial discharges* in cracks, gaps and voids can erode many organic insulating materials and lead to *erosion breakdown.*

2.) For an **electric field, parallel to a surface**, the macroscopic field is theoretically not influenced by the surface, Section 2.4.2.3. Nevertheless, the dielectric strength of such an arrangement is lower than the strength of a comparable gas-insulated gap because the microscopic field is distorted by the *irregularity of the surface* and because only *weakly bound charge-carriers* are released. Furthermore, significant field distortions can be caused by surface contamination, wetting and *pollution layers*. Since the field is *tangential*, the gas discharge also develops parallel to the surface. Often, the discharge is ignited at the *triple-point* between electrode, insulating material and gas. The dielectric strength of a gas-insulated gap could only theoretically be achieved under ideal laboratory conditions.

If arrangements with fields parallel to the surface cannot be avoided in practice, *sufficiently long flashover distances* and a *sufficiently high field efficiency factor* are necessary, e.g. in the case of insulators in GIS or overhead line insulators.

Note: For **post insulators in GIS**, the tangential field component is reduced by *inclination of the surface*. For **overhead line insulators**, the impact of pollution layers is reduced by undulating *screen profiles* with long *creepage lengths* and sometimes by *hydrophobic surface properties*. The field strength at the triple-point is often reduced by an appropriate *electrode configuration*.

3.) For insulation systems with tangentially stressed interfaces against solid or liquid dielectrics, the low strength of tangential surfaces would limit withstand-voltages to very low values, and the high strengths of the dielectrics would only be *partially exploited*. Therefore, **creepage arrangements** (**creepage surfaces)** are used with insulating materials that reach far beyond the electrode edges into the low-field regions, Figure 3.2-33.

Unfortunately, a uniform tangential field distribution cannot be achieved thereby because a strong field stress enhancement exists at the triple-point at the electrode edge. Therefore, *pre-discharges* occur *at very low voltages*, but the breakdown is prevented by the insulating material. If the voltage is increased, a *guided gas-discharge* will develop along the surface (*surface discharge*, *creepage discharge*), which will finally reach the counter-electrode and end up in *flashover*.

Owing to its general importance, the *basic creepage arrangement* (Section 3.2.6.2 and 3.2.6.3) and the *pollution flashover* (Section 3.2.6.5) will be discussed in more detail in order to deduce *methods* for the suppression of surface discharges.

3.2.6.2 Ignition of Surface Discharges

Field distributions for **impulse** and **AC voltage stresses** are normally exclusively determined by the *dielectric displacement field*, i.e. by the permittivities ε_1 and ε_2. Here the *geometry of the electrode edge* has a strong influence, Figure 3.2-35. The field can be described by a purely *capacitive equivalent circuit*, consisting of the capacitances ΔC of the insulating layers and stray capacitances in air ΔC_S, Figure 3.2-34 (left). If there are sufficiently conductive **pollution layers**, additional *surface resistances* ΔR are necessary for the case of AC voltage stress, Figure 3.2-34 (middle). In the case of DC voltages, the field distribution is determined by the conductivities of the insulating materials and the conductive layers; the gas is comparatively high-resistive. The equivalent circuit consists of a purely ohmic lattice network with longitudinal and transverse resistances, Figure 3.2-34 (right).

a) Impulse and AC voltage
(Dielectric displacement field)

At **very sharp electrode edges**, a high *tangential field strength component* exists and *stable glow discharges* can form, Figure 3.2-35 (left). The inception voltage can be estimated from the assumption of a cylindrically symmetric edge field with inner radius R_c and outer radius d

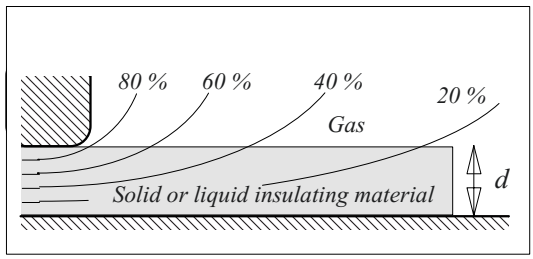

Figure 3.2-33: Creepage surface with equipotential lines (simplified, without considering refraction of the equipotential lines at the interface).

$$V_i \approx E_i \cdot R_c \cdot \ln (d/R_c). \qquad (3.2\text{-}71)$$

The order of magnitude for the *inception field strength* at cylindrical electrodes is given by Eq. (3.2-58). This does not take the interaction with the surface into account.

At **smoothly curved electrode edges**, discharge inception is caused by the *normal field strength component* in the gas-filled interstice, Figure 3.2-35 (right). There, the field strength is enhanced by dielectric field displacement. A discharge is ignited, if the ignition condition is fulfilled at any location within the interstice. During ignition, the surface of the insulating material helps to supply free charge carriers. The *field conditions in an interstice* were already used in Section 2.4.3.3 for estimation of the *partial discharge inception voltage* V_i in a dielectric displacement field, Figures 2.4-18 and -19:

$$V_i \sim \sqrt{\frac{d}{\varepsilon_r}} \qquad (3.2\text{-}72)$$

Note: *Numerical values* can be calculated with the empirical equation (2.4-35).

Since the dielectric strength of the gas-filled gap decreases with gap width, a breakdown is to be expected in the mm range, Figure 2.4-19. Therefore, the first discharge occurs *perpendicularly to the surface* in a comparatively uniform field. Immediately after ignition, the discharge will turn into a *steamer* propagating

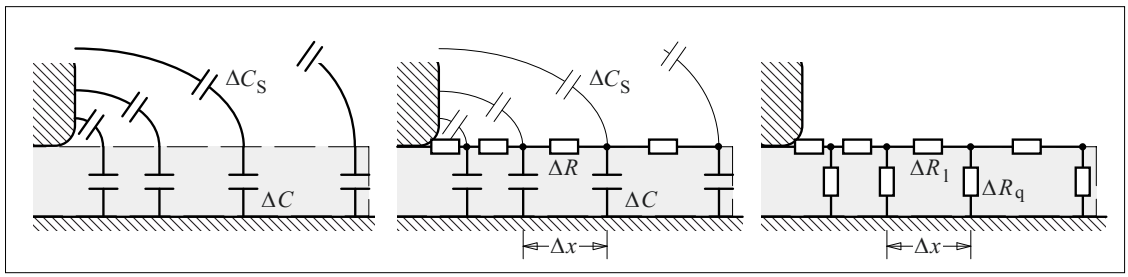

Figure 3.2-34: Simplified description of tangential field distributions on creepage sufaces by equivalent circuits with distributed parameters for different kinds of stresses:
Left: Circuit for impulse and AC stresses (dielectric displacement fields only).
Middle: Circuit with recognition of conductive pollution layers for AC voltages.
Right: Circuit for DC voltages (conduction field only).

parallel to the surface under the influence of the tangential field component ("*creepage discharge*"). Glow discharges do *not* occur.

b) Pollution layers for AC voltage

A calculation of tangential field strength can be performed by means of an *ohmic-capacitive equivalent circuit,* Figure 3.2-34 (middle). Stray capacitances ΔC_S are neglected for this case, although this is not always justified close to the electrode edge [26]. The related surface capacitance per unit length and the related surface resistance per unit length are $C' = \Delta C/\Delta x = \varepsilon_0\varepsilon_r b/d$ and $R' = \Delta R/\Delta x = R_\square/b$. The variables b and d are the width and thickness of the insulating material, $R_\square$ is the specific surface resistance (resistance of a square surface element).

The differential equations (line equations) for current and voltage are set up for an infinitesimal element Δx of the lattice network. An *exponentially decreasing tangential field strength* is derived from the solution for the voltage distribution. If the maximum field strength value at the electrode edge is identified with the dielectric breakdown strength E_{bd} at the interface, the equation can be solved for the *corona inception voltage* V_i:

$$V_i = \frac{E_{bd}}{\sqrt{\omega C' R'}} = \frac{E_{bd}}{\sqrt{\omega R_\square \varepsilon_0}} \sqrt{\frac{d}{\varepsilon_r}} = K \sqrt{\frac{d}{\varepsilon_r}} \qquad (3.2\text{-}73)$$

Formally, this equation is equivalent to Eqs. (3.2-72) and (2.4-35) respectively. Empirical values for K are given there; V_i is calculated as the r.m.s. value, Section 2.4.3.3.

Note: Eq. (3.2-73) is not only valid for plane geometries. Figures 3.2-33 and -34 can also be interpreted with a vertical *axis of rotation*, without the product $C'R' = \varepsilon_0\varepsilon_r R_\square/d$ changing. The width b is to be replaced by the circumference $2\pi r$, which is also canceled out. In the case of a *horizontal axis*, C' is to be calculated according to Eq. (2.3-30).

Note: The experimentally determined constants K do *not* show a clear dependence on surface resistance $R_\square$ [26]. Therefore, it is assumed that partial discharge inception is caused by the *dielectric displacement field* even if there are pollution layers, as long as surface conductance is not too high.

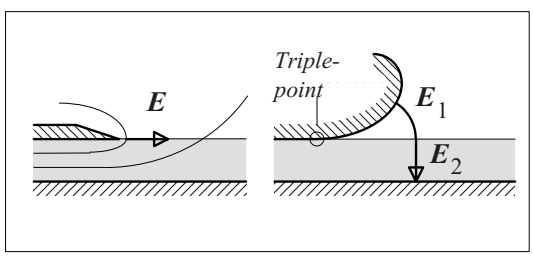

Figure 3.2-35: Ignition of surface discharges by the tangential field component at a sharp electrode edge (left) or by a normal field component at a smoothly curved electrode edge (right).

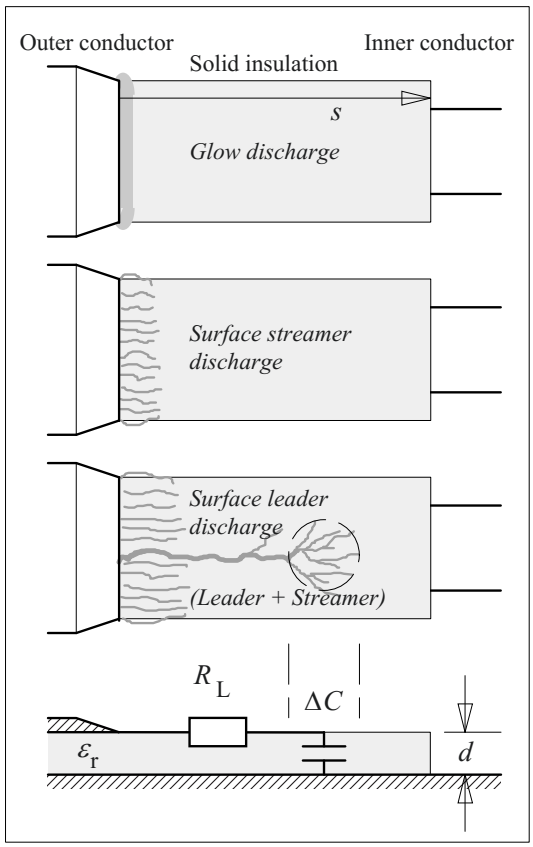

Figure 3.2-36: Development of surface discharges on a cylindrical insulator surface.

c) DC voltage
(Steady-state conduction field)

The lattice network according to Eq. 3.2-34 (right) gives exponentially *decreasing tangential field strength* and an inception voltage according to Eq. (3.2-73), if the specific capacitive conductance $\omega\varepsilon_0\varepsilon_r$ is replaced by the conductivity κ of the insulating material:

$$V_i = E_d \sqrt{\frac{d}{\kappa R_\square}} \qquad (3.2\text{-}74)$$

Conclusion: For all the Eqs. (3.2-71) to (3.2-74), there is only a slight increase of *inception voltage* V_i with *insulating material thickness d*. Dielectric strength is *reduced* by a high relative *permittivity* ε_r in a dielectric displacement field, and it is *enhanced* by a (uniform) pollution layer in a steady-state conduction field, if the *surface resistance* $R_\square$ is sufficiently low and uniform.

3.2.6.3 Development of Surface Discharges

After the inception of partial discharges and at the time of an increase in voltage, a surface discharge develops *similar to a pure gas discharge* in a strongly non-uniform field. The insulating material only acts as a barrier guiding the gas discharge and preventing direct breakdown (*guided gas-discharge*).

Under the influence of tangential field components, *(surface) streamer discharges* develop. At a curved electrode edge, they start directly from the breakdown of the air gap, and at a sharp electrode edge, they emerge from the preceding *glow discharge*, Figure 3.2-36.

Owing to the *high lateral capacitance*, the streamers carry much higher currents than streamers in a point-to-plane arrangement in air. For AC and switching impulse voltages, current densities allowing thermal ionization and inception of *leader discharges* are already reached for streamer ranges of a few centimeters. For a pure gas-insulated arrangement, streamer ranges of approximately one meter would be necessary for leader inception.

The *surface leader discharge* (*creeping discharge*, *creeping spark*) consists of a leader channel with low resistance R_L (similar to a trunk) and a leader head of current-gathering streamers with high lateral capacitance ΔC (similar to branches or bunches).

The length of the leader is determined from the equilibrium between the given voltage drop at R_L and the required voltage for the leader discharge channel, Figure 3.2-36 (bottom). Since the required voltage per unit length for a leader discharge decreases with increasing length, the leader can easily bridge long distances with increasing voltage, and complete flashover can quickly be reached.

Therefore, increasing the *flashover distance cannot* increase the *flashover voltage* significantly!

In practical applications, the flashover voltage V_f is less important than the *inception voltage* for *leader discharges* V_L, which must be prevented in any case for technical insulations.

The *inception of leaders* at V_L can be derived from a simple estimation: If the increasing voltage for AC or switching impulse stresses is approximated by a voltage step with amplitude V_L, ΔC will be charged via R_L with constant voltage. In this case, the *ohmic losses* W_{th} in R_L are equal to the capacitively stored energy $\frac{1}{2}\cdot\Delta C\cdot V_L^2$. If it is also assumed that the leader inception with *thermal ionization* is characterized by exceeding a minimum loss energy $W_{th} \geq W_{min}$, it follows that

$$\tfrac{1}{2}\cdot\Delta C\cdot V_L^2 = W_{th} \geq W_{min} . \qquad (3.2\text{-}75)$$

Thereby, a limit for the *leader inception* can be given:

$$V_L = (2W_{th}/\Delta C)^{0.5} \sim (d/\varepsilon_r)^{0.5} \qquad (3.2\text{-}76)$$

This proportionality is in good agreement with the empirical equation for AC voltages:

$$V_L = 25.8\,\text{kV}\cdot\left\{\frac{\text{pF/cm}^2}{\Delta C/\Delta A}\right\}^{0.44} \qquad (3.2\text{-}77)$$

The specific capacitance per unit-area $\Delta C/\Delta A$ can be calculated from geometry. For plane arrangements it follows that [16]

$$V_L = 75\,\text{kV}\cdot\left\{\frac{1}{\varepsilon_r}\cdot\frac{d}{\text{cm}}\right\}^{0.44} . \qquad (3.2\text{-}78)$$

Note: The factor and the exponent in Eq. (3.2-77) are only weakly dependent on *pressure* and the *nature of the gas*. The application of SF_6 and increasing the pressure do *not* give the same enhancements of dielectric strength as in a uniform field.

Example: Cast-resin bushing without field grading

For a cylindrical cast-resin bushing ($\varepsilon_r = 4.5$) with the inner conductor diameter $D_i = 1$ cm, the inception voltage for leader discharges V_L shall be calculated as a function of the outer diameter $D_a = D_i + 2d$. Eq. (3.2-77) is used for the calculation of a table of values. The surface-related capacitance per unit-area is given by Eq. (2.3-20):

$$\Delta C/\Delta A = 2\pi\varepsilon z \ln^{-1}(D_a/D_i)/(\pi D_a z) = 2\varepsilon\{D_a\ln(D_a/D_i)\}^{-1}$$

Table of values:

D_a	2	4	8	16	cm
d	0.5	1.5	3.5	7.5	cm
$\Delta C/\Delta A$	0.574	0.143	0.048	0.018	pF/cm^2
V_L	33	61	98	151	kV

Obviously, *increasing the insulation thickness* is *not* a very effective **method** for increasing the leader inception voltage V_L. An analogous conclusion can be drawn for the application of materials with *lower permittivity* ε_r; furthermore, there are only a few different materials available. At higher voltages, arrangements with *geometric*, *capacitive* (*dielectric*), *resistive* or *non-linear* field grading are therefore used (Sections 2.4.5, 5.4.5, 7.1.1.4, 7.1.2.1 and 7.1.6)

3.2.6.4 Pollution Flashover

Rain, precipitation from fog, dew or moisture absorption causes *wetting or humidification* of insulator surfaces depending on the atmospheric conditions. In combination with *dirt deposits, electrolytically conductive pollution layers are formed*. Coastal areas with saline fog, locations with road-salt fog, and environments with high air pollution (e.g. by dust, soot, oily particles and dissociable contaminants) are especially at risk.

The field distribution in a *DC field* is determined by pollution layers even at low pollution layer conductivities, Figure 2.4-29. In an *AC displacement field*, only high conduction currents in the pollution layer can influence

the field distribution. In the case of *impulse voltages*, conduction currents are normally negligible in comparison with displacement currents. Nevertheless, an impulse voltage can prolong an already burning AC pre-arc and cause breakdown.

Owing to the spatial and temporal development, **pollution flashover** is also called **creepage flashover**, Figure 3.2-37.

At first, the current density lines of the surface *leakage current* (*creepage current*) are displaced from locations with reduced conductivity (e.g. at dry zones) to areas with higher conductivity, Figure 3.2-27 (a). For leakage currents in the range of 10 to 100 mA *local heating* occurs at locations with higher surface current densities close to the edges of the dry zones. Thereby, water is evaporated and the dry zones are lengthened perpendicularly to the current density lines (b).

Ultimately, the current density is high enough to *ignite a pre-arc* (d) by thermal heating. If the current path were to be interrupted (c), a high voltage ΔV would be built up across the dry zone and a *pre-arc* would also be ignited (d).

Note: The total voltage for *pre-arc inception* can be very low in comparison with the flashover voltage. It depends primarily on the wetting of the surface and on the pollution layer conductivity.

Stable pre-discharges (i.e. pre-arcs) can only exist, if there is a *stable working point* on the gas discharge characteristic, Figures 3.2-2 and -3a. The current is limited by the resistance of the conductive pollution layer in series with the arc. The resistance must be low enough, i.e. the inclination of the resistance line in Figure 3.2-3a has to be so low that it intersects the arc characteristic at working point no. 1.

The drying of the pollution layer in the environment of the root point of the arc causes a *lengthening of the stable burning pre-arc* along the current density lines, Figure 3.2-27 (e). The series resistance of the conductive layer decreases slightly, but the arc voltage increases very significantly. This is equivalent to a shifting of the gas discharge characteristic towards higher voltages, Figure 3.2-3. If the sum of the arc voltage and the voltage drop along the resistive layer is higher than the source voltage, the *arc will be quenched*. If the voltage sum always stays below the source voltage, the prolongation of the arc will lead to *flashover*. This is only possible for a low pollution layer resistance (i.e. for a *high pollution layer conductivity*) or for a low inclination of the resistance line.

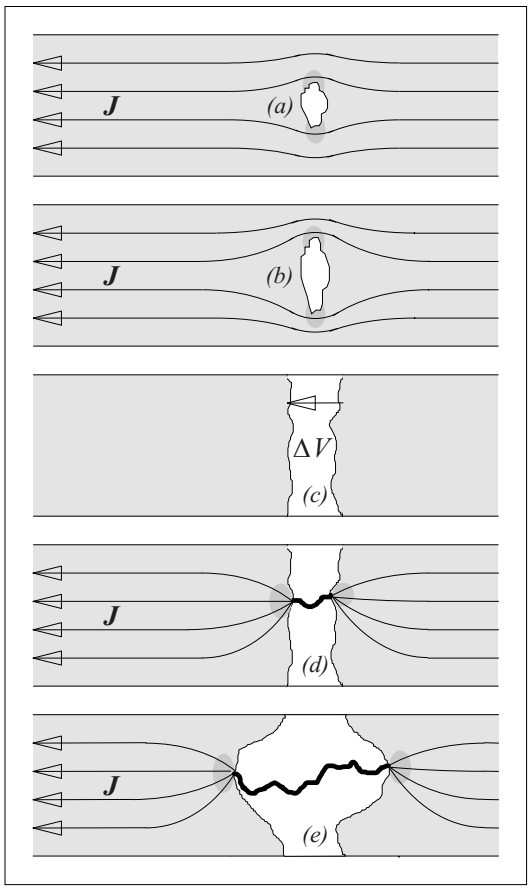

Figure 3.2-37: Phases of pollution flashover:
a) Displacement of the "creepage current" by a dry zone with local heating.
b) Increase of the dry zone by ohmic losses, acceleration of surface drying.
c) Interruption of current flow after surface drying along the whole insulator circumference.
d) Flashover of the dry zone, development of an electric arc (pre-arcing).
e) Extension of the dry zone and the arc length by surface drying.

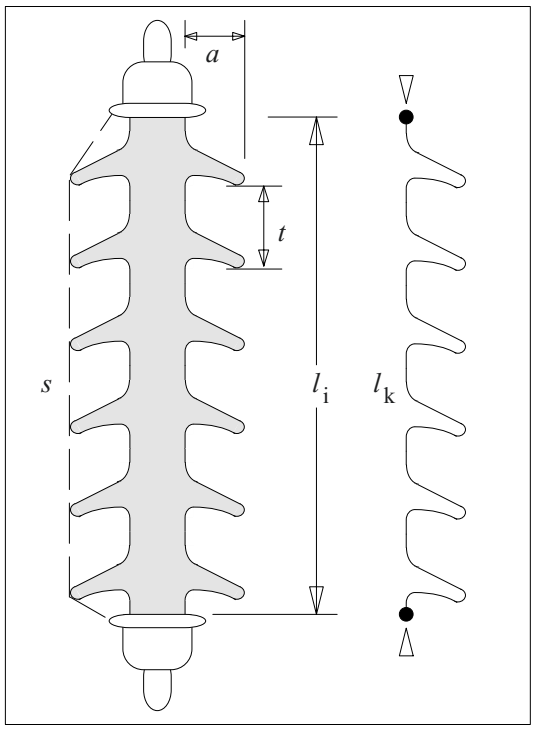

Figure 3.2-38: Outdoor insulator with creepage-path lengthening by means of shed profile.

Note: If the voltage source is weak, the *internal resistance* of the source can cause quenching of the arc and simulate an enhanced *flashover voltage*. Therefore, the determination of flashover voltages requires a *strong voltage source* with a low internal impedance or a low relative short-circuit voltage [56].

The magnitude of the creepage currents is determined by the *resistance* of the insulator surface. The resistance is given by an integration of the resistance element dR along the creepage path l_k:

$$\mathrm{d}R = \frac{\mathrm{d}l_k}{\kappa \cdot \Delta s \cdot b} \qquad (3.2\text{-}79)$$

Δs is the thickness of the conductive layer and b is the position-dependent circumference of the insulator. The *pollution severity* is characterized by the so-called *layer conductivity*, which is defined as product of conductivity and layer thickness:

$$\kappa^* = \kappa \cdot \Delta s \qquad (3.2\text{-}80)$$

Thus, the *surface resistance* R is given by the layer conductivity κ^* and a *shape factor*

$$f = \int_0^{l_k} b^{-1}\,\mathrm{d}l_k \qquad (3.2\text{-}81)$$

as

$$R = f / \kappa^* . \qquad (3.2\text{-}82)$$

Typical layer conductivities are given in [16], i.e.

$\kappa^* = 5$ µS for weak to medium pollution,
$\kappa^* = 10$ µS for medium to heavy pollution and
$\kappa^* = 40$ µS for extremely heavy pollution.

The development of a pollution flashover is also influenced by the **insulating material**. Thermally and chemically resistant surfaces (*porcelain glazes, glass*) are not permanently modified by weathering or by surface discharges in most cases. Long-lasting pre-discharges on surfaces of *organic materials* can cause *erosion* and enhancement of wettability. During *diffusion* of water and contaminants into the bulk material, conductive paths can be generated, which can initiate a so-called *tracking flashover* [22]. Even *silicones* can lose their water-repellent (hydrophobic) properties under the impact of electrical discharges, but a *recovery* of surface properties can occur because of the diffusion of low-molecular silanes [57].

The following **methods** can be used in order to avoid pollution flashover:

1. The basic method is the *lengthening of the creepage path* l_k by means of a **shed profile**, Figure 3.2-38. The ratio of creepage path length l_k to insulator length l_i is determined by the ratio of *shed overhang a* to *shed spacing t*. The ratio $l_k/l_i \approx 2$ is chosen under normal pollution conditions and $l_k/l_i \approx 3$ under difficult conditions. The insulator length l_i or flashover distance s (thread measure) is dimensioned according to the impulse voltage withstand-level. Values between 2.5 and 5 cm/kV are *common creepage path lengths* for outdoor conditions; they are related to the r.m.s. value of the applied operating voltage.

The lengthening of the creepage path (i.e. the increase of the surface resistance) is not the only effect of insulator sheds. They also pro-

vide *protection* of the underside *against rain and dirt deposition* and they help *dry and clean zones* to remain, which are able to withstand the applied voltage. The partial voltages can be kept low by means of a higher number of sheds. For extreme requirements, there are special shed profiles, e.g. the so-called *anti-fog sheds* with additional vertical ribs on the undersides.

2. In the case of severe pollution, the *natural cleaning effect* of rain might not be sufficient, and **regular cleaning** of the insulators would be necessary. Eventually, this can be done automatically by permanently installed *spraying units*. If pollution is extreme, a water-repellent (hydrophobic) *silicone paste* ("*silicone grease*") can be applied every year.

3. **Composite insulators** with *silicone elastomer sheds* ("*silicone rubber sheds*", *SIR sheds*) are a good alternative to the common porcelain insulators. They preserve their *water-repellent property* (*hydrophobicity*) for decades, and they can transfer hydrophobicity to the attaching contaminants by diffusion. Thereby, the formation of coherent liquid films is impeded [9], [57].

Note: The terms "silicone rubber" or SIR are widely used. However, the material is a synthetic elastomer, not a natural rubber.

Note: Composite insulators with hydrophobic SIR sheds have extraordinary surface properties. Nevertheless, it is a disadvantage that the hydrophobicity can be lost under the influence of corona discharges, Section 5.3.4. Coronas can occur on a *bedewed surface* if the tangential background field is above 0.3 - 0.5 kV/mm [471]. The electric field forces deform the water drops and form tips that cause the **water drop corona** affecting hydrophobicity. Close to the fittings, surface field strengths of 0.8 to 1 kV/mm can be reached. Therefore, maximum field strengths should be reduced by an appropriate design, e.g. by means of grading rings. If the corona stress is only temporary and of short duration, the hydrophobicity will recover by diffusion of low-molecular silanes, Section 5.3.4.

The application of SIR sheds has significantly improved the flashover behavior for *DC stresses*, especially for HVDC bushings with rated voltages above 500 kV [7], [8], [10].

4. It was proposed to retrofit DC bushing porcelain insulators that are at flashover risk. So-called *booster sheds* consisting of silicone discs with large diameters are distributed along the insulator length in order to interrupt developing pre-arcs [58], [8].

3.2.7 Spark, Arc and Lightning Discharges

During the breakdown of a gas-insulated gap, a conductive channel is formed by electron avalanches, the current increases and the voltage collapses. Ultimately, a **high-current discharge** develops; it is the consequence of insulation failure, not the cause. However, different kinds of high-current discharges are of great importance in high-voltage engineering: *Spark discharges* (Section 3.2.7.1), *arc discharges* (Section 3.2.7.2) and atmospheric *lightning discharges* (Section 3.2.7.3) will be discussed.

3.2.7.1 Spark discharge

During *breakdown*, the gas-insulated gap is bridged by a streamer at first. Owing to intense *collision ionization* the conductivity of the

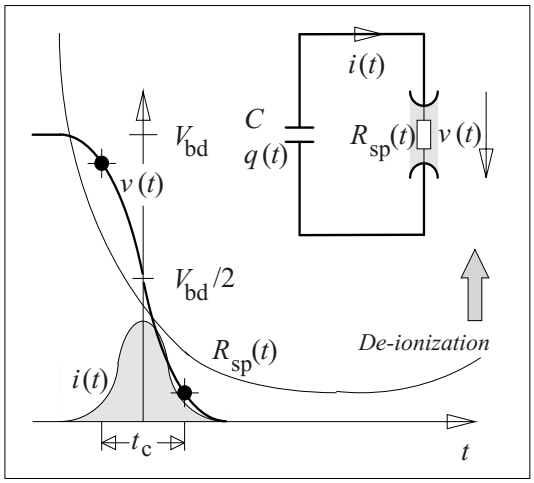

Figure 3.2-39: Spark resistance, spark formation time (time of voltage collapse), voltage and current for the discharging of a capacitance (schematic), see also Figure 3.2-21

channel increases and *spark resistance* $R_{sp}(t)$ decreases from very high initial values down to very low final values, Figures 3.2-21 and -39. In the case of a steady-state source voltage, the *transient spark* develops into a permanent *electric arc* with a constant final current (Section 3.2.7.2). If a *source with finite energy content* is discharged, only transient current and light impulses will occur. After their decay, the discharge gap de-ionizes by *recombination processes* and the spark resistance $R_{sp}(t)$ increases again, Figure 3.2-39.

Note: The time characteristic of the spark resistance is important for equivalent circuit simulations of discharge circuits. They often experience significant *non-linear damping* as a result of $R_{sp}(t)$.

The *time of voltage collapse* t_c from 90 % to 10 % is also known as the *spark formation time*.

Note: The spark formation time can play a role in the *discharge delay* (Section 3.2.4), but often it is short in comparison with the streamer formation delay (formative time lag) and is therefore often neglected.

The short spark formation time in SF_6 is jointly responsible for the *short rise times of fast transients* in gas-insulated switchgear GIS.

The increase in charge carrier numbers through *collision ionization* can be described by an increase dn of electron density n along the distance dx with the effective ionization coefficient α_e:

$$\mathrm{d}n = \alpha_e \, n \, \mathrm{d}x \, . \qquad (3.2\text{-}83)$$

The increase in the electron density with time results from the drift velocity of electrons $u = \mathrm{d}x/\mathrm{d}t$:

$$\mathrm{d}n/\mathrm{d}t = \alpha_e \, n \, u \, . \qquad (3.2\text{-}84)$$

If the electron current density $J_- = n \cdot u \cdot e$ (with the elementary charge e) is approximately equal to the total current density J, the increase in the electron density is

$$\mathrm{d}n/\mathrm{d}t = \alpha_e \, J / e \, . \qquad (3.2\text{-}85)$$

The electron density n at a given time t is calculated by integration:

$$n = \alpha_e \cdot e^{-1} \cdot \int_0^t J(t)\,\mathrm{d}t = \alpha_e \cdot e^{-1} \cdot A^{-1} \cdot \int_0^t i(t)\,\mathrm{d}t$$

$$n = \alpha_e \cdot e^{-1} \cdot A^{-1} \cdot Q_{sp}(t) \qquad (3.2\text{-}86)$$

In this equation, $Q_{sp}(t)$ is the charge that has flowed through the spark until time t. The current density $J(t) = i(t)/A$ is assumed as constant over the cross section area A. The **spark resistance** $R_{sp}(t)$ is calculated with the spark length l_{sp}, the electron mobility μ and the conductivity $\kappa = \mu \, n \, e$:

$$R_{sp}(t) = l_{sp} / (\kappa A) = l_{sp} / (\mu \, n \, e \, A)$$

$$= l_{sp} / \{\mu \, \alpha_e \, Q_{sp}(t)\} \qquad (3.2\text{-}87)$$

Eq. (3.2-87) is **Toepler's spark-resistance law**, which can also be written with the empirically determined Toepler constant k_T:

$$R_{sp}(t) = k_T \cdot l_{sp} / Q_{sp}(t) \qquad (3.2\text{-}88)$$

The Toepler constant is almost independent of pressure and field strength, Tables 3.2-6.

Table 3.2-6: Toepler constants for different gases [16].

Air	k_T =	0.5 ... 0.6 $\cdot 10^{-4}$	Vs/cm
Nitrogen	k_T =	0.4 $\cdot 10^{-4}$	Vs/cm
Argon	k_T =	0.85$\cdot 10^{-4}$	Vs/cm
SF_6	k_T =	0.4 ... 0.8 $\cdot 10^{-4}$	Vs/cm

Note: **Toepler's spark-resistance law** is derived from the idea of *collision ionization*; i.e. it is only valid as long as the *Toepler mechanism* or the *streamer mechanism* can be assumed. If *thermal ionization* has to be assumed, an alternative approach will give a better fit: The **Rompe-Weizel spark resistance law** assumes that the resistance is inversely proportional to the dissipated energy:

$$R_{sp}(t) = \frac{k_{RW} \cdot l_F}{\int_0^t u_F(t) \cdot i_F(t)\,\mathrm{d}t} \qquad (3.2\text{-}89)$$

Both spark resistance laws describe a very fast decreasing spark resistance.

The **spark formation time** t_{sp} shall be estimated for a capacitance C that is charged to the breakdown voltage V_{bd} and discharged via the spark resistance $R_{sp}(t)$, Figure 3.2-29.

With the instantaneous value of the charge in the capacitance

$$q(t) = C \cdot v(t) = C \cdot V_{bd} - Q_{sp}(t),$$

the voltage-time characteristic is calculated according to Eq. (3.2-88):

$$\begin{aligned} v(t) &= R_{sp}(t) \cdot i(t) = \frac{k_T \, l_{sp}}{Q_{sp}(t)} \cdot \left(-\frac{dq}{dt}\right) \\ &= \frac{k_T \, l_{sp}}{C \cdot \{V_{bd} - v(t)\}} \cdot \left(-C \, \frac{dv}{dt}\right). \end{aligned} \qquad (3.2\text{-}90)$$

After separation of the variables v and t, the differential equation (3.2-90) can be integrated and solved for $v(t)$ [46]:

$$v(t) = \frac{V_{bd}}{1 + e^{\frac{V_{bd}}{k_T l_{sp}} t}} \qquad (3.2\text{-}91)$$

Integration constants are determined by the theoretical boundary conditions $v(-\infty) = V_{bd}$, $v(0) = V_{bd}/2$ and $v(\infty) = 0$, Figure 3.2-39. A practical limitation of this infinitely long time is given, for example, by the time interval for the collapse of the voltage $v(t)$ from 0.9 V_{bd} down to 0.1 V_{bd} [16]. It can be calculated from Eq. (3.2-91):

$$t_{sp} = 4.4 \, k_T l_{sp}/V_{bd} = 4.4 \, k_T/E_{bd}. \qquad (3.2\text{-}92)$$

This means that the *spark formation time* t_{sp} is *not* dependent on the value of the discharged capacitance. If a large capacitance has to be discharged, the large charge transfer will cause a low spark resistance and a high current. The spark formation time t_{sp} is mainly dependent on the *breakdown field strength* $E_{bd} = V_{bd}/l_{sp}$ that is given prior to the breakdown incident. Therefore, t_{sp} depends on the *type of gas*. With $k_T = 0.5 \cdot 10^{-4}$ Vs/cm, we calculate for atmospheric standard conditions

in *air* (E_{bd} = 30 kV/cm) t_{sp} = 7.3 ns and

in SF_6 (E_{bd} = 90 kV/cm) t_{sp} = 2.4 ns.

There is only an indirect dependence on *flashover distance* due to the dependence of breakdown field strength on distance. The *dependence on pressure* is strong, and it is given by the breakdown field strength, i.e. if pressure is increased, E_{bd} will increase and t_{sp} will decrease.

Note: From these relationships it is clear that there are very short spark formation times (or times of voltage collapse) for *compressed-gas equipment*, especially with SF_6 gas. Traveling waves with *rise times in the ns-range* (fast transients) can therefore occur in the case of breakdowns or disconnector switching actions,.

Note: The steepness of current increase and voltage collapse is not only determined by the spark formation time but also by the *system properties* of the discharge circuit, e.g. by the *natural frequency* $\omega = (L \cdot C)^{-1/2}$, Figure 3.2-21.

Gas-*insulated lines* must be regarded as *systems with distributed parameters* (traveling-wave transmission-lines). According to the equivalent transmission-line circuit in Figures 2.6-8 and -10, the time constant for the voltage collapse and the current increase is $\tau = Z/L$. With Z = 50 Ω and L = 100 nH (for a 100 mm long discharge channel), we calculate τ = 2 ns. Even in this case, the inductive time constant is significantly longer than the spark formation time (t_{sp} < 1 ns for p > 2 bar).

3.2.7.2 Arc Discharge

During *breakdown of a gas-insulated gap*, a conductive *spark* channel is generated by *collision ionization* and *photoionization* at first. Then, a high current density causes *thermal ionization* within the discharge column and *thermionic electron emission* at the cathode. Owing to the highly conductive arc plasma in the discharge column, anode potential is displaced close to the cathode and high field strengths and *field emission* occur. This causes the total voltage drop along the discharge gap to decrease to very low values of approximately 10 to 100 V. Owing to the intense thermal ionization, the **electric arc** is characterized by an *intense light emission*.

In *circuit-breakers*, the arc develops during the opening of the switching contacts. Shortly before the separation of the contact pieces, the current narrows down to a very small contact area. Owing to the high current densities, the temperatures are sufficiently high for *thermal ionization*; and after the lift-off of the contact pieces, the current flows without any interruption through the thermally ionized channel (electric arc).

For the most part, the voltage drop of the arc is a so-called *cathode fall* because positive ions accumulate directly in front of the cathode. Negative ions cause a significantly smaller *anode fall*. Owing to the high conductivity, the voltage drop within the *arc column* is comparatively small for shorter discharge lengths, and it increases linearly with the arc length. The arc column consists of largely ionized *plasma*.

The low voltage-drop along an electric arc and a completely different **voltage-current characteristic** (see Figure 3.2.2) are explained by a completely different process of charge carrier generation.

It was already mentioned with Eq. (3.2-2) that the decreasing V,I characteristic for a *steady-state condition* of the arc can be derived from the *equilibrium* between the generated Joule heat P_{gen} and the removed heat P_{trans} that is transferred to the environment:

$$P_{\text{gen}} \quad = \quad P_{\text{trans}} \tag{3.2-93}$$

The generated heat power is given by the product of current and voltage P_{gen}, $= V \cdot I$, the removed (transferred) heat power is a function of arc temperature T, arc radius R and arc length l_{arc}, i.e. $P_{\text{trans}} = l_{\text{arc}} R^m f(T)$ [47]. The equilibrium gives

$$V \cdot I \quad = \quad l_{\text{arc}} R^m f(T) \, . \tag{3.2-94}$$

The variables on both sides of the equation are only independent of each other to a first-order approximation. Actually, the current I is a function of arc cross-sectional area πR^2 and of temperature-dependent *conductivity* $\kappa(T)$. These conditions are better described by a modified approach [16]:

$$V \cdot I^n \quad \sim \quad l_{\text{arc}} \tag{3.2-95}$$

With n = 0.5 ... 0.25, the *voltage drop* decreases with increasing *current* and increases nearly proportionally with *length*.

The **properties** of the arc are strongly influenced by environmental conditions:

If the arc is *cooled*, the generated heat power has to compensate for the cooling, and the *voltage drop* will be greater. Depending on the source impedance, the current can also be enhanced. The equilibrium between heat generation and heat transfer will be reached at a higher *temperature*. Typical values within the arc plasma are between 4000 K and 10,000 K, in some extreme cases up to 50,000 K. At 20,000 K, nearly all gas atoms are ionized [2].

The properties of the arc are strongly dependent on *pressure*. The cross sectional area decreases with pressure because the number of charge carriers per unit area increases with pressure. Therefore, the current density also increases. To a first approximation, a proportionality can be assumed:

$$\pi R^2 \sim 1/p \quad \text{and} \quad J \sim p \, . \tag{3.2-96}$$

Also the *voltage drop* along the arc increases with p, and therefore the *power loss density* increases quadratically with pressure.

An increasing *current* mainly causes an increasing *current density*; the arc *cross-sectional area* increases only slowly.

Often, the arc is subject to *magnetic forces*, which are intended to enlarge the current-carrying loops. At higher currents, magnetic forces can become stronger than the buoyant forces on the hot plasma in the arc.

For **AC voltages**, a *load-independent* sinusoidal arc current is assumed, which is determined (i.e. imposed) by the series impedance

and the source voltage of the circuit, Figure 3.2-40. After the *current zero* crossing (1), there is still a residual ionization, and the voltage in the positive current half-wave increases with current owing to the ohmic resistance. If the *ignition voltage* is reached (2), the voltage and current will follow the negative *V,I characteristic of the arc* until the current maximum is reached (3). While the current is decreasing, the voltage increases again, but to a lesser extend because the conductivity of the arc channel has increased in the meantime. Increasing arc voltage and decreasing arc current lead to *extinction* of the arc (4). After the current zero crossing, the behavior is analogous in the negative current half-wave. If the discharge channel is sufficiently *de-ionized* during the current zero crossing, the positive (or negative) current cannot increase again, the arc will be extinguished permanently and the *recovery voltage* increases between the electrodes (5).

The main problems of arc discharges in **circuit-breakers** are the *extinction* of the arc, the *de-ionizing* of the gas volume and the *insulation* of the fast rising *recovery voltage* between the electrodes (contact pieces). Switching consists of three phases:

1. The *extinction of an arc* is caused by a *perturbation of its conditions of existence*. This means that the *required arc voltage* is *increased* so much that a stable working point is no longer possible, i.e. the *V,I* characteristic is displaced upwards so far that it no longer touches the resistance line, Figure 3.2-3a. In this case, the current through the discharge channel decreases and is interrupted. This situation can be achieved by lengthening the arc, increasing the pressure, forced cooling or separation into a number of partial arcs.

For *AC*, the interruption of current occurs during the current zero crossing and the shifting of the *V,I* characteristic impedes the re-ignition.

2. The *de-ionization* of the discharge channel by recombination of charge carriers occurs automatically when the ionized gas cools down after the interruption of the current. De-ionization can be accelerated by forced cooling. As this occurs, the dielectric strength of the insulating gap has to increase faster than the recovering voltage.

Note: For **AC circuit-breakers**, the natural current zero crossing supports de-ionization and facilitates current interruption. For **DC circuit-breakers**, a natural current zero crossing does not exist and current interruption is heavily impeded. It can be supported by reverse currents fed from auxiliary circuits.

3. The *maximum of the recovery voltage*, which has to be insulated by the opened switching gap, can be significantly greater than the operating voltage stresses because of commutation processes and transients (*switching overvoltages*, *internal overvoltages*). The voltage stress during switching operations is simulated by *switching-impulse test voltages* (Section 2.2.3).

The *compressed gas-blast circuit-breaker* with SF_6 has established itself among the different switching principles for *HV power circuit-breakers*. The electron-affine sulfur hexafluoride is both an effective cooling and extinguishing medium for the arc plasma and an dielectrically strong insulating medium. During contact separation, the electric arc is ex-

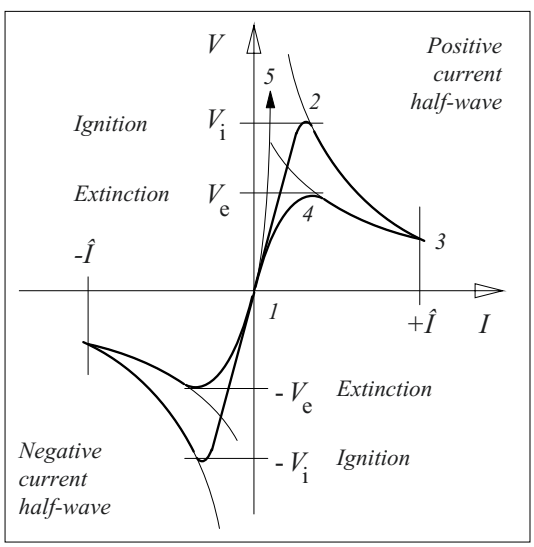

Figure 3.2-40: Electric arc at AC voltage and load-independent imposed AC current with current zero crossing (1), ignition (2), current maximum (3) and extinction (4). Voltage recovery after de-ionizing (5).

posed to high pressure and intense blow-out with SF_6 (Section 7.1.5.2).

Note: The arc plasma contains highly reactive sulfur and fluorine ions that react to form residue-free SF_6 during cooling down. The presence of *water* has to be excluded, in order to avoid the formation of toxic byproducts.

In a *vacuum circuit-breaker*, the current is interrupted in the current zero crossing by deionization of a *metal-vapor plasma*.

Note: Owing to the limited dielectric strength of the vacuum-insulated gap, vacuum circuit-breakers can only be used in the *medium voltage range* (Section 7.1.5.3). Moreover, the fast current chopping would cause fast transients. Nevertheless, the series-connection of synchronously switching vacuum switching tubes is a possible option for replacement of SF_6 circuit-breakers.

3.2.7.3 Lightning Discharges

Atmospheric lightning discharges can cause severe *damage*. In the field of electrical engineering systems malfunctions and destruction are caused by so-called *external overvoltages*. Important systems, e.g. energy transmission grids, communication systems and data transfer nets or important buildings need *lightning protection systems*. Equipment for energy transmission is additionally tested with *standard lightning impulse voltages* in order to guarantee sufficient dielectric strength in case of an external overvoltage. In central Europe, the *probability* for the progression of a lightning discharge down to ground level is approximately 2 lightning strikes per km^2 and year, but there are significant deviations, both locally and globally. However, *external overvoltages* regularly occur in distributed electricity supply systems.

The **formation of thunderclouds** is related to *strong* and *humid air*. Two kinds of thunderstorms can be observed:

1. A *heat thunderstorm* is caused by the summer heating of ground-level air and by an unstable atmospheric layering of warm air close to ground and cold air above. At disturbances of the layering, e.g. at a ground surface unevenness, humid and warm air starts to ascend, accelerates upwards (chimney effect) and cools down owing to the decreasing atmospheric pressure. In the process, the humidity condenses and forms convective clouds, i.e. clouds with vertical development reaching up to 10 km into the troposphere. Heat thunderstorms are typical summer thunderstorms occurring at ground temperatures above 30 °C, mostly in the afternoon and mainly (but not necessarily) on mountain sides.

2. A *front thunderstorm (stormy front)* is caused by a cold front moving under warm and humid air masses, triggering upward currents of air as a result. In the west-wind zone of the northern hemisphere, active front-thunderstorm areas move eastwards in front of low-pressure areas. They often develop in the seasons with changeable weather conditions.

Note: Sometimes *dust storms, forest fires* or *volcanic eruptions* can also cause thunderstorms, but this will *not* be discussed in the following.

In the strong chimney-like *updrafts* (5 to 30 m/s) of a thundercloud, positive and negative *charges* are separated, both by upwards moving water droplets and by downwards falling ice crystals, hailstones and rain. Charge separation are probably caused by many different processes, e.g. atomizing of droplets, bursting of ice crystals and electric influence of dipole charges in droplets, which are disrupted into positive and negative droplets [16], [47].

A *typical charge distribution* of a thundercloud consists of a high-altitude region with positively charged ice crystals, Figure 3.2-41 (left). The center of negative charge is located underneath, at an altitude of approximately 5 km. Downwards falling sleet and hail stones can cause a smaller region with positive charge at a lower altitude and associated with strongly positive rain at ground level.

A thundercloud develops within 30 to 45 min. Finally, the updrafts come to a halt, and cold downdrafts and "*thunder squalls"* occur. Rain falls within the next 30 minutes. As thunder cells can develop repetitively, thunderstorm activity can last for longer periods.

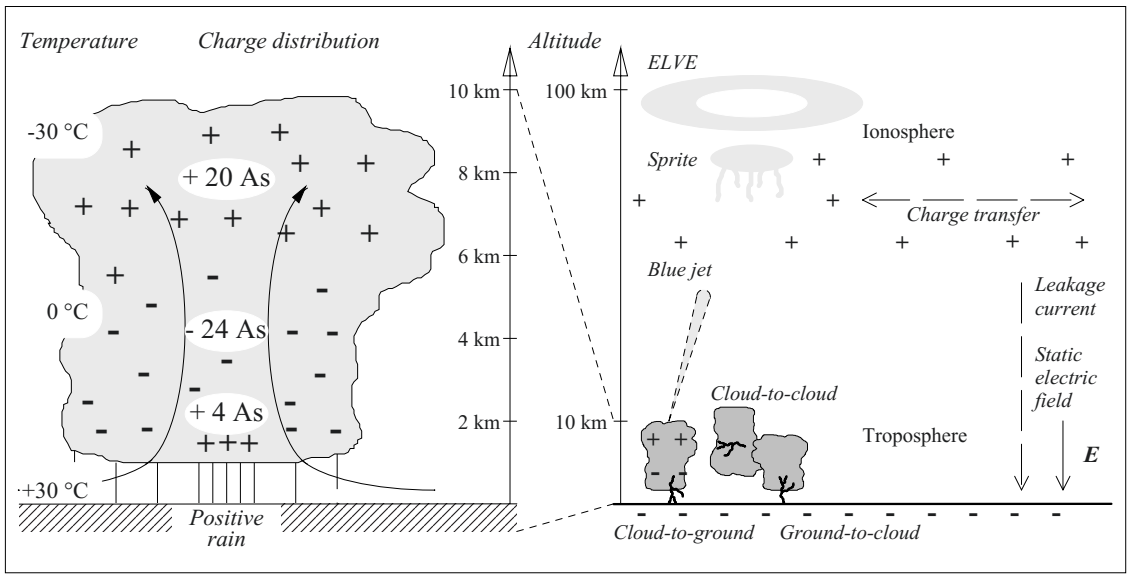

Figure 3.2-41: Charge distribution in a typical heat thundercloud (left) and upper-atmosphere lightning and discharge phenomena (right).

The majority of **lightning discharges** or **lightning flashes** consist of discharges within the cloud (*cloud-to-cloud lightning*), Figure 3.2-41 (right).

A lower percentage of lightning discharges consist of *downward flashes*, i.e. discharges between cloud and earth. They can be identified from discharge branches growing towards the ground, Figure 3.2-42 (left). In most cases, *negative charge* is flowing to ground (negative cloud-to-ground lightning), but a minority consist of *positive cloud-to-ground lightnings*, depending on the charge distribution in the cloud, Figure 3.2-41 (left).

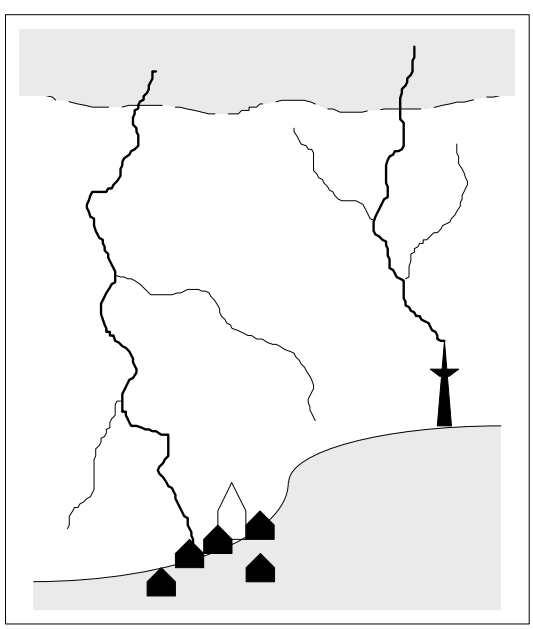

Figure 3.2-42: Downward and upward flashes.

For a very low percentage, *upward flashes* were observed, starting from tall structures on ground. These *ground-to-cloud lightnings* can be identified from discharge branches growing towards the cloud, Figure 3.2-42 (right).

Note: World-wide, there are always a few hundred active thunderstorms. On average, the downward flashes carry *negative charge* to ground; positive *charges* are accumulated in the *ionosphere* and distributed all over the world., A global static electric field is thus generated that is determined by the balance of lightning currents and atmospheric leakage currents, Figure 3.2-41 (right).

Note: At the end of last century, **upper-atmospheric lightning** above the thunderclouds was also observed from space, i.e. *blue jets* between thunderclouds and the lower ionosphere and so-called *sprites* and *ELVEs* (Emissions of Light and Very Low Frequency Perturbations from Electromagnetic Pulse Sources) at very high altitudes between several 10s of km and approx. 100 km, Figure 3.2-41 (right) [483], [484].

In the following, the **development** of a *negative* cloud-to-ground lightning flash is dis-

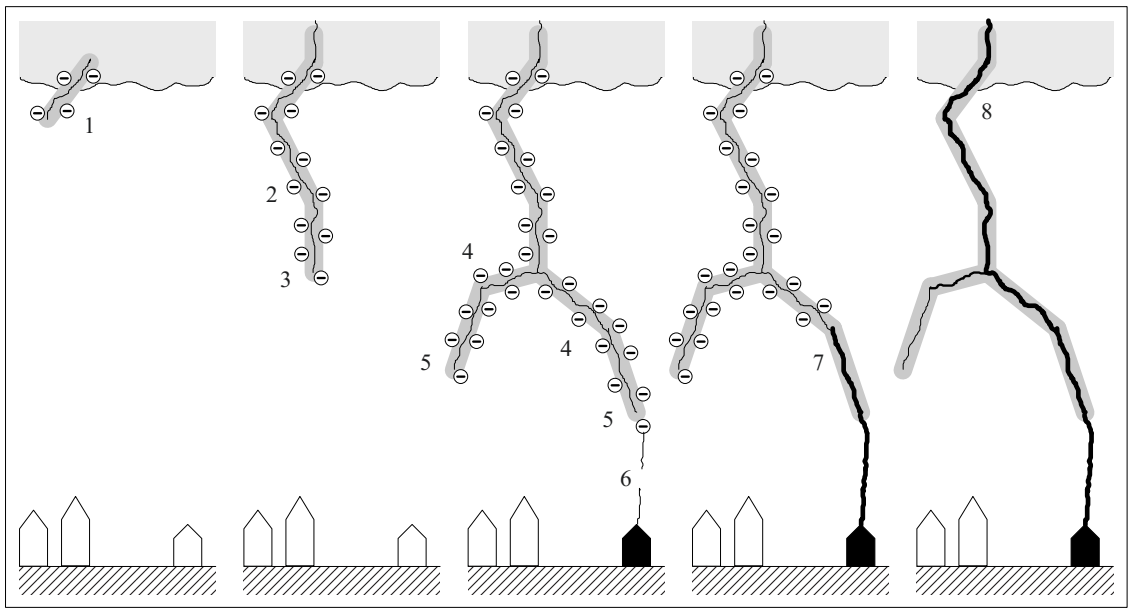

Figure 3.2-43: Development of a negative cloud-to-ground lightning flash:
1 to 5: Descending stepped leader discharges and accumulation of negative space charge (approx. 300 to 1000 µs).
6: Upward and downward (connecting) leaders, initiated by field enhancements at discharge head and ground.
7 to 8: Main discharge (return stroke) with discharge of negative space charge (approx. 10 to 100 µs).
NN: Subsequent flashes following the pre-ionized channel (approx. during 10 to a few100 ms).

cussed in more detail, Figure 3.2-43. There are four stages; the *descending stepping leader discharge* starting from the cloud (approx. 300 to 1000 µs), the *upward and downward leaders* connecting close to the ground, the high-current main discharge (*return stroke*, approx. 10 to 100 µs) and a number of *subsequent flashes* through the pre-ionized channel (within 10 to a few 100 ms).

If the breakdown field strength is exceeded, an electrode-free *bipolar streamer discharge* can start within the cloud and propagate in opposite directions both towards ground (negative side) and into the cloud (positive side). The ionized channel is also referred to as a *descending leader*. Owing to a lack of charges, the channel cannot grow steadily towards ground and the leader propagation stops. Discharges at the opposite end deliver additional charges within 15 to 100 µs, the field strength at the discharge head increases and the next partial breakdown step occurs. Thus, the leader propagates in steps, each with a length of approx. 50 m (*stepped leader*) and with a comparatively low current. The direction of the individual steps is highly irregular because of local field distortions caused by space charges. Branching can also occur as a result of local field stress enhancements. At first, the descending leader discharge path is nearly independent of structures on the ground. Even tall buildings and mountains can be bypassed because they cannot influence the local electric field direction at the discharge head over longer distances.

Close to ground, the descending stepped leader discharge causes very high field stress enhancements and initiates positive *upward* and negative *downward leaders* that are approximately 10 m long. The so-called *connecting leaders* originate from exposed grounded structures and from the discharge head, connect and cause final breakdown between the stepped leader and ground (see point-to-point arrangement, Figure 3.2-30).

Note: Owing to the *limited range of upward and downward leaders*, lightning strikes are also possible alongside higher buildings, towers and mountains. *Air termi-*

nations of lightning protection systems have a limited *cone of protection* only.

The discharge propagates along the pre-ionized channel from ground towards the cloud (*return stroke*) and discharges the negative space charge stored alongside the channel. The *return stroke* is the *main discharge* that is visible as a *lightning flash* and audible as *thunder*. Current magnitudes can reach peak values of from a few kA up to a few 100 kA within a few µs. The current decay can last for a few 100 µs. This behavior can be explained by the large amount of charge in the discharge head allowing a rapid increase of current after contact to ground, Figure 3.2-44.

Note: The *individual current curves differ* significantly. Nevertheless, a *standard lightning impulse voltage* with a front time of 1.2 µs and a time to half-value on wave tail of 50 µs is defined in order to simulate the influences of lightning impulse currents on power equipment by a standardized test method, Figure 3.2-44, Section 6.2.3.

After replenishment of charges from the cloud, the pre-ionized channel can be used for some *subsequent strikes, generally* with lower current amplitudes.

Lightning strikes can cause severe harm and damage to men, animals, buildings, trees and technical systems. In the following **direct and indirect influences** on *electrical and electronic systems* shall be discussed.

Traveling waves, overvoltages and electromagnetic forces are *direct influences* of lightning strikes, e.g. in the phase conductors of a three-phase system. Additionally, heat generation can damage conductors in the impulse current path.

Voltage drops across ohmic and inductive impedances are *indirect influences*. They cause *transient potential differences* between statically grounded parts and they can cause "back flashovers" from grounded conductors into active lines of electric and electronic systems [41]. The strong and time-varying *magnetic field* of the lightning-impulse current *induces* high voltages in loops. They can endanger

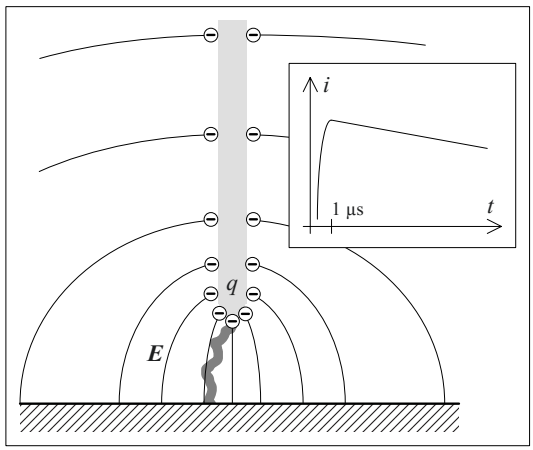

Figure 3.2-44: Current-time characteristic of the return stroke.

electronic systems and they can cause flashovers between conductors without sufficient separation. Section 7.4.1 describes **lightning protection**.

Lightning flashes are described by four **lightning current parameters**, which allow estimation of expected damage:

1. The *peak value* of the current allows us to determine the maximum ohmic voltage drop at *grounding resistances* and to calculate overvoltage amplitudes on *traveling wave lines* (see Section 2.6.1, example). Mostly, $\hat{I}$ is between 5 and 100 kA; sometimes a few 100 kA can occur.

2. The *rate of current rise* $\mathrm{d}i/\mathrm{d}t$ allows the calculation of voltage drops at inductive impulse current diverters and the calculation of *induced voltages* in nearby conductor loops. Therefore, the rate of current rise is the most important parameter for the description of induced voltages in electrotechnical systems. Typical values of the rate of current rise $\mathrm{d}i/\mathrm{d}t$ are between 1 and 100 kA/µs.

3. The *charge* of an impulse current $\int i\,\mathrm{d}t$ is a measure for the heat energy $\int \Delta v \cdot i\,\mathrm{d}t$ generated at the root point of the arc, if a constant voltage drop Δv is assumed at the root point. This energy is related to the *fusing* of metallic conductors. The range is 0.5 up to some 100 As.

4. The *integral of the squared current* $\int i^2 \, dt$ is related to the ohmic losses in the conductors $R \cdot \int i^2 \, dt$ and to the mechanical impulse (momentum) $\int F \, dt$. Typical values are between 10^3 and 10^7 A^2s.

Lightning discharges are further described in Section 7.4.1 on **lightning protection**. *Lightning current parameters* that are assumed for protection purposes are listed in Tables 7.4.1-1 and -2.

3.2.7.4 "Ball Lightning"

For a long time, reports about so-called ball lightning have been comparatively frequent, but so far there is no commonly accepted physical explanation. Therefore, a discussion in a textbook may be too early, but interested readers should be given some information in spite of this, as it might be one of the oldest known high-voltage phenomena of all: There are historical eye witness reports from ancient scholars, mediaeval rulers, Nobel Prize winners and many other people. In modern times, chance pictures and video sequences have been taken, but a scientifically founded and reproducible observation does not yet exist.

Note: There are many diverse and speculative attempts at explanation. They include optical illusions, mental delusions caused by pulsed magnetic fields, methane gas flames, plasma balls, black holes, nuclear reactions and esoteric phenomena. Furthermore, "ball lightning" might be used for different physical phenomena.

Nevertheless, some often described *properties* can be figured out from the various reports. "Ball lightnings" are described as luminous effects with different colors. They occur in conjunction with a thunderstorm, have a spherical shape and can exist for comparatively long times between seconds and minutes. The balls can have destructive effects and explode, or they can be harmless and fade away.

The described phenomena could be related to *plasma balls* that might be generated by lightning strikes into wet soil. In laboratory experiments with pulsed energy transfer into water droplets, spherical plasma-magnetic entities (*plasmoids*) were successfully generated and kept glowing for approximately 0.3 s [440], [485].

Note: In laboratory experiments, the discharge is ignited at a negative rod electrode within a ceramic tube that is open at the top. The tube contains a small amount of water, which is brought into a glowing plasma condition by a discharge, and which expands upwards with high velocity. The discharge plasma is extended across the edge of the ceramic tube and comes into contact with the outer water surface, and the salted water provides a contact to the anode. Owing to the buoyant forces, the expanding plasma is detached from the water surface with a velocity of approximately 1 m/s. Owing to its charge, it takes a spherical shape. The glow duration of 0.3 s is much longer than typical ionization times in gas-discharge plasmas, but it is significantly shorter than observed *durations* in nature. Excitation processes of molecules, which cause a long-lasting *chemiluminescence* in flames, are the object of current research [441], [442]. There could be additional chemical contaminants in the water, on the ceramic tube surface or on the electrodes that influence the color and duration of the glow.

3.3 Discharges in Liquid and Solid Dielectrics

Discharges in liquid and solid dielectrics also develop by the acceleration of electrons, collision ionization and avalanche formation. However, they *cannot* be described by a universal physical theory as is possible for gases with their homogeneous and well definable properties. The groups of "solids" and "liquids" consist of *very many materials* with *very different* physical and chemical properties. They are subject to variations of material compositions, production conditions, contamination, defects and ageing processes. This results in strong *statistical dispersion and changes* of breakdown strengths. The difference between ideal strength (under laboratory conditions) and technical strength (under application conditions) can be more than one order of magnitude.

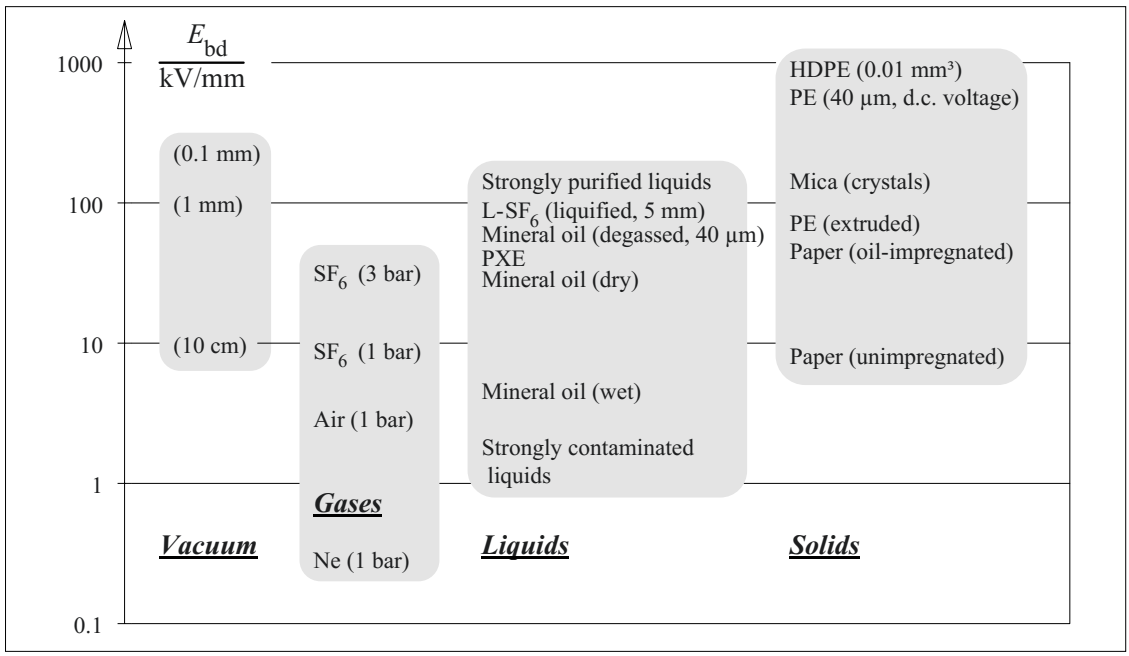

Figure 3.3-1: Ranges for breakdown field strengths at AC voltage (50 Hz) for atmospheric pressure, ambient temperature and insulation thicknesses in the cm-range (other conditions are mentioned in brackets).
Abbreviations: SF_6 *(Sulfur hexafluoride),* L-SF_6 *(Liquified sulfur-hexafluoride),*
PXE (Phenyl-Xylyl-Ethane), PE (Polyethylene), HDPE (High-density polyethylene).

Basically, the inception of discharges is impeded with increasing *density of the material structure* (decreasing free path-length for charge carriers) and with increasing *binding forces* of the electrons. Accordingly, the *dielectric breakdown strength increases from gases through liquids to solids*, but a large number of influences blurs this picture, Figure 3.3-1.

Figure 3.3-1 gives breakdown strengths for liquid and solid dielectrics. *Technically pure materials* can be found in the middle of the given ranges*, highly purified materials* or very thin layers are at the upper ends and *contaminated materials* at the lower ends. For gases, the technically achievable design strengths are significantly closer to the physical limits.

Gaseous, liquid, and solid insulating materials have their **specific advantages and disadvantages**. Without respect to their dielectric strength, they are especially suited as "construction materials" for specific purposes:

1.) **Gases** have the following *advantages*: Low weight, perfect impregnation properties, well defined properties, long-term stability, insensitivity to electrical discharges or self-healing properties (even in case of arcs) and low cost (for air). It is *disadvantageous* that breakdown strengths (at atmospheric pressure) are low and that stresses because of dielectric field displacement are high. Gas (air) is the *"natural" insulating material* (e.g. for overhead lines and switchgears), which is only replaced by liquids or solids if necessary.

2.) **Liquids** have different *advantages*: Good impregnation properties, high breakdown strengths and high thermal conductivities by convection. On the other hand, there are the following *disadvantages*: Higher weight, breakdown-strength degradation by ageing and contamination, thermal expansion, the necessity for sealed housings and higher costs.

Liquids are the *typical impregnation materials* for electrically stressed cavities (in capacitors,

transformers, cables, etc.). They are also used for the convective *transport of heat* (e.g. in transformers).

3.) **Solids** also have specific *advantages*: High breakdown strengths (e.g. for thin films), reduced stresses because of field displacement and their applicability as mechanical construction materials. Low-viscosity resins can be used for impregnation; in the cured state, they allow "dry", i.e. oil-free constructions. It is *disadvantageous* that heat conductivities are low, that electrical discharges can cause irreversible destruction, that weights are high and that there are high technological requirements.

Solids are used in *highly stressed dielectrics* (capacitors, bushings, cables), for the *embedding of conductors* with high surface field strengths (transformers, electrodes, cable terminations) and for *mechanical construction elements* with insulating properties (string, post and housing insulators, switch rods, partition plates etc.).

3.4 Discharges in Liquids

Insulating oils based on **mineral oil** are the most important insulating liquids, Sections 3.4.1 to 3.4.3. They are used in large quantities in transformers both as *insulating* and as *cooling liquids* ("transformer oil"). Furthermore, mineral oil is used as *impregnating liquid* in oil-filled equipment, e.g. in bushings, instrument transformers and capacitors. Additionally, **other liquids** based on natural or synthetic sources are used for special applications, Section 3.4.4.

3.4.1 Discharge Mechanisms in Mineral Oil

Basically, the breakdown strength of mineral oil decreases significantly with voltage-stress time, Figure 3.4.1-1. Owing to multiple *unknown parameter influences* (type, form and number of particles; water content, stressed volume, electrode surface, distance, oil convection, uniformity of the field …), breakdown tests show large differences and *dispersions* which cannot normally be adequately described by **theory**. Therefore, **empirical** parameter dependences are most important for practical dimensioning.

Example: In a weakly non-uniform electrode arrangement, the 1 % breakdown values can be *lower than half* the 50 % breakdown values for long lasting AC voltage application [59], Figure 3.4.1-2. This is a dramatic increase of **statistical spread**, in comparison with short-duration voltage applications (impulse voltage) and in comparison with gas discharges.

The high number of relevant parameters has initiated many **experimental investigations** since the 1950s, in order to find *statistically justified relations* between test conditions and dielectric strength. Nevertheless, there is not yet a consistent theory of oil breakdown which is comparable with the theory of gas dis-

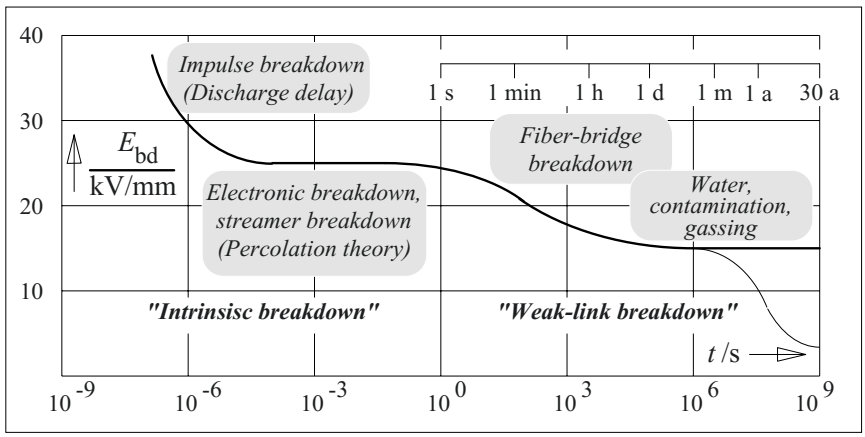

Figure 3.4.1-1: Breakdown strength of a liquid dielectric as a function of voltage-stress time (transformer oil, d= 2.5 mm, V= 200 mm³) without respect to the statistical dispersion which increases with time, see fig. 3.4-2.

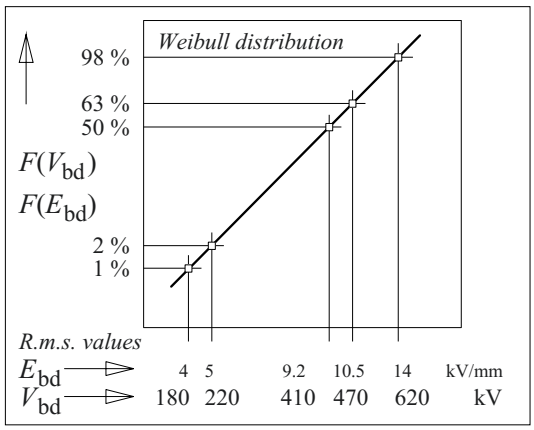

Figure 3.4.1-2: Breakdown frequency as a function of voltage and field strength in technically clean and dry oil at AC voltage (f = 50 Hz, voltage rise rise 8 kV/s) between excentric tubulal electrodes (Da = 600 mm, Di = 80 mm, d = 72 mm, l = 300 mm, field efficiency factor 62 %), oil flow 100 l/min [59].

charges. For *very short voltage-stress times*, the discharge behavior seems to be similar to the discharge behavior in gases, Figure 3.4.1-1, but the direct formation of electron avalanches by collision ionization in an ideal liquid is not conceivable at first glance; free path-lengths are not long enough and the typical breakdown strengths are not high enough.

Note: In the past, it was assumed that the liquid contains *low-density volumes*, which could be seen as oil-vapor "*mircobubbles*" [59]. In these bubbles, free path lengths could be available, allowing collision ionization similar to gas discharges ("**masked gas-discharge**"). The increasing breakdown strength with decreasing stress duration would be equivalent to the *voltage-time characteristics of gas discharges*, Figure 3.4.1-1; and dependences on the static pressure could also be explained consistently, Figure 3.4.2-5. There are different theories for the generation of microbubbles [59]: Low-density volumes could occur even below the boiling temperature because of the *thermal (Brownian) motion of molecules*. Furthermore, it seems to be possible that density differences occur by *electro-hydrodynamic motion* of charged volumes. Another idea assumes that space charges expand by *electrostatic repulsion* causing low-density volumes. Additionally, discharges could be ignited by *charge transfer* between particles and electrodes. High electric field strengths at microscopic tips at electrodes could additionally cause *current injections, local overheating* and density reductions.

As early as 1970, a **physical theory** of oil breakdown was developed on the basis of discharge current measurements and optical imaging, [426]: High local field strengths at electrode tips cause a strong *increase of conductivity*, together with *space charge formation* and equalization of the field distribution. From such an *impulse-free dark-current discharge* or *continuous discharge* (1), luminescent and **thermally ionized discharge channels** erupt repetitively at very high field strength (2). By analogy with gas discharge physics, these channels are referred to as **leaders**, Hauschild [426]. The channels transfer the electrode potential into the liquid with a voltage gradient of approx. 1 kV/mm. The discharges can be stabilized in a strongly non-uniform field. At sufficiently high voltages or in a uniform (or weakly non-uniform) field, the leader channels can reach the counter-electrode and generate the *main discharge*, formed by a high-current *backward leader* (3).

Note: In today's terminology, the described discharge phenomena are often referred to as **primary** (1)**, secondary** (2) **and tertiary** (3) **streamers**. But in terms of discharge physics, this is not correct where **thermally ionized channels** are concerned; these would be better referred to as **leaders** [426]. Today, the term "*streamer*" imprecisely describes the *propagation of low-density volumes* without respect to their physical origin. Please note that gas-discharge physics uses the term "*streamer*" only for a space-charge-related discharge channel generated by *collision ionization*, Section 3.2.3.

Owing to physical investigations, the theory of oil breakdown is now much more sophisticated. Different stages from the first *initial processes* to the final breakdown process (the so-called *streamer development*) can now be described in detail, Section 3.4.1.1 to 3.4.1.4. In the following, physical theories (Section 3.4.1) and empirical parameter dependences (Section 3.4.2) are described and discussed.

3.4.1.1 Stages of Oil Breakdown

By means of high-speed cameras, *shadow images* of different discharge stages can be taken. They show the propagation of *volumes with low density* and thus give a sophisticated picture of oil breakdown, Figures 3.4.1-3 and -7ff. In oil gaps, breakdown processes start at

the *electrode surfaces* and they are related to the generation of *gas-filled microcavities*. Gas discharge processes occur in these cavities.

Note: So far, similarities with gas discharges can be explained (voltage-time characteristic, pressure dependence), but it is not yet clear, whether **microcavities** are the reason for the discharges or whether discharges generate the microcavities. Different mechanisms are discussed in the literature. In all experimental investigations on mere oil gaps without barriers, discharges start at the electrodes. Therefore it is assumed that both the *properties of oil* and the *interaction with the electrode surface* play an important role.

In the following, the **different stages** will be discussed in detail, but an overview is given at first, Figure 3.4.1-3:

(1) **Without a field**, the liquid is in an unordered state. At the interfaces between liquid and electrodes, electrochemical double layers (Helmholtz layers) are formed; they reduce the work function for electrons [402], [404].

(2) After the application of an **electric field**, electrons are injected into the liquid. Structural differences of electrode surface areas, oxides and pollution layers cause strong local differences of the work function and for the injection of electrons. Very high injection current densities of the order of kA/mm² can occur, especially at microtips [423].

Under the influence of a **strong field**, the *conductivity* of the liquid increases non-linearly. Electrons are injected at the *cathode* and build up a negative *space charge* that weakens the field and restricts the emission. At the *anode*, electrons are stripped in the liquid and focused (concentrated) in front of the positive tips. This significantly increases local field strengths.

In the *liquid*, current density lines are concentrated at preferential surface points. At these points, energy is transferred into the liquid causing local enhancements of temperature

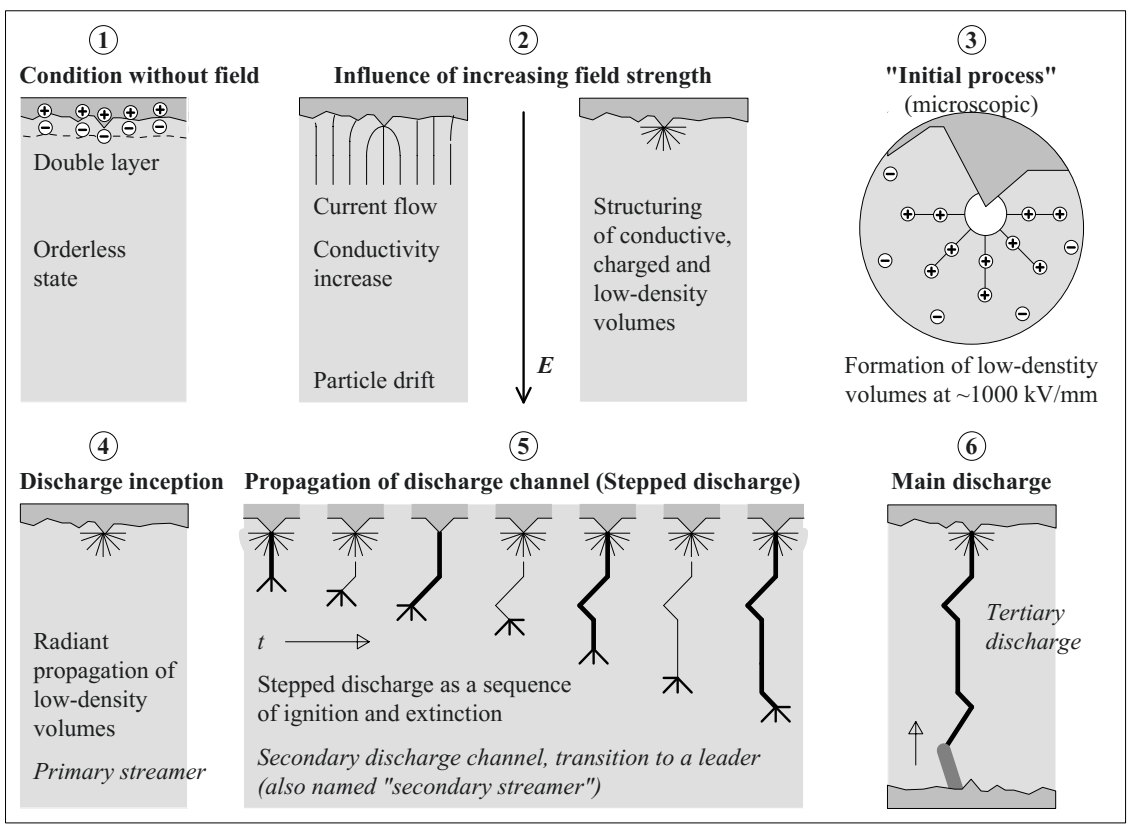

Figure 3.4.1-3: The stages of oil breakdown, see also Figure 3.4.1-10.

and conductivity. The conductive paths are connected to the electrode and charged accordingly. The charged current paths form *semi-spherical* and regular *bunch-like structures* in the liquid because of their electrostatic repulsion. As a result, preferential paths for current flow are imprinted in the liquid (**percolation theory**).

(3) At **very high local field strengths** between 250 and 1000 kV/mm (i.e. far above the macroscopic technical breakdown strength of approx. 25 kV/mm), microscopic *volumes with low density* are generated, which can be regarded as *gaseous*. Their bunch-like and branching structures in the liquid can be detected by shadow images. There are three different theories describing the initial processes of discharge evolution in strong electric fields: (a) discharges caused by collision ionization within the liquid [403], [407], (b) destruction of surface tension [404] and (c) current-induced conductivity increase [310], [423].

Note: In addition to these (intrinsic) **initial processes** in the *liquid* itself, influences of **weak links** (*contaminants*) have to be considered.

(4) Today, the bunch-like and radially expanding low-density regions are referred to as "*streamers*" in the literature. This is not quite precise, because there is no reference to the physical cause. Nevertheless, as long as the *initial* or **primary streamers** are caused by *collision ignition*, i.a. at high local voltage drop, this wording is in accordance with gas discharge theory, cf. Section 3.2.3.

(5) A discrete branched **secondary discharge channel** develops from the uniformly structured *branch-like* **primary streamers** as a *stepped discharge* similar to the leader discharge of a *cloud-to-ground lightning flash*, Figure 3.2-43. As high current densities at low local voltage drops occur during the stepped growth of the channel, thermal ionization, i.e. a **leader discharge** is assumed [426]. Nevertheless, the phenomenological term "*secondary streamer*" is further used in literature without physical reason.

A *positive channel* propagates stepwise and with high velocity (approx. 2 mm/µs) towards the counter electrode, which is always reached. The discharge is interrupted and ignited several times during propagation. A *negative channel* leaves a positive space charge cloud behind which weakens the local field and limits the discharge range and velocity (approx. 0.1 mm/µs). Thus, the negative channel is less dangerous than the positive one [405], [406].

(6) For long streamer lengths or if the counter electrode is reached, the conductive channel is used for a high-current luminescent **tertiary discharge** (main discharge) with high conductivities and temperatures causing oil vaporization, gas discharges, ionization, light emission and voltage collapse.

After this overview, the *stages of oil-breakdown* will be discussed in detail in Sections 3.4.1.2 (The liquid before ignition), 3.4.1.3 (Initial processes) and 3.4.1.4 (Discharge Propagation).

3.4.1.2 The Liquid before Ignition

a) The liquid without a field

Even without a field, there are free charge carriers in the liquid, mainly in the form of positive and negative ions and a few quasi-free electrons. The charge carrier density is determined by the equilibrium of recombination and ionization (dissociation).

At the interface between oil and **electrode**, there is a thin and diffuse *electrochemical double layer* with a thickness of approx. 100 nm. There is a preponderance of negative charge in the liquid, whereas the positive image charges are situated on the electrode [402], Figure 3.4.1-3 (1).

Note: The *microscopic field strengths* can reach 1000 kV/mm. Electrons need an energy of approximately 4 to 5 eV (*work function*) in order to leave the electrode against such a field. Normally, there is an *oxide layer* on the metal electrode surface with traps that can exchange a limited number of electrons with the liquid.

Double layers, energy levels and microscopic field strengths are strongly dependent on *surface roughness*, *surface conditions* and *contaminants,* and they are subject to strong local and temporal variations. This might be one of the reasons for the high *statistical spread of oil-breakdown*, which can often be observed.

b) Impact of an external field

An external field changes the double layers at the **electrodes**. At the *(negative) cathode*, electrons are injected into the liquid and a negative *space charge* is built up. It weakens and homogenizes the field in front of the electrode, thus reducing the injection. The injection process can only start again when the space charge has been removed by charge carrier drift. A repetitive process results that is comparable to the gas-discharge *Trichel impulses*. In front of the *(positive) anode*, the microscopic field is significantly enhanced because drifting electrons, which were generated in the liquid or at the cathode, are concentrated (focused) close to surface in-homogeneities. This explanation corresponds to the observation that breakdowns are caused by *positive streamers* in most cases (**polarity effect**).

In the **liquid**, the *mean free path lengths* are short. Even at *high field strengths*, electrons cannot get enough energy for collision ionization processes and avalanche formation. Therefore, it is hardly imaginable that the processes are comparable to gas discharges; it seems to be more reasonable to compare the processes with the **energy-band model** of an *amorphous solid dielectric*.

Note: The **energy levels** of the charge carriers are described by *erratic energy-band structures* similar to an amorphous solid (conduction and valence bands, traps), Figure 3.5-2. Electrons can move along chain molecules by tunneling and hopping. During the transition between molecules, electrons have to get over higher potential barriers (intermolecular transition). *Quasi-free electrons* in the conduction band are generated by energy transfer from thermal motion, radiation or the electric field.

At low *field strengths*, the ions drift to the electrodes where they are neutralized or accumulated [486]. Thus, the **conductivity** of liquids *decreases* within the *transit time* of the ions. At *higher field strengths*, energy-band structures and potential walls are displaced according to the potential gradient. Consequently, tunneling, hopping and generation of quasi-free electrons in the conduction band are made easier. The conductivity *increases* significantly, Figure 3.4.1-3 (2) left, Section 4.2.2.2.

Note: It is assumed that even "quasi-free" electrons are not completely free. Owing to the high material density, they remain in a permanent interaction with the molecules and lose energy continuously. Therefore an *accumulation up to the ionization energy* seems to be impossible [310]. Nevertheless, there are *controversial opinions regarding this*, Section 3.4.1.3 (a) [402], [407].

c) Imprinting processes in the liquid (percolation)

There is an interesting theory about *imprinting processes in the liquid*: The **percolation theory** [310], [423] assumes that an ideal liquid *without a field* is without any long-range order and remains in a condition of complete *disorder*, which is in contrast to a solid. In this situation, there are no *energy levels* within the liquid which can absorb charge carriers. Under the influence of an *electric field*, the molecules are arranged and a *short-range order* is generated with different energy levels, which are occupied by electrons. Drifting, hopping and tunneling electrons polarize the adjacent molecules and create *new energy levels* that facilitate the motion of subsequent electrons. As a result, coherent *regions with enhanced conductivity* and enhanced current density (allowed zones) are generated. In these regions, electrons "*percolate*" through the oil. In a limited volume, molecules are arranged in regular (short-range) order, Figure 3.4.1-4 (bottom).

Note: "*Percolation*" refers to the **imprinting of preferential directions** for charge carrier movement in the oil by the incipient charge transport itself. This process is analogous to a coffee percolator, in which the water percolates through the coffee powder and impresses macroscopic propagation structures.

Ordered ranges can be built by generating clusters from charge carriers and molecules, they can be extended by charge supply from

the electrodes and they can be connected to each other. Thereby, the *liquid is structured* with temporarily stable *quasi-crystalline* clusters (consisting of up to 10^5 molecules and with dimensions up to 0.1 µm), which are separated by disordered regions. Similarly to an amorphous solid, there are *"allowed zones"*, which can carry electrons and in which electronic charge transport occurs by quantum-mechanical processes (hopping, tunneling) [310], see also Figure 3.5-2. The electronic charge transport through the liquid takes place by charge transfer between the allowed zones. The higher their number and the higher their degree of order, the higher currents can flow.

The *conductive paths* are spherically or semi-spherically arranged under the influence of the local field close to microscopic tips by the *repulsion forces of the space charges*, Figure 3.4.1-3 (2) right.

3.4.1.3 Initial Processes

The actual ignition of the breakdown process is called the *initial process*.

Basically, the **intrinsic breakdown** *of the pure liquid itself* and the **weak-link breakdown** *caused by contaminants* have to be distinguished.

Experiments with very sharp point-electrodes show that the inception of streamers in pure liquids requires very high **local field strength**s of the order of

$$E = 1000 \text{ kV/mm}$$

The inception field strength for positive streamers is lower than for negative streamers (polarity effect), Section 3.4.1.2. The physical nature of the initial processes can be explained by a number of different theories, Figure 3.4.1-

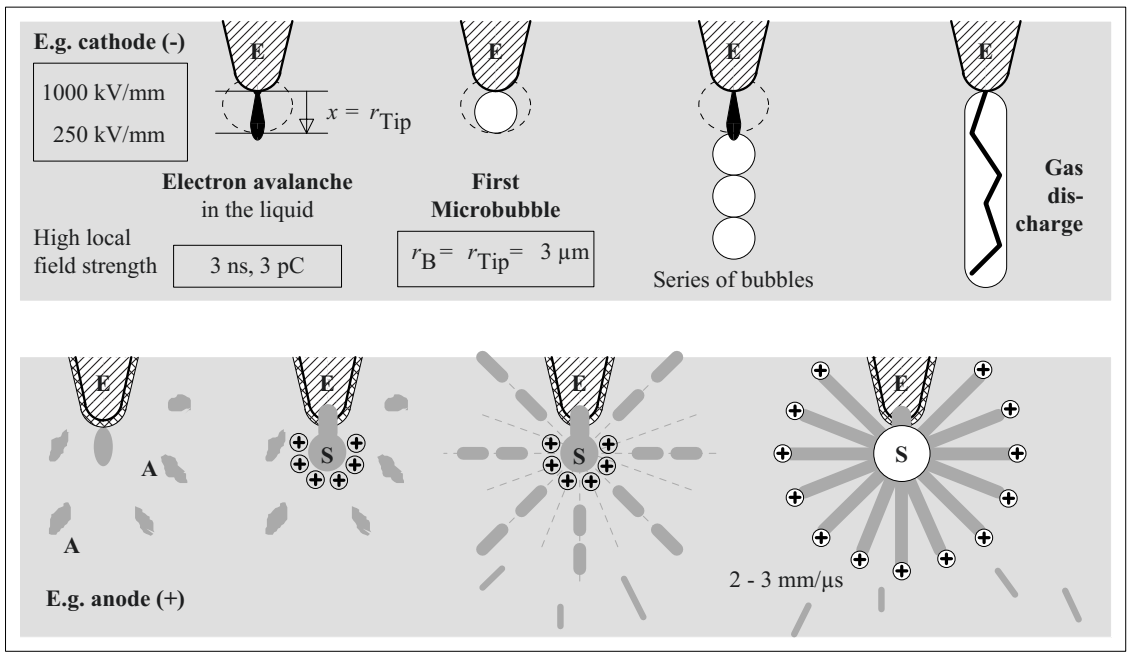

Figure 3.4.1-4: Different theories about initial breakdown processes in insulating oil at an electrode (E) with high local field strength.
Top: Generation of microbubbles by electron avalanches in the liquid at very high local field strengths ("hot micro cavities").
Bottom: Arrangement of allowed (conductive) zones (A) around an interconnected source region (S): Interconnection with the electrode (E), structuring of the conductive zones, current increase and gas formation (G) by vaporization (percolation theory).

4. They describe the initial processes in different ways, *(a)* as *avalanche formation* in the oil itself, *(b)* as a reduction of *surface tension*, *(c)* as an imprinting, structuring and *heating* of the liquid or *(d)* as a thermal instability in wet and conductive *cellulose fibers*. Different technological influences have to be taken into account *(e)*. The sections *a)*, *b),* and *c)* describe initial processes for **intrinsic** breakdowns, sections *d)* and *e)* refer to **weak-link** phenomena.

a) Avalanches in the oil ("hot microcavity")

Tobazéon [403] assumes that collision ionization and **electron avalanche formation** can occur *in the liquid itself* for a field strength of approximately 1000 kV/mm.

Note: Lewis gives the following explanation based on a reduction of the collision cross section with increasing electron energy: At 1000 kV/mm, collisions would be elastic and the electrons would keep their energy, which could be *accumulated up to the ionization energy of approx. 9 eV* [402]. Furthermore, electron exchange processes (Auger processes) could generate high energy electrons at the electrodes [407]. Owing to a simple estimation, Tobazéon's theory is quite plausible, if the situation at a point electrode with a µm radius is compared with a gas discharge: The ratio of oil density (800 kg/m³) to air density (1,2 kg/m³) and the ratio of the inception field strengths of approx. 1000 kV/mm (oil) to 3 kV/mm (air) are in the same order of magnitude.

In a non-uniform field, the range of the avalanches is very limited, because free charge carriers are trapped below 250 kV/mm. As a result of *energy dissipation*, every avalanche causes a **microcavity** or a **microbubble** with a radius approximately equivalent to the point-electrode radius (up to approx. 10 µm). Subsequent avalanches (approx. 3 pC every 3 ns) generate a *series of bubbles* which gives enough length for the ignition of gas discharges and for their development into a so-called *streamer* [403], Figure 3.4.1-4 (top).

Note: For tests with sharp point electrodes, it was observed that only the *positive* streamer inception depends on *pressure* and not the negative streamer [414]. For the *positive* point electrode, it is concluded that there is a concentration of current, overheating and pressure-dependent *vaporization* (see c)). The *negative* streamer is assumed to start with an *electron avalanche* directly in the liquid phase as described above.

b) Destruction of surface tension ("cold microcavity")

Lewis [407] has also shown that the **surface tension** of the liquid is reduced at high field strengths. This means that the cohesion of the liquid-molecules could be broken up at the locations of the highest electric field strength (especially in the double layer at the anode) and a **"cold" microcavity** could occur. In such a cavity, collision ionization processes could occur, and *initial electrons* could be generated by charge transfer between incident charge carriers and the electrode (Auger process). In this case, the electric discharge would be the consequence and not the cause of the initial process.

c) Interconnecting of electrode-liquid interfaces (percolation theory)

According to the **percolation theory**, conductive ("allowed") zones in the liquid are arranged at points of locally focused field lines. The current flow causes an imprinting (percolation), which further increases the conductivity, Section 3.4.1.2 [423].

Note: Kist [310] assumes that the **interfaces** between metal, oxide and liquid block at first, *switch through* after a threshold is exceeded and interconnect an "allowed zone" in the liquid with the electrode, Figure 3.4.1-4 (bottom). This zone becomes an inception or **source region** which is charged from the electrode and creates a **spherical micro-field**. The allowed (or rather conductive) zones are arranged in the **spherical micro-field**. They are enlarged by means of *charge supply* from the electrodes (electrons at the cathode, "holes" at the anode.

Owing to electrostatic repulsion, the growing conductive and charged zones are arranged in tree-like or threadlike spherical structures. The structuring *imprints* **channels** for increased current flow, which causes local heating and *vaporization* of the liquid when energy dissipation becomes high enough. The resulting radial and branched *primary streamers* are oriented in the direction of the microscopic field.

Low-density streamers also play an important role in percolation theory, but they aren't the reason for the current flow. Streamers are the consequence of the current, which already exists because of field-induced ordered states. Electric discharges can be ignited in the gaseous streamers, which were generated by overheating. Thereby, a *pressure dependence* according to a) could be explained.

d) Wet fibers (fiber-bridge breakdown)

There is very good experimental evidence that **wet fibers** reduce AC and DC breakdown voltages and increase statistical spread [59]. Therefore, **weak-link breakdown** *caused by contaminants* and **intrinsic breakdown** *of the liquid itself* have to be distinguished.

Owing to the electrostatic field forces, fibrous impurities can drift in the direction of the electric field lines and line up as fiber bridges, especially during **long stress durations**. Often, the *hygroscopic cellulose fibers* contain water in the percentage range and they form *conductive paths* which are overheated. Evaporated water generates microcavities and causes the so-called **fiber-bridge breakdown** at comparatively low field strengths, Figure 3.4.2-2. These processes are relevant both for *DC* and for *AC voltage stresses* because the stresses of dielectric interfaces do not depend on polarity. In the case of *impulse voltage*, stress duration is not long enough for particle drift.

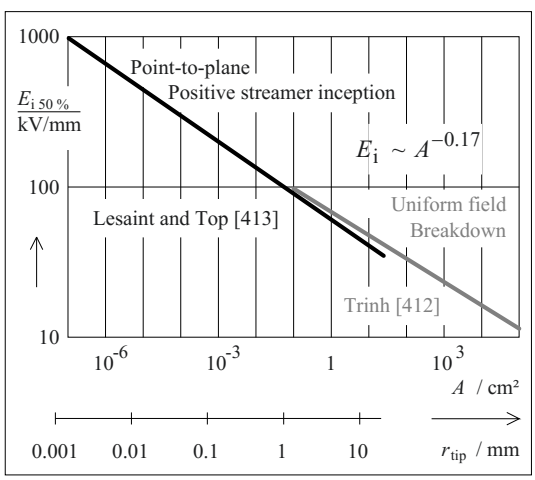

Figure 3.4.1-5: Size effects for ***impulse voltage stresses*** *at point electrodes with different tip radii* r_{tip} *[413] and at plane electrodes with different electrode areas A [412].*

The initial process is a local *thermal instability* (*thermal breakdown*), similar to the processes according to the percolation theory *c)*. However, breakdown occurs at significantly lower field strengths because of the weak links.

e) Technological influences

Statistical investigations show that discharge inception is subject to significant **size effects**. First of all, it seems contradictory that extremely high inception field strengths of 1000 kV/mm occur on highly rounded tips with r_{tip} = 1 µm, and that inception field strengths decrease with increasing radius or electrode area down to macroscopic strength values of approx. 10 kV/mm, Figures 3.4.1-5 and -6. It has been discussed for a long time whether these size effects are **volume, area or distance effects**. [408] … [411].

Note: This ambiguity results from the experimental difficulty of distinguishing these influences: if one of the parameters is changed, the other two cannot be kept constant at the same time. It has been shown that experimental data from distribution functions for a unit volume or for a unit area can be extrapolated over 8 orders of magnitude both by a volume rule and by an area rule. [412].

The oil condition and the type of voltage stress profile are obviously strong influences. These influences can be explained by the difference between **intrinsic breakdowns**, which are determined by the properties of the oil itself (in the case of small "faultless" electrode surfaces), and **weak-link breakdowns**, which are caused by impurities such as particles, water or significant surface defects.

1.) **Intrinsic breakdowns** occur in very *clean oils*, for very *short stress durations* (impulse voltages) and for very *small electrode areas*. They show very high local inception field strengths of about 1000 kV/mm and low statistical spread, Figures 3.4.1-5 (left) and -6 (left).

2.) Breakdown strength decreases with increasing size of the arrangement, including in the case of lightning impulse voltages, Figures 3.4.1-5 and -6. Because stress duration is not sufficient for particle drift, an **electrode-area-related weak-link breakdown** is observed. It is caused by faulty electrode surfaces or by adjacent particles. In this way, a certain influence of the oil quality can be explained.

Note: It was shown experimentally that the assumption of an area rule gives a good fit over more than 12 orders of magnitude, Figure 3.4.1-5 [413], [412]. Additionally, experiments with artificial **field stress enhancements** show that high and constant *microscopic inception field strengths* occur at local tips, even for low *averaged (i.e. macroscopic) inception field strengths* [414]. This means that the local field strength at a field non-uniformity, and not the average field strength, is responsible for streamer inception. In order to explain the size effect according to Figure 3.4.1-5 as an area effect, it has to be assumed that surface defects cause the *field stress enhancement factors* between 10 and 100 and that the probability for the existence of such defects increases significantly with increasing stressed electrode area. First of all it doesn't seem plausible that typical surface roughness causes such extreme field stress enhancements. Therefore, it is assumed that *particles adhering to the electrode surface* cause a strong tip effect [413], [415]. The extreme difference between high microscopic and low macroscopic inception field strengths, which at first appeared to be contradictory, thus seems to be quite plausible to explain.

Note: The size effect for *streamer inception* is interpreted as an area effect here. Nevertheless, *streamer propagation* is of course strongly influenced by the flashover distance, Section 3.4.1.4.

3.) **Volume-related weak-link breakdowns** occur, if *particle-loaded oils* and *long-lasting voltage stresses* (AC or DC voltage) are subject to particle drift and breakdowns at comparatively low voltages with a high statistical spread [59]. Figure 3.4.1-6 [445] shows the strength for an *impulse voltage* (dashed line, see Figure 3.4.1-5) which is not influenced by weak links in the oil volume. For very small insulation arrangements and for *AC voltages*, there are discharge inception field strengths, which are even slightly higher than for impulse voltages [445]. This is explained by injected space charges homogenizing the field distribution for AC voltages and by the small size, for which volume effects do not yet occur, Figure 3.1.4-6 (left). However, there is a significant decrease in AC breakdown strength with increasing size of the insulation arrangement and with increasing particle content of the oil, Figure 3.1.4-6 (right).

The observed size effects can be explained well both by **volume** and by **size effects**. They are consistent with the idea of initial processes, which are triggered at the electrode surfaces by drifting particles from the oil volume.

Note: In particle-loaded oils, the probability of a particle-induced weak-link breakdown increases with the number of available particles per unit area. In particular, oils with *wet fibers* show weak-link breakdowns with a large statistical spread during long-lasting voltage stresses [59]. Obviously, slow **particle drift** through the oil reduces the long-term strength; short-term *impulse strengths* are not dependent on particles. By means of the *addition of conductive particles* it was determined that free particles trigger the discharge at comparatively low field strengths, just at the *instant of electrode contact*. It is assumed that the field strength at the particle's end is significantly increased without a protective

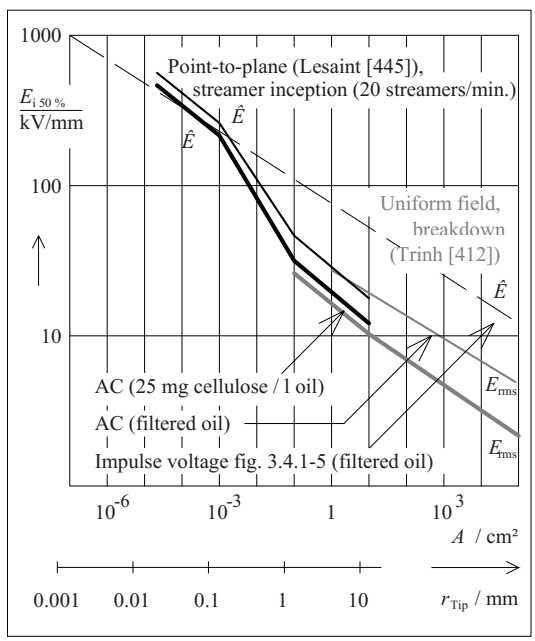

*Figure 3.4.1-6: Size effects for **AC voltage stress** (peak values) for tips with different radii r_{Tip} [445] and electrodes with different areas A [412]. **Intrinsic breakdowns** (for AC only for small areas/ volumes and for impulse voltage) as well as **weak-link breakdowns** (for AC for two different oil qualities).*

space-charge cloud that could reduce the field strength [415].

These processes are not only volume effects but also **distance effects**, because the free oil gap in the field direction determines how fast and how many particles can drift towards the electrode. Furthermore, distance effects play an important role in *streamer propagation*, Section 3.4.1.4.

Conclusion: Initial processes and **discharge inception** depend on microscopic *surface properties* and *oil quality* (particle and water content); they are initiated at the electrode surface. The *intrinsic breakdown* only dominates for very pure oils, for very short impulse voltage stresses or for small electrode areas. With increasing electrode areas, an area-related *weak-link breakdown* affects breakdown strength, (**area effect**). For oils with a high *particle content* and with a sufficiently long voltage stress, a volume-related or distance-related weak-link breakdown dominates because of particle drift (**volume or distance effects**). For *technically purified oils*, the area-related and the volume-related effects can be superimposed.

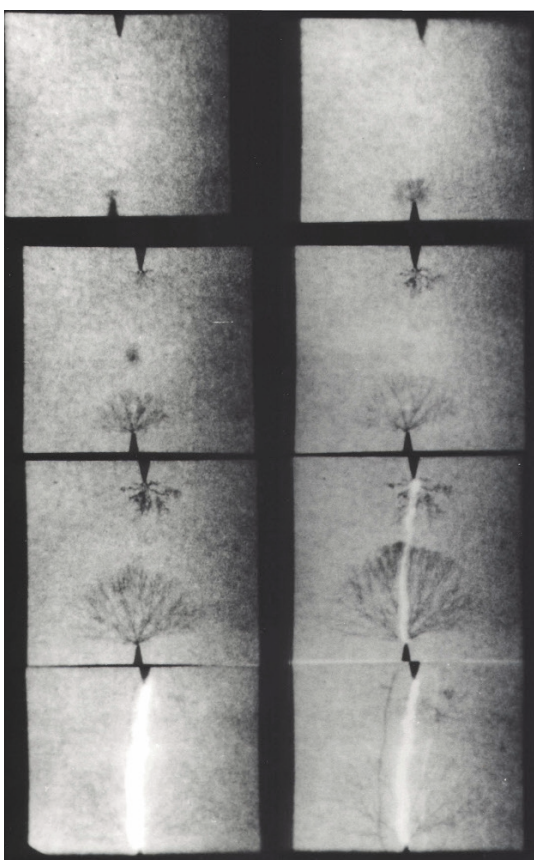

*Figure 3.4.1-7: Negative and positive discharge channels (at the upper and lower tips). **Point-to-point** electrode in insulating oil. The delayed start of the negative discharge corresponds to the polarity effect [424], Figure R. Badent, IEH Univ. Karlsruhe.*

From this the decrease in breakdown strength with stress duration can be explained, Figure 3.4.1-1. The *voltage-time characteristic* plays an important role in the design of insulation systems, and it is characterized by the so-called **impulse factor**, i.e. by the ratio of impulse to AC breakdown strength.

3.4.1.4 Discharge Propagation

After the discharge process is started by an initial process, the discharge develops from the source region. Often, all kinds of *low-density structures* that propagate under the influence of an electric field are often referred to as "*streamers*", irrespectively of wether or not they are *electrical discharges* at all, *streamer discharges* with collision ionization (i.e. streamer discharges in a strict sense) or *leader discharges* with thermally ionized channels, Figure 3.4.1-7.

a) Polarity effect

Positive discharge channels are much more dangerous than **negative** ones because they have a lower *inception voltage* (polarity effect), Figure 3.4.1-7, and they may result in a lower breakdown voltage.

Note: Figure 3.4.1-7 is a sequence of eight shadow images with intervals of 500 ns. There is a positive tip at the bottom and a negative tip at the top of each picture. It can clearly be observed that the visible positive discharge phenomena (at the lower tip) start approximately two intervals earlier than the negative ones (at the upper tip).

Additionally, the *penetration power* and the *range* are larger for **positive channels** than for negative channels. This is due to the fact that a

negative space charge cloud is formed in the region around the **negative** channel owing to highly mobile electrons, and this homgenizes and weakens the local field at the channel's head. For the filament-shaped channels of the **positive** channel, significantly higher local field strengths at the discharge head, better propagation conditions and greater penetration power result, Figure 3.4.1-8. Consequently, *insulation tests* with *positive voltage* usually present tougher stress conditions and are generally explicitly stipulated in the test specifications.

b) Propagation modes

The propagation of discharge channels is generally determined by the arrangement (homogeneity of the field, distance) and hence there can be four different propagation modes whose *propagation velocity* differs respectively by approximately one order of magnitude and which exhibit partially distinctive structural differences. The methods of classification and description of different authors are not consistently the same, Table 3.4.1-1.

Note: The **first mode** with very low propagation velocity occurs only under special conditions at very sharp edged points and is of no significance for many breakdown processes. The practically relevant **propagation modes** no. **two, three** and **four** are sometimes also referred to as *primary-, secondary* and *tertiary streamers* [423], but actually, the last two aren't streamers [426].

c) Propagation in a non-uniform background field

The most important physical investigations were conducted for discharge propagation in a strong *non-uniform field* with *impulse voltages*, far above the 50% discharge voltage of the arrangement. Thus, the discharge can be sparked off in a controlled manner and synchronized with high speed recordings.

1.) Under these conditions, the discharge begins with the regularly structured *primary streamers* (**second mode**), whose filamentous and branched spherical structure is oriented towards the radial microfield in the region around the non-uniform point electrode, Figures 3.4.1-8 and -9. The propagation velocity is in the range of

$$2 \text{ to } 3 \text{ mm/µs}$$

and is stabilized by the build-up of space charge associated with the streamer propagation and by the streamer's charging current (*self-regulation*).

Note: The increasing field strength at the head which results from the discharge growth and which has an accelerating effect is reduced again by the space charge built up in the adjacent channels and by the throttling of the supply of charge.

Note: For this form of discharge, different terms such as "*primary streamer*" [310], "*second mode*", "*micro-crown*" [406] or "*fan-shaped filaments*" [413] are used as descriptions, Table 3.4.1-1.

Table 3.4.1-1: Propagation modes of discharge phenomena (or so-called streamers)in mineral oil

Hauschild [426]			**Leader discharge**	
Top, Massala and Lesaint [405]	**First mode** Slower subsonic discharge	**Second mode** Ultrasound discharge	**Third mode** Very fast discharge	**Fourth mode** Extremely fast discharge
Badent [423]		**Primary streamer**	**Secondary "streamer"**	**Tertiary "streamer"**
Torshin [406]		**First step** "micro crown"	**Step wise discharge propagation**	
*For a strongly **non-uniform field***	**0.1 to 1 mm/µs** Only for very sharp points (r < 1 µm) and for very low voltages	**2 to 3 mm/µs** Normal case with self-regulation by space charges	**~ 10 mm/µs** Start mode at the point as well as just in front of the counter electrode	**> 100 mm/µs** Develops from the streamers that are greatly accelerated in the third mode and is **self-luminous**
*For a quasi **homogeneous field***	(only for negative streamers)		(only for very large increase in the field >50 kV/mm)	

2.) For distances greater than approx.. 50 mm, discrete discharge channels, so-called *secondary streamers* (**third mode**), with a *high velocity* of

10 mm/µs

or more erupt from the primary structure and rapidly pass over the oil gap, since the velocity stabilization caused by space charges loses its effectiveness, Figure 3.4.1-10

In the case of *positive polarity*, wide ranging and irregular discharge channels are formed and they spark through the entire gap in a stepwise sequence of *ignition and extinction* (**stepped discharge** [406]) , Figure 3.4.1-3: After the (re-)ignition of a formerly extinguished channel, the discharge head is connected to the point-electrode potential via a conductive channel. By reducing the potential difference, the discharge is extinguished again, but the charged head is still further accelerated by the field so that a larger potential difference is re-created, which in turn leads to re-ignition of the discharge channel.

Note: The discharge channel is of high impedance and low impedance in phases, and it does not give rise to any permanent collapse of voltage across the channel. That is, there is not initially a permanent thermally ionized channel but there are recurrent collision ionization processes which can finally lead to thermal ionization. In gas discharge physics, this is a *transition* from the **streamer discharge** to **leader discharge** [426].

3.) From this mode, the streamers can change into a faster, high current and self-luminous propagation mode, the so-called *tertiary streamer* (**fourth mode**) at more than

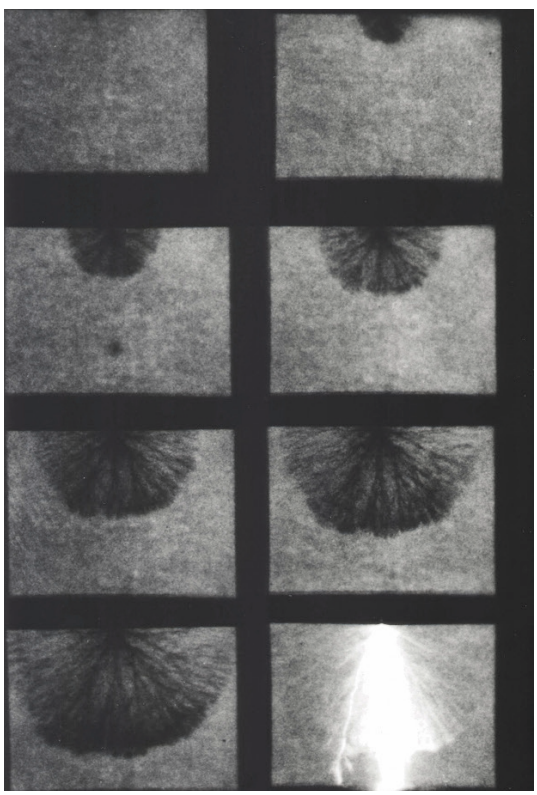

Figure 3.4.1-8: Positive discharge channels (so-called primary streamers) with umbel-shaped or spherical structure [424]. ***Rod to plane*** *in insulating oil, with r = 5 mm and d = 50 mm. Voltage: lightning impulse voltage 1.2/50 µs approx. 250 kV. Light exposure time 100 ns, image distance 500 ns.*

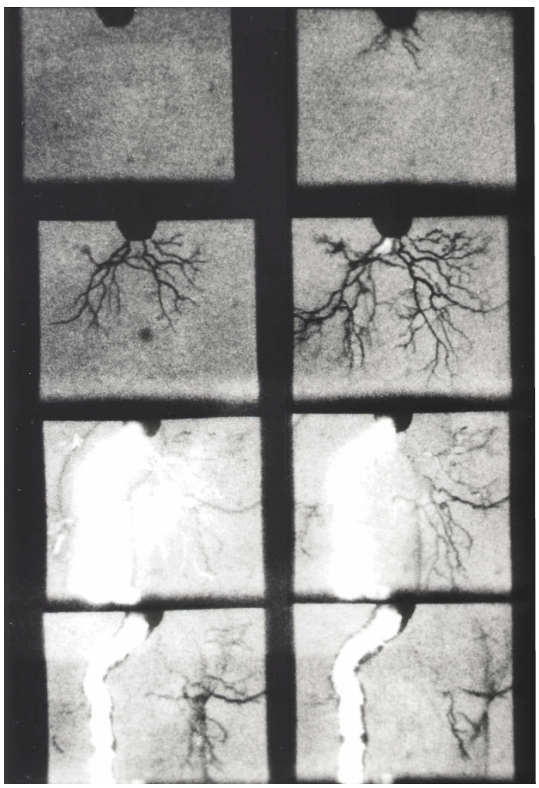

Figure 3.4.1-9: Negative discharge channels (so-called primary streamers) with branched structure [424]. For explanations see Figure 3.4.1-7.

Figures 3.4.1-8 and 9, R. Badent, IEH Univ. Karlsruhe

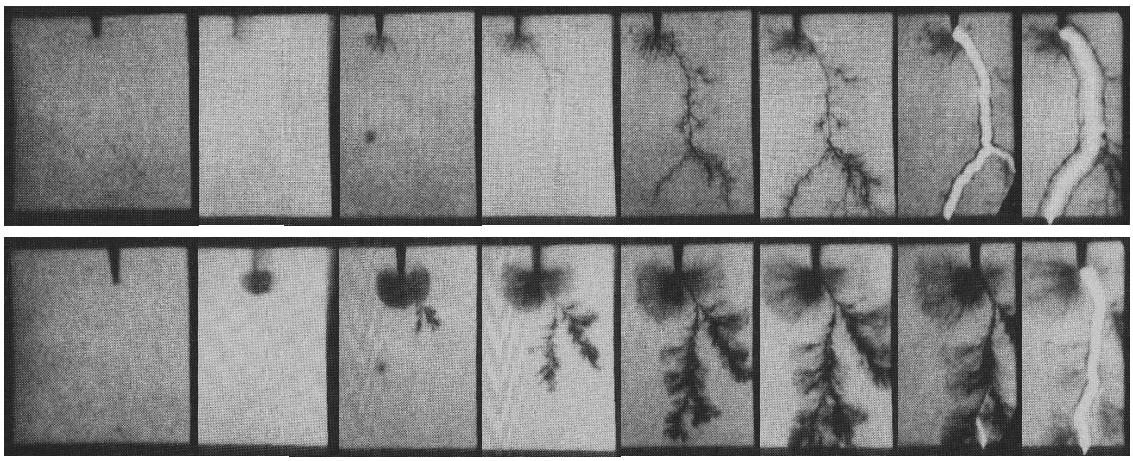

Figure 3.4.1-10: Propagation of negative and positive discharge channels (top and bottom). ***Point to plane*** *in insulating oil. Left to right: regular primary streamers, eruption of fast discrete channels (so-called secondary streamers) and inception of self-luminous main discharge [425], see also Figure 3.4.1-3. Images by R. Badent, IEH Univ. Karlsruhe.*

100 mm/µs.

In the terminology of gas discharge physics, this must instead be referred to as a **leader discharge** [426]. The *main discharge* that leads to this breakdown results in partially discharging of the smaller secondary branches, Figure 3.4.1-8 (bottom right) and to a *blast wave* that can also be identified in the shadow image, Figure 3.4.1-9 (bottom).

Positive and negative channels show different **structures**, Figures 3.4.1-8 to -10. The formation of *negative channels* is less regular and the transition to the so-called secondary streamer is less identifiable in the structural changes. The propagation modes can better be distinguished by the different velocities.

Note: Oil breakdown was also described with the help of the *percolation theory* as a sequence of so-called *streamer discharges* [423], [310], Figure 3.4.1-11: After *creation of a source volume*, *imprinting* of the liquid (*percolation*) and inception of *primary streamers,* higher local field strengths at the streamer head lead to a wide-ranging percolation structure with extended states, increased charge flow and drastically increasing current. This phenomenon, which is described as a *percolation threshold*, is the basis for the wide-ranging *secondary streamer* that erupts from the primary structure with higher propagation velocity in the direction of the macroscopic field. Streamer propagation in oil shows a distinct *polarity effect***:** Umbel-shaped primary streamers are formed at the *positive point electrode* (anode) in the permitted areas of the micro-field at a comparatively slow rate; the transition to secondary streamers requires significantly higher local field strengths, Figure 3.4.1-11 (left). At the *negative point electrode* (cathode), the space charge formed by injected electrons delays streamer inception, Figure 3.4.1-11 (right)

The type of appearing discharge modes depends significantly on the **external conditions**: In a *strongly non-uniform field*, *pre-discharges (primary streamers*) can occur without resulting in breakdown. The prerequisite for this is that the voltage is not too much above the partial discharge inception voltage (discharge inception voltage) or that the stress duration, for example, in the case of an impulse voltage, is so short and the flashover distance is so large that the streamer cannot reach the counter electrode. The range of positive discharges in this case is greater than that of negative ones. For *impulse voltage stress*, the voltage stress can significantly exceed the voltage necessary for breakdown for a brief period ("overstressing"). With adequately large flashover distances, this results in the formation of the sequence of discharge modes as explained above.

d) Discharges in a uniform background field

The above-mentioned d modes are generlly possible also in a uniform or weakly non-uniform background field. However, there are

three significant differences that influence discharge propagation:

1.) In a uniform field, discharges start at *local defects,* whose position is generally not known.

2.) The field strength is relatively high over the entire distance, so that *positive discharge channels* with high penetrating power practically always lead to *breakdown.*

3.) The *large-area electrode* of equal polarity present behind the discharge channel weakens the local field at the discharge head and supports the effect of the space charge which limits and regulates the discharge velocity.

Positive discharge channels, at first, occur as so-called *primary streamers* with the "normal" velocity of 2 to 3 mm/µs. In the case of large flashover distances, the positive channel corresponds to a "*stem with a bunch"* (or a *leader*), whose stem is extinguished and whose bunch drifts away electrode-free until its potential is shifted so much that the stem re-ignites (**stepped discharge**). The relatively *constant propagation velocities* of v = 2 to 3 mm/µs have been observed both in uniform as well as

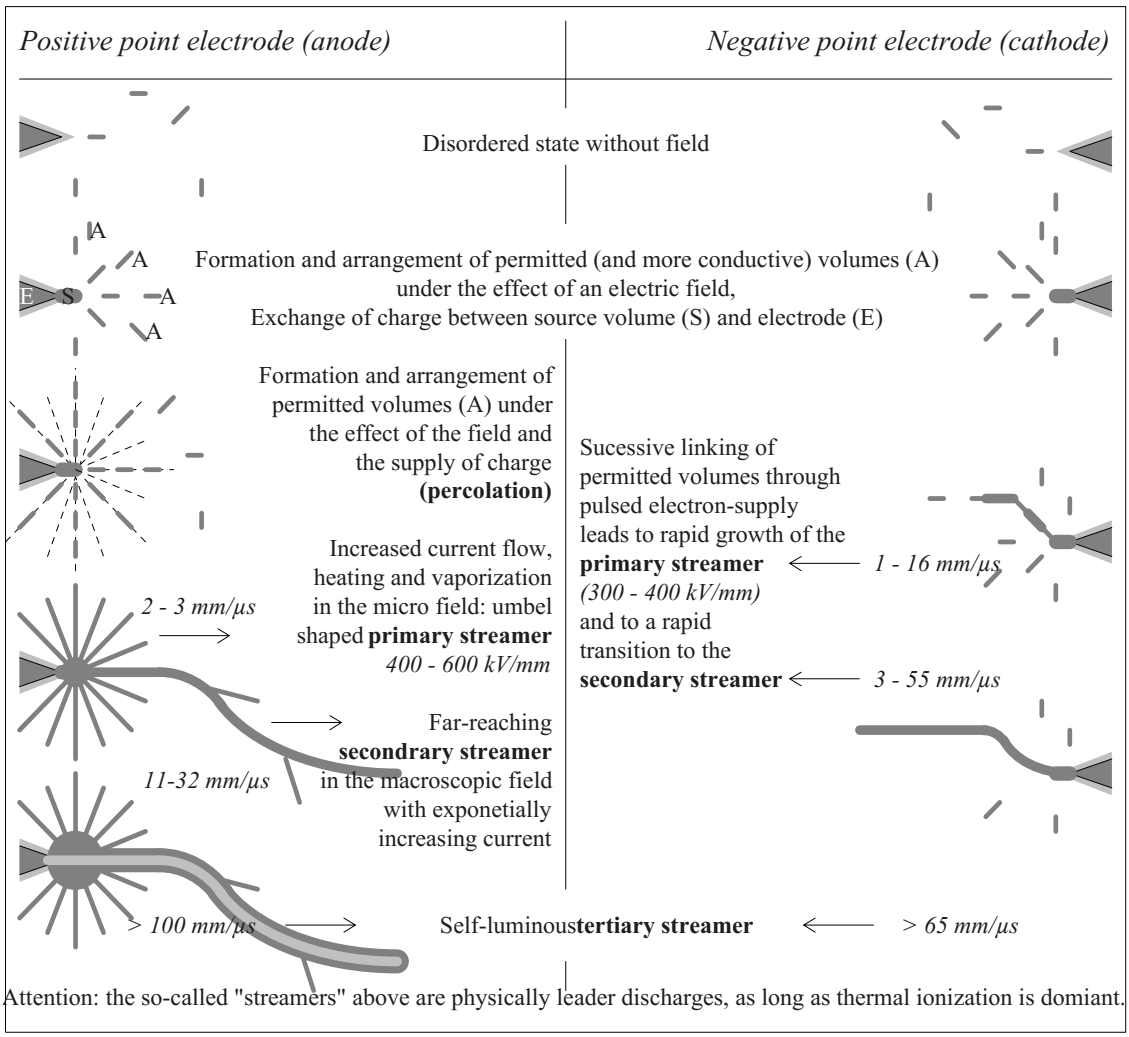

Figure 3.4.1-11: Explanation of breakdown processes in non-uniform oil insulated electrode arrangements through the percolation theory; inception field strengths result from the values of the applied impulse voltage and from the radius of the point, streamer velocities from the temporal distances of shadow images [310], [423].

non-uniform fields. That is, the field around the positive discharge head has distinct *self-regulating properties*. The faster, *secondary propagation modes* with v >10mm/µs are only reported for very high overvoltages from approx. 50kV/mm, which can only be applied as a short-term impulse voltage [405]. In weakly non-uniform fields, Torshin has observed fast discharges with stepwise propagation [406] even for average field strengths of 12 kV/mm.

Negative discharge channels are highly branched and have an almost *ball-shaped (spherical) charge distribution* which homogenizes the field, slows down the discharge and brings it to extinction after a limited **range** [405]. For low voltages, the propagation can occur in a *slow first subsonic mode* at approx. 0.1 mm/µs. If the discharge head has passed through a **field strength minimum** at about half the flashover distance, the "*point of no return*" is reached and this leads to breakdown.

e) Barriers and insulated electrodes

The electric strength of oil insulated gaps can be considerably increased by using insulating *barriers* and *insulated electrodes,* since both the *initial processes* at the electrode surfaces and *discharge propagation* are significantly influenced by this.

Note: In practice, barriers and electrode insulations of high- quality *insulating pressboard* or *transformerboard* (made of *pure cellulose*), which are suitable for impregnation and wetting with oil, have proven to be both technically and economically excellent [27], [82], Section 3.4.2, Section 5.5, Section. 7.1.3, Section 7.2.3 and Section 7.3.4.

Coatings can mask *electrode surface defects*, can hamper *injection* at the cathode and *focussing* of electrons at the anode, prevent the contact of *particles* with the electrode and may restrict the *energy input* into the discharge.

Barriers obstruct the *electron transport* from the cathode to the anode, they prevent *particle drift* over larger distances (distance effect) and they reduce the *weak link volume* (volume effect). Finally, the barriers obstruct the *imprinting* of the liquid (percolation structure) that precedes the breakdown and they may restrict the *length*, *charge and energy consumption of a discharge channel* (barrier effect). It must, therefore, be concluded that the effect of barriers is better for finer *division* of the *oil gaps* in the *field direction*.

Note: It must be noted that introducing barriers and electrode coverings into the field volume causes changes in the **field distribution** which can sometimes be disadvantageous, but which can also often be specifically exploited.

Note: It must also be noted that insulation components of **cellulose** are very *hygroscopic* in dry condition and hence the oil is kept dry over wide ranges. This is an important prerequisite for the high electric strength of insulating oil, see Section 3.4.2.1.

3.4.2 Important Parameters Influencing Breakdown in Mineral Oil

The physical laws of oil breakdown described in Section 3.4.1 unfortunately do not allow the calculation of electric strengths, as is possible, for example, for gas discharges using Paschen's law. The relationships are too complex and too many parameters are involved. Therefore, insulation systems must be designed based on tried and tested **semi-empirical relationships** in order to take the various influencing parameters into consideration [65].

3.4.2.1 Water and Pollution

In the case of **very long stress durations**, a drastic reduction in the strength can occur owing to *water (moisture), pollution and ageing*, Figure 3.4.1-1. In particular, even the **absorption of water** in small quantities leads to a loss of strength, Figure 3.4.2-1.

For a **relative water content** of 100 %, the solvent power of the oil is depleted; this leads to the formation of *free water* in the form of an emulsion with a drastically reduced residual strength of 15% to 20% of the strength of dry oil. This is generally equivalent to a *complete loss of the insulation strength* and must be avoided under all circumstances.

The measure for this is the *solvent power of oil for the water*. As long as the water content in oil remains far below the *saturation limit*, the electric strength also remains high.

Therefore, oil-insulated high-voltage equipment must always be filled with oil that is *dried and degassed* under vacuum to a few ppm of residual moisture. The ingress of water during operation must be prohibited by constructive measures, for example, by air hermetic sealing or with the help of dryers filled with desiccant. Despite this, during the course of time, water content can increase owing to *air contact* of the oil, through *diffusion* via walls and sealing systems or owing to *oil decomposition* (oxidation) as a result of *oil ageing*. Therefore, the oil quality must be checked periodically.

The oil strength is also greatly reduced by **fibers**, especially by *cellulose fibers* along with moisture (**fiber-bridge breakdown**). *Compact particles* cannot bypass larger oil gaps, and therefore, they have a *lesser* influence on the strength [59]. This means that a large flashover distance and a large oil volume favor the formation of moist fiber bridges, Figures 3.4.2-1 and 3.4.2-2.

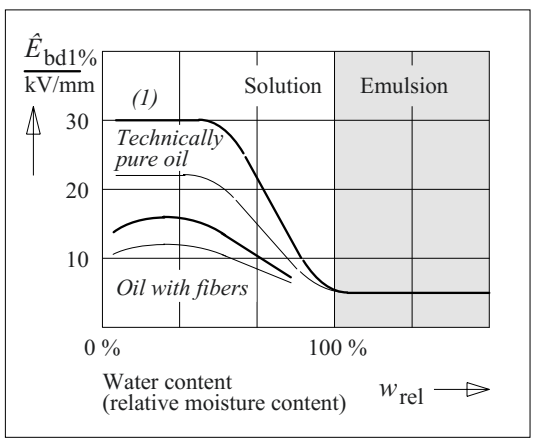

Figure 3.4.2-1: AC voltage strength of technically pure and fiber containing insulating oil [59].
—— d = 1 mm, volume = 14 cm³, with oil flow
—— d = 5 mm, volume = 25 cm³, without oil flow
Curve (1) corresponds to about 50 % breakdown field strength determined according to VDE 0370 section 1 with d = 2.5 mm (r.m.s. value) [16].

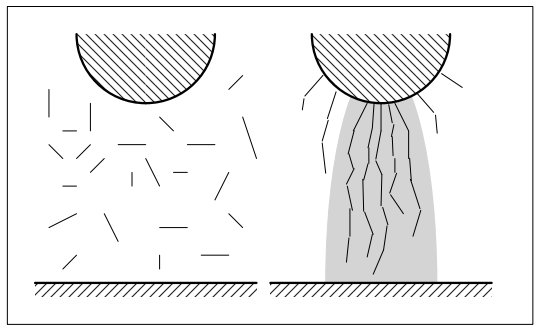

Figure 3.4.2-2: Formation of fiber bridges under the effect of an electric field (right) in an oil loaded with dielectric fibers (left).

For both alternating voltage and for direct voltage, the fibers drift in the direction of electric field gradients, that is in the direction of increasing field strengths, and form linked, largely unbranched *fiber bridges* within seconds to minutes, which reduce both the strength and the *insulation resistance*. The dynamics of fiber bridge formation are greatly accelerated by increasing particle content and especially water content. The formation of a fiber bridge is associated with partial discharges [443], [444].

Note: In contrast to a *solid insulation* that is irreversibly destroyed by a breakdown, *repeated breakdowns in oil* are possible without loss of strength, if the energy is not too large, if the accumulation of **soot particles** is not yet too great and if the resultant **free gas** is removed or released. However, the regeneration capacity of oil is limited and must not be compared with that of *gases*.

The **oil quality can be checked** by determining the *breakdown voltage* in a *standardized test arrangement*, Figure 3.4.2-3. However, oil quality data based on different *test arrangements cannot be directly compared*!

Note: It must be noted that despite similar test conditions and same flashover distance d=2.5mm, *different breakdown voltages* occur for different arrangements and this cannot be interpreted just by different field efficiency factors (degrees of homogeneity) [16]. In the case of ASTM electrodes, the comparatively large *volume* used between the plates and the sharp edged *rims* reduce the strength. The strength is increased again by the increased oil flow in the non-uniform field.

While carrying out the *test according to IEC 60156 (VDE 0370-5)* [177], a sinusoidal alter-

nating voltage (50 Hz) with 2 kV/s is rised until breakdown occurs. The arithmetic mean value from 6 successive breakdown voltages is specified as the r.m.s. value. Gases and breakdown products must be removed from the stressed volume by stirring and a two minute waiting time between the single breakdown tests.

Note: From curve (1) in Figure 3.4.2-1 it can be inferred that the breakdown voltage determined according to or IEC 60156 (VDE 0370-5) only decreases significantly for relatively large relative water contents. Also *sensitivity towards detection* of particles is low. Particles and fibers can be better detected if a cylindrical electrode arrangement with a *larger test volume* is used and the voltage is increased in a *stepped manner with one minute waiting times* [59]. Thus, the probability of the formation of a particle constellation or fiber constellation that causes a breakdown is increased.

3.4.2.2 Temperature Dependence

The influence of **moisture and fibers** on the electric strength of oil is shown in Figure 3.4.2-1 as a function of *relative moisture* or of relative water content. Since the solvent power for water and hence also the *relative* humidity change with temperature, there is a distinct **temperature dependence** of the electric strength. The solubility of insulating oil for water is based on the aromatic content of the oil, on the type of oil and on the ageing status and increases with the temperature, Figure 3.4.2-4.

Spherical cap electrodes	Sphere to sphere	Plate to plate
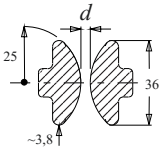	Diameters 12.5 mm	Diameters 25.4 mm Sharp edges
According to IEC / VDE [62]	Electrodes according to UTE [63]	Electrodes according to ASTM [64]
Field efficiency factors for d = 2.5 mm		
$\eta = 0.97$	$\eta = 0.87$	$\eta << 1$
50 % and 63 % breakdown voltages for technically pure, dry and degassed oil [16]:		
63 kV 65 kV	55 kV 57 kV	38 kV 39 kV

Figure 3.4.2-3: Breakdown voltages (r.m.s. values) of insulating oil in different test arrangemets [16].

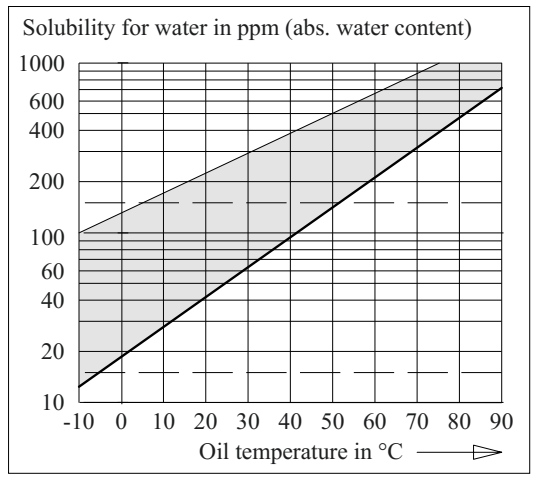

Figure 3.4.2-4: Absolute water saturation concentration in ppm as function of oil temperature for a mineral oil with low aromatic content (approx. 10 %, lower curve) and for aromatics (100 %, upper curve) [59].

Example: "Wet oil" (w_{abs} = 40 ppm)

For example, an insulating oil with low aromatic content (lower curve) attains the saturation concentration (that is w_{rel} = 100 %) at room temperature (20 °C) even for an absolute water content of 40 ppm (40 parts per million = $40 \cdot 10^{-6}$), Figure 3.4.2-4. The electric strength is too low to be of use, Figure 3.4.2-1 (curve 1). For an *increase in temperature*, for example, in a device at operating temperature, the solvent power increases and the *relative water content decreases* at constant absolute water content. According to Figure 3.4.2-1, the electric strength therefore increases again. At 75 °C, w_{rel} amounts to 40 ppm/400 ppm = 0.1 or only 10 %, so that a strength increased by a factor of 6 can be expected. Hence, in the case of wet oil, a very *strong temperature dependence* of the electric strength is observed.

Example: "Relatively dry oil" (w_{abs} = 10 ppm)

For oil dried to a residual water content of 10ppm, a relative water content of w_{rel} = 10 ppm/40 ppm = 0.25 = 25 % occurs at room temperature (20 °C) and results in a high electric strength, Figures 3.4.2-4 and 3.4.2-1 (curve 1). Although the relative water content falls by increasing the temperature, this is no longer associated with a significant gain in strength. Therefore, only a *weak temperature dependence* of the electric strength is seen.

Note: In the case of a *fall in temperature, the* "dry" oil with 10 ppm water content also attains its *saturation concentration* at a temperature between -10 °C and -20 °C. This implies that even this oil is *not yet adequately dried*. Residual moisture of approx. 5 ppm is common.

First and foremost among the problems is a drastic **fall in temperature** during operation. For example, insulating oil in a transformer at summertime ambient temperatures or in an operational temperature state can have a high strength despite a certain amount of water content, since the solvent power of oil is relatively high. In winter, for example, in the switched-off state of the transformer, if drastically reduced temperatures are attained, the *saturation limits* can be *largely reduced* and the absolute water content of the oil can correspond to a *dangerously high relative moisture level*.

Note: In practice, this problem is generally solved by the insulation components made of **cellulose** (paper and pressboard or transformerboard) as they are very *hygroscopic* in the dried state and they can keep the oil dry to a large extent as *moisture traps*. The water content of the oil then results from *equilibrium conditions* between the oil and the cellulose, see Figure 5.5-6, as well as from dynamic *moisture exchange processe*s induced by temperature changes.

3.4.2.3 Pressure Dependence

The breakdown strength is also basically dependent on **pressure**, however the increase in strength with pressure is *significantly less* pronounced than for gases, Figure 3.4.2-5. For alternating voltage stress on oil, according to Figure 3.4.1-2, a *very large statistical dispersion range* around the presented 50 %-values must additionally be taken into consideration. Therefore, the pressure dependence is often ignored in practice. Other parameters are of greater significance.

Note: A drastic fall in strength can also result when *oil that is gas saturated* at higher pressure is suddenly relieved of the pressure. Thus, *free gas* can be released, comparable with an opened mineral water bottle.

The comparison between oil and compressed gases is of interest, Figure 3.4-2.5: *withstand voltages* with lower breakdown voltages for oil are often about half the illustrated mean breakdown values. The technical oil strength is thus comparable with the strength of SF_6 at 3 to 5 bar.

Note: The pressure dependence of the oil strength was earlier perceived as a reference to the theory of a "hidden gas discharge". However, they can also be explained well with the relationships described in Section 3.4.1: under increased pressure, the formation of gaseous *microcavities* is made difficult and in the *gaseous phase of streamers* they also possess increased electric strength under increased pressure.

3.4.2.4 Barriers and Insulated Electrodes, Dependence on Gap Width

According to experience, **volume, gap width, electrode surfaces and electrode coatings** have a significant influence on the strength of insulating oil and this has been well explained with the relationships of gas-discharge physics according to Section 3.4.1.4 *e)*.

With the help of **barriers** oil gaps can be subdivided, gap widths can be reduced and dielectric strength can be increased, because the formation of fiber bridges and the drifting of particles or charge carriers over larger gaps is prevented and the stressed volume is reduced. Furthermore, if necessary, the formation of

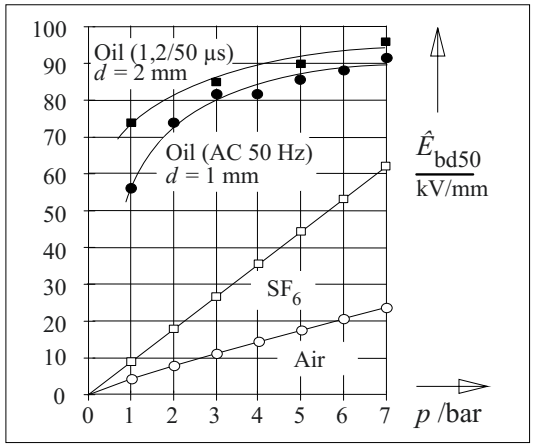

Figure 3.4.2-5: Pressure dependence of electrical strength (50 % breakdown peak-values) for

- ○ *air at d = 2 mm (Eq. 3.2-25 with k = 5),*
- □ *sulfur hexafluoride at d = 2 mm (Eq. 3.2-43),*
- ● *oil at AC voltage and d = 1 mm [60],*
- ■ *as well as oil at lightning impulse voltage (1.2/50 µs) and d = 2 mm [66].*

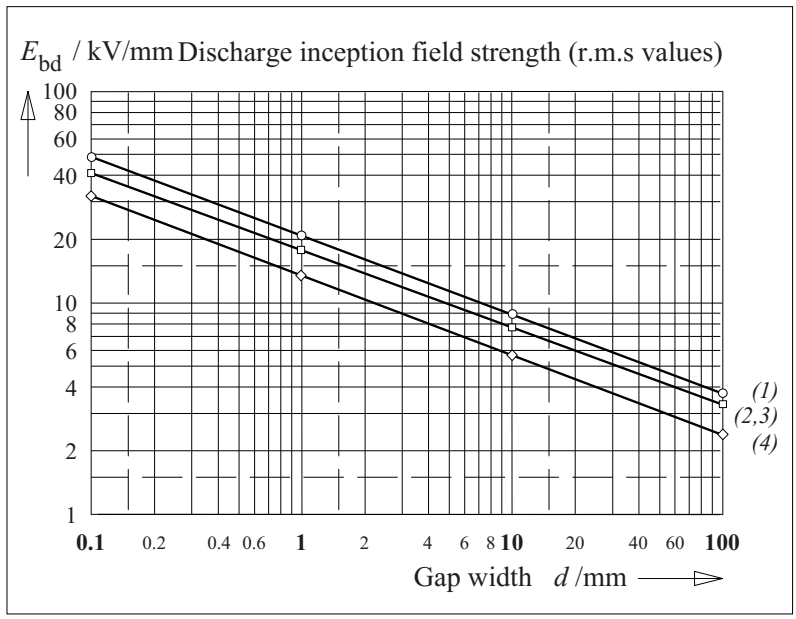

Figure 3.4.2-6:

Electric strength of oil gaps for AC voltage stress (1 minute, 50 Hz) as a function of gap width d for

(1) ○ insulated electrodes and degassed oil,
(2) □ insulated electrodes and gas saturated oil,
(3) □ bare (uninsulated) electrodes and degassed oil,
(4) ◇ bare electrodes and gas saturated oil [27].

The curves are valid for very low discharge inception probabilities in large oil volumes of transformers (design curves).

streamers is limited to the gap width. **Insulation** and coatings of the electrodes influence the initial process of the streamer ignition and the energy input into the streamer may be restricted, which in turn reduces its penetration power, Section. 3.4.1.4 *e)*.

The *inception field strength* for discharges in a *uniform field* increases with decreasing *gap width*. The empirical function

$$E_{bd} = E_0 \cdot (d/\text{mm})^{-a} \qquad (3.4.2\text{-}1)$$

is one of the basic practical dimensioning guidelines for the one-minute *AC voltage test loading* of *oil gaps*, for example in transformers [27], Figure 3.4.2-6. The curves are valid for a low inception probability of discharges.

Note: According to Section 3.1.3 and Figure 3.1-11, Eq. (3.4.2-1) can be interpreted as a statistically motivated *size effect* analogous to Eq. (3.1-19). A *distance effect* must be adopted for this, instead of a volume effect or an area effect. The distribution that is taken as the basis is a two parameter Weibull distribution.

The slope of the straight lines in Figure 3.4.2-6 corresponds to an exponent a = 0.37 [289]. The gap boundaries and the oil quality can be described by the value E_0, which corresponds to the value for d = 1 mm. For example, the following values are used: E_0 = 21.5 kV/mm for *insulated* electrodes in *degassed* oil (1), E_0 = 18.5 kV/mm for *insulated* electrodes in *gas saturated oil* (2), E_0 = 17.5 kV/mm for *bare (unisulated)* electrodes in *degassed* oil (3) and E_0 = 14 kV/mm for *bare (uninsulated)* electrodes in *gas saturated* oil (4).

The breakdown of the oil gap leads directly to *breakdown* for electrodes that are bare (uninsulated) on both sides, and in the case of insulating barriers or insulated electrodes, it leads initially to *partial discharges*.

Eq. (3.4.2-1) and Figure 3.2.4-6 are also approximately applicable to **weakly non-uniform fields**, if potential differences and their respective mean field strengths are to be compared:

$$\Delta V_{bd} = \int_0^d E(x)\,dx \overset{!}{=} E_{bd} \cdot d \qquad (3.4.2\text{-}2)$$

In **strongly non-uniform fields** or along creepage paths (surfaces), Eq. (3.4.2-1) and (-2) cannot be applied. For these instances, a procedure for determining *cumulative field stresses* at the interfaces was specified and this is explained in Section 7.1.3.3 (d) with Figure 7.1.3-12 [274].

Note: The field strengths according to Figure 3.4.2-6 and Eq. (3.4.2-1), (-2) correspond to *very low breakdown probabilities* of the oil gap under consideration. For a comparison with Figure 3.4.1-2, a uniform oil gap with d = 72 mm for bare electrodes in degassed oil is considered. According to Eq. (3.4.2-1), E_{bd} = 3 kV/mm results; with Eq. (3.4.2-2) it is deduced that ΔV_{bd} = 216 kV. According to Figure 3.4.1-2, this would correspond to a *breakdown probability* of less than 2%. The stress on an oil gap in a device, for example for a *short duration AC voltage test,* must be below the values determined according to Eq. (3.4.2-1) or (-2) if an oil gap breakdown must be ruled out with high probability.

Note: The above-mentioned considerations are related to a pure distance effect. However, also a *volume effect or a surface effect* can be detected [59]. With the information on the distribution function (as in Figure 3.4.1-2, for example) and the critically stressed volume, the distribution function for larger volumes can be calculated according to Eq. (3.1-14) to (-17).

In practical arrangements, however, there are not only uniformly stressed volumes but also volumes with varying field strengths. Generally, the volume in which 90% of maximum field strength is exceeded is considered as the *critically stressed volume*. Sinz [59] has however shown that this results in too little volume and proposed to weight the magnitude of individual volume elements with the breakdown probability for the local field strength.

Note: Figure 3.4.2-6 directly shows that the *subdivision of a large oil gap* by impregnated **pressboard barriers** *into several narrow gaps* with insulating boundaries leads to a drastic *gain of strength***.** Thus, considerably smaller *dimensions* can be achieved for transformers. This reduces the *magnetic leakage flux* and especially the *weight* and hence also the *dimensions* and *costs.*

3.4.2.5 Time Dependences, Time Factors

The basic dependence of electric strength on **stress duration** corresponds to the curve in Figure 3.4.1-1. Different reasons are given for this in Section 3.4.1 with reference to discharge physics: For example, (1) a *statistical time lag (ignition delay time*) elapses until the emergence of a start electron, (2) the growth of streamers requires time (*formative time lag*) during which an impulse voltage shall not have died down too far, (3) *particle drift and fiber bridge formation* for direct voltage and alternating voltage are slower processes with longer formation time and (4) *moisture absorption as well as ageing* take place over very long periods of time. This explains, for example, that the 50 % breakdown voltages in the case of a **lightning impulse** v**oltage** for uniform or weakly non-uniform fields are approximately double the values for an **AC voltage** relative to the peak value, Table 3.4.2-1.

Note: For a *comparison of strengths for* **impulse voltage and AC voltage** in Figure 3.4.2-5 it must be noted that the AC voltage strength has still to be converted from the gap width d = 1 mm to d = 2 mm with the help of Eq. (3.4.2-1) so that the AC voltage values must be reduced to about 78 % of the illustrated values. Furthermore, it must be noted that owing to the especially large dispersion for AC voltage breakdowns, the actual stress must be kept significantly lower than the 50 % breakdown voltages. The *technically usable* dielectric strength of oil at AC voltage corresponds approximately to the strength of SF_6 for about 3 bars.

For **increased frequencies** there is a *strength reduction* and no increase in the strength as could be inferred by comparison with the impulse voltage strength [421]. The causes for this are *dielectric losses* that increase greatly from about 1 kHz, leading to *thermal instabilities* and decreasing breakdown voltages, which at 1.5 MHz in a uniform field amount to only about 20% of the initial values at 50 Hz.

Note: This loss of strength is important also for *repetitively switched or square-wave voltages* and for power frequency voltages with high *total harmonic distortion*. Thermal instabilities can occur, especially in insulations with large volumes and poor heat removal, such as in older compensation capacitors with oil-paper insulation. Special care is required also for power electronic apparatus with voltage-source converters and repetitively switched voltages.

For **direct voltage**, especially favorable conditions are given for the drift of impurities and correspondingly low strengths occur, Table 3.4.2-1.

The *lightning impulse voltage*, which is influenced the least by impurities in the oil and which exhibits the lowest dispersion, is selected as a *reference quantity* in Table 3.4.2-1.

Table 3.4.2-1: 50 % breakdown strengths of technically pure and degassed transformer oil for different types of stress for different durations. The strengths are related to the reference value 1 for lightning impulse voltages between bare electrodes and are referred to as ***time factors****:*

Electrodes:		*bare (insulated)* [22]	*bare* [39]
Lightning impulse voltage	1.2/50 µs	**≥ 1**	**1**
Switching impulse voltages	200/5000 µs		0.7
	250/2500 µs	0.7 (0.8)	
AC voltage, peak value			
Voltage rise:			
30 s			0.55
10 $kV_{r.m.s.}$/min			0.35
Stress duration:			
1 minute		0.45 (0.59)	
3 hours		0.36 (0.53)	
Direct voltage			
1 minute		0.20 (0.26)	

For [22]: Values in *brackets* relate to *insulated electrodes*.

For [39]: Values from measurements for lightning impulse voltages up to 1250 kV in a cylindrically symmetric arrangement (R_a = 100 mm, R_i variable).

Example: Oil gap with *d* =2 mm

According to Figure 3.4.2-6, an oil gap with d = 2 mm between bare electrodes has a *"discharge inception field strength"* of about 13.2 kV/mm for a one-minute AC voltage stress. Therefore, the *reliable withstand field strength* lies below E_{bd} = 13.2 kV/mm for the r.m.s. value and below $\hat{E}$ = 18.7 kV/mm for the peak value.

According to Figure 3.4.1-2, the *50 %-breakdown voltage* is larger by the factor 410 kV/220 kV = 1.85 than the 2 % *breakdown voltage*, which is equated in rough approximation with the values according to Figure 3.4.2-6. By extrapolation of $\hat{E}_{bd50} \approx 1.85 \cdot 18.7$ kV/mm = 35 kV/mm to a *lightning impulse voltage stress* of $\hat{E}_{bd50} \approx 2 \cdot 35$ kV/mm = 70 kV/mm (factor 1/0.5 = 2, see Table 3.4.2-1), a value that comes close to the measured 50 % *impulse breakdown field strength* of 74 kV/mm is obtained, Figure 3.4.2-5.

Also for gap widths in mm range, one can deduce from this example that the curves given in Figure 3.4.2-6 correspond to a *low breakdown probability* of a few percent and that the *50 % breakdown field strengths*, in accordance with Figure 3.4.1-2, are *about twice as high*.

Example: Oil gap with d =20mm

An oil gap with d = 20 mm between blank electrodes, according to Figure 3.4.2-6 , has a "discharge inception field strength" of about 6 kV/mm for one-minute AC voltage stress. This corresponds to a breakdown probability of about only a few percent. The *reliable withstand voltage*, therefore, lies below $V = E\ d$ = 120 kV for the r.m.s. value or below 170 kV for the peak value. If this value is extrapolated according to Table 3.4.2-1 to a *lightning impulse voltage* of 170 kV/0.5 = 340 kV, then the breakdown probability is significantly less than that for AC voltage V = 120 kV, since the statistical dispersion of breakdown voltages for lightning impulse voltage is less than that for AC voltage. This implies that this estimation is on "the safe side".

According to Figure 3.4.1-2, the *50 % breakdown voltage* is larger by the factor 410 kV/220 kV = 1.85 than the 2 % breakdown voltage, which is equated to a rough approximation with the values according to Figure 3.4.1.2-6. For *AC voltage*, a value of about $V_{bd50} \approx 220$ kV and $\hat{V}_{bd50} \approx 310$ kV serves as a rough indicative value. For *lightning impulse voltage*, $\hat{V}_{bd50} \approx 310$ kV/0.5 ≈ 600 kV would result as the orientation value. Measured values [39] also correspond to this. If the 1 % breakdown values are set at about 70 % of $\hat{V}_{bd50}$ [66], then for the *1 %-breakdown voltage,* a value with a magnitude of 660 kV·0.7 = 420 kV is estimated.

In the oil channels of transformers, **test stresses** of 5 to 10 kV/mm for *AC voltage* (r.m.s. value) and about double those values for *lightning impulse voltage* are permitted. [23], [67]. The widths of the oil channels must be dimensioned according to Figure 3.4.2-6 in dependence on the local field strengths in the transformers. The permissible *operating field strengths* (r.m.s. values of AC voltage) are substantially lower and range from approx. 2 kV/mm for devices with air contact with the oil up to 5 kV/mm for hermetically sealed devices [16].

The graduation of **test voltages** is taken from Tables 6.1-2 and 6.1-3. It takes the *time factors* into account and shall ensure the coordination of equipment insulations for a particular voltage level (*insulation coordination*). The

large difference between test voltages and operating voltages shall also take the loss of strength owing to *ageing* in decade-long operation into consideration.

3.4.3 Partial Discharges (PD) in Mineral Oil

In highly non-uniform fields, stationary partial discharges (PD) can occur in oil, similarly to PD in gases, during which the streamers stabilize as a result of space charges, without reaching the counter electrode and without resulting in a direct breakdown. The partial discharge inception field strength of **point to plane arrangements** is a more sensitive indicator of gas content, water content and contamination of oil than the breakdown voltage in an approximately uniform field [16], [22], Table 3.4.3-1.

The comparatively high edge field strengths are responsible for the fact that in an appreciable field volume, the field strength is increased so much that primary streamers can be initiated.

From this it is also understood that significantly greater field strengths are possible at the sharp **edges of capacitor foils** than in the uniform field volume between capacitor foils, see Figure 2.4-20 and example in Section 2.4.3.3 ("Edges of metallic foil electrodes in capacitor insulations").

Table 3.4.3-1: Partial discharge inception (PDI) field strengths at hyperbolic point electrodes in oil (r.m.s. values) [16]

Insulating oil	Radius	E_{PDI} kV/mm
Mineral oil (w_{rel} = 10 %)	100 µm	170
Mineral oil (w_{rel} = 100 %)	100 µm	110
Mineral oil	6 µm	785
Phenyl-xylyl-ethane (PXE)	6 µm	981

Example: Edges of metallic foil electrodes in capacitor insulations (Continued from Section 2.4.3.3)

For the numerical example for Eq. (2.4-36) and Figure 2.4-21, at E_0 = 60 kV/mm, an *edge field strength of* E_{edge} = 220 kV/mm was estimated at an ideally round edge (R_{edge} = 6 µm). If a further enhancement of the field is assumed owing to *unevennesses of the edge surfaces*, one arrives at the order of magnitude given in Table 3.4.3-1. Moreover, it must be noted that the rather *cylindrically symmetrical* field at the foil edge decreases more slowly with increasing distance from the edge than a *spherically symmetrical* field at the point electrode. Therefore, partial discharges must be expected at the cylindrical foil edge for *lower field strengths*.

Furthermore, it can be concluded that **conductive particles** which lead to a local field stress enhancement owing to the point electrode effect become less critical with decreasing *particle size* as the local partial discharge inception field strength increases to very large values.

The most common cause for partial discharges in insulating oil is **gas bubbles or gas layers.** The field strength in gas is increased through *dielectric field displacement.* While increasing the voltage, the *Townsend's ignition condition* is reached in the gas for relatively low voltages and this leads to partial discharges.

Free gas in oil, similar to free water, means an *extreme loss of strength*, very much below the strength of technically clean oil and usually below the typical values of test field strengths. Free gas in oil-impregnated devices must be avoided *under all circumstances*.

For estimating the *field strength in oil* during the inception of *partial discharges in gas*, at first the *partial discharge inception field strength in gas* is determined. It is calculated from the breakdown voltage of the gas gap according to *Paschen's Law* (3.2-25) for air and hydrogen or according to Eq. (3.2-43) for SF_6 as well as from the flashover distance d in the gas. For spherical bubbles, the bubble diameter must be used, since the ignition condition is initially fulfilled for this longest possible path while increasing the voltage see Figure 2.4-22. *The inception field strengths in gas* can be converted to *field strength values in oil* with the *field displacement equations* (2.4-38)

for spherical bubbles or with Eq. (2.4-18) for plane gas layers.

Example: Spherical gas bubble in oil

The estimation described gives the effective partial discharge inception field strength according to Eq. (3.4-2) as a function of bubble diameter d in oil with air bubbles under atmospheric standard conditions:

d:	10	100	1000	µm
$E_{\text{oil PDI}}$	20	5	3	kV/mm

These values must be understood as orientation values, since in Eq. (3.2-25) with $k = 5$, no special surface value was used for the feedback factor γ. However, owing to the use of double logarithms, γ has only a weak influence on the result.

The example shows that very *small air bubbles* ($d << 10$ µm) cannot practically worsen the *technical* AC voltage strength of insulating oil (approx. 20 kV/mm for a 1 mm wide oil gap, Figure 3.4.2-6). *Larger bubbles* as well as *gas* layers that are *transverse or longitudinal to the direction of the electric field* must definitely be avoided, however.

Free gas can especially occur owing to *insufficient vacuum* while filling the device with oil or owing to *insufficient degassing* of the filling oil. *Small gas bubbles* could also be released from an oil containing gas owing to flows and turbulences.

Note: Another source of free gas in oil is the water that may be bound in insulation components made of hygroscopic cellulose. Inadmissibly high water content of several percentage points by weight can lead to the formation of bubbles of water vapor at high operating temperatures (bubble effect [446], [447]).

If the *gas absorption capacity of the oil* is adequate, small gas bubbles are even dissolved back into the oil over time. Many days are often required for this, if the gas is trapped in the *back tapers* and only small *contact areas* are available for the oil or if *gas diffusion* through impregnated paper or pressboard barriers is obstructed.

Another dangerous source of gas formation is **partial discharges** at *existing defects*, such as electrode tips or gas bubbles. Along with other fission gases of oil, generally, hydrogen is formed as the key gas. With the help of an analysis of gases dissolved in oil *("gas-in-oil analysis")*, the occurrence of partial discharges can even be subsequently identified, Section 6.4.3.2.

In the case of a *point electrode*, the fission gases are dissolved in oil until the gas absorption capacity is exhausted. The formation of free gas leads to an increasing partial discharge intensity that can increase until breakdown, with irreversible damage to the insulation.

In case of a *gas bubble*, the free gas can *dissolve in the oil* under the stimulating effect of partial discharges. However, the oil must possess the property of *"gas absorbing behavior"* with a high proportion of aromatic compounds, that is to say, it has the property of gas absorption under the influence of partial discharges. Under favorable conditions, therefore, the partial discharge intensity can decrease and can even be *completely quenched* if all the free gas is dissolved. However, if the *gas absorption capacity* of the oil is not sufficient, or if it is not an oil with gas absorbing behavior, then free *hydrogen gas,* which exhibits a lower electric strength than air, is produced. The partial discharge inception voltage decreases and the partial discharge intensity can intensify until breakdown occurs.

Note: The *gas absorbing behavior* is determined according to a procedure standardized in IEC 60628 and described by specifying a *gas absorption coefficient* in µl/min.

3.4.4 Other Insulating Liquids

Also other liquid dielectrics generally show *similar dependences* of electric strength like mineral oil. The strengths that can be attained are basically not different.

Therefore, the application of insulating liquids is especially oriented towards other properties that predestine or exclude a liquid for a specific purpose, as in Chapter 5. *Important prop-*

erties include permittivity, dissipation (loss) factor, conductivity, thermal and chemical resistance, viscosity, pour point, heat removal capacity (thermal conductivity), thermal capacitance, thermal expansion, flash point, combustibility and biological compatibility.

Besides the dominating mineral oils, synthetic *silicone liquids, ester liquids*, *chlorinated hydrocarbons* (askarels or polychlorinated biphenyls PCBs, no longer permitted) and *chlorine free hydrocarbons* as substitutes for the askarels are important. For special applications, even *vegetable oils* (ricinus oil, rapeseed oil), *liquefied gases* (He, LN2) and *de-ionized water* are used, among others, see Section 5.4. The importance of vegetable oils and "*natural esters*" made out of it as substitutes for mineral oil is already given today owing to their better biodegradability, and it will further increase with increasing mineral oil prices.

3.5 Discharges in Solids

Solids basically have a *very high electric strength,* and this strength is distinctly higher than the strength of liquids and gases, Figure 3.3-1. However, it is greatly reduced in the case of technical insulating materials owing to non-ideal material structures, to impurities to defects and to ageing. This implies that the *practically applicable electric strength* is determined more by the individual *manufacturing and application conditions* and less by the physical material properties.

Following discharges, the solid can no longer be regenerated as can gases and liquids through convective material exchange. *Damage* is usually *irreversible*.

In the area of short stress durations, breakdown occurs at very large field strengths owing to electronic collision ionization processes, Figure 3.5-1. We refer to *electrical breakdown* (Section 3.5.1). In case of longer stress durations, the generation of heat in the dielectric can lead to thermal destruction of the insulating material. This so-called *thermal breakdown* (Section 3.5.2) strongly depends on the operational conditions (heat generation, heat removal). Over long periods of time, the electric strength can be drastically reduced owing to *ageing processes* (Section 3.5.3). Erosion of insulation through partial discharges can lead to *erosion breakdown* or *ionization breakdown* respectively. Chemical changes by electric fields and currents can cause so-called *electrochemical breakdown*. Furthermore, there are *non-electric ageing processes* which can reduce the electric strength significantly, e.g. embrittlement, cracking or water absorption.

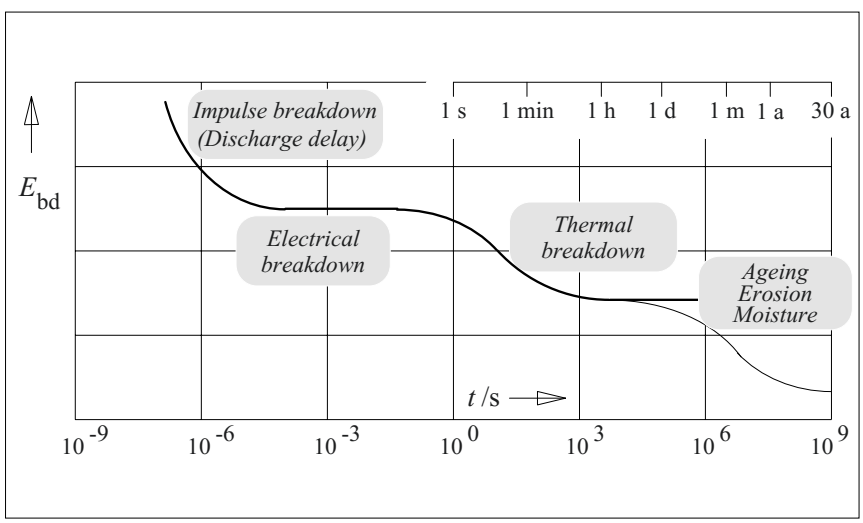

Figure 3.5-1:

Breakdown strength of a solid dielectric as a function of stress duration, without considering the statistical dispersion (schematic).

3.5.1 Electrical Breakdown

Electrical breakdown by the formation of *electron avalanches* requires free electrons and adequate free path lengths for effective collision ionization. According to the energy-band model of solid-state physics, the *conduction band* in insulating materials in which the electrons can move freely is only poorly occupied [25], Figure 3.5-2 (center). Therefore the electrons must be brought into the conduction band from the electrodes *(external field emission),* from the valence band or from occupied states in the forbidden zone *(internal field emission)*, only under the influence of the field, Figure 3.5-2 (right).

Note: Thus, it is assumed that the regular *potential field of the positive atomic nuclei* in an ideal crystal is *distorted* by an *electric field* to such an extent that, from the upper occupied states, the valence electrons can "tunnel" through the potential barriers between the atoms and enter the conduction band. A very low probability exists for this according to the quantum mechanical tunnel effect, which increases with the reduction of the potential to be overcome.

The field strengths necessary for internal field emission in **ideal crystals** are extremely high, and they cannot be achieved in practical insulations. Crystals always exhibit *irregularities* in the form of *dislocations, grain boundaries, crystal impurities and amorphous areas*. This is exhibited as additional states (traps, donor states) in the "forbidden zone" that are below the conduction band, from which electrons can be released even at lower field strengths. Crystal defects and grain boundaries form preferred directions for the breakdown ("*directional breakdown*" [68]).

Note: Energy-band models are also used to describe electronic processes in amorphous **solids** and in **liquids**. They are characterized by less clearly separated bands and by a larger number of intermediate energy levels.

Crystalline materials are not only *mineral materials* such as quartz and mica, but also *high polymer synthetics* such as polyethylene, in which both crystalline and amorphous areas can be formed simultaneously.

For thin *polyethylene films* (d is about 100 µm, DC voltage stress) $E_{bd} \approx 800$ kV/mm at 20 °C and $E_{bd} \approx 300$ kV/mm at 100 °C. For *epoxy resin molded materials,* $E_{bd} \approx 400$ kV/mm was measured with impulse voltages for $d = 3$ mm [39].

Loss of strength occurs with increasing **temperature** through additional free electrons caused by thermal activation.

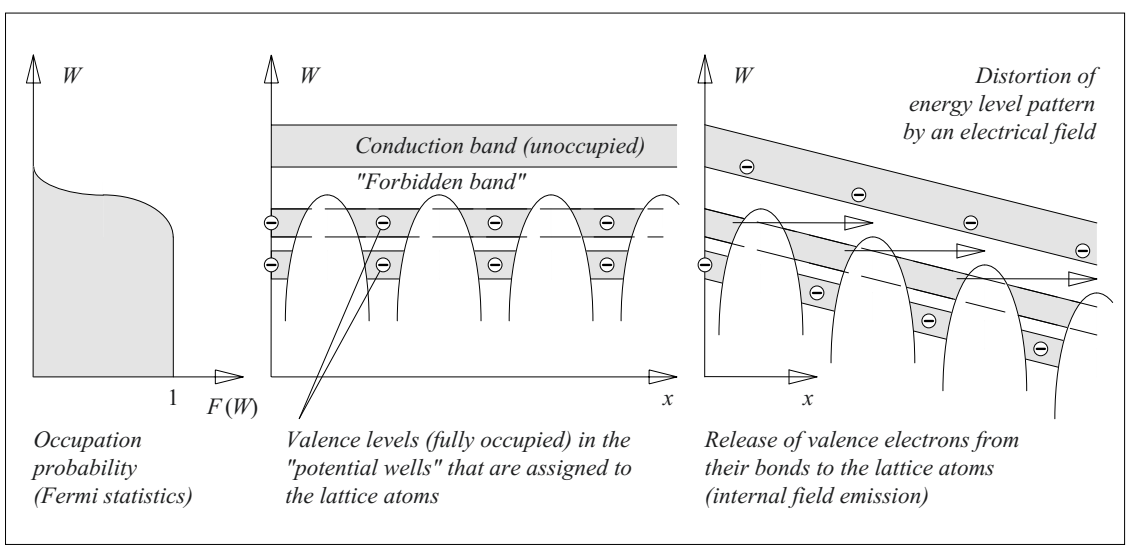

Figure 3.5-2: Occupation probability of energy levels in energy-band models (left), periodic potential field of an ideal non-conductive crystal with potential barriers between individual atoms (center) and release of valence electrons owing to the quantum mechanical "tunnel effect" under the effect of an electric field (right).

Electrical breakdown exhibits a distinct **volume effect**. This pertains to a *statistical size effect,* since the probability for defects causing breakdown increases with the volume, see Section 3.1.3, Figure 3.1-11 and Eq. (3.1-19)

Moreover, there is a *physically* explainable loss of strength with insulating material thickness d, which is a **thickness effect,** owing to *negative space charges* at the positive electrode. The thickness of the space charge layer and the local field stress enhancement increase with the thickness of the insulating material.

For *high density polyethylene,* for the example of AC voltage it is specified that E_{bd1} = 800 kV/mm for a volume $V_1 = 10^{-5}$ cm^3 and E_{bd2} = 600 kV/mm for a volume $V_2 = 10^{-3}$ cm^3 [39]. Extrapolation to larger volumes (V_3 = 100 cm^3) leads to breakdown field strengths that are lower by about one order of magnitude (E_{d3} = 70 kV/mm). Practical values, depending on the quality of the material, are even lower and may only achieve a few 10 kV/mm.

3.5.2 Thermal Breakdown

Insulations in which the *supplied* (*input) thermal power* P_{sup} is constantly higher than the *removed thermal power* P_{rem} are constantly heated up and ultimately thermally destroyed. This process of **thermal breakdown** may take place within seconds or possibly even gradually over many hours, depending on the thermal conditions of the insulating body, Figure 3.5-1 (*thermal instability*).

In practice, the following factors favor the development of the described thermal instability:

- *High dissipation factor (loss factor)* tan δ of the insulating material, that is to say, high dielectric power loss P_δ.
- Increased dielectric losses owing to the *total harmonic distortion* of the applied voltage.
- *Disproportionately high increase of dissipation factor (loss factor)* and dielectric power loss with the temperature T.
- *Heat supply* from outside, for example, by the *ohmic losses* P_I of a neighboring conductor.
- *Poor heat removal* to the surroundings, for example, owing to a high *ambient temperature,* owing to a *thick insulating material* (for high voltages) or owing to low *thermal conductivity of* the insulating material.

Note: Generally, thermal breakdown is also possible in *liquids*, for example, when convection is hampered by blockage of oil channels. Generally, however, heat transport owing to liquid flow prevents thermal instability. Dielectric losses in *gases* are extremely low; hence, a thermal breakdown cannot occur.

Example: Compensation capacitors

Thermal breakdowns can occur, for example, in older compensation capacitors with oil-paper dielectrics. The relatively large losses and the compact structure for the realization of bigger capacitance values can lead to thermal instability at increased voltage or in the case of harmonics with higher frequencies. Even modern compensation capacitors with low-loss polypropylene film dielectrics are at thermal risk by the increase in the

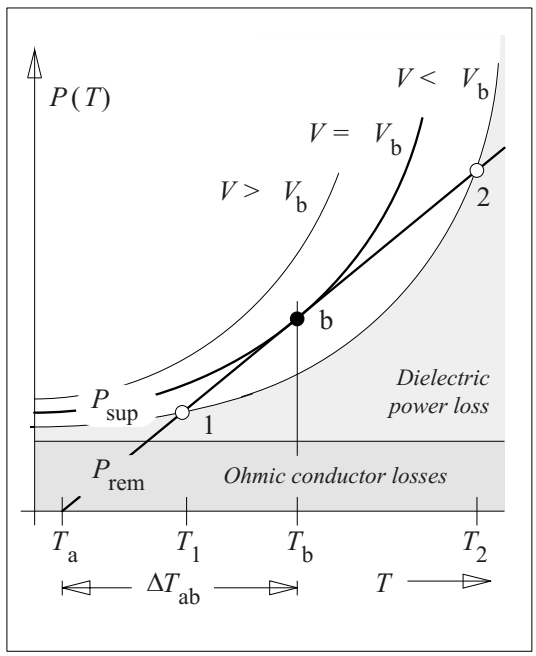

Figure 3.5-3: Balance of supplied and removed heat for thermal breakdown with stable (1) and instable (2, b) working points for determining the so-called thermal breakover voltage.

harmonic distortion factors in the network, as the power loss increases with the frequency, Eq. (3.5-2).

Example: Epoxy resin bushing

Bushings between the hot oil of a transformer and the gas volume of an enclosed switchgear are specially thermally stressed: the heat supply through the conductor, the relatively high dielectric losses of some epoxy resins at higher temperature and the high ambient temperature lead to a situation in which a thermal equilibrium can occur only for a very high insulating material temperature. The thermal stability, therefore, must often be verified by means of a thermal stability test.

Note: The so-called *RIP (resin-impregnated paper) bushings* are made of a crepe paper core with alumina grading layers impregnated with an epoxy resin, see Sections 5.3.3.1 and 7.1.2.3.

Example: Thermal stability test

Thermal stability is verified by *simultaneous* stress of a test object with voltage *and* current. Thermal stability, which is a steady-state condition, is assumed if the observed parameters, such as dissipation factor tan δ or conductor temperature, do not vary over a period of 5 hours.

Example: Thermal breakdown owing to ageing

Even a successful thermal stability test offers no guarantee of thermal stability over a long period of time. In the case of *mineral oil-impregnated paper*, a significant increase in the dissipation factor can occur owing to thermally accelerated ageing. In insulations with unfavorable heat transmission conditions, for example in thick-walled insulated bushings, this can result in exceeding the thermal stability limit, Figure 3.5-7.

No breakdown strength with the meaning of a material specific quantitiy can be given for thermal breakdown. The **breakdown voltage** ("*breakover voltage"*) for a *specific arrangement* is derived from consideration of the *balance of supplied and removed heat,* taking the geometry and ambient conditions into account, Figure 3.5-3.

The **supplied thermal power** P_{sup} results from the sum of the power loss P_δ in the dielectric and the heating effect of the externally supplied ohmic losses in the conductor P_I:

$$P_{sup} = P_\delta + P_I \qquad (3.5\text{-}1)$$

P_I is independent of temperature to a first approximation. Owing to the exponential increase in conductivity, $P_\delta(T)$ and the dissipation factor tan δ also increase exponentially with the temperature, Figure 3.5-3:

$$P_\delta = V^2 \omega C \cdot \tan \delta(T)$$

$$= V^2 \cdot \omega C \cdot \tan \delta_a \, e^{\beta(T - T_a)}. \qquad (3.5\text{-}2)$$

Note: The *frequency dependency* included in Eq. (3.5-2) leads to a strong increase in losses with increasing frequency. Additionally, also the dissipation factor often increases with an increase in frequency. Thus, thermal problems can occur at *high frequencies*, for power electronic *switching impulses* and, often unexpectedly, even for AC line voltages with high *harmonic contents*, Section 4.2.4. Assuming linear materials, dielectric power loss results from the superposition of loss components that are associated with the individual components of the frequency spectrum, see Eq. (4.2-20).

The **removed heat** P_{rem} is proportional to the heat transmitting surface $A(x)$, the thermal conductivity λ and the gradient of insulating material temperature grad $T = \partial T/\partial x$ in the direction of heat flow x:

$$P_{rem} = \lambda \cdot A(x) \cdot \partial T/\partial x \qquad (3.5\text{-}3)$$

In Figure 3.5-3, it is assumed for simplification that the insulating material temperature T is location-independent. The removed heat is then determined by the heat transfer at the surface of the insulating material and is proportional to the difference $(T - T_a)$ between T and ambient temperature T_a. P_{rem} can be plotted as a straight line against T.

In the stationary state, supplied and removed heat are equal (*thermal balance*):

$$P_{sup} = P_{rem} \qquad (3.5\text{-}4)$$

If the applied voltage is lower than the breakover voltage ($V < V_b$), a *stable working point 1 and an unstable working point 2* are possible.

For temperatures $T > T_1$, the removed heat is greater than the supplied heat. The *stable working point 1* with the insulation temperature T_1 is re-adjusted by cooling down. It does *not* lead to breakdown. Only when the temperature of the insulating material is pushed above T_2 by a *temporary additional heat supply* is the arrangement *no longer thermally stable,* since the supplied heat is permanently greater than the dissipated heat.

On increasing the voltage further, the losses in the dielectric also increase until $P_{sup}(T)$ and $P_{rem}(T)$ no longer intersect, and in any case it leads to thermal escalation: the voltage is above the breakover voltage ($V > V_b$).

If, in *the borderline case of the thermal breakover voltage* ($V = V_b$), both the power curves touch each other at an *unstable* point b, this leads to *thermal breakdown*. Owing to the idendity in gradients, the following applies at the "breakover point":

$$\partial P_{sup}/\partial T = \partial P_{rem}/\partial T \qquad (3.5\text{-}5)$$

Note: From Figure 3.5-3 it can be seen which measures can be applied to *shift* the thermal breakdown to *higher voltages*:

By using *dielectrics with lower losses or by reducing the ohmic losses in the conductor*, the power curves for $P_{sup}(T)$ for uniform voltage are shifted downwards. The breakover voltage is only attained after increasing the losses $P_{sup}(T)$ by increasing the voltage.

A steeper increase in the power lines $P_{rem}(T)$ results from more *effective heat removal*, for example by *cooling*. Thus, higher losses $P_{sup}(T)$ and a higher voltage are necessary to attain the breakover voltage.

A reduction in the *ambient temperature* T_a shifts the power line $P_{rem}(T)$ to the left. Here too, higher losses $P_{sup}(T)$ and a higher voltage are necessary to attain the breakover voltage.

Using equations (3.5-1) to (3.5-5), the thermal breakover voltage (breakdown voltage) can be calculated for different arrangements. This always shows that the *breakdown voltage no longer increases linearly with the insulating material thickness d*. Moreover, significant variations occur depending on the arrangement.

Global thermal breakdown and local thermal breakdown are distinguished, Figure 3.5-4. In the first case, general ("global") warming

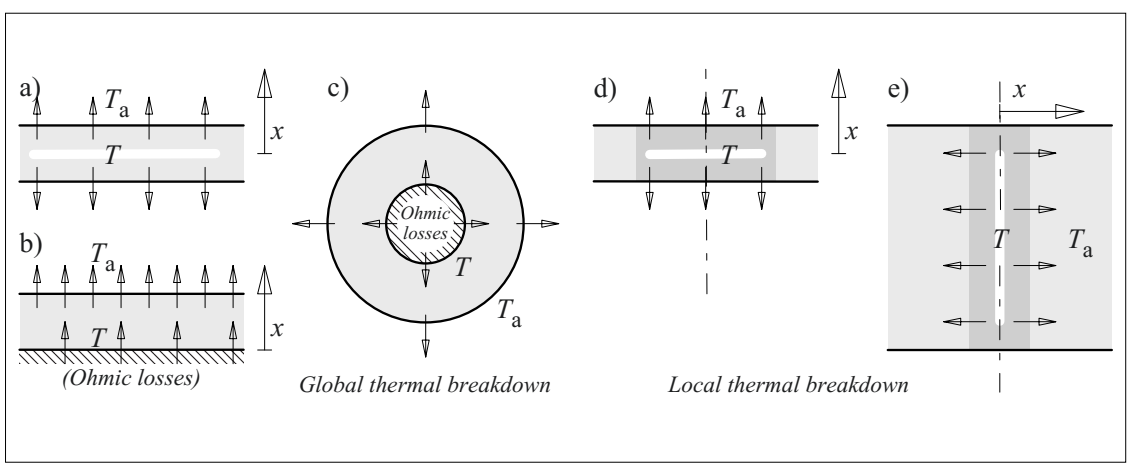

Figure 3.5-4: Heat flow for global and local thermal breakdown for example arrangements.
The areas of highest temperature T (hot spots) are marked with white bars.
a) Plane arrangement with global heating and heat transfer through the electrodes on both sides.
b) Plane arrangement wiht heat transfer on one side and with additional thermal loading by ohmic losses.
c) Coaxial arrangement with thermal loading by ohmic losses (for example, cables or bushings).
d) Plane arrangement with local heating and axial heat transfer through the electrodes on both sides.
e) Plane arrangement with local heating and radial heat transfer into the cooler dielectric.

takes place in a homogeneous dielectric with uniform stress. In the second case of a non-uniform or non-uniformly stressed dielectric, only a locally restricted (local) warming occurs, which in the case of thermal instability leads to the formation of a breakdown channel. In the literature, for example, instances a) and e) are calculated according to Figure 3.5-4 [16].

For plane arrangements with heat removal on both sides through the electrodes according to Figure 3.5-4 a) and d) (Kreifuß approach), a thermal breakover voltage V_b that is *independent of insulation thickness d* results from Eq. (3.5-1) to (-5).

Note: Instead of a derivation, a *plausibility consideration* is presented here: by *doubling the insulation thickness d*, and for the same applied voltage *V*, the field strength is halved and the specific power loss (power loss density) is reduced to one fourth. Owing to the doubled volume, the *power loss is halved*, see also Eq. (3.5-2), with halved capacity. Owing to doubling of the insulation thickness, the thermal resistance is also doubled and the *removed heat* for the same temperature difference is *halved*. In a presentation according to Figure 3.5-3, therefore, only the two curves $P_{sup}(T)$ and $P_{rem}(T)$ *are reduced in equal measure.* Therefore, the *same temperatures* develop in the insulating material, and the breakover condition is attained for the *same voltage.*

Significantly different values for the thermal breakover voltage are obtained for *different materials*, Table 3.5-1 [47]. In the case of *thin insulations*, these values *cannot* be attained, since the breakdown is not caused thermally but electrically. The *significance* of the thermal breakover voltage is that the *breakdown voltage strength of lossy dielectrics can not be increased further* by increasing the *thickness* of the dielectric. The limits are a few cm for dielectrics with comparatively high losses and a few 10 cm for low-loss dielectrics.

Note: Table 3.5-1 also shows that some materials, under unfavorable heat transfer conditions, are *not suitable for high-voltage insulations*. For example, PVC cables can at the most be used up to the medium voltage range. Even in the case of cast resins, an increase in losses in the region of the glass transition temperature can lead to thermal problems depending on the type of resin. Although oil-impregnated paper is suitable as a high-voltage insulating material, it can however lead to thermal instability in the case of extremely high field strengths (in capacitors) and in the case of poor heat removal (for large capacitances),

Table 3.5-1: R.m.s. value of thermal breakover voltage for different materials in a plane arrangement according to Figure 3.5-4 a) and d) for f = 50 Hz and T = 20 °C.

Quartz (depending on the purity)	2....20 MV
Mica (depending on the purity)	7....18 MV
Steatite (depending on density)	1.5...9.8 MV
Hard porcelain (dto.)	0.4...2.8 MV
Glass (20 °C)	2.....6 MV
Glass (350 °C)	0.1...0.2 MV
Polyethylene (PE)	3.....5 MV
Capacitor paper	3.5...4 MV
Sulfate paper	0.6 MV
Polyvinylchloride (PVC)	0.1...0.2 MV

According to Figure 3.5-4 e) (Wagner approach), *for a narrow channel of increased conductivity with lateral heat dissipation*, the same power loss per unit length occurs, if both the voltage *V* and the channel length *d* or the insulation thickness *d* are doubled. However, experience shows that the breakover voltage is not *proportional* to thickness *d* but to the *root of d*:

$$V_b \sim d^{1/2} \qquad (3.5\text{-}6)$$

Apparently, the radius *r* of the discharge channel increases with increasing insulating material thickness or channel length *d*. Therefore, the heat-producing volume grows more than proportional to *d* and the breakover voltage increases more slowly than the insulation thickness *d*.

Generally, the thermal breakover voltage is not only dependent on the m*aterial* but also on the *arrangement,* on the external *heat sources and* on different *ambient conditions* (temperature, heat transfer). Therefore, with simplifying *analytical calculation*, only simple cases can

be discussed and general trends are described (see above.).

In many cases, the insulating material volume can be divided into thermally similar volumes for a *calculation*. For example, for the case of bushings, *discretization into the insulation layer volumes* between electrically and thermally highly conductive metallic grading layers makes sense. The solutions for all partial volumes lead to an equation system which can be solved iteratively, for example.

Below the breakover voltage, an iterative solution converges on a temperature distribution. Above the breakover voltage, there is no convergence.

In very complex cases, a *non-linear thermal field calculation* with temperature dependent material parameters must be carried out on the basis of an *electric field calculation*. The *method of finite elements* is generally applied for this.

3.5.3 Ageing, Erosion Breakdown and Lifetime

a) Ageing processes

Solid insulations may not be stressed over long periods with the voltages and field strengths that are possible for short periods owing to electrical and thermal breakdown, Figure 3.5-1. There are many mechanisms that lead to *ageing* and to a reduction in the quality of solid insulations and enforce the setting of *relatively low operating field strengths*:

- Mechanical, chemical and thermal stresses as well as weather influences and radiation can lead to *brittleness* and formation of *cracks*.
- Partial discharges and creepage currents in existing or newly formed defects (cavities, conductive points, pollution layers, and cracks) particularly attack organic insulating materials. Progressive erosion ultimately leads to so-called *erosion breakdown*.
- Under the effect of penetrating moisture, the material structure can change owing to *hydrolysis* (for example, depoymerization, decomposition of bondings or delamination of fiber reinforced materials).
- Under the combined effect of *moisture* and electric *fields*, conductive tracks caused by electrochemical changes can appear, they initiate so-called *electrochemical breakdown* (e.g. formation of "*water trees*" in polyethylene cables).
- Owing to thermal stress of insulating materials, *conductivitie*s and *dissipation* (*loss) factors* can increase. This can lead to completely changed *field distributions* for *DC voltages* and to *thermal instabilities* or *thermal breakdown* for *AC voltages*.

The danger of the above mentioned ageing mechanisms depends primarily on to what extent the mentioned effects on the insulating material can be foreseen and **preemptively** ruled out during *design and production.*

b) Lifetime characteristics

The so-called **lifetime characteristic** is an important dimensioning tool, which is determined with the help of constant-voltage tests according to Figure 3.1-13. It primarily describes the ageing of insulation under the effect of an electric field, Figure 3.5-5.

The *curves of lifetime characteristics* are dependent not only on the type of material but also on various other *conditions*. For example, for polyethylene films, the type of impregnation (air, SF_6 or oil) is decisive for its service lifetime, but in contrast *short term strength* is hardly influenced, Figure 3.5-5. The loss of service life is especially drastic in the case of partial discharge erosion owing to air impregnation. In the case of epoxy resin insulations, the high strengths of the actual resin (EP 1) are not made use of in technical insulations, since local increases of field strength enhancements

caused by production only allow a reduced background field (EP 2). In bulk insulations with large volume, the probability of inhomogeneities that increase field strengths increases, so that an additional reduction in strength must be expected (EP 3) according to the statistical law of size (size effect).

The service lifetime of insulation can therefore only be determined through *experiments with samples* that were manufactured under the *actual production conditions*.

The **lifetime stress relationship** according to Eq. (3.1-21) is

$$\hat{E}_{bd}/\hat{E}_0 = (t_{bd}/t_0)^{-1/k}. \qquad (3.5\text{-}7)$$

According to Eq. (3.1-22) a double logarithmic representation results in a straight line with the gradient -1/*k*. Here the *lifetime exponent k* is characteristic of a specific ageing mechanism. If the ageing mechanism changes in the course of time, then the gradient of the lifetime lines also changes.

With the values from Tables 3.5-2, and for a known short term strength $\hat{E}_0$ (for a stress duration t_0), the *lifetime* t_{bd} for a stress $\hat{E}_{bd}$ can be roughly estimated according to Eq. (3.5-7).

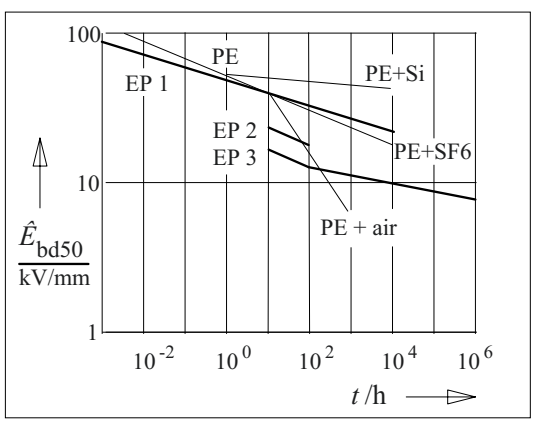

Figure 3.5-5: Lifetime characteristic for different dielectrics at AC voltage [22]:
PE: PE films in air, SF6 and silicone oil.
EP 1: Epoxy resin in model arrangement (d =1 mm).
EP 2: Insulation sample with locally increased field through corrugated metal foil layers [69].
EP 3: Like EP 2 in large volume insulations.

Table 3.5-2: Guide values for the short duration strengths (1 minute), lifetime exponents and operating field strengths (30 years) for some insulations for f = 50 Hz and T = 20 °C [22], [16], [23].

Dielectric	Application	k	$\hat{E}_{bd}$ (1 min) kV/mm	$\hat{E}_{op}$ (30 yr.) kV/mm
Polyethylene	Cables		140	3 ... 7
PE + SF_6	Films	9	> 200	
PE + Oil	Films	30	> 200	< 40
Paper + Oil	Capacitors	30...40	180	< 40
	Cables	30...40	55 ...80	< 20
	Transformers		20 ...30	3 ... 7
Porcelain	Insulators		125	1 ... 3
Epoxy resin		12	125	1.5... 4

Note: Frequently, lifetime characteristics are extrapolated from experiments ranging over several months up to 30 years ($2.6\ 10^5$ h). Owing to the associated uncertainties, *operating field strengths must be specified* much below the 1 % breakdown values at the time of the nominal service life (for example, at 30 years).

The ageing effect of other **environmental influences** must be simulated through practice oriented *experiments*. Often, short term electric strength and other material properties are determined after artificial ageing under intensified conditions (accelerated ageing). The "conversion" of artificial ageing time under intensified conditions to actual ageing periods is, however not generally possible.

c) Examples of ageing

1.) For example, the *influence of air humidity or direct exposure to water* can be simulated by immersing in water at 50 °C or 100 °C. Thus, of diffusion processes and **hydrolysis processes** are accelerated. In this way, comparative material investigations can be carried out in an accelerated time scale. Such investigations are especially important for all types of *compounds and interfaces*, such as bondings, vulcanizations, fiber reinforced plastics or epoxy resins with fillers in which the chemical bonds can be weakened or broken by hydrolysis.

2.) **Material compatibilities**, similarly, are generally investigated at increased tempera-

tures to attain acceleration. Thereby, the compatibility of dielectrics, casings, paints, seals and conductor materials with liquid and gaseous *impregnating media* must be verified. Incompatibilities can be seen inter alia in the form of swelling, dissolution, chemical decomposition, gas formation or weakening of mechanical and electric strength.

3.) Increases in *temperature and moisture* have a strong accelerating influence on the ageing of organic insulating materials. In particular, *paper* is *mechanically weakened* by **depolymerization** of cellulose molecules, that is to say through decomposition into components with shorter chain lengths. Figure 3.5-6 (Bouvier diagram) distinctly shows that poorly dried paper and high operating temperatures lead to an extremely accelerated decomposition of paper. That is, *high operating temperatures*, for example in transformers, require *well dried paper* (relative water content of the paper $w < 0.5$ %).

4.) In the case of *oil-paper insulations*, ageing

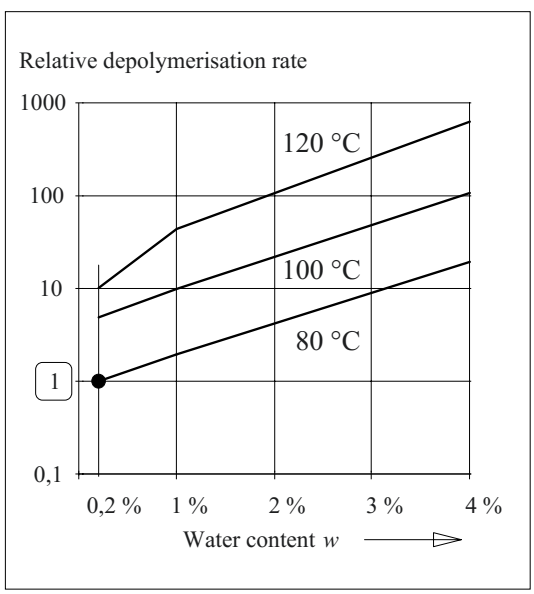

Figure 3.5-6: Relative depolymerisation rate of paper as a function of water content for various temperatures (Bouvier diagram according to [70]) with the reference value 1 for w = 0.2 % and T = 80 °C.

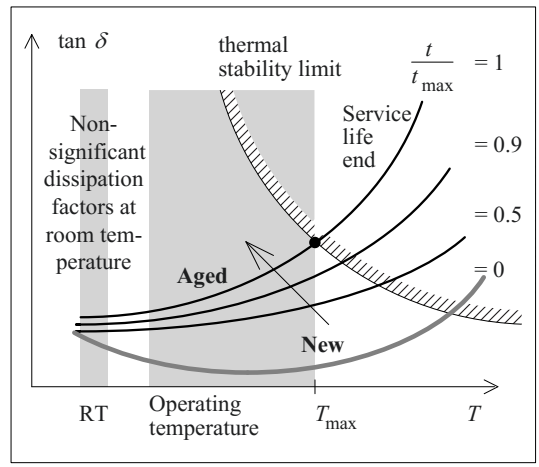

Figure 3.5-7: Worsening of thermal stability of an oil-paper dielectric due to increase in dissipation factor at power frequency, caused by ageing during the lifetime (schematic).

can also lead to an **increase in the dissipation (loss) factor**, which can only be detected at increased **operating temperatures**, Figure 3.5-7.

This is due to high thermal stress in the regions around the hot spot of the insulation. Thus, the insulating oil is decomposed and this process is accelerated by increased *temperatures, oxygen* and *catalytically* effective materials. Conductive and polar decomposition products are formed.

It is especially critical that these increases in dielectric losses *cannot be identified* through diagnostic dissipation factor measurements at power frequency and at normal **ambient temperatures**, Figure 3.5-7 (left).

With increasing *temperature,* the losses of aged materials also increase more intensely than those of new insulations, Figures 5.5-2 and 3.5-7, so that under suitable conditions (operating temperature, insulation thickness, heat removal and ambient temperature) there is a risk of further *overheating* with accelerated thermal *ageing* leading to acute thermal *instability* or *thermal breakdown*, Figure 3.5-3. The thermal stability limit of insulation is only reached at high temperatures for new materials (with lower losses), Figure 3.5-7 (lower

curve). During the course of ageing, the losses increase and always limit the **permissible temperatures** to *steadily decreasing values*. The end of service life is reached if the thermal stability limit is reached at the maximum possible operating temperature, Figure 3.5-7 (upper curve).

Note: For the *diagnosis* of this dangerous development, *on-line monitoring* that is not yet currently available would be ideal, Section 6.4.8.2. In the case of off-line diagnostic measurements at room temperature, *PDC analysis* can be applied as greatly increased polarization currents indicate a well-advanced ageing process [236], [392], [398], Section 6.4.7.6 *f)*, Figure 6.4.7-9.

5.) Another example is ageing through *erosion* of solid insulation by partial discharges associated with **repetitive pulse stresses,** such as in *impulse capacitors*, in *motor insulations* with *enamel-insuated wires* or in *oil-pressboard barrier systems*, see Sections 7.3.3 and 7.3.4.

3.6 Partial Discharges (PD)

Partial discharges (PD) are discharges that affect **only a part of the insulation distance** and that do not immediately lead to breakdown, they take place *in all types of insulation systems*. Often, partial discharges do not affect short-term electric strength. However, in the case of organic insulating materials, *erosion* due to partial discharges, mainly in case of frequent and repetitive discharge impulses at **AC voltage** and **repetitive impulse voltages**, leads to a usually *drastically reduced service life*. Hence, the occurrence of partial discharges is an important criterion for the evaluation of *insulation quality* also for DC voltage.

In the case of **DC voltage**, discharge frequency and erosion efficiency are enormously reduced, and the question can be raised whether PD at DC voltage is still a danger for the insulation system. The answer is: “That depends”. For example, charge displacments on interfaces or the charging of surfaces by corona discharges can lead to field distortions and flashovers. Hence, the occurrence of partial discharges is an important criterion for the evaluation of *insulation quality* also at DC voltage. Nevertheless, the interpretation of PD is much more difficult than the interpretation of PD at AC voltage.

The *intensities* of partial discharges as well as a few *other parameters* (e.g. *PD inception* and *PD extinction voltages*) are generally measured while testing the withstand voltage of a device. Thus, the criterion for passing a high-voltage test is not only the short-term strength but also the partial-discharge behavior (intensity limits, inception and extinction voltages) that has been *recommended* in the standards for specific categories of devices (e.g., high-voltage transformers, high-voltage cables etc.), or which has been individually *agreed upon* between the manufacturer and the customer.
In the following sections, the *causes* of partial discharges (Section 3.6.1), important *sources of partial discharge* (Section 3.6.2) and characteristic *properties* (Section. 3.6.3) are described. Based on this, experienced high-voltage engineers can, in many instances, present an intuitive *diagnosis* on the cause of defect and the location of defect. The methods of modern *data processing* allow a multitude of extensive methods of analyses for which there are different possible approaches (Section 3.6.3). The actual *measuring technique* for acquisition and diagnosis of partial-discharge data is described in Section 6.4.2.

3.6.1 Causes of Partial Discharges

Causes of partial discharges are local *increases in field strength* (for example, at conductive points or through field displacement) or local *reductions in electric strength* (e.g. owing to gas-filled cavities). During discharge processes, there is a large difference between DC voltage, AC voltage and impulse voltage. Partial discharges have the greatest technical significance for AC voltages due to the erosion of sensitive materials.

A distinction is made between *corona discharges* at conductive electrode tips in air or in

gas insulated arrangements, *internal partial discharges* within insulation and *surface discharges* at interfaces. During partial discharge measurements, interfering signals are also recorded that belong to the so-called *background noise level* and which are neither associated with the external nor with the internal insulation of the tested device. A great technical effort must be made to reduce the background noise to a tolerable level, Sections 6.3.8 and 6.4.2.

3.6.1.1 Corona Discharges

According to Section 3.2.5, corona discharges occur in the *strongly non-uniform field* of a gas insulated electrode arrangement, if the *ignition voltage* is exceeded when the voltage is increased. They occur for **AC voltages** in an area of *maximum voltage,* as long as the voltage is higher than the corona inception voltage, Figure 3.6-1. For this, the **ignition voltage** at a *negative point* is slightly lower than one at the *positive point* (polarity effect).

For a *peak electrode at high-voltage potential*, corona discharges appear at first in a negative maximum of the voltage cycle when the voltage is increased. For a *peak electode at earth potential*, corona inception accordingly takes place at a positive maximum, Figure 3.6-1. For a further increase in voltage, partial discharge inception follows *in the other half-cycle*.

Note: The *inception voltage* for the discharges must not be confused with the **breakdown voltage** of a point to plane arrangement which is at much higher values for strongly non-uniform arrangements. The breakdown voltage is significantly lower at a *positive point* than at a *negative point,* since the field strength at the negative plane is increased by the formation of a positive space charge (see Section 3.2.5.2 Polarity Effect).

The discharges are a *close sequence of current impulses*, which discharge a partial capacitance of the discharge gap and appear as current impulses *i(t)* in the capacitively closed external electrical circuit. After an impulse, the space charges built up during the discharge must first recombine or drift away before another discharge can ignite, so that a relatively regular sequence of impulses occurs (*Trichel impulses*, see Section 3.2.5.2 and Figure 3.2-25).

In the case of **DC voltage**, a continuous corona discharge results from *an uninterrupted sequence of current impulses* after exceeding the ignition voltage, Figure 3.6-5 (top right no. 2).

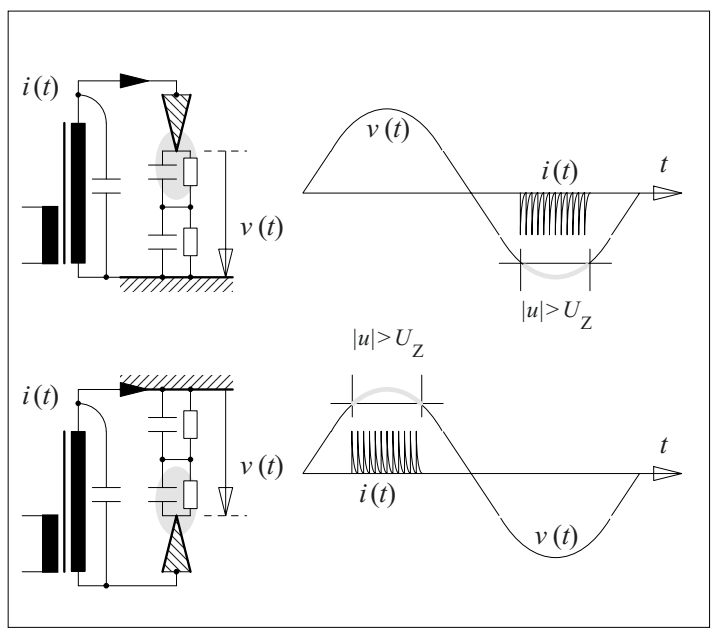

Figure 3.6-1: Corona discharges in a gas-insulated point-to-plane electrode arrangement for slightly exceeding the partial discharge inception voltage:

Top: Point to high voltage, plane to earth potential.
Bottom: Point to earth potential, plane to high voltage.

The discharges begin for negative polarity of the point in the respective half-cycle. For a further increases of voltage, discharges are also ignited in the other half-cycle.

The discharges occur as a close sequence of current impulses (Trichel impulses).

Discharge current impulses occur even for **impulse voltages** after exceeding the ignition voltage. However, generally they cannot be filtered out from very large and rapidly changing surge currents. Therefore, the discussion of partial discharges is restricted to *AC and DC voltage stresses* here.

Note: Corona discharges, which occur in air outside of a device, i.e. outside of a solid, liquid or encapsulated insulation, are also described as **external partial discharges**.

Note: Corona discharges at sharp edges in a *test set up* can lead to an unacceptably high *noise level* for partial discharge measurements. Therefore, if corona discharges in the *negative* or *positive half-cycle* are detected, points and edges on the *high-voltage side* or on the *ground side of the test set up* must first be checked.

3.6.1.2 Internal Partial Discharges at AC Voltage

Internal partial discharges occur in defects within solid or liquid insulations. Defects are frequently formed by *gas-filled cavities* or *bubbles*. During partial breakdown in a cavity, **field changes** occur that are associated with *charge transfers* in the cavity and at the external electrodes Figure 3.6-2 (top left and middle). The latter can be recorded by sensitive partial discharge measurements that are decribed in Section 6.4.2.

Whenever the voltage at the cavity experiences a voltage excursion corresponding to the ignition voltage, the next discharge takes place.

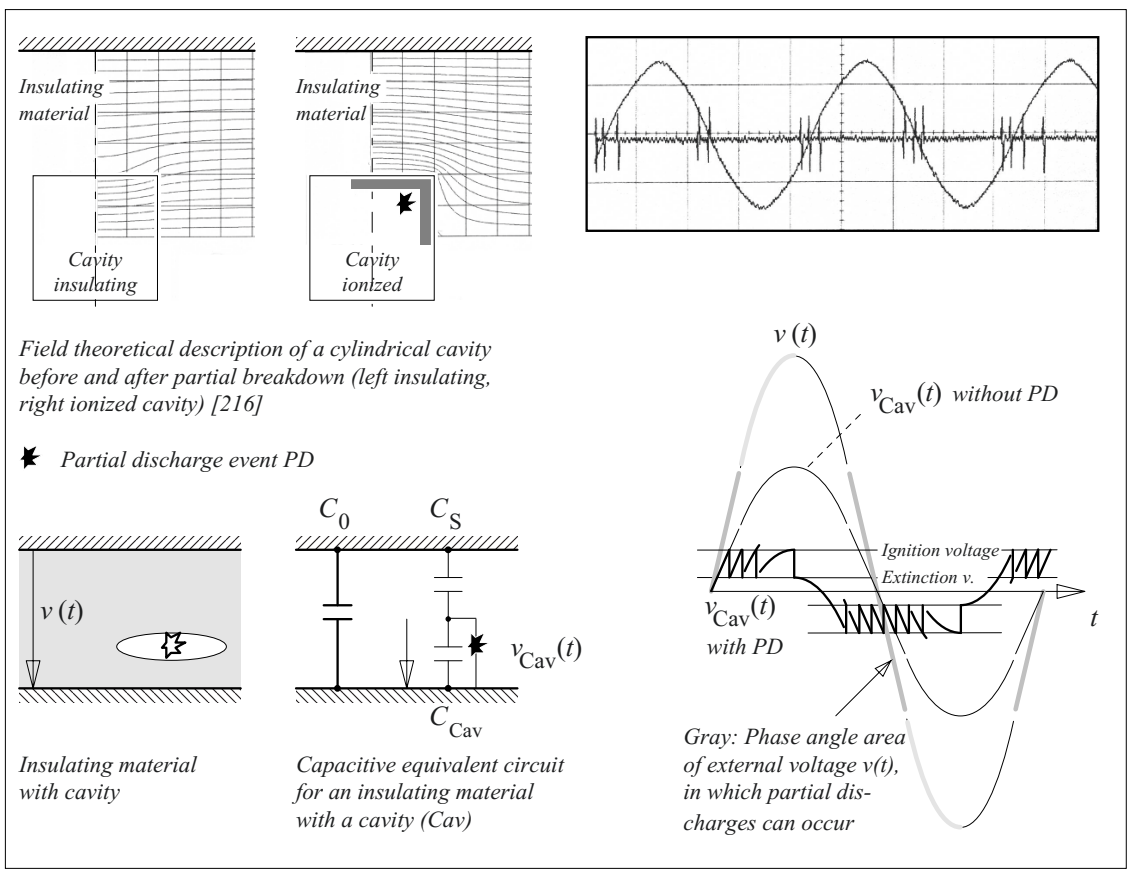

Figure 3.6-2: Internal partial discharges (PD) at AC voltage in a gas-filled cavity.
Top: Field theoretical model with equipotential lines before and after the partial discharge event (left and right) with measured test voltage curves and partial discharge impulses (extreme right).
Bottom: Equivalent circuit model for a cavity (left). External voltage v(t) and cavity voltage without PD well as cavity voltage with PD, i.e. along with ignition and extinction of PDs.

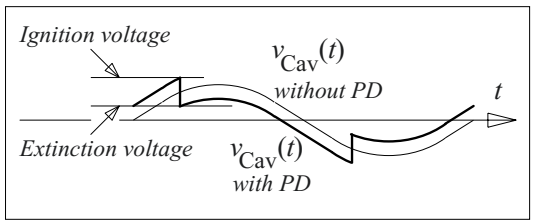

Figure 3.6-3: Existence of partial discharges below the partial discharge inception voltage, i.e. without the peak value of the cavity voltage attaining the value of the ignition voltage.

Therefore, internal discharges occur typically in the *area of larger voltage-time gradients* at regular intervals with *equal voltage excursions*, as the re-charging of the defect is primarily performed in a capacitive way, Figure 3.6-2 (top right).

Note: Analytical calculations are possible for spherical and ellipsoidal cavities [209]. The example according to 3.6.2 (top) was evaluated with the help of *numerical field calculations* and the calculated and measured charge values matched well [216]. In practice, however, geometries are almost always unknown and hence quantitative calculations are impossible. Principal considerations are therefore usually restricted to a simple **capacitive equivalent circuit**, Figure 3.6-2 (bottom). Strictly speaking, this is however not correct since the equipotential surfaces do not exactly coincide with the cavity surfaces so that the *allocation of capacities* is at best possible as an approximation.

In a simplified **capacitive equivalent circuit**, an individual partial discharge impulse can be described as the discharge of a *cavity capacitance* C_{Cav}. The recharging is carried out for **AC voltage** by the capacitive displacement current that flows via the partial capacitance C_S. that is assumed in series. C_0 approximately corresponds to the total capacitance of the insulation arrangement, that is, $C_0 >> C_S$. Besides, $C_{Cav} >> C_S$ and often even $C_0 > C_{Cav}$ can be assumed:

$$C_0 \quad (>) \quad C_{Cav} \quad >> \quad C_S \qquad (3.6\text{-}1)$$

With no ignition of partial discharges, the *cavity voltage* $v_{Cav}(t)$ follows the *external voltage* $v(t)$ according to the capacitive divider ratio of C_S and C_{Cav} with no phase shifts, Figure 3.6-2 (bottom right).

If the cavity voltage exceeds the *ignition voltage* V_{bd} of the gas gap (see Paschen's law Eq. (3.2-35), (-42) and (-43)) and if an *initial electron* is available, the cavity voltage collapses down to the value of an *extinction voltage* V_{ex}. The cavity capacitance is *recharged* capacitively via C_S with unchanged rate of voltage rise. That is, the individual partial discharge event acts similarly to a downward *displacement of voltage curve* by the voltage difference $\Delta V = V_{bd} - V_{ex}$, Figure 3.6-2 (bottom right).

Depending on the cavity voltage magnitude, *multiple partial discharges* can often occur up to the voltage maximum, i.e. the ignition voltage can be reached, voltage breakdown can occur and the voltage curves can be displaced by ΔV several times. In the *next half-cycle*, the repeated displacement of the cavity voltage curve leads to a very *early attainment of the ignition voltage*, possibly even *before the zero crossing* of the externally applied voltage $v(t)$. In Figure 3.6-2 (bottom right), the *phase relation of the partial discharges* is marked by grey shading of the voltage curve $v(t)$. A typical discharge area begins *before the zero crossing* and extends along the *voltage curve ascending towards the maximum*.

Note: When the AC voltage is increased, the *first discharge* might take place at an phase angle close to the maximum, since the ignition voltage V_{bd} is attained there for the first time, but

in the next and in subsequent half-cycles *discharges* already occur *during the increase in voltage* before the negative or positive maximum is reached as a result of the voltage curve displacement.

On lowering the AC voltage, the *partial discharges can continue to exist*, even when the peak value of the cavity voltage *no longer attains the value of the ignition voltage*. As a result of the displacement of the voltage curve by ΔV in each half-cycle, the ignition voltage is exceeded at least once for each half-cycle, Figure 3.6-3. Theoretically, the **partial discharge extinction** (PDE) could be around 50 % below the **partial discharge inception** (PDI). Actually, reductions of around 10 to

35% are observed. "Partial discharge inception"

Generally, devices must be dimensioned in such a way that the *operating voltage is always below the partial-discharge extinction voltage*, so that partial discharges that are ignited by a temporary *over-voltage* are definitely quenched again at the operating voltage.

Note: The regular discharge sequence according to Figure 3.6-2 is substantially disturbed in practice. For lower voltages, the lack of initial electrons in small cavities mainly leads to a *statistical dispersion of partial discharge inception voltages*. A regular discharge only occurs for higher voltages, since initial electrons are available owing to ionization in the cavity.

Note: The simple *equivalent circuit* according to Figure 3.6-2 offers only an inaccurate description of the *actual field distribution*. For example, the *conductivity of insulating material or conductive decomposition products* at the surface of the cavity can lead to a phase shift of the cavity voltage. Even a temporary reduction of the field strength in the cavity is in fact possible through diffusion of conductive discharge products, [71].

Note: During the *inception of a partial discharge,* impulses occur according to the *streamer mechanism,* since no conductive electrodes are available for the release of new initial electrons. Thus, inception voltages occur that have values about 10% above the values expected according to Paschen's law. The half-value width of the impulses is accordingly *very short* at a few ns [67].

In the literature, the *inception field strength* for *streamer discharges* in cavities is specified with [209]

$$E = 25.2 \frac{\mathrm{V}}{\mathrm{m \cdot Pa}} \cdot p \cdot \left[1 + \frac{8.6}{\sqrt{pd/\mathrm{m \cdot Pa}}}\right] \qquad (3.6\text{-}2)$$

Depending on the material, the cavity surfaces become so conductive through *ageing based on partial discharges* that the discharge changes from the streamer mechanism to the *Townsend mechanism* within a period of few minutes to an hour. The inception voltages, then, correspond to *Paschen's law.* The *half-value width* of the impulse increases to 80 to 800 ns for flashover distances of 0.1 to 1mm. Since approximately the same charge is transfered, the *current amplitude* is significantly lower. [67].

In the case of internal partial discharges, it must be noted that the streamer inception is delayed under certain circumstances owing to the **statistical ignition delay**. Figure 3.6-4 shows the example for spherical cavities in epoxy resin. The smaller the diameter *d* of the cavity, the lower is the probability of the presence of an initial electron and that much greater is the average ignition delay time or the statistical dispersion time t_S until the emergence of an initial electron and until the start of streamer development. Thus, there is a risk that a cavity up to a specific size in the mm range remains undiscovered during a one-minute **AC voltage test** if the partial discharge could not be initiated early enough. However, the probability of discharge inception increases in practical tests, since cavities do not appear alone but form a part of a larger volume. Moreover, the inception probability increases if the field strength significantly increases beyond the static inception field strength of the cavity.

Example: Air bubble in insulating oil

For insulating oil with spherical air bubbles, it shall be specified at which field strengths in the insulating oil (background field E_0) partial-discharge inception and partial-discharge extinction are to be expected.

The field strength E_1 in the gas bubble is increased by field displacement relative to the field strength E_0 in oil (see Figure 2.4-22). According to Eq. (2.4-38) it follows that $E_1 = 1.222\ E_0$ with $\varepsilon_{r1} = 1$ (air) and $\varepsilon_{r2} = 2.2$ (oil). During an increase in the voltage, the ignition condition is at first fulfilled at the longest path in the center of the

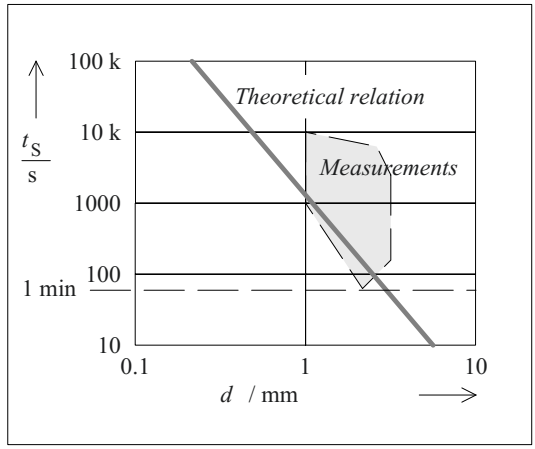

Figure 3.6-4: Ignition delay in spherical cavities as a function of diameter d [209].

bubble. Assuming Paschen's law, according to Eq. (3.2-35) the following is applicable:

$$\hat{V}_{\mathrm{bd}} = \hat{E}_1\, d = 1.222\, \hat{E}_0\, d = B\, pd/\ln(A\, pd/k).$$

With the constants A = 1130 (bar mm)$^{-1}$, B = 27.4 kV/(bar mm) and k = 5, the *partial-discharge inception field strength in oil* under atmospheric standard conditions (T = 293 K, p = 1 bar) is

$$E_{0\,\mathrm{PDI}} = 15.9\ \mathrm{kV/mm}\ /\ln(226\, d/\mathrm{mm}), \qquad (3.6\text{-}3)$$

after conversion to r.m.s. values.

This results in the numerical values mentioned in Section 3.4.3 for the "spherical gas bubble" example. In the case of *partial-discharge extinction field strength*, up to 30% lower values must be adopted.

3.6.1.3 Internal Partial Discharges at DC Voltage

Also in case of DC voltage stresses, internal partial discharges can occur in defects within solid or liquid insulations such as in *gas-filled cavities* or *bubbles*. During partial breakdown in a cavity, **field changes** occur that are associated with *charge transfers* in the cavity and at the external electrodes Figure 3.6-5 (top left and middle). The latter can be recorded by the same sensitive partial discharge measurement methods as for AC voltages, cf. Section 6.4.2.

Whenever the voltage at the cavity experiences a voltage excursion corresponding to the ignition voltage, the next discharge takes place.

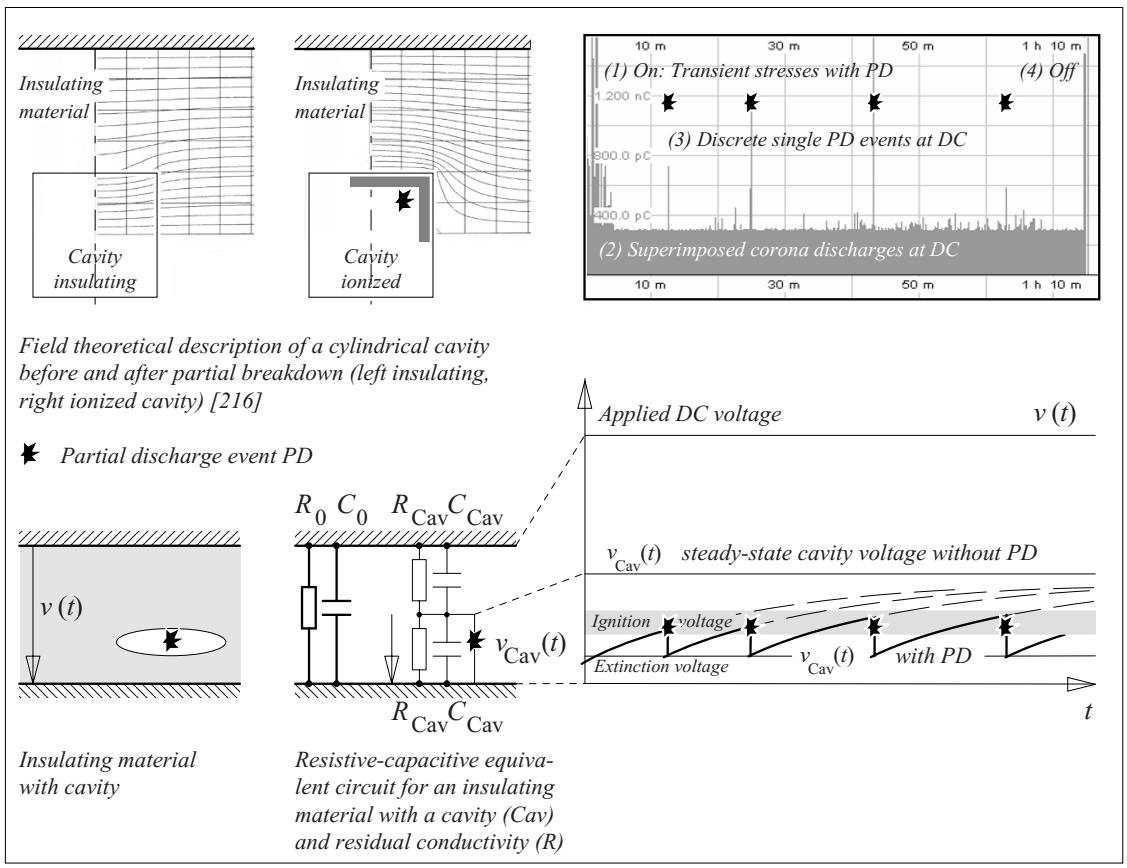

Figure 3.6-5: Internal partial discharges (PD) at DC voltage in a gas-filled cavity. Field theoretical model with equipotential lines before and after the partial discharge event (left and right) with measured test voltage curves and partial discharge impulses (extreme right). Equivalent circuit model for a cavity (left). External voltage v(t) and cavity voltage without PD well as cavity voltage with PD, i.e. along with ignition and extinction of PDs.

For an applied constant DC voltage, the cavity must be re-charged via the highly-resitive insulation material, which can take very long times in the range of minutes. Therefore, internal discharges at DC voltage typically occur *after long periods of time*, Figure 3.6-5 (top right).

Note: In practice, geometric conditions of the insulation defects are almost always unknown and hence quantitative *field calculations* are impossible. Principal considerations are therefore usually restricted to a simple **resistive-capacitive equivalent circuit**, Figure 3.6-5 (bottom), which is an extension of the capacitive equivalent circuit according to Figure 3.6-2 (bottom). Strictly speaking, this is however not correct since the equipotential surfaces do never exactly coincide with the cavity surfaces so that the *allocation of capacities and insulation resistance* is at best possible as an approximation.

If a **DC voltage is switched on**, an initial capacitive *displacement field* and a subsequent *transition process* occur, in which the defects can also be re-charged capacitively so that an *increased but decreasing PD activity* can be observed, Figure 3.6-5 (top right no. 1). The figure shows a practical **example** which includes the superposition of a permanent external *DC corona* (no. 2).

For a steady-state DC voltage stress, the recharging of a discharged cavity capacitance C_{Cav} can only happen very slowly with the time constant $R_S \cdot C_{Cav}$ via the high insulation resistance R_S being in series with C_{Cav}, Figure 3.5-6 (top right no. 3 and bottom right). Whenever the ingnition voltage is reached, PD events occur comparatively regularly, but with scattering of times and amplitudes as the the ignitition voltage is scattering and cannot be well defined. The PD events at DC voltage are significantly less frequent than for AC voltage, and they are in the range of seconds, minutes or hours. This large spread is caused by the fact that conductivities of insulating materials can easily vary over several orders of magnitude.

The long time constants require very *long durations* of **DC voltage withstand tests**, sometime in the range of several hours, in order to reach the steady states within the insulation system that must be tested. Unfortunately, also after a long test duration, "spontaneous" breakdowns are still possible without any preceding indication by partial discharges.

Also the **interpretation of PD measurements** at DC voltage is significantly complicated, mainly as there is no relation to a *phase angle* or to a *voltage difference* [465], [512], [513], cf. Section 3.6.3.2.

3.6.1.4 Surface Discharges

Creepage discharges frequently develop from electrode edges similar to corona discharges. Therefore, their inception is often dependent on the magnitude of the currently existing **AC voltage** $v(t)$. If this increases during the voltage half cycle, the length of the streamer and the intensity of the discharges become greater. Thus, creepage discharges frequently exhibit intensities *increasing from the zero crossing to the peak*, Figure 3.6-8. A polarity effect is produced with the involvement of the electrode.

Note: If the discharge channel only burns normal to the surface and has not yet deviated into surface direction, the conditions can be described according to Figure 3.2-34 (left) by an equivalent circuit which corresponds to the equivalent circuit for internal partial discharges according to Figure 3.6-2. *Directly after the partial discharge inception* these discharges would be comparable with internal partial discharges.

In the case of *increased voltage*, the surface discharges can bridge *long lengths* with the formation of streamers. Thus, irregular impulses with large charge transfer and half value widths of several 10s of ns occur.

In the case of **DC voltage**, surface discharges can no longer be fed by capacitive displacement currents. However, surfaces can accumulate *surface charges*, e.g. due to *DC corona.* Then, the surface charge can be partially discharged by single, high-current and far-reaching *surface discharge impulses* that can possibly lead to flashover.

3.6.2 Sources of Partial Discharges

Typical sources of partial discharges in gaseous, liquid and solid insulating materials are described in the following sections.

For the estimation of *partial discharge inception voltages/ field strengths*, refer

- to Section 3.2.5.3 *(corona inception)* with Eq. (3.2-58),
- to Section 3.2.6.2 *(surface discharges)* with Eq. (3.2-71) to (-74) and also (2.4-35),
- to Section 3.2.2.4 *(Paschen's law)* with Eq. (3.2-35), (-42) and (-43),
- to Section 3.4 *(oil breakdown)* with Figure 3.4.2-6 and Table 3.4.3-1, as well as
- to Section 3.6.1 *(partial discharge causes)* with Eq. (3.6-2) and (-3),

3.6.2.1 Sources of Partial Discharges in Gases

Typical sources of **corona discharges in gases** are closely rounded *point* s and *edges,* conductors with (very) *small diameters* and sharp-edged *particles*, Figure 3.6-5 (top). In practice, surface defects, scratches, roughness and dirt deposits on electrodes as well as conductive particles, e.g. in the form of metal chips, often lead to partial discharges. Production and assembly of gas-insulated switchgear (GIS) therefore require special care and partial discharge testing is carried out after assembly.

Surface discharges in gases represent one of the basic problems of high-voltage engineering, Figure 3.6-5 (bottom). In practice, they are suppressed for example by capacitive potential grading (for bushings), by geometrical field grading (for cable entrance fittings) as well as by elongations of creepage paths and hydrophobic surfaces (for insulators), see Section 2.4.5.

3.6.2.2 Sources of Partial Discharges in Liquids

Small radii of curvature in conductors, *points* and conductive *particles* are less critical than in gases owing to the higher strength in liquids, Figure 3.6-6 (top left).

In liquids, the release of **gas** in the form of *bubbles or gas layers* has a serious effect, Figure 3.6-6 (top right). Owing to field displacement, already electrically weak gas bubbles are yet more heavily stressed so that partial discharges are initiated in oil *at very low background field strengths*, see Eq. (3.6-3).

Furthermore, **water (moisture)** causes a significant reduction in electric strength, especially when drop-shaped water is released. Oil-insulated devices must, therefore, be well *dried* and filled with *degassed and dried* oil under *vacuum*.

Also *tangential overstresses* of insulating material surfaces, such as at the metallic foil edges in *capacitor dielectrics* and in the *pressboard barrier systems* of transformers, can lead to surface discharges, Figure 3.6-6 (center and bottom).

In the pressboard barrier system, partial discharges can even occur as a result of the breakdown of individual *oil gaps,* for example, by the formation of *fiber bridges*.

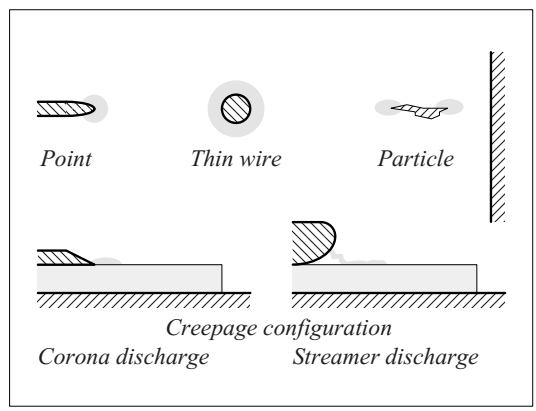

Figure 3.6-5: Partial discharge sources in gases.

3.6.2.3 Sources of Partial Discharges in Solids

Owing to the high electric strength of solid insulating materials, partial discharges are practically always caused by **defects** in the dielectric. These defects almost always consist of *cavities* which are filled with lower molecular components from the surrounding media owing to diffusion processes. Therefore, lower electric strength can often result from *air-filled* cavities, in which the stresses are greatly increased owing to field displacement, Figure 3.6-7.

Cavities closed on all sides usually occur owing to incompletely degassed cast resins or owing to secondary chemical reactions (for example, for polyurethane resins containing moisture), Figure 3.6-7 (top left). Also, progressive *erosion*, for example owing to "water trees" in polyethylene cable insulations, ultimately leads to the formation of cavities, Figure 3.6-7 (bottom right). Moreover, *detachments* between electrode and dielectric as well as *cracks and gaps* in the dielectric can occur owing to reaction shrinkage, mechanical stresses, brittleness and inadequate adhesion, Figure 3.6-7 (top left and right). Extended cavities occur also in *incompletely impregnated layers* such as those between smooth polymeric films in capacitor dielectrics.

Extended *delaminations* in fiber-reinforced materials *are* especially dangerous. These can allow large insulation gaps parallel to the electric field to be bypassed by gas or probably even by diffused water, Figure 3.6-7 (bottom left). Critical *interfaces parallel to the electric field* are also produced by pushing cable entrance fittings on to the cable dielectric, Figure 3.6-7 (bottom right).

After a discharge, solids *no longer* have the ability to regenerate, as in gases and liquids. That is, partial discharges lead to a *progressive erosion* and therefore must definitely be prevented. This results in extreme requirements for the **production quality** of solid insulations. *Vacuum casting* of cast resins, the *impregnation* of interfaces, the use of *bonding agents (sizing, silanization)* for fiber-reinforced materials or materials containing fillers and the use of *semi-conductive layers at* the interfaces between insulating materials and electrodes shall be mentioned as key words.

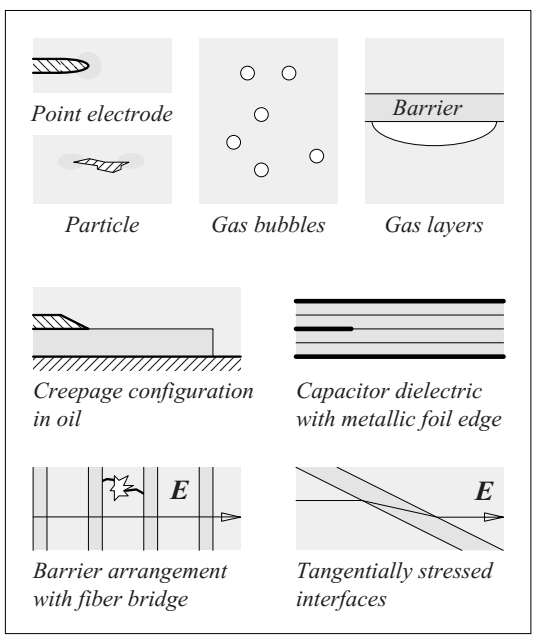

Figure 3.6-6: Partial discharge sources in liquids.

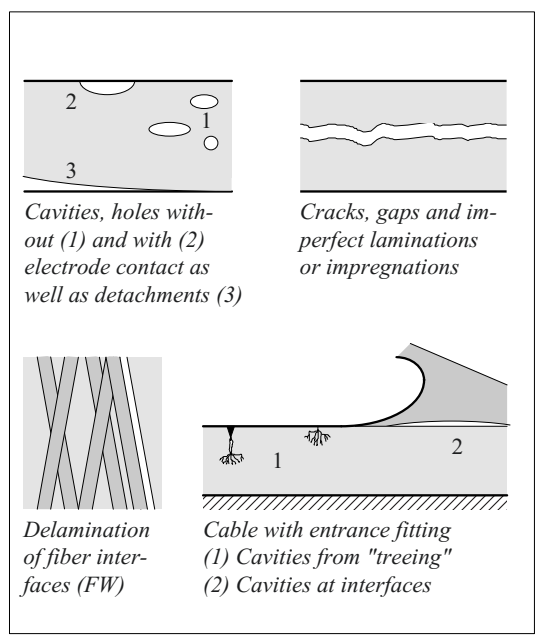

Figure 3.6-7: Partial discharge sources in solids.

3.6.3 Classical Interpretation of Partial Discharges

3.6.3.1 Classical Interpretation of Partial Discharges for AC Voltage

According to Section 3.6.1, different causes for partial discharges also appear in different partial discharge phenomena with characteristic properties. As a result, the **type and location of the defect** can be presumed in many cases. However, even modern diagnosis systems very often fail owing to the *multitude* of probable sources of partial discharges, to the *complexity* of insulation systems and to the *superimposition* of partial discharges from different defect sources.

The measured *intensity* of partial discharges is not so helpful for error diagnosis since only the “apparent charge” at the connections of the test object and not the "actual charge" of a partial discharge impulse itself can be recorded, see Section 6.4.2.2. However, *meaningful parameters* in the discharge images that can be represented with an oscilloscope are

- *phase angle* of partial discharges,
- polarity effects,
- impulse frequency and impulse regularity,
- changes in intensity with the voltage,

as well as

- the ratio of *inception voltage to extinction voltage* (hysteresis).

Figure 3.6-8 shows a few **characteristic partial discharge images** with their reference to the applied AC voltage as a *phase-resolved pattern*. The amplitude of an impulse on the screen of the oscilloscope is an indicator of the *impulse charge*, if the *current impulses* are amplified and *integrated* in a partial discharge measuring circuit by a sensitive partial discharge measuring device. The relevant partial discharge measuring technique is described in Section 6.4.2.

Figure 3.6-8 reflects the respective state shortly after the *inception of partial discharges*, and the images change considerably for higher voltages. Moreover, the figures represent *single defects* whose images are not blurred owing to the overlapping of different effects.

Corona discharges at points appear owing to the polarity effect both in *gases* (a) and *liquids* (b) as regular impulses of constant magnitude close to the AC voltage peaks at the negative point electrode. Thus, it can be distinguished

whether the discharges take place on the *high-voltage side* (left side in the figure) or on the *ground side* (right side in the figure). The frequency of the impulses increases with the voltage.

In *liquids*, larger irregular discharges occur when the point is of positive polarity. In *gases,* this can be observed only for distinctly increased voltages.

Discharges in **cavities** (shrink holes, bubbles, gaps, cracks, detachments ...) and on **surfaces** can be identified from a phase position for an *increase in the voltage* to the maximum.For a *contact to an electrode* (c), different images appear in the half-cycles owing to the polarity effect. Here the larger impulses occur at the positive electrode. Here too, discharges on the *ground side and on the high-voltage side* can be distinguished. Discharges *without contact at an electrode* (d) show a comparable image in both half-cycles.

Caution: Unfortunately, the development of phase-resolved partial discharge pattern is intensely dependent on the *voltage shape*. That is, a voltage highly distorted by *harmonics* no longer gives the partial discharge images known from sinusoidal voltages. It is therefore essential to use an **undistorted sinusoidal test voltage profile** for the interpretation.

a)
Corona discharge in gas
at a point, against a plane. Regular impulses with constant amplitude, frequency increasing with the voltage.

b)
Corona discharge in oil
at a point, against a plane. gegen eine Platte. Smaller, regular impulses with constant amplitude, frequency increasing with the voltage.

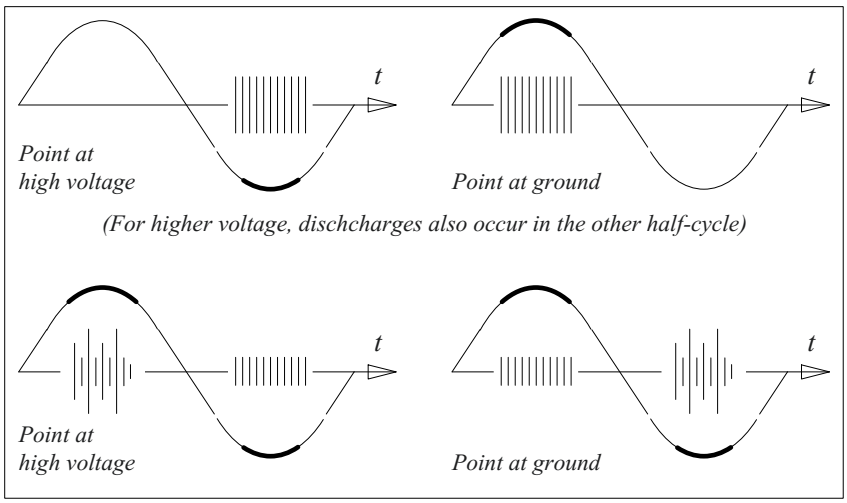

c)
Cavity discharge or surface discharge
with one-sided ***contact to an electrode*** *(Surface discharges can be identified through irregular and intensive streamer discharges at higher voltages).*

d)
Cavity discharge or surface discharge without electrode contact,
discharges between ***insulated conductors.***

e)
Creepage discharge or surface discharge

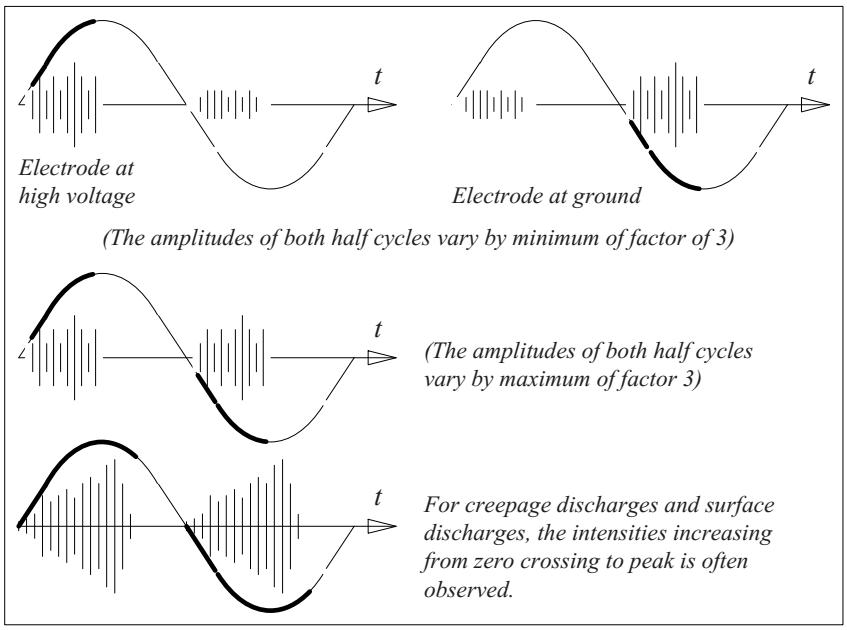

f)
Contact noise
(left) and

g)
Discharges from electrodes on floating potential
(right).

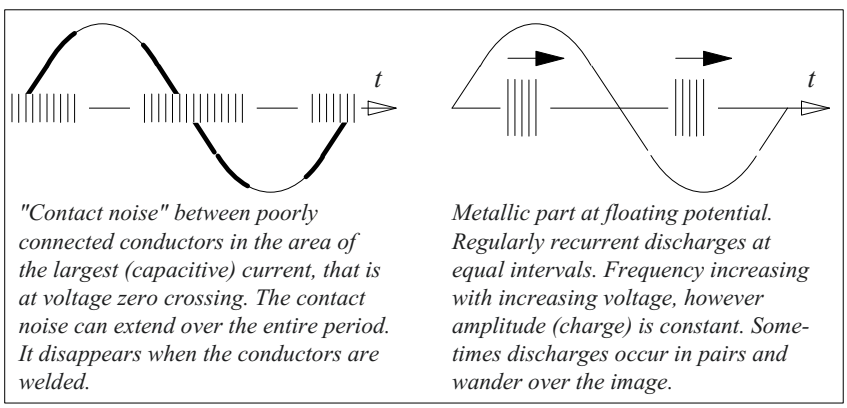

Figure 3.6-8: Characteristic partial discharge pattern for the observation with the oscilloscope. The impulse amplitude is a measure for the apparent charge [67], [72].

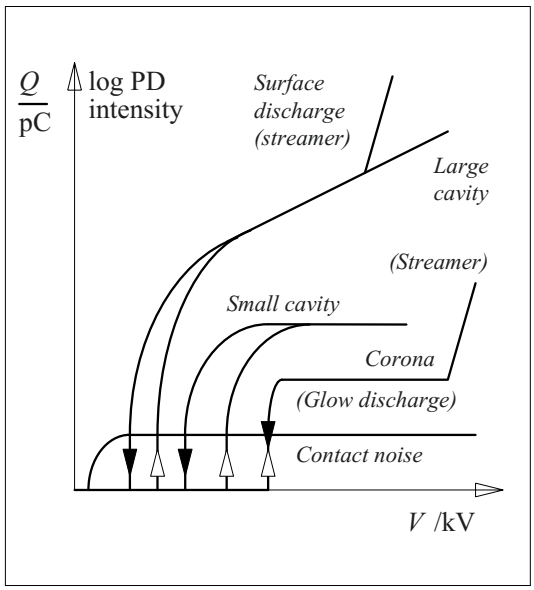

Figure 3.6-9: Characteristic curve of partial discharge charge intensity Q against voltage V.
▻ *PD inception (PDI)* ◣ *PD extinction (PDE)*

At higher voltages, *surface discharges* show very intense and irregular streamer-discharges that can bridge across larger stretches of surface and which frequently show a growing intensity with the voltage amplitude (e).

Contact noise (f) occurs for poorly connected conductors (electrodes, connecting leads, shields) in the area of maximum capacitive charging current (that is, near *voltage zero*), if the non-connected metallic part is connected by a flashover and recharged by a current impulse.

Metallic parts at floating potential (particles, chips, free electrodes ...) can be recharged or discharged by partial discharges (g). This causes impulses of constant amplitude to occur at constant intervals. The frequency increases with the voltage. Impulse groups that drift across the image often occur.

Another important criterion for the identification of partial discharges is the curve for **partial discharge intensity** (partial discharge intensity or apparent charge *Q*) **against the voltage**, Figure 3.6-9. A logarithmic charge scale is recommended for this.After the inception of discharges*, corona discharges* do not significantly change their intensity until there is a change in the discharge mechanism (streamer inception). Inception voltage and extinction voltages are nearly identical; a small difference can only be caused by the ignition delay.

In case of *cavity discharges and surface discharges*, in accordance with Figure 3.6-3, the extinction voltage is distinctly lower than the inception voltage. For large cavities and for surface discharges, a steady increase in the intensity with the voltage is observed. Surface discharges finally develop into streamer discharges of high intensity.

For the practical execution of partial discharge analysis, the **evaluation and diagnosis scheme** according to Figure 3.6-10 has proven its value. It is based on the observation partial discharge images with an oszilloscope and on the determination of partial discharge intensities (apparent charge in pC) with a classical partial discharge measuring device [73]. The *partial discharge images* and their *phase angles* are plotted on ellipses (to save space).

Note: There are also partial discharge measuring devices that show the partial discharge images on an ellipse.

Note: For **transformers**, the *measured phase relation* of a partial discharge to the phase-to-ground voltage does not necessarily correspond to the actual phase angle of the impulse at the defect point, since, according to the location of the defect, different voltages (for example, three phase-to-ground voltages and three phase-to-phase voltages) can be responsible for the partial discharges.

Note: Under favorable circumstances, the location of the defect can be roughly concluded by three-phased recording of partial discharges. Great progress in defect localization for different equipment was achieved by the *synchronous multi-channel PD measurement*, Section 6.4.2.7.

In a *hysteresis test,* which must not be carried out too far above the partial discharge inception voltage, the ratio *of partial discharge in-*

ception voltage to partial discharge extinction voltage is determined. In doing so, one can generally distinguish between corona discharges on the one hand and cavity discharges and surface discharges on the other hand.

During a *voltage increase test* according to Figure 3.6-9, information may be gained about the size of the cavities and the existence of surface discharges.

In a *continuous test* at constant voltage, the discharge behavior can vary significantly, so that indications on the risk of partial discharges may be given. For example, gas bubbles in insulating oil can completely dissolve or can steadily increase under the effect of partial discharges. Thus, partial discharges can die out or lead to breakdown, depending on the type of oil, see Section 3.4.3.

For a *contact to an electrode* (c), different images appear in the half-cycles owing to the polarity effect. Here the larger impulses occur at the positive electrode. Here too, discharges on the *ground side and on the high-voltage side* can be distinguished. Discharges *without contact at an electrode* (d) show a comparable image in both half-cycles.

Caution: Unfortunately, the development of phase-resolved partial discharge pattern is intensely dependent on the *voltage shape*. That is, a voltage highly distorted by *harmonics* no longer gives the partial discharge images known from sinusoidal voltages. It is therefore essential to use an **undistorted sinusoidal test voltage profile** for the interpretation.

At higher voltages, *surface discharges* show very intense and irregular streamer-discharges that can bridge across larger stretches of surface and which frequently show a growing intensity with the voltage amplitude (e).

Contact noise (f) occurs for poorly connected conductors (electrodes, connecting leads, shields) in the area of maximum capacitive charging current (that is, near *voltage zero*), if the non-connected metallic part is connected by a flashover and recharged by a current impulse.

Metallic parts at floating potential (particles, chips, free electrodes ...) can be recharged or discharged by partial discharges (g). This causes impulses of constant amplitude to occur at constant intervals. The frequency increases with the voltage. Impulse groups that drift across the image often occur.

Another important criterion for the identification of partial discharges is the curve for **partial discharge intensity** (partial discharge intensity or apparent charge Q) **against the voltage**, Figure 3.6-9. A logarithmic charge scale is recommended for this. For a *contact to an electrode* (c), different images appear in the half-cycles owing to the polarity effect. Here the larger impulses occur at the positive electrode. Here too, discharges on the *ground side and on the high-voltage side* can be distin-

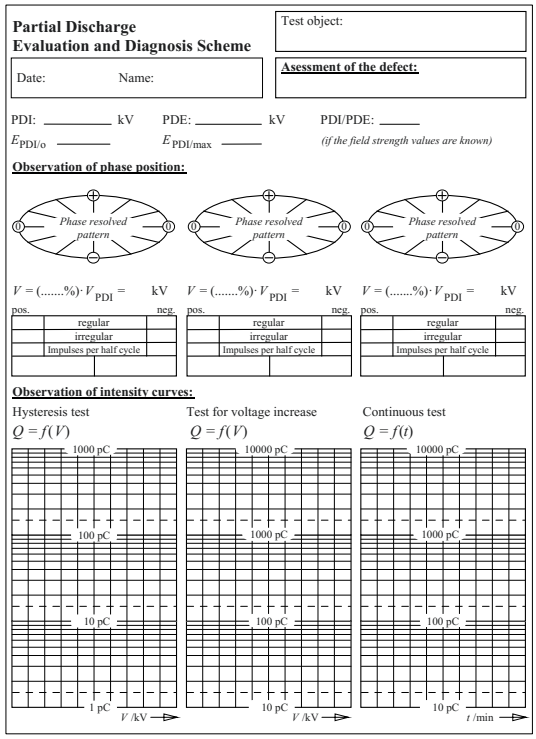

Figure 3.6-10: Partial discharge diagnosis scheme for the documentation and the evaluation of partial discharge observations with the help of an oscilloscope and a classical PD measuring device [73].

guished.

Discharges *without contact at an electrode* (d) show a comparable image in both half-cycles.

Caution: Unfortunately, the development of phase-resolved partial discharge pattern is intensely dependent on the *voltage shape*. That is, a voltage highly distorted by *harmonics* no longer gives the partial discharge images known from sinusoidal voltages. It is therefore essential to use an **undistorted sinusoidal test voltage profile** for the interpretation.

At higher voltages, *surface discharges* show very intense and irregular streamer-discharges that can bridge across larger stretches of surface and which frequently show a growing intensity with the voltage amplitude (e).

Contact noise (f) occurs for poorly connected conductors (electrodes, connecting leads, shields) in the area of maximum capacitive charging current (that is, near *voltage zero*), if the non-connected metallic part is connected by a flashover and recharged by a current impulse.

Metallic parts at floating potential (particles, chips, free electrodes ...) can be recharged or discharged by partial discharges (g). This causes impulses of constant amplitude to occur at constant intervals. The frequency increases with the voltage. Impulse groups that drift across the image often occur.

Another important criterion for the identification of partial discharges is the curve for **partial discharge intensity** (partial discharge intensity or apparent charge Q) **against the voltage**, Figure 3.6-9. A logarithmic charge scale is recommended for this.

Note: The **classical partial discharge interpretation** is often made more difficult by the superimposition of partial discharges on several defects.

The described criteria are generally only applicable to a single (dominant) defect or to the overlapping of congeneric errors. The differentiation between *similar, but different errors* is often not possible. Again, great progress in differentiation between different defects was achieved by the *synchronous multi-channel PD measurement*, Section 6.4.2.7.

Despite intensive research, for a long time it has not been possible to go beyond the limits of classical partial discharge diagnosis. But modern data technology today allows **advanced computer aided interpretation approaches**, Section 6.4.2.6 ff.

The entire topic of data acquisation and evaluation of electrical and non-electrical partial discharge signals is dealt with in Section 6.4.2.

3.6.3.2 Interpretation of Partial Discharges for DC Voltage

The interpretation of partial discharge events for DC is not yet as developed as that for AC voltages. Since a *phase relation* to an AC voltage cannot be produced, the above mentioned classical visualization and interpretation procedures are largely missing. Even the definition of *inception voltages* and e*xtinction voltages* is not possible because of the long-lasting transition processes in the insulation system and the long durations between single discharge impulses.

Possible remaining **parameters** are the *impulse shape* or the *frequency spectrum* and the *apparent charge* of an individual impulse, the *time difference* to the preceding and to the following impulse, the *apparent charge* of the preceding and the following impulse, the *impulse frequency* (repetition rate) as well as the *temporal development* of the discharge process.

Traditionally, for direct voltages, **individual partial discharge impulses** are plotted *against time*. Generally, DC partial discharge impulses occur regularly, but only very rarely.

For **internal discharges**, that is for discharging a defect within an insulating material, the defect must at first be recharged, usually via very large insulation resistances and with very long time-constants. **During a DC voltage withstand test,** it is often required that only a specific number of impulses of a specific magnitude may occur within a time window.

Even external **interference impulses** can be significantly more difficult to identify than for AC voltages, since they are individual events without any phase relation.

Note: **Corona discharges** in air behave totally different; they occur in the form of very frequent regular discharges, which are determined by space charge formation, Section 3.2.5.2.

It was therefore proposed that the φ, Q, N pattern for AC voltages are *to be* substituted by Δt, Q, N pattern for DC voltages [465]. This implies that **time difference** Δt between successive impulses would appear instead of the phase angle φ.

It was shown that in this way a differentiation between different types of defect is possible. *External discharges* in air are represented, for example, by very small time differences and by a low statistical spread of the charge Q. For *internal discharges*, time differences occur that are longer by many orders of magnitude and these are slightly dispersive for strongly scattered charge values.

Based on the above-mentioned parameters, **histograms** can be calculated that differ for the basic types of defects and that enable a *diagnosis* of insulation systems right through to initial approaches for automated classification [512], [513].

The **impulse form** is another starting point for the interpretation which provides very good classification results on lab-scale samples and with a high-frequency and distortion-free coupling between discharge location and a broadband PD measuring system [514]. However, it is problematic that the impulse form normally is greatly distorted on the path between the source and the sensor, as with AC voltages.

A great step forward for partial discharge diagnosis for AC voltages and DC voltages is given by the **synchronous multi-channel PD measurement** of impulses from the same source, Section 6.4.2.7: by developing amplitude relations or propagation time relations, all impulses can be assigned to a certain, although perhaps as yet unknown source. In this way, the separation and identification of interference sources and partial discharge sources is considerably improved.

3.7 Vacuum Breakdown

In many cases, the insulation of higher voltages is even necessary in a vacuum, such as in X-ray tubes, transmitting tubes, image tubes, accelerators, superconducting equipment, satellites or vacuum switches, Section 7.1.5.3.

3.7.1 Physical Process

While considering the electric strength of a vacuum, it is *not* enough to consider only the limiting case of *Paschen's law* for $pd \rightarrow 0$: in vacuum and as well as in gases with very low pressures, there are practically no gas particles between the electrodes, the free path lengths are significantly larger than the electrode distances and no increase in charge carrier number can occur owing to collision ionization.

Theoretically, Paschen's law would subsequently lead to an infinitely high breakdown voltage; see Section 3.2.2.4, Figure 3.2-13 and Eq. (3.2-38).

Of course, an infinitely high breakdown voltage cannot be attained even in a vacuum; it is other physical processes, primarily at the electrodes, which determine the vacuum breakdown [316]:

a) Breakdown between electrodes

The *breakdown* is initiated by processes at the *electrode surfaces* that are not dependent on (very low) gas pressure. Thus, a *metal vapor* is formed in which the breakdown takes place by collision ionization [23], [67], [316]:

At the cathode surface, at very high local *microscopic field strengths* E_μ, a *field emission* of electrons in the vacuum takes place. The work function or potential barrier for frequently used metals (copper, stainless steel) amounts to about $\phi = 4.5$ eV and is overcome beyond about $E_\mu = 1000$ kV/mm by the quantum-mechanical tunnel effect, Figure 3.7-1. Owing to field stress enhancements at *microtips* or at conductive channels in oxide films, significantly lower *macroscopic field strengths* E_m are sufficient for field emission:

$$E_\mu = \beta \cdot E_m \qquad (3.7\text{-}1)$$

The field stress enhancement factor β can be considered as the reciprocal of a microscopic field efficiency factor and is of the order of magnitude of a few 100 to a few 1000. Thus, even for field strengths of the order of magnitude of 1 to 10 kV/mm, field emission processes must be expected.

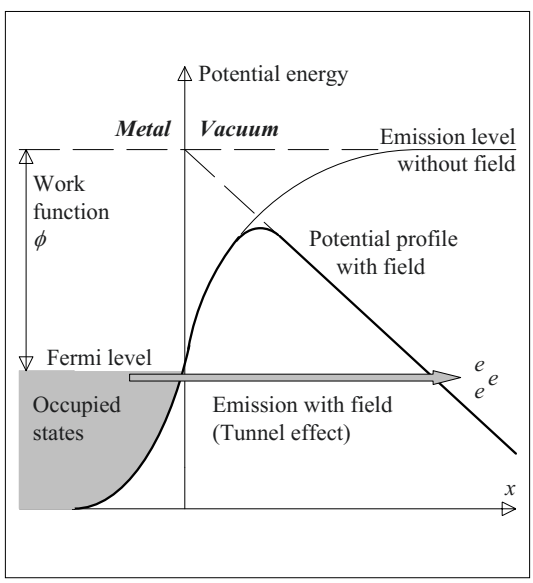

Figure 3.7-1: Field emission at the cathode surface during vacuum breakdown.

Electron emission can initiate breakdown by two processes:

1.) The microtips heated by the field emission current vaporize explosively and release the metal vapor responsible for the breakdown. For this **cathode-initiated breakdown**, local current densities above 10^8 A/cm^2 are possible.

2.) For **anode-initiated breakdown**, the electrons released at the cathode owing to *field emission* are accelerated as an electron beam towards the anode which is locally heated up until the anode material vaporizes. This also results in X-ray bremsstrahlung. New initial electrons are generated at the cathode as a result of feedback. In the course of a *generation mechanism*, finally metal vapor plasma is formed [16].

Note: Adsorbed *gas layers* can also vaporize at the anode surface under electron bombardment and facilitate ionization processes and avalanche processes. At the cathode, adsorbed gas layers can reduce the work function.

Breakdown processes induced by field emission can be expected to have approximately *constant* breakdown field strength.

For *larger distances* of 5 to 10 mm, processes gain influence under the **participation of charged particles.** They are accelerated in the field and create a microplasma on impact on the electrode. Critical velocities for this are approx. 100 m/s. Thus, a *non-linear* relation between breakdown voltage and distance results, Figure 3.7-2.

Moreover, the migration of particles takes time so that short-term lightning impulse stresses give rise to more rapidly increasing strengths with increasing distances than long-term AC voltage stresses.

b) Conditioning

In an electrode arrangement, an improvement of the microscopic *surface structure* and a considerable increase in the breakdown strength can be attained by means of *conditioning* (partly above 300 %). It is assumed that emission centers for pre-discharge currents, that is microtips or gas layers, are reduced and micro-particles are removed during the conditioning process.

Current conditioning, thermal conditioning and spark conditioning are approved conditioning procedures. *Spark conditioning* consists of a larger number of breakdowns during which breakdown voltages increase. The *energy* of the breakdowns must be limited by protective resistors to an extent so that no new microtips can be created. An (undesired) degradation of the arrangement is described as *deconditioning.*

A prerequisite for the relatively high electric strength in a vacuum is the high *quality of the vacuum.* Even low gas densities lead to a drastic loss of strength to the point of the Paschen minimum, Figure 3.2-13. Therefore, not only the electrodes must be conditioned. Other components (shields, insulators) can also contain adsorbed gas layers and these must be removed by annealing. The quality of the vacuum can be maintained over a long period of time with getter materials of rare earths.

3.7.2 Technical Strengths

a) Strength for AC and impulse voltages

The previous explanations show that the strength of an electrode arrangement under vacuum depends on many *parameters* and can therefore vary, depending on the test set up.

For *very small distances* (d < 2mm), *field emission induced* breakdowns and constant breakdown field strength are expected. This corresponds to a *linear* dependence of breakdown voltage on the electrode distance:

$$V_{bd} \sim d \qquad (3.7\text{-}2)$$

For *larger distances*, for which accelerated particles initiate the breakdown, the icrease of breakdown voltage V_{bd} is often approximated by the square root of the distance d, Figure 3.7-2. The introduction of an exponent α is more precise:

$$V_{bd} \sim (d/\text{mm})^{\alpha} \qquad (3.7\text{-}3)$$

The exponent, however, varies from $\alpha = 1$ to about $\alpha = 0.3$ depending on the distance [316]. The following is valid as a *rough approximation* for the r.m.s. value of the *breakdown AC voltage* [67]:

$$V_{bd\,rms} \approx 30\ \text{kV} \cdot (d/\text{mm})^{1/2} \qquad (3.7\text{-}4)$$

The *impulse voltage strength* is not very much different from the AC voltage strength. As a guide,

$$\hat{V}_{bd} \approx 30 \ldots 40\ \text{kV} \cdot (d/\text{mm})^{1/2} \quad \text{for } d < 2\text{mm}$$

and (3.7-5)

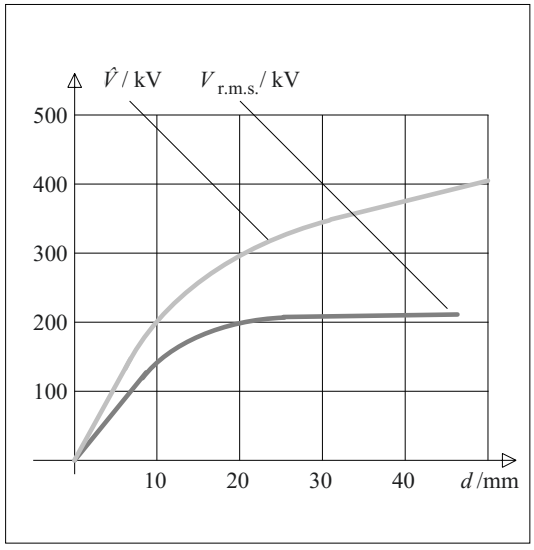

Figure 3.7-2: AC voltage strength and lightning impulse voltage strength in vacuum (according to [316]).

$$\hat{V}_{bd} \approx \quad 60\ \text{kV}\cdot(d/\text{mm})^{1/2} \quad \text{for } d > 2\text{mm}$$

are given in [67].

A more exact investigation of vacuum breakdown shows that there is a distinct dependence on the *material* and the *condition of the electrodes*.

b) Breakdown along surfaces

The strength at the *surfaces of insulating material* (glass, ceramics) is distinctly reduced in vacuum owing to emission processes.

The starting points are the *triple points* between the metal electrode, insulator and vacuum, Figure 3.7-3. Owing to microscopic field displacement, comparatively low macroscopic field strengths are sufficiently high for the emission of electrons. At the insulator surface, comparatively loosely bound electrons can be released owing to collision ionization (*secondary electron emission*) and an avalanche can be formed ("electron cascade"). Thus, the surface is charged and adsorbed gas layers are detached and ionized.

Measures for increasing the strength at the interfaces are especially

- a specific *reduction of the field strength* at the triple point to prevent electron emissions,
- a *conical design* of the triple point,
- a *coating* of ceramic surfaces with CuO_2 and Cr_2O_3,
- a *polishing* of the surface or
- an *annealing* at 1000 °C for removing absorbed gas layers.

Example: In *vacuum circuit-breakers*, the tangential stress of ceramic surfaces in the area of the triple point must be completely avoided in practice by covering the surfaces largely with *metallic shields*, Section 7.1.5.3 and Figure 7.1.5-3.

These shields, along with electric field grading, also serve as protection against the direct depositing of metal vapor plasma on the insulator surface. Owing to this, increasingly conductive layers would be formed on unshielded insulator surfaces over a period of time, which would have a very negative effect on the electric strength of the interfaces.

3.7.3 Applications

a) Classical applications

The classical application areas of vacuum insulation are *electron tubes, vacuum interrupters* and *picture tubes*. Although they are increasingly losing significance owing to semiconductor technologies, *x-ray tubes* and *vacuum circuit-breakers* are still of high importance, they are described in detail in Sections 7.4.4 and 7.1.5.3. A few special applications are mentioned here.

b) Magnetic insulation

Impulse generators for generating *high power impulses* with extreme peak values in the MV, MA and TW ranges (*pulsed power* technol-

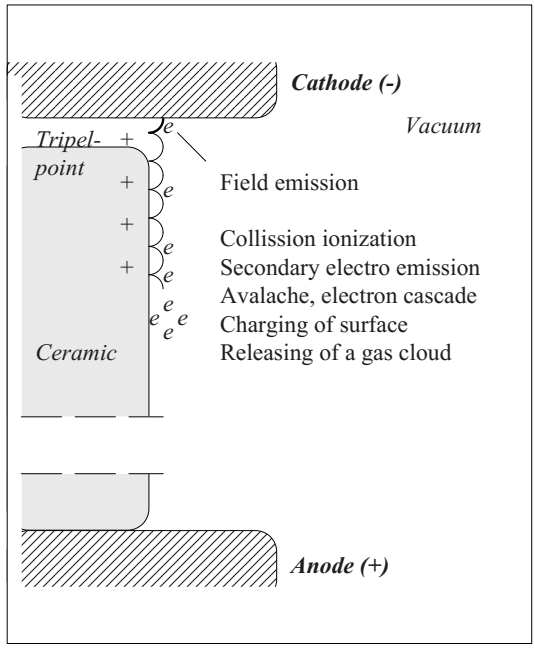

Figure 3.7-3: Reduced surface strength in vacuum.

ogy), use the so-called line generators with energy storage, traveling wave transmission lines and water insulation with higher permittivity for the temporal and spatial compression of impulse energy, see Section 2.6.3.3 and 6.2.3.2 d). Often, the impulse must be transferred to a line insulated with vacuum and to the matched load, for example to a so-called particle beam diode in which ions or electrons are highly accelerated.

The impulse traveling on a *vacuum insulated line* (guided TEM-wave, Section 2.6.1), is thus linked to a strong magnetic field. The electrons emerging from the cathode, owing to the forces of the electric field, are forced on to a curved track by the *Lorentz force* of the magnetic field and ideally led back to the cathode. Above a critical current value, the electron bombardment of the anode required for vacuum breakdown is inhibited (*magnetic insulation*) [439].

Note: At the front and rear of the impulse, current and magnetic field strength are reduced so that the magnetic insulation is no longer effective. However, if the impulse is considered as a guided TEM wave, then, according to Eq. 2.6-10 and -12, even a lesser stress is given through the electric field.

c) Insulations for different pressures

Insulation systems, caused by external circumstances, can sometimes be exposed to different pressures down to the level of a vacuum and they must still retain their insulating properties under all circumstances.

An example is the insulation of devices, which are transported from the Earth's surface into space. Thus, the *Paschen minimum* with an extremely low strength of approx. 330 V is passed, if air or the subsequent **space vacuum** are provided as the insulation medium, Figures 3.2-13, -24, Table 3.2.3.

The environment of **superconducting installations** is evacuated as thermal insulation has to be guaratueed, see Section 7.5. Large magnetic coils, such as those seen in nuclear fusion technology or in particle accelerators, must be discharged quickly in special instances, for example during a quench (loss of superconductivity), so that the ohmic heat loss occurring in the expanding normal conductive area does not lead to damage [450]. For this purpose, the coil is usually connected in series with an external ohmic load resistor. The voltage thus enforced reaches the tens of kV range and effects a discharge of the coil according to $\partial i/\partial t = V/L$. In this situation, the conductor insulation as well as the surrounding vacuum can still work as insulation. However, if gas should enter into the vacuum space owing to leakages and the conductor insulation should exhibit weak spots (for example, small cracks), here too the Paschen curve will be traversed and the insulation fails when the Paschen minimum is approached.

Therefore, in the given examples it is necessary to design the insulation systems in such a way that they include the so-called **"Paschen strength"**. This is, for example, possible when all voltage carrying conductors are enclosed by a solid and "*electrically sealed"* (that is, gap free) insulation, on whose external surface the ground potential is applied as a closed shell with the help of conductive covering, comparable with the semi-conductive layers (screens) on a cable insulation. The external vacuum volume or gas volume that may have low strength, is thus maintained *completely free of field*. In this case, for superconducting insulation systems, there exists the difficulty that the electric strength must also be assured at low temperatures close to absolute zero. This has especially to be considered during the choice of suitable insulating material (coefficients of thermal expansion, crack formation) and suitable processing techniques. "

The Paschen strength, i.e. the strength against discharges in the Paschen minimum, can neither be tested under atmospheric pressure nor under evacuated conditions. The completely assembled insulation system must instead be tested in a vessel that can be evacuated and in the relevant gas (such as air, nitrogen, helium)

at different pressures. [451]. After adjusting the different pressure levels, the test voltage is applied in each case for a specific period. Thus, the Paschen curve including the minimum is passed through (**Paschen test**). For this, no discharge between the conductors and ground coverings or walls of housing may occur. The Paschen test is well suited for finding production defects that cannot be identified at other pressures.

4 DIELECTRIC SYSTEM CHARACTERISTICS

In addition to the **electric strength** dealt with in Chapter 3, there are *many other important characteristics* of insulating materials:

The electric field is significantly influenced by **dielectric properties,** i.e. through different *polarization phenomena* that are usually described by parameters such as *permittivity* and *dielectric dissipation factor* and by the *conductivity*, cf. Section 2.4. They will be dealt with in detail in Chapter 4.

Other characteristics such as surface resistance, tracking resistance, arc resistance and water repellence (hydrophobicity) are more related to the **surface area** and less to the material volume itself. Material-specific data are given in Chapter 5.

Further, the insulating materials, according to a common and adequate terminology of the past, are always **"construction materials"** for devices or installations [81]. Important characteristics are already compiled and summarized in Section 2.2. The *characteristic profile* of an insulating material must be compatible with the technical *requirements.* I.e. *mechanical, thermal and chemical characteristics* as well as their *processing technology* must always be taken into consideration and it is of utmost significance in many cases (Chapter 5).

4.1 Polarization in the Time and Frequency Domain

In Section 2.4.1, the dielectric characteristics such as "conductivity" and "polarization" were explained without taking the **time-based transients** into consideration. The explanation was only about the fact that the orientation of dipoles according to the type of polarization mechanism needs time and energy and thus, for high frequencies, the dipoles cannot follow the field or can only follow it with a delay, as in Figure 2.4-5. This result in far-reaching consequences dealt with below in the time and frequency domain.

4.1.1 Description in the Time Domain

The **system characteristics** of a dielectric can be determined, for example, in the time domain by *measuring a step function response*, i.e. with the help of a step voltage or a field strength step function, Figure 4.1-3.

$$E(t) \quad = \quad E \cdot \sigma(t) \qquad (4.1\text{-}1)$$

$\sigma(t)$ is the so-called unit step function. $E(t)$ is the **dielectric system response** in the time domain. The *vacuum field* is formed under a very large charging current impulse by the field step and, according to Eq. (2.4-7), the charge density $\varepsilon_0 E$ results at the electrodes, Figure 4.1-1 (left). The delayed orientation of dipoles (*polarization*) creates additional charges on the electrodes with a charge density increasing with time $P_i(t)$, Figure 4.1-1 (center).

Note: Generally there are *many polarization mechanisms* that are denoted by different indices *i*. The polarization thus results from the superposition of individual mechanisms:

$$P(t) \quad = \quad \sum_i P_i(t) \qquad (4.1\text{-}2)$$

After the dipoles are orientated, a *steady-state current* flows, Figure 4.1-1 (right):

$$J \quad = \quad \kappa \cdot E \qquad (4.1\text{-}3)$$

These procedures can be described for linear materials with the help of a **network model**, Figure 4.1-2. The formation of the vacuum field corresponds to the charging of the *vacuum capacitance* C_0. The steady-state current flows for $t \rightarrow \infty$ through the *DC resistance* R_∞. When describing the delayed and time-varying polarization $P_i(t)$, it is assumed that the rate of change $\partial P_i/\partial t$ is proportional to the actual difference between $P_i(t)$ and the steady-state end value $P_i(\infty)$ (Debye approach):

A. Küchler, *High Voltage Engineering*, VDI-Buch,
DOI 10.1007/978-3-642-11993-4_4

$$\frac{\partial P_i}{\partial t} = \frac{1}{\tau_i} \cdot \left[P_i(\infty) - P_i(t) \right] \quad (4.1\text{-}4)$$

This differential equation produces a polarization that is exponentially tending towards $P_i(\infty)$:

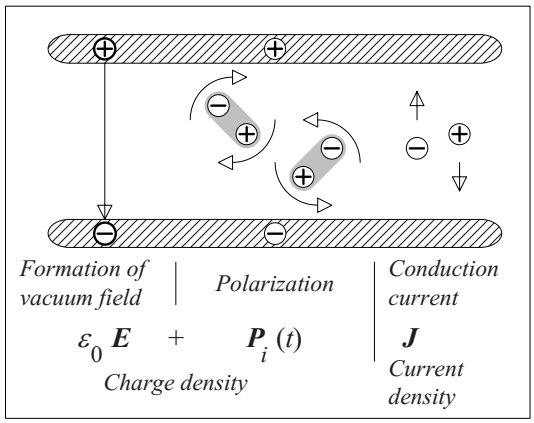

Figure 4.1-1: Phyisical processes in a dielectic after application of a step field.

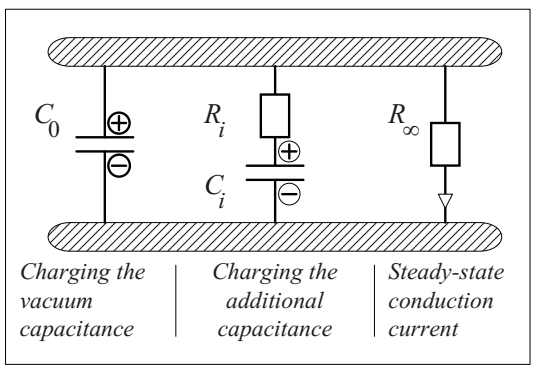

Figure 4.1-2: Network model of the dielectric.

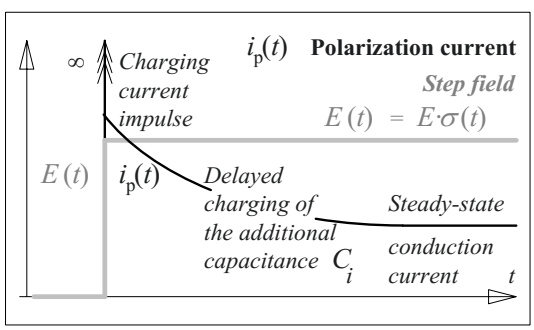

Figure 4.1-3: Dielectric system response in the ***time domain.***

$$P_i(t) = P_i(\infty) \cdot \left[1 - e^{-\frac{t}{\tau_i}} \right] \quad (4.1\text{-}5)$$

Note: A *generalization* that goes beyond the exponential approach according to Eqs. (4.1-4) and (-5), is given in the literature [269]. However, most of the practical problems can be resolved and demonstrated using the *exponential approach* described.

According to Eq. (4.1-5), polarization corresponds to a charge density that is exponentially tending to an end value, and this is also described in the network model by the *RC*-charging of an *additional capacitance* C_i via a *resistance* R_i with the time constant

$$\tau_i = R_i \cdot C_i \,, \quad (4.1\text{-}6)$$

Figure 4.1-2 (center). Since several polarization mechanisms are generally effective, they must be summed up according to Eq. (4.1-2). In the network model, this corresponds to the parallel connection of *RC*-elements with different indices i or different parameters R_i and C_i and different time constants τ_i.

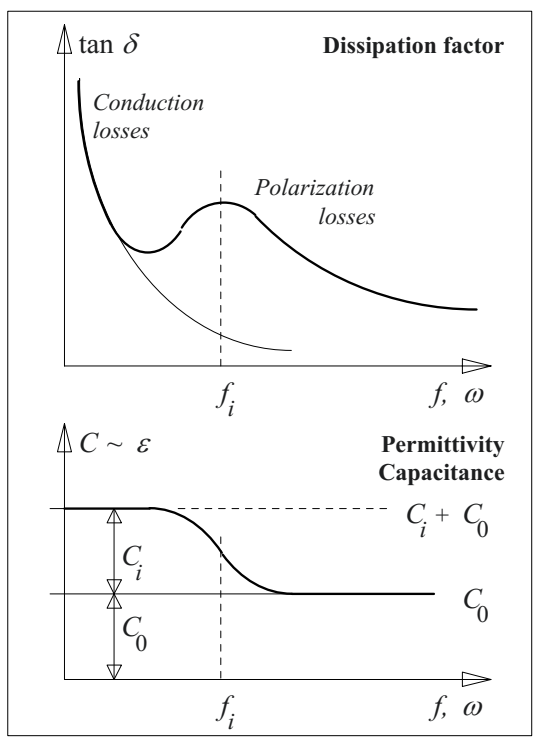

Figure 4.1-4: Dielectric parameters in the ***frequency domain.***

The **polarization current** as a response to the step field in the **time domain** can be directly assigned to the elements of the network model, as in Figures 4.1-2 and -3. It contains all the information that is necessary to form a dielectric equivalent circuit: The integration of the initial current gives the charge and therefore the **initial capacitance** C_0:

$$C_0(\Delta t) = \frac{1}{V} \cdot \int_0^{\Delta t} i_p(t) \cdot dt \qquad (4.1\text{-}7)$$

Note: However, this is only the **vacuum capacitance** if the integration interval is chosen to be so short that no polarization phenomenon has yet been included. This is practically impossible. It is therefore better to speak of the **"initial capacitance"** (or **"high-frequency capacitance"**) $C_0(\Delta t)$, whose magnitude depends on the considered time interval Δt and on the included polarization mechanisms.

The **direct current resistance** R_∞ results from the stationary end value of the polarization current $i_p(\infty)$:

$$R_\infty = V / i_p(\infty) \qquad (4.1\text{-}8)$$

Note: According to the standards (e.g. [157]) the measurement of volume "resistance" is performed with varying and sometimes very short measuring durations. This is of no physical significance, since not only the resistive conduction current flowing through R_∞ is recorded but also the polarizing current in an unknown state of transition, i.e. also the charging current of the additional capacitances C_i is recorded. Improved methods for determination of end values of resistance or conductivity can be found in Section 4.2.2.3 and 6.4.1.2.

The **polarization equivalent circuit elements** R_i and C_i representing polarization phenomena can likewise be determined from the polarization current: for $t = \Delta t$, the initial current impulse has decayed and the polarization current is largely the charging current of the still uncharged capacitance C_i flowing through the **resistance** R_i. The steady-state current component through R_∞ must be subtracted:

$$R_i = \frac{V}{i_p(\Delta t) - i_p(\infty)} \qquad (4.1\text{-}9)$$

If *multiple polarization mechanisms* must be considered, then instead of an individual element R_i, a *parallel connection of multiple resistances R_i is used.*

The **capacitance** C_i can be determined from the *time constant* of the current decay according to Eq. (4.1-6), but only if a single polarization mechanism dominates. If several polarization mechanisms overlap, *the sum of additional capacitances* can be determined from the total charge that has flowed by integration of the charging current:

$$\sum_i C_i = \frac{1}{V} \cdot \int_{\Delta t}^{\infty} [i_p(t) - i_p(\infty)] \cdot dt \qquad (4.1\text{-}10)$$

Complete dielectric equivalent circuits can be determined by so-called *"curve fitting",* i.e. by approximation of the measured polarization currents $i_p(t)$ with the help of exponential functions which have to be simulated with associated *RC*-elements [229], [230].

Until now it has been assumed that the decreasing polarization currents must be interpreted as **charging currents** of additional capacitances C_i and not as **time variable conductivities** (which is conceivable, for example, in the case of oil with ion drift processes, Sections 4.2.2.2 and 4.3.2.3). Both of these options can be distinguished by measuring the **depolarization current** or the discharge or relaxation current $i_d(t)$ after disconnecting the voltage and short circuiting the test object. For a linear system according to Figure 4.1-2, the depolarization current is supplied from the fully charged capacitances C_i (if charging time was long enough) and corresponds to the time profile of the charging current i_p. It thus indicates the **charge stored** through polarization.

The *proportion of the conduction current* as well as the **conductivity** are derived from the *difference* of currents that are shifted in time relative to one another $i_p(t)$ and $i_d(t+t_L)$, see Figure 4.2-8 and Eq. (4.2-6d).

Note: Polarization current measurements are used inter alia to determine **material properties** for insulation designs. Section 7.2 Another important application is

the **dielectric diagnosis** of operating equipment**,** in which circuit elements are calculated from current measurements to draw conclusions regarding the wetting or ageing state of an insulation, Section 6.4.7.6.

4.1.2 Description in the Frequency Domain

By analogy with the description of dielectric properties in the time domain, treatment in the **frequency domain** is also possible based on Figures 4.1-1 and -2:

The transformation of Eqs. (4.1-4) and (-5) into frequency domain gives a complex polarization $\underline{P}$ and a *complex permittivity* $\underline{\varepsilon}^*$, Section 4.2.4. The real part essentially describes the dependence of **capacitance** C or **permittivity** ε on the frequency f or the angular frequency ω respectively, Figure 4.1-4 (bottom). The imaginary part describes an additional phase shifting δ being induced by *dielectric losses*. Phase angle between voltage (stimulation) and current (response) is $\varphi = 90° - \delta$. The losses are generally specified by the **dissipation factor** $\tan \delta$ which equals the ratio of dissipation losses to capacitive reactive charging power, Figure 4.1-4 (top) and Eq. (4.2-13). The recording of these parameters (especially the complex permittivity) against frequency results in the **dielectric system response** in the frequency domain.

The parameters of the frequency domain traditionally have great significance for describing dielectrics. The relationships are explained in detail in Section 4.2.3.

The *frequency dependences* can be explained clearly with the help of Figures 4.1-1 and -2:

At *very high frequencies*, the dipoles cannot follow the rapidly varying field and only the vacuum field is created. In the network model, this corresponds to a dominant displacement current through C_0. A capacitance measurement for high frequencies, therefore, would give only the value C_0 which often comes close to power frequency capacitance. The dissipation factor tends to zero, Figure 4.1-4.

At *very low frequencies*, all dipoles can follow the field with no delay. As a result, the electrodes are additionally charged. In the network model, this corresponds to a charging of all capacitances C_0+C_i or $C_0+\Sigma_i C_i$. A capacitance measurement for very low frequencies would thus give the value of the sum of capacitances, Figures 4.1-4. The dissipation factor tends towards infinity, as in the ratio of dissipation losses to reactive power, the reactive power $\omega C_0 V^2$ tends towards zero, and the ohmic losses V^2/R_∞ largely remain constant.

In the case of *medium frequencies*, the dipoles lag in following the field and perform mechanical work that is supplied to the medium as heat (the so-called dielectric losses or dissipation of heat). In the network model, this corresponds to the losses of the charging current in R_i. The capacitance measurement would result in a mean value. The dissipation factor shows a maximum of polarization losses in the transition region, Figures 4.1-4.

4.2 Dielectric Parameters

In the following sections, dielectric parameters that are important in practice, such as *permittivity* ε_r (Section 4.2.1), *conductivity* κ (Section 4.2.2), *dissipation factor* $\tan \delta$ (Section 4.2.3) and *complex permittivity* $\underline{\varepsilon}^*$ (Section 4.2.4) are considered for insulating materials. The **measurement** of dielectric parameters is described in Section 6.4.1.

Widely different substances are grouped under the collective term **insulating materials,** which exhibit a common characteristic: relatively *low conductivity*, Figure 4.2-1. However, conductivities are still significantly different for gaseous, liquid and solid insulating materials.

Gases possess nearly *ideal dielectric properties,* although the electric strength is low: Besides the extremely low conductivity κ, the

constant permittivity $\varepsilon_r \approx 1$ and the low losses must especially be mentioned.

Liquid and solid dielectrics are characterized by a few common attributes:

- The *conductivity* is, generally, 3 to 6 orders of magnitude higher than for gases.
- *Permittivities* are generally higher than 2 and lower than 7 for common insulating materials. However, there are substances with significantly higher values, Figure 4.2-2.
- Permittivity, conductivity and losses are dependent on *temperature, frequency* and *stress duration.*
- The *losses* increase with the temperature and are greater for AC voltage than for DC voltage.

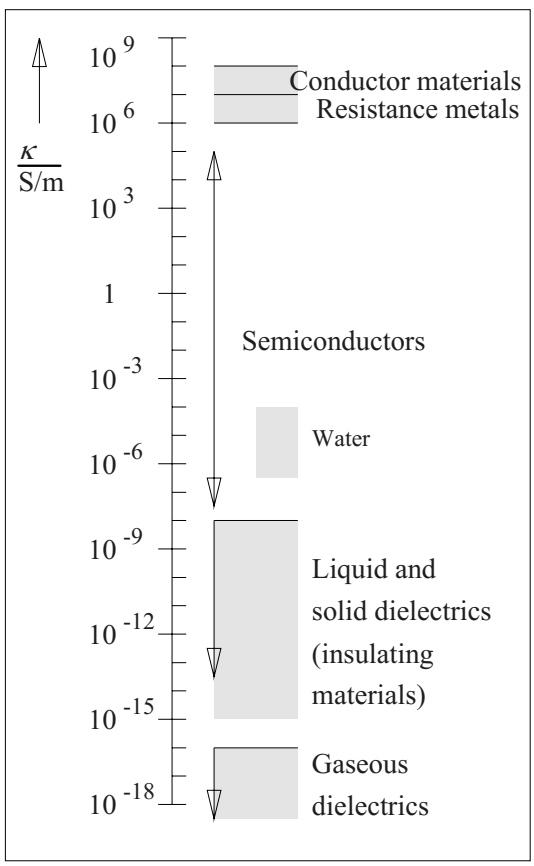

Figure 4.2-1: Electrical conductivity for conductors, semiconductors and insulating materials.

- The *electric strength* is lower for AC voltage stress than for DC voltage stress and impulse voltage stress.

4.2.1 Permittivity ε_r

The occurrence of relative permittivities $\varepsilon_r > 1$ through **polarization** of charge carriers and electrical dipoles in insulating materials has already been explained in detail in Section 2.4.1.2. Here, guide values for technically important materials and their basic dependences on different parameters are compiled.

4.2.1.1 Polarization Mechanisms

Materials which exhibit neither significant orientation polarization nor lattice polarization have permittivities in the range of 2. This includes, for example, mineral oil and many thermoplastic synthetic materials with symmetric non-polar molecules, Figure 4.2-1.

Several organic insulating materials with complex and stronger polarizable molecules and groups have higher permittivity of up to about $\varepsilon_r = 7$ owing to **orientation polarization**. Important examples are cellulose, duroplastic cast resin (e.g. epoxy resin) and a series of thermoplastic synthetic materials. Extreme values are attained, for example, for water ($\varepsilon_r = 81$) or glycerin ($\varepsilon_r = 40$).

In many inorganic insulating materials, **lattice polarization** leads to largely increased permittivity of up to $\varepsilon_r = 10$.

In dielectrics with interfaces orthogonal to the electric field (for example in capacitors or in transformers with pressboard barriers in oil), in materials with fillers (e.g. epoxy resin with quartz powder) and in mixed dielectrics, *interfaces between partial capacitances* with different time constants ε/κ occur (see Figure 2.1-16). For very low frequencies, only *partial capacitances with the higher resistances* are charged so that it results in a high capacitance

or a high resultant permittivity. Owing to the charges accumulated at the interfaces, we refer to **interfacial polarization** (see Figure 2.4-23).

4.2.1.2 Frequency Dependence (Dispersion)

Fig 4.2-3 shows the fundamental profile of permittivity ε_r and polarization losses against frequency from the electrical engineering viewpoint and the optics for different polarization mechanisms. The profiles correspond to the relationships explained in the example of a single polarization mechanism in the Section 4.1.2 and Figure 4.1-4.

In mixed dielectrics with **interfacial polarization** (that is with polarity reversals of the more resistive insulating layers), ohmic losses occur with increasing frequency since the more resistive layers are charge reversed via the resistances of the more conductive layers. Finally the total capacitance, the resultant permittivity and the losses decrease again, if the displacement current through all layers dominates the conduction current, so that the series connection of the partial capacitances is effective, Figure 4.2-3.

With increasing frequency, the dipoles can no longer follow the field with no lag and the permittivity decreases, Figure 2.4-5.

The *decay of the different polarization mechanisms* takes place in steps for different frequencies, starting from the **interfacial polarization** through the **orientation polarization** and the **lattice polarization** to **atomic polarization**, Figure 4.2-3. In particular, the decay of orientation polarization can occur in multiple steps depending on the size and mobility of the molecular groups that are polarized.

Note: For very high frequencies, the frequency dependence (dispersion) is no longer described through the *permittivity* ε_r as a function of frequency, but only with the quantities of optics as a *refractive index* against the wave length. Basically, the relationship

$$\varepsilon_r = n^2 \qquad (4.2\text{-}1)$$

is applicable, but only if frequency or wavelength coincide.

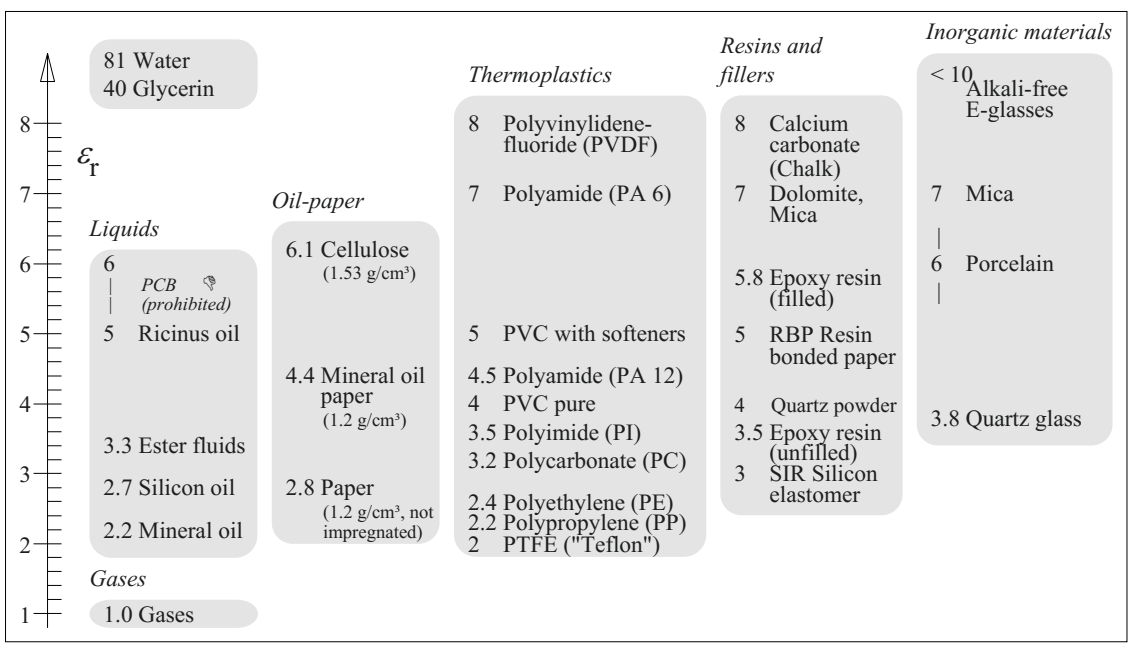

Figure 4.2-2: Permittivities of technically important materials at technical frequencies (up to 1 MHz) under atmospheric standard conditions (T = 20 °C, p = 1 bar) as orientation values.

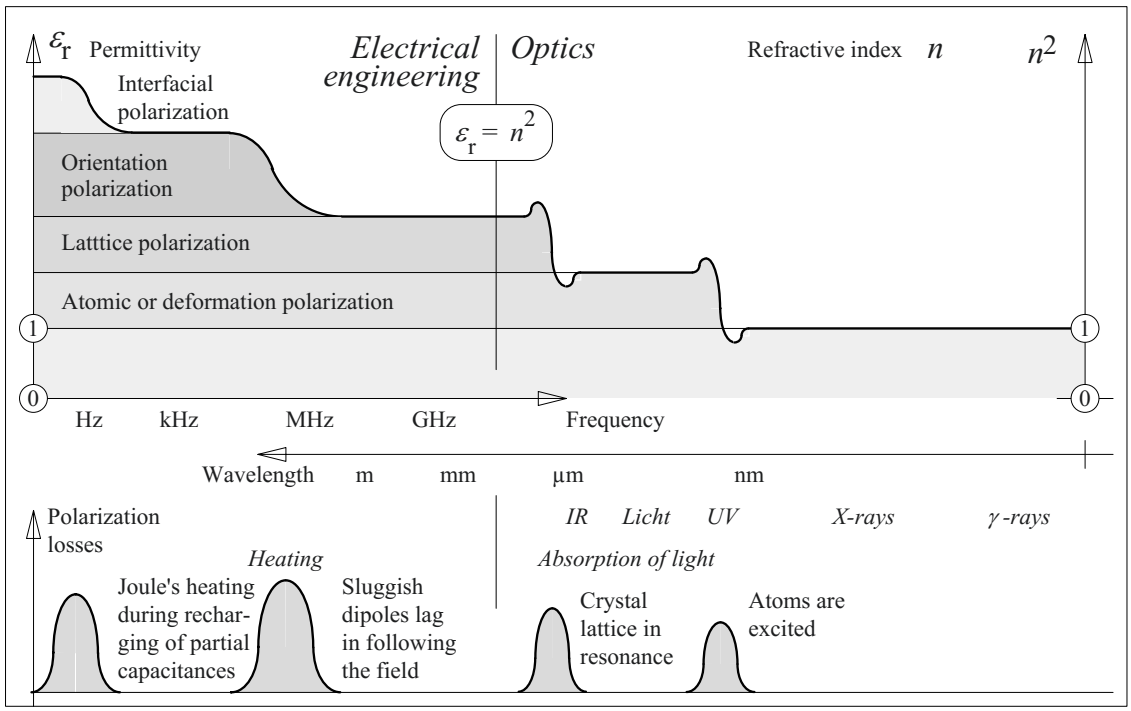

Figure 4.2-3: Dispersion (frequency dependence) of permittivity and polarization losses from the electrical engineering viewpoint (left side) and the optics viewpoint (right side), schematic representation.

Example: Water

In the visible light region, water has a refractive index $n = 1.333$. This corresponds to a permittivity $\varepsilon_r = n^2 = 1.8$. However, for low (electro-technical) frequencies, owing to pronounced orientation polarization of water molecules $\varepsilon_r = 81$. In the micrometer wave region, large polarization losses occur which can be used in so-called "microwave" chambers for dielectric heating of water based media.

4.2.1.3 Temperature Dependence

The temperature dependence of permittivity ε_r is primarily caused by *orientation polarization*, see Figure 2.4-5. With increasing temperature, the "frozen" dipoles at first become *mobile*, so that orientation polarization can be effective. The permittivity frequently increases in multiple steps, corresponding to the "defrosting" of different polarization mechanisms, Figure 4.2-4. At the same time, the increase of temperature can also lead to changes of the conductivities and to the inception of *interfacial polarization*.

The steps in the profile of the permittivity ε_r correspond to maxima of the *dissipation factor* $\tan \delta$, which however, can often no longer be or can only poorly be identified in the cumulative curve, Figure 4.2-4. At higher temperatures, the influence of the strongly increasing *conductivity* is dominant. For further increases in temperature, the *thermal agitation* disturbs the orientation of the dipoles, and ε_r again decreases, Figure 4.2-4.

Increases in the permittivity often result from a transformation of the material structure, for example close to the *glass transition temperature* T_g.

Example: Epoxy resin

The thermosetting epoxy resin loses its considerable mechanical strength above the *glass transition temperature* T_g without melting. As a result of the softening, polar molecule groups become more mobile and ε_r distinctly increases. Depending on the epoxy resin, T_g lies above approximately 100 °C. Even for temperature increases from 20 °C to 80 °C, there is an increase in permittivity by up to 20 %.

4.2.1.4 Field Strength Dependence

Often, permittivity, conductivity and dissipation factor increase with increasing field strength.

Note: For example, for *unfilled epoxy resins*, even for field strengths of approx. 42 kV/mm (that is, for about 20 to 50 % of the breakdown field strength), an increase in the permittivity by about 10 to12 % is observed (T = 20 °C); at 80 °C these values are increased to about 15 to 20 % [16]. By using fillers, the field strength dependences can be reduced.

In *liquid dielectrics* (e.g. in mineral oil) there are significant field strength dependences of *conductivity* and *dissipation factor*, already at low field strengths. This is caused by the field-dependent processes of charge carrier *drift*, charge carrier *generation* in the volume and charge carrier *injection* at the electrodes, see Section 4.3.2.3.

4.2.1.5 Mixed Dielectrics

In layered dielectrics and in mixtures of substances, the *resultant permittivity* $\varepsilon_{r\,res}$ can be calculated from the permittivities of the components.

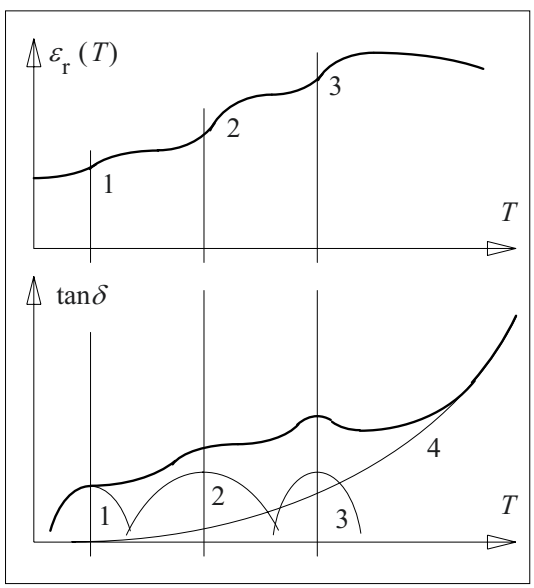

Figure 4.2-4: Temperature dependences of permittivity and dissipation factor for a material with three different polarization mechanisms (1 to 3) and with increase in conductivity (4).

For a **layered dielectric** with n layers and with interfaces orthogonal to the field, $\varepsilon_{\mathrm{r\,res}}$ results from the resultant capacitance, Eq. (2.4-28):

$$\varepsilon_{\mathrm{r\,res}} = d\,/\{d_1/\varepsilon_{\mathrm{r1}} + ... + d_n/\varepsilon_{\mathrm{rn}}\} \qquad (4.2\text{-}2)$$

For **mixtures of substances,** the resultant permittivity is derived from the relative percentage by volume v_1 to v_n as an approximation according to the empirically substantiated *Lichtenecker's law of mixtures*:

$$\ln \varepsilon_{\mathrm{r\,res}} = v_1 \cdot \ln \varepsilon_{\mathrm{r1}} + ... + v_n \cdot \ln \varepsilon_{\mathrm{rn}} \qquad (4.2\text{-}3)$$

Note: With the help of Eqs. (4.2-2) and (-3), the *temperature coefficient* of $\varepsilon_{\mathrm{r\,res}}$ can be determined from the temperature coefficients of the material components by differentiation with respect to the temperature T. By selection of materials with positive and negative coefficients, *compensation of temperature dependences* is thus possible. This is applied during the production of temperature stable capacitors.

Eqs. (4.2-2) and (-3) are applicable under the assumption of a predominantly dielectric displacement field. For very slowly changing processes (or for highly conductive mixture components), higher capacitances and *higher resultant permittivities* result when the more conductive partial capacitances can be regarded as being short circuited (**interfacial polarization**). In Eq. (4.2-2), this extreme case can be considered with $\varepsilon_{\mathrm{r}\,k} \to \infty$. In Eq. (4.2-3), $\varepsilon_{\mathrm{r}\,k} \to \infty$ does not give any meaningful result.

4.2.2 Conductivity κ

In the strict sense, conductivity refers to so-called *direct current conductivity (DC conductivity),* which according to Section 4.1.1, Eq. (4.1-8) and Figure 4.1-3, can be determined from the **end value** of the so-called polarization current, which is a steady-state conduction current. Conductivities in the broader sense that are determined (prematurely) from polarization currents after finite measuring periods, should actually be termed as "*apparent conductivities*", since their cal-

culation still includes polarizing current components that aren't conduction currents.

For stresses with *DC voltage,* for *transition processes* and for *low frequency* AC voltages, the formation of *electric fields* is (co)determined by the conductivities κ, if the conduction current cannot be neglected against the displacement current (see Section 2.4.4). Moreover, the conductivity leads to *losses* in the case of AC voltages, which at higher temperatures, often dominate compared to polarization losses (see Section 4.2.3).

Conductivity is caused by freely mobile charge carriers and is comparatively low in insulating materials, Figure 4.2-1. For the multitude of the conduction processes, differentiation into **ionic conduction** and **electron conduction** (N-type conduction) is common [16].

4.2.2.1 Conductivity in Gases

In *gases*, a very low conductivity is seen owing to a low number of ions that are created owing to collision ionization caused by radiation (see Section 3.2 and Figure 3.2-1). Radiation can increase the conductivity of gases by many orders of magnitude and this can be utilized in the radiation measurements.

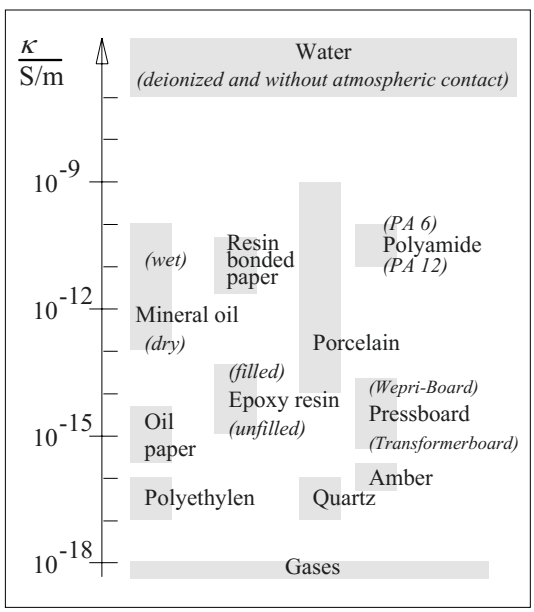

Figure 4.2-5: Conductivities at room temperature (orders of magnitude [2], [16], [82], without taking diverse parameters into consideration, see text).

Under standard atmospheric conditions, at very low field strengths, an **initial conductivity** of $\kappa_{initial} = 2.5 \cdot 10^{-14}$ to $5 \cdot 10^{-14}$ S/m for air is mentioned [16], [24]. This value results from the equilibrium between the generation and recombination of charge carriers. It is valid only for so long as there is no *saturation*, i.e. as the flowing current remains clearly below the *generation rate* for new charge carriers. For atmospheric air in the vicinity of the Earth's surface, the generation rate amounts to $\partial n/\partial t = 1$ / s cm³. The elementary charge $e = 1.6 \cdot 10^{-19}$ As and the air gap width d give rise to a **saturation current**

$$J_{sat} = e\,(\partial n/\partial t)\,d = 1.6 \cdot 10^{-19}\ \text{A/cm}^2\ \text{d/ cm}. \qquad (4.2\text{-}4)$$

If d = 10 cm, this current corresponds to an approximation value according to Eq. (3.2-1). The current attains the saturation current, according to $E_{sat} = J_{sat} / \kappa_{initial}$, even at field strength values in the range of V/m that are much below the relevant values for insulation. At higher field strengths, according to $\kappa = J_{sat}/E$, conductivities must be estimated with the constant saturation current value which gives rise to *extremely low values* (Figure 4.2-5) and extreme *non-linearity.*

Note: The conductivity of gases increases greatly owing to ionization. This can be induced, for example, by *photoionization* caused by radiation, by *collision ionization* at high field strengths (from approx. 2.5 kV/mm in normal atmosphere, see Section 3.2) or by *thermal ionization* at high temperatures (for example, in the vicinity of spark plugs in combustion engines).

4.2.2.2 Conductivity in Liquids

Ionic conduction dominates in liquids. Positive and negative ions are formed owing to dissociation of impurities. Free electrons play a role only at high field strengths; at low field strengths they are attached to molecules or they recombine with positive ions.

During step voltage response measurements on liquids, there are a falling current profiles, Figure 4.2-6. Here they do **not** relate to *linear polarization processes*, according to Figures 4.1-2 and -3, but to a *time-variant conductivity* due to *ion drift* and *charge accumulation* close to the electrodes, cf. Section 4.3.2.3.

Note: For insulating oils, *depolarization current measurements* often supply very small currents after only a few seconds. But after *polarity reversal*, higher currents are measured again. That is, the charge carriers wer accumulated as *space charge* close to the electrodes, and without applied voltage, they can be hold by the mirror charges on the electrodes for long periods. With the voltage applied already after a few seconds a low residual current is measured. It must therefore be attributed to a low **residual conductivity** [270], [271], [456], [486], cf. Section 4.3.2.3..

At lower field strength, insulating oils show an **initial conductivity** that results from the equilibrium between generation and recombination of charge carriers. Since in an *alternating field*, overall there is no removal of charge carriers, the initial conductivity is retained and we refer to it as **AC conductivity**, too.

For an *applied direct voltage*, the charge carriers migrate to the electrodes and they are accumulated there. Charge carrier density and conductivity decrease, Figure 4.2-6. That is, the number of freely mobile ions decreases steadily after some time. The **transit time** τ is dependent on the ion mobility μ, the oil gap width d and the field strength E:

$$\tau = d/(\mu \cdot E) \qquad (4.2\text{-}5)$$

Thus, the **conductivity of the liquid** is not only dependent on *temperature* (by way of the ion mobility μ) but also on *time, field strength* and *oil gap width*!

Example: For E = 1 kV/mm, d = 2mm and at room temperature, a transit time of τ = 6 s was measured for a new insulating oil [271]. In *HVDC insulations*, viewed in the field direction, there are significantly larger oil gaps in the centimeter range and hence transit times in the range of a few *minutes* are possible.

After the removal of ions, for an applied *constant field strength* which leads to the permanent removal of ions, a *new equilibrium* is set at a *lower level of conductivity* and this is also described as **DC conductivity**, Figure 4.2-6.

This **conductivity end value** is extremely dependent on field strength, as an intensely increased creation of new charge carriers is initiated for field strengths above 2 to 3 kV/mm [82], [271], Figure 4.2-7. The implied *minimum of conductivity* results from the opposing effects of a depletion of charge carriers and the generation of free charge carriers with increasing field strength, see also Section 4.3.2.3 and Figure 4.3-6.

Note: In **used oils**, increased conductivities occur owing to acids and metal ions that have been delivered by

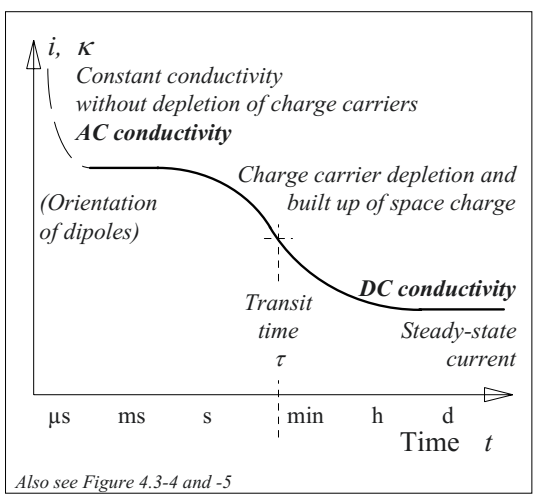

Figure 4.2-6: Reduction in current and conductivity with the stress duration in an insulating liquid.

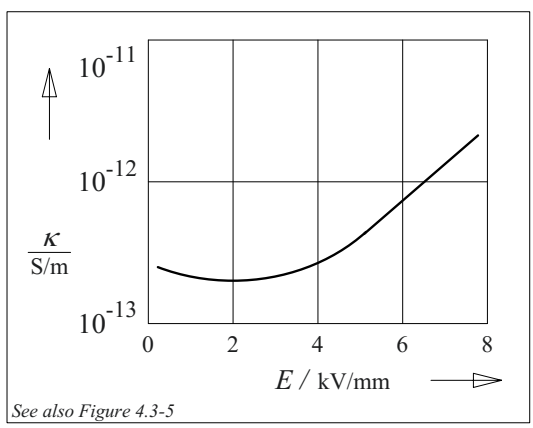

Figure 4.2-7: Field strength dependence of mineral oil conductivity at room temperature [82], [271].

electrodes. Thus, the described changes in conductivity can sometimes be masked.

Section 4.3.2.3 describes the **nonlinear conduction behavior** by *equivalent circuits* and by *multi-physics approaches*, Figures 4.3-5 and 4.3-6.

4.2.2.3 Conductivitiy in Solids

In *solids* too, charge transport at low field strengths takes place predominantly by ionic conduction. For high field strengths close to the electric strength limit (breakdown strength), also electron conduction is involved.

In **step voltage response measurements,** at room temperature, the conductivity can often be identified as a *steady-state end value* only after very long times of several hours, days or even weeks since the currents are still dominated by *polarization phenomena* even after long measuring periods. At higher temperatures, the end values are identified earlier.

By assuming *linear system properties*, the material characteristics can yet be determined from the step function response by approximating the current profile for $t > 0$ with exponential functions that are correlated with *RC*-elements (curve fitting), see Figure 4.2-8 as well as Section 4.1.1 with Figure 4.1-2. Thus, the entire information is incorporated *in a single measurement*.

$$i_\mathrm{p}(t) = \frac{V}{R_\infty} + \sum_i \left(\frac{V}{R_i} \mathrm{e}^{-\frac{t}{\tau_i}}\right) \qquad (4.2\text{-}6)$$

The current component V/R_∞ caused by the **conductivity** corresponds to a theoretical end value $i_\mathrm{p}(\infty)$, which can be developed more precisely with the help of *depolarization current* $i_\mathrm{d}(t)$: After the charging time $t = t_\mathrm{L}$, the equivalent capacitances C_i are charged by polarization current components to differently high fractions of the diagnostic voltage V:

$$v_{C_i}(t_\mathrm{L}) = V \cdot \left(1 - \mathrm{e}^{-\frac{t_\mathrm{L}}{\tau_i}}\right) \qquad (4.2\text{-}6a)$$

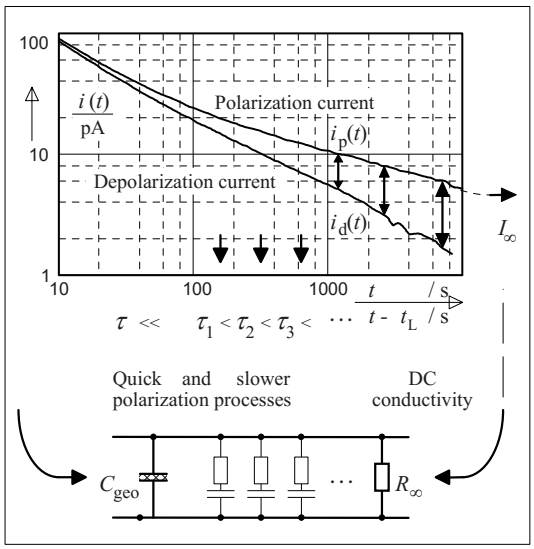

Figure 4.2-8: PDC measurement and equivalent circuit model for linear solid materials.

After short circuiting the test object, for $t > t_\mathrm{L}$, exponentially decaying *depolarization current components* occur and these are dependent on the attained charge status and these comprise system properties with the exception of DC resistance R_∞, which is short circuited during depolarization:

$$i_\mathrm{d}(t) = -\sum_i \left(\frac{v_{C_i}(t_\mathrm{L})}{R_i} \mathrm{e}^{-\frac{t-t_\mathrm{L}}{\tau_i}}\right) \qquad (4.2\text{-}6b)$$

If the polarization current and the depolarization current are shifted by t_L relative to each other and added, the related current components compensate each other partially:

$$i_\mathrm{p}(t) + i_\mathrm{d}(t + t_\mathrm{L}) = \frac{V}{R_\infty} + \sum_i \left(\frac{V}{R_i} \mathrm{e}^{-\frac{t}{\tau_i}} - \frac{v_{C_i}(t_\mathrm{L})}{R_i} \mathrm{e}^{-\frac{t}{\tau_i}}\right)$$

$$\overset{(4.2-6a)}{=} \frac{V}{R_\infty} + \sum_i \left(\frac{V}{R_i} \mathrm{e}^{-\frac{t+t_\mathrm{L}}{\tau_i}}\right) \qquad (4.2\text{-}6c)$$

Eq. (4.2-6c) represents a significantly *better approximation* for the end value of the polarization current caused by conductivity than Eq. (4.2-6), since the exponential terms result in smaller values. For very long measuring peri-

ods and charging times, that is for $t+t_L >> \tau_i$, the exponential terms can be largely neglected and the following is valid as an approximation:

$$i_p(t) + i_d(t + t_L) \approx \frac{V}{R_\infty} = I_\infty \qquad (4.2\text{-}6d)$$

If the magnitudes of the consecutive currents $i_p(t)$ and $i_d(t)$ are mutually shifted by the charging time t_L on the time axis, the described system-theoretical relationship can be recognized, Figure 4.2-8. The sum (or the difference of the magnitudes) of the two currents, which are mutually shifted by t_L, allows an improved *estimation for the end value of the polarization current*, even at earlier times t, Figure 4.2-8 (top).

Note: The conductivity end value can also be calculated by the **charge difference method** (CDM): charges result from the integration of the measured currents. The charge difference forms approximately a straight line increasing with time, and the gradient converges relatively rapidly towards the conductivity end value, Section 6.4.1.3, Figure 6.4.1-5, [427], [392], [428]. This type of conductivity determination is advantageous for diagnostic measurements for which there is not enough time as well as for overlying disturbances which can averaged out by integration.

Note: In Figure 4.2-8, slower polarization processes are represented by *RC*-elements. The vacuum capacitance C_0 and quickly changing polarization processes, which cannot be recorded for a step function response measurement with finite rise time, are summed in the so-called geometrical capacitance C_{geo}, see Figure 4.3-2.

a) Oil-impregnated cellulose products

Oil-impregnated cellulose is an important group of materials, which are used in the form of **impregnated insulation paper** (OIP oil-impregnated paper) and also as **pressboard**. For dry materials, the conductivities determined according to Eq. (4.2-6d) are only slightly dependent on the **field strength** in the range of 1 to approx. 20 kV/mm. For higher field strengths, an *increase in conductivity* by about 20 % at 30 kV/mm was observed, perhaps caused by the non-linear characteristic of the insulating oil. [271].

The conductivity of impregnated paper increases with the **water content** w. For wetted samples, on the basis of preliminary laboratory examinations for new material [234], [231], an exponential relationship is assumed, according to which the end value of DC conductivity

$$\kappa_{board}(\infty) \approx \frac{\kappa_{oil}(\infty)}{K_1} + K_2 \cdot e^{\frac{w}{K_3}} \qquad (4.2\text{-}7)$$

is dependent both on the *water content* w of the board or paper as well as on the *conductivity of the impregnating oil* $\kappa_{oil}(\infty)$, Figure 6.4.7-4. This corresponds to a conduction current along *moisturized fibers* and background conductivity due to *oil-filled capillaries*.

Note: The constants $K_1 = 300$, $K_2 = 0.00018$ pS and $K_3 = 0.714$ % are *guideline values* only for new materials *at room temperature.* For other temperatures, a **temperature correction**, according to Eq. (4.2-9) is necessary.

Water content and **ageing products** or **deterioration products** do not only increase conduction currents but also *polarization currents*. Depending on the polarization mechanism, the increase occurs in the time range of seconds, see Figure 6.4.7-9, or even after very long periods [392], see Section 6.4.7.6 b). Thus, not only *conductivity* but also *RC elements* for the description of polarization according to the Figures 4.1-2 or 4.2-8 must be adapted depending on the state of the material.

b) Highly polymerized substances

In *highly polymerized substances* such as polyethylene, polypropylene or epoxy resin, the conductivity is comparatively very low, Figure 4.2-5. Freely moving ions are present in much lower concentration than in oil-impregnated pressboard or paper. Freely moving electrons are not available even for high field strengths. Charge transport is rather affected by so-called “hopping” of electrons from one trap to the next. This results in extremely reduced charge carrier mobility.

Note: Since no regular crystal structure is generally present, the *energy-band model* with valence band and conduction band is not applicable to high polymer insulating materials. Owing to irregularities in the crystalline structure, there are a large number of *traps* between the unoccupied conduction levels, in which the electrons

are no longer attached to a specific atom, and the occupied valence levels. The traps are partly occupied by electrons (donor states) and are also partly unoccupied. For current conduction, the electrons must not be raised from the low lying valence levels to the conducting levels. Electrons in traps are raised to the conduction level and can again settle down in other traps. Under the effect of the field, "*hopping*" occurs in the direction of the field.

Note: In **composite materials**, a higher conductivity is possible even for high polymer basic material if, for example, fibers that are admixed with it are conductive either intrinsically or owing to wetting. In **silicone materials**, based on the admixture of lower molecular components (silanes), ionic conductivity can be present to a certain extent.

c) Porcelain

Porcelain and ceramics, depending on the mixture components used, can exhibit differently high ionic conductivities which are generally quite large in comparison with other insulating materials, Figure 4.2-5.

4.2.2.4 Influence of Field Strength and Temperature

The order of magnitude of conductivities can be stated only very inaccurately for different materials, Figure 4.2-5. The conductivity is dependent on the **parameters** *stress duration, field strength, temperature, water content, purity, and material composition*. Therefore, the conductivity can easily fluctuate over some orders of magnitude, despite of apparently similar conditions. Determining reliable values presents a serious problem, especially in field calculations for HVDC-transmission devices [7], [10], [82], [271] (see Section 2.4.4).

With time, charge carrier depletion in an insulating material volume results from the withdrawal of mobile charge carriers for the electrodes. It can be observed as **time dependence** of electrical conductivity, especially for fluids, see Section 4.2.2.3. Therefore, it is often difficult to compare the conductivity values.

With increasing **field strength**, the conductivity is at first constant. For *liquids,* even conductivity minima at 1 to 2 kV/mm are observed [271]. Probably, available ions here are exhausted by the field with no new ions being formed. In the case of higher field strengths, the conductivity in liquids increases owing to additional ions as a result of dissociation processes and by injection of electrons from the cathode, Figure 4.2-7. In mineral oil, the increase is from field strengths of about 2 kV/mm at 20 °C and from about 0.8 kV/mm at 70 °C. Significantly higher values are applicable for synthetic insulating liquids [16]. As an approximation, an exponential law with positive exponent m is applicable for constant temperature:

$$\kappa = \kappa_0 \cdot (E/E_0)^m \qquad (4.2\text{-}8)$$

In *solid insulating materials*, the field strength dependence is significantly weaker.

For increasing **temperature**, the ion mobility and the number of electrons raised to the conduction levels exponentially increase. For both ionic conduction as well as for electron conduction, the so-called Arrhenius equation

$$\kappa = \kappa_\infty \cdot e^{-W/kT} \qquad (4.2\text{-}9)$$

can be determined with the material specific *activation energy W* and with the Boltzmann constant $k = 1.3807 \cdot 10^{-23}$ J/K. In a logarithmic representation, straight lines result, Figure 4.2-9. With the help of the presented examples, the following statements can be made:

- The increase in conductivity with temperature can amount to 4 to 5 orders of magnitude between *ambient temperatures* and *operating temperatures*.
- Conductivities of *different substances* can vary by several orders of magnitude.
- The *conductivity ratio* between different substances can vary substantially with increasing temperature.

This results in serious technical consequences:

Example 1: Thermal stability: The exponential increase in conductivity leads to an exponential increase in *dielectric power loss*, and hence in unfavorable thermal conditions a *thermal breakdown* according to Figure 3.5-3 can be initiated (see Section 3.5.2). Insulations

with relatively high losses (e.g. resin-bonded paper, various resins), poor heat dissipation (solid, unfilled insulating materials), greater insulation thickness (for voltages of a few 100 kV) and high ambient temperatures (e.g. in hot transformer oil) are crucial.

Example 2: Field displacement in pressboard barriers at DC voltage: In layered dielectrics, *pressboard barriers* of transformerboard *under oil* are *extremely highly stressed* by fields orthogonal to the interfaces. The barriers must practically insulate the entire voltage, whereas the *oil gaps are largely unloaded*, Figure 2.4-23.

Example 3: Barrier systems for a direct voltage bushing: Fig 2.4-28 shows a bushing in a barrier system of poorly conductive pressboard (transformerboard) in more conductive oil. According to Figure 4.2-9, the conductivity ratio between oil and pressboard amounts to about 1000:1 at *room temperature*. A *uniform potential distribution* in the axial direction thus results in the oil gap. At an *operating temperature* of 100 °C, the conductivity ratio reduces to about 30:1. The potential grading effect of barriers is thus greatly reduced. The radial resistance must be maintained high enough, even at operating temperatures, by using an *adequate number of barriers*. *Temperature gradients* can cause problems as they can lead to conductivity gradients and *field displacements*.

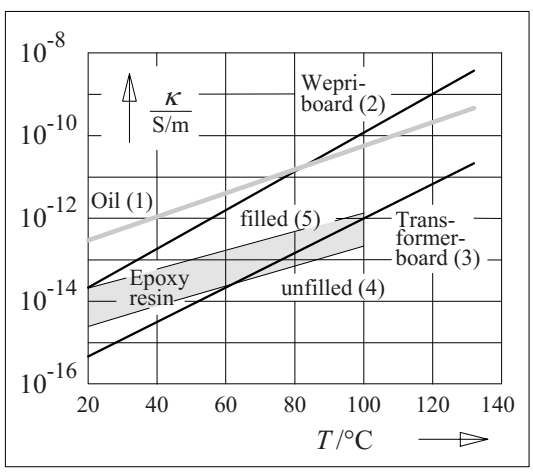

Figure 4.2-9:Temperature dependence of apparent conductivity at E = 0.5 kV/mm (low field area).
(1) Mineral oil, steady-state values [82].
(2), (3) Pressboard (Wepri board and Transformerboard), steady-state values [82].
(4), (5) Epoxy resin (unfilled and filled), 5 minutes values [16].
Note: The steady-state conductivity values are much lower than the 5 minutes conductivity values.
Note: Bisphenol-A epoxy resin with liquid dicarboxilic acid anhydride hardeners and aminic accelerator (4), filled with 350 parts per weight of Al2O3.

4.2.3 Loss or Dissipation Factor tan δ

For a *dielectric at AC voltage*, the current $\underline{I}$ of the voltage $\underline{V}$ leads by an angle of approximately $\varphi \approx 90°$, Figure 4.2-10. Owing to polarization losses and conductivity losses, the phase angle φ deviates by a "*loss angle*" δ from 90°. The current component $\underline{I}_\delta$ ("in-phase current", "active current") is in phase with $\underline{V}$ and results in the real power that is dissipated in the dielectric, i.e. the dielectric *power loss* $\underline{P}_\delta$. The current component $\underline{I}_C$ leads $\underline{V}$ by 90° and results in *capacitive reactive power* $\underline{Q}_C$.

According to Figure 4.2-10, the loss angle δ is defined by the loss factor (dissipation factor):

$$\tan\delta = \frac{I_\delta}{I_C} \quad . \tag{4.2-10}$$

With the power quantities

$$P_\delta = V \cdot I_\delta \tag{4.2-11}$$

and

$$Q_C = V \cdot I_C \tag{4.2-12}$$

the *loss* (*dissipation*) *factor* is also given by

$$\tan\delta = \frac{P_\delta}{Q_C} \quad . \tag{4.2-13}$$

The **loss factor** (dissipation factor) tan δ therefore also specifies the ratio of dielectric power

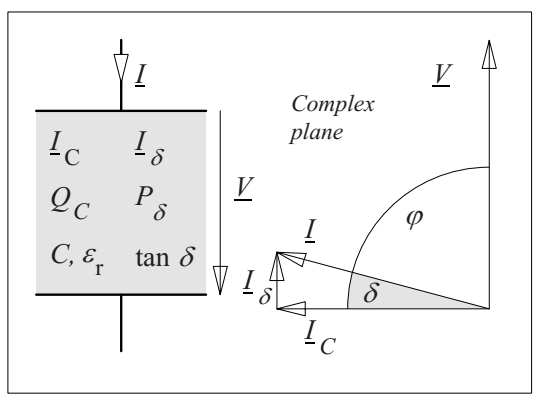

Figure 4.2-10: Description of lossy dielectrics with active current, power loss and loss factor (dissipation factor) using the complex AC calculation methods and phasor diagrams.

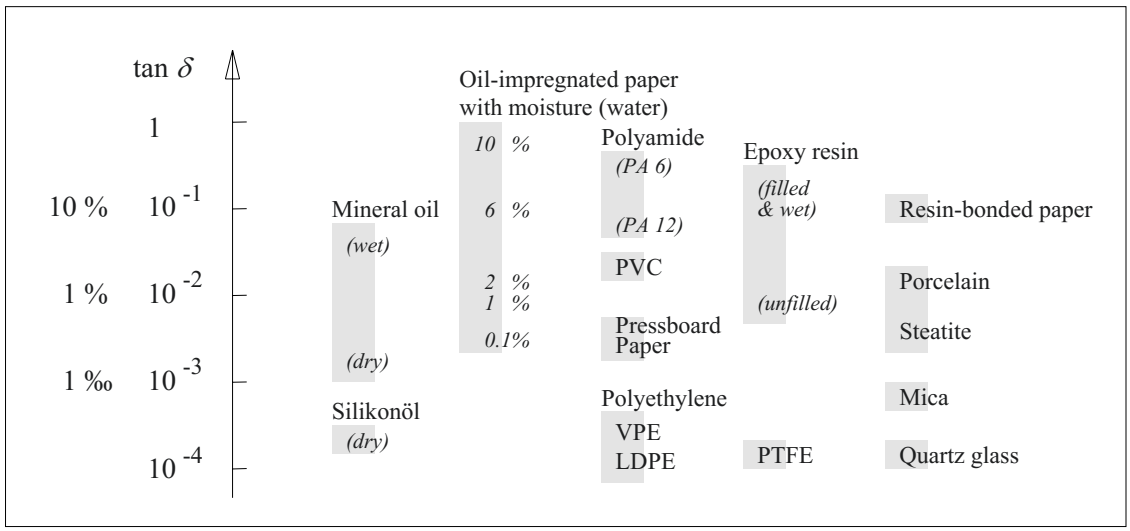

Figure 4.2-11: Dissipation factors (loss factors) at power frequency (50 Hz) and room temperature.

loss P_δ to capacitive reactive power Q_C in a dielectric. If the capacitive reactive power is known, the dielectric power loss can be directly stated with the dissipation factor:

$$P_\delta = (\tan\delta)\cdot Q_C \qquad (4.2\text{-}14)$$

Note: In the English language, the quantities **loss angle** δ, **loss factor** tan δ, **dissipation factor** cot φ and **power factor** cos φ are used for the description of dielectric losses, Figure 4.2-10. tan δ and cot φ are identical, and for a small angle δ, even the *power factor* cos φ can be compared, Table 4.2-1.

Table 4.2-1: Description of dielectric losses:

δ **Loss angle**	0.0573°	0.573°	5.71°	45°
tan δ **Loss factor**	10^{-3}	10^{-2}	0.1	1
cot φ **Dissipation factor**				
cos φ **Power factor**	10^{-3}	10^{-2}	0.0995	0.707

Nevertheless, **dissipation factor** is a very common wording in *high voltage engineering*, and it will be used predominantly in this book, instead of **loss factor**.

The dissipation factor tan δ is a *material parameter*, which according to Eq. (4.2-13) is determined by the *polarization losses and the conductivity losses*, Figure 4.2-10. The dissipation factors are greater than is to be expected on the basis of *DC conductivity*. In the case of liquids, this is because *AC conductivity* is larger than the DC conductivity (see Figure 4.2-6). Especially for solids, the dissipation factor includes additional polarization losses that occur largely owing to *orientation polarization* and *interfacial polarization*.

Figure 4.2-11 shows that substances which have relatively high permittivity owing to *orientation polarization* (for example, PVC, polyamide, epoxy resin, cellulose, resin-bonded paper, see Figure 4.2-2), also exhibit relatively large (polarization) losses. **Moisture** results in a great increase in losses owing to water molecules that can be easily polarized as well as owing to an increase in conductivity. This is especially crucial for *moisture sensitive substances* such as paper, pressboard, polyamide and reinforced and filled synthetic materials.

This results in strong dependences on the parameters such as **frequency** and **temperature**, Figures 4.2-13 and 2.4-5.

The dissipation factor increases with the conductivity and hence possibly also with the **field strength**. On inception of strong partial discharges there is a sudden increase in losses ("*partial discharge bend*"), and some decacades ago, this was considered as a rough indicator for the occurrence of partial discharges. This is still of practical importance in partial

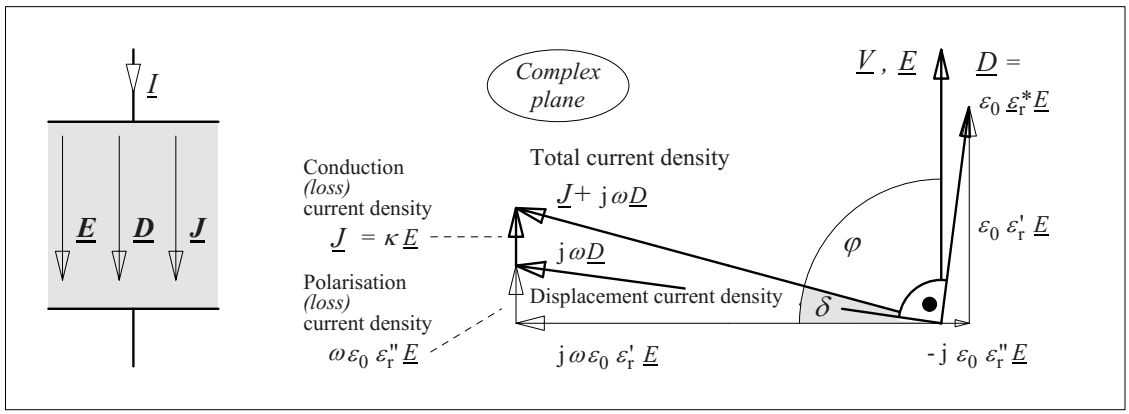

Figure 4.2-12: Description of lossy dielectrics with conduction losses and polarization losses by means of phase shift of field quantities in a complex phasor diagram (for AC voltage).

discharge-resistant insulations of generators and resin-bonded paper bushings.

Generally, materials with low dissipation factors (generally under 10^{-2} = 1 %) are used for *high voltage insulations*, in order to avoid **thermal instabilities** and thermal breakdowns. In that connection, it must be noted that increased *operating temperatures* prevail in devices, which also lead to distinctly increased losses. It is a problem that the dissipation factor values measured *at ambient temperature* still do not give any indication of dissipation factors and thermal stability at increased operating temperatures. Along with the *material properties*, the *insulation design* and *heat transmission conditions* also play a decisive role in evaluating the thermal stability, see Section 3.5.2.

4.2.4 Complex Permittivity

For a material with losses owing to conductivity *and* orientation polarization, it is assumed that the *electrical polarization* $P(t)$, according to Eqs. (2.4-7) and (4.1-4), shows a lag in following the electric field $E(t)$. For a *single* polarization mechanism with the *relaxation time* τ, and for example assuming a step field $E(t) = E_{stat} \cdot \sigma(t)$, an exponential approximation to the stationary end value is obtained, Eq. (4.1-5).

Note: Polarization P should not be confused with the power loss P_{δ}.

In the *alternating electric field*, the phase lag in polarization is expressed by a *phase shift* between the electric field $E(t)$ or the voltage $v(t)$ and the electrical displacement density $D(t)$. That is, in a *(complex) phasor diagram*, the complex phasor for the r.m.s. value $\underline{D}$ lags in phase with regard to the complex phasors for the r.m.s. values $\underline{E}$ or $\underline{V}$, Figure 4.2-12.

Note: By assuming a uniform field or by taking very small field areas into consideration, the *vectorial character* of field quantities $\underline{\boldsymbol{E}}$, $\underline{\boldsymbol{D}}$ and $\underline{\boldsymbol{J}}$ needs not be considered.

Formally, the phase lag of $\underline{D}$ can be described with a decomposition into two phasors $\varepsilon_0\varepsilon_r' \underline{E}$ and $-j\varepsilon_0\varepsilon_r'' \underline{E}$. The first phasor corresponds to the standard displacement density that is not out of phase. the second phasor lags by -90° corresponding to the multiplication with –j. With the approach

$$\underline{D} = \varepsilon_0 \underline{\varepsilon_r}^* \underline{E} \qquad (4.2\text{-}15)$$

the phase displacement is thus described by a **complex permittivity**

$$\underline{\varepsilon_r}^* = \varepsilon_r' - j \cdot \varepsilon_r'' . \qquad (4.2\text{-}16)$$

The *real part* ε_r' equals the standard (relative) permittivity ε_r; the *imaginary part* $-\varepsilon_r''$ can be correlated with the polarization losses via the

phasor diagram of current densities, Figure 4.2-12:

The displacement current density $j\omega\underline{D}$ which leads $\underline{D}$ by 90° is composed of *purely capacitive* component $j\omega\varepsilon_0\varepsilon_r'\underline{E}$ and polarization *(loss)* current density $\omega\varepsilon_0\varepsilon_r''\underline{E}$. With the conduction *(loss)* current density phasor $\underline{J} = \kappa\underline{E}$, *total* current density $\underline{J} + j\omega\underline{D}$ results.

According to Figure 4.2-12, the *dissipation factor* (loss factor) is given by

$$\tan\delta = (\kappa + \omega\varepsilon_0\varepsilon_r'')/(\omega\varepsilon_0\varepsilon_r') = \tan\delta_L + \tan\delta_{Pol}\,. \qquad (4.2\text{-}17)$$

The dissipation factor components that have to be assigned to the conductivity losses and polarization losses are

$$\tan\delta_L = \kappa/(\omega\varepsilon_0\varepsilon_r') \quad \text{and} \quad \tan\delta_{Pol} = \varepsilon_r''/\varepsilon_r'\,. \qquad (4.2\text{-}18)$$

Figure 4.2-13 represents the profile of dissipation factor $\tan\delta$ and relative permittivity $\varepsilon_r = \varepsilon_r'$ against **frequency** and against **temperature**. The analytical derivation, assuming a lag in dipole orientation according to Eq. (4.1-4), results in [25]

$$\varepsilon_r' = \varepsilon_\infty + (\varepsilon_{stat} - \varepsilon_\infty)/[1 + (\omega\tau)^2] \quad \text{and}$$
$$\varepsilon_r'' = \omega\tau\cdot(\varepsilon_{stat} - \varepsilon_\infty)/[1 + (\omega\tau)^2]\,. \qquad (4.2\text{-}19)$$

In this, the decrease in ε_r' with *frequency* can be noticed. The loss-determining component ε_r'' has a maximum at the frequency $f = 1/\tau$.

Instead of a theoretical derivation, the presented curves should be made physically plausible.

Frequency dependences:

At low frequencies, the dipoles follow the field practically without any lag, and depending on the temperature this results in a static permittivity ε_{stat}, Figure 4.2-13 (top left), see also Figure 4.2-3. Above the frequency $f = 1/\tau$, the dipoles can no longer follow the rapidly changing field and the *permittivity* falls to ε_∞.

The *polarization losses* have a *maximum* in the frequency range of $f = 1/\tau$, because although the dipoles can still follow the field, impacts and other interactions cause a lag (phase shift) with a *withdrawal of energy*. In the case of lower frequencies $f << 1/\tau$, there is no phase displacement between $\underline{D}$ and $\underline{E}$; for higher frequencies $f >> 1/\tau$, the dipoles cannot move at all, Figure 4.2-13 (bottom left). With increasing temperature, the dipoles become more mobile, the relaxation time τ decreases and the loss maximum is shifted to higher frequencies.

The *conductivity losses* must be superimposed on the polarization losses. Owing to Eq. (4.2-18), the dissipation factor $\tan\delta_L$ infinitely increases with decreasing frequency $\omega \to 0$ because the ratio of power loss to reactive power increases accordingly.

Temperature dependencs:

The *permittivity increases* at first with increasing temperature because the dipoles become more mobile. For this, with increasing frequency, ever higher temperatures are necessary to make the "frozen" dipoles sufficiently mobile, Figure 4.2-13 (top right).

With further increasing temperature, the thermal agitation disturbs the orientation of dipoles and hence the permittivity again decreases.

In the range of increasing dipole mobility, a maximum of *polarization losses* results, Figure 4.2-13 (bottom right).

The superimposed *conductivity losses* with the conductivity $\kappa(T)$ according to Eq. (4.2-9) lead to an exponential increase in the dissipation factor with temperature. According to Eq. (4.2-18), a greater increase must be expected at lower frequencies.

Practical curves:

Practical curves often comprise a *superimposition* of various polarization mechanisms. Thus, they are related more to the representation in Figure 4.2-4. Moreover, there are large differences between different *materials*, different *material states* (e.g. ageing, moisture) and different *insulation designs* (interfacial polarization). Loss maxima and step levels in the permittivity profile can frequently no longer be clearly identified.

Note: For the practically important **oil-impregnated paper**, the dissipation factor reduces for increasing temperatures up to about 50 °C and beyond that it again sharply increases. This "*bath-tub curve"* has a favorable impact on the *thermal stability* of oil-impregnated insulations at increased operating temperatures.

Unfortunately, the dissipation factor minimum disappears for wetting and ageing of insulation owing to which wetting and ageing represent a risk for the thermal stability of insulations.

Harmonics:

Often, not only the dissipation factor at a certain frequency has to be considered: **harmonics in the network** can lead to significant reactive currents and losses. Also **power electronic switching impulses** with steep switching edges always exhibit a pronounced *harmonic spectrum* with high amplitudes V_i. In these cases, the total dielectric power loss results from the superposition of loss components resulting from the individual harmonics, wherein the insulating material is considered as linear.

$$\begin{aligned} P_\delta &= P_{\delta 0} + P_{\delta 1} + P_{\delta 2} + ... \\ &= \sum_{i=0}^{\infty} (\tan\delta)_i \cdot (\omega_i C \cdot V_i^2) \end{aligned} \qquad (4.2\text{-}20)$$

Since the reactive power $\omega_i C \cdot V_i^2$ increases proportionally to the frequency ω_i, the associ-

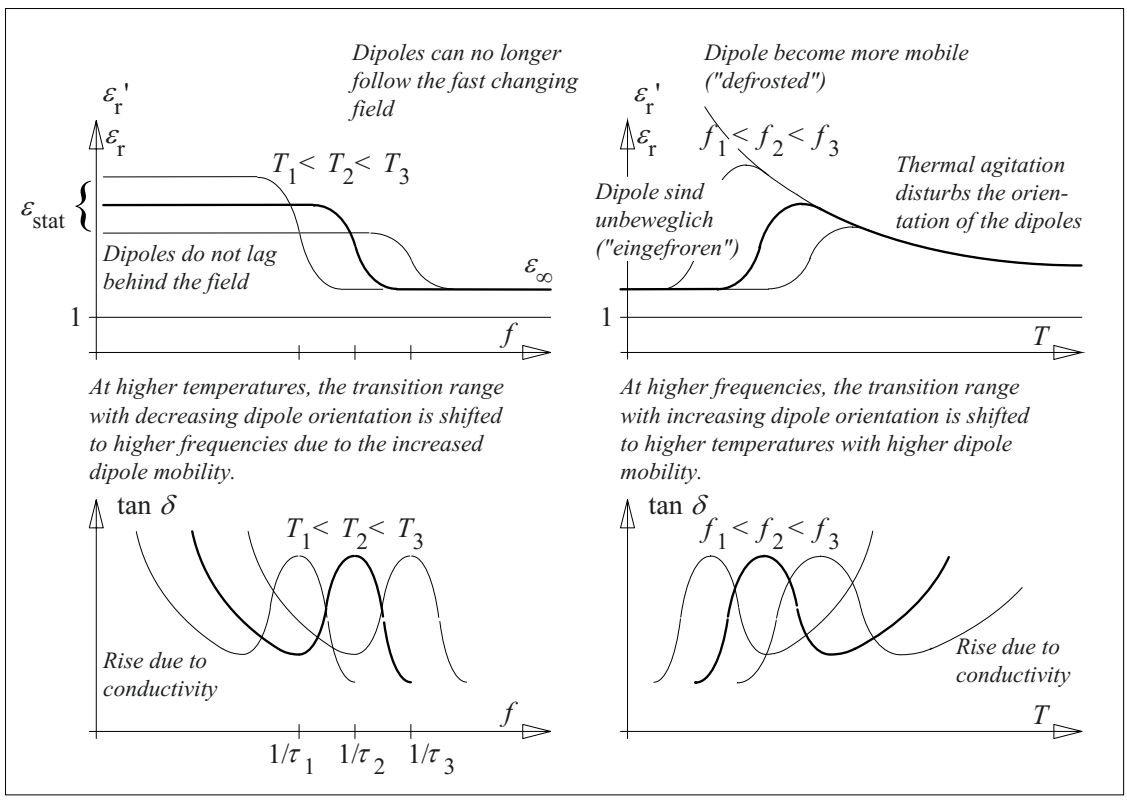

Figure 4.2-13: Basic dependence of relative permittivity and loss factor (dissipation factor) on the parameters temperature and frequency for a dielectric with orientation polarization (schematic, see Figure 2.4-5).

ated loss components also increase. In addition, the dissipation factor $(\tan\delta)_i$ often also increases with frequency, especially since various polarization mechanisms normally overlap, which is not represented in Figure 4.2-13.

Thus, for high harmonic content, unexpectedly **high thermal stresses** can occur owing to dielectric losses, along with the risk of *thermal instability* (*thermal breakdown*), see Section 3.5.2.

Example: The *oil-paper capacitors* formerly used for **reactive current compensation** were thermally capable of coping with the losses for the fundamental component $f = 50$ Hz. However, the increasing harmonic content in the network has led to an intolerable thermal load. As a result, the oil-paper dielectric has been replaced by *low loss synthetic dielectrics*.

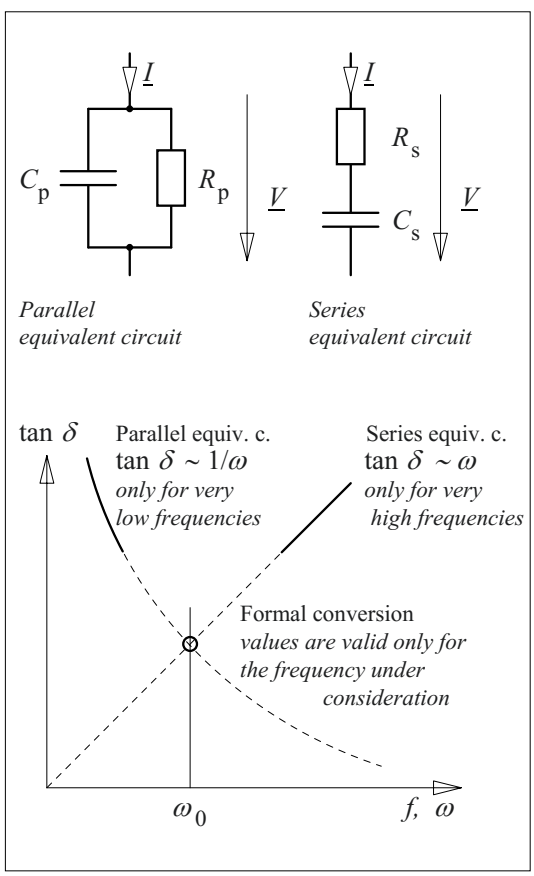

Figure 4.3-1: Parallel equivalent circuit and series-equivalent circuit (top) with conversion at a fixed frequency (bottom).

Note: In the case of **rectangular switching impulses,** the losses can be computed from the harmonic spectrum according to Eq. (4.2-20). An alternative would be a **calculation in the time domain**, by computing the loss energy ΔW_p created by the polarization during a switching operation. The loss energy is calculated from the polarization current:

$$\Delta W_p = \int V \cdot i_p(t) \cdot dt \qquad (4.2\text{-}21)$$

With the *switching frequency*, the number of *switching processes for each time unit* and from that, the *power loss* is calculated. For a dissipation factor assumed to be independent of frequency, a power loss created by a *square wave voltage* is about four times greater than that created by a *sinusoidal voltage* of equal frequency [284].

4.3 Description of Dielectrics

Simple equivalent circuits of capacitances and resistances can *only* describe the properties of dielectrics in an *incomplete way*.

Nevertheless, the **classic parallel and series equivalent circuits** (Section 4.3.1) are still a valuable calculating aid if restricted to *one* frequency or a narrow frequency range. The flaw in simple equivalent circuits lies in their inability to correctly simulate complex physical interrelationships. Extended material-related equivalent circuits, which can be determined from **dielectric systems responses** in *time domain* or *frequency domain*, offer a better simulation of dielectric properties (Section 4.3.2). For the description of **insulation systems** of various materials, multiple equivalent circuits must be combined in a geometry-oriented arrangement (Section 4.3.3).

4.3.1 Classic Parallel and Series Equivalent Circuits

Parallel and series equivalent circuits consist of a single *equivalent capacitance* and a single *equivalent resistance* respectively, Figure 4.3-1. The **dissipation/ loss factors**, according to Eq. (4.2-10), result from the ratio of real power (that is converted into resistance) to

reactive power (that is assigned to the capacitance).

For the *parallel equivalent circuit*

$$\begin{aligned}\tan\delta &= P_\delta / Q_C \\ &= [V^2 / R_\mathrm{p}] / [\omega C_\mathrm{p} \cdot U^2] \\ &= 1/(\omega C_\mathrm{p} R_\mathrm{p}) \,. \end{aligned} \qquad (4.3\text{-}1)$$

Note: The hyperbolic decrease in the dissipation factor with frequency ~ $1/\omega$ included in the above would only be physically correct for materials whose losses can be assigned exclusively to a constant *conductivity*. Generally, this may only be assumed for very low frequencies. In the limiting case of ω approaching zero, even the reactive power approaches zero, but the power loss remains finite owing to the ever available conductivity, so that the dissipation factor tends towards infinity. Practically, this is important below mHz.

The *series equivalent* circuit leads to

$$\begin{aligned}\tan\delta &= P_\delta / Q_C \\ &= [R_\mathrm{s} \cdot I^2] / [I^2 / (\omega C_\mathrm{s})] \\ &= \omega C_\mathrm{s} R_\mathrm{s} \,. \end{aligned} \qquad (4.3\text{-}2)$$

Note: The linear increase of dissipation factor with the frequency ~ ω present in the above would only be physically correct for arrangements whose losses can be exclusively assigned to a constant *series resistance*, for example on the basis of supply lines or contact resistances. However, this is not the case with pure dielectrics.

This means that both the equivalent circuits are *not* capable of correctly describing the **frequency dependence** of the dissipation factor, Figures 4.3-1 and. 4.2-12.

However, the *parallel equivalent circuit* enables the physically correct description of *conductivity losses.* Therefore, for very low frequencies, there is a correlation with the actual profiles.

The physical interpretation of a *series equivalent circuit* consists of an ideal capacitor that is connected through a *series resistance* which is not negligible. In particular, the capacitor impedance $1/(\omega C_\mathrm{s})$ decreases very sharply at high frequencies and R_s increases owing to the skin effect and may no longer be ignored.

The losses of any dielectric at *one* fixed frequency can be formally described by both the series equivalent circuit and the parallel equivalent circuit. However, the elements of the equivalent circuits, that is, C_p and R_p and C_s and R_s respectively, are applicable *only for the considered frequency*. A change in the frequency without adjusting the circuit elements leads to incorrect results!

For a specific frequency ω_0, a **conversion of the elements** of both the equivalent circuits is possible by equating the complex impedances $\underline{Z}_\mathrm{p} = 1/[1/R_\mathrm{p} + \mathrm{j}\omega C_\mathrm{p}]$ and $\underline{Z}_\mathrm{s} = R_\mathrm{s} + 1/(\mathrm{j}\omega C_\mathrm{s})$ and the dissipation factors, according to Eqs. (4.3-1) and (-2). From both the conditions, the following results for the equivalent capacitances

$$\begin{aligned} C_\mathrm{p} &= C_\mathrm{s} / (1 + \tan^2\delta) \\ \text{and} & \\ C_\mathrm{s} &= C_\mathrm{p} \cdot (1 + \tan^2\delta) \end{aligned} \qquad (4.3\text{-}3)$$

as well as for the equivalent resistances

$$\begin{aligned} R_\mathrm{p} &= 1 / (\omega C_\mathrm{p} \cdot \tan\delta) \\ \text{and} & \\ R_\mathrm{s} &= (\tan\delta) / (\omega C_\mathrm{s}) \\ \text{or} & \\ R_\mathrm{p} &= R_\mathrm{s} (1 + 1/\tan^2\delta) \,. \end{aligned} \qquad (4.3\text{-}4)$$

The equivalent capacitances C_s and C_p are therefore, not exactly equal. In practice, however, the difference is usually negligible in the case of dielectrics with dissipation factors $\tan\delta < 10^{-1}$.

In a dielectric with low losses, the p*arallel equivalent resistance* R_p is very large, according to Eq. (4.3-4). Very small values are obtained for the *series equivalent resistance* R_s.

Several equations can be used for the calculation of **power loss** P_δ of a dielectric:

Under the condition $C_p \approx C_s \approx C$, generally the following is applicable, according to Eq. (4.2-10)

$$P_\delta = Q_C \tan\delta = \omega C V^2 \tan\delta . \qquad (4.3\text{-}5)$$

In the *equivalent circuits* 4.3-1, the following results for the power loss

$$P_\delta = V^2 / R_p \quad \text{and} \quad P_\delta = R_s \cdot I^2 . \qquad (4.3\text{-}6)$$

For the *power loss density*, according to Eq. (4.3-5), considering an infinitesimal volume $\Delta V_{vol} = \Delta A \cdot \Delta x$ with uniform field $E = \Delta V/\Delta x$, the generally applicable relation is

$$\begin{aligned} p_\delta &= \Delta P_\delta / \Delta V_{vol} \\ &= \omega(\varepsilon' \Delta A/\Delta x)(E\,\Delta x)^2(\tan\delta) / (\Delta A\,\Delta x) \\ &= \omega\,\varepsilon_0\,\varepsilon_r'\,(\tan\delta)\,E^2 \\ &= \omega\,\varepsilon_0\,\varepsilon_r''\,E^2 . \end{aligned} \qquad (4.3\text{-}7)$$

Example: Coaxial cable

By means of the power loss density p_δ, the dielectric heat generation (power dissipation) P of a coaxial cable (length l, outer and inner radii R_a and R_i) can be calculated by integration over the volume of the cable. The electric field strength E in Eq. (4.3-7) is expressed by Eq. (2.3-21):

$$P = \iint_{V_{vol}} p_\delta \, dV_{vol} = \frac{\omega\varepsilon'(\tan\delta)V^2}{\ln^2\frac{R_a}{R_i}} \int_{R_i}^{R_a} \frac{1}{r^2} 2\pi r l \, dr$$

$$= \frac{2\pi l\,\omega\varepsilon'(\tan\delta)V^2}{\ln\frac{R_a}{R_i}} \qquad (4.3\text{-}7a)$$

For a PE cable with R_a/R_i = e, $\varepsilon' = \varepsilon_r \cdot \varepsilon_0$ = 2.3·8.85 pF/m and tan $\delta = 10^{-4}$, the following dielectric power dissipation at f = 50 Hz is given in dependence on the voltage V (r.m.s. line-to-ground voltage):

V_m, line-to-line in kV	12	24	36	123	245	420
V, line-to-ground in kV	6.93	13.9	20.8	71.0	141	242
P/l in W/km	0.19	0.77	1.74	20.3	80.4	236

It is interesting to note that the absolute value of the dielectric power dissipation does not depend on the absolute value of the cable diameter, but on the ratio of the radii only.

For a high-quality polymeric-insulated cable, the dielectric losses are very small and can often be neglected in comparison with the ohmic loss in the conductor. For an oil-paper-insulated cable with ε_r = 4.4 and tan $\delta = 3\cdot10^{-3}$, the dielectric power dissipation is approximately sixty times greater than that calculated above, and it can further increase during the ageing of the cable.

4.3.2 Description of Dielectric Material Properties

Generally, more complex dielectric material properties can be described by means of the **dielectric sytem response** according to Eq. (4.1-1). For practical applications, it is used for determination of *material-related equivalent circuits* or *physical description models* that represent dielectric properties much better than simple parallel or series equivalent circuits according to Section 4.3.1.

Important applications of equivalent circuits for the description of materials are in the area of *dielectric diagnostics*. Under this, one seeks to draw conclusions regarding the magnitude of the equivalent elements from dielectric measurements and correlate them with the material properties, in order to make statements about the insulation condition and the ageing condition, Section 6.4.7.

Another application is the description of *high voltage DC fields* and the related transition processes in which slow polarization occurs

and which can substantially influence the currents and fields, Section 7.2.1.

Solid materials can often be regarded as linear and are modeled with the help of **dielectric equivalent circuits** (so-clled material-related equivalent circuits), Section 4.3.2.1 and 4.3.2.2. *Liquid insulating materials* generally exhibit a distinct non-linear behavior and therefore must be described with suitable **functional relationships**, Section 4.3.2.3.

4.3.2.1 Linear Polarization Equivalent Circuit for Solid Materials

For *linear materials*, a linear equivalent circuit for describing different polarization mechanisms can be developed by expanding the basic parallel equivalent circuit, Figure 4.3-1 and 4.3-2. Many *solid materials* behave largely linearly with respect to field strength and hence *linear equivalent circuits* can be used. Strong **polarization** is often characteristic here. It causes *depolarization currents*, which exhibit similar current-time characteristics and similar magnitudes as the preceding polarization currents, cf. Figure 4.2-8. This can be described in the following way:

A linear material equivalent circuit consists of the vacuum capacitance C_0 and the insulation resistance R_∞ to allow for the dielectric constant ε_0 and the conductivity κ. The increase of the capacitance or the permittivity by material polarization as well as the occurrence of slower polarization mechanisms is taken into account by the parallel connection of *RC-elements* according to Figures 4.1-1 and -2. Here the series resistance R_i delays the charging and discharging of the additional capacitance C_i according to the time constant

$$\tau_i = R_i C_i \qquad (4.3\text{-}8)$$

in accordance with Eqs. (4.1-5) and (-6). τ_i corresponds to the *relaxation time constant*(s) for a polarization mechanism with the index *i*. The charging and discharging of C_i corresponds to the binding and release of charge during polarization and depolarization respectively.

Some of the polarization mechanisms have

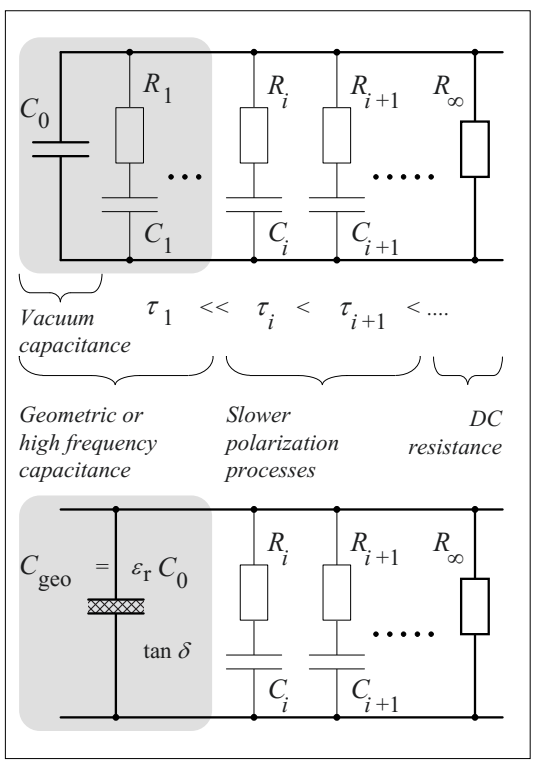

Figure 4.3-2: Equivalent circuit for the description of polarization processes in general and simplified form (top and bottom).

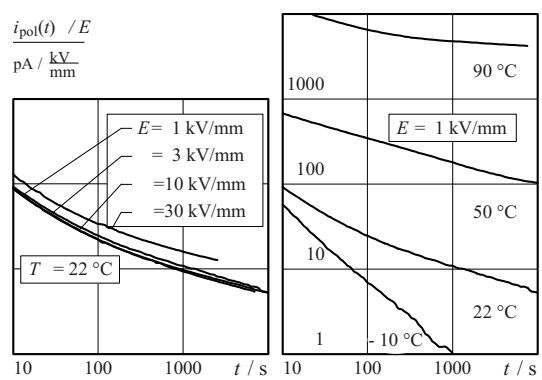

Figure 4.3-3: Field-strength dependence and temperature dependence of dielectric system responses for a dry oil-impregnated Transformerboard [271].

such small relaxation time constants that they need not be taken into account in the frequency domain that is under consideration. Therefore, the related series resistances can be ignored and the then parallel partial capacitances can be combined into a *"geometrical capacitance"* or a *"high-frequency capacitance"*

$$C_{\text{geo}} = \varepsilon_{\text{r}} C_0 . \qquad (4.3\text{-}9)$$

It must be noted here that this capacitance, depending on the frequency, can still exhibit losses (shades areas in Figure 4.3-2), which, for example, can be described with the help of a loss factor (dissipation factor) tan δ. Then, only *slower polarization mechanisms* are taken into account by *RC*-elements, Figure 4.3-2 (bottom).

The **elements of a dielectric equivalent circuit** can be determined by polarization and depolarization current measurements or step response measurements in the **time domain**, Figure 4.1-3. For this purpose, the charging current impulse must be integrated up to the time of interest, from which a *geometric capacitance* can be calculated. For longer durations, the *polarization elements* R_iC_i result from a curve-fit with exponential functions having different time constants τ_i, Figure 4.2-8. The *DC resistance* can be estimated according to Eq. (4.2-6) from the sum (or difference of magnitudes) of the polarization and depolarization currents that are displaced in an overlapping manner, without having to measure it for "infinitely long" periods.

According to system theory, it is equivalent to determine the *circuit elements* by **frequency domain analysis,** which is performed by the measurement of capacitance and dissipation factor or complex permittivity as a function of frequency. An equivalent circuit can then be generated from measured or calculated frequency responses by curve fitting.

In linear materials, the **equivalent elements** are generally suited to simulate *real polarization mechanisms* in a physically correct manner. Nevertheless, as the equivalent elements in practice are determined by *pure mathematical curve fitting*, they *cannot directly* be related to *particular physical polarization mechanisms*. That is, a single *RC* element could for example represent the superposition of several polarization mechanisms with similar time constants.

Polarization and conduction processes, dielectric system responses and equivalent circuit elements are primarily subject to variation with parameters such as *field strength*, *temperature* or *water content*.

Example: For a dry oil-impregnated **transformerboard** Figure 4.3-3 shows a specific *non-linearity* only at higher field strengths, probably caused by the non-linearity of the oil. Furthermore, there is a distinct *temperature dependence*, which especially manifests itself as a reduction in the time constants and an increase in the currents with increasing temperature.

The especially important dependence on temperature is looked at closely in Section 4.3.2.2.

4.3.2.2 Dependence on Temperature

The dielectric equivalent circuit according to Figure 4.3-2 can be used for the description of linear dielectric behavior of materials both in the *frequency domain* and in the *time domain*, i.e. also for the calculation of the frequency-dependent spectrum of dissipation factor or the time-dependent curve of the polarization current, Figure 4.3-4 (right) and (left). Here, the equivalent circuit elements and the associated *dissipation factor spectrum* as well as the associated *polarization current* are only valid for the currently considered temperature.

Note: The assumption of **linear material behavio**r is an *approximation* only. Nevertheless, it is often appropriate mainly for *solid materials* and at *low field strengths*.

It is already shown in Figure 4.2-13 (bottom left) that the *dissipation factor spectrum* is shifted with temperature rightwards to higher frequencies because of *increasing conductivity* of the material and *increasing mobility* of the dipoles. Figure 4.3-4 (left) shows a typical ex-

tract (schematic), e.g. for oil-impregnated paper, with a minimum close to power frequency.

In the equivalent circuit, increasing conductivity and increasing dipole mobility correspond to a reduction of the resistance R an the resistances R_i with the time constants τ_i. The *charge* that is stored or displaced during polarization is assumed to be *independent of temperature* to a first approximation, so that the capacitances C_i can be regarded as constant [501].

According to this concept, the behavior of the material with increasing temperature can be described both in the *frequency domain* as a single shift of the dissipation factor curve towards higher frequencies and in the *time domain* as a double shift of the current curve towards shorter times and higher amplitudes, Figure 4.3-4.

For oil-impregnated paper and pressbord, it

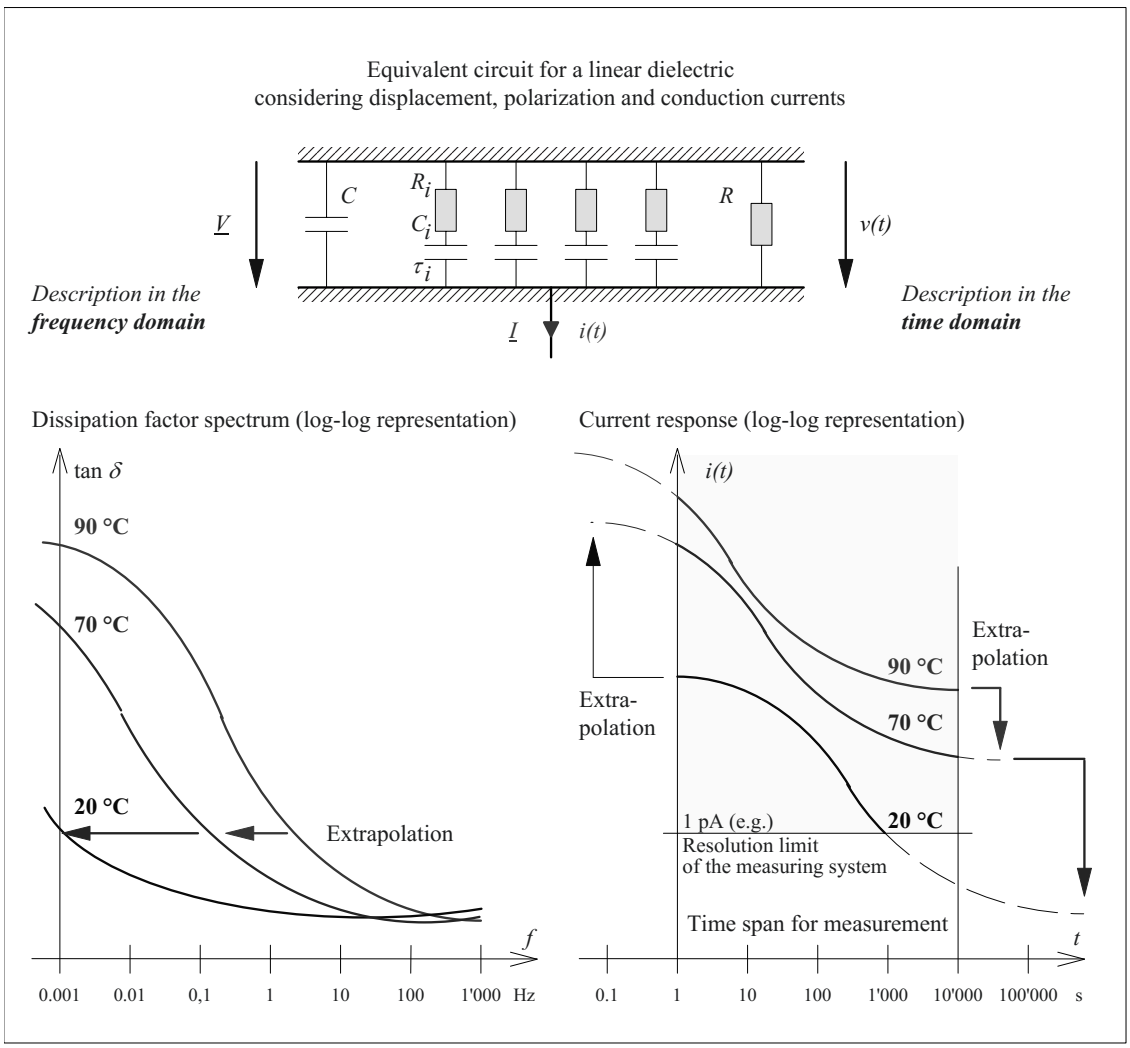

Figure 4.3-4: Conversion of dielectric system responses in the frequency domain (left) and in the time domain (right) performed between different temperatures by "shifting" of the curves (schematic). Measurement: solid curves. Extrapolation: dotted curves.

was shown that the DC resistance R and the resistances R_i can be recalculated for other temperatures according to the *Arrhenius equation* Eq. (4.2-9) assuming the same activation energy [501], [511]. For a first-order approximation, the equivalent capacitances C and C_i need not to be changed. This represents a *physical hypothesis* according to which polarization phenomena exhibit similar temperature dependences (i.e. interfacial polarization is directly related to conductivity and orientation polarization to dipole mobility) and according to which the amount of polarizable charge does not change with temperature.

The recalculation of the curves has a high practical value: For a linear material, the complete **dielectric system response** and the **DC conductivity** that were measured at higher temperatures (e.g. 90 °C and 70 °C) in a feasible time span (e.g. 1 to 10'000 s) and at a high current amplitude can therefore be *extrapolated* to *lower temperatures* (e.g. 20 °C), to *longer times* (e.g. 100'000 s) and to *very low current magnitudes* below the measuring sensitivity (e.g. 1 pA), even without the possibility for direct measurement in this range, Figure 4.3-4 (right).

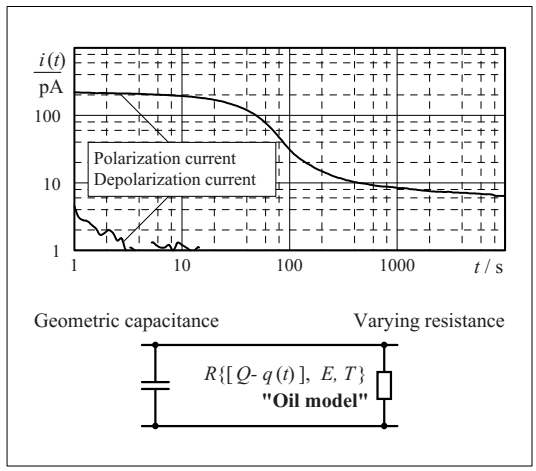

Figure 4.3-5: Modeling for a non-linear insulation liquid, see also Figure 4.2-6.

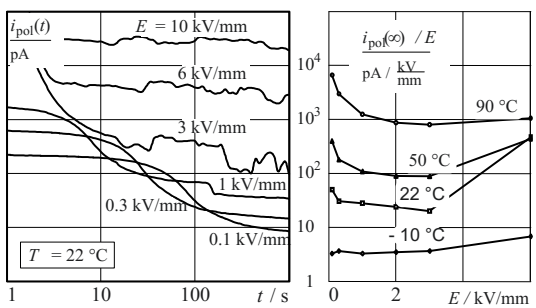

Figure 4.3-6: Field-strength dependence and temperature dependence of dielectric system responses for a new oil [271], see also Figure 4.2-7 .

4.3.2.3 Drift, Diffusion and Injection in Liquids

Insulating liquids show a strongly *non-linear* behavior, and they cannot be described with linear equivalent circuits that were discussed before for the solid materials.

a) Physical processes

Insulating liquids exhibit time-variant polarization currents during polarization and depolarization current measurements, but they exhibit practically no depolarization currents after a depolarization time of a few seconds, Figure 4.3-5. This can be explained in the following way:

(1) At **low field strengths**, conductivity or the current through the liquid decreases during the time of voltage application as the **intrinsic charge carriers** (ions) drift towards the electrodes with different and field-strength-dependent velocities and transit times, cf. Figure 4.3-6 (left). A large amount of this charge is not neutralized at the electrodes but forms *space charge layers* of opposite polarity close to the electrodes (*heterocharges*). The distribution of the **space charges** is determined by an equilibrium of the *drift current* in the electric background field and the oppositely directed *diffusion current* that is caused by the

concentration gradient of the accumulated charge carriers of equal polarity.

Thereby, *local field strength* and injection of charge carriers at the elektrodes are intensified resulting in a steady-state conduction current which is also dependent on the background field strength (global or average field strength resp.), Figure 4.3-6 (left). This causes a small reduction of field strength in the bulk of the liquid.

(2) If the **voltage is switched off**, and the electrodes are short-circuited, only a very small *depolarization current* is flowing as the electrically influenced counter-charges (so-called *mirror charges*) on the electrodes hold the space charges for a long time, Figure 4.3-5. This can lead to very long *relaxation times* before the liquid has returned to the its original state (*memory effect*).

(3) Nevertheless, if the **polarity is reversed**, the space charges are free again, and the polarization current has an amplitude as high as it is expected from the originally present intrinsic charges [486]. Here, it takes some time for all of the accumulated charge carriers to start to move which is comparable to the *dissolving of a "traffic jam"*. Therefore, the current increases at first. Then it decreases as the charge carriers reach the counter electrode. Finally it approaches the steady-state value [503], [504]. The time, when the current reaches its maximimun, is the "*time of flight*", when most of the charge carriers are moving or "flying" respectively.

(4) At **high field strengths** (i.e. with effect from approx. 2 kV/mm), strong **injection** of *homocharges* (mainly electrons at the cathode) starts to increase conduction current significantly. Then, a large number of ions and charged particles is drifting between the electrodes and results in comparatively high and fluctuating currents, Figure 4.3-6 (left). Even in this case, space charges are built up by an equilibrium of drifting and diffusing charge carriers, whereby the local field strength is reduced in front of the injecting electrodes and is increased in the bulk of the liquid.

(5) If voltage or background field strength is increased, current increases disproportionately until **breakdown** takes place.

Figure 4.3-6 (right) gives an example of the so-called *"bath-tub curve" of oil conductivity* which can be explained by the described behavior, i.e. at low background field strengths by a depletion of intrinsic charge carriers by the electric field forces (drift motion) and at high background field strengths by a flooding by injected charges.

b) Global description with equivalent network elements

For a global description of an oil gap, it was proposed to use an equivalent circuit based on a variable resistance [271]. However, polarization phenomena and local field strength enhancements are neglected.

The dielectric equivalent circuit reduces essentially to that of a *geometrical capacitance* for very fast (high frequency) polarization phenomena and a **time-variant conductivity**, which has already been described under Section 4.2.2.2.

Here, the dependence of conductivity or resistance on different parameters must be considered, Figure 4.3-6. The **initial conductivity** $\kappa(0)$ is reduced for an applied field E by *ion transport* (*ion drift*). According to Eq. (4.2-5), the time constant or the *transit time* τ is proportional to the gap width and the reciprocal of the field strength, Figure 4.3-6 (left). After the removal of ions, a new charge carrier equilibrium or a **final conductivity** $\kappa(\infty)$ is set, which is intensely field strength dependent and increases sharply above 2 kV/mm, Figure 4.3-6 (right).

Note: It is interesting that the end values of conductivity apparently exhibit a **minimum** in the range between 1 and 3 kV/mm, Figure 4.3-6 (right). This can be explained as follows: At very *low field strengths*, the ef-

fect of the field on the number of charge carriers is only weak and the *initial conductivity* is almost maintained. With *increasing field strength*, the final conductivity decreases owing to *depletion of charge carriers*, before *new charge carries are again injected from the electrodes or released from traps* and lead to a sharp increase in the conductivity at *high field strength*.

These processes cannot be described by linear equivalent circuits. Instead, a functional relationship, a so-called **physical "oil model"** is proposed [271], in which the initially available amount of charge $Q(0)$ is calculated from the initial current $i_p(0)$ and the transit time τ:

$$Q(0) = i_p(0) \cdot \tau \qquad (4.3\text{-}10)$$

Note: Both the quantities can be read directly from the polarization current profile. Thus, the ion transit time τ, according to Eq. (4.2-5) is dependent on the ion mobility μ, on the gap width d and the field strength E.

If the the initially available amount of charge $Q(0)$ is reduced by the charge

$$q(t) = \int i_p(t) \cdot \mathrm{d}t\,, \qquad (4.3\text{-}11)$$

which is already transported by $i_p(t)$, the actual current carrying amount of charge $Q(t)$ and from this the **current** $i_p(t)$ is given:

$$Q(t) = Q(0) - \int i_p(t) \cdot \mathrm{d}t \qquad (4.3\text{-}12)$$

$$i_p(t) = \frac{Q(t) \cdot \mu}{d} \cdot E(t) + i(\infty, E(\infty)) \qquad (4.3\text{-}13)$$

$Q(t)$ reduces to zero after all the transition processes elapse, and an **end value of the current** $i(\infty)$ remains, which results from the e*nd value of the field strength* $E(\infty)$, Figure 4.3-6 (right).

Note: The dependences of conductivity on time t, field strength $E(t)$ and gap width d included in Eqs. (4.3-10) to (-13) were experimentally checked [271].

c) Multi-physical description

A *linear equivalent circuit* according to Section 4.3.2.1 is not suitable for the description of the complex behavior of conduction phenomena in liquids.

Functional relationships, which describe the variation of conductivity by ion movement and by the effect of higher electric field strengths, can be used in the form of a *nonlinear equivalent circuit* according to Section 4.3.2.3 b) if space charges and local field stress enhancements in the oil are neglected, Eq. (4.3-10) to (…-13). Here, the material condition is assumed to be homogeneous which is a rough approximation only.

In reality, additional phenomea occur which are described in Section 4.3.2.3 a). That relates essentially to the built up of *space charges* and to *local field stress enhancements*, especially close to the interfaces. These processes can be described by a **multi-physical approach**, i.e. a set of differential equations that couples the different relevant physical processes. In doing so, the *motion of charge carriers or ions* must generally be considered in accordance with the universal *Boltzmann transport equation*. For example, the starting point is given by *Fick's laws of diffusion* that describe how particle flow is driven by the particle *concentration gradient*. In the *Nernst-Planck equation* the drift current is added, i.e. the flow of charged particles driven by the *electric field forces*. Finally, the **Poisson-Nernst-Plank equation** extends this approach to include the *interaction of charged particles* among each other.

This approach, which is used in biochemistry and electrochemistry for the description of conduction processes in electrolytes and membranes, can also be used for the description of *insulating liquids* and *liquid-impregnated fiber materials* [503], [504]. With this, it becomes possible to calculate charge *injection* at the electrodes due to very high local field strengths by means of the *Fowler-Nordheim equation*, charge carrier *drift* due to potential gradients (electric field forces resp.) and charge carrier *diffusion* due to concentration gradients. The build-up of *surface charges* and *space charges* in transient and steady states is determined by the transition processes and

equilibrium conditions for the charge carrier flows or currents respectively.

4.3.3 Description of Geometrical Properties

If insulation consists not only of a single (uniform) dielectric, **geometry-related polarization effects** (interfacial polarization) occur at the interfaces, and these effects cannot be differentiated from **material-related polarization effects** by means of dielectric measurements. If an equivalent circuit according to Figure 4.3-2 is established for the complete insulation, then the geometrical properties and material properties can no longer be distinguished. The equivalent circuit loses most of its *physical* significance. It is therefore sensible to **discretize** the insulation *geometry* and assign the elements to *material specific* equivalent circuits.

The *influence of geometry* will first be explained at a layered arrangement of two parallel equivalent circuits (Maxwell's two-layer model) connected in series, Section 4.3.3.1, before discussing layered arrangements in which the *material polarization as well as complex insulation geometries* are considered, Section 4.3.3.3.

4.3.3.1 Maxwell's Two-layer Model

Maxwell's two-layer model consists of the series connection of two parallel equivalent circuits, Figure 4.3-7. Thus, a physically exact description of **interfacial polarization** at the interface of two *layered "conductive" dielectric* is provided.

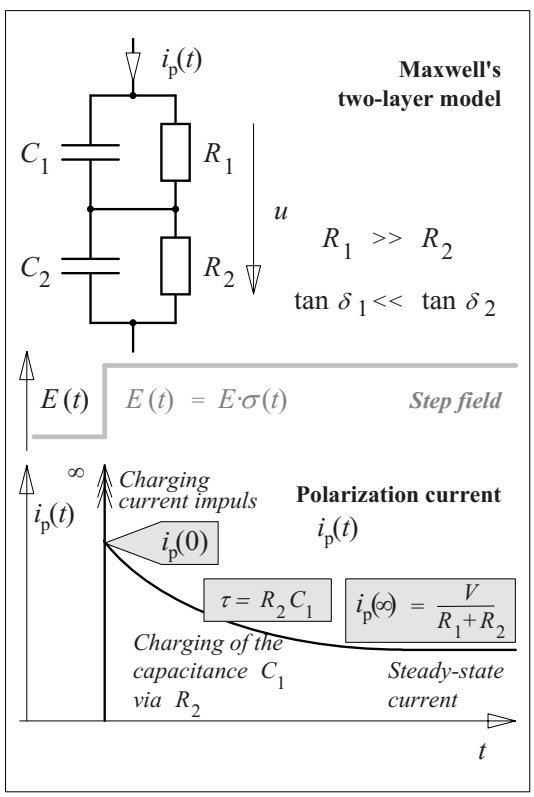

Figure 4.3-7: Maxwell's two-layer model in the ***time domain.***

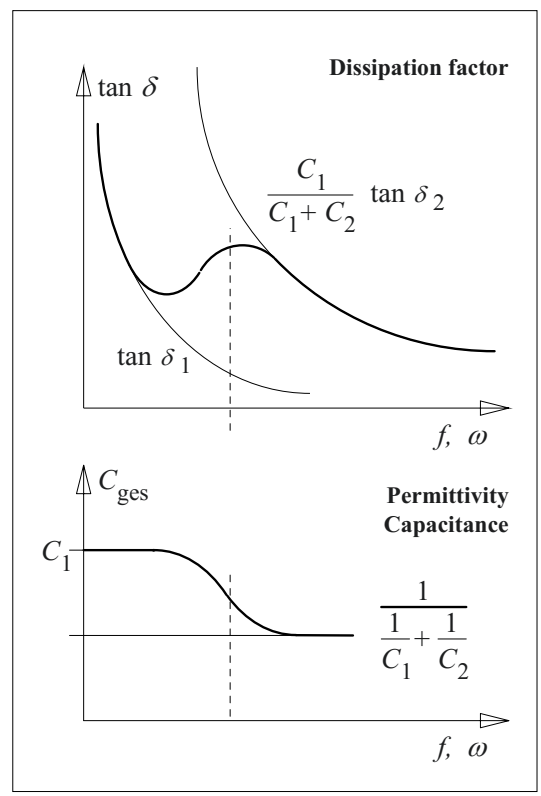

Figure 4.3-8: Maxwell's two-layer model in the ***frequency domain.***

a) Discussion in the time domain

The dielectric **system response in the time domain** at first results in a high capacitive *charging current impulse*, Figure 4.3-7. Subsequently, an approximately exponential *recharging of capacitance* C_1 takes place via the smaller resistance R_2 with the *time constant*.

$$\tau \approx R_2 \cdot C_1 . \qquad (4.3\text{-}14)$$

The initial *current* $i_p(>0)$ is primarily driven by the partial voltage applied at R_2 as a conduction current through R_2 and thus contains the information about the magnitude of R_2. A more precise calculation which considers the displacement current through C_2 is included in Section 6.4.7.6 with Eq. (6.4.7-6).

The *steady-state end value* of the current results from the series connection of both the resistances:

$$i_p(\infty) = \frac{V}{R_1 + R_2} \qquad (4.3\text{-}15)$$

If $R_1 >> R_2$ is valid, then information about the magnitude of R_1 is included in this.

Note: In Section 2.4.4.3 the recovery voltage of a capacitor has already been calculated with Maxwell's two-layer model, see Figure 2.4-31. It is also apt for the description of **dielectric diagnostic measurements** in layered insulations, if to a first approximation only *interfacial polarization* is assumed and material polarization is ignored, see Section 6.4.7.

b) Discussion in the frequency domain

In the frequency domain, the frequency dependence of the parameters of capacitance C and dissipation factor tan δ are especially significant. Instead of a derivation of detailed formulae for the resultant capacitance C and the resultant dissipation factor tan δ, only the limiting cases will be considered for high and low frequencies that are for $\omega \to \infty$ and for $\omega \to 0$. For this, it is assumed that dielectric 1 has significantly lower losses than dielectric 2 (that is, tan $\delta_1 <<$ tan δ_2 and respectively $R_1 >> R_2$).

$\omega \to 0$:

With decreasing frequency, the displacement current through C_2 becomes small compared to the conduction current through R_2. To a rough approximation, R_2 can be considered as a short circuit for C_2, so that the *capacitance* C approaches the value C_1, Figure 4.3-8 (bottom). The *dissipation factor* tan δ approaches the dissipation factor tan δ_1 of the non-short circuited medium with decreasing frequency, Figure 4.3-8 (top).

$\omega \to \infty$:

With increasing frequency, the displacement currents prevail and the resultant *capacitance* reduces to the value of the series connection of partial capacitance C_1 and C_2, Figure 4.3-8 (bottom). The *dissipation factor* is primarily determined by tan δ_2 at higher frequencies, since tan δ_1 reduces to negligibly small values. However, the power loss $\omega C_2 \cdot V_2^2 \cdot$tan δ_2 produced in the dielectric 2 must be related to the reactive power $\omega C \cdot (V_1+V_2)^2$ at the resultant capacitance. This gives the resultant dissipation factor tan $\delta \to$ (tan δ_2)$\cdot C_1/(C_1+C_2)$, Figure 4.3-8 (top).

Therefore, the **frequency responses** of the capacitance and the dissipation factor in the two-layer model include also a remarkable *formal correlation* with the frequency responses with the assumption of *orientation polarization*, Figure 4.2-13.

Additionally, there is a *formal correlation* with regard to the **temperature response**: An increase in temperature leads to a reduction in the resistances R_1 and R_2 and an increase in the dissipation factors tan δ_1 and tan δ_2 respectively. *Thus, the effect of an increase in tem-*

perature is equivalent to the effect of a decrease in frequency.

This behavior is also found for the assumption of *orientation polarization*, Figure 4.2-13 (right).

Note: Therefore, while considering the frequency responses, it must also be ensured that *geometrical and material specific properties* are not confused.

4.3.3.2 Simple Layered Arrangements

The above described Maxwell's two-layer model gives only an incomplete description of a layered insulation, since material polarization is not taken into consideration.

For a more accurate consideration, **a step function response measurement** will be considered *in the time domain*: A step voltage or step field is applied to layer of two transformer board barriers (each of 1 mm) with an intermediate oil gap (2 mm). As a step function response, the *polarization current* is measured in a guard-ring electrode arrangement [271].

A comparison between **measurement and simulation** shows that the simple *Maxwell's two-layer model* supplies currents that are much too small for short periods (currents induced by polarization are missing), but it reproduces *interface polarization* properly for longer periods, Figure 4.3-9 (a).

A simulation with *linear equivalent circuits,* according to Figure 4.3-2, in which *polarization effects* are also taken in to account using *RC* elements, leads to significantly improved results, Figure 4.3-9 (b).

Note: The simulation of *non-linear oil* by a linear equivalent circuit is *physically not correct*. On changing the field strengths or dimensions, the correlation between measurement and simulation is not that good while using the same oil-equivalent circuit.

The physically correct simulation of the oil by a *non-linear oil model* according to Eq. (4.3-10) to (-13) shows good correlation between measurement and simulation for short and long measuring durations, Figure 4.3-9 (c).

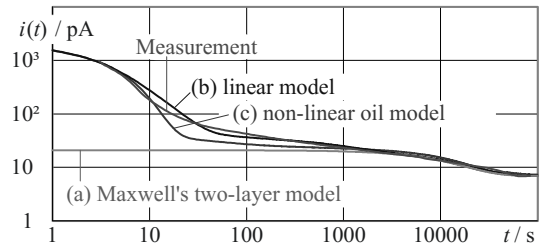

Figure 4.3-9: Comparison of measurement and simulation with different dielectric models for an example of a step response measurement for an insulation of two Transformerboard barriers (1 mm each) and an oil gap (2 mm) [271].

Note: For medium measuring durations, *deviations can be identified and this is attributed to the fact* that the functional relation of the oil model only takes one single *dominant ion type* with a short transit time into consideration. A more accurate *description* must include **additional types of ions** with longer transit times.

As a *conclusion* it can be stated that *linear and non-linear dielectric models* that have been determined from material measurements are also suitable for properly describing the transition behavior of layered insulations.

4.3.3.3 Complex Geometries

The layered arrangements dealt with in Sections 4.3.3.1 and 4.3.3.2 represent simple, **one-dimensional plane arrangements,** in which *interfaces* between different materials are also simultaneously *equipotential surfaces*, which can be used for demarcating areas that are differently simulated, Figure 4.3-10 (top).

Each area is thus assigned to its own dielectric equivalent circuit. The elements of the equivalent circuit (Index "E") must be determined from the material equivalent circuit (Index "M") by a *conversion* with geometrical distance and area relationships:

$$\frac{R_E}{R_M} = \frac{d_E}{d_M} \cdot \frac{A_M}{A_E} \qquad (4.3\text{-}16)$$

$$\frac{C_E}{C_M} = \frac{d_M}{d_E} \cdot \frac{A_E}{A_M}$$

This principle is also applicable to **one-dimensional rotationally symmetric arrangements,** if the interfaces can be considered as *equipotential surfaces* due to the symmetry. However, for the calculation of equivalent circuit elements, the relationships of the plane field in Eq. (4.3-16) for R_E and C_E must be substituted by those of a cylindrically symmetric field, Eq. (2.3-20). However, in the case of thin layers, it can again be approximately calculated assuming plane geometry.

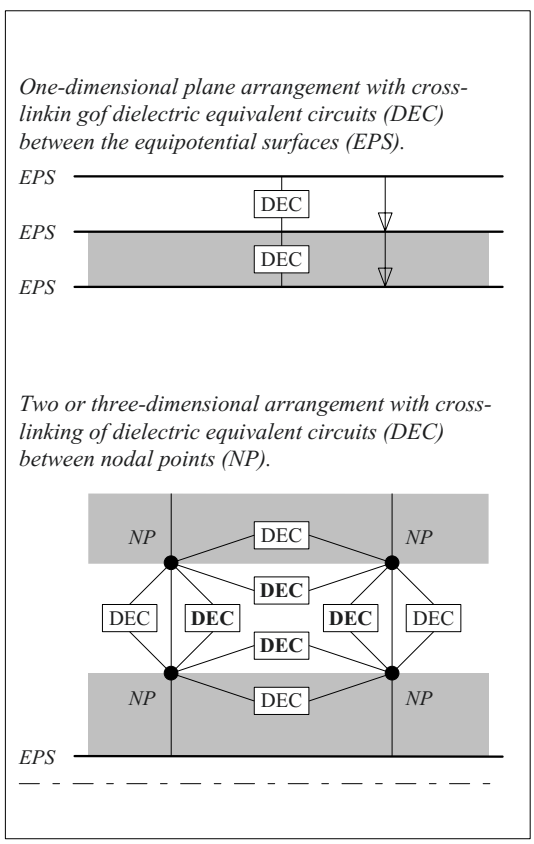

Figure 4.3-10: Description of insulation systems with dielectric equivalent circuits (DEC).

An **application example** is the *simulation of transformer insulations* for *dielectric diagnosis*, Section 6.4.7 with Figures 6.4.7-2, -6 and -10. But it must be noted that along with *cylindrically symmetric layering* of oil gaps and barriers, there are also areas with *spacers* and *oil channels* that are in parallel and disturb the cylindrically symmetric field. They can be included in a simplified manner using parallel equivalent circuit elements.

In true **two or three dimensional arrangements**, *interfaces are generally no longer equipotential surfaces.* Hence, "equipotential points", so-called nodal points or nodes, must be selected for meshing. Between adjacent nodal points, dielectric equivalent circuits are interconnected in two or three dimensions, Figure 4.3-10 (bottom). For the conversion of equivalent circuit elements analogous to Eq. (4.3-16), the geometrical dimensions of the network element under consideration must be considered in the spatial directions that are defined by the equivalent circuit element.

Since the number of equivalent circuit elements is very large, the procedure described is extremely complex even for *comparatively simple insulation* arrangements. As a result, a network for calculation of two or three dimensional field distributions is generated, similar to that for numerical field calculations.

Numerical field calculation programs would be actually better suited to calculating complex, spatial field distributions. In the time domain, till now, *transient field calculation programs* could only take the *permittivity and conductivity* of a material into consideration (which corresponds to a simple parallel equivalent circuit), but not material-specific polarization processes. However, Figure 4.3-9 shows that the *interfacial polarization,* which is *dominant after longer times,* can be properly calculated for that times, even with simpler material models.

An **application example** is the insulation for *high voltage direct current transmission*

(HVDC transmission). In complex insulation arrangements the transition processes are influenced by polarization effects and lead to time-varying field stresses that are difficult to understand, see Sections 2.4.4 and 7.2.

5 INSULATING MATERIALS

The electric strength and the dielectric properties of insulating materials were dealt with in Chapters 3 and 4 as basic high voltage engineering material properties, without going into the details of special features of individual materials. Often, however, *non-electrical properties* of a "construction material" are crucial to their use and practical application.

Chapter 5 will therefore deal with *special properties* of a few important insulating materials. The following are considered for this:

- *The importance* of an insulating material in high voltage engineering *applications,*
- Its basic *material structure*,
- Special dielectric properties,
- Other special properties and
- *Technology* (manufacturing, processing) and *performance* in operation.

A *systematic classification* of insulating materials cannot be done readily. As a principle of classification, for example, physical states of matter (gaseous, liquid, solid), the chemical structure, the processing technology, or the areas of application can be considered. Each principle of classification leads to a classification, which comes across as illogical from another point of view. In the following *classification*, therefore, *groups of substances* are formed, which appear significant on the basis of specific high voltage engineering features:

5.1 *Gases* (air, SF_6, alternative gases)

5.2 *Inorganic solid insulating materials* (ceramics, porcelain, glass, mica)

5.3 *Highpolymer synthetic materials*, i.e. thermoplastic insulating materials (polyethylene, PVC...) as well as thermosetting plastics and elastomers (epoxy resin, polyurethane, silicone elastomers)

5.4 *Insulating liquids* (mineral oil, synthetic fluids, vegetable oils)

5.5 *Fibrous materials* (paper, pressboard, synthetic materials)

The extensiveness of the topic and the variety of materials do not nearly allow an exhaustive approach. The presentation therefore must be restricted to *certain important fundamentals and points*. The user requires the exact details of the respective manufacturer in each case. Moreover, he must assure its suitability for the given application by means of his own tests for himself.

5.1 Gases

All gases are ideal *embedding media and impregnation media* owing to their ability to uniformly fill accessible cavities. Even closed cavities can be filled by diffusion processes (usually very slowly).

Note: These properties are also present in *liquids*, but to a lesser extent.

Atmospheric air is the *naturally available insulating material* for all "outdoor insulations".

Unfortunately, the *electric strength* in the case of atmospheric air is comparatively poor and even sulfur hexafluoride (SF_6) only attains the strength of liquid dielectrics in the compressed condition (see Section 3.2). *Immediate recurrence of electric strength* after flashovers and discharges through recombination of free charge carriers is of advantage. Even due with *ageing*, there is no change in the properties under practical conditions.

The *dielectric properties* are exceptionel provided that a high constant relative *permittivity*

$$\varepsilon_r = 1.0 \qquad (5.1\text{-}1)$$

and an extremely low *dissipation factor*

A. Küchler, *High Voltage Engineering*, VDI-Buch,
DOI 10.1007/978-3-642-11993-4_5

$$\tan \delta << 10^{-4} \qquad (5.1\text{-}2)$$

can be expected nearly under all application conditions.

- The *application of gases* includes, for example,
- *external insulations* (air as natural embedding insulating material),
- enclosed, often *compressed gas* insulated devices (SF_6, N_2, air and "alternative gases" as embedding insulating material),
- *circuit-breakers* (with SF_6 as insulating medium and extinguishing medium),
- gas impregnated *film insulations* (with SF_6 as impregnating medium) and
- *measuring capacitors and reference capacitors* (with air and SF_6 as temperature independent and frequency independent dielectrics).

Note: Gases are also used in *liquid form* at very low temperatures both as insulating medium and as cooling medium for *superconducting devices*, see Section 5.4.6.

5.1.1 Air

Air as natural ambient medium does not require any special "processing" or treatment.

The dimensioning of devices must take the changes of electric strength with *pressure and temperature* into consideration, see Eq. (6.3-2) as well as Section 3.2.

The use of *synthetic air* as an alternative gas for encapsulated switchgear is discussed in Section 5.1.3.

Moreover, it must be noted that *admission of atmospheric air* can have an unfavourable *influence on other insulations*:

Owing to *rainfall* or deposition of atmospheric humidity (condensation on colder surfaces), the surface strength decreases.

Solid insulating materials can absorb moisture due to diffusion and possibly accumulate at the interfaces (e.g. filled or fiber reinforced organic materials).

In case of *insulating oils*, the electric strength is reduced due to absorption of moisture and gases. Oxygen and moisture can also accelerate ageing.

The conductivity of *de-ionized water* increases by many orders of magnitude due to absorption of CO_2 from the atmosphere.

5.1.2 Sulfur Hexafluoride (SF_6)

Owing to its electron-affine properties, SF_6 is the most important *insulating gas* as well as *extinguishing gas* in high voltage engineering. It is used for the insulation of enclosed switchgear systems (Section 2.6.3.1) and gas-insulated transmission lines (Section 7.1.1.3). It is also used as extinguishing and insulating gas in high voltage circuit-breakers (Section 7.1.5.2) and in some cases in medium voltage circuit-breakers.

SF_6 has about three times *higher electric strength* than air, see Section 3.2. In association with increased pressures of 3 to 5 bars, electric strengths that are about a factor of 10 above the strength of atmospheric air can be attained. High voltage switchgears thus have a drastically reduced area and volume requirement and can even be set up for reasonable costs within cities or buildings.

Additional information on the strength of SF_6, for example even in non-uniform fields, is also given in the specialist literature, such as [22], [28], [55].

Note: Even higher strengths can be attained for a series of *fluorocarbon compounds* and *chlorofluorohydrocarbon compounds* (CFC) [22]. However, more or less all of them have unfavorable properties, such as a reduced temperature range, an increased toxicity or a classification as a hazardous greenhouse gas or as hazardous for the ozone layer.

Note: Also SF_6 has a very high *global warming potential* and must not be released into the atmosphere. It has to be used, processed and re-used in closed circuits with low leakage rates.

SF_6 is distinguished from all other gases with high electric strength owing to a unique characteristic profile:

1. A relatively low *temperature of condensation* (T_K = -63°C at p = 1 bar) allows its use even at low ambient temperatures. The *phase diagram* of SF_6 shows that at pressures of several bars condensation must be expected in *climatically cold zones*, Figure 5.1-1. For example, SF_6 condenses at a temperature of -30°C for a pressure of 5 bars. By *mixing* it with N_2, the temperature of condensation can be reduced, since the (partial) pressure of SF_6 is reduced. The electric strength of the *gas mixture* remains high even for a high proportion of N_2. For example, a gas mixture with an SF_6 proportion of 20 % still has about 70 % of the electric strength of pure SF_6 gas [22], Figure 5.1-2.

2. Moreover, the SF_6 molecule is chemically very *stable* under natural ambient conditions; this implies that it is *not toxic.*

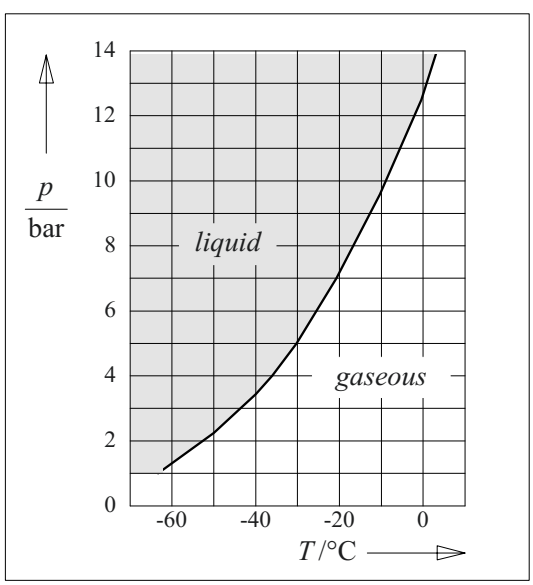

Figure 5.1-1: Phase diagram of sulfur hexafluoride.

Note: SF_6 is *invisible, odorless and heavier than air*, i.e. it presents a risk of *suffocation* within rooms, test vessels, tubs and sinks that can be filled with SF_6 with the displacement of air without this being noticed. Therefore, effective *ventilation* must always be provided.

3. Owing to the effect of *flashovers and switching arcs*, SF_6 molecules are broken down into their components, which are so reactive that they immediately re-combine to form inert SF_6 molecules. The advantage here is that it does not involve a hydrocarbon and hence carbon deposits cannot be formed.

However, in the case of flashovers or in switching arcs, potential remanents of *moisture or oxygen* lead to the formation *of toxic substances* through secondary reactions. On opening enclosures, they can be seen as white powder or they can be identified from the putrid smell of hydrogen sulfide H_2S. Inhalation of the gas or contact of the powder with the skin must definitely be avoided.

The gas in *gas insulated switchgear* (GIS) is therefore *dried* and *hermetically sealed* against the environment. A possible gas loss is registered by the pressure drop; this generally amounts to a maximum of 1 % per year. The total gas volume is subdivided into *part volumes* by partition insulators so that the effect of a leakage is locally restricted. For mainte-

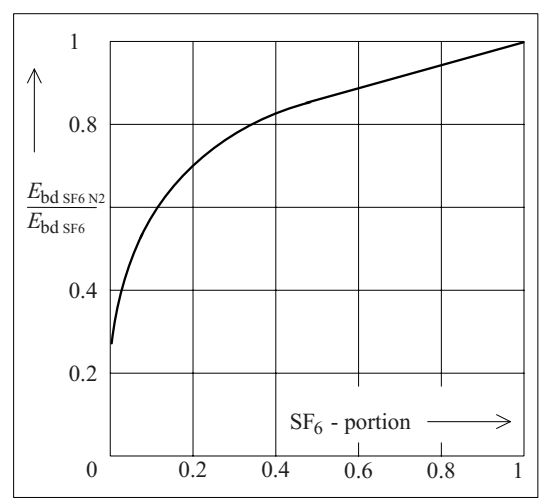

Figure 5.1-2: Electrical strength of mixtures of nitrogen and sulfur hexafluoride [22].

nance purposes, the entire SF_6 filling of an installation is pumped into the reservoir of a *processing station* and is used for refilling after drying and filtering. The containers should be *opened* only outdoors or in well-ventilated environments; an unchecked release of gas must be avoided.

The electric strength of SF_6 is affected by the presence of *particles and impurities*. The hazards due to particles can be avoided by *particulate traps* in the form of spaces with low field strengths in which particles can be deposited or by *insulating coating* of the outer (grounded) electrode that hampers the charging of the particles. Assembly of installations must be carried out with particular care, not only during *production* but also during *final assembly* at the site. The internal strength of an installation can therefore be proven only by means of partial discharge measurements *after* completing the final assembly, Section 6.4.2.

Note: Particles in gas-insulated switchgear can lift off and jump under the force of the electric field. A *jumping particle* causes a partial discharge impulse that can be measured. Nevertheless, the the designed service field strength should be lower than the *lift-off field strength* of the remaining particles.

SF_6 affects the *ozone layer significantly less* than the chlorofluorohydrocarbons (CFC). However, a 23900-times larger *global warming potential* (GWP, time frame 100 years) in comparison to CO_2 is noteworthy [316]. Although only small quantities are used in power engineering, special measures are undertaken to restrict its release into the atmosphere. Thus, steps are taken to reduce the quantity of SF_6 by *mixing* with N_2 and to minimize the release into the atmosphere by low *leakage rates* and through *closed reprocessing cycles*. SF_6 circuit-breakers were replaced in the medium voltage domain largely by *vacuum circuit-breakers*, but they continue to dominate as before in the high voltage applications, Section 7.1.5. *Fully adequate alternatives* are currently not yet known.

5.1.3 Alternative Insulating Gases

Among insulating gases, *sulphur hexafluoride* (SF_6) has an absolutely dominant position because of its extraordinary profile of properties. Dielectic strength is approximately three times higher than the strength of air, the gas is inert and non-toxic, and it can be used in a wide range of temperatures. The high global warming potential is a disadvantage. Today, loading of the atmosphere with greenhouse gases is avoided by specifying very low leakage rates, by using closed cycles and by using small gas quantities in electrical equipment. But owing to the development of global energy infrastructure, total gas volumes of switchgear, switches, instrument transformers and especially *gas-insulated lines* increase drastically. As a result, the interest in *alternative insulating gases* is also increasing.

The insulating gases **synthetic air** (so-called "clean air"), **nitrogen** (N_2) or **carbon dioxide** (CO_2) at **high pressure** show up with many favorable properties that are also given for SF_6, such as chemical stability, non-toxicity, nonflammability and low boiling temperature. Moreover, they are even much better with respect to global warming potential, decomposition product toxicity and boiling temperature. Nevertheless, dielectric strengths at comparable pressures are significantly lower, which requires technical solutions with a complex, *heavy-weight pressure-resistant encapsulation* or a dimensioning with *longer insulation distances*.

Among the above mentioned gases, **synthetic air** has some advantages: As the composition is very close to atmospheric air, release to the atmosphere or into rooms doesn't cause any danger. In contrast to CO_2, no global warming potential is given. In comparison with N_2, the electronaffine oxygen causes a slight improvement of dielectric strength. In the case of an emergency requirement, the insulating gas can be refilled at little effort directly from the atmosphere.

Note: In order to avoid the use of SF_6 circuit-breakers in a SF_6-free switchgear, **vacuum interrupters** are included. However, today they are only available up to the lower high-voltage levels.

Because of the low dielectric strength of the above mentioned atmospheric gases, an intensive research for dielectrically strong electronaffine **alternative gases** is still going on.

As already discussed in Section 3.2.2.3, a high **electron affinity** of the gas molecules is required for an effective attachment of electrons and for a high *dielectric strength*. This can be achieved by the use of *electronegative elements* (such as F or Cl) and by a favorable *isomeric structure* of the molecule which both can cause energy levels for attached electrons. Also *collisions or interactions* of electrons with the molecules of an eventually used *carrier gas* (e.g. air, nitrogen or CO_2) have an influence on the attachment processes.

Very high dielectric strengths can be reached with a number of **chlorinated and fluorinated hydrocarbons**, but many of them, such as CCl_4, C_2F_5CN and CF_3CN, are omitted due to their *toxicity*.

Furthermore, alternative gases should neither be corrosive nor flammable, and they should have a low global warming potential (GWP), a low ozone depletion potential (ODP) and a low boiling point which allows the use at low ambient temperatures.

Note: A low *ozone depletion potential* is generally given for fluorinated hydrocarbons if they do not contain chlorine [509].

Finally, only a limited number of candidates remain, such as isomers of **Fluoronitriles**, e.g. $(CF_3)_2CFCN$ which has approximately twice the dielectric strength than SF_6, or the **Fluoroketones** $CF_3C(O)CF(CF_3)_2$ (*C5K ketone*) and $C_2F_5C(O)CF(CF_3)_2$ (*C6K ketone*), which is also used as *cooling agent* owing to its low global warming potential. A selection is given in Table 5.1-1. None of these gases reaches the properties of SF_6 or the above mentioned requirements in all respects.

Especially the comparatively high *boiling temperatures* of alternative gases require mixing with a **carrier gas** (buffer gas) in most of the cases. Then, the dielectrically effective gas can be used at a low *partial pressure* with a low *boiling temperature* without having low gas pressure in the equipment. Similar to SF_6, carrier gases can be used in a high concentration without loosing the electroaffine properties of the dielectrically effective gas. Some reductions of the dielectric strength must be accepted, but at the same time the *toxicity* of fluoroketones and fluoronitriles and the *global warming potential* of fluoronitriles is also

Table 5.1-1: Properties of selected alternative insulating gases according to [509]

Insulating gas	Sulphurhexafluoride SF_6	Fluoro ketone (C5K) $C_5F_{10}O$	Trifluoroiodomethane CF_3I	Hydrofluoroolefin HFO1234zeE	Hydrochlorofluoroolefin HCFO1233zd	Fluoronitrile C_4F_7N
Boiling point *) Sublimation point	-64 °C *)	+ 26.5 °C	-22.5 °C	-19 °C	+ 18.3 °C	-4.7 °C
GWP (CO_2: 1)	22,800	1	0.4	6	7	2,100
Ozone depletion potential	0	0	very low	0	very low	0
Flammability	no	no	no	no	no	no
Toxicity LC50 4h/rat (ppm)		>20,000	160,000 mutagene	>207,000	120,000	<15,000
Dielectric strength (LI) at -15 °C		85 % of SF_6 (air as a carrier gas)	120 % of SF_6	100 % of SF_6	90 % of SF_6 (air as a carrier gas)	120 % of SF_6 (air as a carrier gas)

drastically reduced for the gas mixtures in comparison with the unwanted properties of the pure gases.

Nitrogen, *air* and *CO_2* are considered as carrier gases (buffer gases).

If the gas mixture shall be used as a **breaking gas** in *circuit-breakers*, CO_2 should be used because of its superior arc extinguishing properties. Eventually, a small quantity of O_2 can be added for binding of cabon and decomposition products, and for the improvement of arc extinguishing properties.

During *partial discharges* (to a smaller extend), during *flashovers* and especially during *arcing* in switches, severe **decomposition of the alternative gases** takes place, and it cannot be compensated completely by recombination as for the simply constructed SF_6 molecule. Thereby, the *dielectric strength* can be further reduced, especially for low concentrations of the alternative gases. Furthermore, *highly toxic decomposition products* are generated, and their components and their hazard potential are not yet investigated completely, and absorbers or catalysts are not yet available [509]. Decomposition of the gases can be detected from a *pressure increase* in the gas volume.

Note: For the design of the *sealing systems i*t must be considered that the carrier gas molecules are smaller than the SF_6 gas molecules.

As an **example**, an alternative gas miture of a fluoronitrile with CO_2 shall be mentioned [510]. With a concentration of 6 percent by mole (equivalent to 22 percent by weight) of a branched isomer of the *heptafluorobutyrnitrile* $(CF_3)_2CFCN$ an application down to -25 °C is possible, the global warming potential decreases to 462 and is only 2 % of value given for SF_6. The gas mixture is not classified as toxic any more [510].

In summary, compact gas-insulated switchgear and gas-insulated lines can principally be insulated with alternative gas mixtures today. Nevertheless, they must be designed according to the given characteristic profiles of the gas mixtures, a simple replacement of SF_6 in existing equipment is not yet possible at the moment. The use of alternative gas mixtures as breaking gases is a controversial issue.

5.2 Inorganic Solid Insulating Materials

Inorganic solid insulating materials in the form of porcelain, glass, and mica products are generally characterized by a *high temperature resistance* and are insensitive to *chemical influences, weather influences, radiation and partial discharge stresses*. Moreover, in comparison to other insulating materials, they have a relatively *high thermal conductivity* and in many cases, a very *high mechanical strength*.

However, in the case of *mica products* the good properties of mica deteriorate owing to organic binding agents.

5.2.1 Porcelain and Ceramics

External insulations which are produced in the form of mechanically stable suspension insulators, supporting insulators and housing insulators are predominantly made of *mechanically* strong porcelain. Moreover, ceramics and porcelain are suitable for all *thermally highly stressed* insulations, such as immersion heaters, spark plugs or thermally conductive insulations for the assembly of power semiconductors. Owing to a closed porous surface (glazing), excellent *weathering resistance* and impassivity against the effect of *chemicals* are provided. Only hydrofluoric acid, concentrated phosphoric acid and long acting hot sodium hydroxide and potassium hydroxide can be corrosive for porcelain glazings.

The *surface resistance* strongly decreases for relative air humidity above 80% or for direct wetting by the formation of moist, conductive layers and hence the risk of *pollution flashovers* increases. Dirt deposits have a particularly negative effect. The moderate surface

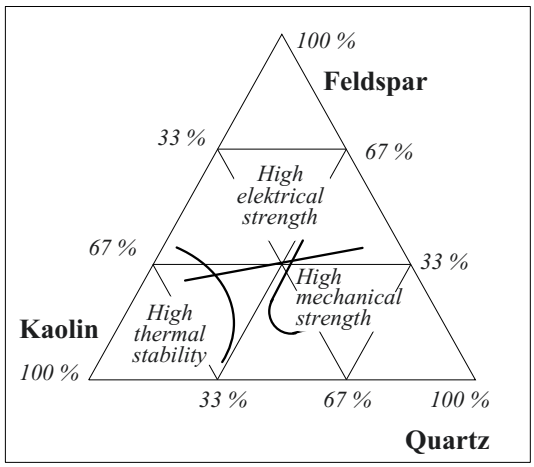

Figure 5.2-1: Properties of quartz-porcelain with regard to the composition porcelain paste.

properties of porcelain must be taken into consideration during design through ample creepage lengths (see Section 3.2.6.4 and Figure 3.2-28). Silicone composite insulators have significantly better hydrophobic properties, i.e. water-repellent surface properties, and in the case of difficult ambient conditions, they are increasingly replacing porcelain insulators, Section 5.3.4 and 7.2.4.2.

Note: Moreover, *ceramic substances and metal oxides* are used as capacitor dielectrics at lower voltages, such as ferroelectric ceramics with extremely high permittivity or thin layers of aluminum oxide in electrolytic capacitors.

In **spark plugs,** insulators made of aluminum oxide ceramics are used, wherein the miniaturization of the spark plug body leads to very high field strengths, even for impulse voltages of a few 10 kV, and requires a corresponding material development. During production, the insulation bodies are pressed and subsequently fired, Section 7.4.6. The extensive use of spark plugs in automobile engineering leads to the fact that a large proportion of ceramics for high voltage applications is used in this field.

For **manufacturing** porcelain insulators, the mineral raw materials *feldspar* (alkali aluminum silicate), *kaolin* (aluminum silicate) and *quartz* (SiO_2) or *aluminum oxide* are finely ground with water and mixed to give a moldable mass. The composition of the porcelain paste determines the mechanical, thermal, and electrical properties of the finished insulator, Figure 5.2-1. Thus, Aluminum **oxide-porcelain** has better mechanical properties and can be better processed than **quartz-porcelain**.

In an extruding machine, the soft *paste* is formed into cylindrical blanks. In this process, gas bubbles must be removed by the action of a *vacuum*. After drying to a water content of approx. 15%, the insulator achieves the desired shape by pressing or lathing, Figure 5.2-2.

After drying further, the formed body is provided with a coating of low melting point minerals by dipping into an immersion bath or by spraying, and this forms a closed glassy coating (*glaze*) in a subsequent firing process.

A solid *sintered product* is obtained from the porcelain paste in the kiln at 1400 to 1500°C for approximately 40 to 50 hours. It consists of crystals in a molten glass phase primarily comprising feldspar. Drying, firing and sintering results in *large shrinkage* of about 15 to 20 %.

Note: A reduced shrinkage of about 5 %, better mechanical properties and a lower dissipation factor are obtained for *steatite*, which comprises lardite (soapstone, magnesium silicate) instead of kaolin. Manufac-

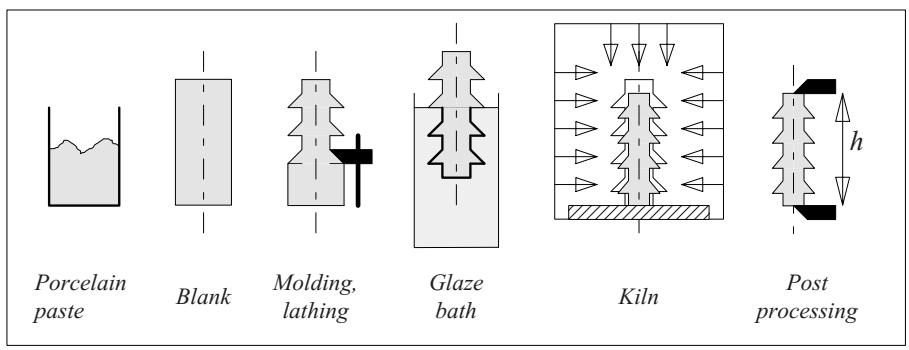

Figure 5.2-2: Manufacture of porcelain insulators

turing larger insulators is, however, not possible and hence steatite is mainly used in high frequency engineering.

Owing to the intense shrinkage, which cannot be exactly defined, it is very difficult to *produce parts with dimensional accuracy* and only larger tolerances are achievable. Narrow-tolerance dimensions must be refinished by *grinding.*

5.2.2 Glass

Glass can be used instead of porcelain for smaller **insulators,** for example**,** *cap-and-pin insulators*. Damages and cracks can be visually identified. However, the mechanical stress that can be applied is lesser than that for hard porcelain. Insulating glass (E-glass, Pyrex glass) may only contain very little alkali oxide (< 0.8 %, "alkali free"), and thus no large, conductive layers with alkali ions are formed when moisture is deposited on the surface.

Moreover, glass is used in the form of thin **fibers** for mechanical *reinforcement of plastics* (glass-fiber reinforced plastics, GRP). Appropriate surface treatment (silanization) of fibers is essential for electric strength as this facilitates a *reliable bonding* between fiber and polymer (generally, cast resin). Detachments must definitely be prevented in order to avoid adsorption of moisture that is diffused into the material (see Section 3.4.2.3, Figure 3.4-6).

The fibers, in the form of strands, help in the *reinforcement of rods* (e.g. in composite insulators with reinforced epoxy resin rods and silicone sheds) During the manufacture of filament wound pipe*s* (FW-pipes) according to the "filament winding" procedure, fiber strands are drawn through a resin bath and are wound in a crisscross manner in several layers on a winding mandrel on which the hardening takes place. Moreover, the glass fibers are inserted in the form of *fiber mats* for the reinforcement of pipes, plates or any resin bodies. For this application, *vacuum casting* is necessary to ensure freedom from cavities.

Glass fibers can also be used in oil as mechanical bonding agents.

The basic component of **glass** is *quartz* (Silicon dioxide SiO_2), which is present in non-crystalline form in a supercooled molten mass.

Pure *quartz glass*, owing to its very high melting point, can only be used for a few special applications, such as for transmitting tubes. For this, along with the extreme thermal resistance, very low dissipation factor is also a decisive factor ($\tan\delta = 1... 30 \cdot 10^{-4}$).

For *simple glass quality* (mirror glass, alkali glass) approx. 20 to 30 % alkali oxides are added to lower the melting point. However, owing to sharply increased volume conductivity and surface conductivity, its application as electrical insulation glass is generally not possible, Table 5.2-1.

Almost "*alkali-free" glasses* contain *boroxide* (B_20_3) for lowering the melting point (borosilicate glasses). Owing to their good electrical properties, they are used largely for electrical insulation (E-glasses), Table 5.2-1.

Lead glasses with the addition of lead oxide were earlier used as capacitor dielectric owing to their high permittivity and low losses, Table 5.2-1.

Table 5.2-1: Guide values for the dielectric properties of various types of glass [16], [47].

	ε_r	$\tan\delta$ ‰ 50 Hz	κ S/m 20°C	κ S/m 300°C
Simple glass quality (with alkali oxides)	4 ... 8	100 ... 10	$< 10^{-6}$	10^{-3}
Lead glass (with lead oxide)	8 ... 10	10 ... 1	$< 10^{-8}$	
E-glass (with boroxide)	approx. 6	< 1	$< 10^{-11}$	10^{-8}
Quartz glass (without supplements)	approx. 4	3 ... 0.1	10^{-16}	

5.2.3 Mica Products

Mica is a naturally occurring mineral. The so-called potassium mica (potassium-aluminum double silicate, "*muscovite"*) is predominantly suitable for application in high voltage engineering. Owing to its crystal structure, it can be divided into *very thin plates* and can be processed to form larger insulations with *binding agents* (mainly epoxy resins and silicone resins as well as enamels).

Pure mica in the form of muscovite has very good electrical properties ($\varepsilon_r = 7$, $\tan\delta < 1$ ‰, E_{bd} = 50...150 kV/mm). The properties of phlogopite (magnesium mica) are slightly poorer.

Special properties of mica products are the *resistance against partial discharges* as well as a high *thermal resistance* of 130°C to 500°C, depending on the binding agent. Mica based insulations are, therefore, suitable for insulations that are thermally stressed and for those in which partial discharges during operation due to cavities or delaminations cannot be ruled out. Generally, the thermal and electrical properties of mica insulations are affected by the unavoidable binding agent.

Micanites are products of mica plates with binding agent that are used for thermally stressed commutators, machine insulations, immersion heaters, spools and tube holders.

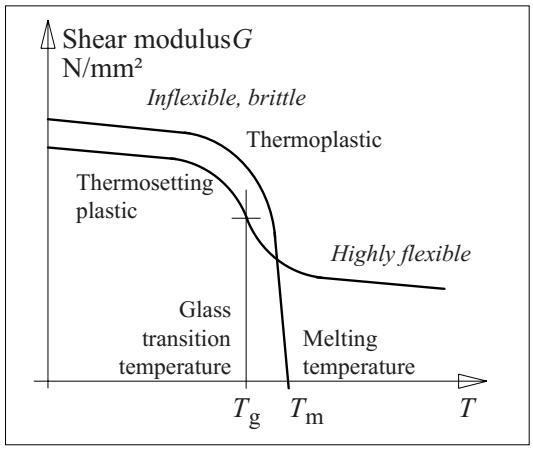

Figure 5.3-1: Shear modulus G as function of temperature for thermoplastic and thermosetting plastic materials (schematic).

Mica films are a type of *mica paper*: mica that has been freed from crystal water by baking is processed as a suspension in a paper machine to form a thin, paper-like mica insulation film. It can be applied to different *carriers,* e.g. of paper, glass silk, polyester fleece or polyester silk, along with *binding agents* and must be protected with a *liner* [319]. This material is used in machine insulations and generator insulations as well as in dry transformers for taping of conductors. If necessary, it is impregnated with resin and hardened, see Section 7.1.6.2.

5.3 Highly Polymerized Plastics

Highly polymerized plastics occur in many different substances. There is a correspondingly wide palette of different properties, processing options, molding options and application options. Hence, the following presentation can only deal with a few important points as examples. For detailed information, the specialist literature and the datasheets of the manufacturer must be referred to [88], [89], [90], [91].

Characteristically, polymers have a relatively low *thermal stability*. In some cases thermopolymeric materials melt only very slightly above 100 °C. However, specific fluorinated hydrocarbons and silicones can also be stressed with temperatures of a few 100 °C. The temperature dependence of the shear modulus (as a measure of the resistance of a material against mechanical distortion) generally differs for *thermoplastic* and *thermosetting* substances, Figure 5.3-1.

The *weight* of polymers is very low compared to porcelain or glass. Comparably low *mechanical strength* must be frequently improved with reinforcements (composite materials). Also the relatively low *thermal conductivity*

can be increased to a certain extent with mineral-based fillers.

The resistance of polymers against the influences of *weather, radiation* and the effect of *chemicals* or *media in the environment* can vary depending on the material. Therefore, compatibility tests under realistic conditions are often necessary before use. Here problems such as *diffusion of moisture* and *hydrolytic decomposition* (e.g. in case of adhesive bonds and composite materials) are of importance.

Maximum possible *electric strengths* can be attained with polymers (e.g., thin foils), but they are strongly dependent on the processing. Unfortunately, partial discharges at defects can often lead to very rapid *erosion*.

The *conductivities* of polymers are very low when compared to ion-conductive substances such as porcelain and glass. *Permittivity* and *polarization losses* depend on the dipole moments of the molecules.

5.3.1 Reactions of Formation and Cross-linking

Highly polymerized plastics result from linking of low molecular components (*monomers*) to high-molecular chain molecules (*polymers*). Here the cross-linking of molecules can take place in one, two or three dimensions. There are three different formation reactions:

- Under **polymerization** similar monomers are linked by breaking double bonds to form a high-polymer chain molecule without the *separation of by-products*, Figure 5.3-2. If at least two different types of monomer are cross-linked, this is known as co-polymerization.
- Under **polycondensation** different kinds of monomers are linked by *separation of low-molecular reaction products,* such as water or ammonia. The reaction products often lead to cavity formation, and hence polycondensation products are generally not used for highly stressed insulations, Figure 5.3-2.
- During **polyaddition**, different types of monomers are linked *without the separation of by-products*. It gives rise to high-quality insulating materials.

The mentioned poly-reactions can lead to thermoplastic, thermosetting and elastomer materials depending on the type of spatial cross-linkage. This classification does not relate to the type of the above-mentioned formation reactions, but to the behavior during heating, Figure 5.3-1:

Thermoplastic polymers (thermoplastics)

If the cross-linking of molecules is largely linear, then chain molecules can be displaced relative to each other if the Van der Waals forces are weakened during heating. That is,

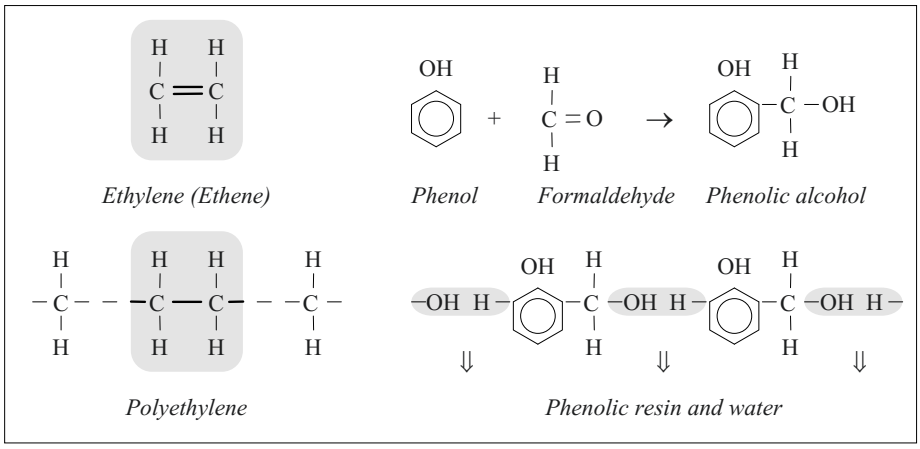

Figure 5.3-2: Examples of polyreactions: polymerization and polycondensation with elimination of water.

the substance can *melt* and can *solidify* again on cooling, i.e. it is *thermoplastic*, Figure 5.3-1. This enables thermal processing by casting, pressing, extrusion, blowing and welding.

Thermoplastic materials, for example, are used for cable insulations (polyethylene, PVC), capacitor dielectrics (foils) and for casings.

Thermosetting polymers

In a multidimensional cross-linking between the chain molecules, the resultant bond can no longer be broken due to heating. Only dissociation of the Van-der-Waals' bonds occurs and results in softening. However, melting is *no longer possible*, since the three-dimensional cross links between the chain molecules still exist. The material exhibits duroplastic behavior, Figure 5.3-1. Above the glass transition temperature T_g, duroplasts remain in a flexible state that is determined by the tightness of the cross linking. In the case of further heating, an irreversible *thermal decomposition* of the material structure occurs.

Note: The glass transition temperature generally corresponds to an increase in the *permittivity* and to a *polarization loss maximum,* since polarizable dipoles become mobile, Figures 4.2-2 and -12.

The formation reaction (hardening) must take place according to the required shape. A *subsequent change in the shape* is possible only by mechanical post-processing (grinding, turning and milling), but it is no longer possible by heating. The shape stability of thermosetting polymers under mechanical stress is of advantage because the spatial cross-linking counteracts the standard *"creepage"* of the material in thermoplasts and hence only a reversible elastic distortion occurs.

Typical thermosetting polymers are *cast resins*, which harden in a mold. They are used for manufacturing insulation bodies and for casting assembly components. Even cross-linked polyethylene (XLPE) in cable insulations, whose molding is done via extrusion in thermoplastic condition, is subsequently transformed into a duroplastic medium due to irreversible cross-linking of chain molecules among each other.

Elastomeric polymers

Elastomers are *thermosettings* that exhibit an *elastic behavior* even at operating temperatures, owing to very loose spatial cross-linking. Molding takes place through cross-linking in the provided form by casting. Subsequent processing is generally not possible.

Elastomers are used, for example, as sealants, for flexible-line insulation and for the sheds of composite insulators as well as for cable fittings (silicone elastomers).

5.3.2 Thermoplastic Insulating Materials

5.3.2.1 Polyethylene (PE and XLPE)

Polyethylene, as a thermoplastic material that can be readily extruded, is largely used for the *insulation of cables* from the medium voltage range up to the 500 kV level.

Polyethylene is produced from the polymerization of ethylene (ethene) molecules, Figure 5.3-2 (left). Depending on the method of preparation, variously structured materials are produced:

a) In the case of the *low-pressure method* polymerization takes place in the presence of catalysts at ambient temperature and pressures of a few bars. Thus, a *high-density polyethylene* (HDPE) is produced, which consists of linear chain molecules. They are arranged parallel to each other in space-saving crystalline regions that are interrupted by smaller amorphous regions. The melting temperature lies at about 135 °C. However, the degradation of the crystalline regions starts at only about 100 °C.

b) In the case of the *high-pressure method*, polymerization takes place under pressures of 1500 to 3000 bars at 200 °C. This results in a *polyethylene of lower density* (LDPE: low-

density polyethylene) from partly branched chain molecules. They disturb the formation of crystalline regions of parallel chains and hence larger amorphous regions of lower density occur. The melting temperature is at about 110 to 115 °C, but the crystalline regions start degrading even at -20 °C. Hence, the *continuous emperature resistance* is only about 70 °C.

When compared to many other insulating materials, polyethylene exhibits excellent **dielectric properties**:

Its non-polar, symmetrical molecule results in low *permittivity* (ε_r = 2.3) and very low *losses* (tan $\delta < 10^{-4}$).

Thin layers (d < 1 mm) give rise to very high *breakdown field strengths* (E_{bd} > 100 kV/mm). For production samples of high voltage and extra-high voltage cables of cross-linked polyethylene XLPE (l = 100 m), strengths for $E_{bd50\%}$ of 40 to 50 kV/mm (r.m.s. value for short-duration AC voltage stresses for up to an hour) and respectively of above 150 kV/mm (peak value for lightning impulse voltage stress) are reported; data on dispersion and service life are given in the literature [324].

Note: Breakdowns occur largely in the *amorphous regions* in which donor states seem to exist, from which electrons can be more easily released than in the crystalline regions.

Initially, only lower *operating field strengths* of 2 to 5 kV/mm were applied owing to the sensitivity to partial discharges and owing to field distortions by the build up of space charges. With increasing improvement in production technology for the development of higher voltage levels, the operating field strengths could be increased up to approx. 15kV/mm, Section 7.1.1.2, Figure 7.1.1-3.

The processing of polyethylene during the manufacture of cable insulations is carried out by extrusion, Figure 5.3-3 (top right). The internal conducting layer, insulation and external conducting layer are applied on the conductor in a triple extrusion head, Figure 5.3-3 (bot-

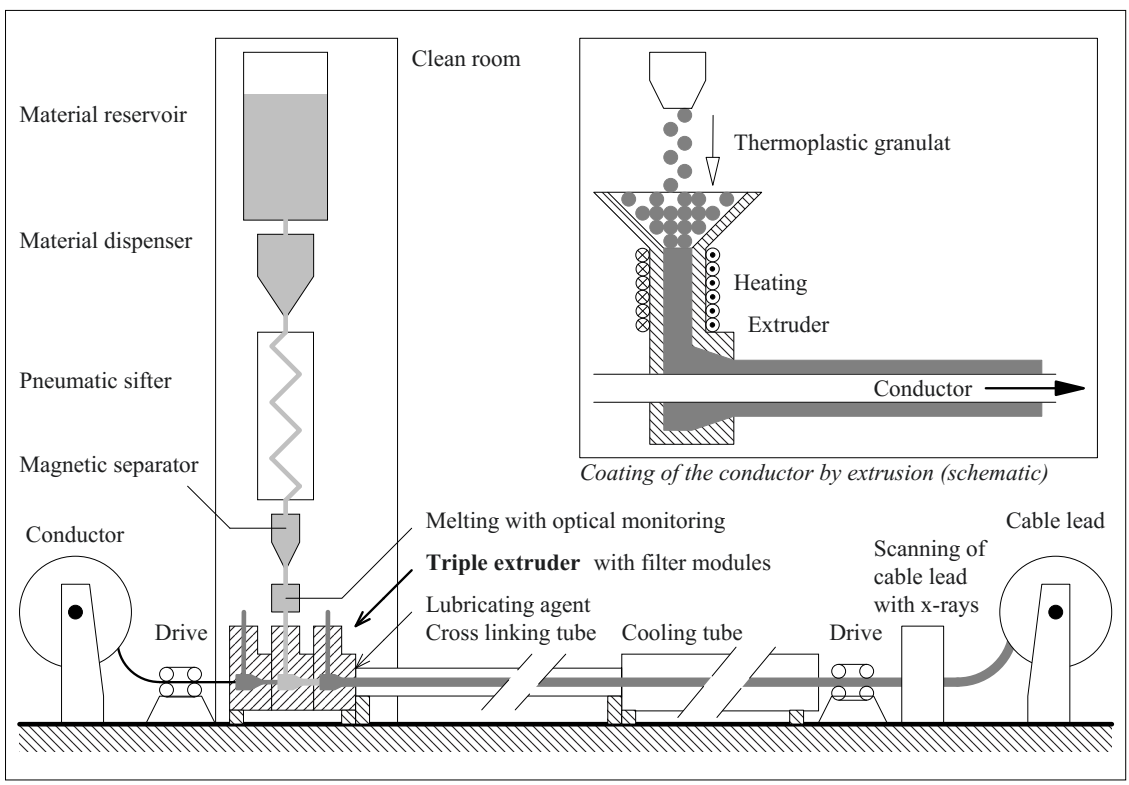

Figure 5.3-3: Manufacturing a high voltage XLPE cable lead by triple extrusion in a horizaontal procedure.

tom). While manufacturing extremely stressed extra high voltage cables, special quality assurance measures are applied [325]. The thermoplastic granulate is purified under clean room conditions by pneumatic sifters and magnetic separators. Melting and compaction as well as optical detection of particles in the melt are carried out in the extruder. Additional safety can be ensured by using filter modules at the outlet of the extruder.

Owing to low permanent temperature resistance and the creepage of the material under mechanical and thermal stress, a three-dimensionally **cross-linked polyethylene** (XLPE) is used in cables. Cross linking takes place *after* extrusion of thermoplastic insulation, for example by electron bombardment. This results in a thermosetting condition at ambient temperature and an elastomeric condition at higher temperatures with a certain degree of *residual mechanical strength*, see Section 5.3.3.5. The *stability of shape* of polymer molecules that are cross-linked to each other, which prevents the creepage of the material, is of special significance. *Permanent temperature resistance* increases to about 90 °C.

Cross linking can occur through the direct effect of radiation or through reaction with peroxides that are added to the polyethylene. The temperature of about 200 °C necessary for the reaction can be attained, for example, by heat supply through steam, nitrogen or ultrasound.

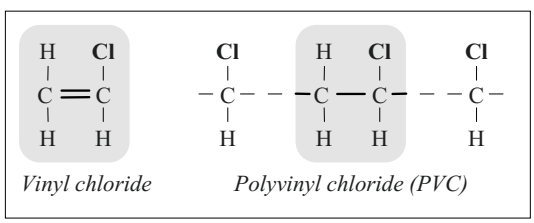

Figure 5.3-4: Polymerization of vinyl chloride.

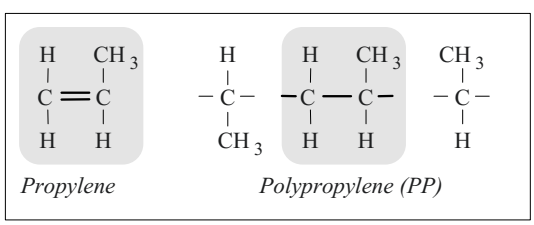

Figure 5.3-5: Polymerization of propylene.

For the so-called *horizontal method*, the cable core is drawn through the heated horizontal tube with the help of an internal lubricant. In the tube, cross-linking takes place with admixed *peroxides* [325], Figure 5.3-3.

The **service life** of polyethylene insulations is often reduced owing to so-called *"water trees"*. This refers to conductive tree-shaped structures which are formed by electrochemical processes under the effect of the electric field and in the presence of diffused moisture. The growth of the "tree" in the direction of the field ultimately leads to the formation of finer discharge channels (so called "electrical trees") and leads to insulation breakdown, see Section 7.1.1.2.

For insulations that are exposed to UV radiation, embrittlement occurs owing to cross-linking reactions. Dark, absorbing fillers (e.g. carbon black) are therefore admixed for outdoor applications, e.g. in cable sheaths.

5.3.2.2 Polyvinyl Chloride (PVC)

Vinyl chloride prepared from ethylene and chlorine is catalytically polymerized under pressure to form polyvinyl chloride (PVC), Figure 5.3-4. This gives rise to a more brittle plastic that has a permittivity of $\varepsilon_r = 4$ owing to the polar Cl atoms. By admixing polar *flexibilizers*, which interact with the polar Cl atoms, a flexible and elastic mixture is obtained. This greatly increases the permittivity and dissipation factor. For a cable mixture with a flexibilizer portion of 20 to 25%, $\varepsilon_r = 5.3$ and $\tan\delta = 30$ to 50% approximately. Typical operating field strengths are under 3 kV/mm.

Owing to the high losses, PVC is used as a *dielectric* only in the low voltage range, currently only up to 10kV for shorter medium voltage cable runs. *Cable sheaths* are manufactured from PVC also for higher voltages.

In PVC, ageing due to the flexibilizer diffusing out is a problem. In the event of fire, corrosive gases (e.g. hydrochloric acid HCl) are formed.

5.3.2.3 Polypropylene (PP)

Polypropylene (PP) is obtained by polymerization of propylene (propene), Figure 5.3-5. This involves the methyl side groups ($-CH_3$) pointing outwards in a twisted chain sequence. Thus, a higher *degree of regularity* is attained which favors the crystallization and leads to a largely *non-polar* character of the chain molecule. The space required by the side groups is responsible for a relatively low density [49], [89].

The *electric strength* and the *dielectric properties* (ε_r = 2.3 tan $\delta < 10^{-3}$) are comparable with polyethylene. The *thermal resistance* is distinctly better than that for other bulk plastics such as PE, PVC and polystyrene (PS): The crystallite melting point lies at 160 to 168 °C, and hence continuous use up to 105 °C and a temporary stress up to 150 °C are possible. Low temperature flexibility is limited to about -20 °C.

Along with high dimensional stability under heat, especially a relatively high degree of *hardness, rigidity and strength* at lower *density* must be mentioned. Polypropylene exhibits a *low water adsorption* and is highly resistant to *chemicals.* In chlorinated and aromatic oils, a *swelling* occurs on heating.

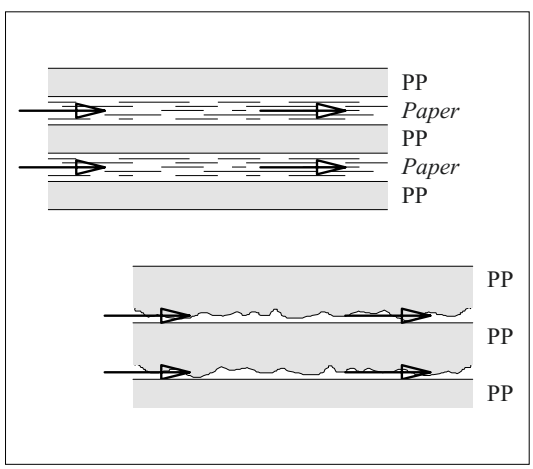

Figure 5.3-6: Impregnation of a mixed dielectric (top) and an "all-film" dielectric (bottom).

Thin **insulating films** for *capacitor dielectrics* are at first extruded with a sheet die and are cooled down as a 1-3 mm thick film on a roller. By extreme extension in the longitudinal and transverse directions, the molecules are aligned and the mechanical properties are vastly improved. Insulating films can also be manufactured by blowing or casting.

A *rough surface* or imprinting creates *impregnation channels* for the layers of films and these enable the penetration of impregnating agents, Figure 5.3-6 (bottom). By diffusion, even cavities enclosed on all sides, e.g. formed by closely lying aluminum foils, are impregnated. Paper layers are no longer required as an *impregnating wick* for low viscosity impregnating agents and an adequate "space-factor" (> 10%).

For *AC voltage,* the films in the all-film dielectric can be more heavily stressed because electrically weaker paper is not present. Also for *DC voltage*, significantly better volume utilization is achieved in all-film dielectric, since the electric field is forced out of the paper owing to difference in conductivity.

Note: The *permissible field strengths* are especially oriented towards *field distortion at the edges* of the conductive foils; see Figures 2.4-20, -21 and -30. They must be determined for real production samples by durability tests. *Operating field strengths* for multilayer dielectrics with d_{total} = 50 µm can be in the range of 20 to 30 kV/mm (50 Hz, r.m.s. values). *Transient strengths* are two to three times higher. Thus, lower values are more applicable to paper dielectrics and higher values to all-film dielectrics.

Polypropylene is also suitable as a **construc-**

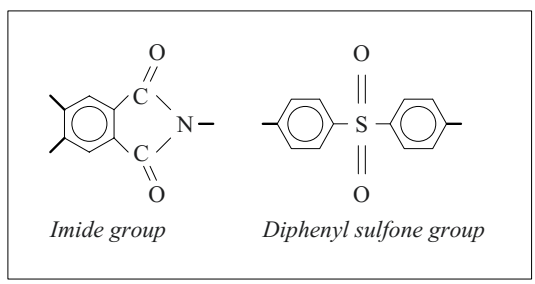

Figure 5.3-7: Components of polyimide (left) and polysulfone (right).

tion material, e.g. for housings (casings) owing to its good mechanical properties. It can be processed by injection molding or extruded. PP parts can be joined by heated tool welding or hot gas welding. Reinforced PP modifications are available for increased mechanical stresses.

5.3.2.4 High-temperature Resistant Thermoplastics

Polymers of pure CH compounds can no longer be used for temperatures that are distinctly above 100 °C. Significantly higher temperatures for continuous use are obtained in the case of polymers which, along with *benzene rings*, also comprise *oxygen atoms, nitrogen atoms or sulfur atoms*, Figure 5.3-7.

Polyimides (PI) comprise the so-called imide group. They can be temporarily stressed up to 300 °C and are suitable for *continuous use temperatures* of 250 °C. Polyimide films are used in highly thermally loaded capacitor dielectrics ($\varepsilon_r = 3.5$ tan $\delta = 3 \cdot 10^{-3}$). **Polyamide imides (PAI)**, which comprises additional amide groups, have a continuous use temperature of 220 °C and additionally exhibit a high *ultimate tensile strength*.

Polysulfones (PSU), and the **Polyethersulfones (PES)** derived from it, can be used for up to 150 °C and 200 °C respectively.

5.3.2.5 Polyamides (PA) and Aramides

Polyamides are formed by *polycondensation* of dicarboxylic acids and diamines with the separation of water:

$$\text{HOOC - R - COOH} + \text{H}_2\text{N - R - NH}_2 \rightarrow$$

$$\text{..... - OC - R - } \mathbf{CO - NH} \text{ - R - NH - .....}$$

$$+ \text{H}_2\text{O}$$

This pertains to a group of different thermoplastic substances that are characterized by comparatively high *mechanical tensile strength, toughness and abrasion resistance*. Therefore, they are often used as fiber reinforced material for insulating, mechanically loaded parts such as bracings, threaded rods, screws, nuts or casings. Their operation is possible even at very low temperatures.

The *types of polyamides* are characterized by the length of the carbon chains in the compositions of chain molecule (PA 6 to PA 12). The polar carbon amide groups -CO-NH- that form the links, increase the permittivity, the dissipation factor, water absorption and the melting temperature according to their relative proportions in the molecule:

PA 6 $\varepsilon_r = 7$ tan $\delta = 300$ ‰ water absorption 4 %

PA 12 $\varepsilon_r = 4.5$ tan $\delta = 50$ ‰ water absorption. >1 %

Owing to the high water absorption, the dimensional stability of the molded components is adversely affected by *swelling*.

The *melting temperature*s lie between 220 °C (PA 6) and 178 °C (PA 12). Owing to the beginning softening, *the continuous temperature resistance* is restricted to values between 75°C (PA 6) and 65°C (PA 12). Mechanical and thermal properties can be improved through *fiber reinforcement*.

Polyamides are not used for the highest electrical stresses owing to their high water absorption, high losses and the relatively high conductivity (10^{-10} S/m for PA 6 to 10^{-11} S/m for PA 12).

For **aramides**, R must be replaced by benzene rings in the above reaction equation. Aramide fibers attain high tensile strengths and they are stable up to about 300 °C.

Aramides are used for the manufacture of *pulp moldings* ("Nomex®-Board" [82]) and *aramide papers*. In the case of high *thermal loads*, they can fulfill the function of cellulose containing insulations, e.g. in transformers. The electrical properties of oil-impregnated materials are comparable with paper or pressboard.

5.3.2.6 Polytetrafluoroethylene (PTFE)

Extremely temperature resistant polytetrafluoroethylene (PTFE) is obtained by the polymerization of tetrafluoroethylene, Figure 5.3-8. The trade name is, for example, "Teflon®" (Du Pont).

This is a thermoplastic material that does not melt in the conventional manner on attaining the crystal melting temperature. At 380 °C, the viscosity of the melt is still so high that the standard processing methods for thermoplastics cannot be applied. Thermal decomposition starts at a temperature above 400 °C.

For manufacturing the molded parts, the PTFE in powder form must be *sintered* at about 380 °C in a gel-like condition. Cavities can be reduced by simultaneous pressurization, but they cannot be totally eliminated. The production of extruded parts (profiles, conductor insulations) is possible with a paste of PTFE-powder and lubricating agent, generally benzene (paste extrusion). After the extrusion the lubricating agent is evaporated and the PTFE is sintered. PTFE products are very expensive owing to poor processability and complex production methods.

Because of low intermolecular forces, the material flows even under low mechanical loads. PTFE is therefore suitable as a *lubricating agent* and as a *sealant* in threaded joints ("Teflon-tape"). Mechanically loaded parts must be fiber reinforced.

The regular structure of the molecule leads to very low *permittivity* of solids and liquids at comparable density (ε_r = 2.05). The *dissipation factor* is very low (tan $\delta = 10^{-4}$). Both the properties remain constant over a wide range of frequencies since there is no orientation polarization. Hence, PTFE is used in *high frequency engineering* for connectors, bushings and capacitor dielectrics.

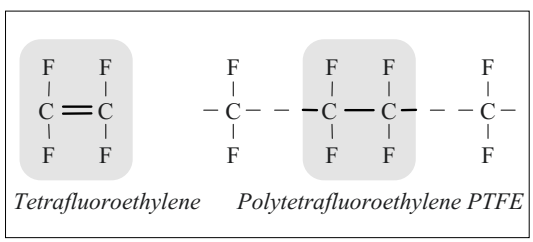

Figure 5.3-8: Polymerization of Tetrafluoroethylene.

PTFE exhibits creepage resistance and arc resistance, but owing to its porosity it is very *sensitive to partial discharges***.** Therefore, the continuous dielectric strength amounts to only 2 to 6 kV/mm.

The use of PTFE in high voltage engineering is restricted to special applications in which a high *operating temperature* (up to 260 °C) or noninflammable substances are necessary. Other options for application are available owing to the resistance of PTFE to *chemicals and weather influences.*

Note: There are still more **fluorine-based polymers** that can be more easily processed but their properties do not entirely correspond to the properties of PTFE [16], [88], [89]. Significantly different dielectric properties are seen in **polyvinylidenefluoride** (PVDF) with a permittivity ε_r = 8 and a dissipation factor tan δ = 0.1 (at 1 MHz). PVDF has a high mechanical strength and toughness. It melts at 175 °C and can be thermoplastically processed. It is used for wire sheathings and cable sheathings as well as for films.

5.3.2.7 Polymethylmethacrylate (PMMA), Acrylic Glass

The thermoplastic polymethylmethacrylate (PMMA) or the *acrylic glass* is obtained by the polymerization of methacrylic acid methyl ester (methyl methacrylate)

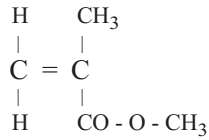

and this is known by the commercial name *"Plexiglas®"*. Despite moderate dielectric properties (ε_r = 3.8 and tan δ = 6 % at 50 Hz), owing to excellent *light transmitting capacity* it finds some uses, even in electrically stressed

environments, for example for viewing glasses, transparent appliances, optically high quality components or as light conductors.

5.3.3 Thermosetting Materials and Elastomers

Thermosetting substances and elastomers are obtained by a *cross-linking reaction* between the molecule chains. That is, a firm spatial network is formed in which the molecules are chemically linked to each other, and this can no longer be broken down by heating as in the case of thermoplastics, therefore melting or liquefaction is no longer possible.

The **cross-linking** can take place *directly* in the course of the chemical hardening reaction (such as for resins or silicone elastomers) or *subsequently* in the case of thermoplastic substances which are cross-linked by adding chemicals or through electron bombardment (such as for cross-linking of thermoplastic PE to XLPE). In this case, the thermosetting or elastomeric condition results generally during the manufacturing process of the insulation components.

Below the **glass transition temperature** the molecule chains, in addition to the cross-linking, are strongly bonded by intermolecular forces; to an extent they are "frozen" and in the so-called *thermosetting (duroplastic)* condition; the material is hard and brittle. On heating way above the glass transition temperature, the intermolecular forces are overcome, causing the thermoplastics to attain the liquid state. However, in the case of thermosetting materials the chemical cross linkages continue to be intact so that only a softened *elastomeric* state is obtained. On cooling down, the molecules return to their original position, the substance exhibits the property of **contour accuracy** or of **shape memory**. The well-known *flow* of thermoplastic substances under mechanical stress is prevented by the cross- linking. Therefore, *elastomers* are especially well suited to applications with continuous mechanical stress (sealants, cable entrance fittings, cable joints, shrinkable sleevings).

During the processing of more rigid thermosetting materials below the glass transition temperature, there are considerable *restrictions*, such as a subsequent change in form is no longer possible or is possible only by mechanical finishing. On the other hand, there are also *other processing options* which open up extensive areas of application for the thermosets as **cast resins** and as **adhesives**:

- The user can change the processability and molding material properties by the *formulation* of the reaction components. This is done, for example, by the addition of fillers, dyes or accelerators.
- Molding material can be cured at comparatively *low temperatures*, sometimes even at room temperature. Thus, all types of casting are possible, e.g. for structural components, cable joints or transformer windings. Moreover, there are many applications such as coatings, sheathings and finishing (varnishing). Epoxy resins are also especially suitable for adhesive bonding.
- *Composite materials* can be made directly by the manufacturer of a device. Examples are the production of fiber reinforced parts (e.g. GRP), production of resin-impregnated insulations based on paper or other fibrous materials, as well as application of silicone shields to other insulation bodies.

Epoxy resins have a special position among the thermosetting insulating materials. Further, polyurethanes and silicone resins as well as various elastomers and shrinkable sleevings are also of importance.

5.3.3.1 Epoxy Resins (EP)

Epoxy resins are polymer compounds which consist of the so-called *epoxy groups* with a braced three ring system, Figure 5.3-9. Owing to their instability, these groups can be used for building up macromolecules and for spatial

cross-linking. By breaking up the three ring system and transposing H-atoms, links are formed to adjacent molecules without the lower molecular reaction products being formed (*polyaddition*). Epoxy resins are thus especially suitable as **casting resins** for the manufacture of high quality insulation parts. Owing to the reactivity of epoxy groups, epoxy resin is also applicable as an **adhesive**.

a) Resin and hardener

Reaction resin that is not yet cross-linked ("*resin component*") is produced by stepwise synthesis of macromolecules from monomers and the formation of new epoxy groups. Depending on the chain length, the reaction resin is liquid *("liquid resin")* or solid *("solid resin")* at room temperature and must first be melted for further processing.

The resin well-established in electrical engineering is based on a monomer compound of 2 moles phenol with 1 mole acetone and is therefore, named as *bisphenol A*. *Cycloaliphatic resins* free from aromatic compounds have a high resistance to creepage currents (tracking resistance) and are considered for outdoor insulators. However, they have not gained acceptance in preference to the classic porcelain and to hydrophobic silicone composite insulators. Further, there is a series of special resins for higher thermal stresses, for flame resistant molding materials or for flexible materials.

The reaction resin reacts after mixing it with the hardener *("hardener component")* with the formation of spatial cross links to a thermosetting molding material. Generally amines and anhydrides are used as hardening agents.

For *amine-cured systems*, for example, diamines with two NH_2 groups form bonds between resin molecules

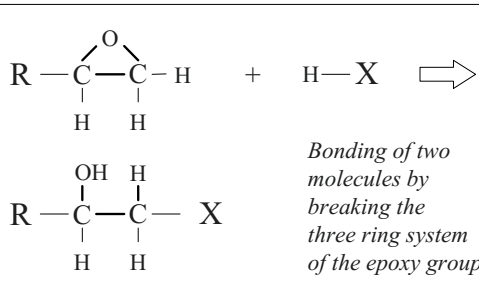

Figure 5.3-9: Reaction of the epoxy group.

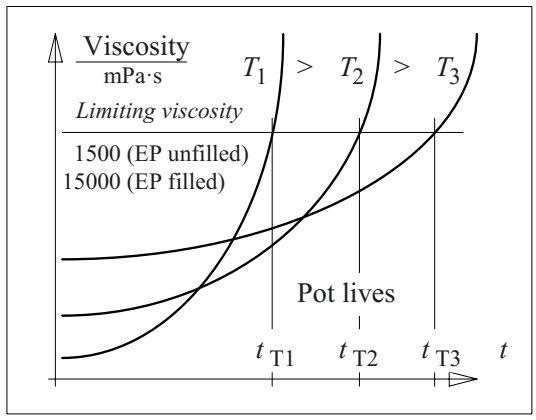

Figure 5.3-10: Isothermal rise in viscosity till the limiting viscosity within the pot life (schematic).

by reacting with the reactive epoxy groups according to Figure 5.3-9. Aliphatic amine hardeners can be used even at room temperatures, but they give rise to low glass transition temperatures of only about 50 °C. Cycloaliphatic and aromatic amines react at increased temperature and give rise to glass transition temperatures of up to 100 °C and 160°C respectively.

A popular *anhydride hardener* is phthalic anhydride, which must first be melted. Therefore it is particularly used for solid resins. Other anhydride hardeners can be processed already at moderately increased temperature.

b) Reaction process

After mixing the resin and hardener, the hardening process begins and this leads to an increase in the *viscosity*, and this in turn restricts the *processing time*. For a comparison of reaction resin masses, the isothermal viscosity rise (that is, for constant temperature) until attaining the limiting viscosity index is observed. The time required for this is termed as *"pot life"*, Figure 5.3-10. The higher the *temperature* of the resin mass, the thinner is the resin liquid at the beginning of the hardening process and the shorter is the pot life. That is, the available processing time is shortened by increasing the temperature.

Curing of the reaction resin mass is associated with a *chemical reaction shrinkage* that is caused by closer packing of chemically linked molecules. Figure 5.3-11 represents the increase in volume of liquid reaction resin mass and the cured material against temperature. The *gelling line* lies between the liquid state

and the cured state. At first the shrinkage occurs in the *liquid phase* (A-B) and can be balanced by the resin mass flowing in. After *gelling* this is no longer possible; the rigid body shrinks further owing to ongoing cross-linking processes which are not yet completed (B-C). Thus, *mechanical stresses* are built up. After successful chemical curing, further *physical cooling shrinkage* occurs owing to a fall in temperature to the service temperature (C-D).

From Figure 5.3-11 it is clear that a *temperature increase* during curing owing to reaction heat (A-B'-C') leads to a reduction in the proportionate shrinkage in the free flowing phase. This increases the mechanical stresses owing to the greater shrinkage in the solid phase. For large castings, *isothermal curing* (A-B-C) at the *lowest* possible temperature must be the aim.

Design and production technology must take the characteristics of shrinkage into consideration to avoid *stress cracks*. For unfilled resins, the reaction shrinkage can amount to up to 3%.

Note: The reaction shrinkage for *liquid resins* is larger than that of *solid resins*, since a considerably larger number of smaller molecules must be cross-linked. The cooling shrinkage, on the other hand, is greater for solid resins owing to higher processing temperatures. An effective method for reducing the shrinkage is the use of *mineral fillers* (e.g. quartz powder).

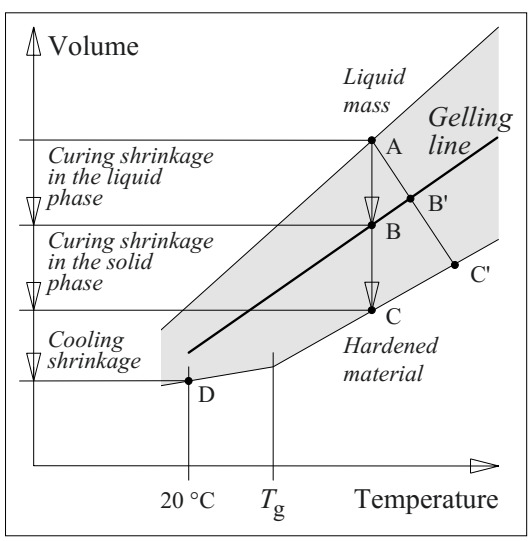

Figure 5.3-11: Components of shrinkage during the curing and hardening of reaction resin mass and during cooling down of the hardened material [90].

Mechanical stresses can occur if free shrinkage in the gelled state is obstructed in the mold. *De-molding* in the gelled, but not yet cured condition may help in this respect. A complete curing must be achieved by a subsequent tempering.

Curing is an *exothermic reaction*, that is, *heat* is released and this causes the reaction to proceed more rapidly within a larger volume than at the cooled surface. Therefore, effective *heat removal* must be provided.

Note: The generation of heat depends on the number of reacting epoxy groups. Their number can be significantly reduced by using *fillers* and by using *long chain solid resins*.

c) Fillers

Mineral fillers can be included up to a *degree of filling* of 55 to 65 percent by weight. Higher degrees of filling are not possible, since then the complete embedding and wetting of filler particles in the resin matrix is not guaranteed. Fillers are used less for a reduction in the cost of the molding material but they can help in *improving a number of properties*:

Fillers reduce the *reaction shrinkage* and the *generation of heat* during the curing reaction. Thus actually makes the production even of *large castings* possible.

Crystalline quartz powder is the standard filler, and this helps in increasing the mechanical strength and thermal conductivity. Adsorption of moisture at the grain surfaces is a problem and this can be overcome by s*ilanization* of quartz powder. Quartz powder *cannot* be used in SF_6-installations owing to the formation of conductive Si-F compounds under the effect of decomposition products of SF_6 (hydrofluoric acid).

Dolomite (Ca-Mg carbonate) and *aluminum oxide* are suitable for SF_6 installations; however, they lead to reduced mechanical strength.

A number of **other fillers** can be used to achieve special properties, such as aluminum

hydroxide $Al(OH)_3$ for high *tracking resistance* and *flame retardance* (by separation of water of crystallization), amorphous quartz powder or glass beads for low *thermal expansion*, aluminum oxide Al_2O_3 for high *thermal conductivity*, fibrous fillers (short glass fibers, Wollastonite) for better *crack resistance*, as well as aluminum hydroxide or chalk for good *mechanical machinability*.

Note: Specially improved properties must often be bought with other disadvantages, such as with poorer mechanical properties or with poorer flow of the reaction mixture (for fibrous fillers).

d) Technology

Accurately weighed components (resin, hardener, accelerator, fillers, dye and additives) must be **mixed** under *vacuum* to ensure adequate **degassing** and to obtain void free products, Figure 5.3-12. For *thin-film degassing*, a spiral conveyor feeds the reaction resin mass into a mixer tube to an end cone on which the mass can be degassed in a thin layer of large area. In the case of solid resins, for anhydride hardeners, as well as for highly filled and highly viscous preparations, a heating process must be carried out to attain a satisfactorily low viscosity for processing.

For **classical vacuum casting**, the degassed mixture is sucked out in the absence of air into a mold that is evacuated and treated with parting agent, Figure 5.3-13. A resin reserve remains in the inlet connections and in the riser to compensate the volume shrinkage in the liquid phase. With the help of specific *temperature gradients*, a reaction is controlled in such a way that the gelling starts as far away as possible from the connecting sleeves (point A) so that the liquid resin mixture can flow as long as possible.

After gelation, the reaction shrinkage in the solid phase leads to detachment from the mold walls and leads to shrink coating of molded components. Generally, filled resins are used for avoiding *stress cracks.*

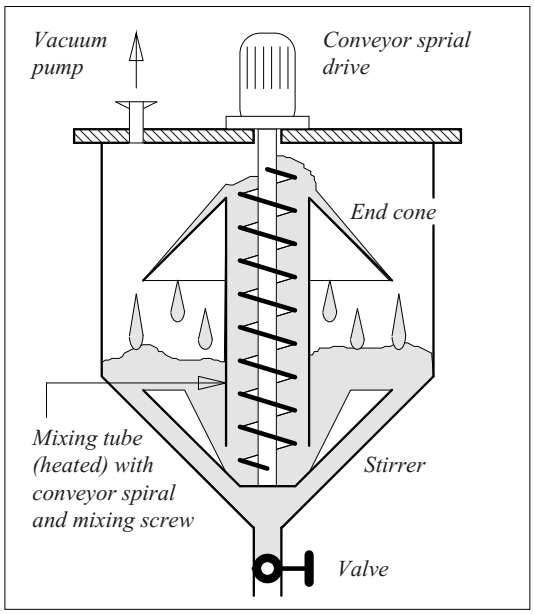

Figure 5.3-12: Mixing and degassing of reaction resin mass through thin film degassing.

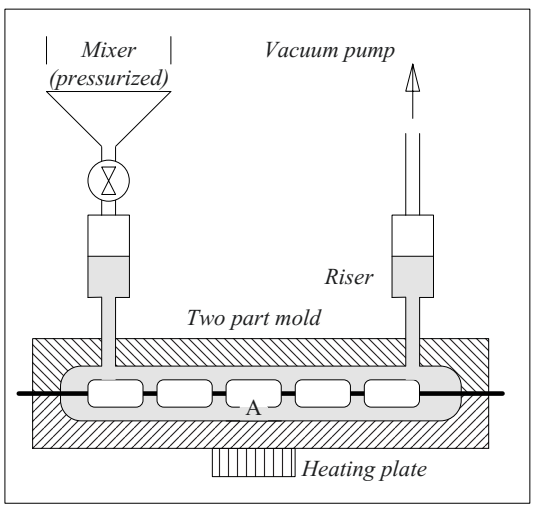

Figure 5.3-13: Example of the encapsulation of a high voltage resistance with a filled reaction resin compound under vacuum.

Note: The function of the riser in an evacuated mold can be fulfilled by a free resin surface. Through a given temperature gradient, the gelling process progresses from bottom to top. The cured component, e.g. an insulator, must then be mechanically reworked to the specified dimension.

A typical *application of vacuum casting* is the casting of larger components in small numbers

of units, such as the encapsulation of windings for *dry-type transformers*.

Under the **pressure gelation process**, the reaction resin mass is gelled in a comparatively hot mold at a pressure of 2 to 5 bars. Thus, the gelation begins very quickly and extensively at the mold wall. Owing to high pressure, the resin mass is pushed out of the mixer while still in the semi-liquid condition. *Short molding cycles* are possible even for *larger castings* owing to rapid gelation at higher temperatures. The effort for the pressure-resistant design of molds and mixers is especially worthwhile for the automatic production of components in larger numbers of units.

Unfilled cast resin must be used for **vacuum impregnation** since fillers would lead to rapid blockages in narrow impregnating channels such as in filters. Moderate mechanical properties, large shrinkage and intense exothermic reaction of unfilled resin are only put up with for *electrically highly stressed parts*, e.g. for windings of larger electrical machines and generators, for spools and dry (oil free) bushings, Figures 5.3-14, -15.

Large machine parts are impregnated in an autoclave under vacuum in an *impregnating bath*. The liquid reaction resin mass with anhydride hardeners is set up to be so inert that the impregnating bath continues to be usable for *a few years*. Curing is done by heat supply and by the action of an accelerator within the material to be impregnated, Figure 5.3-14.

Bushings made of *resin-impregnated paper* (RIP) are manufactured as cylindrical crepe paper windings that are several meters long and contain metallic foils. The crepe paper is dried and impregnated in the axial direction under vacuum, Figure 5.3-15. This involves several *extreme conditions* and they necessitate perfect process control: The pot life of the reaction resin mass must be long enough to enable complete filling of the mold and impregnation of the paper winding. During the exothermic curing reaction, the heat generated by the unfilled masses must remain within

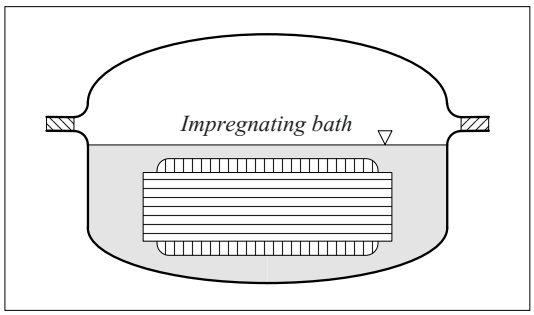

Figure 5.3-14: Vacuum impregnation of a stator winding in an inert impregnating bath.

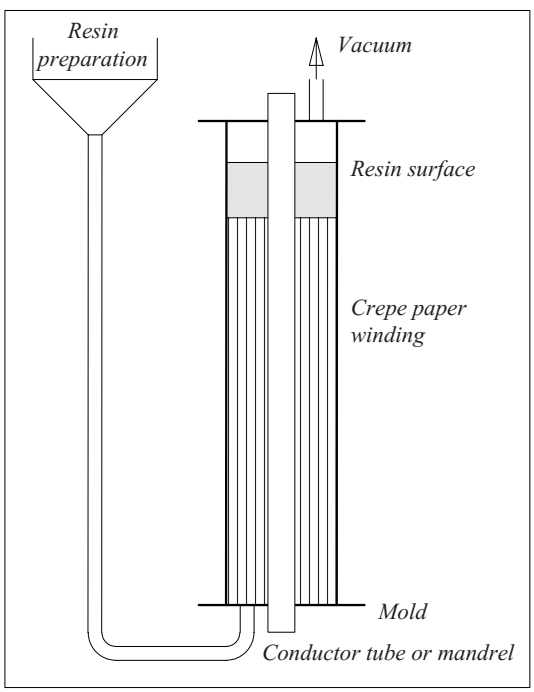

Figure 5.3-15: Vacuum impregnation of large crepe paper windings for RIP bushing insulation core.

controllable limits. During shrinkage in the liquid phase, the resin is replenished in the axial direction through the channels in the crepe paper. After the gelation, the winding is detached from the external mold and it shrinks on the conductor tube in the radial direction.

e) Fiber reinforced epoxy resins

Fiber reinforced components for high voltage engineering, such as tubes, composite insulators or switch rods must form a void free, moisture resistant, stress resistant and durable

bond between the fibers and the resin matrix. *Silanization* acting as a size is necessary for this. The components can be manufactured using a *vacuum impregnation process* for example. High quality tubes can also be manufactured using the *filament winding* (FW) *procedure*. Using this method, glass fiber rovings soaked with reaction resin mass are coiled on a mandrel such that the mechanical stress on the fibers under load produces tension. The resin is cured subsequently.

f) Adhesives

Single-component adhesives based on epoxy resin are used in the form of an already mixed powder which is melted and cured under the effect of heat.

Note: Heat cured powder reaction resin mixtures can also be used for *powder coating* of electrode surfaces. Thus, the hot components are dipped in an atmosphere of powder for a specific duration.

Two-component adhesives are obtained in prefabricated containers in the correct mixture ratio. Large-scale application is in two component mixers with static mixer tubes, Figure 5.3-16. Important applications are, for example, the attachment of porcelains to large housing insulators for bushings and instrument transformers, or the attachment of insulators with metallic armatures.

While *designing the adhesive joints,* it must be noted that these may only be provided for pressure load, tensile stress or combined tensile and shear stress. Peeling stresses and non-uniform tensile loads must be avoided.

The *long-term stability* and hydrolysis resistance of important adhesives must be determined through proper *endurance tests* at increased mechanical stress, similar to that while determining electrical service life time lines.

g*) Electrical properties*

The electrical and dielectric properties of epoxy resins depend strongly on the type of *reaction resin mixture* and on many *production parameters*.

The *electric strength* of epoxy resin in general is dealt with in Section 3.5 (Figure 3.5-5, Table 3.5-2). A description of *dielectric properties* is given in Chapter 4 (Figures 4.2-2, -5, -9, -11).

Guide values for *permittivity* at room temperature and power frequency are ε_r = 3.5... 4 for unfilled materials and ε_r = 5.8 for filled materials (approx. 40 weigth percent Al_2O_3). Depending on the filler substance, other (generally lower) values are obtained.

Dissipation factors for unfilled materials are less than 10^{-2} and slightly higher for filled materials. They increase sharply with temperature (rise in conductivity, as well as polarization losses near the glass transition temperature) and can lead to thermal instability in the case of thick, electrically and thermally heavily stressed insulations.

Moisture adsorption on non-silanized surfaces of fillers or glass fibers causes a sharp increase in losses and results in a sharp fall in electric strength in the case of fiber reinforced materials.

5.3.3.2 Polyurethanes (PU)

Linear urethanes with thermoplastic properties are obtained by polyaddition of di-isocyanates

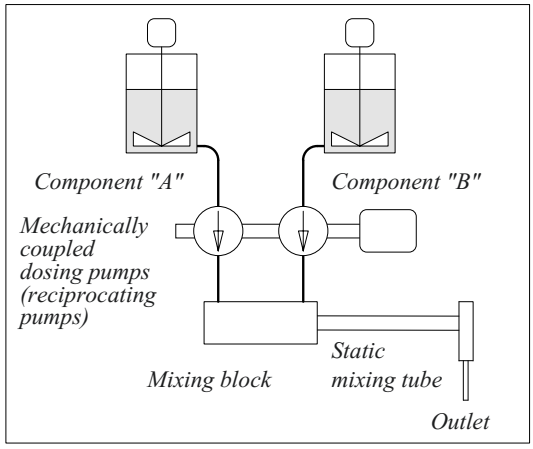

Figure 5.3-16: Principle of a two-component mixer (simplified).

and diols (dihydric alcohols):

$$O{=}C{=}N\text{- R -}N{=}C{=}O \;+\; HO\text{- X -}OH \;\rightarrow$$

$$O{=}C{=}N\text{- R -(NH)-(CO)-O- X -}OH$$

Under this, the bonding urethane group -(NH)-(CO)-O- results from the transposition of an H atom without the elimination of lower molecular reaction products. *Cross links* are possible via NH groups as well as by using isocyanates with three O=C=N groups. Polyols (polyhydric alcohols) such as ricinus oil (castor oil) are used as a reaction agent.

Polyurethanes are substances with *thermosetting or elastic properties*. Although they offer a very wide range of materials and they can be formulated for specific properties, their use in the high voltage engineering field has remained comparatively low until now. The reasons for this are as follows:

Isocyanates react with *moisture* with the formation of CO_2 gas which can lead to *cavity formation.* This problem can be overcome by the addition of *zeolites* that absorb water or by processing without air contact in a two-component mixer.

After the preparation of the reaction resin mass, the reaction takes place relatively rapidly even at low temperatures, hence the available *processing period is short*. Polyurethanes are, thus well suited to castings at room temperature. However, using a mixing plant is recommended owing to short pot lives.

The *thermal resistance* is comparable with the thermal resistance of cold-curing epoxy resins. Generally, maximum operating temperatures of 50 °C to 120 °C are attained. However, special polyurethanes have even much higher glass transition temperatures.

The *electrical properties* are slightly poorer than those of epoxy resins. Guide values at room temperature [88] are for a

thermosetting PU $\varepsilon_r = 4$ (1 MHz),
$\tan\delta = 2\cdot10^{-2}$ (1 MHz),
$\kappa = 10^{-11}$ S/m

and for a
PU elastomer $\varepsilon_r = 7$ (1 MHz),
$\tan\delta > 5\cdot10^{-2}$ (1 MHz),
$\kappa = 10^{-10}..10^{-12}$ S/m.

Positive properties of polyurethanes are high *tracking resisitance,* high *toughness* and high *elasticity*. Foamed elastic polyurethanes exhibit the property of compressibility. They are used as fine-pored **foam** for subsidiary insulations, for example, between epoxy resin core and housing insulator in a bushing for compensating thermal expansions. Electric *field strength, pore size* and *type of gas* must be matched to each other so that no discharges are ignited in accordance with *Paschen's law*.

Typical *applications* of polyurethanes are in the *low voltage range*, e.g. for castings of assembly components, insulation parts for moist interior rooms or for foams. Moreover, wires are insulated with *PU varnishs*. In the *medium voltage range*, elastic PU casting compounds for cable fittings are used as standard.

5.3.3.3 Phenolic Resin and Resin-bonded Paper (RBP)

Phenolic resins are obtained by polycondensation with the elimination of water, Figure 5.3-2. Phenolic resins are a *classic*, *but obsolete substance* of high voltage engineering that was used up to the voltage level 220kV.

By *impregnating paper with liquid resin,* processing into plates, rolled laminated tubes or bushings and subsequent curing at increased temperature, oil-free insulation parts could be manufactured for the first time from so-called *resin-bonded paper* RBP (commercial name e.g. "Pertinax"). However, to avoid stress cracks in large scale insulations, the papers were not completely impregnated so that mechanical stresses could be reduced by the *delamination of paper layers*. In such insulations, since they are not completely free from air, *partial discharges* must be taken into consideration. However, they last a relatively long

time owing to the relatively high *partial discharge resistance* of the phenolic resin.

Resin-bonded paper has a relatively high *permittivity* ($\varepsilon_r \approx 5$), high *conductivity* ($\varepsilon \approx 10^{-11}$ S/m) and high *losses* ($\tan\delta \approx 0.1$). The given values relate to $T = 20$ °C and $f = 1$ MHz. The *short-duration electric strength* is comparable with the strength of other high polymer insulating materials.

Insulating components made of resin-bonded paper are not always gas-tight and oil-tight parallel to the paper layers. *Infiltrating oil* can re-impregnate the available cavities and thereby lead to a *rise* in the *capacitance* of the insulation. Owing to the effect of partial discharges, yellow "*X-wax*" is thus formed by decomposition and cross-linking of oil molecules.

While dissecting electrically highly stressed resin-bonded paper insulations, often interesting, widely branched discharge traces are seen between the paper layers.

Today, void free resin-impregnated paper RIP insulation is state of the art. However, resin-bonded paper RBP bushings are still in use.

5.3.3.4 Elastomers and Shrinkable Sleevings

Elastomers are spatially cross-linked macromolecules which return to their initial position without experiencing any permanent change in shape, even after a mechanical extension, owing to their *contour accuracy* and their *shape memory*. Popular substances are, for example, ethylene propylene rubber (EPR) or silicone elastomers. Elastomers, when compared to thermoplastics, have a very wide elastic range in which the *extension* is *reversible,* since the *cross-linking* of molecules does not allow mutual relative displacement. Insulation systems with high mechanical flexibility are thus possible, e.g. **flexible cables** that are not laid in a fixed position. Furthermore, elastomers can be compressed or extended for long periods without losing their restoring forces through material flow processes. Along with the usual technical applications, such as for **sealing**, this is especially important for **cable joints** and **cable entrance fittings,** which must contact the cable insulation with adequate *surface pressure* to guarantee the high voltage strength of the joints, Section 7.1.4.4.

Note: Such **joints** generally contain a lubricating agent to compensate for unevenness and to fill voids.

Cable insulations are manufactured from extruded thermoplastic polyethylene by subsequent spatial cross-linking, Section 5.3.2.1 Thus, a thermosetting **cross-linked polyethylene** (XLPE) is obtained, which does not melt at increased temperatures but changes to an elastomeric condition. Hence, even at increased operating temperatures of up to 90 °C, the flow of the material is inhibited.

A special form of elastomers is **shrinkable sleevings**. They are elastic only at increased temperature, that is, above the glass transition temperature. They are stretched in that state by compressed gas and subsequently cooled down below the glass transition temperature. In this way, the stretched condition is frozen since the intermolecular forces no longer allow any change in the position of the molecules. Only when heated, these bonds are released and the sleeving shrinks to the original dimensions, which are predetermined by the spatial cross-linking of macromolecules (*contour accuracy, shape memory*).

While *manufacturing* shrinkable sleeving, at first a tube is *extruded* from thermoplastic material (for example, from polyethylene PE). Subsequently spatial *cross-linking takes place*, e.g. by bombardment with electrons. Owing to this, the bonds of hydrogen atoms are broken, giving rise to free valences and this enables the polymer molecules to cross-link with one another. At room temperature, such a cross-linked sleeving still has *thermosetting* properties owing to intermolecular forces. By *heating* above the glass transition temperature, the sleeving becomes *elastic and* can be *stretched* to the desired dimension by compressed gas. After *cooling down* in the stretched condition,

it is again frozen into the thermosetting condition.

The *user* can change the stretched sleeving into the elastic state again by heating, in which the sleeving tries to shrink to its original dimensions. During this so-called **heat-shrinking technique**, the sleeving largely adapts itself to form fit the body to be shrink-wrapped, but no permanent force is exercised on the substrate after cooling down.

In contrast, there is a so-called **cold-shrinking technique**, whereby the sleeving is made of permanent elastic material (e.g. of silicone elastomer). It is mechanically widened on a supporting base (e.g. a plastic spiral or mandrel) and is applied to the body to be shrink-wrapped by removing the supporting base. A certain amount of residual extension of the sleeving remains, which leads to a permanent *surface pressure* on the substrate and which, along with the lubricating agent, allows *joints* of very high voltage strength.

5.3.4 Silicones

5.3.4.1 Properties of Silicones

The chemical relationship of the s*ilicon atom* with the carbon atom allows the formation of analogous compounds with exceptional properties. The simplest monomer compounds are the methane-related silane and the long chain silanes derived from it, Figure 5.3-17.

Polymer *silicone compounds,* for example, are obtained from methyl silanols by polycondensation. That is, two OH groups are attached to form an oxygen bridge -O- with the elimination of H_2O, Figure 5.3-17. *Silicones* are macromolecules made of a very stable inorganic skeleton with Si- and O-atoms that is surrounded by organic groups R, Figure 5.3-17. The monomer structural unit R_2SiO formally corresponds to a ketone R_2CO, and hence the macromolecule is referred to as "silico-ketone" or as "**silicone**" [49].

By *spatial cross-linking (vulcanization)*, thermosetting *silicone resins* and also *silicone elastomers* (SIR, *silicone rubber*) are obtained. Silicone elastomers are exceptionally elastic, extensible and have a very high contour accuracy. Their properties are greatly influenced by the degree of cross-linking and by mineral fillers that are added to resins and elastomers, generally with percentages ranging from 30 to 70 %. In high voltage engineering, the following groups of materials are especially important:

1. **Silicone resins** are spatially heavily cross-linked thermosetting materials whose glass transition temperature lies above the working temperature. They are used as temperature resistant substances.

2. **Silicone elastomers** (so-called "silicone rubbers") are spatially less strongly cross-linked so that the glass transition temperature lies below the working temperature and an elastomeric (extensible) condition exists. Areas of application are hydrophobic insulators (Section 5.3.4.2), contour accurate and permanently elastic insulation bodies (Section 5.3.4.3) as well as insulations and sheathing for flexible cables.

3. **Silicone gels** are spatially cross-linked only to a very small extent and have a higher pro-

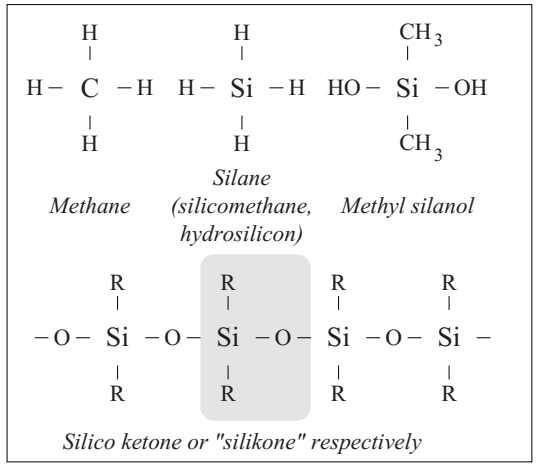

Figure 5.3-17: Monomer and polymer silicon compounds as well as alalogies between carbon chemistry and silicon chemistry.

portion of silicone fluid. This results in a sticky state with greater spreading power and higher breakdown strength, and hence they are well suited to electrically highly stressed joints or interfaces (Section 5.3.4.3).

4. **Silicone pastes** (so-called "silicone grease") are spatially no longer cross-linked; however, the chain length of the molecule is so large that a paste-like condition exists. They can be used, for example, in filling electrically stressed joints or for applying to porcelain insulator surfaces for (temporarily) increasing the hydrophobicity.

5. **Silicone liquids** (so called "silicone oils") are no longer cross-linked for short chain lengths and hence a liquid state exists. They can be generally used as a substitute for mineral oil, Section 5.4.3.2. For cost reasons, however, this happens only when it is necessary owing to technical requirements (temperature resistance, fire protection).

Silicones that are cross-linked can be differentiated as *RTV silicone,* i.e. room temperature vulcanization silicone, and *HTV silicone*, i.e. high-temperature vulcanization silicone or heat-curing silicone respectively. HTV silicone has been preferred in the past owing to its better mechanical properties. RTV silicones have improved so much in their properties in the meantime that they are increasingly used at low temperatures owing to their simpler processability (*LSR liquid silicone rubber*). It is common practice to use a two-component mixer system for the components A and B which react by polyaddition, Figure 5.3-16.

Silicones are not inflammable and can be used over a *wide range of temperature* (-60 °C to 180°C) without any significant change in properties. Silicones are *highly resistant* to chemicals, weather influences and ageing.

The wide-meshed cross-linking of **silicone elastomers** allows a *comparatively high diffusion* of gases, water vapor or oil molecules. Hence, the suitability of silicones as *sealing material* must be tested in each case. For example, oil impermeability can be attained with fluorinated silicone elastomers. In the case of **silicone gels**, this property has a positive effect, since the *trapped gas* in seams can escape by diffusion. [472].

The *permittivity* of unfilled silicones is $\varepsilon_r = 2.8$ to 3, with fillers between 3 and 6, in special cases it is even at 15 to 20. The *dissipation factor* tan δ amounts to about 0.5 to 1 % and the *conductivities* are between 10^{-13} and 10^{-11} S/m for unfilled and filled materials. Owing to the non-polar properties of molecules, the dielectric properties vary significantly less with temperature than for other elastomers. Silicones are generally *tracking resistant* and have high *breakdown strength* that is comparable with other polymers.

Note: By filling with carbon black, *conductive mixtures* are obtained and these can be used in *cable fittings* for potential grading electrode contours.

5.3.4.2 Hydrophobic Insulators

Surface hydrophobicity must be mentioned as an excellent property, Figure 5.3-18. Silicones are thus the ideal material for *outdoor insulations* under conditions of severe *pollution*. Precipitation forms *isolated water droplets*, which are held together on polluted surfaces by the surface tension of water, Figure 5.3-18 (top right and middle). Comparable porcelain surfaces, on the other hand, are hydrophilic, water flows to form a large area of moist film, Figure 5.3-18 (top left). The *contact angle* Θ [92] is suitable for the quantification of hydrophoby: a large contact angle is obtained for hydrophobic surfaces, whereas easily wettable surfaces lead to small contact angles and the drops run to form a film. When a drop runs on to the insulator surface, the contact angle can be differentiated as the advancing angle Θ_a and the receding angle Θ_r. The latter determines whether the flowing drop leaves behind a *moist film*. Moist films can bridge over large stretches of the insulator and initiate a *pollution flashover*.

Note: An additional option for qualitative estimation of hydrophobicity is a simple *flashover test*: a plate like material sample (125 x 125 x 5 mm^3), which has been wetted earlier in an aqueous saline solution (κ = 100 µS/cm) is placed between two plate electrodes (D = 70 mm) following a defined dripping period (1 min) and stressed several times with AC voltage until flashover occurs [9], [57]. The results can be useful in identifying significant differences depending on the surface condition. The flashover test is thus even suitable for comparative evaluation of different pre-stresses and different methods of surface treatment.

Silicone sheds have the ability to prevent the formation of continuous films, even under *intense rain*, and to facilitate isolated drops rolling off, Figure 5.3-19. The *surface resistance* is maintained at a high level, a continuous moist film does not form. Porcelain insulators that are coated with silicone paste ("silicone grease") exhibit a similar characteristic. On the other hand, the surface resistance of clean *porcelain surfaces* collapses by many orders of magnitude at relatively low rain intensities and the individual drops flow together to form a tight water film [7], [9], [10].

Experiments have shown that several weeks of *pollution* on porcelain surfaces under outdoor conditions leads to the breakdown of hydrophobicity even for much lower rain intensities. The performance of silicone surfaces has not changed [57].

Long term experience has proved that silicone sheds, even after many decades, retain their hydrophobic character even under the conditions of industrial pollution [9], [93]. The hydrophobicity extends even to the deposited *dirt layer*. The low-molecular components of silicone which diffuse out and which are formed within the shed material are held responsible for this.

The hydrophobicity on the stressed areas can be *temporarily reduced* by flashovers, corona discharges or treatment with aggressive solutions. However, low-molecular components that diffuse out lead to an automatic *regeneration*. With the help of silicone liquid ("silicone oil"), the hydrophobicity can be immediately restored [9], [57].

Note: Dew on the silicone surfaces can be a reason for corona discharge. A so-called **dewdrop corona** occurs at the dew drops which are distorted to form peaks due to the field forces. The dewdrop corona can be avoided by limiting the field strengths to 0.3 to 0.5 kV/mm

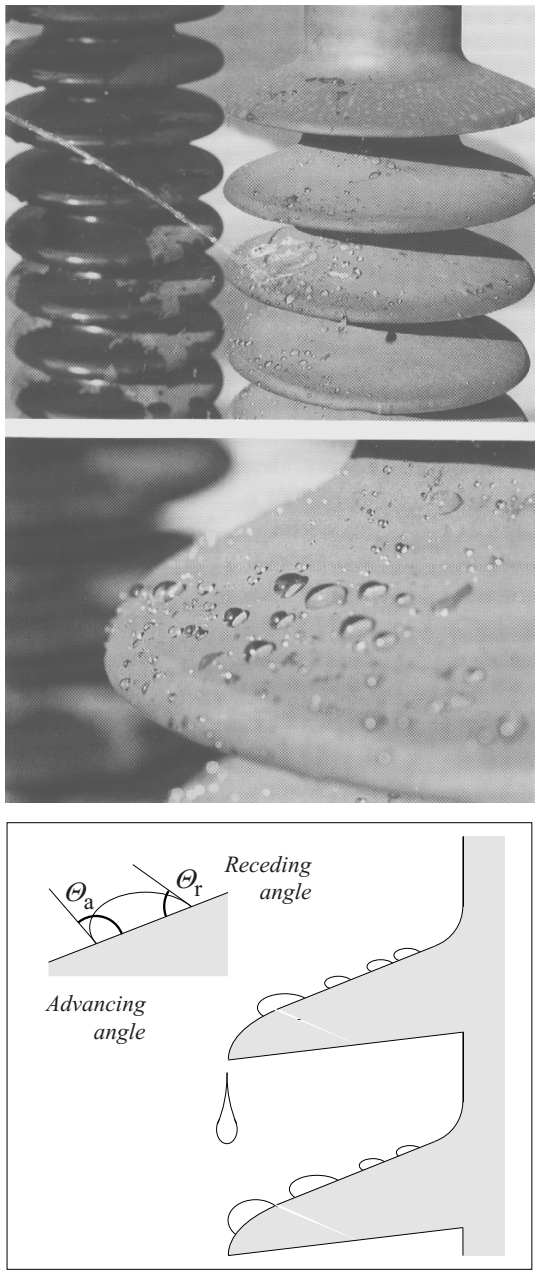

Figure 5.3-18: Drop formation on the surface of a hydrophobic silicone-shed insulator (top right, middle and bottom) in comparison to the formation of a moist film on the hydrophilic surface of a comparable porcelain (top left) [9], [57]. Photo insulators: HSP Hochspannungsgeräte GmbH, Troisdorf.

[471], Section 3.2.6.4.

The *excellent surface properties* of silicone give rise to the question of whether the usual *creepage distance* of 2.5 to 5 cm/kV for porcelain (related to the r.m.s. value of the applied operating voltage, see Section 3.2.6.4) can be shortened. Long term investigations with silicone sheds on bushing insulators for more than a decade have shown that even in severely polluted, humid and salty atmospheres, without intermediate cleaning, reliable operation with creepage distances between 1.7 and 2 cm/kV is possible [57], [93]. Despite this, creepage distances are often designed according to the guidelines approved for porcelain. It must also be noted that corona discharges can occur for local field strengths that are too high when there is dew on the surface [471] (see above).

Note: In the case of *HVDC bushings* above 500 kV, the application of bushings with silicone sheds is often considered as the only secure way to avoid flashovers under non-uniform rain [8], [93], see Figure 2.4-29.

Important **applications** of silicone elastomers are as *insulators fit for outdoors* (insulator rods, housing insulators for instrument transformers and bushings), push-on *cable fittings* with *potential grading* and thermally resistant flexible *cable insulations*.

Different methods can be applied for manufacturing **composite insulators**, Figure 5.3-20. In each case, the surface of the fiber –reinforced tube or rod must be treated with a *bonding agent* (primer), and this guarantees a permanent and hydrolysis resistant chemical bonding between the substrate and the sheds.

Note: The vulcanization and bonding of silicones can be hampered by chemicals (e.g. by amines for adhesives and epoxy resins) and by their vapors.

Individual *prefabricated sheds* are vulcanized with a RTV silicone (cross-linking at room temperature) on the pre-treated surface of the insulator tube and on the already applied sheds, Figure 5.3-20a. Using individual sheds allows a high degree of flexibility with respect to spatial dimensions and the choice of material (HTV silicone or RTV silicone) owing to lower molding costs.

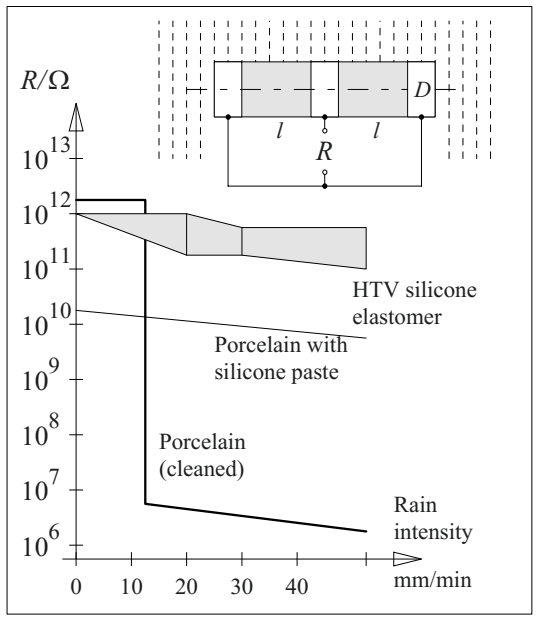

Figure 5.3-19: Resistance of cylindrical surfaces (D = 70 mm, l = 188 mm) for vertical rain (conductivity 100 µS/cm).

The sheds can also be directly cast in a top opening mold with RTV silicone *on a pretreated insulator tube*, Figure 5.3-20b. After gelation, the mold migrates downward into the position for casting the next shed. Great flexibility with respect to spatial dimensions is obtained by using very simple molds.

The *cast of the complete insulator* on the pretreated substrate needs expensive, longitudinally divided molds, Figure 5.3-20c. The flexibility is thus severely restricted, but it results in very short cycle times that enable batch production of larger numbers of units. For longer insulation lengths, many successive castings are conducted. The parting seam of the mold running longitudinally must be subsequently smoothened if possible to avoid the accumulation of dirt.

Note: Composite insulators are impressive not only owing to their *excellent surface properties*. They also have a much lower *weight* compared to porcelain. Moreover, *greater safety* is also provided, e.g. in the case of an internal short circuit or for devices filled with

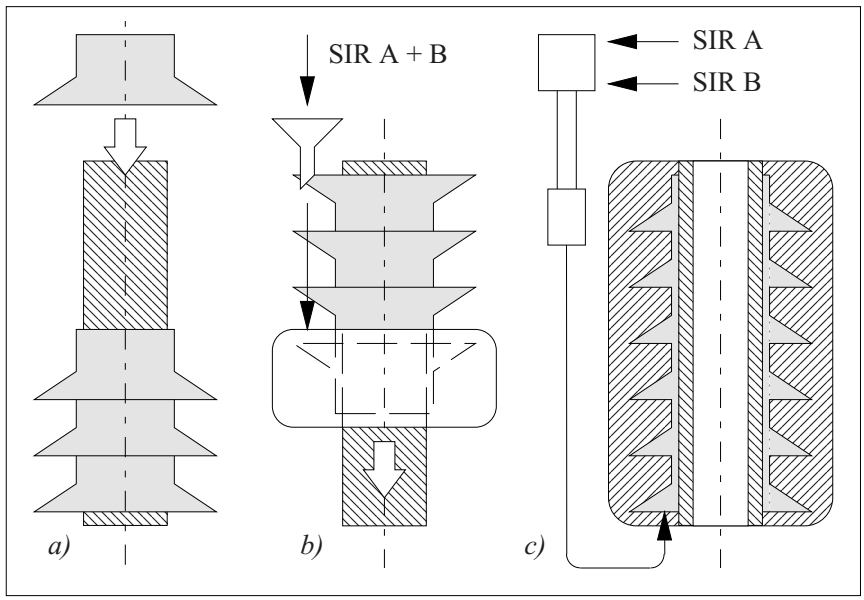

Figure 5.3-20: Manufacture silicone-shed composite insulators on a glass-fiber reinforced insulating tube or insulating rod:

a) Application of prefabricated HTV- or RTV-sheds.

b) Casting of individual sheds with a RTV casting compound in a mold migrating downwards.

c) Casting of a complete insulator in a single split mold.

compressed gas: there are no sharp-edged porcelain pieces if the housing insulator bursts [57], [93], Figure 7.1.2-4.

5.3.4.3 Other Applications of Silicones

In **cable entrance fittings** and in **cable joints**, conductive silicone is used for a potential grading ground electrode (deflector), which is cast in insulating silicone, Figure 5.3-21. The flexibility of the silicone enables close and permanent contact to the surface of the uncovered cable insulation while pushing-on the "grading cone". The permanent elastic properties of the silicone elastomer enable the continuance of a permanent mechanical stress, which takes care of the necessary contact pressure on the uncovered cable insulation. A high quality joint over a long period of time is only made possible by the permanent elasticity of the SIR.

Note: The contacting of the deflector with the outer semi-conductive layer (insulation screen) of the cable insulation and the quality of the joint, which is highly stressed in the normal and tangential directions, are of particular significance.

Other applications of permanently elastic elastomers have been described under Section 5.3.3.4.

The properties of **silicone gel** for electrically highly stressed interfaces and joints are also of interest: owing to its high degree of *stickiness*, adhesion is good on many substrates. Owing to the low degree of cross-linking in the gel, *cross-linking* with the substrate is often even

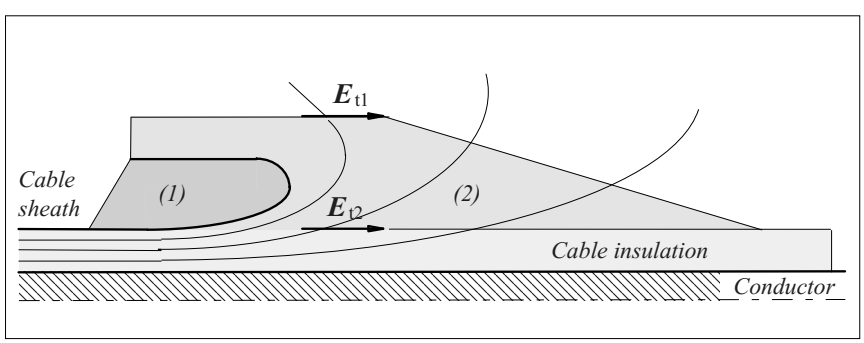

Figure 5.3-21: Potential grading in a cable entrance fitting through a ground electrode (so-called "deflector") made of conductive silicone (1) and a "grading cone" made of insulating silicone (2).

possible. The voids formed by the surface roughness can be completely filled for force-fit connections under pressure, owing to the high proportion of *silicone liquid* in the gel. Furthermore, the *trapped gas* can easily diffuse out under sufficient contact pressure so that a high quality interface is obtained.

Breakdown tests for **two-component systems** of basic material (silicone elastomer, polyethylene, epoxy resin and porcelain) with a silicone gel have shown that the *longitudinally stressed interface* with the polymeric basis materials has an electric strength that can correspond to (at least) the strength of the pure gel [472]. Only the interface with the porcelain corresponds to standard high voltage engineering expectations and is of lower strength, since apparently the roughness here is greater and the adhesion is lower [472].

5.3.5 Nano-dielectrics

5.3.5.1 Introduction

Substances with special properties determined by nanosized fillers have been in use for a long time without the relationship between the properties and nanofillers being known. Historical examples are Roman glasses, whose fascinating optical properties were created by nanoparticles of gold, or oriental sword blades whose carbon content in the form of nanotubes gave rise to excellent mechanical strengths. It only became known towards the end of 20th century that the properties of a basic material can be drastically changed by relatively low quantities of nanostructured fillers.

Since then, efforts have been made specifically to develop so called “nanocomposites” with improved properties. For this, particles with dimensions of a few 10s of nm are mixed with a proportion of very few weight percents of up to about 10 %.

Note: The *nanostructuring* of nanoparticles can be three-dimensional (particles in the form of powder), two-dimensional (rods, tubes) or one-dimensional (plates).

Surprisingly, this achieved exceptional changes in properties that are completely unknown for fillers in the µm range. At first, there was greater interest in the resultant high mechanical strength or high thermal resistance. As early as 1994, Lewis had described the consequences of nanostructuring for dielectrics by a drastic enlargement of the microscopic interfaces and had used the term “nanometric dielectrics” [448].

Inorganic nanoparticles, as fillers in polymers, have the ability to cause a so-called nanostructuring of the surrounding polymer molecules and effect large improvements of the electrical and dielectric properties [416] [487]. The interfaces between the nanoparticles and the polymers and the reduced distances to the neighboring particles play a special role in this. Properties that were not attainable until now for dielectrics are thus attained, e.g. hydrophobicity and self-cleaning surfaces, reduced build-up of space charge, better resistance against treeing and erosion or higher resistance to partial discharges. Nanocomposites, therefore, possess a special innovation potential also in high voltage engineering.

Well-known inorganic materials are used as **fillers,** such as aluminum oxide Al_2O_3, silicon dioxide SiO_2, titanium dioxide TiO_2, magnesium oxide MgO or so-called layered silicates LS. Popular polymer materials such as polyamide PA, polypropylene PP, cross-linked polyethylene XLPE, epoxy resin EP or silicone elastomers SIR are considered as basic materials (matrix). Therefore, the special properties of nanodielectrics arise primarily from the small diameter of the filler particles and not necessarily from special materials.

Manufacturing procedure requires the mixing of particles with diameters in the nm range into organic polymers in the liquid phase, such as resin components or thermoplastics. For this, a few percentages by weight must be homogeneously and completely dispersed. This is technologically very complex and expen-

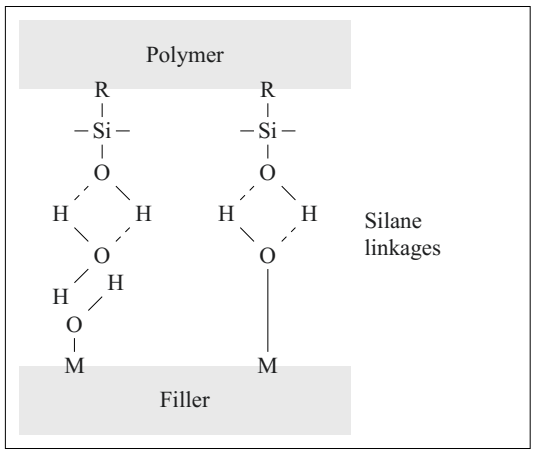

Figure 5.3-22: Silane linkages between filler particles and polymer molecules.

sive, but very important since the desired property improvements can only be attained by optimal distribution of the nanoparticles.

Note: The use of nanoparticles is still at a very early stage and many physical and chemical interdependencies are not yet completely known. The probable **risks** of handling nanoparticles, therefore, should not be simply ignored. Still, high chemical activity exists in many cases owing to extremely large particle surfaces and the small particles can penetrate deep into the biological systems down to the level of individual cells [449]. The medical and pharmaceutical sciences want to use these properties, specifically for new therapy approaches.

5.3.5.2 Principle of Nanostructuring

Nanoparticles, like other fillers, can form a compound with the polymer matrix, e.g. through silanes, Figure 5.3-22. The special feature here is the large particle surface area, which leads to comparatively wide-ranging and comprehensive **structuring** or **self-organization** of the surrounding polymer molecule chains parallel or perpendicular to the surface, Figure 5.3-23.

The range of the structuring imparted by the particle surface area can amount to a few 100 nm. For the common filler particles in the µm range, this has no effect on the actual basis material (matrix material), since the distances also lie in the µm range and thus are much greater than the range of the structuring, Figure 5.3-24 (top). With nanoparticles, on the other hand, even the distance of the particles is in the order of magnitude of 100 nm, so that the structured layers in the environment of the particle comprise a large part of the total volume, Figure 5.3-24 (bottom). Thus, the material on the whole acquires completely new properties.

Note: An **interactive zone** with multiple charge double layers is formed at the surface of a nanoparticle with a diameter of about 10 to 50 nm (Tanaka model [416]): comparatively large bonding forces act on a first layer that is a few nm thick. Deep traps are formed in the second layer of about 10nm thickness. Local microscopic volumes in a third layer of several 10s of nm thickness act as traps for charge carriers and ions.

The interactive zones at the particle surfaces not only lead to structuring of the surrounding polymer matrix, but also influence the injection of charge carriers at high local field strengths at the electrodes (Schottky emission).

The structuring imparted by the particles results, for example, in a firm and regular structure of the base material. Polymer chains are immobilized and the glass transition temperatures are shifted. This can manifest itself in higher mechanical strength, in higher thermal resistance, in larger resistance against erosion and in changed electrical properties.

5.3.5.3 Dielectric Properties

The typical **electrical and dielectric properties** of nanocomposites are substantially

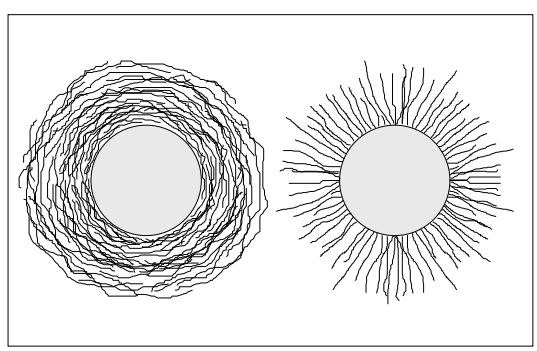

Figure 5.3-23: Alignment of polymer chain molecules parallel or perpendicular to the surface of nanoparticles (self-organization, schematic).

changed in comparison with amorphous polymers without structuring [487]. For the application as dielectrics, the following effects are significant:

1.) Increasing the *resistance against partial discharges, treeing and erosion* as well as the *tracking resistance.*

Owing to the forces in the interactive zones, segmented structures occur from nanoparticles (nanosegmentation) and quite strong bonding forces exist between these (first and second layer). The eroding effect of electrical discharges takes place at first in the spatially limited areas with weaker bonds (third layer).

2.) Reducing the *space charge build-up*.

The negative extensions of the charge double layers of the structured arrangement of nanoparticles increase the potential thresholds at the electrodes for charge carrier injection. The microscopic field stress enhancements caused by space charges are distinctly reduced because of this.

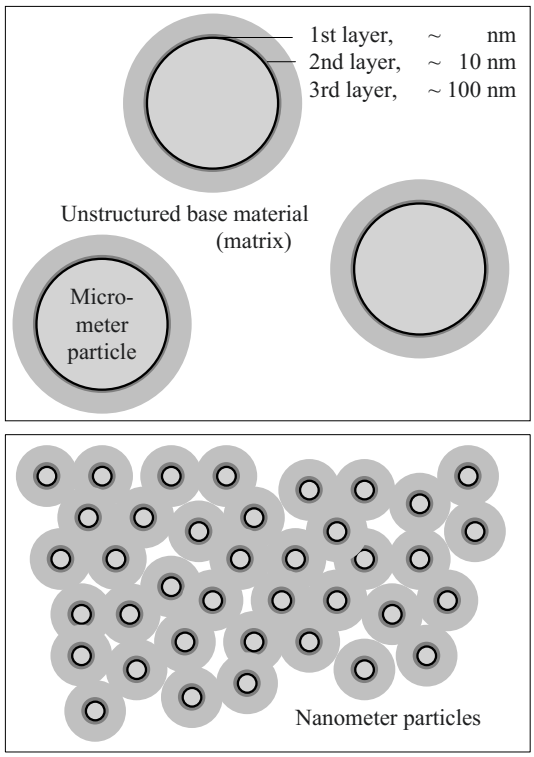

Figure 5.3-24: Incomplete structuring of base material by micrometer particles (top) and extensive tructuring by nanometer particles (bottom), schematic representation.

3.) Improved or unchanged *breakdown strength*.

4.) Partly slight reduction of *permittivity* owing to reduced interfacial polarization and because of immobilization of polymer chains.

5.) Changes in the *dissipation factor* with temperature and frequency caused by the complex structure of the interfaces and owing to shifts in glass transition temperatures.

6.) Increase or decrease in *conductivity*.

Depending on whether the nanoparticles used act as ion traps or contribute to ionic impurities, charge carrier densities are decreased or increased.

5.3.5.4 Applications

For most of the **applications** in high voltage engineering, the high costs of nanocomposites are not yet in reasonable proportions to the attainable improvements. However, there is potential for numerous applications and this will increasingly lead to practical applications.

Table 5.3.5-1: Possible applications for nanocomposites [416], [460]

Application	*Material*	*Advantages*
Motor windings	Polyimides	PD resistance
High voltage machine windings	Epoxides	PD resistance
Cast resin transformers	Epoxides	PD resistance, thermal resistance
AC cables	XLPE	Resistance against treeing
Capacitors	PP	Voltage strength
DC cables	PE, XLPE	Reduction of space charges
External Insulation	SIR	Tracking resistance, hydrophobicity
Switchtgears	PE, Epoxides	Space saving

Example: A possible application example is *enameled wires in converter-fed motors,* which are subjected to quickly rising repetitive impulses. Partial discharges in the air filled cavities can lead to a progressive erosion of insulation for conventional wires. Wires in which the partial discharge resistance of 15µm thick polyesterminide insulation was significantly increased by nano-

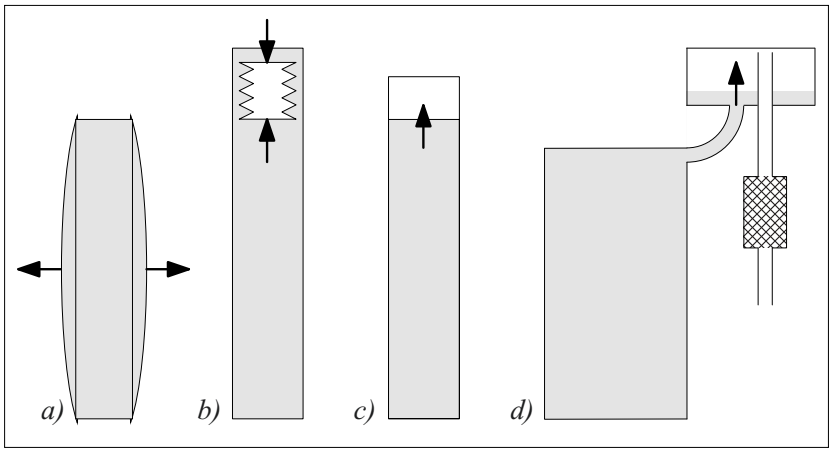

Figure 5.4-1: Compensation of thermal expansion of insulating liquids:

a) Hermetically sealed housing (tank) with rectangular cross section.

b) Hermetically sealed housing with metallic expansion cell or bellow.

c) Hermetically sealed housing with gas cushion.

d) Open housing with expansion tank (compensator) and dryer.

particles based on layered silicates (phyllosilicates) have been reported in literature [459]. Even with filling ratios between 1 and 5 %, service life extensions of several orders of magnitude were attained.

5.4 Insulating Liquids

The main task of insulating liquids is the *impregnation* of cavities of all types with a medium that has an electric strength as high as possible. Compared to gases, liquids have the advantage of significantly higher electric strength even under normal pressure. Even the field displacement in the liquid is less owing to higher permittivity. Additionally, in transformers insulating liquids must remove the occuring *ohmic heat losses* convectively.

Note: Earlier, insulating liquids were also used as extinguishing media in circuit-breakers ("*switchgear oils*"). This application, however, has been pushed to the background since the introduction of compressed gas-blast circuit-breakes and vacuum circuit-breakers. Only *on-load tap changers* in transformers operate in oil.

5.4.1 Technology of Insulating Liquids

The application of insulating liquids requires proper handling with respect to structural *design*, *processing*, i*mpregnation* and *condition monitoring* during operation:

The *structural design of a device* must take the **thermal expansion** of the insulating liquid and of other materials present in the device into consideration. The volume expansion coefficient of insulating liquids amounts to approximately 7 to $10 \cdot 10^{-4}$/K. That is, for a temperature enhancement of 100 K, the volume increases by 7 % or even by 10 %.

Rectangular housing cross sections or *cooling ribs* with walls that can be arched are often used in oil-filled, hermetically sealed capacitors and medium voltage distribution transformers, Figure 5.4-1a. In hermetically sealed devices with cylindrical cross sections such as in bushings, the volume is compensated by *compressible expansion cells* or *expansion bellows*, Figure 5.4-1b. The same purpose is fulfilled by a compressible *gas cushion*, e.g. of nitrogen, which has a lower volume, Figure 5.4-1c. However, the electric strength in this case is reduced owing to the gas dissolving in oil; see Figure 3.4.2-6 (curves 2 and 4). But the exsolution of gas bubbles from mineral oil with temperature variations under standard conditions is not to be expected [94].

Note: Devices with gas cushions (bushings, capacitors, and instrument transformers) shall not be inclined or may only be inclined to the extent that the gas cannot reach the impregnated insulations ("active parts") and cannot settle there. This is generally applicable even during transportation.

Large transformers compensate the thermal expansion via an *expansion tank*, which is in

contact with the atmosphere via a dryer, Figure 5.4-1d.

Before filling a device, the insulating liquid must be subjected to **drying and degassing**. For this, the liquid is led into a degassing column under vacuum at increased temperature through a pack of Raschig rings, on which the liquid in thin layers can be degassed over a long period of time (*thin-film degassing*) [47], Figure 5.4-2. The conditions must be chosen in such a way that highly volatile fractions are not distilled off. Mineral oil can be dried at 50 to 60 C and 10^{-2} mbar to a residual water content of 0.5 to 5 ppm.

Note: Along with the degassing of oil, it must also be ensured that *insulation to be impregnated is dried*. Cellulose-based insulations can hold large quantities of water (depending on the drying state from less than 0.5 to 6 %).

Impregnation process is generally started with a *vacuum phase*, so that there is no trapped gas any more, Figure 5.4-2. Then, the insulating liquid is led in. The actual "*impregnation*" is achieved by a subsequent pressurization. Therefore, the wording "vacuum impregnation" is not quite correct; it should better be replaced by "vacuum-pressure impregnation".

If the housing *cannot be completely evacuated* (e.g. for mechanical reasons), impregnation based on the capillary effect can still be considered in the case of fibrous insulations. However, the liquid level may only be increased so slowly that there is no occlusion of larger volumes of gas. Even after the impregnation, *small gas bubbles* can be dissolved in the liquid by diffusion if the bubbles are in *contact with a sufficiently large volume of liquid*. Void-free impregnation can be proven by a sensitive *partial discharge measurement*. Owing to slow diffusion and dissolution processes, this can sometimes only be successfully tested after a *waiting time of several days*.

Insulating liquids in large devices must be subject to a **diagnosis** on a regular basis to enable the documentation of parameters such as moisture, ageing and any discharge processes. The parameters to be observed depend on the type and the application of insulating liquid.

5.4.2 Mineral Oil

Mineral oils are the most frequently used insulating oils. As low viscosity oils, they are useful in the filling of *transformers (transformer oils)*, impregnation of *oil cables* (*cable*

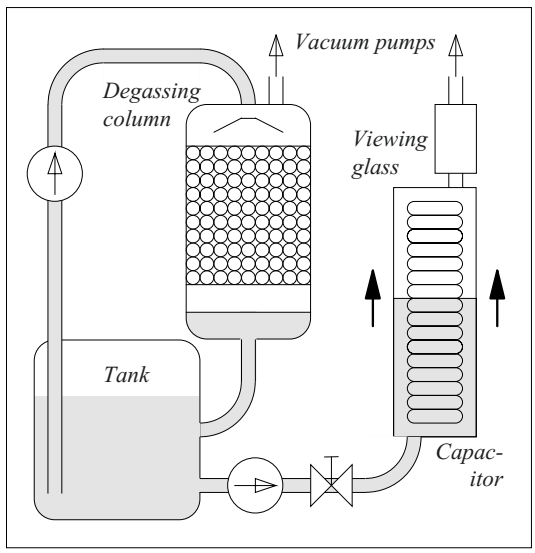

Figure 5.4-2: Processing of insulating oil and impregnation of a capacitor (schematic).

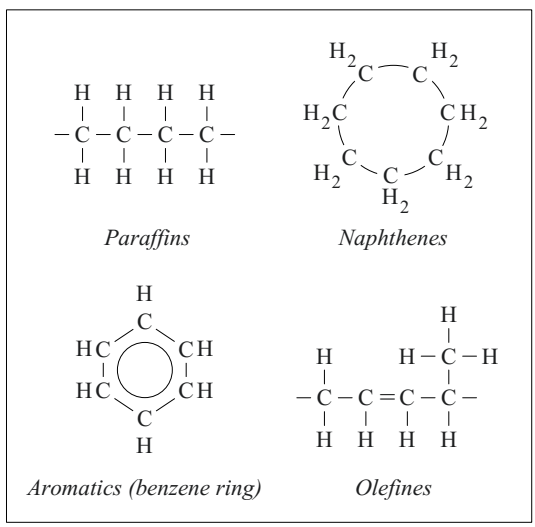

Figure 5.4-3: Basic constituents of insulating mineral oil (transformer oil).

oils), capacitors, instrument transformers and bushings, as well embedding *compact high voltage equipment* (e.g. impulse generators, power supplies for lasers and X-ray machines).

Note: The depletion of reliable *crude-oil reservoirs* led to the development of **gas-to-liquid oil** (GTL) made of *natural gas* by Fischer-Tropsch synthesis. It guarantees constant properties, high ageing stability and very low electric conductivity.

Classic **mineral oils** are obtained from *crude oil* by refining, hydrogenation and if necessary, by the addition of inhibitors. They comprise the following as **basic components** (Figure 5.4-3):

- *paraffins* (chain molecules without double bonds) and isoparaffins (with branching),
- *naphthenes* (circular hydrocarbons *without* double bonds),
- *aromatic compounds* (hydrocarbons with benzene rings), as well as
- *olefins* (chain-like or circular molecules *with* double bonds).

Long chain *paraffins* obstruct the flow of oil at low temperatures. Insulating oils that must also be suitable for low temperatures, therefore contain a higher proportion of *naphthenes*. *Olefins* are chemically vulnerable owing to unsaturated double bonds and greatly reduce the ageing stability of the oil. Olefins should not be present in substantial quantities in insulating oil.

Also *Aromatic compounds* lead to accelerated ageing on exposure to oxygen and light. They can oxidize to polar molecules, can add ions or other molecules, can also chemically bond once the double bonds are broken or can cross link with one another. Aromatic compounds also even have the advantageous property of *gas absorbing behavior*, i.e. the molecules adsorb hydrogen under the effect of partial discharges (see Section 3.4.3). *Gas absorbing aromatic oils* are therefore often used in hermetically sealed insulations that are electrically highly stressed (e.g. for capacitors and bushings with very high field strengths at the edges of metallic foils). Special *ageing resistant oils* are preferred in transformers owing to the influx of air, to higher temperatures and to the catalytic effect of conductor materials. Ageing stability is achieved by naphthene-based oils and chemical *inhibitors*.

Note: After **refining** at 180 to 200 °C, the mineral oil comprises, depending on the origin of the oil, especially paraffins and naphtenes as well as a larger proportion of monocyclic and polycyclic aromatic compounds (approx.. 20 %). By **hydrogenation**, the double bonds of aromatic compounds can be saturated by the addition of hydrogen and are thus converted into considerably more stable naphthenes. A steam pressure of 50 to above 100 bars is built up at increased temperature for this and the reaction must be catalytically accelerated. For producing special **gas absorbing oils,** monocyclic *aromatic compounds* can again be added which are slightly more ageing resistant than the originally available aromatic mixture. The reduced ageing stability of gas absorbing oils can be improved again by the addition of *inhibitors*, but this is used up through oxidation during the course of time, especially under the effect of oxygen. Since insulating oil is obtained from natural mineral oil, even small quantities of sulfur are present in it at first. The so-called **corrosive sulfur** can attack the conductor materials. Therefore it is now common practice to eliminate the corrosive sulfur from the oil.

The **ageing** of mineral oil largely takes place through different *oxidation mechanisms* that require the presence of oxygen and the effect of heat, radiation or partial discharges, Figure 5.4-4. Copper catalytically accelerates the reaction; therefore, it should not be laid as a bare conductor in the oil.

The *dissipation factor* increases irreversibly owing to the integration of polar OH-groups. *Acids* and insoluble *oil sludge* are formed. The oil *resinifies* owing to cross links over oxygen bridges. *Water* is produced as a condensation product and reduces the electric strength.

A particularly dangerous reduction in electric strength is caused by the formation of so-called *X-wax:* under the effect of partial discharges or of very high alternating electric field strengths, any available oxygen oxidizes the oil molecules. These are then cross-linked under prolonged stress. An insoluble *wax* as well as *hydrogen gas are formed*; the gaseous form can be separated and destroys the electric

strength. X-wax is observed, for example, in older oil cables, at the metallic foil edges in AC capacitors and impulse capacitors, in delaminated resin-bonded paper bushings with infiltrated oil as well as in incompletely impregnated insulations.

The following methods can be used for the **analysis of oil condition**:

Breakdown measurements can only identify heavy wetting of oil. The *direct determination of moisture* through titration (Karl Fischer titration) is more significant. However, the cellulose-based insulation frequently extracts the moisture from oil and hence high moisture values occur only in extreme cases.

Ageing (Oxidation) of oil can also be recognized from enhanced values of the *dissipation factor* tan δ, Figure .5.4-5.

Moreover, the ageing condition can also be determined from neutralization of free acids *(neutralization number)* or free and bonded acids *(saponification number)* by potassium hydroxide. An oil change is generally recommended when the neutralization value for 1 g of oil exceeds the value of 0.5 mg of KOH.

Note: Gas-in-oil analysis, i.e. the analysis of gases dissolved in oil, does not give any direct

Mechanism	*Consequences*	*Measures *)*
a) Breaking double bonds and addition of polar groups (oxidation): 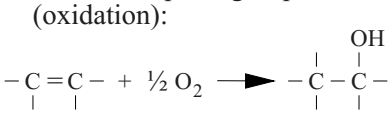	Dissipation factor irreversibly increases due to polarization losses. Cross-linking and gumming.	Use of oils with low percentage of unsaturated hydrocarbons (olefines). *) see below
b) Oxidation of oil molecules (effect of PD, UV or light): 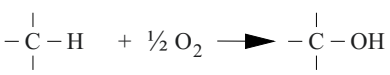	Dissipation factor increases due to polarization losses. Decomposition products, acids, oil sludge.	Regeneration through fuller's earth treatment is only possible to a limited extend. *) see below
c) Oxidation and polycondensation (effect of PD, UV or light): 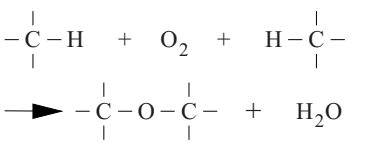	The breakdow strength reduces due to the synthesis of water, conductivity and dissipation factor increase, see Figures 3.3-4, 4.2-5 und 4.2-10. Cross-linking leads to formation of oil sludge and gumming.	By drying of oil, breakdown strength, conductivity and dissipation factor can (partially) be regenerated. *) see below
d) X-wax formation (high alternating field strengths, effect of PD): 1.) Bonding of oxygen through oxidation of oil molecules, see b). 2.) Subsequent cross-linking: 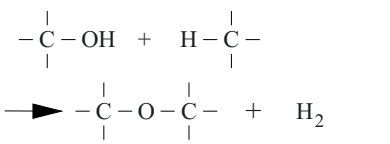	Irreversible increase in polarization losses due to oxidation. Gumming, formation of X-wax, decrease in volume and gas formation (hydrogen) through cross-linking.	Paritial discharge free design. Void-free impregnation. Use of gas-absorbing oils. *) see below
*) General measures:	Closure against influx of air or access to oxygen and moisture, as well as measures against the effects of PD, UV, light and catalysts (copper). Application of inhibitors which break the oxidation chain.	

Figure 5.4-4: Ageing of mineral oil by oxidation processes.

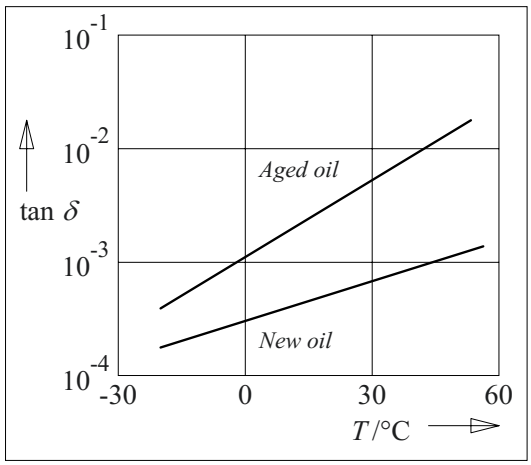

Figure 5.4-5: Dissipation factors of aged transformer oil and of new transformer oil [23].

information about the condition of the oil, but it indicates the defects in the device. For example, it can distinguish between electric arcs, partial discharges, overheating in different temperature ranges and decomposition of cellulose [95]… [100]. This and other methods of analytical and electrical diagnostics are described in Section 6.4.

The **regeneration** of aged mineral oils is possible to a limited extent. Dissolved gases and moisture can be completely eliminated by *drying* or *degassing*. Polar components which increase losses can be partially absorbed by a specially prepared *bleaching clay* (*fuller's earth*, *aluminum silicate*). Gumming (resinification) and X-wax formation can no longer be reversed.

Ageing of insulating oils is a major problem in highly thermally stressed *transformers* in which the oil is in contact with the atmospheric oxygen through the expansion tank. Preventive **measures** against ageing are the *encasement* of copper based conductors, the utilization of oils with *ageing stability* having low content of aromatic compounds as well as the use of *inhibitors*, which break the oxidation chain and get attached to the oil molecule. Inhibitors are consumed over time and must be replenished. Oils in *hermetically sealed devices* (bushings, capacitors, converters, hermetically sealed transformers and apparatus) are at lower risk of ageing and hence even the use of *gas-absorbing oils* with a high content of aromatic compounds is possible.

The **electric strength** and **dielectric properties** of mineral oil have already been described in Section 3.4 and Chapter 4. In particular, see Figures 3.3-1, 3.4.1-2, 3.4.2-1, -2, -4, -5 and -6, Table 3.4.2-1 and 3.4.3-1 and Figures 4.2-2, -5, -6, -7, -9 and -11.

5.4.3 Synthetic Insulating Liquids

Synthetic insulating liquids are generally applied owing to special properties that are not provided by mineral oils.

5.4.3.1 Polychlorinated Biphenyls (PCB)

Polychlorinated biphenyls were used as fire resistant insulating liquids and cooling liquids in transformers and as impregnating agents of higher permittivity (ε_r = 4 .... 6 at 20 °C and 50 Hz) in capacitors. They can be bio-accumulated and are difficult to biodegrade. Moreover, under the effect of great heat, highly toxic decomposition products (dioxins) are formed. Hence, the production of PCB was stopped in the Federal Republic of Germany in 1983 for example. Existing devices had to be replaced or filled with non-hazardous liquids while observing limiting concentrations. Disposal is carried out by high temperature incineration.

5.4.3.2 Silicone Liquids ("Silicone Oils")

Silicone liquids consist of linear polymers of limited length *without* spatial cross-linkages. The macromolecule consists of an inorganic skeleton with Si and O atoms that is enclosed by methyl groups, for example, Figures 5.3-17 and 5.4-6. Often silicone liquids are also called "silicone oils".

Silicone liquids are characterized by a high *flash point* (> 300 °C according to ASTM D

92) and a *high fire point* (> 335 °C). These values are twice as high as for mineral oils. Moreover, silicone liquids are chemically stable and thus *ageing resistant*. Even in the presence of air, at 150°C silicone liquids have practically unlimited stability [88]. Compared to mineral oil, *thermal transmission properties* are not so favorable; the volumetric *thermal expansion coefficient* is higher (10^{-3}/K).

Physiologically, toxicologically and ecologically, polydimethylsiloxane (n = 35) is considered as *non-hazardous*; it decomposes in the environment into non-hazardous decomposition products of water, carbon dioxide and silicic acid [101]. Similar to mineral oils, the classification is according to the German water polluting category WGK 1 (mild water pollutant) for example.

At ε_r = 2.7 (20 °C)... 2.3 (200 °C), the *permittivity* is slightly higher than that for mineral oil. The *dissipation factor* varies only slightly over a *wide frequency and temperature range* (up to 10 MHz and up to 200 °C respectively) and is very low at tan $\delta = 1 \ldots 2 \cdot 10^{-4}$.

Silicone liquids have a slightly lower *electric strength* than mineral oils. Moisture has a similar strength reducing influence. Lower electric strength for *larger oil gaps* is a disadvantage for their application in high voltage transformers.

Owing to its high pricing, silicone liquid is only used as an insulating liquid when it is necessary on the basis of *thermal stress* or as *fire protection*. Furthermore, *silicone pastes* made of silicone liquid with silicic acid are useful for *hydrophobizing* of porcelain surfaces. However, the effectiveness is limited in time. Instead of regular renewal, using a SIR composite insulator is often preferred, see Section 5.3.4.

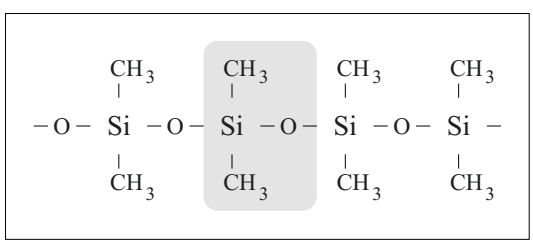

Figure 5.4-6: Polydimethyl siloxane.

5.4.3.3 Other Organic Liquids

Synthetic insulating liquids for **transformers** are preferred over mineral oil, especially when *thermally resistant, flame-retardant* or *environmentally compliant* substances that are not hazardous to water are required.

Along with silicone liquids, **ester liquids** [102] which have already been tried and tested in distributing transformers are especially considered. *Pentaerythritol tetraester*

$$C(CH_2 - O - CO - R)_4$$

(e.g. "Midel 7131" [101], [103]) is produced by *esterification* of the tetra-alcohol pentaerythritol and mono-carboxilic acids [488]. As compared to mineral oil, higher permittivity ε_r = 3.3 and a slightly higher dissipation factor tan $\delta \geq 10^{-3}$ are observed. Owing to thermal ageing at 150 °C, tan δ increases within 2000 h by about a factor of 10. The electric strength is at comparable values. However, owing to a *high water absorption capacity* (2700 ppm at 20 °C), it is only dependent on water content to a very small extent up to 500 ppm. This also applies to the dissipation factor. It must be noted that there are a low *pour point* of -50 °C and high values of *flash point* (257 °C) and *fire point* (310 °C) which are almost double the values of typical mineral oils.

Insulating liquids for **capacitors** are today less used in the impregnation of paper, but are increasingly used for the impregnation of very *low-loss film dielectrics (*all-film dielectrics) with lower permittivity. The high permittivities of polychlorinated biphenyls (PCB) are therefore no longer necessary. Frequently demanded properties are a *low viscosity* for the impregnation of films placed one upon another, a high *electric strength* for withstanding

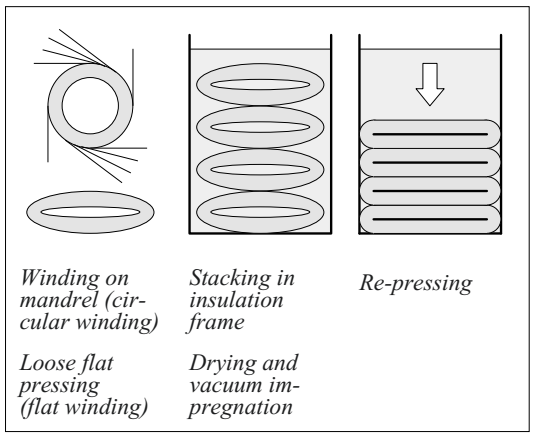

Figure 5.4-7: Production of all-film capacitors with synthetic liquids (schematic).

the high edge field strengths at the metallic foil edges and a high *gas-absorbing capability*.

For a long time, *polyisobutylene*

$$.... - CH_2 - C(CH_3)_2 - ....$$

has been used as a chemically resistant impregnating agent for cables, capacitors and metal paper (MP) capacitors. It has similar properties to mineral oil (ε_r = 2.2). The viscosity depends on the chain length [88].

Thermally stable, low viscosity insulating liquids with a *high gas absorption capacity* comprise benzene rings, i.e. they have an aromatic character. Examples of this are mentioned as *dodecyl benzene* from the series of alkyl benzenes, *phenyl-xylyl-ethane* (PXE), *mono-isopropyl-biphenyl* (MIPB), *benzyl neocaprate* (BNC), *ditolylether* (DTE, "Baylectrol 4900", from Bayer) as well as mixtures of *mono benzyl toluene* and *dibenzyl toluene* (M/DBT, "Ugilec", "Jarilec", from Prodelec) [16], [104] to [107]. Furthermore, there are also fluorinated and chlorinated insulating liquids.

Capacitors with **all-film dielectrics** are mainly used as *compensation capacitors* owing to their low losses for AC voltage. They are considerably less sensitive to increased power loss for distortions than paper insulated capacitors.

All-film dielectrics with synthetic insulating liquids can be stressed partially with *field strengths* up to 100 kV/mm (1 Minute, 50 Hz-r.m.s. value, in the area of the uniform field at d = 50 µm). This implies that electric strengths that are about twice as high as those in mineral oil-impregnated paper can be attained.

Note: The dielectric strength in capacitors is not determined by the field strengths in the homogeneous area of the dielectric, but by the sharply increased *field strengths at the edges* of the conductive foils, see Figure 2.4-20.

Owing to a compact method of construction, employing expensive insulating materials is useful even for other applications, such as for *grading capacitors, impulse capacitors* or *measuring capacitors*. By choosing suitable insulating materials, the temperature dependence of precision capacitors can be partly compensated.

The *impregnation of all-film capacitors* requires a raw or punched film surface and a loose assembly of the capacitor winding to ensure an adequate “space factor” for a surface covering penetration of the impregnating agent, Figure 5.4-7. Circular windings that were wound on a mandrel are pressed into loose flat windings with adequate space factor after the removal of the mandrel. Several flat windings are stacked in an insulating frame, electrically connected via inserted metal strips (reed contacts), dried under vacuum and impregnated under vacuum, see Figure 5.4-2. The capacitor pile is pressed in the impregnated condition. A *paper insulated capacitor* can be pressed already after drying since the fibrous structure of the dielectric ensures the absorption of the liquid, see Figure 5.3-6 and Section 5.3.2.3.

5.4.4 Vegetable Oils and “Natural Ester Liquids”

In the initial stages of high voltage engineering, *resin oils* were used as voltage resistant impregnating agents for transformers [81]. But owing to their low ageing stability and their inclination to gumming, they were very soon

replaced by mineral oils. Nevertheless, there are still a few applications of **vegetable oils** for insulation, Section 5.4.4.1.

Note: Nowadays, vegetable oils are mainly used as *raw materials* for the manufacture of wire enamels and impregnating resins, based on polyester resins and polyurethane resins. Linseed oil, wood oil, soya oil, ricinus oil and turpentine oil are used for this [88].

Meanwhile, there is a strongly increasing interest in so-called **natural ester liquids** which are made of renewable raw materials (seed oils) and which provide a number of very favorable properties such as biodegradability, non-inflammability, no hazard to water, low viscosity and sufficient electric and dielectric properties as well as sufficient ageing stability, Section 5.4.4.2.

5.4.4.1 Vegetable Oils

Ricinus oil has until now been an important electrical insulating material for DC voltage capacitors and impulse capacitor. *High permittivity* at $\varepsilon_r = 4.5$ is advantageous for *capacitive energy storage* of high energy density for this. Moreover, *impulse capacitors* with ricinus oil-paper insulation have an *about ten times longer service life* than capacitors with mineral oil-paper insulation.

The *field strength reduction at the sharp foil edges* for impulse stresses owing to the higher permittivity is considered responsible for this. Moreover, it is assumed that the *viscous ricinus oil* cannot be as easily eliminated as the viscous mineral oil owing to electrostatic alternating forces on the metallic foils, and hence the formation of partial vacuums and gas bubbles is hindered. Furthermore, ricinus oil could have higher *resistance* to *partial discharges* occurring during the impulse discharges at the foil edges. However, the erosion of insulation for impulse discharges is also greatly determined by the resistance of the paper or the film to partial discharges.

The *dissipation factor* of ricinus oil is about 5 times higher than the *dissipation* factor of mineral oil. The dielectric properties are also strongly temperature dependent. Hence, ricinus oil is not used for AC voltage stresses but more for DC voltage stresses and impulse voltage stresses as well as for insulation in physical devices and in laboratories [22].

Ricinus oil must be dried, filtered and treated with fuller's earth and activated carbon. Owing to *high viscosit*y, impregnation is possible only at increased temperatures. The advantage is that the high viscosity prevents the leakage of an impregnated winding at room temperature. Ricinus oil solidifies at -10 to -18 °C and therefore *cannot be used at low temperatures*.

Meanwhile, even **rapeseed oil** is also considered as insulating liquid for high voltage devices owing to the growing interest in renewable and biodegradable raw materials. The *electric strength* corresponds to approximately that of mineral oil at the same *relative moisture*, whereby the *water absorption capacity* of rapeseed oil is more than a factor of 10 greater than that of mineral oil. The requirements for the breakdown strength of new oils are fulfilled. The *dissipation factor* is about a factor of 10 greater than that of mineral oil. Thus, the *dissipation* factors at 90°C are far above the (for mineral oil!) stipulated value of 0.5% [399]. Experiments with a 20kV/250 kVA *distributing transformer* have in principle shown the suitability of rapeseed oil as a cooling medium and insulating medium [400].

Note: In the comparative *ageing tests* on the transformerboard that was impregnated with mineral oil or with ageing stabilized rapeseed oil, the boards impregnated with rapeseed oil and the associated oil unexpectedly aged slower than the conventional comparative samples [401]. However, based on the structure of rapeseed oil, a comparatively lower *ageing stability* was expected.

5.4.4.2 Natural Ester Liquids

Pure vegetable oils (seed oils) are biodegradable, difficult to inflame and not hazardous to water. Unfortunately, viscosity is comparatively high and ageing stability is insufficient for many applications. These drawbacks can be overcome by the so-called "natural ester fluids".

The denomination as "*natural ester fluid*" might be misunderstood, the final product is

not natural, it is a result of chemical processing, but the raw materials are natural seed oils.

Easily available *seed oils* (e.g. rapeseed, soya, sunflower) are used as renewable raw materials. From these, a tri-ester is produced by *esterification* of tri-alcohols and fatty acids. A further processing allows the generation of mono-esters by a transesterification reaction. The final product consists of mono-esters, of tri-esters or of mixtures from *mono-esters*, *tri-esters*, *seed oils* and *inhibitors* [488], [489], [490].

Depending on the raw materials and process technology, properties of natural ester fluids can vary in a wide range. *Low viscosity* and good *low-temperature behavior* can be achieved by a high percentage of unsaturated fatty acids. Improved *oxidation stability* is possible by a high percentage of saturated fats. An optimized balance of different seed oils and additives provides insulating liquids that have a high environmental safety, high fire safety, compatability with transformer materials, sufficient oxidation stability, low viscosity, low pour point and good electrical properties [489].

Therefore, natural esters are already widely used in *distribution transformers*, especially for environmentally sensitive applications. The usage for *high voltage transformers* as well as for *retrofitting* of aged transformers is possible and is tested.

However, *natural ester fluids* are not completely equivalent to *mineral oils*; there are the following basic similarities and differences [489] [290] [491] [292]:

- The *breakdown strength* is comparable, but a higher sensitivity to electrode surface area is reported (*area effect*).
- *Dissipation factor* (a few percent at 90 °C) and *acidity* are higher and increase significantly during ageing.
- Natural esters are less stable with respect to *oxidation*, protection against the access of oxygen might eventually be necessary.
- Natural esters *dissolve much more water* than mineral oil (approximately 200 to 1000 ppm at 20 °C), therefore, new equilibrium diagrams for liquid and solid insulations have to be established [492].
- The *viscosity* is higher, therefore natural ester fluids are less efficient for the convective heat transfer in transformers.
- The *pour point* is higher, therefore the low-temperature limit has to be chosen accordingly.
- The *flash point* is higher.
- The *biodegradability* is much better, i.e.degradation is faster.

In any case, the limits of the individual (natural) ester formulation have to be considered carefully.

5.4.5 Water

Water has a high electric strength for *voltage stresses of very short duration*, and it complies with the impulse voltage-time characteristics of other liquid insulating materials. $\hat{E}_{\mathrm{bd50}}$ amounts to about 40kV/mm for a breakdown time of 1 µs and falls to about 20 kV/mm for a breakdown time of 10 µs. For *stresses of long duration*, water is heated and vaporized even at low field strengths owing to its high conductivity, and this initiates the breakdown [22].

Water has a *high permittivity* at $\varepsilon_{\mathrm{r}} = 81$ owing to its highly polar molecule. Under completely de-ionized conditions, the conductivity due to the dissociation of water molecules amounts to about $\kappa = 10^{-7}$ S/m, and this corresponds to a *self-discharge time constant* $\tau = \varepsilon/\kappa = 7$ ms. In contact with air, the conductivity increases owing to the dissolution of CO_2 and the formation of dissociated carbonic acid up to about $\kappa = 10^{-4}$ S/m, and this corresponds to a self-discharge time constant $\tau = \varepsilon/\kappa = 7$ µs. Therefore, energy can only be stored in water

insulated capacitors for *a very short period* of time.

Note: Breakdown strength and specific resistance can be distinctly increased by mixing with **ethylene glycol** [475]. The bivalent alcohol $C_2H_4(OH)_2$, known as an antifreeze compound and a solvent, is highly polarizable like water but does not form ions. For a proportion of approx. 70 %, the *breakdown strength* increases by about 39 %, *conductivity* decreases from 8 10^{-6}·S/m to $2.5 \cdot 10^{-6}$ S/m and *permittivity* falls from about 80 to 68.5 [475]. As per Eq. (2.1-13), an increase in the *energy density* by approx. 48 % is associated with it. An increase in the self-discharge time constants through reduced conductivity and lowering of the freezing point is also of advantage. The *toxicity* of ethylene glycol must be considered.

An important **application** is the *high-power impulse technology* (*pulsed power* technology) described in Sections 2.6.3.3, 6.2.3.7 and 7.4.2. Under this, very compact water insulated lines are charged within about a few µs from conventional capacitor batteries by oscillation. At a voltage maximum, the lines are discharged within a few 10 ns as a travelling wave. This results in an extreme space and time compression of the stored energy that is required for basic physical research and for ignition impulses in nuclear fusion experiments [14], [15], [40], [42], [43], [108].

Water is also used as a *switching medium in spark gaps*. By discharging an energy storage capacitor, the electrically stored energy can be quickly transformed into the energy of an *acoustic shock wave* in a water insulated spark gap. In *medical technology*, this is useful for destroying renal stones, in *production technology* for material transformation and in *recycling* for separating material fractions. Moreover, the pulse power technology described above is also used for water insulated point-to-point spark gaps (made of rods). The breakdown time depends on the distance of the electrodes and on the magnitude and profile of the applied voltage.

Furthermore, in high voltage engineering, *water resistors* are used for current limitation and as filter elements in high voltage circuits or as load resistors in impulse voltage circuits. Owing to the corrosion hazard at the electrodes and to the probable separation of gas, the use of transparent pipes or tubes is recommended. The conductivity should be adjusted in a defined manner by the release of small quantities of salt (for copper electrodes, for example, with copper sulfate $CuSO_4$). During the design stage, the adequate removal of resultant heat must be ensured.

Water is also used for potential grading for cable tests in *cable test terminations*, Figure 5.4-8. Under this, the resistance must be adjusted in such a way that there is no overloading of the voltage source and the heat losses can be dissipated.

5.4.6 Liquefied Gases

For the utilization of *superconductivity* in power engineering (see Section 7.5), an impregnating agent suitable for low temperatures is necessary [111]. All the technically applied insulating liquids today can only be used for temperatures above approx. -60 °C. For use at lower temperatures, liquefied insulating gases such as *sulfur hexafluoride* (LSF_6, liquid SF_6), *nitrogen* (LN_2, liquid N_2) and *helium* (LHe, liquid He) are available for example. For LN_2 and LHe, strengths that can be compared with other liquid insulating materials are specified [109], Tab. 5.4-1.

Table 5.4-1: Breakdown strengths of liquid gases at normal pressure given as 63% value (peak value). Breakdown probabilities under 1% must be expected to occur at about half of the specified values [109].

Arrangement	$\hat{E}_{bd63}$ (LHe)	$\hat{E}_{bd63}$ (LN_2)
Sphere-to-plane (D = 50 mm, d = 1 mm)		
AC (60 Hz)	39.0	68.5 kV/mm
DC positive	54.5	72.4 kV/mm
DC negative	50.9	74.4 kV/mm
Coaxial cylinders (L = 100 mm. d = 2.3 mm)		
AC (60 Hz)	19.7	23.1 kV/mm
DC positive	20.4	23.9 kV/mm
DC negative	19.2	24.0 kV/mm

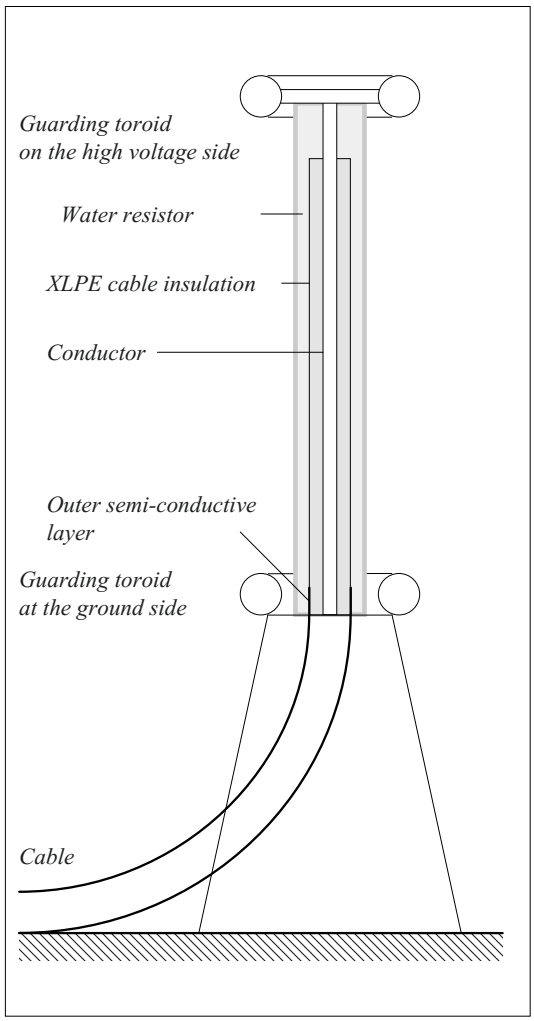

Figure 5.4-8: Cable test termination (schematic).

Breakdown is initiated by thermal gas bubbles [110]. This leads to a pronounced volume effect and area effect, as well as to a *large dispersion* of breakdown field strengths. Therefore, low breakdown probabilities of < 1 % must only be expected at much lower field strengths (about half of the above mentioned values) [109].

For a larger range of flashover distances, the following breakdown field strengths $\hat{E}_{bd}$ (peak values) are given in a sphere-to-plane arrangement (D=50mm), for LN_2 under normal pressure and for LSF_6 at 22 bars [22]:

		LN_2	LSF_6
d =	05 mm	$\hat{E}_{bd}$ = 80 kV/mm	90 kV/mm
	1 mm	55 kV/mm	90 kV/mm
	2 mm	40 kV/mm	90 kV/mm
	5 mm	30 kV/mm	90 kV/mm
	10 mm	25 kV/mm	-
	20 mm	19 kV/mm	-

The strength of liquefied insulating gases is heavily dependent upon *pressure*. Strengths are specified for LSF_6, which approximately correspond to that of gaseous SF_6 with the same density as that which occurs for the respective pressure above the liquid [22].

The use of *high-temperature superconductivity* enables **insulation with LN_2,** whose boiling point is 77K under normal pressure**.** This enables the heat removal capacity to be reduced approximately by a factor of 100 in comparison with LHe with a boiling point of 4.2 K.

For the **volume effect and area effect,** exponents (-0.148 and -0.172 according to [109]) were determined that are smaller than the exponents assumed for the *distance effect* in insulating oil (approx. -0.37), Figure 3.4.2-6. For LN_2, the following is given as the empirically determined **distance effect** 331], [332].

$$E_{bd(DC)} = (29\ \text{kV/mm}) \cdot (d/\text{mm})^{-0.2} \quad (5.4.6\text{-}1)$$

The breakdown is initiated by thermal gas bubbles at the electrode surfaces and in the volume. In contrast to insulating oil, **bubble formation** in LN_2 is *unavoidable:* While operating close to the boiling point, it is not only the heating at quenching (loss of superconductivity), but probably even the AC losses in operation (which cannot be totally avoided even for superconductivity, see Section 7.5) that leads to bubble formation at the conductor surface. The design of the insulation, therefore, must also take into consideration the presence of bubbles that can be noticed from a distinct reduction in the breakdown voltage,

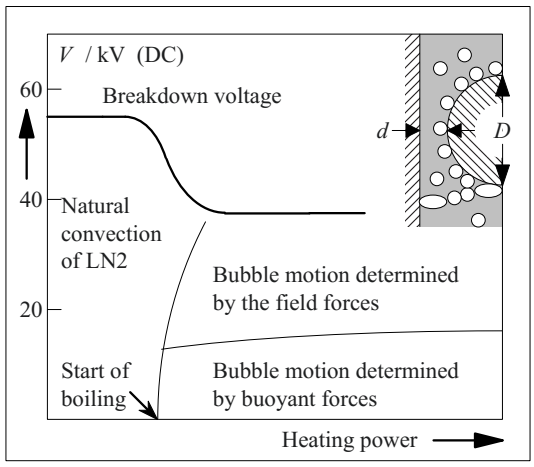

Figure 5.4-9: Influence of thermal gas bubbles on the breakdown behavior of LN_2 in a cylinder-to-plane arrangement with d=2mm and D=10mm. The grounded, horizontally placed cylinder was heated [332].

Figure 5.4-9. The bubbles deform under the effect of the electric field and form chains [332]. Thus, the electric strength approximates to the **value of gaseous nitrogen** (GN_2), very rapidly for small gaps ($\leq$ 0.5 mm) and slightly slower for larger gaps ($\geq$ 1 mm) with intensified heating and intensified bubble formation [333].

Approximately comparable profiles were determined for the strength for AC, DC positive and DC negative (for peak values, see also [333]).

In the case of **impulse voltage**, a fundamentally different characteristic is seen: during the *liquid phase* - similar to insulating oil - the impulse strength is far above the AC strength (a factor of 1.5 relative to the AC peak value and 2.2 relative to the AC r.m.s. value [333]), but the strength reduces in the *gas bubble phase* to the value of the gas strength, so that there is no significant difference between impulse strength and AC-strength, Figure 5.4-10. There is no distortion of the gas bubbles for impulse voltage stress, and hence the decease is slower, i.e. only for higher heating power. But basically it is ascertained that thermal gas bubbles especially lead to *loss of high impulse voltage strength!*

The effect of bubbles in LN_2 **is less hazardous** than in insulating oil: however, owing to a low *permittivity* of ε_r = 1.44 in spherical bubbles, the *field stress enhancement* amounts to only about 11 % (for AC and impulse voltages). Furthermore, the *gas density* of bubbles in the low temperature range at about 77 K is approx. 3.8 times higher than at the room temperature of 293 K. According to *Paschen's law*, this leads to a significantly higher electric strength owing to correspondingly reduced free path lengths, Section 3.2.2.4. Measurements have been reported, according to which even the AC-strength in LN_2 in the range of 0.5 to 1 mm, approximately follows Paschen's law for GN_2 at 77 K ($\hat{E}_{bd}$ = 12.5 kV/mm for d = 1 mm [333]). Other sources also recommend the *strength of nitrogen gas at 77 K to be chosen* as the limiting value [334] (AC r.m.s. value: 6.4 kV/mm, LI peak value: 15 kV/mm, for d = 10 mm in each case).

Measures for **increasing the electric strength** would include preventing the formation of bubbles by having operating temperatures *far below the boiling point* (the lower limit is the melting point of nitrogen at 63 K) as well as by *increasing the pressure*, which delays boiling and increases the strength [335].

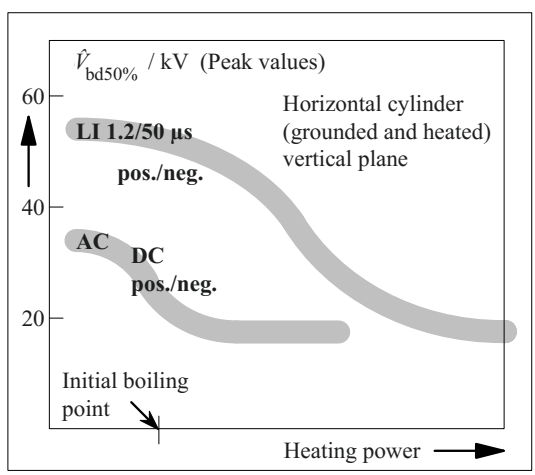

Figure 5.4-10: Reduction of AC voltage strength and loss of impulse voltage strength under the effect of thermal gas bubbles in LN2 in a cylinder-to-plane arrangement with d=1 mm, D = 10 mm and l= 20 mm [333].

5.5 Fibrous Materials

Impregnated paper and impregnated pressboard consisting of fibrous materials are used as dielectrics and dielectric barriers in capacitors, cables, bushings, instrument transformers and transformers. *Plates, tubes and other molded components* are largely used in transformer construction as dielectric barriers. Fibrous materials are one of the most important insulating materials of high voltage engineering. The properties must always be considered with regard to an **impregnating agent**, Figure 5.5-1. In combination with *mineral oils* or other insulating liquids, high electric strengths can be attained by *impregnation* of cavities and pores between the fibers. Without impregnation, fibrous materials possess unacceptably low strengths.

Note: Although the strength of papers can also be increased by *compressed gases*, it is less common. The high impregnability of gases allows the use of electrically resistant foils with lower permittivity and accordingly less field displacement into the gas-filled gaps.

The main component of paper and pressboard is *cellulose* (Section 5.5.1), for which short-term temperatures up to 120 °C can be allowed, but this ages unacceptably fast for operating temperatures above 90 °C. Higher temperatures are possible with *synthetic fibrous materials* (Section 5.5.2).

5.5.1 Paper and Pressboard

Paper and pressboard acquire their electric strength only by impregnation with insulating oil, Section 5.5.1.1. The actual insulating materials are therefore not paper and pressboard, but **oil-impregnated paper** OIP and impregnated pressboard. Dielectric properties are dependent on a series of different parameters, Section 5.5.1.2. Significant reductions in strength are possible as a result of ageing and absorption of water (or moisture resp.), therefore condition assessment is of great significance for OIP, Section 5.5.1.3. The special features of OIP dielectrics must be taken into consideration during manufacturing and processing, Section 5.5.1.4.

5.5.1.1 Electric Strength

The high electric strength of impregnated fibrous materials depends on the *barrier effect of fibers*, which subdivide the volume into a large number of very closely placed oil gaps or pores with high electric strength, Figure 3.4.2-6.

For a theoretical *assessment of partial discharge inception field strengths* in oil-filled pores of impregnated paper or pressboard, see Eq. (3.4.2-1), case (1) and (2), Table 5.5-1.

Table 5.5-1: Theoretically estimated partial discharge inception field strengths (r.m.s. values) in the oil filled pores of impregnated paper or pressboard.

Oil condition	degassed	gas-saturated
	E_{PDI}	E_{PDI}
Pore width	kV/mm	kV/mm
1 µm	270	220
3 µm	180	148
10 µm	115	95
30 µm	76	64

Under this, pore widths in the range of 1 ... 3 µm are associated with thin, highly compressed insulating papers, and pore widths of 10 … 30 µm are associated with less strongly compressed, thicker materials.

These inception field strengths in the pores are attained owing to *field displacement* even for lower mean field strengths. In the *ideal case*, a *spherical oil filled pore*, according to Figure 2.4-22 and Eq. (2.4-38), increases the field strength in oil by about 25% relative to the surrounding cellulose. This implies that the following is valid:

$$E_{\text{fiber}} \leq 0.8\, E_{\text{Oil}} . \qquad (5.5\text{-}1)$$

For this it was assumed that for mineral oil ε_r = 2.2 and for the cellulose fiber ε_r = 5.1 [82] to ε_r = 6.1 [103]. In the *worst case, a parallel level layering* or de-lamination of individual layers is applicable with Eq. (2.4-17):

$$E_{fiber} \leq 0.4\, E_{\mathrm{Oil}}\,. \qquad (5.5\text{-}2)$$

For *highly compressed material* (density δ = 1.25 g/cm^3), oil absorption amounts only to about 8 %. The relative permittivity of the mixed dielectric is about ε_r = 4.5 and for average field strength it is approximately

$$E_{\mathrm{mean}} \approx 1.1 \ldots 1.3\, E_{fiber}\,. \qquad (5.5\text{-}3)$$

In *weakly compressed material* (density δ = 0.8 g/cm^3) oil absorption amounts to almost 50 %. The relative permittivity of the mixed dielectric is about ε_r = 3.7 and for average field strength it is approximately

$$E_{\mathrm{mean}} \approx 1.4 \ldots 1.6\, E_{fiber}\,. \qquad (5.5\text{-}4)$$

The theoretically determined values can be verified with difficulty from *measurements*, because in a test set up of two electrodes and a material sample between them, the *weakest point* lies *in the oil filled interstice* at the electrode edge, Figures 2.4-18 and -19. This implies that outside the material, normal and at higher voltages even tangential discharges are ignited and these erode the cellulose and lead to breakdown (*edge breakdown*). The inception of partial discharges in homogeneously stressed areas of the material is therefore *not* achieved.

Depending on the radius of curvature at the foil edges, measured *apparent r.m.s. partial discharge inception field strengths* $E_{\mathrm{PDI}} = V_{\mathrm{PDI}}/d$, ($d \approx 50$ µm) lie between 55 and 70 kV/mm for capacitor dielectrics and between 60 kV/mm (d = 0.2 mm) and 20 kV/mm (d = 4 mm) [27], [82] for pressboard. They reduce with the density of the material because the field displacement in the oil-filled interstice increases. The *apparent breakdown field strengths* are higher; they increase with the density of the material because the resistance to partial discharge erosion increases.

For the *strength* at *lightning impulse voltage*, in accordance with Table 3.4.2-1, values are applicable that are two to three times higher than the r.m.s. values of partial discharge inception field strengths. Values measured between spheres (D = 25 mm) of 60 kV/mm (d = 10 mm) to 135 kV/mm (d = 0.2 kV/mm) are specified for pressboard [27]. The strengths of thinner capacitor dielectrics are slightly higher.

Operating field strengths are much below the mentioned values to rule out a breakdown even for many years of operation. Common r.m.s. values are for

capacitors ($d \approx 50$ µm)	20 ... 30 kV/mm,
low-pressure oil cable	10 ... 16 kV/mm,
hermetically sealed devices (instrument transformers, bushings)	3 ... 5 kV/mm
and transformers with air admission	2 kV/mm.

Tangential stresses on a paper surface or on a pressboard surface under oil can be applied almost up to the values of a comparatively long oil gap, because the fibrous surface structure exhibits a barrier effect for the tangential stress. Microscopically, there exists a steady transition from the oil medium into the fibrous material. Incomplete wetting of the surface is not possible. In practice, however, the tangential stresses are often restricted to about 70% of the oil gap values.

5.5.1.2 Dielectric Properties, Moisture and Ageing

a) Permittivity

The *permittivity* of impregnated paper and that of pressboard depends on the density of the material and on the impregnating agent, Figure 5.5-1.

b) Dissipation factor (loss factor)

The *dissipation factor* of mineral-oil-impregnated paper has a polarization maximum in the range of -80 to - 60 °C at 50 Hz, Figure 5.5-2. Thus, the usual operating temperatures are

between the polarization maximum and the conductivity rise in a loss minimum of about tan $\delta = 3 \cdot 10^{-3}$ ("*bath-tub curve*"). For used oil-impregnated paper, the minimum disappears, Figure 3.5-7. An ageing-induced or moisture-induced rise in dissipation factor can lead to *thermal breakdown* in the case of unfavorable heat transmission, for example, in thick-walled insulations.

c) Moisture influences

The performance of oil-impregnated paper and pressboard is heavily determined by the **water content or water content** of the cellulose:

- For a water content of more than 0.1%, conductivity and dissipation factor begin to rise exponentially.
- Up to a water content of 1 to 2%, the breakdown strength is practically not influenced, but beyond that it reduces to very small values. The dissipation factor amounts to about tan $\delta = 10^{-2}$.
- For a water content of about 10%, there is practically no more electric strength. The dissipation factor is about tan $\delta = 1$.

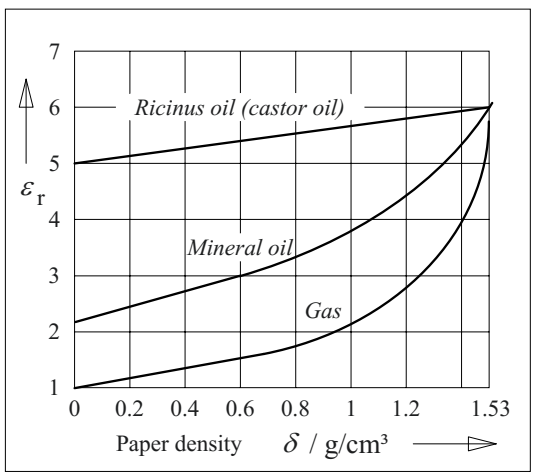

Figure 5.5-1: Permittivity of ipmregnated paper or pressboard for different impregnating agents as a function of paper density (volumic mass) [16], [82].

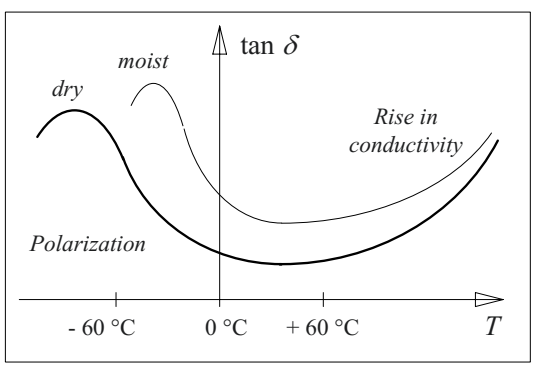

Figure 5.5-2: Dissipation factor or loss factor for oil-impregnated paper or pressboard ("bath-tub curve"), see also Fig. 3.5-7.

Hence, paper and pressboard must be **extremely well dried**, generally down to a water content of a maximum of 0.5 to 0.3%.

More extensive drying by increasing the temperatures could cause appreciable ageing of the cellulose. Considering *short-duration electric strength* at room temperature, water contents of up to 2% can be accepted. However, at high operating temperatures, *de-polymerization* of cellulose molecules would therefore be accelerated by more than a factor of 10, Figure 3.5-6. From the perspective of *ageing stability,* this is unacceptable. Moreover, moist cellulose would release dangerous steam bubbles at high temperatures. Residual moisture of 0.3 to 0.5 % is thus a compromise that enables good dielectric properties, high breakdown strength and a *long service life*.

d) Conductivity

The conductivity of oil-impregnated paper OIP and pressboard is increasingly gaining importance since it directly determines the performance of DC voltage insulations, Section 7.2, and furthermore since it is used as a diagnostic

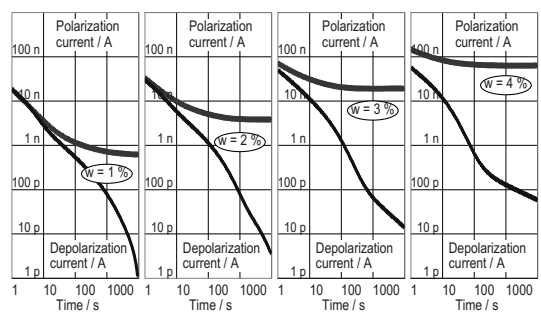

Figure 5.5-3: Determination of dielectric properties of oil-impregnated transformerboard T IV by PDC-measurements for different water contents.

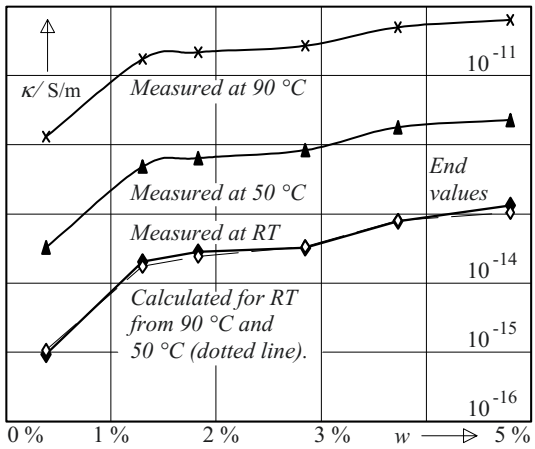

Figure 5.5-4: Conductivities of OIP at E = 0.1 kV/mm for different water contents w and three temperatures, determined by the charge difference method CDM [429]. Verification of the Arrhenius relation by back calculation of room temperature RT values from measurements at 50 °C and 90 °C, Eq. (4.2-9), Figure 4.2.9.

indicator for OIP insulations, Section 6.4. The conductivity is determined by ion conduction in the oil-filled capillaries as well as by charge carrier transport along cellulose fibers which are wetted to a greater or lesser extent. For a polarization and de-polarization current measurement (PDC measurement), the conduction current overlays the polarization processes; it increases sharply with the water content, Figure 5.5-3. From the de-polarization current it can be seen that even the polarization processes (to a lesser extent) are influenced by the water content.

Conductivity depends not only on the water content, but also on several other parameters, especially on the temperature, Figure 5.5-4. The *temperature dependence* results from increases in the number of charge carriers and from increases of charge carrier mobility; it follows the Arrhenius relationship according to Eq. (4.2-9). This can be verified from Figure .5.5-4, since the values reverse calculated from 90 °C and 50 °C to room temperature agree with directly measured values.

The conductivity increases exponentially with increasing *water content*, both for OIP as well as for pressboard, Figure 5.5-5, Eq. (4.2-7). The structural differences between homogeneous pressboard and OIP made of thin individual layers have an effect on the conductivities, Figure 5.5-5: paper layers impregnated with high-resistive oil exhibit comparably low conductivities for high water contents, probably because high-impedance oil gaps between the moist and conductive paper layers act as resistance-enhancing layers. Paper layers impregnated with low-resistive oil do not exhibit this phenomenon, but increased oil conductivity also causes an increase in the conductivity of the impregnated material for low water contents.

Note: Eq. (4.2-9) and Figure 5.5-5 were determined with different oils and with different wetting procedures. Hence the values differ from each other.

The conductivity distribution in paper and pressboard is not completely uniform; it is assumed that higher conductivity is present at the surface zones in which the *conductivity of oil* is of importance [429], [436]. The oil conductivity has a significant influence on the conductivity of the impregnated material when it has a high value and if the cellulose is not heavily wetted [429], [436].

Conductivity shows only a very low *field strength dependence*, which is probably caused by the non-linearity of the oil conductivity.

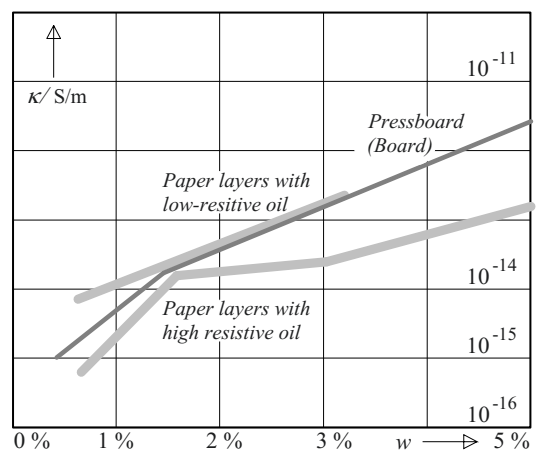

Figure 5.5-5: Conductivities of oil-impregnated paper OIP (light grey curves) and pressboard (Transformerboard, dark grey curve) for different water contents w for high and low resistive insulating oils. Schematic representation for room temperature [429], [436].

Also *ageing* has at least an indirect influence on the conductivity. Ageing is generally understood as de-polymerization of long chain cellulose molecules, which can weaken the mechanical strength. Whether and how this can be identified in dielectric measurements is subject of discussion. However, in the course of ageing, especially also the oil is damaged and this is noticed from an increase in conductivity and polarization processes in the oil-cellulose mixed dielectric, Figure 6.4.7-9.

5.5.1.3 Condition Assessment

An **assessment of the ageing condition** of cellulose-based insulation can be carried out on material samples by determining the average *degree of polymerization* (DP value) according to IEC 450. New cellulose molecules consist of 1300 to 1400 glucose molecules. Cellulose chains are shortened by the ageing processes. The limit for operational reliability is seen for a DP-value of 150 to 200, at which the cellulose is brittle and fragile. For the determination, cellulose is dissolved in copper ethyldiamine; the viscosity of the solution is a measure of the average chain length [84]. A disadvantage of the process is that it is necessary to extract the material samples. The method allows only local evidence.

The analysis of cellulose-decomposition products that are dissolved in oil enables an integral statement about the ageing condition of a device. *Furfuran derivates (furfurals, furfurols)* are determined by *liquid chromatography*, according to IEC 61198 (VDE 0380- 6) [84], [112], [493]. On the basis of experience to date, definite quantification of cellulose decomposition has not been possible. It must be noted that an oil exchange flushes out the available decomposition products. In *Gas-in-oil analysis*, the presence of CO and CO_2 give an indication of the decomposition of cellulose owing to thermal overheating or electrical discharges. The type of defect can be determined based on the other fault gases arising from the decomposition of mineral oil, see Section 6.4.3.2.

The determination of the *water content in oil* and the application of **equilibrium curves** allow only very inaccurate conclusions about the *water content in the cellulose*, Figure 5.5-6. The highly hygroscopic cellulose extracts the moisture from the oil, so that even for unacceptably wet paper or pressboard (e.g. $w = 3$ %), in the equilibrium condition a very dry oil condition is measured (i.e. $w \leq 5$ ppm at 20 °C). Only at very high temperatures, it is possible to prove low paper moistures (e.g. 0.5%) by appreciable moisture in oil (e.g. 15 ppm at 100 °C). A comparison between moisture in oil and moisture in paper is allowed only on setting an equilibrium condition. This can take a long time.

Note: In **transformers**, in which mostly locally and temporally varying temperatures are present, it is generally *not* possible to assume an *equilibrium condition*: determination of moisture in paper using equilibrium curves in accordance with Figure5.5-6 is therefore not possible, see also Section 6.4.7.

Meanwhile, also methods of **dielectric diagnostics** are employed. I.e. a diagnosis voltage is applied to the insulation system. The *response* of the dielectric system in the form of currents or voltages can be assessed in the *time domain or frequency domain*, Section 6.4.

For a detailed presentation of **diagnosis procedures**, see Sections 6.4.7 and 7.1.3.6.

5.5.1.4 Manufacture and Processing

Paper and pressboard are manufactured from so-called *wood pulp,* which largely consists of cellulose fibers. *Cellulose* is a natural macromolecule, which can be considered as a condensation polymer of glucose (dextrose), Figure 5.5-7. By cross-linkages via the polar hydroxyl groups, crystalline areas are created which gives rise to a *fibrous structure* with capillaries and a large surface area. This explains the hygroscopic character of cellulose, which in equilibrium with air binds 5 to 10 % of its weight in the form of water. High quality cellulose is obtained from alpha-cellulose with a degree of polymerization of about 2000 and

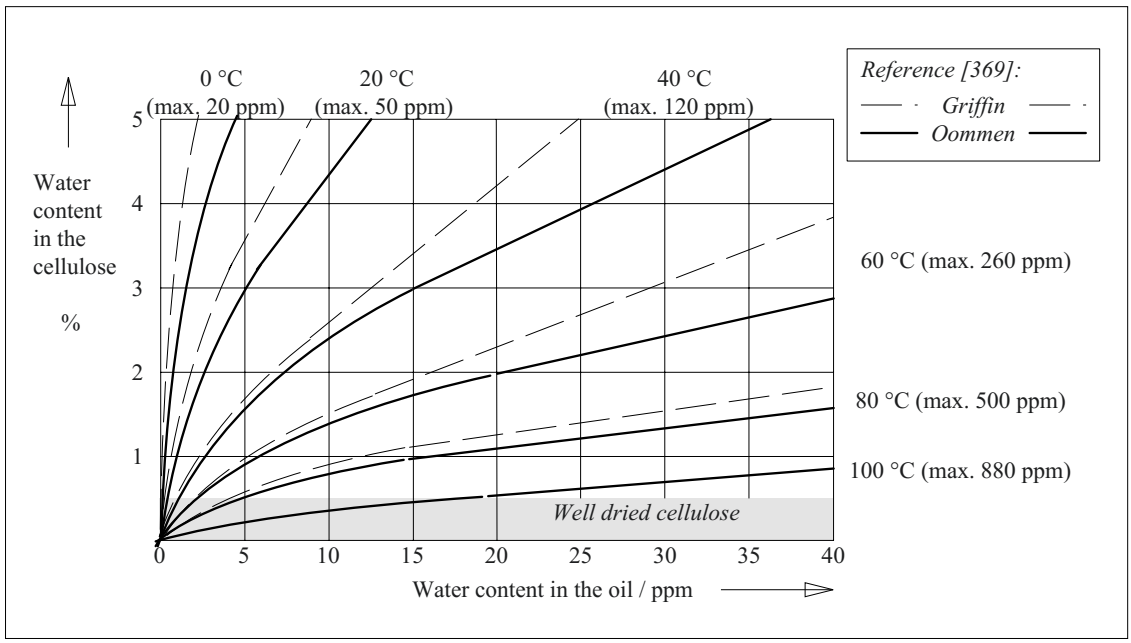

Figure 5.5-6: Water content in mineral oil and cellulose in equilibrium for different temperatures. Saturation concentration of water in oil for the respective temperatures is given in the brackets. The curves specified in the literature do not always concur with each other [369].

a low proportion of so-called hemicellulose with a degree of polymerization under 200. Hemicellulose facilitates the formation of hydrogen bridges and thereby increases the strength of the fibers if their proportion is less than 10% [27].

The best and strongest fibers are provided by pine woods which are at the limit of their natural environment of growth, such as northern spruce and pines. In particular, they contain *slowly and thickly grown fibers*. However, wood pulp from other sources, such as birch, poplar, wheat straw or from cotton scrapings, linen scrapings and waste hemp are often also added.

For *obtaining wood pulp*, the raw material must be chopped down and also chemically and thermally processed to remove interfering components (lignin and resins). Wood pulp used for electrotechnical applications is largely obtained by alkaline decomposition by boiling with sodium hydroxide and sodium sulfide (sulfate pulping). Finally, it is necessary to wash it out with care in clean and non-conductive water.

For the **manufacture of paper and pressboard**, the (sulfate) wood pulp is dissolved in

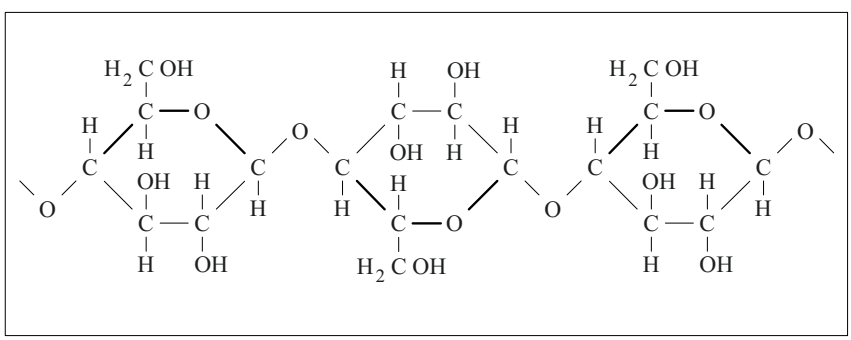

Figure 5.5-7:

Macromolecule of cellulose.

water, broken down to individual fibers and finely *ground* to obtain a dense material with many contact points between the fibers.

Note: Wood pulp for insulating paper and insulating pressboard is not bleached. Binding agents and fillers are not added either.

At the *paper machine*, the aqueous suspension (99 % Water) is cast continuously by passing through a *sieve* in which approx. 10 to 20% of water drips off. After a few 10s of meters, the moist paper web is lifted off and dehumidified between *press rollers* and woven felts until a water content of about 65 to 70% is achieved. It is further *dried* by intense heating for a resultant water content of 4 to 8%. This is followed by cooling down on cooling rollers, smoothing between rollers, cutting to specific widths and winding [88].

For manufacturing thinner capacitor papers, the machine-smooth paper is *calendered*, i.e. additionally pressed under high pressure between the rollers of a so-called *calender*. This gives high compression and a smooth surface.

The manufacture of **pressboard** is similar to that of paper. However, the moist web lifted off the sieve is immediately wound on a roller until the desired plate thickness of several mm is attained. Owing to the high proportion of water, individual paper layers are still deeply interconnected. By cutting open in the axial direction, a moist panel is formed and this, similarly to paper, passes through a press section and dryer section and is subsequently stacked.

Molded components made of pressboard, e.g. flange rings and caps for transformer insulations, can be manufactured by thermoforming from wetted pressboard panels or by manual couching of wet paper layers on molds.

Paper is processed by winding. *Conductors* are wound with paper tapes in an overlapping manner, Figure 5.5-8. For example, *high voltage cables* require insulations of several cm thickness made of "cable paper" (80 to 130 µm). *Bushing cores* are obtained by continuous winding of broad paper webs, in which, on attaining the respective diameter, metallic foils of graduated lengths are inserted for capacitive grading, Figure 5.5-9. *Capacitor dielectrics* are manufactured by simultaneous winding of metallic capacitor foils with several thin "capacitor papers" (10 to 30 µm) and/or polymeric films, Figure 5.5-10.

Note: While connecting the metallic foils via contact strips, the *inductance of the capacitor* is greatly determined by the position of the contact strips. An especially low inductance set up results without contact strips, when both the metallic foils are shifted against

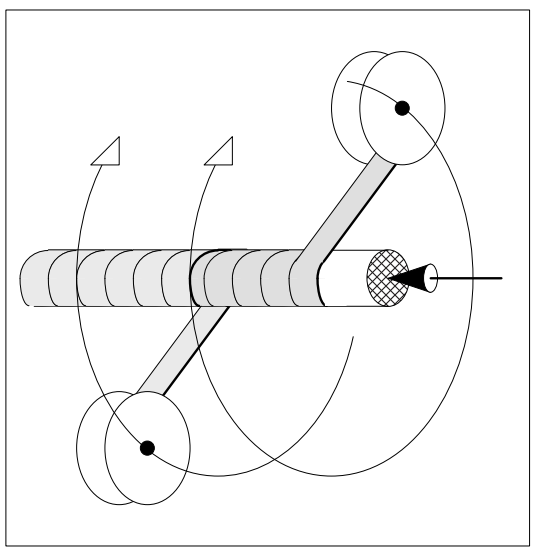

Figure 5.5-8: Winding a conductor with overlapping paper tapes (Cable or tape winding).

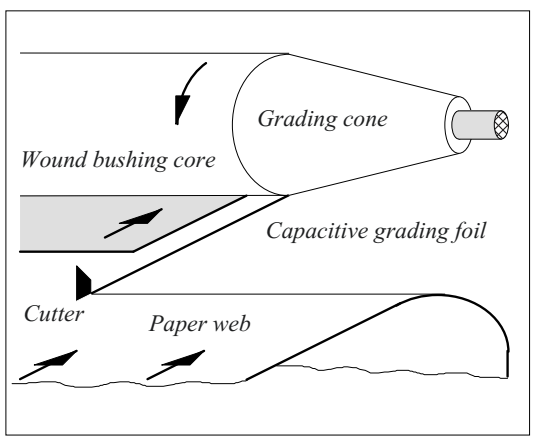

Figure 5.5-9: Winding of a bushing with running through paper web and inserted capacitive grading foils.

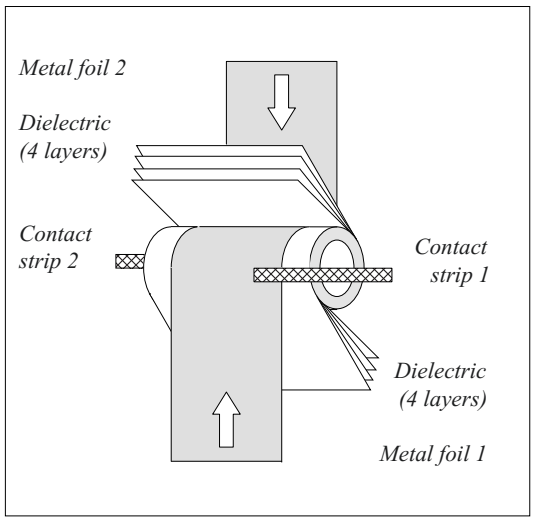

Figure 5.5-10: Winding of a four-layered capacitor dielectric with contact strips.

each other towards left and right and are contacted across the whole area at the front side of the capacitor winding [113].

While processing the paper, the assembly of a **multilayer dielectric** must always be guaranteed. Owing to technologically unavoidable defective spots and holes, a single paper does not have an insulation effect, i.e.

"**one paper is no paper**!"

Individual defective spots are only covered by stacking several layers. Adequate coverage is necessary also for *abutting edges* between strips and webs, Figure 5.5-11. Practical insulations are therefore made out of 4 to 5 layers. Analogously, this is also applicable to insulations of polymeric films.

Note: Frequently, oil-filled cavities, which are considerably larger than the pores within the paper, form *defects* in the assembly of dielectrics. These must be taken into account during the estimation of *electric strength*, see Table 5.5-1 and Figure 3.4.2-6.

The insulation body manufactured by winding as well as other cellulose-based parts must be **dried and impregnated under vacuum** in order to obtain an ageing-stable, void-free insulation that is also free of partial discharges. Negligible residual moisture of about 0.1% can be attained only at high temperatures (up to 120 °C) and under vacuum, Figure 5.5-12.

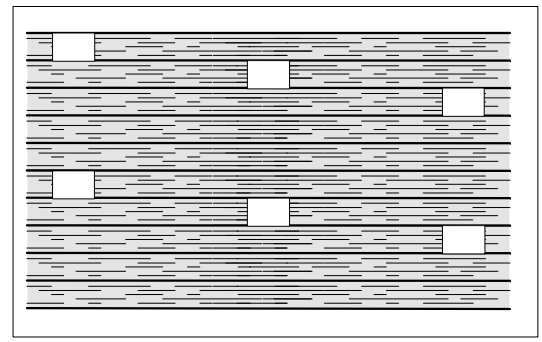

Figure 5.5-11: Coverage of defective spots or abutting edges in a multilayered dielectric.

For this, the pressure in the degassing tank must be selected to be at least one order of magnitude lower than the desired *partial water vapor pressure* to ensure a pressure difference for rapid moisture diffusion from the inner parts of the insulation to the surface.

Example: For drying to a residual water content of 0.1%, according to Figure 5.5-12, a temperature of 120 °C at a partial water vapor pressure $\leq$ 3 mbar is necessary. For ensuring an adequate pressure difference, a pressure in the degassing tank of around 0.1 mbar is generally necessary.

The following *phases* are passed through during drying and impregnation, Figure 5.5-13:

a) Dielectric is mainly *heated up* by convection, for example by heating kerosene vapor (*vapor-phase*), which condenses on the still cold insulation [114]. In the case of trans-

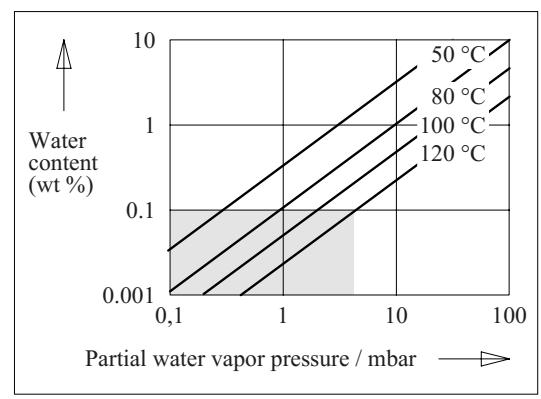

Figure 5.5-12: Water content of cable paper (wt % with regard to the dry weight of the paper) as a function of partial water vapor pressure at different temperatures [16].

former windings, the heating can be accelerated by the ohmic losses of current (Joule effect) in the conductors. Here, owing to the inductive reactive impedances, heating is carried out at low frequencies so that low voltages that can be handled under vacuum conditions are adequate (*LFH: low-frequency heating*) [70]. The rise in temperature should not be more than 10 °C/hour for the protection of the paper or pressboard [27]. Owing to the high temperatures, an atmosphere that contains oxygen (air) shall *not* be used to avoid rapid ageing through oxidation. Heat transmission by *radiation heating* under vacuum is generally not enough, since heavily evaporating water in the initial stages leads to significant evaporative cooling.

b) Water also evaporates significantly during subsequent *evacuation*. The desired end pressure is therefore often not attained immediately and the insulation temperature falls again, Figure 5.5-13.

Note: Temporary reductions in pressure (*reduction in intermediate pressure*) already in the heating up phase can lead to an acceleration of water transport to the surface. They are therefore used in modern plants for the **optimization of process control** [114].

c) Temperature and pressure must be maintained at the desired values by *radiation heating and evacuation* until the *drying is completed*. The drying procedure is at first supervised by the *quantity* of *water* deposited in a condensation trap. In the medium vacuum phase, the *dissipation factor* is observed for the insulation with the longest diffusion paths. Information about the drying state is also given by the *pressure rise* that is measured within a specific period after the vacuum

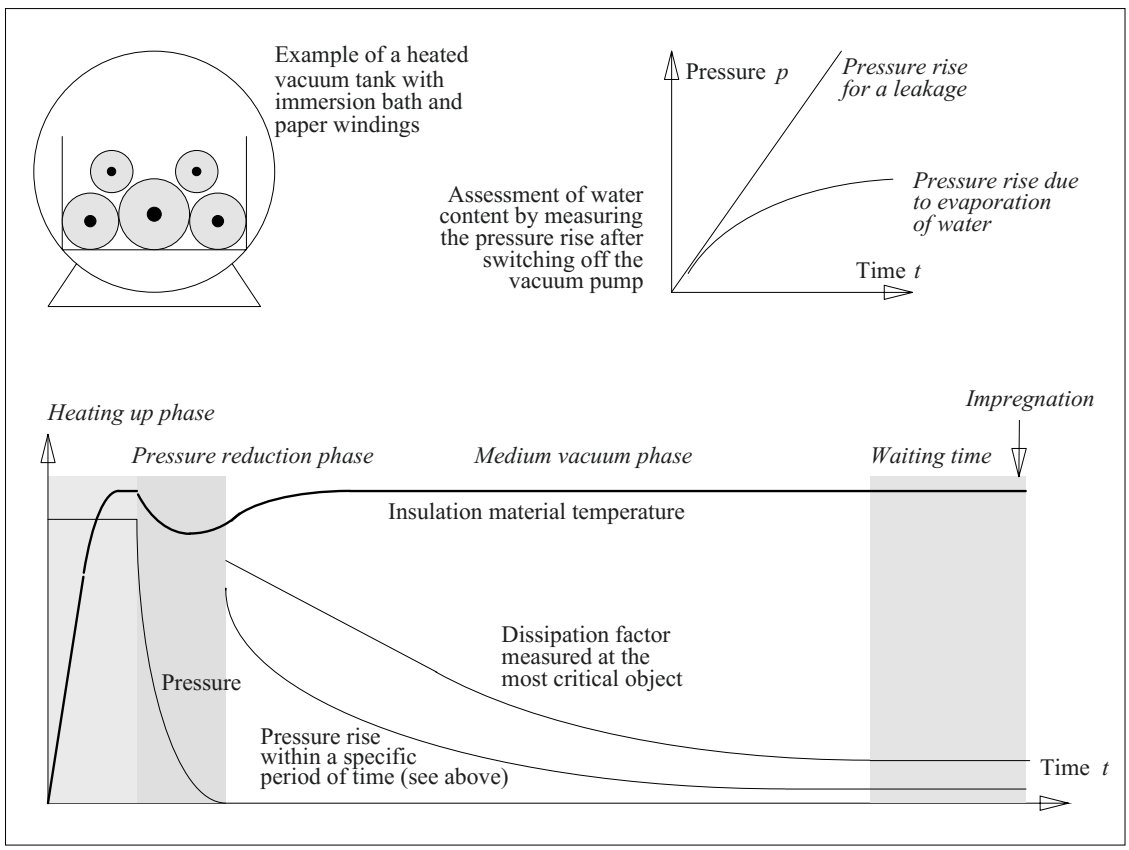

Figure 5.5-13: Monitoring the drying progress of cellulose-based insulations by observing the temperature parameters: pressure, pressure rise (within a specific period after switching off the vacuum pump) and dissipation factor (for the object with the least rate of drying).

pump is switched off. In a hermetically sealed tank, *partial water vapor pressure* equilibrium occurs after a long time, and this, in accordance with Figure 5.5-12, gives information about the (average) residual moisture.

All the procedures mentioned provide *integral information* which does not allow any direct conclusion on the local water content. If the measurable parameters are no longer changing, an additional *waiting period* is allowed, Figure 5.5-13. Objects with large surfaces and small thicknesses can be dried within a few days, but under unfavorable diffusion conditions it can even take several weeks. For example, the moisture for big bushing cores must diffuse over several meters in the axial direction to the front side areas, since the metallic grading layers obstruct diffusion in the radial direction.

During drying, a *shrinkage* that cannot be exactly defined before must be taken into consideration and it makes prior determination of the final dimensions of the finished product difficult.

d) After drying, the insulation is *flooded under vacuum with dry and degassed oil* to prevent the entry of air and moisture.

e) Thereafter, the vessel with the paper windings immersed in oil can be *pressurized*. *Impregnation is finally completed* by compression and dissolution of residual gas bubbles.

f) Oil-impregnated cellulose-based insulations should only *be in contact with atmosphere* for a *short while* since the oil only delays absorption of moisture and does not prevent it. Atmospheric moisture absorbed by oil, in accordance with Figure 5.5-6, is again absorbed by cellulose fibers. I.e. only a *limited temporary storage under oil* is possible after the impregnation. *Assembly* must then be carried out in an air-tight housing or in a transformer protected by a dryer, Figure 5.4-1.

Note: **Subsequent drying** of wetted transformer insulations at the installation site, for instance, is possible with the help of *low-frequency heating* (*LFH*): while heating up the oil-filled transformer, temperature equilibrium is created by the circulation of oil. After emptying the oil, fine drying is carried out under vacuum with simultaneous low-frequency heating of windings by a frequency converter. Subsequently, the transformer is filled with new oil or with the used oil that has been conditioned in parallel under vacuum [70]. During this, it must be noted that the *impregnation of insulation already containing oil* is more difficult, so that larger gas bubbles might be trapped and could dissolve in oil only after a longer period.

5.5.2 Synthetic Fibrous Materials

Synthetic fibrous materials in the form of papers or pressboard type panels and molded components for high temperatures are prepared from *aramide fibers*, see Section 5.3.2.5.

Since stiff and smooth extruded fibers of crystalline aramide have no bonding with one another and do not become felted, manufacturing products with satisfactory mechanical properties was not possible for a long time. The necessary *bonds with the crystalline fibers* could only be formed by flocculation or by moist fibrillated fibers of amorphous amides.

The further manufacture of aramide-papers and Nomex ® board (Du Pont) is similar to the manufacturing process of paper and pressboard from cellulose.

Aramide products are characterized by a high *long-term heat resistance* of 220 °C. Cellulose is thermally decomposed even at temperatures above 120 °C with the elimination of gases.

During *drying*, geometrical data are largely constant. The *mechanical strength* is distinctly reduced when compared to cellulose-based products. Owing to their *impregnability*, aramide products have similarly good *electrical properties* as cellulose products. They exhibit an increasingly greater resistance to *partial discharges* and practically negligible *ageing* [82], [101]. The high cost is a disadvantage.

6 TESTING, MEASURING AND DIAGNOSIS

High voltage engineering production is especially vulnerable to small defects, which can develop into serious consequences.

Even long before the idea of comprehensive quality assurance for common industrial property with ISO 9000 ff was thought of, high voltage engineering was dependent on *reliable quality control* (Section 6.1). Under this, testing in the high voltage test laboratory with the *generation and measurement* of *extreme test parameters* is especially significant (Sections 6.2 and 6.3) [141], [498]. In addition, *diagnosis and monitoring* of the condition of devices (Section 6.4) are of greater significance today, since owing to high costs, unnecessary premature re-investments should be avoided. On the other hand, the risk of damage with greater consequences must also be kept to a minimum.

Note: Tests, measurements, and diagnoses are conducted based on **standards and specifications**. The involved parties (e.g. manufacturers, customers, testing institutes) agree upon their application or the customers request their application. Standards generally do not describe any binding physical, technical or legal rules; they are rather made up of recommendations and compromises that are formulated in committees to describe the state of the art and to handle varied interests.

At the national level, important standards are the German *VDE Vorschriften* (Verband der Elektrotechnik Elektronik Informationstechnik, i.e. Association for Electrical, Electronic and Information Technology, Frankfurt a. M.) often being identical with *DIN standards* and the *European EN standards*. At the European level, *IEC (CEI) standards* (International Electrotechnical Commission) are prevalent; they are increasingly adopted in EN, DIN, and VDE specifications so that the actual *content-based* standardization activity is largely shifted to the international committees of the IEC. At the US-American level, *IEEE standards* (The Institute of Electrical and Electronic Engineers, New York) are of greater significance. Finally, *CIGRÉ recommendations* (Conseil International des Grands Réseaux Électriques, Paris) should also be mentioned. Moreover, there are still a large number of other standards institutions, especially at the national level of individual states.

6.1 Quality Assurance

The objective of quality assurance is to guarantee the properties of a product or the properties of a service provision agreed upon between the client and the contractor.

In this context, it is not attaining the "highest possible quality", but rather reliable *reproducibility* of agreed properties or properties specified in the standards that are most significant.

6.1.1 Quality Assurance Systems

For attaining this objective, manufacturers and service providers install their own **quality assurance systems** that are respectively described in a *Quality Management Handbook*. Important quality assurance elements are described in ISO 9001. The quality assurance system is checked at regular intervals through *internal audits*. Further, the option to allow *external institutions to audit and certify* the quality assurance systems is also available. In many cases, customers also conduct their own audits of important subcontractors.

The *quality management handbook* is a collection of in-house specifications that are to be continuously updated. It contains information about the responsibilities of the highest-level management and officers. By determining the qualification features of employees and training methods, quality should become independent of individual persons. The full contract cycle is described including contract review, design, purchasing, production, testing, dispatch, customer service, documentation and handling of complaints.

Important components of a quality management handbook are the *quality specifications*,

A. Küchler, *High Voltage Engineering*, VDI-Buch,
DOI 10.1007/978-3-642-11993-4_6

such as production specifications, specifications for materials and parts or test specifications. Specifications that include manufacturing expertise are not always published.

6.1.2 Certification and Accreditation

Integration of **high voltage test facilities** into quality assurance systems is dependent on whether they have to be operated as independent institutions or as a section of a high voltage production plant. In addition to *certification* within a quality assurance system in accordance with EN 29001 (and also ISO 9001), high voltage test facilities can also obtain an *accreditation* through an national accreditation agency, for example, through the German accreditation body DAkkS (Deutsche Akkreditierungsstelle GmbH, which includes Deutsche Akkreditierungsstelle Technik DATech since 2009), based on the principle of ISO/IEC 17025, Figure 6.1-1 (left). This is a formal approval that a testing facility is competent for the execution of the specified tests or types of tests. A prerequisite for accreditation is the independence of the testing institution, which is greater than that expected for certification [115], [116].

Note: Like many other institutions in economics, research and teaching, also test laboratories, high voltage laboratories and calibration labboratories can be accredited for specific activities by *accrediting agencies*. For this, the agencies are integrated in a network of national and international accreditation hierarchies, Figure 6.1-1 (left). In the course of an accreditation process, the accredited institution (after considerable bureaucratic groundwork, on payment of charges and with limited validity period) is certified that it follows the guidelines (minimum requirements) of the agency. The influence, supervision tasks and competence of national institutions are thus passed on in many areas to the network of accrediting agencies.

6.1.3 Calibration

The focus of quality assurance in high voltage laboratories is the **calibration of measuring equipment**, since incorrect high voltage me-

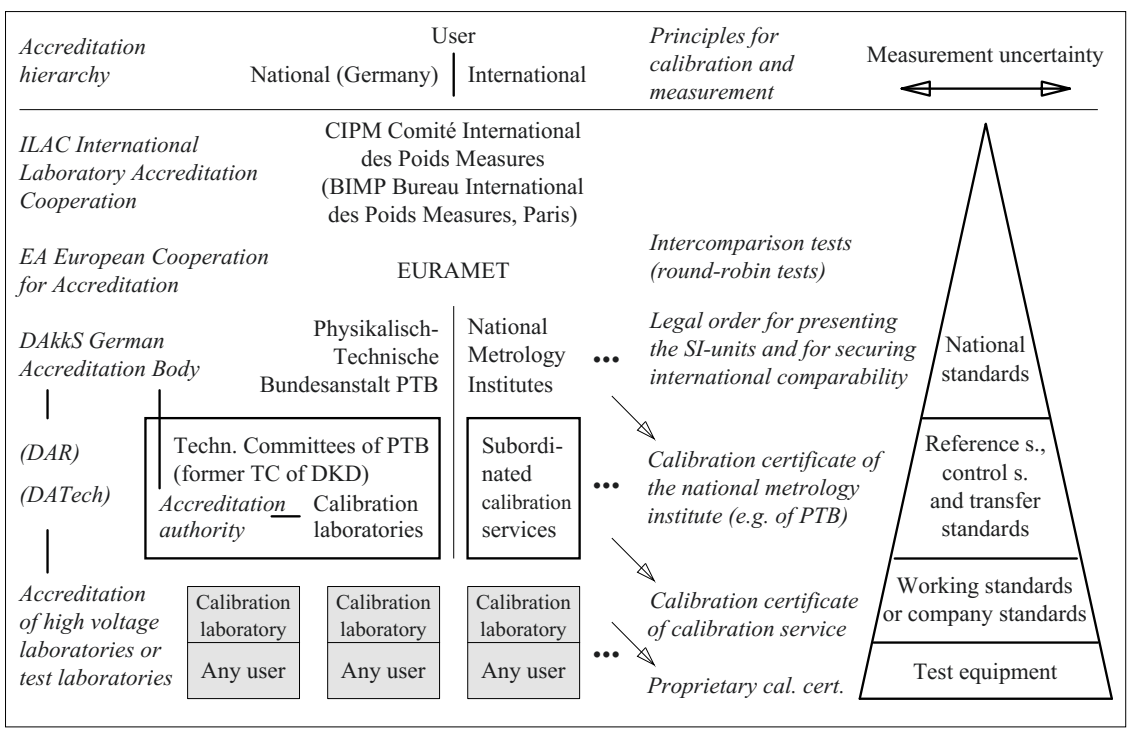

Figure 6.1-1: Hierarchy and bureaucracy for traceability of measuring system calibration with respect to the national metrology standards (Note: DAR, DATech and DKD are now parts of DAkkS and PTB).

asurements can lead to increased overloads or underloads of the devices during the tests. This results in increased risks both with regard to test damage and with regard to the non-identification of faultive insulations during the tests.

The *calibration intervals* and the *calibration specifications* to be applied must be referred form a *directory for measuring and test equipment.* The result of the calibrations must be documented in a *calibration report*.

The basic principle of calibration is the *complete traceability* of the measuring devices used to the *national and internationally reconciled standards* [120], [389]. This gives rise to a hierarchy of calibration standards, whose *measurement uncertainty* increases from the top towards the bottom, Figure 6.1-1 (right). The national standards are provided by a *national metrology institute* in most of the industrial countries, and in Germany it is provided by the *Physikalisch-Technischen Bundesanstalt PTB (Federal Institute for Physics and Technology)* in Braunschweig, Figure 6.1-1 (center). Uniformity of standards of metrology institutes in different countries is developed by international cooperation, for example, in the form of intercomparison tests (round-robin tests).

Subordinate to the above are *calibration services* (such as the former *German calibration service DKD*, whose technical committees are now taken over by the PTB), often consiting of a large number of calibrating laboratories. They get their own standards to be calibrated by the higher-level metrology institute and they carry out a large number of calibrations of the calibrating devices or test devices of the *users*. The *calibration certificate* of the respective higher level is the basis for calibration or measurement on the lower level. The certificate records the *measurement uncertainty* of the measuring device used that is found in the calibration.

The **measurement uncertainty** of the measuring or test device at the lowest level may be no greater than 1/3rd of the tolerance permitted for the measuring parameter. The higher level calibration standards must have a lower measurement uncertainty, which again may be no greater than 1/3rd of the measurement uncertainty of the lower level standard or test device. The requirements for the total measurement uncertainties for high voltage measuring systems are given in Table 6.1-1.

The specification of a **measurement uncertainty** u is based on estimated values for the measured variable X and for the standard deviation σ of individual measured values x_i. This relates to the specification of *confidence intervals*, which can be determined for random errors from a knowledge of the distribution function. Frequently, however, not all systematic errors can be detected; they are therefore treated as random errors and are taken into account in the measurement uncertainty u through estimated confidence limits [117].

Table 6.1-1: Requirements for the total measurement uncertainty for measuring systems according to EN 60060-2 (IEC 60060-2) [116].

	Measuring system	Working standard	Reference standard	National standard
DC voltage				
Mean value	3%	1%	0.3%	0.1%
Ripple	10%	3%	1%	0.3%
AC voltage				
Peak value	3%	1%	0.3%	0.1%
Switching impulse and lightning impulse voltage				
Peak value	3%	1%	0.5%	0.3%
Time	10%	5%	1.5%	1.2%

For a large number of *n individual measured values* x_i, such as, for example, for voltage measurements with a sphere gap, the arithmetic mean value x_m, in accordance with Eq. (3.1-2), is used as an estimate for the expectation value μ of the measured variable X. The empirical standard deviation s of the individual measured values x_i are obtained in accordance with Eq. (3.1-5). For a finite number of measured values, the mean value x_m deviates from the expectation value μ of random variable X. While assuming a Gaussian normal distribu-

tion, the standard deviation of the mean value is estimated as [119]

$$s_m = s/n^{1/2} . \qquad (6.1\text{-}1)$$

If only one individual measured value x_i is available, this can then be considered as the estimated value x_m, but the standard deviation is unknown. The specification of a standard deviation requires the estimation of an upper and lower limit x_U and x_L based on possible influencing variables, e.g. based on the accuracy class of the measuring device used. The mean value between the limits can be used as the estimated value for the measured variable:

$$x_m = (x_U + x_L) / 2 \qquad (6.1\text{-}2)$$

For the standard deviation of the mean value, the estimated value

$$s_m = (x_U - x_L) / 12^{1/2} \qquad (6.1\text{-}3)$$

is given [118].

Often, an output quantity Y is a *function of several variables* X_1, X_2... X_n that *contain measurement uncertainties*. The deviation dy of measurement result $y = f(x_1, x_2, ..., x_n)$ can be determined as the total differential from the individual deviations weighted with the respective partial derivatives [119]:

$$dy = dx_1 \cdot \partial y/\partial x_1 + dx_2 \cdot \partial y/\partial x_2 + ... dx_n \cdot \partial y/\partial x_n$$

By squaring, quadratic and mixed terms are obtained and these are mutually cancelled owing to equally probable positive and negative deviations. Only the quadratic terms that are interpreted as squares of *empirical standard deviations of the mean values* remain:

$$s_{y_m}^2 = \sum_{i=1}^{n} (s_{x_{im}} \cdot \partial y / \partial x_i)^2 \qquad (6.1\text{-}4)$$

For this, small empirical standard deviations s_x << x_m and a Gaussian normal distribution are presumed.

While assuming a Gaussian normal distribution, a *measurement uncertainty of*

$$u = 2 \cdot s_{y_m} \qquad (6.1\text{-}5)$$

corresponds to a *confidence interval* of 97.7 % for the mean value y_m, see Section 3.1.2.2.

Example: Measurement uncertainty of divider ratio of a voltage divider

The following variables are measured with an oscilloscope:

V_1 = 111 V,
measurement uncertainty u_1 = 1 % · 160 V = 1.6 V

V_2 = 0.3 V,
measurement uncertainty u_2 = 1 % · 0.4 V = 4 mV

The standard deviations are estimated with Eq. (6.1-3):

$s_1 = (3.2 \text{ V})/ 12^{1/2} =$ 0.924 V

and

$s_2 = (8 \text{ mV})/ 12^{1/2} =$ 2.309 mV

With the mean value of the voltage ratio

$r =$ $V_1/V_2 = 370$ (*)

the square of the estimated standard deviation from Eq. (6.1-4) and Eq. (*) results:

$s_r^2 = s_1^2 \cdot (1/V_2)^2 + s_2^2 \cdot (-V_1/V_2^2)^2$
$= 17.6$

The measurement uncertainty of the divider ratio with Eq. (6.1-5) is approximately

$u_r = 2 \cdot s_r = 8.39.$

The result of the measurement corresponds to the confidence interval for the divider ratio of $r + u_r$ = 378.4 to $r - u_r$ = 361.6. With respect to the mean value of the divider ratio r = 370, this gives a measurement uncertainty of $u_r/r = \pm 8.39/370 = \pm 2.3$ %.

6.1.4 Insulation Coordination

6.1.4.1 Principle of Insulation Coordination

The operational safety of high voltage devices, installations and systems as well as the quality of insulation must be proven by **high voltage**

tests. Necessary tests and test voltage levels for this are specified in the context of so-called **insulation coordination**. Insulation coordination includes

- the analysis of operating *voltages and overvoltages*,
- the selection of the *dielectric strength of operational equipment* that is provided for a specific voltage level and
- the selection of *protection levels* for the surge arresters.

The procedure is first basically described in the standards, [121], [122] and subsequently in detail in an application guideline [123], Figure 6.1-2:

The starting point is the analysis of all classes and types of *operating voltages and overvoltages in the network.*

Note: This analysis is carried out with the objective (initially independent of the level of highest voltage for equipment V_m) of covering the real operating stresses by a number of standardized withstand voltages. Only in the last step is the insulation level defined this way assigned to the standardized values of V_m.

1.) From the analysis of real *operating stresses in the network*, so-called **representative voltages** V_{rp} are determined in different *categories* in the first step. These categories are related to the *type and duration of the stresses*, see Fig-

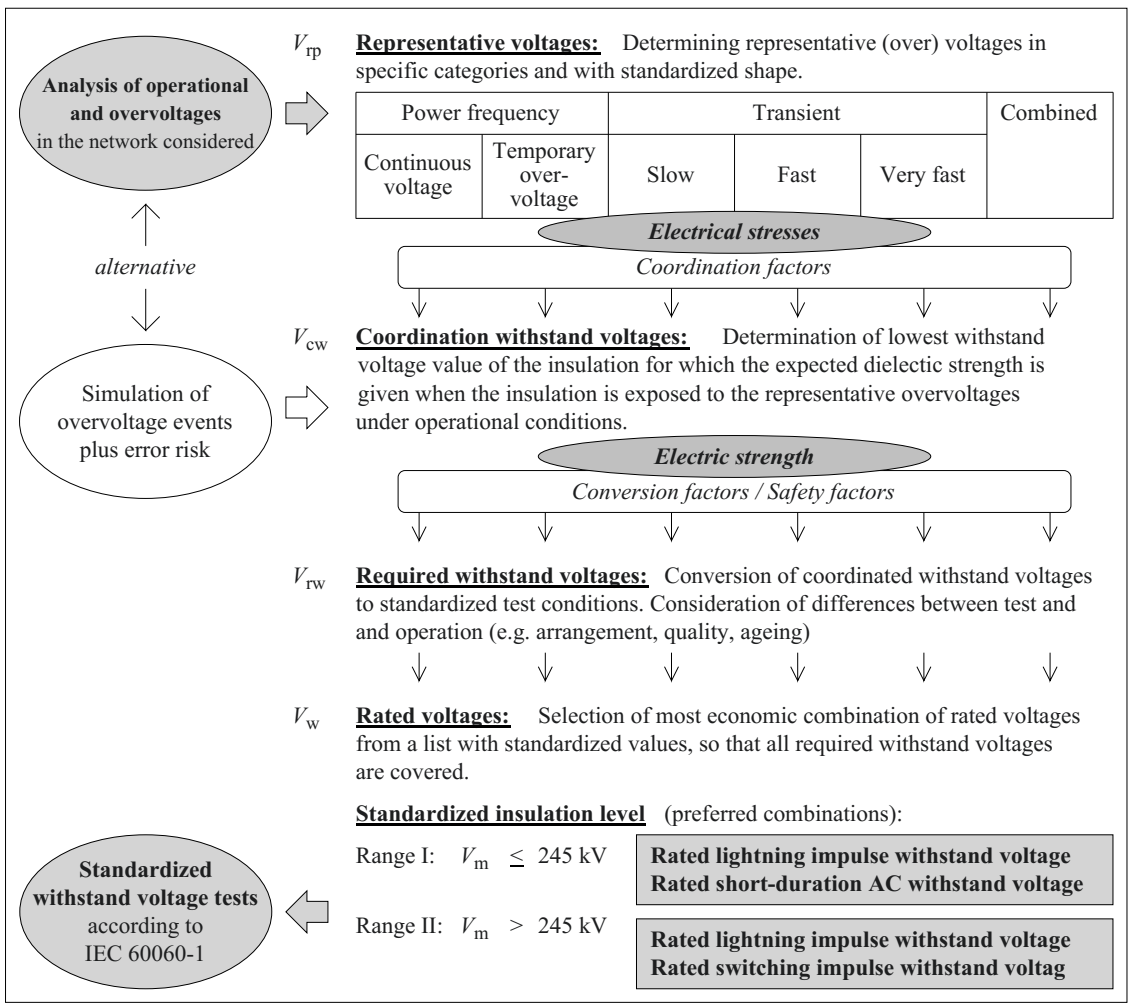

Figure 6.1-2: Procedure for insulation coordination in a network according to IEC 60071-1 [121], [122], [123].

ure 6.1-2 (top) and Figure 2.2-4. While determining the representative voltages, the method must also take account of the performance of the available **surge arresters**, which generally lead to the limiting but not the elimination of overvoltages. Thus, they have a decisive influence on the magnitude of the representative voltages, see Section 6.1.4.3.

Table 6.1-2: Standardized insulation levels in range I: (1 kV < V_m ≤ 245 kV)

Highest voltage for equipment		Short-duration AC withstand voltage	Lightning impulse withstand voltage
	Reference value		
V_m	$\frac{V_m\sqrt{2}}{\sqrt{3}}$		
R.m.s. value	Peak value	$\frac{\text{Peak value}}{\sqrt{2}}$	Peak value
kV	kV	kV	kV
Phase-to-phase	Phase-to-earth	Phase-to-earth	Phase-to-earth
3.6	2.9	**10**	**20**
			40
7.2	5.9	**20**	**40**
			60
12	9.8	**28**	**60**
			75
			95
24	19.6	**50**	**95**
			125
			145
36	29.4	**70**	**145**
			170
72.5	59	**140**	**325**
123	100	*185*	**450**
		230	**550**
145	118	*185*	*450*
		230	**550**
		275	**650**
170	139	*230*	*550*
		275	**650**
		325	**750**
245	200	*275*	*650*
		325	*750*
		360	**850**
		395	**950**
		460	**1,050**

Note: Usually, the phase-to-earth withstand voltages are also applied to the phase-to-phase insulation. If the values given in italics seem not to be adequate, to prove that the reqired phase-to-phase withstand voltages are fulfilled, additional phase-to-phase withstand voltage tests are necessary.

2.) In the second step, the *electric strength of the insulation* in the form of **coordination withstand voltages** V_{cw} is specified such that *error rates* that are still *acceptable* in the network are obtained. For this, the *representative voltages* and their *frequency distribution* as well as the *properties of insulation* (breakdown probability) must be known through previous analyses. This is a *technical and economic optimization* of the insulation. The acceptable error rate assumed here is not a technical variable; it is more a result of economic and social considerations.

Note: Since the variables mentioned are generally only *inaccurately* determined, in practice the coordination withstand voltages are recommended to be set a little higher in order to obtain additional safety through *oversizing*.

The relationship between representative voltages (that is, stress in the network) and the coordination withstand voltage (that is, the electric strength of the insulation) is established through *coordination factors* that can result from deterministic considerations or from statistical analyses [123].

The **coordination-withstand voltages** V_{cw} are the lowest withstand voltage values for which the expected dielectric strength in the respective (over) voltage category is just achieved.

3.) In the third step, through aditional conversion with a *safety factor*, the differences between *operating conditions and test conditions* must be considered, such as different atmospheric conditions (for air insulations), different arrangements of devices, variation of the product quality, installation quality or ageing influences. This gives the **required withstand voltages** V_{rw} for testing.

4.) Instead of the required withstand voltages, **standardized test voltage values** must be chosen in the fourth step, Table 6.1-2 and -3.

However, they must not all be tested individually, since a specified strength in one category (e.g. short-duration AC voltages) can also imply a specified strength in another category (e.g. switching impulse voltage).

Note: Corresponding relationships are not generally applicable, but they vary according to the type of insulation.

5.) In the fifth step, with the help of *test conversion factors*, individual **rated voltages** V_w are selected from the standardized values, in which it must be ensured that all required withstand voltages are covered by this, Tables 6.1-2 and -3.

A *combination of rated voltages* is described as a **standardized insulation level,** which can

Table 6.1-3: Standardized insulation levels in range II (V_m > 245 kV)

Highest voltage for equipment U_m	Reference value $\frac{U_m\sqrt{2}}{\sqrt{3}}$	**Switching-impulse withstand voltage**			**Lightning-impulse withstand voltage**
		Longitudinal insulation *(a)*	Phase-to-earth	Phase-to-phase *(b)*	*(c)*
R.m.s. value kV	Peak value kV	Peak value kV	Peak value kV	Peak value kV	Peak value kV
300	245	**750**	**750**	**1,125**	**850**
		750	**850**	**1,275**	**950**
					1,050
362	296	**850**	**850**	**1,275**	**950**
		850	**950**	**1,425**	**1,050**
					1,175
420	343	**850**	**850**	**1,360**	**1,050**
		950	**950**	**1,425**	**1,175**
		950	**1.050**	**1,575**	**1,300**
					1,425
550	429	**950**	**950**	**1,615**	**1,175**
		950	**1,050**	**1,680**	**1,300**
		950	**1,175**	**1,763**	**1,425**
		1,050	**1,175**	**1,763**	**1,550**
800	625	**1,175**	**1,300**	**2,210**	**1,675**
		1,175	**1,425**	**2,423**	**1,800**
		1,175	**1,550**	**2,480**	**1,950**
		1,300	**1,550**	**2,480**	**2,100**
1,200	980	**1,425**	**1,550**	**2,635**	**2,100**
		1,550	**1,675**	**2,764**	**2,250**
		1,675	**1,800**	**2,880**	**2,400**
					2,550

Notes: *(a) "Longitudinal insulation" between different parts of a grid, e.g. between the open contacts of a disconnector. Tests are performed as combined tests with AC voltage (peak value is equal to the reference value) and with SI voltage of opposite polarity (peak value is the given SI voltage).*

(b) Peak value for the according relevant test with combined AC voltage and SI voltage.

(c) The lightning impulse voltages apply to both phase-to-phase and phase-to-earth insulation. For longitudinal insulation, tests are performed analogously with (a) as combined tests with AC voltage (peak value is equal to the reference value) and with LI voltage of opposite polarity (peak value ist the given LI voltage).

(d) If applicable, AC voltage tests are described in the standards for equipment.

(e) Tests with chopped lightning impulses are especially important for transformers, and they are performed with higher voltages.

be assigned to the *highest voltage for equipment* V_m. The rated *lightning impulse voltage* and the rated *short-duration AC voltage* are recommended as the *preferred combination* for the lower voltage levels (range I, $V_m \leq 245$ kV) and the rated *lightning impulse voltage* and rated *switching impulse voltage* are recommended for higher voltage levels (range II, $V_m > 245$ kV), Tables 6.1-2 and -3.

Note: Other or extended specifications can be made for specific operating equipment for the *respective conditions* to be covered, e.g. see Section 7.1.3.5 (Transformer Tests).

In special cases even tests with DC voltages, with non-power-frequency AC voltages or with special impulse voltage shapes are necessary, such as for example for HVDC transmission components, DC-voltage operated devices, cables or impulse capacitors, see Figure 2.2.-4.

6.1.4.2 High Voltage Tests

Depending on the **function of the insulation**, high voltage tests for the proof of dielectric strength require the application of test voltages between phase and earth (*phase-to-earth* or *line-to-ground insulation*), between energized conductors (*phase-to-phase* or *line-to-line insulation*) or between different points of the grid (*longitudinal insulation*), Figure 6.1-3. In **three-phase AC systems**, the line-to-line insulation is the insulation between the phases in most of the cases. In the follwing, test voltages are described for three-phase AC systems.

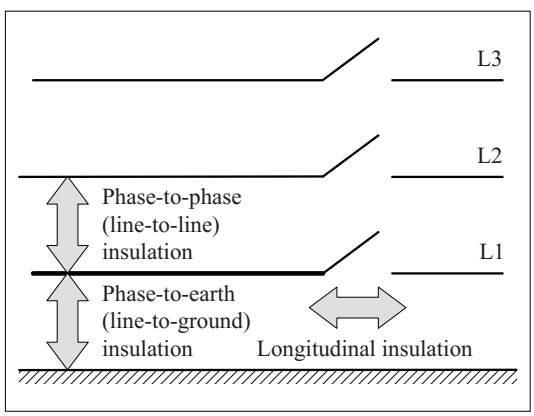

Figure 6.1-3: Insulations in a three-phase AC system that have to be tested, phase L1 is chosen as an example.

Generally, high voltage equipment is characterized by a so-called **nominal voltage** V_n, e.g. by V_n = 380 kV or 400 kV. Due to the requirements of insulation coordination, the rating of the insulation is determined by the **highest voltage for equipment** V_m within the considered group of similar nominal voltages, that is V_m = 420 kV for the example mentioned above [498]. The **standardized withstand voltages** for high voltage tests according to Tables 6.1-2 and 6.1-3 are related to this value, and the tests should show the compliance of the insulation with the **rated voltage** V_r. The general standard IEC 60071-1 gives the following possibilities,

- short-duration *AC voltage* tests,
- *switching impulse voltage* tests,
- *lightning impulse voltage* tests and
- *combined* voltage tests.

Tests for steep-front impulse voltages should be specified in the standards for special devices.

For the insulation levels specified in the standards, in the case of *non self-restoring insulations*, it is a so-called *assumed conventional withstand voltage*, for which no breakdowns are permitted. In the case of *self-restoring insulations* (e.g. pure gas gaps), a *statistical withstand voltage* with a specific number of breakdowns can be allowed. Verification is achieved by high voltage tests in the form of **type tests, routine tests or special tests** based on test programs given in the standards or agreements. *Lower test voltages* are often stipulated for **repeat tests**, e.g. after long lasting operation.

For a *reference voltage,* different *test voltage levels* that correspond to different degrees of safety are mentioned. The selection of the test voltage level is based on the amplitude of the *overvoltages to be expected*, which can vary, e.g. based on the neutral point treatment. Moreover, different rated withstand voltages apply *depending on the operating equipment*. For example, higher values are stipulated for isolating distances than for high voltage de-

vices (insulators, bushings, power transformers, instrument transformers, cables, …). Requirements for neutral point insulations and insulations in rotating machines are lower.

In many cases, a higher withstand voltage must be proven for the **internal insulation** of an equipment than for the **external insulation** which often can flash over without causing irreversible damage.

Details are obtained from the specialist literature [498] and from the applicable standards and specifications agreed between the manufacturer and customer.

6.1.4.3 Surge Arresters

a) Application of surge arresters

Using **surge arresters** for the protection of operational resources is especially required, if lightning overvoltages or high switching overvoltages are to be expected. The protection parameters of arresters must be coordinated with the electric strength of the insulation [124], Figure 6.1-4.

The **protection levels** V_{pl} and V_{ps} for lightning impulse voltages and switching impulse voltages must be much below the *rated withstand voltages* of the insulation to be protected, so that overvoltages are definitely limited to values for which there is only a negligibly small probability of an electrical breakdown of insulation in the network. Here we refer to *protective ratio*.

Note: Besides, the protection level must be significantly higher than the **permanent operating voltages**, in order to avoid a faulty response or overheating owing to leakage currents. The selection of a surge arrester thus represents an *optimization task*; some usable data are presented as an extract in Table 6.1-4 [124].

A *protection level* is defined by the maximum

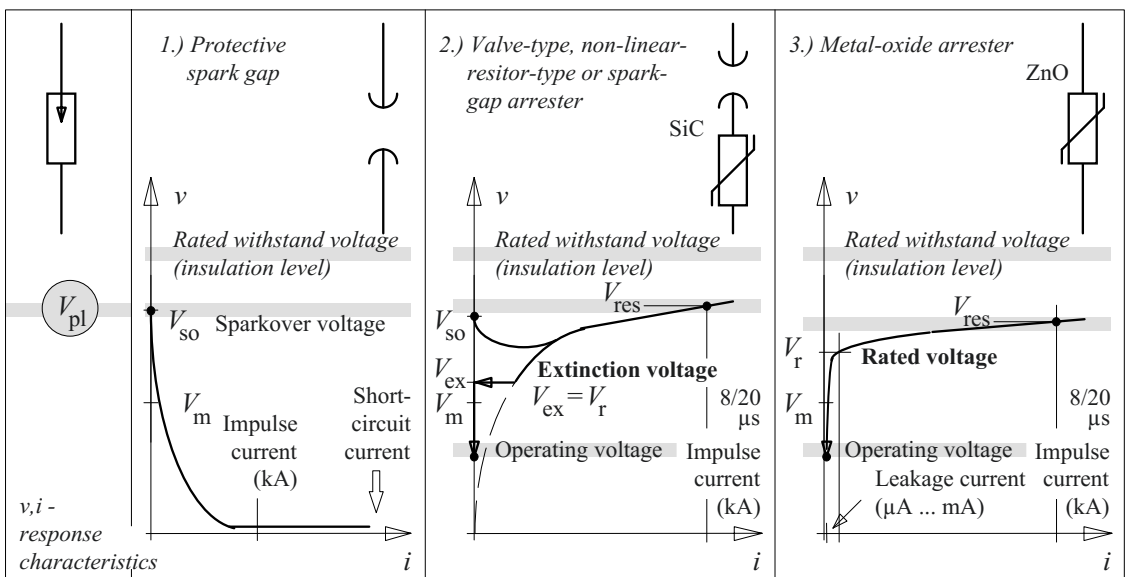

Protection level	V_{so} *Sparkover voltage*	V_{so} *Sparkover voltage* or V_{res} *residual voltage*	V_{res} *Residual voltage*
Extinguishing	*Network protection*	V_{ex} *Extinction voltage*	V_r *Rated voltage*
Permanent current	*No*	*No*	*Leakage current*

Figure 6.1-4: Functional principles of different overvoltage protection elements.

voltage occurring at the arrester. This is either the *sparkover voltage* V_{so} of spark gaps or the maximum residual voltage V_{res} occurring during the leakage impulse current, which results as a voltage drop at the non-linear resistors, Figure 6.1-4.

Note: In the context of *insulation coordination*, the values V_{so} and V_{res} respectively can be considered as *representative over voltages* at the location of the arrester. Thus, they are always significantly below the *rated switching impulse withstand voltages* and *rated lightning impulse withstand voltages* which are applied to verify the insulation level of the insulation to be protected, as in Figure 6.1-2.

Note: Generally, arresters are installed between the conductor and ground. The protection levels V_{pl} and V_{ps} thus correspond to the *representative line-to-ground overvoltages*.

Note: In the case of *overvoltages that increase rapidly*, arresters have only a *protection zone* that is limited in terms of line length, Section 2.6.3.2. For this, according to Figure 2.6-17 and Eq. (2.6-22), higher *representative overvoltages* V_{rp} can occur depending on the transit time τ between the arrester and the object to be protected and depending on the rate of rise in the overvoltage $\partial v/\partial t$. These overvoltages can be above the sparkover voltage or the residual voltage and above the lightning impulse voltage level V_{pl} of the arrester [123]:

$$V_{rp} = V_{max} = V_{pl} + 2 \cdot \Delta v = V_{pl} + 2 \cdot \tau \cdot \frac{\partial v}{\partial t} \qquad (6.1\text{-}6)$$

Therefore, a *short, low-inductance connection* of the surge arrester is required. Data about the coordination withstand lightning impulse voltage V_{cw} resulting from V_{pl} and about a *protection zone* L_p derived from a lightning strike rate and an acceptable error rate are specified in the standards, [124].

Overvoltage impulses give rise to large pulsed **leakage currents**. The current-carrying capacity or the energy consumption capacity of an arrester is thus classified by a *nominal discharge current* (8 µs /20 µs for front and back). 5 or 10 kA are recommended for range I (V_m over 1 to 245 kV) and 10 or 20 kA are recommended for range II (V_m over 245 kV) [124].

b) Types of surge arresters

The task of surge arresters is to limit transient lightning overvoltages and switching overvoltages, Figure 6.1-4.

1.) A coarse protection can be attained through **protective spark gaps**, Figure 6.1-4 (left). They are often found in the form of *metal parts* (so-called *arcing horns*) on both sides of outdoor insulators, in which the critical task is to keep the arc away from the insulator surfaces in the event of an insulator flashover. For very fast transient overvoltages the sparkover voltage results from the *impulse voltage-time characteristic* of the highly non-uniform electrode arrangement, with possibly greater spark formation time in accordance with Figure 3.2-22.

It is also disadvantageous that the subsequent current and the *arc* driven by the line voltage, are generally not self-quenching, but must be detected by the power system protection as *current to ground* and must be disconnected by power circuit-breakers.

Note: For this type of overvoltage protection, it must be noted that *rapid voltage breakdowns* can become a risk to operating equipment. Hence, spark gaps are *not* recommended as surge arresters in IEC 60099-5 [124].

2.) Better protection is offered by a **valve-type arrester** (**non-linear-resistor-type arrester** or a **spark-gap arrester**), in which a non-linear resistor made of silicon carbide SiC is connected in series with a spark gap, Figure 6.1-4 (center). The *sparkover voltage* V_{so} is determined by the spark gap. After the breakdown and during the leakage impulse current, the non-linear -resistance of the SiC restricts the voltage to a *residual voltage* of V_{res}. During the subsequently arising permanent power frequency voltage, the current decreases so much owing to the non-linear SiC resistance characteristic that the arc in the spark gap extinguishes below the *extinction voltage* V_{ex}. Normal operating voltage can then be applied over the extinguished spark gap. The extinction spark gap is necessary because exces-

sively large currents and thermal stresses would occur in the SiC at a permanently applied operating voltage.

Table 6.1-4: Parameters of metal-oxide arresters for networks with grounded neutral point, used in Germany [124]

Nominal voltage V_N kV	Continuous voltage V_c min. kV	Rated voltage V_r min. kV	Residual voltage V_{res} for	
			Nominal leakage impulse current max. kV	Switching impulse current max. kV
10	8	12	35	-
20	16	24	70	-
30	24	36	105	-
110	75	126	310	260
220	160	216	530	440
220*	160	240	600	500
380	260	360	900	750
380*	260	396	1000	830
* For generator transformers				

Note: In the case of non-linear-resistor-type arresters, the *extinction voltage* V_{ex} is used as *rated voltage* V_r to which the other characteristic values are related to [309].

3.) **Metal-oxide arresters** comprise non-linear resistors of zinc oxide ZnO which can be permanently subjected to a *continuous voltage* V_c without a spark gap and without the arrester being thermally overloaded by resistive (leakage) currents, see Figure 6.1-4 (right) and Table 6.1-4. The non-linear performance is very much more pronounced than for SiC, and hence only currents below 1 mA flow at normal operating voltages. A response voltage is not defined, since if an overvoltage occurs the non-linear characteristic is followed according to the leakage current amplitude up to a *residual voltage* V_{res}, which defines the protection level at which the voltage is limited by the arrester. The magnitude of the residual voltage is, however, dependent on the gradient of the voltage rise. With the disappearance of the overvoltage, the current also falls to the lower initial value in accordance with the *v,i*-characteristic and an extinction spark gap is not necessary.

Note: The *rated voltage* U_r is the r.m.s. value of a power frequency voltage, to which the arrester can be exposed for 10s. This value is close to the bend in the *v,i*-characteristic, and hence can be compared with the extinction voltage of non-linear-resistor-type arresters with spark gap.

Note: For long columns of arresters (for high voltages), parasitic currents through *stray capacitances* must be considered: similar to capacitive voltage dividers, they lead to an *unequal voltage distribution* along the longitudinal capacitances of the arrester column. Thus, the tablets of ZnO stacked on one another act in different regions of the non-linear *v,i*-characteristic and can possibly be thermally overloaded. Corrective measure is possible through *field grading* in the vicinity of the arrester (external grading) or through *grading capacitors* (internal grading).

6.2 Generation of High Voltages

In the following sections, the generation of *high AC voltages, DC voltages and impulse voltages* for test purposes is described. The methods discussed for the generation of high test voltages are applicable in other technical fields too.

High voltage test fields and **high voltage test laboratories** are generally an electromagnetically shielded room and/or a hall to maintain the *background noise level* at a minimum during partial discharge measurements; they also include high voltage sources for three basic test voltages, namely *AC voltages, DC voltages and impulse voltages*. Owing to the large flashover distances necessary for air, high test voltages also require large hall dimensions, Figure 6.2-1.

Note: Test voltage sources up to 3200 kV for lightning impulse voltages and 1500 kV for DC voltages and 1200 kV for AC voltages are necessary for the new voltage levels 1000 kV AC (UHVAC Ultra High AC Voltage) and 800 kV DC (UHVDC Ultra High DC Voltage).

In any case, i.e. regardless of the size of the test facility, working with high voltages requires special safety **measures** that are to be found in the respective **updated and applica-**

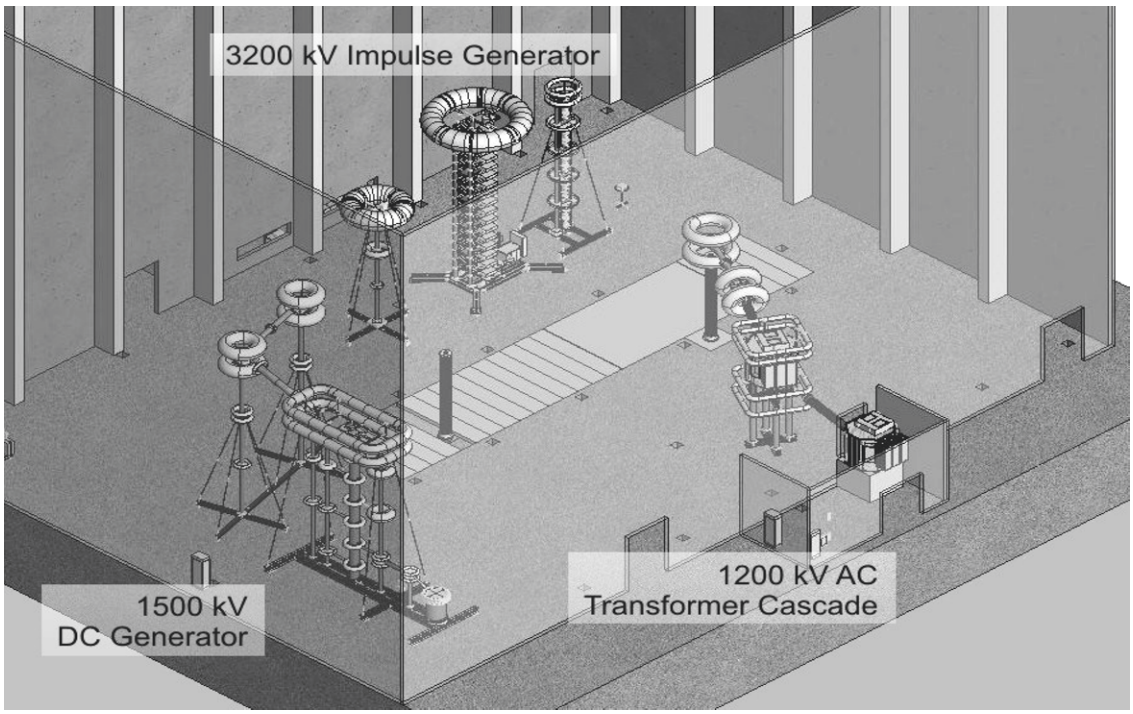

Figure 6.2-1: Shielded UHV ultra high voltage test laboratory with 1200 kV AC voltage cascade, 1500 kV DC voltage generator and 3200 kV impulse voltage generator, hall dimensions 35 x 50 x 30 m^3 (b x l x h), photo HSP Hochspannungsgeräte, Troisdorf/Highvolt, Dresden, year of construction 2007.

ble standards and they also require special *qualifications and training* for the personnel. Depending on the purpose of the high voltage equipment, there are different specifications, such as for test fields, for switchplants or for high voltage supplies in devices.

Important **safety elements** in a **high voltage test laboratory** are the *barricading* of the high voltage room with *protection against contact* and adequate *safety clearances* between parts that conduct high voltage and ground potential as well as *marking* the areas through warning labels and warning lights indicating the switching status. Barricades and other grounded parts of the installation must be connected to the *grounding system* of the laboratory in a reliable and visible manner. For this, a radial grounding arrangement of unsheathed *ground wires* in which a broken wire could be identified anywhere is established. The entries of the high-voltage room must be included in a *safety circuit*, whose opening leads to immediate deactivation of the high voltage source. Automatic *grounding switches* can further enhance safety.

Before entering the high voltage room, the high voltage source must be visibly switched off in two stages with the help of the *power circuit-breaker and the disconnector*. Then the installation parts on the high voltage side must be *manually grounded* with the help of an *earthing stick*. The earthin stick must subsequently be connected to the high voltage generator to make a *permanent and visible grounding connection* before starting work on the plant.

Instrument leads or control wires which lead into the high voltage room and which could displace the high voltage potential outwards must have a *grounded sheath* and are to be protected by *surge arresters*.

Capacitors and other **capacitances** can still carry charge, even after disconnecting the high voltage source, or can be recharged by *recov-*

ery voltages even after a temporary short-circuit. Especially with regard to **DC voltage generators,** capacitances form one of the largest *safety risks*. It is therefore recommended (but not sufficient) to provide a rapid discharge through discharge resistances or automatic grounding switches. Furthermore, capacitances must always be reliably and continuously *short-circuited*. In the case of a series connection of capacitors, this is applicable even to the individual *partial capacitances*. Establishing a grounding connection is not sufficient if a *direct short circuit* of all *partial capacitances* is not simultaneously guaranteed.

Note: Risks due to charged capacitors exist especially for *improper handling of electrical devices*, which include *high voltage direct current supplies*.

6.2.1 Generation of AC Voltages

6.2.1.1 Principles of Generation

Test voltage values are always specified as

peak values divided by $\sqrt{2}$

Figure 6.2.1-1: 500 kV/ 125 kVA test transformer with oil-filled tank and with porcelain bushing in the HV test laboratory of Hochschule Würzburg-Schweinfurt.

since peak values are decisive for breakdown [133]. In the case of sinusoidal voltages, division by $\sqrt{2}$ allows a *comparison with the r.m.s. values* of the operating voltage.

Different principles are provided for generation of high AC test voltages, Figures 6.2.1-1 and 6.2.1-2.

Single-phase test objects of *low capacitance* (e.g. insulators, bushings, grading capacitors, components of single-phased encased switchgear, instrument transformers, voltage dividers, surge arresters) are tested with **single-phase test transformers**; the supply is generally from the low voltage network at power frequency, Section 6.2.1.2, Figure 6.2.1-1 and Figure 6.2.1-2 (left). *Special designs* allow the testing of ground-free test objects or the generation of voltages balanced to ground. Very high test voltages can be attained by the *cascaded arrangement* of comparatively small, insulated test transformers, Section 6.2.1.3. Appreciable voltage rises sometimes occur in the case of capacitive loads and in no-load operation, Section 6.2.1.4.

For test objects with *high capacitances* (e.g. cables, large enclosed switchgear and capacitors with large capacitances), the common test transformers and test voltage sources are often too weak owing to high capacitive reactive power, and they are very heavy to transport or not even available. For **on-site tests,** high voltage generation by transportable **series resonance test systems** with high voltage reactor coil is possible, whereby either the frequency of the supply voltage or the inductance of the reactor coil (adjustable-gap inductor) must be tuned to resonance. The resonance should be in a range, which must still be considered as "close to operating frequency", Section 6.1.2.5, Figure 6.2.1-2 (center).

Note: Generally, the compensation of capacitive reactive power is also possible through *parallel compensation* (parallel resonance test systems). However, a high voltage *test transformer* is also necessary for this, along with the high voltage *compensation reactor*. The application of a series resonance system is thus generally the more economical solution.

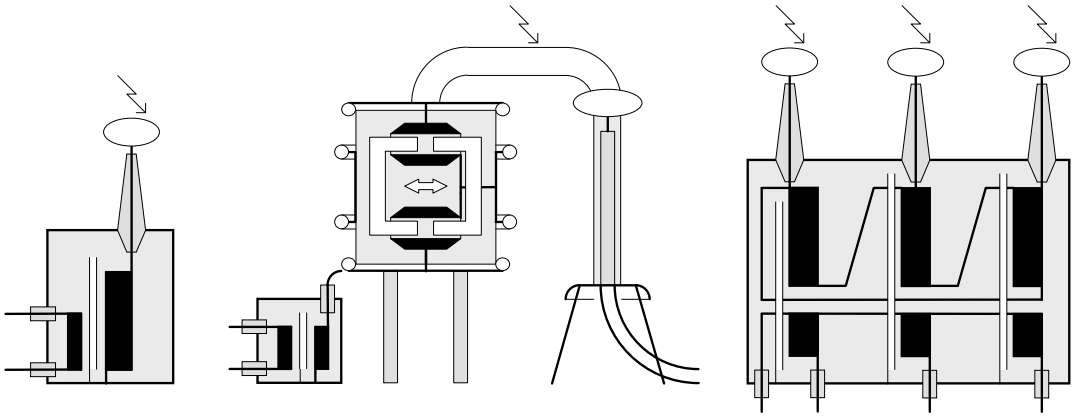

Single-phase test transformer for test objects of lower capacitance (generally for power frequency f = 50 or 60 Hz).

Single-phase series resonance test system for test objects of higher capacitance with excitation transformer (left), high voltage inductor (center) and cable with termination (right). The circuit is tuned to resonance via the frequency or the adjustable-gap inductance.

Three-phase testing of a power transformer with induced AC voltage in the high voltage winding through excitation of the low voltage winding with increased frequency (generally 100 or 120 Hz).

Figure 6.2.1-2: Generation of high AC test voltages with test transformers (left), series resonance systems (center) and through the AC voltage induced in the test object (right).

The reduction of capacitive reactive power can also be achieved by applying **voltages of very low frequency** (VLF, $f = 0.1$ Hz) [128], [129], [130]. The voltages are, for example, sinusoidal or they exhibit a square-wave voltage with a half-wave oscillation for charge reversal (the so-called cosine-square voltage), Section 6.2.1.6. The VLF test can be carried out on-site with *light, mobile systems*. They are therefore set up for *laid medium voltage cables* as an alternative to the DC voltage test that is no longer considered relevant.

Three-phase and single-phase *power transformers* cannot be tested at power frequency (50 or 60 Hz) because owing to the saturation of the iron core, the voltages cannot be increased significantly above the voltages occurring during operation. As per the law of induction, significantly higher induced test voltages

$$v_{ind} = \partial \Phi / \partial t \quad \text{and} \quad \underline{V}_{ind} = \omega \, \underline{\Phi} \qquad (6.2.1\text{-}1)$$

are only possible with **increased frequency,** since the magnetic flux Φ must be restricted owing to iron saturation. It is a standard practice to feed the transformer on the low-voltage side with doubled frequency, and the high voltage side insulation is then tested with the induced AC voltage, Figure 6.2.1-2 (right) [131]. Testing with the **induced AC voltage of increased frequency** can in principle be applied to all types of power transformers, test transformers and instrument transformers, Section 7.1.3.5.

6.2.1.2 Test Transformers

Test transformers generate high and (to the extent possible) distortion free test voltages at comparatively small powers. *Test transformers* and *power transformes* are very different, based on **design and construction**, Table. 6.2.1-1.

Test transformers are generally designed to be *single-phase*. They have a relatively large *transformation ratio*. Owing to the high voltages to be insulated, comparatively large insulation gaps, and therefore even large magnetic leakage fluxes or *large relative short-circuit voltages* v_{sc} occur. The iron-core is designed in such a way that the flux density remains in an approximately linear region of the magnetization characteristic.

Table 6.2.1-1: Characteristic features of power transformers and test transformers

Power transformers		***Test transformers***
Voltage transformation during transmission of (large) power	*Task*	Voltage transformation for generating higher test voltages
Generally, three-phase (Figure 6.2-1, right)	*Structure*	Generally single-phase (see Figure 6.2-1 left)
Large	*Nominal power*	Comparatively low
Lower, e.g. 123 kV/20 kV = 6.15 e.g. 20 kV/ 0.4 kV = 50	*Transmission ratio*	Larger, e.g. 500 kV/0.4 kV = 1250 e.g. 100 kV/0.23 kV = 434.8
Design for high durability under operating conditions with high thermal stress and ageing	*Insulation*	Design for withstanding high voltages with low thermal stress and slower ageing
Lesser, due to lower voltages to be insulated v_{sc} = 5%.....15%	*Stray inductance*	Comparatively high, owing to thicker insulation between primary voltage winding and secondary voltage winding v_{sc} = 15%.....25%
Maximum saturation degree of magnetization characteristic for weight reduction	*Iron core*	Low saturation degree of magnetization characteristic in linear region in order to achieve distortion-free and linear transformation
Permanent operation, mostly below the nominal apparent power	*Operation*	Short test intervals (overload is possible), partial permanent operation

Single-phase test transformers can be manufactured with different **insulation systems**. In Figure 6.2.1-3, the respective arrangements of the low-voltage winding (narrow) and high-voltage winding (broad) on the limb of the iron core are illustrated. In order to avoid unnecessary insulation gaps, the windings are interlaced in such a way that minimum possible potential difference is obtained between them and relative to the core.

For *oil-filled transformers*, the winding insulation consists of oil-impregnated paper and pressboard, Figures 6.2.1-3 a), b) and d). *Gas-impregnated windings or windings cast with resin* can be insulated with polymeric films, Figure 6.2.1-3 e) and c).

Note: In the case of windings cast with resin (*encapsulated-winding dry-type transformer*), a *completely cavity free insualtion* can hardly be attained, and thus they can generally only be employed free of partial discharges for voltages up to about 100 kV, and therefore are only suitable for the *medium voltage range*.

Conductive housings (tank construction) require high voltage bushings or partition insulators, Figure 6.2.1-3 a), b) and e), that can be absent for *insulating housings* (*insulating housing construction*), Figure 6.2.1-3 c) and d). However, insulating enclosures have poorer heat dissipation to the surroundings.

Gas-insulated switchgear (GIS) can be tested with directly *flange-mounted and encased transformers* [132]. The low weight of SF_6-impregnated transformers is advantageous for on-site tests, Figure 6.2.1-3 e). The *stray capacitance* of the high voltage electrode (across the winding) to the housing and core can be used along with a low-voltage measuring electrode for *voltage measurements* and *partial discharge measurements* [125].

If the *iron core is laid at ground potential*, then the entire high voltage must be insulated within the high voltage winding and against the core. These stesses can be halved if the high voltage winding is divided and the *core is laid at half-potential*, Figures 6.2.1-3 b) and c). For one-sided grounding of the high voltage winding, the core and housing are at half

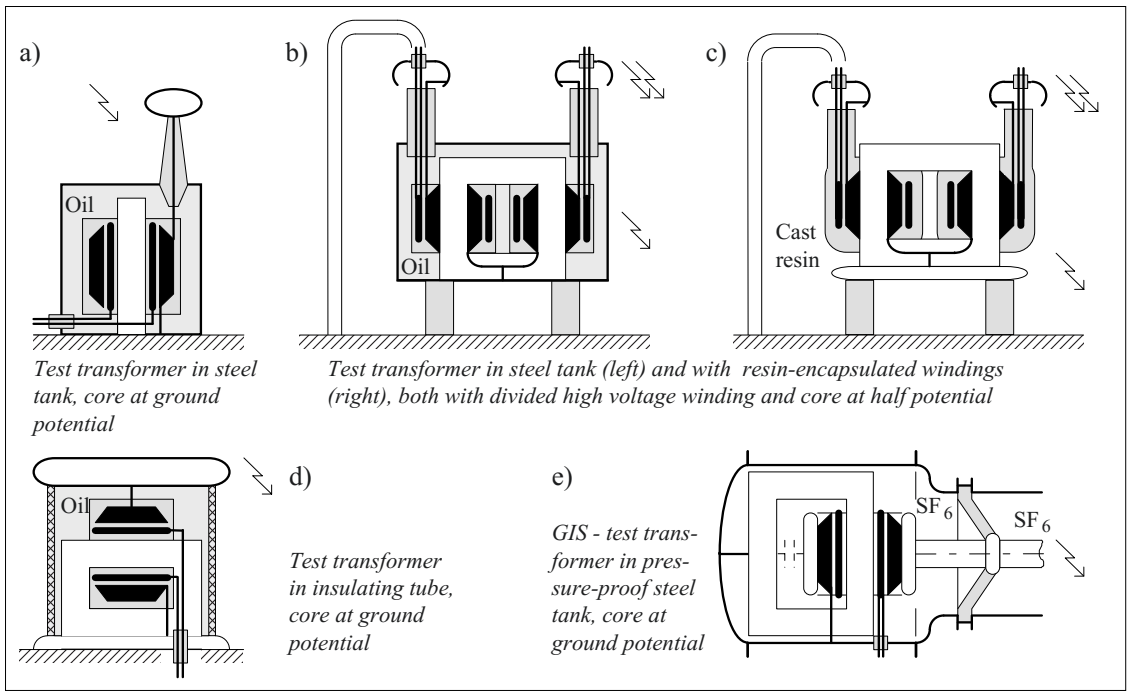

Figure 6.2.1-3: Connection and assembly of test transformers with oil insulation, cast resin insulation and compressed-gas insulation.

the potential of the high voltage and must be insulated against ground. *Connections for low voltage windings,* which are at the potential of the respective high voltage connections, are fed out through the bushings within the (hollow) high voltage winding termination. For one-sided grounding of the high voltage winding, see Figures 6.2.1-3 b) and c), this can be used for a low voltage side excitation of the transformer.

Note: The symmetrically constructed transformer even facilitates the generation of *a voltage balanced to ground* if the core is laid at ground potential. Thus, a low voltage winding at core potential is necessary for excitation. However, this is *not* illustrated in Figure 6.2.1-3.

6.2.1.3 Cascade Arrangement

Voltages of individual transformers are connected in series by the cascaded arrangement of test transformers, Figures 6.2.1-4a and -4b. Thus, highest AC test voltages of up to several MV can be generated with comparatively compact test transformers.

The whole transformers are insulated against ground according to their housing potential. High voltage windings (H) are connected in series. The radii of curvature of shields and electrodes must increase stage-by-stage owing to increasing voltage.

In the first stage, the low voltage excitation takes place with an *excitation winding* (E) lying inside the HV winding and being connected to the core potential. An *coupling winding* (C) lying outside the HV winding and being connected to high voltage potential supplies the current for the excitation winding in the second stage. The lines between coupling winding 1 and excitation winding 2 are led within the inner conductor of the bushing at high voltage potential. The excitation winding of the third stage is supplied with power from the coupling winding of the second stage.

The *relative short-circuit voltage* of the cascade rises sharply with an increase in the number of stages.

Higher thermal stress on the lower stages is also a disadvantage. Hence, the *number of*

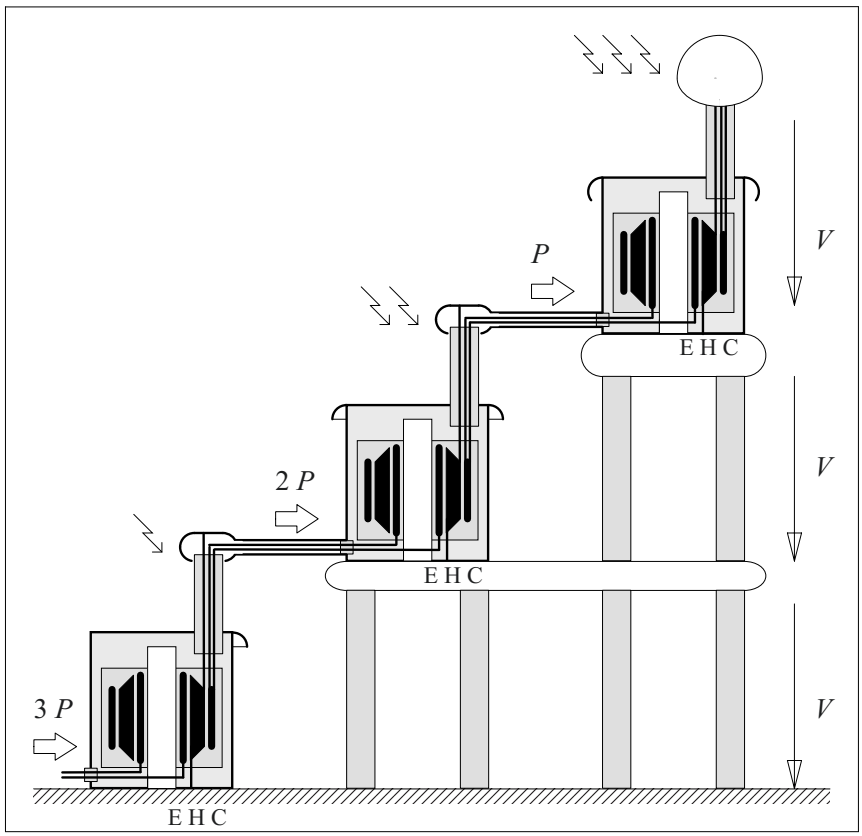

Figure 6.2.1-4a: Generation of very high AC test voltages in a three-stage cascade assembly.

E: Excitation windings
H: High voltage windings
C: Coupling windings

stages is restricted to three in practice for most of the cases.

Note: Cascade connections can even be set up from test transformers with two connections that are symmetrical to the core, Figures 6.2.1-3 b) and c). Both the low voltage windings that lie on the outer side of the HV winding are at the potential of the associated high voltage connection, and they can therefore be used as excitation winding and as coupling winding.

6.2.1.4 Capacitive Voltage Rise in Transformers

Test transformers are largely *capacitively loaded* by the capacitances of the insulation arrangements to be tested, by capacitive voltage dividers and by coupling capacitors for partial discharge measurements. Owing to winding capacitances, even in no-load operation, there exists a certain amount of capacitive load. Thereby, along with the relatively large *stray inductance* of test transformers, substantial *capacitive voltage rises* (*resonant overvoltages*) can result, Figure 6.2.1-5.

For a large capacitive load current I, the magnetization current through the main inductance, the core losses and thus the magnetizing impedance can be neglected. The capacitive voltage rise thus results from a simplified *transformer equivalent circuit diagram* which consists of the leakage impedance $\underline{Z}_L = R_W + jX_L$ only and which is related to the high voltage side. $\underline{Z}_L$ can be determined in a short-circuit test. R_W is the sum of the winding resistances converted with the voltage transformation ratio $a = V_{N2}/V_{N1}$:

$$R_W = R_{W1} \cdot a^2 + R_{W2} \qquad (6.2.1\text{-}2)$$

L_L and X_L respectively is the sum of the converted stray inductances and leakage reactances respectively:

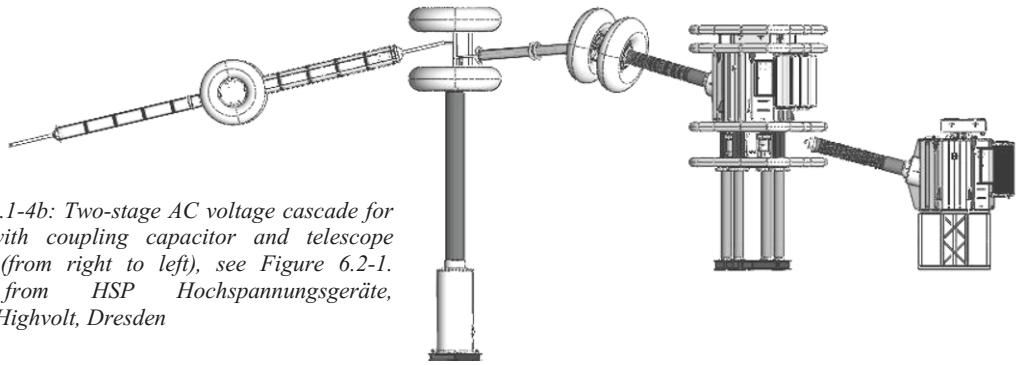

Figure 6.2.1-4b: Two-stage AC voltage cascade for 1200kV with coupling capacitor and telescope electrode (from right to left), see Figure 6.2-1. Figure from HSP Hochspannungsgeräte, Troisdorf/Highvolt, Dresden

$$L_L = L_{\sigma 1} \cdot a^2 + L_{\sigma 2} \qquad (6.2.1\text{-}3)$$

$$X_L = X_{\sigma 1} \cdot a^2 + X_{\sigma 2} \qquad (6.2.1\text{-}4)$$

Due to the capacitive load C_2, the complex resonance voltage ratio η is

$$V_2/\underline{V}_1' = (\mathrm{j}\omega C_2)^{-1}/[R_W + \mathrm{j}\omega L_L + (\mathrm{j}\omega C)^{-1}]$$

and the magnitude is (6.2.1-5)

$$\eta = V_2/V_1' = [(1-\omega^2 L_L C_2)^2 + (\omega R_W C_2)^2]^{-1/2}.$$

Owing to the capacitive voltage rise, the magnitude of the generated secondary voltage *cannot* generally be concluded from the magnitude of the preset primary voltage, i.e. an *independent measurement of secondary voltage* is always necessary.

Example: Test transformer with capacitive load

The following test transformer is considered:

$a = V_{2N}/V_{1N}$ = 100 kV/220 V = 454.5

$a = I_{1N}/I_{2N}$ = 22.7 A/50 mA

R_{W1} = 0.5 Ω, R_{W2} = 20.66 kΩ, v_{sc} = 14.4 %

1.) At first, the *elements of the transformer equivalent circuit diagram* related to the high voltage side must be determined:

With Eq. (6.2.1-2), R_W is = 124 kΩ. In the short-circuit test, the current I_{2N} = 50 mA is driven by the voltage $V'_{sc1} = v_{sc} \cdot 100$ kV = 14.4 kV. This corresponds to an impedance Z_L = 288 kΩ. From $Z_L^2 = R_W^2 + X_L^2$, the elements X_L = 260 kΩ and L_L = 827 H are determined.

2.) *Maximum possible load capacitances* for full high voltage V_2 = 100 kV shall be calculated for continuous operation ($I = I_N$) and transient overload ($I = 2 \cdot I_N$).

The capacitances are calculated from $V_{2max}/I_{2max} = 1/(\omega C_{max})$:

C_{max} = 1.6 nF for I = 50 mA (permanent operation)

and

C_{max} = 3.2 nF for I = 100 mA (transient overload).

3.) For the range of C = 0 to 3 nF, the *capacitive voltage rise* η and the *maximum permissible primary voltages* V_1 are specified.

With Eq. (6.2.1-5), the following values are obtained for different load capacitances:

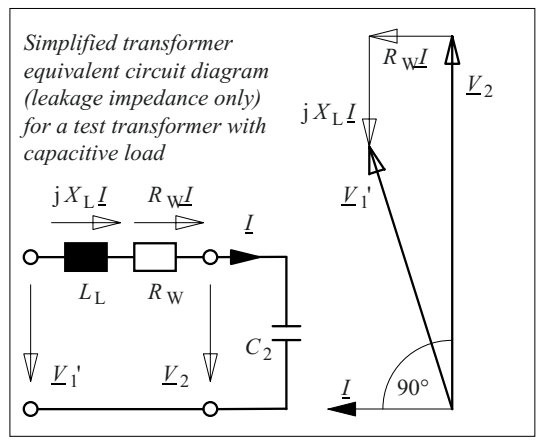

Figure 6.2.1-5: Voltage rise caused by capacitive load of a test transformer.

C/nF	0	0.5	1	1.5	2	2.5	3	3.5
η	1	1.04	1.09	1.14	1.19	1.25	1.31	1.37
V_2 /kV	100	100	100	100	100	100	100	100
V'_1/kV	100	96	92	88	84	80	76	73
V_1 /V	220	211	202	193	185	176	168	161

4) For a load capacitance $C = 6$ nF, the *maximum possible high voltage* and the related primary voltage shall be determined.

The voltage rise factor $\eta = 1.78$ for $C = 6$ nF. In continuous operation ($I = I_N$), the following is valid

$$V_2 = I_{2N}/(\omega C) \quad = 26.5 \text{ kV}$$

and

$$V_1 = v_2/(a \cdot \eta) \quad = 32.8 \text{ V}.$$

For transient overload ($I = 2 \cdot I_N$), the maximum values are twice as large:

$$V_2 = 56 \text{ kV and } V_1 = 65.6 \text{ V}$$

Note: Generation of high frequency high voltage with *iron-free* **Tesla transformer** is likewise based on a resonant overvoltage. A capacitance C_1 is discharged across a spark gap and across the low voltage winding in an oscillating manner. C_1, the stray capacitance C_2 at the high voltage side and the stray inductance of the transformer determine the resonance frequency. Each discharge event is followed by a *high-frequency oscillation package* in the range of about 10 to 100 kHz. The oscillation decays owing to the damping of the resonant circuit.

6.2.1.5 Series Resonance Test Systems

Series resonance test systems are especially used for single phase **on-site tests** on the test objects with high capacitance, such as for installed *cable runs*, Section 7.1.15, for on-site assembled gas-insulated *switchgear* and for gas-insulated *transmission lines* (GIL), Section 7.1.1.3. The *quality control of the installation and the assembly* respectively or the assessment of the insulation condition and the verification of *availability* are carried out by withstand voltage tests and partial discharge tests. Thus, the on-site testing concept follows the basic concepts of insulation coordination, i.e. the test stresses shall be **representative** of *the operating stresses* [121], [122], [123], [133], and [375]. However, the direct usage of test transformers for test objects with high capacitance is not possible owing to the power supply required.

Example: For a cable with a length of $l = 10$ km and with a capacitance of $C' = 250$ nF/km, at a test voltage of $V = 400$ kV (r.m.s. value) and $f = 50$ Hz, a *capacitive reactive testing power* of $S = (2\pi f)\,(C'l)\,V^2 = 126$ MVA is obtained. Such a power is not available at the medium voltage level and the low voltage level.

This problem can be technically and economically solved with a *series resonance test system*. In a series resonance circuit of a *reactor inductance* and a *test object capacitance*, a high test voltage results from a resonant overvoltage, Figure 6.2.1-2 (center) and -6. For tuning to resonance, either the **inductance** of the high voltage reactor (via an adjustable gap in the magnetic circuit) or the **frequency** of the supply voltage (via a frequency converter) is tuned, [125], [126], [127], [355].

The resonance circuit can be supplied with a low voltage V_E and a low power by an *excitation transformer*: in the *case of resonance*, the reactor inductance supplies the capacitive reactive power required by the test object capacitance, the voltage source only has to cover the very low *power loss* of the resonance circuit, which is produced in an equivalent series

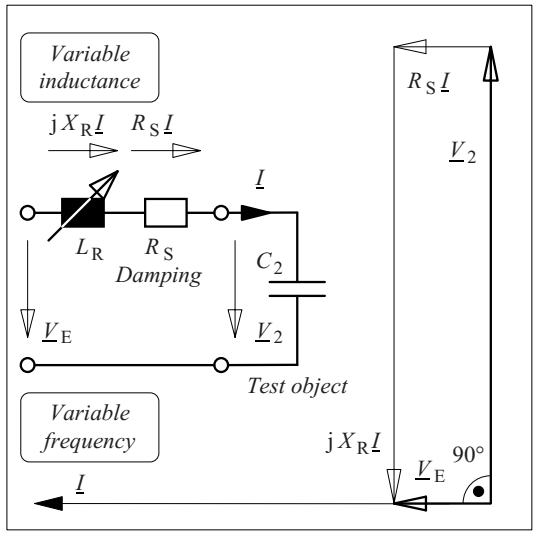

Figure 6.2.1-6: Generation of high AC voltages in series resonance with variable inductance (reactor) or variable frequency (30 to 300 Hz) for test objects with high capacitive reactive current.

resistance R_S, Figure 6.2.1-6:

$$P_S = R_S I^2 = V_E I \qquad (6.2.1\text{-}6)$$

The series resonance system can thus manage with a very low *power input*. However, the excitation transformer and the reactor coil must be designed for the *high capacitive reactive current (charging current) I*. Furthermore, the high voltage reactor is generally *lighter* than a comparable transformer. Moreover, it can be *modularly transported* and can be connected in series (or parallel) on-site, in order to attain the maximum possible test voltages (or currents). Figures 6.2.1-7 and -9 show the corresponding *cascading*.

In the case of resonance, the following is applicable:

$$\omega_0 = 2\pi f_0 = \frac{1}{\sqrt{L_R C_2}} \qquad (6.2.1\text{-}7)$$

According to Eq. (6.2.1-5) and (6.2.1-7), the *resonance ratio* V_2/V_E is

$$\eta = \frac{V_2}{V_E} = \frac{1}{\omega_0 C_2 R_S} \; . \qquad (6.2.1\text{-}8)$$

It corresponds by Eqs. (6.2.1-6) and (-8) to the *quality factor q of the resonance circuit* and to the ratio of the *capacitive reactive power* S_2 to the power loss of the resonance circuit respectively:

$$q = \frac{S_2}{P_S} = \frac{\frac{1}{\omega_0 C_2} \cdot I^2}{R_S \cdot I^2} = \frac{V_2}{V_E} = \eta \qquad (6.2.1\text{-}9)$$

The quality factor or the resonance ratio that can be attained are determined by *the losses of the test circuit*, which especially result from the winding resistances and from the iron losses of the *reactor*, because the test objects generally have very low losses. For reactors with *variable inductance*, the values are about q = 50, whilst for reactors with *fixed inductances*, q = 100 to 200 is specified [379].

A great advantage of resonance test systems is that in the event of a *breakdown* in the test object, the resonance circuit is detuned, the high voltage immediately disappears and the *short circuit current* remains very low since it is driven only by the weak excitation transformer and is also limited by the reactor.

a) Variable inductance

Adjustable reactors can be built in, for example, *insulating housing design*: the two-leg core is divided and comprises an oil gap that can be adjusted by an insulated spindle, Figure 6.2.1-2 (center). The winding is divided between the upper and lower legs; the core is at half potential and is externally shielded by ring-shaped electrodes. The reactors can be assembled in series in self-supporting manner because of their modular design, Figure 6.2.1-7. Thus, modular resonance test systems are possible for very high voltages [126], [127]. In the case of a constant test voltage frequency ω_0, the ratio of maximum to minimum test object capacitance is obtained in accordance with Eq. (6.2.1-7) from the adjustable ratio of inductances, which amounts to about 20:

$$C_{2max}/C_{2min} = L_{Rmin}/L_{Rmax} \qquad (6.2.1\text{-}10)$$

Note: A variable inductance can be implemented in the form of a *variable low voltage inductance* that can be looped into the high voltage circuit through a test transformer. However, it is a disadvantage that an additional transformer is required.

Note: Cable test illustrated in Figure 6.2.1-7 is conducted with a *cable test termintionl* in which the space between the uncovered bare cable insulation and the housing insulator is filled with slightly conductive *water for resistive potential grading*, Sections 5.4.5 and 7.1.1.5, Figure 5.4-8.

b) Variable frequency

An innovation in high voltage test techniques are series resonance circuits that are tuned via the *variation in frequency* with the help of **frequency converters** for *fixed inductance. Fixed inductances* are highly reliable and have low losses, so that a *very high quality factor* or a very advantageous ratio of *input power to*

testing power of approximately 1:100 to 1:200 is obtained.

By changing the **frequency**, there is a deviation to some extent from the power frequency of 50 or 60 Hz. However, today a larger range of frequencies from a few 10s of Hz to a few 100 Hz is considered as *"close to the operating frequency"* [355]. IEC 60060-3 provides a frequency range of 10 to 500 Hz [390], while IEC 62067 restricts the frequency range for tests on cables with a nominal voltage above 150 kV to f_{min} = 20 Hz to f_{max} = 300 Hz [356]. In the case of a fixed inductance L_R , the ratio of maximum to minimum test object capacitance, in accordance with Eq. (6.2.1-7), is obtained from the ratio of adjustable frequencies:

$$1/L_R = \omega_{min}{}^2 C_{2max} = \omega_{max}{}^2 C_{2min}$$

$$C_{2max}/\, C_{2min} = (f_{max}/\, f_{min})^2 \qquad (6.2.1\text{-}11)$$

That is, a frequency ratio of 300 Hz/ 20 Hz = 15 results in a *capacitance range* of $C_{2max}/\, C_{2min} = 15^2 = 225$ that can be *used* for tests. This range is adequate in many practical cases, but can be extended further by series and parallel connection of reactors.

Note: The **weight of a test system** plays a major role for the mobile application. For systems with *fixed inductance* and with *variable frequency*, particularly *low values* of approx. 1 kg/kVA with regard to the 50 Hz testing power result. The *optimization of the overall system* is the reason for this: the design of reactor core for a lower frequency (e.g. 30 instead of 50 Hz), indeed leads to an increased weight in iron, but it can also be compensated by a lower test reactive power. The fixed reactor has no movable parts and can therefore be made lighter and more compact than a variable reactor. Furthermore in a fixed reactor the magnetic circuit can be designed to be optimal and with lower leakage flux by subdividing into many sub-gaps. Ultimately, a regulating transformer can be dispensed with owing to the supply of power through a frequency converter.

Figure 6.2.1-8 shows the example of a *mobile test system* with a high voltage reactor in a *tank construction* [355]. With this, similarly to oil transformers with steel tanks, effective cooling and *permanent operation* at high power over a long period are possible.

A *filter circuit* against supply-side interferences, a coupling capacitor for **partial discharge measurements** and the test object are

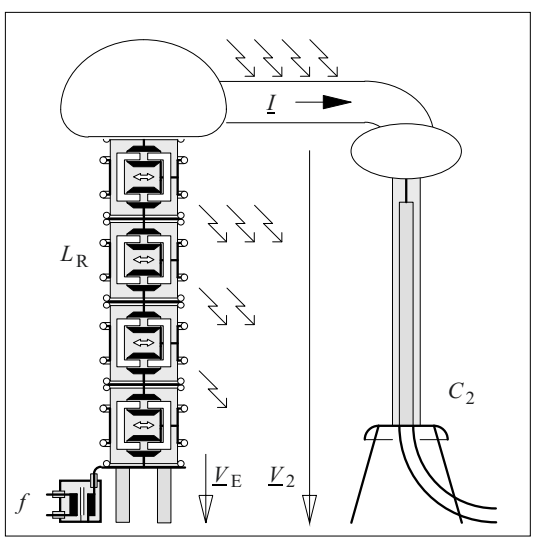

Figure 6.2.1-7: Generation of high AC voltages in a series resonance system with adjustable inductances or adjustable frequencies, high voltage reactors in series connection, schematic (left) and a 1700 kV - 3 A - 50 Hz series resonance system with reactors, compressed-gas capacitor and coupling capacitor, photo Haefely Test AG/ Hipotronics Inc. (right).

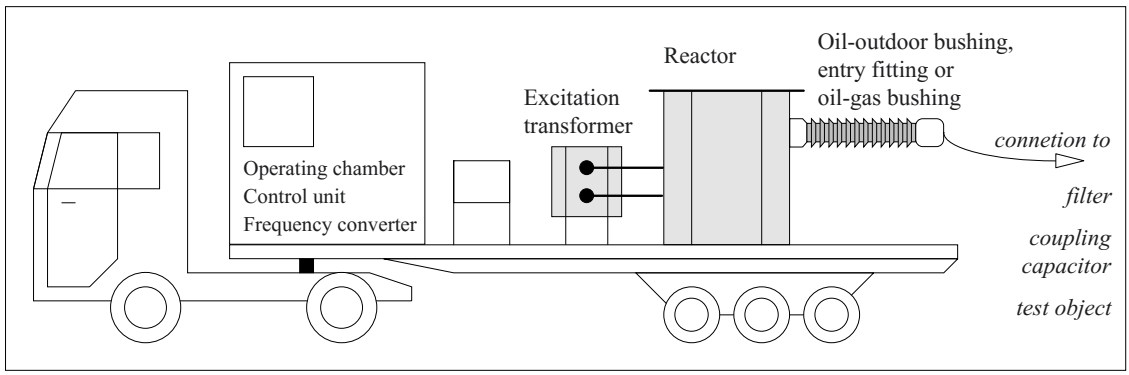

Figure 6.2.1-8: Mobile resonance test system with variable frequency for 90 A and 150 kV [355] (schematic).

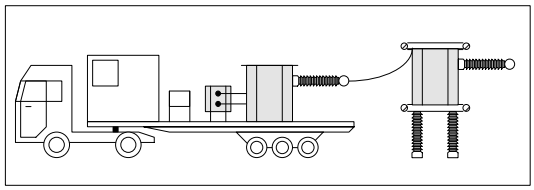

Figure 6.2.1-9: Mobile resonance test system with series connection of reactors [357] (schematic).

connected to the bushing, see Section 6.4.2. The advantage is that the series resonance test circuit already forms a filter. However, the circuit is excited by the frequency converter with rectangular voltages whose broad frequency spectrum cannot be completely filtered out. Since the four switching impulses of the source are known, they can be considered for the evaluation of a partial discharge measurement in the time domain. [379].

Instead of *oil-outdoor* **bushings**, even *oil-gas bushings* or *entry fittings* can be used, resulting in hermetically sealed on-site test systems.

For the extension of the range of test voltages, similar **reactors** can be positioned on post insulators and *connected in series* [357], Figure 6.2.1-9. For a cascading of reactors, however, the *insulating housing construction* is preferred, which allows the direct stacking of reactors. Moreover, the weight can be reduced by replacing the oil insulation by SF_6

Note: The many advantages of frequency-variable resonance test systems can be expected to lead to an increasing expansion of *on-site* use, and in special cases even for *stationary* use.

6.2.1.6 Requirements for Test Voltages in Laboratories and On-site

During on-site tests, even with the above mentioned test voltage sources, the *requirements* of IEC 60 060-1 for AC test voltages often *cannot be fulfilled*. Owing to this, in practice, considerable variations have been developed with respect to type of voltage, voltage waveform, frequency, tolerances and test procedures. The new standard IEC 60 060-3 shall, therefore formulate *(general) requirements* that *can be economically implemented on-site* [375], [390], Table 6.2.1-2 and Figure 6.2.1-10. Device-specific standards can thus comprise additional refinements or limitations. On-site tests on cables are described in Section 7.1.1.5 with Table 7.1.1-1.

A **test** in accordance with **operating conditions** should be conducted, as far as possible, *close to the operating frequency* (AC). For all the test stresses varying from the operating conditions, it must be asked whether the test provides *representative results*.

A strong dependence of the short-duration withstand voltage with *frequency* was shown for **VPE cable samples** [377], Figure 6.2.1-10. Therefore, for VLF tests and DC voltage tests, considerably higher withstand voltages must be expected. Owing to this, the magnitude and duration of the *test voltage stress* are *graded* according to the frequency, see Section

7.1.1.5, table 7.1.1-1. However, since the **frequency dependence** apparently corresponds to a change of breakdown mechanism, fixed *relation*s of test voltage values for significantly different frequencies unfortunately *cannot* be specified. Investigations on artificially damaged cable test objects made of cross-linked polyethylene (XLPE), however, have shown a high **selectivity** of breakdown voltage at f = 0.1 Hz for *mechanical damage* and for *"water trees"* [376]. Moreover, ample experience with VLF tests for medium voltage cables is available which enables a condition estimation of the aged cable.

The decision about the *type of test voltage* that must be applied is therefore greatly dependent on the query to be answered: a *proof of withstand voltage in accordance with operation conditions* requires a frequency close to the operating frequency. *Diagnostic statements* are also possible in other frequency ranges.

Different types of test voltages are discussed in the following sections:

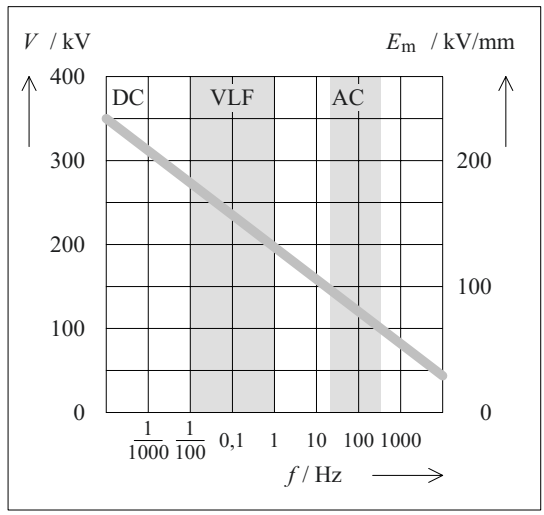

Figure 6.2.1-10: Withstand voltages determined for XLPE cable samples as a function of test voltage frequency [377].

a) DC voltage tests

In the past, DC voltage tests with high test levels (for cables 4 V_0) were common for oil-filled cables and paper-insulated mass-impreg-

Table 6.2.1-2: Requirements for laboratory tests and on-site tests for AC voltage equipments [375], [390].

Note: **Test voltage levels** see Table 7.1.1-5.		**Tests in laboratory** *(test field)*	**On-site tests**
Note: **Impulse voltage tests** see Section 6.2.3.		IEC 60 060-1	IEC 60 060-3 *) device-specific variations
a) **DC voltage DC** *(no longer common for AC voltage operating equipment)*	*Frequency f*	**DC voltage**	**DC voltage**
	Ripple-factor	< 3 %	< 3 %
	Tolerance for test voltage	± 1 % (< 1 min), ± 3 % (> 1 min)	± 3 % (< 1 min), ± 5 % (> 1 min)
	Measurement uncertainty	± 3 %	± 5 %
b) **Very low frequency voltage VLF**	*Frequency f*	Not common	**0.01 – 1 Hz**
	Voltage wave form		Sine to rectangle, test voltage is peak value (sometimes r.m.s. value*)
	Tolerance for test voltage		± 5 %
	Measurement uncertainty		± 5 %
c) **Damped AC voltage DAC** (Oscillating voltage)	*Frequency f*		**20 – 1000 Hz**
	Damping		< 40 % for each period
	Tolerance for test voltage		± 5 %
	Measurement uncertainty		± 5 %
d) **AC voltage** close to **operating frequency** (power frequency)	*Frequency f*	**45 – 65 Hz**	**10 – 500 Hz** (cable **20 – 300 Hz***)
	Sinusoidal $\hat{V} / V_{\text{r.m.s.}}$	$\sqrt{2}$ ± 5 %	$\sqrt{2}$ ± 5 % (or $\sqrt{2}$ ± 15 % and $0.98 < \hat{V}_{\text{pos}} / \hat{V}_{\text{neg}} < 1.02$)
	Tolerance for test voltage	± 1 % (< 1 min), ± 3 % (> 1 min)	± 3 % (< 1 min), ± 5 % (> 1 min)
	Measurement uncertainty	± 3 %	± 5 %

nated cables, as well as for electrical machines, since even large capacitances could be tested with transportable equipment at low input power and meaningful conclusions about the insulation condition could be made, Table 6.2.1-2 a), Figure 6.2.1-11 a).

However, it was shown for XLPE cables that the DC voltage test is *not sensitive* even at high test levels for many of the very serious errors. This is because eroding partial discharges can occur with a high repetition rate for operational AC voltages but not for DC voltages. On the other hand, DC voltages could be hazardous for the test object owing to *space charge built up*, Section 7.1.1.5. These differences can also be explained by the fact that the *field distributions* in the insulation are determined by permittivities for operational AC voltages and by conductivities and transition processes for DC voltages. Consequently, completely different stresses can occur during testing and during operation, see Section 2.4.4.

Note: Tests with DC voltages for *HVDC applications* are described separately, Section 6.2.2 and 7.2.

b) Very Low frequency (VLF) voltages

For voltages with very low frequencies, space charge build up should be avoided by the *periodic changes in polarity*, Table 6.2.1-2 b), Figure 6.2.1-11 b). In addition, eventual defects can be identified by *partial discharges* with low repetition rates. However, it is not always clear whether the *capacitive field distributions* for the power frequency also occur during testing in the very low frequency range between 0.01 Hz and 1 Hz. This depends on the selected frequency, on the conductivities of the materials and on the geometrical structure of the insulation, Section 2.1.4.3.

Note: In addition to the voltage test, it is recommended to evaluate the global ageing condition of cable insulations by comparative or voltage dependent **dissipation** (or loss) **factor measurements** at 0.1 Hz [378]. The significance of dissipation factor measurements is debatable, and hence, so-called *isothermal relaxation current analysis* (IRC-analysis) is recommended as an alternative [223], [224], Section 6.4.7.4.

VLF withstand voltage testing for the very low frequency f = **0.1 Hz** is developed for on-site testing the laid medium voltage cables, which generally takes place at three times the nominal voltage (phase to ground voltage) 3 V_0 with a test duration of 1 h, Section 7.1.1.5 with Table. 7.1.1-1. All voltage waveforms between sine wave and rectangular wave are allowed and the test voltage is the *peak value* [375], [390], Table 6.2.1-2b). In practice, a *sinusoidal AC voltage* and the so-called *cosine-rectangular voltage* are mainly used, Figure 6.2.1-11 b).

Note: At 0.1 Hz, the capacitive charging power (reactive power) is smaller by a factor of 500 than at 50 Hz, so that the test equipment is very compact and can be transported in very compact **cable measuring coaches**. These generally include the equipment for *voltage tests* with 0.1 Hz and with DC voltages as well as extensive measurement equipment for the acoustic and electrical *runtime location of cable defects*, for *cable diagnosis* as well as for *dielectric measurements* (dissipation factor measurements and partial discharge measurements).

Note: The **sinusoidal 0.1 Hz test voltage** can**,** for example, be generated by slowly increasing and decreasing of voltages from two different sources with positive and negative polarity. The **cosine-rectangular voltage** is generated by charging the cable capacitance from a DC voltage source. After about 5 s, a reactor is connected in parallel so that an oscillation process is initiated, this approximately corresponds in duration to the power frequency. At the negative voltage peak, a switch disconnects the oscillating circuit and the cable retains the charge state with opposite polarity. The loss-related voltage reduction is balanced by a DC voltage source. After another 5 s, the next oscillating charge reversal of the cable is performed.

c) Damped AC voltage

Damped AC voltages can be generated on-site by *charging* the test object capacitance from a DC voltage source with subsequent *discharge* via an inductance, Table 6.2.1-2 c), Figure 6.2.1-11 c). A *decaying, damped oscillation*, a so-called **"oscillating voltage"** occurs and its frequency, likewise, can be set in the range of f = 20 to 1000 Hz "close to the operating frequency". This results in *field distributions* of the test object that correspond to the fields at operating frequency; however, the stress is not

continuous and has only a transient, *pulsed character*. Ignition delay for inception of partial discharge, or the change in partial discharge intensities with the stress duration, therefore cannot be observed. In addition, the prior DC charging of the test object does not correspond to the operating stress. *Test voltage* is the peak value V_p and it is identical with the charging voltage.

d) AC voltage

With the help of series resonance testing systems, it is possible to test even test objects with large capacitance with *continuous* AC voltages close to the **operating frequency**, Section 6.2.1-5. For this, it is assumed that *capacitive field distributions* present in operation are also present within the permitted frequency range of 10 to 500 Hz (for cables 20 to 300 Hz, see Section 7.1.1.5, Table 7.1.1-1) and that no changes occur in the *breakdown processes* [377], Figure 6.2.1-10. Therefore, test systems with corresponding variable frequency can be employed [375], [390], Table 6.2.1-2 d), Figure 6.2.1-11 d). The *test voltage* is the peak value divided by $\sqrt{2}$.

Continuous AC voltage tests close to the operating frequency are most comparable with the *test stresses in the laboratory* and with the *operating stresses*.

6.2.2 Generation of DC Voltages

High DC voltages serve as *test voltages* for HVDC components and cables as well as *supply voltages* for various technical applications, such as video terminals, X-ray equipment, electron microscopes, capacitor chargers, dust precipitators (electrostatic precipitators), paint-spraying devices and surface coating devices.

High DC voltages are obtained from AC voltages by *rectification* (Section 6.2.2.1), mostly in connection with a *voltage multiplier circuit* (Section 6.2.2.2). In the case of lower voltages,

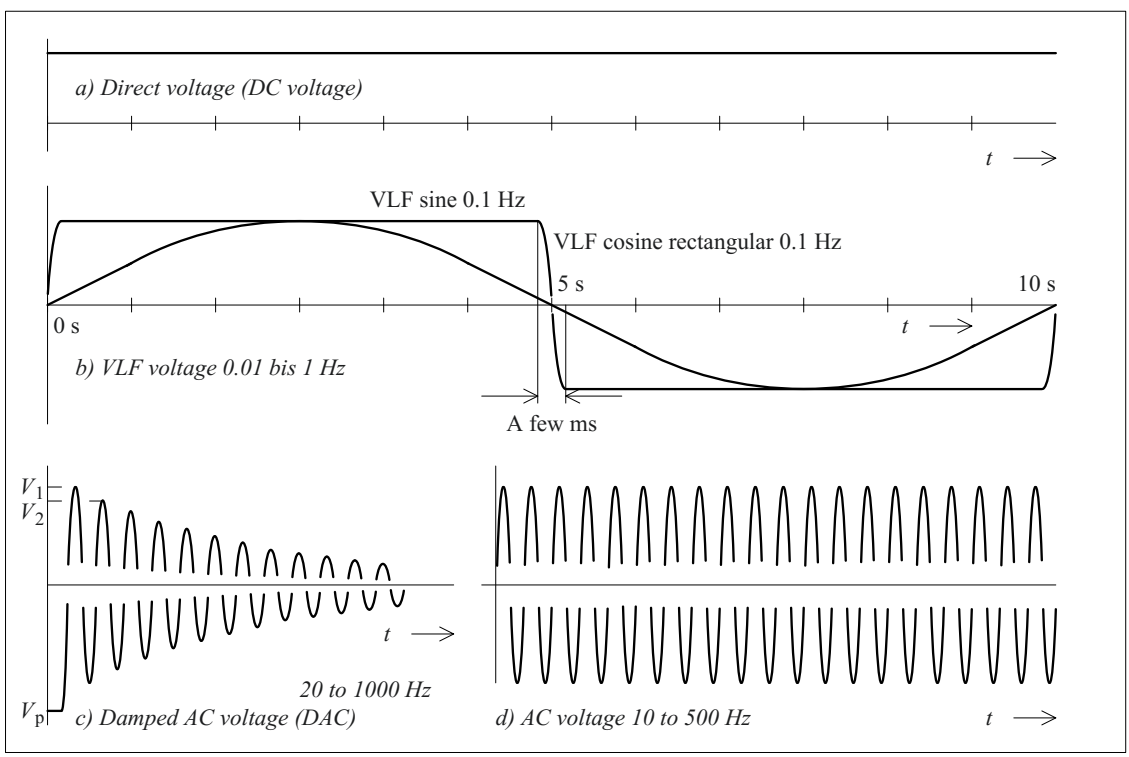

Figure 6.2.1-11: Test voltage waveshapes for on-site tests.

supply is often via a *switched-mode power supply* (Section 6.2.2.3). Using *electrostatic generators* is restricted to special applications at very high voltages (Section 6.2.2.4).

Direct voltages are often superimposed by periodic functions. Therefore, IEC 60060-1 [133] defines the *arithmetic mean value* as the DC test voltage.

$$V_{=} = \overline{v(t)} \qquad (6.2.2\text{-}1)$$

The ripple $\delta v = 0.5(v_{max} - v_{min})$ is described by the *ripple factor* ("ripple factor")

$$\delta v/V_{=} = 0.5(v_{max} - v_{min})/V_{=} . \qquad (6.2.2\text{-}2)$$

It should not be more than 3% for DC voltage tests.

6.2.2.1 High-voltage Rectifier

High-voltage rectifiers always consist of a *series connection of several semiconductor diodes* whose reverse voltage is restricted to a few kV. This is a problem for *potential distribution in the reverse blocking state,* since an unequal voltage distribution would lead to overstress and destruction of individual diodes. Voltage distribution determined largely by undefined junction capacitances and blocking-state currents can be made more uniform by *parallel grading capacitors* and *grading resistors* for the grading of time-varying voltages and steady-state DC voltages respectively, Figure 6.2.2-1. In forward direction, i.e. in the coducting state, the diodes are protected by *series resistors*.

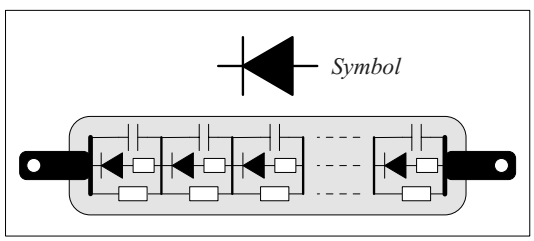

Figure 6.2.2-1: Capacitively and resitively graded high-voltage rectifier.

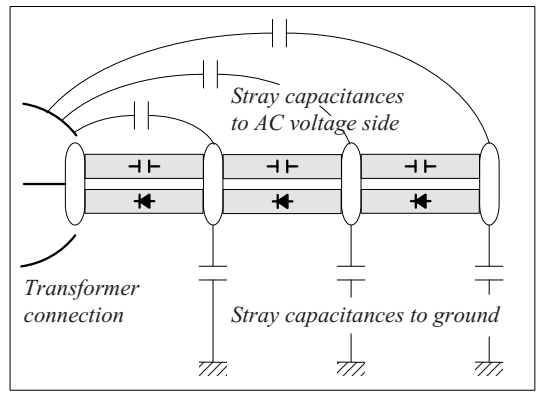

Figure 6.2.2-2: Linearization of potential distribution in the reverse blocking state by grading capacitors parallel to the high-voltage rectifiers.

For *spatially extended rectifiers* that are used for very high voltages of many 100 kV, a non-linear voltage distribution along the series connection of the individual rectifiers occurs, owing to *undefined stray capacitances* to the groundside and to the AC voltage side, Figure 6.2.2-2. Voltage distribution can be lineraized by parallel *grading capacitors*. For this, sufficiently large longitudinal currents must be present, relative to which the transverse currents over the stray capacitances are negligible.

6.2.2.2 Rectifier Circuits

AC voltage sources available in high voltage laboratories are often supplemented with a capacitively graded *rectifier* and a *smoothing capacitor* to form a **half-wave rectifier circuit**, Figure 6.2.2-2 and -3 (top): After connecting the AC voltage, the capacitor is charged to the peak value $\hat{v}$ during the positive half wave. The charging current must be restricted to the permissible value by a series resistor. Full charging within a quarter period presumes a small charging time constant $RC \ll T/4$. After the voltage peak, the rectifier blocks and a connected load R_L is supplied during a period $t \leq T$ from the charged smoothing capacitor. By exponentially discharging with the time constant $R_L C$, the voltage v_C drops until the transformer voltage v_T is

increased to an extent that recharging occurs. The *voltage stress of the rectifier* in the *blocking state* results from $v_R = v_T - v_C$ and can amount to a maximum of $v_{Rmax} = 2 \cdot \hat{v}$.

For a **symmetrical voltage doubling circuit**, only *half as large a rectifier* and *half as large an AC voltage* v_T are necessary for generating a comparable DC voltage v_C, Figure 6.2.2-3 (bottom). After connecting the AC voltage, the lower partial capacitance C_1 is charged to $v_{C1} = +\hat{v}$ during the negative half-wave via rectifier 1.

Thereafter, the right transformer connection is present at half DC voltage potential $v_{C1} = +\hat{v}$. In the positive half-wave, the partial capacitance C_2 is also charged to $v_{C2} = +\hat{v}$ via rectifier 2. The total voltage is $v_C = v_{C1} + v_{C2} = +2\hat{v}$.

A series resistor limits the current during charging. Under load, the smoothing capacitances are discharged between the recharging phases. C_1 is recharged in the negative half-wave and C_2 in the positive half-wave.

Note: A symmetrical doubling circuit that was connected asymmetrically to the ground potential on the DC side was described. Thus, there is a need for a special *symmetrical transformer* whose high voltage winding is at half of the DC voltage potential and therefore may *not* be connected to ground potential. The insulation must be rated for the mixed voltage $v_{C1} + v_T$.

For independent DC voltage sources with their own individual AC voltage supply, the **Greinacher multiplier** (Greinacher cascade) has been accepted and this is characterized by two important advantages, Figure 6.2.2-4: The first one is that the power can be supplied with a *transformer winding grounded on one side*. Another is that very high voltages can be generated by a *series connection of many rectifier stages* with proportionally low partial voltages. Moreover, the charging current can be limited by dimensioning the capacitors.

The Greinacher-cascade consists of an *booster column* with booster capacitors C_B, a *rectifier*

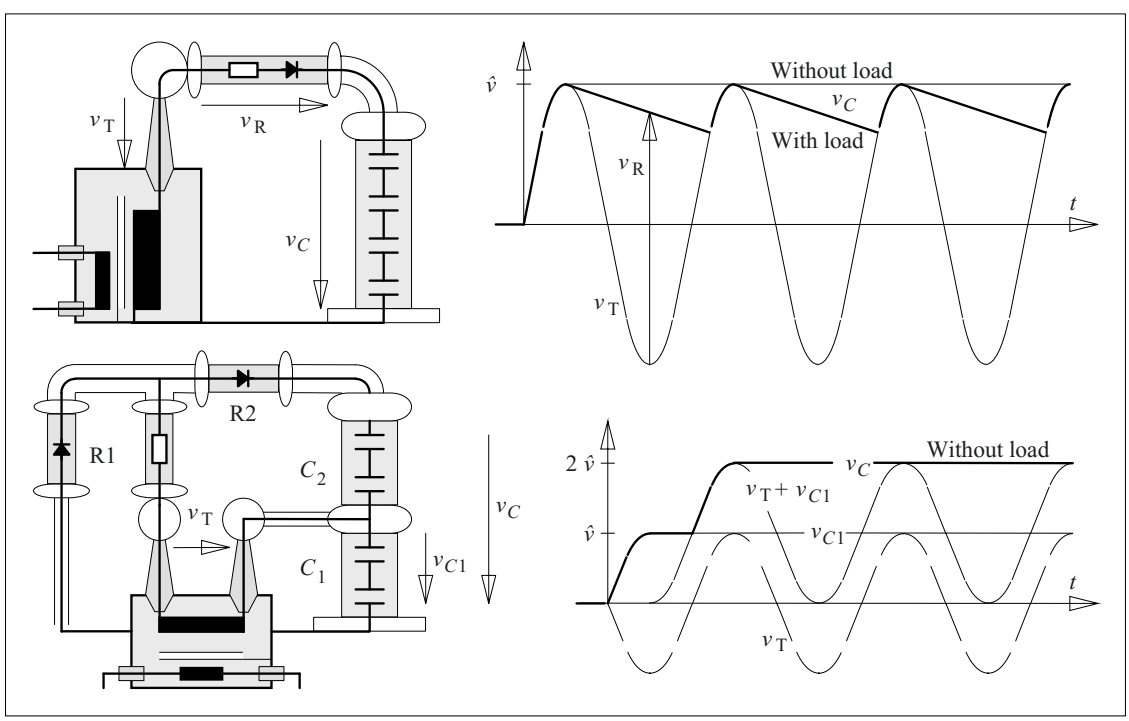

Figure 6.2.2-3: Half-wave rectifier circuit (top) and symmetrical voltage doubling circuit (bottom).

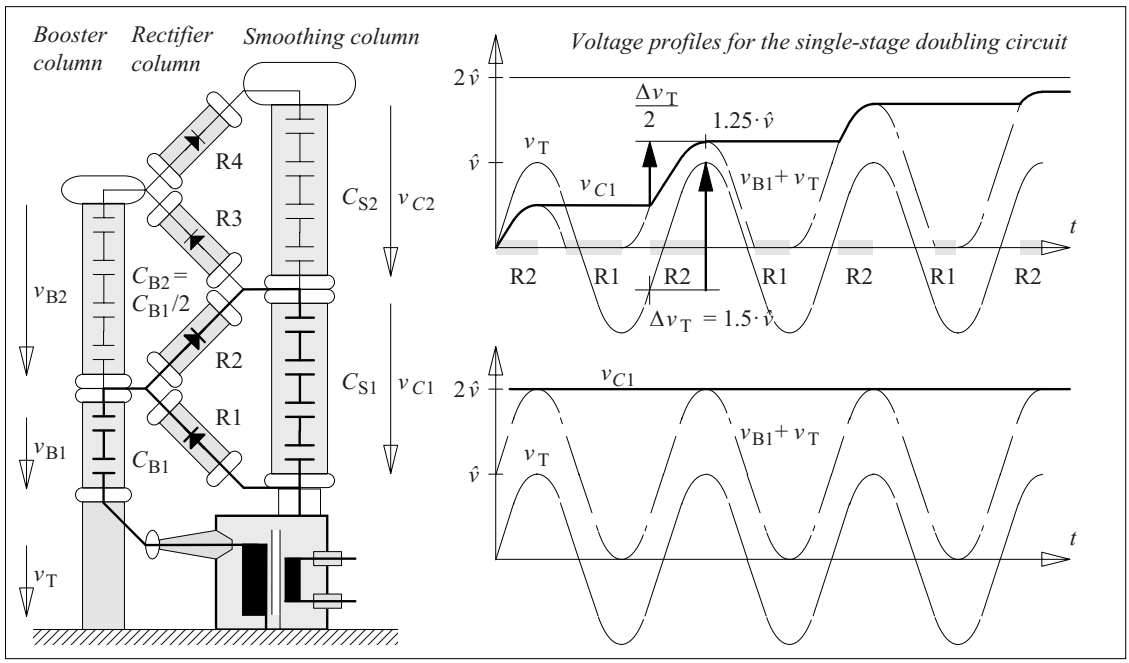

Figure 6.2.2-4:

Principle of Greinacher cascade as two-stage doubling circuit (top left).

Voltage profiles for a single-stage doubling circuit (top right) after connecting the AC voltage and in the stationary unloaded condition respectively (below). For multi-stage multiplier circuits, charging processes are slower due to re-charging processes between the smoothing column and the booster column.

1500 kV UHVDC-cascade for a HVDC test laboratory (right), figure HSP Hochspannungsgeräte, Troisdorf / Highvolt, Dresden.

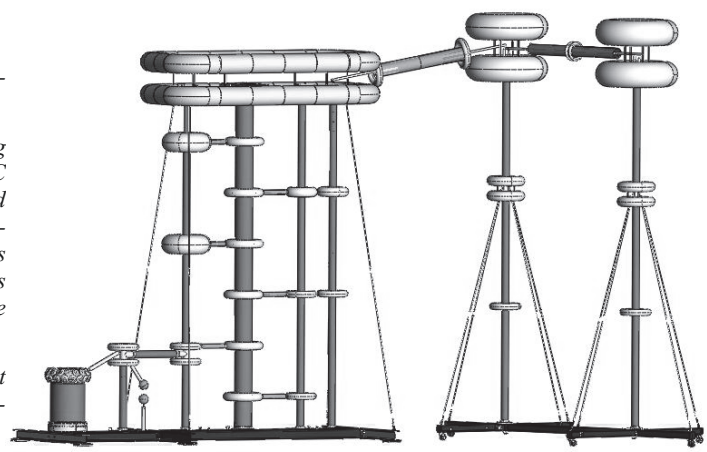

column, a *smoothing column* with smoothing capacitors C_S and often even a *divider column* with a resistive voltage divider that is not illustrated in the figure.

The voltage profiles are illustrated in Figure 6.2.2-4 for a single stage *doubling circuit*. That is, the associated circuit comprises only the *circuit part* drawn in bold in Figure 6.2.2-4 (left). In the stationary, unloaded condition, the booster capacitor C_{B1} is charged via R_1 to $v_{B1} = +\hat{v}$. The oscillating total voltage $v_{S1} + v_T$ is rectified by R2 and charges the smoothing capacitor C_{S1} to $v_{C1} = 2 \cdot \hat{v}$.

The *charging procedure* takes place in *steps*, the voltage v_{C1}, for a single-stage doubling circuit, *asymptotically* approaches the end value $v_{C1} = 2 \cdot \hat{v}$, Figure 6.2.2-4 (top right).

After *connecting the transformer*, R2 is conducting in the positive half-wave and v_{C1} (bold curve line) follows the transformer voltage v_T in accordance with the *capacitive divider ratio* of C_{B1} and C_{S1}. As long as R2 is conducting, the voltage v_{C1} is always equal to the total

voltage $v_T + v_{B1}$. The profiles shown in Figure 6.2.2-4 are applicable *for equal capacitances* $C_{B1} = C_{S1}$ and $v_{C1} = v_T/2$ as long as R2 is conducting.

R2 blocks at the *positive voltage peak*. The capacitor voltages remain the same at the attained values $v_{C1} = \hat{v}/2$ and $v_{B1} = -\hat{v}/2$. The voltage $v_T + v_{B1}$ (dotted curve line) again decreases with v_T. At $v_T + v_{B1} = 0$, R1 is conducting and C_{B1} is subsequently recharged to v_T. As long as R1 is conducting, the total voltage $v_T + v_{B1}$ is always equal to zero.

At the *negative voltage peak*, $v_{B1} = +\hat{v}$ is attained and R1 closes. Thereafter, $v_T + v_{S1}$ increases following the profile of v_T. As soon as the instantaneous value of the capacitor voltage v_{C1} is attained, R2 is conducting again and C_{S1} is *charged again*. Thus, the *residual voltage rise* for the transformer voltage $\Delta v_T = 1.5 \cdot \hat{v}$ only leads to a voltage step by $\Delta v_{C1} = \Delta v_T/2 = 0.75 \cdot \hat{v}$ at C_{S1} owing to capacitive voltage division over C_{B1} and C_{S1}.

At the *positive voltage peak*, R2 blocks and the capacitor voltages remain the same at the attained values $v_{C1} = 1.25 \cdot \hat{v}$ and $v_{B1} = +0.25 \cdot \hat{v}$. *Analogous continuation* of the described processes leads to the illustrated voltage profiles, whereby the voltage steps Δv_T and $\Delta v_{C1} = \Delta v_T/2$ become progressively smaller from period to period.

Theoretically, the voltage can be increased as high as desired by *connecting many doubling stages in series (cascading)*. For example, the booster capacitor $C_{B2} = C_{B1}/2$ of the *second doubling stage* is charged up to $2 \cdot \hat{v}$ in the negative AC voltage half-wave from the charged smoothing capacitor C_{S1} of the first stage via R1 and R3. In the positive half-wave the transformer voltage v_T thus "shifts" the voltage of the booster column up to $v_T + v_{B1} + v_{B2} = \hat{v} + \hat{v} + 2 \cdot \hat{v} = 4 \cdot \hat{v}$ (at the positive peak). This allows the voltage of the second smoothing capacitor to also increase up to $v_{S2} = 2 \cdot \hat{v}$. In the unloaded steady state, the following is generally applicable for n doubling stages:

$$V_{=} = \bar{v}_S = 2 \cdot n \cdot \hat{v} \qquad (6.2.2\text{-}3)$$

Owing to the recharging processes between the booster column and the smoothing column, the asymptomatic charging of the Greinacher cascade to the end value takes ever-increasing times *with increasing numbers of stages n*. Since a permanent discharge of the smoothing column is caused by the *load current*, an increase in the number of stages does not always lead to an increase in the *attainable DC voltage* (output voltage mean value in accordance with Eq. (6.2.2-1)). Ripple increases significantly in accordance with Eq. (6.2.2-2). The analysis shows that the stationary DC voltage decreases linearly with the load current I [16]:

$$V_{=} = \bar{v}_S = 2 \cdot n \cdot \bar{v} - \frac{I \cdot f(n)}{f \cdot C} \qquad (6.2.2\text{-}4)$$

Larger load currents require a small *number of stages n*, large *capacitance values C* or an increased *frequency f*.

DC voltage sources with **greater load capacity** up to the MV range and up to the 100 mA range can be implemented with Greinacher cascades in which several *booster columns* operate on a single smoothing column. For this, *transformers balanced to ground* (two booster columns) or *three-phase transformers* (three booster columns) are considered for AC voltage sources [22]. Furthermore, the individual stages of a rectifier cascade can each be supplied by a *transformer cascade* (transformatory support).

6.2.2.3 Switched-mode Power Supplies

The extensive use of high DC voltages as *supply voltages in devices* (for example, for lasers, capacitor charging devices, ozone producers, electrostatic precipitators, x-ray devices, spray paint equipment, coating devices, copiers) and for mobile *test equipment* (e.g. cable testing vehicles) has led to the development of switched-mode power supplies up to several 10s of kV. They are considerably *lighter and more compact* than comparable 50 Hz power supply units because, owing to high clock frequencies in the 10 kHz range, a comparatively light HF transformer with ferrite core can be used: in accordance with the law of induction $v_{ind} = -\partial\Phi/\partial t$, low magnetic fluxes are essentially adequate for transformation for high frequency flux changes.

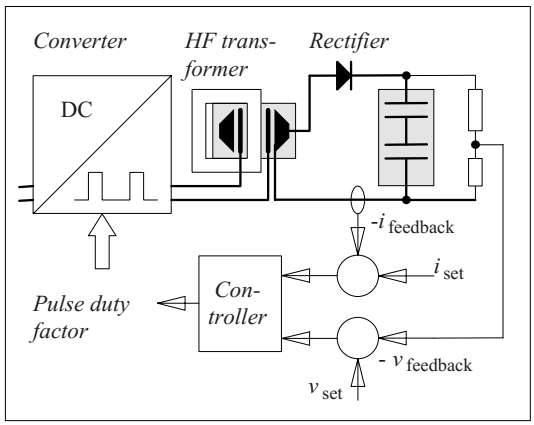

Figure 6.2.2-5: Capacitor charging device with constant-current charging (schematic).

An *electronic power converter*, e.g. a DC step-down converter, generates periodic rectangular impulses with the help of switched power semiconductors. These impulses can be transformed with a high-frequency-compatible *ferrite core transformer*. After *rectification and smoothing*, the output DC voltage results. The high clock frequency leads to very short discharge periods between the recharge phases. This allows a higher current load capacity or smaller smoothing capacitors. Switched-mode power supplies can cause strong power system perturbations owing to non-sinusoidal currents and hence appropriate filters must be provided.

With switched-mode power supplies, pulse-width-modulated *capacitor charging devices* with *constant-current charging* can also be implemented, Figure 6.2.2-5. For this, the controller develops the command variable (reference variable) in the form of the pulse duty factor T_{on}/T from the difference between setpoint (target) value and (actual) feedback value of the charge current. On attaining the target voltage, the changeover to floating operation takes place.

Through constant-current charging, significantly higher *efficiencies and lower charging times* are possible than for conventional *RC* charging with a maximum efficiency of $\eta = 50$ %. This is very positive for battery-operated devices or for limited power input.

Another advantage of switched-mode power supplies is the easy adaptability to *different supply voltages*. Switched-mode power supplies are, therefore, especially suitable for mobile systems with on-board power supply operation or battery operation.

6.2.2.4 Electrostatic Generators

Electrostatic generators generate high DC voltages practically without any *ripple*. Moreover, very *high voltages* can be attained with relatively little technical complexity. However, generally only low *load currents* in the µA to mA range are possible. For nuclear physics accelerators, compressed gas insulated devices up to 25 MV have been built [16].

In the past 300 years, electrostatic generators, at first based on frictional electricity, have contributed significantly to the physical understanding of electricity. However, electromagnetic generators have replaced them for large-scale generation of electrical energy owing to the comparatively low energy density of the electric field.

The principle of electrostatic generators is based on the *separation of charge carriers* by *friction*, by *electric influence* in electric fields or by *corona discharges* in non-uniform fields, Figure 6.2.2-6. Charge separation by friction is caused by breaking an intimate interconnection of two charge-carrying interfaces. For this, at least one of the two materials must be a good electrical insulator. Charge

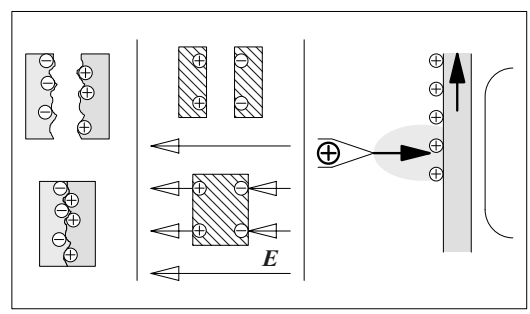

Figure 6.2.2-6: Charge separation through friction (left), through electrostatic induction (centre) and through a corona electrode (right).

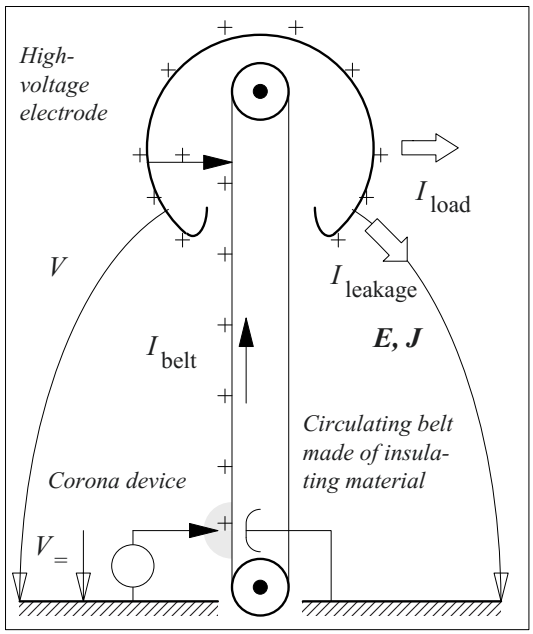

Figure 6.2.2-7: Van de Graaff generator or belt generator

separation by electric influence (i.e. electrostatic induction) is possible when two conductors are separated within the electric field and transversely to the direction of the field.

For generating higher voltages, the separated charges are fed to the *collector electrodes against the forces of the electric field*. Insulating discs, belts or drums are used for this purpose.

Note: The principle of generating higher voltages can be explained on a *plate capacitor* with constant plate charges $+Q$ and $-Q$: The distance of the plates is increased by means of mechanical work. The voltage increases with decreasing capacitance according to $V = Q/C$ proportionally to the plate distance. The applied mechanical work is stored as electric field energy.

The **belt generator (Van de Graaff generator)** has been extensively used, and it is *theoretically suitable for the generation of any desired high DC voltages*, Figure 6.2.2-7. With a *corona device*, charge carriers are sprayed on the surface of a *circulating belt of insulating material* and transported on the band against the force of the electric field. In the field-free internal space of a hollow high-voltage electrode, the charges are passed over a metallic

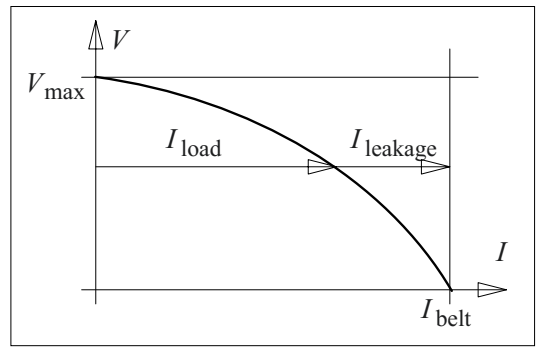

Figure 6.2.2-8: Load characteristic of a van de Graaff generator (belt generator).

contact to the high-voltage electrode. The transported charges are accumulated on the outer side of the electrode, whereby the voltage increases in accordance with

$$V = Q/C\,. \tag{6.2.2-5}$$

Charges and voltages can increase until a steady-state condition is reached, i.e. equilibrium *between the leakage current plus load current* and the charge transport of the band:

$$I_{leakage} + I_{load} = I_{belt} \tag{6.2.2-6}$$

An unrestricted voltage rise is practically *not* possible, since a disproportionate rise of the leakage current occurs at the latest on exceeding the *corona inception voltage*. Under load, the voltage falls down, Figure 6.2.2-8. The charge transport of the belt is restricted by the *surface charge density* σ, the *belt velocity* u and the *width* of the belt b:

$$I_{belt} = \sigma \cdot u \cdot b \tag{6.2.2-7}$$

The surface charge density is restricted by the *breakdown field strength of the surrounding gas.* For a thin belt with a uniform field on both sides, the following is applicable if the edge fields are ignored:

$$\sigma_{max} < 2 \cdot D_{max} = 2 \cdot \varepsilon_0 \cdot E_{max} \tag{6.2.2-8}$$

The belt generator must therefore be understood as a constant-current source with the source current given by Eq. (6.2.2-7). An increase in current can be attained with broader

belts, higher band velocity and higher electric strength (i.e. through compressed-gas insulation).

The magnitude of the attainable voltage is determined by the magnitude of the insulation resistance, the corona inception voltage and the magnitude of the belt current.

Van de Graaff generators with large insulation distances, high quality support insulators and compressed-gas insulation can be designed for maximum voltages up to 25 MV. Devices for large currents of multiple mA (for lower voltages in the MV range) are designed as **drum generators** with higher peripheral speed, larger drum width and multiple corona units and receiver units distributed over the circumference.

Note: The formation of a charged **thundercloud** (cumulonimbus) can be compared with the charge accumulation in a Van de Graaff generator. The charge transport thus takes place by upwinds, see Section 3.2.7.3.

6.2.3 Generation of Impulse Voltages

Impulse voltage tests simulate overvoltages in electrical power systems such as three-phase networks. The classic differentiation into *"external overvoltages"* (lightning impulse overvoltages) that are caused by atmospheric discharges and "*internal overvoltages"* (switching impulse overvoltages) that occur owing to switching processes in the network must be supplemented by rapidly varying transient effects *("fast transients")* occurring along with flashovers and switching processes.

6.2.3.1 Impulse Voltage Waveforms

In order to achieve international comparability, the multitude of overvoltage phenomena is reduced to standardized *lightning impulse voltages and switching impulse voltages* for test purposes [133], [134]. For these test voltages, parameters that describe the *voltage rise*, *peak value* and the *decay in the wave tail* within specific tolerances are specified, Figures 6.2.3-1a and 6.2.3-1b and Table 6.2.3-1. An exact specification of the profiles is not obtained, since in practice, superimposed interferences and oscillations cannot be avoided. This is especially so for very high voltages, spatially extended impulse circuits and non-capacitive test objects.

Note: Other transient test parameters are *chopped-wave lightning impulse voltages, impulse currents* for testing switches and arresters, "synthetic" test stresses of impulse currents and impulse voltages for switching tests as well as *extremely rapidly varying impulses* in the ns range.

For tests in a laboratory or **test facility**, *aperiodi*c voltage profiles are specified, Table 6.2.3-1 (left). In the case of **on-site tests**, the idealized voltage waveforms often cannot be adhered to. Therefore, even strongly *oscillating* impulse voltages are used that are defined in IEC 60060-3 by their *envelope curves* with time parameters that are considerably widened, [375], [390], Figure 6.2.3-2, Table 6.2.3-1 (right).

Note: Allowing oscillating voltages has the advantage that higher peak values can be attained than would be possible for non-periodic discharge of the impulse generator, see Eq. (6.2.3-1).

a) Lightning impulse voltages

Based on real lightning current-time characteristics (see Section 3.2.7.2 with Figure 3.2-44) or the over-voltages caused by them, **lightning impulse voltages** are defined by the *peak value* $\hat{V}$, the *front time* T_1 or T_f and the *time to half-value (on wave tail)* T_2 or T_h which is also called *tail time* T_t. In the case of **chopped lightning impulse voltages**, which are intended to simulate the action of very rapid voltage changes, the *chopping time* T_c is used as an additional parameter, Figure 6.2.3-1a.

Strong distortions are frequently superimposed during the rise of impulse voltages. Real waveshapes, therefore, can often only be inter-

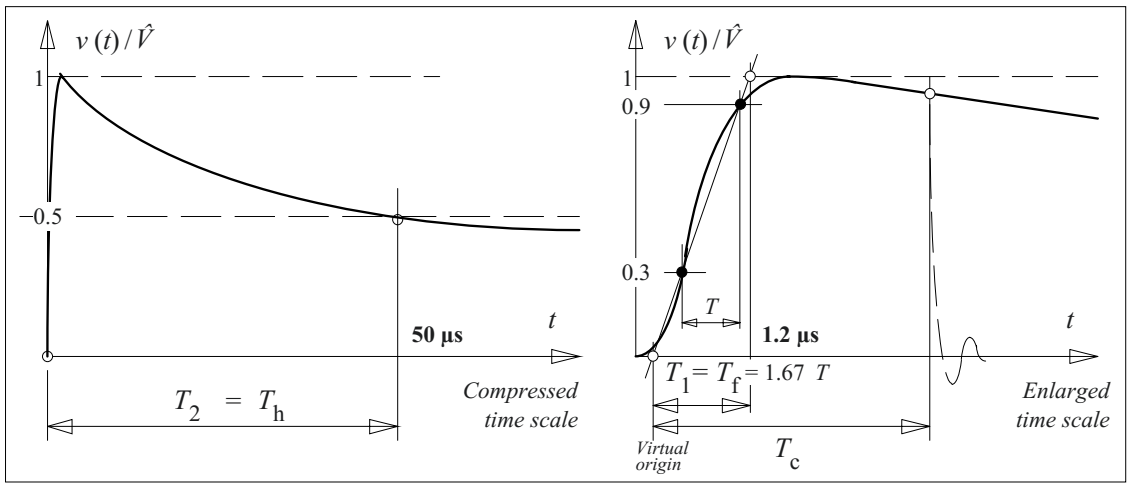

Figure 6.2.3-1a: Definition of characteristics of an aperiodic lightning impulse voltage (LI) 1,2/50 µs.

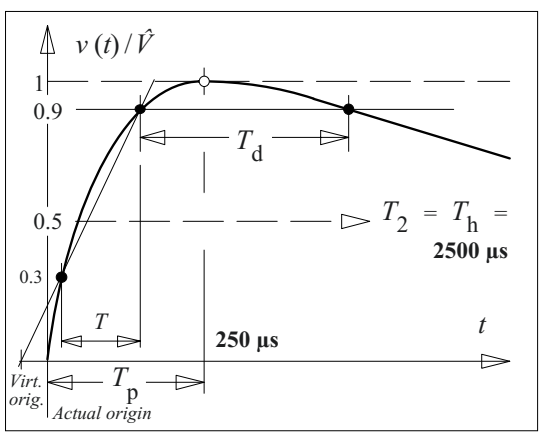

Figure 6.2.3-1b: Definition of characteristics of an aperiodic switching impulse voltage (SI) 250/2500 µs.

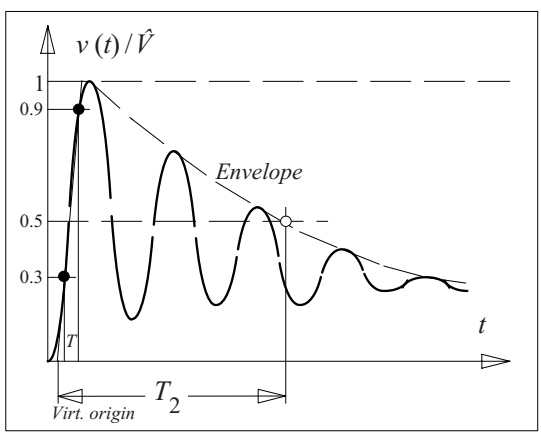

Figure 6.2.3-2: Oscillating lightning or switching impulse voltage for on-site tests (OLI or OSI).

preted inaccurately with the common definition of a *rise time* from 10 to 90 %. Determining the **front time** T_1 or T_f from 0 to 100 % on a substitute line that is drawn through the 30 % and 90 % points of the waveshape curve is more practical, Figure 6.2.3-1a. The *virtual origin (zero reference point)* for determining the time to half-value on wave tail and the chopping time are also defined using the substitute line. The time T between 30% and 90% values is related to the front time by a simple geometrical equation, Figure 6.2.3-1a (right):

$$T_1 = T_f = 1.67 \cdot T \qquad (6.2.3\text{-}1)$$

For the **standardized lightning impulse voltage** "1.2/ 50", a *front time* of 1.2 µs (permissible deviation ± 30 %) and a *time to half-value* of 50 µs (permissible tolerance ± 20 %) are specified. *Chopping times* are generally in the range of 2 to 5 µs. These and other characteristic values are presented in Table 6.2.3-1 against the less restrictive parameters for **on-site tests** with oscillating impulse voltages [390].

Note: Often, even for tests with *standardized aperiodic lightning impulse voltage* in the laboratory, **oscillations** are superimposed to the impulse voltage waveshape in the front area and in the area of voltage maximum. While determining the peak value, the amplitude of the overshoot must not be more than 5%.

Superimposed oscillations are especially important when testing *transformers*. The evaluation of the impulse voltage curve is therefore explained in detail in

Section 6.2.3.4 with Figure 6.2.3-9: The current unsteady evaluation procedure is replaced by a steady, frequency dependent evaluation method using a *frequency-dependent weighting* of the superimposed *oscillation* by means of a filter function , cf. IEC 60060-1 [133], [498].

b) Switching impulse voltages

Switching impulse voltages are characterized by the *time to crest* T_{cr} or *time to peak* T_p and by the *time to half-value (on wave tail)* $T_2 = T_h$. or *tail time* T_t respectively.

Note: If the test object causes a back-swing, then instead of the time to half-value on wave tail, the *crest duration* T_d, during which the voltage exceeds 90 % of the peak value, can be specified along with the *time to zero crossing* T_0.

For the **standardized switching impulse voltage** "250/2500", a *time to crest* of 250 µs (permissible deviation ± 20 %) and a *time to half-value (tail time)* of 2500 µs (permissible deviation ± 60 %) are specified. These and other characteristic values are presented in Table 6.2.3-1 against the less restrictive parameters for **on-site tests** with oscillating impulse voltages [390].

Note: The large *tolerances* of the time parameters mentioned are necessary in practical test operation, since the connected test objects are elements of the respective impulse circuits and they can greatly influence the impulse voltage waveform.

The d*efinition* of the **time to crest** value T_{cr} or time to peak T_p between the *actual zero refer-*

Table 6.2.3-1: Requirements for laboratory tests and on-site tests with impulse voltages [375], [390].

Note: Tests for AC voltages see Section 6.2.1.6	**Tests in laboratory** *(test facility)*	**On-site tests**	
	IEC 60 060-1 see Figure 6.2.3-1a and -1b	IEC 60 060-3 See Figure 6.2.3-2	
a) **Lightning impulse voltage**	**Aperiodic lightning impulse voltage** LI (Lightning impulse)	**Oscillating lightning impulse voltage** OLI (Oscillating LI)	
Front time	**1.2 µs** ±30 % or 0.84 to 1.56 µs	**0.8 to 20 µs**	Time parameter from envelope curve
Time to half-value on wave tail, tail time	**50 µs** ±20 % or 40 to 60 µs	**40 to 100 µs**	
Measurement uncertainty of time parameters	± 10 %	± 10 %	
Tolerance of peak value	± 3 %	± 5 %	Peak value of oscillation
Measurement uncertainty of peak value	± 3 %	± 5 %	
Superimposed oscillations	± 5 % (averaging depending on freq.)	allowed, 15 to 400 kHz	
b) **Switching impulse voltage**	**Aperiodic switching impulse voltage** SI (Switching impulse)	**Oscillating switching impulse voltage** OSI (Oscillating SI)	
Time to crest (time to peak)	**250 µs** ± 20 % or 200 to 300 µs	**20 to 400 µs**	Time parameter from envelope curve
Time to half-value on wave tail, tail time	**2500 µs** ± 60 % or 1 to 4 ms	**1 to 4 ms**	
Measurement uncertainty of time parameters	± 10 %	± 10 %	
Tolerance of peak value	± 3 %	± 5 %	Peak value of oscillation
Measurement uncertainty of peak value	± 3 %	± 5 %	
Superimposed oscillations		allowed, 1 to 15 kHz	

ence point of the voltage curve and the moment at which the *peak value* is attained includes some *uncertainty* in determining both these times. In practice, this leads to difficulties, especially for automatic determination by transient recorders. It is therefore proposed that the *approved method* of determining the *time parameters for lightning impulse voltages* should be adopted: the rise would then be characterized by the time T between the 30 % and 90 % values. To allow a comparison with the previously common parameters, a **conversion** between the *time parameter T and the time to crest* T_{cr} or T_p with the help of factors is currently under discussion, for example,

$$T_p \overset{!}{=} 2.4 \cdot T \,. \qquad (6.2.3\text{-}2)$$

Moreover, it is recommended to exactly define the time parameter with the help of a *virtual origin*. Although IEC 60060-1 (general test conditions) [133] is not yet "harmonized" in this regard, an appropriate modification is already taken into consideration in the new IEC 60060-3 (on-site tests) for oscillating switching impulse voltages [375], [390].

6.2.3.2 Single-stage Impulse Voltage Generators

Standardized lightning impulse voltages and switching impulse voltages are generally generated in **capacitive impulse circuits** by charging a *load capacitance* C_L from an energy storage capacitance C_D (*discharge capacitance* or *impulse capacitance*), Figure 6.2.3-3. Here the total *load capacitance* includes the capacitance of the test object, the capacitance of the impulse voltage divider and possibly an additional load capacitance.

Following the ignition of the switching spark gap G1, the load capacitance C_L is charged via the *damping resistance* R_F ("*front resistance*", which determines the *front time*) from the discharge capacitance C_D (that is charged to V_0). Here, an *exponential voltage rise* occurs and its time constant τ_1 is determined largely by R_F and the series connection of capacitances C_L and C_D, Figure 6.2.3-3 with Eq. (6.2.3-3b). Simultaneously, a slower *exponential discharge* of the capacitances C_L and C_D occurs via the *discharging resistance* R_T ("*tail resis-*

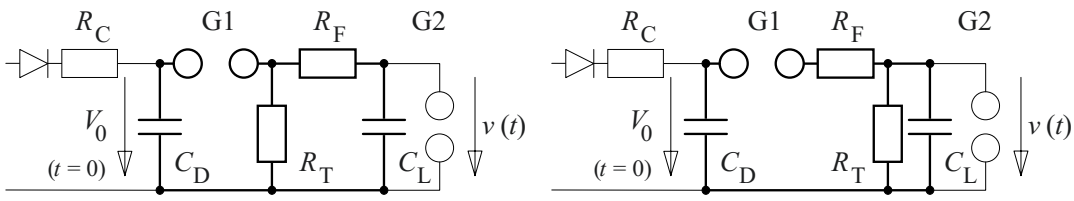

Basic circuit 1 ***Basic circuit 2***

$$\eta = \frac{\hat{V}}{V_0} = \frac{C_D}{C_D + C_L} \qquad (6.2.3\text{-}3a)$$ *Voltage efficiency*

$$\eta = \frac{\hat{V}}{V_0} = \frac{R_T}{R_T + R_F}\,\frac{C_D}{C_D + C_L}$$

$$\tau_1 = R_F \frac{C_D C_L}{C_D + C_L} \qquad (6.2.3\text{-}3b)$$ *Front time costant*

$$\tau_1 = \frac{R_T R_F}{R_T + R_F}\,\frac{C_D C_L}{C_D + C_L}$$

$$\tau_2 = R_T (C_D + C_L) \qquad (6.2.3\text{-}3c)$$ *Wave tail time constant*

$$\tau_2 = (R_T + R_F)(C_D + C_L)$$

Figure 6.2.3-3: Basic single-stage circuits for the generation of double exponential impulse voltages in capacitive impulse circuits with approximation equations for the characteristic values of the impulse voltage profile.

tance", which determines the *time to half-value on wave tail* or *tail time* resp.) with the time constant τ_2, Figure 6.2.3-3 with Eq. (6.2.3-3c). C_L and C_D are thus also connected in parallel by the spark gap G1. The *peak value* of the resultant impulse voltage $v(t)$ does *not* reach the value of the charging voltage V_0, since after ignition of the spark gap, the charge stored in C_D is distributed to C_D and C_L. The *voltage efficiency* $\eta = \hat{V}/V_0$ is therefore less than one, Eq. (6.2.3-3a). Solving the *differential equation* describing the network results in a *double exponential voltage-time characteristic*, Figure 6.2.3-4:

$$v(t) = V_0 \cdot \eta \cdot \frac{\tau_2}{\tau_2 - \tau_1}\left(e^{-\frac{t}{\tau_2}} - e^{-\frac{t}{\tau_1}}\right) \qquad (6.2.3\text{-}4)$$

The approximation equations (6.2.3-3a, b, c) for time constants and voltage efficiency are valid under the assumption $R_T C_D \approx \tau_2 >> \tau_1 \approx R_F C_L$.

The parameters *front time* T_1 and *time to half-value* T_2, which are defined for **lightning impulse voltages,** are proportional to the time constants τ_1 and τ_2:

$$T_1 = \quad T_f = \quad K_1 \cdot \tau_1 \qquad (6.2.3\text{-}5)$$

$$T_2 = \quad T_h = \quad K_2 \cdot \tau_2 \qquad (6.2.3\text{-}6)$$

Constants K_1 and K_2 are dependent on the impulse voltage wave form, Table 6.2.3-2.

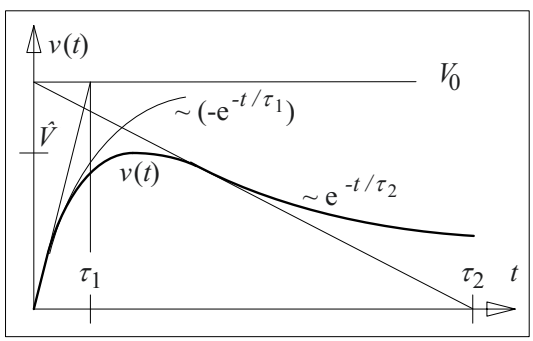

Figure 6.2.3-4: Double exponential impulse voltage.

Table 6.2.3-2: Constants for the determination of front time and time to half-value on wave tail.

	Impulse voltage wave form			
	1.2/5	**1.2/50**	1.2/200	250/2500
K_1	1.49	**2.96**	3.15	2.41
K_2	1.44	**0.73**	0.70	0.87

Lightning impulse voltage impulses can be generated with the standardized parameters by appropriate dimensioning of the circuit elements. Equations that are only slightly different are applicable for the two *basic circuits*, which differ in the position of the discharge resistance, Figure 6.2.3-3 with Eq. (6.2.3-3a,b,c).

The maximum amount of charging voltage V_0 is restricted by the sparkover voltage of the switching spark gap G1. Generally, the electrode distance is set so wide that the gap does not break down spontaneously. Thus, it is purposefully ignited by a *trigger impulse* that generates an ignition spark at a *trigger electrode* and thereby triggers the main discharge, Figure 6.2.3-5. The *trigger generator* must be at the potential of an electrode or an additional coupling capacitor must be used.

Note: Below the breakdown voltage of a spark gap, a limited voltage range exists in which the field strengths

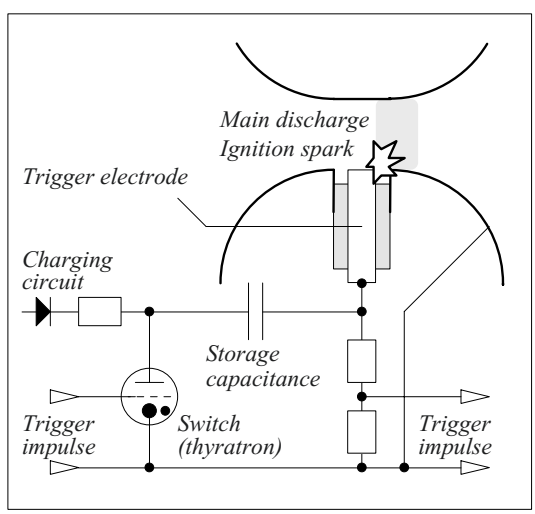

Figure 6.2.3-5: Triggering of the main discharge in a spark gap by an ignition impulse.

are still adequate for triggering by an ignition impulse [108]. It is best to determine the *triggering range* for a given arrangement empirically. The voltage at the spark gap should be chosen at the center of the triggering range to maintain the minimum possible probabilities of a *spontaneous breakdown* on the one hand and of an *ignition failure* on the other hand.

Note: Instead of triggering by an ignition spark, it is also possible to shift the potential of an *intermediate electrode* to such an extent that the main discharge is triggered [108].

Chopped impulse voltages are generated by a *chopping spark gap* G2. The chopping time T_c is adjusted either by the electrode distance or is also determined by *triggering*.

Even the parameters of **switching impulse voltages** result from the time constants τ_1 and τ_2. For *time to crest* (*time to peak*) and *time to half-value* (*tail time*), the following is approximately applicable,

$$T_{cr} = \frac{\tau_1 \tau_2}{\tau_2 - \tau_1} \ln \frac{\tau_2}{\tau_1} \qquad (6.2.3\text{-}7)$$

and

$$T_2 = \tau_2 \cdot \ln \frac{2}{\eta} \qquad (6.2.3\text{-}8)$$

under the assumption $T_2 = T_h > 10 \cdot T_{cr}$ [135].

Example: Dimensioning of an impulse circuit

A discharge capacitor C_D = 10 nF (V_0 = 140 kV) and a capacitive voltage divider with a high-voltage capacitance C_V = 200 pF are provided for an impulse circuit setup. The impulse circuit elements shall be dimensioned according to basic circuit 1 in such a way that a *lightning impulse voltage* 1.2/50 is generated at a test object capacitance C_T = 800 pF.

The *time constants* τ_1 = 405 ns and τ_2 = 68.5 µs result from T_1 = 1.2 µs and T_2 = 50 µs with Eq. (6.2.3-5) and -6 as well as Table 6.2.3-2.

The total load capacitance is $C_L = C_V + C_T$ = 1 nF. Thus the *discharging resistance (tail resistance)* R_T is obtained from Eq. (6.2.3-3c) as $R_T = \tau_2 / (C_D + C_L)$ = 6.2 k Ω. The *damping resistance (front resistance)* is $R_F = \tau_1 (1/C_D + 1/C_L)$ = 450 Ω according to Eq. (6.2.3-3b).

According to Eq. (6.2.3-3a), the *voltage efficiency* is $\eta = C_D / (C_D + C_L)$ = 91 %. Therefore, at V_0 = 140 kV, an *impulse voltage peak value* $\hat{V} = \eta \cdot V_0$ = 127 kV is obtained. A higher voltage efficiency $\eta \approx 1$ is obviously obtained only under the condition

$$C_D >> C_L . \qquad (6.2.3\text{-}9)$$

The energy stored capacitively in C_D is described as so-called *"impulse energy"*, and it amounts to about W = 100 J for V_0 = 140 kV. The impulse energy is largely transformed into ohmic heat losses in the elements R_F and R_T, and to a smaller extent also into losses in the spark resistance of the switching spark gap G1 as well as in the capacitors and in the test object.

Often, the **properties of the test object** change the *form of the impulse voltage* to such an extent that the permissible tolerances are no longer maintained: *large test object capacitances* increase the *rise time constant* τ_1, but the influence on the wave tail time constant τ_2 is weak for comparatively large discharge capacitances. The *front time* is *adjusted* by changing the damping resistor R_F. In a modular system, for example, the given resistances can be used in series connections and parallel connections. When using a tape-type resistor web, there is generally the option to make adjustments by bridging sections.

Note: Resistor webs are made woven of insulating fabric tapes with meander-shaped continuous resistance wires of large length. *High voltage resistors* consist of series connections of many low-inductance partial resistors that can be immersed in oil or embedded in cast resin to increase the voltage strength.

6.2.3.3 Multi-stage Impulse Voltage Generators

The voltage of a single-stage impulse circuit is mainly restricted to approximately 100 to 300 kV by the voltage rating of the components. Multi-stage generators according to Erwin Marx, so-called **Marx generators,** are used for higher impulse voltages. By *parallel charging* of stages, short-duration *series connection* of the discharge capacitors and *series discharging*, a temporary multiplication of voltage occurs, Figures 6.2.3-6 and 6.2.3-7.

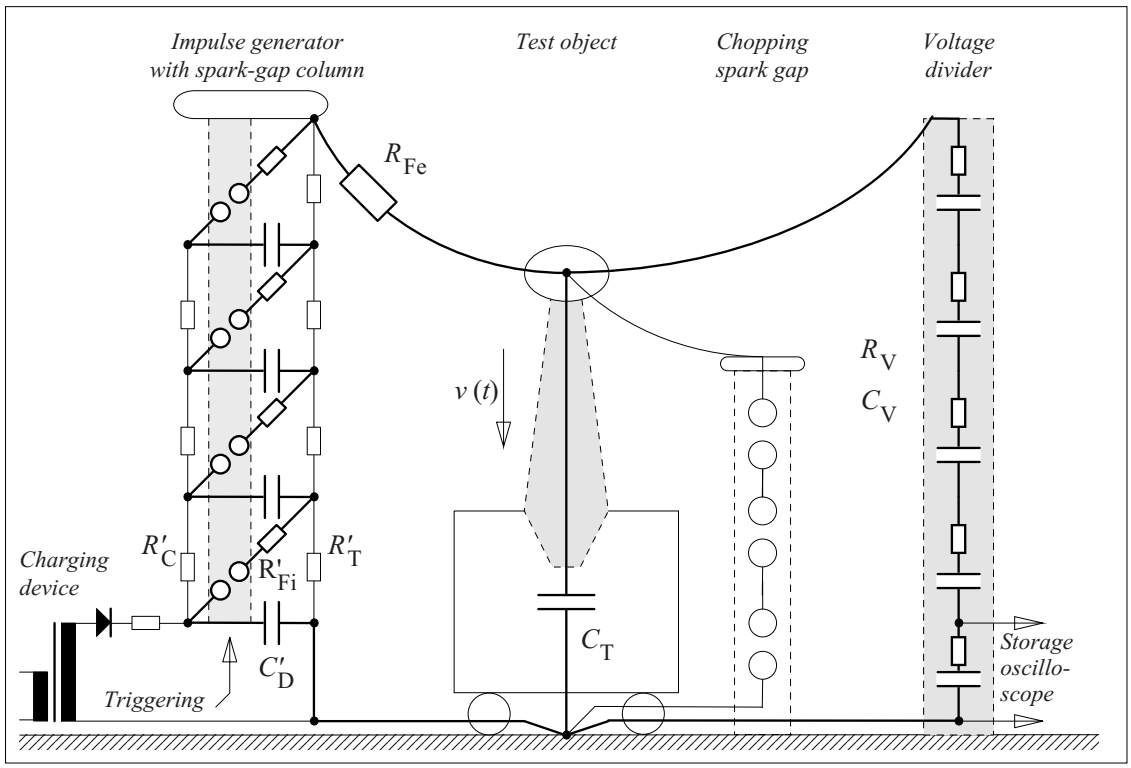

Figure 6.2.3-6: Multi-stage impulse generator or "Marx generator" with related impulse circuit, see Fig. 6.2.3-7.

Charging of discharge capacitances C_D' takes place in a *parallel connection* on two bus bars via charging and discharging resistors R_C' and R_T'. Therefore, the charging device needs only be dimensioned for the single-stage voltage V_0.

All discharge capacitances C_D' are connected *in series* by igniting the switching spark gaps. For n stages, the *summated charging voltage*

$$V_{0\Sigma} = n \cdot V_0 \qquad (6.2.3\text{-}10)$$

is available *at the generator head* in a resulting discharge capacitance

$$C_D = (1/n) \cdot C_D' \qquad (6.2.3\text{-}11)$$

The *resultant load capacitance* consists of the sum of the test object capacitance and voltage divider capacitance:

$$C_L = C_T + C_V \qquad (6.2.3\text{-}12)$$

Note: Voltage divider capacitance C_V is often chosen to be large compared to the test object capacitances, which therefore have only a weak influence on the front time.

The load capacitance $C_L \approx C_V$ is charged via the resultant (front-time) damping resistance R_F, which is the sum of the internally distributed damping resistances R_{Fi}', the concentrated external damping resistance R_{Fe} and the resultant damping resistance of the voltage divider R_V:

$$R_F = n \cdot R_{Fi}' + R_{Fa} + R_V \qquad (6.2.3\text{-}13)$$

The discharge capacitances are discharged via the resistances R'_T and R'_C with the switching spark gaps ignited. If $R_C' >> R_T'$ is selected, the *resultant discharging resistance (tail resistance)* is given by

$$R_T = n \cdot R_T'. \qquad (6.2.3\text{-}14)$$

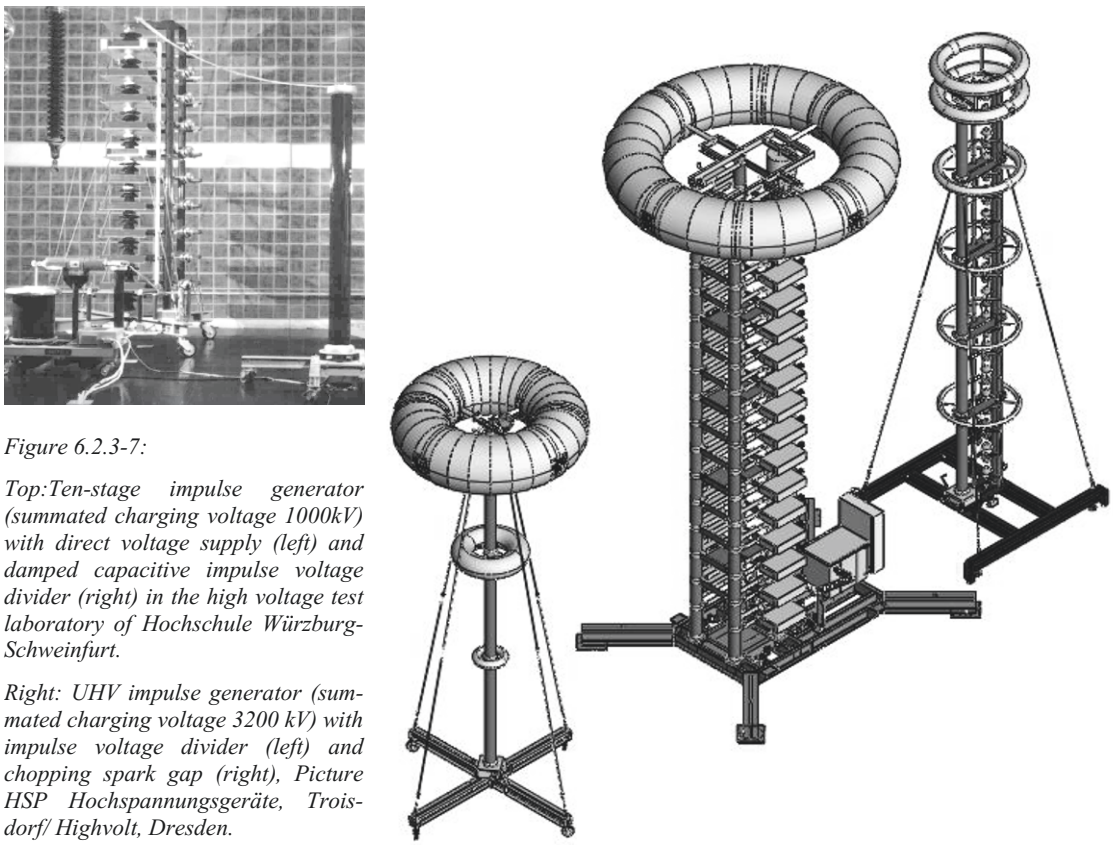

Figure 6.2.3-7:

Top:Ten-stage impulse generator (summated charging voltage 1000kV) with direct voltage supply (left) and damped capacitive impulse voltage divider (right) in the high voltage test laboratory of Hochschule Würzburg-Schweinfurt.

Right: UHV impulse generator (summated charging voltage 3200 kV) with impulse voltage divider (left) and chopping spark gap (right), Picture HSP Hochspannungsgeräte, Troisdorf/ Highvolt, Dresden.

For the calculation, Eqs. (6.2.3-1) to (-3) can be applied with the resultant parameters (C_D, C_L, R_F, R_T) or with the parameters of the individual stages (C_D', $C_L' = n \cdot C_L$, $R_F' = R_F/n$ and R_T'). Multiplication circuits are possible for both basic circuits 1 and 2.

Note: Modern impulse generators are frequently designed to be *modular*, i.e. the stages can be connected in different combinations, *in series or parallel*. This results in greater flexibility for adaptation of the generator to different test objects as well as for **on-site-tests**.

All spark gaps must be adjusted in such a way that they do not automatically ignite for an applied direct voltage V_0. **Fireing** of the generator is caused by *triggering the lowest spark gap* that connects the two first discharge capacitors in series. Thereafter, the doubled loading voltage occurs at the *second spark gap* and owing to high *overvoltage,* it results in a rapid breakdown. Here it is assumed that the *stray capacitances* to *ground* temporarily maintain the upper electrode of the second spark gap approximately at ground potential. The *other spark gaps* are progressively ignited from bottom to top by ever-increasing overvoltages.

The arrangement of discharge gaps one above the other in a *spark gap column* should ensure that the *UV-radiation* emitted by the first discharge generates start electrons at the electrode surfaces of the higher spark gaps and thereby minimizes the *ignition delay time* and *statistical dispersion* ("jitter").

Note: Complete ignition of impulse generators can be improved by *additional capacitors* to ground in the lower stages if the stray capacitances are not adequate for reliable ignition. For large generators, *simultaneous triggering of multiple successive stages* is often useful to achieve reproducible ignition with less dispersion. Finally, for extreme requirements regarding jitter, potential-free laser triggering is possible.

Note: Dirt on the electrode surfaces frequently causes non-triggered spontaneous ignitions. It is therefore recommended to burn away any dirt by multiple *test triggers* and to check for reliable operation.

Arrangement of impulse circuit elements is carried out in accordance with Figure 6.2.3-6 in such a way that the impulse generator is connected directly to the test object. The voltage divider must be connected in a separate circuit *starting from the test object* to record the voltage at the test object as accurately as possible. To avoid oscillations and inductive coupling impedances, the **high voltage connections and ground connections** must be made while keeping insulation distances at the shortest paths possible. Reference conductors are arranged radially to a *central reference point* and are grounded centrally, Figure 6.2.3-6, Section 6.3.8.

Note: High-voltage conductors must not be provided with large *radii of curvature* as for DC voltages and AC voltages. Owing to very short-duration transient voltage stress, the dielectric strength can be ensured by adequate *distances*.

6.2.3.4 Overshoot and Back Swing

Owing to parasitic properties of the test circuit or the test object that is connected, the impulse voltage waveform can considerably be distorted and it can be deviate from the double-exponential function according to Eq. (6.2.3-4). Mainly the overshoot in the front of the voltage curve (a), the definition of a test voltage amplitude (b) and the back swing in the tail of the voltage curve (c) is a matter of concern.

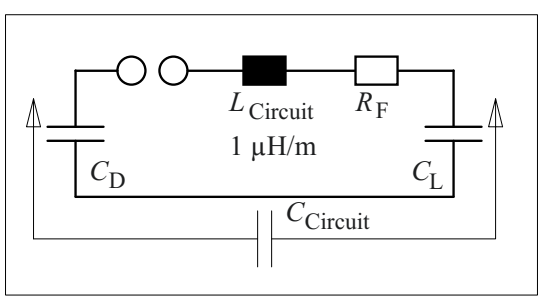

Figure 6.2.3-8: Damping of an impulse circuit by the resultant damping resistance.

a) Overshoot

In the case of *spatially extended impulse circuits*, i.e. especially for multi-stage generators, appreciable **circuit inductances** and oscillations occur. They can be ignored in to a first approximation if there is at least a *critical damping of the circuit*. By the damping resistance (front resistance) R_F. For a simple *RLC* series resonant circuit, this results in a damping condition in accordance with Figure 6.2.3-8:

$$R_F \geq 2 \cdot \sqrt{\frac{L_{\text{Circuit}}}{C_{\text{Circuit}}}} \qquad (6.2.3\text{-}15)$$

The series connection of the discharge capacitance and the load capacitance must be considered as the *circuit capacitance*. The *circuit inductance* can be roughly estimated from the *length of the electric circuit* of the oscillating circuit with 1 µH/m, see Figure 6.2.3-6 with a boldly drawn discharge circuit. The *damping resistance (front resistance)* includes the internal and external damping resistances as well as the voltage divider resistance R_V, if the divider capacitance represents the major proportion of the load capacitance.

Example: Spatial extension of an impulse circuit

The maximum possible spatial extension of the impulse circuit shall be estimated for the example (C_D = 10 nF, C_L = 1 nF, R_F = 450 Ω) calculated in Section 6.2.3.2.

The effective capacitance results from the series connection of C_D and C_L to C_{Circuit} = 0.909 nF. For R_F, a possible damping by a divider resistance is *not* considered, since the load capacitance is concentrated largely in the test object capacitance (C_T = 0.8 nF). $L_{\text{Circuit}} \leq$ 46 µH is obtained with R_F = 450 Ω from Eq. (6.2.3-15). This corresponds approximately to a maximum circuit length of $l \leq$ 46 m.

For *large impulse generators or high load capacitances* (with accordingly small damping resistances), compliance with the damping condition according to Eq. (6.2.3-15) can lead to difficulties.

Note: Following the response of the *chopping spark gap*, a high frequency oscillation occurs at first in the

circuit of the test object and the chopping spark gap, and it is only very poorly damped.

b) Test voltage amplitude

The exact performance of an impulse circuit can only be determined by *network analysis*. However, the knowledge of all relevant equivalent netework elements is generally not given for that.

Therefore, it is a practical difficulty to determine the **test voltage amplitude** from a measured impulse voltage curve which contains superimposed oszillations to a greater or lesser extent, Figure 6.2.3-9 (top left). Thus, significant differences Δv between the extreme value $\hat{V}_e$ of the measured curve and the peak value $\hat{V}_b$ of the double-exponential base curve according to Eq. (6.2.3-4) can occur.

The previously used discrete (and meanwhile obsolete) procedure that the *test voltage amplitude* $\hat{V}_t$ below 500 kHz must be inferred from the *extreme value* $\hat{V}_e$ of the oscillating voltage and above that from the peak value $\hat{V}_b$ of an *averaged curve (base curve)*, Figure 6.2.3-9 (below, grey curve), does not correspond to the continuous breakdown behavior of insulations in dependence on stress duration.

Therefore, IEC 60060-1 describes the following **evaluation procedure** based on a continuous curve [133], [489], Figure 6.2.3-9: The recorded oscillating impulse voltage $v_{rec}(t)$ is approximated by a double-exponential base curve $v_b(t)$ according to Eq. (6.2.3-4). The difference between recorded curve and base curve is the residual curve $v_r(t)$, it represents the superimposed oscillating content, Figure 6.2.3-9 (top left). This oscillating content is filtered according to the so-called *k*-factor

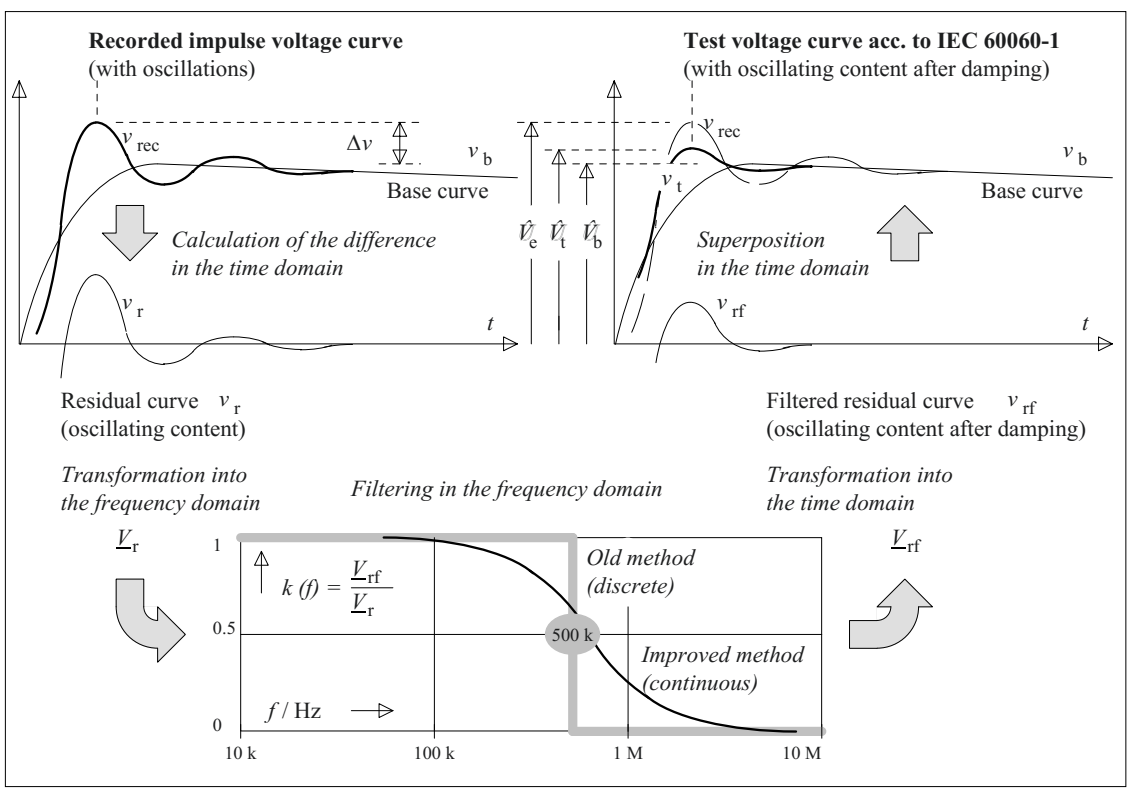

Figure 6.2.3-9: Method for the determination of the test voltage curve from a measured impulse voltage with superimposed oscillations. Damping of the ocillating content according to Eq. (6.2.3-16) and IEC 60060-1.

curve

$$k(f) = 1 / (1 + 2.2 \cdot (f / \mathrm{MHz})^2) \qquad (6.2.3\text{-}16)$$

in the frequency domain, and this results in a frequncy-dependent damping.

Note: This **filter characteristic** represents the characteristic of breakdown voltage as a function of stress duration which was empirically determined for many insulating materials. Corresponding investigations have been performed, for example, with the basic high voltage materials such as air, SF_6, popyethylene and oil [293].

Accordingly, for a slow overshoot with correspondingly long stress duration ($f << 500$ kHz), the amplitude is not damped at all ($k = 1$); and for a high-frequency overshoot with correspondingly short stress duration ($f >> 500$ kHz), the oscillating contents are completely damped ($k = 0$).

The *test voltage curve* $v_t(t)$ with the amplitude $\hat{V}_t$ is calculated by superposition of the base curve $v_b(t)$ and the filterd residual curve $v_{rf}(t)$ in the time domain, Figure 6.2.3-9 (top right).

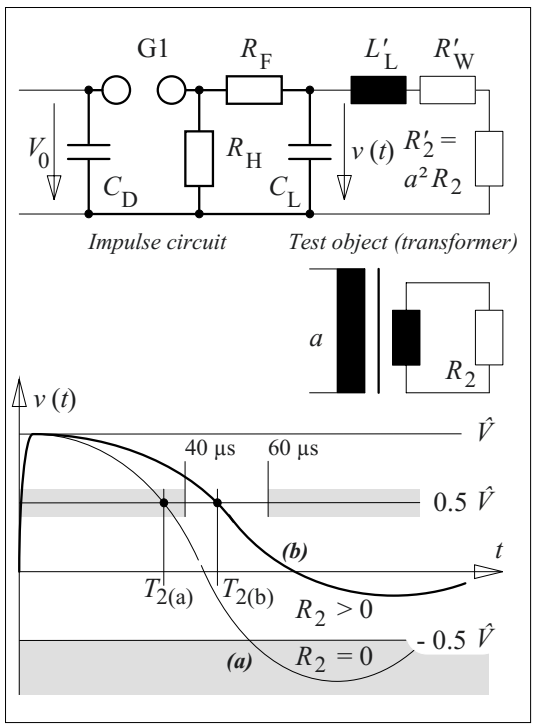

Figure 6.2.3-10: Lightning impulse voltage test of a single-phase transformer (a) with a damping of back-swing by a resistive termination of the low-voltage winding (b).

Note: The test voltage curve that is calculated according to the describe procedure is also used for the determination of **the time parameters** (front time $T_f = T_1$ and time to half-value $T_h = T_2$ or tail time T_t resp.).

Note: A **simplified manual calculation** of the test voltage amplitude can be based on the fundamental oscillation of the oscillation spectrum: depending on the frequency of the fundamental oscillation, it is weightened with the appropriate *k*-factor and then it is superimposed to the base curve. However, components of higher frequencies are not regarded in this case.

c) Back swing

During the impulse voltage testing of *transformers*, particularly large changes in the *wave tail of the impulse voltage* occur, since the low *short circuit impedance* of the transformer is parallel to the discharging resistor if the low voltage winding of the transformer is short-circuited, Figure 6.2.3-10 (top). In particular, the leakage inductance $L_\sigma' = L_L'$ of the transformer leads to "back-swings" that must be restricted to 50 % [52]. The winding resistance of the transformer R_W' is not enough for this in most of the cases. The impulse voltage waveform must be given a profile conforming to the standards by connecting a resistance R_2 to the low-voltage winding, whose value is multiplied with the square of the transformation ratio *a* for a transformation to R_2' on the high-voltage side, Figure 6.2.3-10 (bottom).

Note: The complex structure of transformer windings, in conjunction with the impulse circuit, leads to resonances that manifest themselves as intense *superimposed oscillations* in the impulse voltage waveform *v(t)*, cf. to Section b).

6.2.3.5 Impulse-current Generators

Impulse currents are frequently used in association with *impulse voltages* for test purposes and they are generated similarly to impulse voltages by discharging *capacitive energy storage capacitors*. They should therefore be discussed briefly in this context.

For **double exponential impulse currents,** the *front time* T_1 and the *time to half-value* (*tail*

time) T_2 are standardized. The tolerance range is $\pm$10 %. However, the front line must be defined through the 90% and the 10% point of the curve profile for the definition of front time! Back swing may not exceed 20% of the peak value; the amplitude of oscillations at peak current must remain under 5%.

Standardized *exponential impulse currents* are, for example, 8/20 and 4/10, the numbers respectively specify the front time and time to half-value (tail time) in µs. *Overvoltage protection devices* (spark gaps, arresters) must be tested with exponential impulse currents with regard to their current carrying capacity following to their response. Moreover, tests for *electromagnetic compatibility* (EMC) of complex systems such as aircraft require the simulation of lightning strikes by impulse currents.

Exponential impulse currents are generated from capacitor banks, in which discharge capacitors are connected in parallel and charged up to voltages of approximately 100 kV. Discharging takes place in parallel via minimal length paths of equal length via a switching spark gap and the test object (load), Figure 6.2.3-11.

Owing to the circuit inductance, the current does not follow an ideal exponential function. It is rather a *damped oscillation* of a series resonance circuit. For the relationship between the current parameters T_1, T_2 and $\hat{I}$ and the network elements of the impulse current circuit, refer to the relevant literature [16].

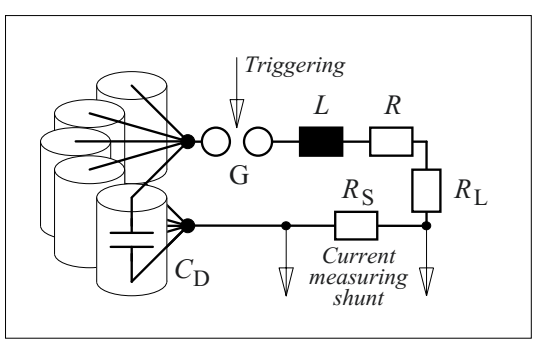

Figure 6.2.3-11: Generation of exponential impulse currents from a capacitor bank (schematic).

Rectangular or long-duration impulse currents shall represent *discharge currents,* which, after the response of the *overvoltage protection devices*, are fed from long cables charged to operating voltage. The duration T_d for which the current is larger than $0.9 \cdot \hat{I}$ is standardized. T_d is largely in the range from 500 to 3200 µs [16].

Rectangular impulse currents and long-duration impulse currents are generated by discharging *LC lattice networks*, whose capacitances have been charged in advance. Thus, an electrically long line is simulated by concentrated components, Figure 6.2.3-12. The rectangular impulse current simulates the traveling wave process to be emulated.

Note: Strictly speaking, *power frequency short-circuit currents* up to the 100 kA range with current-flow durations in the seconds range are *not* impulse currents. They are fed from the rotating mass of high-performance motor-generator sets or from high-capacity high-current transformers.

6.2.3.6 Combined Test Circuits

Many electrical power engineering equipments are stressed both by *high voltages* as well as by *high currents*. Corresponding high-power test sources are impossible to implement with reasonable technical effort. Instead of this, one applies combined test circuits to generate high currents and high voltages in *separate low-power circuits*. With the help of a control unit, the time sequence of current stress and voltage stress is aligned in such a way that the stresses correspond to the conditions in service or according to the test requirements, Figure 6.2-13 and -14.

The *response behavior* of **overvoltage protection devices** is checked with impulse voltages. The *discharge capacity* is tested by the immediately subsequent feed-in of an impulse current, Figure 6.2.3-13.

Switching devices must be capable of *interrupting* a specific power frequency *current* and

of insulating the *recurrent voltage* across the switching contacts that open.

The current-breaking capacity is tested with so-called "synthetic test circuits", in which a motor-generator set supplies the power frequency current which is to be interrupted. Interrupting the current through the test object is followed by triggering of the impulse voltage circuit, which simulates the recurrent voltage by an oscillating voltage in a *RLC*-circuit, Figure 6.2.3-14.

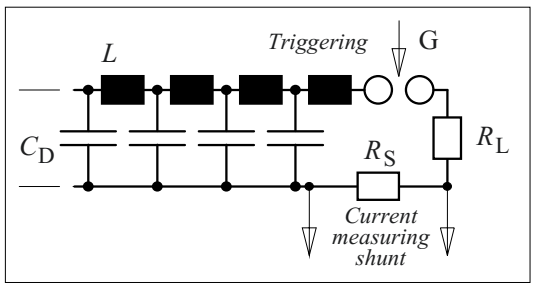

Figure 6.2.3-12: Generation of rectangular impulse currents by discharging lattice networks (schematic).

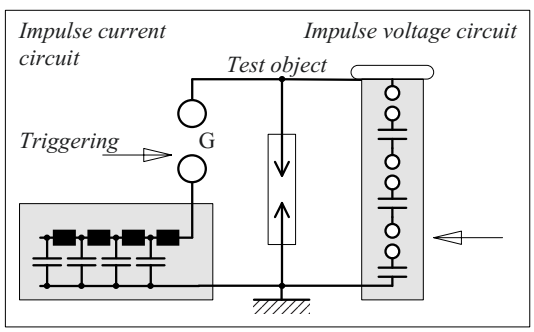

Figure 6.2.3-13: Testing an overvoltage arrester with impulse voltage and impulse current (schematic).

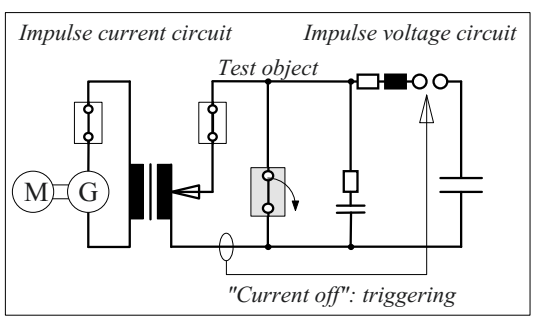

Figure 6.2.3-14: "Synthetic test circuit" for testing the breaking capacity of switches (schematic).

6.2.3.7 Special Impulse Generators

Many technical applications require impulses that do not correspond to the impulse voltages that are standardized for insulation tests. A few *examples* are given in the following sections:

a) Rectangular impulse voltages help in determining system properties or transmission properties of measuring systems by *step-response measurements*. Generally, voltages are relatively low, since it is not important to test the insulation but only to achieve a sufficiently high signal level. High voltages are only necessary for testing non-linearities.

In the case of lower voltages, it is possible to use *electronic function generators*. Higher rectangular voltages of up to a few 100 V are generated by the parallel connection of charged capacitances to the test object. A low inductivity assembly and adequate damping of oscillations must be ensured for this.

Rectangular voltages in the kV range can be generated with *line generators (cable generators)*, see Section 2.6.3.3 and Figure 2.6-18. For this, a charged line is connected to the load through a low-inductive switch. Discharging the line by traveling waves ideally leads to a rectangular voltage impulse. According to the equivalent transmission-line circuit in Figure 2.6-8, the rise-time constant for a resistive load R is practically exclusively determined by the inductance L of the switch and the characteristic (line) impedance Z, i.e. the following is applicable: $\tau = L/(R + Z)$. For a capacitive load C, such as for a capacitive voltage divider, C is exponentially charged with the time constants $\tau = ZC$ if the inductance can be neglected. Depending on the voltage, electronic switches, relays with mercury contacts, switching tubes (thyratrons) or switching spark gaps are used as switches.

b) Very rapidly rising impulses in the ns range are used for the simulation of electromagnetic wave fields for testing of the *electromagnetic compatibility (EMC)* of devices and systems.

For example, the immunity to the so-called *nuclear electromagnetic puls*e (NEMP, HEMP *high altitude electromagnetic pulse*), that is expected for a nuclear explosion outside the earth's atmosphere, is tested with a double exponential impulse whose rise time T_r is = 4 ns and whose time to half-value on wave tail T_2 is = 200 ns [41].

The test object is exposed to the transient electromagnetic wave field in a *parallel-plate line*, Figure 6.2.3-15. The supply is from a charged capacitor bank that in principle belongs to an impulse voltage circuit (discharge capacitance C_D). The unavoidable inductance of the discharge circuit L_D prolongs the attainable rise time too much. A so-called *secondary circuit* is therefore necessary, which can be designed to be of considerably *low inductance*, since significantly smaller insulation distances and overall dimensions are possible owing to the only short-duration voltage stress. That is, $L_T << L_D$ is applicable. The transfer capacitance C_T is charged in oscillating manner from the discharge capacitance C_D via G1 and L_D. At the maximum capacitor voltage $v_T(t)$, G2 ignites and leads to a rapid *voltage rise* $v_R(t)$ at the load with the time constant L_T/R. The *decrease in the tail of the impulse* is determined by the discharge of C_T through R.

In the so-called "*transfer operation"*, $C_T \approx C_D$ is chosen. Under this, the oscillation ideally transfers the total charge from C_D to C_T, Figure 6.2.3-15. In the so-called "*peaking operation"*, $C_T << C_D$ is chosen. This results in still smaller inductances and rise times in the secondary circuit.

c) High-power impulse technology: In many technical applications, high-voltage impulses are necessary for the *power supply of devices*, Section 7.4.2. The determining parameters for this are always a specific *pulse energy* or *pulse power* and the pulse frequency or the *repetition rate*. The standard voltage range extends up to several 10 kV.

Generally, the impulse is generated by the discharge of a capacitive energy storage device consisting of *pulse-resistant* capacitors in a low inductance discharging circuit. For repetitive operation, a short charging time and a high efficiency (i.e. low losses) are necessary. Owing to this, the simple mains-operated charging equipment is increasingly being replaced by switched-mode power supply units with *constant-current charging,* see Section 6.2.2.3. Switched-mode power supply units are particularly also suitable for mobile systems owing to their lower weight.

Important applications are compiled in Section 7.4.2, such as the generation of **acoustic shock waves** under water for *medical purposes*, for *production* or for *recycling*. Other applications arise for **pulsed light sources**, i.e. for *pulsed lasers*, *flash devices* and *UV sources* for chemical processing technology (e.g. harden-

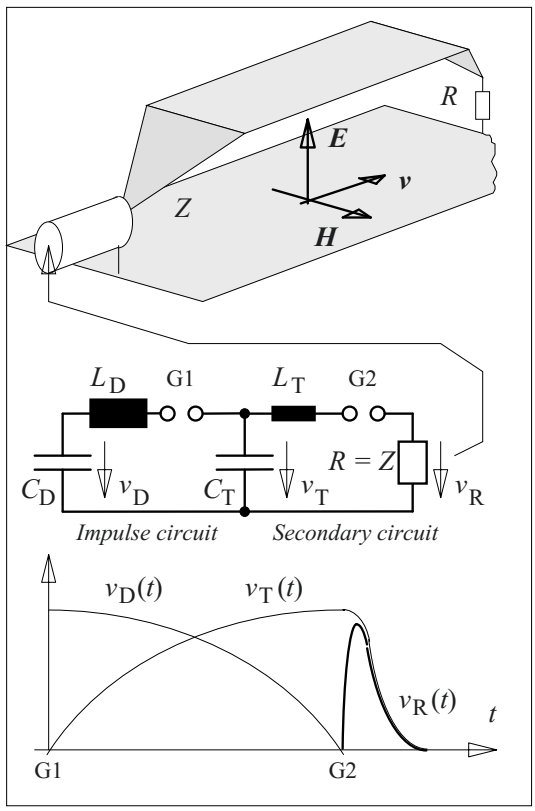

Figure 6.2.3-15: Impulse circuit with secondary circuit for generating quickly rising impulses for the supply of a NEMP-simulator.

ing of photosensitive enamels and resins).

Electrostatic precipitators can be operated with impulse voltages to improve the separating performance for high resistive dusts. *Back corona* caused by charged dusts and the associated partial breakdowns and precipitator breakdowns are avoided by pulse operation. [136].

Moreover, different **test procedures** are based on the application of high voltage impulses, e.g. acoustic-electrical *cable fault location* (localization of discharge noises), *simulation of overvoltages* (hybrid generator for impulse voltages and impulse currents, burst generator, network disturbance simulator [41]), and the *simulation of electrostatic discharges* ("ESD pistol").

d) Pulsed power: The term "pulsed power" is coined for extreme impulses as used in fundamental *physical research, material research* and as ignition impulses for *nuclear fusion experiments* [138].

In extreme cases, pulsed powers in the TW range, voltages in the MV range and currents in the MA range are required for load impedances of a few Ohms. The rise times are typically approximately in the order of 10 ns and the half-width values are a few 10ns [15], [42], [43], [137].

Although the impulse energies for this are only in the range of a few 100 kJ, such impulses *cannot* be generated directly from conventional energy storage capacitors since, even with compact oil insulated constructions, the circuit inductances are too large. Therefore, the energy must be transferred by oszillation to *ever more compact and lower inductive circuits*, Figures 6.2.3-15 and -16. The electric strength of ever-decreasing insulation distances is ensured by the ever-decreasing stress duration.

That is, a **spatial and temporal "compression"** of energy takes place towards the output.

Many circularly arranged and *synchronously triggered modules* energize pulsed lasers or particle emitting diodes that are focused on a "target". *Extreme power densities* thus occur at the center of the arrangement, see Figure 2.6-20. The final impulse generation takes place according to the principle of *line generators* by discharging a traveling wave transmission line, see Figures 2.6-18 and -19.

Figure 6.2.3-16 shows a sketch of an implemented module that must be understood as

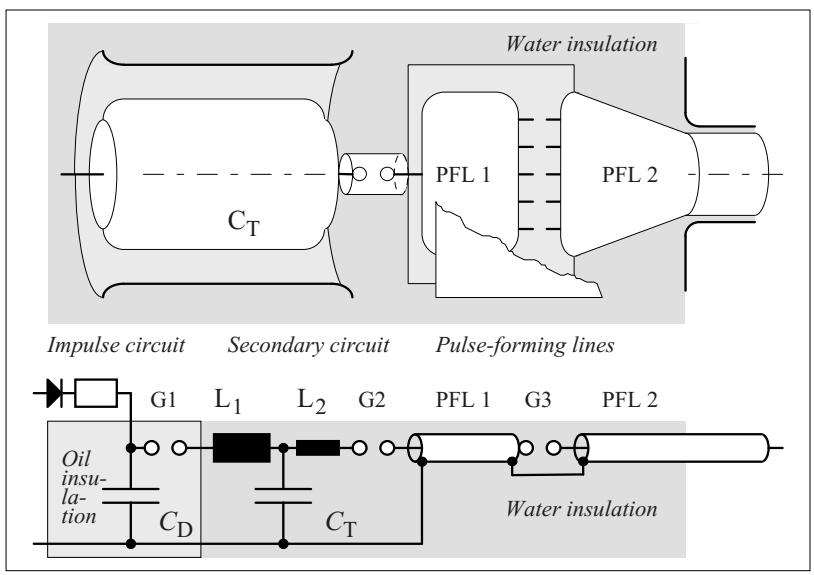

Figure 6.2.3-16: Pulse power generator for terawatt impulses with voltages and currents in the MV range and MA range, consisting of conventional capacitive energy storage (impulse circuit), water-insulated transfer capacitance (secondary circuit), pulse-forming traveling wave line (PFL 1) and output line (PFL 2) in a schematic representation [15], [137]. Parallel modules are synchronized by triggering the spark gaps 1 (impulse circuit) and 2 (secondary circuit).

part of an installation of 36 circularly arranged synchronous modules [15], [137].

From a multi-stage impulse voltage circuit *with conventional discharge capacitors* C_D, after ignition of the generator spark gaps (G1), a *transfer capacitance* C_T is charged in an oscillating manner via the relatively large circuit inductance L_1 within a few µs. *Complete energy transfer* ideally takes place in the case of equal capacitances. C_T can be insulated with *de-ionized water* owing to the short stress duration. The high relative permittivity $\varepsilon_r = 81$ and the high electrical short-term strength allow a very compact and low-inductiv structure, e.g. in coaxial form, Figure 6.2.3-16 (top). From the transfer capacitance, an even more compact *pulse-forming parallel-plate line* (PFL 1) is charged in oscillating mode via a comparatively low inductance L_2 in less than 1 µs.

The final *output impulse* results from the ignition of the spark gap 3 in accordance with the line generator principle, see Figure 2.6-18. The *water insulation*, owing to the high permittivity or the low wave propagation velocity u_{Water}, allows a very short overall length l_1 of the pulse-forming line PFL 1. For a half-value width T_H = 50 ns, a single propagation time $\tau_{PFL1} = T_H/2$ = 25 ns is necessary, see Figure 2.6-18. With u_{Water} = 3.3 cm/ns, l_1 = 83 cm is obtained (in comparison, u_{Vacuum} = 30 cm/ns). An extremely low inductance of spark gap G3 is necessary for a short impulse rise time. It therefore consists of *parallel* water-insulated rod spark gaps that are *decoupled* by the propagation time according to the rod lengths. The gaps can therefore ignite in parallel.

Note: **Synchronous ignition and triggering of parallel discharge channels** is an important prerequisite for generating rapidly rising impulses and for synchronizing of multiple modules. *Laser triggering* of gas insulated spark gaps of parallel rods *("rail-gap spark gaps"),* in which the initial electrons are released from *metallic aerosols* (suspended matter) by laser induced photo emission in the entire field volume, is an interesting innovation [139], [140].

The *output impulse* propagates as a traveling wave on an output line (PFL 2) towards the load. Here, different *modifications* are possible, such as conversion from plate geometry to coaxial geometry, impedance variation, polarity change or voltage increase and power increase owing to reflections and the delayed response of further spark gaps [43].

Further concepts include complete filling of the space with plate line geometries, the stacking of several generator levels and flexible line connections for adapting to different load impedances [14].

6.3 High Voltage Measurement Techniques

The measurement of high field strengths, high voltages, and high currents places special requirements on the measuring systems used for it. The most important principles and their suitability for the measuring of different quantities are discussed in the following sections. Additional information is given in the specialist literature [141].

6.3.1 Measuring Spark Gaps

6.3.1.1 Sphere-to-sphere Spark Gap

The sphere-to-sphere spark gap (sphere gap) is the classic high-voltage measuring equipment for *direct* measurements of voltages. In breakdown tests, the ***peak value*** of the voltage $\hat{V}$ before the breakdown is concluded from the *flashover distance d*, Figure 6.3.1-1. Tables give breakdown mean values under standard atmospheric conditions for the specified diameters D = 2/ 5/ 6.25/ 10/ 12.5/ 15/ 25/ 50/ 75/ 100/ 200 mm and for different distances; Table 6.3.1-1 comprises an extract [142], [143]. The tabulated relationships apply for a weakly non-uniform field here, i.e. the sphere diameter D must be considerably larger than

the flashover distance d. As a rule-of-thumb formula, the peak value of the voltage to be measured is

$$\hat{V} \,/\, \mathrm{kV} < D \,/\, \mathrm{mm}\,. \qquad (6.3.1\text{-}1)$$

In the case of greater non-uniformity of the field, the dispersion increases, and also the field between the spheres is increasingly influenced by the structures in the surroundings. Therefore, the surroundings of the sphere gap must be kept free of field-distorting structures within a *protection zone*.

Note: The spherical *protection zone* is generally determined with a radius $B > 2{\cdot}D$ around the breakdown point P. The minimum radii must also be between $B = 14{\cdot}d$ for small sphere diameters and $B = 6{\cdot}d$ for large sphere diameters. The *height A* of the breakdown point P above the grounded floor shall lie between $7{\cdot}D$ and $9{\cdot}D$ for small sphere diameters and between $3{\cdot}D$ and $4{\cdot}D$ for large sphere diameters. The exact gradation can be obtained from the standards [142], [143].

The current limiting *series resistor* R_S also acts as protection against transient overvoltages, e.g. resulting from discharges at other points of the test circuit. It must be dimensioned in such a way that the voltage across the capacitance of the sphere gap is not appreciably decreased. Its capacitance can amount to several 10 pF.

Note: The series-resistance values shall be between 0.1 MΩ and 1 MΩ for AC power frequency voltages and for DC voltages. For higher frequencies and for impulse voltages, smaller resistances must be chosen. For the damping of oscillations in impulse circuits, a few 100 Ω are generally adequate; 500 Ω (and 30 µH) should not be exceeded.

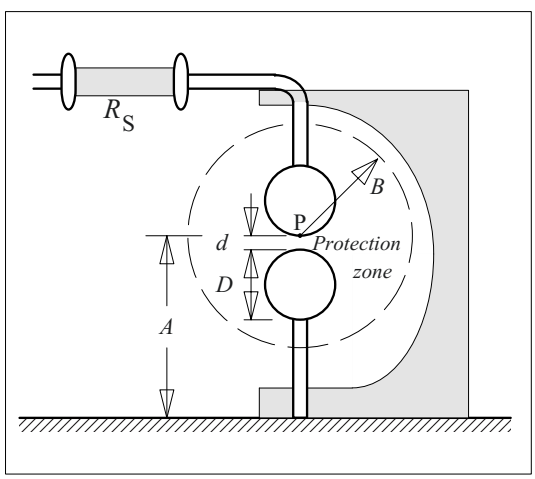

Figure 6.3.1-1: Sphere gap with series resistor.

The particular advantage of the sphere gap is its *simple and universal applicability*. It is suitable for determining **peak values** for **DC voltages, AC voltages** as well as **switching impulse voltages** and **lightning impulse voltages** ($T_2 \geq 50$ µs), since the impulse voltage-time characteristics remain flat down to the µs range. For a sphere gap grounded on one side, a *polarity effect* for *impulse voltages* results from field distortions at larger flashover distances only, because the field strength at the grounded electrode is reduced owing to the surrounding grounded structures and is increased at the voltage electrode (asymmetry relative to ground).

Note: According to Section 3.2.5.2, it might be assumed that the breakdown voltage for a positive voltage electrode (or "point") should be lower than for a negative electrode. However, the opposite is observed in reality, Table 6.3.1-1. For this, better starting conditions for electron avalanches at the negative point are important since the first avalanche leads to a breakdown in a weakly non-uniform field (streamer mechanism). For impulse voltages, no field-distorting space-charge cloud can be formed.

Some disadvantages of the sphere gap are the collapse of the measured voltage during breakdown and the dispersion of the individual breakdown values, which necessitates *pre-ionization* (with UV light or laser light) and forming a *mean value* of many breakdown values. Before a measurement, any deposited dirt must be burnt away by *cleaning breakdowns* until reproducible, less dispersed values are obtained. Additionally, there is neither a direct nor a continuous voltage display.

The sphere gap mainly helps in **check measurements**, i.e. if *another measuring system* has to be checked. Under this, the voltage is repeatedly increased until breakdown for an exactly known distance d. Owing to de-ionization of the gap, the interval between the breakdowns must be at least 30 s. An average breakdown value is obtained from the readings

of the measurement system to be checked. It can be compared to the voltage value that is associated with the distance *d* and the prevailing atmospheric conditions.

Note: For **measuring an AC voltage**, the voltage is increased slowly ten times until breakdown. The resulting standard deviation of the displayed values must not exceed 1%.

For the **measurement of an impulse voltage**, the amplitudes of successive impulses are increased in steps of approx. 1 % of the expected breakdown value until breakdown. The trials repeated for ten times should result in a standard deviation of 1 % for a lightning impulse voltage and of 1.5 % for a switching impulse voltage. Alternatively, the breakdown mean value can be determined according to the up-and-down method with at least 20 impulse voltage stresses in 1 % steps, Figure 3.1.1-b).

Measurements for direct voltages are problematic since dust deposits can lead to large dispersions. Therefore, using a rod-to-rod spark gap provides better results, Section 6.3.1.2. For measurements with a sphere gap, a constant air flow of 3 m/s is recommended if necessary, as well as a very large number of breakdowns until a stable value is achieved.

The table value (standard value) $\hat{V}_{\mathrm{bd50(0)}}$ is valid under the *standard* a*tmospheric condi-*

Tabelle 6.3.1-1: Peak values of 50 % breakdown voltage on uni-polar grounded sphere gap in kV for different sphere diameters D and flashover distances d for DC voltage, AC voltage and negative impulse voltage (left columns) as well as positive impulse voltage (right columns) under standard atmospheric conditions (T = 20 °C, p = 1013 mbar = 1013 hPa = 760 Torr).

The impulse voltages are valid for times to half-value on wave tail longer than or equal to 50 µs; the polarity effect for positive impulse voltages is marked by numbers in italics (see the note in the text). Numbers presented in bold correspond to the values of the uniform field and are valid also for larger sphere diameters D. Measurement uncertainties are assumed for AC voltage and impulse voltage for d < D/2 at ±3 % and for DC voltage for d < 0.8·D/2 at ±5 %, the values presented in brackets rerfer to larger, unexplained dispersions.

$\frac{d}{\mathrm{cm}}$	D = 5 cm		D = 10 cm		D = 15 cm		D = 25 cm		D = 50 cm		D = 75 cm		D = 100 cm		$\frac{d}{\mathrm{cm}}$
	= ~ -\	/+	= ~ -\	/+	= ~ -\	/+	= ~ -\	/+	= ~ -\	/+	= ~ -\	/+	= ~ -\	/+	
0,5	17,4	17,4	**16,8**	**16,8**	→										0,5
1	32,0	32,0	**31,7**	**31,7**	→										1
1,5	45,5	*46,2*	**45,5**	**45,5**	→										1,5
2	57,5	*59,5*	**59,0**	**59,0**	→										2
2,4	65,5	*69,0*	69,5	*70,0*	**70,0**	**70,0**	→								2,4
3	(75,5)	*(81,0)*	84,0	*85,5*	85,5	85,5	**86,0**	**86,0**	→						3
4	(88,5)	*(97,5)*	105	*109*	110	*111*	**112**	**112**	→						4
5			123	*130*	133	*136*	137	*138*	**138**	**138**	→				5
6			(138)	*(148)*	152	*158*	161	*163*	**164**	**164**	→				6
7			(150)	*(163)*	169	*178*	184	*187*	189	189	**190**	**190**	→		7
8					(185)	*(196)*	206	*211*	214	214	**215**	**215**	→		8
9					(198)	*(212)*	226	*233*	239	239	240	240	**241**	**241**	9
10					(209)	*(226)*	244	*254*	263	263	265	265	**266**	**266**	10
12					(229)	*(249)*	275	*291*	309	*311*	315	315	**318**	**318**	12
14							(302)	*(323)*	353	*357*	363	363	**366**	**366**	14
16	Area with						(326)	*(350)*	392	*402*	410	*411*	**414**	**414**	16
18	increased dispersion and						(347)	*(374)*	429	*442*	453	*458*	**462**	**462**	18
20	externally influenced field						(366)	*(395)*	460	*480*	492	*505*	**510**	**510**	20
24									515	*540*	565	*585*	595	*600*	24
30									(585)	*(620)*	665	*695*	710	*725*	30
40									(670)	*(715)*	(800)	*(835)*	875	*900*	40
50	*Detailed tables are given in the relevant standards [142], [143]*										(895)	*(940)*	1010	*1040*	50
60											(970)	*(1020)*	(1110)	*(1150)*	60
70													(1200)	*(1240)*	70

Area with almost uniform field

$\frac{\hat{V}_{\mathrm{bd50(0)}}}{\mathrm{kV}}$

tions

temperature T_0 = 20 °C,

atmospheric pressure p_0 = 1013 mbar

and

absolute humidity h_0 = 8.5 g/m^3,

and it must be converted to the applicable peak value $\hat{V}_{bd50}$ under the given atmospheric conditions (T, p, h). Changes in the **air density** and the *humidity* are corrected. The dependence of the breakdown on pressure and temperature results directly from Paschen's law, Section 3.2.2.4. An increased **air humidity** leads to an increased electron affinity and thus to an increase in the breakdown voltage. A *simplified conversion*, which ignores the slight curvature of the Paschen curve, assumes proportionality between breakdown voltage and relative air density δ. The absolute humidity h is considered by applying a correction factor k:

$$\hat{V}_{bd50} \approx \hat{V}_{bd50(0)} \cdot \delta \cdot k \qquad (6.3.1\text{-}2)$$

$$\delta = \frac{p}{p_0} \cdot \frac{273\,\mathrm{K} + T_0}{273\,\mathrm{K} + T}$$

$$k = 1 + 0.002 \cdot \left(\frac{h / \mathrm{g\,m^{-3}}}{\delta} - 8.85 \right)$$

Note: Owing to long years of painful experience in practical training, it shall be mentioned that *measured values* are given on the left and *standard (table) values* are given on the right hand side of Eq. (6.3.1-2)!

Note: Conversion to standard conditions in *non-uniform field* is described in Section 3.2.5.5

The sphere gap was formerly often used as a *simple and clear calibration tool* for other measurement systems. However, the measurement uncertainty of 3 % (for a confidence interval of 95 %) that can be attained for AC voltages and impulse voltages or 5 % for DC voltages is *no longer adequate* for a reference system according to the standards, see Table 6.1-1. However, the application as a *measuring system for AC voltages and impulse voltages,* predominantly for **check measurements,** is possible if a standard deviation of 1% is attained for AC voltages and lightning impulse voltages and a deviation of 1.5% is attained for switching impulse voltages. The measurement uncertainty can be reduced a little more by an *individual calibration* of a sphere gap with an accordingly suitable reference measuring system.

A breakdown provides a very clear and direct proof of voltage stress. Therefore, sphere gaps still have great practical value for *quick and indicative check measurements*.

Note: Sphere gaps can also be used as *protective gaps*, as *chopping spark gaps* and as *modifiable capacitances* in high voltage laboratories. There are **vertical** and **horizontal** sphere gaps.

6.3.1.2 Rod-to-rod Spark Gap

Since the accuracy of the sphere gap for DC voltages is distinctly poorer than for AC voltages and impulse voltages, the vertical or horizontal *rod-to-rod spark gap* is recommended for **relatively high DC voltages**, [142], [143], Figure 6.3.1-2.

The rods must have a *rectangular* and *sharp-edged* cross section (side length 15 to 25 mm) so that corona discharges and an exactly reproducible breakdown behavior occur. For flashover distances between 250 and 2500 mm, there is a largely linear relationship that is explained by the growth of the *streamer discharges*:

$$\hat{V}_{bd50(0)} = 2\ \mathrm{kV} + d \cdot 0.534\ \mathrm{kV/mm} \cdot \qquad (6.3.1\text{-}3a)$$

Note: Under 120 kV, this relationship is no longer valid since the streamer discharges are initiated only above 120 kV.

With respect to the **air density**, correction of the standard value is carried out in accordance with Eq. (6.3.1-2). Similar to Eq. (3.2-70b), a *considerably larger influence of* **humidity** is observed here than in the uniform field of a sphere gap:

$$k = 1 + 0{,}014 \cdot \left(\frac{h / \mathrm{g\,m^{-3}}}{\delta} - 11 \right) \quad (6.3.1\text{-}3b)$$

Eq. (6.3.1) is valid in the humidity range from 1 to 13 g/m^3 and allows a voltage determination with an estimated uncertainty of 3 % for a confidence interval of not less than 95 % [142], [143].

Note: There are tests that have detected even smaller standard deviations (< 1 %) and measurement uncertainties (±2 %) [144]. For round rods (D = 20 mm) and rounded off rod ends, the following is applicable:

$$\hat{V}_{\mathrm{bd50}} = \delta \cdot [V_0 + d \cdot 5.1\ \mathrm{kV/cm}] \cdot [0.051 \cdot (8.65 + h/\mathrm{g/m^3})]^{0.25} \quad (6.3.1\text{-}4)$$

Here, V_0 is 20 kV for positive DC voltages, V_0 is 15 kV for negative DC voltages and h lies between 4 and 20 g/m³.

6.3.2 Electrostatic Voltmeter

Electrostatic voltmeters provide an *absolute voltage measurement*, that is, voltage measurement can be traced back to measurement of other physical quantities (force and distance), Figure 6.3.2-1. In a computable electric field,

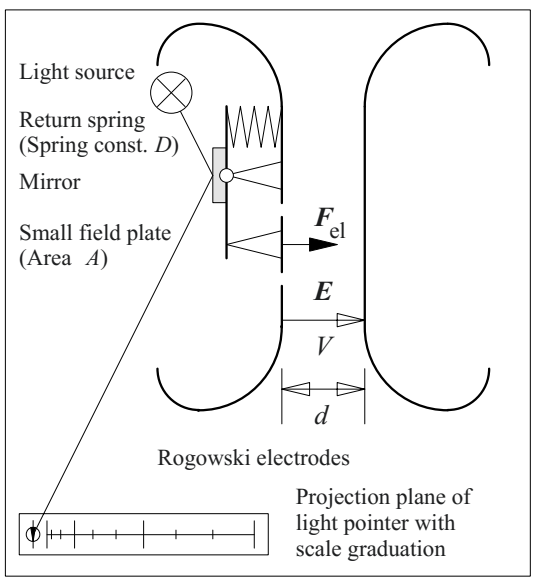

Figure 6.3.2-1: Electrostatic voltmeter (voltmeter according to Starke and Schröder).

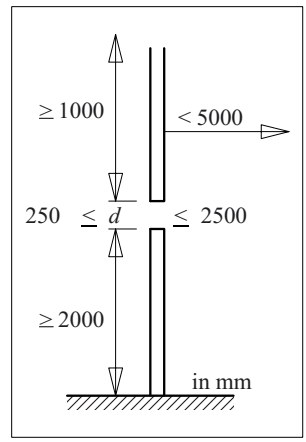

Figure 6.3.1-2: Rod-to-rod spark gap for the measurement of high DC voltages, rectangular rod cross-section.

i.e. in a uniform field for example, an eccentrically supported small plate is deflected so far by the *force of the field* until the field force corresponds to the *force of a return spring*. Using a mirror, the deflection x is displayed by projection of a pointer image on a scale divided into voltage values. With equilibrium of forces

$$F_{\mathrm{el}} = 0.5\ \varepsilon_0\, A\, V^2/d^2 = F_{\mathrm{Spring}} = D \cdot x\ ,$$

the deflection is proportional to *the square of the voltage* and inversely proportional to the square of the electrode distance:

$$x \sim V^2/d^2 \quad (6.3.2\text{-}1)$$

The reading for *DC voltages* is independent of the polarity. In the case of *AC voltages*, the system cannot follow the pulsating force owing to its mass inertia, and hence the mean value of the square of the voltage is displayed. This is therefore a **true r.m.s. measurement** that is independent of the voltage waveform. Displaying impulse voltages is *not* possible. High *accuracy* (up to 0.1%) is only achieved in the upper section of the voltage measuring scale owing to the square-law dependence of the reading on the voltage; the accuracy falls steeply for lower voltages. A selection of the *measuring range* is possible in accordance with Eq. (6.3.2-1) by changing the electrode distance d.

The exceptional property of electrostatic voltmeters lies in their extremely **low feedback** to

the voltage source via the very high insulation resistance and via the comparatively low capacitance between the electrodes. Electrostatic voltmeters can therefore be used for the *measurement of DC potentials*, even in the case of high-resistive arrangements and high internal impedances of the voltage source.

A compact construction with a closed housing is designed for up to a few 10 kV. Above 100 kV, rounding off the electrode edges gives rise to such large dimensions that compressed-gas-insulated designs are used. Electrostatic voltmeters are precision instruments with sensitive adjustment mechanics and projection optics. Generally, they are used only under the controlled conditions of a laboratory.

6.3.3 Field Sensors

6.3.3.1 Electrically Short Sensors

Classic field sensors record **time-varying electric and magnetic field strengths** by a *displacement current* coupled in a *sensor surface* or by a *rotational voltage* induced in a *sensor loop*, Figure 6.3.3-1 (top, left and right). Here, the sensors are assumed to be spatially concentrated or "electrically short", so that lumped circuits with *lumped equivalent network elements* can be specified, Figure 6.3.3-1 (bottom). Broadband measurement of extremely rapidly varying processes is possible through appropriate *small sensor dimensions*. For a known field geometry, such as in uniform or coaxially symmetric fields, conclusions about the voltage, the current or the electromagnetic wave processes can be drawn from the measured variables.

Important applications are, for example, the broadband measurement of *fast transients* and *partial discharge impulses* in gas insulated switchgear, the *directional coupler technique* for directionally selective measurement of partial discharge impulses and interference impulses [215] or the measurement of pulse forming processes of p*ulse power* technology [5], [145], [146], [147], [148].

Note: The sensitivity of the capacitive and magnetic sensors to unwanted magnetic and capacitive coupling is reduced with the help of a symmetrical structure, Figure 6.3.3-1.

Since the signals are proportional to the *time derivatives* of field quantities, generally they must be *integrated*. Integration can be performed actively by broadband integration amplifiers or by numerical integration of the digitized signals. However, in the case of extremely rapidly varying processes for a capacitive sensor, *direct passive integration* by a defined sensor capacitance C_S that shall be only loaded with a high impedance R_S is recommended. For a magnetic sensor, the self-inductance L_S of the magnetic sensor loop along with a low-impedance load R_S can be used for passive integration, Figure 6.3.3-1 (bottom).

Note: The capacitive sensor with a capacitive load C_S can also be interpreted as a *capacitive voltage divider*, if the coupling of the displacement current is described by a high-voltage stray capacitance C_{HV}, Figure 6.3.3-1 (bottom center).

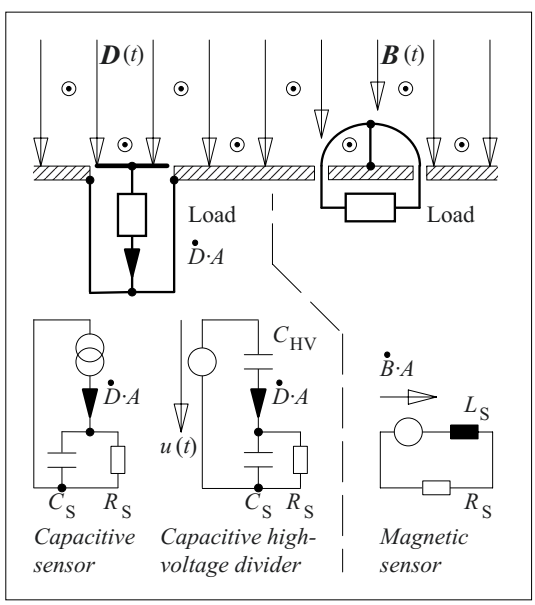

Figure 6.3.3-1: Coupling of displacement current in a capacitive sensor surface and induction of a rotational voltage in a magnetic sensor loop (top, left and right) with equivalent network representations (bottom).

6.3.3.2 Electrically Long Sensors

In the case of extremely rapidly changing field variables or spatially extended sensors, such as Rogowski coils, the runtime events in the sensor must also be considered [145], [146]. That is, the sensor itself must be understood as a system with *distributed parameters* or as an "*electrically long*" traveling wave line with the characteristic impedance Z, Figure 6.3.3-2, also see Section 2.6.

It could be proven that even electrically long sensors are suitable for measuring *extremely rapidly varying processes* if they are operated either with a very high-impedance load ($R >> Z$ for capacitive sensors) or with a very low-impedance load ($R << Z$ for magnetic sensors respectively) and if the *distributed coupling* in the sensor is *synchronous and with equal amplitude* at each position. That is, the sensor understood as a traveling wave line in the x-direction, must be arranged perpendicular to the direction of propagation in the *phase plane* of the electromagnetic (TEM) wave [5], [149], [150], Figure 6.3.3-2.

For spatially non-uniform coupling, the sensor signal includes information both about the *location dependence* and *time dependence* of the field quantity in the form of convoluted location functions and time functions. The spatial field distribution along the sensor contour in the x-direction can then be determined for a known time function by numerical deconvolution [5].

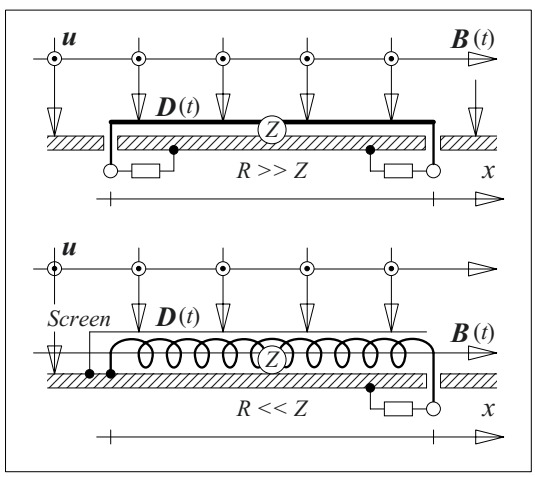

Figure 6.3.3-2: Spatially extended (electrically long) capaxitive and magnetic sensors (top and bottom) as systems with distributed parameters and distributed coupling in the phase plane of a TEM wave [5].

6.3.3.3 Potential-free Probes

The spatial measurement of electric and magnetic fields can be done with the sensor principles described in Figure 6.3.3-1 and with potential-free probes that are *positioned to be potential-free in the respective measurement location*. Signal transmission takes place wireless via radio transmission or in an optical path, for example, via optical waveguides.

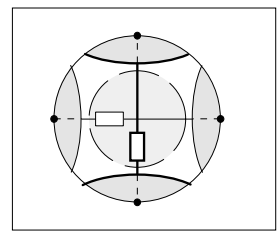

Figure 6.3.3-3: Potential-free capacitive probe for measurement of displacement currents in the three spatial directions with six measuring surfaces.

For capacitive sensors, two measuring surfaces are necessary for each field strength component. For *three-dimensional measurements*, spherical probes with six measuring surfaces are used [151], Figure 6.3.3-3. Owing to local distortion of the electric field by conductive spheres, *spatial resolution* is limited, see Figure 2.3-17.

Another option for potential-free measurements is the use of electrooptical sensors, Section 6.3.3.5.

6.3.3.4 Generator-mode Sensors ("Field Mills")

Static, stationary and very slowly changing fields neither couple with appreciable displacement currents in static surfaces, nor do they induce appreciable voltages in static loops. However, in so-called electro-mechanical "*field mills"* or *"generator-mode sensors"*, *mechanical movement of the sensor* causes a time-variation of the dielectric displacement at the sensor surface or of the magnetic flux in the sensor loop; and this results respectively in

displacement currents or induced voltages that are proportional to the electric or magnetic field strength, see Figure 6.3.3-1.

As an example of the measurement of static electric fields, a **fieldmill voltmeter** is considered, Figure 6.3.3-4. Sector-pattern measuring surface rotates in the field shadow of a grounded aperture. Thereby, the effective area $A(t)$ varies sinusoidally. For a static displacement density $\boldsymbol{D}$, a sinusoidal *current* $D \cdot \partial A/\partial t$ can be tapped at the axle, since the charge that is bound to the measuring surface (or induced by the electric field) changes with the size of the effective area $A(t)$.

Note: It is also possible to use a fixed measuring surface in the field shadows of a rotating, grounded aperture.

Note: Another generator-mode principle is realized in an *oscillatory voltmeter*: vibration of the measuring surface causes distance changes and changes in capacitance between high-voltage and ground side.

Generator-mode sensors are *field strength measuring devices*, which can also be used for *measuring voltage*, i.e. as "voltmeters" for a known field geometry or based on calibration. Compared with electrostatic voltage measuring devices, this *has also practically no effect* on the voltage source and draws no energy from the source. Furthermore, the *linear relationship* between field strength and current as well as significantly *higher sensitivity* are advantageous. Thus, generator-mode sensors are suitable for high-impedance measurements of constant or very slowly changing variables, such as for recovery voltages or DC potentials.

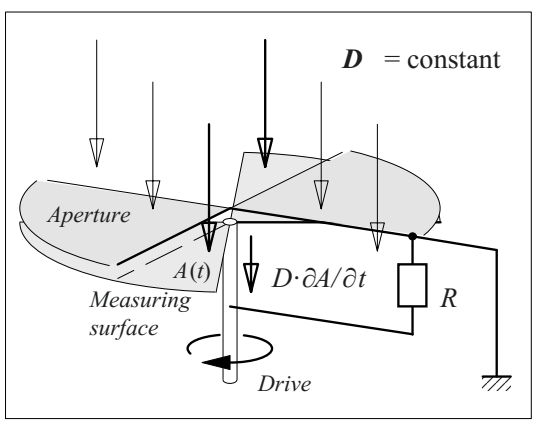

Figure 6.3.3-4: Measurement of static and steady-state electric fields by variation of measuring surface area A(t) with time in the field shadow of a grounded aperture (fieldmill voltmeter).

6.3.3.5 Electro-optical and Magneto-optical Field Sensors

Electric or magnetic fields can influence the optical properties of different materials, and hence the *polarization state* can be modulated by light. Thus, there are very attractive options for *potential measurements and reaction-free field strength measurements* in high voltage engineering. At the same time, high bandwidths can be attained. In particular, induced double refraction (Kerr effect and Pockels effect) as well as induced optical activity are used (Faraday effect), Figure 6.3.3-5.

a) Induced birefringence (double refraction)

A birefringent material has two different refractive indices and phase velocities for light that oscillates parallel to and perpendicular to the so-called optical axis. This anisotropy can be predetermined by the molecular or crystalline structure or can be caused or influenced (induced double refraction) by *external influences* (mechanical strains, electric fields).

Note: Generally, optically effective microscopic structures are orientated very rapidly by electric fields (the so-called *relaxation time* for the standard insulating liquids is in the sub-nanoseconds range); in solids, however, the *usable bandwidths* can be restricted by piezoelectric effects.

Under the effect of an **electric field**, even in isotropic substances, an *optical axis* that is parallel to the field is induced, Figure 6.3.3-5. Linearly polarized light whose polarization direction is set, for example, at 45^0 to the optical axis, is thus split into *two rays* of equal intensity that *oscillate perpendicularly to each other.* The two rays propagate with different phase velocities and thereby experience a *phase shifting* $\Delta\varphi$.

Under the so-called **Kerr effect** $\Delta\varphi$ is proportional to the square of the field strength:

$$\Delta\varphi = 2\cdot\pi\cdot K\cdot l\cdot E^2. \qquad (6.3.3\text{-}1)$$

Here, l is the effective length of the optical path in the field. The Kerr constant K is dependent on the material, the temperature and the wavelength of the light. E is assumed to be constant.

Example: Approximately, $K = 3\cdot10^{-15}$ m/V^2 for **insulating oil** [366]. With a field strength $E = 3$ kV/mm and effective length $l = 10$ cm, $\Delta\varphi = 1°$ is obtained. Therefore, in many materials, high field strengths and long lengths are necessary to attain an appreciable phase displacement.

Note: If the field strength E is not constant along the optical path x, the phase shifting must be calculated by integration:

$$\Delta\varphi = 2\cdot\pi\cdot K\cdot\int_0^l E^2(x)\,\mathrm{d}x \qquad (6.3.3\text{-}1a)$$

Few naturally birefringent crystals exhibit the linear **Pockels effect** [141], [152]:

$$\Delta\varphi \sim l\cdot E. \qquad (6.3.3\text{-}2)$$

Here, the direction of propagation of the light is along the natural optical axis so that the natural double refraction is not effective. Double refraction that is effective for the light is induced by an external field.

Superimposition of phase shifted light components results in **elliptically polarized light**, Figure 6.3.3-5. In the special cases, $\Delta\varphi = \pi/2$, $3\pi/2$ ... results in circular polarized light, for $\Delta\varphi = \pi$, 2π ... linear polarized light reappears.

In the arrangement according to Figure 6.3.3-5, a *second polarizer is* used as an *analyzer* to transfer the modulation of the polarization state into an *intensity modulation:* in the case of crossed polarizers (+/- 45° with respect to the induced optical axis), the intensity after the analyzer for $\Delta\varphi = 0$ is equal to zero. Even for $\Delta\varphi = \pi$, polarized light is again obtained, but with planes of polarization rotated by 90°, so that the total intensity can pass through the analyzer. For arbitrary phase displacements $\Delta\varphi$, the *intensity ratio* $I_2/I_1 \sim E_{L2}^2/E_{L1}^2$ (after/before the analyzer) can be calculated from the field components of the elliptically polarized light $\boldsymbol{E}_L = \boldsymbol{E}_{L||}+\boldsymbol{E}_{L\perp}(\Delta\varphi)$ emerging from the analyzer:

$$I_2/I_1 = \sin^2(\Delta\varphi/2) \qquad (6.3.3\text{-}3)$$

Very strong *non-linear characteristics* for **intensity modulation** are obtained from Eq. (6.3.3-1) and also (-1a) and (-3). For small phase shifts or small field strengths, *sensitivities are very low*. For very large angles $\Delta\varphi >$ 90°, characteristics are not unique since Eq. (6.3.3-3) is a periodic function. For a measurement, it must therefore be tracked in which section of the characteristic the measurement is made, Figure 6.3.3-6.

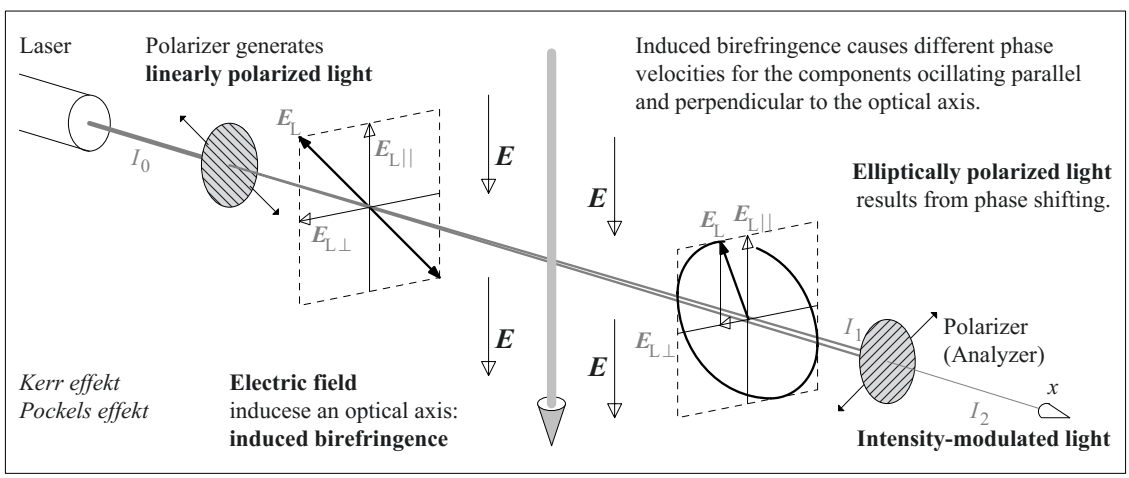

Figure 6.3.3-5: Elektro-optical field strength measurment through induced birefringence.

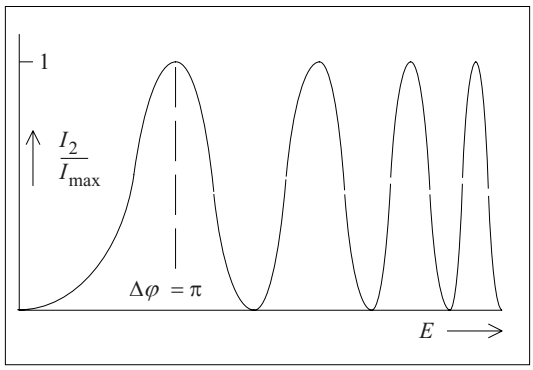

Figure 6.3.3-6: Characteristic of a simple Kerr cell.

Note: Intensity variations do not only arise from phase shifts but also from intensity variations of the *light source* or from (slow) changes in the optical path. Therefore, the intensity signal containing the field strength information must be related to a *reference signal* obtained, for example, by means of a beam splitter.

The characteristic illustrated for the quadratic *Kerr effect* in Figure 6.3.3-6 is analogously also applicable to the linear *Pockels effect*, but the maxima and minima follow at equal intervals, because the phase shift increases linearly with the field strength in accordance with Eq. (6.3.3-2).

b) Induced optical activity

For optically active materials, the *plane of polarization* of traversing light is *rotated*. Here, there are material causing anti-clockwise or clockwise rotation (direction of view against the direction of light). This natural optical activity can be used inter-alia for determining the concentration of solutions (e.g. sugar solutions).

Note: Optical activity can be described by different phase velocities for two oppositely rotating *circularly polarized waves*, which on superimposition always result in linearly polarized light, but with rotated direction of polarization. Analogously to the double refraction (birefringence) of linearly polarized waves dicussed above, this is described as *circular double refraction (circular birefringence)*.

In some materials (e.g. in *quartz* or in light-conducting *fiber optic glasses*), optical activity can be induced parallel to the direction of propagation by magnetic fields, Figure 6.3.3-7. This so-called **Faraday effect** shows a linear dependence of the angle of rotation α on the magnetic flux density B:

$$\alpha = V \cdot l \cdot B. \qquad (6.3.3\text{-}4)$$

Here, V is the so-called Verdet constant (and not a voltage). With two crossed polarizers, the modulation of the polarization state can be converted into an *intensity modulation*, whereby minimal intensity is obtained at $\alpha = 0$ and maximum intensity is obtained at $\alpha = \pi/2$. Also in this case, a quadratic relationship is applicable:

$$I_2 / I_1 = \sin^2 \alpha \qquad (6.3.3\text{-}5)$$

With Eq. (6.3.3-4), this forms a non-linear characteristic that is not unique. Figure 6.3.3-6 is likewise applicable; however, the maxima and minima follow at equal intervals, because the angle increases linearly with magnetic flux density B in accordance with Eq. (6.3.3-4).

c) Analysis of characteristic curves

Crossed polarizers according to Figures 6.3.3-5 and -7 are suitable, for example, for cells for intensity modulation in which the full range between maximum and minimum intensity is to be used. For measuring purposes, especially for small phase shifts or for small angles of rotation, *non-linearity* and *low sensitivity* are a disadvantage. Improved evaluation options are described in the following sections.

Induced optical activity: If in Figure 6.3.3-7, the *analyzer is turned back by 45°*, this acts as

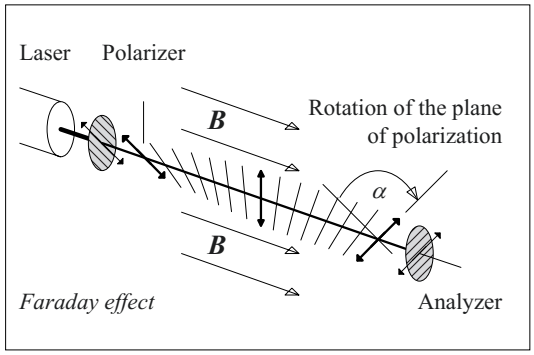

Figure 6.3.3-7: Induced optical activity.

an additional rotation of the plane of polarization by +45°. In accordance with Eq. (6.3.3-5), the *working point* shifts into the area of half intensity

$$I_2/ I_1 \quad = \sin^2(45°+\alpha) \approx ½+\alpha \qquad (6.3.3\text{-}6)$$

and into the *linear region of the characteristic* with the *highest sensitivity*, Figure 6.3.3-8.

Note: For **magneto-optical current transformers** very long effective lengths in the field direction and large angles of rotation α can be attained by winding optical wave guides, so that multiple maxima and minima are passed through. Signals must be *numerically evaluated.*

Another option is that a *reference current* must be set by a control circuit in such a way that the rotation of the plane of polarization caused by the field to be measured is reversed (compensated) in a *second Faraday cell*.

Induced birefingence: A *linearization* that is comparable with Eq. (6.3.3-6) and an *increase in sensitivity* of the *optical characteristic* are possible, even for induced birefringence (Kerr effect and Pockels effect), if the working point is adjusted for half the intensity and maximum gradient according to Eq. (6.3.3-3) for one of the components by a *phase shift* by $\Delta\varphi = 90°$:

$$I_2/I_1 = \sin^2(45°+\Delta\varphi/2) \approx ½+ \quad \Delta\varphi/2 \qquad (6.3.3\text{-}7)$$

The adjustment of this working point is *not* made by rotation of the analyzer, but by a so-called $\lambda/4$ plate, which effects a phase displacement of orthogonal light components by a *quarter of the wavelength*, that is by the above-mentioned 90°, and thus generates *circularly polarized light*.

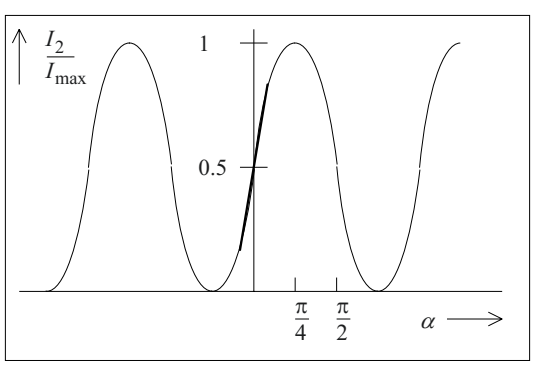

Figure 6.3.3-8: Linearization of the characteristic.

Note: Unfortunately, even for linearized optical characteristic, the **Kerr effect** is still *non-linear*, Eq 6.3.3-1. Therefore, for slowly changing fields, it is recommended to *superimpose* on the field to be measured a known *alternating field* with the angular frequency ω. The fundamental component of the light intensity with ω is then directly *proportional* to the field strength [366]:

For the measurement of a DC field E_0, the Kerr cell characteristic can be linerarized by modulation with a commparatively weak sinusoidal field $E_1 = \hat{E}_1 \cdot \sin(\omega t)$ which is superimposed to the measured field [494], [495]. The resulting field $E = E_0 + E_1$ gives the intensity

$$I_2 \sim E^2 = (E_0 + E_1)^2 =$$

$$E_0{}^2 + 2\, E_0\, \hat{E}_1 \cdot \sin(\omega t) + \hat{E}_1{}^2 \cdot \sin^2(\omega t)\,. \qquad (6.3.3\text{-}8)$$

The three components with the different frequencies $\omega = 0$, ω and 2ω can be separated by means of filters. The second term is proportional to the measured quantity E_0 and the third term can be used as a reference signal.

d) Applications

While using electrooptical sensors it must be noted that the signals can also be superimposed by the mechanical *elasto-optic effect* (birefringence induced by mechanical stresses). Electro-optical sensors must, therefore, be protected against *mechanical stresses and vibrations*. Further, it must be noted that the constants in Eqs. (6.3.3-1), (-2) and (-4) do not only depend on the material but also on the *wavelength* of the light used and on the *temperatur*e, so that according *corrective calculations* may be necessary.

In optical systems, fluctuating *intensities* (caused by the light source) or changes in the *optical path* (caused by contaminations or ageing) must be monitored and compensated (*drift compensation*). This is simpler to implement for short periods in test-setups than in instrument transformers for current and voltage, from which a very high *long-term stability* (durability) is expected.

Note: Options for drift compensation are optical *reference paths*, *modulation* of light intensity, regulated *compensating circuits* as well as methods for determin-

ing *phase shifts* $\Delta\varphi$ and *angles of rotation* α independently of intensity.

Owing the to difficulties mentioned, **application options** of electro-optical effects are still restricted to a few special cases:

Magneto-optic measuring transformers were developed based on the Faraday effect in optical fibers [368], see Section 6.3.5.2 with Figure 6.3.5.3 (c),

Kerr cells with larger Kerr constants (e.g. in nitro benzene) are used for the switching and modulation of light flux.

Potential-free field strength measurements are feasible with *Pockels cells* [152].

The Kerr effect is often the only option for the measurement of electric field *distributions in transparent insulating liquids*, such as in insulating oil or in water. Here, the application spectrum extends from the measurement of stationary or slowly changing fields in HVDC insulation and for electrostatic charges [366], [367], [494], [495] up to very rapidly changing periodic or transient fields of pulsed power technology in the ns range [153].

6.3.4 Voltage Dividers

Generally, high voltages are divided by many orders of magnitude (e.g. from the MV range into the 100 V range) by voltage dividers down to a level which facilitates reading with measuring instruments, oscilloscopes and transient recorders or further processing in electronic circuits and computers. A high-voltage divider always consists of a high-voltage arm (high-voltage section) and a low-voltage arm (low-voltage section) in series.

6.3.4.1 Response Characteristic

The extrapolation of the divider ratio calibrated at low voltage by many orders of magnitude to the high voltage level requires **linearity** of the components used with respect to the voltage. High voltage and low voltage sections of a divider may not change with **temperature** (or only in the same manner), so that the divider ratio is maintained even for temperature fluctuations.

Note: Temperature-independent capacitances occur in *compressed-gas capacitors*. For other capacitor dielectrics, a certain amount of *compensation* is attained by the combination of materials with positive and negative temperature coefficients. For special requirements, the *room temperature* may have to be maintained constant.

The large extent of a high voltage divider leads to distributed **stray capacitances** towards ground and high voltage electrodes. Thereby, the dynamic system behavior changes in an undefined manner and is also generally dependent on frequency, see Section 6.3.4.3.

The **dynamic response characteristic** of voltage dividers is especially important for the proper transfer of fast impulse voltage signals. It is generally determined not by frequency response measurements but by *step response measurements*, Figure 6.3.4-1.

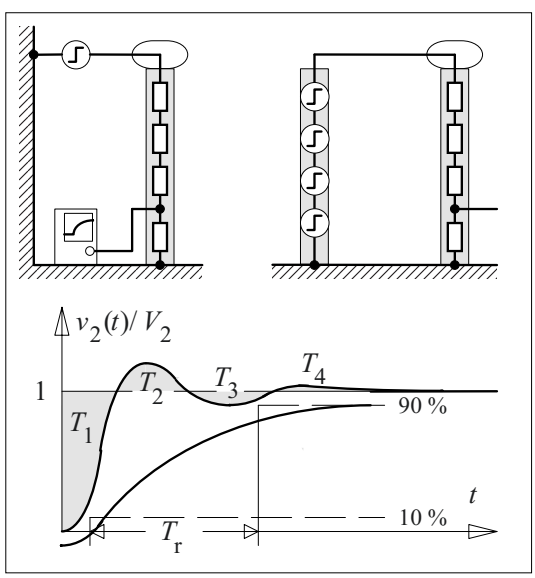

Figure 6.3.4-1: Step-response measurements at a voltage divider with concentrated and with distributed step generator (top left and right). Overshooting and aperiodic profile of step-response function with definition of a response time and a rise time (bottom).

The step-function fed into the head of the divider generates an aperiodic or slightly overshooting step-response. For this, the overshooting must not exceed 5%. In high voltage measurement techniques, sometimes the rate of rise is characterized by the **response time** T_{resp} and this is defined as the difference of the areas under the ideal step function and under the normalized step-response function $g(t) = v_2(t)/V_2$:

$$T_{resp} = \int_0^\infty [1 - g(t)]\,dt = T_1 - T_2 + T_3 - ... \qquad (6.3.4\text{-}1)$$

However, the response time is not sufficient for the characterization of of dynamic system properties, as already shown by examples with negative response times, e.g. if there is a high overshooting.

A better characterization is given by the **rise time** T_r between the 10 % and 90 % amplitude values [141]. For multiple independent elements of a measurement setup, (e.g. step function generator, divider, attenuator and oscilloscope) individual rise times are added geometrically:

$$T_r = [T_{r1}^2 + T_{r2}^2 + ... + T_{rn}^2]^{1/2} \qquad (6.3.4\text{-}2)$$

Note: Here a so-called *Gaussian system* is assumed, whose attenuation increases quadratically with the frequency. This assumption is fulfilled with satisfactory precision for many cascade connections with low-pass characteristics [141].

Example: Step-response measurement

Step-function generator, divider, attenuator and oscilloscope each exhibit a rise time of 1 ns. According to Eq. (6.3.4-2), the rise time of the recorded signal is T_r = 2 ns.

For exponentially increasing voltage-time characteristics, e.g. for *RC* elements and *LR* elements, the rise time T_r corresponds to 2.2 times the time constant τ:

$$T_r = 2.2 \cdot \tau \qquad (6.3.4\text{-}3)$$

In Gaussian systems, for *rise time* and 3 dB *bandwidth B*, the applicable relationship is

$$T_r \cdot B = 0.35. \qquad (6.3.4\text{-}4)$$

Note: For dividers with *extremely low rise times*, the *electromagnetic radiation* emanating directly from the step function generator gives rise to distortions in the step-response. They can be suppressed if the divider is situated in the cylindrical phase plane of the TEM wave which is generated by spatially distributed and synchronized step function generators [18], [19], Figure 6.3.4-1 (top right).

6.3.4.2 Divider Designs

a) Resistive voltage divider

Resistive voltage dividers are exclusively suitable for *DC voltage measurements*, Figure 6.3.4-2 (a). Owing to stray capacitance to ground, a *RC* lattice network occurs with a distinct low-pass behavior. For resistances on the high-voltage side in the GΩ range and stray capacitances in the 10 pF range, the magnitude of the divider ratio

$$r = V_2/V = R_2/(R_1 + R_2) \qquad (6.3.4\text{-}5)$$

decreases considerably even for frequencies of a few 10 Hz. The divider is no longer suitable for network frequency AC voltages.

Note: For a more accurate conclusion, a quantitative analytical estimation of the frequency response by complex calculation with a simplified equivalent circuit is possible, Section 6.3.4.3 includes an example.

b) Resistive-capacitive voltage divider

Resistive-capacitive voltage dividers (compensated resisitve voltage dividers) according to Figure 6.3.4-2 (b) are in principle suitable for all types of voltages if they fulfill the *compensation condition*

$$R_1 C_1 = R_1' C_1' = R_2 C_2 \,. \qquad (6.3.4\text{-}6)$$

The compensation condition implies that the resistive and capacitive divider ratios of the two parallel divider columns must be equal, Figure 6.3.4-3 (curve 2). Ideally, a frequency

independent divider ratio r or a rectangular step-response results.

$$r = v_2(t)/v(t) = R_2/(R_1 + R_2)$$
$$= C_1/(C_1 + C_2) \qquad (6.3.4\text{-}7)$$

If the compensation condition is not fulfilled, a frequency-dependent divider ratio or a step response with exponential transition processes results, Figure 6.3.4-3 (curves 1 and 3).

Note: If C_2 is too small, we have *under-compensation*, since C_1 is not adequately compensated. In the first instant, the capacitive divider ratio is effective and it results in a voltage step that is too high. If C_2 is too large, we have *over-compensation*, Figure 6.3.4-3 (curve 3). The capacitive divider ratio gives a very low initial voltage.

Note: During the design process of the divider, the parallel capacitances C_1' must be chosen to be so large that the stray capacitances to ground are negligible.

The divider is *only conditionally* suited for *impulse voltage measurements,* since the undamped capacitive column along with the measuring circuit inductance can lead to resonances, which must be suppressed by additional external damping resistances, see section d).

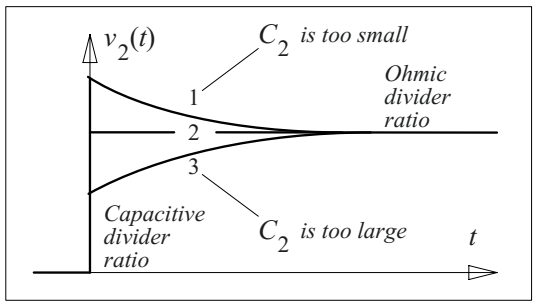

Figure 6.3.4-3: Step responses of a compensated resistive voltage divider for the cases of under-compensation (1), compensation (2) and over-compensation (3).

Despite good dynamic system behavior, **high voltage dividers** for very high voltages are not designed as compensated ohmic dividers, because *two high-voltage divider columns* are necessary for this. Often there is also no requirement for such a divider since test devices

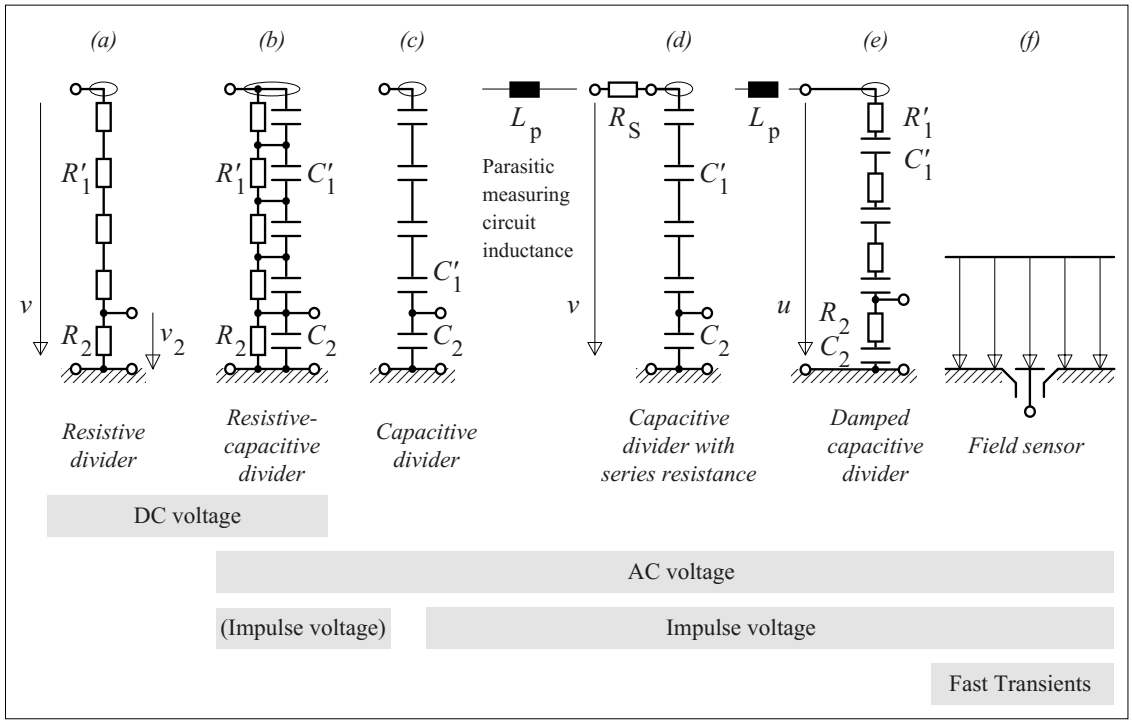

Figure 6.3.4-2: Designs of high-voltage dividers and their suitability for different types of voltages.

for AC voltages, DC voltages and impulse voltages are generally already equipped with special dividers. Besides, two separate dividers can be used more flexibly.

Compact **high voltage probes** of up to several 10 kV are designed as compensated voltage dividers. Spatially separated high-voltage and low-voltage sections of C_1/R_1 and C_2/R_2 are connected via a matched coaxial line, which includes a distributed resistance for attenuation of traveling-wave oscillations. The probe is balanced with a series-connected signal shaping network [141]. The probe forms a mached unit with the actual head, the connecting line and the termination network, lengthening of the connecting cable is generally *not* possible.

Note: Other areas of application of the compensated divider are compact structures *in devices* with low voltages or *secondary dividers* of high bandwidth in the low voltage range.

c) Capacitive dividers

Capacitive voltage dividers, Figure 6.3.4-2 (c), can *not* be used for DC voltage measurements, since a completely undefined resistive divider ratio results from undefined insulation resistances and from the load impedance. Capacitive dividers are especially suitable for *AC voltage measurements* in a wide frequency range, because although stray capacitances bring about a change in the magnitude, there is **no frequency dependence** of the divider ratio

$$r = v_2(t)/v(t) \qquad = C_1/(C_1 + C_2) \qquad (6.3.4\text{-}8)$$

In the case of *impulse voltage measurements*, similar to compensated dividers, sufficient external damping of the measuring circuit must be ensured, see section d). Owing to their simple construction, capacitive dividers are generally used in small, e.g. single-stage impulse circuits up to the 100 kV range.

d) Capacitive divider with series resistor

Capacitive voltage dividers lead to relatively weakly damped measuring circuits whose inductances increase with the height of the divider. For critical damping, a damping resistor whose resistance depends on the measuring circuit inductance and the divider capacitance is necessary according to Figure 6.2.3-8 and Eq. (6.2.3-15), see Figure 6.3.4-2 (d).

Example: For a divider with 500 pF and a circuit inductance of 20 µH (that corresponds to a measuring circuit length of about 20 m), a damping resistance of $R_D \geq 100\ \Omega$ is obtained.

It must be noted that a damping resistance R_D and a divider capacitance C_1 form a *RC*-element whose rise time

$$T_r = 2.2 \cdot R_D C_1 \qquad (6.3.4\text{-}9)$$

must be much shorter than the rise time of the impulse voltage to be measured.

Example: In the above-mentioned example, a *rise time of the divider* of $T_r = 2.2 \cdot R_D C_1 = 110$ ns results, and this is still adequate for the measurement of a *lightning impulse voltage* of 1.2/50 µs. Nevertheless, *fast transients or traveling waves* in the ns range can no longer be measured.

e) Damped capacitive dividers

Damped capacitive dividers (Series-damped capacitive dividers, "Zaengl dividers") are the typical *impulse voltage dividers* for high and highest voltages. Damping resistors are integrated into the divider column in a distributed arrangement in series with the capacitors, Figure 6.3.4-2 (e), not only to damp the *inductance* of the low voltage circuit, but also to suppress *traveling waves* that could be formed on a long un-damped divider column. At high frequencies, the ohmic divider ratio is effective owing to low capacitive impedances, and the capacitive divider ratio is effective at low frequencies owing to high capacitive impedances. If the compensation condition

$$R_1 C_1 = R_1' C_1' = R_2 C_2 \qquad (6.3.4\text{-}10)$$

is met, a divider ratio *independent of frequency* theoretically results. Damped capacitive dividers with distributed resistances therefore (if they fulfill the compensation condition) have a

significantly *higher upper cut-off frequency* than capacitive dividers with concentrated series resistors.

Damped capacitive dividers cannot be used for *DC voltage measurements* since no defined parallel resistances exist, similarly to capacitive *dividers*. The lower cut-off frequency is determined by the discharging of C_2 through the coupling circuit.

f) Field sensors

Very fast *traveling wave processes* and *fast transients* can be measured with field sensors that are integrated into the ground electrode and which take up the displacement current components of electromagnetic waves, Figure 6.3.4-2 (f). Field sensors are described in detail in Section 6.3.3.

6.3.4.3 Stray Capacitances

The large extent of a high voltage divider leads to distributed **stray capacitances to ground**, through which currents are carried over to ground, bypassing the low voltage section, Figure 6.3.4-4. Thus, the *transmission ratio* changes in an undefined manner and is also largely *frequency dependent*.

Example: Ohmic divider with stray capacitance to ground

Instead of the divider ratio, the current $\underline{I}$ through the divider column is calculated taking into consideration a *stray capacitance to ground* that is assumed to be concentrated. Here the comparatively small low voltage resistance can be ignored, Figure 6.3.4-5 (top). The analysis of the network with the help of a complex calculation leads to the following current magnitude:

$$I = \frac{V}{R \cdot \sqrt{1 + (\frac{\omega CR}{4})^2}} . \qquad (6.3.4\text{-}11)$$

In the case of *DC voltages*, the *undisturbed* divider current $I_0 = V/R$ results. For *AC voltages*, the divider current and divider ratio are *frequency dependent* (*low-pass performance*), Figure 6.3.4-5 (bottom). For example, for R = 1 GΩ, C = 10 pF and f = 50 Hz, a ratio of I/I_0 = 0.79 is obtained. That is, the error already amounts to 21%.

Only the purely **capacitive divider** remains *independent of frequency*, even under the effect of stray capacitances, because the entire

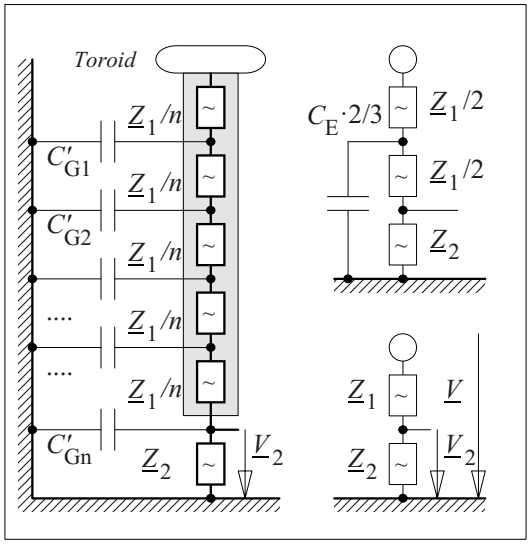

Figure 6.3.4-4: High voltage divider with distributed stray capacitances to ground (lattice network structure), as well as equivalent circuits with and without concentrated stray capacitances to ground.

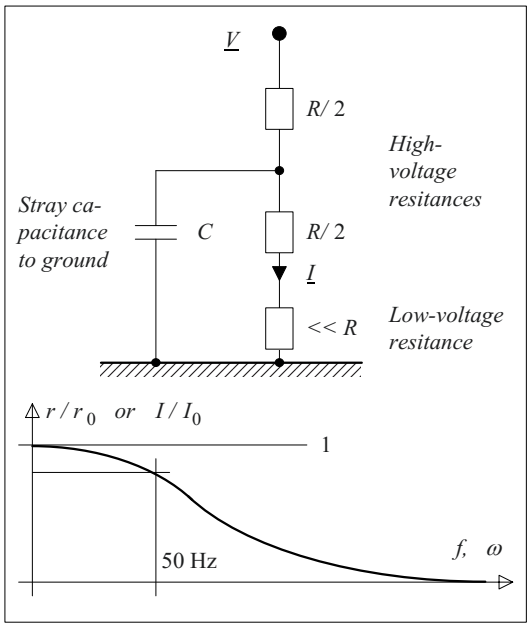

Figure 6.3.4-5: Resitive divider with stray capacitances.

equivalent network consists of capacitances. Therefore, it is suitable for the measurement of impulse voltages and AC voltages over a wide range of frequencies. However, here too, the magnitude of the divider ratio is changed by a constant absolute value.

Various **corrective measures** against the effect of stray capacitances are possible:

- A field grading *toroid* of large size which is mounted at the top of the divider column enforces a field direction parallel to the divider in the area around the divider, so that no displacement current flows in the transverse direction. However, very large toroid diameters are necessary for this.
- Using a *funnel-shaped top electrode and ground electrode* is favorable since they considerably reduce the feedthrough between the environment and the divider column, Figure 6.3.4-6. Furthermore, displacement currents, which are coupled via stray capacitances on the high-voltage side, are de-coupled again on the ground side in a symmetrical structure so that there is considerable compensation of the interferences in the measurement signal.
- In the case of *compressed-gas capacitors*, the high-voltage electrode can be designed in such a way that it shields the measuring capacitance against the surroundings, Figure 2.3-3 (center).

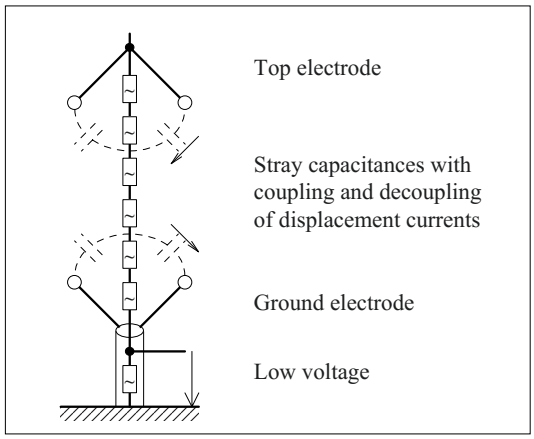

Figure 6.3.4-6: Measures against stray capacitances.

- By selecting *larger divider capacitances* in the nF range, transverse stray capacitances in the pF range can often be ignored.
- With *large distances* to the walls and with *low overall height* of the divider, the transverse stray *capacitances* can be kept small.
- In some cases, *calibration* of the divider in the *original test circuit arrangement* at the application site is necessary.

6.3.4.4 Low-voltage Arms

For divider ratios of the order of magnitude of $r = 1{:}10^3$ to $1{:}10^4$ and for high-voltage capacitances in the range of 100 pF to 1 nF, very large capacitances result for the *low-voltage arm.*

With $C_2 = 1$ µF and a parasitic self-inductance $L_2 = 100$ nH (corresponding to a line length of about 100 mm), for example, a *series resonance* with a frequency of $f_2 = 0.5$ MHz or a period of $T_2 = 2$ µs occurs. The oscillation, for example, can be induced by the impulse voltage 1.2/50 µs to be measured and can lead to considerable measurement errors.

It is therefore necessary to design low-voltage arms to be *extremely low-inductive* to shift the self-resonances into a frequency range in which the measurement is no longer distorted.

Very *low-inductive capacitors*, *if possible with frontal contact areas* and without connecting wires, must be used first for this, Figure 6.3.4-7, Section 7.3.3.2. The capacitors must be connected in parallel with lowest-possible inductance. The best solution is a circular arrangement between metallic *circular discs* and with a measurement tap on the axis. By using the *coaxial arrangement* of capacitors and taps, magnetic field-filled loops are minimized.

Note: If a smaller divider ratio is opted for, low-voltage capacitances are also smaller and resonance frequencies are higher. The higher output voltage of the divider must then be further divided with a *secondary divider.*

6.3.4.5 Coupling Circuits

Capacitive and damped capacitive dividers must be loaded with special *coupling circuits*, so that the divider ratio remains largely *independent of frequency*. The use of measuring cables of different lengths must be possible for this, other than for high-voltage probes with fixed cable lengths.

As an *example*, the coupling of a high-impedance oscilloscope to a damped capacitive divider is explained, Figure 6.3.4-8:

For very quickly changing signals, the impedance of the low-voltage arm corresponds to the resistance $R_2 << Z$. This is loaded with high resistance by the series connection of the series resistance $Z\text{-}R_2$ and the cable impedance Z, i.e. with $(Z\text{-}R_2)+Z \approx 2Z$. A traveling voltage wave with the amplitude $v_2(t)/2$ at the cable input travels into the cable, it corresponds to the low voltage $v_2(t)$ of the divider that is divided by a factor of 2. At the end of the cable, the high-resistance input impedance of the oscilloscope $R >> Z$ is similar to open-ended line termination, at which the traveling voltage wave is reflected with doubled value $2 \cdot v_2(t)/2 = v_2(t)$, so that the original amplitude occurs again. The returning wave is absorbed nearly without reflection at the input side by $(Z\text{-}R_2)+R_2 = Z$, because C_2 exhibits a very low impedance.

Note: By charging the oscilloscope input capacitance (approx. 15 pF) via the cable impedance (approx. 50 Ω), the *rise time of the measurement system* is increased by a proportion of approximately 1.7 ns that is to be added in accordance with Eq. (6.3.4-2).

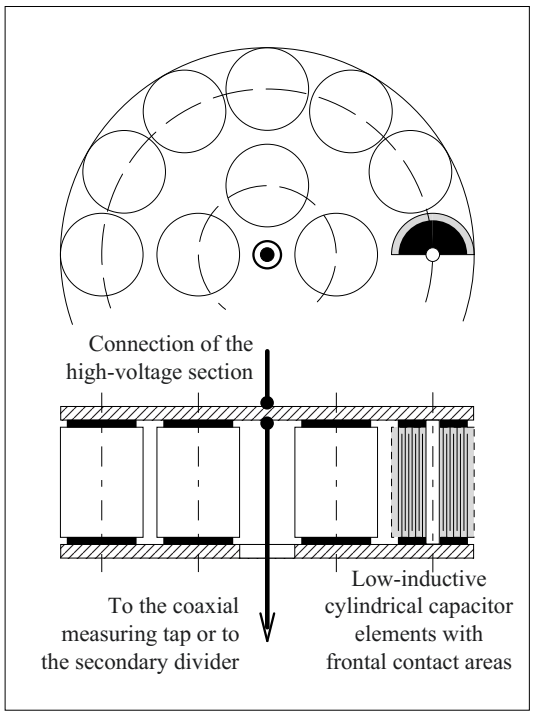

Figure 6.3.4-7: Low-inductive design of a capacitive divider's low-voltage arm.

For *slowly changing processes*, the capacitive divider ratio is effective. Thus, the cable capacitance C_C lies parallel to C_2 and this slightly distorts the divider ratio. C_2 is chosen to be so large in the µF range that standard cable lengths do not have any undue distortion. A discharge with a time constant in the range of seconds takes place via $R \approx 1$ MΩ, so that even very slowly changing processes can be measured.

Other coupling circuits are given in the specialist literature [141].

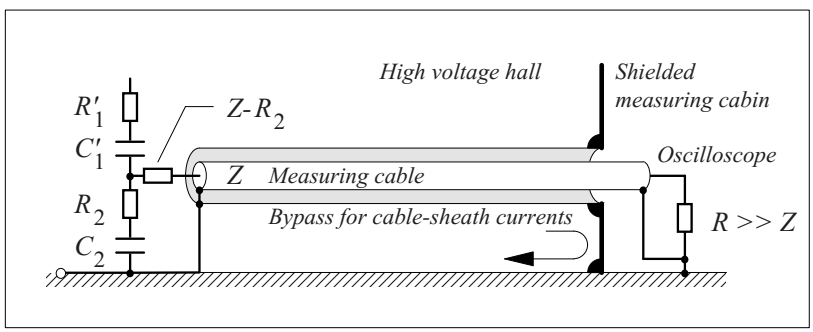

Figure 6.3.4-8: Coupling of a high-impedance oscilloscope to the low-voltage arm of a damped capacitive divider via a measuring cable with an additional shield as a bypass for the defined conduction of cable-sheath currents.

6.3.5 Instrument Transformers

Instrument transformers serve as operating equipment of the electrical supply network primarily for recording the *voltages and currents* at *operating frequency*. They must be measured in the *normal operating condition* of the network with a precision defined by the accuracy class. Moreover, *disturbances* in the network (over-voltages/under-voltages, short-circuit currents) must be detected.

Instrument transformers are designed to be *single phase*; three units are required for three phase systems.

Instrument transformers are increasingly manufactured with *silicone-shed composite isolators* and with *oil-free dielectrics* (cast resin or film insulation with SF_6), since the explosion of oil-filled equipment with porcelain insulators can lead to considerable consequential damages.

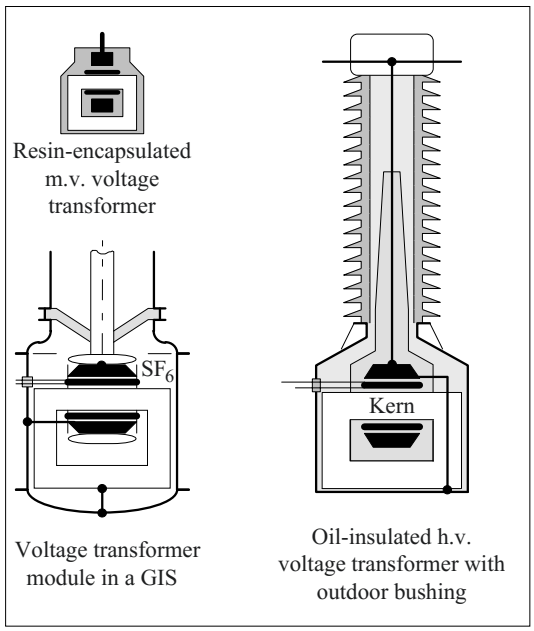

Figure 6.3.5-1: Inductive voltage transformers.

6.3.5.1 Voltage Transformers

a) Inductive voltage transformers

Inductive voltage transformers are comparable with *test transformers* that are excited on the high-voltage side and are loaded on the low-voltage side with a measurement impedance, Figure 6.3.5-1. For adequate loading, the capacitive voltage rise (resonant overvoltage) is negligible. Voltage transformers are operated at operating voltage in the approximately linear region of the magnetization characteristic. From the transmission ratio, the high voltage V_1 is obtained:

$$V_1 = V_2 \cdot n_1/n_2 \qquad (6.3.5\text{-}1)$$

Recording the r.m.s. value is of importance here. It was previously implemented by a true r.m.s. responding instrument; today the r.m.s. value is determined by the evaluation of the digital signal. The upper *cut-off frequency* of the inductive voltage transformer amounts to a few kHz in the medium-voltage range and for high-voltage transformers it decreases to a few 100 Hz.

Inductive voltage transformers are largely used in the *medium voltage range*, frequently in dry construction as *resin-encapsulated transformers*, Figure 6.3.5-1 (top left). There are also voltage transformers for the *high-voltage range* that are insulated with films and SF_6 and are used in gas-insulated switchgear, Figure 6.3.5-1 (bottom left). Classic oil-insulated voltage transformers consist of a transformer insulated with oil and paper in a dead-tank construction and an outdoor-oil bushing, Figure 6.3.5-1 (right).

b) Capacitor voltage transformer

At high voltages, iron cores and windings of inductive voltage transformers are very large, therefore it is more economical to use **capacitior voltage transformers** together with inductive transformers in *resonance circuits* (*resonance capacitor transformers*), Figure 6.3.5-2 (left). The high voltage V_1 is divided by a *capacitive divider* down to a medium voltage V_2 in the range of approx. 10 to 30 kV. The measurement devices with the load resis-

tance R are connected as so-called *burden* via a *reactor* (inductance L) and an *inductive voltage transformer*. The inductive transformer can thus be designed as a compact medium-voltage transformer.

The inductance L and the capacitance C_1+C_2 form a *resonance circuit* at the fundamental power frequency of the network f_0. In the case of resonance

$$f_0 = 1/\{2\pi\,[L(C_1+C_2)]^{1/2}\}, \qquad (6.3.5\text{-}2)$$

the voltage V_R is independent of the *magnitude of the burden (load) R* so that the reading is basically independent of the number of measurement devices connected in parallel:

$$\underline{V}_R/\underline{V}_1 = C_1/(C_1 + C_2) \qquad (6.3.5\text{-}3)$$

Note: Eq. (6.3.5-3) can be derived from the equivalent circuit in Figure 6.3.5-2 (bottom right) by complex calculation with the condition Eq. (6.3.5-2). For illustration purposes, no-load operation ($R' \to \infty$) for which a *capacitive divider ratio* results owing to the lack of a load is considered. For the loaded divider ($R' < \infty$) a *voltage decrease* is to be expected and it is directly balanced by a *resonance overvoltage*.

The fact that the output signal was independent of the *load* and the possibility to even supply the older protective relays with *higher power consumption* was of great advantage in the days of analog power system management.

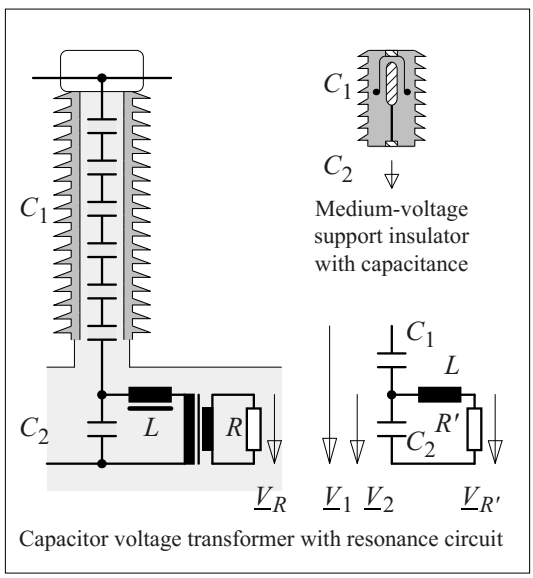

Figure 6.3.5-2: Capacitor voltage transformer.

Pure **capacitive voltage transformers (dividers)** can supply only very high-impedance loads with lower power consumption. Hence, the signal that has been capacitively divided must be further processed electronically. Thus, a constant load for the divider, a higher *bandwidth* for recording the signal as well as unlimited options for *further processing* of signals with respect to power system management and with respect to network protection are achieved. An inductive voltage transformer is no longer required.

Capacitive, resistive or **compensated voltage transformers (dividers)** can be used even in the *medium voltage range*, Figure 6.3.5-2 (top right). For example, it is possible to encapsulate a cylindrical capacitor or resistor elements in an epoxy-resin **support insulator** [363], [364]. Thus, the transformer or divider does not take up its own space and can contribute to the simplification of medium-voltage switching systems. Along with an electronic evaluation unit, the low-voltage elements are connected to the lower side of the insulator.

6.3.5.2 Current Transformers

a) Inductive current transformers

Inductive current transformers must carry the conductor(s) at high-voltage potential as *primary winding* via a transformer-type current transformation unit, Figure 6.3.5-3 (a), (b). If the conductor is directly fed through a circular closed iron core, the primary winding consists of only one turn. The inductive current transformer is thus comparable to a Rogowski coil (but *with an iron core*), see Figure 6.3.7-1. The *secondary winding* at low-voltage potential consists of many turns. It supplies the transformed current into the secondary circuit and this must *not be interrupted* (!) to prevent overvoltages and therefore has to be protected with *overvoltage arresters*.

Note: Short circuit currents are often indicated to be too *low* owing to saturation of the iron core and owing to the suppression of the direct current component.

b) Current transformers with high-voltage insulation

In **medium voltage applications**, it is common to use compact and dry inductive current transformers that are embedded in *cast resin* (*resin-encapsulated current transformers*). Moreover, *Rogowski coils* and inductive *magnetic field sensors* with electronic signal integration can be integrated in components of switchgear assemblies, for example in cable connectors [365].

In **high voltage applications**, the high voltage difference between the primary winding and the secondary winding at ground potential places particularly high demands on the *insulation* within the current transformer.

In the case of classic **crossed-ring-core transformer**, the conductor is fed into the grounded tank and out again with the help of a capacitively graded bushing, Figure 6.3.5-3 (a). The bushing is thus thermally loaded by the doubled primary current. Within the transformer, the high voltage is to be insulated between primary winding and the core, tank and secondary winding. The classic insulation system is oil-paper with a bushing insulator made of porcelain.

At the so-called **top-assembly current transformer**, the tank with the inductive transformer is at the high-voltage potential and forms the head of the transformer, Figure 6.3.5-3 (b). The core and secondary winding are at ground potential and must be insulated against the tank and conductor (primary winding) at high-voltage potential. The supply wires for secondary windings are fed into the head with an inverse capacitively graded bushing that is only loaded by secondary current. Films that have been impregnated with SF_6 and silicone-shed composite insulators are implemented as the insulation system. In this way, exploding porcelain and burning oil are prevented in the event of damage.

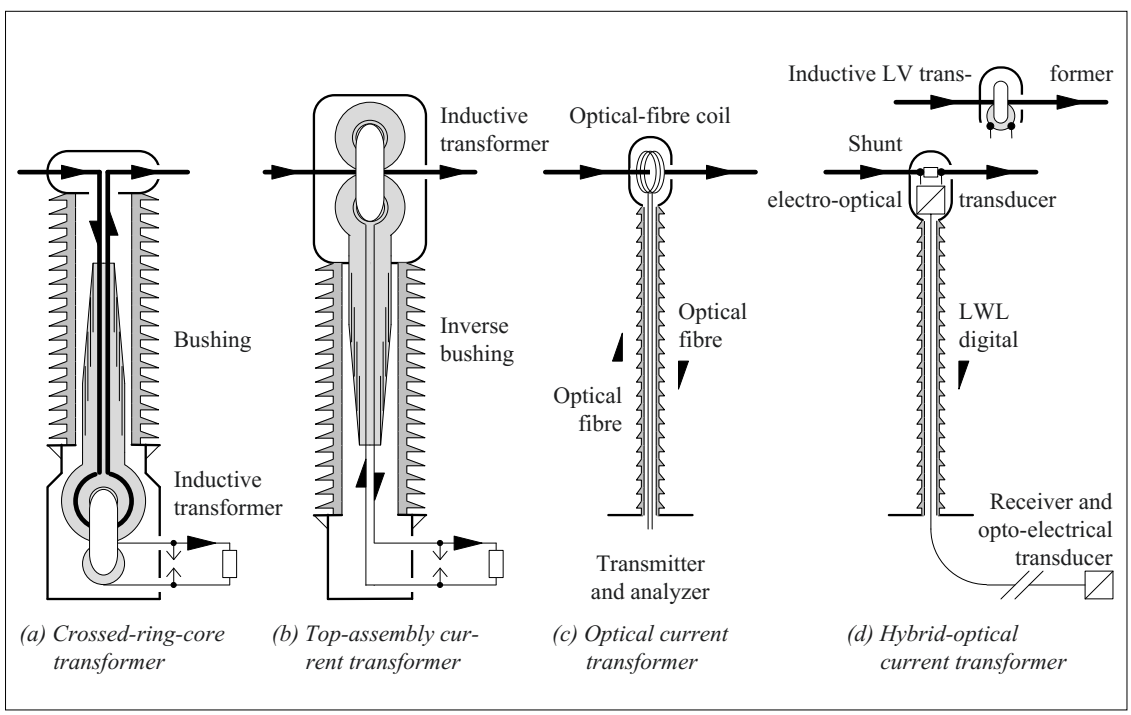

Figure 6.3.5-3: Current transformers.

c) Transformers without high-voltage insulation

With respect to insulation technology, favorable conditions for the installation of current transformers are found in *bushings* and *gas insulated switchgear*. Here the conductor is fed centrally through the circular iron core and the secondary winding without interruption. The current transformer is placed in an *area that is shielded* from the electric field, such as above the grounded grading layer of the bushing, Figure 6.4.8-3, or in an ring groove in the outer conductor of a coaxial arrangement, Figure 6.3.7-1. The transformer must have an adequate internal diameter to be able to accommodate the bushing or the conductor insulated by the SF_6 gas.

d) Current transformers with potential separation

Modern options for potential free signal transmission allow completely new current-transformer concepts. Current signals can be recorded directly on the conductor at the high-voltage potential and, for example, can be transmitted via optical waveguides across *any potential differences* to a receiving unit at *any position*, Figure 6.3.5-3 (c), (d).

A **magneto-optical current transformer**, for example, can be employed with a coil shaped *optic fiber* wound around a conductor [368]. The magnetic field parallel to the fiber causes a rotation of the plane of polarization of the polarized light. The angle is proportional to the length of the light path and the strength of the magnetic field (*Faraday effect*). This rotation can be recorded by various methods; in the simplest case, the modulation of the polarization condition is converted with the aid of an optical polarizer and analyzer into an intensity modulation [141], see Section 6.3.3.5. While designing the current transformer, compensation for *intensity fluctuations* in optical system and for *temperature influences* on the optical properties must be carried out. Moreover, it must be noted that even *mechanical* loads and vibrations can influence optical properties. The high bandwidth of the analog optical transmission is an advantage. An auxiliary power supply at high-voltage potential is not necessary.

Hybrid-optical current transformers measure the current at the high-voltage potential with a conventional *inductive current transformer* (for alternating current) or with a *current–sensing resistor* or measuring *shunt* (for direct current). Thus, the measurement signal is provided with precision and reliability known for conventional current transformers and without any problems with regard to insulation. The electrical signal is transmitted in *digitized* form over the *optical path* to the receiver at ground potential. The need to supply the electronics at high-voltage potential with *auxiliary power* is a disadvantage. For this purpose, optical, capacitive or inductive transmission procedures are considered.

6.3.6 Measurements of R.m.s. Value, Peak Value and Harmonics

The peak value that is significant for breakdown is primarily to be recorded during measurements in the *high voltage laboratory*. The measurement of r.m.s. values is important in the *power supply network*. Various circuits are available for this along with series impedances, capacitances, transformers and dividers. A few examples are given in the following sections.

Resistive and capacitive series impedances along with r.m.s.-responding current measurement instruments are used in measuring the *r.m.s. value* of power frequency AC voltages. Ohmic series resistors are also suitable for measuring *DC voltages*. With capacitive series impedances, it must be noted that in the case of *voltages having harmonic distortions,* incorrectly high values are shown since the harmonic contents of the voltage drive disproportionately large currents owing to their higher frequencies:

$$I_k = k \cdot \omega_0 C \cdot V_k \qquad (6.3.6\text{-}1)$$

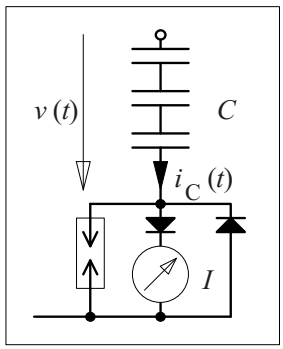

Figure 6.3.6-1: Measurement of peak value of AC voltages according to Chubb-Fortescue.

For series impedances, hazardous contact voltages can occur on the low-voltage side if the current path is interrupted. An overvoltage protective circuit must prevent this.

The circuit according to **Chubb-Fortescue** enables the measurement of the *peak value* $\hat{v}$ for periodic *AC voltages*, Figure 6.3.6-1. The current $i_C(t)$ that is impressed by the capacitive series impedance is proportional to the derivative of the voltage with respect to time:

$$i_C(t) = C \cdot \partial v / \partial t \qquad (6.3.6\text{-}2)$$

The reading i_M of a moving-coil instrument corresponds to the mean value of the rectified current that is developed by integration of the positive half-wave oscillation between $t = 0$ and $t = T/2$:

$$i_M = \frac{1}{T} \int_0^{T/2} C \frac{\partial v}{\partial t} \, dt = \frac{C}{T} \int_{-\hat{v}}^{+\hat{v}} dv \qquad (6.3.6\text{-}3)$$

Here the instants $t = 0$ and $t = T/2$ correspond to the current zero and the negative and positive maxima of the voltage respectively. Proportionality between the displayed mean value of the rectified current and the voltage peak value results from Eq. (6.3.6-3):

$$i_M = C \cdot f \cdot 2 \cdot \hat{v} \qquad (6.3.6\text{-}4)$$

Note: If the voltage profile shows *intermediate maxima*, additional current zeros occur and result in a faulty reading.

Note: The diode that is anti-parallel to the measurement branch obstructs the charging of capacitance *C*.

While using voltage dividers, the peak value can be measured by **peak detection and peak value storage**. Here, charging a measurement capacitor C_M via a diode prevents the decrease in stored measurement voltage for a decreasing divider voltage, Figure 6.3.6-2. This principle can generally be used for *AC voltages and impulse voltages*.

The described basic circuit according to *Davis, Bowdler, and Standring* is subjected to systematic errors due to the discharging of C_M, the parallel connection of C_2 and C_M in the recharging phase and the parallel connection of the discharging resistance R_D and the low voltage capacitance C_2. Therefore, a series of improved circuits, such as a *two-branch circuit* (with an equalizing branch) for AC voltage measurements according to *Rabus*, circuits with no-current, *controlled charging* by active components or *sample and hold* elements with operational amplifiers for the storage of non-recurrent processes are available [141].

Note: Reading electronic peak voltage measurement devices is often sensitive to *unwanted electromagnetic coupling* by impulse voltages. Besides ensuring the necessary electromagnetic compatibility, the displayed peak value must also be definitely checked using the oscillographic recording of the impulse voltage profile.

The possibilities of **digital signal processing** also include the calculation of *r.m.s values and peak values* from the signal-time characteristics recorded with high bandwidth. This can also be used for examining the harmonic distortion spectrum in the supply network by

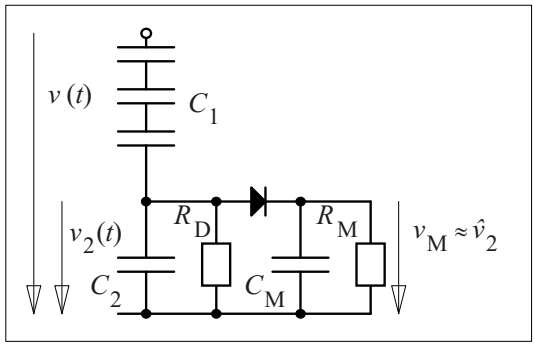

Figure 6.3.6-2: Basic circuit for peak detection and peak value storage in a measurement capacitor.

Fourier analysis, which is gaining importance since the increasing number of power electronic consumers and operating equipments lead to non-sinusoidal currents and voltage drops at the network impedances. Owing to this, the recommended "voltage quality" is possibly impaired [154]. *Transition processes* in the network to some extent lead to increased deviations from the stationary operating condition [155] and must be recorded by relevant broadband measurements with transient storage.

6.3.7 Current Measurement

Measurement of currents with *inductive current transformers* in the power supply network was described in Section 6.3.5.2. **Current probes**, whose magnetic circuit can be opened like tongs to enclose a conductor at low voltage, are based on the same principle. Depending on the type of the magnetic material used and the connected signal amplifier, even large bandwidths are possible.

So-called **Rogowski coils** are inductive current transformers that can be used even for extremely *rapidly changing currents*. Here, according to the theory of electrically long magnetic sensors, it must be ensured that the coil with the surrounding shield forms a traveling-wave line with constant characteristic impedance, which is operated in short circuit mode and for which the magnetic coupling is uniformly distributed over its circumference, Figure 6.3.3-2, Section 6.3.3.2, [5], [145], [146], [149], [150]. This implies that a Rogowski coil arranged *concentric to the current conductor* can measure current profiles, whose *rise times* are considerably *shorter* than the *propagation time along the coil*, Figure 6.3.7-1. For the commonly *undefined arrangement*, the current rise times must be considerably *longer* than the propagation time along the coil, so that the signal is not superimposed by transient oscillations based on spatially non-uniform signal coupling.

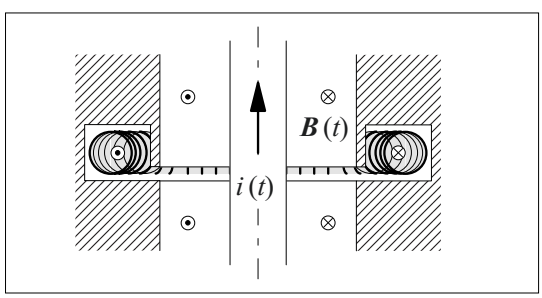

Figure 6.3.7-1: Toroidal Rogowski coil without iron core, with slitted shield and with concentric current conductor for the measurement of rapidly varying currents i(t).

Rapidly varying currents can also be measured with **current measuring resistors (shunts)**. However, the problem here is that *current path and measuring circuit* are often coupled not only by the ohmic measuring resistance but are also magnetically coupled so that measuring voltage is not proportional to the current.

It is therefore recommended to use *coaxially symmetric current measuring shunts*, in which the measuring tapping is placed in the center of a cylindrical resistor tube in a *space free of magnetic field*, Figure 6.3.7-2. Current is returned via a coaxially symmetric arrangement on a mounting flange. The *rise time* of the shunt is restricted by the effect of the current displacement. That is, a current step can be noticed within the tube with a delayed rise in voltage at the measuring tapping. Rise times can be achieved in the ns range for very thin tubes of resistance alloys.

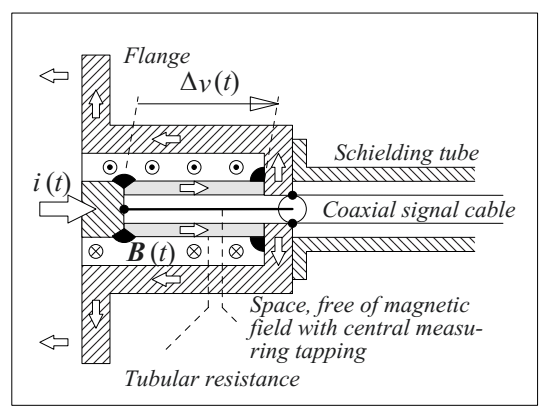

Figure 6.3.7-2: Coaxial current measuring shunt without electromagnetic induction in the measuring circuit.

Note: For *low resistive shunts*, only a low signal level results in a possibly severely disturbed electromagnetic environment. Therefore, it can be necessary to use an *additional cable shield* (e.g. in the form of a flanged tube) as a bypass for cable sheath currents.

Currents can also be measured with the help of **magneto-optical methods** (*Faraday effect*). In many crystals, such as in quartz, the *optical activity* is induced by magnetic fields, which then leads to a rotation of the polarization plane of polarized light, Section 6.3.3.5 and 6.3.5.2. In particular, the option to implement *potential-free sensors* is an advantage. An optical *Rogowski coil* can be formed with the aid of optical waveguides that are wound around the conductor that conducts the current, Section 6.3.3.5 b).

6.3.8 Electromagnetic Compatibility (EMC)

High voltage measurement technology has always meant the assurance of electromagnetic compatibility in an especially strongly disturbed environment. Therefore, experiences and knowledge of the high voltage measurement techniques form an important foundation of modern, generally applicable EMC-philosophy. The electromagnetic compatibility is by itself a large independent special discipline that will not be dealt with here [41], [141]. In the following section, only a few important EMC measures in *high voltage laboratories* are discussed, Figure 6.3.8-1.

High voltage testing fields are electromagnetically *shielded* in order to carry out sensitive **partial discharge measurements** at low background noise level. Supply lines and control lines are guided via *lead-in filters*. Before measuring a partial discharge, the background noise level must be checked by measurement. Values around 1 pC can be achieved with good shielding. Under the conditions of industrial test fields as well as for onsite measurements, optimal shielding is not always achievable. In many cases, electromagnetic compatibility can only be achieved through *narrowband partial discharge measurement* in a slightly disturbed frequency domain. Interference-free partial discharge measurement is discussed in detail in Section 6.4.2.5.

For **impulse voltage measurements**, the shielded room serves as a *protective shield* for sources of interference from the environment. Within the room, coupling through electromagnetic fields is reduced by *separations* of large dimensions. It is a rule of thumb that the distance of the devices should be approximately equal to their height. Coupling impedances are prevented by a *common mass point*

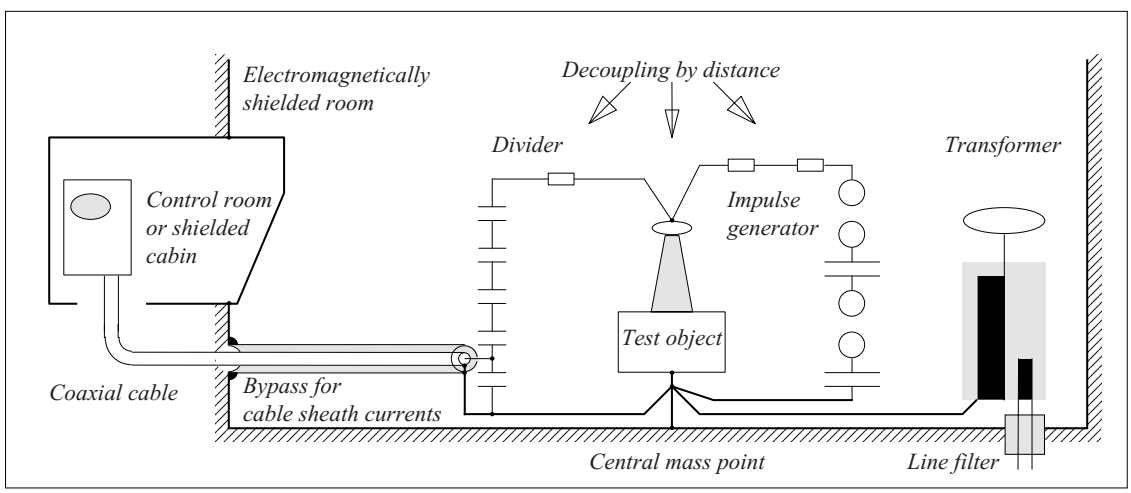

Figure 6.3.8-1: Ensuring electromagnetic compatibility for impulse voltage tests (schematic).

with very short connection lines. In particular, the connection of the divider parallel to the test object must be made so that no voltage drops occur at the supply lines on the ground side or on the high voltage side.

Cables must be led from the hall on *short paths* such that no looping occurs in which induced voltages can drive cable sheath currents. I.e. cables must be *bundled* and must be laid as directly as possible on the shielding structures.

Cable sheath currents cause voltage drops at the coupling impedances of the cable sheath, which can completely distort the measurement signal especially at low signal levels. Therefore, if possible, a *large signal level* is chosen within the room and the signal is once again divided outside the shielded room, if necessary. Cable sheath currents can also cause electromagnetic influences outside the shielding. Therefore, it is often necessary to lay an *additional cable shield as a bypass* for the cable sheath currents. On the input side, it is directly connected to the reference conductor (i.e. to the common mass point). On the other side, the bypass must have such a good circumferential contact with the shielding of the room that the cable sheath currents pass to the shielding practically *completely*.

The amount of interference coupling into a cable can be ascertained by *preliminary tests* with signal conductors that are short circuited (and possibly also interrupted) on the input side.

6.4 Diagnosis and Monitoring

Along with high voltage tests for verification of withstand voltages, diagnostic methods are absolutely essential to obtain more differentiated conclusions about the *condition of a device and respectively, its insulation*. This, at first, pertains to ordinary type tests, routine tests and service tests. Reliable conclusions are particularly important, especially for decade-long aged equipment, which on the one hand must be taken out of the network in advance before the occurrence of a crucial damage, and which on the other hand, owing to its high replacement value, should not be replaced before the expiry of its technically probable lifetime. Ultimately, also the investigation of damages requires a suitable set of diagnostic tools.

The informative value of the diagnostic methods still does not come up to the questions posed in many cases. This especially pertains to the question of the expected *remaining service life* of a device.

Important methods are the dielectric measurements of classic parameters such as capacitance and dissipation factor at power frequency, conductivity and the dielectric system response (Section 6.4.1). Partial discharge measurements (Section 6.4.2), chemical analyses (Section 6.4.3), insulating material tests (Section 6.4.4) as well as optical and acoustic methods (Section 6.4.5) also come under this. New methods for determining system properties (Section 6.4.6) and dielectric diagnoses (Section 6.4.7) have now become increasingly valid and significant. Diagnostics are generally carried out in the plant or in the high voltage test field. Increasingly onsite diagnoses ("*off-line diagnosis*") are also being carried out. Moreover, the interest in "*online diagnosis*" is also on the rise and even in permanent "*online monitoring*" during operation (Section 6.4.8), especially for valuable or strategically important equipment, such as large transformers or bushings [156].

6.4.1 Dielectric Measurements

6.4.1.1 Dissipation Factor and Capacitance

Dissipation factor and capacitance are material-specific and device-specific parameters. Compliance with specified values is checked by measurements. *Trend analyses* provide details about changes. For example, increases in

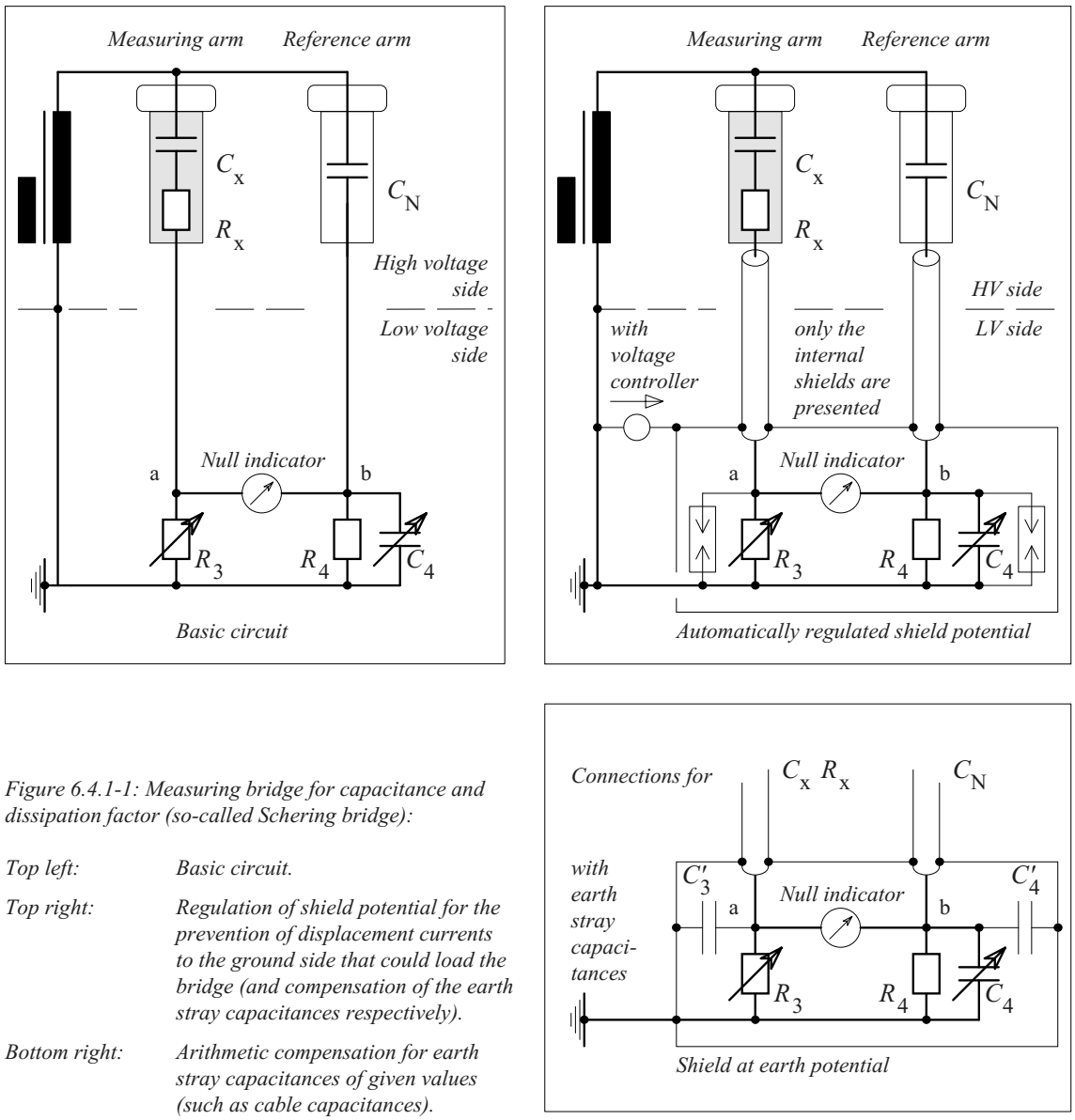

Figure 6.4.1-1: Measuring bridge for capacitance and dissipation factor (so-called Schering bridge):

Top left:	*Basic circuit.*
Top right:	*Regulation of shield potential for the prevention of displacement currents to the ground side that could load the bridge (and compensation of the earth stray capacitances respectively).*
Bottom right:	*Arithmetic compensation for earth stray capacitances of given values (such as cable capacitances).*

bushing capacitance or capacitor capacitance indicate breakdowns of partial capacitances. For resin-bonded paper bushings, a rise in capacitance can even be caused by oil-impregnation of the not entirely voidless insulation body. Loss of impregnating agent or a disconnected contact can be indicated by a fall in capacitance. Increased dissipation factors, for example, occur owing to infiltrating moisture and as a result of structural changes owing to ageing, see Section 4.2.3.

Note: With a rise in voltage, the inception of intense partial discharges becomes noticeable also through a rise in dissipation factor. Determining partial discharge inception via the "*partial discharge kink" of the dissipation factor graph* is, however, very insensitive and was in practice only during the initial stages of high voltage engineering.

The classic **basic circuit** for determining capacitance and dissipation factor is the *C*-tan δ measuring bridge according to *Schering* ("Schering bridge"), Figure 6.4.1-1 (top left).

It is distinguished from common AC measuring bridges by the fact that the test object (C_x, tan δ_x) is realistically stressed with *high voltage,* while all trimming elements are *at low voltage*. C_N is a very low loss, high voltage capacitor, for example a gas-insulated high voltage capacitor, with exactly known capacitance (standard or reference capacitor).

The balanced condition of the bridge, at which the *null indicator* shows no voltage, is

$$\underline{Z}_x / \underline{Z}_3 = \underline{Z}_N / \underline{Z}_4 , \qquad (6.4.1\text{-}1)$$

and it can be evaluated best with a *series equivalent circuit* for $\underline{Z}_x$:

$$\underline{Z}_x / \underline{Z}_3 = \underline{Z}_N \cdot \underline{Y}_4$$

$$\frac{R_x + \frac{1}{j\omega C_x}}{R_3} = \frac{1}{j\omega C_N} \cdot \left(\frac{1}{R_4} + j\omega C_4\right)$$

The following results from the real part and the imaginary part

$$R_x = R_3 \cdot C_4 / C_N ,$$

$$C_x = C_N \cdot R_4 / R_3 \qquad (6.4.1\text{-}2)$$

and

$$\tan \delta_x = \omega C_x R_x = \omega C_4 R_4 .$$

Under this, **ground stray capacitances** can lead to inaccurate results. In particular, the cables between the bridge and the high voltage components have capacitances C_3' and C_4'. They are in parallel to the bridge impedances $\underline{Z}_3$ and $\underline{Z}_4$, Figure 6.4.1-1 (bottom right). However, the following *remedial measures* are available:

1. *Double-shielded cables* and housings are used. External shields remain grounded, *internal shields* are dynamically maintained at the potential of the bridge points a and b of the balanced bridge by an electronic *voltage controller*. Thus, in the absence of a potential difference between the internal shielding and the inner conductors (bridge points a and b), displacement currents do not flow. Displacement currents between internal and external shields are fed by the voltage controller and they do *not* load the bridge.
2. Even without voltage controller, the shielding and bridge points a and b can be brought to the same potential by manual trimming of a third bridge arm *("auxiliary arm according to Wagner")*, so that the stray capacitances remain ineffective [141]. If an ungrounded high voltage source is available, a single grounded shielding can also be used.
3. Further, there is the option to compensate the phase displacement angle caused by ground stray capacitances with a *RLC-network* in arm 3.
4. If the ground stray capacitances are defined and known, what is mostly the case for coaxial measuring cables, an *arithmetic correction of the result* is made. From the balancing condition (6.4.1-1), with $1/\underline{Z}_3 = \underline{Y}_3 = 1/R_3 + j\,\omega\, C_3$' and $1/\underline{Z}_4 = \underline{Y}_4 = 1/R_4 + j\,\omega\,(C_4 + C_4$') and in accordance with Figure 6.4.1-1 (bottom right) to a good approximation

$$\tan \delta_x = \omega C_x R_x \approx \omega C_{4+}C_4')\, R_4 - \omega C_3' R_3$$

is obtained.

With the balanced value $\tan \delta_{x0} = \omega C_4 R_4$ in accordance with Eq. (6.4.1-2), the following is obtained for the *dissipation factor correction*:

$$\tan \delta_x = \omega C_x R_x \approx \tan \delta_{x0} + \omega C_4' R_4 - \omega C_3' R_3 \qquad (6.4.1\text{-}3)$$

The capacitance measurement value in accordance with Eq. (6.4.1-2) is hardly influenced by the stray capacitances.

Along with the basic circuit according to Schering, different **variants** were developed [141]. For example, there are special bridge circuits for *large capacitances*, for large *dissipation factors* and for *grounded test objects*. The *universal C-tan δ measuring bridge* allows simplified balancing with a complex comparator, with which the balancing is performed in dependence on the magnitude and phase angle of the diagonal bridge voltage V_{ab}. Moreover, there are bridges with *current comparators*. In addition to manually balanced bridges, there are also automatically balancing versions.

Computer-based measuring systems work according to the principle of a vectorial impedance measurement in the frequency domain, Figure 6.4.1-2. The dissipation factor tan δ_x that is sought is thus determined from the currents in the measurement arm and in the reference arm, i.e. from the phase displacement δ_x of the fundamental modes. For this purpose, for example, analog current signals recorded in both the arms are integrated, digitalized, fiber-optically fed into a digital signal processor (DSP) and processed further with a discrete Fourier transform (DFT) [204]. Depending on the speed and precision of the A/D conversion and the capacity of the processor, high precision and extremely short measuring durations can be achieved, which in practice facilitates the automatic *monitoring* of dielectric parameters in *real time*. The ability to calculate other parameters, such as capacitances, series resistances or parallel resistances, dissipation factor, power factor, power loss, voltage and frequency is an additional advantage.

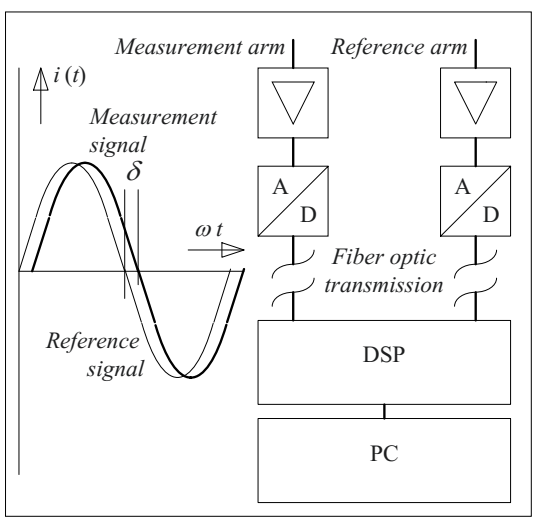

Figure 6.4.1-2: Computer-based measurement of the dissipation factor from the phase difference of the currents in the measurement arm and reference arm (as in [204]).

Capacitances and dissipation factors can also be determined from **resonance frequency and damping** of oscillating circuits. For this, a charged capacitance, for instance, is discharged in oscillation ("*oscillating voltage").* It is an advantage that even very large capacitances, such as in cables, can be measured. The accuracy is, however, not comparable with a bridge measurement, since other imperfect elements with losses (circuit inductance, switching elements) are included in the measurement result.

For determining **permittivity**, an accurately defined field geometry is necessary, in which the field distortions at the edges must be avoided by a *guard-ring arrangement,* Figure 6.4.1-3. Relative permittivity is obtained as the quotient of the measured insulating material capacitance and the calculated (or measured) vacuum capacitance:

$$\varepsilon_r = C_x/C_0 \qquad (6.4.1\text{-}4)$$

Coaxial guard-ring arrangements are used in compressed gas insulated reference capacitors (so-called *compressed-gas capacitors*) and in test vessels for liquid insulating materials. Plane guard ring arrangements are used for testing flat insulating material samples.

6.4.1.2 Insulation Resistance, Conductivity

Insulation resistance R_{In} between two electrodes results from a resistance network which emulates different materials and surfaces. Usually, a parallel connection of the **volume resistance** R_V and the **surface resistance** R_S, is considered:

$$R_{In} = R_V + R_S \qquad (6.4.1\text{-}5)$$

The values are determined by the *conductivity* of the material and by the *surface condition*. The *volume resistance* is accordingly dependent on stress duration, field strength, temperature and water content (see Section. 4.2.2). Typical values can be referred from Figures 4.2-5 to -9. *Surface resistance* is heavily dependent on the type, quantity, distribution, and wetting of pollution layers (see Section. 3.2.6.4 and 5.3.4). It is specified as resistance between opposite edges of a square and typically lies between 10^6 and 10^{13} Ω.

First of all, the measurement of insulation resistance for devices gives an indication of the presence of isolating gaps. In the context of trend analyses, ageing and wetting of cellulose-based insulations or contamination of oils can be tracked, for example. Surface resistances give information about the hydrophobicity of differently contaminated, aged or treated surfaces for instance, Figure 5.3-19.

With the help of guard ring arrangements, volume resistance and surface resistance of insulating material samples can be differentiated, Figure 6.4.1-4 (top and bottom resp.). While *measuring the volume resistance* between the high voltage electrode and the measurement electrode, current flowing through R_G is not measured and R_S is parallel to the low impedance measuring device. Even while *measuring the surface resistance* between the measuring electrode and the guard ring electrode, the current over R_G remains without any influence and R_V is parallel to the low impedance measuring device.

Note: The surface resistance can also be measured between two 10 cm long parallel blade-shaped electrodes that are pressed against the surface at a distance of 1 cm [157].

Similar to the determination of permittivity, a well defined field geometry in which field distortions at the edges and surface currents are prevented by a *guard ring arrangement* is also necessary for determining **conductivities**, Figure 6.4.1-4. The conductivity κ and the resistivity ρ for plane arrangements

$$\kappa = \frac{1}{\rho} = \frac{1}{R_D} \cdot \frac{d}{A}. \qquad (6.4.1\text{-}6)$$

are calculated from the volume resistance

$$R_D = \frac{1}{\kappa} \cdot \frac{d}{A}.$$

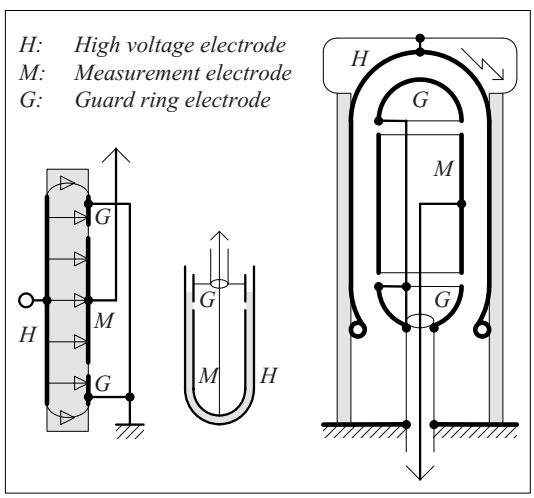

Figure 6.4.1-3: Plane insulation material sample with plane guard ring arrangement (left) and coaxial guard ring arrangements for testing liquids (center) and for a compressed-gas capacitor (right).

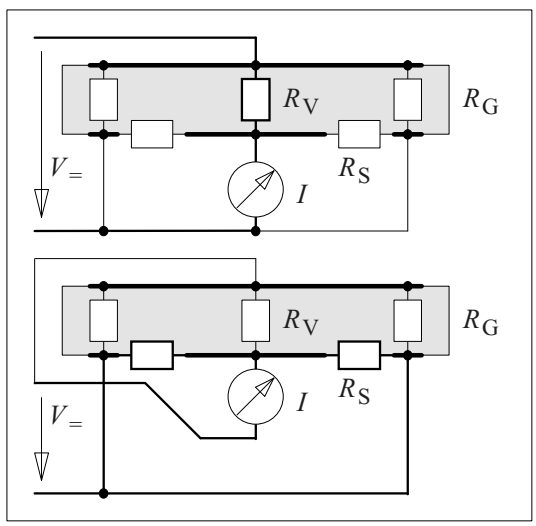

Figure 6.4.1-4: Measurement of volume resistance (top) and surface resistance (bottom) in a guard-ring electrode arrangement.

Solid insulating materials are usually measured on flat *plate-shaped samples* in plane electrode arrangements. However, it is also possible, to apply electrodes and guard rings as conductive coatings on *differently shaped bodies*. For *liquid insulating materials*, there are measuring cells of two concentric cup-shaped electrodes with a liquid-filled insulation gap. Similar to a compressed-gas capacitor, a guard ring is found in the upper area, Figure 6.4.1-3.

In conductivity measurements, it must be noted that the measured currents for **solid insulating materials** are influenced not only by its own direct current conductivity but also by *polarization processes* for long periods, Sections 4.2.2 and 4.3. Therefore, measurement must continue until the value of the *direct current conductivity* can be identified from a constant *steady-state end value* of the current. In practice, such an end value is often not attained, therefore measurement values are specified for *different periods of measurement* such as 1, 2, 5, 10, 50 and 100 minutes [157], [386].

Note: However, one should not come to the false conclusion that here it deals with real *conductivity values or resistance values*; they also include polarization current components. Therefore, it is better to use terms like *"apparent conductivity"* and *"apparent insulation resistance"* respectively.

Note: A new method, the **charge difference method** (CDM), under which the conductivity end values can be estimated by the calculation of charge differences from the polarization current measurements and depolarization current measurements (PDC-measurements), is described in Section 6.4.1.3 [427], [392], [428].

For **liquids**, the *decrease in conductivity* caused by ion drift in an electrical DC field plays an especially significant role, Section 4.2.2.2. Therefore, there is a special specification for the measurement of insulating liquids using trapezoidal AC voltages, with which the charge carrier depletion, which would be caused by the ionic drift, is prevented. With the rise in voltage, capacitive displacement current flows and conduction current flows during the stable phase at constant voltage. This allows both the measurement of permittivity and the measurement of the initial value of conductivity without charge carrier depletion (i.e. the so-called *AC conductivity*) [270], [385]. However, this value is different from the steady-state values obtained after prolonged DC field stresses.

6.4.1.3 Dielectric System Response

Capacitance, dissipation factor and conductivity are parameters which describe only a small section of the dielectric system properties. It is more comprehensive to measure a complete *dielectric system response*, which in the case of a linear dielectric or insulation system, enables the establishment of a complete equivalent circuit, Figure 4.3-2, Section 4.3.2.1. The above-mentioned classic parameters can be derived from it. These measurements are carried out on material samples in a *guard-ring arrangement*, through which it is ensured that only the current is measured which flows directly through the material and that the surface currents are made ineffective by discharging them via the guard ring, Figure 6.4.1-4 (top).

System responses can be measured in both the time domain and the frequency domain, see Sections 6.4.7.6 and 6.4.7.7. Basically, both the measurements are equal; a conversion is possible in the case of a linear system. However, this prerequisite is not always fulfilled, e.g. for an oil-insulated or oil-impregnated arrangement with non-linear insulating materials.

a) Measurements in the time domain

For measurements in the **time domain**, a stabilized direct voltage is applied as a step function on the object to be measured. The *polarization current* $i_p(t)$ flowing through the object results from a capacitive charging current impulse directly after connecting; it is subsequently determined by the polarization mechanisms that are effective in the material and that subside with time, and it finally tends towards an end value that is determined by the *conduc-*

tivity of the material. After a long period, the high frequency capacitance is charged, and moreover charge is stored at the interfaces and in the aligned dipoles. In the equivalent circuit according to Figure 4.3-2, these processes are physically correctly described by a capacitance, by *RC* elements for different polarization mechanisms and by a resistance for the conductivity.

After disconnecting the voltage and short circuiting the object, a *depolarization current* $i_d(t)$ is flowing owing to the charge stored by the preceding polarization. In the equivalent circuit according to Figure 4.3-2, this corresponds to the charge stored in the *RC*-elements. Even in the depolarization current, complete system information is contained, with the exception of information about the insulation resistance that is short-circuited during depolarization.

Note: Depolarization current measurements are not influenced by *surface resistances* since they are short circuited during the measurement. Owing to this, dielectric measurements are possible even for insulations on which no guard ring arrangement can be implemented (e.g. on cables). However, the signal no longer contains information about the conductivity.

The analysis of polarization currents and depolarization currents is known as *PDC analysis*, Section 6.4.7.6.

Note: A common task is the measurement of so-called **direct current conductivity**

$$\kappa = \frac{1}{\rho} = \frac{1}{R_V} \cdot \frac{d}{A} = \frac{I_\infty}{V_=} \cdot \frac{d}{A}, \qquad (6.4.1\text{-}7)$$

which can be determined from the end value I_∞ of the decreasing *polarization current* $i_p(t)$, i.e. theoretically only after an infinitely long time and in practice, often only after hours or days, Figure 6.4.1-5 (left), Section 6.4.1.2:

$$i_p(t) \rightarrow I_\infty \qquad (6.4.1\text{-}8)$$

Convergence occurs much faster when the *difference in the magnitudes of the polarization current and the depolarization current* $i_p(t)$ and $i_d(t)$ is developed, since in both the currents redundant information about the polarization effects cancel out with opposite signs and because the *conductivity component* is present only in the polarization current, Figure 6.4.1-5 (left). For this comparison, the depolarization current must be shifted in time by the polarization duration t_p or charging time t_C as polarization current and depolarization current are not flowing simultaneously and the measurements are performed with the time shift $t_p = t_C$:

$$i_p(t) - i_d(t + t_p) \rightarrow I_\infty \qquad (6.4.1\text{-}9)$$

A new method, the so-called **charge difference method** CDM, is based on the *integration* of $i_p(t)$, giving the total charge $q_p(t)$ that has flowed, and on the integration

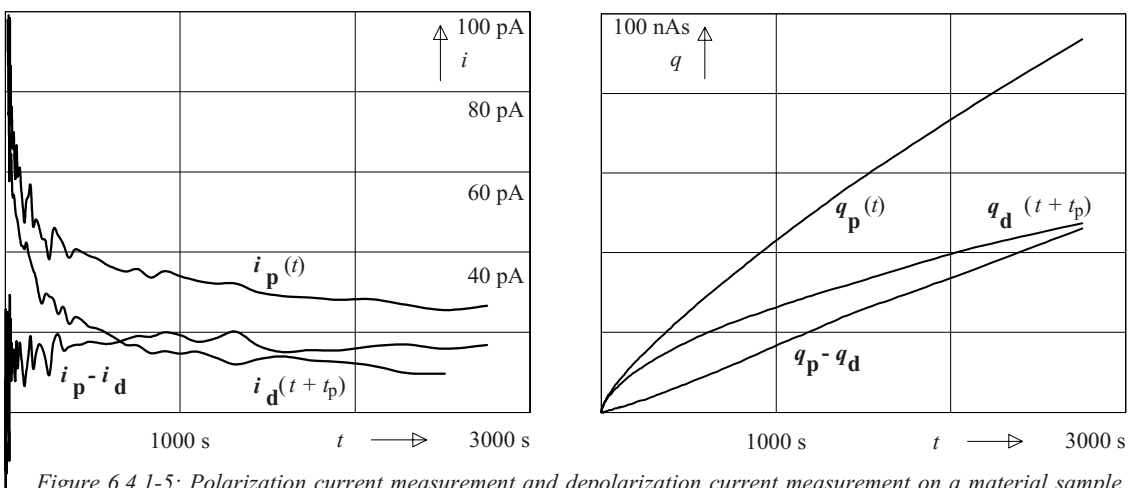

Figure 6.4.1-5: Polarization current measurement and depolarization current measurement on a material sample of oil-impregnated paper with the difference in the magnitudes of currents i_p and i_d (left) as well as evaluation of current measurements by integration (right). q_p is the total charge that has flowed, q_d is the stored and released charge. The gradient of the charge difference function q_p - q_d is approximately proportional to the conductivity (charge difference method CDM [427]). Superimposed interferences (left) are averaged out by integration (right).

of $i_d(t+t_p)$, giving the released charge $q_d(t+t_p)$ that has been stored before, Figure 6.4.1-5 (right), [427] to [429]. The *difference of charge magnitudes* $q_p(t) - q_d(t+t_p)$ is approximately equivalent to the unstored charge that has been discharged as conduction current via the insulation resistance. From the gradient of the *charge difference function,* a good estimation for the conductivity end value can be derived quite early. Here it is particularly of advantage also that the interferences present in the current signals can be averaged out by the integration.

b) Measurements in the frequency domain

For measurements in the **frequency domain**, the object is subjected to a sinusoidal voltage until a *steady state* is achieved (at least four periods). An *impedance* is determined from the stationary current flowing through the object. By measurement at many different frequencies, the frequency dependence of the impedance is determined point-by-point, and from this the frequency dependence of the *complex permittivity* $\varepsilon = \varepsilon' - j\varepsilon''$ as well as the magnitudes of the capacitance C and the dissipation factor $\tan\delta$ are calculated. Its analysis is described as *frequency domain spectroscopy* FDS, Section. 6.4.7.7.

Note: A measurement in the *time domain* often appears to be more advantageous than in the frequency domain:

1. For measurements in the *frequency domain*, a large number of individual measurements are necessary to measure C, $\tan\delta$ and $\varepsilon = \varepsilon' - j\varepsilon''$ over a large frequency range. Here, for each individual measurement point one must wait for a steady state to be reached (i.e. at least four periods). Owing to this, very long measuring times are necessary, especially for very *slowly changing processes* in the range of 10^{-3} to 10^{-4} Hz. Instead of this, the measurement period in the time domain is only a fraction of this, since a single voltage step is sufficient for recording the complete system information.

2. For measurement in the time domain, it is simply possible to apply *voltages of any magnitudes*. As a result of this, there is great freedom with regard to the field strength load during the measurement and the insulation can be stressed similarly to the actual operational conditions, for example, for DC voltage insulation systems (HVDC) or for diagnostic purposes. Lower voltages are adequate for diagnostic examinations. In the frequency domain, on the contrary, it is extremely difficult to implement frequency variable voltage sources with large amplitudes. Therefore, the voltages must generally be restricted to the range of a few 100 V, which is, however, often adequate for diagnostic measurements.

3. Processes in the time domain are often more directly accessible to the human *imagination* than processes in the frequency domain, for which an additional measure of abstraction is necessary.

Note: The strong point of *time domain measurement* lies in the measurement of slowly changing processes and in the use of higher voltages. *Frequency domain measurements* are advantageous for very high frequencies, since corresponding time domain measurements would require extremely rapid voltage steps and very high sampling rates.

Note: It is necessary to complete the measurement with a *depolarization* both in the time domain as well as in the frequency domain, in order to avoid influences on the subsequent measurements by the previous loading (*memory effect*). That is, in the frequency domain, the same number of both positive and negative periods must be passed through from zero crossing to zero crossing. In the time domain, the depolarization can be attained by an equivalent stress with opposing polarity or by a long-term short circuit.

6.4.2 Partial Discharge (PD) Measurement and Diagnosis

The *formation and clear interpretation* of partial discharges from the viewpoint of gas-discharge physics has already been discussed in Section 3.6. Many practically relevant cases can already be assessed with the phase-resolved diagrams (phase-resolved pattern) described there, if the test voltage function corresponds to a distortion-free sinusoid, Figure 3.6-8. Here, the methods for measured-value acquisation, signal processing, evaluation and further computer-aided diagnosis shall be described.

The partial discharge measuring technique requires two different perspectives to be distinguished: according to one perspective, partial discharge measurement is used in the context of **quality assurance** during high voltage testing in order to confim specific and specified partial discharge levels according to standardized procedures [476], [477], the so-called IEC- partial discharge measurement. On the

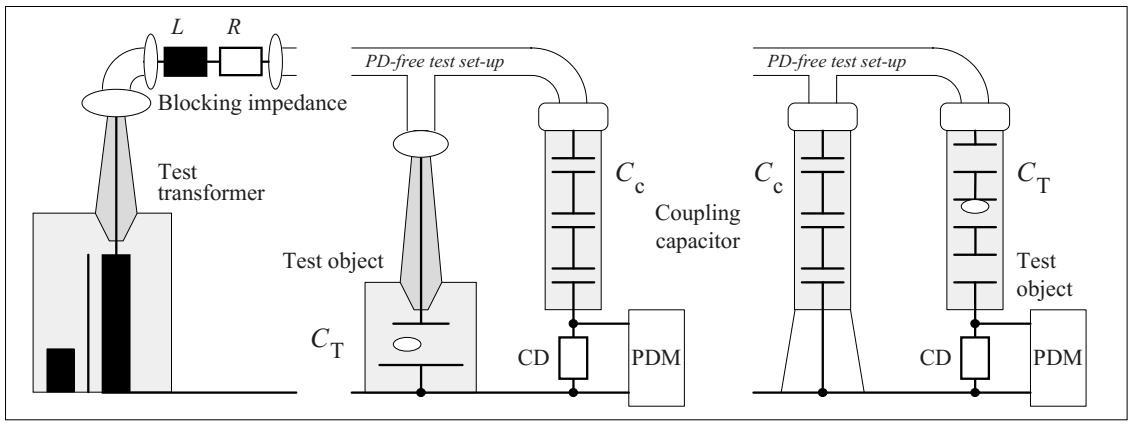

Figure 6.4.2-1: Parital discharge tests on grounded and earth-free test objects (left and right) with blocking impedance, coupling capacitor, coupling device (CD), partial discharge measuring device (PDM) and PD-free test set-up.

other hand, partial discharge measurement is also an efficient **instrument for diagnosis and research,** which allows considerably more thorough analyses of insulation faults, often even with new and non-standardized procedures or with measurement circuits or parameters that are not recommended according to the standards.

With the common partial discharge measuring technique in the kHz-range (Sections 6.4.2.1 to 6.4.2.4), the questions of interference signal suppression and partial discharge diagnosis must also be considered (Sections 6.4.2.5 and 6.4.2.6). The separation of several overlapping signal sources and sources of interference is also newly possible with synchronous multichannel partial discharge measurement (Section 6.4.2.7). In addition to the classic measuring procedure, the ultra-high frequency UHF technique and a few non-electrical methods are also of importance (Sections 6.4.2.8 and 6.4.2.9).

6.4.2.1 Partial Discharge Measurement Circuit

The measurement of partial discharge impulses requires a special *measuring technique*, Figure 6.4.2-1. A *coupling capacitor* with capacitance C_C.is connected in parallel to the *test object* with capacitance C_T which is also connected to the test transformer via a blocking impedance [476]. In the case of a partial discharge, a pulsed compensating current flows in the circuit of C_C and C_T. The partial discharge current impulse can be measured as voltage impulse using a *coupling device* (CD) that is situated either in the arm of the test object or in the arm of the coupling capacitor.

Note: **Coupling out of partial discharge signals** can also be performed at the *measuring tap of a bushing*; in this case, the bushing capacitance adopts the function of the coupling capacitor. Non-conventional coupling out using *capacitive or magnetic sensors*, *Rogowski coils* and *antennae* can also be considered if there is adequate sensitivity in the frequency domain under consideration and if calibration of the partial discharge measurement circuit is possible, see Section 6.3.3. They are the prerequisite for newer approaches to partial discharge analysis, e.g. for the analysis of impulse shape (time-resolved analysis) or for the analysis of extremely high-frequency components in the frequency spectrum of the signal, see Section 6.4.2.6. Further, field probes and antennae can be used onsite for the localization of partial discharges in stationary electrical equipment.

Note: Coupling devices are often networks with band-pass or high-pass behavior, e.g. consisting of a parallel connection of inductance and resistance. Owing to this, an overload of the sensitive partial discharge measuring device by the power frequency voltage is avoided.

Often, decoupling of the entire partial discharge circuit from the network side through a *blocking impedance* acting as *low-pass filter* (e.g. series connection of R and L) is helpful to suppress conducted interferences. Also, the

parallel connection of transformer winding capacitances is prevented which would reduce the sensitivity of the measuring circuit, Figure 6.4.2-1 (left).

Note: Damping of external interferences is also possible using a so-called *bridge circuit*, in which the coupling devices are present both in the arm of the test object as well as the arm of the coupling capacitor (so-called Kreuger bridge). External current impulses cause common-mode signals at both the coupling devices. Partial discharges in the test object (or in the coupling capacitor) lead to differential-mode signals.

The overall *test set-up* must be *free of partial discharges*. That is, along with the use of appropriate devices (transformer, coupling capacitor), adequately rounded supply lines, toroids and fittings are necessary. Moreover, all metallic parts must be maintained at defined potential through contacting.

Note: The partial discharge measurement circuit described here can be used for both AC voltage as well as **DC voltage**. Partial discharge impulses for DC voltage, however, occur essentially more *rarely and irregularly* than for AC voltage, since a discharged defect is recharged not by displacement currents but by much lower conduction currents. Therefore, the partial discharge measuring device cannot provide a continuous charge reading, but the *charge of individual impulses* must be recorded over time. A criterion for the withstanding of a DC voltage test is therefore, for example, charge *and* counting of individual impulses within a longer observation period.

Note: **Partial discharge measurement for DC voltage** is to a large extent susceptible to external *interferences* and to interferences in the measurement set-up. For AC voltage, individual current impulses are conspicuous in view of regular and repetitive partial discharge impulses or they are averaged out. In the case of direct voltage, there is no comparable differentiating possibility and greater *effort* must be applied *to the suppression (of interference) and shielding*. In Section 6.4.2.7 c), a new method is described as to how interferences and partial discharge can be differentiated with *synchronous multi-channel measurement*.

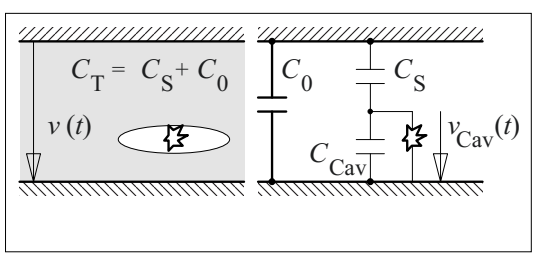

Figure 6.4.2-2: Simplified equivalent circuit for describing internal partial discharges in a test object.

6.4.2.2 Apparent Charge, Partial Discharge Energy

a) Apparent charge

According to Figure 3.6-2, internal partial charges are described by an equivalent circuit and by the *discharging of a cavity capacitance* C_{Cav} on exceeding the ignition voltage or breakdown voltage V_{bd}, Figure 6.4.2-2. The **real charge turnover**

$$\Delta Q = C_{Cav} \cdot \Delta v_{cav} = C_{Cav} \cdot V_{bd} \qquad (6.4.2\text{-}1)$$

cannot be measured at the terminals of the *test object.* The voltage drop at the cavity Δv_{Cav} is identical to the ignition voltage V_{bd} of the cavity: $\Delta v_{Cav} = V_{bd}$. However, owing to the voltage division at C_S and C_0, it only causes a negligible small *voltage dip at the terminals of the test object*

$$\Delta v = \Delta v_{Cav} \cdot C_S/(C_S + C_0) = V_{bd} \cdot C_S/C_T \qquad (6.4.2\text{-}2)$$

assuming that the test object is inductively decoupled from the rest of the measuring circuit during several nanoseconds.

Note: In Figure 6.4.2-2 and in Eq. (6.4.2-2) it is assumed with $C_T = C_S + C_0$ that the cavity has a significantly smaller thickness than the insulating material in series. In consequence, it is also assumed that the cavity capacitance C_{Cav} is significantly larger than the series capacitance C_S and that C_{Cav} can be neglected in the series connection with C_S.

This voltage dip according to Eq. (6.4.2-2) is so small that it cannot be measured directly. Instead of this, the *charge that flows out* from

the coupling capacitor and recharges the test object is measured. For this purpose, the coupling device is regarded as the current measurement resistance and the signal is integrated in the partial discharge measuring device in order to calculate the charge that is flowed. During this, it is not important whether the current is measured in the arm of the coupling capacitor or in the arm of the test object, see Figure 6.4.2-1. This charge which can be measured, is described as the "**apparent charge"**

$$Q_A = C_T\,\Delta v = \Delta v_{Cav} \cdot C_S = \Delta Q\; C_S/C_{Cav} \qquad (6.4.2\text{-}3)$$

for which it is assumed that the voltage dip Δv can be fully compensated by an constant-voltage source.

This apparent charge Q_A is much smaller than the real charge turnover Q. Unfortunately, the relationship according to Eq. 6.4.2-3 is completely unknown, since the type, position and size of the defect are not known, thus there is no information about the "transmission ratio" C_S/C_{Cav}. Despite this, the *apparent charge* Q_A has proven in practice its value as a **parameter for the specification of partial discharge intensity**. This is also theoretically comprehensible, since the apparent charge is related to the *energy dissipation* in the defect and to the *size of internal cavities*, cf. b) and c) [67]:

b) Partial discharge energy

The **energy dissipation** W_{PD} **in the defect** and the discharge frequency are responsible for the eroding effect of partial discharges. The partial discharge energy can only be indirectly estimated from the parameters measured externally at the test object terminals on the basis of the following consideration: the energy dissipation is equal to the capacitive energy stored in the cavity capacitance C_{Cav} before the partial discharge event. On the assumption of a complete discharge of the cavity by Δv_{Cav}, the following is approximately valid:

$$W_{PD} \approx \frac{1}{2} \cdot C_{Cav} \cdot \Delta v_{Cav}^2 = \frac{1}{2} \cdot \Delta Q \cdot \Delta v_{Cav}$$

According to Eq. (6.4.2-3), ΔQ is related to the externally measurable apparent charge Q_A by the capacitive divider ratio C_S/C_{Cav} . Δv_{Cav} is likewise obtained via the capacitive divider ratio from the peak value of the externally measurable partial discharge inception voltage $\sqrt{2}\,V_{PDI}$ or from the externally measurable voltage difference of the AC voltage $\Delta V_{n,n+1}$ between two successive partial discharge impulses n and n+1. Thus, an expression that comprises only parameters that can be measured externally is obtained for the energy dissipation in the cavity:

$$W_{PD} \approx \frac{1}{2} \cdot (Q_A\,\frac{C_{Cav}}{C_S}) \cdot (\sqrt{2}\,V_{PDI} \cdot \frac{C_S}{C_{Cav}})$$

$$\begin{aligned} W_{PD} &\approx \frac{1}{2}\sqrt{2} \cdot Q_A \cdot V_{PDI} \\ &\approx \frac{1}{2} \cdot Q_A \cdot \Delta V_{n,n+1} \end{aligned} \qquad (6.4.2\text{-}4)$$

The unknown capacitive divider ratio falls out, since charge parameters and voltage parameters are divided in inverse ratio.

The *partial discharge inception voltages* are often comparable for devices of the same voltage level, so that the *apparent charge* can also be considered as a relative guide to the *energy of the discharging impulse*.

c) Size of the cavity

According to Eq. (6.4.2-3) and (-1), *apparent charge* also increases with the breakdown voltage of the cavity and thus with the flashover distance d and the **size** of the *cavity*:

$$\begin{aligned} Q_A &= \Delta Q \frac{C_S}{C_{Cav}} = C_{Cav} V_{bd} \frac{C_S}{C_{Cav}} \\ &\sim V_{bd} \sim d \end{aligned} \qquad (6.4.2\text{-}5)$$

d) Determination of limit values

Eq. (6-4.2-4) suggests that for *high voltage levels* (with high partial discharge inception voltages), *lower apparent charges* are acceptable than for lower voltage levels, if there is the same acceptable energy dissipation in the cavity [67]. This gradation is actually seen in current test practice. However, this has not resulted from the presented theoretical considerations, but over many decades of test experience.

For the magnitude of acceptable partial discharge intensities, there are neither general specifications nor theoretical justifications. Generally, values from *practical test experience* are stated in the device specific standards. Mostly, **during testing**, the test voltage is applied. On reducing the voltage, the partial discharge intensity should not exceed the specified charge value Q_A for a defined voltage value (significantly above the operating voltage). During this, it must be ensured that in operation, partial discharges that could be ignited by an overvoltage are in any case extinguished again **at the operating voltage**.

Generally, **charge values** that are accepted for a **test** for highly stressed insulations (operating field strength $\geq$ 3 kV/mm) are between Q_A = 1 and 10 pC, if a *sensitive insulating material* such as polymeric films, epoxy resin or oil-impregnated paper is involved.

Generator insulations with a high percentage of partial discharge-resistant *mica* can exhibit discharges in the range of 1000pC; 10000 pC is considered to be hazardous [67]. *Glass and porcelain* exhibit an even higher resistance to partial discharges. *Corona discharges* in air, and even on ceramic surfaces, are considered non-hazardous.

Partial discharge tests for *transformers* are mandatory for voltages of V_m > 72.5 kV. The levels are 100 pC for 1.2 $V_m/\sqrt{3}$ and 250 pC for the one hour PD measurement voltage of 1.58 $V_r/\sqrt{3}$ or 1.5 $V_m/\sqrt{3}$, see Section 7.1.3.5 with Figure 7.1.3-14. These levels are considered generous and values are generally well below them. It can be assumed that for an apparent charge of 500 pC, there is a serious problem in the transformer [206].

With regard to **erosive ageing** of insulating materials, both the discharge intensity Q_A and the discharge frequency N are important. In sensitive organic insulating materials, a *charge rate* of

$$N\,Q_A = 2 \text{ nC/min} = 33 \text{ pC/s} \approx 1 \text{ pC/ period}$$

is considered safe. This value should be valid for both AC voltage and for DC voltage [207].

6.4.2.3 Sensitivity and Calibration

a) Sensitivity

According to Eq. (6.4.2-2), the discharge of the defect leads to a voltage dip Δv at the test object connections, which, in accordance with Eq. (6.4.2-3), can be compensated completely by the outflow of apparent charge Q_S from a constant-voltage source. But, since the coupling capacitor does not form an ideal voltage source, a voltage dip of Δv^* remains. This implies that the entire apparent charge is not compensated, but only the **measurable charge**

$$Q_M = C_C \cdot \Delta v^*. \qquad (6.4.2\text{-}6)$$

For the charge balance, the following applies:

$$\Delta v^*(C_C + C_T) = Q_A = C_T\,\Delta v\,. \qquad (6.4.2\text{-}7)$$

For $C_C >> C_T$, Δv^* approaches zero, i.e. it is a constant-voltage source. For $C_C << C_T$, Δv^* approaches Δv, i.e. no charge compensation takes place.

From Eqs. (6.4.2-6) and (-7), the relationship between measurable charge and apparent charge is obtained:

$$Q_M = Q_A\,C_C/(C_C + C_T) \qquad (6.4.2\text{-}8)$$

For $C_C >> C_T$, Q_M is equal to Q_A. For smaller values of C_C, Q_M also decreases. Especially for *large test object capacitances* (such as for

capacitors, cables or layer windings of transformers), a significantly *reduced sensitivity* of the partial discharge measurement circuit must therefore be expected.

Note: The relationship between Q_A and Q_M can be determined by an **indirect calibration**. Under this, current impulses of constant charge quantity are passed via the parallel circuit consisting of C_C and C_T, so that the partial discharge measurement device shows a signal corresponding to Q_M. If an equal current impulse is directly passed via the coupling device, the reading corresponds to the apparent charge Q_A. The ratio of the readings corresponds to the sought *calibration factor*

$$k_c = Q_A/Q_M = (C_C + C_T)/C_C . \quad (6.4.2\text{-}9)$$

The *apparent discharge* Q_A is used as a measurement parameter for quantification of partial discharges. A conclusion from Q_A about the *actual charge turnover* ΔQ in the defect would be desirable. Unfortunately, Eq. (6.4.2-3) provides only a basic relationship that cannot be practically evaluated, since the ratios of parameters and capacitances cannot be specified for an unknown defect. However, in general $C_S << C_T$, so that, generally, $\Delta Q >> Q_A$ can be assumed.

b) Calibration

In practice nowadays, a **direct calibration** is carried out. That is, the current impulses of the calibration are fed with known charge quantity Q_0 *via the terminals of the test object* and compared with the indicated charge value Q_{ind}. Generally, partial discharge measuring devices can be set in such a way that displayed charge values correspond to the supplied charge. During the measurement, the displayed charge corresponds to the apparent charge Q_A.

While carrying out a **calibration**, a few important points must be considered [476]:

1. Calibration must be carried out without high voltage, but *in the original and complete test circuit* including the test object, since all the lumped capacitances and stray capacitances are also included in the sensitivity of the test circuit. Each change, therefore, requires a new calibration.

2. The calibrator itself shall be made up of a fast step-function generator connected in series with a capacitance C_0 . With the step voltage V_0, the charge $Q_0 = C_0 \cdot V_0$ is coupled into the test object via C_0. The calibrator thus simulates the capacitive coupling of partial discharge impulses from a defect. C_0 must *not be higher than 10 % of the test object capacitance*, in order not to influence the setup too strongly.

3. The connection of the calibrator capacitance C_0 should be done close to the high voltage terminal of the test object, so that the calibration charge is not partially lost via the stray capacitance of a supply line.

4. *Charge values* that approximately correspond to the *partial discharges* to be measured should be used for calibration. Here, however, it must be ensured that the calibration impulses are significantly larger than the *background noise level*. The *frequency* of the calibration impulses should be at least 2 for each period of the AC voltage.

5. The *rise time* T_r of the step voltage V_0 must be so small that the calibration impulse exhibits a *frequency spectrum* whose limit frequency is higher than the limit frequency of the partial discharge impulses to be measured. With the common, rather low-frequency filter settings of the partial discharge measuring devices (see Section 6.4.2.4), it is ensured that the partial discharge impulses and the calibration impulses have spectral amplitude densities that are comparable within the frequency band $f_1 < \Delta f < f_2$ which is used for the measurement.

Note: These requirements are generally fulfilled with T_r < 60 ns. $T_r < 0.03/f_2$ is applicable for broadband devices with $f_2 > 500$ kHz.

6.4.2.4 Signal Processing and Signal Evaluation

Owing to complex system properties of the measurement circuit, current impulses that can be measured with the coupling device are

mostly not of significance with regard to **classic partial discharge diagnostics**. Current impulses must be integrated to form the "charge" parameter. The "*quasi-integration*" undertaken for this purpose can be carried out by *broadband and narrowband partial discharge measuring devices*.

Note: Interference voltage meters and radio interference meters (RIV-meters) were originally developed for communications engineering and they were used at the early beginnings of partial discharge measurement technique. Although they do no longer fulfill the requirements of IEC 60270, they can be used for orienting measurements and with great care, even for quantitative information.

Important parameters of classic diagnostics are the *apparent charge* Q_A (*partial discharge intensity* PDI), *phase position* with reference to the power frequency fundamental mode, the *discharge frequency N*, as well as the *partial-discharge inception voltage* and the *partial-discharge extinction voltage* (PDI and PDE), see Section. 3.6.

The **reading of a partial discharge measuring device** is proportional to the apparent charge of the largest regularly recurring impulses. If the impulse frequency N falls below 2 impulses per 50 Hz period (i.e. less than 100 per s), the amplitudes in accordance with Table 6.4.2-1 are weighted with less importance. The *inertia* of earlier analogous pointer-type instruments is thus replicated.

Tab 6.4.2-1: Weighting of the reading of a partial discharge measuring device with respect to impulse frequency N.

Impulse frequency N/s	1	2	5	10	50	$\geq$100
Reading in % $\pm$ 5 %	40	60	81	90	99	100

Note: Following the radio interference meters, the so-called **CISPR evaluation characteristic** was in use in the past, Figure 6.4.2-4. It was based on the idea adopted from acoustics that a few large impulses should be rated just as high as many smaller ones. The damaging effect of partial discharges is, however, so complex that the application of this simple idea is not justified.

a) Broadband partial discharge measuring devices

The performance of broadband partial discharge measuring devices will first be explained with the example of an analog *RC-Integration*, Figure 6.4.2-3. For $R_m << R$, the partial current

$$i_C(t) = i(t) \cdot R_m / R \qquad (6.4.2\text{-}10)$$

charges the capacitance C to the voltage $v(t)$, which is proportional to the charge that has flowed until this time:

$$v(t) = \{ \int i_C(t) \mathrm{d}t \} / C \sim \int i(t) \mathrm{d}t \qquad (6.4.2\text{-}11)$$

This charge value is ideally stored in C. Owing to the finite time constant $\tau = R \cdot C$, however, a gradual *discharge* occurs. The maximum $\hat{v}$ of voltage $v(t)$ is proportional to the charge Q, if the *integration time constant* τ is sufficiently long compared to the *impulse duration* τ_i:

$$\tau = R \cdot C >> \tau_i \qquad (6.4.2\text{-}12)$$

The time constant τ, however, should not be too large, so that successive impulses can be distinguished Practical values are in the µs range.

The *RC* integration element can also be interpreted as a *low pass* in the *frequency domain*.

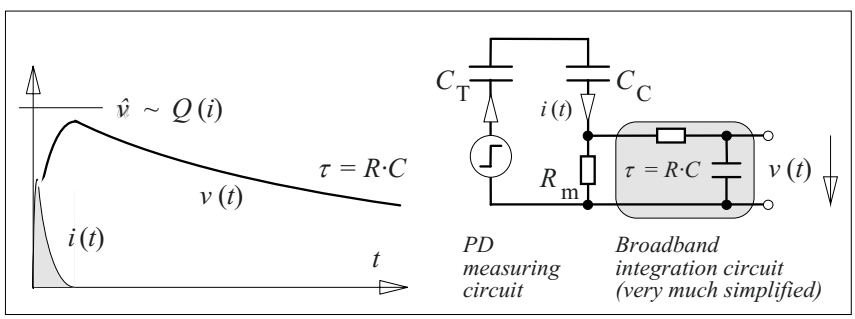

Figure 6.4.2-3: Broadband integration of a compensating current i(t) in a PD measuring circuit by a RC low pass.

The requirement for a large time constant $\tau = R \cdot C$ corresponds to the requirement for a low *upper cut-off frequency* of the low pass. For practical measuring devices, this lies in the 100 kHz range. Systems with significantly higher limit frequencies would no longer work as integrators, but would transfer the current impulse more or less unchanged.

Note: Even for current impulses lasting for a longer period, the condition (6.4.2-12) is probably no longer fulfilled and hence an integration error can result.

Owing to the *low signal amplitudes*, active integration amplifiers were used in the past. Today, the input signal is immediately digitalized in totally **digitalized measuring devices** and then processed further in digital form. Thus, a high level of flexibility with regard to the integration procedures and further evaluations is obtained.

Practical partial discharge measuring devices have no low pass characteristic, but have a *bandpass characteristic* for blocking network frequency and other low frequency signal components below approx. 10 kHz. According to IEC 60270, the *upper cut-off frequency* f_2 should be at 500 kHz, the *bandwidth* Δf between 100 kHz and 400 kHz and the *lower cut-off frequency* f_1 between 30 kHz and 100 kHz. [476].

When determining the filter characteristic of the bandpass, the coupling device (with circuiting), connecting line and partial discharge measuring device must be regarded together as one unit, for which the resultant frequency response must be considered. Mostly *damped oscillating impulse responses* occur, and these no longer have a similarity with the shape of the original impulse. Only the amplitude is proportional to the *apparent charge* (*quasi-integration*) and *polarity* can be identified from the largest half-wave. Occasionally, tuning of the filters is inadequate and hence the information about the polarity of the impulse can be lost. The *resolution for successive impulses* is determined by the damping of the oscillations and generally is in the µs range.

b) Narrowband partial discharge measuring devices

Narrowband partial measuring devices have very *intensely oscillating impulse responses*. That is, the impulse response is in the form of a sine beat that rises and decays, whereby the frequency of the oscillation corresponds to the center frequency (mid-frequency) f_C of the filter. The duration of the oscillation is determined by the bandwidth Δf. Information about the polarity of the impulse is thus completely lost. It can be shown that the amplitude of the oscillation is proportional to the *charge* of the exciting impulse [141], if the spectral amplitude density of the partial discharge impulses is constant in the frequency domain covered by the filter [477]. This implies that for the selection of the *centre frequency*, a frequency range must be selected in which the reading does not vary with the frequency.

According to IEC 60270, the *bandwidth* Δf should be between 9 kHz and 30 kHz and the *center frequency* f_C between 50 kHz and 1 MHz [476]. A common bandwidth is the value adopted from the CISPR [158] for interference voltage receivers (or radio-interference meters) $\Delta f = 9$ kHz, which corresponds to an impulse resolution time of approx. 220 µs.

Narrowband partial discharge measuring devices with tunable filters have the advantage that in an *electromagnetically disturbed environment* (such as in industrial production units), a frequency band with comparatively little disturbance can be selected. Poor resolution of rapidly successive pulses and loss of polarity information is a disadvantage.

c) Interference voltage measuring devices

Historic precursors of partial discharge measuring devices are the interference voltage measuring devices (radio-interference meters) of communications engineering. These are tunable measurement receivers with *bandpass characteristics*, which are also suitable as narrowband partial discharge measuring devices for the quasi-integration of impulses. *Their*

reading is a voltage V_{RIV} in µV and not a charge in pC, as in partial discharge measuring devices. For calibrated interference voltage measuring devices, the following relationship is applicable

$$V_{RIV} = Q_M \cdot R_m \cdot \Delta f \cdot a / \sqrt{2} \ . \quad (6.4.2\text{-}13)$$

R_m is the resistance of the coupling device, Δf the bandwidth and Q_M the (measurable) charge flowing through R_m. The factor a increases with the frequency N of the impulses in accordance with a *weighting characteristic*, Figure 6.4.2-4. The interference voltage for N = 100 impulses per second (corresponding to one impulse per AC half-cycle) is the reference value with the weighting factor a = 1. The weighting characteristic results originally from a circuit with rectifier (for peak-value storage), a resistive-capacitive network and a pointer-type instrument with mechanical inertia.

Example: For a bandwidth Δf = 9 kHz, a coupling device R_m = 60 Ω, a factor a = 1 (i.e. N = 100/s) according to Eq. (6.4.2-13), an interference voltage V_{RIV} = 1 µV corresponds to a measurable charge Q_M = 2.62 pC.

Note: The relationship between Q_M and Q_A can be determined by calibration in accordance with Eq. (6.4.2-9). However, the **calibration** is overall made difficult owing to different weighting characteristics according to Figure 6.4.2-4 and Table 6.4.2-1, since the reading pertains not only to the frequency of the partial discharge impulses to be measured, but also to the frequency of the calibrator impulses. The calibration is applicable only to the cases in which the frequencies coincide. In other cases, the charge values must be converted to the given frequencies. Interference voltage measurement devices with weighting functionality that can be turned off are therefore often more suitable.

Note: The weighting characteristic takes into account the subjective perception that for *radio reception, many small impulses* cause similar interference to a *few large impulses*. Also for partial discharges, many small impulses can be likewise considered to be similarly damaging to a few large impulses. However, the processes of erosion breakdown are dependent on a number of hardly ascertainable parameters, so that the above-mentioned qualitative dependence *cannot* be included in a weighting characteristic.

d) Digital partial discharge measuring devices

Because very quick and efficient computers are available, partial discharge measuring devices have now been completely implemented in digital form. This means that the signal measured at the coupling device is digitalized immediately and in real-time. Only then, it is *digitally filtered, integrated and further processed*. This has resulted in completely new options for partial discharge measurement, partial discharge analysis and the suppression of interference impulses, Section 6.4.2.7. For example, bandwidths, center frequencies and cut-off frequencies are completely freely adjustable; the distinction between narrowband and broadband devices and the restriction to a few center frequencies defined in the standards becomes obsolete; and time-based correlations between individual impulses can be determined. A wide electromagnetic interference signal spectrum can be monitored, so that frequency ranges can be chosen with minimum background noise levels. This is a great advantage for the onsite testing technique.

6.4.2.5 Interference-free measurement

Partial discharge measurement circuits are designed for the sensitive measurement of the smallest impulses in the pC range. Therefore, they are also particularly sensitive to all types of interferences. Interference-free measurement of partial discharges, therefore, is one of the major challenges of the practical applica-

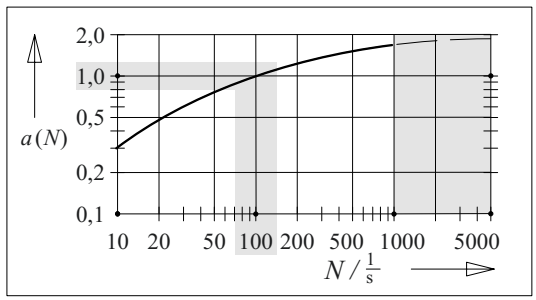

Figure 6.4.2-4: CISPR weighting characteristic for interference voltage measuring devices. For high impulse frequency N > 1000/s, it can lead to erroneous displays due to lack of impulse resolution.

tion of high voltage measurement technology. Therefore, before a partial discharge measurement is performed with high voltage, it must first be checked without voltage whether the so-called **background noise level** is lower than the signal to be measured. Moreover, it must be verified that the **the set-up** without a test object is **free from partial discharges** under voltage. In the following section, the most important sources of interference and appropriate countermeasures are listed:

1. **External electromagnetic radiation** can be damped over a broadband range by a *high voltage room shielded on all sides*. Background noise levels lower than 1 pC can be attained.

2. **External conducted interferences**, e.g. by power electronic switching impulses on the low voltage side of the power supply, are often damped by inductances and winding capacitances of the test transformer as well as by current limiting resistors on the high voltage side. If necessary, *filters* connected with low inductance to the hall shield must be used on the low voltage side.

3. **Narrowband interference sources** (e.g. transmission equipment) can be **blocked** with a *narrowband partial discharge measuring device* by adjusting the center frequency in an undisturbed frequency range. This is a helpful solution for onsite measurements, in which shielding is generally not possible. It is disadvantageous here that the information about polarity and impulse shape is lost.

4. **Impulse interference sources with constant phase relationship** can be *gated out* by choosing an appropriate *time window*. This option, available for many partial discharge measuring devices, is helpful for orienting measurements, but it is largely *not accepted*, since there is the risk that also the signals to be measured are blocked.

5. **Metal parts at floating potential** can be discharged periodically to the high voltage side or the ground side. Only a good tidiness of the high voltage laboratory with well defined contacting of all conductive parts helps here.

6. Poor, loose or **undefined contacts** can cause the so-called “contact noise”that can be avoided by well defined, e.g. by screwed or wedged conductor connections.

7. **Partial discharges in a test set up (**at edges or points on the high voltage side or the ground side) must be prevented by adequately rounded shield caps. Directional microphones and low-light amplifiers have proved useful as aids for fault location.

Onsite partial discharge measurements in an electrical installation are especially difficult, since large external interferences can be eliminated neither by a hall nor by filters or shield caps. There are a number of approaches, but these do not allow the background noise level of a laboratory measurement to be achieved:

1. Partial discharges are measured with a **bridge measurement,** both in the *leg of the test object* and in a *reference leg* (instead of the coupling capacitor) and they are synchronously recorded [67]. *Common mode signals* must be assigned to external interferences, push-pull signals to the test object (or the coupling capacitor).

2. By the so-called **directional coupler technique**, i.e. by *partial discharge measurement at two different points* (e.g. left or right of a cable joint), it can be distinguished whether the impulse source is between or beyond the measuring points. In this way, both external interferences can be identified and **localization** or spatial demarcation of the partial discharge source is possible. For that purpose, currents and magnetic fields caused by the partial discharge impulses must be observed. External sources cause *common-mode currents*, sources between the measuring points cause push-pull currents. Broadband magnetic sensors or Rogowski coils can be

used for the measurement of partial discharge currents [215], Section 6.3-7.

3. Many more methods are now available to attenuate narrowband and broadband interference sources with the aid of **digital filters**:

   By transformation in the frequency domain and **adaptive filtering** of interference lines, *narrowband interference sources* can be gated out. *External (corona) interference sources* can be separated from internal discharges by **comparing** two signals (e.g. a current signal and a voltage signal), in which one of the signals must be filtered in such a way that the *transmission properties* of both the channels correspond to each other. Interference is similarly suppressed as described in item no. 1, i.e. by *calculating the difference*. For current signals and voltage signals, the direction of interference propagation can be determined by *calculating the product* [215].

   Another approach is the separation of *random interference signals* from the desired partial discharge signals by **neural networks**. For this, a *time-resolved signal shape analysis* is used. It requires a broadband output signal coupling and signal processing up to the VHF range, i.e. up to about 100 MHz, [249].

4. New options for interference signal suppression are also offered by fully **digital partial discharge measuring devices,** in which the *interference signal spectrum* can be analyzed and the *center frequency* and *bandwidth* can be adjusted so that the lowest possible background noise level occurs, Section 6.4.2.4d).

5. Greater progress in interference signal suppression is attained by the **synchronous multi-channel partial discharge measurement**, Section 6.4.2.7. Synchronously measured and related impulses can be identified by their characteristic amplitude relationships or time relationships and assigned to specific interference sources or partial discharge sources. By this, selective *blocking of individual interference impulses* (so-called "**gating"**) is possible.

6.4.2.6 Partial Discharge Diagnosis

Owing to the complexity of the discharge processes, many partial discharge events evade direct physical interpretation according to Section 3.6.3. Modern data techniques could thus make progress by signal analysis, by statistical methods, by pattern recognition methods and by the correlation of synchronous impulses. The decisive breakthrough, namely the reply to the questions

- "Where is the defect?"
- "What type of defect is it?"
- "How severe is its damaging effect?"
- "How are multiple defects to be differentiated?"
- "How does it impact durability?"

has not yet yielded a full response in the general form. Partial discharge diagnosis is, therefore, apparently an everlasting challenge for high voltage engineering research. A few approaches will be described in the following sections. Particular progress is represented by synchronous multi-channel partial discharge analysis, and the following Section 6.4.2.7 is dedicated to this.

a) Classic interpretation

Classic parameters of partial discharge diagnostics are the partial discharge intensity or the *apparent charge*, the *inception voltages* and *extinction voltages* and the *phase position* of partial discharge impulses.

The partial discharge intensity refers to the so-called *apparent charge* Q_A that can be measured externally on the test object terminals. Actual maximum permissible values are derived on the basis of experiences. However it is **not** possible to make a general statement

about the magnitude and hazard of partial discharges within the insulation and about the expected sevice life, since the specific stresses on volumes or surfaces and the signal coupling paths in an (unknown) defect cannot be specified. Moreover, the readings of partial discharge measuring devices depend more on the amplitude of the strongest of the impulses and less on the frequency N which is also relevant for the ageing processes.

The *inception voltages* and *extinction voltages* V_{PDI} and V_{PDE} serve as indicators of production defects and they shall show that, under operating conditions, no damaging discharges can take place. The problem with this is that the inception and extinction of a partial discharge must be defined by a possibly less significant intensity threshold. Additionally, a considerable ignition delay can often be found for closely localized defects [209].

In the case of a *sinusoidal* **AC voltage**, without appreciable distortion by harmonic oscillations, the *phase position* of the impulses gives important indications of the physical environment of the discharge for simple defect situations (e.g. internal/external discharge, contact to electrodes), Section 3.6.3, Figure 3.6-8. The phase-resolved partial discharge patterns are based on a **deterministic physical approach** which facilitates the understanding of the patterns. But on the other hand, it no longer meets the complexity of the situation in many cases. For example, by the superimposition of events from *different defects,* the clearness of partial discharge patterns is lost. Moreover, the interpretation often reflects *subjective* experiences and feelings. A frequent source of error is that for *non-sinusoidal voltages,* false conclusions can be drawn from the phase position of the impulses; and the phase positions can additionally be shifted owing to the *buildup of space charges* [214].

The possibilities for partial discharge interpretation for **DC voltages** are far more limited, since phase relationships cannot be established. Instead of this, it is recommended that *time differences* between successive impulses are considered [465]. This allows basic types of defects to be distinguished, Section 3.6.3.2, but for the development of partial discharge interpretation methods that are illustrated in the following section, this has had no further significance: they are practically exclusively fixated upon AC voltage still. Only *synchronous multi-channel partial discharge measurement* offers a new option, including for DC voltages, for associating the impulses with different defects and different interference sources, Section 6.4.2.7.

b) Statistical approaches

Modern data techniques have opened up new options for processing large data quantities and for statistical partial discharge analyses. **Statistical approaches** for *analysis systems* are based on maximum possible acquisition of impulse data, on data reduction by the storage of some selected impulse parameters, on calculation of new parameters, on determination of *distribution functions* and on the comparison with reference databases. This allows *probabilities* for the presence of different types of defects or "*degree of correlation*" with known defects to be specified [74], [78], [79]. No physical explanation is provided for this, but only a statistically substantiated similarity is ascertained. Reference to discharge physics is often sought through *phase-resolved patterns,* in which so-called "cloud plots" are created by superposition of many periods. This enables the frequency of the discharges to be visualized additionnally by using a three dimensional image or by color gradation, [74] to [80], [204], [212], [213].

Note: There is also the possibility here of *misinterpretation through harmonic distortion influences and space charge influences* associated with the phase-resolved representation.

For digital evaluation, the partial discharge impulses must at first be *recorded* with high bandwidth and *unaltered* as far as possible, then digitalized, filtered and then must be *stored* in connection with other measurement values (voltage, time). This is restricted to a few impulse parameters to reduce the data

volume. By *numerical signal processing*, along with the development of classic parameters (charge, phase position, frequency), other parameters (such as polarity, energy and amplitude) and time constants are developed. Owing to this, during the increasing and decreasing of the test voltage, an extensive *data record* is created, which is *compressed* by creating statistical distribution functions and which can be *further processed* based on different methods and approaches. This involves the important distributions *impulse frequency* against the phase angle or the *impulse amplitude* against the phase angle. It is, however, largely common to analyze a dozen different distributions. The availability of an extensive *database* with *explicitly* identifiable defects is a decisive factor for the validity of statistical analyses.

*Note: T*he reading of a classic partial discharge measuring device can thus be numerically simulated based on the recorded data.

The **visualization** of data records is often carried out with multi-dimensional histograms, in which, for example, parameters such as charge Q_A, frequency N and phase position φ are represented three dimensionally as a so-called *"φ,Q,N-pattern"*. In the simplest form, these are so-called *"cloud plots*", in which partial discharge events summed over several periods are represented as charge points against the phase position. The frequency N is represented in the third dimension either by the density of the cloud points, by a color gradation (see Figure 6.4.2-5 center) or by three dimensional bars.

Along with the subjective evaluation of partial discharge patterns, the aim is to ascertain the *concurrence* of measured data records with reference measurements by means of **expert systems**, in order to achieve an allocation to *type of defect and location of defect*. For this purpose, parameters and distribution functions are compared, correlations are determined and the methods of *pattern identification* or *"fuzzy logic"* are applied. One can also attempt to relate discharge parameters and types of defect via a neural network using a *neuronal approach* [75], [76], [77]. This allows the interpretation of partial discharges to be raised from the subjective level to the level of automated objective comparison. In many cases, this is a great advantage for test practice [210].

Partial discharge analysis systems generally do not give any absolute information about the type of defect, but determine a *degree of correlation* of the measured partial discharge data with previously measured *references*. An allocation to a defect category is possible for sufficiently large database with known defect instances. A statement about the hazard of the partial discharge or about the service life of the insulation is thus at most possible only very indirectly on the basis of operating experiences.

The *interpretation of phase-resolved patterns* such as cloud plots or the *φ,q,n-patterns* is

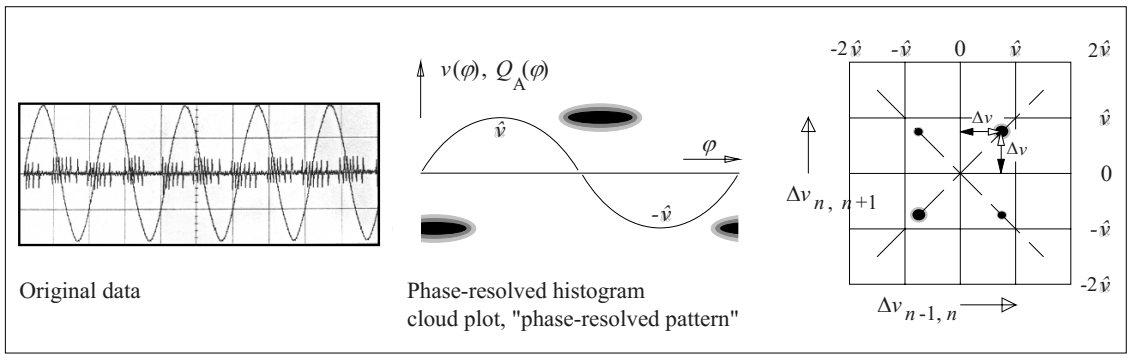

Figure 6.4.2-5: Partial discharge diagnosis for a model body (cylindrical cavity 1 x 1 mm in epoxy resin) with original data (left), phase-resolved cumulative representation (center) and pulse sequence analysis (right).

associated with several **fundamental problems**:

1. The *deterministic relationship* between individual successive and related impulses is lost during the summation of several periods, as is still clearly identifiable in the original data of the example, Figure 6.2.4-5 (left).
2. Phase-resolved representations are *not clear* if the *test voltage is distorted*, especially when intermediate maxima occur. Then several rising and falling flanks of the voltage can occur, in which discharges of varying polarity result. The partial discharge pattern would be completely changed.
3. Phase position can also be shifted owing to superimposition of *space charging fields*.
4. *Multiple defects* are hardly kept apart without additional methods. **Synchronous multi-channel partial discharge measurement** has now been proven as an efficient method for separation of multiple partial discharge sources. This method is able to assign the source of individual impulses and to resolve overlapping partial discharge patterns into individual pattern and to analyze them separately, Section 6.4.2.7.

c) Pulse sequence analysis

The above-mentioned difficulties do not occur with the pulse sequence analysis method, or appear only to a lesser extent. With a pulse sequence analysis, a *deterministic relationship* between successive impulses should be made noticeable by redefined discharge parameters, [211], [214]. The test voltage change Δv between two partial discharge events is observed.

Note: It is a so-called **autocorrelation method,** in which the measured impulses are correlated with each other and not with an external parameter (e.g. phase position).

For example, Figure 6.4.2-5 (left) shows *internal discharges* in a cavity, which "in accordance with the textbook" and analogous to Figure 3.6-2 ignite in the area of the steepest voltage gradient $\partial v/\partial t$, always after passing through the same voltage difference Δv. If the voltage difference between the events n and $n+1$ is applied over the voltage difference between the events n-1 and n, points occur on the diagonals of the pattern for *related*, *equally high voltage differences*, Figure 6.4-2-5 (right). The position of the points is determined by the voltage difference Δv. This voltage difference is characteristic of the defect and independent of the test voltage waveform. In contrast to the phase-resolved pattern (cloud plots), here *sharp patterns* occur, since neither the space charge induced phase displacements nor test voltage distortions play a role here.

A *second defect* would be indicated by another voltage difference. If unrelated impulses appear successively, statistically dispersed voltage differences arise, similar to stochastic *interference impulses*. Then it can be identified that the impulses do not have a deterministic relationship with each other.

Also pulse sequence analysis shows characteristic patterns that can be physically substantiated. While internal discharges occur in the pattern diagonals (see above), *external discharges* have very small voltage differences, and they are concentrated at the origin.

Thus, pulse sequence analysis promises to give an additional contribution to defect detection. However, here also, the question of the life time of insulation under the effect of partial discharge erosion cannot be answered.

Note: With pulse sequence analysis it could be shown that the sequence of partial discharge events is *very much more deterministic* than that which can be identified with statistical analysis. For example, the dispersion of the phase position of the impulses that had been assumed until now as coincidental could be attributed to a systematic cause i.e. could be attributed to superimposition of *space charge fields*. For the evaluation of voltage differences Δv, therefore, many sharp partial discharge patterns occur that are not blurred by statistical averaging and which allow a new and more precise physical interpretation of events [214].

With the superposition of several defects, the ability to identify uniquely is often lost, simi-

larly to the phase-resolved representation. However, a unique identification can be achieved, even in the case of multiple partial discharge sources, by separation of impulses with the aid of **synchronous multi-channel partial discharge measurement**, Section 6.4.2.7.

d) Analysis of impulse shape

The analysis of the impulse shape requires a highly broadband signal recording to obtain an *undistorted image of the signal* (*time-resolved analysis*). Theoretically, the impulse shape or the high frequency spectrum contains information about the type and size of the defect [67], [77]. Unfortunately, the impulses can only be coupled out via broadband field probes in favorable circumstances, such as in gas-insulated switchgear, Section 6.3.3.1.

In most cases, the recording of the unaltered impulse shape is not possible; it always more or less reflects the system properties of the transmission path. Despite this, the information on the transmission path can help in the allocation of an impulse to a specific defect source. Thus, it supplements the options for *synchronous multi-channel partial discharge measurement*, which offers an efficient method for the isolation of different partial discharge sources, Section 6.4.2.7.

e) Electrical detectionof partial discharges

There are a few methods for the spatial localization of partial discharge sources, which are *only* applicable *in special cases*:

With the **directional coupler technique** described in Section 6.4.2.5, not only can the interferences be detected, but the direction of partial discharge sources can also be identified. By the measurement of *partial discharge current at two different points* (e.g. left and right of a cable joint), it can be distinguished whether the impulse source lies inside or outside the measurement points. External sources cause *common-mode currents* and sources between the measuring points cause push-pull currents. Broadband magnetic sensors or Rogowski coils can be used for the measurement of partial discharge currents [215], Section 6.3-7.

In large systems with distributed parameters, propagation time measurements of partial discharge impulses can indicate the location of the defect (**reflectometry**).

Note: With a new approach, it is attempted to determine the *properties of the transmission path in transformers* with a calculated "**curve fitting"** of a measured impulse shape and hence to infer the location of the origin of the partial discharge within the transformer winding. For different transmission paths, a theoretical impulse shape is calculated with the aid of network models and compared with measured ones to be able to identify the suitable transmission path in an iterative process [208].

6.4.2.7 Synchronous Multi-channel Partial Discharge Measurement

A basic problem of partial discharge diagnostics lies in the separation and analysis of different partial discharge signal sources and partial discharge interference sources, which mutually superimpose. Until recently, the unsolved task in this context was to assign signals to multiple different sources and then to individually analyze these according to their type and source.

Note: There is an interesting analogy for this: The ornithologist (bird lover) likes to identity different types of birds and different locations of their origin from various superimposed voices, Figure 6.4.2-6. The technology used for this is based on a *multi-channel measurement* with the aid of two ears for separating different locations as well as *multi-frequency measurement* for analysis of different voices.

a) Principle of synchronous multi-channel measurement

For spatially extended insulation systems, such as *generators, transformers or cable systems*, **multi-channel synchronous comparative measurements** can help in the separation and identification of individual defects, allocation to the relevant phases and suppression of interference sources [217], [272], [422], [455], [461], [463]:

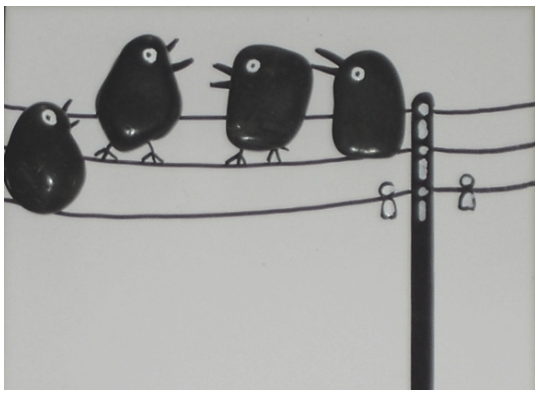

Figure 6.4.2-6: Analogy for multi-terminal/multi-channel-/multi-frequency partial discharge measurement in an insulation system, Image: A. Küchler.

During the so-called synchronous multi-channel partial discharge measurement, the partial discharge impulses are simultaneously recorded in multiple channels, that is, either **at different points** (e.g. at the three phases) or **at different center frequencies**. Complete digital processing of all signals provides the option to store the entire history of the partial discharge processes, even down to every individual impulse, and to subsequently evaluate it on demand, without time pressure and even with different methods.

The basic idea of synchronous multi-channel partial discharge measurement is that a single impulse that originates from a partial discharge sorce is synchronously measured in different channels and forms a *group of related signal impulses* within a time frame, Figure 6.4.2-7. The impulses of a group always have the same *characteristic amplitude relationships and time differences* with regard to each other. These relationships are characteristic of the defect and of different propagation paths (damping and run time). This makes it possible in principle to individually attribute each measured partial discharge impulse to a specific defect source.

Example: In Figure 6.4.2-7, defect 1 can be identified at recurrent amplitude relationships q_1/q_2 and q_1/q_3 as well as recurrent time differences $t_3 - t_1$ and $t_3 - t_2$. Defects 2 and 3 are distinguished from defect 1 by their impulse patterns. Although they are not different from each other in their amplitude relationships, they are different in time sequence or in time differences.

Information about the **attribution of individual partial discharge impulses to different defects** can thus be obtained with the aid of temporally related *impulse groups*. For the first time in the history of the partial discharge measuring technique, it is thus possible to overcome a problem that could not be solved until now: even for multiple superimposed defect sources, the attribution, sorting and **separation** of individual impulses according to the different defects can now be undertaken. By sorting individual impulses, the standard cumulative representation (φ,Q,N-pattern, pulse sequence analysis) can be disintntegrated in separate diagrams for individual defect sources which can be separately analyzed, Figures 6.4.2-8 to -12.

Synchronous **multi-channel** partial discharge measurement can be performed either by

- measurement at multiple points with multiple measuring units (synchronous **multi-point** partial discharge measurement) or by
- measurement at one point, where multiple channels are realized through parallel measuring units with synchronously running filters at different center frequencies (synchronous **multi-frequency** partial discharge measurement).

Note: In a *three-phase system*, synchronous multi-channel partial discharge measurement does not necessarily have to be carried out at the three phases, although it is natural to measure three phase systems accordingly.

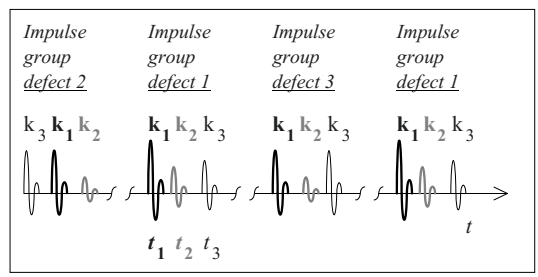

Figure 6.4.2-7: Superposition of partial discharge impulses that are synchronously acquired by three channels k_1, k_2 *and* k_3 *(schematic presentation).*

Note: Naturally, combinations of the above-mentioned methods are also possible, e.g. measurement at multiple points at different frequencies or measurement at a point with multiple units at different frequencies.

Note: A *narrowband measurement* is sometimes recommended for suppression of interferences during on-site measurements. For transformers, it should be ensured that the *center frequency* falls outside the resonance range of the transformer to prevent the alteration of signal amplitudes [273].

b) Visualization

For distinguishing different defect sources, **visualization** of *amplitude relationships or time differences* is very helpful, since these can be clearly designed for three-channel measurements. It will be explained in the example of the **amplitude correlations** of a three-channel measurement. Under this, the highest of the three measured and related charges, e.g. q_{L1}, is set in the ratios q_{L1}/q_{L2}- 1 and q_{L1}/q_{L3} – 1 to the two smaller charges. These ratios are used as *coordinates* to "localize" the defect in a so-called three axis **star diagram**, Figure 6.4.2-9. A *physical defect location* (*or defect source*) in the device is virtually *transformed into a point in the star diagram*, whereby the relationship between the *actual defect location* in the device and the *virtual defect location in the diagram* needs certainly not be simple or known.

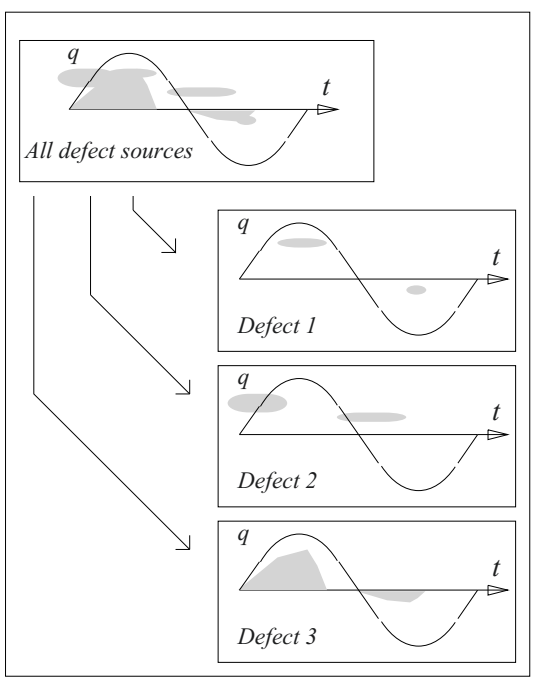

Figure 6.4.2-8: Separation of defect sources.

Defects *between L1 and ground* have the same "distance" to the adjacent phases L2 and L3 and should therefore lie close to line "L1". Defects *between L1 and L3* are also placed between L1 and L3 in the star diagram, since the coordinate $q_{L1}/q_{L3} - 1$ assumes the value zero owing to the equality of charges $q_{L1} = q_{L3}$.

Note: The **correlation** of three synchronous signals can also be realized by the *direct* as axis-parallel vectors. In doing so, the length of the vectors corresponds to the respective **amount of charge** on a linear or logarithmic scale. Another option is the visualization of **time differences** between synchronous impulses. Under this, the impulse triple, depending on the impulse sequences and time differences, is transformed into such a point on the star diagram that there is a relation between the actual partial discharge location and the location in the diagram [463].

Note: According to the terminology of the inventors, these diagrams for three-channel measurements are generally described as "**star diagrams"** [217] and as **3PARD** (*three-phase amplitude relation diagram*), **3PTRD** (*three phase time relation diagram*) or **3CFRD** (*three center frequency relation diagram*) respectively [422], [454], [463].

A particular advantage of star diagrams is that *different defects* each form a *characteristic cluster*. This allows each impulse triple to be "marked" and attributed to *a partial discharge source or interference source.* The clusters can be separated and analyzed individually in a phase-resolved representation.

Example 1: All impulses that are measured *in all three phases* as *common-mode signals* of equal strength are conidered as **external interferences**. They give rise to a value of zero for coordinate formation. The origin or zero point is thus a type of "trash can" into which these symmetrical interference impulses can be moved. However, there are also external interferences which occur asymmetrically and are thereby also represented as asymmetrical to

the axes of the star diagram. However, like other partial discharge sources, they too form characteristic clusters that can be separately extracted, analyzed and identified, see also Example 3.

Example 2: The test voltage was fed in at phase L2 of the stator of an asynchronous motor and synchronous **multi-point measurement** was carried out at all three phases. The star diagram shows two distinct clusters, Figure 6.4.2-10. After separation of the clusters, the individual representation of phase-resolved cloud plots (φ,*Q*,*N*-pattern) shows that Cluster 1 represents an interference source which is sychroneous with the mains. Cluster 2 shows internal partial discharges, which are symmetrical with respect to phase L3 and L1, as corresponds to the connection of the test voltage to L2.

Note: The above-mentioned two-dimensional star diagram of *charge relations* is only a visualization example. The diagrams, for instance, can also be extended to *three dimensions* to be able to illustrate additional impulse parameters for better differentiation (e.g. *impulse polarity*). Instead of *charge relations, relationships of measurement time differences* can also be developed [422]. Of course, measurements can also be carried out with a different number of channels. Furthermore, a resolution into individual cloud plots is possible also for the occurrence of multiple clusters.

Example 3: Partial discharge measurements were carried out on a medium voltage insulator under oil with a single partial discharge measuring device, i.e. *at a single* connection point. Three channels were formed with three synchronous filters that were operated with different center frequencies [461]. It was thus a synchronous **multi-frequency measurement** with a so-called 3 CFRD (three center frequency relation diagram), Figure 6.4.2-11 (top left). In the classic PRPD pattern (phase-resolved PD pattern), superimposed sources and interferences cannot be kept apart from each other, Figure 6.4.2-11 (top right). However, in the multi-frequency star diagram 3CFRD, three clusters result that can easily be distinguished, Figure 6.4.2-11 (left). After reverse transformation, they can be separately analyzed in the phase-resolved representation:

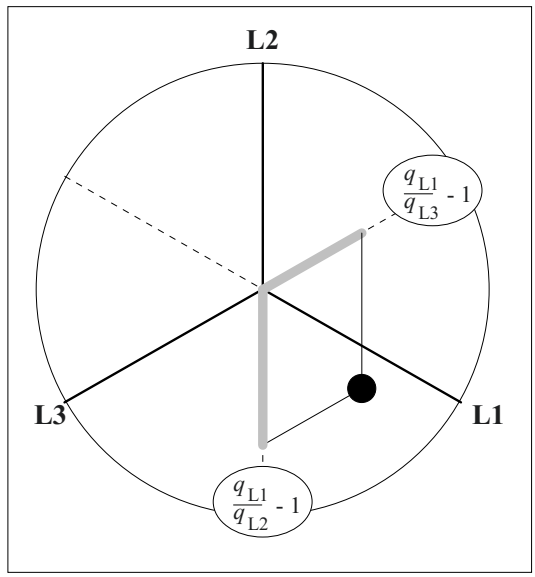

Figure 6.4.2-9: Visualization of a defect location in the so-called star diagram.

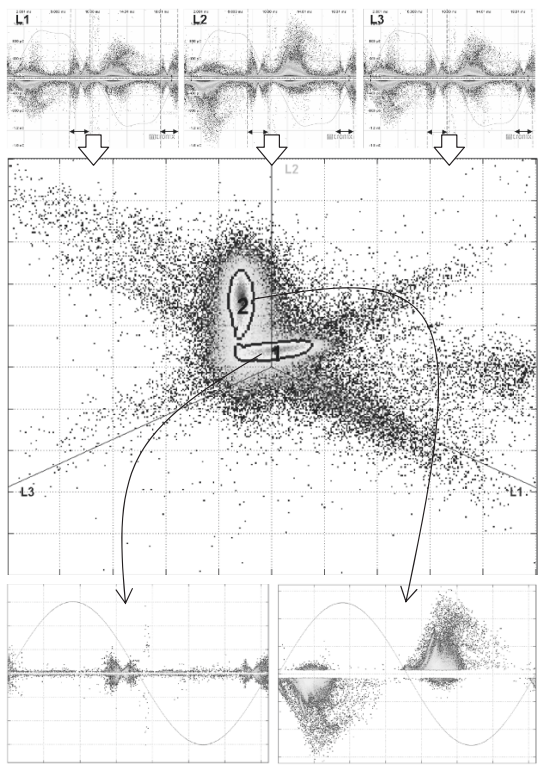

Figure 6.4.2-10: Three-channel PD measurement at the stator of a 10 kV-7 MW asynchronous motor, single-phase test voltage. Top: visualization of interference signals (Cluster 1) and PD (Cluster 2) in multipoint star diagram Below: analysis of individual clusters, phase-resolved representation. Images: Omicron/ R. Plath.

the three patterns can be attributed to the disturbed environment, to a network synchronous impulse interference source that is synchronous with the power system and to an internal partial discharge source, Figure 6.4.2-11 (right).

With this method, it is possible to specifically rid the partial discharge patterns or partial discharge measurements from particular interference sources and also to analyze different partial discharge sources independently of each other. This even allows the partial discharge intensity caused solely by the defect to be determined [461].

Note: Synchronous multi-frequency measurement (3CFRD) is the first method which performs the **separation** of defects and interferences at a single connecting point and simultaneously provides a **classic partial discharge measurement** that is in conformance with IEC 60270, provided one of the bandpass filters can be adjusted to be in conformance with the standard. *Considering the hardware*, the measurement is a *single channel* measurement at a single connecting point. However, *considering the signal processing, three channels* in the frequency domain are formed by three bandpass filters.

c) Partial discharge measurement at DC voltage

Synchronous multi-channel partial discharge measurement provides the option for the first time to separate different partial discharge sources and interferences even at DC voltage [454], [455]. Since three phases are not available for use in the direct voltage test set-up, the channels must be connected to different locations that are isolated by impedances or must be formed by selection of different center frequencies. Thus, even for DC voltage, it is ensured that different sources of signal can be measured with different amplitudes in the different channels and can thereby be separated.

Example 4: Figure 6.4.2-12 shows a three-channel partial discharge measurement with three different center frequencies at DC voltage. Two distinctly distinguishable sources of partial discharge as well as interferences can be identified.

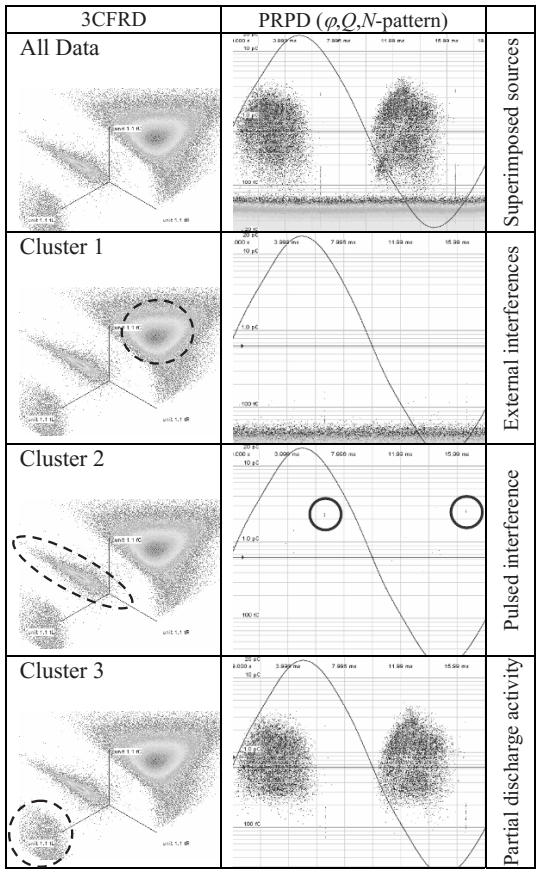

Figure 6.4.2-11: Multi-frequency star diagram (3CFRD) for separation of different partial discharge sources and interference sources [461].

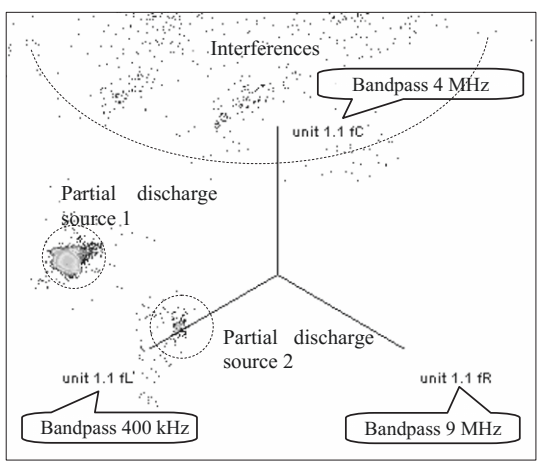

Figure 6.4.2-12: Visualization of a multi-channel partial discharge measurement for direct voltage in multi-frequency star diagram 3CFRD (see text) [454].

Note: The discrimination of interference sources and signal sources is especially important and complex for DC voltage, since often only very few individual impulses occur, and all of these must be counted. Owing to this, the DC partial discharge measurement is especially susceptible to individual interference impulses. Standing, phase-related partial discharge patterns which facilitate an interpretation at AC voltage are not available for DC voltage. Separation by synchronous multi-channel measurement is, therefore, a great step forward.

6.4.2.8 UHF Partial discharge Diagnosis

Partial discharge impulses do not only exhibit the relatively low frequency spectrum used for classic measurement. It has been shown that, especially for partial discharges in gas-insulated switchgear (GIS) and depending on the type of defect, even *very high-frequency spectral components* (UHF ultra high frequency) can occur up to the region of about 2 GHz. Since many sources of interferences (mobile phones, radar, television, outdoor corona) are predominantly narrowband or transmit in lower frequency ranges, a very high **signal to noise ratio** is possible with a relatively *narrowband measurement* in the range of 100 MHz to 2 GHz, even for an onsite measurement [218].

The most important **application** of UHF partial discharge diagnosis is the checking of a GIS that is *assembled at the construction site*, which can only be checked component-wise in the factory before transport and assembly. Functional verification of the entire system must be carried out after *onsite* assembly. In particular, it involves the detection of **contaminations** in the form of *hopping or fixed particles*. Moreover, *cavities* may be detected in cast-esin components (post insulators, teminations). In principle, UHF diagnosis is also possible **online**, that is, at operating voltage [260], Section 6.4.8.4.

Note: Owing to the favorable signal-to-noise ratio in the UHF range, it is also suggested to carry out *online partial discharge measurements on the cable accessories* in the UHF range [262].

UHF diagnosis requires largely undamped transmission paths in the device and a very broadband coupling of signals. Both conditions are satisfied in **gas-insulated systems**. In devices and equipment with liquid and solid dielectrics, such as **cables or transformers**, a significantly higher damping and very often also complex transmission paths do exist. Thus, the applicability of the UHF diagnosis is significantly limited.

The signal is extracted by *broadband capacitive* **sensors** Section. 6.3.3.1. They are either directly mounted in the assembly openings in the grounded outer conductor of a switchgear (flush with the inner surface of the conductor) or subsequently applied to the glass panels of viewing windows as so-called “window sensors”. If multiple sensors are distributed in the system, the **partial discharge source** can be **located** accurately to a few 10 cm using propagation time measurements as well as damping induced amplitude differences. For this, if need be, an *acoustic partial discharge measurement* is additionally included, Section 6.4.2.9.

Note: Another possible application of UHF diagnosis is the *localization of partial discharges in transformers* by recording the propagation time differences of multiple sensors [263].

The amplified sensor signals can be fed via a multiplexer into an *oscilloscope* and into a *spectrum analyzer* for time domain and frequency domain measurements, Figure 6.4.2-13. Similar to the classic partial discharge diagnosis process, the UHF signals can be represented with regard to the test voltage phase in which similar *partial discharge patterns* occur, and these can be interpreted in a comparable manner [218]. For this, even *classic partial discharge diagnosis systems*, e.g. for the phase-resolved representation, can be used along with converters for the conversion of high frequency sensor signals [260].

In contrast to classic partial discharge measurements, UHF measurements *cannot be directly calibrated,* since there is generally no clear relationship between the apparent charge of a PD impulse and the reading of UHF sensors.

Note: Instead of calibration of a sensor, until now a so-called "**sensitivity check**is used which is carried out in multiple steps: (1) At first, an artificial defect is inserted into the system to be tested, whose partial discharge intensity is measured with a calibrated classic partial discharge measurement system (e.g. 5 pC). Simultaneously, the UHF spectrum of the defect is recorded in the vicinity of the defect with the sensor to be tested. (2) Subsequently, at the defect location, a reference impulse with a short rise time (< 0.5 to 1 ns) is fed in and its amplitude is changed such that the best concurrence with the UHF spectrum of the artificial defect results. (3) The *reference impulse* determined in this way can later be used as a reference for partial discharge impulses with intensity corresponding to that of the artificial defect (in the example, 5 pC). The accuracy is restricted (+/-30%). Moreover, the reference impulses for different systems and different installation locations must be specified again each time. Sensitivity check is thus very complicated.

Owing to excellent correlation options, the s*ynchronous multi-channel measurement* explained in Section 6.4.2.7 allows a **calibration** of individual UHF impulses for the first time [462]. Moreover, the method is also simple and even conforms to the standards: For each impulse, the UHF signal and classic partial discharge signal are synchronously recorded. Since the classic signal can be quantified via a classic calibration, this even gives the relationship of the related (synchronous) UHF partial discharge impulse to the classic apparent charge Q_A in accordance with Eq. (6.4.2-3).

This implies that it is now possible to use the advantages of UHF partial discharge measurements, which are frequently less affected by interferences, and simultaneously to supply the relevant value of apparent charge Q_A to each individual UHF partial discharge impulse in accordance with the standard.

6.4.2.9 Non-electrical Methods of Partial Discharge Diagnosis

The recording of *electrical* partial discharge impulses is an *ever applicable* method, which also facilitates *quantitative intensity data*. Although optical, acoustic and chemical methods cannot be universally used, in special cases they are of great importance, see Section 6.4.5:

Optical discharge measurement enables very precise localization in gases and other transparent media.

For example, even external corona discharges of up to approx. 10 pC can be seen with *low-light-level amplifiers*. This generally requires a complete darkening to prevent outshining by the ambient light.

Detection can now be carried out even with *daylight UV cameras* by selective filtering of UV discharge light. This involves special cameras superimposing a UV image with the partial discharges and a normal light image with the view of the discharge location [219]. This makes it possible to efficiently monitor *outdoor sub-stations*.

The *volumes of encpsulated switchgear* can be monitored with *light detectors*.

Using **acoustic propagation time measurements**, discharges in *transformers* and other devices can be localized precisely to several cm. Under this, microphones for the detection of *structure-borne noise* are mounted at multiple points of the transformer tank. The time differences between related signals of different measuring points are evaluated for a *triangulation* of the discharge location. Uncertainties arise through refraction, reflection or material

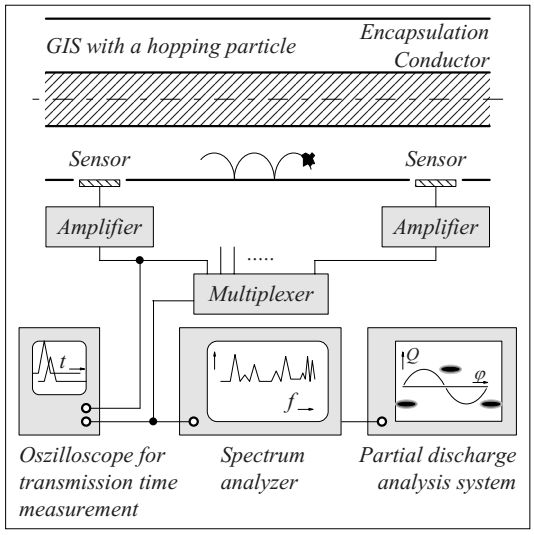

Figure 6.4.2-13: UHF partial discharge diagnosis.

induced propagation time variations. Background noises must be damped by opting for a suitable frequency band in the ultrasonic range. Further, external corona discharges can be detected with **directional microphones** that are especially sensitive in the ultrasonic range.

Acoustic partial discharge measurement is an important aid for defect location in test fields and in transformer tests.

Chemical analyses of insulating oil (*gas-in-oil analysis*) can detect decomposition gases in very low concentrations ($\geq$ 1 ppm). Under this, however, the immediate partial discharge events are not measured. It is rather an integral method that provides information about the elapsed period, Section 6.4.3.2.

6.4.3 Chemical Analyses

Electrical diagnosis methods are effectively supplemented by physical and chemical methods.

Physical parameters, such as gas pressure in gas-insulated switchgear, the oil level in oil-filled devices*,* gas formation in transformers (Buchholz relay) or the insulating material temperature help in online monitoring or the routine checking of devices and systems.

Chemical analyses are especially important for the diagnosis of *oil-paper insulation*. They enable the determination of water content (Section 6.4.3.1), of cracked gas dissolved in oil (Section 6.4.3.2), of dissociation products of cellulose (Section 6.4.3.3) and of the degree of polymerization (Section 6.4.3.4).

The *numerous other chemical and physical methods of examination* that result from the many insulating materials used will not be dealt with in detail here. In practice, the suitability of materials must often be checked under conditions close to the application. For example, frequent questions of interest are related to temperature resistances, ageing resistances or hydrolysis resistances, material compatibility, mechanical strengths, glass transition temperatures, pot lives, thermal expansion, hydrophobicity, material compositions, contaminations and many other parameters.

6.4.3.1 Determination of Water Content

Moisture has a strong *strength-reducing effect*, Figure 3.4.2-1. Moisture in cellulose-based insulations accelerates thermal ageing through *de-polymerization*, in which water can again be the dissociation product, Figure 3.5-6. Drying during production and long-term closure against moisture are therefore basic prerequisites for high-voltage resistant oil-paper insulations. Water content must therefore be checked on a routine basis in order to carry out drying processes and sealing measures in time.

Determining the **breakdown strength** of oil provides useful results for water content only *when the moisture level is very high* and is close to the saturation concentration, Figure 3.4.2-1. Moreover, the result is influenced by other parameters, such as temperature and particle content. Therefore, a breakdown measurement can give only a *rough guide*.

More exact determinations of low water contents in *mineral oil* and other *low viscous fluids* are possible by **Karl Fischer titration** [220]. For this, careful *sample extraction* without the entry of additional moisture is necessary at first: a dry syringe is rinsed with the oil to be analyzed before the actual oil sample is taken. The ingress of air must be strictly avoided during this process. The oil sample is introduced through an air tight diaphragm in the analysis container with conditioned solvent (e.g. methanol), in which all moisture has earlier been directly bound by the dosed addition of a titrant (stand-by operation).

The actual *analysis* is carried out by the dosed addition of titrant until the moisture released from the sample is completely bound. This is detected by a change in the conductivity.

The titrant can be added with a dosing pump (*volumetric method*). The water content of oil is calculated in ppm from the quantity of the titrant and from the weight of the oil sample. In the *coulometric method* [220], the iodine necessary for the titration is formed electrolytically from iodine ions directly in the analysis container:

$$2\,J^- - 2\,e^- \rightarrow J_2$$

Since one mole of water reacts stochiometrically with one mole of iodine, the amount of electricity necessary for preparing iodine is proportional to the quantity of water.

Different solvents and titrants are available for Karl Fischer titration [221]. In the case of *silicone liquids*, special reagents are necessary, since water molecules get deposited on siloxanes by hydrogen bonds [16].

Note: In the case of *highly viscous fluids*, water content can be determined according to the vaporization procedure explained below for pressboard or by dilution with very dry solvent.

Determination of moisture in **solid cellulose based insulations** is difficult. Indeed theoretically it can be determined via *equilibrium curves* from the water content in the oil and the temperature, Figure 5.5-6. Practically, however, owing to very long diffusion time constants, the *absence* of an equilibrium status should be assumed. Moreover, even for very low measured water content in oil (e.g. 5 ppm), the equilibrium water content in paper can still be up to several percent. Moreover, the curves of different authors differ from each other. Measurements of **insulation resistance** and the new methods of **dielectric diagnosis** (Section. 6.4.7) have also not yet been established as quantitative methods for the determination of moisture.

Destructive testing by direct chemical analysis of *paper samples* remains a safe option. They must be brought from the test object under oil directly to the examination with the exclusion of air contact. In the case of air contact, the hygroscopic cellulose would quite rapidly absorb additional moisture. Paper samples, for example, can be cut under oil from the top layer of the insulation, for development models or discarded devices, also from electrically *un*stressed parts of the insulation. The analysis is based on **Karl Fischer titration,** in which the moisture must first be removed from the cellulose. There are three methods:

1. *Direct titration:* The sample is *directly* brought *into the titrating container* with the solvent. The problem here is that the moisture, especially for thicker samples, is released only very slowly, so that additional moisture can eventually penetrate into the measuring system during the extraction time. This drift of the measuring system must be determined with a dummy measurement and must be subtracted. Direct titration is often applicable only for very thin samples (paper).

2. *Extraction with methanol:* The sample is stored in *previously dried solvent* for over 2 hours, and its water content can be analyzed similarly to that of an oil sample. It is often advisable to mix oil-releasing components into the solvent. The water content of the solvent must be determined with a dummy test specimen and must be subtracted [220].

3. *Evaporation method:* The sample is dehumidified in a separate oven at approx. 130 to 140 °C (partially to 170 °C) in a dry *stream of carrier gas*. The gas bubbles through the solvent and releases the water. The drift of the measuring system during the extraction time must be determined by a dummy measurement and must be subtracted.

Note: The extraction temperature is a critical compromise: it must be high enough to push out all water and it must remain low enough that there are no significant new quantities of water owing to de-polymerization.

6.4.3.2 Gas-in-oil Analysis

Electrical discharges and local overheating decompose the insulating oil and the cellulose. The resultant type of *decomposition gases* complies with the energy density in the defect and the insulating materials involved (mineral

Table 6.4-1: Characteristic decomposition gases of insulating oil for the defect indication in transformers [96].

Type of gas and maximum normal gas concentration after multi-year operation of transformers [98] *µl/l or ppm resp.*			Electric discharges			Local overheating			Decomposition of cellulose
			Electric arcs	Sparks	PD	>1000°C	1000 ... 300°C	<300°C	
Hydrogen	H_2	*200*	🔑	🔑	🔑	●	○	○	
Methane	CH_4	*50*	●●	●	●	●●	●	●	
Ethane	C_2H_6	*15*	○	○	○	○	○	🔑	
Ethylene (Ethene)	C_2H_4	*60*	●●	●	○	🔑	🔑	●	
Acetylene (Ethyne)	C_2H_2	*15*	🔑	🔑	● *)	●	○		
Propane	C_3H_8		○			○	○	●●	
Propylene	C_3H_6		●	○		●	●●	○	
Carbon monoxide	CO	*1000*							🔑
Carbon dioxide	CO_2	*11000*							●●

Key gases: 🔑 Associated gases: larger proportion: ●● smaller proportion: ● unspecific: ○

*) only for high energy density

oil, cellulose). Analysis of *fault gases* dissolved in the oil can provide valuable information about the deterioration process.

Note: Meanwhile, it is also proposed, to analyze the collected fault gases in the Buchholz relay and to assess them with the aid of gas exchange models [420].

a) Interpretation of gas-in-oil analyses

The **interpretation** of measured gas concentrations allows the identification of different types of defects with the aid of characteristic *key gases* and *accompanying gases*, Table 6.4-1. Gas-in-oil analysis has, therefore, developed into one of the most important *diagnosis methods* for oil-filled devices, such as *transformers, measuring transformers, bushings, oil-filled cables* and oil-filled *switchgear*.

Electrical discharges lead to separation of hydrogen and, with high energy density in electric arcs and sparks, can also lead to low-molecular unsaturated hydrocarbons (acetylene). *Thermal overheating* causes a decomposition of oil molecules by *pyrolysis* at the so-called hot spot. This even results in appreciable quantities of hydrocarbons with longer chains being formed with two and three carbon atoms. Defects during *decomposition of cellulose* can be identified through carbon monoxide and carbon dioxide. In the process, oxygen atoms are obtained from the cellulose molecules, Figure 5.5-7

For distinguishing different types of defect, a number of empirically substantiated criteria were developed that are not based on the absolute concentrations but on the **ratios** of different gas concentrations, Figure 6.4.3-1. They initially apply to transformers, but can also be applied to other oil-filled devices [95] to [100], [163], [164], [165]. IEC 60599 recommends an interpretation on the basis of three so-called *basic gas quotients* [393], Table 6.4-2.

For a **rough classification**, partial discharges (PD) are characterized by $CH_4/H_2 < 0.2$, discharges (D) are characterized by $C_2H_2/C_2H_4 > 0.2$ and thermal defects (T) by $C_2H_2/C_2H_4 < 0.2$. In the case of *bushings*, we assume $CH_4/H_2 < 0.07$ for partial discharges (PD), $C_2H_2/C_2H_4 > 1$ for discharges (D), $C_2H_4/C_2H_6 > 1$ for thermal defects (T) and $CO_2/CO < 1$ or > 20 for thermal defects in paper (TP).

Developing useful ratios requires the measured gas concentrations to be significantly greater than the *quantification limit* and that at least one value in the ratio to be calculated must be above the **significant gas concentration**. There are distinct differences between various electrical equipment, Table 6.4-3.

Calculation of ratios can be inaccurate owing to already **present gas concentrations**. The causes are, for example, CO_2 absorption from the atmosphere (up to 300 µl/l), CO_2 generation through paper ageing or oil oxidation, H_2 production through reaction of steel with water, from protective coatings or from overheated core plates, as well as the basic concentrations that are present owing to natural ageing or previous defects. Where possible, such influences must be **corrected**, e.g. by the evaluation of *concentration variations (trend analysis)*.

Often, the common classification with *defect codes* of ratios is not very vivid. It is therefore common to use **graphic illustrations** Sometimes.

Thus, a *nomogram* [98] is shown as an example, in which the measured gas concentrations are marked on logarithmic scales and are connected by straight lines, Figure 6.4.3-2. The ratios can be identified in the illustrated form by the slopes of the straight lines. They can be related to the basic types of defect, such as *electric arc (D), partial discharge (PD), pyrolysis/ overheating (T) and decomposition of cellulose or paper* (TP) with the aid of a legend.

The described nomograph shows a series of advantages for the practical application: interpretation of the data is very clear, high gas concentrations are immediately obvious and differences are especially clear for comparative representations in the same image. This is especially valuable for the comparison of similar objects as well as for trend analyses for the same object.

The *gas concentrations* are determined not only by the energy conversion in the defect but also by the time, the oil volume and by the diffusion time constants. For the assessment of an analysis result, the *types of gases* and their *relations to each other* are therefore more important than the concentration values. The development of concentration values against time is, however, an important criterion with regard to a *trend analysis,* in order to decide about the removal of operating equipment from the network. The difficulty in this is that the defect can be escalated up to a breakdown within very short periods. Annual or half-yearly *control measurements* are therefore not always adequate to identify hazardous developments. *Continuous monitoring* with simple and robust measuring systems is desirable for large transformers [166].

b) Extraction of fault gases

With the exception of the less common analysis of free gases from the Buchholz relay, the

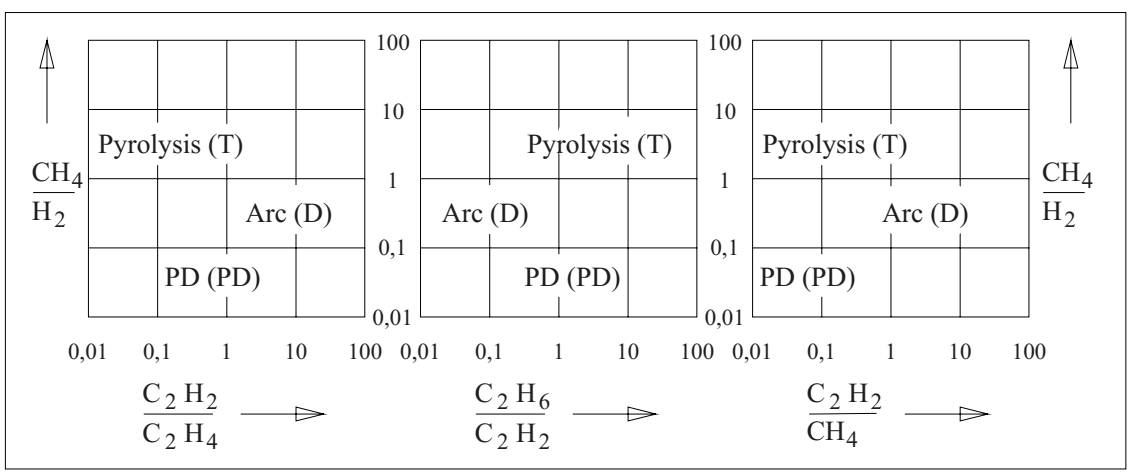

Figure 6.4.3-1: Allocation of the three basic types of defects "pyrolysis" (thermal overheating, T), "arc" (electric arc, spark discharge, D) and "PD" (partial discharge, PD) to the characteristic ratios [98].

gas-in-oil analysis at first requires the **extraction** and **compression** of the dissolved gases. For this purpose, an *oil sample* is generally drawn with a syringe without contact with air and injected into an evacuated *degassing container*, Figure 6.4.3-3 (left).

With the classic measurement, a special mercury-piston pump, the so-called **Toepler pump**, creates a partial vacuum and sucks off the evaporating gases, which are compressed in a *collecting burette*, Figure 6.4.3-3.

Note: The piston of the *Toepler pump* comprises of a mercury level moving up and down in a glass cylinder. This ensures an ideal impermeability. The influx and delivery of gases is carried out via electromagnetic valves that are contactlessly controlled. A great disadvantage of the classic Toepler pump is the large quantity of mercury contained.

Meanwhile, there are mercury-free alternatives that are available for degassing: during the **vacuum extraction**, the fault gases evaporating in the degassing container are fully com-

Table 6.4-3: Typical 90 % or 95 % values that were observed in individual networks. Variations in other networks are possible [393].

Values in µl/l (or ppm)

Gas	*Transformers*	*Bushings* **)	*Measuring transformers*	*Oil-filled cables*
H_2	60 -150	140	6 – 1000 **300** *)	150 - 500
CO	540 - 900	1000	250 – 1100 **300** *)	40 - 100
CO_2	5100 - 13000	3400	800 – 4000 900 *)	220 - 500
CH_4	40 - 110	40	11 – 120 **30** *)	5 - 30
C_2H_6	50 - 90	70	7 – 130 **50** *)	10 - 25
C_2H_4	60 - 280	30	3 – 40 **10** *)	3 - 20
C_2H_2	3 - 50	2	1 – 16 **2** *)	2 - 10

*): Suggestion for maximum permissible values for closed measuring transformers without need for action.

**): Suggestion for typical values for bushings.

Table 6.4-2: Gas-in-oil analysis according to IEC 60599 [393].

Case		*Basic gas quotients:*	$\frac{C_2H_2}{C_2H_4}$	$\frac{CH_4}{H_2}$	$\frac{C_2H_4}{C_2H_6}$
PD	**Partial discharges,** in the form of cold corona discharges, associated with X-wax formation or small perforations in paper.		not significant	< 0.1 < 0.2 *) < 0.07 **)	< 0.2
D1	**Discharges of low energy**, associated with larger perforations in paper (holes), carbonization of paper surface (creepage path formation) or carbon particles in oil (similar to on-load tap changers in transformers).		> 1	0.1 – 0.5	> 1
D2	**Discharges of high energy,** with energy conversion (often identifiable by disconnection), associated with extensive decomposition of paper, molten metal at the discharge base points or extensive carbonization of oil.		0.6 – 2.5	0.1 – 1	> 2
T1	**Thermal defects upto 300 °C,** associated with brownish coloration of paper		not significant	> 1, not significant	< 1
T2	**Thermal defects between 300 °C to 700 °C**, Associated with carbonization of paper		< 0.1	> 1	1 - 4
T3	**Thermal defects above 700 °C**, associated with carbonization of oil and if applicable, with metal colorations (above 800 °C) or molten metal (above 1000 °C).		< 0.2	> 1	> 4
TP	**Thermal defects in paper**		$\frac{CO_2}{CO}$	< 3 ***) < 1, > 20 **), ***)	

*): valid for measuring transformers, **): valid for OIP bushings

***): the CO_2 and CO values should be corrected by the background values from paper ageing, oil oxidation and absorption of CO_2 from the atmosphere (for open devices, upto 300 µl/l).

pressed in a valve block with a multi-stage vacuum pump and an automatically controlled on-off valve [419]. This allows a high sensitivity to be attained. Automation even enables *online monitoring* in continuous operation.

Note: For automated systems, it is also possible to allow the evaporating gases in a degassing container to enter into an evacuated tubular *filling loop*. In this, the gas is subsequently compressed by an auxiliary gas which pushes the fault-gas plug into the gas chromatograph [166].

A simple to use, but slightly less sensitive method is **partial vacuum degassing**, in which the oil, for example, is sucked in with the aid of a syringe and partially degassed, Figure 6.4.3-4. The evaporated gas can be compressed with the same syringe and injected into the gas chromatograph [419].

Note: Another option for partial extraction of gases dissolved in oil is by using permeable membranes.

In the case of transformers, the **free gas** collected in the *oil expansion vessel* (Buchholz relay) can also be evaluated in addition to the analysis of gases dissolved in oil. In the *equilibrium condition*, the ratio of the gas concentrations of the liquid phase to the gaseous phase is given by the so-called *Ostwald coefficients*, such that the analysis is generally possible with the converted concentrations in accordance with Table 6.4-2. However, an equilibrium condition is often doubtful, since the dynamics of gas generation processes and gas exchange processes must always be considered [420]. For this, the *concentration comparison* between the liquid phase and the gaseous phase can give information about the dynamics of the progression of defects [393].

c) Determination of gas quantities

The gases to be analyzed are added to the carrier gas stream in a **gas chromatograph** (*mobile phase* of Ar, He or N_2) and pass through a capillary ceramic *separation column*. Different propagation times are obtained by the interaction with the surface (*stationary phase*), depending on the type of gas. The emergence of a gas component at the outlet of the column is

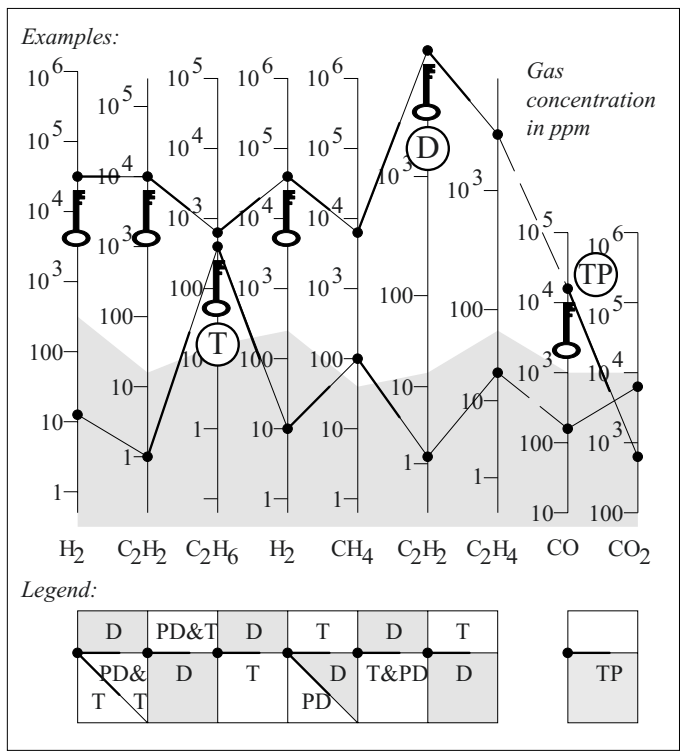

Figure 6.4.3-2: Nomograph for interpretation of decomposition gases dissolved in oil [98]:

The measured gas concentrations are applied on a logarithmic scale in ppm and are connected to each other by straight lines. The slope of the line is a measure of the concentration ratio. Allocation to the three basic types of defects is conducted with the help of the legend. It specifies the angular fields through which the lines pass for different types of defects:

D: Electric arc, sparks (discharges)
T: Pyrolysis, overheating (thermal defect)
PD: Partial Discharges
TP: Thermal decomposition of paper

Two analysis examples with key gases:

1.) D and TP:
Severely damaged oil-paper core of a bushing with partial breakdown of 15 % of the insulation layers.
2.) T:
Indication of thermally stressed oil.

Concentration range below the significant gas concentration limit is shaded in grey.

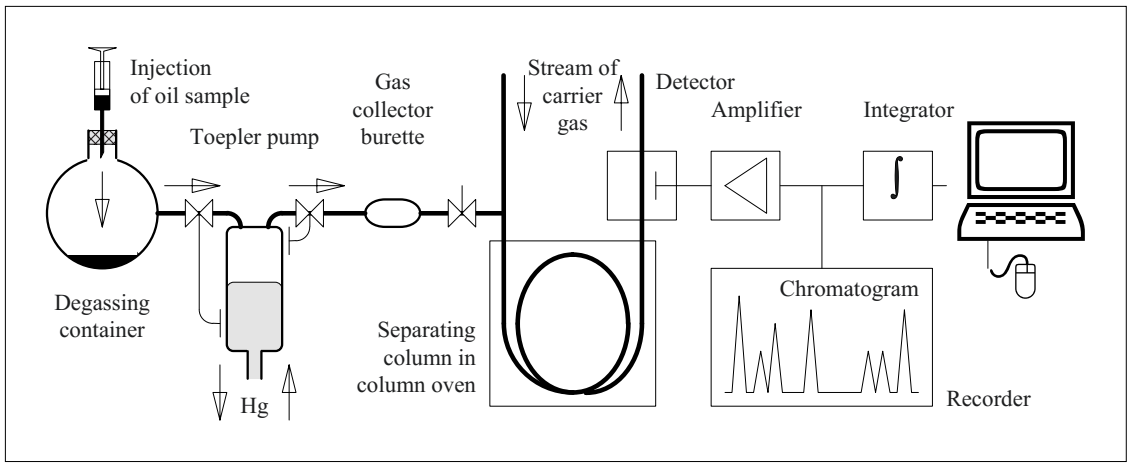

Figure 6.4.3-3: Gas-in-oil analysis system with oil sample injection, degassing, collection and chromatograph.

registered by a *detector* and plotted in the *chromatogram* as a peak. The attribution of peaks to different types of gases is dependent on the individual properties of the column and must be undertaken with the aid of a so-called "*calibration gas"* of known composition. Quantitative evaluation is carried out by the *integration* of areas under the peaks.

Note: For inflammable gases, a *flame ionization detector* (FID) can be used as a detector which burns the gases in a hydrogen flame and registers the change in conductivity occurring due to ionization in the gas. CO and CO_2 are catalytically converted beforehand to hydrocarbon compounds. Hydrogen and non-inflammable gases such as N_2 and O_2 must be measured by thermal-conductivity detectors (TCD) via the change in the thermal conductivity in the gas stream. werden.

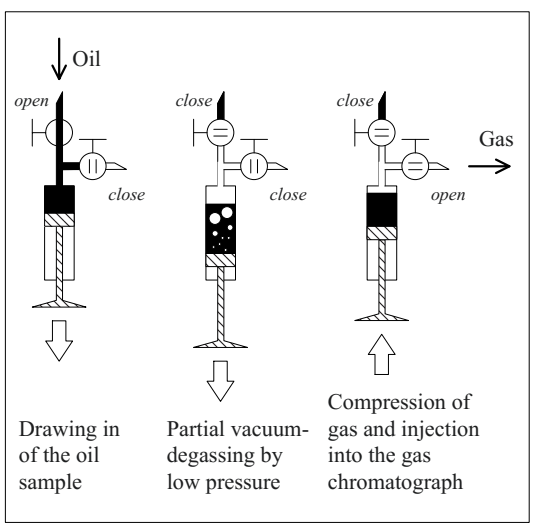

Figure 6.4.3-4: Partial vacuum-degassing of insulating oil.

For *automated measuring systems for continuous online monitoring* of large transformers, **infrared-spectrometers** are also available for use and they can measure the relevant fault gases with the exception of hydrogen. Therefore an additional sensor is necessary for hydrogen [166].

6.4.3.3 High-pressure Liquid Chromatography (HPLC)

Cellulose chains are shortened during the *ageing of cellulose* by depolimerisation. *Furfuran derivatives* that are partially soluble in oil are obtained (furfurals, often also described as furfurols or furanes). These high-molecular compounds *cannot* be determined by the gas chromatographic method.

For the *analysis*, decomposition products are extracted with solvents or silica-gel columns (liquid-liquid extraction and liquid-solid extraction). The separation of decomposition products is performed by *high-pressure liquid chromatography* (HPLC: high pressure/ performance liquid chromatography). In a separating column, the decomposition products transported by a *liquid mobile phase* are decelerated at different rates by addition to a sta-

tionary phase and are registered by a UV detector [84], [112], [167], [168].

Note: The stationary phase consists of pellets with a diameter of approx. 5 µm in a steel column with a diameter of approx. 4mm. Hydrocarbon chains are linked at the spherical surface made of SiO_2 atoms. Non-polar molecules are thus decelerated more than polar molecules. Owing to the narrow cavities, high pressures up to 400 bars are necessary for movement of the mobile phase. [49].

Similar to gas-in-oil analysis, the analysis of furane derivatives provides *integral data* about the entire oil-impregnated *volume* and about the entire *period* in which the oil is neither changed nor processed. That is, even the inaccessible internal areas of the insulation are monitored. However, in practice, there is not yet a verified relationship between the *degrees of polymerization* of aged cellulose-based insulations and the content of furane derivatives in insulating oil. For the assessment of the ageing condition, therefore, there is still no standard interpretation pattern [84], [112].

6.4.3.4 Determination of Degree of Polymerization of Cellulose

The average number of glucose molecules in a chain molecule of cellulose is described as the *mean degree of polymerization* (DP value), Figure 5.5-7. In the new state it is around 1300 to 1400 and reduces owing to *thermal ageing*, especially in the presence of *moisture*, Figure 3.5-6. Owing to this, cellulose becomes fragile and brittle. On mechanical grounds, the limit for the operational safety of transformers is seen at a DP value of 150 to 200 [84].

According to IEC 60450, the DP-value is determined by dissolving *cellulose samples* in copper ethyldiamine. The viscosity of the solution is a measure of the average chain length of cellulose molecules.

Paper samples must be taken from electrically unloaded sections of insulation for the analysis. These *random samples* are not always representative of the ageing condition of the hot spot.

6.4.4 Insulating Material Tests

Properties of insulation materials are determined and checked by a number of chemical and physical methods. This should be restricted to the most important *electrical test procedures* in this context. Their application is described in the standards (e.g. IEC or DIN VDE group 3).

6.4.4.1 Dielectric Measurements

Dielectric measurements on the insulating materials have already been described in the context of dielectric measurements on devices in Section 6.4.1. Important parameters are the *permittivity* ε, *dissipation factor* $\tan\delta$, *volume resistance* R_V and the *surface resistance* R_S, [178].

Measurements are carried out in *guard-ring arrangements*, to obtain a well defined field geometry and to avoid inaccurate measurement owing to leakage currents, Figures 6.4.1-3 and -4. In the case of solid and flat plate-type insulating materials, ring-shaped and circular-shaped electrodes are placed on the surface or applied with conducting varnish. Measurements on liquid insulating materials are carried out in special cylindrical measuring cells, Figure 6.4.1-4.

Important parameters that can influence the result of measurement are *frequency and temperature*. *Air humidity* is also of significance for determining the surface resistance.

6.4.4.2 Breakdown measurements

Breakdown voltages, to a large extent, are influenced by many different parameters, see Section 3. For this reason, properly defined conditions for breakdown measurements are specified in the *standards* to facilitate a *comparison* between different materials.

The **results** are strongly dependent on the *electrodes* used, on the *embedding medium*

and on the *rate of voltage rise*. Consequently, they are **not comparable** for varying test conditions. The breakdown voltages that are determined are therefore not "material properties", but only comparative values for test objects that are tested under *exactly the same conditions*. Information on *breakdown strength without* the details of **exact test conditions** is *worthless*.

Furthermore, the breakdown strength determined under *standard conditions* often varies significantly from the strength relevant to the application. The user must therefore develop the appropriate strength for his *application purpose* from the general dependences in accordance with Section 3, or determine them experimentally under application-oriented conditions.

Problems during breakdown measurements often result from field strength enhancements at the *electrode edges*, from *surface discharges,* from the influence of the *rate of voltage rise* and from the *statistical dispersion* of measurement values.

a) Electrode arrangements

For the testing of **liquids** in accordance with IEC 60156 [176] - [177], a distance d = 2.5 mm between spherical electrodes (D = 12.5 to 13 mm) or partially spherical electrodes (spherical caps) is used, Figure 6.4.4-1 (left). The latter show only a weakly non-uniform field on their axis (η = 0.97) and the field strength decreases outwards. Other standards specify other electrode arrangements and different measurement values are obtained, Figure 3.4.2-3.

According to IEC 60243 [173]-[175], solids in the form of **boards and films** can be tested, for example, between disc-shaped **electrodes** (D_1 = 25 mm, D_2 = 75 mm or $D_1 = D_2$ = 25 mm), Figure 6.4.4-1 (center). Under this, the stress is applied *perpendicular to the surface* or *perpendicular to the layers* in layered or laminated materials.

For many other test objects, which cannot be tested between disc-shaped electrodes (bands, strips, pipes, tubes, cylinders, cast materials, solid shaped pieces etc.), the standard allows a *widely different range of electrodes* (rods, foils, spheres, pins). Furthermore, specifications are provided for tests *parallel to surfaces* or *parallel to the layers* in layered or in laminated materials.

Electrode arrangements with insulating material samples form often typical "*creepage surfaces*" with very low inception voltages for surface discharges, see Section. 3.2.6. In the case of test stresses perpendicular to the surface, the inception of creepage discharges should be avoided, so that inaccurate breakdown measurement values do not occur as a result of erosion of the dielectric in the electrode edge area. Thus, the testing under *air* is restricted to very thin films. By **embedding** the electrodes and the test sample in a dielectric with high electric strength and with a field displacing effect, i.e. with a high permittivity, the inception of surface discharges can be shifted up to a few 10 kV, according to Eq. (2.4-35). Theoretically, the *strength of the interstice* for *AC voltage* must fulfill the condition

$$(\varepsilon_r \cdot E_{bd})_{interstice} > (\varepsilon_r \cdot E_{bd})_{insulation}. \quad (6.4.4\text{-}1)$$

And for *DC voltage*, the condition

$$(\kappa \cdot E_{bd})_{interstice} > (\kappa \cdot E_{bd})_{insulation} \quad (6.4.4\text{-}2)$$

must be fulfilled, Figure 2.4-18. Generally, the strength of the interstice increases steeply with narrowing gaps, Figure 2.4-19. In practice, (dried) transformer oil is often used as an embedding medium, whereby it must be ensured that the material to be tested is not changed by the oil, e.g. by swelling or unwanted impregnation.

Note: Even while testing completed and finished insulation systems, the inception of surface discharges often represents a voltage limiting factor. Along with embedding in oil or SF_6, *potential grading measures* are also feasible, e.g. by capacitively grading layers made of metallic foils, or by resistively grading layers made of conducting varnish [26]. In particular, non-linear mate-

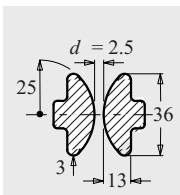

Partially spherical electrodes for liquids (IEC 60156)

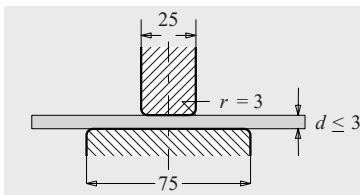

Electrode arrangement for films and boards up to 3 mm with embedding (IEC 60243-1)

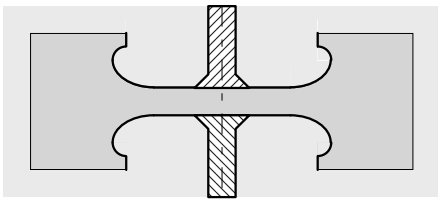

Electrode arrangement with worked or with recast Rogowski electrodes for greater insulation material thickness

Figure 6.4.4-1: Determination of breakdown voltages for liquids and solids.

rials whose conductivity increases with the electric strength are advantageous.

For the breakdown of **thick-walled solid insulations**, owing to higher voltages, adequately *rounded electrodes* must be *embedded in the material*, Figure 6.4.4-1. This is very difficult and generally cannot be implemented for routine tests, but can only be applied for basic investigations. Electrodes can be embedded, e.g. by casting in the spheres or Rogowski electrodes with the reaction resin compound to be tested. For given solid material samples, the electrode contour must be carved out and given a conductive coating. By additional embedding in insulating oil, voltages above 100 kV can be attained.

b) Voltage rise

The AC test voltage applied to the electrodes is increased up to breakdown. For **liquids**, a voltage rise of 2 kV/s must be used [177]. In the case of **solids,** there are different types of voltage increase [173]:

- During *short term testing*, the majority of breakdowns occur after 10 to 20 s (rate of rise 0.1, 0.2, 0.5, 1.2 or 5 kV/s).
- During the 20 s or 60 s *step testing*, the voltage is increased in 20 or 60 s steps, whereupon it is started with about 40 % of the expected breakdown voltage. The voltage is increased by 5 to 10 % of the initial value for each step.
- While *testing with low or very low rates of voltage rise*, the majority of breakdowns occur between 120 to 240 s or between 300 and 600 s, and the initial value is about 40 % of the expected breakdown voltage.
- For *withstand voltage test*, the specified voltage must be withstood over a given period.

c) Statistical dispersion, evaluation

Owing to the statistical dispersion of breakdown voltages, a *mean-value calculation* from several individual values is necessary for *estimation* of the 50 % breakdown voltage V_{bd50}.

For *insulating liquids*, AC breakdown voltage is determined in kV as a *mean value* of 6 measurement values in accordance with IEC [176], [177]. Gas bubbles and decomposition products must be eliminated by stirring and two minutes waiting time between the breakdowns, see Section 3.4.1.

For *solid insulating materials*, 5 samples are broken down. The test result is the *median* (that is, the mean value of the series) of the breakdown voltage in kV or the breakdown strength in kV/mm. If a single value deviates by more than 15 % from the median, the number of samples must be increased from 5 to 10 [173].

For *thorough examinations*, the type and the parameters of the *distribution function* must be

estimated from a larger number of breakdowns, in order to allow statements about the breakdown probabilities, see Section 3.1.

d) Tests with impulse voltage or DC voltage

The preceding explanations and the above-mentioned standards for *AC voltage* are *analogously* applicable to breakdown tests of solid insulations with impulse voltage and DC voltage [173]. Special features are given in the supplementary standards [174], [175]. Two- to three-fold higher breakdown values must often be expected for DC voltage and impulse voltage.

In **DC voltage tests**, the type of voltage rise is restricted to short-time testing, testing with low or very low rate of voltage rise and the withstand voltage testing [174]. For **impulse voltage testing**, the applied voltage stress consists of subsequent series of 3 equal lightning impulse voltage pulses 1.2/50 µs. The test is started with about 70% of the expected breakdown voltage. With each series, the voltage is increased by 5 to 10 % of the initial value [175].

6.4.4.3 Creepage Currents and Tracking Resistance

The so-called *creepage currents* flow on the surface of electrically stressed insulating materials, and their magnitude is determined by the surface resistance. Creepage currents can be concentrated on narrow current paths similar to the case of pollution flashover. This results in a local thermal and electro-thermal stressing of the surface. Moreover, owing to drying, small partial arcs can occur. Depending on the *resistance* of the insulating material *to these stresses*, conductive or non-conductive *creepage current traces or tracks* are created, which can be two-dimensionally extended or linearly engraved. Conductive creepage current traces lead to flashover, non-conductive traces favor at least the deposit of dirt and reduce the hydrophobicity. Thereby they also weaken the strength of the surface, see Section 3.2.6.4.

a) Determination of proof and comparative tracking indices

According to IEC 60112, the tracking resistance is determined by a **proof tracking index** and a **comparative tracking index** [169]: from a drop dispenser, 50 drops of a conductive solution is added on to the surface between two electrodes at which a power frequency AC voltage is applied, Figure 6.4.4-2. The failure criterion is a current $I > 0.5$ A for a period $t > 2$ s or the appearance of a continuous flame. On test objects that have withstood the test without failing, the depth of erosion is

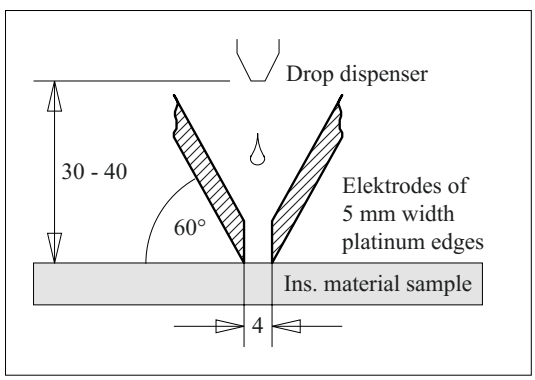

Figure 6.4.4-2: Determination of comparative tracking index CTI according to IEC 60112 [169].

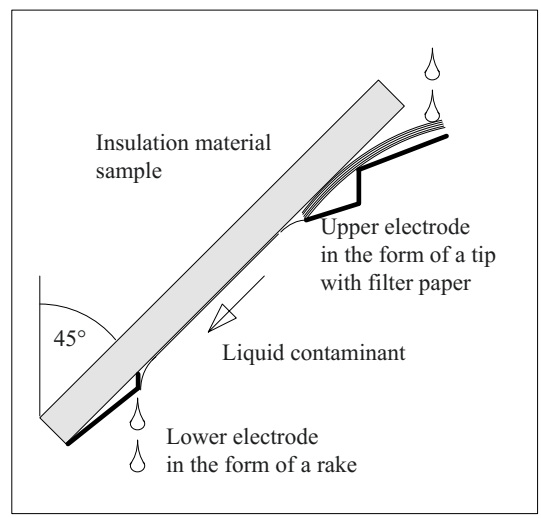

Figure 6.4.4-3: Determination of resistance against tracking and erosion under severe ambient conditions, IEC 60587 [172].

measured.

The *proof tracking index* (PTI) is described as a specified voltage value, for which a particular number of samples (generally 5 units) are checked and withstand the test with 50 drops.

The *comparative tracking index* (CTI) is determined as the maximum voltage for which 5 test objects withstand the test sequence with 50 drops. Moreover, it must be proven that a test sequence with 100 drops is withstood at 25 V below this value.

The method is used to differentiate between materials with relatively low to good resistance against tracking, even under humid environmental conditions. Materials for high voltage outdoor usage, however, must be checked with more stringent methods.

b) Inclined-plane test

Thus, IEC 60587 describes another test method for evaluating the **resistance against tracking and erosion** under severe ambient conditions Figure 6.4.4-3 [172]: a conductive solution provided with a spreading agent (conductivity 2.5 mS/cm, 23 °C) flows from the upper to the lower electrode on the underside of an inclined plane specimen *(inclined-plane test*). The applied power frequency AC voltage feeds a creepage current which leads to partial arcs and as the case may be, to erosion and tracking. Two methods are specified:

In the case method 1 (*constant tracking voltage),* voltages of 2.5, 3.5 or 4.5 kV are applied. The voltage value is determined at which no breakdown occurs during a six hour test period for 5 test objects. Both a current increase above 60 mA and the growth of a creepage current track over a length of 25mm is considered as a failure criterion.

In the case of method 2 *(stepwise tracking voltage)*, the voltage is applied in steps of 250 V, and the voltage is determined which 5 test objects withstand for one hour without failure. The increase of the current above 60 mA is considered as failure criterion.

c) Cyclic test (Rotating wheel dip test)

The inclined plane test is considered unsuitable for *silicone elastomers*, since the hydrophobic properties are suppressed by the spreading agent [381]. Therefore, a **cyclic test** oriented towards the operating stresses was developed for evaluation of the resistance against tracking and erosion (IEC 61302 [382]). In that case, at least 5 identical rod-shaped test objects (diameter 25 mm, creepage path 140 mm, inclined by 15° to the horizontal) are assembled on a rotating wheel and are alternately dipped into a conductive liquid and exposed to an electrical AC stress of 10 kV at the surface three times every minute. The failure criterion is a leakage current above 300mA or a flashover.

6.4.4.4 Arc Resistance

Although *flashovers* along the surfaces should be avoided by suitable dimensioning, they are, however, not generally impossible. Many insulating materials, therefore, must be arc resistant, i.e. they should not be unacceptably severely affected by the *thermal effect of arcs* and discharges.

Table 6.4-4: Significance of arc-performance index *LV as per DIN VDE 0303 section 5.*

Index *)	**1**	**2**
First digit	Length of the arc path is **< 20 mm**	**≥ 20 mm** **)
Second digit	Arc path under the arc is **non-conductive**	**conductive** **)
Third digit	Arc path after cooling down is **non conductive**	**conductive** **)
Fourth digit	Changes in the specimen are **not significant**	**significant** **)

*) If no clear allocation is possible, the index "0" is assigned.

**) Exact description of allocation criteria must be referred from VDE 0303 section 5.

a) Resistance test to low-voltage, high-current arc discharges

Performance of high-temperature-resistant materials that are stressed by *arcs of low voltage and high current* is evaluated on the basis of the so-called **low voltage-high current-arc test**, in accordance with DIN VDE 0303 section 5 [170]: an arc is ignited at the surface of the insulating material with two pointed carbon rods to which a *DC voltage* (220V) is applied via a protective resistor of 20 Ω. By moving the negative electrode with a speed of v = 1 mm/s, the arc extends up to current chopping. The test result is specified as an *arc-performance index* LV with four digits, Table 6.4-4.

Example: Arc-performance index

The evaluation **LV 1.2.0.1** signifies that the arc length is smaller than 20mm, that the path under the arc is conductive, that the material can be classified as neither conductive nor non-conductive after cooling down and that the specimen does not show any significant damage.

Note: The earlier standard classification into six stages of L1 to L6 is replaced by the (neutral) LV-classification. The following are considered as equivalent substitutes:

L1 = LV 2.2.2.2, L2 = LV 1.2.1.2, L3 = LV 2.2.1.0,
L4 = LV 1.1.1.2, L5 = LV 2.1.1.1, L6 = LV 1.1.1.1

b) Resistance test to high-voltage, low-current arc discharges

Substances are evaluated with respect to *high voltage arc resistance* in accordance with IEC 61621 by a resistance test to **high-voltage, low-current arc discharges** [171]:

Arcs are ignited with a test transformer (12.5 kV) between two electrodes (d= 6.35mm) lying on the *dry* surface of the insulating material and are limited to *specific currents* by protective resistors on the low voltage side. The test begins with 10 mA. During a minute, the duration of current is respectively increased (1/8, 1/4, 1/2 s). Subsequently the test currents of 10, 20, 30 and 40 mA each flow continuously for one minute. The maximum test duration is thus 420 s. The failure criterion is the disappearance of the arc in the material or burning of the sample. For the 5 test objects, the arc resistance is determined as the *time to failure* (median, minimum and maximum).

6.4.4.5 Additional Tests for Insulating Materials

The above-mentioned tests represent only a selection from different options. Other than the general tests (e.g. for the influences of moisture or UV radiation), there are a number of material-specific methods (e.g. for silicone elastomers) that must be obtained from the respective *material-specific standards or device-specific standards* [381].

6.4.5 Optical and Acoustic Diagnosis Methods

6.4.5.1 Optical Waveguides

In high voltage engineering, optical waveguides are largely used in the *of potential-free transmission signals* in digital or analogue signal transmission paths and also as *sensors* for magnetic fields, temperatures, mechanical tensions, pressures or light emissions.

Important examples of the **galvanic isolation** for *signal transmission* are potential-free field probes, Section 6.3.3.3, optical and hybrid-optical current converters, Section 6.3.5.2, differential voltage measurements at high voltage potential or the transmission of *control pulses*, e.g. for triggering spark gaps or for the triggering of thyristor valves. Moreover, galvanic isolation is often necessary in *computer networks and in measurement systems* for reasons of electromagnetic compatibility. Further, fiber optics can be used for the *transmission of auxiliary energy* for potential-free electronic systems. However, owing to the moderate laser efficiency, the power levels are mostly restricted to the mW range.

Optical waveguides can be used directly as **sensors**, e.g. for monitoring *oil levels* in bushings. In extended *gas-insulated switchgear*, the optical measurement of light emissions can be employed in the individual chambers for localization of discharges. Mechanical stresses, temperature changes and magnetic fields vary the optical properties (i.e. the so-called optical activity) of glass fibers, Section 6.3.3.5. This results in new application ideas that are still in the research or prototype stage, such as, for example, *magneto-optic current transformers*, Section 6.3.5.2, *thermal monitoring* of cables, overhead-line conductors or transformer hot spots and potential-free *pressure sensors or light sensors* for partial discharge detection in transformers [372], [373].

Note: All optical fibers, which bypass the potential differences, may comprise neither conductive sheaths nor encasements or finishings. They must possess adequate *creepage distances*, which, for example, can be attained by a spiral-shaped arrangement. Thereby, even the *tangential stress* in the direction of the fiber can be maintained low. For protection against environmental influences, the optical fiber is often led within a *silicone-shielded composite housing insulator* and *foamed* with a compressible medium, Figure 6.3.5-3 c), d). For the installation of optical waveguides in electrically highly stressed media (e.g. oil), under certain circumstances they must be *void-free* and corresponding electric strength must also be specified.

6.4.5.2 Visual Diagnostics

Efficient tools for visual diagnostics are available in different spectral ranges [374]:

With the help of **low-light amplifiers**, *corona discharges in outdoor installations and indoor installations* can be located through their light emission, e.g. on sharp-edged fittings or on contaminated or wetted surfaces. However, the prerequisite is *complete darkness,* since low ambient light already leads to overdriving of the device. Hence, in practice, the use of low-light amplifiers often remains restricted to completely blacked out high voltage test fields.

Meanwhile, there are also **daylight UV cameras**, which capture the daylight image and the UV light image of corona discharges separately for the different spectral ranges and superimpose them. This results in new options for visual diagnostics, e.g. in new options for inspection flights along overhead transmission lines [219] or for the localization of partial discharges in high-voltage test fields.

Infrared cameras allow the visualization of hot spots or non-uniform heating for thermally highly stressed components, e.g. on conductors and contacts [266], on bushings, on cooling elements of transformers, on overhead lines or on surge arresters. The so-called **thermography** or **thermographic imaging** is of increasing importance for the supervision of thermally stressed equipment.

Endoscopes are used for the visual inspection of generators, transformers or switchgear. In future, endoscopes may even possess sensory capabilities, Section 6.4.5.1.

6.4.5.3 Acoustic Diagnostics

Corona discharges can also be acoustically located by **directional microphones**. For the coaxial combination of the microphone with a laser, the located discharge position can be marked by the receiving point of the laser beam.

Discharges within the equipment can be located by externally applied microphones for the **structure-borne noise**, see Section 6.4.2.9. Potential-free microphones are used on insulating material surfaces, and often even on grounded surfaces, for safety purposes and for electromagnetic compatibility.

Acoustic localization is especially important during the *testing of transformers*, in order to be able to localize the area to be repaired. For this, time differences between the signals of multiple microphones are analyzed (triangulation). They correspond to acoustic propagation time differences for different paths. However, location is often difficult owing to complex sound propagation conditions, parallel paths and reflections.

For **cable fault locating**, charged high voltage impulse capacitors are discharged into a defective cable. The time difference between the discharge current signal and the discharge sounds is a measure of the distance of the defect. In the vicinity of the defect, exact location of the defect can be detected by repetitive discharge sound and with the aid of a ground microphone.

Note: The clamping force for transformer windings is a decisive factor for mechanical stability in the case of a short circuit. It has been shown that the windings react to impulse current loads with movements of varying amplitude depending on the clamping force. Thus, *transient pressure surges in oil* occur, which induce a damped oscillation with a periodic time of several seconds and with amplitudes in the range of few 10 mbar. The pressures are dependent on the squares of the current amplitudes. *A trend estimation of the clamping force* is enabled by the so-called **transient oil pressure measurement** in the pipe to the oil expansion vessel and by the conversion of the measured pressure p_{Meas} to the pressure p_{SC} in the case of a short circuit [371]:

$$P_{\mathrm{SC}} = p_{\mathrm{Meas}} \left(\hat{\imath}_{\mathrm{SC}} / \hat{\imath}_{\mathrm{Mess}}\right)^2 \qquad (6.4.5\text{-}1)$$

For $p_{\mathrm{SC}} < 20$ mbar, the winding is assumed to be stable enough, for $p_{\mathrm{SC}} > 50$ mbar, it is assumed to be too loose.

6.4.6 Determination of System Properties

Turn-to-turn faults in transformers, displacement of windings, partial breakdowns in capacitor windings or between grading layers in bushing, short circuits in cables and other *electrical or geometrical changes* in devices lead to changed *electrical system properties*. They can be diagnosed during classic impulse voltage tests (Section 6.4.6.1), by the calculation of transfer functions (Section 6.4.6.2), by frequency-response measurements (Section 6.4.6.3) and by reflectometry (Section 6.4.6.4). *Dielectric system properties* can be measured in the time domain and the frequency domain. This generally yields diagnostic information about material properties, e.g. about oil conductivities or water contents in oil-paper insulations. This topic is dealt with in detail in Section 6.4.7.

6.4.6.1 Impulse-current Waveshapes

Only in the extreme case of a voltage breakdown, insulation defects can be definitely identified on the waveshape of an *impulse voltage* during the classic lightning impulse voltage test. Generally, the voltage waveshape is barely influenced by minor changes in the test object. For a sophisticated analysis, therefore, interference-free recording of transient *impulse current waveshape* is necessary, cf. Section 6.3-7 and Section 8.

Note: For *transformers*, the current through the tested windings, the neutral-point current, the current over the insulated tank (tank current), the inductively or capacitively transmitted current in another winding system or the total current can be analyzed. Test circuits are given in the literature and the relevant standards [52], [159], [160].

Generally, the current waveshapes of the *test impulses* (with full test voltage amplitude) are compared with each other and with the current waveshapes of the so-called *calibrating shots* (with half the amplitude). The current waveshapes that are ocillating to a greater of lesser extend should be *congruent* taking the amplitude scale into consideration. Different current waveshapes in the course of a test sequence are sensitive indicators for changed geometric or electrical characteristics in the windings, e.g. for partial breakdowns that lead to interturn faults.

Note: System properties of a winding arrangement also depend on the *tapping position of the tap changer*. Hence, the measurements are comparable only when the tapping positions are equal.

6.4.6.2 Transfer Functions, Frequency Response Analysis FRA

Impulse current waveshapes are dependent not only on the system properties of the test object, but also on the waveshape of the applied voltage. Therefore, one strives for the development of a *system function* which is *specific for the test object* and whose *changes* are monitored.

Note: In principle, this is feasible for all the equipment, but the tests are especially aimed at **large transformers** for which the increased costs of diagnosis are justified [160]. The diagnosis objective is the detection of *winding displacements, winding deformations and turn-to-turn faults* (interturn faults)..

A *transfer function* (TF) is generally calculated in the *frequency domain* from the input current $\underline{I}_1(j\omega)$, from the output current $\underline{I}_2(j\omega)$ or from the output voltage $\underline{V}_2(j\omega)$ by relating them to the input voltage $\underline{V}_1(j\omega)$, in fact, as a complex transfer function $\underline{TF}$ of the input current (admittance function), of the output current or the output voltage:

$$\underline{TF}_{I1/V1} = \underline{I}_1(j\omega)/\underline{V}_1(j\omega) = \underline{Y}(j\omega) \qquad (6.4.6\text{-}1)$$

$$\underline{TF}_{I2/V1} = \underline{I}_2(j\omega)/\underline{V}_1(j\omega) \qquad (6.4.6\text{-}2)$$

$$\underline{TF}_{V2/V1} = \underline{V}_2(j\omega)/\underline{V}_1(j\omega) \qquad (6.4.6\text{-}3)$$

For comparative purposes, the representation of the **amplitude spectrum** $TF(f)$ against the frequency f is suitable.

Broadband sensors are necessary for the measurement, e.g. current and voltage sensors mounted on the bushings of a transformer on the high voltage side and the low voltage side, Figure 6.4.8-3.

Transfer functions can be measured directly in the *frequency domain* (frequency response measurement), but only at very low voltages.

Transfer functions can be developed by *Fourier transform* even from the functions $v_1(t)$, $i_1(t)$, $i_2(t)$ and $v_2(t)$ measured in the *time domain* during a lightning impulse voltage test. They can therefore significantly extend the informative value of an impulse voltage test. Under this, it is not important whether a complete or chopped lightning impulse voltage or another transient voltage shape is involved. In particular, for testing and monitoring purposes, this results in significant advantages compared to frequency response measurement:

- *Additional measurements*, before and after an impulse voltage test, are *omitted*.
- Changes which only have an effect for a *full test voltage* can be immediately identified.
- In peinciple, there is a possibility of "*online monitoring*" in the network through analysis of operation-induced transient processes [161], [391].

Note: A prerequisite for the development of transmission functions by transformation is that the analyzed system is *passive, causal, time-invariant* and *linear*. Linearity can be assumed for transformers for frequencies **above 1 kHz**, since most of the magnetic sheet steel types do not show appreciable magnetization there [391].

Problems result, e.g. from the *quantizing uncertainty* which affect the measurement signals in the form of noise and lead to *tolerance bands* for the transfer functions. Further, the following **influences** must be considered:

1. *Tapping position*
   (change in system properties),
2. *Temperature* (damping of amplitudes),
3. *Measurement impedances* and
4. *Method of terminal connection*.

Moreover, there are special requirements for *electromagnetic compatibility* during the measurement of current shapes and voltage shapes [162]. The most direct possible **connection of the analyzer** to the terminals of the transformer by the shortest possible path is of decisive significance for the reproducibility of the measurements. The connection routing must be accurately documented.

Comparable results are only possible for **identical measuring conditions**. Therefore, FRA cannot give an absolute, but only a relative statement and a reference measurement is always necessary. The consideration is generally restricted to a *frequency domain* **under 1 MHz** owing to the diverse influences of interference.

A comparison of different systems has produced concurrence in a frequency range of 10 to 500 kHz [474]. Measurement procedures in the time domain with subsequent transforma-

tion could not properly represent the whole frequency range. By standardization of the connection technique on the high-voltage bushings, reproducibility of the results could be achieved up to approx. 1.5 MHz. The low voltage bushings are shorter, and hence are less critical with respect to the connection technique.

Since the result is presented in the form of graphic amplitude profiles, the **interpretation** requires the availability of comparable reference curves and a high degree of experience. The interpretation can be facilitated by *network simulations*, since this allows the influence of winding changes on the measured curves to be viewed [474]. However, this requires an accurate knowledge of the transformer design and is associated with greater effort, and hence the simulation is reserved for more fundamental investigations.

Note: For the advanced concept of the development of **online transfer functions,** impulses that are generated in the regular network operation through lightning overvoltages or switching overvoltages should be used**.** The problem here is that not all exciting impulses show adequate *continuous spectrum* and thus, are not always suitable for the analysis. Further, there must be a clear identification and allocation of *excitation* and *response* which can be made difficult owing to overlapping of multiple peaks and owing to reflections in the network environment of the test object. Further, it was shown that varying temperatures and varying resistances in the regulator windings cause damping of amplitudes of varying intensity, but the position of the *dominant points of resonance* is apparently very marginally influenced [391].

6.4.6.3 Frequency Response Measurements

System properties can be determined at low voltages both by *frequency response measurements* with sinusoidal AC voltages of varying frequency and by *impulse response measurements*.

Frequency response measurements are a common tool for setting up *equivalent circuits* for the calculation of transient and high-frequency phenomena in *installations*, *networks* and *systems*. For this, especially the *points of resonance* at which significant *voltage overshoots* and overvoltage stresses can occur, is of concern.

Frequency-dependent voltage distributions and *resonances* within devices can lead to overstressing of specific parts of the insulation that are adequately dimensioned for operation frequency stress. For example, the validity of equivalent circuits that are related to transformer windings can be verified by frequency response measurements. However, direct measurement of voltage distributions requires actual windings or winding models with freely accessible turns.

Determination of *dielectric* system properties in time and frequency domain is described in Section 6.4.7.

6.4.6.4 Reflectometry

Also *propagation time measurements* on *systems with distributed parameters* represent a method for determining specific system properties in the time domain. Propagation time measurements are especially suitable for the *cable fault locating*, during which the propagation time of test impulses between the measurement point and the reflecting fault location is determined.

Note: The exact localization of defects is thus carried out by *acoustic detection* of noises that occur during the discharging of high voltage capacitors on defective cables.

6.4.7 Dielectric Diagnosis

Classic dielectric diagnostics is based on simple equivalent circuits that are valid for *power frequency* and that describe properties such as capacitance C, dissipation factor tan δ and insulation resistance R_{ins}, Section 4.3.1. This enables statements about a few basic dielectric properties to be made.

More accurate information is possible by the measurement of *complete dielectric system responses,* from which *equivalent circuits of higher order* can be derived and various *po-*

larization mechanisms can be described (Section 4.3.2.1, Figure 4.3-2). Material changes, e.g. by *wetting* or by thermal *ageing*, can often be identified by the change in the dielectric system responses and in the assigned equivalent circuit elements respectively.

Summarizing contributions are given in the related literature [239] to [242] and [468] to [470]. In the following sections, the dielectric methods are first distinguished according to the time domain and frequency domain methods (Section 6.4.7.1). Moreover, the selectivity of the measurements, which can be influenced by the selection of measuring electrodes, must be taken into consideration (Section 6.4.7.2). Subsequently, methods that are often discussed, such as discharge voltage analysis (Section 6.4.7.3), IRC analysis (Section 6.4.7.4), recovery voltage analysis (6.4.7.5), PDC analysis (Section 6.4.7.6) as well as frequency domain analysis (Section 6.4.7.7) are considered, see also Section 6.4.1.3.

6.4.7.1 Time and Frequency Domain

There are a number of approaches to dielectric diagnostics that are based on the analysis of voltages and currents in the **time domain** or **frequency domain**, Figure 6.4.7-1, and they offer various options, Table 6.4-5.

In **frequency domain**, *capacitances* and *dissipation factors* are recorded for different frequencies by a large number of individual measurements so that dielectric system properties can be completely measured (FDS frequency domain spectroscopy, FDA frequency domain analysis). For this, each individual measurement requires a steady state which can only be assumed after about four periods. Hence, measurement periods are very long if low frequencies shall be recorded. Moreover, it is very difficult to generate high diagnosis voltages both at low and high frequencies.

The same and complete information about the system properties can be obtained by **step response measurement in the time domain** in a single measurement, so that the measurement durations become significantly shorter. The generation of higher diagnosis voltages is comparatively easy. Determination of fast changing processes is difficult, since a correspondingly high sampling rate is necessary. For step response measurements in the time domain, after applying or disconnecting a di-

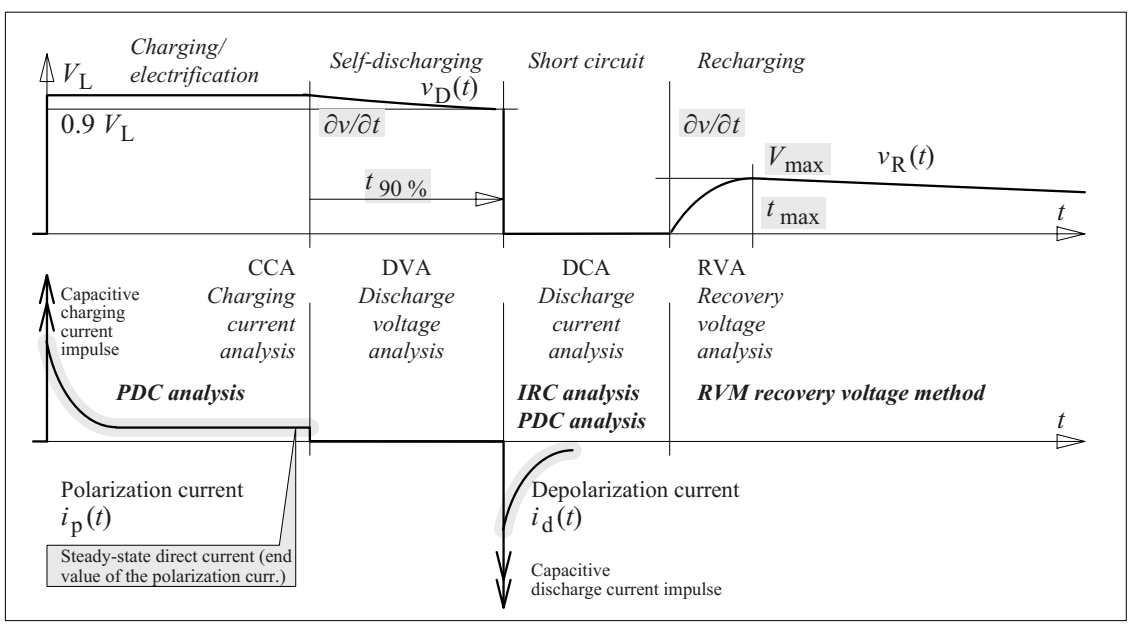

Figure 6.4.7-1: Dielectric diagnostics in the time domain [33] (cf. equivalent circuit in Figure 4.3-3).

agnosis voltage, the *relaxation currents* in the form of *polarization currents or depolarization currents respectively* are recorded (PDC polarization and depolarization currents), Figure 6.4.7-1. For linear systems, the variables of the frequency domain and all other diagnostic parameters can be derived from this using transformations [230].

Note: Even the combination of **time domain measurements and frequency domain measurements** is possible: since the measurements for very low frequencies in the frequency domain lead to very long measurement durations, it is better to document *slow processes* with a step-response measurement in the time domain (PDC measurement). This, on the other hand, cannot determine *the fast changing processes* and hence rapidly varying processes must be measured in the frequency domain at higher frequencies. It was therefore proposed that the two approaches be combined and the time domain measurement be transformed into the frequency domain and then a cohesive dissipation factor curve should be formed [467].

Note: Furthermore, there are other methods which do not use the entire system information, but are content with *only particular characteristic parameters*. This includes *dissipation factor measurements* for a specific frequency in the **frequency domain**, e.g. 50 Hz or 0.1 Hz, and in the **time domain**, development of characteristic current ratios, so-called *polarization indices* or *adsorption coefficients*, *discharge voltage analysis*, which measures the self-discharge of a loaded capacitance, *isothermal relaxation current analysis* (IRC), which evaluates the depolarization current after a specific charging cycle and short circuit cycle, as well as *recovery voltage analysis* (RVM recovery voltage method), which also considers the recovering voltages at a polarized and temporarily short-circuited test object.

6.4.7.2 Selective Measurements

Dielectric measurements can include different parts of an insulation, depending on which terminals (electrodes) are accessible and between which ones the measurement is made, Figure 6.4.7-2.

Often, only two electrodes are accessible at the test object, one of which is grounded, such as, for example, for laid *cables*. Only **integral measurements,** which incorporate all insulation currents, surface currents and leakage currents, can be carried out.

The same applies also for *transformers* if the discharge voltages (DVA) or recovery voltages (RVM) are to be measured, because discharge and voltage recovery are influenced by all currents flowing between the windings and the grounded parts, Figure 6.4.7-2 (left).

Note: For *insulations between an electrode and ground*, current measurements in the time domain and the frequency domain (PDC, IRC and FDS) are also possible when potential-free voltage sources are used, Figure 6.4.7-2 (left).

For **selective measurements,**two earth-free electrodes are necessary, Figure 6.4.7-2 (right). At one of the electrodes *(1),* the diagnosis voltage is applied, the measurement current (PDC or FDS respectively) is tapped at the second electrode *(2).* The *third grounded electrode (3)* works like a *guard-ring electrode* and carries the leakage currents and surface

Table 6.4-5: Properties and special features of dielectric diagnosis methods in time domain and frequency domain.

Analysis methods		Complete *system-information*	*Integral* two-electrode measurement	*Selective* three-electrode measurement	Exclusion of parasitic *surface/ leakage currents*	*Conductivity* measurement	Analysis-software for *complex geometries*
Polarization **current**	PDC	yes	possible	possible	possible	given	known
Depolarization **current**		*no*	possible	possible	given	*not possible*	known
Isothermal relaxation **current**	IRC	*no*	possible	possible	given	*not possible*	*not known*)*
Discharge **voltage**	DVM	*not known*)*	possible	*not possible*	*not possible*	possible	*not known*)*
Recovery **voltage**	RVM	*not known*)*	possible	*not possible*	*not possible*	Possible	*not known*)*
Frequency domain	FDS	yes	possible	possible	Possible	possible	known
Measurement at discrete **frequency**	50/ 60/ 0.1 Hz	*no*	possible	possible	possible	*not possible*	*not known*)*

not known):* currently, no usage or application is known regarding this

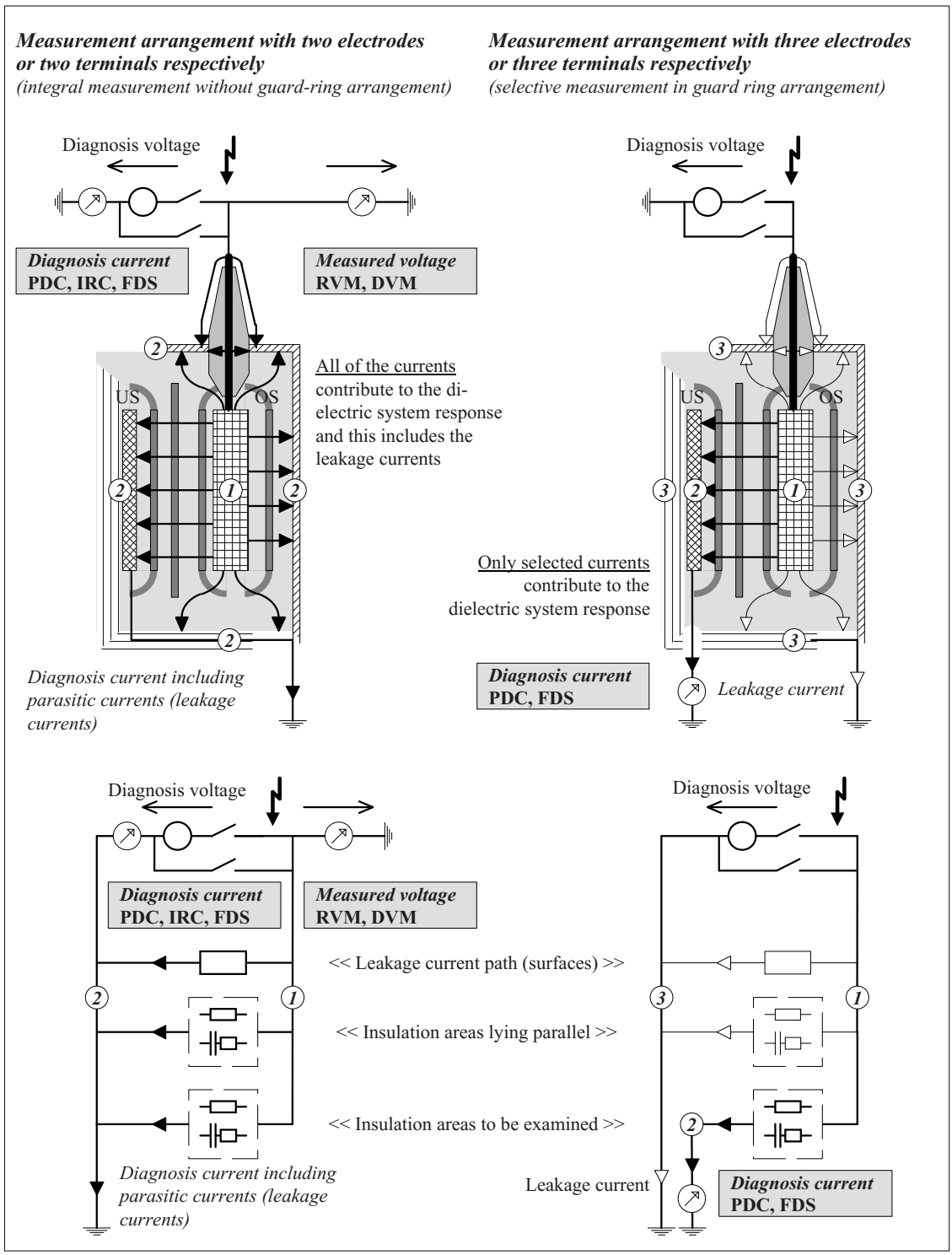

Figure 6.4.7-2: Integral and selective measurement of dielectric system response with the help of different methods, explained for the example of a transformer. Left: Measurement arrangement with two electrodes. Right: Measurement arrangement with three electrodes.

currents without influencing the measurement, see Figure 6.4.1-4. In this manner, different areas of the insulation system can be selectively picked out, e.g. the insulation between HV (higher voltage teminal) and ground, HV and LV (lower voltage terminal), LV and ground or individual bushing insulations.

The methods mentioned are described in the following chapters.

6.4.7.3 Discharge-voltage Measurement

Discharge-voltage measurements (DVM), in principle, can be designed very easily with a DC voltage source. After disconnecting the voltage source, the voltage decreaseses owing to self-discharging through the insulation resistance of the test object. Measured variables are the initial gradient of the voltage decrease during the self-discharging as well as specified periods (e.g. $t_{90\%}$), Figure 6.4.7-1. The input impedance of the voltage measuring system must be much higher than the DC resistance of the insulation to be measured. For high-resistance insulations, electrostatic voltmeters or fieldmill voltmeters are therefore necessary in some cases, cf. Sections 6.3.2 and 6.3.3.4.

The profile of voltage $v_D(t)$ gives information about the resistive components of the equivalent circuit that describes the material. Since DC resistances of oil-paper insulations are heavily dependent on the water content [222], a realistic diagnosis is possible. However, it must be noted that surface resistances, parallel current paths and measurement impedances can lead to inaccuracy in the measurement.

6.4.7.4 IRC Analysis

During the isothermal relaxation current analysis, a dielectric, previously polarized by DC voltage, is discharged. The discharge current (relaxation current or depolarization current respectively) is recorded [223]. Surface resistances and insulation resistances lie in parallel to the low-resistance current measurement impedance and do *not* influence the measurement. This means that surface resistances cannot distort the measurement. However, information about the DC conductivity, which is an important moisture indicator for oil-paper insulations, is also not provided.

IRC-analysis especially provides significant results where polarization processes exist with **pronounced time constants** which are significant for particular material conditions. If the polarization mechanisms in the depolarization current

$$i_d(t) = \sum_j I_j \cdot e^{-t/\tau_j} \qquad (6.4.7\text{-}1)$$

are described by exponentially decreasing depolarization current components, after multiplication with the linearly increasing time function t, the product

$$t \cdot i_d(t) = \sum_j I_j \cdot t \cdot e^{-t/\tau_j} \qquad (6.4.7\text{-}2)$$

has **maxima** exactly at the positions of the time constants $t = \tau_j$.

Note: This can be easily shown with extreme value determination for the current-time product according to Eq. (6.4.7-2) if the derivate with respect totime is set to zero.

Thus, for a small number of pronounced polarization mechanisms, there is the distinct possibility of visualizing the position of material-specific time constants as maxima of the function **current multiplied by time.**

Note: For more than three time constants, it is difficult to distinctly separate the components from each other. Hence, the method is not applicable for oil-paper with continuously distributed time constants.

Note: The depolarization current profile is also determined by the duration of the previous polarization time. That is, after a **discharge period** comparable with the **charging time**, the depolarization current is very small since hardly any charge is stored in the dielectric. Therefore, the time constant of the current drop is caused not only by insulating material but also by the measurement method.

Application examples are the classification of new and water-tree damaged *medium voltage plastic-insulated cables* [224] as well as the

evaluation of the hardening status of *epoxy resin materials* [225]. In theses cases, homogeneous insulations are examined with a special charging time of 1800 s in order to achieve comparability. In the case of plastic-insulated cables, IRC-analyses allow the setting of priorities during renovation of cable runs.

6.4.7.5 Recovery Voltage Analysis

Recovery voltage analysis or recovery voltage method (RVM) respectively is the oldest dielectric diagnosis method. It was based on the experience that a polarized dielectric can be recharged on its own from the charges stored in the dielectric, even after a temporary short circuit. It is required that the insulation is not loaded at all or is only loaded with very high resistance, Figure 6.4.7-3. That is, the input impedance of the voltage measurement system must be very much higher than the insulation resistance of the insulation to be measured.

Note: Recovery voltage measurement (in the open-circuit condition), is thus comparable with a *depolarization current measurement* (in the short-circuit condition): in both cases, the voltage signal and the current signal respectively are caused by the charge previously stored by polarization.

A major problem of recovery voltage analysis is that *only two-electrode measurements* are possible. The influences of *parasitic surface currents and leakage currents* are fully involved in the measurement, because the entire polarized dielectric always contributes to the recovery voltage. Moreover, selective measurements between ungrounded electrodes are not possible.

Recovery voltage not only presents a danger in high voltage engineering, but also includes information about the structure and condition of the insulation.

a) The occurrence of recovery voltages

The formation of recovery voltages is already explained in Section 2.4.4.3 for the process of *interfacial polarization* in a **multi-layer dielectric,** see Figures 2.4-31 and 6.4.7-3. From this, in the case of a transformer insulation consiting of oil ducts or oil gaps (O) and barriers (B), it is concluded that layers which are oppositely but equally charged to $v_O(t=0) = -v_B(t=0)$ during the short circuit, undergo self-discharging at different rates, owing to different conductivities, if the short circuit is opened. The time constants are $\tau_O = R_O C_O$ and

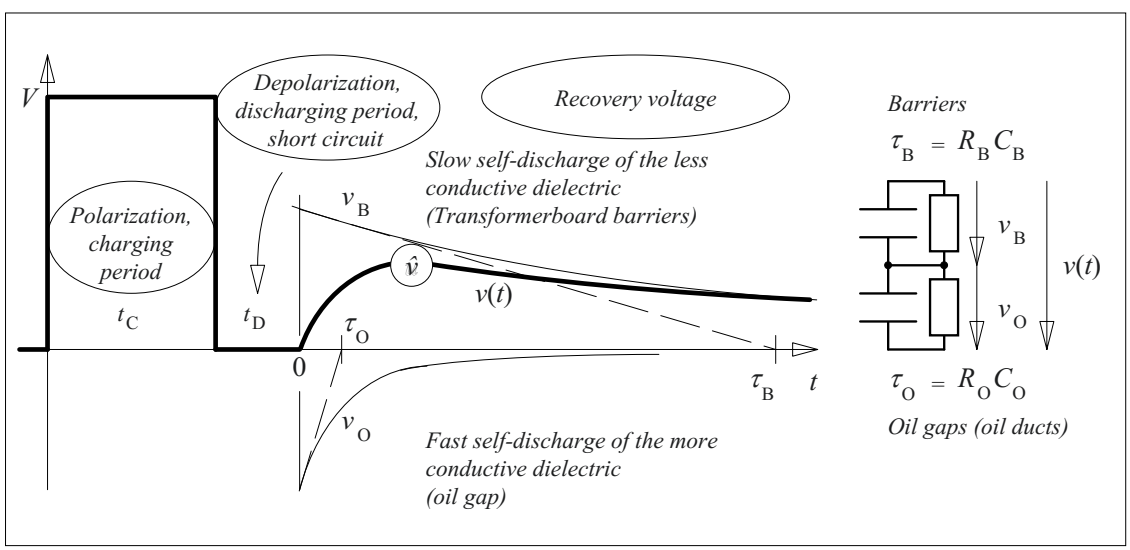

Figure 6.4.7-3: Occurence of recovery voltage through interfacial polarization in a multi-layer oil-paper dielectric, such as in a transformer.

$\tau_B = R_B C_B$. Under superimposition, at first an increasing, and subsequently a decreasing total voltage (or differential voltage respectively) $v(t) = v_O(t)+v_B(t)$ occurs and this is effective as a recovery voltage.

Recovery voltages can be explained even for **homogeneous dielectrics** with *material-specific polarization processes*, Figure 4.3-2: after removing the short circuit, the discharged (high frequency or "geometric") capacitance C_{geo} is recharged from the equivalent circuit elements $R_{pol}C_{pol}$ that describe polarization and that still carry charge. Finally, it is discharged through the DC resistance R_{ins}.

b) The so-called "polarization spectrum"

In the past, a special measuring method had made use of the term "Recovery Voltage Method" RVM (owing to which other options of recovery voltage analysis were ignored). This is a special test procedure that consists of a series of many recovery voltage measurements with varying charging times and discharging times [32], [83]: the charging time and the discharging time of the test object are in a fixed ratio (e.g. t_C:t_D = 2:1). By *series measurements* with varying charging times t_C, but with a fixed time ratio t_C:t_D, it is intended to excite different polarization mechanisms differently or to scan the different time constants respectively.

A representation which applies the maxima $\hat{v}$ of individual recovery voltages over the associated charging times t_C is described as a "polarization spectrum". This is misleading, since the term spectrum is generally used in the frequency domain and not in the time domain.

c) Interpretation of "polarization spectra"

The interpretation of "polarization spectra" at first presented a major problem, because it was postulated that the position of the maximum in a "polarization spectrum" (the so-called *characteristic time constant*) should be in direct relationship with the *water content* of transformer barriers [32], [83]. This resulted in contradictory and debatable results [86], [87], [226].

A correct interpretation must consider that in barrier systems along with material-specific polarization processes, even highly distinct (and often dominant) *interfacial polarization* occurs, and it depends considerably on the geometrical structure and the oil conductivity, Figure 6.4.7-3. Therefore, influences of **water content**, of **geometrical structure** and of **oil conductivity** can be distinguished in the measurements only with great difficulty [222]. An interpretation approach which takes all these influences into consideration is currently not known.

Note: Increased *barrier conductivity* (e.g. through moisture) leads to a shortened time constant τ_B, increased oil conductivity (e.g. through oil ageing) leads to a shortened time constant τ_O, Figure 6.4.7-3. Both effects thus shift the maximum of the recovery voltage (and also the characteristic time constant of the polarization spectrum) to earlier times.

Another problem is a very *time-consuming measuring procedure,* in which a large number of recovery voltages must be documented. Each individual measurement includes the charging phase, discharging phase and recovery phase as well as a depolarization phase, in which the insulation must be discharged to the extent that the next measurement will not be influenced.

Note: The same information can be determined in a considerably shorter period from a single *step-response measurement* (i.e. in a single charging phase) by conversion, see Section 6.4.7.6.

All recovery voltage measurements are carried out as two-electrode measurements to ground and thereby face the problem of *surface resistances* lying parallel to the dielectric to be measured, Figure 6.4.7-2 (left). As a result, shorter discharge time constants τ_B can occur and increased water content levels in barriers can be faked respectively.

d) Other approaches

When determining the "polarization spectrum", only the peak value of an individual recovery voltage curve is evaluated, i.e. only a fraction of the information that is contained in the signal can be used. The complete *evaluation of individual curves* would be considerably more efficient. For example, the information about the time constant τ_O and also about the oil conductivity is included in the initial steepness s, Figure 6.4.7-3.

In the case of interfacial polarization according to Figure 6.4.7-3, a new *"p-factor*"

$$p = \hat{v} / (s \cdot t_{max}) \qquad (6.4.7\text{-}3)$$

was proposed [227]. It contains recovery voltage amplitude $\hat{v}$, initial steepness s and the time t_{max} at which the maximum occurs, and it depends only on the ratio of time constants τ_B/τ_O. This results in a certain amount of *temperature compensation* that can be advantageously used, e.g. for comparing paper-insulated medium voltage cables [228].

Furthermore, it is also proposed to examine dielectric system responses at different polarization voltages. *Non-linearities* are valued as indicators of damage, but the correlation with the insulation condition is not yet completely known [223].

6.4.7.6 PDC Analysis

a) PDC measurement

PDC measurement (PDC: Polarization and Depolarization Currents) measures the **polarization current** $i_p(t)$ or the charging current respectively for applied DC voltage, Figures 6.4.7-1 and 6.4.7-2 (right). Therefore, it is a **step response measurement**, from which the properties of a *linear insulation system* can be calculated, e.g. in the form of an *equivalent circuit*, Figure 4.2-8. It is especially advantageous that the entire information (for lower frequencies) can be obtained in *a single measurement*, see Section 4.2.2.3.

The measurement of **depolarization current** $i_d(t)$ or discharge current respectively, after the charging or polarization time $t_C = t_p$ and during the short circuit of the test object, also provides the properties of the insulation, with the exception of the DC resistance R_∞ which remains short-circuited during depolarization.

If the magnitudes of the actually successive currents $i_p(t)$ and $i_d(t)$ are shifted relatively to each other on the time axis by the charging time t_C, the described relationship according to system theory becomes obvious, cf. Section 4.2.2.3 with Figure 4.2-8. The sum of the two currents (or the difference in current magnitude respectively) provides an estimate of the **end value** of the *polarization current* in accordance with Eq. (4.2-6d) if the current values are taken at times that are shifted by t_C. Another effective method for early estimation of conductivity end values is the **charge difference method** described in Section 6.4.1.3.

The *capacitance* C_{geo}, which is valid for rapidly changing processes, can be determined by integration of the charging current impulse on switching on the DC voltage. For the description of slower polarization processes, the remaining *RC* elements are established through an approximation of the measured curves with the aid of exponential functions [229], [230]. The determination of equivalent circuits describing dielectric materials through PDC measurements has already been explained in Sections 4.1.1, 4.2.2.3, 4.3.2 and 4.3.3.

Since the PDC measurement is as a step-response measurement, it contains the *entire system information* if linear systems are assumed. *All other diagnostic parameters*, such as recovery voltages, "polarization spectra" or frequency responses of capacitance and dissipation factor can be calculated by appropriate transformation or by using the established equivalent circuit describing the material. Good agreement is obtained with the correspondent measurements, which are all considerably more complex than the PDC measurement [232].

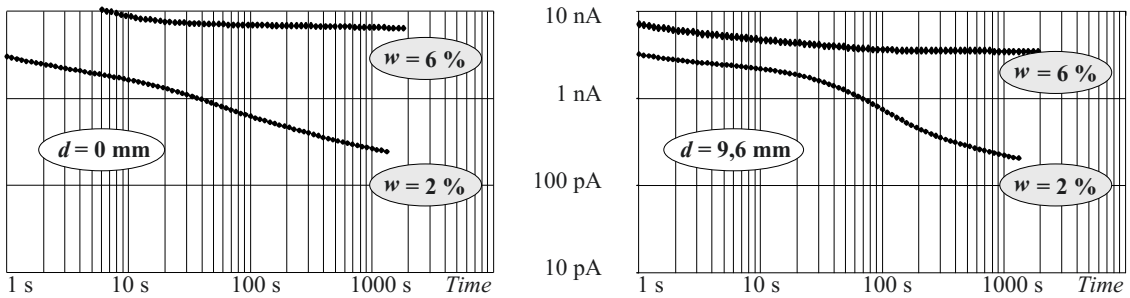

Figure 6.4.7-4: Polarization currents, measured at insulation models made of two Transformerboard barriers (each 1 mm) with an intermediate oil gap. Measurements for differerent water contents of barriers and for different oil-duct widths d = 0 mm (homogenous arrangement, left) and d= 9.6 mm (multi-layer arrangement, right) [233].

b) Analysis of homogeneous insulations

In the case of **homogeneous insulations**, such as in *cables* or *bushings*, the material properties can be directly determined according to the described procedures, and they can then be compared with the *reference data*. Figure 4.2-8 in Section 4.2.2.3 shows a dry oil-impregnated transformer board reference [231]. In the case of wetted samples, owing to orienting laboratory investigations of new materials, it is assumed that the end value of the DC conductivity is dependent on both the *water content w* of the barriers and also on the *conductivity of the impregnating oil* $\kappa_O(\infty)$, Figures 5.5-3 to 5.5-5 and 6.4.7-4 (left) [234], [231], 429], [436]. This corresponds to a conduction of current along the *wetted fibers* and a basic conductivity owing to *oil-filled capillaries*.

Note: Eq. (4.2-7) in Section 4.2.2.3 gives an experimentally determined relationship, which is, however, not always valid and is still the subject of *ongoing research* [428], [429], see Section 4.2.2.3 a).

Note: In the case of **aged materials**, also deterioration products deposit on the cellulose fibers. In in many cases, they can increase the conductivity and the polarization currents similarly to water. Ageing processes of oil and paper under the effect of temperature, light, oxygen, water and metal ions can be of a totally different chemical nature.

Therefore, additional information is necessary for a *differentiation of ageing influences and moisture influences* on dielectric measurements. This difficulty is generally not only related to PDC measurements, but basically to *all dielectric methods*.

Example: The above-mentioned considerations helped, for example, to correctly identify the **wetting condition** of service-aged "dry" oil-paper bushings from *low end values of the current* and also to select **severely aged** objects on the basis of *increased initial values of the current* [231], [236], Figure 6.4.7-9.

In this case, it was particularly significant that the objects that were selected at *room temperature* using PDC measurement showed high dielectric losses at *operating temperature* and at power frequency exhibiting the risk of thermal instabilities [392], [398].

c) Performance of multi-layer insulations

The performance of multi-layer insulations can be explained with an example of plane insulation model made of two new Transformerboard barriers (Weidmann T IV, 1 mm) and an intermediate oil duct or oil gap, Figure 6.4.7-4. In the polarization currents measured in a guard ring arrangement, the influences of parameters such as water content in the barriers *w* and oil gap width *d* (or the geometrical proportion of the layers respectively) can be easily identified:

In **moist** barriers with high water content (*w*= 6%), the polarization currents rapidly attain a high steady-state end value. In **drier** barriers (*w*=2%), the polarization currents decrease slower and attain a significantly lower end value. These end values are largely equal for both homogeneous and multi-layer insulations, because the end values of the polarization current are mainly determined by the high resis-

tance of the barriers. Therefore, they also correspond to Eq. (4.2-7).

A **multi-layer arrangement** influences the time characteristic of the transient process: That is, the barrier capacitance is predominantly charged via the oil gap resistance. Thus, the time constant of the current decrease corresponds to approximately the product of oil gap resistance and barrier capacitance. The **homogeneous insulation** is the limit case of a very small oil gap resistance. The polarization current then decreases very much faster and is especially determined by material-specific polarization processes according to Figure 4.2-8, and no longer by the macroscopic multi-layer arrangement.

The **conductivity of the oil** principally determines the initial values of currents, since at first, the barrier capacitances are charged via the oil gap resistances. In mult-layer insulations, high initial currents are synonymous with high oil conductivities.

Note: On the described insulation models, also *recovery voltage analyses* were carried out, which did not show any comparable clear differentiation of the parameters water content and the insulation geometry. Some implausible results can be attributed to the fact that recovery voltage measurements cannot in principle be carried out in guard ring arrangements, and as a result are influenced by undefined surface currents in the test vessel and in the test set-up [222].

A greater advantage of PDC analysis is the option to associate the *oil conductivities and barrier conductivities* with the *initial values and end values* of the polarization current if oil conductivity is much higer than barrier conductivity:

After connection to the voltage and very fast charging of the capacitances, the barrier capacitance is *initially* recharged via the **oil gap resistance** which consequently deteremines the current value. After *long periods*, the current is determined through the series connection of the oil resistance and the **barrier resistance**. Generally, the latter dominates if the barriers are dry enough, cf. *Section g)* with Eqs. (6.4.7-6) and (-7).

With guard-ring-type connection of the windings, **leakage currents** can be ruled out and **selective measurements** of parts of the insulation are possible.

d) Analysis of transformer insulations

Analysis of transformer insulation needs to consider both the complex insulation geometry, Figure 6.4.7-5, and the material-specific polarization processes:

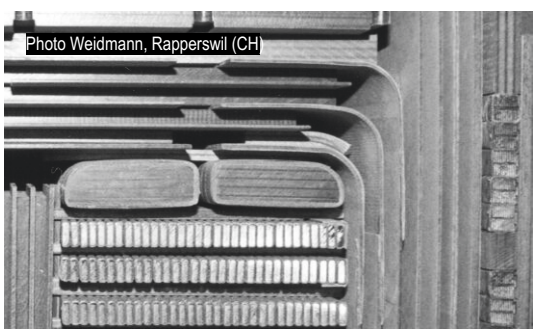

Figure 6.4.7-5: Transformator insulation with oil ducts (or oil gaps resp.), barriers, spacers and parallel oil channels.

Figure 6.4.7-6: Complete modelling for diagnosis measurements between HV winding and LV winding.

X, Y, Z: Relative portions of thicknesses and areas.

Leakage currents to core and tank are not involved in PDC measurements and FDS measurements, but in RVM measurements. The measurement current is the superpostion of several components.

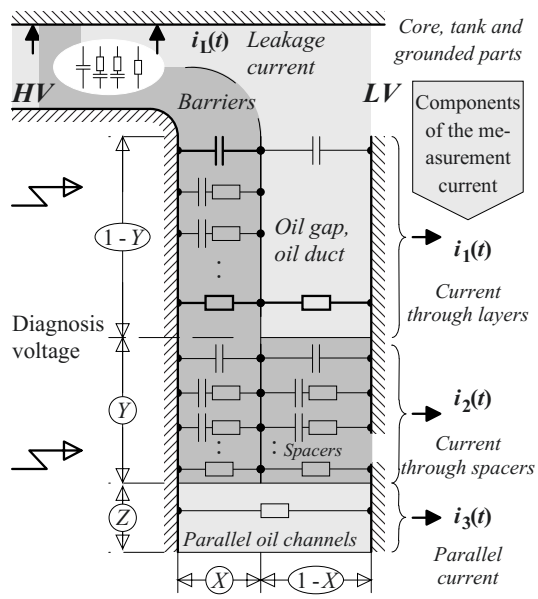

In the **complete model of a multi-layer transformer insulation**, the insulation between the considered windings must be represented by material-specific equivalent circuits for the *barriers, spacers, oil gaps* and parallel *oil channels*, Figure 6.4.7-6. The measurement current is therefore composed of three components $i_1(t)$ through the *layers* of oil and barriers, $i_2(t)$ through the *spacers* and $i_3(t)$ through the *parallel oil channels*.

Note: Even the insulation against grounded components would be simulated with comparable models. However, they are unnecessary for PDC and FDS measurements, since *leakage currents* are not involved in these measurements.

PDC analysis is carried out with the currently available diagnosis software by **"curve fitting"**, i.e. by *comparing the measured and calculated polarization currents and depolarization currents* [229], [230]: for the calculation, *geometrical insulation data* must be put in and *material-specific equivalent circuits*, which represent different barrier-conditions (different water contents) and different oil conductivities, must be selected. By varying the material data, the calculated curves are made to agree with the measurements. The **water content of the barriers** is obtained from the best fit and the **oil conductivity** is obtained from its initial value. For this, the calculation is done taking the measuring temperature into consideration.

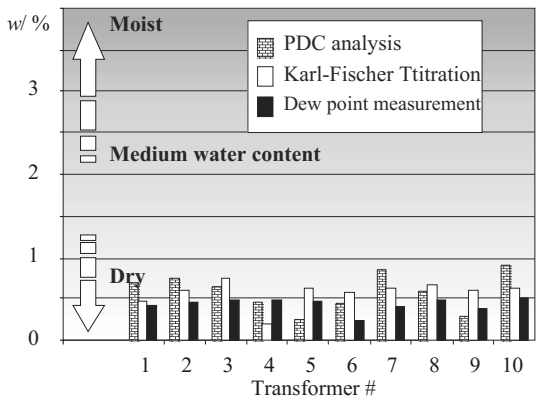

Figure 6.4.7-7: Comparision of diagnosis methods for new high voltage transformers [235].

e) Analysis examples

Meanwhile, PDC analysis could successfully be used in various applications:

For *newly manufactured* (and thus, dry) *transformers*, a matching classification of the residual water content was achieved with dew point measurements in the evacuated tanks, as well as by *Karl Fischer titration* on paper samples and also by *PDC measurements* on transformers [235], Figure 6.4.7-7.

Note: The *dew point* is that temperature at which the humidity present in a gas condenses (during a decrease in temperature), i.e. at which the relative humidity has increased to 100%. Therewith, the absolute humidity of

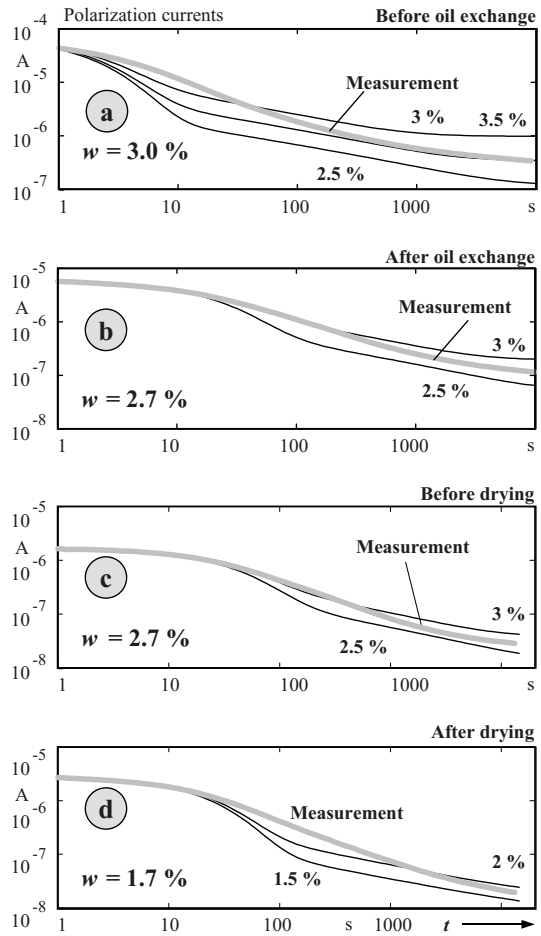

Figure 6.4.7-8: PDC diagnosis by "curve fitting" as per number d) for a 300 MV transformer, before and after an oil exchange (a and b) as well as before and after drying of core-and-coil assembly (c and d) [233], [232].

the gas and the *water vapor partial pressure* can be specified. In equilibrium, this is correlated to the water content of paper.

An interesting example is the *monitoring of reconditioning processes* on an aged 300 MVA transformer, Figure 6.4.7-8. Before and after an oil exchange respectively, and before and after drying of the core-and-coil assembly, PDC analyses were carried out by "curve-fitting" (see in this Section, *paragraph d)*). As expected, they show that with the oil exchange only a little amount of water was extracted. Moisture decrease ascertained during the drying corresponds to the extracted water quantity [233], [232].

f) Related questions

For *bushings*, it has been shown that even objects that possess comparable water contents (identifiable by comparable polarization current end values), but are *aged differently*, can be distinguished by PDC measurements in a time period of a few seconds [236], [231], [428], Figure 6.4.7-9, see also *Section b)*.

Basically, the differentiation of **ageing influences and moisture influences** is a problem yet to be solved, for which only very few approaches exist [237], [238]. As already explained in *paragraph b)*, also the deterioration products can lead to an increase in polarization currents and conductivities, and therefore cannot always be differentiated from moisture by dielectric diagnosis alone. Another problem is that the moisture that can be detected by dielectric diagnosis can originate from ageing processes (through depolymerisation of cellulose) and also from external sources (e.g. from leakages, diffusion processes or air contact).

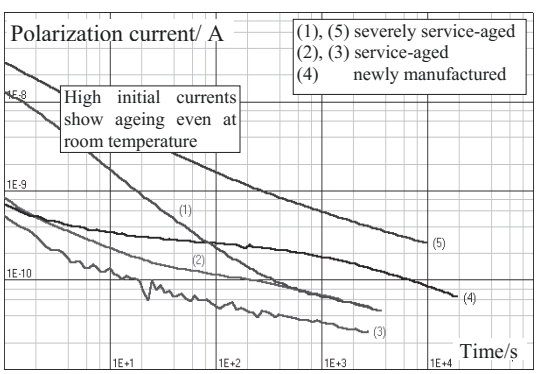

Figure 6.4.7-9: PDC diagnosis of ageing condition of 400 kV oil-paper (OIP) bushings aged in service [428]. Advanced ageing is evident from significantly enhanced initial values of the polarization current.

In dielectric measurements on **bushings**, **external influences** can lead to a change in the quantities to be measured when leakage currents have access to the free ends of the grading layers. In the frequency domain there is sometimes an *apparent decrease in the dissipation factor*, eventually leading down to negative values [243]. In the time domain, polarization currents and depolarization currents can be modified, eventually, leading to *polarization reversal* [244], [398].

Until now parasitic influences for greatly increased **oil conductivities** have not been included in the analyses. They can cause increased currents through microscopic *oil-filled capillaries* and in transformers also increased currents through *macroscopic oil ducts*. In both cases, the end values of the polarization currents are increased and increased moisture values are simulated [231].

For diagnosis by curve-fitting the necessary **geometric data** are sometimes either not available at all for use or only incompletely available.

g) Simplified diagnosis

Even for incompletely known geometry data, a simplified diagnosis can be conceived in which two different measurement instants $t \geq 0$ as well as $t \rightarrow \infty$ are taken into consideration [231], Figure 6.4.7-10 (top).

For the **initial value** of the polarization current $i_p(0)$, the current through the layers dominates, i.e. $i_p(0) \approx i_{p1}(0)$ is valid, Figure 6.4.7-10 (bottom left). The current is obtained as the solution of the network-differential equation:

$$i_p(0) \approx \frac{V}{R_O(0)} \cdot \left(\frac{C_B}{C_O + C_B}\right)^2 + V \cdot \sum_j \left(\frac{1}{R_{pj}}\right) \cdot \left(\frac{C_O}{C_O + C_B}\right)^2 \quad (6.4.7\text{-}4)$$

R_{pj} stands for the resistances assigned to individual *RC* elements, which describe the polarization of the board.

Note: For *multi-layer insulations*, generally $C_B >> C_O$ is valid, so that the first term dominates, which is correlated with the resistance of the oil gap R_O and the **oil conductivity** respectively,:

$$i_p(0) \approx \frac{V}{R_O(0)} \cdot \left(\frac{C_B}{C_O + C_B}\right)^2 \quad (6.4.7\text{-}5)$$

In the case of *homogeneous insulations*, $C_O \rightarrow \infty$ is valid and hence the second term, which is largely determined by the **polarization processes**, dominates:

$$i_p(0) \approx V \cdot \sum_j \left(\frac{1}{R_{pj}}\right) \quad (6.4.7\text{-}6)$$

The **end value** of the polarization current results approximately from the steady-state currents i_{p1} and i_{p3} through the layers and eventually, through parallel oil channels, Figure 6.4.7-10 (bottom right):

$$i_p(\infty) \approx i_{p1}(\infty) + i_{p3}(\infty) = \frac{V}{R_B + R_O(\infty)} + \frac{V}{R_3} \quad (6.4.7\text{-}7)$$

If the first tem is assumed to dominate, then $i_p(\infty)$ mainly contains information about R_B and the **barrier conductivity** respectively, and with Eq. (4.2-7) an estimate of **water content of the barriers** *w* can be given.

From Eq. (6.4.7-4) and (-7), the correlations of the initial value of the current with the oil conductivity and of the end value of the current the with the barrier conductivity mentioned in *Section c)* are obtained.

For the practical evaluation, it is recommended to measure **initial values and end values** of the polarization current. According to Eq. (4.2-6d), this allows to estimate the end value from the sum (or the difference in magnitude respectively) of the polarization current and depolarization current, even after finite periods, Figure 6.4.7-10 (top).

If the Eqs (6.4.7-4) and (-7) are correlated with geometric relationships for capacitances and resistances, a physically substantiated correlation between a measurable **characteristic current ratio** and the *conductivity ratio* between oil and board is obtained:

$$\frac{i_p(0)}{i_p(\infty)} \approx \frac{i_p(t = 1\text{s})}{i_p(t) + i_d(t + t_C)} \quad (6.4.7\text{-}8)$$

$$\frac{i_p(0)}{i_p(\infty)} \approx \frac{\frac{\kappa_O(0)}{\kappa_O(\infty)} \cdot \frac{d_O}{d_B}}{\left[\frac{d_O}{d_B} + \frac{\varepsilon_O}{\varepsilon_B}\right]^2 \cdot \left[\frac{1}{\frac{d_O}{d_B} + \frac{\kappa_O(\infty)}{\kappa_B(\infty)}} + Z \cdot X\right]}$$

Here, *Z* and *X* are the surface ratios and thickness ratios in the barrier system according to Figure 6.4.7-6:

$$Z = \frac{A_3}{A_1 + A_2} = \frac{A_{Oil(Parallel)}}{A_{Barrier}}$$

$$X = \frac{d_B}{d_B + d_{Oil}} = \frac{d_{Barrier}}{d_{Total}} \quad (6.4.7\text{-}9)$$

The conductivity of the board can be determined from the *conductivity ratio* $\kappa_Ö(\infty)/\kappa_B(\infty)$ and the *oil conductivity*, and it can be correlated with the *water content* via Eq. (4.2-7).

Note: The current ratio $i_p(0)/i_p(\infty)$ is **not** equivalent to the **classical polarization index,** which is formed at arbitrary times without considering the dynamics of transient processes. Instead, it is a **characteristic current ratio**, which has a distinct correlation to the conductivity ratio and thus corresponds to a *physical meaning*.

Note: An advantage of the ratio formation is a **lower sensitivity to temperature variations**. If the temperature is known, then furthermore an additional arithmetic

temperature correction for the current ratio can even be made.

Note: The current ratio is suitable for the estimation of the **influence of parallel current paths** through parallel oil resistances R_3, Figures 6.4.7-6 and -10. The initial current hardly changes, because the surface ratio $A_3/A_1 = Z$ is small. In the steady-state current, an addiitional current component through R_3 occurs. From the ratio of polarization currents, it can be identified that the parallel current path with the surface ratio Z leads to a decrease in the current ratio, and thus has a similar effect as a reduction in the conductivity ratio of oil/board or an increase in the **water content** respectively. The disturbing effect of the parallel current path is especially large for **severely aged oil** and a large oil/board conductivity ratio, since the denominator in Eq. (6.4.7-8) is small and the influence of the interference term $Z{\cdot}X$ is large in that case [231].

h) Bushing diagnosis

Bushing insulations at first appear as comparatively simple cylindrically symmetric insulations between the inner conductor and the outermost metallic grading layer, the so-called ground layer. The dielectric in between is divided into a larger number of partial capacitances by the conductive grading layers, Figure 6.4.7-11.

In normal operation, the gound layer is connected to earth via the *measuring tap*. For measurement purposes, this connection is opended so that the current flowing through the dielectric can be extracted. But it has now been proved that under unfavorable conditions (e.g. for contaminated and wetted surfaces or for highly conductive transformer oil), *leakage currents* can flow between the free ends of the grading layers and the voltage side or the ground side. These currents are added to (or subtracted from) the signal current at the measuring tap, and thereby cause an *error* that is difficult to quantify [398].

Conductive paths *to the voltage side* increase the measurement signal; conductive paths *to the ground side* reduce the measurement signal, ranging down to a two-fold polarity reversal. These influences are at the maximum when the coupling is around the middle of the grading contour and when the covering insulation layers above the ends of the grading layers is very thin or the radial resistance is relatively low.

Note: These effects can be explained by the fact that all partial capacitances are at first charged by a *positive* current when connecting a positive diagnosis voltage. For example, a conductive path to the *ground side* is considered. It partially discharges the outer partial capacitances at the ground side and temporarily leads to a current in the reverse (*negative*) direction via the measuring tap. In the steady-state, all charge reversal processes are completed and the steady-state current is again *positive* [430]. The entire process is therefore associated with a two-fold polarity reversal of the current.

These changes of *polarization currents* described in the **time domain** correspond to the changes of *dissipation factor* in the **frequency domain,** ranging down to negative values.

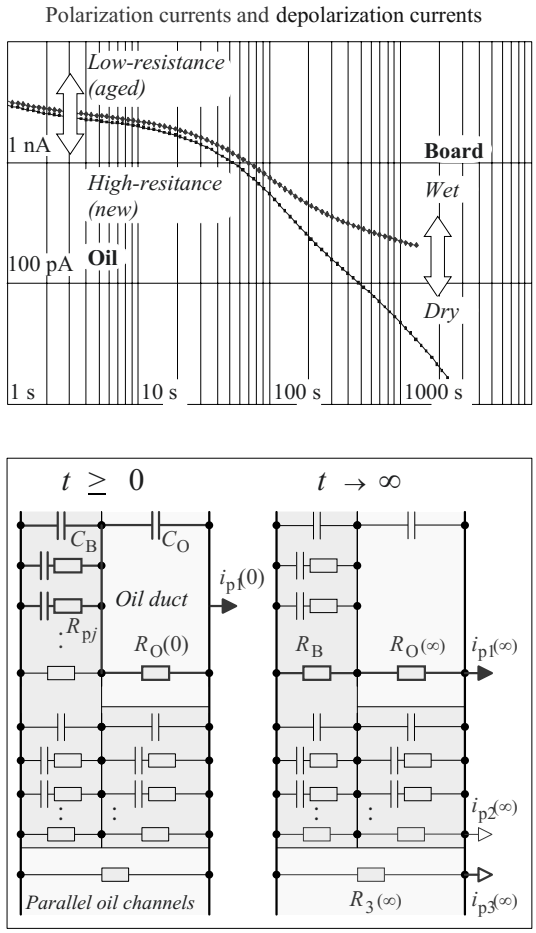

Figure 6.4.7-10: Differtiation of characteristic equivalent circuit elements by a selection of different measuring times.

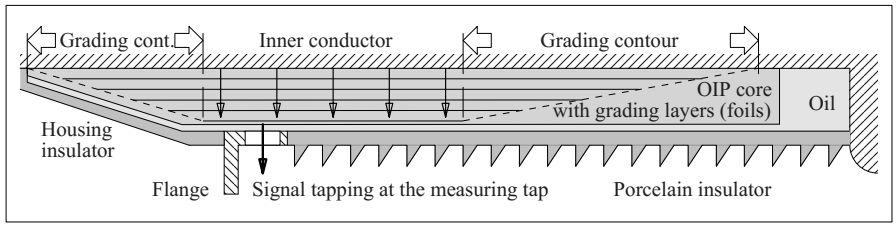

Figure 6.4.7-11: Dielectric measurements on the measuring tap of an oil-paper bushing.

Note: The described processes were originally discussed at first in the **frequency domain**, in order to explain the phenomenon of "*negative dissipation factors"* [243].

All these changes of currents or dissipation factors are only *apparent* in nature, i.e. they do *not* give any information about changes in the bushing dielectric. It must therefore be ensured by suitable measuring procedures that the measured parameters are really associated with the dielectric.

Cleaning of *bushing surfaces* and avoiding measurements during humid *weather conditions* are useful measures.

A method has now been developed, with which the *upper and lower limits* for the polarization current and the dissipation factor of the bushing dielectric can be determined [430], [434]: For this, a **conductive bandage** is put circumferentially on the bushing at the center of the grading contour (*worst-case bandage*). In the case of a *grounded bandage*, current components are branched off and the remaining current via the measuring tap is too low (lower limit). If the *bandage is at diagnosis voltage*, additional current components are fed in, and the resulting measurement current is too high (upper limit). A grounded bandage behind the *edge of the grounded grading layer* can act as a guard-ring electrode and draw off the surface currents so that the measurement signal is improved. A complete **measurement** is thus obtained from three or four individual measurements with and without bandages, Figure 6.4.7-12:

1. Measurement with worst-case bandage *at ground* (lower limit).
2. Measurement with worst-case bandage *at diagnosis voltage* (upper limit).
3. Measurement *without bandage* (classical, possibly inaccurate measurement).
4. Measurement with *guard-ring bandage* behind the edge of the grounded grading layer (optional, for improved estimation of the current through the bushing dielectric).

Example: In Figure 6.4.7-12 it can be clearly identified that the relative influence of the parasitic surface currents is increasingly smaller with increasing currents in the main dielectric (e.g. through *wetting or ageing*). The *bandage measurements* which lie close to each other show the measurement result as very reliable, on the

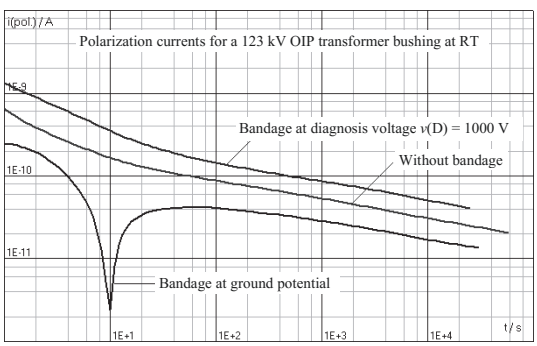

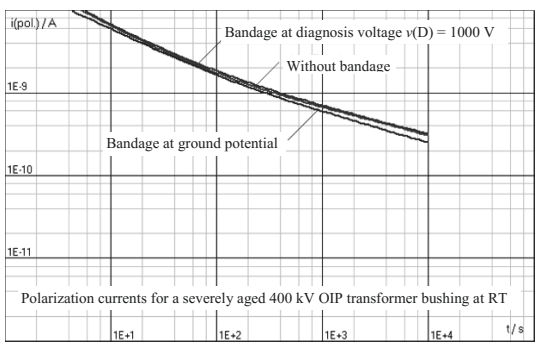

Figure 6.4.7-12: PDC measurements on high voltage bushings with bandages in the center of the grading contour (worst-case bandages) for demarcating the scope of the current through the bushing dielectric [428], [430], [434]. Left: new 123 kV OIP bushing. Right: severely aged and thermally unstable 400 kV OIP bushing (also refer to figure 6.4.7-9).

right in the figure. For new bushings with low currents, the bandage measurements are comparatively far apart from each other, on the left in the figure. The conductivity ratio of the *main insulation* and the *insulation of the top layers* can be concluded from the distance of the curves [434].

6.4.7.7 Frequency Domain Analysis

For capacitances and dissipation factors measured at *power frequency* (50 or 60 Hz) and room temperature, only a very weak dependence on water content or ageing condition is indicated.

The power frequency dissipation factor of oil-impregnated paper rises steeply with the water content at *increased temperature* (70 °C). Appropriate measurements are, however, possible only in exceptional cases. At *room temperature*, increases in dissipation factor that are dependent on water content occur at very *low frequencies* (mHz range). At low frequencies, the dissipation factor generally increases because the reactive power decreases and thereby the ratio of real power to reactive power rises.

From the point of systems theoretically, the measurement of capacitances and dissipation factors in the **frequency domain** (FDS: Frequency Domain Spectroscopy) is equivalent to a step-response measurement in the **time domain** (PDC measurement) for linear systems, and it is possible to transform the results [239], [240], [241]. Therefore, many explanations for PDC measurements can also be transferred into the frequency domain.

a) Instead of a step-response measurement, the system properties and the related equivalent circuits can also be determined by *frequency response measurement* for the real part and the imaginary part of complex permittivity, in accordance with Eq. (4.2-16), Figure 6.4.7-13.

Note: The equivalent circuit comprises the DC resistance, polarization processes recorded during the measurement and a so-called geometric capacitance C_{Geo}. It integrates the vacuum capacitance C_0 and those high frequency polarization processes that lie outside the considered frequency domain, Figures 4.3-2 and 4.2-8.

For practical measurements, capacitances and dissipation factors must be recorded as a function of frequency *in a series of individual measurements*. This requires a *steady state* to be awaited for each individual measurement, which can be assumed to be available after about four periods. Measuring lower frequencies can therefore result in long measuring periods.

It is advantageous that the measurements, such as PDC measurements, can be executed in a type of "*guard-ring arrangement*" to eliminate leakage currents, Figure 6.4.7-2.

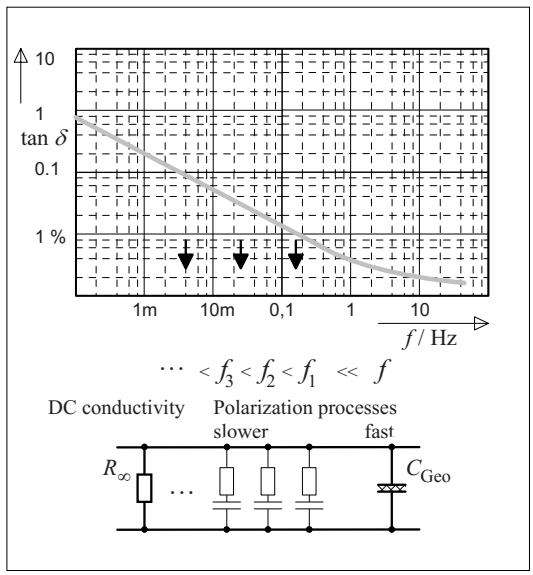

Figure 6.4.7-13: Frequency domain analysis for a homogeneous insulation.

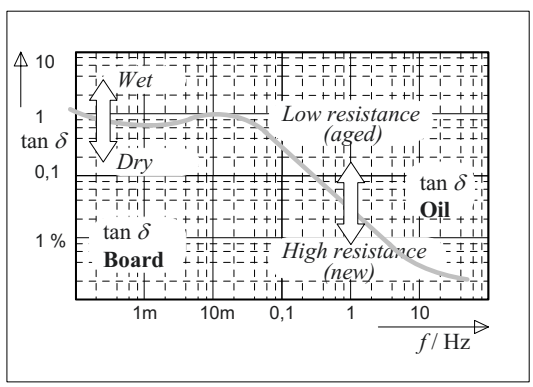

Figure 6.4.7-14: Frequency domain analysis for a multi-layer insulation.

b) In *homogeneous insulations*, the influence of water content is manifested by a sharp rise in dissipation factor, especially for very low frequencies, but not for the power frequency. This can be explained by the moisture-induced exponential increase in the conductivity in accordance with Eq. (4.2-7): at low frequencies, the parallel resistance $R_\infty = R_p$ especially determines the losses. According to Eq. (4.3-1), a decrease in this resistance corresponds to an increase in power loss or an increase in the dissipation factor.

c) The *performance of multi-layer insulations* will be explained with the example of a layered arrangement of an oil gap and barriers. The basic correlations are explained in Section 4.3.3 with Figure 4.3-7: at **higher frequencies**, the capacitively divided voltage drops largely across the capacitance of the oil gap, which is assumed to be lower. The measured dissipation factor, therefore, must be largely attributed to the **oil gap**. The higher barrier capacitance acts like a short circuit. At **lower frequencies**, the generally lower oil gap resistance acts like a short circuit because the capacitive reactances increase. Therefore, the measured dissipation factor must be largely attributed to the **barriers**, Figures 6.4.7-14 and 4.3-2.

d) Transformer insulations, as explained earlier with Figure 6.4.7-6, must be simulated by a complex equivalent circuit oriented towards the geometry. Based on this, and similar to PDC analysis, frequency responses can be calculated and can be fitted with the measurements (curve-fitting) to determine the best fitting material parameter.

e) The oil exchange in a 300 MVA transformer is mentioned *as an analysis example*; see Figure 6.4.7-8 (a) and (b). The curves transformed from the time domain into the frequency domain, at low frequencies and before and after the oil exchange, result in practically unaltered dissipation factors, which corresponds to a hardly altered water content. At higher frequencies, the insulation shows significantly lower losses, which correspond to the substantially improved quality of the exchanged oil. Measurements at 0.1Hz agree with the calculated frequency responses [233].

f) Additional questions here, similar to those of PDC analysis, refer to the ability to distinguish between moisture effects and ageing effects, to the effect of external environmental influences on measurements on bushings [243] and to the effects of oil conductivities and parallel current paths.

6.4.7.8 Dielectric Diagnosis in Time Domain and Frequency Domain

According to systems theory, PDC analysis and frequency domain analysis are methods which *correspond to each other* in the time domain and in the frequency domain if linear systems are considered. All the above-mentioned considerations about the effects of water, deterioration products, surface currents and other parameters are, in principle, valid in both the time domain and the frequency domain, as, for example, the comparison of Figures 6.4.7-10 and -14 shows. Therefore, the *efficiency* and the *problems* of the two methods can be *compared* [468].

Both methods, for example, are able to differentiate the properties of oil and of oil-impregnated pressboard barriers in multi-layer *oil-paper insulations*. However, the accuracy in *determining the water content* is restricted, since a series of other parameters that are difficult to control is of significance [436]. This includes, for example, that the differentiation of *water* and *deterioration products* in oil-impregnated insulations is difficult, because both increase the conductivity and thereby produce a similar effect in the dielectric system response. However, it has been shown that deterioration products also invoke polarization processes with shorter time constants and thereby can be measured at shorter times or at higher frequencies, see Figure 6.4.7-9.

A few more differences between the **practical applicability** of PDC analyses and FDS analy-

ses are mentioned: as against the information that can be obtained in *a single step response measurement* during PDC measurement, a *series of measurements* is necessary during FDS analysis, which can especially significantly extend the measurement durations for low frequencies. Further, during PDC measurement, even *very high voltage steps* can very easily be used to investigate non-linearities with the aid of external DC power supply units [271]. For FDS measurement, the *frequency-variable sinusoidal voltage* is *restricted* to lower values by the amplifier. PDC analysis reaches its limits at *faster processes* or higher frequencies respectively, which occurs as a result of the time resolution during digitalization. It is therefore easier to measure fast changing processes in the *frequency domain*.

A new method combines the **advantages of both systems** [467], Figure 6.4.7-15: *slow* processes are measured by a polarization current measurement in the *time domain* and *fast* processes by a dissipation factor measurement in the *frequency domain*. With regard to a pure frequency domain measurement, the measurement time is reduced by about 75%. For a coherent representation, the measurements are transformed from the time domain into the frequency domain and further analyzed there.

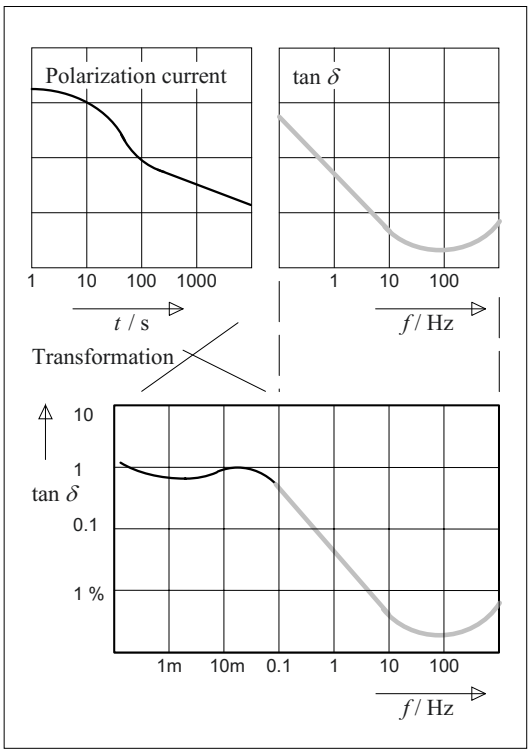

Figure 6.4.7-15: Combined time domain and fequency domain analysis for a multi-layer insulation [467].

6.4.8 Online monitoring

Complex technical systems (such as power stations or networks) and important components (such as large generators and large transformers) are monitored not only within the inspection periods, i.e. "**offline**" in the disconnected state, but are also monitored permanently "**online**" during operation to enable a response to dectable defect evolutions just in time.

Dependable operation of **electrical insulations** *up to the end of the nominal lifetime* was initially expected, based on factory tests and according to a safe design. Continuous online monitoring of electrical insulations did *not* appear to be *necessary* and moreover, was *too expensive*.

This point of view has now changed such that the operator of electrical equipment is more than ever interested in *online monitoring* of his devices, *including the insulation*. The following reasons are responsible for this:

- Many operating devices have long exceeded their *nominal lifetime* and continue to be operated in an *unknown ageing condition;* a preventive replacement investment is no longer made without a condition assessment.
- The cost pressure during the manufacture of electrical equipments reduces the safety margins, including the dimensioning of insulation systems. Operation in the *limit-rating range* (from electrical and thermal viewpoints) is increasingly expected from insulations.

- The cost pressure while operating power stations and networks leads to the provision of less redundancy and lower *stand-by capacities*, so that the strategic significance of individual and possibly vulnerable equipment increases. On the other hand, increasingly fewer *personnel* and lower technical *competence* are available, so that it is increasingly difficult to assess the plants on the basis of experience and to respond adequately in case of emergency.
- The *costs for monitoring systems*, comprising sensor technology, signal transmission technology and signal processing technology, are declining and hence online monitoring systems are increasingly described as an economically viable option. Moreover, the *performance* and the *reliability* of the systems are continuously rising.
- For the operators of networks, monitoring systems eventually provide valuable information about the *evolution of fault events* (fault history).

In the following sections, the online monitoring of transformers (Section 6.4.8.1), bushings (Section 6.4.8.2), rotating electrical machines (Section 6.4.8.3) and XLPE cables (Section 6.4.8.4) is considered. Under other equipment (Section 6.4.8.5), mainly switchgears with their components are summarized.

6.4.8.1 Monitoring of Transformers

The high strategic significance of large transformers has already led to the early development of transformer monitoring in the form of the *Buchholz protector*. This involves trapping the gas formed in the transformer as a result of discharges. The fault gas is trapped in the oil expansion vessel, which is closed at the top, and it is detected via the displacement of oil. This, however, is just a protective device which is activated only for very large gas quantities when the defect is already at an advanced stage.

Note: Actually, it is important to record small quantities of fault gases in oil (especially hydrogen) with *gas sensors.* Therise in fault-gas contents should then cause a sophisticated gas-in-oil analysis, see Section 6.4.3.2. It is, however, also recommended to analyze the gas content in the oil expansion vessel with regard to fault gas content and correlate it with the fault gas content in oil using gas exchange models [250].

Transformers are now equipped with very well advanced **monitoring systems** [251] [252] as in Figure 6.4.8-1. They are largely used in monitoring classic parameters such as current, voltage, oil level or temperatures. Moreover, maintenance-intensive on-load tap changers are monitored. Furthermore, properties of the insulating oil, e.g. water content [248] or hydrogen gas content (which indicates partial discharges), are analyzed during operation, with sensors or by sample extraction.

Note: Continuously operating sensors are thus the better solution since, for sample extractions, practical analysis intervals are so long that this is not an online monitoring any more.

The monitoring system records a large number of data that are continuously analyzed and evaluated. Thus, the data are available for automatic control (e.g. for cooling circuits). Operational management of the power system continuously acquires relevant information about the condition of the equipment and is warned in advance about the emergence of critical situations.

In relation to this, **temperature monitoring** with the aid of multiple temperature sensors is of great practical importance. The loading capacity of the transformer is especially restricted by reaching the maximum permissible temperatures for the insulating materials used. The directly measurable *upper oil temperature* and the temperatures of *hot spots* within the windings, which cannot be directly measured, are significant here. The hot- spot temperature is calculated with the aid of a **thermal transformer model**, in which the heat sources (copper losses owing to load current, iron losses owing to applied voltage), the ambient temperatures, the thermal capacitances and the thermal transmission conditions (taking the cooling into consideration) are involved.

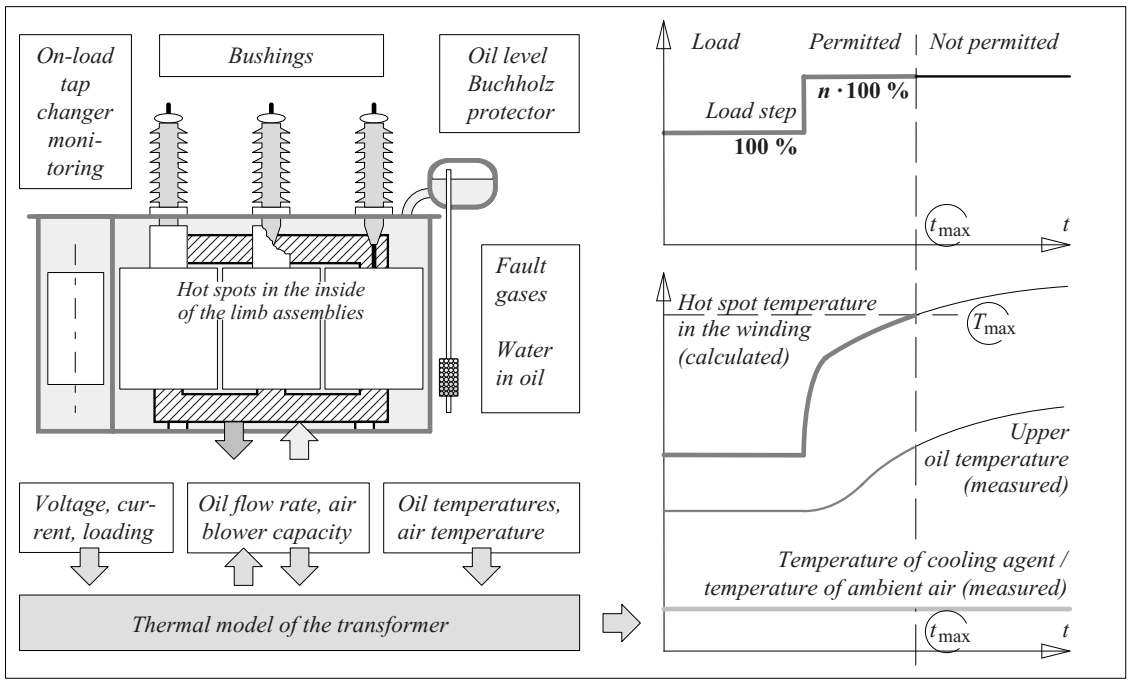

Figure 6.4.8-1: Important components of transformer monitoring (left) and transient temperature profiles for change in load condition (right).

The so-called *homogeneous-body model,* in accordance with IEC 60354 (meanwhile replaced by IEC 60076-7, Loading guide for oil-immersed power transformers), can be upgraded to a *two-body model*, in which shorter thermal time constants (in the range of few minutes) are used for the winding and longer time constants (in the range of hours) are used for oil, core and tank [251], Figure 6.4.8.2. Thus, the transient temperature profiles for load changes or changes in the ambient temperature can be calculated and predicted online, Figure 6.4.8-1 (right). Predictions of the permissible overload duration under the actual load conditions and ambient conditions are thus made from the material-specific temperature limits, Figure 6.4.8-1. For oil-impregnated paper, the permissible continuous hot-spot temperature is 120 °C; the hot-spot temperature may not exceed 140 °C for an overload with 1.5 times the nominal current for a maximum duration of 30 minutes [295], [296]. The maximum permissible load duration t_{max} is thus obtained from the maximum permissible temperature T_{max}, as in Section 7.1.3.6.

The thermal reserves as well as the actual and estimated load capacity of the transformer are calculated using the transformer model. The **cooling system** *can* thus *be controlled* and the data are provided for effective operation and for optimal utilization of the equipment [251], [252].

Note 1: The large mass of the transformer (especially as a result of the oil and iron core) is associated with a very large *thermal capacitance,* which accounts for *thermal time constants* in the hours range for large transformers. This allows **short-term load conditions** which are significantly above the maximum permissable values in the steady-state condition, Figure 6.4.8-1 (right).

Note 2: Transformers, which reach the temperatures mentioned under continuous operation or very frequently, are subjected to **accelerated ageing**. Reducing the load can considerably extend the *lifetime* of the insulation.

Note 3: A heavily *wetted paper insulation* allows only considerably lower **temperature limits**, since outgassing and vaporization take place [251]:

$$T_{HS_{max}} = 166\,°C - 13\,K \cdot \frac{w_{Paper}}{\%} \qquad (6.4.8\text{-}1)$$

For a water content of w = 5 % only about 100°C can therefore be tolerated.

Remark 4: **Bushings** have a considerably lower thermal capacitances and significantly shorter thermal time constants. The overload capacity of a transformer is thus often limited by the bushings. Hence, it is useful to include the bushings in the monitoring, Section 6.4.8.2.

Monitoring the on-load tap changers is an important component of transformer monitoring [297]. Malfunctions can lead to serious damage to windings. The load and number of *switching operations* are recorded for monitoring purposes. Moreover, the time-characteristic of the mechanical *drive torque* can be tracked during a switching process. It is compared with references and limit values to be able to trace the *erosion of switching contacts* [252]. An additional task is the *monitoring of oil* in the switching compartment that is subjected to rapid ageing owing to switching arcs.

New diagnosis methods, such as dielectric methods, electrical and acoustic partial discharge measurements, chemical-analytical sensor technology or the online determination of system-theoretical transfer functions are involved only in the form of *experimental setups* or *conceptual studies* in monitoring systems. Furthermore, there are ideas for extensive **optical monitoring systems** with *optical waveguide sensors* for currents, voltages, temperatures, partial discharges and moisture in the core-and-coil assemblies of transformers [372].

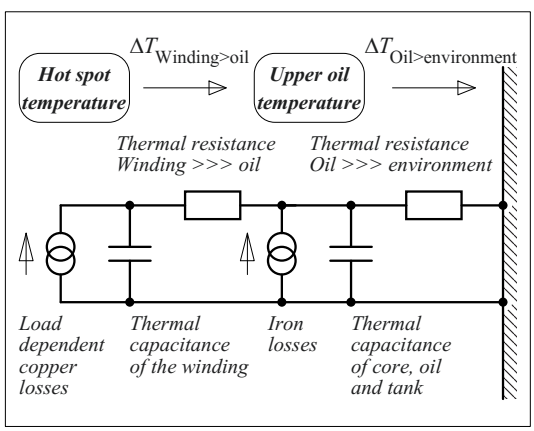

Figure 6.4.8-2: Thermal two-body model for a transformer (according to [251]).

6.4.8.2 Monitoring of Bushings

Owing to their large numbers, bushings are generally not monitored online since this involves high costs which are not proportionate to their comparatively low value.

On the other hand, bushings are the "bottlenecks of energy transport" and thus they are of *great strategic significance* for highly expensive transformers and switchgears. Additionally, they are subjected to *especially high thermal and electrical stresse*s. For example, this can lead to the accelerated ageing of oil-paper insulations in the case of high continuous loads, such as in the machine transformers of power plant units working to full capacity. Moreover, bushing damage is one of the most common causes for transformer failures. The question of bushing monitoring is therefore raised ever more frequently.

Classic monitoring parameters that can be tracked online are *oil level, oil pressure and* various *temperatures*, Figure 6.4.8-3.

For *electrical measurements,* bushings generally have an access to the outermost *grading layer* (to the so-called ground layer) via the *measuring tap*, which is normally connected to ground potential but can also be separated from it for measuring purposes. Usually, the measuring tap is used for **offline diagnosis**, i.e. for the measurement of *capacitance, dissipation factor, insulation resistance, polarization currents* and *depolarization currents.* However, measurements can only be taken during occasional maintenance intervals, rather *at random,* and this is by no means comprehensive. This cannot be called monitoring. This is also due to the fact that a dissipation factor measured at a random *ambient temperature* is in no way meaningful with respect to the often much higher *operating temperatures*. Hence, a reliable diagnostic statement is not even guaranteed. Also for this reason, monitoring under operating conditions would be desirable. The measuring tap is also the specified connection option for this, Figure 6.4.8-3.

Note: A few acutely hazardous situations, such as excessive temperatures or oil losses, can be detected via sensors and can be reported to the monitoring system of the transformer. The temperature of the hot spot can be estimated with the aid of a thermal model [246].

However, it would be highly desirable to be able to observe the **ageing process** already at an early stage by monitoring the dielectric parameters. The *power frequency dissipation factor at operating temperature* is especially considered for this: at increased temperatures, it is indicating ageing and moisture. Moreover, a threat to the insulation from dielectric ohmic heat loss can be immediately detected, so that even short-term, *thermally escalating situations* can be directly measured as shown in Figures 3.5.7 and 5.5.2. Monitoring the dissipation factor under operating temperature would therefore be especially interesting, since the relationship between the thermal-electrical load capacity and the actual load, i.e. the **actual safety marigin** which theoretically cannot be determined, could be read online from this.

Note: During the *dissipation factor measurement*, it must however be considered that also *contamination and wetness* of the *insulator surface* can influence the results.

Partial breakdowns between the grading layers of the bushings can be detected by *increasing the capacitances*. Cyclic monitoring at the frequency of maintenance intervals is not adequate, since partial breakdowns can escalate to total breakdown in a very short time. For this reason, it is recommended to implement online monitoring that is sensitive to capacitance *variations* [245]. Thus, in an extreme case, it might even be feasible to operate the dielectric until failure (i.e. until the first partial breakdown), to have an **alarm** immediately before further, spontaneously caused breakdowns and to initiate automatic emergency measures via the power system protection.

Note: In the case of the old *resin-bonded paper(RBP) bushings*, increases in capacitances can also be caused by *subsequent oil absorption* by incompletely resin-impregnated paper layers. However, these capacitance variations occur continuously and not suddenly or in steps as in the case of partial breakdowns.

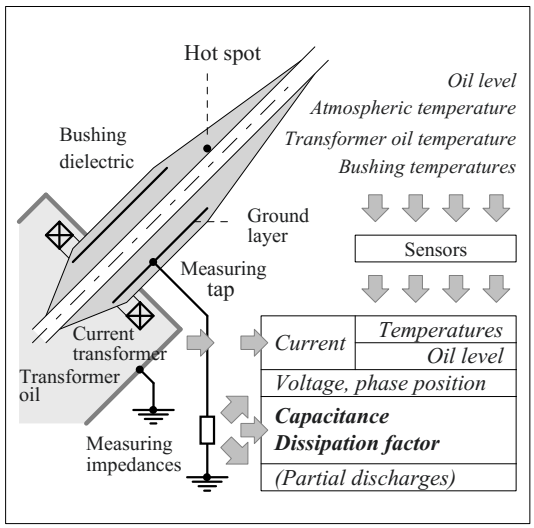

Figure 6.4.8-3: Online monitoring for bushings.

Measuring the current flowing via the measuring tap of the bushing is not sufficient for the **measurement of capacitance and dissipation factor**. The voltage magnitude must be known to be able to determine the *capacitance,* and a **reference measurement arm,** against which the phase displacement can be determined, is necessary to determine *dissipation factor*. These prerequisites are given for an offline-measurement in a bridge circuit or in a dielectric analyzer [204], but not for an online measurement with unknown and varying voltage.

There are three approaches to **online monitoring**:

(1) The bushing along with a low voltage impedance is assembled as a *voltage divider* and its *low voltage impedance* is designed to be *switchable*. Therefore, measurements are undertaken at short intervals with two different dividers (but with the same voltage) and both the unknown C and tan δ are calculated from this. First experiments with *capacitance monitoring* were absolutely successful [245], [252], but the precision achieved so far is not yet adequate for determining the dissipation factor.

(2) It is also feasible to make *comparative measurements* between the *three bushings of a three-phase system*. Small deviations from the standard phase displacements by 120° indicate that ageing does not occur completely synchronously in all phases. Thus only *relative* and not absolute data are obtained from this [247]. Synchronous variations in all three phases cannot be detected. Further, problems occur owing to the isolation of fundamental components and harmonic distortions or asymmetrical loads and voltages. A recommendation for the elimination of temporally scattering network interferences consists of graphically illustrated pattern recognition with the aid of a cloud representation; the changes in the measurement values should be made visible by displacement of the cloud [247].

(3) A new approach consists of obtaining a *reference signal from external sources* that are independent of the bushings to be monitored, e.g. via capacitive probes from the *electric stray field to the three phases* of the three-phase system [431], [432]. The measurement signal recorded at a bushing can be compared with this reference signal. This does not involve absolute determination of the dissipation factor, but monitoring of *dissipation factor variations*: the phase difference between the reference arm and the measurement arm must first be determined as an initial state; ageing-induced variations of the dissipation factor are then indicated by the variation in the phase difference. Dissipation factor variations can be determined with a high accuracy of few parts per thousand, if the signals are digitalized, filtered, compared, statistically evaluated and monitored over long periods [433],[435]. It is also advantageous that individual objects can be monitored independently of each other in both single-phase and three-phase systems.

Basically, the bushing capacitance can also be used for the **outcoupling of partial discharge impulses** via the measuring tap. Onsite measurements at bushings are very problematic since the low signal level of partial discharge sources in the bushing are frequently overlaid by the many times larger interference levels from the environment.

Note: Outcoupling of partial discharges at the measuring tap of bushings are already used today in shielded test laboratories to monitor the entire test circuit. Owing to this, a separate coupling capacitor is unnecessary in some cases.

6.4.8.3 Monitoring of Rotating Machines

Generators and large drives (high voltage machines) are expensive and strategically important equipment, for which a higher expense for diagnosis and monitoring is economically justified.

For **offline diagnosis**, with regard to maintenance intervals, generally the *partial discharge performance* and the *variation in the dissipation factor* $\Delta(\tan \delta)$ as a function of voltage, the *insulation resistance* or other dielectric parameters are considered and are compared with experienced data of the performance of similar generators. Especially for offline diagnosis, the visual inspection (e.g. endoscopy) of crucial machine components is of great significance. However, there is a series of parameters which must be monitored **online** [352]:

Moderate voltages up to few 10 kV and very high currents up to the range of 30 kA especially lead to high thermal loads in large, compactly built turbo generators, and this must be controlled by **temperature monitoring** and active cooling, e.g. with water-cooled conductors. An additional recommendation for the **identification of hot spots** is to chemically analyze the cooling air with respect to thermal reaction products [253].

In large turbo-generators, the **cooling water** must be transported twice over the voltage difference against earth, de-ionized for this purpose and continuously monitored with regard to its *residual conductivity.* In addition, **hydrogen gas** is used as a cooling medium for large turbo-generators, owing to its high heat transfer capability and to lower friction losses in the so-called “air” gap between rotor and stator. Hydrogen gas requires reliable moni-

toring of gas pressure, leakage rates and escaped gas in the environment of the generator. Even the smallest possible quantities must be indicated by gas sensors long before a flammable air-gas mixture can be formed.

The stator insulation system of generators and large motors consists of partial-discharge-resistant mica-based tapes, impregnated with synthetic resin, and of conducting layers on the internal side and external side of the winding elements (rods or coils). Very small cavities within the insulation are unavoidable in production, which leads to non-critical **partial discharges during the operation** of the machine even in new insulation systems.

The dielectric is subject to high thermal and mechanical alternating stresses, see Section 7.1.6. These can lead to detachments, gap formation as well as mechanical loosening, and to increased partial discharge activity as a result. Partial discharge resistant mica plates present in the dielectric are responsible for preventing erosion breakdowns. In this respect, the machine insulation, in contrast to pure organic insulating materials, is quite insensitive, even to high partial discharge levels. **Partial discharge monitoring** therefore, not only has to monitor the risk of partial discharge erosion; variations in the partial discharge performance are also used as an *indicator* of variations in the structure of the generator insulation induced by thermal-mechanical stresses. To a large extent, generator failures are attributed to electrical breakdowns of the stator insulation owing to local mechanical/thermal overstress [257].

A “normal” partial discharge intensity lies in the range of few nC and is thus significantly higher than the intensities from other interference sources connected via the power system. Owing to the resultant *high signal-to-noise ratio*, partial discharge monitoring for generators (e.g. in nuclear power stations) or strategically important drives (e.g. for the oil pumping or water pumping) can be employed for the supervision of normal partial discharge activity.

There are many approaches to the **diagnostic evaluation** of partial discharge signals right from *phase-resolved interpretation* of broadband signals in the classic frequency domain [254] or in the VHF range for a few 10 MHz [255] through to the localization of defects by *comparison of propagation times* in the time domain [256].

Investigations of electrically aged generator rods at 1.6 V_n show that during the course of ageing, the *partial discharge intensity* increases by about one order of magnitude and an ever-increasing *voltage dependence* occurs. Moreover, phase-resolved *partial discharge pattern* vary in a significant manner [257]. Artificial defects at the generator rods (internal defects, damaged semi-conductive layer (corona screens), damaged potential grading on the winding head insulation) show clearly distinguishable partial discharge pattern [258]. Further, it is proposed *to correlate the signals of the three phases with one another* for comparative purposes and for the suppression of interferences [259].

6.4.8.4 Monitoring of XLPE Cables and Fittings

High-voltage cables with XLPE insulation are practically maintenance-free and achieve very long lifetimes if the conductor temperatures remain under 90 °C and the ingress of moisture is prevented. The task of monitoring is above all to monitor these conditions. Moreover, temperature monitoring can show the currently still available load capacity of the cable and thereby contribute significantly to the economical utilization of the cable lines.

Temperature measurements are carried out with *optical waveguides* in the cable sheath into which the laser light impulses are fed. A location-dependent *temperature profile* can be generated from the light that is backscattered owing to temperature gradients. Along with the load current and the cable data, the *remaining load capacity* can be determined with the aid of a mathematical model [264].

Water sensors are likewise integrated into the cable sheath. They consist of wires that are encased by a plastic braiding. The *insulation resistance* between wires an sheath is measured, it decreases with ingressed moisture. *Defect location* is possible by the measurement of the longitudinal resistance of the sensor [264].

XLPE high voltage cables are subjected to a sensitive partial discharge test in the factory, so that **partial discharges** are generally no longer to be expected in the laid cable. Moreover, a classic partial discharge measurement at the cable terminations is often not useful owing to the damping of partial discharge impulses for greater cable lengths.

Despite this, partial discharges can occur in operation owing to assembly faults of **fittings** (cable entrance fittings, cable joints). For an online measurement, the *directional coupler technique* [215] is specifically applied therefore, with measurement points on both sides of the fitting to be checked [265], cf. Sections 6.4.2.5 (Interference-free Measurement) and 6.3.3 (Field Sensors). Of various options for directionally selective measurement of impulses, those directional coupling sensors have proven their worth which consist of two successively placed capacitive measurement surfaces that cover each other and produce different signal magnitudes depending on the *direction of wave propagation*, Figure 6.4.8-4.

By using two directional couplers on both sides of a cable fitting, it can be decided whether the partial discharge source lies between the directional couplers, thus within the fitting to be monitored, or whether the impulses come in from the left side or the right side and thereby must be rated as *external interferences*. Where there are multiple impulse sources, different impulses can be sorted to some extent, i.e. different *locations of origin* can be assigned. Thereby, a high sensitivity of up to about 1 pC can be achieved [265].

Note: Along with the described online monitoring methods, there are also extensive **offline test techniques** for testing the newly laid cable lines or for condition assessment of the aged cable lines. In view of the high cable capacitances, basically the availability of a sufficiently powerful test voltage source is a major problem.

The previously popular *DC voltage test* is today viewed as *meaningless,* especially for XLPE cable insulations which are extremely resistant to DC voltage. Other test methods with *series resonance systems* (variable frequencies up to a few 100 Hz), "*oscillating voltages*" (damped oscillations) or very *low frequencies* (VLF 0.1 Hz sine or cosine-rectangular voltages) manage with low-power sources. Therefore, they can be implemented in mobile test systems. These methods are described in detail in Section 6.2.1 (generation of AC voltages).

The purpose of the tests is to provide proof of withstand test voltage levels and to perform partial discharge measurements as well as dissipation factor measurements.

6.4.8.5 Monitoring Other Equipment

Transformers, generators and cables are expensive and strategically important equipment that is very difficult to repair or is very expensive to repair after an insulation failure. Moreover, they are especially exposed to thermal, electrical and to some extent, even mechanical stresses (in the case of short circuits and for generators), oxidative attacks (by the influx of atmospheric oxygen into oil-paper dielectric in transformers) or the effect of moisture. These conditions are not the same for other equipment. Moreover, for almost all types of equipment there are properties that can be monitored online.

a) Gas-insulated switchgear

In switchgear, the pressure of **SF_6 gas** must be monitored above all else. Loss of pressure leads to loss of *electric strength*, whereby emergency running properties must still exist at ambient pressure in any case, i.e. adequate strengths must remain for the operating voltage. Pressure losses or gas losses must also be avoided because SF_6 as a *"greenhouse gas"* is to be held in closed circuits.

Experimentally, there are also *fiber-optic sensors*, with whose help **partial discharges** are

assigned to individual chambers of an encapsulated switchgear.

Furthermore, it is possible to couple out the *UHF spectrum* of **partial discharge events** via capacitive sensors that can even be fitted as "window sensors"to the windows in the enclosures of old assemblies, e.g. to detect free particles in the system, see Section 6.4.2.8. For online measurement, it is possible to check old systems under operating voltage with mobile test systems at random or in a routine manner [260], [261]. In the case of strategically important systems, many measurement points can be cyclically and continuously monitored with a single analysis system via a multiplexer [260]. External interferences or interferences by switching operations can be identified through simultaneous appearance in all phases.

b) Outdoor switchgear and overhead lines

Also for **overhead lines**, temperature monitoring by optical waveguides in the overhead conductor is feasible. Similar to cables, a *temperature profile* can be recorded and optimal utilization of overhead lines is effected up to the actual thermal limits.

Also (random) monitoring of the **contact points** with the aid of an *infrared camera* is of practical significance *(thermography, thermographic imaging)*. Owing to ageing processes and corrosion, the contact resistance increases, local overheating can occur and the stability of the contact can be lost. With the help of measured temperatures, the contact resistance can be calculated based on a thermal equivalent circuit, and a statement about the remaining service life is made [266].

Some other monitoring procedures, such as the *visualization* of corona discharges on **overhead line fittings** with UV filters (Section 6.4.2.9), are only used for commissioning tests, for random inspections or in substantiated suspicious cases.

For inspecting **composite insulators**, *UV radiation measurements* and measurements with low-light amplifiers are especially considered in order to be able to detect corona discharges or other discharges at the silicone surfaces [267], which can lose their hydrophobicity owing to electrical discharges [9], [57]. Local heating can be identified from the *infrared radiation* [267]. Occasionally, potential distributions are measured by *field sensors* and compared with numerical field calculations to be able to identify uneven potential distributions on insulation strings or field stress enhancements on the sheds or fittings [267].

c) Surge arresters

For monitoring **metal-oxide surge arresters**, the use of *surge counters*, the measurement of *leakage current* with the evaluation of its third harmonic component or its resistive component as well as potential-free *temperature measurement* with *surface wave sensors* (which are scanned by microwaves) are considered [268] along with the visual inspection of surge marks in the *series spark gaps* (which requires sophistcated experience). In view of the high reliability of the arrester and the high costs of monitoring, which generally has to be implemented with unreliable electronics, the usefulness of the mentioned methods is still debatable [268].

d) SF_6 circuit-breaker

For SF_6 circuit-breakers, monitoring is mainly restricted to monitoring the gas pressure and

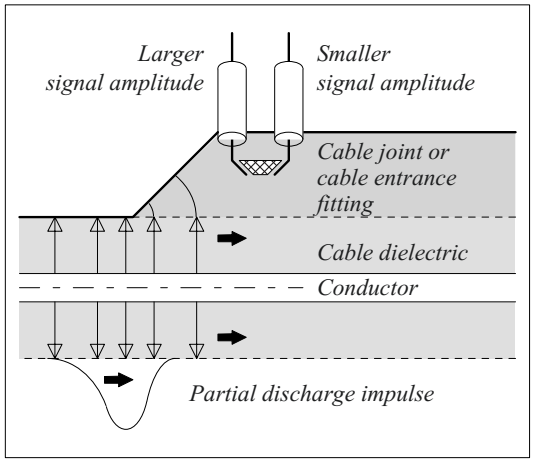

Figure 6.4.8-4: Directional coupler technique.

the hydraulic systems. Further developments are related to measurement and evaluation of *gas parameters* (pressure, mixture ratio and temperatures), *mechanical parameters* (switching speeds, switching paths), *spring drives* or *hydraulic drives* [268]. The objective of monitoring is to be able to change over to condition-based maintenance intervals.

7 APPLICATIONS

After describing the *principles* and the *technologies* of high voltage engineering in the earlier Sections, *typical applications* will also be presented by way of example. The range of probable applications does not allow a complete and thorough overview. However, special monographs are available for most of the topics. Moreover, reference should be made to previous Sections, which have already dealt with many application examples.

7.1 Typical Insulation Systems for AC Voltages

7.1.1 Cables and Accessories

Cables used for transmission of electrical energy must conduct high currents, insulate the respective operating voltages and overvoltages and withstand diverse environmental influences. Now XLPE cables are almost exclusively installed for all voltage levels owing to economical and ecological advantages and to very good operating experience [417]. Owing to the long service life of cable installations, many old types of cables are still being used to a great extent [311].

For example, in the German 110 kV network, there are cable installations with a system length of approximately 4600 km. Until 2002, only about 25% of this was XLPE cable, but about 22% was low-pressure oil-filled cable, about 36% was external gas-pressured cable and about 17% was internal gas-filled cable [311].

With the exception of low voltage cables, the electric field in power cables is confined to the volume of the dielectric by inner and outer semi-conductive layers, the so-called conductor and insulation screens. As a result of this, partial discharges in undefined cavities are eliminated. A nearly *cylindrically symmetric electric field,* which is calculated and optimized according to Section 2.3.1.3, occurs in such a *radial-field cable*....

Note: Owing to a temperature gradient, a conductivity gradient results, which leads to significant *field distortions* and space charges in the case of *DC voltage stress*, as in Figure 2.4-27.

Cables are designed as *single-conductor cables and three-conductor cables* (single-core or three-core cables) with different insulation systems [179], Figure 7.1.1-1a) to g).

A reliable insulation requires a close, cavity-free contact between the conductors and the dielectric. It is guaranteed by *inner and outer semi-conductive layers* acting as *conductor screen* and *insulation screen*. In the case of paper-insulated cables, they are made of graphite paper or copper strips. In polyethylene cables, semi-conductive layers are applied by extrusion of a semi-conductive PE mixture onto the inner conductor and onto the dielectric, which is extruded in the same way (multiple extrusions), as in Figures 7.1.1-2 and 5.3-3. A stranded-conductor *shield* with current carrying capacity, a *bedding layer*, a *diffusion barrier*, an *armour* and a *sheath* are arranged on the outer semi-conductive layer (insulation screen), in order to in ensure protection against mechanical damage, against diffusion of moisture and against oil leakage, all in addition to the electrical function. This can be implemented in different ways depending on the design of the cable.

7.1.1.1 Paper-insulated Cables

The classic cable insulation consists of many layers of *paper strips* (cable paper d= 80 to 130 µm) that are wound helically and staggered against each other, as in Figure 5.5-8. Gaps between adjacent edges of paper are covered by the following paper layers. These gaps allow for the displacement of paper strips when the cable is bent, Figure 5.5-11. Additional layers of the cable structure are wound on the dielectric. After drying, impregnation is carried out with a so-called mass of mineral oil

A. Küchler, *High Voltage Engineering*, VDI-Buch,
DOI 10.1007/978-3-642-11993-4_7

and resins that is viscous at ambient temperature *(paper-insulated mass-impregnated cable)* or with low-viscosity mineral oil *(oil-filled cable)*.

Note: For new productions, these cable designs are replaced by *polymeric cables* of extruded and cross-linked polyethylene, except for few exceptions (cables for high-voltage direct-current transmission), cf. Section 7.1.1.2. However, owing to the long service life of old cable installations, these old designs are still in use.

Mass-impregnated cables have the advantage that the impregnating agent does not leak out at cable joints or as a result of damage. However, temperature changes or load changes create the risk of cavity formation through detachments. Therefore mass-impregnated cables can only be used up to the *medium voltage range*, as in Figure 7.1.1-1 a) and b).

Note: If three conductors are led within a common outer conductor (*belted cable*), *interstices* between the conductor insulations are also stressed electrically, Figure 7.1.1-1 a). Hence, they can only be used up to a voltage level of 10 kV. If three radial-field cables are installed as *three-core cable or triple-sheath cable*, as in Figure 7.1.1-1 b), voltage levels up to 30 kV can be used. In the high voltage range, *thermal stability* is no longer guaranteed.

An *external gas pressure cable* is made of a mass-impregnated cable in which cavity formation is inhibited by an external pressure on a lead sheath. The slightly oval cross-section allows for the necessary deformation. For this purpose, the cable must be conducted within a compression-proof steel pipe (so-called *pipeline compression cable*), Figure 7.1.1-1 c). Through this, protection against the leakage of impregnating agent is also provided. In Germany, usage is up to a voltage level of 110 kV,

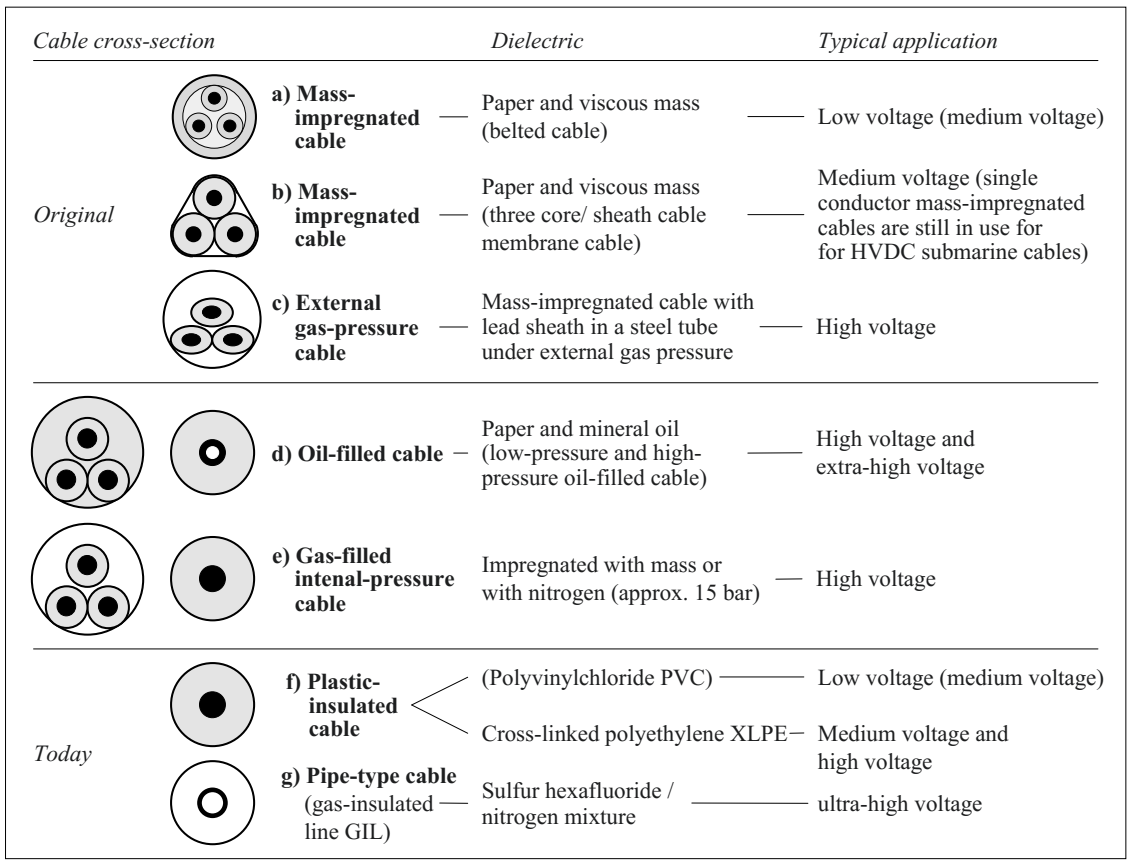

Figure 7.1.1-1: Typical cable cross-sections for different insulation systems (schematic representation). Inner conductors, outer conductors, conductive layers, pipes, binding bands and sheaths are uniformely plotted in bold.

in other countries rarely up to a voltage level of 275 kV.

Note: HVDC submarine cables must be mentioned as an application of *single-conductor mass-impregnated cables* which is still up to date, cf. Section 7.2.5.

In **oil-filled cables**, the paper is impregnated with low-viscosity mineral oil, Figure 7.1.1-1 d). This results in high-quality and thermally stable insulation that is suitable for application up to the extra-high voltage range. In the case of *low-pressure oil-filled cables*, thermal expansion must be compensated by expansion tanks. For this purpose, oil channels for the oil exchange are formed either through hollow conductors (single-conductor cables) or through the interstices between conductor insulations (three-core cables). Up to a voltage level of V_m = 525 kV, *high-pressure oil-filled cables* (oilostatic cables) with pressures of 14 to 16 bar can be used.

Note: Despite their high-quality insulation, oil-filled cables will more and more be replaced by XLPE cables even in the high extra-voltage range, since oil losses pose a risk to the environment, and on the contrary solid dielectric offers advantages also during operation.

The *ageing* of oil-paper insulated cables, both for oil impregnation and mass impregnation, is comparable with the ageing of similar systems in power transformers, measuring transformers or bushings. Ageing mechanisms are, for example, cavity formation, oil ageing, depolymerization or wetting. Hence, corresponding diagnosis methods such as analyses of insulating oil, partial discharge measurements or dielectric measurements are also applied, cf. Section 6.4.7.

In **gas-filled internal-pressure cables**, cavities are impregnated with compressed gas of high electric strength (N_2, approx. 15 bar), Figure 7.1.1-1 e).

7.1.1.2 Plastic-insulated Cables

The first plastic-insulated medium voltage cables were made of **polyvinylchloride (PVC)**. However, owing to high dielectric *losses* in the high voltage range, there is no longer thermal stability, Sections 5.3.2.2 and 3.5.2. Since it is cheap, PVC is used even today in the low voltage range as insulating material and sheathing material.

Currently, the dominant insulating material in all new medium voltage cables and high voltages cables is **cross-linked polyethylene (XLPE),** Section 5.3.2.1. VPE Cables are increasingly replacing and displacing the classic mass-impregnated cables and oil-filled cables and are now qualified up to 500 kV [325], Figure 7.1.1-1 f).

Owing to the solid *dielectric*, no oil systems or compressed-gas systems are necessary and there is no risk of oil loss, gas loss or pressure loss. Furthermore, XLPE has excellent *electric strength* and, owing to low losses, *thermal stability* is very also good. The *low long-term heat resistance*, which amounts to only about 90° C even for cross-linked material, is a disadvantage, Section 5.3.2.1. When laying the cables, special care must therefore be taken to ensure good *heat dissipation* during service operation. Hence it is often recommended not to install multiple cables in bundles.

Medium voltage cables, high voltage cables and extra-high voltage cables are **manufactured** as single-conductor radial-field cables by *multiple extrusion* of inner semi-conductive layer (conductor screen), PE dielectric and outer semi-conductive layer (insulation screen) on the conductor in one manufacturing process (triple extrusion). The quality and the electric strength of cable core depend essentially on the care and cleanliness in this process step, Section 5.3.2.1 with Figure 5.3-3. Multiple extrusion guarantees an intimate connection between semi-conductive layers (screens) and dielectric which was not always achieved for old cable designs. Subsequently, *cross-linking* of polyethylene (PE) to XLPE takes place in the three extruded layers. In the case of the so-called *horizontal method*, the extruded core is drawn with the aid of a lubricating agent through the heated cross-linking pipe, in which peroxides, that were admixed prior to this, cause spatial cross-linking. The use of a hori-

zontal movement enables eccentricities in the core to be largely avoided [325]. Thereafter, semi-conductive tapes, wires, bedding layers, armour and a diffusion barrier are *wound* onto the cable core, Figure 7.1.1-2. The outer sheath is again *extruded* from PE or PVC.

For the **dimensioning** of XLPE cables, quite low *operating field strengths* of around 2 to 4 kV/mm (r.m.s. values) were at first used for medium voltage levels. This resulted in these cables having a strength far above the test requirements. With increasing experience and improving production technology, the operating field strengths for higher voltages were raised further up to 15 kV/mm, in order to be able to specify the diameter of cables at an acceptable level for transport and laying, Figure 7.1.1-3.

Note: This approach contradicts the high voltage engineering law of enlargement (*statistical size effect*), according to which larger insulations have a lower strength, Section 3.1.3. However, this is possible because the *strength reserves of the XLPE material* have not been exploited by far at low voltage levels, cf. Section 5.3.2.1.

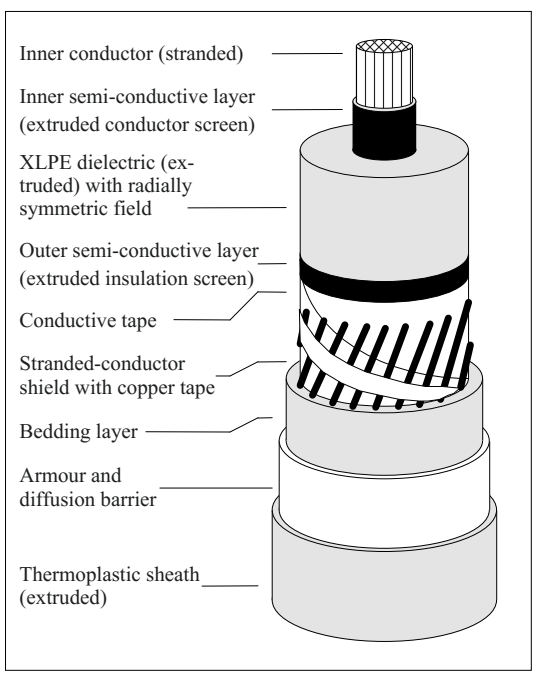

Figure 7.1.1-2: Design of a single-conductor XLPE high voltage cable (schematic representation).

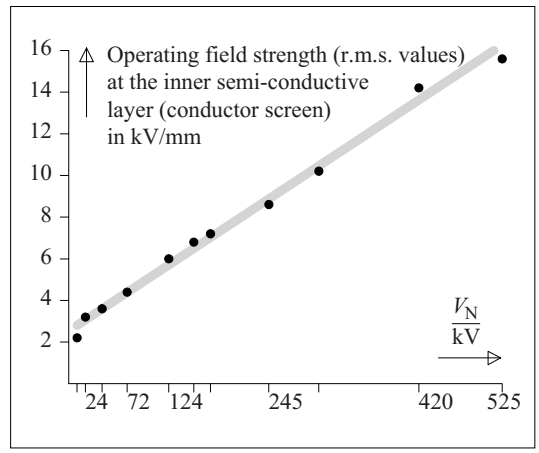

Figure 7.1.1-3: Typical operating field strengths in XLPE cables [312].

Electrical *weak points* occur especially due to faults during assembly of *cable accessories* and rarely in the cable dielectric itself.

The **ageing** *of XLPE dielectric* must not be compared with that of oil-paper insulations: there is neither thermal ageing nor cavity formation. However, there is a certain amount of *sensitivity to moisture ingress,* which has caused problems with the first XLPE cable designs: under the effect of the electric field, in the presence of moisture and owing to electrochemical processes, small tree-like structures, so-called *"water trees",* are formed which increase the local field owing to the high permittivity of water and grow in the direction of the field. Although they form an obvious sign of cable ageing, they can only be the cause of instantaneous hazard when fine discharge channels, so-called *"electrical trees"*, develop from them. The length of "water trees" is considered an ageing indicator, since it has a (weak) relationship with the residual strength of the insulation [311]. However, a section of cable has to be cut out for determining the water tree lengths. Furthermore, IRC analysishas been found to be a method that allows a statement about the overall ageing condition of the cable, Section 6.4.7.4.

By the modification of materials, construction and production processes, the *sensitivity to*

"water trees" is reduced to such an extent that even in the presence of free water, a service life of 40 to 50 years is expected. Therefore, further measures are often omitted for medium voltage cables [311].

High voltage cables and, to some extent, also medium voltage cables are designed to be *longitudinally watertight*, by embedding a swelling tape or swelling powder (water blocking powder) in the **sheath**. High voltage cables generally have a *laterally watertight* design in the form of a diffusion resistant metallic sheathing. The most insensitive covering is the *corrugated aluminum sheath*, furthermore *lead casings* and, as a lighter alternative, even an *aluminum-composite layer sheath* of a laminate of aluminum foil with a PE sheath have been proven of value.

The designs so far are related to fixed cables to be laid for power transmission and power distribution. In the industrial application, however, there is also a large demand for **flexible cables**, which, for instance, must supply large drives with medium voltage in sometimes very rough environments. *Flexible insulating materials*, e.g. *silicone elastomer,* are used for the flexible cables, cf. Section 5.3.3.5. Conductors are manufactured by *stranding* of many individual wires and this requires special expertise, so that alternating mechanical stresses (e.g. during regular coiling and uncoiling) can be borne without damage.

7.1.1.3 Gas-insulated Lines (GIL)

The technology of metal-enclosed tubular conductors, which is known from gas-insulated switchgear, can also be used in **gas-insulated lines (GIL)** and **pipe-type cables** for power transmission over longer distances, Figure 7.1.1-1 g). The GIL combines the advantages of cables and overhead lines [313]: similarly to a cable, the system is *enclosed* and *shielded*, but permittivity and *capacitance* are lower. Moreover, the dielectric *cannot age*, it cannot be *thermally overloaded* and it is *self-healing*. New and highly advantageous properties are very low *magnetic field strengths* outside of the line (even in comparison with cables). Additionally, the GIL doesn't pose any danger to the *environment,* even for very high short circuit currents [314].

Examples of use are the replacement of *cables*, e.g. for reducing the *fire hazard* in tunnels, especially also in publicly accessible areas, replacement of *overhead lines*, e.g. owing to space requirements or for aesthetic reasons, as well as *reducing the magnetic field strengths* in the environment of power transmission routes.

In a first generation, a length of over 100 km was installed and experience of about 30 years was obtained. A *new generation* is distinguished by improvements, especially by introducing a N_2/SF_6 gas mixture, by elastic connections of aluminum pipes, by using standardized modules, by automatic welding, by direct installation in the ground with the help of pipeline installing methods and by increasing the rate of installation. Through this, distinct reductions in cost can be achieved, which make the GIL an economical alternative in the case of *high power levels* above approximately 1000 MVA.

Similarly to gas-insulated switchgear, an *on-site test* with mobile resonance systems (possibly as segmented testing) is necessary for the GIL after assembly to detect assembly faults. UHF diagnosis is recommended for *partial discharge measurements* [313], Section 6.4.2.8.

7.1.1.4 Cable Accessories (Cable Fittings)

The end of a cable with uncovered and bare conductor insulation according to Figure 7.1.1-2 represents a *creepage configuration* with an extremely low partial discharge inception voltage, cf. Sections 2.4.5 and 3.2.6 with Figure 3.2-35. It is therefore necessary to provide for a field grading at the *edge of the outer conductor* and for increasing the dielectric strength in the environment of the bare cable

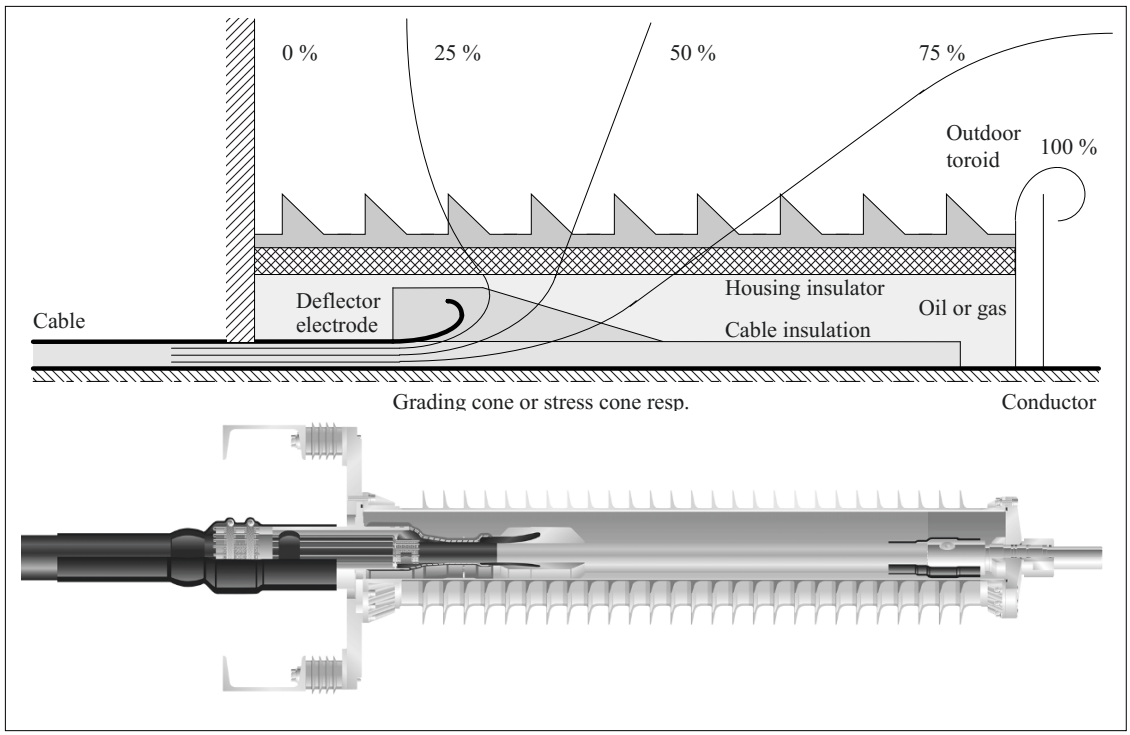

Figure 7.1.1-4: Cable termination with grading cone (stress cone) and housing insulator. Top: Diagram with equipotential lines. Bottom: Sectional view, 145 kV termination, photo Tyco Electronics now TE Connectivity.

insulation [180], [464]. There are different technologies available for this (geometrical, capacitive, refractive, resistive and non-linear field grading or potential grading, respectively) and these are explained in Section 2.4.5. In particular, geometrical field grading is applied for cable accessories. However, there are also solutions for the medium voltage range using refractive, resistive and non-linear grading.

Note: *Resistive grading* is especially proposed for the new *HVDC cable fittings* in order to handle the migration of electric fields at DC stress owing to temperature variations and related conductivity variations [496], Section 7.2.5.5.

The field grading media can be applied in the form of tubes, tapes, elastomer bodies or layers, for example, using the slip-on technique, the hot-shrinking technique, the cold-shrinking technique and the winding technique. A few examples are considered in the following sections.

a) Cable terminations (cable entrance fittings)

An **outdoor cable termination** for a high voltage XLPE cable shall be considered as an example, Figure 7.1.1-4. A *grading cone* (or *stress cone* respectively) of ethylene-propylene elastomer (EPR ethylene-propylene rubber) or silicone elastomer (SIR silicone rubber) with integrated conductive *deflector electrode* is placed on the bare *cable insulation* and contacted with the outer *semi-conductive layer (insulation screen)* of the cable; cf. also Figure 5.3-21. Assembly is analogous to the assembly of cable joints by the slip-on technique or the cold-shrinking technique, Section 7.1.1.4b).

At least for the high voltage levels, the grading cone or stress cone is situated in a *housing insulator* (porcelain insulator or composite insulator made of glass-fiber-reinforced plastic tube and silicone sheds) containing a highly insulating medium (e.g. oil, oil-type filling mass, SF_6-gas). The equipotential lines are widened by the grading contour of the deflec-

tor electrode in such a way that in the outside space and in the *interface* between cable and stress cone, lower tangential field strengths result that can be handled. The stress cone must fill that space in which the field strength would be too high for the surrounding insulating medium. The diameter of the *housing insulator* is to be designed large enough, so that unacceptable field strengths do not occur in the adjoining atmosphere. Generally, optimization is by field calculation.

A steady *contact pressure* through radial extension of the *permanently elastic* stress cone is necessary for increasing the strength of the *interface* between the stress cone and the cable insulation. The inside diameter of the stress cone is smaller than the outside diameter of the uncovered cable insulation. The quality of the *tight push fit* and the operational reliability of the cable are largely dependent on the *care* taken during assembly.

The conductive deflector must also be connected at the earth potential of the outer semi-conductive layer (insulation screen) with great care, i.e. without cavities forming against the cable insulation, e.g. by means of semi-conductive tapes and through a press fit on the outer semi-conductive layer of the cable.

For XLPE medium-voltage cables, one-piece *slip-on cable terminations* (or *cable entrance fittings* respectively) made of silicone elastomer with integrated deflector and outdoor shed profile are provided, Figure 7.1.1-5 (top left). Even for XLPE high-voltage cables and XLPE extra-high-voltage cables, elastic slip-on stress cones are used and the traditional winding technique is replaced. The slip-on elements can be manufactured in the factory under optimal conditions and pre-checked; and they can be assembled relatively easily, thus increasing the reliability of the cable terminations.

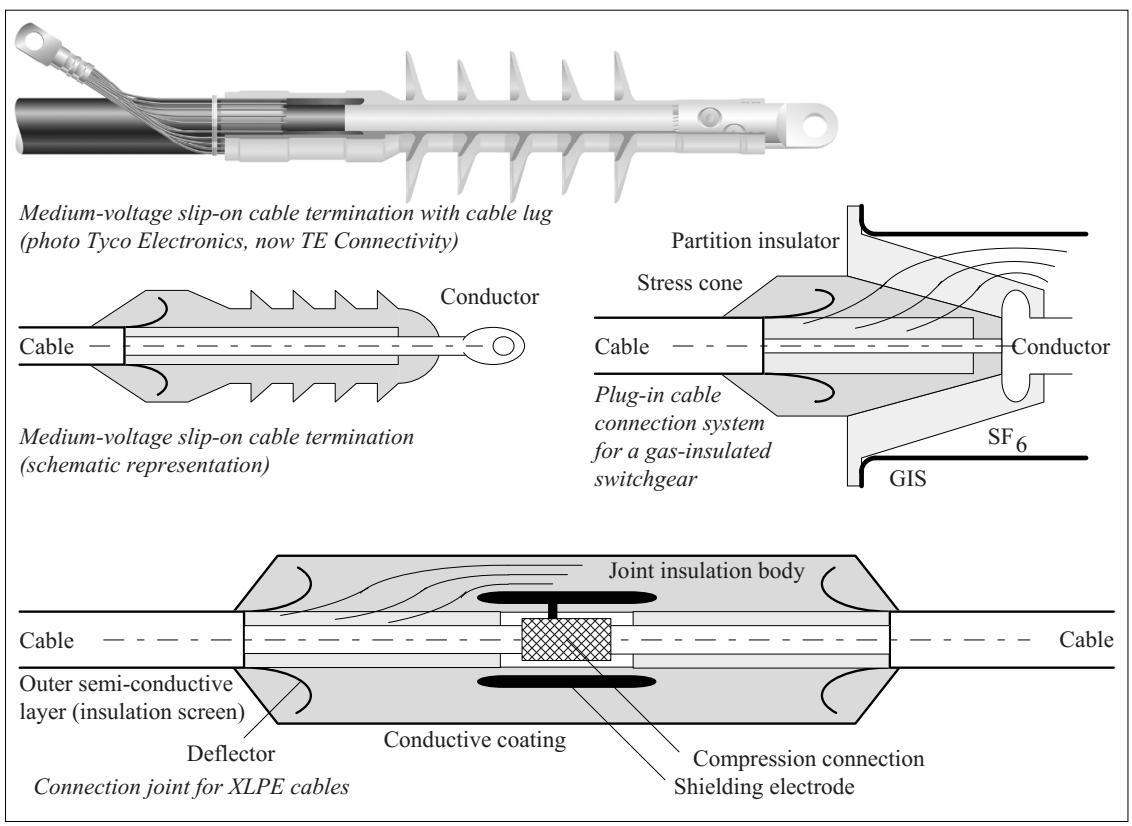

Figure 7.1.1-5: Examples of cable accessories.

Figure 7.1.1-6: Permanent elastic connecting joint of silicone elastomer for XLPE medium voltage cables. Top: Joint body with conductive deflectors for geometric field grading (left and right, earth potential) and with "Faraday cage" for covering the metallic through connector (center, high voltage potential). Bottom: Joint mounted according to cold-shrinking technique, cf. Figure 7.1.1-7. The sheath is connected on both sides by coil springs, the outermost layer is formed by the external tube. Photos Tyco Electronics, now TE Connectivity.

Note: In the case of *paper cables*, which are used less and less frequently, the stress cone is coiled from insulation paper and it is impregnated with oil to be free of cavities. A funnel-shaped metallic cone that is pressed against the stress cone is used as a *deflector*. Alternatively, field grading can also be carried out with metallic foils, i.e. with *capacitive grading layers* in the stress cone (grading cone). The insulator diameter can be reduced in this way, cf. Section 7.1.2.

Note: For cable tests, special **cable test terminations** with resistive potential grading using *water* are used, Section 7.1.1.5.

In **plug-in cable connector systems,** e.g. for *transformers* or for *gas-insulated switchgear*, the elastic stress cone completely fills the partition insulator [181], [182]. This leads to another highly stressed interface. The field distributions results from the deflector geometry and electrode geometry, Figure 7.1.1-5 (top right). Filling the joints with oil is necessary above V_m = 145 kV.

b) Cable joints

Cable joints are used for connecting two cable sections. In the case of XLPE cables, prefabricated *slip-on joints* of EPR or silicone elastomer can now be used up to the highest voltages, Figure 7.1.1-5 (bottom). Along with the assembly of the joints by *slipping on*, it is possible to assemble pre-stretched joints (*cold-shrinking technique*), Figures 7.1.1-6 and -7, or shrinkable joints (*hot-shrinking technique*), Section 5.3.3.4.

Two deflectors and a shielding electrode of conductive elastomer are cast in the joint body. The shielding electrode ("Faraday-cage") covers the junction of the two conductors. The earth potential of the outer semi-conductive layers (insulation screen) on the cable continues into a conductive coating of the joint insulation body. There is a highly stressed *interface* between the joint insulation and the cable insulation, which must be carefully executed. The explanations given for slip-on terminations (lubricant, press fit, and freedom from cavities) are valid analogously. For assembly, the joint must first be completely pushed over one of the cables. After establishing the conductor connection, the joint is pulled back into its final position [180]. Two methods are specially considered for the assembly:

1. In a **slip-on termination**, the grading cone is pushed with the aid of a lubricating paste and radially stretched with the build-up of mechanical stress. The *press fit* created in this way ensures an interface contact that is free of partial discharges, wherein cavities in the interface are filled by the *lubricating paste* used for sliding.

2. During the so-called **cold-shrinking technique**, the permanent elastic elastomer body is initially stretched on a spiral and stored in this state. During the assembly, the expanded body is applied over the cable insulation and is let

onto the surface by removing the assembly spiral, Figure 7.1.1-7, cf. Section 5.3.3.5. For this, a certain amount of extension must remain to guarantee the press fit.

Note: The traditional *taped joints* are manufactured on-site from self-bonding EPR tapes with a winding machine. They are used for up to 220 kV.

Note: In the case of *paper insulated cables*, the joint insulation is wound from insulation paper and impregnated with oil. Metallic funnels are used as deflectors.

7.1.1.5 Testing Cable Systems

Test voltages for cable systems and its components are related to the

R.m.s. value of line-to-ground voltage V_0

with which the cable dielectric is stressed in operation, Table 7.1.1-1.

Tests for **individual cables and accessories** include (also similar to other operating equipments) *development tests, type tests, selection tests* and *routine tests*. After these tests, however, additional processing steps which have a definitive influence on the quality of the insulation are necessary: While *installing the cables*, large mechanical stresses occur which can lead to damage. The subsequent *assembly of accessories* requires manual operations on the insulation system itself, so that even with all the necessary care, a certain amount of error risk cannot be completely ruled out. For this reason, additional tests must be undertaken for the **already laid and assembled cable system**. This includes the *system type test, long term test, qualification test* and *on-site test*.

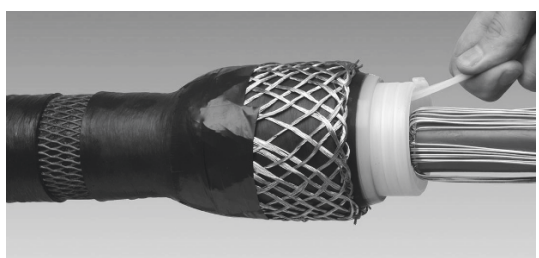

Figure 7.1.1-7: Assembly of a permanent elastic joint by cold-shrinking technique: Joint (including outer tube) that is pre-stretched and present on a spiral is arranged over the connecting point and is lowered by pulling out the spiral (left to right in the image), Figure 7.1.1-6 shows a section after the assembly. Photo Tyco Electronics, now TE Connectivity.

New cable systems, e.g. for development of new voltage levels, must be subjected to extensive **qualification tests**, and indeed *as a system*, i.e. with cables, joints and terminations [326].

Pre-qualification tests for a *400 kV XLPE cable section,* with which the operating stress of 35 years should be simulated, are mentioned as an *example* [327]:

Test voltage:	400 kV (1.7 times rated voltage)
Conductor temperature:	90 to 95 °C
Load cycles:	Heating cycles 12h/36 h
Test duration:	8760 h (one year)

Lightning impulse voltage test and switching impulse voltage test after completion of the tests (1175 and 950 kV resp.)

An additional qualification test with enhanced requirements was carried out for the *joints* with 100m long cable units:

PD measurement:	1.7 V_0 = 400 kV, q < 5 pC
Long-duration test:	2 V_0 = 460 kV, 30 days Heat cycling test 8/16 h, 90-95 °C, temperature monitoring and PD monitoring
Lightning impulse voltage:	1425 kV, 10-times pos, 10-times neg.
PD measurement:	1.7 V_0 = 400 kV, q < 5 pC
Long duration test:	1.7 V_0 = 400 kV, 4 days

The routine test of individual components and the **on-site test** for *verifying the operational readiness* of his individual cable system are of maximum significance for the operator, Table 7.1.1-1.

a) Routine test

High voltage cables are tested in their complete manufactured length **in the factory**, in order to verify the *freedom from cavities* of the

Table 7.1.1-1: Voltage tests for cables and cable systems [356].

	Routine tests (for cables)			**On-site tests** (for cable systems)		
Standard	*Frequency*	*Voltage*	*PD*	*Frequency*	*Voltage*	*PD*
1 kV < *U* < 40 kV						
DIN VDE 0276-620	49 - 61 Hz	3.5 Vo/ 5 min	2.0 Vo/ 2 pC	45 - 65 Hz **0.1 Hz**	2.0 Vo/ 60 min 3.0 Vo/ 60 min	--- ---
IEC 60502	49 - 61 Hz	3.5 Vo/ 5 min	1.73 Vo/ 10 pC	49 - 61 Hz 49 - 61 Hz **DC**	1.73 Vo/ 5 min Vo/ 24 h 4.0 Vo/ 15 min	--- --- ---
40 kV < *U* < 150 kV						
IEC 60840	49 - 61 Hz	2.5 Vo/ 30 min	1.5 Vo/ no detectable PD	49 - 61 Hz **20 - 300 Hz**	Vo/ 24 h 1.73 - 2 Vo/ 1 h	--- ---
Obsolate:	49 - 61 Hz		1.5 Uo/ 10 pC	49 - 61 Hz **DC**	1.73 Vo/ 5 min 3.0 Vo/ 15 min	--- ---
150 kV < *U* < 500 kV						
IEC 62067	49 - 61 Hz	2.5 Vo/ 30 min 2.0 Vo/ 60 min	1.5 Vo/ 10 pC	49 - 61 Hz **20 - 300 Hz**	Vo/ 24 h 1.1 - 1.7 Vo/ 1 h	--- ---

cable by partial discharge measurement at AC voltage in the context of the **routine test**. This gives rise to two problems: on the one hand, very high *capacitive charging currents* must be supplied, and this is possible with appropriate powerful test transformers or series resonance test systems, Section 6.2.1.5. On the other hand, very high voltages must be applied and this requires special *test terminations*, Figure 6.2.1-7. They consist of an insulation housing, in which the cable with bare insulation projects over a very long length. The gap between housing and insulation is filled with *water*, which effects a *resistive potential grading* through the axial conduction current.

XLPE cable must be practically *free of partial discharges* owing to the sensitive dielectric. The PD intensities mentioned in Table 7.1.1-1, therefore, must not be considered as tolerable PD levels, but rather as a practicable specification with regard to realizable measuring sensitivities and the background noise level. New specifications stipulate *"no identifiable discharges from the test object"* [356].

b) On-site test

Weak points of cable systems generally do not lie in the cable insulation but in the *joints* and *terminations* with their interfaces. In addition to the manufacturer's tests of the components, **on-site testing** of *assembled cable systems* is necessary for verifying operational readiness, Section 6.2.1.6.

Testing longer cable lengths with power frequency is very difficult owing to high capacitive charging currents. Therefore, for paper-insulated cables, a *DC voltage test* was originally initiated, in which even very long cable lengths could be tested with comparatively compact systems. However, XLPE cables exhibit a very poor sensitivity to damage of the dielectric, so that even incisions in the dielectric or nails driven into it were not detected in the DC voltage tests. Very high DC voltage levels can furthermore induce preliminary damage to the dielectric. DC voltage tests, therefore, are only applied to check the intactness of the external *cable sheathing*.

Note: Owing to the very low conductivity of XLPE, *space charges* or *surface charges* can build up during a DC voltage test, which can be discharged only very slowly and can even present a risk for the electric strength of the insulation.

Considerably better reproduction of the real operating stresses is provided by **AC voltage tests**. In practice, tests with *low frequency voltages* of 0.1 Hz (sinusoidal or cosinusoidal-rectangular) with *damped AC voltages* (oscillating voltages) or with *AC voltages close to power frequency* (f = 20 to 300 Hz) are carried out, Section 6.2.1.6, Table 6.2.1-2, Figure 6.2.1-10. The relevant test technique is described in Section 6.2.1.5.

Partial discharge measurements would be desirable also for on-site tests. However, owing to the usual interference levels, they can be executed only in special cases and then only with difficulty. Therefore, there are no relevant specifications for this, Table 7.1.1-1 (right). Despite this, PD measurements can be used, for example, for verifying the assembly quality of cable accessories: with the help of the *directional coupler technique* described in Section 6.4.2.5, it is possible to differentiate whether a PD impulse has occurred in the joint or outside using two sensors on both the sides of a cable joint.

After long-term operation, dielectric **diagnosis measurements** on *installed cables* can give indications of the ageing (in paper cables) or water-tree damages (in XLPE cables). In the case of a breakdown, a **defect can be localized** via the propagation time difference between an electrical signal and an acoustic ground-borne sound signal.

7.1.2 Bushings

Leading a conductor through an opening in a grounded wall ("bushing") presents a creepage configuration with low partial discharge inception voltages, Figure 3.2-35 and -36. Bushings must increase the strength to such an extent and the field distribution must be homogenized to such an extent that test stresses and operating stresses are withstood. That is, for walls, substations, transformers and generators, bushings fulfill the same function as cable terminations for cables.

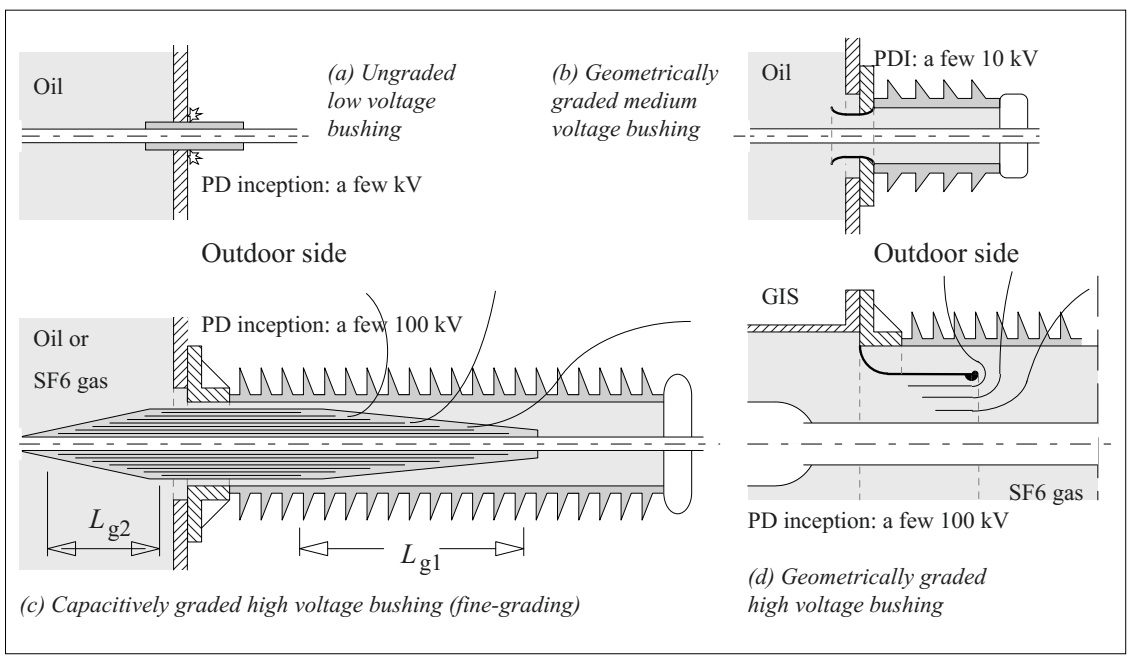

Figure 7.1.2-1: Ungraded and graded bushings with typical orders of magnitude of partial discharge inception (PDI).

7.1.2.1 Field Grading or Potential Grading

Ungraded bushings are suitable only for low voltages of a few kV owing to the discharges at the edges on the wall side, Figure 7.1.2-1(a). In the medium voltage range, e.g. in distribution transformers, economical *hollow porcelain bushings* are used, Figure 7.1.2-1(b). Owing to its *oil filling,* about ten times higher electric strength results in the area of ground-side edges. Up to the voltage level of 123 kV, bushings can be implemented with acceptable diameters by rounding of edges, formation of double-sided *deflector geometry* (on both sides) and coatings of conductor and grading electrode.

However, high voltage bushings generally have a **capacitive field grading**, since this allows the diameter to be kept small, Figure 7.1.2-1 (c). On the cylindrical, longitudinally graded *conductive grading layers*, a potential distribution results, which is determined by the mutual capacitances [183]. For this, the aim is uniform potential grading along both the grading lengths L_{g1} and L_{g2}.

The potentials of the grading layers even influence the *field distribution* outside the bushing core and homogenize the field distribution at the surface of the housing insulator and in the adjoining media respectively. Under this, it can be imagined that the grading layers pass on to the corresponding equipotential surfaces, cf. also Figure 1-1. It has been approved that the grading length L_{s1} should be chosen to be about half the length of the flashover distance and must be placed somewhere in the center.

Note 1: In the case of a bushing between two media with different electric strengths, both the *grading lengths* can be different such as between oil and air or SF_6 and air. Wall bushings (air-air) or oil-gas bushings respectively have two comparably long grading lengths.

Note 2: It has been approved that the grading must be designed to be finely graded as a so-called **fine grading** with radial distances of approximately 1 to 3 mm. For this, metallic foils are wound along with an insulating medium (paper, crepe paper, film) which must be made suitable for high voltages by drying and impregnation. This leads to a favorable relationship between the *creepage discharge inception voltage* at the grading-layer edges and the actual applied voltage, cf. Section 3.2.6. Since *the highest local field strengths* appear at the **grading-layer edges**, these should be embedded in an *electrically strong medium* and should not emerge un-insulated at the surface of the core.

Fine-grading and high voltage resistant embedding of the grading-layer edges are measures which guarantee the insulation function even for high *lightning impulse voltage stresses.*

If the grading is designed as a **coarse grading** with only a few cylindrical grading electrodes, considerably higher edge field strengths occur at the grading-layer edges. Possibly, other designs of self-supporting grading electrodes with rounded edges are selected in these cases. Owing to this, the overall larger insulation diameters are obtained.

Similar to cable terminations according to Figure 7.1.1-4, also **geometrically graded bushings** can be implemented up to the high voltage range, Figure 7.1.2-1 (d). In order to limit the field strengths at the insulator surfaces, at the conductor and at the electrode to the respective permissible values, a grading electrode is necessary, which is arranged at an adequate distance above the conductor and under the insulator and has a sufficiently large rounding. Owing to this, much larger diameters are obtained for the bushing insulator than for a comparable capacitively graded bushing, cf. Figure 7.1.2-1 (d), (c).

Other grading methods, based on materials of increased conductivity (**resistive field grading**) or increased permittivity (**refractive grading**), can be generally applied also for bushings, but have not yet been widely spread.

7.1.2.2 Calculation of Capacitive Grading

For the calculation of a capacitive field grading, for **undivided end-to-end grading layers**, the two grading lengths L_{g1} and L_{g2} are integrated into one resultant grading length L_g, Figure 7.1.2-2 (top):

$$L_g = L_{g1} + L_{g2} \qquad (7.1.2\text{-}1)$$

The following is applicable to *axial and radial field strengths*

$$E_{ax} = -\Delta V/\Delta x \qquad (7.1.2\text{-}2)$$

and

$$E_{rad} = \Delta V/\Delta r. \qquad (7.1.2\text{-}3)$$

Assuming a capacitive voltage division, the partial voltage ΔV is calculated from the total voltage V, the total capacitance C and the partial capacitance $\Delta C = (\varepsilon \cdot 2\,\pi r \cdot x)/\,\Delta r$:

$$\Delta V = V \cdot C/\Delta C = V \cdot C \cdot \Delta r/(\varepsilon \cdot 2\pi r \cdot x) \qquad (7.1.2\text{-}4)$$

In this, $2\pi r$ and x are the circumference and the length respectively of the cylindrical layer under consideration. By a transition to infinitesimal sections $\Delta x \rightarrow \mathrm{d}x$ and $\Delta r \rightarrow \mathrm{d}r$, *differential equations* are obtained from Eqs. (7.1.2-2) and (-3) with Eq. (7.1.2-4). They determine the profile of the grading contour [22]:

$$E_{ax}(r,x) = -V \cdot \frac{C}{2\pi\varepsilon} \cdot \frac{1}{x \cdot r} \cdot \frac{\mathrm{d}r}{\mathrm{d}x} \qquad (7.1.2\text{-}5)$$

$$E_{rad}(r,x) = V \cdot \frac{C}{2\pi\varepsilon} \cdot \frac{1}{x \cdot r} \qquad (7.1.2\text{-}6)$$

Note: The simplest solution is obtained under the assumption of constant *radial field strength in the dielectric* according to Eq. (7.1.2-6). According to $x \sim 1/r$, the length of the grading layers is shortend hyperbolically with the radius. According to Eq. (7.1.2-5), the axial field strength is dependent on x and r in this case. That is, a *non-linear voltage distribution along the surface* results, which adversely affects the voltage distribution at the housing insulator surface. Since the electric strength along the surface is generally considerably lower than that within the insulation body, a solution for which the *field strength at the surface remains constant* is mostly sought. A certain amount of non-uniformity of radial field strength in the insulation body must then be accepted and taken into consideration during dimensioning.

For a *linear axial voltage distribution at the surface*, Eq. (7.1.2-5) must be solved under the condition $E_{ax}(r,x) = V/L_g$ = constant. After isolating the variables x and r, integration from the *external ground layer* (x_n, r_n) up to any grading layer (x, r) gives the conditional equation for the grading layer length x:

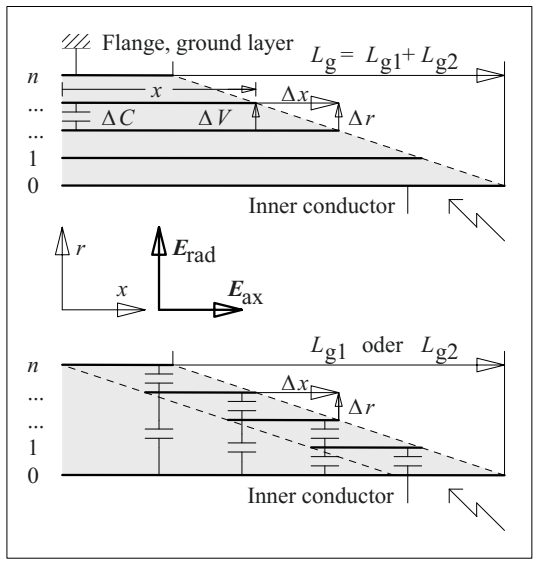

Figure 7.1.2-2: Capacitive grading in a bushing core, both as an overall grading (top) and as a boundary-area grading (bottom).

$$x_n^2 - x^2 = -L_s \cdot \frac{C}{\pi\varepsilon} \cdot \ln\frac{r_n}{r} \qquad (7.1.2\text{-}7)$$

The overall capacitance C is considered here as constant parameter and is determined by applying the *geometrical boundary conditions* $x = x_0$ and $r = r_0$. After elimination of C, the grading layer length x is calculated:

$$x = \sqrt{x_n^2 + (x_0^2 - x_n^2)\,\frac{\ln(r_n/r)}{\ln(r_n/r_0)}} \qquad (7.1.2\text{-}8)$$

Note: Another approach for solving differential equations (7.1.2-5) and (-6) is the specification that the ratio of $E_{rad}/E_{ax} = a$ shall remain constant. This gives a declining linear relationship between r and x that is $x = b - a \cdot r$. The quantity b can be determined by the definition of boundary conditions for $x = x_0$ and $r = r_0$. However, the field strengths are constant neither in the axial nor in the radial direction.

When calculating **unilateral boundary-area gradings**, non-negligible stray capacitances to the inner conductor (and probably even to the outer conductor) must also be considered along with the partial capacitances between the grading layers, Figure 7.1.2-2 (bottom). This results in a *lattice network* of *longitudinal capacitances* and *parallel capacitances.* The magnitude of the parallel capacitances can

only be estimated from the geometrical data. Exact values require knowledge of the *field distribution*.

Increased currents flow through the outer partial capacitances and cause increased voltage drops and a *non-linear voltage distribution* at the surface. A linear voltage distribution is achieved when the outer capacitances are increased by extending the length of the layers or by displacement of the position of the layers into internal areas of the bushing core.

Note: The *dimensioning* of the grading can be performed, for example, iteratively [26]: for given constant edge distances Δx and insulation thicknesses Δr, the potential differences ΔV are calculated for a *given initial condition,* taking the lattice network structure into consideration. Depending on the deviation from the mean value V/n, the overlapping lengths of the layers are changed. Any further iteration step consists of a recalculation of potential differences with subsequent *correction of the overlapping lengths*.

Note: the *edges of the conductive grading layers* shall not come up to the surface of the insulation body neither for the boundary-area grading nor for the overall grading. Bare electrodes reduce the electric strength in the adjoining gas gaps or oil gaps, cf. Figure 3.4.2.6. Moreover, the maximum field strength occurs at the edges, so that this area should be appropriately embedded in a *medium of high electric strength*.

7.1.2.3 Designs

Capacitively graded bushings are manufactured in various designs depending on the purpose of the application, Figure 7.1.2-3. *Flashover distances* and *creepage path lengths* result from the respective ambient conditions, cf. Section 3.2.6.4 and Figure 3.2-38. Significantly shorter lengths are adequate under oil and compressed gas. *Diameters* are determined from the permissible stress of the dielectric in the bushing core. Standard operating field strengths lie between 2 and 4 kV/mm for high-quality large-volume insulations, cf. Section 3.5.3 with Figure 3.5-5 and Table 3.5-2.

The classic bushing insulation is made of **oil-impregnated paper (OIP)**. The bushing core is formed by winding of paper web material, in which metallic foils are inserted as grading layers after a specific radius increase in the mm range, Figure 5.5-9. After heating up the

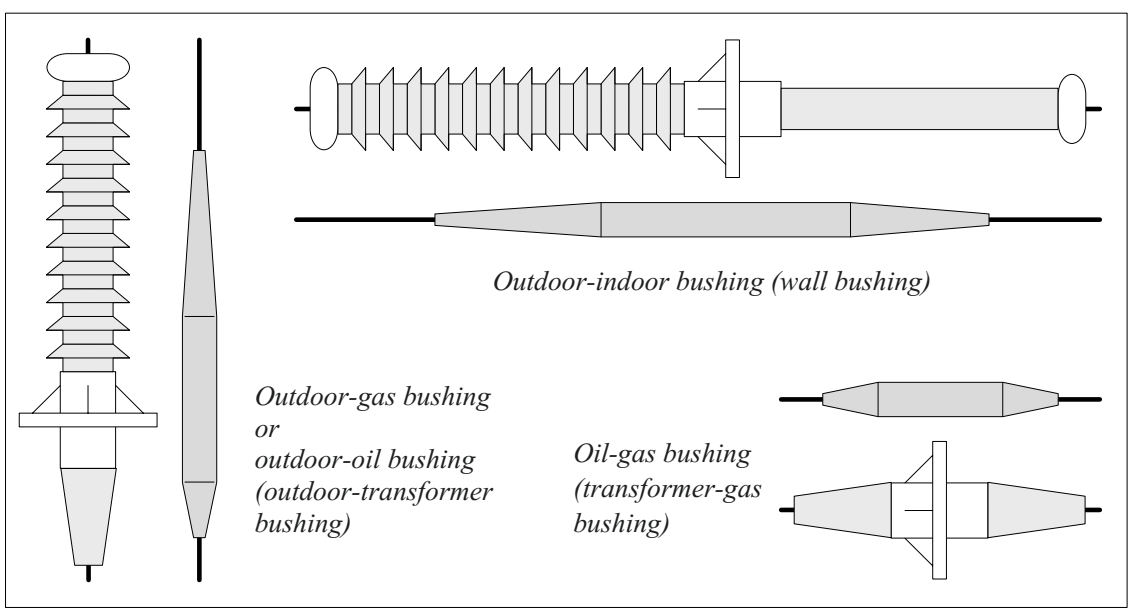

Figure 7.1.2-3: Comparison of capacitively graded high voltage bushings of the same voltage level for different applications with the appropriate bushing cores (i.e. insulating bodies). Grading contours are under the cones.

winding and drying under vacuum and temperature, impregnation can be carried out under vacuum with dried and degassed oil, cf. Section 5.5.1.4 with Figure 5.5-13.

Note: Analogously to the so-called "*hard-paper winding"* (resin-bonded paper winding), the oil-impregnated paper winding is also referred to as "*soft-paper*".

Subsequently, the impregnated winding or core respectively is assembled in a *bushing housing* consisting of a flange, housing insulators and top fittings. The evacuated housing is finally filled with oil. These economical oil-impregnated bushings are preferred for use in transformer manufacturing. The comparatively small quantity of oil in the bushings is not a big issue for an oil-filled transformer.

In the past, oil-free ("dry") bushing cores made of **resin-bonded paper (RBP)** or *hard paper* respectively were wound from *phenolic resin-impregnated paper* and hot-cured. Thereby, the paper layers are bonded, but the resulting body is not completely impregnated, it still contains some air. Cavities, and thereby partial discharges, can not be avoided therefore, cf. Section 5.3.3.3. For new bushings, resin-bonded paper is thus no longer state of the art, but is still in use in old systems. This is possible as RBP has a comparatively high resistance to partial discharges. However, the risk of erosion breakdowns is significantly higher than for modern insulation technologies.

Today, oil-free ("dry") bushing cores made of **resin-impregnated paper (RIP)** are wound from *crepe paper*, dried and impregnated with unfilled *epoxy resin* under vacuum which guarantees a cavity-free insulating body [69], cf. Figure 5.3-15. During shrinkage of the resin during the curing process, the crepe paper can follow without mechanical stress due to its waviness. Moreover, well-defined small-scale wrinkling is specified for the smoothly inserted metal foils. The impregnation and curing of cavity-free bushing cores with a length of several meters is possible, but presents the greatest challenges to the production technology, cf. Section 5.3.3.1 d).

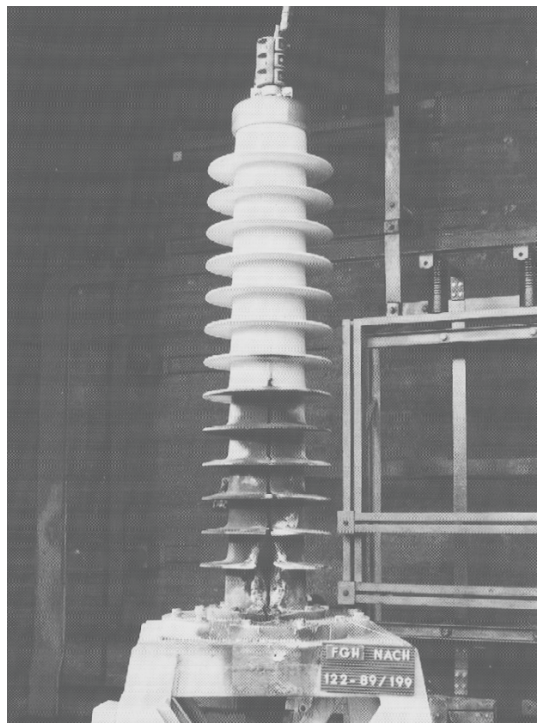

Figure 7.1.2-4: 123 kV RIP bushing with silicone sheds after an internal short circuit (40 kA, 0.5 s, 50 Hz) [57]. Photo by HSP Hochspannungsgeräte, Troisdorf.

RIP bushings have a series of *advantages* when compared to oil-insulated bushings: There are neither problems of leakage nor environmental impacts from escaping oil. Even for higher thermal loading, neither oil ageing nor gas bubble formation lead to deterioration of the dielectric properties. In the case of damage, an oil fire cannot occur, Figure 7.1.2-4.

RIP cores have either directly vulcanized silicone sheds on the outdoor side or they are assembled in a porcelain housing insulator or a glass-fiber-reinforced composite insulator with silicone sheds. The *secondary insulation* in the gap between the bushing core and the housing insulator can be formed by oil, by compressed SF_6 gas or by compressible *foam* which must be electrically sufficiently strong and adequately thermally conductive.

In the future, oil-free ("dry") bushing cores made of **resin-impregnated synthetics (RIS)** might more and more be wound also from

synthetic fabric and impregnated with filled resin under vacuum. It is advantageous that drying times can be drastically reduced and that the insulating body is less sensitive to humidity. In order to reduce shrinkage and ensure mechanical properties, impregnation must be performed with a filled resin, and this is a big challenge. Today, RIS technology is only applicable to the lower high voltage levels therefore.

Note: Using **gas-impregnated film dielectrics** is not common owing to comparatively higher costs. Nevertheless, voltage transformers and current transformers often contain SF_6 gas. Therefore, they make use of this insulation technology for the design of potential grading systems quite often, cf. Section 6.3.5.

Capacitive grading is also possible with a smaller number of **metallic cylinders in SF_6**, which are fixed by insulating spacers (*coarse potential grading).* However, relatively large diameters are the result of this. Moreover, large insulator diameters also occur for **geometrical grading**. In gas-insulated switchgear (GIS), the insulating gas of the system must also ensure the internal insulation of the bushing, Figure 7.1.2-1 (d).

Hollow porcelains and *composite insulators* made of glass-fiber-reinforced hollow cylinders with *silicone sheds* are used as **outdoor side housing insulators**, cf. Section 5.3.4. In the case of resin-impregnated insulating bodies, *silicone sheds* can be vulcanized directly on the bushing core. Above all, the advantage of composite insulators*,* in addition to the hydrophobicity of the surface and lower weight, is a reduced hazard potential in the case of internal short circuits, Figure 7.1.2-4. Porcelain fragments flying around must *not* be expected even with major defects.

Oil side or gas side housing insulators in transformers or substations are generally cast resin parts with cast-in shield electrode for covering the conductor connections.

Note: Resin-impregnated bushing cores do not require any oil side or gas side housing insulators. Owing to this, very simple *oil-gas bushings* and *oil-oil bushings* are possible, which are practically made of only one insulating body with a fitted flange. In the case of hot surrounding media (transformer oil) and very high voltages, the thermal stability must be checked, cf. Section 3.5.2.

7.1.3 Transformers

Transformers are used as *power transformers* for the transmission of electrical energy between different voltage levels, as *test transformers* for the generation of test voltages and test currents and as *measuring transformers* or *instrument transformers* even for the measurement of currents and voltages.

Along with single-phase transformers, mainly *three-phase high voltage power transformers* play a significant role. Especially at the highest voltage levels, they are expensive and strategically important components of the electric power systems. Figure 7.1.3-1 shows the example of a typical *oil-insulated construction* with the three-limb *iron core*, with the three *limb assemblies* comprising concentric windings and with the three high voltage *bushings*. Additionally, important components are the *on-load tap changer* for varying the transformation ratio under load by switching between the winding taps and the automatically controlled *cooling circuit* of the oil through which the heat loss of the transformer is carried to the heat exchanger. The oil expansion vessel absorbs the thermal expansion of the oil. In the case of gas accumulation, the so-called *Buchholz relay* triggers an alarm. Nowadays, the operating condition of strategically important transformers is increasingly monitored online with the aid of *monitoring-systems* and thermal models.

The *structure of the insulation* is determined by the voltage stresses in the windings, between the windings and against the core and the tank. Weight and leakage inductance of a transformer are the result of the insulation distances and gap widths between windings, layers and turns. Therefore, it is always necessary to look for a very compact but reliable *insulation design*.

Although modern transformers exhibit very low losses (approximately 0.2 to 0.5 %), the *heat removal* from the insulation also has a high significance, since very large power is transmitted: for example, a relative loss of

0.2 % for an 800 MVA transformer would correspond to a power loss of 1.6 MW! Since the power loss of windings increases approximately with the square of the current, the insulation in a weakly loaded transformer is subjected to considerably lower *thermal loads* and in a transformer that is overloaded within a short time, it is subjected to considerably higher *thermal loads*.

Note: Extreme thermal loads occur, for example, in *traction transformers*: in order to save on the weight of the iron core, the magnetic flux density of the core is driven to the extent that large hysteresis losses and appreciably larger relative losses occur.

A large number of *different designs* of transformers is available for diverse applications, but they are not dealt with here. The same applies to various *specific characteristics* that result, for example, from different *vector groups* or the integration of *on-load tap changers*.

In the following section, only the most important *transformer insulation systems* are discussed and the focus is on oil-paper insulation that is still dominant in the high voltage area.

7.1.3.1 Oil-filled Transformers and Dry-type Transformers, Reactors

a) Transformers with oil-board insulation

Oil-filled high voltage transformers are insulated by low viscosity *insulating liquids* (generally, mineral oil) and impregnated *fiber materials* (generally, of pressboard or transformerboard based on cellulose respectively). Thereby good *heat removal* through convection, a high thermal capacity for short-duration *overload* and high quality *insulation* of oil channels and solid barriers are guaranteed simultaneously, cf. Sections 5.4 and 5.5. Furthemore, the hygroscopic behavior of the cellulosic fibers maintains the oil in a *dry condition* with a high dielectric strength.

The insulation consisting of oil and board (pressboard) is discussed in detail in the following Sections 7.1.3.2 to 7.1.3.5 owing to its importance in high voltage power transformers. Other insulation systems do not yet have corresponding significance for high voltage transformers, and therefore will be explained only briefly in the following sections:

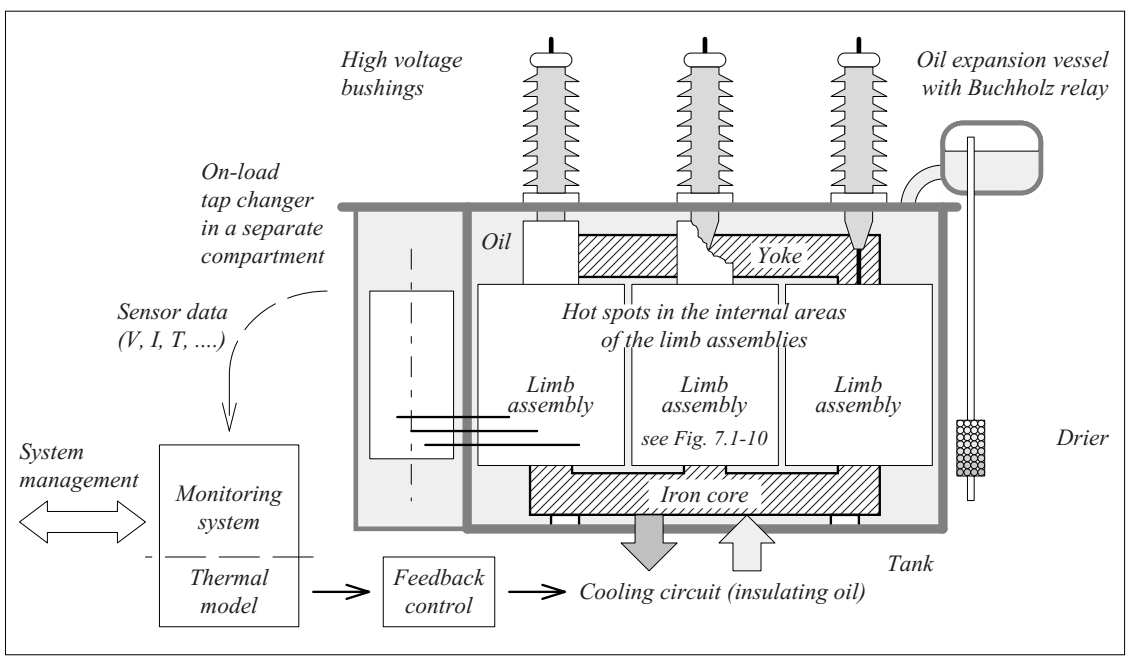

Figure 7.1.3-1: Components of on oil-insulated high voltage power transformer (schematic representation).

b) Dry-type transformers

Resin-encapsulated windings or resin-bonded windings are used for so-called **dry-type power transformers** and **voltage transformers** in the medium voltage range. In these applications, the windings are insulated by polymeric films or fiber materials. High *field strengths* cannot at all be tolerated owing to air inclusions between the layers. *Heat removal* by conduction of heat through the resin encapsulation is considerably poorer than the convective heat removal in oil-insulated transformers. Therefore, it leads to power rating limitations and often even to high temperatures which necessitate the use of thermally stable materials (e.g. aramide fibers, polyimide films). Dry-type transformers have vertical cooling channels between core and windings, between the windings and even inside the windings themselves to improve removal of heat.

By eliminating hygroscopic materials (cellulose), time-consuming drying procedures (such as with pressboard-insulated core-and-coil assemblies) can be avoided during production. Moreover, an open structure without a tank is possible.

The oil-free construction, which is less hazardous for the environment is also advantageous. Therefore, despite their higher price, dry transformers are often used as medium voltage distribution transformers.

c) Gas-insulated transformers

Dry-type transformers for the high voltage range can be implemented in a *compressed-gas tank under SF_6* by means of gas-impregnated *polymeric film insulation*. They are used, for example, as **measuring voltage transformers** or **test transformers** in gas-insulated sitchgear, cf. Section 6.2.1.2. The oil-free construction is especially advantageeous in gas-insulated switchgear, in which the insulation medium SF_6 is already present. But even in outdoor switchgear, SF_6-insulated instrument transformers have been established owing to low fire load. Although gas-insulated **power transformers** are possible in principle, they do not currently represent an economical alternative to oil-filled transformers in many cases owing to the high costs of the pressure-resistant tank. Nevertheless, the oil-free construction is of great value for seismic prone regions.

d) Cable transformers

Another idea for manufacturing dry, high voltage transformer windings from wound and externally cooled *XLPE cables* is described in Section 7.1.6.3 along with similar applications (cable generators).

e) Superconducting transformers

The vision of superconducting transformers with considerably lower losses is associated with new concepts of the construction of insulation systems based on *liquid nitrogen*, cf. Section 7.5.

f) Reactors

Also high voltage reactors are designed similarly to high voltage transformers, and hence they are not described separately. Instead of a closed iron core, they use one with a single gap or a distributed gap which determines the inductance. The winding is similar to a *transformer high voltage winding*. All types of transformer insulation can be used for the insulation systems. Examples are *oil-paper insulated* reactors with an in-tank design for large reactive power ratings or low-weight *compressed-gas insulated* reactors for mobile use. Applications are *shunt reactors* for the compensation of reactive power, *filter reactors* in AC circuits and *smoothing reactors* in HV-DC converter stations as well as *series-resonance test reactors* for on-site AC testing, cf. Section 6.2.1.5.

7.1.3.2 Windings and On-load Tap Changer

The windings can be designed as a foil windings (sheet or strip windings), multi-layer windings or disc windings, Figure 7.1.3-2.

Foil windings, sheet windings or **strip windings** are wound from sheet material or strip material (e.g. from copper foils, sheets or strips respectively) along with the interlayer insulation, Figure 7.1.3-2 (top). Since the total winding voltage V occurs across the very narrow front sides of the winding, the foil winding is a typical *low voltage winding*. The advantage here is that as a result of the broad strip-shaped conductor, a favorable distribution of the currents and the electro-mechanical forces in the case of short-circuit currents occur Furthermore, the construction is mechanically stable, and it can easily be manufactured. The *interturn insulation*, owing to the very low turn-to-turn voltage, has no insulation function in the usual sense, but has a distancing function between the turns to prevent turn-to-turn faults. High temperatures often require the use of *temperature-resistant materials*, e.g. of aramide fibers or polyimide films. *Paper* is also used in oil-insulated transformers. During drying, the long axial diffusion paths between the conductor foils must be considered. Residual moisture would form conductive bridges and could lead to thermal instabilities even at very low voltages.

In the case of a **layer winding** or **multi-layer winding**, turns are laid next to each other and one layer is laid above the other, Figure 7.1.3-2 (center). A paper winding on the conductor or an oil-proof enamel coating serves as the *interturn insulation* (or *turn-to turn insulation* respectively). Between the layers, the interlayer voltage, which is the doubled voltage per layer, must be insulated by the *interlayer insulation* of wound and oil-impregnated paper layers or pressboard layers. Vacuum drying and vacuum impregnation must be carried out with special care here, since the remaining residual gas cannot diffuse easily from the compact multi-layer insulation into the surrounding oil.

Note: In the case of dry-type transformers with resin-enclosed windings, interlayer insulation is carried out using polymeric films.

The full winding voltage V occurs over the relatively narrow front side of the winding.

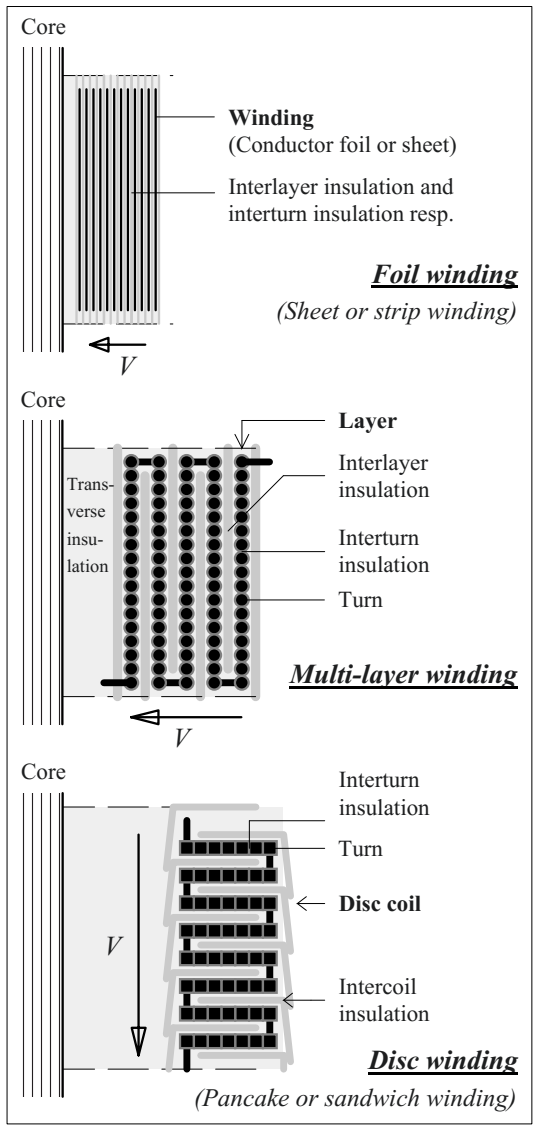

Figure 7.1.3-2: Foil winding, multi-layer winding and disc (sandwich or pancake) winding.

Therefore, cylindrical multi-layer windings are mainly used in the *medium voltage range,* but for cost reasons they are now even used up to 123 kV.

By shortening the layer lengths with increasing radius, multi-layer windings with a *potential grading* in the axial direction up to half the winding height are achieved. This principle is especially appropriate for windings that must be insulated only on one side against the surrounding, e.g. as for single-phase test trans-

formers, Figure 6.2.1-3 a), d) and e). The outer connection to the center of the winding is used as a high-voltage terminal and the inner one as a ground connection.

High voltage windings and extra-high voltage windings are designed as **disc windings** consisting of stacked *disc coils,* in which one turn is laid over the other forming a spiral coil, Figure 7.1.3-2 (bottom). Individual discs are alternately connected to each other at the inner ends and at the outer ends which results in a series connection. Winding terminals are arranged at the front sides.

Note: Disc windings are also called *pancake windings* or *sandwich windings*.

Note: The entire winding can be wound from a continuous conductor (winding wire) as a so-called *continuous turned-over winding* or *inverted winding.* This shall be explained for a pair of two consecutively wound discs, Figure 7.1.3-2a. The first spiraliform disc (a) - (b) is regularly wound ourwards on the winding mandrel, i.e. from the inner end (a) to the outer end (b). With the same conductor, and continuative to this, the winding of the second disk is also started inside on the mandrel (c) and it is also wound outwards (d), i.e. from the inner end (c) to the outer end (d), Figure 7.1.3-2a (top). Then, the wire at the external end of the second disk is fixed on the mandrel again (d), Figure 7.1.3-2a (middle). During further rotation of the winding mandrel, the second disc is now turned-over or inverted in such a way that the external end returns inside (d) and that the internal end (c), which is the connection to the first disc, is positioned at the outside Figure 7.1.3-2a (middle and bottom). Finally, the second disc is pushed towards the first disc along with simultaneously thightening of the winding wire. Then, the next pair of discs can be wound in the same manner [184].

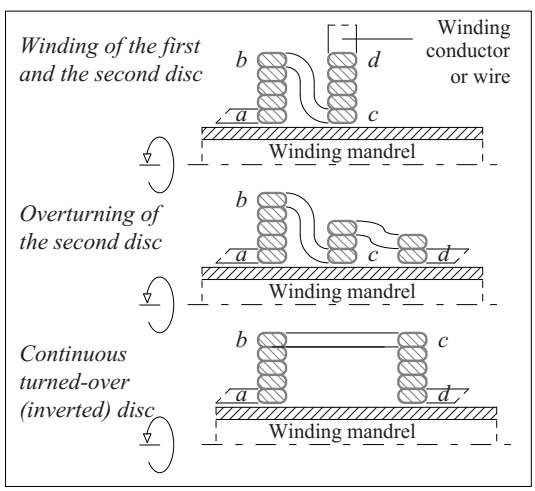

Figure 7.1.3-2a: Manufacturing of a continuous turned-over (inverted) disc winding on a horizontal mandrel [184].

As a first approximation, the total winding voltage V is uniformly distributed over the entire winding length so that windings can be designed for very high voltages. Across the narrow front sides, there is the relatively low partial voltage of an individual disc only. A paper winding on the conductors serves as the *interturn insulation*. The *intercoil insulation (coil-to-coil insulation)* cosists of discs, edge protection rings and spacers made of pressboard [27]. Individual disc coils are often spaced so far apart that the insulating oil can flow past the windings and remove the heat loss. This construction also facilitates vacuum drying and allows reliable impregnation of the insulation, Figure 7.1.3-4b (top left).

For *AC voltage*, the **voltage distribution in the windings is** linear according to the number of turns. In the case of *lightning impulse voltage*, the effects of *capacitances* between turns, layers and discs as well as between winding and the surroundings prevail, Figure 7.1.3-3. The lattice network structure of the capacitances causes a *non-linear voltage distribution.* Hence, in the case of lightning impulse voltage

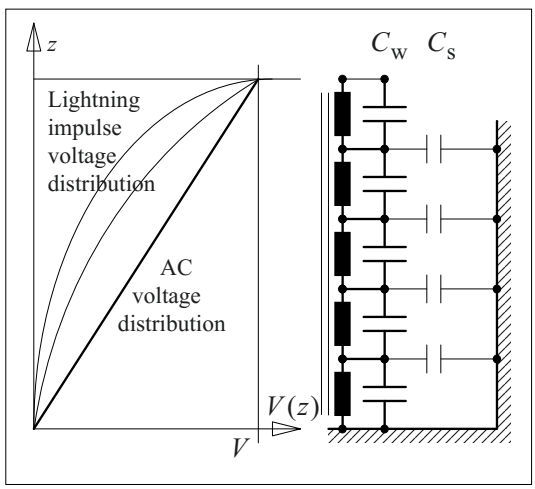

Figure 7.1.3-3: AC voltage and lightning impulse voltage distribution in a high voltage winding.

stresses, turn-to-turn faults preferably occur at the upper end of the stressed winding. *Multilayer windings* perform better than disc windings owing to their large winding capacitances, provided that the layers are of equal lengths or capacitances. In *disc windings*, an increase in the longitudinal capacitances in the highly stressed upper winding area is possible by changing the sequence of interconnection of the disc coils. This results in a change from a series connection of disc-to-disc capacitances to a series-parallel connection [67]. Additionally, the effect of earth stray capacitances can be compensated by stray capacitances to a *screen* at high voltage potential [184].

Note: During frequency response measurements, transformer windings exhibit multiple *resonances*, whose excitation can lead to overstressing of windings or of winding parts. Detailed analyses necessitate much more complex equivalent circuits [191].

Taps of high voltage transformers windings are generally located on the ground side ends of the windings which are designed as regulating windings. With the aid of an **on-load tap changer**, the *tranformation ratio* of a transformer can be changed under load, i.e. without interrupting the current. The changes are performed stepwise according to the steps set by the *taps* For this, a new current-free tap is pre-selected by a so-called *tap selector*. The so-called *diverter switch* or *load transfer switch* then connects the original current-carrying tap and the new current-free tap in parallel via resistances (circulating currents are limited by the resistances), before the connection to the original tap is opened and closed to the new tap without resistance. For transformers up to about 123 kV and currents up to about 600 A, the functions of tap selector and diverter switch even can be combined in a so-called *selector switch*. For this, the tap-changing operation is always performed between adjacent taps with the aid of rotating resistance-linked and resistance-free contacts [184], [297].

On –load tap changers operate under *oil* that is loaded, degenerated, and polluted by contact abrasion and by breaking sparks and hence should *not* come into contact with the insulating oil of the transformer. Therefore, on-load tap changers are arranged in *separate compartments* within or outside the transformer tank, Figure 7.1.3-1. The taps are voltage-carrying conductors and must be fed into the tap-changer compartment with the aid of an insulating partition wall.

To facilitate quicker switching operation and to prevent mechanical wear and degeneration of tap-changer oil, the application of *vacuum switches* can be used as diverter switches (load transfer switches). Furthermore, the use of *thyristors* and *hybrid concepts* is discussed [380].

Note: Fully power electronic tap changers still have problems with current commutation, with losses, with the fault current ratings and with the large number of thyristors. In contrast to mechanical switches, which preferably change the tap connections of the high voltage windings because of the lower currents there, thyristors should change the tap connections of the low voltage windings, since in this case fewer thyristors have to be connected in series. However, in this case new transformer designs would be necessary.

7.1.3.3 Design of Oil-board Insulation

a) Insulation design

Along with the insulation within the windings, the insulation of *high voltage windings and high voltage conductors* relative each other, against the low voltage windings, against grounded components (core, tank) and against the windings of other phases, is also necessary. Adequately dimensioned *oil gaps* must be provided for this purpose, Figure 7.1.3-4a.

Note: In Figure 7.1.3-4a, the *classic construction* with a low voltage winding, high voltage winding and compensating winding is schematically represented. Under this, Figure 7.1.3-4b shows the *typical insulation components*, but in the form of an *autotransformer (single-winding transformer*) for coupling between a 220 kV network and a 400 kV network. The compensating winding is located internally on the core.

The dielectric strength of the oil gaps can be considerably increased with *pressboard barriers,* which divide the wider oil gaps into narrower sub-gaps, Section 3.4.2.3 Figure 3.4.2-6.

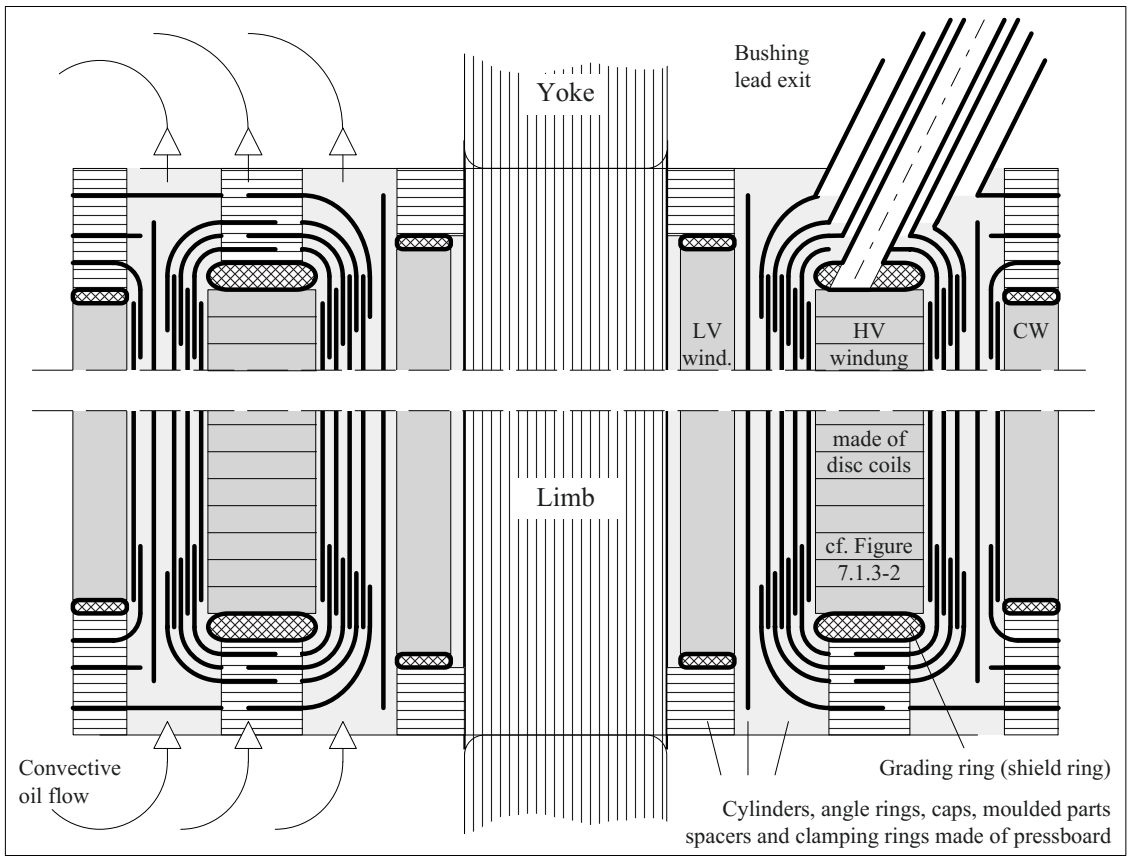

Figure 7.1.3-4a: Insulation system of a classic high voltage power transformer with core, low voltage winding LV, high voltage windingHV and compensating winding CW (schematic representation from inside towards outside).

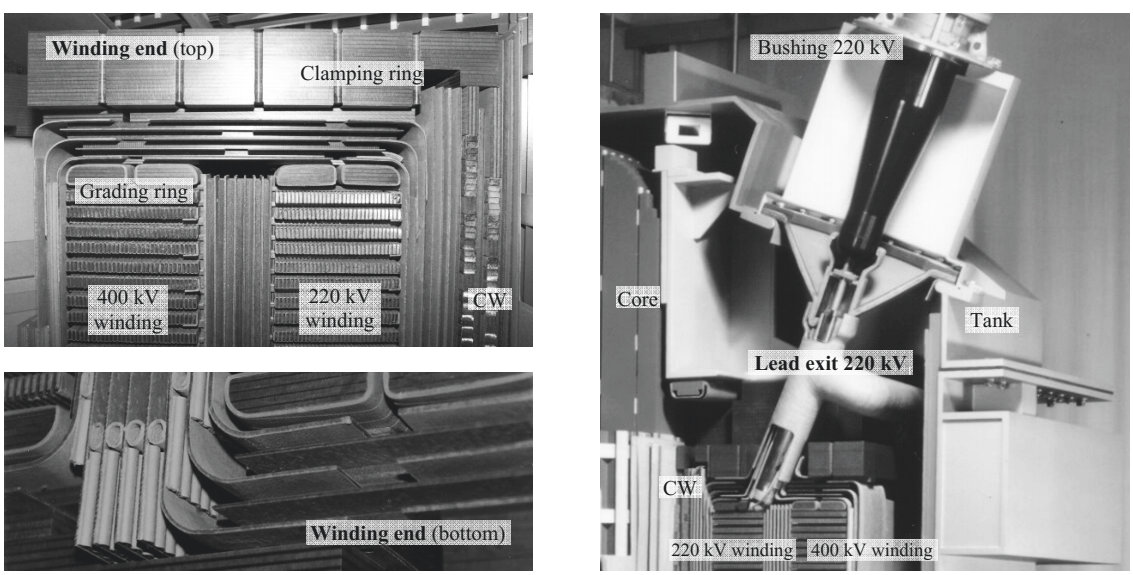

Figure 7.1.3-4b: Typical insulation components in the arrangement of a 200 / 400 kV autotransformer. The upper ends of the 400 kV and the 220 kV windings have the same potential, the 400 kV lead exit is present at the outer side of the winding but not visible in the photo, cf. Figure 7.1.3-6. Photo of insulation model: Weidmann, Rapperswil (CH).

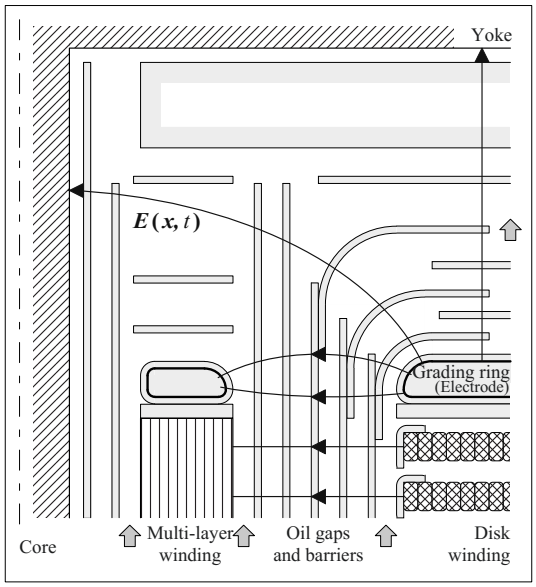

Figure 7.1.3-5: Dielectric stressing of a barrier system at the upper end of a high voltage winding (schematic representation) [274].

Owing to this, smaller distances, lower leakage inductances and a lower transformer weight are possible. It is desirable that the barriers follow approximately the *profile of equipotential surfaces* since then the stress on the oil gaps is normal and not tangential to the pressboard surface.

Especially high field strengths are created at the exposed *edges of the winding ends* below the grounded yoke of the iron core. Therefore, the winding ends are covered by metalized and rounded *grading rings* or *shield electrodes*. If the windings are not directly grounded, the *lower winding ends* must also be insulated against the core and the housing, Figures 7.1.3-4 and 7.1.3-5.

Pressboard barrier systems consist of cylinders, angle rings (flange rings), caps, discs, manually formed parts, spacers and clamping rings. The fixing is carried out with oil-proof casein glue that can be impregnated. Here it is important that the *closed barrier surfaces* are designed perpendicular to the direction of the field. This can be ensured by overlapping the cylinders and shaping the insulation components, Figure 7.1.3-5.

However, *heat removal* through oil flow in the oil ducts between the barriers necessitates gaps and openings which must be mutually displaced so that the oil gaps are *always* subdivided in the direction of the field. Axial cooling channels can also be created within multi-layer windings by windings of corrugated board between the layers.

Forces occurring in the case of a short circuit tend to considerably enlarge the leakage flux gap (*normal force*) and compress the winding (*contraction force*) [184]. They must be taken up via an adequately stable clamping of the windings by spacers and by clamping rings [27], [65], [82]. High dimensional accuracy must be maintained to avoid shearing forces.

Windings, together with the barriers, spacers, grading rings (shield electrodes), angle rings and caps, are braced upwards and downwards against the core by *clamping rings* of laminated wood (densified laminated wood, beechwood veneers compressed with synthetic resin) or laminated pressboard (bonded pressboard panels). Here, laminated pressboard is used in the areas of higher field strengths and wood in the areas with lower field strengths.

Concentric windings, barriers and supports on a limb together form a structural unit and an insulation component. It is therefore referred to as *limb assembly*, Figure 7.1.3-1.

Also the high voltage conductors are led to the bushings or to adjacent windings through cylindrical barrier systems, the so-called *lead exits*, Figures 7.1.3-6 and -7. The oil volumes of the transformer and the lead exits are often separated by partition insulators in order to enable assembly tasks to be carried out on the lead exits and bushings without lowering the transformer oil level. For this, so-called *drip-proof sealed end caps* of epoxy resin or of pressboard are used, as well as pressboard *Faltenbalgs or bellows* with creepage path extensions for very high voltages, Figure 7.1.3-6.

Sections 5.4 and 5.5 describe the *processing and preparation of the insulating materials.*

b) Design of cylindrical barriers

> The **function of barriers** is especially to increase the *dielectric strength of the oil gaps* by subdividing the gaps into narrower sub-gaps.

The *dielectric strength* of the oil gaps and the barriers results from the relationships presented in Sections 3.4.2.3, 3.5 and 7.3.4. In the case of AC test voltages, field strengths up to 10 kV/mm are possible in oil ducts of a few mm gap width, Figure 3.4.2-6, Eq. (3.4.2-1).

The **leakage flux gap of the transformer** between the low voltage winding and the high voltage winding is designed largely *cylindrically symmetrically*. To a first approximation, the electric field in this range can often be considered as a uniform one, Figure 7.1.3-8a. According to Figure 3.4.2-6 and Eq. (3.4.2-1) respectively, a specific oil gap width d results for a voltage to be insulated, Figure 7.1.3-8a (top). If the oil gap is subdivided into narrower sub-gaps by the barriers, the strength is increased so that the same voltage can be insulated over a shorter distance d, Figure 7.1.3-8a (center). Owing to the higher permittivity of pressboard, the field is largely displaced from the barriers into the oil gaps, Figure 7.1.3-8a (bottom). Thus, the **oil gaps** are the actual insulation distances; the *barriers* essentially provide *separation.*

In order to design the most compact transformer, the *smallest possible* insulation thickness d must be determined. It is obtained from the ratio of voltage V to insulation thickness d, which must be maximized [274]. Wherein n is the number of oil gaps, $n+1$ is the number of barriers. The indices "B" and "Oil" represent the barriers and oil gaps, also cf. Figure 7.1.3-8a:

$$\frac{V}{d} = \frac{1}{d}\cdot\left[(n+1)\cdot V_{\mathrm{B}} + n\cdot V_{\mathrm{Oil}}\right] \qquad (7.1.3\text{-}1)$$

$$= \frac{(n+1)\cdot\frac{\varepsilon_{\mathrm{Oil}}}{\varepsilon_{\mathrm{B}}}d_{\mathrm{B}} + n\cdot d_{\mathrm{Oil}}}{(n+1)\cdot d_{\mathrm{B}} + n\cdot d_{\mathrm{Oil}}}\cdot E_{\mathrm{Oil}}$$

Figure 7.1.3-6: Cut-away model of a removable 400 kV lead exit system with a Faltenbalg (bellow) at half the winding height. Photo: Weidmann, Rapperswil (CH).

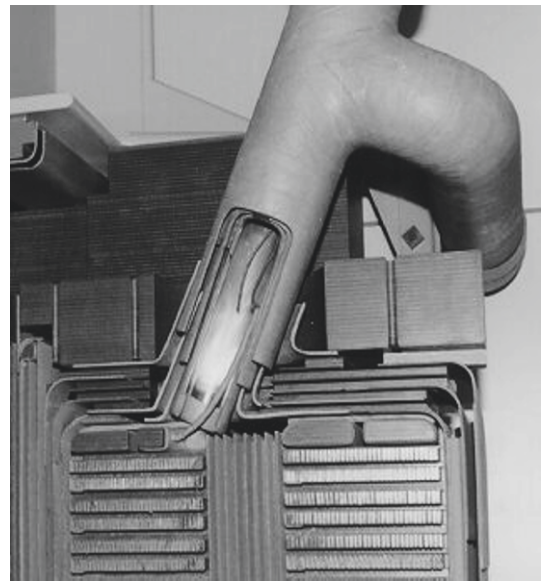

Figure 7.1.3-7: Connection of a 220 kV Lead exit system of concentric barriers to the windings of an autotransformer, cf. Figure 7.1.3-4b. Foto of the cut-away model: Weidmann, Rapperswil (CH).

With Eq. (3.4.2-1), the following is obtained

$$\frac{V}{d} = \frac{(n+1)\cdot\frac{\varepsilon_{\mathrm{Oil}}}{\varepsilon_{\mathrm{B}}}d_{\mathrm{B}} + n\cdot d_{\mathrm{Oil}}}{(n+1)\cdot d_{\mathrm{B}} + n\cdot d_{\mathrm{Oil}}}\cdot E_0\cdot\left(\frac{d_{\mathrm{Oil}}}{mm}\right)^{-a} \qquad (7.1.3\text{-}2)$$

The maximum ratio *V/d* results for the *smallest possible barrier thickness* d_B. However, at d_B = 2 mm, a *practical lower limit* is reached, because the barriers at the overlapping points must be angularly sharpened, because they must remain dimensionally stable during the drying process and also because they require a certain amount of resistance against sporadic partial discharge events [274], [285]. Under this basic condition, the maximum ratio *V/d* is obtained for the *narrowest possible oil gap* d_{Oil} with a maximum possible number *n*. This condition also has its practical limitations: The oil gaps must be wide enough to make up for manufacturing tolerances and to allow undisturbed *oil circulation*.

Note: The described result with the thinnest possible barriers is correct **only for AC voltage and impulse voltage insulation**. For *DC voltage insulations*, field displacement conditions are completely different and the barriers must insulate a voltage close to the total voltage. Therefore, the *barriers* require *adequate thickness*; cf. Section 7.2.3 with Figure 7.2.3-5.

c) Design of lead exits

For the dimensioning of lead exits, a *radial (cylindrically) symmetric field* can approximately be assumed in the environment of the conductor. High field strengths at the conductor surfaces can be reduced by sufficiently large *conductor diameters* and, if necessary, by a thick **paper wrapping**. A comparable optimization example is explained in Section 2.4.3.1 (but with other materials, i.e. with cast resin in air instead of paper in oil). The disadvantage here is the low strength of the remaining *large free oil gap*, which is additionally stressed by field displacement from the paper wrapping. The accumulation of fibers and particles is thus held responsible for a large *dispersion* of breakdown voltages and for a comparatively *low strength* at very high voltages [274], [286].

Similar to a uniform field, also in a non-uniform field substantial increases in the dielectric strength can be achieved by subdivision of

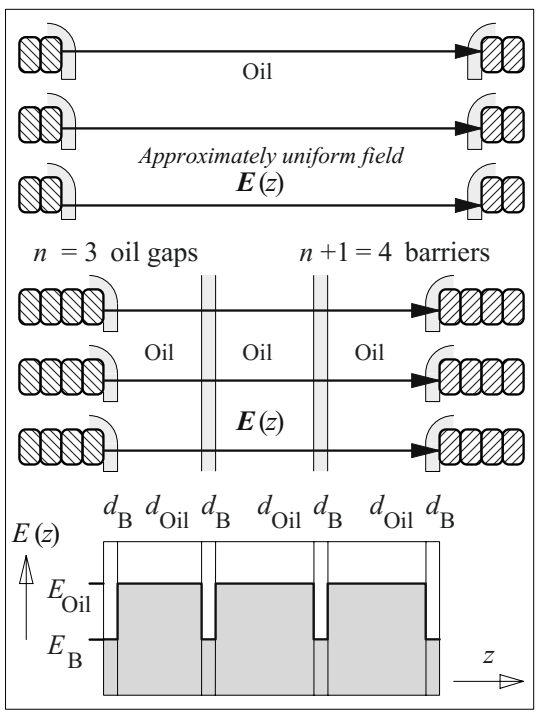

Figure 7.1.3-8a: Transformer leakage flux gap between two windings with a large oil gap (top) and with barriers for subdividing it into electrically stronger subgaps with smaller volumes (center and bottom) [274].

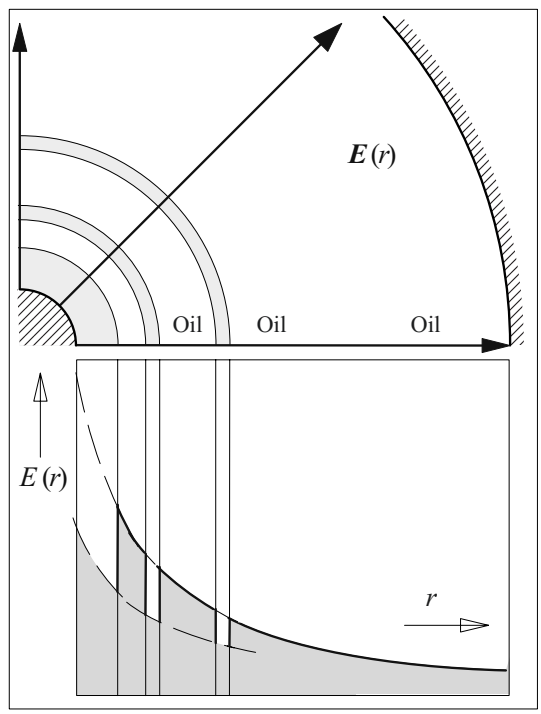

Figure 7.1.3-8b: Barriers in the lead exit of a transformer between high voltage conductor and tank with adjustment of gap width and dielectric strength to the local field stress in a nonuniform field [274].

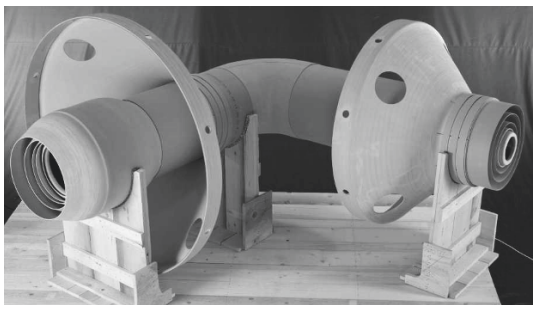

Figure 7.1.3-9: Insulation system of a lead exit with bushing side (left) and winding side (right) for 1000 kV, photo: Weidmann, Rapperswil.

the oil gap with the aid of barriers *concentrically* arranged around the conductor, i.e. with a so-called **lead exit system**, Figures 7.1.3-6, -7, -8a and -9. The gap width and the strength of the oil gaps can be *adjusted* to the magnitude of the *local field stress*, Figure 7.1.3-8b. Owing to this, smaller conductor diameters and smaller external dimensions are possible [274]. Lead exit systems can be implemented up to the highest transmission voltages of more than 1000 kV in a compact design, Figure 3.1.3-9.

d) Design for non-uniform and tangential fields (creepage paths)

The field distribution at the *winding ends* in the area of the **shield electrodes**, at the **bracings**, at the **supports** or at the **Faltenbalgs** (**bellows**) can generally no longer be determined analytically and must be optimized with numerical field calculations. In these areas, *non-uniform field distributions* occur, whereby the field vectors can also be inclined to the barriers, Figure 7.1.3-10.

It must first be noted that the length applicable to the strength calculation according to Eq. (3.4.2-1) and Figure 3.4.2-6 respectively, is not the geometrical gap width *d,* but rather the larger **effective gap width** d_{eff} *in the field direction* $\boldsymbol{E}$*,* Figure 7.1.3-10.

Furthermore, **tangential field components** $\boldsymbol{E}_{\tan}$ can occur, representing a critical stressing at high voltage interfaces. However, in this context oil-pressboard interfaces are an ex-

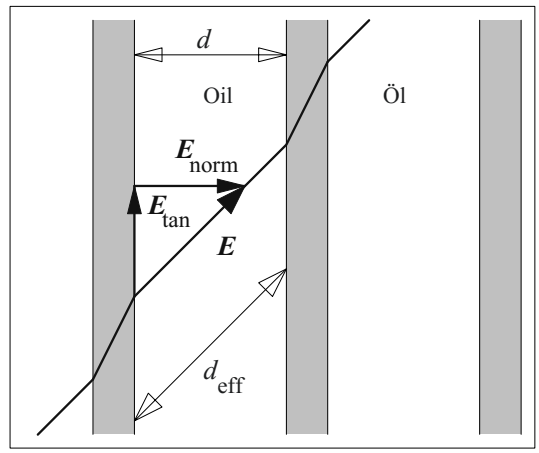

Figure 7.1.3-10: Tangential and normal field components as well as effective gap widths.

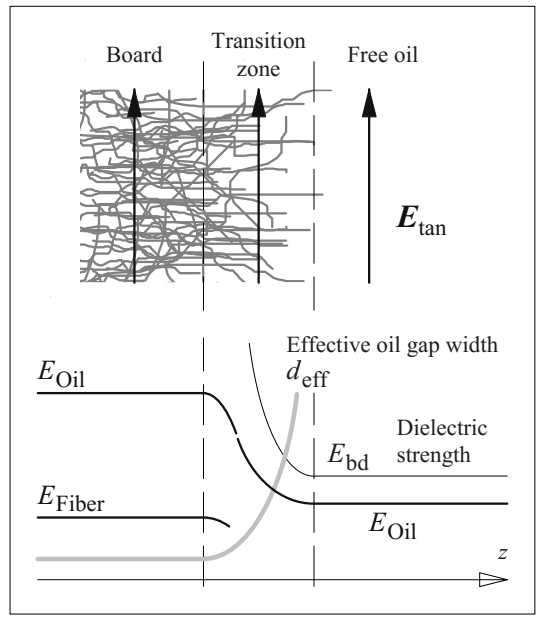

Figure 7.1.3-11: Oil-pressboard interface for a tangential field stress (microscopic presentation) with comparison between dielectric strength and electric stress profile (schematic representation).

ception: the fiber structure of the board results in a *quasi-steady transition* from the pressboard into the free oil, Figure 7.1.3-11 (top). The capillary forces prevent the wetting problems that are known for smooth surfaces. Moreover, the very small oil gap width between the pressboard fibers (with high electric strength) increases quasi-steadily outwards, whereby the dielectric strength *steadily* de-

creases to the values of the free oil gap. Fibers projecting into oil act in practice as microscopic barriers for the tangential field components, Figure 7.1.3-11.

Based on these theoretical considerations, it would be expected that the **tangential electric strength** corresponds to the strength of a free oil gap [274]. Experimental tests have actually shown that this assumption is correct for short tangential paths, but lower values can result for longer paths [286]. The 63 % breakdown field strength $E_{\mathrm{bd63\%}}$ lies above the values of design curves for a free oil gap according to Figure 3.4.2-6, and a roughly comparable length dependence can be observed [287]. In practice, tangential design stresses are frequently limited to about 70 % of the permissible stresses for free oil gaps [274].

Electrical stresses can be associated with highly **non-uniform field strength profiles**, especially in *long oil gaps* and for tangential stresses along *creepage paths*. The application of design curves according to Eq. (3.4.2-1) and Figure 3.4.2-6 is thus generally associated with difficulties:

- A very conservative approach could be one in which local *maximum field strengths* are to be restricted to values that are obtained for the total insulation path from the above-mentioned design curves. Although on one hand it is safe, this could result in *oversizing,* since the arrangement would not be stressed according to its strength over large paths.
- On the other hand, it would be dangerous to compare *average field strength values* with the design curves. In highly non-uniform fields, very low average values can be obtained, although partial insulation paths are highly stressed and probably overstressed. Average field strengths can therefore only be considered for weakly non-uniform fields, cf. Eq. (3.4.2-2).

For the evaluation of **non-uniform field strength profiles** in long oil gaps, it is therefore recommended that average field strengths shall be determined for *various interval lengths* along a *criticalfield line* which shall be compared with the design curves according to Eq. (3.4.2-1), Figure 3.4.2-6 [274], [288], Figure 7.1.3-12:

A long oil gap with non-uniform field strength profile as in Figure 7.1.3-12 a) and b) is considered for this. Starting off with the maximum field strength values, *average field strengths*

$$E_{\mathrm{av}}(z) = \frac{1}{z} \cdot \int_0^z E(z')\,\mathrm{d}\,z' \qquad (7.1.3\text{-}3)$$

are now calculated for *various interval lengths or path lengths* from z = 0 to $z = d$, Figure 7.1.3-12 c) (lower curve). These average field strengths are compared with the *design values* permissible for the oil gap of the respective length z according to Eq. (3.4.2-1), Figure 7.1.3-12 c) (upper curve).

The ratio of the permissible to average field strengths

$$q = \frac{E_{\mathrm{bd}}(z)}{E_{\mathrm{av}}(z)} \qquad (7.1.3\text{-}4)$$

is considered as a *safety factor q* for the intervals of length *z,* Figure 7.1.3-12 d). For a *critical interval length* z_{crit}, this results in the smallest safety factor q. However, if the strength of the arrangement has to be guaranteed, it must still satisfy the condition $q \geq 1$.

Note: Breakdown tests have shown that the voltages determined in this way correspond to a *low breakdown probability* of about 2 % [289].

For the **tangential stress along creepage paths**, e.g. along the barrier surfaces, the same evaluation concept can be applied: At first the tangential field strength values along the creepage path are rearranged to a new *profile with steadily decreasing values*. The *average field strengths values for different creepage path intervals z* are calculated as per Eq. (7.1.3-3). For the calculation of safety factors analogously to Eq. (7.1.3-4), and for reasons of precaution, the tangential dielectric strength of the barrier surface must be assumed only

with about *70% of the dielectric strength of the oil*:

$$q = \frac{0.7 \cdot E_{\mathrm{bd}}(z)}{E_{\mathrm{av}}(z)} \qquad (7.1.3\text{-}5)$$

Note: It is reported that with this evaluation concept, the partial discharge inception voltage at a 400 kV Faltenbalg (bellows) was predicted as 882 kV, which comes quite close to the *measurement value* of 950 kV, [288].

7.1.3.4 Manufacture

The manufactureof a high voltage transformer starts with the stacking of the **iron core** of thin, and magnetically soft iron sheets in the horizontal position. The sheets are insulated against each other by phosphatized layers in order to avoid eddy currents. At the beginning, the build-up of the core is performed without a yoke, since the windings must first be arranged on the limbs after the erecting of the core into the vertical positon.

The **windings** are made individually on horizontal or vertical winding benches with winding mandrels that are adjustable in diameter. Multi-layer windings are wound, for instance, horizontally on a pressboard cylinder as a support. Disc windings can be wound, for exam-

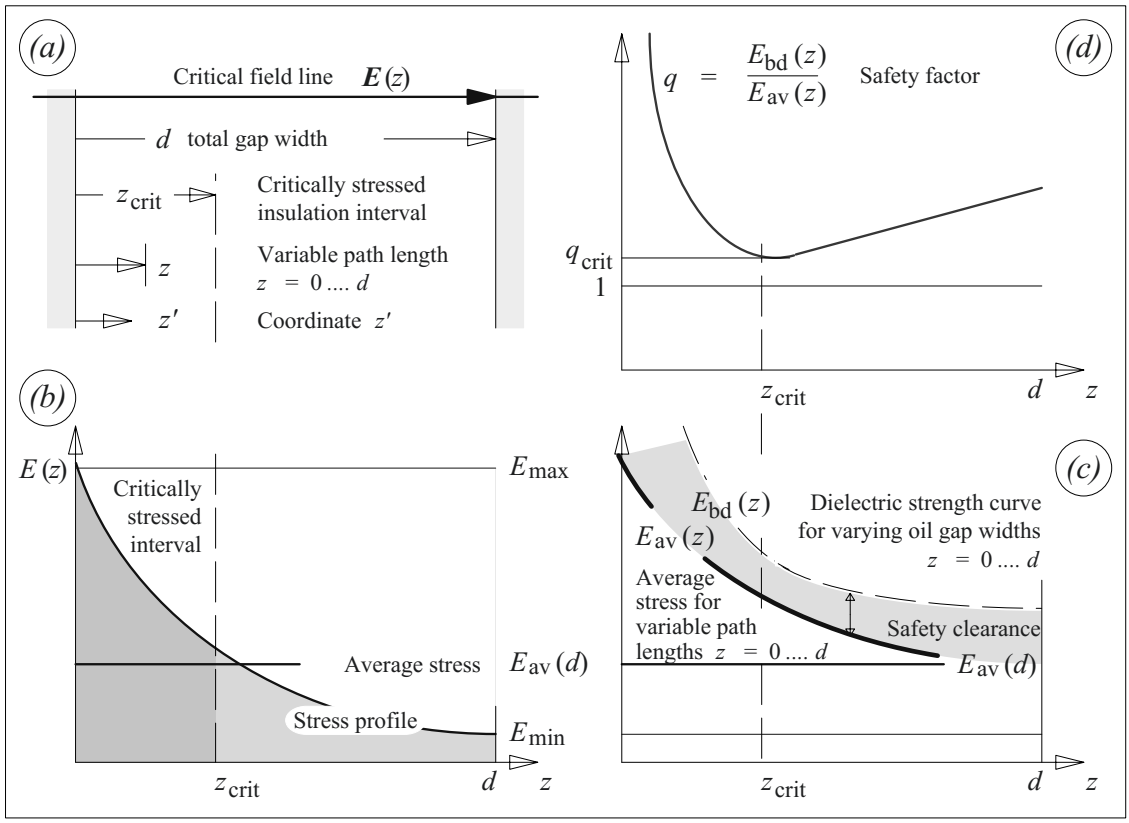

Figure 7.1.3-12: Evaluation of cumulative field stresses für non-uniform field strength profiles [274], [288].

(a), (b): Long oil gap or long creepage path with highly non-uniform field strength profile.

(c) Starting off with the maximum field strength values, avearge field strengths $E_{av}(z)$ for increasing path lengths z= 0 to z= d are calculated (lower curve) and compared with the design values according to Eq.(3.3-1)that are applicable for the oil gaps or creepage paths of the considered length z (upper curve).

(d) From the ratio of permissible to average field strength $E_{bd}(z) / E_{av}(z)$, a safety factor q results for an interval of length z. The saftey factor is smallest at the critical interval length z_{crit} . For this, the condition $q \geq 1$ must always be fulfilled.

ple, in vertical or horizontal positions as spirals with the discs lying one above the other or one besides the the other respectively. Winding processes require a lot of manual work, many experiences owing to complicated winding diagrams and great care, especially owing to the great sensitivity of the insulation and owing to the fact that it cannot be inspected later. The wound conductors are often wrapped with a thin paper layer to avoid contact between bare metal and the oil gaps, whereby the paper wrapping should not obstruct the transfer of heat to the oil. Since cellulose-based insulation components shrink during the subsequent drying, appropriate length compensation must already be ensured during winding. Windings with unfavorable drying conditions are sometimes pre-dried, since moisture can only diffuse out of multilayer windings and foil windings in the axial direction, as in bushings, for instance.

The windings and formed components of the barrier system are assembled for complete **limb sets** and set on the limbs of the vertically erected iron core. By interconnecting the windings and closing the iron core with the yoke, a complete **core-and-coil assembly** is built up. It must be subjected to intensive drying.

While **drying**, effective heat transfer is carried out at first in the heat-up phase by hot kerosine vapor, since the heat of evapouration must be supplied and large masses must be heated up (vapor-phase method). The temperature rise during this should not be too rapid in order to protect the fiberboard materials that are still moist [27]. In the pressure decreasing phases and medium vacuum phases, temperature is maintained by radiant heating; cf. Section 5.5.1.4 with Figure 5.5-13.

Flooding of the core-and-coil assembly with degassed and dry oil takes place in the transformer tank under **vacuum.** For a partial-discharge-free insulation, it is necessary that the rising oil can completely displace the gas upwards through the ducts and openings in the barriers. Residual gas adhering to the surfaces and trapped in undercuts must be completely dissolved in oil after the final *pressurization* and during an adequate *impregnation period.*

Note: Ageing-resistant oils are preferred for transformers since the thermally stressed oil stays in contact with the atmospheric oxygen via the oil expansion vessel.

7.1.3.5 Transformer Testing

Transformers have insulation systems of extremely complex designs with many model-based variants. Testing a finished transformer therefore includes a very extensive program of *routine tests, type tests and special tests* that are cofigurated differently depending on the individual transformer. Therefore, only a few basic intentions are explained in the following sections; details are presented in the standards and, in addition, can be agreed between the manufacturer and the client [290], [291], [52], [292].

Routine tests include the measurement of winding resistance, transformation ratio (including phase angle rotation), short-circuit impedance, load loss (short-circuit loss), no-load loss and no-load current. Moreover, various *high voltage tests* or *dielectric tests* (see below) and functional tests on the tap changers are necessary.

Temperature rise tests as well as a number of further *high voltage tests* (see below) must additionally be provided as **type tests**.

Special tests include special *dielectric tests* (see below), the measurement of *capacitances*, *dissipation factors* and *insulation resistances*, *short-circuit tests*, determination of transmission behavior for transient voltages as well as measurement of zero impedances, distortions of no-load currents, noise levels and power consumtion of oil pumps and cooling fans.

From the point of view of high-voltage engineering, **high voltage tests** (**dielectric tests**) are of special significance for verifying

insulation quality. It must be noted that dielectric strength is dependent on the *duration of the stress*, Figures 3.4.1-1 and 3.5-1. For the design of oil gaps in transformers, different dielectric test levels, the so-called *rated insulation levels* or *design insulation levels* (DIL), are applied for chopped-wave lightning impulse voltage (LIC), for full-wave lightning impulse voltage (LI), for switching impulse voltage (SI), for AC voltage for one minute and for AC voltage for one hour, Figure 7.1.3-13. Accordingly, the *dielectric test stresses* acting for different durations are staggered in their levels, Tables 6.1-2, -3 and 7.1.3-2.

The **type of tests to be carried out** is based on the highest voltage for equipment V_m (highest r.m.s. value of voltage between two phases, for which the insulation is designed), Table 7.1.3-1. In the case of the induced voltage tests, the test levels are determined in relation to the rated voltage V_r, Figure 7.1.3-14, but may also be related to V_m for the tests with partial discharge measurements, cf. Sections *e)*, *f)* and *g)* below. Generally, the amount of testing for the routine tests increases with the voltage: For $V_m > 72{,}5$ kV, partial discharge measurements (IVPD) and full-wave lightning impulse voltage withstand tests (LI) are mandatory. For

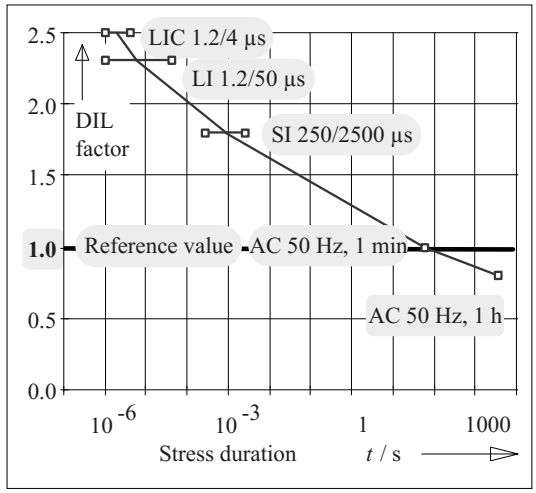

Figure 7.1.3-13:
Design values for the electric strength of oil gaps as a function of stress duration in comparison to the one-minute AC voltage strength (r.m.s. value), expressed as a Design Insulation Level (DIL) [274].

Table 7.1.3-1: High voltage tests on power transformers (selection) according to IEC 60076-3 [52].

Insulation	**Highest voltage for equipment** V_m	**Tests**					
		Lightning impulse voltage		**Switching impulse voltage**	**Applied AC withstand voltage**	**Induced voltage** *(e)*	
		Full wave LI *(a)*	**Chopped wave** LIC *(b)*	SI *(c)*	AV *(d)*	**Withstand test** IVW *(f)*	**Test with PD measurement** IVPD *(g)*
Uniform	$V_m \leq$ **72.5 kV**	**Type test**	Special test		**Routine test**	Routine test ⟶	Special test *)
Uniform**)	$V_m >$ **72.5 kV**	**Routine test**	Special test	Special test	**Routine test**	Routine test ⟶	**Routine test *)**
Non-uniform**)	$V_m \leq$ **170 kV**	**Routine test**	Special test	Special test	**Routine test**	Routine test ⟶	**Routine test *)**
Uniform and non-uniform	$V_m >$ **170 kV**	Included in LIC ⟶	**Routine test**	**Routine test**	**Routine test**	Replaced by SI	**Routine test**

Note *): The requirements of the IVW withstand test can be incorporated in the IVPD test with PD measurements so that only one test is required.

Note **): Differences refer to tests that are not shown in this table (Line terminal AC withstand test LTAC, cf. [52])

V_m > 170 kV, withstand tests with chopped-wave lightning impulse voltage (LIC) and switching impulse voltage (SI) must additionally be performed, but the latter replace the short duration induced voltage withstand test (IVW).

The **test voltage levels**(dielectric test levels, insulation levels) are stated in the relevant standards [290], [291], [52], an extract for V_m > 170 kV is given in Table 7.1.3-2. Up to V_m = 170 kV, the values largely correspond to the values in Table 6.1-2. Additionally, chopped-wave lightning impulse witstand voltages (LIC) are specified that are 1.1 times the LI peak values. Furthermore, a few additional test voltage values are also given which represent common practice in some parts of the world or which can be used in some special cases.

Table 7.1.3-2: Test voltages for withstand voltage tests on transformers related to the highest voltage for equipment winding V_m > 170 kV

V_m	**LI**	**SI**	**AV** or **LTAC**
r.m.s. value	peak value	peak value	$\frac{\text{peak value}}{\sqrt{2}}$
kV	kV	kV	kV
245	**650**	**550**	**275**
	750	**620**	**325**
300	**850**	**700**	**360**
	950	**750**	**395**
362	**1050**	**850**	**460**
	1175	**950**	**510**
420	**1300**	**1050**	**570**
	1425	**1175**	**630**
550	**1550**	**1300**	**680**
	1675	**1390**	
	1800	**1425**	
800	**1950**	**1550**	
1100	**2050**	**1700**	
	2100	**1675**	
1200	**2250**	**1800**	

Note: ***LIC values (chopped wave)*** *are calculated from LI values (full wave) by multiplying with a factor 1.1.*

Note: Some of the values are not in accordance with IEC 60071-1 but they represent existing practice in some parts of the world.

Note: Dotted lines represent special cases.

Note: The table represents values given in IEC 60076-3 in extracts only.

a) Full-wave lightning impulse voltage tests (LI)

Fast rising voltages cause voltage distributions within the transformer that are determined mainly by the *capacitances* and by the *resonant behavior* of the whole system. Thus, the voltage distributions and dielectric stresses can be completely different from those during AC and switiching impulse stresses. Therefore, testing must be performed accordingly with a fast rising voltage impulse, the so-called **full-wave lightning impulse voltage**. Testing the winding terminals with full-wave lightning impulse **withstand voltage** shall verify the lightning impulse voltage strength between the *terminals* and ground, between the terminals and the remaining windings and *along the tested winding* [52], [292].

For oil-filled transfomers, test with *negative polarity* is recommended to avoid external flashovers. After a *calibrating shot* (reference impulse with a voltage between 50 % and 70 % of the full test voltage), three *full-wave impulse tests* must be withstood. The test is successful if there are no significant differences between voltage and current transients recorded from the reference impulse and those recorded from the full test voltage.

Note: Current transients are a very sensitive indicator of impedance changes and internal faults, see below.

All the winding terminals to be tested are stressed successively in the impulse voltage test sequence. The other winding terminals are grounded directly or via low resistances. In the case of a *delta connection*, two phase windings are always in parallel with the test voltage.

Note: One, more or all of the impulses may be specified by the purchaser's enquiry and order to be of *positive poalrity*. Then, additional reference impulses may be necessary and the test sequence shall be agreed between manufacturer and purchaser [52].

If **non-linear elements** or **surge arresters** are built into the transformer for the limitation of overvoltages, they may operate during the test and cause differnet voltage and current curves

at different test voltage magnitudes. Thus, a direct comparison between reference impulse and test impulses is not possible any more. The test sequence shall at least contain a reference impulse below the threshold value of the non-linear elements. Therefore, three reference impulses a) with 50 to 60 %, b) with 60 to 75 % and c) with 75 to 90 % of the full test voltage magnitude are recorded. After the three full test voltage impulses, the reference impulses are repeated as accurately as possible in the reversed order. The test is successful if the transient impulse voltage and current curves do not differ significantly at the same test voltage magnitude and if the successive impulses exhibit curves that can be expected from the behavior of the non-linear elements. Further information is given in IEC 60076-3 and -4.

In the case of lightning impulse voltage tests on transformers, it is especially difficult to attain the standardized **test voltage parameters** within the permissible tolerances ($T_1 = T_f$ = 1.2 µs ±30 %, $T_2 = T_h$ = 50 µs ± 20 %, overshooting ≤5 %, back swing ≤ 50 %, test voltage ± 3 %), cf. Section 6.2.3. Therefore, IEC 60076-3 describes a number of special rules and exceptions for impulse tests on transformers:

In particular, high winding capacitances slow down the *voltage rise* and increase the *front time*. This can be counteracted by decreasing the damping resistance in the impulse circuit. However, the condition for overdamping is often violated as a result of this, and hence *oscillations* are superimposed on the voltage waveform.

Note: Depending on the given situation, IEC 60076-3 [52] gives the following guidelines:

- If the maximum relative overshoot magnitude is 5 % or less, the test voltage value may be taken from the measured voltage waveshape as the extreme value $\hat{V}_{test} = \hat{V}_{extr}$ according to Section 6.2.3.4 and Figure 6.2.3-9.
- If the maximum relative overshoot exceeds 5 % the damping resistance and the front time may be increased to reduce the overshoot. For transformers with $V_m \leq 800$ kV, the front time shall not exceed 2.5 µs. If the relative overshoot magnitude still exceeds 5 %, then the test voltage value shall be taken from the so-called test voltage function according to to Section 6.2.3.4 and Figure 6.2.3-9. In these cases, the tested windings must receive a chopped-wave lightning impulse test, in order to provide a high-frequency stress.
- For very large transformers with $V_m > 800$ kV, it might be difficult to achieve a front time of less than 2.5 µs. Then, a longer front time may be accepted by agreement between purchaser and manufacturer.

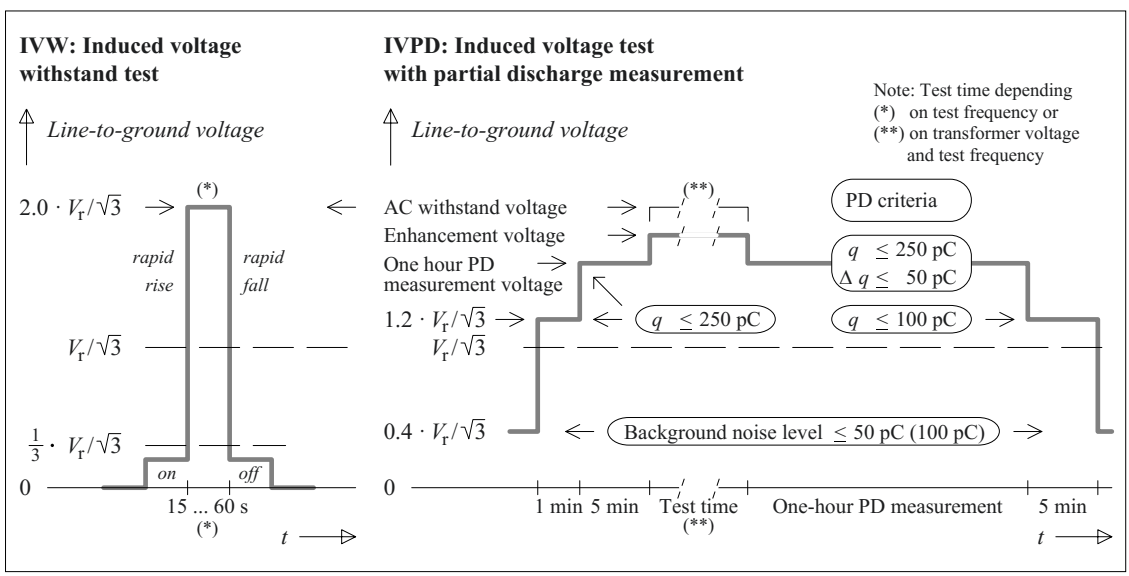

Figure 7.1.3-14: Transformer testing with induced voltage withstand test (IVW) and induced voltage test with partial discharge measurement (IVPD) according to IEC 60076-3 [291], [52].

In the *tail of the impulse voltage*, a very much slower *back-swing* can occur, since the leakage inductance of the transformer and the low-voltage-side winding capacitances form a resonance circuit that is weakly damped only. Thus, the time to zero-crossing is shortened and the time to half-value (tail time) can eventually fall below the still tolerable value of 40 µs. In this case, it can be agreed that even shorter tail times down to 20 µs may be acceptable if the thereby shortend stress duration is compensated by an increased test voltage magnitude. For each 2 µs by which the tail time is less than 40 µs, the test voltage shall be increased by 1 %..

Note: Eventually, these resonances can be damped by *resistances*, which are connected to the *low-voltage-side terminals*, to such an extend that the back swing is less than 50 % and that the tail time remains within the tolerance zone, Figure 6.2.3-10.

The criterion for a **successful impulse testing** is not only withstanding the impulse voltage. *Diagnostic statements* that can be derived from the variations of the **transient currents** are also of great significance: by comparing the currents between reference impulses at reduced voltage and test impulses at full test voltage, *turn-to-turn faults* (*interturn faults*) or mechanical *displacements* and *deformations* of windings can be detected, for example. For these measurements, the neutral point current, the winding current, the current transmitted to the adjacent windings or the tank current as well as the voltages transmitted to the untested windings are suitable [292].

Note: The **interpretation** of current comparisons necessitates special experience to be able to differentiate common variations from real fault indications. In particular, for *chopped-wave impulse voltages*, different *chopping times* can lead to varying oscillation behavior, especially to varying amplitudes. However, variations of oscillation frequencies must be assessed as critical.

Note: The **interference-free measurement** of transient currents requires a very low inductive and broadband (generally coaxial) *current measuring shunt* as well as effective *shielding measures* against the electromagnetically highly disturbed test environment, cf. Section 6.3.7 and 6.3.8. Current profiles can be **recorded** in analog or digital form, wherefore special demands are made on transient recorders with regard to *bandwidth* and *resolution* [292]. It is important that digitally recorded data are stored as **raw data** and are not subjected to further mathematical processing (filtering, smoothing), since this gives rise to the risk of deletion of fault indications.

Changes in the test object can be identified not only from the changes in the transient *current waveforms* in the **time domain**, but also from the derived *transfer impedances* or *transfer admittances* (or *transfer functions*) in the **frequency domain**, cf. Sections 6.4.6 and 6.3.7. The advantage of transfer functions is that they are no longer dependent on the test voltage waveform. For the analysis, it is recommended to use the *admittance function* $I(\omega)/U(\omega)$ since the voltage spectrum does not have any zero points [292].

Note: Partial breakdowns in the windings are evident, for example, from the displacement of poles in the admittance function, *partial discharges* from the flattening of poles and *variations in the external test circuit* from changes in the current and voltage waveforms for an unchanged transfer function [292].

b) Chopped-wave lightning impulse voltage test (LIC)

Testing with **chopped-wave lightning impulse voltage** (LIC) is performed along with the full-wave lightning impulse voltage test, in order to apply high-frequency stresses to the transformer insulation, as they can occur during breakdowns, resonance excitations or transient overvoltages. The *peak value* must be *1.1 times* the full impulse voltage amplitude; the **chopping time** must be between 3 and 6 µs.

Note: A *chopping time* between 2 and 3 µs can be accepted if there is an according agreement and if the peak value of the test voltage is achieved before the chopping.

The *breakdown of the test voltage* shall be as fast as possible and the time to the first zero-crossing shall be as short as possible. Thus, no additional impedances shall be used in the chopping circuit. Nevertheless, the *back-swing*

of the test voltage must be restricted to 30 % in order to avoid high stesses with opposite polarity. If necessary, damping of the chopping circuit must be performed with the lowest possible impedance required for this purpose.

The *test sequence* is combined with the full-wave impulse voltage testing:

Impulse number	Impulse type	Impulse waveform	Impulse peak value
1	reference	full	50 … 70 %
1	**test**	**full**	**full**
2	**test**	**chopped**	**enhanced**
2	**test**	**full**	**full**

The test is successful if there are no significant differences between voltage and current transients recorded from the reference impulse and those recorded from the full test voltage.

Note: If *non-linear elements* or *surge arresters* are built into the transformer, three reference impulses a) with 50 to 60 %, b) with 60 to 75 % and c) with 75 to 90 % of the full test voltage magnitude are recorded. After the full-wave test voltage impulses and the chopped-wave test impulses, the reference impulses are repeated as accurately as possible in the reversed order.

c) Switching impulse voltage test (SI)

Slowly rising voltages cause voltage distributions within the transformer that are determined mainly by the *turn ratios* and by the behavior of the *magnetic circuit*. Thus, the voltage distributions and dielectric stresses come close to those during AC and switiching impulse stresses. Therefore, testing must be performed accordingly with a slowly rising voltage impulse, the so-called **switching impulse voltage**. Testing with switching impulse **withstand voltage** shall verify the switching impulse voltage strength for the terminals and the connected windings to ground and to the other windings. It is an important requirement for transformers that are subject to a long-duration test with induced AC voltage (IVPD), especially *when short-duration induced voltage withstand testing (IVW)* at high test levels is *not* provided or is *not* possible.

Note: The *switching impulse duration* is similar to the duration of a *power frequency AC half-wave.* Consequently, the *dielectric strengths* of insulations are comparable for both the switching impulse stress and the short-duration AC stress. Especially for transfomers with very high rated voltages, it would be difficult to provide the required very high AC test levels, and the switching impulse voltage test is chosen instead of this. According to Figure 7.1.3-13, there are differences between the dielectric strengths at SI and AC (1 min) which must be regarded by choosing differently high test voltages.

Testing with *negative polarity* is recommended to avoid external flashovers. After a *reference impulse* of a voltage between 50 % and 70 % of the full test voltage, *three full test impulses* must be withstood. In order to avoid the influence of magnetic saturation on the voltage waveform of successive impulses, *demagnetizing impulses* with opposite polarity and reduced level are necessary after each test impulse.

The termials of a winding to be tested are grounded on one side (at the neutral point, if present) and connected to the impulse generator on the other side. The transient current is always measured on the grounded side. Then all the windings are stressed successively in the impulse voltage test sequence.

The test is *assessed* by comparing the recorded transient voltages and currents.

In order to avoid the magnetic saturation of the iron core, the **impulse voltage waveshape** is purposely different from the standard waveshape of 250/2500 µs which is intended for equipment without saturable magnetic circuit. The waveshape should exhibit a *time to peak* of at least 100 µs, remain above 0.9 $\hat{V}$ *for* at least 200 µs and exhibit the first zero crossing (*time to zero*) after 1000 µs at the earliest.

Note: Considering the given limits for the maximal magnetic flux density that is possible without saturation, the *shortening of time to peak* and time to zero is necessary as *higher induced test voltages* can only be

achieved by a faster changing voltage (i.e. by a *higher derivate of the voltage with respect to time*). Because of the same reason, also AC testing must be performed at higher testing frequencies (e.g. at 100 Hz or 120 Hz instead of 50 Hz or 60 Hz respectively).

d) Appplied AC voltage test (AV)

Tests with an externally **applied withstand AC voltage** (external voltage) should verify the *AC voltage strength of the tested winding and of their terminals* against ground and against the other windings and parts of the transformer which all are grounded.

The voltage is applied as a single-phase AC voltage to all the terminals of the tested winding, including the neutral terminal. Thus, there is *no* turn-to-turn voltage, and the AV test can *not* replace an induced voltage test.

Tests last for 60 s, approximately at the rated frequency f_r (i.e. $f \geq 0.8\ f_r$). The test voltage value is the measured peak value divided by $\sqrt{2}$. The magnitude of the test voltage depends on the transformer design, for the details refer to IEC 60076-3 [52].

e) Induced AC voltage tests

Tests with **induced AC voltage** are performed with the transformer connected and excited exactly as it will be for service. Testing is carried out by excitation of the test object on the low-voltage side or by excitation from another winding being suited for that purpose. Then, symmetrically induced AC voltages appear at all the line terminals, with no voltage at the neutral. Also, turn-to-turn voltages are induced. The test is performed with a single phase voltage on a single phase transformer and with a three phase voltage on a three phase transformer respectively.

In order to reach the increased test voltage level at a given magnetic flux which is limited by saturation of the magnetic core, *increased frequencies* are necessary. If the induced voltage shall approximately be doubled in comparison with the service voltage, also the frequency must be doubled (100 or 120 Hz instead of 50 or 60 Hz respectively) at a given magnetic flux density, cf. Section 6.2.1.1.

There are two types of tests with induced voltages, Figure 7.1.3-14:

- The **induced voltage withstand test** (IVW) is a *short-duration withstand test* at approximately twice the rated voltage, cf. Section *f)*. It shall verify the withstand strength of the insulation against short-duration AC overvoltages.
- The **induced voltage test with partial discharge measurement** (IVPD) is a *long-duration test* with an *enhancement voltage* and a *one-hour PD measuring phase*, cf. Section *g)*. The test shall verify that the transformer will be free from hamful partial discharges under normal operating conditions.

Both tests can be combined, if the enhancement voltage level in the IVPD test is raised up to the withstand voltage level of the IVW test.

For the determination of the *test voltage value*, both the r.m.s. value and the peak value divided by $\sqrt{2}$ are measured. The lower of both the values is considered as the test voltage value.

f) Induced voltage withstand test (IVW)

The **induced voltage withstand test** (IVW) is performed for transformers with $V_m \leq 170$ kV according to Section *e)*. The test is intended to verify the *short-duration* AC withstand strength of all *terminals* and *windings* among each other and against earth as well as the strength *along the windings*.

The test voltage (phase to earth) is $2 \cdot V_r / \sqrt{3}$ and the test duration at full test voltage is 60 s, Figure 7.1.3-14 (left). However, if the test frequency f_T exceeds twice the rated frequency f_r, the test duration t_T is reduced, maintaining the number of periods.

$$t_T = (120\ \text{s}) \cdot f_r / f_T \qquad (7.1.3\text{-}6)$$

In any case, test duration must not be less than 15 s.

Note: The *partial discharge behavior* of the transformer is not investigated during the induced voltage withstand test (IVW) but during an additional test with *long-duration* partial discharge measurements (IVPD), see below and Figure 7.1.3-14 (right).

Note: For *transformers with higher voltages* (V_m > 170 kV), short-duration withstand capability against overvoltages is verified by the switching impulse withstand voltage test (SI), cf. Section *c)*.

g) Induced voltage test with PD measurement (IVPD)

The **induced voltage test with partial discharge measurement** is intended to verify that transformers with V_m > 72.5 kV will be *free of harmful partial discharges* under normal operating conditions and after short-duration AC overvoltages. For transformers with $V_m \leq 72.5$ kV, the test can be applied as a special test. The **test sequence** (i.e. test voltage vs. test duration) and the related *partial discharge criteria* are definded according to Figure 7.1.3-14 (right):

- The *background noise level* at $0.4 \cdot V_r / \sqrt{3}$ must be below 50 pC (or 100 pC for shunt reactors resp.) both before the test and after the test. These levels are defined with respect to the achievable background noise levels in the high voltage transformer test fields.
- At the beginning of the test, a *test voltage* of $1.2 \cdot V_r / \sqrt{3}$ and the so-called *"one-hour PD measurement voltage"* of $1.58 \cdot V_r / \sqrt{3}$ are applied, at least for one minute and for five minutes respectively. The PD level must not exceed 250 pC in these cases.
- In order to see whether enhanced AC voltages can ignite additional partial discharge activity, a so-called *"enhancement voltage"* of $1.8 \cdot V_r / \sqrt{3}$ is applied for a short duration that is also given by Eq. (7.1.3-6). Only for the very large transformers with V_m > 800 kV, the test duration with the enhancement voltage is increased by a factor of 5.

  Note: If an enhancement voltage with magnitude of $2 \cdot V_r / \sqrt{3}$ is used this test can *substitute for the induced voltage withstand test* (IVW) on transformers with $V_m \leq 170$ kV, cf. Section *f)*.
- Then, the test voltage is reduced to the *one-hour PD measurement voltage* with a magnitude of $1.58 \cdot V_r / \sqrt{3}$. During the one-hour test, the PD level must not exceed 250 pC and must not increase by more than 50 pC. During the last twenty minutes of the one-hour test, the PD level must not exhibit any rising trend and no sudden and enduring increase must occur.

  Note: In the case of old transformers, it is assumed that intensities of 500 pC can indicate a serious insulation problem [294].
- Finally, the *test voltage* is reduced to a magnitude of $1.2 \cdot V_r / \sqrt{3}$, at least for five minutes. The PD level must not exceed 100 pC in this case. This test should verify that the transformer is free of partial discharges even after preceding AC overvoltages.

Note: For the one-hour PD measurement voltage and for the enhancement voltage, *higher voltage levels* may be used if specified by the purchaser. In particular, a *one-hour PD measurement voltage* of $1.5 \cdot V_m / \sqrt{3}$ and an *enhancement voltage* of $\sqrt{3} \cdot V_m / \sqrt{3}$ may be used if higher.

Amongst others, also the quality of the impregnation and the formation of gas in the insulating oil can be detected from the results of the *partial discharge measurements*. Partial discharge measurements should therefore be carried out *after the* withstand voltage tests. With the occurrence of discharges, the transformer must not be rejected immediately; a specific waiting time can possibly lead to the dissolving of free gas bubbles and the disappearance of partial discharges. If not, additional diagnostic measures are necessary, e.g. by acoustic localization attempts.

7.1.3.6 Operation, Diagnosis and Maintenance

a) Thermal stressing

During service operation of the transformer, **thermal stressing** of the oil and paper owing to heat loss in the core (no-load loss) and owing to ohmic loss in the windings (load-dependent loss $\sim I^2$) plays an especially important role: heavy continuous loads, associated with high continuous temperatures, accelerate the ageing of oil and paper, while transient excess temperatures damage the cellulose.

The permissible **hot-spot temperatures** at the conductor surface are considered to be 120 °C for continuous operation and 140 °C for short duration (for a maximum of 30 min at 1.5 times rated current) [251], [295], [296]. At these temperatures, severe ageing already occurs [305]. For example, a continuously *highly loaded generator transformer* ages considerably faster than an only *moderately loaded line transformer*. Therefore, cooling as well as monitoring and regulation of temperatures have great significance for long-term maintenance of value. Supporting monitoring systems were described in Section 6.4.8.1.

The loading capacity and overload capacity of oil-filled transformers is given with regard to load magnitude and load duration in the standards (IEC 60076-7 [295], [296]). Important parameters are the *ambient temperature* and the *cooling method*. If the permissible **continuous load** at 20 °C is specified as 100 %, then, depending on the cooling method, a higher continuous load is permissible at lower ambient temperatures (e.g. 124 % to 137 % at -25 °C) and a lower continuous load is permissible at higher ambient temperatures (e.g. 81 % to 87 % at 40 °C). *Deviations* from this are possible in the following situations:

1. **Normal load fluctuations** which do not yet lead to accelerated ageing, can temporarily be 1.5 times or 1.3 times higher than the above-mentioned continuous load (for small and medium or for large transformers respectively). Phases with increased load must be compensated by longer phases at lower load in order to compensate for the consumption of service life.

2. If necessary, **longer lasting overloads** up to 1.8, 1.5 or 1.3 times the contiuous load are possible (for small, medium or large transformers), sometimes even for *weeks or months*. In these cases, an increased *rate of using life* is permitted, but without thermal decomposition of the insulation (pyrolysis) and without exceeding the maximum temperatures in the steady state.

3. For a very **short-duration emergency operation**, whose duration is less than the thermal time constant of the transformer and which should *not exceed 30 minutes*; overloads up to 2.0, 1.8 or 1.5 times the nominal power are permitted. In these cases, a distinct *rate of using life* occurs. The *transient temperature characteristics* would exceed the maximum permissible *thermal limits* if the duration were too long, Figure 6.4.8-1 (right).

Note: The above-mentioned load factors for *small, medium and large transformers* are related to nominal apparent powers up to 2.5 MVA, up to 100 MVA and above that.

In the case of large transformers, monitoring of the above-mentioned conditions and the knowledge of thermal reserves require an exact image of critical temperatures, which generally *cannot be measured directly*. Nevertheless, transient temperature characteristics can be calculated simultaneously with the varying load by means of detailed **equivalent thermal networks** [304], Figure 6.4.8-1 (right) and 6.4.8-2. Thus, *prognoses* can be made for hot-spot temperature which cannot be measured directly and for the maximum *permissible duration* of an overload state.

Note: The thermal loading capacity of transformers is not only determined by heating up of windings and oil. Thermal limits must be regarded also for the connected *components* (**bushings** and **on-load tap changers** [297]). Owing to comparatively very *short thermal time constants*, the components can significantly and temporally restrict the overload capacity of the

transformer. For the specification of components, this must be taken into consideration through the specification of correspondingly higher nominal values.

b) Ageing, damaging and diagnosis

After year-long or decade-long service operations, it is practically impossible for the operator to estimate the insulation condition and residual service life. **Ageing** and **damaging** can occur during operation owing to *thermal loads* (hot-spot temperatures), *electrical discharges* (partial discharges, arcs), *chemical influences* (oxidation, hydrolysis, electrolysis, catalytic reactions) or *mechanical loads* (short-circuit current forces, easing of bracings). Moreover, changes in the **components (***bushings, on-load tap changers, magnetic circuits, cooling system, control system and monitoring system)* must be considered.

Attempts to identify an *up-to-date insulation conditions* are made using a large number of **diagnostic methods** that are explained in Section 6.4. A consistent picture is generally obtained only by taking multiple indicators into consideration, on the basis of relevant standards and experiences as well as by *trend analyses* of different parameters [294], [298], [299], [300], [301]. Therefore, in the following sections only a few fundamentals can be described, a few *critical values* are mentioned in brackets as a very rough *guide*:

Oil analyses are of outstanding significance owing to easy availability of oil samples: **reduction of dielectric strength** of oil can be detected directly by *breakdown voltage measurements* (> 30... 50 kV [301], Figure 3.4.2-3) and indirectly by measuring *relative water content* (w_{rel}< 20... 30 % [294], Figure 3.4.2-1) and *particle concentration*. Progressive **ageing** can be identified by the *change in the color* of the clear insulating oil from yellow to dark brown, by an increase in the *dissipation factor* (< 0.3... 1 % at room temperature [298], [294] and < 100 % at 90 °C respectively [301]), by the *acidity* (neutralization number < 0.18... 0.5 mgKOH/g [294], [298], [301]), by the *interfacial tension* (> 24 dynes/cm [294]) or by the formation of insoluble *sludge*.

Gas-in-oil analyses are the most effective tool for detection and classification of **thermal, electrical and chemical defects,** Section 6.4.3.2 [300].

Analyses of paper samples provide *direct evidence* of the properties of solid insulation. But the sampling is very complex, destructive and generally not representative, since samples can be extracted only from the edge areas and never close to the hot spot. Complete or critical **loss of mechanical strength** of cellulose fibers can be detected from the fiber length, i.e. at *average degrees of polymerization* (DP-values) below 200 or 400 respectively [299]. **Dielectric strength, rate of ageing** (Figure 3.5-6) and **thermal loading capacity** (Eq. 6.4.8-1) depend on the *water content of the paper*, which should be normally below 2% [294].

Indirect statements about **paper quality** are possible via *gas chromatography analyses and liquid chromatography analyses* of the oil. **Decomposition of paper** is indicated by *CO* (< 1400 ppm), CO_2 (< 10000 ppm) and *furfural* (< 15 ppm) [299]. For *furanes*, an approximate relationship to the *average degree of polymerization* is specified (250 ppb corresponds to DP 400, 1000 ppb corresponds to DP 330 to 230, 2500 ppb corresponds to DP 200 [299]).

Note: The determination of the *water content in paper* from the water content in the oil with the aid of *equilibrium curves* is not possible or only possible in a very inaccurate manner, since the setting of *equilibrium states* would require constant temperatures over very long periods. Generally, these equilibrium states cannot be reached for transformers in the field.

Dielectric measurements are to an incrasing degree used for the analysis of **water content in paper**, cf. Section 6.4.7. Interpretation requires good experience to be able to isolate the parameters oil conductivity, geometry, ageing and water content [231], [237]. Although measurements can be carried out selectively between individual windings, a more precise

spatial resolution is not possible, and hence the moisture profiles, which are definitely present within the insulation, cannot be identified, Section 6.4.7.2.

Power frequency dissipation factors and **insulation resistances** of the main insulation between the windings can be sharply increased owing to severe **ageing of oil** or by **conductive deposits** on the insulating material surfaces. *Dissipation factors* should remain below 0.9 to 2 % [298], [294].

Electrical repeat tests are rarely used on service-aged transformers for diagnostic purposes owing to the related efforts. Retests are carried out with *reduced test levels*, for example with 80 %. Hence, *partial discharge measurements* (q < 500 pC [295] or 500... 2500 pC respectively [298]) as well as the comparison of *transfer functions* are especially suitable for diagnosis, Sections 7.1.3.5, 6.4.2 and 6.4.6.

For strategically important large transformers in the power grid, even *online monitoring* can be economically justified to detect rapidly progressing defects, even between routine checks, Section 6.4.8.1.

c) Maintenence of value

Also for transformers, a fall in the dielectric, mechanical and thermal strength occurs in the course of normal ageing. Additional damage can accelerate the loss in strength, Figure 7.1.3-15. Previously, maintenance activities or reinvestments were undertaken after specific time intervals had elapsed (*time-based maintenance*). Since large transformers are highly expensive operating equipment, it is now common to carry out measures for the maintenance of value on the basis of diagnostic condition analyses to attain a maximum possible service life (*condition based maintenance*), Figure 7.1.3-15. It is also feasible to operate a transformer until the actual breakdown (*event-based maintenance*). However, this strategy is only useful for small transformers that can be directly replaced and in which measures for the maintenance of value would be disproportionately expensive.

Measures for the conservation of value and for the life extension of oil transformers are especially

- oil processing or oil exchange if need be,
- drying the insulation,
- replacement of windings as well as
- maintenance and exchange of components (on-load tap changers, bushings, gaskets).

In the following section, mainly the first two points are taken into consideration [299].

Oil is especially damaged by the absorption of gas (oxygen), water, deterioration products (acids, sludge) and particles as well as by the decomposition of inhibitors.

Water or **moisture** and **gas** in oil can be simultaneously eliminated by a *vacuum-degassing system*, Figure 5.4.2. The costs necessary for the application of heat and vacuum must be considered. Furthermore, owing to the corresponding partial pressure gradients, water and oxygen can be removed rapidly and effectively from the oil by *blowing-out with dry nitrogen*. This results in a reduction of ageing accelerating components O_2 and H_2O, however saturation with nitrogen occurs. Drying and elimination of oxygen is also possible by the formation of *nitrogen foam* at low air pressure. Water alone can be eliminated with

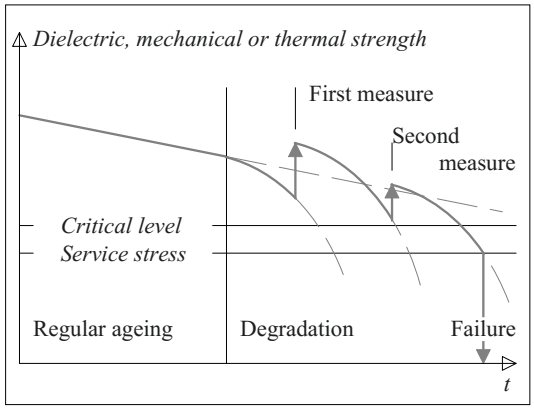

Figure 7.1.5-15: Measures for the maintenance of value on transformers (schematic representation).

the aid of *water absorbing (hygroscopic) filter materials* (cellulose, molecular sieve, zeolites [306], micro-fiber glass). The saturated filters must be replaced or regenerated (dried) in time; moreover the release of particles (e.g. cellulose fibers) must be avoided.

Particles (e.g. moist fibers, metal, and carbon) must be separated from the oil by *filtration*. For a good filter efficiency (even for small particles), oil flow rate, filter and pore size must be coordinated. The filter on its own must not act as a source of fibers or bubbles formed by partial vacuum. Filtering in the bypass is less effective than filtering during draining of oil and refilling with oil.

Sludge and **deterioration products**, which increase the dissipation factor of oil, can be absorbed by *aluminum silicate* (bleaching earth, fuller's earth). Residues of low solubility in the solid insulation must be dissolved away by *flushing oil* or by the operating oil at increased temperatures. For heavy accumulations of sludge, the surfaces must be *sprayed* or *washed* with oil and also subjected to heat-vacuum cycles.

The **water content** (or the moisture resp.) **in solid insulation** practically cannot be reduced by (one-time) drying of oil, because the oil comprises only a few 10 ppm, but the cellulose contains a few percent of water. Concentration difference amounts to about a factor of 1000 and the major proportion of water (approx. 99 %) is bonded in the cellulose. **Effective drying** can be achieved in various ways with *high temperatures* in the insulation and low *water saturation vapor partial pressures* in the environment:

1. Multiple circulation of **hot oil (**85 to 100 °C) through the transformer and degassing system.

2. **Spraying** of windings with hot oil (90 to 120 °C) under **vacuum** at 5 - 10 mbar, fine drying at 1 mbar.

3. **Combination processes** with cyclic hot air heating and spray oil heating as well as cyclic vacuum drying and oil circulation drying.

4. **Vapor-phase drying** by evaporation and condensation of a solvent for heat transmission to the windings, with separation of condensate and water, with subsequent re-evaporation of the solvent by pressure reduction and with a fine-drying phase under vacuum [302].

5. Resistive **heating of windings** at 110 to 120 °C with direct current or alternating current of low frequency *(LFH Low-frequency heating)*, draining of oil, drying under **vacuum** and filling with reclaimed oil; repetition of the cycle if necessary [307].

Note: Moisture-containing solid insulation shrinks owing to the removal of water during drying and hence the *bracing of windings can be loosened* during intensive drying.

Note: Drying tests with the LFH method on a 110 kV / 31.5 MVA transformer (year of construction 1955, sorted out) resulted in *reduction of water content* from 2 to 2.7 % down to 0.5 to 1.5 % (measured with Karl Fischer titration on material samples). The reduction depended on the position and thickness of the barriers, strips, moldings and thrust pads made of pressboard. The *winding pressure* is reduced by up to 30 %, which corresponds to a winding length variation of nearly 0.1 %, similar to what would also occur when cooling the transformer by 40 K [308].

Online measures for permanent cleaning and drying of oil use the oil which is circulated in a bypass as a *transfer medium*. Thereby, water and deterioration products can be removed from the windings (very slowly and over a long period of time). Even for a short-time processing, the removal of particles and water from the oil has a strength increasing influence.

The operation of transformer must not be hampered by the drying systems, e.g. owing to the risk of oil losses, gas bubble formation or heating of oil. This can be achieved, for example, by connecting the drying system to the oil expansion vessel.

Note: If the fault gases present in oil are to be retained as indicators for the *gas-in-oil analysis*, no degassing under vacuum must be carried out for the drying of oil. Instead, only *absorption in hygroscopic filter materials*, such as cellulose [303] or zeolites [306], may be used. Cellulose filter should be cooled so that a higher water

content can result in the filter than in the insulation of the transformer.

Note: Online oil drying is not so much a measure for subsequently drying a heavily wetted transformer. It is more appropriate that, even for *newer transformers,* online drying systems are used *preventively* in order to compensate for the slow wetting process with a (likewise slow) dehumidification process.

7.1.4 Capacitors

High voltage capacitors for AC voltages are used in various applications, Figure 7.1.4-1:

- In high voltage circuit-breakers in the open state, with multiple breaker gaps connected in series, **grading capacitors** guarantee a well-defined capacitive voltage distribution.
- **Coupling capacitors** are used as *carrier-frequency coupling devices* for coupling high frequency signals into power lines. Coupling capacitors are also used for the decoupling of pulse-shaped *partial discharge signals* in laboratories, in test fields or for monitoring of equipment.
- **Compensation capacitors (power-factor correction capacitors)** are to compensate for the lagging reactive power in the grid.
- **Measuring capacitors** as reference capacitors in bridge circuits, as capacitive series impedances, as impedances in capacitive voltage dividers and as coupling capacitors for decoupling partial discharge impulses.

Note: Special features of **DC capacitors and impulse capacitors** are discussed in Sections 7.2 and 7.3.

Capacitors consist of a *housing* and an "*active part*", which consists of a highly stressed dielectric between two electrodes. Depending on the application, various forms of housings, bushings and connections are used, Figure 7.1.4-1.

7.1.4.1 Structure of the Dielectric

For optimal utilization of the volume available, a dielectric which allows the maximum possible *energy density*

$$w = \tfrac{1}{2}\,\varepsilon E_{\max}^{2} \qquad (7.1.4\text{-}1)$$

must be chosen. Above all, the dielectric must exhibit a high *permissible field strength* $E_{\max}$ and also a relative *permittivity* ε_r as high as possible.

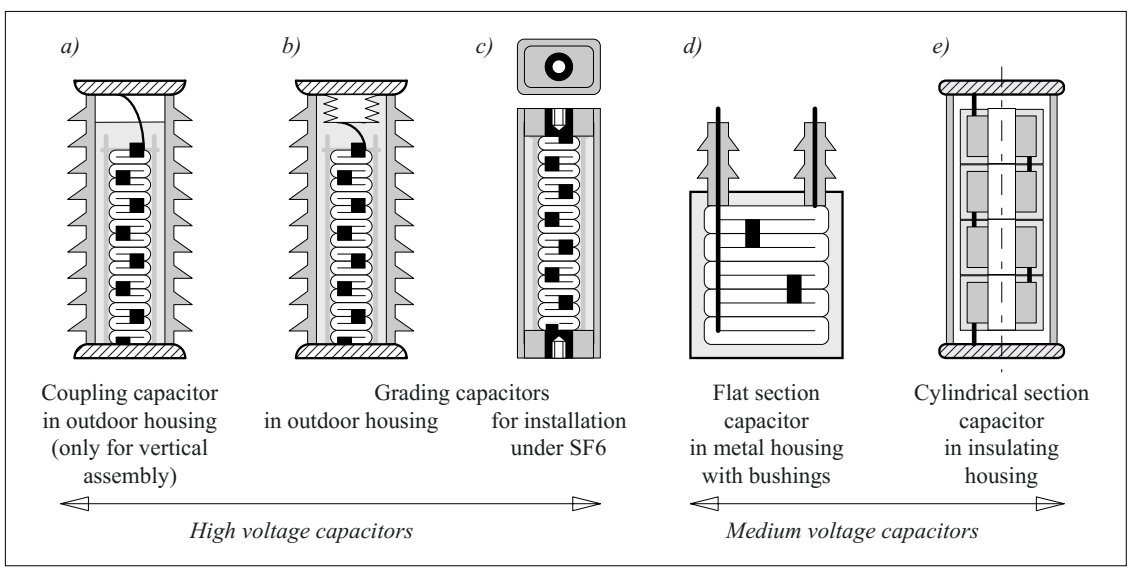

Figure 7.1.4-1: Examples of high voltage and medium voltage capacitors in various designs (schematic).

High energy densities can be achieved with *oil-impregnated paper*, with *mixed dielectrics* of paper and polymeric films and with "*all-film" dielectrics*. In the case of special requirements, the classic mineral oil is even replaced by low-viscosity synthetic insulating liquids, Section 5.4.3.3.

Capacitor elements are formed by winding paper (and/or polymeric films) with two metallic foils, Figures 5.4-7 and 5.5-9. The energy density is at a *maximum* when the dielectric is formed from only a limited number of thin layers, Section 2.4.3.3: For *large insulation thickness*, the field strength in the area with uniform field between the metallic foils is restricted to low values, because high *edge field strengths* occur at the sharp edges of the foils, Figure 2.4-20. With decreasing insulation thickness, the ratio of E_{edge}/E_0 improves and the energy density in the dielectric increases, Figure 2.4-21. For very *small insulation thicknesses*, the fixed dead volume of metal foils leads to a reduction in the resultant average energy density, Figure 2.4-20 and Eq. (2.4-37).

In practice, maximum energy density can be achieved for insulation thicknesses of several 10 µm, which generally result from windings of four or five layers of 10 to 20 µm thick *capacitor papers* and/or *polymeric films*. Short-term permissible r.m.s. values of field strength in homogeneous fields lie at about 50 V/µm (= 50 kV/mm). Owing to this, a single capacitor element can only insulate test voltages of a few kV. Therefore, high voltage capacitors are made of a *series connection* of many *individual elements*. For this purpose, the cylindrical capacitor elements are removed from the winding mandrel, pressed to form flat sections and stacked in an insulating rack. Contacting is either by metal strips that are placed in the winding (cf. Figure 5.5-10) or by the metal foils projecting out of the winding on the face sides to the left and right (Figure 2.4-20 top).

Note: The type of contacting and the position of the contact strips influences to a large extent the contribution of a capacitor element to the *inductance* of the electrical circuit [113], cf. Section 7.3.3.2 (so-called "capacitor inductance"). Low inductances can be achieved, especially for flat butting contacts of all single turns on the face sides.

Increasing the permissible field strengths is not only possible by using *polymeric films* and synthetic *insulating liquids*. *Rounding of the metal foil edges* also leads to a decrease in the local electrical stess, e.g. as a result of turning over the foil edges or of laser-cut melted edges.

7.1.4.2 Drying and Impregnation

If the dielectric contains **paper**, the sections that are stacked and connected in the insulation rack are dried at increased temperature under vacuum, re-pressed and flooded with oil under vacuum, Figures 5.4-2 and 5.5-12. Capacitance compensation can be effected on the impregnated stack by opening previously established contact bridges. In this way, the short circuit is removed from adjustment elements. After assembly of the stack in the housing, evacuation, flooding with oil and final pressurization are carried out.

In **mixed dielectrics**, papers and polymeric films are wound one upon the other. Thereby, paper serves as an *impregnating wick*, by means of which the impregnating agent infiltrates into the volumes between the films, Figure 5.3-6. Gaps that are not in contact with the paper can also be impregnated (with delay) by diffusion through the polymeric films. During service operation, mixed dielectrics are not stressed uniformely any more: Owing to *field displacement,* electrical stress in the polymeric films is generally increased and in the papers generally reduced. Thereby, the *paper volume* contributes less to energy storage and should therefore be kept as *small* as possible. Moreover, the dielectric strength of the paper often establishes the limits for the strength of the whole dielectric.

In **all-film capacitors**, paper is totally dispensed with in order to be able to fully utilize

the high dielectric strength of the polymeric dielectric. Nevertheless, impregnation is possible with *low-viscosity insulating liquids* (Section 5.4.3.3), but it requires a rough or embossed surface of the polymeric films, Figure 5.3-6. An adequate *space factor* between the films, which lie upon each other, is a prerequisite for impregnation. Loosely stacked windings are directly dried *in the housing* for a brief period under vacuum, impregnated and re-pressed in the "wet" condition, see Figure 5.4-7.

For gas-insulated switchgear, all-film capacitors can also be designed **oil-free** with SF_6 gas impregnation in a closed and pressure-tight insulating housing.

7.1.4.3 Capacitor Designs

Capacitors in the **high voltage range** mostly have an *insulating housing*, because no volume for transverse insulation is lost and because additional high voltage bushings are unnecessary in that case, Figure 7.1.4-1 a), b), and c). In order to maintain a practical construction height during the series connection of many capacitor sections, high voltage capacitors are generally stacked with flat elements and not cylindrical elements. In the **medium voltage range**, the complexity of transverse insulation and bushings is significantly lower, so that even *rectangular metallic housings* are used. Along with flat capacitor elements, they offer advantageous space utilization, Figure 7.1.4-1 d).

Capacitors for *outdoor installation* require a weather-resistant **housing** with an appropriate creepage path extension, Figure 7.1.4-1 a) and b). Porcelain insulators with sheds are largely used. For *indoor installation* or for application under *compressed gas* (e.g. SF_6), smooth or slightly profiled insulation housings are adequate. In capacitors having an upright position, the **thermal expansion** of the dielectric and impregnating liquid can be compensated by a *gas cushion* (generally, N_2), Figure 7.1.4-1 a) and e). For liquid-filled capacitors, any desired mounting position is possible by using *expansion bellows* or *expansion cells*, Figure 7.1.4-1 b), or by using *deformable rectangular housings* for the compensation of thermal expansion in the completely liquid-filled housing, Figure 7.1.4-1 c) and d). Thus, especially compact designs are created for use in gas-insulated switchgear; also cf. Figure 5.4-1.

7.1.4.4 Measuring Capacitors

Measuring capacitors must fulfill special requirements. In many cases they are therefore quite different from the described designs.

First of all, **oil-impregnated flat section capacitors** are used as *coupling capacitors* in partial discharge measuring circuits and as high-voltage capacitors in capacitive *voltage dividers*. For this, it must be checked whether the voltage dependence of the capacitance is within tolerable limits. In the case of special requirements, the temperature dependence of a capacitance can be compensated by a combination of dielectric materials with different temperature coefficients of relative permittivity.

For special requirements of linearity, i.e. of capacitance stability with respect to voltage, temperature and frequency, so-called **compressed-gas capacitors** can be used. They are insulated with compressed gas and designed with geometrically well defined capacitance in a guard ring arrangement, Figure 6.4.1-3. As a result of the guard ring arrangement, no sensitivity with respect to earth stray capacitances occurs in *compressed-gas dividers.* Compared to other technical insulating materials, the dielectric is extremely low-loss, linear, and insensitive regarding temperature and frequency. Therefore, it is well suited for *reference capacitors or standard capacitors* in bridge circuits, Figure 6.4.1-1. However, owing to the large insulation distances in gas insulations, only relatively small capacitance values are possible.

7.1.5 Circuit-breakers

The task of power circuit-breakers is the reliable interruption of *operating currents and short-circuit currents* as well as the safe insulation of the *recovery voltage* across the opened switching contacts [20], [47], [186]; cf. Section 3.2.7.2. For the selection of a circuit-breaker, above all the specific *current characteristics* of the breaker, such as

I_r rated current,

i_p peak short-circuit current,

I_{th} thermally equivalent short-time current

as well as

I_b symmetrical short-circuit breaking current

must be compared with the actual stresses occurring in the electrical power network. In the case of short-circuit currents with initial aperiodic components (so-called "DC components"), the stressing of the interrupter assembly is greater and more powerful circuit-breakes must sometimes be chosen [20].

Note: In addition to power circuit-breakers, there are other switching devices which serve for various other tasks, must not fulfil the same specifications and will not be discussed further here: For example, *disconnectors* guarantee the establishment of a safe isolating gap without having to interrupt the currents. *Grounding switches* must ensure a reliable connection to ground. *Load interrupter switches* can interrupt the operating currents and to certain degree also overload currents, but are not able to switch short-circuit currents. *Switch disconnectors* combine the functions of load interrupter switches and disconnectors [20].

7.1.5.1 Development of Switching Devices

The first high-capacity power circuit-breakers were **oil circuit-breakers**, in which the arc is burning in bulk oil after disconnecting the switch contacts. By heating up, vaporizing and decomposition of oil, as well as by heat transfer, energy is extracted from the arc until it is extinguished. The long arc extinction time (10 to 20 half waves), restricted breaking capacity and the risk of inflammation and explosion led to the development of so-called **small-oil-volume circuit-breakers** and of **oil-free circuit-breakers**. In these breakers, the arcs burn in a very narrow arcing chamber, which comprises notches for holding the liquid extinguishing medium (oil or water respectively). Here, an effective cooling of the arc is achieved by the adiabatic expansion while retracting the moving contact, by the heavily exhausting vaporized extinguishing medium and, if applicable, by an enforced liquid flow.

A very simple principle was realized for smaller switching capacities in the medium voltage range by the so-called **hard-gas circuit-breaker** (**gas-evolving circuit-breaker**). Under this, a gaseous extinguishing medium evolves as an arc decomposition gas in the form of hydrogen and crystallization water at the inner surface of an expulsion tube made of solid insulating material.

Through the development of **air-blast circuit-breakers** (**compressed-air circuit-breakers**) it is possible to abstain from any kind of extinguishing liquid. Here, the arc is blown with compressed air under 15 to 21 bar and high velocity. Thereby the arc is so intensely cooled that it is extiguished in the first or second current zero crossing. In the case of a *free-jet circuit-breaker*, the compressed air blows on the openly burning arc. In an *arcing-chamber circuit-breaker*, the air is compressed in a closed chamber during the movement of the switching contact [47].

With the development of **SF_6 compressed-gas circuit-breakers** for the medium voltage range, high voltage range and extra-high voltage range (of about 20 to 400 kV) and development of **vacuum circuit-breakers** that dominate in the medium voltage range, the above-mentioned switching principles were passed, but to some extent they are still in use in the grid.

Due to the high *global warming potential* of SF_6 gas that might escape into the atmosphere, alternative solutions both for insulating appli-

cations and arc-extinction applications are discussed. In the case of circuit-breakes, both **vacuum circuit-breakers** and **CO_2 compressed-gas circuit-breakers** are considered for the future.

High voltage switches earlier had to be implemented basically through *series connection of several capacitively graded interrupter units*. For this purpose, a single SF_6 compressed-gas interrupter chamber is meanwhile adequate for up to 400 kV.

Note: The *series connection* of several medium-voltage *vacuum interrupter chambers* in order to meet the high-voltage switching requirements is not yet sufficiently solved owing to very stringent conditions for *synchronism* of the units.

7.1.5.2 SF_6 Compressed-gas Circuit-Breaker

Sulfur hexafluoride (SF_6) is an electron-affine gas and possesses superior **insulation properties.** Therefore, is suitable especially for the insulation of the recovery voltage over the clearance of the open contacts. For low ambient temperatures, mixtures of SF_6 and nitrogen are used; cf. Section 3.2 and 5.1.2.

Moreover, SF_6 has excellent **arc-extinguishing properties**, since lot of energy is required to break SF_6 down into an arc plasma. Therefore, a very rapid and practically complete regeneration of SF_6 molecules along with the recombination of charge carriers and recovery of electric strength occurs after extinguishing the arc. Another advantage of SF_6 is that, unlike many other electron-affine gases, free carbon is not formed as a decomposition product [187].

a) Functional principle

There are two principles for SF_6 power circuit-breakers: In the *puffer circuit-breaker*, the arc extinguishing gas is blown with the help of a piston into the nozzle of the extinction cham-

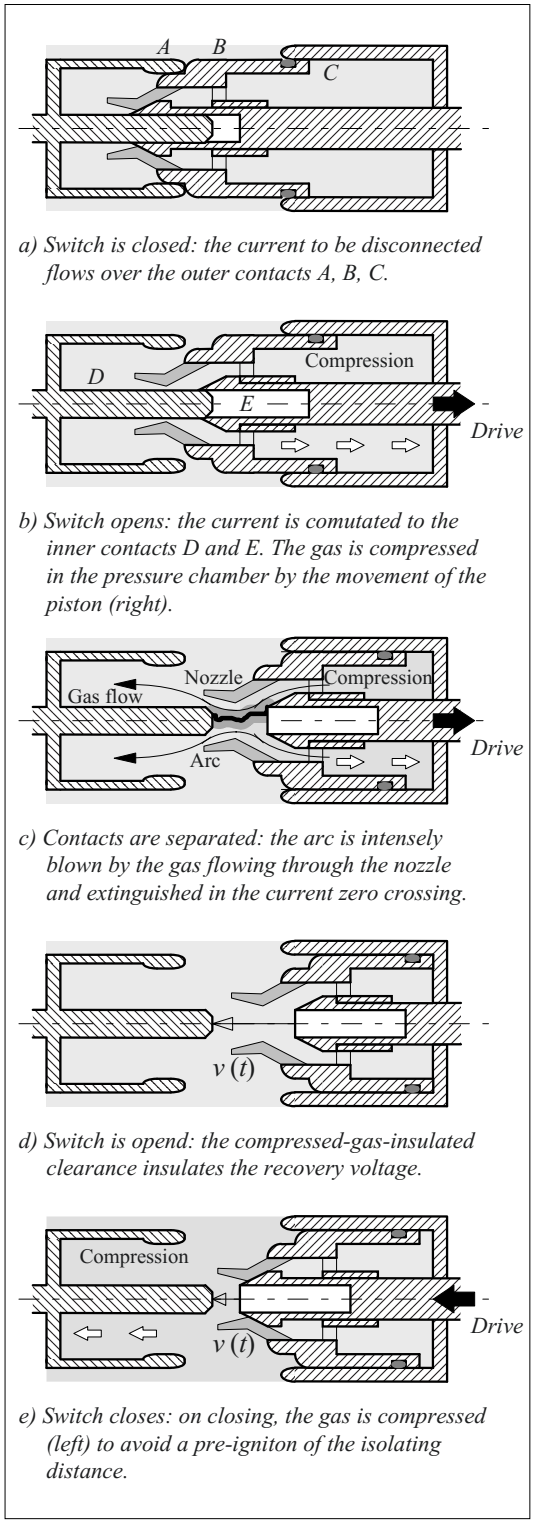

a) Switch is closed: the current to be disconnected flows over the outer contacts A, B, C.

b) Switch opens: the current is comutated to the inner contacts D and E. The gas is compressed in the pressure chamber by the movement of the piston (right).

c) Contacts are separated: the arc is intensely blown by the gas flowing through the nozzle and extinguished in the current zero crossing.

d) Switch is opend: the compressed-gas-insulated clearance insulates the recovery voltage.

e) Switch closes: on closing, the gas is compressed (left) to avoid a pre-igniton of the isolating distance.

Figure 7.1.5-1: Principle of a compressed-gas puffer circuit-breaker, a) to d) while opening, d) and e) while closing (schematic).

ber, Figure 7.1.5-1. In the *self-blast circuit-breaker*, the compression pressure that is necessary for arc extinction is generated by the thermal expansion of the arc. For this, however, adequately high currents are necessary. Therefore, actual switches often combine both the principles.

In an enclosed **puffer circuit-breaker**, the current flows over the outer, very low resistive copper contact pieces A, B and C, Figure 7.1.5-1 a). On opening the switch, the contact tube E pulls the contact piece B towards right by means of a limit stop within about 30 ms, Figure 7.1.5-1 b). The energy for the drive originates from a *spring energy store* or a *compressed-air energy store*. At first, the contact between the contact pieces A and B is separated and the current is commutated to the inner *tungsten-copper contacts* D and E. Contact piece B simultaneously works as piston by which the SF_6 gas is compressed into a *pressure chamber*. After separation the contacts D and E, the arc is formed, and as soon as the *nozzle* made of polytetrafluoroethylene PTFE is cleared, this arc is blown intensively in the axial direction by the gas flowing out of the pressure chamber, Figure 7.1.5-1 c).

Owing to intensive *cooling*, the heat removal in the area of current zero crossing far exceeds the supplied Joulean heat $R \cdot i^2$ which leads to a fall in temperature of the arc plasma. Below approximately 3000 K, the plasma largely loses its high conductivity and the arc extinguishes, already in the first *current zero crossing* in modern switches. In this process, it must be taken care that the current chopping does not occur before the current zero crossing because high rates of current change $\partial i/\partial t$ can cause serious over-voltages $L \cdot \partial i/\partial t$ at the inductive equipments in the electrical power system. Even a *current chopping* at 4 A can be critical.

Even after the arc is extinguished, the cooling must be continued by blowing in order to deionize the isolating gap. *Strength recovery* of the gas-insulated gaps must be faster than the rise in the recovery voltage $v(t)$, Figure 7.1.5-1 d). This, for example, can be achieved for a 110 kV circuit-breaker for pressures of 4 to 6 bar and opening velocities of 4 to 5 m/s. If breakdowns occur again, owing to lack of strength of the isolating gap or owing to higher transient recovery voltages in the network, this is characterized as *re-ignitions* (until 5 ms) or *arc-backs* (after 5 ms). In these cases, the arc must be extinguished in the next current zero crossing. The amount of compressed gas is enough for several extinguishing trials. Therefore, the magnitude of *transient recovery voltages* in the network is of high significance for successful arc extinction [20].

Note: A breakdown of the gap during dielectric strength recovery is described as a *thermal arc-back* if the conductivity of the gas is still too high or as a *dielectric arc-back* if the charge carriers are not yet cleared out of the gap.

On *closing* the switching contacts, at first, the nozzle is closed by the contact tube E, Figure 7.1.5-1 e). Subsequently, the circuit-breaker gas is compressed in the left section of the arcing chamber. The resultant pressure rise prevents an early and untimely breakdown. Breakdown and arcing occur just before the galvanic contact of the contact pieces is made, so that the thermal stress remains low and fusing or contact welding are avoided. This is referred to as so-called *switch-on safety*.

b) Arcing models

The permissible breaking currents are determined by very complex gas dynamic processes in the arcing chamber which are difficult to describe. Hence, the designs of the circuit-breakers were done in the past mostly on the basis of experience and experiments. Rising short-circuit power levels in the network, associated with the demand for reliability of circuit-breakers, require a better understanding of the arcing behavior. This has two objectives:

First, the interaction of the switch with the electrical network shall be described using **global models**. For this, it's not necessary to have a thorough understanding of the physical processes. Often it is adequate to describe the

arc as a "black box" with a two terminal network model. Based on the global macroscopic arc properties, a differential equation for the conductance G of the arc plasma is often derived from an energy balance:

$$\frac{1}{G}\cdot\frac{\partial G}{\partial t} = \frac{1}{\tau}\cdot\left(\frac{v\cdot i}{P} - 1\right) \qquad (7.1.5\text{-}1)$$

Eq. (7.1.5-1) is comparable with the spark resistance laws according to Section 3.2.7.1. v and i are arc voltage and arc current, P and τ are model parameters which are again dependent on G and i and which must be determined empirically. Some modifications of this model are described in the literature [317].

Secondly, improved **physical models** shall provide a deeper insight into the behavior of the arc and shall enable the optimization of circuit-breaker properties. For this, physical processes in the arc and during the interaction with the cold gas flow as well as interaction with the nozzle and the electrodes must be studied and understood in detail. The correct description here includes the conservation equations for energy, mass and impulse in their full form. Non-linear properties of gases must be described with chemical reaction equations that reflect the atomic interactions [317]. In this regard, there are research activities for several questions yet to be solved, such as thermodynamic properties of SF_6, measurement of plasma-state variables, flow simulation (turbulences, ultrasound), influence of Teflon vaporization or dielectric strength recovery after the arc extinction.

c) Arcing chambers and circuit-breaker units

Arcing chambers can be used directly in an *encased or compressed-gas-insulated substation*, but the gas volume of the arcing chamber is separated from the volume of the switchgear. For *outdoor installations*, a weatherproof housing insulator is necessary. The series connection of the circuit-breaker units is carried out, for example, in T-form with parallel grading capacitors and with a drive fed through the post insulator, Figure 7.1.5-2. In the case of open contacts, the grading capacitors of about 200 pF provide a uniform voltage distribution.

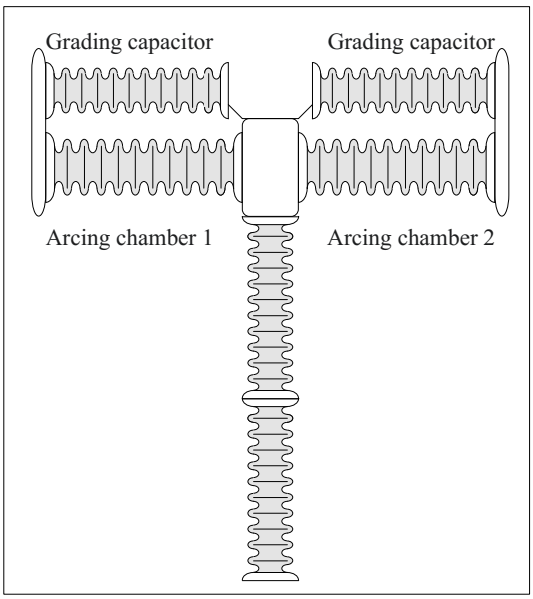

Figure 7.1.5-2: Series-connection of two circuit-breaker units in an outdoor installation (schematic).

Compared to oil-based circuit-breakers, gas-blast circuit-breakers with inert and non-toxic SF_6 gas are very *safe and low-maintenance*. Gas decomposed in the arc actually reacts completely again to form SF_6. Hermetically and permanently sealed *medium voltage circuit-breakers* only have to be monitored with respect to the gas pressure.

In the intensive arcs of *high voltage circuit-breakers* and in the presence of small contents of the gases O_2 and H_2O, secondary reactions occur to a greater extent, and toxic and corrosive *decomposition products* are formed., They are bound to some extent by absorbers. Moreover, fluorides in powder form result from reactions with metallic electrodes. High voltage circuit-breakers must therefore be opened periodically for removing the solid decomposition products. This requires special safety measures to be followed to avoid contact with and inhalation of *toxic decomposition products*. SF_6 gas is pumped out before opening and re-conditioned in a closed cycle.

SF_6 circuit-breakers are designed for a large number of normal *switching operations*. Despite this, *wear* does occur, so that regular *maintenance activities* are required in consultation with the ciruit-breaker manufacturer. *Inspections* are necessary, especially after the very rare interruptions of large short-circuit currents in the extreme range. Meanwhile there are proposals for status-oriented maintenance, whereby various electrical, mechanical and gas-analytical parameters are measured during switching operations and compared with the reference values [318].

SF_6 gas must be held in closed cycles for yet another reason: owing to its *greenhouse effect,* it has 23900 times larger global warming potential (GWP, time horizon of 100 years) compared to CO_2. Although only small quantities are produced (1995 approx. 8500 t/a, of which about a third for power engineering devices), unmonitored release into the environment is no longer permitted. Alternatives for SF_6 circuit-breakers are available today only to a limited extent: in the medium voltage range, the vacuum circuit-breaker has achieved a share of above 80%, SF_6 switches are still at about 10%. In the high voltage range and the ultra-high voltage range, currently there are no alternatives yet to SF_6. Vacuum circuit-breakers could reach the lower high voltage ranges (up to 110 kV) in the near future. Nevertheless, higher voltages would require series connections of very well synchronized interrupting units.

7.1.5.3 Vacuum Circuit-breaker

Vacuum is well suited as a switching medium, since the arc is formed by the current flow over a **metal-vapor plasma** of electrode material. Even in the first zero crossing of the current, an extremely fast *de-ionization* of the discharge gap occurs due to radial *diffusion, recombination* and *condensation* of the heavy metal atoms at the electrodes. During the recovery of the voltage across the separated contacts, residual charge carriers are withdrawn and this leads to rapid recovery of dielectric strength of the opened vacuum gap, especially for small contact distances [316].

Note: However, the rapid de-ionization has the disadvantage that *small currents* of a few 10 A are already chopped before the zero crossing and with a high rate of current change $\partial i/\partial t$. Therefore, overvoltages can be induced in inductive operating equipment ("current chopping"). This still presents obstacles to the use of vacuum circuit-breakers in high voltage switchgear.

Note: Owing to the rapid de-ionization, also a *breakdown spark in the circuit-breaker* may extinguish at the next current zero crossing without leading to a short circuit of the network. This leads to a *conditioning* of the electrode surfaces. For example, micro-tips that are burnt away by sparks can be considered as the cause of self-healing breakdowns.

The **dielectric strength** of vacuum gaps amounts to about $\hat{V}$ = 20 kV already at d = 0.5 mm and increases to about $\hat{V}$ = 100 kV for d = 3 mm, cf. Section 3.7. In a medium-voltage vacuum circuit-breaker the recovery voltage can be withstood even after a very short period after the opening of the contacts, since only short switching paths are necessary and the de-ionization of the metal vapor-plasma takes place very rapidly by the deposition (condensation) of heavy metal ions on the electrodes in the span of the current zero crossing. This is a decisive advantage of the vacuum technique compared to switching devices with compressed gas, especially in the medium voltage range [316].

Vacuum circuit-breakers are made of large-area contacts pressed against each other in a two-piece *ceramic vacuum tube* made of aluminum oxide Al_2O_3, Figure 7.1.5-3. The movement of the moving contact that amounts to only about one centimeter is conveyed via a *metallic bellow expansion joint*. With a sealing that is soldered under vacuum, a *gasket-free and hermetically closed set-up* is possible, which must hold the vacuum *without maintenance* during the entire service life of the circuit-breaker. Special requirements are placed on the quality of the vacuum interrupter tube, since a *loss of vacuum* is not detected and inevitably would lead to breakdown.

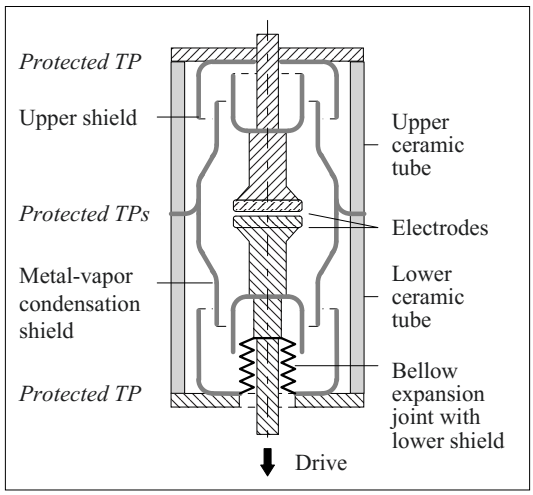

Figure 7.1.5-3: Medium voltage vacuum interrupter.

Ceramic surfaces under vacuum represent especially critical weak points of the insulation, Section 3.7. Therefore, they must be protected by overlapping *concentric shields* of metal (e.g., copper with low gas emissions, so-called oxygen-free copper OFC) against the deposition of *metal vapors*. Another important function of the shields is the protection of *triple points* (TP) against high electric field stresses, i.e. the provision of a so-called "field shadow" at the junction of ceramics, metal and vacuum, so that no electron emissions can take place there which would lead to avalanche formation and flashovers via secondary electron emission at the ceramic surfaces, Figures 3.7-3 and 7.1.5-3.

The metal-vapor condensation shield in the middle position is fixed on a potential-free ring between the upper and the lower ceramic tube. In the case of open contacts, it is maintained capacitively at half-potential.

Highly pure, gas-free and highly thermoresistant materials must be used as *electrode materials*, e.g. the sinter material CuCr (50/50), so that the arcs cannot release unacceptable quantities of gas. Released gas atoms are bonded by absorbers ("getters") made of reactive rare-earth elements.

During a **current-breaking process**, *metal-vapor plasma* and a high-current arc are formed in the gap between the separating contacts. The arc contracts under the magnetic forces (pinch) and the electrodes are thermally heavily stressed in the two root points of the arc. Metal vapor that is formed during melting and vaporization of electrode material does not only delay the de-ionization at the current zero crossing, it also decreases the dielectric strength of the gap for the recovering voltage. Therefore, special electrodes are used, on which *a contracted arc does not stick* to a fixed root point [316], Figure 7.1.5-4:

For the so-called *radial-field contacts (RMF, radial magnetic field)* or spiral contacts respectively, the current is guided by the geometrical shape of the electrodes in such a way that radial magnetic field components B_{rad} are formed. Along with the axial direction of current flow, an azimuthal Lorentz force results, which propels the arc in a circle on the electrode surface, Figure 7.1.5-4 (left). The use of this contact system is restricted to currents of up to approximately 31.5 kA and to smaller contact distances of up to 10 mm.

Higher currents and larger contact distance are possible, if the arc can be held in the *diffuse state*, i.e. at lower current density. For this, *axial-field contacts (AMF, axial magnetic field)* are used, in which axial magnetic field

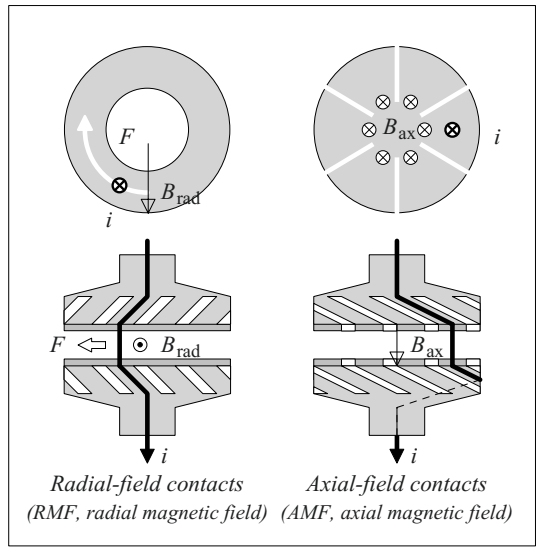

Figure 7.1.5-4: Electrode configurations for vacuum circuit-breakers (schematic).

components B_{ax} are generated by the geometrical structure of the electrodes or by external coils, Figure 7.1.5-4 (right). Slots impede the formation of eddy currents by B_{ax}. The axial magnetic field *prevents the contraction* of the arc in the following manner:

Owing to Lorentz forces, electrons and ions describe helical paths around the axial magnetic field lines. The path radii of ions are greater than the path radii of electrons owing to higher centrifugal forces. Thus, the current is led via concentric plasma tubes of electrons (internally) and positive ions (externally). Since the charges of same polarity in the plasma tubes repulse each other, the contraction of the arc (pinch) is substantially hindered.

Individual vacuum circuit-breakers can switch off *currents* of a few 10 kA for *voltages* of several 10 kV. Vacuum circuit-breakers are especially suited to the **medium voltage range** ($V_m \leq 84$ kV), since the breakdown strength of vacuum rises only slightly with the flashover distance, cf. Section 3.7. However, the vacuum circuit-breaker has many advantages in the medium voltage range; it has therefore widely gained acceptance.

In the **high voltage range**, vacuum circuit-breakers have not been considered until now as an *alternative for compressed gas-blast circuit-breakers* owing to the small increase in dielectric strength of the vacuum with the distance. Nevertheless, the application of SF_6 is now subject to increasing restrictions, and hence vacuum circuit-breakers are again being more strongly evaluated as a possible alternative. For high voltage use, there are two feasible options [316]: on the one hand, medium voltage vacuum interrupters can be connected in series, for which exact coordination of switching instants must be ensured. On the other hand, single-stage circuit brakers are being tested up to 168 kV as laboratory samples. From the insulation point of view, for example, additional potential-free shields, which provide capacitive field grading, are necessary. The practical use must at first be expected in the lower high-voltage range ($\leq$ 123 kV). For the higher voltage levels, the SF_6 circuit-breaker continues to be indispensable.

7.1.6 Electrical Machines

Electrical synchronous and asynchronous machines are used both as generators and as motors. They consist of a *rotor* and a *stator*, Figure 7.1.6-1. The rotor generates a magnetic field $\boldsymbol{B}$ that rotates with the rotation of the rotor and that induces alternating voltages in the stationary windings of the stator. The stator consists of a cylindrical iron-core stack made of sheet metal with a concentric opening for the rotor. *Stator windings* are inserted in *axial slots* on the inner side of the core stack and are uniformly distributed over the circumference.

The machine insulation must insulate the *conductors against each other and against the iron sheets of the stator*. The conductors emerge from the slot ends at the front ends of the iron core stack and are interconnected in the *winding overhangs*, Figure 7.1.6-1 (left). The design of the insulation varies greatly depending on the size and age of the machine [319]. For small machines that are stressed only with *low voltage*, the conductors are wound as enamel-insulated wires directly into the slots, Section 7.1.6.2. For *large machines*, preformed and insulated *conductor bars* or so-called *integral coils* are accomodated in the slots and connected at the front end and at the back end in the winding overhangs, Section 7.1.6.2. Even the largest generators in the GW range are stressed only with *medium voltage*, since the insulation problems for higher voltages cannot be solved with conventional machine insulation systems. Therefore, a so-called generator transformer is always necessary for the supply of electrical power into the high-voltage system.

Note: As an experiment, the vision of a *cable generator* was therefore developed, in which, owing to the high dielectric strength of the XLPE cable insulation, the high voltage is directly generated and hence the generator transformer can be dispensed with, Section 7.1.6.3.

7.1.6.1 Low-voltage Motors

During the manufacture of low voltage motors, *slot liners* made of cutted and folded insulation sheets are first placed into the slots. Subsequently, *enamel-insulated or coated wires* are inserted with the aid of special *automatic winding machines*. In doing so, there are always numerous wires put into a slot. Insulating sheets are placed between different phase windings in the area of the winding overhang forming the so-called *interphase insulation*. Then, the stator carrying the windings is *immersed* in varnish, *sprayed* with varnish or, for higher requirements on the insulation quality, *impregnated* under vacuum with polyester resin or epoxy resin.

The function of immersion in varnish or impregation with resin is first to protect the winding against *moisture* and to provide mechanical *stabilization* of the insulation under vibration to prevent abrasion. Moreover, the *heat transfer* shall be improved. The type of insulating materials used is primarily chosen according to the thermal stresses (temperature

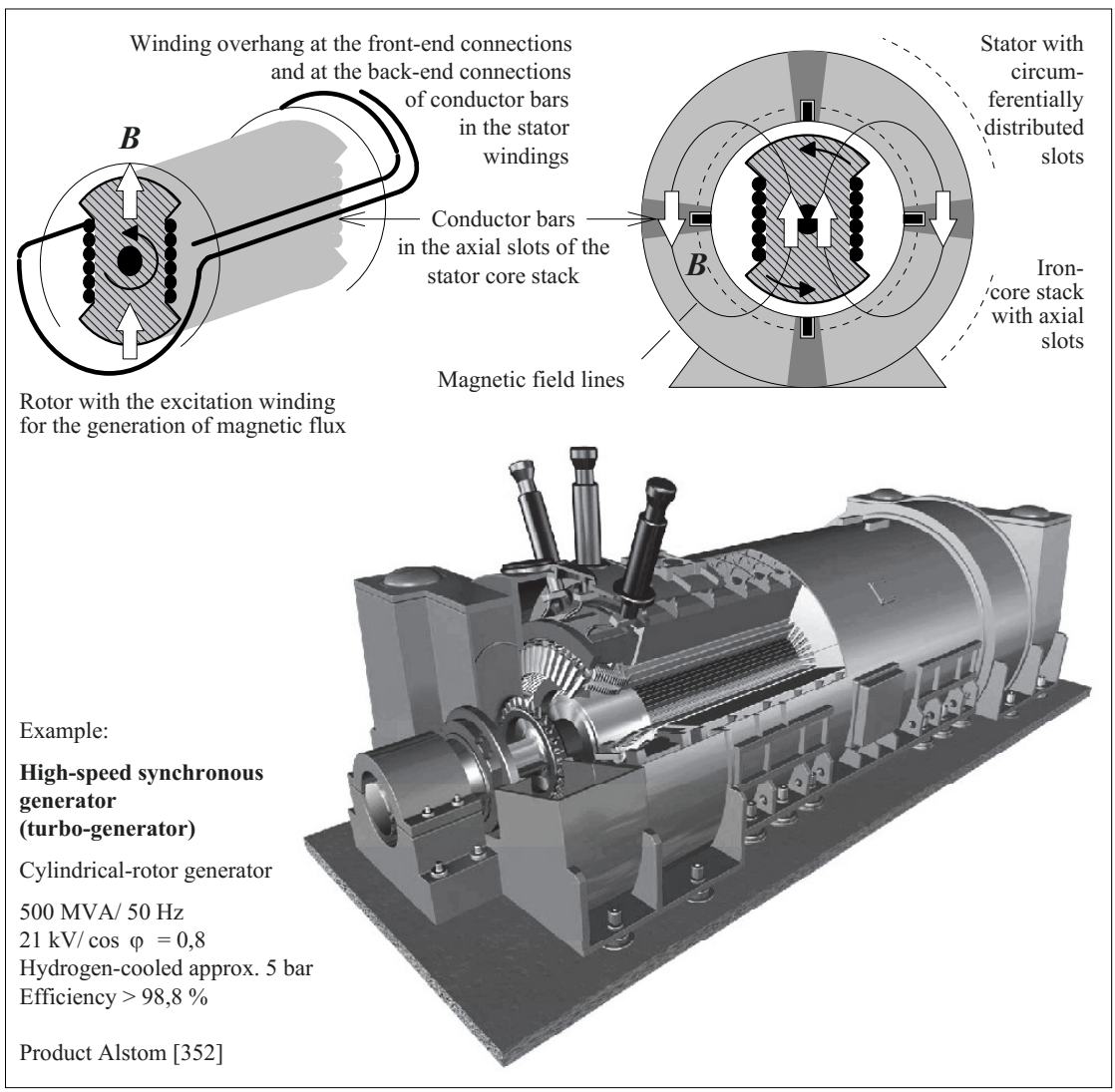

Figure 7.1.6-1: Principle and construction of an electrical synchronous machine (schematic).

class) to be expected during operation [319].

Low voltage insulations are generally not free from cavities, but for the standard operating AC voltages of a few 100 V, no eroding *partial discharges* occur in these cases. However, power *supply with converters* over longer cable runs can be problematic: owing to their high rate of rise of voltage, switching impulses propagate as traveling waves and increase the voltage by reflection at the motor impedance to about double the value. If turn-to-turn voltages in the phase termination area become too high, partial discharges of high repetition rate occur in the cavities and lead to rapid erosion of the sensitive enamel insulation and subsequently to turn-to-turn faults. Some example remedies are (adequately voltage-resistant) *low-pass filters, cavity-free* insulations or specially *coated insulating materials* with increased partial discharge resistance.

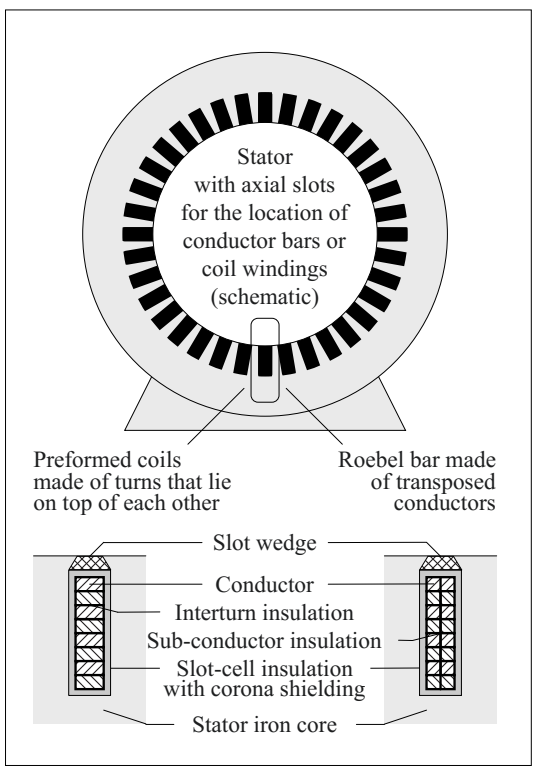

Figure 7.1.6-2: Insulation in the stator of a rotating machine (schematic). Only one winding layer is illustrated. Generally, there is one upper and one lower layer in the slot.

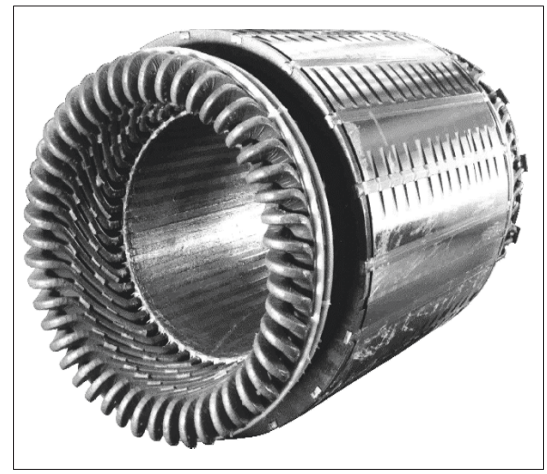

Figure 7.1.6-3: Stator windings of a high voltage motor with winding overhang. Photo Siemens AG, Nuremberg

Note: The sensitivity of an insulation to *converter impulses* can be checked by a *step test with impulse voltages* with increasing amplitude. By simultaneous *impulse current measurement*, a partial insulation failure can be detected long before it leads to complete breakdown. The results can even be correlated with the results of *partial discharge measurements* [320].

7.1.6.2 Machines for High Powers

For motors and generators for high powers, the use of high voltages would generally be advantageous. However, even for the so-called *"high voltage machines"*, it is restricted to rated voltages of about 27 kV, since the insulation problems for higher voltages cannot be solved with the classic machine insulations systems. Owing to limited voltage levels, large power generators must always supply their power via *generator transformers* to the high voltage and ultra-high voltage levels.

Owing to comparatively low voltages, currents and conductor cross sections are very large. For example, in a 1300 MVA generator, at V_r = 27 kV, operating currents are approx. 28 kA.

a) Winding arrangement and insulation design

In the *axial slots* of the stator, preformed coil elements (insulated bars or preformed coils) are inserted, fixed with slot wedges and con-

nected at the front end and at the back end in the winding overhang to form so-called *bar windings or preformed windings,* Figure 7.1.6-2 and -3. Large conductor cross sections must be established with several parallel *sub- conductors*, which must be regularly cross-connected for uniform current distribution (*transposed conductor, Roebel bar*), Figure 7.1.6-2 (right). In the case of very large currents, some of the sub-conductors are designed to be hollow and are cooled with water.

Note: *Cooling water* must be passed to conductor potential via insulating tubes (mostly of polytetrafluoroethylene PTFE) and must be kept *de-ionized* to the extent that leakage currents in the liquid are not too large.

For the so-called *preformed winding*, the conductors of a winding layer that are accommodated in a slot, are connected in series to form multiple turns of a coil, Figure 7.1.6-2 (left). In contrast, the sub-conductors in a *transposed conductor* (or *Roebel bar* resp.) are connected in parallel, Figure 7.1.6-2 (right). In the case of a *double-layer winding*, tow coils are accommodated in one slot above each other (upper layer and lower layer).

The conductor insulation, either as *interturn insulation* or as *strand insulation*, is stressed only with very low voltages. The full operating voltage lies between the conductor stack and the stator iron core across the *slot-cell insulation,* which acts as the *main insulation*. It is also described as coil insulation, Roebel bar insulation, ground insulation or slot armour.

For operating voltages in the kV range, the main insulation must be shielded against cavities and delaminations by means of an inner and outer *semi-conductive layer* (inner and outer *"corona shielding"*) in order to avoid partial discharges. The outer corona shielding largely helps with good electrical contact of the main insulation to the grounded stator iron core in order to prevent discharges between the stator iron and the insulation surfaces of bars or coils. The surface resistance of the outer layer, however, must not be so low that appreciable eddy currents can flow between the adjoining iron sheets.

The *electric field* between the inner and outer semi-conductive layers (corona shields) is less homogeneous than in a cable, and owing to the rectangular cross section, field stress enhancements occur at the edges of the sub-conductors, Figure 7.1.6-4 (left bottom). Originally, field strengths (at the broad and flat side of the conductor rods) were restricted to values below 2 kV/mm to largely rule out partial discharges in cavities, but now, owing to improved insulation systems, field strengths of up to 3 kV/mm are used and even higher values are under discussion [319]. Nevertheless, insulation thicknesses of a few mm only allow voltages of a few 10 kV.

The conductors emerging from the front ends of the stator are interconnected in the so-called winding overhang to form turns and windings or coils respectively, Figure 7.1.6-3. For that

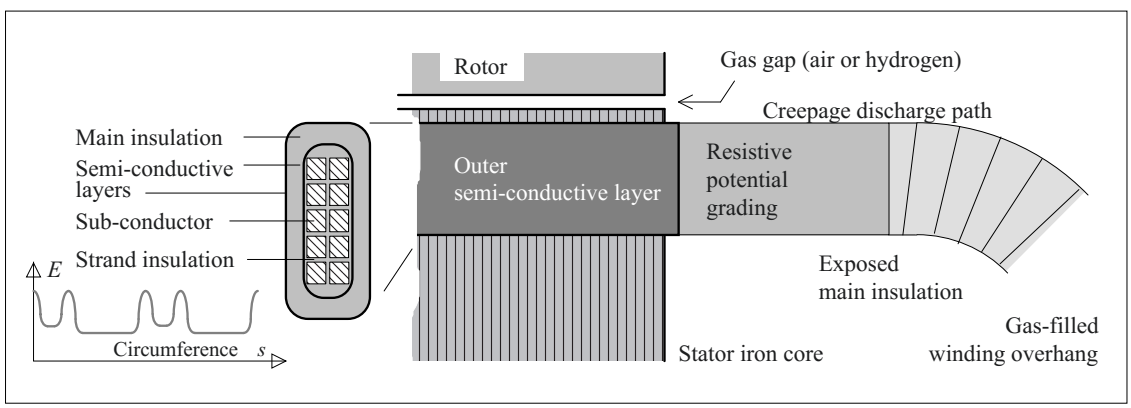

Figure 7.1.6-4: Generator winding insulation (schematic).

reason, the main insulation must be continued continuously as an *overhang insulation*, Figure 7.1.6-4.

The exit points of the conductors at the front end of the iron core stack represent *classic creepage configurations;* cf. Section 3.2.6.2 with Figures 3.2-33 to -35. Therefore, a *resistive potential grading* by semi-conducting varnish or tapes is used for the suppression of surface discharges. The potential grading is performed along a lattice network of longitudinal resistances and transverse capacitances or stray capacitances towards the high voltage side, Figures 7.1.6-4 and 3.2-34 (center). *Nonlinear materials* (e.g. based on silicon carbide), whose conductivity increases with the field stress, are especially effective, because this causes the field to be displaced away from the areas with higher field strength. Potential grading is also possible by the application of *capacitively grading layers* [22], [26], [45], Figure 7.1.2-2 (below). The flashover distances in gas in the winding overhang area must also be adequately dimensioned, and with this there is also a voltage restriction to less than 30 kV.

b) Insulating materials and production

The machine insulation system in operation is not only subjected to high electric field strengths, but also to remarkable mechanical forces, thermal expansions and thermo-mechanical stresses. Therefore, freedom from cavities and partial discharges cannot be guaranteed. Only inorganic *ceramics or mineral materials* can resist persistent partial discharge erosion. In practice, *mica products* have proven to be useful, Section 5.2.3.

The base material of *mica tapes* is *mica paper*: Mica that is released from water of crystallization and processed to a foil similar to paper is applied on a *carrier material* (paper, glass silk, polyester fleece or polyester silk) with a *bonding agent* and protected by a *facing* [319], Section 5.2.3. Depending on the process, the tapes comprise higher or lower quantities of bonding agent.

The actual insulation is formed by *winding* the preformed conductor with the *mica tapes*. The bonding agent is not yet hardened at this stage.

The insulation is either hardened with the bonding agent that is still present in the liquid form in the mica tapes, or the wrapped-up tapes are flooded under *vacuum* with *polyester resin* or *epoxy resin*, exposed to pressure, impregnated and hardened (VPI process: *vacuum pressure impregnation*); cf. Section 5.3.3.1 with Figure 5.3-14. Here, the accelerator and the hardener that are present in the impregnating resin penetrate also the mica tapes, which initially contained only little resin, and also harden them.

The described processes can be carried out either for the individual not yet assembled conductors or for the complete, ready-made stator (with dryly inserted windings). Best results are achieved with the *complete-stator impregnation* with epoxy resin (i.e. with the so-called global VPI). It requires very large vacuum-tight and pressure-proof vessels (so-called *autoclaves*) and this can now be carried out for machines of more than 200 MVA [319].

Note: In the past, the insulation was designed based on *bitumen* and *mica splittings*. With this approach, it was especially problematic that shear stresses can be invoked by thermal expansion in the insulation while heating by the internal copper conductors. Even though this technique has now become outdated, there are still old, safely dimensioned generators with long residual lifetimes present in the network.

For the described production processes, there are many manufacturer-specific and historically developed variants [319].

c) Generator operation and diagnosis

Large, strategically important generators and drives must be diagnosed not only in the course of inspection intervals but must also be monitored online if possible. The methods employed here are described in Section 6.4.8.3. For example, *partial discharges and changes of dissipation factor* with voltage or *insulation resistances* are measured offline. The online monitoring of *temperatures, me-*

chanical vibrations as well as *partial discharge behavior* in the context of trend analyses is of great significance [352].

Owing to the numerous different insulating materials and design variants, comparable *groups* are formed by the manufacturers and the development of measured parameters is tracked over their lifetimes. Thus, it can be determined whether an individual machine is operating within the standard limits of its group.

Damaged insulations can be often repaired by replacing the respective conductor.

7.1.6.3 Cable Generators, Cable Machines

The limited dielectric strength of mica-resin dielectric and the insulation problems in the winding overhang restrict the rated voltages of conventional "high voltage machines" to about 30 kV, Figures 7.1.6-5 and -6 (top). Therefore, a visionary concept was proposed, in which the existing voltage limits are exceeded by using *XLPE high voltage cables*, Figures 7.1.6-5 and -6 (bottom) [321]. Cable generators were at first implemented as so-called *powerformers*™ in demonstration projects for relatively low voltages (e.g. 45 kV, 10 MVA) in order to show the basic technical feasibility [322]. Meanwhile, generators according to this principle are operated even with voltages of 136 kV (turbo-generator 42 MVA) and 155 kV (hydro-electric generator 75 MVA). The principle of the cable generator can also basically be applied to other **electrical machines**.

With the concept of the **cable generator**, not only a single Roebel bar or a single preformed coil is accommodated in one slot of the stator: a greater number of cables can be inserted so that *multiple turns* can be formed for the induction of higher voltages, Figure 7.1.6-6 (bottom). This results in considerably larger *diameters* and very much higher weight in comparison to a conventional generator, see Figure 7.1.6-6 (top). The diameter of the cable generator is also enlarged as there is a two-fold cable insulation between two turns laying side by side, although there would only be a very small interturn voltage to be insulated.

In the area of the *winding overhang*, a simple structure results: the cable can be led from one slot to the next without interruption and with a closed insulation screen, so that the potential grading at the surface that was previously necessary is eliminated, and almost no power-frequency electric field leaks from the cable insulation into the surrounding space.

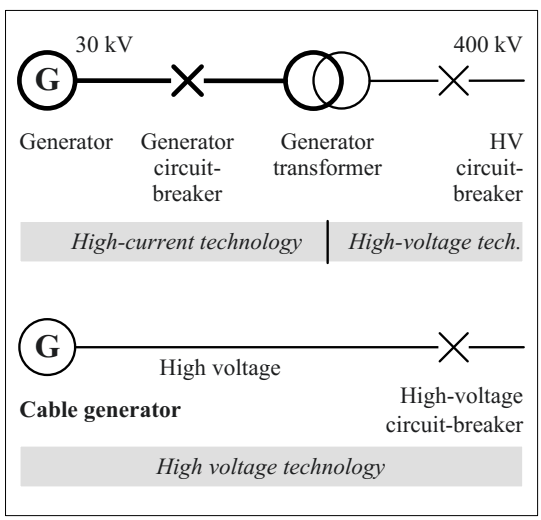

Figure 7.1.6-5: Conventional generator (top) and vision of a high-voltage cable generator (bottom).

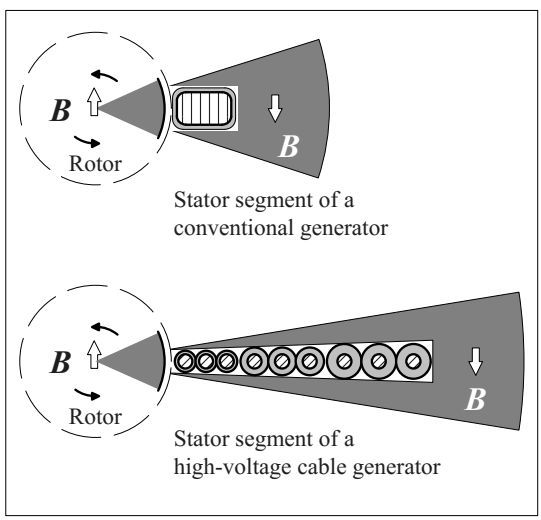

Figure 7.1.6-6: Dimensional comparison between conventional and HV cable generator (schematic).

The insulation of the cable can be adapted to the local magnitude of voltage along a phase winding from the high voltage side to the neutral point (stepped insulation thickness, star connection). Individual cable sections, whose lengths are also restricted for production reasons, must be connected in the winding overhang by *cable joints*. In order to avoid parasitic eddy current loops, the cables must not have highly conductive sheaths or screens. A *semi-conductive insulation screen* is nevertheless required to force the electric field into the cable dielectric, at least at power frequency.

Note: A simplified installation concept without generator switch and generator transformer, lower currents and conductor losses as well as slightly increased efficiency, lower conductor temperatures and a simplified cooling system are listed as **advantages of the cable generator**. Furthermore, increased thermal time constants and a higher overload capacity, probably owing to the large mass of the generator, are also assumed.

Note: **Advantages of the conventional generator** are its technology that is well proven over many years with a long and known service life, the known dynamic performance of the stator (e.g. the natural frequencies of the stator teeth), the partial-discharge-resistant as well as thermally and mechanically highly stress-resistant dielectric, the lower weight of individual components (transport, modular construction) as well as the decoupling of the generator from power-system perturbations (overvoltages) by the impedances of the generator transformer.

Note: It was also proposed to use high voltage windings of cables with semic-onductive external screens for **cable transformers** [323], e.g. as so-called *dry formers*™. Conductors that are insulated on all sides for the full voltage lead to a relatively large winding cross section. This can be counteracted by a smaller number of windings and an increased magnetic flux, i.e. with an enlarged iron core. The no-load loss and part-load loss increase as a result. Short-circuit loss is comparatively low owing to the large conductor cross sections. Owing to the cooling air channels present between the windings, relatively low thermal time constants and a lower overload capacity, especially for very high short-duration overloads result.

Special requirements are imposed for cooling, since the temperature difference between the cooling air and the permissible conductor temperature is comparatively low and the electrical insulation also simultaneously acts as thermal insulation.

7.2 Typical Insulation Systems for DC Voltages

7.2.1 Electrical Stess, Strength and Design for DC Voltage

For stressing insulations with DC voltage, a **"rethinking"** is necessary in view of the fact that the intuitive assessment of high voltage problems is often based upon experiences with AC voltage stresses. Therefore, dielectric and thermic stresses and the behavior of materials are often considered as especially problematic, i.e. as **"the seven plagues of the HVDC insulation system"**:

1. Undefined and varying **conductivities** determine steady-state DC field distributions.

2. Multiple **polarization processes** determine transient field distributions.

3. The development of **space charges** and **surface charges** cause spacially and temporally variable field strength enhancements.

4. Behavior of materials can be strongly **non-linear** or field-dependent respectively.

5. Behavior of materials is strongly dependent on **temperature**.

6. Temperature gradients and field-strength gradients cause undefined and variable **gradients** of material properties.

7. Altogether, field distributions are not at all stable, i.e. **spatial-temporal field migrations** occur.

In the following sub-sections 7.2.1.1 to 7.2.1.4 dielectric stesses, electric strengths, material properties and insulation design are discussed for DC voltage. After that, examples for typical DC insulation systems in high-voltage

equipment and high-voltage components are described.

7.2.1.1 Dielectric Stresses at DC Voltage

There exists an *analogy* between the **steady-state conduction field** (for DC voltage) and *dielectric displacement field* (for AC voltage and impulse voltage): the conductivity κ corresponds to the permittivity ε. However, completely different **field distributions** often occur in practice. Basic relationships and a few applications are discussed in Section 2.4.4.

In the case of DC voltage stresses, the situation is complicated by the fact that the **conductivity values** vary by many *orders of magnitude,* and furthermore, *vary* greatly in some cases with the parameters such as stress duration, field strength, temperature, water content and pollution, Section 4.2.2. This can also be accompanied by the formation of *space charges* and *surface charges*. Field distributions that are dependent on the time or the operating state occur.

Another time dependence results from **transition processes** after the application, change or switch-off of a "direct" voltage. *Steady states* are often established with time constants in the range of hours. This can lead to transient *overstressing*, Section 2.4.4.3. These transition processes must be taken into consideration with sufficiently long *test durations*. DC voltage tests therefore often last over several hours.

Especially high stresses often occur immediately after **polarity reversal**: In the preceding steady state, *surface charges and space charges* have been built up which relieve electrical stresses in the areas of the insulation system that have a higher conductivity. After the polarity reversal, the displacement field that is associated with the high voltage variation at polarity reversal is constructively superimposed on the existing space-charge fields and surface-charge fields. Thus, very high field stresses can occur for a short duration which can be a danger for highly resistive materials such as cross-linked polyethylene (XLPE) in DC cables.

Note: Polarity reversals occur in traditional HVDC transmission systems with **line-commutated converters** (**LCC**) in order to reverse load flow direction, as the thyristor valves must carry the current always in the same direction. Now, **voltage source converters** (**VSC**) with IGBT switching transistors are coming up. Here, load flow direction is reversed by *reversing current direction*, polarity must not be reversed any more and *XLPE cables* can be used.

Furthermore, DC insulation systems are often stressed with **mixed voltages** (pulsating voltages), i.e. with both *DC voltage* and superimposed *AC voltage*. Booster capacitors in rectifier units with voltage multiplier connetions, high voltage cables to be tested with DC voltage and different components for high-voltage direct-current transmission (HVDC transmission) are mentioned as examples.

7.2.1.2 Dielectric Strength at DC Voltage

The **dielectric strength** for DC voltage *per se* is not different than for AC voltage, as can be identified in the example of gas breakdown in a homogeneous field; cf. Table 6.3.1-1.

However, there are practically important differences with regard to the **dielectric stresses** in a macroscopic and in a microscopic scale. Thereby, the so-called "**DC voltage strength**" of an insulation system or an insulating material can either be *increased or decreased*. The circumstances that are responsible for this are often difficult to understand and to quantify. Therefore, the topic DC voltage strength is often regarded as a "book with seven seals".

The main concerns are already mentioned above: *conductivities* and *conduction processes*, *polarization processes*, *space charges* and *surface charges*, *non-linearities*, *temperature dependences*, *gradients* of temperature and material properties as well as spatial-temporal *field migrations*. They require a specific analysis of the individual insulation problem.

A particularly significant loss of dielectric strength results at the *surfaces*, especially for external insulations, owing to non-uniform *contamination and wetting*, Figure 2.4-29.

The erosion of *insulating materials* by internal *partial discharges* is very much delayed, since the defective spots can only be recharged very slowly via the insulation resistance after a discharge. Therefore, a comparatively long time passes before the next discharge impulse occurs.

Some *examples* shall be mentioned here:

- The development of space charges in a non-uniform field leads to a pronounced *polarity effect* in *gases* and *liquids*, Section 3.2.5.2.
- In *liquids*, the strength falls owing to drifting impurities; cf. Section 3.4.2 with Table 3.4.2-1.
- In a *multi-layer dielectric*, with a field orthogonal to the interface, the field is sometimes displaced from a material with a higher conductivity and a lower dielectric strength (e.g. oil-imregnated paper) into a material with a lower conductivity and a higher dielectric strength (e.g. polymeric films). In these cases, this leads to an increased DC voltage strength of the insulation system.
- Even close to the *edges of the metallic foils in capacitors*, a relief of the stress takes place for DC voltage owing to a more conductive impregnation gap, Figure 2.4-30.
- The dielectric strength of *gaps and joints* depends on the distribution of the (more conductive) filling medium and its contacting to the electrodes. Gaps with increased conductivity have a potential-grading effect in the longitudinal direction if they are set properly with a preferably constant width, Figure 2.4-34. In contrast, narrowings of gap-width can result in significant field stress enhancements.

7.2.1.3 Dielectric Properties of Materials

The dielectric properties of insulating materials in HVDC insulation systems were until now described with *simple parallel equivalent circuits*, according to Figure 4.3-1. Here, only two basic properties are considered, the *permittivity* ε_r and the steady-state *conductivity* κ which is also known as DC conductivity. Insulating materials are properly described when the stresses result either from relatively rapidly varying displacement fields (e.g. for impulse voltage, power frequency AC voltage, switching on, polarity reversal) or from very long-lasting steady-state conduction currents (for DC voltage after very long periods).

After switching on or polarity reversal of a DC voltage, transition processes take place in a period of time in which currents and field strengths are influenced by *further dielectric properties* in addition to the basic properties ε_r and κ:

At first, it must be considered wether the material behaves nearly **linear** or significantly **nonlinear**, see subsection *a)*. In **solid materials**, *polarization phenomena*, play an important role, see *b)*. In **liquid dielectrics**, conduction processes and field stresses are determined predominantly by *charge carrier drift*, *charge carrier diffusion* and *charge carrier injection*, see *c)*. **Gases** are extremely high-resistive, but corona discharges and charge carrier drift can cause *charge accumulation* on highly resitive interfaces, see *d)*. **Multi-layer dielectrics** and **complex insulation systems** are discussed in the subsections *e)* and *f)*. In all kinds of dielectrics, *space charges* and *surface charges* can be built up which will severely change the field distributions.

For the **measurement of conduction processes and dielectric properties** it is especially important that the measurements are carried out under exactly *comparable* conditions and exactly under the conditions that occur in the device during *test* or in *operation*. This pertains to

(1) the **material condition** (density, thickness, water content, contaminations, particle content, batch etc).

(2) the **temperature**,

(3) the **field stress** and

(4) the **measurement duration**.

A complete picture is provided only by long-lasting *step response measurements* of the dielectric system with recording of **polarization currents and depolarization currents** (PDC) for all above-mentioned parameters [436]. These requirements can only be satisfied with great difficulty and the standards used today fall short and are not suitable for this purpose [456]. Therefore, it is recommended to measure polarization and depolarization currents (PDC analysis) which consist of displacement current components, polarization current components and conduction current components [500], Figure 7.2.1-1.

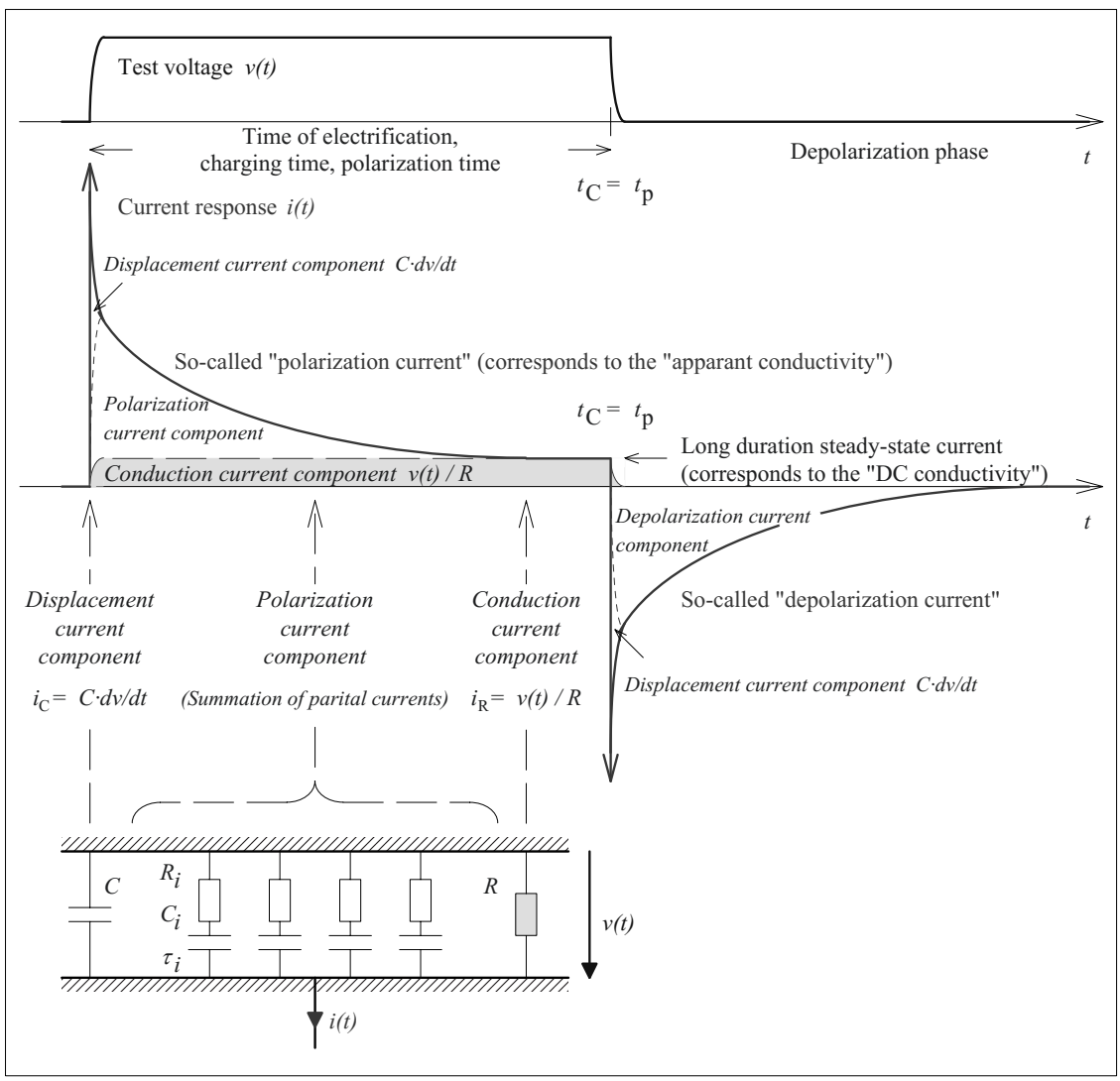

Figure 7.2.1-1: Determination of dielectric properties of a HVDC insulation material by means of PDC analysis (top). Different components of the so-called polarization and depolarization currents are related to the elements of a polarization equivalent circuit (bottom) describing the dielectric properties of a linear material [500].

a) Description of linear and non-linear materials

For **linear materials**, the abovementioned current components are related to capacitances, *RC* elements and resistances respectively, Figure 7.2.1-1 (bottom). Thus, a *polarization equivalent circuit* is provided describing the dielectric properties of a HVDC insulating material for a wide scope of applications. The assumption of linear material behavior is a rough *first-order approximation* only. Nevertheless, it is often appropriate mainly for *solid materials* and at low field strengths.

Note: Firstly, **DC conductivity** can only be determined from the steady-state current after a long time of electrification. As long as the measurement current is still decreasing, the resultant conductivity values must clearly be denoted as **apparent conductivities**. Nevertheless, DC conductivities can be estimated from still decreasing currents by use of the *current difference method* or the *charge difference method*, cf. Figure 6.4.1-4 (left and right).

Furthermore, it is possible to measure steady-state currents at higher temperatures after a shorter time and to calculate the values at a lower temperature according to the *Arrhenius equation* if the material is linear. For this, it is first of all necessary to calculate the activation energy from two measurements at elevated temperatures (e.g. 90 °C and 70 °C), cf. Figure 5.5-4.

In Section 4.3.2.2 it also described that not only the DC resistance R but also the resistances R_j can be recalculated for other temperatures according to the *Arrhenius equation* assuming the same activation energy [501]. For a first-order approximation, the equivalent capacitances C and C_j need not to be changed. For a linear material, the complete **dielectric system response** and the **DC conductivity** that were measured at higher temperatures (e.g. 90 °C and 70 °C) in a feasible time span (e.g. 1 to 10'000 s) can therefore be *extrapolated* to *lower temperatures* (e.g. 20 °C), to *longer times* (e.g. 100'000 s) and to *very low current magnitudes* below the measuring sensitivity (e.g. 1 pA), even without the possibility for direct measurement in this range, Figure 4.3.4 (right).

Non-linear materials cannot be described by equivalent circuits with linear elements that represent global properties of the dielectric. Therefore *multi-physical approaches* must be chosen taking into account a number of phenomena such as

(1) *charge injection* at the electrodes due to very high local field strengths,

(2) *charge carrier drift* due to potential gradients (electric field forces resp.) and mobility,

(3) *charge carrier diffusion* due to concentration gradients and mobility as well as

(4) local build-up of *surface charges* and *space charges* due to interfaces and gradients of temperature and field strength.

For example, Figures 4.3-5 and 4.3-6 show the non-linear behavior of an insulating oil which is further described in subsection *c)*.

b) Solid dielectrics

In solid materials, also *polarization phenomena* occur in addition to *conduction* (in the time span relevant for HVDC stresses). They lead to increased currents that decay over time, and they cause charge storage and release, Figures 4.1-1 to 4.1-3 and 6.4.7-4. At field strengths below 10 kV/mm, solids generally behave linear and the mentioned polarization processes can be considered in an equivalent circuit with additional *RC elements* with different time constants; Figure 7.2.1-1 (bottom), Section 4.3.2.1 and Figure 4.3-2. Linear equivalent circuits are therefore often sufficient.

There are strong *temperature dependences;* see Figures 4.2-9 and 4.3-3 (right). Conductivity follows the so-called Arrhenius equation Eq. (4.2-9).

The *water content* of cellulose based insulating materials is especially of significance, i.e. the absorption of water can lead to steeply increased conductivities or conduction currents and to steeply increased polarization currents [429], [436]; refer Eq. (4.2-7).

Field strength dependences are not so strongly evident in oil-impregnated materials (e.g. pa-

per or pressboard) or in polymeric materials (e.g. epoxy resin or polyethylene) at low field strengths and are observed only at high field strengths above 10 kV/mm, Figure 4.3-3 (left). The reason for such a nonlinearity is *charge carrier injection* from the electrodes which causes the filling of traps and the built-up of *space charges* [502]. This results in a *space-charge-limited current* that increases with the square of the voltage.

Especially in polymeric materials with very low conductivity, *space charges* and trap charges can persist for very long time. Thereby, very high local electric stresses are caused in case of polarity reversal.

c) Liquid dielectrics

The strongly *non-linear* dielectric behavior of insulating liquids and therefore also of insulating oil was described in, Section 4.3.2.3 with Figure 4.3-5 and -6.

At *low field strengths*, oil conductivity decreases during the time of voltage application as the intrinsic charge carriers (ions) drift towards the electrodes and form space charge layers of opposite polarity (heterocharges). Thereby, local field strength is increased.

Without voltage, only a very small *depolarization current* is flowing as the electrically influenced counter-charges on the electrodes hold the space charges for a long time.

Nevertheless, if the *polarity is reversed*, the space charges are free again, and the polarization current has an amplitude as high as it is expected from the originally present intrinsic charges [486].

At *high field strengths* (i.e. with effect from approx. 2 kV/mm), injection of homocharges from the electrodes starts to increase conduction current significantly. If voltage or background field strength is further increased, current increases therefore disproportionately until *breakdown* takes place.

Figure 4.3-6 (right) gives an example of the so-called *"bath-tub curve" of oil conductivity* which can be explained by the described behavior.

The complex behavior of conduction phenomena in oil cannot be described by *linear equivalent circuits. Nonlinear equivalent circuits*, which descricbe the nonlinear behavior of oil by functional relationships, can be used if space charges and local field stress enhancements in the oil are neglected. A *multi-physical approach* is given by the *Poisson-Nernst-Planck equation* considering charge injection and charge carrier drift due to field forces, diffusion processes and interaction of ions, cf. Section 4.3.2.3 [503], [504].

For *practical applications*, e.g. for design purposes or for condition assessment of HVDC transformers, conduction behavior of oil plays an important role, but it cannot be adequately determined by measurements according to standards or by theoretical calculations. Therefore, CIGRÉ has recommended to characterize the conduction behavior of insulating oil by measurement of polarization currents at three "*characteristic stress points*" with respect to the abovementioned "bath-tub curve": (1) at very low field strength after a short time shorter than 1 s, (2) at 1 kV/mm after one hour and (3) at 6 kV/mm after one hour [500].

Note: Conductivity data for insulating oil, can only be used for HVDC insulation calculations with the *utmost care*. If the conditions under which the conductivity values were determined are not exactly known, then the values cannot be used. For example, the conductivity values measured *according to the standards* are related to the *initial conductivity* (often also referred to as AC conductivity) for reasons of comparability [270], [283], while for HVDC calculations, *steady-values* of the conductivity must be known. These are quite sensitive to temperature and field strength, Figure 4.3-6. Even oil types, electrode materials, contaminations and ageing conditions can exercise great influence on conductivities [271],

[500]. The influence of water content (moisture content) is of less significance, if it is very much below the saturation concentration.

d) Gaseous dielectrics

At low field strengths, gases have a conductivity that is significantly lower than the conductivities of solid and liquid dielectrics, Saturation current densities are also very low due to a very small number of ions in the gas, cf. Figure 3.2-1 and -2.

Conductivities and saturation current densities can vary over many orders of magnitude depending on the intensity of ionizing processes (e.g. UV light, X-ray, radioactive radiation, cosmic radiation) that have access to the *gas volume*.

Furthermore, a number of phenomena must be considered that are related to the *gas-solid interfaces*:

(1) Conductive contaminations e.g. water or wet layers on the surface cause a *non-uniform surface conductivity* and severe field distortions leading to surface discharges and flashover at comparatively low voltages.

(2) A solid material with a comparatively *high volume conductivity* behaves like an electrode. If the surface is rough or has edges, corona discharges can occur in the gas and a significant corona current can be fed via the resistance of the solid insulating material.

(3) Charge carriers that drift along the electric field lines out of a large gas-volume can be accumulated at the surface of a solid material with a *very low surface conductivity* (*electrostatic charging*). If a corona source is within the range of the field, charge accumulation can be significantly intensified. This gives rise to field distortions, and the risk of suface discharges and flashovers is increased.

Note: In air, electrostatic charging is especially dangerous for high-resistance polymeric materials (e.g. polyethylene, silicone, epoxi resin) under dry air conditions with a relative humidity below 30 %. These problems can be avoided by *higher air humidities* or by *less resistive materials* (e.g. glass, resin-bonded paper) which both increases the surface conductivity to the extend that accumulated charges come into contact with surface charge carriers and can be discharged.

e) Multi-layer insulations

In the following, an oil-pressboard insulation in a converter transformer is chosen as an example.

In simple planar multi-layer insulations, interfacial polarization can be simulated with a simple *RC* parallel equivalent circuit. After a long time, when the effects of interfacial polarization are dominant, good consistency of simulations with current measurements can be achieved [271]. In shorter time periods, additional polarization processes in solids as well as non-linear oil properties must be considered [456], Figure 4.3-9.

The effect of *polarization processes* in **solid materials** is that *larger currents* flow over longer periods than those that would be expected from the steady-state DC conductivity. Increased currents in the solid insulation components increase and especially prolong the voltage drops and *stresses at the oil gaps* that are connected in series [271].

Note: In a simplified manner (which is physically not entirely correct), the described effect can be compared with an increased *"apparent conductivity"*, at least as long as only polarization currents are flowing. Depolarization currents can no longer be explained using this simplification.

Owing to the *increased initial conductivity* in **liquids**, *oil gaps* are at first *relieved* in transition processes, since the polarization currents that are given by the barrier properties lead to lower voltage drops. This acts against the field-strength-increasing influence of initially increased polarization currents in the barriers.

The duration of the relief is dependent on the *transit time τ of ions* through the free oil gap, i.e. it is dependent on the effective oil gap width (in the direction of field), Eq. (4.2-5).

Further, the decline in the number of charge carriers for new and *highly resistive oils* can lead to very *low steady-state conductivities* and very *large time constants* in insulation systems.

Thus, the transition processes proceed very slowly and the stresses on the oil gaps *last longer*, Figure 7.2.3-7 (bottom). During the *polarity reversal*, a partial compensation between the actual field that is still in transition and the superimposed displacement field results in the oil, so that the *peak stress in oil* is *reduced*.

Moreover, the *non-linear behavior of the insulating oil* at very high field strengths leads to a *conductivity rise*, which in turn causes a fall in the field strength. Only a simulation that takes this non-linear correlation into consideration, can therefore clarify which field strengths develop in the insulation system [271], [486], [504]. Linear equivalent circuits are *not* suitable for this.

f) Complex insulation systems

Also in this sub-section, the converter transformer insulation is considered as an example:

Owing to the non-linear increase of oil conductivity with the field strength, also the *conductivity ratio* between oil and barriers is increased, and the grading effect of the barriers for *steady-state stresses* is thereby improved.

The effect of *non-linear oil properties* as well as the effect of *polarization currents in solids* on the complex *transition processes* in insulation arrangements, especially on the tangential stresses at bushing surfaces and barrier surfaces (as illustrated as an example in Figure 7.2.3-9), is the subject of research [456], [486], [500], [503], [504].

7.2.1.4 Design of Insulation Systems for DC Voltage

The designer of DC insulation systems is faced to a number of specific difficulties. In principle, they require consideration of the following steps:

1. **Steady-state** DC field distributions are conduction fields and must be calculated by means of *conductivities*.

2. In the case of **polarity reversals** or **voltage variations**, steady-state or transient field distributions and displacement fields must be *superimposed*.

3. **Transient processes**, which can sometimes last for very long times, must be investigated up to the time when *steady-state* is reached.

4. The **variations of conductivities** must be well-known for the relevant parameter field (inter alia, *temperature, field strength, time, ageing*), must be quantitatively described and must be taken into consideration.

5. Parameter dependences that cannot be quantified, must be considered **by worst-case estimations**.

6. A **robust design** must be chosen which meets the stresses according to the worst-case scenarios.

7. Relevant **multi-physics phenomena** that are not always included in the applied simulation models, such as *temperature gradients, charge carrier drift, charge carrier injection* or *space charge formation*, must be considered by further on refined multi-physics simulations. If this is not possible, qualitative analyses must be performed and appropriate *safety factors* must be chosen for the design.

8. The **variation of important parameters** (such as *operational temperatures*, *temper-*

ature gradients in the insulation or variation of conductivities during *ageing*) should kept *as small as possible*, should be monitored by *diagnostic measures*, if possible, and should be assessed with respect to *reliability and safety* of the insulation.

Examples for typical DC insulation systems in high-voltage equipment and high-voltage components are described in the following sections.

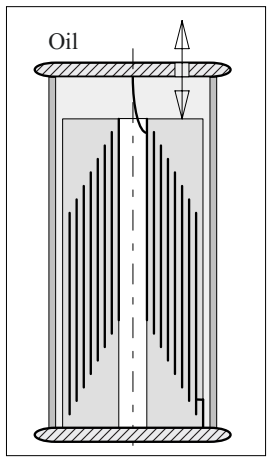

Figure 7.2.2-1:

DC capacitor for the use in an oil-filled device. Single capacitor element with internal series connection of partial capacitances and potential grading at the front ends. Compensation of the thermal expansion by the surrounding oil.

7.2.2 Capacitors for Direct Voltage (DC Capacitors)

The basic **structure** of capacitors for direct voltage (DC capacitors) is not different from the structure of AC capacitors. DC capacitors likewise consist of impregnated *individual capacitor elements* connected in series in a housing, Figure 7.1.4-1.

Compact high voltage capacitors can also be implemented with internal series connections in a single capacitor winding element, Figure 7.2.2-1. The capacitor element is made by winding of a paper web similar to how a bushing is made. The metallic foils are inserted axially offset. Along with the series connection of partial capacitances, the foils simultaneously cause an axial grading of the potential.

When using the capacitor in an oil-insulated device, e.g. as a smoothing capacitor for the voltage source of an X-ray device, thermal expansion can be compensated via a connection opening to the surrounding oil.

The **stressing of the capacitor dielectric** was explained above in Section 2.4.4.1 and 2.4.4.2 with Figures 2.4-23 and 2.4-30:

Oil gaps are largely relieved from field stress owing to their higher conductivity. In a mixed dielectric made of oil-impregnated paper and polymeric films, the DC field is displaced into the latter, which accordingly must be designed to be strong; the paper must rather be considered as an electrically less heavily stressed impregnating wick.

At the **foil edges**, a stress reduction results from currents and the accumulation of space charges in the impregnating gap between the insulation layers, Figure 2.4-30 (bottom). Therefore, the **DC voltage strength** of the capacitor dielectric is higher by about a factor of two than the *AC voltage strength*: the foil edges are relieved from stress, the field is generally displaced from the more conductive and weaker materials into the more resistive and stronger materials. Eroding partial discharges at power frequency cannot occur, cf. Section 7.2.1.

Nevertheless, in the case of a **polarity reversal** or for **back-swinging discharges**, the accumulated charges lead to severe field stress enhancements, partial discharges and reduced service life.

However, for *booster capacitors* in DC voltage multiplier circuits, the lower AC voltage strength must be taken as a basis, since a distinct *AC voltage stress* exists at the beginning of the charging process, Figure 6.2.2-4.

DC voltage capacitors are frequently also used as *energy storage capacitors* in *impulse cur-*

rent circuits, Section 7.3.3. Thereby, the service life is significantly reduced. Terminations and contacts in the capacitor must be designed for very large *impulse currents.*

When applying a (direct) voltage, the **voltage distribution** in a capacitor (or in a series connection of capacitors) is at first inversely proportional to the *partial capacitances,* owing to the capacitive charging current. Ideally, this distribution should also be equal to the steady-state distribution on the basis of the *insulation resistances*.

For series connections, it must therefore be strictly ensured that the capacitors are *identical*, even with respect to the insulating material and the insulating material temperature. In the case of diverse insulation resistivities, the voltage distribution is modified.

Stressing capacitors with DC voltage is associated with a few typical **hazards** for the user, which do not arise the in case of AC voltage applications:

Even after disconnecting the voltage source and opening the safety circuit, a charge can still be present at the *capacitances*. It must be dissipated by **safety measures** (discharge resistances, automatic and manual discharge, permanent short circuit).

A further danger arises from the voltage that recovers after removing a short circuit (*recovery voltage*). It results from charge reversal processes in the dielectric and leads to the recharging of the main capacitance, Figures 2.4-31, 4.3-2 and 6.4.7-1. Therefore, capacitors that have been stressed with DC voltage must remain *permanently short-circuited*.

Danger also occur from a *series connection* of capacitors that are not identical: in the case of a short circuit of the two external terminals, dangerous residual voltages between the intermediate terminals and the external terminals can still remain. Therefore, *all* terminals must be included in the short circuit.

Attention! As a preceding DC stressing can never be completely ruled out, the requirement of a **permanent, reliable and readily visible short circuit** of all capacitor terminals is always valid for **all openly accessible DC, AC and impulse capacitors** if they are unused at the moment.

7.2.3 HVDC Transformers

7.2.3.1 Dielectric Stresses

Converter transformers in the converter stations of high-voltage direct-current transmission systems (HVDC transmission systems) have high-voltage bushings that project into the **converter hall** and supply the converter-bridge circuits, Figure 7.2.3-1. These, for example, consist of a series connection of two bridges that are each fed by transformer windings in the star connection and delta connection to reduce the ripple of the DC voltage (twelve-pulse three-phase bridge connection), Figure 2.2-2.

The rectifier valves are connected in series and parallel in the so-called **valve towers** and are provided with circuits for uniform *potential distribution* and for potential-free *ignition*. The valve towers are surrounded by *shielding electrodes* which are at the potentials of the shielded bridge units being connected in series. For reasons of protection against earthquake, the valve towers are suspended from the ceiling in the converter hall. DC voltage is led through **wall bushings** into the outdoor substation.

With transmission voltages of 800 kV, previously valid insulation limits were broken. Safe design of the operating equipment leads to extremely high test voltages and design voltages [466], Table 7.2.3-1. This results in dimensions that have been unknown until now, both for the internal and external insulation of the whole installation and in particular also for HVDC transformers [453], Figure 7.2.3-2.

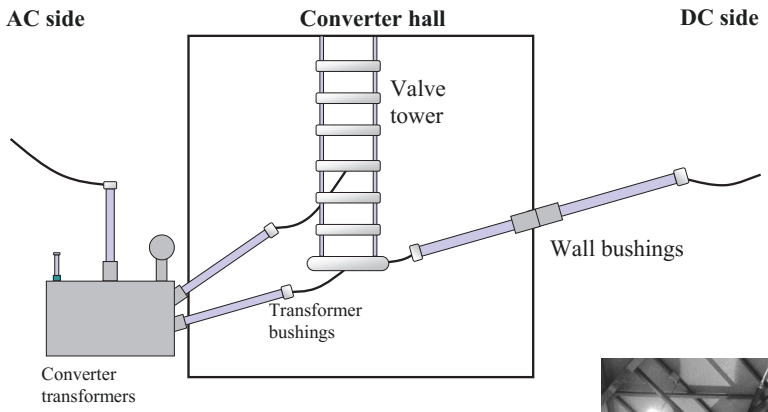

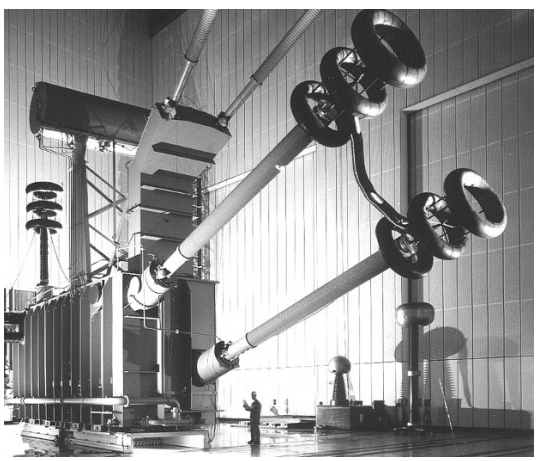

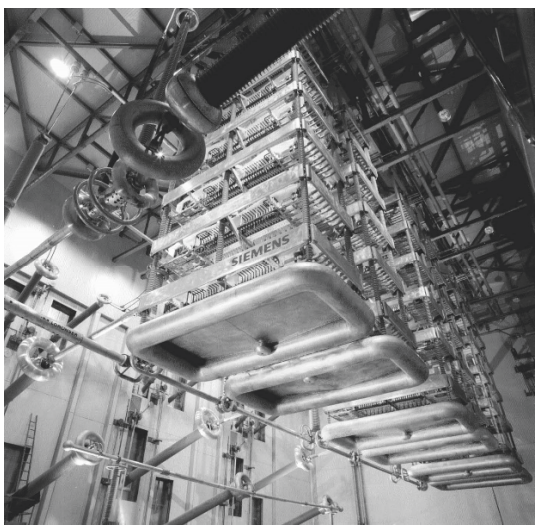

Figure 7.2.3-1:

Basic construction of a HVDC converter hall (left).

500 kV converter transformer in a transformer test field (bottom left) and converter hall with valve towers and transformer bushings (bottom right).

Photos Siemens.

Table 7.2.3-1: Test voltages and design voltages for an 800 kV DC system [466]: (1) Transformer valve side, (2) Transformer-bushing valve side, (3) DC wall bushing, (4) DC switchgear.

Voltage in kV	*(1)*	*(2)*	*(3)*	*(4)*
SIL (Protection level)	1,344	1,344	1,344	1,330
SIL (Withstand volt.)	1,600	1,760	1,600	1,600
BIL (Protection level)	1,344	1,344	1,344	1,579
BIL (Withstand volt.)	1,800	1,980	1,800	1,950
AC (Test voltage)	905	1,054	---	---
DC (Test voltage)	1,250	1,455	1,200	1,200
PR (Test voltage)	965	1,124	1,000	1,000

Maximum test voltages and design voltages are generally required for the transformer bushings, since an especially high level of safety is necessary for these strategically important components, Table 7.2.3-1 *(2)*. The technological leap becomes especially clear from the the transformer bushing dimensions and specifications that have never seen before [432], Figure 7.2.3-3 and Table 7.2.3-2.

Note: **Type test voltages and routine test voltages** for the highest voltage levels are still specified very much *depending on the respective project* as long as standardized values are not yet available for this.

For example, the values that are listed in Table 7.2.3-2 are type test values for 844 kV *converter-transformer bushings*. However, these values are partly also stipulated as routine test values (BIL withstand voltage 2090 kV, AC 60 min at 1100 kV). For *wall bushings*, slightly different values can be used, e.g. for type tests SIL 1800

kV and BIL 2105 kV, and for routine tests respectively BIL 2105 kV, AC 1 min at 1002 kV, DC 1224 kV as well as DC-PR 1020 kV.

In the transformers, the insulation of the high voltage windings is stressed, at the same time, not only by induced AC voltages but also by superimposed DC voltages, that is to say, by the so-called *pulsating or undulating*.

Further, critical DC voltage stresses occur also for **wall bushings** in the converter halls, where problems arise above all with the *external insulation* owing to contamination and wetting, cf. Section 7.2.4.2.

In addition to the **steady-state DC field stresses** and **pulsating field stresses** that mainly occur in operation after a long time,

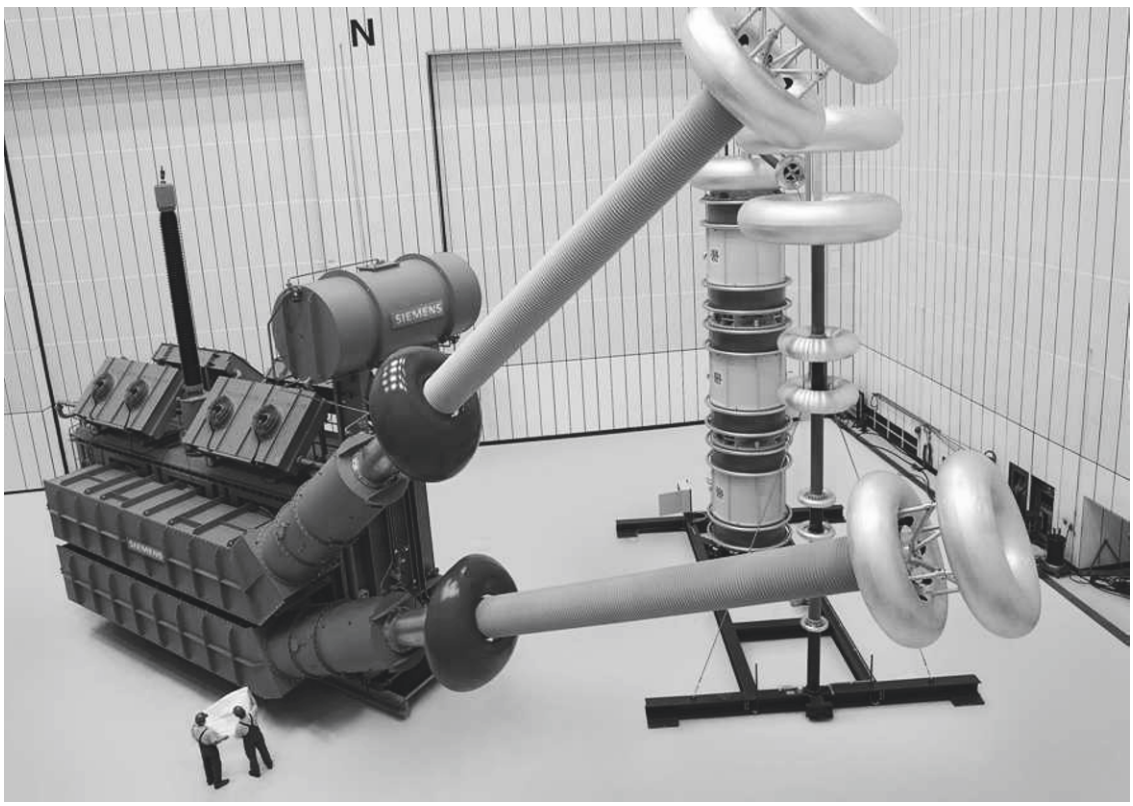

Figure 7.2.3-2: The world's first 800 kV HVDC converter transformer with AC bushing (left, in an upright position) and HVDC bushings for both the winding terminations on the converter side (in the foreground and in an inclined position) after the final acceptance tests in the high voltage test field [453] (5000 MW HVDC system Yunnan-Guangdong in the southwest of China, photo Siemens).

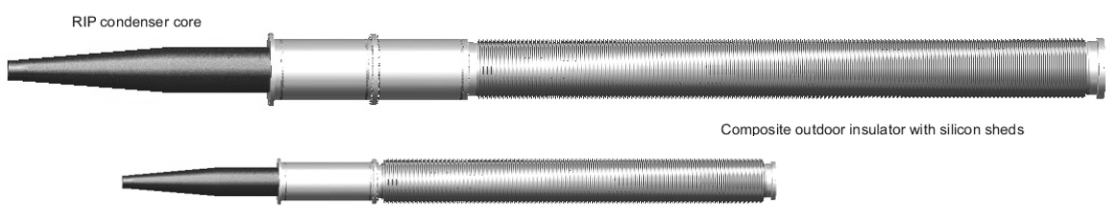

Figure 7.2.3-3: Technological leap in conjunction with the transition from 400 kV to 800 kV HVDC systems, illustraded with the example of cast-resin-impregnated RIP transformer bushings [432] (length 8.1 and 13.5 m respectively; other technical data in Table 7.2.3-2, photo HSP Hochspannungsgeräte GmbH, Troisdorf).

stresses occur as a result of **connecting** to DC voltage **or polarity reversal** of DC voltage owing to high dielectric displacement currents and **transition processes** (transients), in which critical stresses can occur that cannot be directly identified from the initial and final values.

Note 1: In conventional HVDC systems with a *current-source DC-link*, **polarity reversal of DC voltage** is necessary if the *direction of power flow* is to be reversed; the *current direction* remains the same in this case (CSC *current source converter*).

Note 2: In HVDC systems with *voltage-source DC link*, reversal of the power flow direction is possible by *reversal of the current direction* for constant voltage polarity, i.e. **without polarity reversal** (VSC *voltage source converter*). Systems with lower voltages (up to approx. 100 kV) can be operated by phase-fired control, i.e. in the switching mode with square-wave voltage pulses; cf. Section 7.2.6. However, very high voltage transients occur. Therefore, *multi-level converters* are used for higher voltages. They can precisely reproduce the sinusoidal time characteristic of the AC voltage by means of charged capacitors that are connected in series by transistor switches. That's why multi-level converters have comparatively low *filtering requirements*. Nevertheless, the *ohmic loss* of the transistor switches is slightly higher than the loss of the thyristor switches in the CSC systems so that VSC technology is not yet used for the highest transmission powers.

Table 7.2.3-2: Comparison between 800 kV HVDC converter transformer bushings and previous 400 kV bushings, as per Figure 7.2.3-3 [432].

844 kV UHVDC		***412 kV HVDC***
Bushing data		
844 kV	*Voltage*	**412 kV**
3.600 A	*Curent*	2.200 A
3.000 MW	*Power*	**906 MW**
13,5 m	*Length*	8,1 m
4.000 kg	*Mass*	800 kg
2.400 kg	*Resin mass*	**440 kg**
26.000 N	*Bending stress*	5.000 N
Test voltages		
1.100 kV, 1 h	*AC*	750 kV, 1 min
1.455 kV, 2 h	*DC*	900 kV, 1 h
2.090 kV	*BIL*	1.550 kV
1.843 kV	*SIL*	1.300 kV

Steady-state DC voltage stresses, stresses after polarity reversal (PR) and transient stresses shall be covered by special HVDC test cycles, Figure 7.2.3-4. They are described in detail in the following sections.

7.2.3.2 AC and Steady-state DC Voltage Stresses

a) Barrier systems

In the case of *AC voltage stresses*, **barrier systems** are used in oil-insulated devices for subdivision of the *oil gaps* into sub-gaps with higher dielectric strength [27], Figure 3.4.2-6 and Section 7.1.3. The barriers must fulfill this function also in oil-insulated HVDC devices with pulsating field stresses. The barriers are arranged approximately parallel to the equipotential surfaces, as in AC voltage transformers. The basic formation of electric AC fields and DC fields is explained in the example for a field section assumed to be uniform [274], Figure 7.2.3-5.

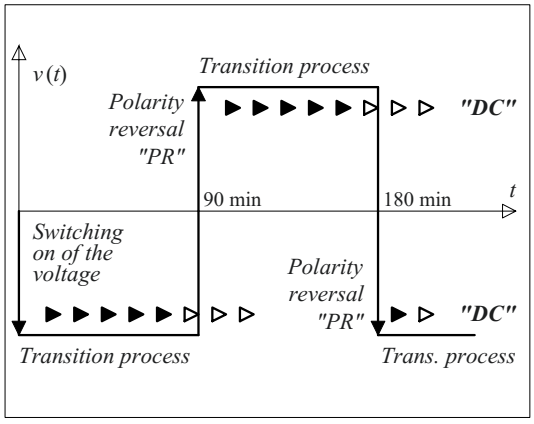

Figure 7.2.3-4: Typical HVDC test cycle.

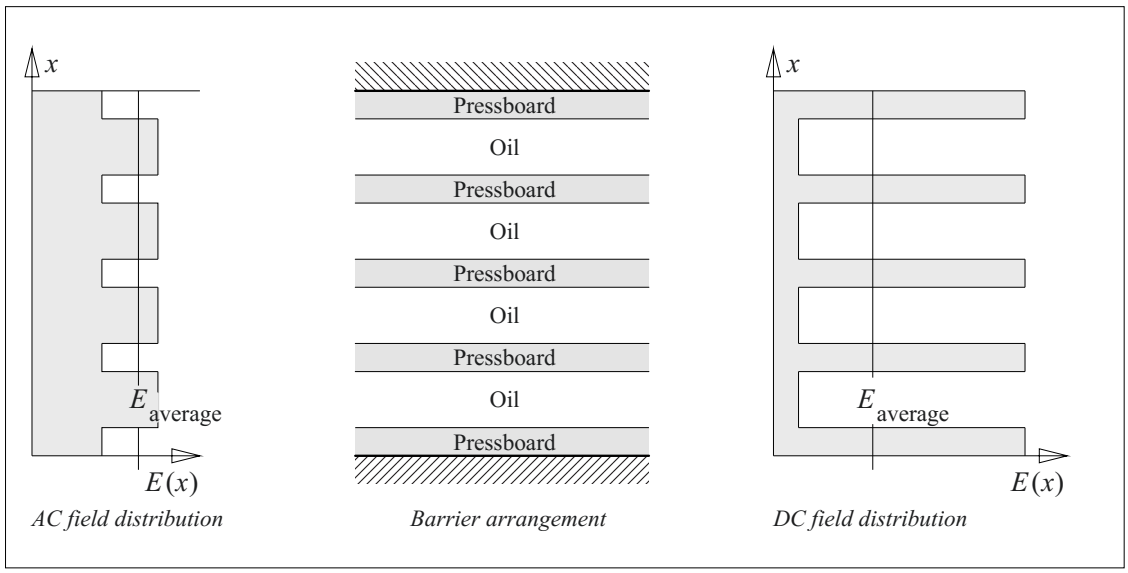

Figure 7.2.3-5: Field stressing of materials in a planar barrier arrangement (center) for AC and DC voltage stresses (left and right) with a ratio of permittivities of 2:1 and with a ratio of conductivities of 1:10 (pressboard : oil) [274].

Since the electric AC field is displaced from the pressboard barriers (ε_r = 4.4) into the insulating oil (ε_r = 2.2), the oil gaps are higher stressed than the barriers, Figure 7.2.3-5 (left). It would therefore be advantageous to select thin barriers as in a conventional transformer, so that the oil gap widths are not excessively reduced. This, however, conflicts with the requirement for DC voltage strength.

For *DC voltage stress*, the electric field is displaced from the more conductive oil (e.g., with $\kappa = 10^{-12} ... 10^{-13}$ S/m) into the pressboard that is less conductive by about two orders of magnitude (e.g., with $\kappa = 10^{-15}$ S/m). Thus, a field stress relief of the weaker oil takes place, but the applied voltage must be insulated largely by the barriers, Figure 7.2.3-5 (right). Therefore the DC voltage strength is not determined by the oil gap width, but by the thickness and number of the *pressboard barriers* [82].

Thus, a *design compromise* with adequately wide oil gaps and adequately thick barriers must be made to satisfy conflicting requirements for AC voltage strength and DC voltage strength [274].

b) Gaps bordered by high-resistance barriers

In **oil gaps** that are bordered by high-resistance barriers, e.g. between overlapping barriers, a steady-state current flows *parallel to the surface* in the steady-state DC voltage condition, Figure 2.4-34a. The potential difference across the barrier is approximately equal to the voltage drop along the overlapping length of the barriers. The length of the overlap must correspond to this stress.

The *design of oil gaps* between lowly-conductivity boundaries can be used specifically for grading the DC voltage distribution between the electrodes [7], [10], [276], [277]. A uniform voltage distribution requires a uniform *gap cross section* between the two electrodes.

Also the *contact to the electrodes* must be of large area and adequately conductive. Pressboard coating of electrodes, which is useful for AC voltage, must not obstruct current access to electrodes for DC voltage.

Narrowing of gaps would lead to an increase in field strength by constricting the current flow lines.

c) Transformer bushing

An **HVDC transformer bushing** for *AC voltage stress and DC voltage stress* is considered as an example, Figure 7.2.3-6 (left and right). The connection between conductor and bushing is shielded by an *electrode*. It is coated with pressboard in order to increase the dielectric strength of the adjacent oil gap. The bushing is considered both without and with a *barrier system*, Figure 7.2.3-6 (top and bottom). This arrangement has already been discussed in Section 2.4.4.2 as an example of a typical DC voltage field, Figure 2.4-28.

For *AC voltage*, the capacitive grading layers of the bushing and the electrode geometry determine the spatial distribution of the equipotential lines, Figure 7.2.3-6 (left). Thin *barriers* have only a slight influence on the field distribution (Figure 7.2.3-6 left, top and bottom). The barriers in the lead-exit area are adjusted to the profile of the equipotential lines in order to sub-divide the oil gaps in the direction of the electric field and to increase their dielectric strength. The stress applied is predominantly radial and is concentrated on the oil gap.

For *DC voltage*, an intense field concentration occurs around the electrode if there are no barriers, since the resistive potential distribution within the bushing core is decoupled from the surrounding oil by a generally high-resistive insulation cover layer, Figure 7.2.3-6 (right top).

For DC voltage, a *barrier system* leads to a completely changed field distribution and it can therefore be used specifically for resistive field grading, Figure 7.2.3-6 (right bottom). The radial stress persists in the conductor and electrode area. In the oil gaps, however, stress is largely reduced and almost the entire voltage drop occurs in the less conductive *pressboard barriers*, cf. Figure 7.2.3-5. The barrier dimensioning must be appropriate for this stress. In the *axial oil gap* between bushing surface and the barrier ends, an **axial conduction current** flows, which homogenizes the potential distribution in the axial direction and corresponds to an axial field stress, cf. also Figure 2.4-28 and 2.4-34a. This current through the axial "grading gap" must be provided with a large area access to the conductor. Considering the AC stresses, this area must be covered by the insulated shield electrode. An oil gap with a *continuously even cross section*, uniform current density and uniform field strength would be optimal. Constrictions that lead to increased current density and increased field strength are critical here.

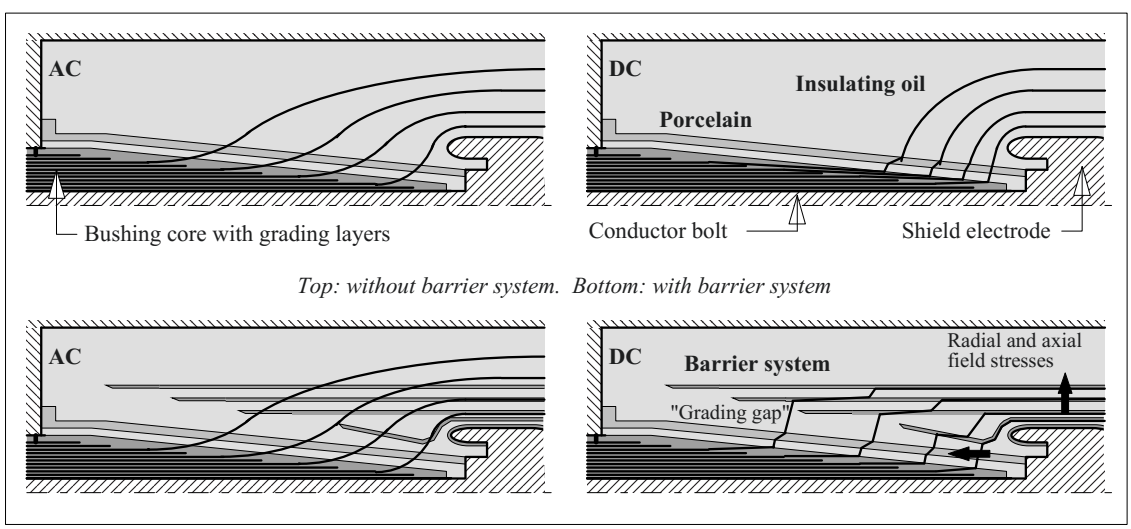

Figure 7.2.3-6: HVDC transformer bushing at AC voltage (left) and at steady-state DC voltage (right), without barrier system (top) and with barrier system (bottom). The 20 % equipotential lines are illustrated (schematic).

Note: In addition, some bushings have a housing insulator made of porcelain and an internal oil gap. The axial potential distribution can also be significantly influenced in this way.

The field grading effect of the barriers is based on the large *conductivity difference* between oil and pressboard. If this difference reduces, e.g. by using less conductive insulating oil, the grading effect of the axial oil gaps deteriorates. Also for increased *temperatures*, field grading deteriorates, since the conductivity difference between the oil and the barriers decreases, Figure 4.2-9, and in extreme cases it can completely disappear.

Within the **bushing**, and for *AC voltage*, a capacitive voltage distribution takes place which causes potential grading even in the surrounding dielectrics. For *DC voltage*, the resistive voltage distribution between the grading layers corresponds to the capacitive voltage distribution, provided a temperature gradient and conductivity gradient do not lead to distortion [188]. However, penetration to the more conductive oil in the barrier system is negligible to a first approximation. The bushing thus requires an adequately dimensioned radial insulation over the grading layers, since internal and external potential gradings are in general different and can, for example, vary with the temperature.

7.2.3.3 Stresses during Voltage Variations

Voltage variations generate dielectric displacement fields which are superimposed on the existing fields. The stresses will first be explained for a simple oil barrier system, Figure 7.2.3-7 (top).

On **connecting a DC voltage,** field strengths are distributed according to the permittivities; for the simple oil barrier system it is approximately in the ratio

$$\frac{E_{\mathrm{Oil}}}{E_{\mathrm{B}}} = \frac{\varepsilon_{\mathrm{B}}}{\varepsilon_{\mathrm{Oil}}} = \frac{4.4}{2.2} = \frac{2}{1}, \qquad (7.2\text{-}1)$$

Figure 7.2.3-7 (left). Subsequently, and in a transient process, the field strengths in oil and pressboard tend to approach a steady-state condition

$$\frac{E_{\ddot{\mathrm{O}}}}{E_{\mathrm{B}}} = \frac{\kappa_{\mathrm{B}}}{\kappa_{\ddot{\mathrm{O}}}} << 1 \qquad (7.2\text{-}2)$$

with a completely changed field distribution. Whether the steady state is reached, depends on the *time constant*

$$\tau = R_{\mathrm{Oil}} C_{\mathrm{B}} \qquad (7.2\text{-}3)$$

with which the barrier capacitance is charged via the oil gap resistance. Therefore, steady-state conditions are achieved at high oil conductivities and small time constants (e.g. after ageing in operation), Figure 7.2.3-7 (center), but not necessarily at low oil conductivities and large time constants (e.g. for routine testing), Figure 7.2.3-7 (bottom).

Note: It must be noted that conductivity ratios and DC field distributions can be greatly varied by **temperature variations** and **temperature gradients**. This can lead to the situation that stress conditions that were not covered in the *tests* are possible in *operation* [275], [278], [279]. It is therefore advisable to carry out *field calculations* and field studies with various feasible conductivity ratios, so that *worst-case scenarios* can be identified [281].

The **stress after the polarity reversal** (PR) can be estimated by determining the *field condition before the voltage variation* $\boldsymbol{E}_{\mathrm{bef}}$. The voltage step during PR then superimposes a field-strength step in the form of a *dielectric displacement field* $\Delta\boldsymbol{E}_{\mathrm{AC}}$ (similar to an "AC"-alternating field), whose magnitude corresponds to the voltage swing $\Delta V = +V - (-V) = 2\ V$ and thereby a particularly high stress is generated. In the case of linear systems, the magnitude of the *polarity reversal stress* (PR) is

$$\boldsymbol{E}_{\mathrm{PR}} = \boldsymbol{E}_{\mathrm{bef}} + \Delta\boldsymbol{E}_{\mathrm{AC}}(\Delta V{=}2V). \qquad (7.2\text{-}4)$$

For the oil gaps with the previously *lower stresses*, very *high stress peaks* thus occur, since the superimposed dielectric displacement

field again meets a capacitive field distribution according to Eq. (7.2-1).

Polarity reversal stresses in the oil gaps are strongly dependent on the *initial state*. For the simple barrier system as in Figure 7.2.3-7, the equal step height leads to different stresses: For a high oil conductivity, a very high peak stress in oil occurs which quickly decreases; and for a low oil conductivity, a significantly lower peak stress in oil is generated, but it lasts significantly longer. Again, the time constants according to Eq. (7.2-3), with which the insulation system tends towards the new steady state, are important.

7.2.3.4 Transition Processes (Transients)

a) Two-layer arrangement

In a **two-layer arrangement**, e.g. made of oil and oil-impregnated pressboard in the barrier system of a transformer, the transition processes proceed approximately exponentially between the initial state (e.g. a capacitive voltage distribution after connection or polarity reversal of a DC voltage) and the final state (e.g. a resistive voltage distribution after a very long time).

Note: Deviations from the exponential profiles owing to *polarization currents* and as a result of *non-linearities* are discussed in Section 7.2.1.3.

Basically, the above-mentioned transients have already been described in Section 2.1.4.3 with Figure 2.1-16 for a *plane capacitor dielectric* and in Section 7.2.3.3 with Figure 7.2.3-7 for a *plane transformer barrier arrangement*.

Depending on the test duration, *initial states and final states*, need not always correspond to the capacitive field distribution and resistive field distribution respectively, because the field distributions caused by previous stresses are to be superimposed, cf. Figure 7.2.3-7. Low oil conductivity causes, for example, large time constants and slow transition processes, so that before the polarity reversal, oil is still under stress and the pressboard experiences reduced stress, Figure 7.2.3-7 (bottom). Therefore, the displacement field superimposed during the polarity reversal is partially compensated by the previous field, especially in the oil, so that a reduced peak stress in oil results.

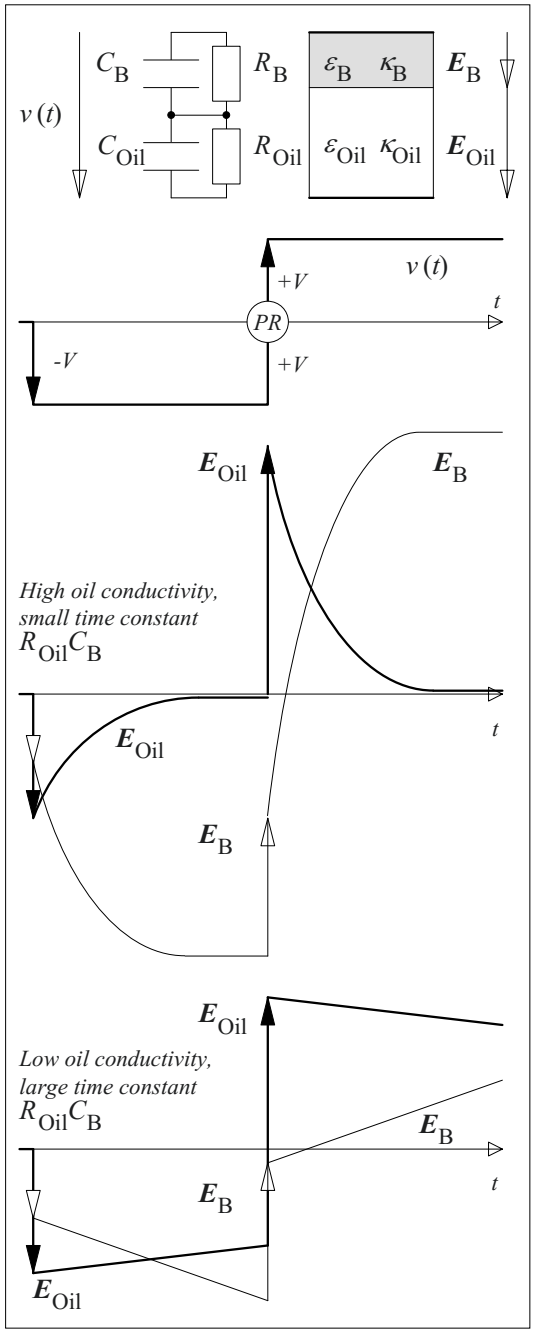

Figure 7.2.3-7: Stressing of an oil barrier system on connection and polarity reversal of a DC voltage for high and low oil conductivity (top and bottom).

Here, the transition processes proceed largely **exponentially decreasing or increasing** and without intermediate maxima, so that the *maximum stresses* can be determined from the *initial states* (for the oil) and from the *final states* (for the pressboard). However, for very highly resistive materials with large time constants, steady states are reached only after very long periods, which probably do not occur in practice for short-duration DC voltage stresses.

b) Three-layer arrangements

In a **three-layer arrangement**, e.g. made of oil, oil-impregnated paper and synthetic material, the transition processes proceed in complex form after switching on or polarity reversal of the voltage [7], [10], [276], [277], Figure 7.2.3-8.

Note: A similar case (plastic barriers between two different oils) has already been discussed in Section 2.4.4.3 with Figures 2.4-32 and -33 as an example of a transition process.

Based on the capacitive field distribution, which stresses all three materials according to their permittivities, the field stress at first decreases in the *most conductive layer* (generally, in the oil gap) but the capacitances of higher resistive layers are thereby charged and stressed to a greater extend. These *less conductive layers* (pressboard and plastic) must therefore additionally take over voltage drops from the oil gap. Thereby, both experience an initially increasing field stress. In the further course of the transition process, also the material of *medium conductivity* (e.g. pressboard) is discharged, so that the applied DC voltage must finally be insulated largely by the material with the *lowest conductivity* (e.g. plastic). For the material with the medium conductivity, the first increasing and then reducing stress causes *a transient voltage overshoot* or a **field strength maximum**, which cannot be detected from the initial state and the steady state.

Here too, the initial states can be displaced by preceding stresses and the steady states can possibly be reached only after very long periods.

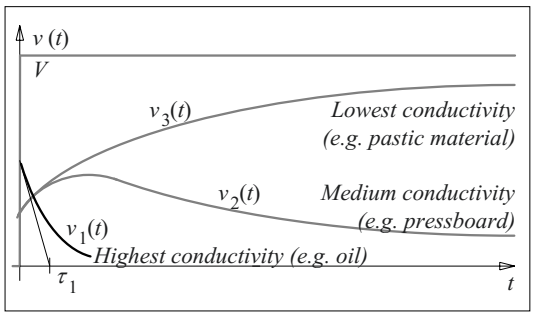

Figure 7.2.3-8: Transition processes (transients) in a three-layer dielectric after switching on a DC voltage v(t).

c) Complex insulation systems

In complex insulation systems, **spatial and temporal displacements** *of field stresses* (*field migrations)* occur within the insulation system similarly to the field displacements between the insulating materials described in Figure 7.2.3-8. These processes can be examined, for example, with spatially cross-linked equivalent circuits [280] or with transient numerical field calculation [282]. Below, the field migrations will be explained in a clear and simplified representation:

As an example, the polarity reversal of a DC voltage at two **overlapping barriers** was already explained in Section 2.4.4.3 with Figure 2.4-34.

Directly after the reversal of polarity, high field strengths in the oil gap as well as a zig-zag-shaped potential pattern with high, but opposite stresses in the oil and in the barriers result from the superimposition of conduction fields and displacement fields according to Eq. (7.2-4). Additionally, “islands” with potentials above 100% and below 0% occur that are to be attributed to positive and negative surface charges.

A practically important example is the interaction of **the bushing and the barrier system** in a HVDC transformer, Figure 7.2.3-9. The oil is regarded as significantly more conductive than the bushing core and barriers. For DC voltage, the oil gap thus fulfills the field grading function explained in Figure 7.2.3-6.

Moreover, the barriers increase the dielectric strength of the oil gaps in the radial direction.

For the *simplified schematic representation*, the barrier system according to Figure 7.2.3-9 (top) is aggregated in a tapered equivalent barrier, Figure 7.2.3-9 (1) to (6). A numerical calculation is possible, e.g. with spatially cross-linked equivalent networks [280]. Some especially important equivalent elements are indicated in the figure.

Transition processes start with the **connection of a negative DC voltage (1)**. Here, the permittivities that are described by spatially distributed partial capacitances are the dominant properties. Therefore, an electric *displacement field* that corresponds to an AC field results at first.

Immediately thereafter a **transition process (2)** begins, during which, basically, the capacitances of the highly resistive materials (barriers and bushing core) are charged in the radial direction via the more conductive oil gaps, Figure 7.2.3-9 (2). In the lower area of the insulation (L), the charging of barriers proceeds faster than in upper area of the insulation (U) owing to smaller capacitances of the thicker barriers: thus, the equipotential lines displaced into the bushing insulation must pass over into the barrier system close to the electrode. This causes a *high tangential (axial) transient stress* in the lower end of the oil gap close to the

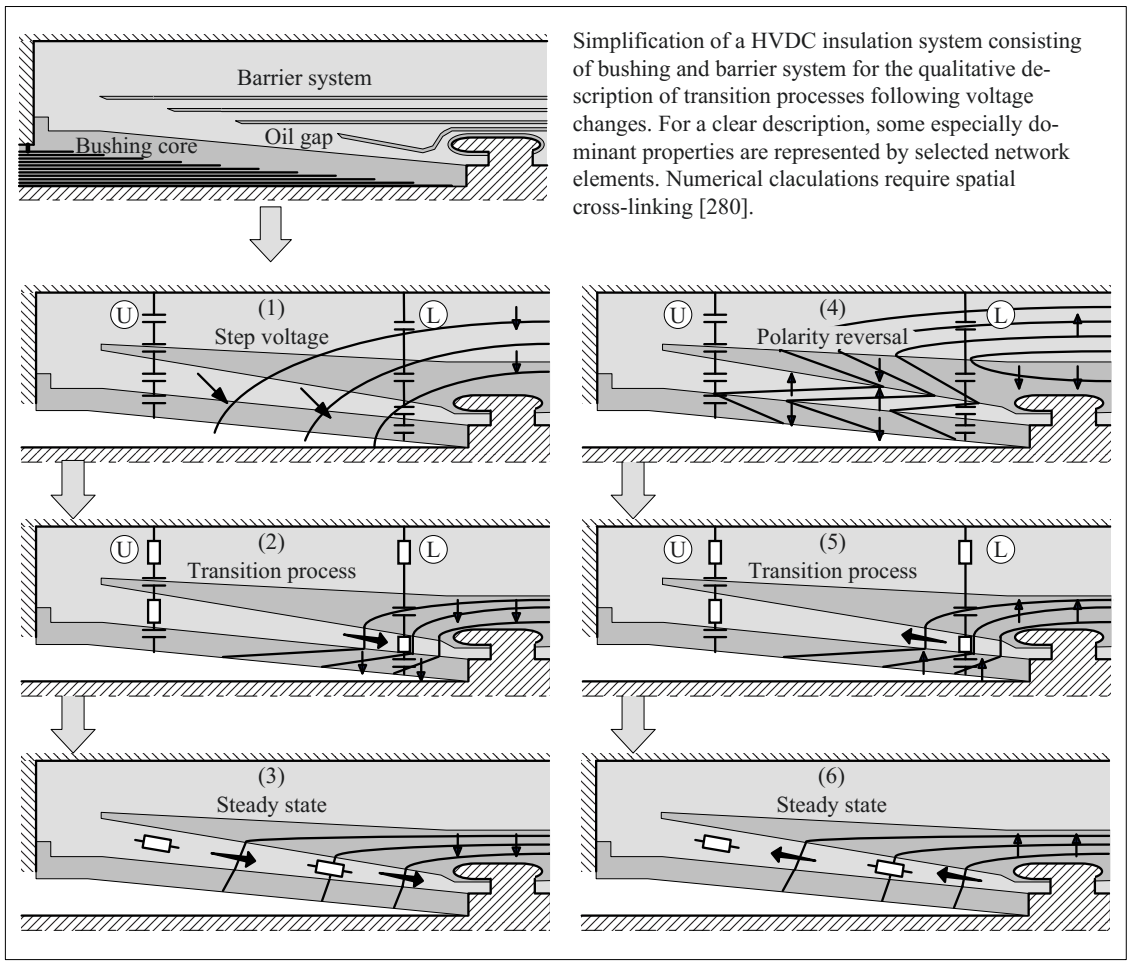

Simplification of a HVDC insulation system consisting of bushing and barrier system for the qualitative description of transition processes following voltage changes. For a clear description, some especially dominant properties are represented by selected network elements. Numerical claculations require spatial cross-linking [280].

Figure 7.2.3-9: Transient phenomena in a HVDC insulation [280] after connection of the voltage (1 to 3) and after reversal of the polarity (4 to 5) in a 25 % equipotential plot (schematic).

electrode, which can significantly exceed the steady-state stresses [280].

Subsequently, a **steady state (3)** occurs, in which the *axial conduction current* flowing in the oil gap determines the axial electric field strength by the magnitude of its current density. In case of a suitable *gap geometry*, a uniform current density homogenizes the field stress. Whether this steady state is achieved depends on the time constants of the materials (especially determined by the oil conductivity) and on the duration of the voltage stress.

During the **polarity reversal (4)**, a dielectric displacement field which corresponds to the *doubled voltage swing* $\Delta V = 2 \cdot V$ is superimposed on the preceding field state according to Eq. (7.2-4) and the *oil gap is extremely stressed*. This scenario has already been explained in detail in Figure 2.4-34 for overlapping barriers.

In the subsequent **transition process (5),** the still charged radial capacitances of the barriers and the bushing top layer insulation are first *discharged* and then *charged again* (i.e., finally *charged reversely*) with different time constants in the lower (L) and upper (U) areas of the insulation. Thereby, the radial stresses in the oil gaps are reduced. Here too, the field displaced into the bushing insulation must pass over into the barrier system close to the electrode. Again, this causes *high axial transient stresses in the oil* adjacent to the bushing.

Finally, here too a **steady state (6)** results, provided the time constants are sufficiently small or the stress time is sufficiently long.

In order to **keep the described processes under control** by the insulation system, a *coordinated design of all components* is required with regard to the geometrical contours of all components, with regard to the properties of all the insulating materials used and with regard to extensive test experience and operating experience [280]. For field studies, it is recommended to carry out calculations with different feasible conductivity ratios to determine the *critical scenarios* [281].

7.2.4 HVDC Bushings

The design of DC bushings is very much similar to the design of AC bushings, cf. Section 7.1.2. However, some important differences must be considered. must be considered.

7.2.4.1 Internal Insulation

At first, it must be noted that potential grading in the bushing core, which is designed as a *capacitive grading*, must act as a **resistive grading** during steady-state DC voltage application. Due to identical capacitive and resisitve geometries, the potential distribution is basically identical for both of the cases if there is no temperature gradient in the core. This can be shown by a step response measurement during which a *transition from the capacitive to the resistive potential distribution* occurs [505], [506], Figure 7.2.4-1 (top).

Note: The insulating layers between the grading layers act similar to a compensated resistive-capacitve **voltage devider** which exhibits a *frequency-independent divider ratio* and which can be used from impulse voltages, to AC voltages, transient voltages and DC voltages, cf. Figures 6.3.4-2 (b) and 6.3.4-3.

Similar to a cable insulation, the bushing insulation encloses the current-carrying conductor which produces **heat loss**. As the enclosing electrical insulation is also an effective thermal insulation, a *temperature gradient* develops which causes a *conductivity gradient*. As a result, the stress is reduced on the inner layers and increased on the outer layers. The reason for this is the *space charge* that is built up due to the conductivity gradient.

This effect of **potential shifting**, which can also described as **field migration**, was already described for a cable in Section 2.4.4.2, Figure 2.4-27. Meanwhile, it could be verified for a bushing by measurements: i.e. in a step-response measurement, the expected capacitive potential distribution passes over into a *significantly displaced resistive distribution* with a high stress on the outer layers, Figure 7.2.4-1 (center). For a bushing core with a constant

temperature, a current step or a temperature step at the conductor results in a *synchoneous run-off of thermal an electrical transients* which again end up in a displaced resistive potential distribution, Figure 7.2.4-1 (bottom) [505], [506].

The effect of the grading core on the *potential distribution* in the **sourrounding media** is significantly weaker than for AC voltage as the *field-grading conduction currents* at DC voltage are significantly smaller than the corresponding displacement currents at AC voltage. Thereby and by the highly resistive cover layers of the insulation, the *potential distribution within the bushing core* is more or less *decoupled* from the *external potential distribution*.

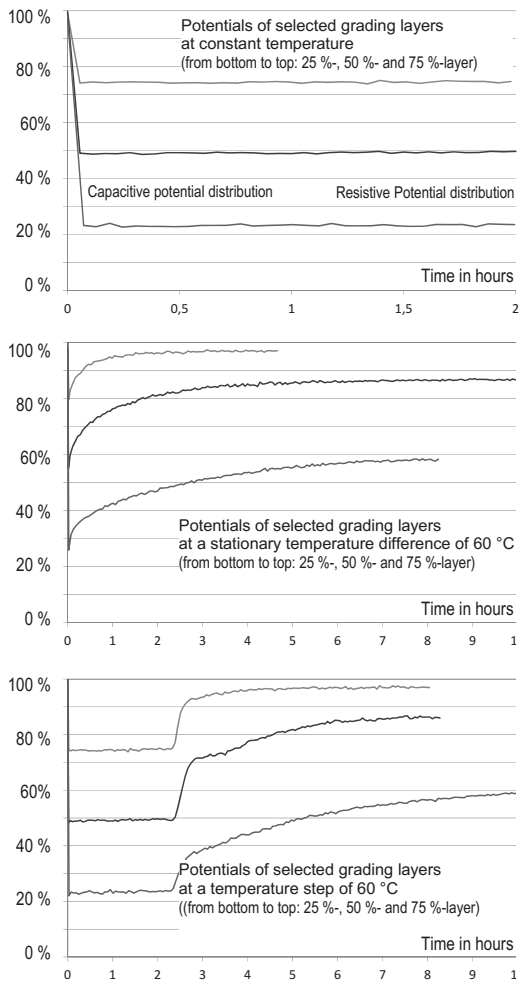

Figure 7.2.4-1: Transient potentials of grading layers in a DC bushing at a constant temperatur (top), for a stationary temperature gradient (center) and for a temperature step (bottom), all measured with a fieldmill voltmeter [505], [506].

In *HVDC converter transformers*, as already explained with Figure 7.2.3-6, an *external grading in the oil* is realized by means of barrier systems, oil gap geometries and electrode contacts. In the case of transient processes, the interaction of internal and external potential grading can become very complex, cf. Figure 7.2.3-9.

7.2.4.2 External Insulation

Usually, bushings are also links between the internal insulation (e.g. in a transformer or a GIS) and the external insulation (e.g. indoor or outdoor). For DC voltage, the design of the external insulation is especially difficult so that long creepage paths, large dimensions and hydrophobic surfaces are necessary. The Figures 7.2.3-1 to -3 and Table 7.2.3-2 give an impression.

External insulation poses a problem for systems of high voltage direct current transmission, especially at high voltages above 500 kV. Deposits of dirt and wetting cause *conductive pollution layers*. For *AC voltage*, surface currents are mostly negligible compared to the capacitive displacement currents, so that the potential distribution is not significantly changed. For *DC voltage*, the field distribution is, however, largely determined by the surface currents. Potential grading measures inside the device are no longer effective in the case of extensive wetting at the surface, Figure 2.4-29.

In unfavorable cases, e.g. during *non-uniform rain*, the high voltage potential is displaced on the insulator surface [8], [58]. Especially unfavorable is the effect of a *horizontal mounting position*, because this even allows wetting of the underside of the sheds.

Potential displacement leads not only to *axial flashover*. In bushings, also extreme *radial*

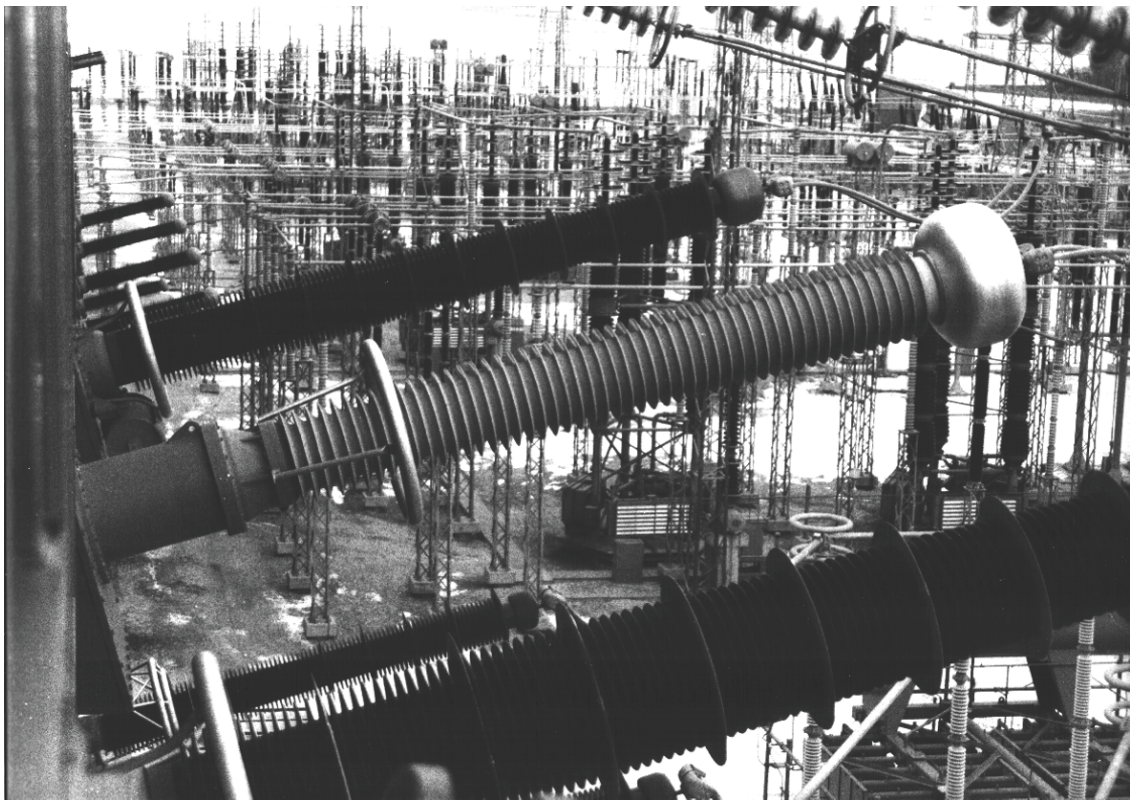

Figure 7.2.4-2: 545 kV HVDC wall bushings at a converter hall (Manitoba Hydro, Winnipeg, Canada). For increasing flashover voltage for non-uniform rain, OIP porcelain bushings are retrofitted with so-called booster sheds. One of the bushings is designed oil-free with hydrophobic silicone shed composite insulator [7], [8], [9], [93], Figure 7.2.4-3. Photo HSP Hochspannungsgeräte GmbH, Troisdorf.

stresses are created between the surface carrying high voltage potential and the ground layer or another grading layer at low potential below the surface. A *radial breakdown* leads to a short circuit, which may *destroy the porcelain* and can ignite the *oil filling*.

The property of the *porcelain surface* to lose its hydrophobicity owing to contamination and rain, and thereby to enable water drops to flow and wet the surface, causes the formation of continuous films of moisture. This can be identified by the reduction of the surface resistance, Figure 5.3-19.

An effective countermeasure is to use composite insulators with hydrophobic *siliconesheds*, Figures 5.3-18 and 7.2.4-2. Individual drops remain insulated, so that continuous conductive bridges cannot be formed. On the existing porcelain insulators, the same effect can be achieved temporarily by coating with *silicone paste* or with a *coating* made of room-temperature vulcanization *silicone* (RTV coating). Coating is, however, not a longlasting solution.

An increase in the flashover voltage by a certain amount also results from so-called "*booster sheds",* Figure 7.2.4-2: with silicone discs of large diameter, which are distributed over the insulator length, the pollution flashover should be delayed by interrupting the prearcs [8], [58], Section 3.2.6.4. However, with this, the cause of the problem, i.e. the potential displacement on the surface is not combated. It only results in delaying the formation of continuous pre-arcs. Nevertheless, it is advantageous that this measure can be applied later on to improve the reliability of critical systems.

Example: Oil-free HVDC wall bushing with silicone rubber sheds

Figures 7.2.4-2 and -3 show a flashover-resistant 545 kV wall bushing for high voltage direct current transmission with *silicone rubber sheds* on the outdoor side. *GRP pipes* are used as housing insulators, which pose no risk of exploding porcelain in the event of damage. Moreover, a significantly reduced weight results. The combustible oil-paper insulation is replaced by a solid *vacuum impregnated RIP bushing core made of epoxy resin;* cf. Sections 7.1.2.2 and 5.3.3.1 with Figure 5.3-14. *Compressed SF_6* or *polyurethane foam* is used as subsidiary insulation between the bushing core and the housing insulator [7] ... [10], [93].

Note: A special feature results from the condition that an epoxy-resin-impregnated core cannot be manufactured in any desired length. For a very long bushing, the outdoor side and the indoor side must be assembled from two separate outdoor-gas and indoor-gas bushings which are connected in a short SF_6 pressure tank under a shield electrode. The entire arrangement is clamped on a continuous conductor bolt with spring assemblies in the shield toroids.

In comparison to porcelain bushings, significantly smaller dimensions and masses are achieved, Table 7.2.4-1.

Table 7.2.4-1: 545 kV HVDC wall bushing as per Figure 7.2.4-3 in comparison with conventional design with porcelain and oil-paper insulation [8].

Electrical test data:			
Lightning impulse voltage	full wave	+/-	1675 kV
	chopped wave	-	1845 kV
Switching impulse voltage	under rain (105 Ω m, horiz. 1.2, vert. 1.4 mm/min)	+/-	1300 kV
AC voltage	50 Hz, 72 seconds		750 kV
DC voltage	negative, 2 hours		500 kV
	polarity reversal, 1 min		
	positive, 0.5 hours		500 kV
	positive, 1 hour		795 kV
PD-measurement	for AC voltage and DC voltage		

Important technical data:	*Conventional bushing*	*Bushing as per Figure 7.2.4-3*
Mass	3700 kg	2600 kg
Creepage path		
outdoor	21.8 m	13,7 m
indoor	7.6 m	3.6 m
Flashover distance		
outdoor	5.5 m	4.3 m
indoor	3.2 m	3.6 m
Specific creepage path at 500 kV		
outdoor	43.6 mm/kV	27.3 mm/kV

7.2.5 HVDC Cables and Accessories

7.2.5.1 DC Cables

At first sight, DC cables and their accessories are not very much different from the designs for AC voltage, Section 7.1.1. In the DC cable, the electric field is also formed in a defined manner between the conductor screen and the insulation screen within a highly resistant dielectric, and in the accessories, a grading of

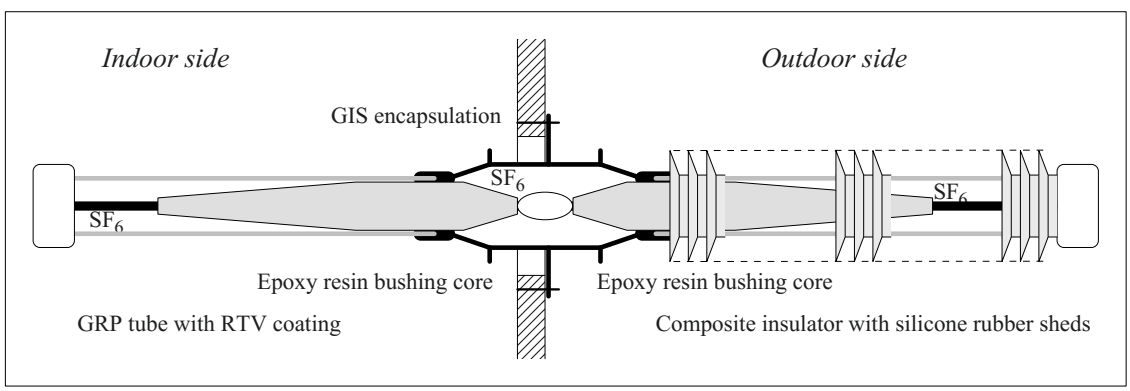

Figure 7.2.4-3: Oil-free 545 kV HVDC wall bushing with composite insulator carrying silicone rubber sheds for a HVDC converter station as per Figure 7.2.4-2, design HSP Hochspannungsgeräte GmbH, Troisdorf [7]...[10], [93].

the electric field must also be performed in the DC case.

Nevertheless, some special *features of DC voltage stress* and of *material behavior under DC stress* must be regarded. They are especially related to field distortions by *space charges*. In a current-carrying cable, for example, a temperature gradient develops which causes a radial conductivity gradient. Due to the conductivity that is increased towards the conductor, the electric DC field is displaced outwards and space charge is built up. Thus a severe misgrading of the potential can occur culminating in an overstressing of the outer insulation (*stress inversion*). This effect was basically explained in Section 2.4.4.2 by means of Figure 2.4-27 and experimentally demonstrated for a DC bushing, see Figure 7.2.4-1.

Depending on the *field of application*, very different cable technologies are used [507], Figure 7.2.5-1. While AC cables are limited in length (as long as there is no reactive-power compensation) to some 10 km up to just over 100 km due to high capacitive reactive power, an *electrically caused length limitation for DC cables does not exist*. Therefore, they are especially suited as submarine cables with very long transmission lengths. The design of *submarine cables* is similar to the design of land cables. Additionally, they need a mechanically very resistant *armour* made of spirally circulating steel wires in order to avoid damages by ships' anchors or by tensile forces that occur during cable laying and by sagging cables on the seabed.

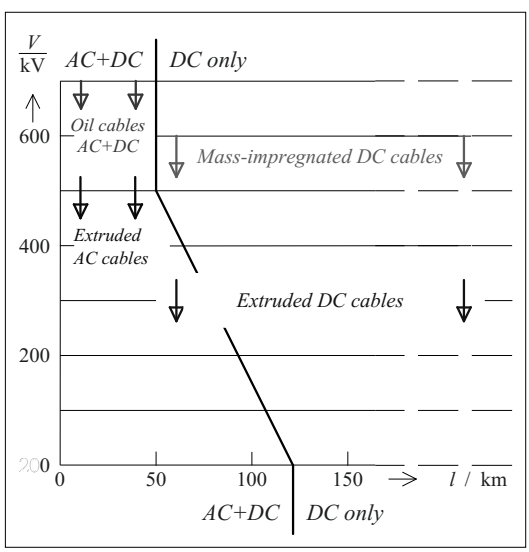

Figure 7.2.5-1: Typical fields of application for different cable technologies under AC and DC voltages (schematic).

DC cables can transmit significantly *higher powers* than AC cables owing to the following root causes: The *permissible operating voltages* are higher, as the dielectric is only stressed with the voltage V that is directly related to the transmission power and not with an AC peak voltage that would be higher by a factor 1.41. Additionally, the *permissible load currents* are higher, as reactive power needs not to be transmitted, as current displacement or skin effect does not occur, and as eddy currents neither generated in the conductor nor in the armouring wires. Lowest ohmic conductor losses and highest transmission powers are acieved with *copper conductors*, but *aluminium conductors* are are also used because of cost reasons or because of its lower weight. Furthermore, also *dielectric losses* are lower as the dielectric does not show polarization losses at DC voltage but only comparatively low conduction losses. Nevertheless, at high DC voltages, thick insulations are used and high field strengths occur. This results in poor heat dissipation of the ohmic conductor losses and in significant *ohmic loss density* within the dielectric:

$$p_{\mathrm{diel}} = \kappa \cdot E^2 \qquad (7.2\text{-}5)$$

In order to avoid the risc of *overheating*, *thermal runaway* or *thermal breakdown*, the *conductivity* κ of the insulating material must not be too high.

Basically, **paper-insulated DC cables** and **plastic-insulated DC cables** are distinguished. The former have a lesser problem with build-up of space charges due to the higher conductivitiy of the oil-impregnated paper or the mass-impregnated paper. Thus they can be used for current-source converter stations where the power flow direction must be re-

versed by polarity reversal. The latter are comparatively low-loss, leightweight, oil-free and cost-efficient, and they can be transported in longer lengths. However, due to the space-charge problems, they are not yet used for the highest operating voltages, and they are normally used in HVDC current-source converter stations only, where the power flow direction can be reversed without polarity reversal.

7.2.5.2 Paper-insulated HVDC Cables

a) Oil-filled Cables

The *highest operating voltages of more than 600 kV*, both for AC and DC voltages, can be achieved with paper-insulated self-contained **oil-filled cables**, Figure 7.2.5-1. The insulation wound of *lapped paper layers* is dried and impregnated under vacuum with low-viscosity oil. The cable has a hollow conductor which enables the compensation of the thermal expansion of the insulation by displacement or suction of oil. Due to the viscosity of the oil, this is only possible for *lengths up to 50 km*, so that longer continuous cables cannot be operated. The low-viscosity oil imposes several additional disadvantages: the cable must be tightly sealed, there is a *risk of oil-leakage* and active *auxiliary system*s for the oil supply are required.

b) Mass-impregnated Cables (MI and PPLP)

Mass-impregnated (MI) paper cables and **polypropylen lapped paper (PPLP) cables** can be used up to 600 kV, Figure 7.2.5-1. The insulations consist of wound and lapped layers of paper or polypropylene and paper. Conductor screen and insulation screen are made of semi-ocnductive paper. The cable is dried under vacuum and impregnated with the so-called “mass”, i.e. with an oil that has a high viscosity at ambient temperature. Impregnation is performed at elevated temperature and in a low-viscosity state.

During operation, the thermal expansion and contraction is compensated by radial deformation of the lead sheath. In this process, cavities and gaps with reduced electric strength can occur close to the conductor screen and the insulation screen. The electric field stress can therefore be reduced in this region by more conductive paper layers.

Mass-impregnated cables can be manufactured nearly in any length and they do not loose oil in case of a damage. Thus, the mass-impregnated cable is the traditional but still the high-end solution for power cable transmission at high transmission power, at high DC voltages and over long distances.

7.2.5.3 Plastic-insulated HVDC Cables

Plastic-insulated cables made of **extruded and cross-linked polyethylene** (**XLPE** cables) can be manufactured at relatively low cost, completely without oil and with comparatively low weight and small diameter. For *AC applications* up to *very high operating voltages above 500 kV*, they have therefore almost entirely prevailed against paper-insulated cables and they have performed very well, Figure 7.2.5-1. Consequently, extruded XLPE cables are also desired for *DC applications*, but the application is unfortunately complicated due to the build-up of *space charge*, so that the higher voltage levels must be opend up step-by-step by newly developed insulating materials.

Unfortunately, also the production of long XLPE cable lengths is not possible as the polymeric material already starts cross-linking within the extruders which must therefore be cleaned regularly. Long lengths must therefore be assembled with *factory joints* or with cable joints that are mounted *on-site*.

XLPE dielectrics are not yet used for the highest transmission voltages in HVDC systems, since **space charge** would be removed only very slowly owing to low conductivity. Space charges are caused by temperature gradients, conductivity gradients, charge carrier injection and traps in the cable dielectric, Figure 2.4-27 and 7.2.5-2.

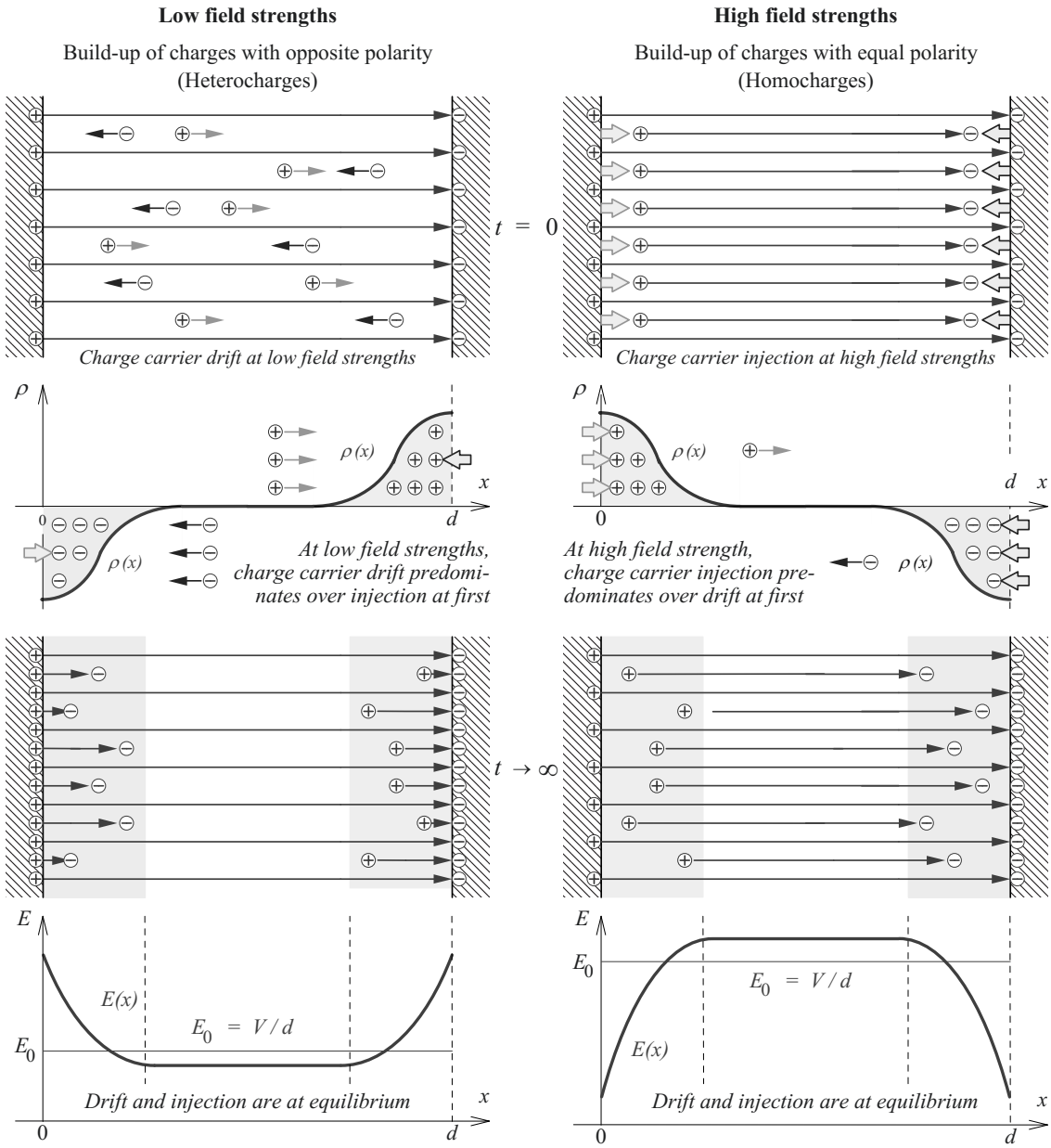

Figure 7.2.5-2: Build-up of space charges in a highly resistive dielectric at low field strength (left) by accumulation of existing charge carriers as "heterocharges" and at high field strength (right) by accumulation of injected charge carriers as "homocharges", as well as enhancement and reduction of the local field strength close to the electrodes (left and right respectively).

Even if there is no temperature gradient, space charges are built up in highly resistive dielectrics (e.g. in XLPE insulations) by the *drift* of existing charge carriers at low field strengths and also by *injection* of charge carriers at the electrodes at high field strengths, Figure 7.2.5-2 (left and right respectively). The injected charges can be accumulated in *traps* in the dielectric and at microscopic *inhomogeneities* (e.g. at the interfaces between amorphous and crystalline regions). For long lasting or for steady-state DC voltage stress, field strength

enhancements (by so-called "*heterocharges*" i.e. charges of opposite polarity) or field strength reductions (by so-called "*homocharges*", i.e. charges of same polarity) can be caused especially close to the electrodes, Figure 7.2.5-2 (bottom).

The described space charges are especially dangerous at **polarity reversal** as the displacement field that is related to the high voltage swing and the remaining space charge field are locally superimposed constructively, cf. Figure 7.2.3-7.

Therefore, XLPE cables are not yet used in the traditional *line-commutated converters* (LCC). They are only used in the new systems with *voltage source converters* (VSC) and *without polarity reversal*. Here, power flow direction is reversed by reversing the current direction, cf. Section 7.2.1.1.

Now, development of cable technology allows the use of HVDC XLPE cables up to 320 kV [496], [497]. Successful tests on 500 kV XLPE DC voltage cables have been reported [315], [507].

The challenges especially exist on the side of material development. The risk of thermal instability (runaway) at very high field stresses shall be reduced by lower conductivity of the insulating materials. The accumulation of space charge must be reduced by better chemical cleaniness, lower amount of impurities and lower content of polar cross-linking by-products [507].

7.2.5.4 Emerging HVDC Cable Technologies

Today, traditional cable technologies with long-term experience are challenged also for DC applications by extruded cables that have lower costs in production, laying and operation.

Mass-impregnated cables can be used up to 600 kV and **self-contained oil-filled cables** have been qualified for 800 kV [507].

Meanwhile, **XLPE cables** are qualified for 500 kV. Nevertheless, higher voltages and polarity reversal operation still require drastic improvements with respect to space charge accumulation and removal. This can already be achieved very effectively by **nanofillers** (nano-structured fillers) such as metal oxides like MgO or SiO_2 and carbon black. But the biggest challenge is a sufficient dispersion of the filler particles in full scale procuction quantities [507].

New candidates for extruded cable insulation that avoid the drawbacks of XLPE dielectric with and without nanofillers are **non-cross-linked thermoplastic materials** with a higher melting point. They are based on PP/PE compounds such as the **high-performance polypropylene thermoplastic elastomer** (HPTE). First of all, the possibility of melting down and recycling of thermoplastic materials is a big advantage. Although this cable technology is now used for medium voltage AC applications only, a high potential for a wide range of high voltage applications for AC, DC and combined voltages is expected. Qualification tests for 320 kV DC are reported [507].

High-temperature superconducting (HTS) **cables** can be made of PPLP insulation impregnated with liquid nitrogen. Limiting factors are the possible lengths of cooling systems and the limited lengths of HTS material tapes. Up to now, demonstation projects are realized for AC systems, but there are promising advantages for potential DC applications. Even at comparatively low voltages of approx. 200 kV, superconducting cables would allow very high currents and very high transmission loads of several GW in comparatively small corridors [507].

7.2.5.5 HVDC Cable Accessories

Also DC cables have **creepage surfaces** at their ends if the are not terminated by cable joints or by cable entrance fittings, Figure 7.2.5-3 (1). After the inception of corona discharges at the edge of the partially removed

cable sheath, streamer discharges and leader discharges, which can be observed under AC voltage stress, cannot develop as there is no displacement current that can feed high-current surface discharges. Nevertheless, accumulated space charges and surface charges cause flashover at comparatively low voltages, so that field grading is absolutely necessary.

Field grading techologies that were described in Section 7.1.1.4 are also used for **DC voltage cable accessories**. For *oil-impregnated and mass-impregnated cables*, cable joints and entrance fittings are wound of paper and impregnated on site. For *polymeric cables*, prefabricated joints and entrance fittings made of elastomeric material are slipped or shrinked on the bare cable insulation, Figure 7.2.5-3.

DC voltage cable accessories require special attention with respect to the electric field stresses in the cable and in the accessory itself which are predominantly determined by the **conductivities** of the involved materials.

Unfortunately, many **materials** that are used for AC voltage are not applicable for DC voltage as conductivities are not stable under long lasting DC voltage stress due to *ion drift*, and because of the accumulation of field-distorting *space charges* and *surface charges*. Furthermore, conductivities in adjacent materials can differ by some orders of magnitude and significant field migrations can occur owing to t*emperature gradients* and *transient temperature variations*. These problems are described in the following for the examples of geometrically and resistively graded accessories.

In the case of **geometrically graded cable entrance fittings and cable joints**, Figure 7.2.5-3 (2) and (3), the DC field distribution for constant and similar conductivities in adjacent insulating materials is theoretically comparable to the field distribution at AC voltage. Owing to an operational temperature gradient from the inside out, the field stress is displaced towards the earthed deflector electrode. This distortion could be considered by an according design of electrode geometry. Nevertheless, if the cold cable would be switched on with a homogeneous temperature distribution, a field stress concentration would then occur at the high voltage electrode. Unfortunately, a *design optimum* that covers both of the situations cannot be found easily, as the conductivities are neither well known nor stable [496], [497].

Alternatively, resistively graded accessories are possible, Figure 7.2.5-3 (4). Here, potential grading in axial direction is achieved by a spe-

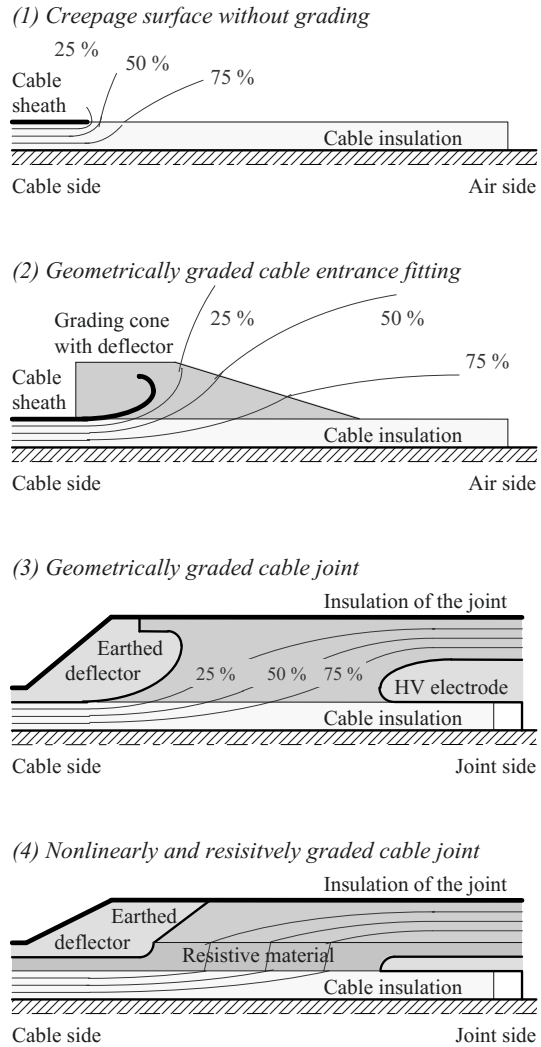

Figure 7.2.5-3: Cable assesories at DC voltage, (1) creepage surface without grading, (2) geometrically graded cable entrance fitting, (3) geometrically graded cable joint and (4) resistively graded cable joint.

cifically designed *semiconductive layer* between earthed deflector and high voltage electrode. Due to the constant diameter, the grading layer is situated at a comparatively constant temperature. Also here, the *design optimum* cannot be found easily: on one hand, the semiconductive layer must carry a sufficiently high current for effective field grading, and on the other hand, it must not be heated up inadmissibly by ohmic loss [496].

Real cable systems must withstand both *DC voltage stresses* and *impulse voltage stresses*. Therefore, also **combinations** of resistive and geometric grading are built.

7.2.5.6 HVDC Cable Testing

HVDC cable systems are qualified in yearlong endurance tests with numerous load cycles at high DC voltage. For this purpose, two basic applications must be distinguished [507], [508]:

In the conventional **line-commutated converters** (LCC) with *thyristor valves*, the direct current is always flowing in the same direction. A reversal of power flow direction can only be achieved by *reversal of voltage polarity*. Consequently, load cycles with polarity reversals of the voltage must be included during the *endurance tests*. Under applied DC voltage, *transient impulse voltage stresses* are tested for both DC polarities at opposite impulse polarity with full impulse peak magnitude.

In the new **voltage source converters with DC link** (VSC) and with multi-level converter topologies that use *IGBT switching transistors*, the DC voltage has always the same polatity. Here, a reversal of power flow direction is achieved by *reversal of current flow direction* while different voltage magnitudes are set in the converter stations. Consequently, polarity reversals during the *endurance tests* can be omitted. Under applied DC voltage, *transient impulse voltage stresses* are tested for the same impulse polarity up to the full impulse peak magnitude and for opposite impulse polarity only with a reduced peak magnitude.

Note: Owing to their low losses, **LCC installations** can be built up to the highest transmission powers of several GW. Unfortunately, polymeric cables which can safely be reversed in polarity are not yet available for the highest transmission voltages because of space charge accumulation in the dielectrics.

In **VSC installations**, polymeric cables can be used without polarity reversal and the introduction of the first polymeric cable for 500 kV DC transmission is expected. The compact design without large filter units and the black-start ability without connection to a strong three-phase power gid are very advantageous. Nevertheless, transmission power is limited to approximately 1 GW and the losses are still higher than the losses of LCC installations.

VSC installations are largely used for the connection of *offshore wind energy farms* or *offshore power consumers* via polymeric DC cables with medium transmission lengths.

7.2.6 High-frequency Chopped DC Voltages

7.2.6.1 Applications

For the connection of *offshore wind energy farms* or *offshore power consumers* via DC voltage cables, especially HVDC converters with DC link, constant polarity and *multi-level converter* topologies are used. They can model the sinusoidal shape of the AC voltage curve even for very high voltages without high-frequency chopping (pulse-width modulation) of the DC voltage and without complex filtering on the AC side.

Pulse-width modulation with *high-frequency chopped DC voltages* is used for DC equipment up to about 100 kV, in particular for switched-mode power supplies and for the converter feed of electrical machines.

Note: Other applications for chopped DC voltages can result from the vision of *energy transmission networks and energy distribution networks* of low loss and space-saving *DC systems*. Energy is exchanged between various DC voltage levels via input side converters, very compact *high-frequency transformers* and output side converters [284].

Furthermore, it is possible to exchange energy analogously between *three-phase AC systems* of different voltage levels (and even different power frequencies). Then, a heavyweight power-frequency transformer will possibly not be required any more.

7.2.6.2 Insulation Problems

New types of thermal and electrical problems result from the chopping of DC voltages of several 10 kV. They are not direct DC voltage problems, but they occur in DC voltage systems and hence they will be discussed in this context:

Dielectric losses for *square-wave voltages* are about *four times larger* than for the sinusoidal fundamental component of equal amplitude, even for a frequency-independent dissipation factor. With high-frequency chopping, a linear rise of power loss with *switching rate* also occurs, Eq. (4.2-14) and (...-20) respectively. I.e. for a switching rate of 10 kHz, the fundamental component alone would lead to 200 times increased dielectric losses, and the square-wave voltage to 800 times increased dielectric losses when compared to a sinusoidal 50 Hz voltage. A possible *dissipation factor increase* with frequency is not yet considered here.

These considerations show that only very *low-loss insulations* can be used and that the insulation concepts must include *dissipation of larger heat quantities*, in order to avoid thermal instabilities ("thermal breakdowns"); cf. Section 3.5.2.

In the case of **partial discharges**, high chopping rates lead to a significantly *accelerated partial discharge erosion*. Therefore, dimensioning and production of insulations must guarantee prevention of partial discharges to an even greater extent than now. Insulations that must be stable over long periods tend to require larger *insulation distances or insulation thicknesses*.

Additional problems result with fast and **steep switching edges** and with **high switching rates** because of the *spatial dimensions* of systems (transformer windings, cable lengths), which can no longer be viewed as *electrically short*, so that traveling waves, reflections, standing waves, resonances and voltage overshoots must be reckoned with.

An *example* is given by low voltage motors that are supplied from inverters over longer cable lengths, in which the steep switching edges generate traveling waves which are reflected with doubled magnitude at the motor impedance and which very rapidly can damage the insulation by high-frequency partial discharge erosion [285].

7.2.6.3 Test Techniques

The common *high voltage test methods* are no longer adequate for this. For thermal reasons, high frequency stresses must be simulated, for example with **resonance transformers** further developed from the classic Tesla transformer [284]. Rapidly varying stresses can be simulated with **impulse voltage tests** with simultaneous observation of partial discharge impulse currents [285]. Actual square-wave voltages have 20,000 switching edges per second at 10 kHz. The development of adequate **square-wave test generators** poses new and high requirements for high voltage test technology. A possible *concept* includes, for example, two oppositely charged high voltage capacitors, which are alternatingly connected to the test object via power electronic switches that are suited for high voltages [284].

7.3 Typical Insulation Systems for Impulse Voltages

7.3.1 Electrical Stress and Strength

Impulse voltage stresses and field distributions result predominantly from the *dielectric displacement field*. Therefore the permittivity must be considered as the most important material property.

In insulations that are complex in arrangement, for example in transformers, the voltage distribution is based on the overall *system properties*. Therefore, isolated consideration of the dielectric is not adequate, additionally inductances, stray capacitances and magnetic couplings must be considered, cf. e.g. Figure 7.1.3-3.

In spatially extended systems and for very rapidly varying processes respectively, e.g. for fast transients, a description of the *systems with distributed parameters* is necessary, Section 2.6.

In the case of impulse stresses**, external insulation** is very *insensitive to pollution layers* on insulator surfaces, since the displacement currents are practically always larger than the conduction currents over the pollution layers.

In case of *lightning impulse voltage* and for *large flashover distances and non-uniform fields in atmospheric air*, also the rounding of electrodes is not as important as for DC voltage and AC voltage. Even with the inception of *pre-discharges*, the *propagation velocities* of streamers and leaders respectively are often not sufficient to reach the counter-electrode during the stress period of a *lightning impulse voltage*, cf. Eq. (3.2-44). That is to say that the *range* of pre-discharges is restricted because the voltage requirement of the pre-discharge must be covered in the comparatively weak electrical background field, Figure 3.2-28. For arrangements similar to *point-to-plane arrangements*, orders of magnitude of breakdown voltages are roughly estimated from the length-related voltage requirement or voltage drop of streamer discharges (approx. 5 kV/cm for $d < 1$ m) and leader discharges (approx. 1 kV/cm for $d > 1$ m), cf. Sections 3.2.4 and 3.2.5 with Figures 3.2-27 and -29.

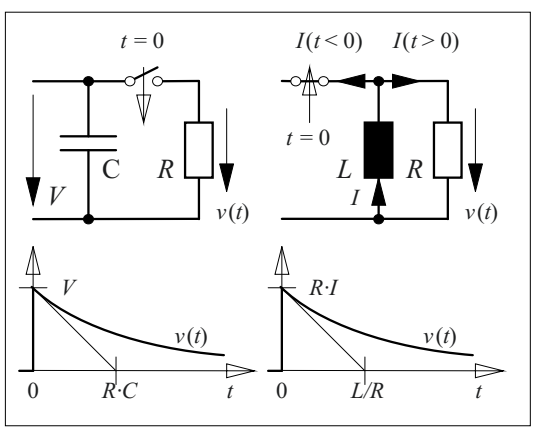

Figure 7.3-1: Generation of high voltage impulses from capacitive and inductive energy storage devices.

Impulse voltage strength decreases with increasing stress duration, cf. Section 3.2.4 (*impulse voltage-time characteristic*). Thus, the dielectric strength at *switching impulse voltage* is more comparable to the strength at AC voltage because of the longer stress duration.

Liquid and solid insulating materials are basically stronger for short stress durations than for long-lasting stresses, Figure 3.4.1-1 and 3.5-1. Many breakdown processes require longer periods for their development, such as fiber bridge formation in liquids, thermal breakdown in solids or erosion in materials that contain voids. Generally, about *two to three-fold higher strength* is assumed for lightning impulse voltage compared to short duration AC voltage strength.

Some examples are discussed in the following.

7.3.2 Energy Storage

The generation of electrical impulses necessitates an *energy storage device*, from which the impulse energy can be very rapidly released. *Energy storage capacitors* or *impulse capacitors* are predominantly used for this, because of the following reasons, Figure 7.3-1 (left):

- They can store energy over longer periods with minimum losses.
- Very rapid release of energy in low-inductance impulse circuits is possible.

In principle, electrical energy can be stored with significantly higher energy density in the magnetic field of a *current-carrying coil*, Fig-

ure 7.3-1 (right). By opening a switch between the current source and the storage inductance, the coil current commutates from the source to the load that is connected in parallel and generates a high voltage impulse.

However, in practice the application of this principle leads to significant *problems*:

The interruption of the direct current requires a very complex *opening switch*. The interruption of extreme currents can actually be managed by blasting away the conductor.

In the loaded state, the maximum current flows and causes continuous *ohmic losses*. They require sufficient removal of heat, large conductor cross section, large conductor weight and a continuous re-supply of energy. Long lasting storage is not possible without using a resistance-less (*superconducting*) conductor, Section 7.5.

Short-duration inductive intermediate storage takes place only in special impulse generators, Section 6.2.3.7. For this, the energy of the impulse is transferred in an oscillating manner from one capacitive storage device to another via the circuit inductance in order to increase the pulse power.

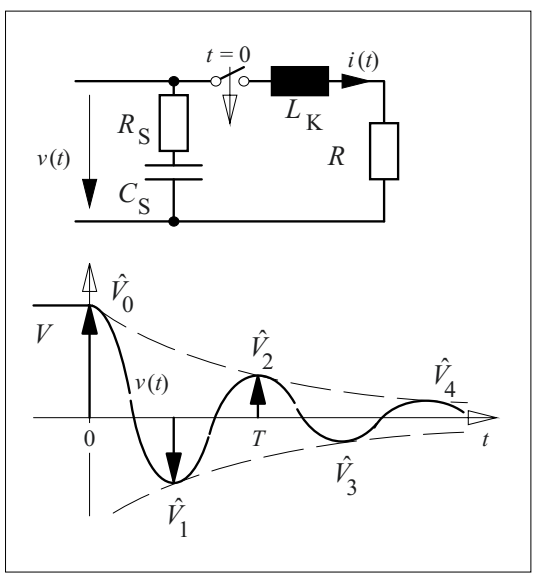

Figure 7.3-2: Oscillating discharge of an energy storage capacitor.

7.3.3 Impulse Capacitors

(Energy Storage or Surge Capacitors)

7.3.3.1 Capacitor Design

Energy storage capacitors, impulse capacitors or *surge capacitors* respectively serve as energy sources for all practical impulse circuits. They can be directly charged from a DC voltage source. Impulse capacitors are basically constructed similarly to AC voltage capacitors or DC voltage capacitors from a series connection of **several capacitor windings** in a **housing**, Section 7.1.4 and 7.2.2.

It is shown that the service life is not restricted by the steady-state DC voltage stress in the loaded condition, but owing to **transient stresses** during the discharging. In general, owing to circuit inductances and resistances, *damped oscillation profiles of capacitor voltage* and *discharge current* occur, Figure 7.3-2. The impulse capacitor is, therefore, usefully described by the series equivalent circuit (C_S, R_S), Section 4.3.1.

In the case of *weak damping*, the amplitude of the current can be roughly estimated by equating capacitively and inductively stored energy:

$$½ \cdot L_K \cdot \hat{I}^2 \quad \leq \quad ½ \cdot C_S \cdot \hat{V}^2 \qquad (7.3\text{-}1)$$

In the case of *strong, overcritical damping*, an exponentially decreasing current with a comparatively low initial value results:

$$\hat{I} \quad = \quad V/(R + R_S) \qquad (7.3\text{-}2)$$

The mechanical and thermal loading capacity of **connections and contacts** must correspond to the resultant *discharge currents*. The current density for single-point contacting of thin metal foils via *contact strips* is especially critical here. Contacting with the inclusion of the entire length of the winding is possible if the metal foils project from both face sides of the winding, Figure 2.4-20. When stacking cylindrical sections and by series connection of flat sections, *butting contacts* with low current density are established.

7.3.3.2 The so-called "Capacitor Inductance"

Impulse circuits must often have especially low inductance in order to quickly transfer the stored energy to a load circuit or to avoid unwanted oscillations. Here, **circuit inductance** is *also* influenced by the design of the capacitor.

Note: Often a parasitic **"capacitor inductance"** is attributed to the capacitor [189]. This is physically *not* correct since the inductances are defined only for *closed electrical circuits* [113]. Nevertheless, so-called "partial inductances" are calculated from the magnetic field energies of partial volumes, which are then attributed to the capacitor component and not to the entire electrical circuit.

Particularly low-inductance circuits are possible with butt-contacted cylindrical capacitor sections [113]. Higher inductances are achieved by stacking flat capacitor sections. In this respect, windings with strip contacts are less favorable than windings with butting contacts. The two *contact strips* of a winding must not be displaced laterally against each other, because the wound metal foils then form a coiled arrangement, in which the resultant currents flow in the circumferential direction and cause a strong axial magnetic field. In the case of a non-displaced arrangement of the contact strips, the currents are compensated in the circumferential direction.

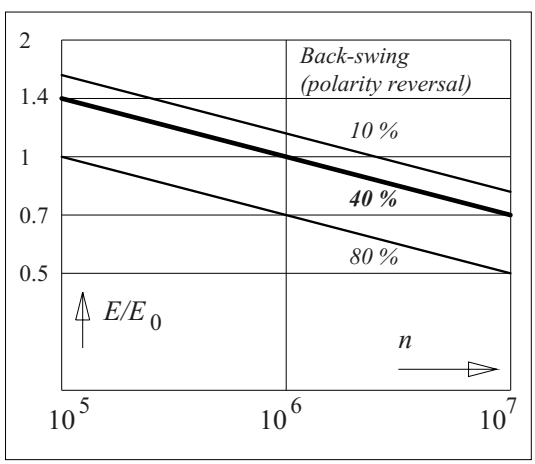

Figure 7.3-3: Service live of an impulse capacitor as a function of field stress and back-swing.

Note: If metal strips are used for contacting, the electrode foils form long *strip lines* in the circumferential direction [113]. They extend from the contact point to both the sides up to the beginning and to the end of the foils in the winding, cf. Section 2.6. Validity of an electrically short (quasi-stationary) approach must be verified checking the *propagation times*.

7.3.3.3 Dielectric and Service Life

While *charging* the capacitor, the field distribution in the dielectric corresponds at first to the dielectric displacement field, Figure 2.4-30 (top). Intense stressing of the foil edges is, however, not as critical as it is for AC voltages, since periodically burning partial discharges cannot develop. With time, the field distribution rather changes to a *steady-state DC distribution*, in which the field stress at the foil edges is reduced by the slightly more conductive impregnating gap, Figure 2.4-30 (bottom). The impregnating gaps thus acts like protruding (semiconductive) extensions of the electrode providing a resistive grading. Owing to this, for pure DC voltage stress, significantly higher field strengths are permissible than for AC voltage.

A critical **stress** occurs at the foil edges for *oscillating discharges*, Figure 7.3-2. At the time of the voltage back-swings, a dielectric displacement field occurs with heavy stresses at the edges. Moreover, the polarity of the foil edge at the maximum of the *back-swing* is opposed to the polarity of the space charges in the impregnating gap. Partial discharges occur in the form of *surface discharges*, which erode the insulating materials. The **service life** of the capacitor is thus determined by the number n of capacitor discharges until *erosion breakdown*, Figure 7.3-3. The service life is not only dependent on the magnitude of the *field strength*, but also on the intensity of the *back-swing*. A low circuit damping leads to an oscillation with large amplitude, long duration

and severe erosion. Owing to this, the service life is shortened, Figure 7.3-3. A reduced service life is also caused by a rise in the *frequency* and *temperature.*

Note: In impulse capacitors stressed for a longer duration, the eroding effect of *surface discharges* at the electrode edges can be seen in a border of wax-like decomposition products (X-wax) on the surface of the solid insulating materials. The final *erosion breakdown* occurs at the edge of the metallic foil and, depending on the dissipated energy, burns a larger or smaller hole in the dielectric, Figure 7.3-4.

The service life of impulse capacitors is often specified for a *back-swing ratio* $\hat{V}_1/\hat{V}_0 = 40$ %. Stronger back-swings can drastically shorten the service life for equal field strengths, Figure 7.3-3. Deviation from other nominal data (voltage or respectively, field strength, frequency and temperature) can also lead to significant variations in service life.

Lifetime characteristics mark a specific confidence level. This implies that for the stress given by the characteristic a breakdown probability still exists, e.g. 1%, 10% or even 50% depending on the specification for the characteristic.

In order to **increase the service life**, *edge field strengths* can be reduced with molten metal foil edges (*laser-cut*) or with *folded edges*. *Impregnation with castor oil* increases service life by a factor of 10 when compared to a mineral oil-impregnation. In this case, the positive factors are higher permittivity (stress reduction at edges for transient stress), higher conductivity (stress reduction at edges for steady-state stress), higher viscosity (resistance to gas formation during alternating electromechanical stress) and the behavior during partial discharges, Section 5.4.4. Also the replacement of paper, which is sensitive to partial discharges, by more resistant *polymeric films* effects an increase in the service life.

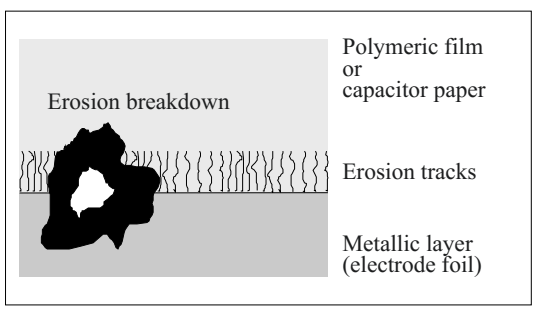

Figure 7.3-4: Unwound dielectric of an impulse capacitor with erosion tracks and erosion breakdown.

7.3.4 Barrier Systems

Pressboard or transformerboard in oil transformers are used for subdivision and for increasing the strength of oil gaps in case of AC voltage, Section 7.1.3.3, and for the insulation of the applied voltage in case of DC voltage, Section 7.2.3.2. In the case of an impulse voltage, as with AC voltage, the stress is applied to the oil gaps. Hence, the effect of barriers must be seen here too as an increase in strength owing to the subdivision of oil gaps.

The course of the breakdown processes was determined with high-speed shadow image photography in a point-to-point electrode arrangement (r = 50 µm, s = 12 mm) with barriers (d = 2 mm) [310], [285]:

Primary streamers occur independently of the barriers as a result of local field stress enhancements in oil at the positive and at the negative point electrodes, Figure 7.3-5 (top). The occurrence of primary streamers and *secondary streamers* in oil was described in Section 3.4.1. They transfer *charge to the barrier surfaces* and lead to the deposition of saponified oil, but do not yet lead to thermal damage of the cellulose.

Note: In the laboratory experiments, streamers could be released only at the *point electrodes*, but *not* electrode-free *between two barriers* [310].

The development of far-reaching *tertiary streamers* leading directly to breakdown is prevented by the barriers. Instead, a (likewise) high-current *partial discharge*, a so-called

"microdischarge", is noticed. It leads to the discharge of the capacitance between point electrode and barrier surface and it transfers the potential of the point electrode to the *barrier surface*, Figure 7.3-5 (top). This results in a considerable *increase in the dielectric strength*, since the inception of microdischarges, in contrast to tertiary streamers in a free oil gap, does not yet immediately lead to breakdown, Figure 7.3-5 (bottom).

Note: As a rough estimation, if it is assumed that a capacitance of 0.2 pF (A = 50 mm^2, s = 5 mm) charged up to 100 kV is discharged, a *charge turnover* of at least 20 nC and an *energy dissipation* of 1 Ws results.

The charge transferred to the barrier surface spreads in the form of a circular *surface discharge* and leads to thermal *damage of the topmost paper layers*. A breakdown occurs only when the peak voltage $\hat{V}$ greatly exceeds

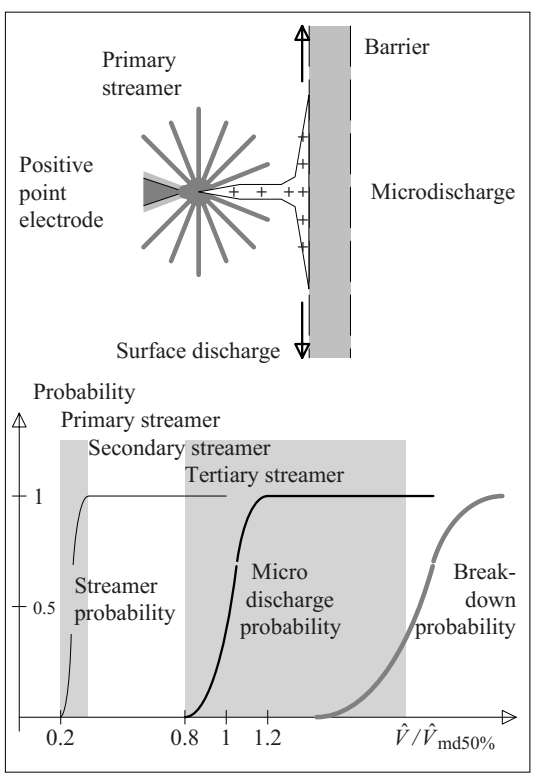

Figure 7.3-5: Charging of barrier surfaces by so-called microdischarges (top). Probabilities for the occurrence of streamers, microdischarges and breakdowns as a function of the peak voltage [310].

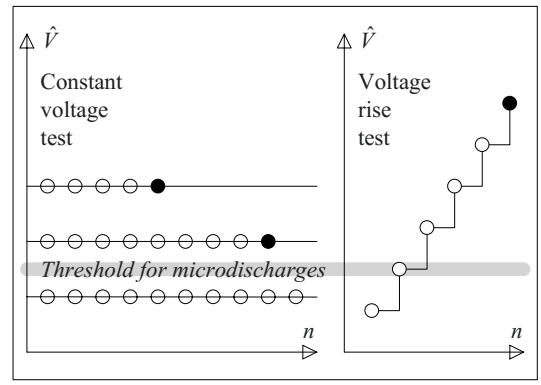

Figure 7.3-6: Constant voltage tests and voltage rise tests show the damage of barriers owing to repetitive discharges above the threshold for microdischarges (schematic) [285].

the inception voltage for microdischarges $\hat{V}_{md50\%}$, Figure 7.3-5 (bottom), or when the barrier is *eroded* owing to repetitive stress with microdischarges.

Repetitive voltage stresses with constant peak value give rise to lower breakdown voltages than stepwise increased individual stresses (step test) [285], Figure 7.3-6. This shows that *repetitive stresses* above the inception threshold for microdischarges lead to the *erosion* of cellulose.

Furthermore, it is noticed that the integration of *barriers* leads to a considerably smaller *dispersion* of breakdown voltage when compared to a free oil gap [285], and this can be explained by the reduced oil gap width and by the changed breakdown process.

Note: It is possible that also the strength increasing effect of barriers for *AC voltage* is based on reduced *dispersion* for the breakdown voltage of narrower oil gaps, Figure 3.4.2-6.

As a **consequence**, the following is adhered to: Barriers provide a strong *increase in the dielectric strength* against individual impulses even above the threshold for pre-discharges. Repetitive stresses can damage and *erode* the barriers if pre-discharges (microdischarges) occur. This is applicable also for test stresses. Therefore, *repeat tests* must normally be performed with reduced test voltages. For infor-

mation about the permitted number of impulses above the pre-discharge threshold, a *service life characteristic* is necessary, cf. also Section 7.3.3.3.

7.4 Other Applications

High voltage engineering provides indispensable technologies which in the first place offer solutions for important tasks in many areas of engineering. In the following sections, some examples are described in brief.

7.4.1 Lightning Protection

Lightning discharges are discussed from the viewpoint of discharge physics under Section 3.2.7.3. However, they have considerable associated risks, and therefore require an effective lightning protection.

7.4.1.1 Ensuring EMC

Strictly speaking, the objective of lightning protection is to protect persons, systems and buildings against the effect of lightning discharges, in this respect lightning protection is also a topic of high voltage engineering. It is related to the effects of **direct lightning impact** (LEMP Lightning Electromagnetic Pulse) and the **indirect effects** of a distant event that can be coupled via electromagnetic fields or via lines or the ground. The measures that must be taken here for ensuring *electromagnetic compatibility* (EMC) must also be planned with regard to **other interference sources** and depending on the protection requirements. This includes *switching operations* and *system perturbations, electrostatic discharges, nuclear electromagnetic impulses* (NEMP) as well as *transmitters*.

Lighting protection concepts should be developed on the basis of a **risk analysis**[478]. It must quantify the existing risk, so that economical protection measures can be devised with which the risk of damage is reduced to the *acceptable residual risk*.

In order to reduce the risk in a systematic procedure, the **lightning protection zone concept** (LPZ concept) was developed, in which the residual risk continuously decreases from the outermost zone LPZ 0 to the inner zones LPZ 1, 2, … . For a high protection requirement, even possibly rare but high-current lightning is taken into consideration (*hazard level / lightning protection level* I), for a lower protection requirement, a design for frequently appearing lightnings with lower intensity is adequate (hazard levels / protection levels II, III and IV), Table 7.4.1-1. That means, depending on the hazard level that is dealt with, the components of lightning protection must be designed for the lightning current parameters stated in the table.

Table 7.4.1-1: Maximum lightning current parameters and non-exceedance probability.

Lightning protection level LPL	**I**	**II**	**III**	**IV**
First impulse current $\hat{I}$ / kA	200	150	100	
T_1 / µs	10			
T_2 / µs	350			
Q_{impulse} / C	100	75	50	
$W/R = \int i^2 \mathrm{d}t$ / MJ/Ω	10	5.6	2.5	
Subsequent current $\hat{I}$ / kA	50	37.5	25	
T_1 / µs	0.25			
T_2 / µs	100			
$\mathrm{d}i/\mathrm{d}t$ / kA/µs	200	150	100	
Long-duration current Q_{long} / C	200	150	100	
T_{long} / s	0.5			
Non-exceeding probability for the above mentioned parameters in %	0.99	0.98	0.97	

In the standards, four lightning protection classes I, II, III and IV are specified, which are dependent on the corresponding hazard classes

and to which strict construction rules apply. A distinction must be made between class-dependent rules (rolling sphere radius, mesh size) and class-independent rules (conductor cross sections, materials). The following information is rather exemplarily and should help in understanding such specifications, but they cannot be a substitute for thorough study of the standards [478], [479].

In the following sections the classic measures of lightning protection are first explained. A distinction is made between the *external lightning protection*, which leads the lightning current on a defined path, and the *internal lightning protection* against the effects of currents, fields and overvoltages. Subsequently, the integration of these measures into a *lightning protection zone concept* is explained.

7.4.1.2 External Lightning Protection

The **external lightning protection system** of an object includes an air termination system with down leads and a grounding system [192] [478].

An air termination system is an exposed conductor arrangement, from which an *upward leader* is formed against the descending lightning stroke. The upward leader connects with a *downward leader* coming from the head of the descending leader (*connecting leaders*), Figure 3.2-43. Under this, a *final breakdown distance* r = 20 to 45 m breaks down.

According to the *"geometrical-electrical model"*, the head of the descending leader comes close to the ground or the air termination system up to the distance r, Figure 7.4.1-1. From this point, connecting leaders develop downwards to the ground or to the air termination system respectively. In the vicinity of the air termination system, a *protected zone* is formed, from which (with high probability) an upward leader will no longer start, since it is in the field shadow. This protection zone can be determined by unrolling a so-called "*rolling sphere*" with the radius r, Figure 7.4.1-1. In a complex system, also the necessary positions of air terminations are thereby obtained by unrolling the "*rolling sphere"* on ground. All the contact points between sphere and grounded structures must be protected by an air termination device. Small radii (20 m) are adopted for high protection requirements and larger radii (30, 45, 60 m) for lower requirements, Table 7.4.1-2.

Table 7.4.1-2: Minimum lightning current parameters, appropriate lightning sphere radii and probabilities for exceeding minimum peak values.

Lightning protection level LPL	**I**	**II**	**III**	**IV**
Smallest peak value $\hat{I}$/kA	2.9	5.4	10.1	15.7
Radius of rolling sphere r/m	20	30	45	60
Probability for exceeding the above mentioned smallest peak value in %	99	97	91	84

A frequently used simplification for low air termination devices below 20 m is a conical protection zone under a *protection angle* α, in which it is assumed that the intersection areas of the conical and original protection zone coincide, Figure 7.4.1-1:

$$\alpha = \arctan\left(\frac{d}{h} + \frac{r \cdot d}{h^2} - \frac{r^2}{h^2}\arccos\frac{r - h}{r}\right)$$

with (7.4.1-1)

$$d = \sqrt{r^2 - (r - h)^2}$$

For r = 20 m and h =10 m, the frequently used value of

$$\alpha = 45°$$

is obtained.

Note: For *high-rise buildings*, a lateral strike can even occur below the tip, according to the geometrical electrical model. The concept of a protection angle of is no longer applicable.

Roof ridges are protected by a *lightning conductor* that lies above the ridge, Figure 7.4.1-2. Inclined roof areas and flat roofs must be protected by *meshes*. On applying the rolling

sphere, there must be no contact with the underlying roof. A mesh width of 5 m x 10 m without significant elevation above the roof surface is often considered as sufficient, Table 7.4.1-3. A rectangular block-shaped protected zone can be formed under large flat roofs with air terminal rods arranged at regular intervals. Metallic parts (roof gutters, roof windows) must be connected to the air termination system; projecting units (chimneys, antennae) must be protected by additional air terminal rods.

For determining the position of air termination devices, there are the methods described above, i.e. the

- **rolling sphere method** and the therefrom derived
- **protection angle method** according to Eq. (7.4.1-1)

and additionally the

- **mesh method**. For this, the roof and in high buildings even the side walls, are covered with meshes that must be selected such that the smaller the rolling sphere radius is assumed the tighter the mesh must be chosen, Table 7.4.1-3.

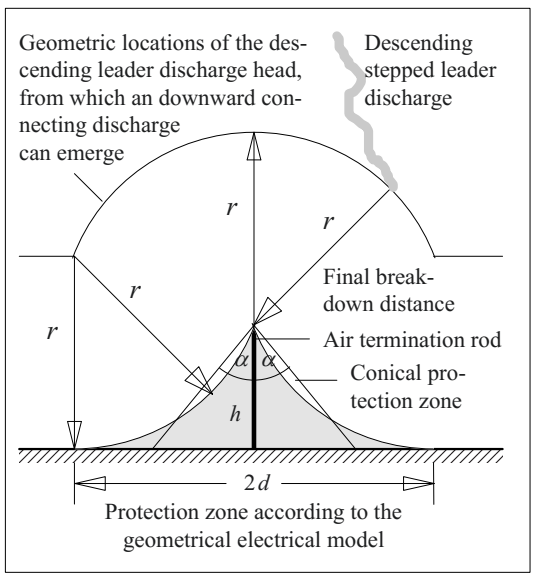

Figure 7.4.1-1: Definition of protection zones in the vicinity of an air termination rod (lightning rod).

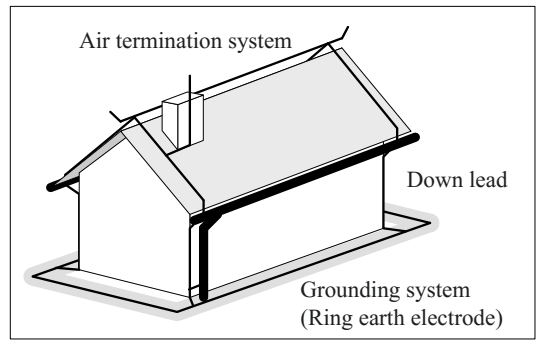

Figure 7.4.1-2: Meshed construction of an external lightning protection system for a building including roof gutters and down pipes (schmatic example).

Table 7.4.1-3: Mesh method

Lightning protection level LPL / Hazard class	**I**	**II**	**III**	**IV**
Radius of rolling sphere *r*/m	20	30	45	60
Mesh width *w*/m	5	10	15	20

A *low-inductance path* of the lightning current to ground is important. In simple cases, 20 m is considered as the maximum distance between direct **down leads** to the earth [193]. However, it is avisable here to lead the down leads at least via all the roof corners and edges of the building, in order to protect the building under a *low-inductance cage* ("Faraday cage") with the best possible *meshing,* Figure 7.4.1-2.

Note: An optimal meshing is possible in a *reinforced concrete construction* by bonding all the reinforcement steel mats to each other and by including them in the lightning protection system before grouting.

Note: High voltage transmission lines are protected by *overhead ground wires.* The overhead line towers act as down leads to ground.

The down leads are connected to the **grounding system.** In the best case, it consists of a large area *foundation earth electrode*, i.e. the steel reinforcement of the concrete foundation is used as a ground electrode. Another option is the provision of a *ring earth electrode* as a closed ring around the building. When using *single earth electrodes* there is the risk of asymmetrical rise in potential, which can be reduced by a *ring circuit* laid around the building, however. A maximum possible symmetrical conduction of the current over

multiple down leads causes partial compensation of the magnetic field components in the building and reduces the magnitude of induced overvoltages.

Note: The grounding system must be electrically separable from the down leads at **inspection joints** in order to periodically check the *earthing resistance*. The electrical contact of different metals present in the earth leads to electrochemical *corrosion* of the less noble metal. If necessary, a permanent electrical isolation by *isolating spark gaps* must be provided.

7.4.1.3 Internal Lightning Protection

a) Equipotential Bonding

Internal lightning protection systems require at least an **equipotential bonding** in the basement of the building to prevent hazardous potential differences between the lightning protection system and the installations of the building in case of a lightning stroke. The equipotential bonding includes the mutual and low-inductance electrical connection of the external lightning protection system, of all metallic pipes (heating, water, gas) and also of all electrical wiring systems.

Note: These connections need only to be effective in case of a lightning stroke. They can be realized by *direct galvanic contact* if possible, via *isolating spark gaps* if electrochemical corrosion must be considered or via *lightning current arresters* if operational voltage differences are present.

In large buildings, an **equipotential bonding network** that provides an interconnection in all three spatial directions is necessary. In this way, inductive impedances and the potential differences attributed to them are reduced to the lowest possible values.

In case of large spatial extent of *conductor loops* in the building, high overvoltages can be induced by the *quickly varying magnetic fields* of the lightning currents. Especially flashovers owing to induced voltages and potential increases at **neighboring points** between the external lighting protection system and the building installations must be ruled out with direct electrical connections (i.e. by *equipotential bonding*) or sufficient distances (*separation distance* for building protection and *safety distance* in the lightning protection zone concept). The necessary minimum distances increase with increasing loop area between the proximity point and the equipotential bonding bar. For high rise buildings, therefore, multiple equipotential bonding is provided at different levels.

b) Overvoltage Protection

Unfortunately, the measures of equipotential bonding cannot eliminate overvoltages completely. Therefore, electrical equipment and systems normally need an additional **overvoltage protection**. One problem in this context is that protective devices which can lead high lightning currents respond comparatively slowly (**coarse protection**), and that electronic protective devices which respond very quickly (**fine protection**) can be destroyed by high impulse currents. Thus, an according coordination is necessary, Figure 7.4.1-3.

Note: **Lightning current arresters** respond to overvoltages and are capable of conducting lightning current. However, as spark gaps, they represent only a *coarse protection*, since owing to impulse voltage-time characteristics, significant overvoltages above the static sparkover voltage is possible; Section 3.2.4.2. Sensitive devices must be additionally protected by an electronic *fine protection*, for example, by a **protective diode** SD, which responds quickly and for defined low voltages, Figure 7.4.1-3. However, it is important here that coarse protection and fine protection are activated in a time-

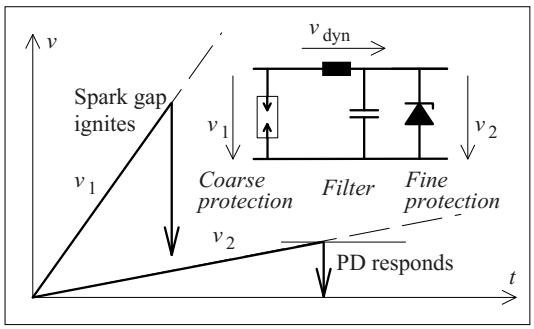

Figure 7.4.1-3: Coarse protection (spark gap) and fine protection (protective diode PD) with low-pass filtering (schematic).

staggered manner. This can be achieved with so-called "**energetic decoupling**". That means, a *dynamic voltage drop* v_{dyn} between the coarse protection and the fine protection, which significantly delays the voltage rise at the fine protection v_2, must be ensured using **filter elements** (e.g. longitudinal inductances and transverse capacitances). As a result, the overvoltage v_1 can activate the coarse protection even before the voltage at the fine protection and at the elements to be protected achieves values that are too high.

7.4.1.4 Lightning Protection Zone Concept

Modern lightning protection concepts for important and sensitive systems, for example, for computer centers, subdivide the volume to be protected into several **lightning protection zones** (LPZ) with different safety standards, Figure 7.4.1-4. Under the external lightning protection system, closed shields are used for demarcation of the zones (building shield, room shield, and device shield). *All* lines and pipes that enter through a shield are directly included into a local equipotential bonding system with mutually coordinated lightning current and surge arresters. This basically results in effective protection against the direct effect of *lightning current*, against the penetration of *magnetic fields* and against *line-conducted overvoltages* [192], [194], [195], [196], [478]. **Example:** As an example, Figure 7.4.1-4 shows the *protection of electronic systems* in a *simple building*: Here, **LPZ 0a** is the absolutely unprotected volume in which a direct stroke of lightning is possible. **LPZ 0b** is the volume that is not captured by the rolling sphere owing to the *air termination system;* and no direct lightning strike is therefore to be expected in this volume. Nevertheless, this volume is exposed to field influences without protection. **LPZ 1** is the so-called protected

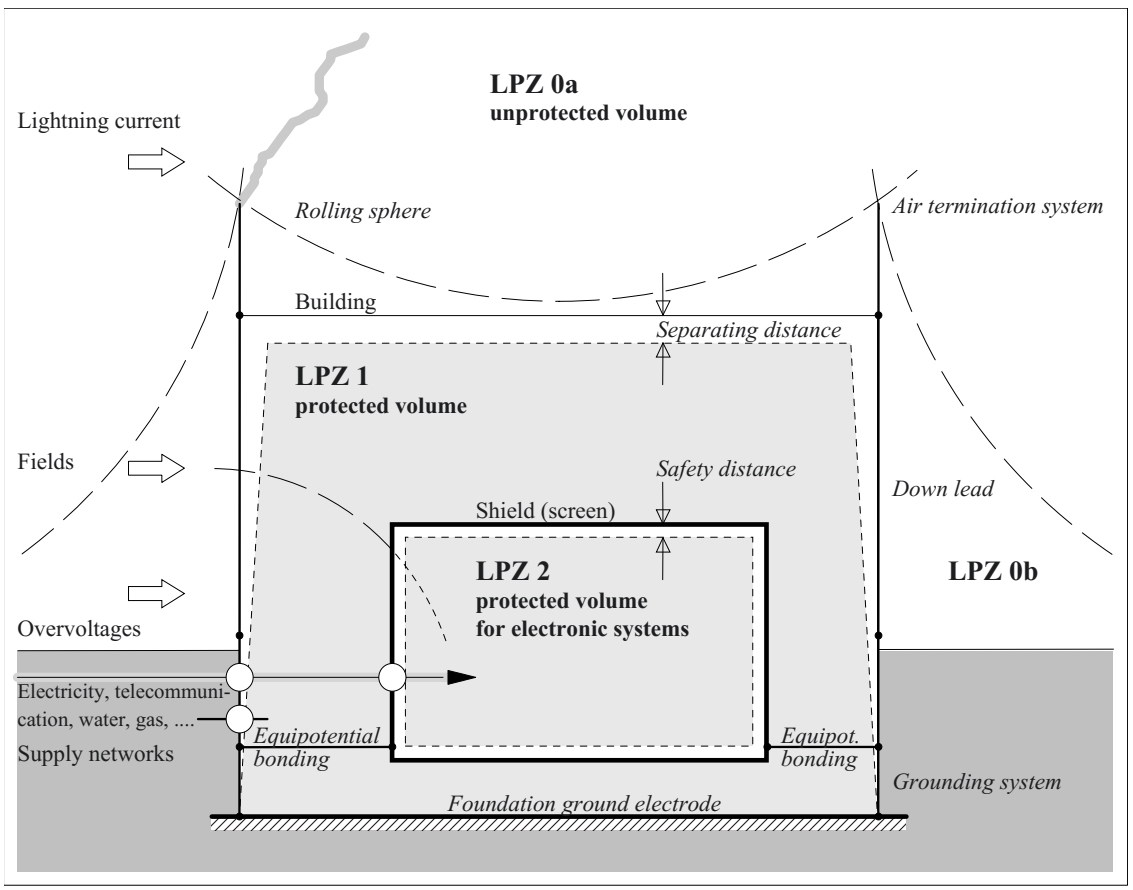

Figure 7.4.1-4: Lightning protection zone concept (schematic example).

volume. A *separation distance* must be maintained from the building envelope or the external lightning protection arrangement respectively, which protects against flashovers owing to induced voltages and potential increases. The necessary separation distance always increases with the height of the building. Since here LPZ 1 is not enclosed by a shield, electronic systems are not yet adequately protected. **LPZ 2** then provides an often adequate protection for electronic systems with an enclosing *shield,* with the *equipotential bonding arrangement* for the supply lines and with an internal *safety distance*. If the building and thereby LPZ 1 should be provided with a closed shield, for instance if a new building is designed, even and hence LPZ 1 can be used for the operation of electronic *devices* that are *insensitive to interferences* and LPZ 2 for the operation of *interference-sensitive equipment*.

7.4.2 Pulsed Power Technology

7.4.2.1 Impulse current circuits

Impulse current circuits include a voltage source, usually a capacitive energy storage device, a circuit-breaker, pulse forming elements and a load, Figure 7.4.2-1. There are also special devices for triggering and measurement.

Different designs of impulse circuits are already described in Sections 2.6.3.3 (*traveling wave generators*) and 6.2.3 (*generation of impulse voltages*). Extreme impulse powers up to the terawatt range are possible using *pulsed power technology* with water insulated intermediate storage devices and traveling wave lines, [14], [15], [40], [42], [43], Section 6.2.3.7 d), Section 5.4.5 and Section 2.6.3.3.

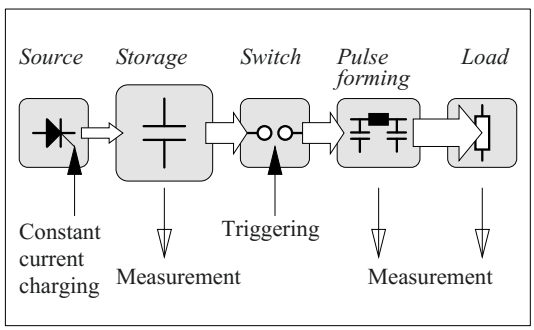

Figure 7.4.2-1: Impulse generator (schematic).

The *storag*e of energy, especially in capacitors with high pulse loading capacity is discussed in Section 7.3.2 and 7.3.3.

Triggering of impulse generators is carried out for low voltages and currents with power electronic switches or switching tubes (thyratrons). High voltages and high currents require electrically or laser-optically ignited switching spark gaps, Figure 6.2.3-5. Here, low jitter is important for the synchronization of multiple generators [108], [139], [140], [190], Section 6.2.3.7 d).

The *measurement* of fast-transient impulses requires very broadband sensors and dividers, [145] ... [154], cf. Section 6.3.3, 6.3.4 and 6.3.7.

In the following sections, various civil **applications**, i.e. non-military applications**,** of *pulsed power technology* for various purposes are presented.

7.4.2.2 Acoustic Shock Waves

Acoustic shock waves in liquids can be used for *medical applications* (e.g. lithotripsy), for example, or for *high-speed material transforming,* Figures 7.4.2-2 and 7.4.2-3. For this purpose, storage capacitors of several 100 pF are charged to a few 10 kV and connected via a triggered switching spark gap to another water spark gap at the focal point of an elliptical reflector. The impulse energy is partially transformed in water into the energy of an acoustic shock wave and focused on the object arranged at the second focal point. The object or the patient must be protected against the electrical effect of the high voltage impulse by a grounded screen grid. In the case of repetitive operation, energy storage capacitors have only a limited service life and must be regularly replaced, Section 7.3.3.

Note: Shock waves can also be generated with electromechanical converters via a membrane. Another alternative is lithotripsy by ultrasound.

In **medicine,** acoustic shock waves are used for *fragmenting* kidney stones, urethral calculus gall stones and bile-duct stones as well as for treating calcifications in the shoulder, for tennis elbow and calcaneal spur. Moreover, it was also ascertained that shock waves help the *blood circulation* and the healing of bone fractures and necroses of the femoral head [353].

In the case of medical *shock wave therapy*, the positioning of patients, the focusing of shock waves (with a focus of a few mm) and the triggering of many repetitive impulses are carried out under continuous X-ray monitoring, Figure 7.4.2-2. Fragmented stones can be flushed through the discharge paths of the urethra or bile ducts; crumbled calcaneal deposits must be dissolved in the body.

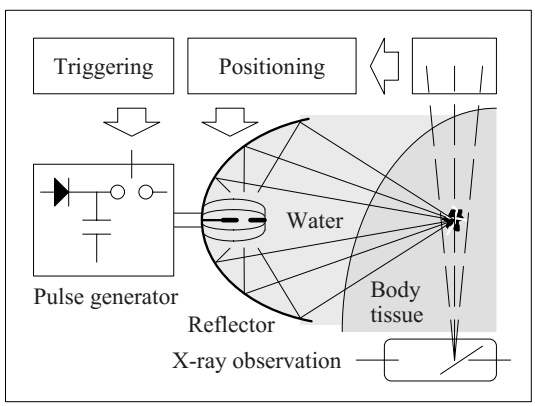

Figure 7.4.2-2: Focusing acoustic shock waves for lithotripsy / fragmentation of kidney stones (schematic).

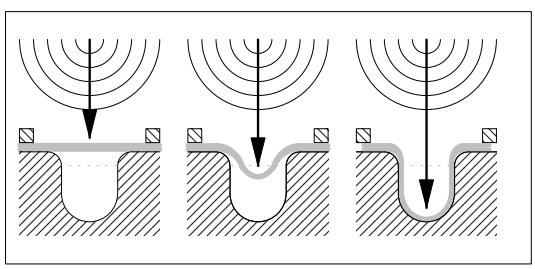

Figure 7.4.2-3: High-speed material transformation using shock waves (schematic).

7.4.2.3 Pulsed Particle Beams and Laser Beams

Very high pulse power can be transferred onto the *surface* of a target in an very short time and *extreme states of materials* can be achieved using pulsed particle beams of electrons or ions or using laser impulses.

Applications include testing deformation mechanisms in *nanocrystalline materials* and in *monocrystals* or testing the bonding strength of *protection layers and functional layers* on material surfaces with high-energy impulses.

For this purpose, for example, pressure impulses are generated with the help of p*roton beams* (1.7 MeV particle energy, 50 … 60 ns pulse duration, 55 kJ beam energy) or *laser impulses* (Nd:YAG, 50 J, 7 ns pulse duration). The effect of the impulses can be investigated by the measurement of speed profiles at the reverse side of the target by laser-doppler velocimetry or by follow-up examinations of microstructures by electron microscopy and X-ray diffractometry [354].

Another application is the *surface modification* of materials with pulsed *electron beams* (150 to 350 keV particle energy, a few 10 µs pulse duration). For adequate beam energy density (3 … 20 J/cm²), *metallic and ceramic surfaces* can be melted to the penetration depth of the electrons (approx. 100 µm) with a single impulse. Owing to the underlying cold material, extremely rapid chilling (quenching) takes place with a rate of change of 10^7 to 10^9 K/s. This results in *amorphous or nanocrystalline surfaces* with improved hardness, abrasion resistance and corrosion resistance. The advantage here is that relatively large areas of up to several 100 cm² can be treated. Moreover, thin foils can be fused on the surface of the material and alloyed as thin layers in the parent metal to improve corrosion properties [358], [359].

The pulsed electron beams are thus generated in so-called *vacuum diodes,* in which the cathode is covered with carbon fiber bunches. The

high voltage impulse extracts the electrons from it by explosive field emission.

Furthermore, there are other applications of high power impulses, e.g. for generating *mega-gauss fields* or for pumping *impulse lasers*, including the *excimer laser*.

7.4.2.4 Electrodynamic Generation of Nanocrystalline Materials

Thin wires can be explosively broken down into very small particles with diameters of less than 80 nm using high *pulsed discharge currents*. Depending on the gas atmosphere, oxidic, nitridic or metallic *nanopowders* are formed, which are separated from the gas stream by centrifugal force separators and electrostatic filters. Larger quantities of nanopowders require repetitive *wire explosion systems* (e.g. 1 Hz repetition rate and 4 kJ pulse energy for 227 mm long wires).

The nanopowders can be used for manufacturing elastic or conductive ceramics. Sinterable bodies (green compacts) result from *magnetic pulse compression* with pressures of up to 10^5 bars, by which the pressed parts are compressed to 80% of their theoretical density. Subsequent sintering is carried out with mm waves [354].

7.4.2.5 Electrodynamic Fragmentation

Electrodynamic fragmentation of *composite materials* is carried out with the help of pulsed **high voltage breakdowns** through the non-conductive solid to be broken down [362]. If an impulse energy of 10 to 300 J/cm is deposited within a few µs in the initial plasma channel, which is only a few 10 µm wide, temperatures of around 10^4 K and pressures up to 10^4 bar result. The *effect of the breakdown* is thereby comparable with a *chemical explosion* in a borehole, whereas the temperature of the spark channel is about 10 times higher and its radial expansion is about 10 to 100 times larger. Moreover, the energy release can be better adjusted and can be carried out repetitively.

It is also advantageous that the electrical breakdown proceeds along the *grain boundaries and material boundaries*, so that a significantly better **separation** of different components is effected than for a mechanical crushing (selective fragmentation). Even the reflection of acoustic shock waves at inhomogeneities, such as enclosures, grain boundaries or material boundaries, generates tensile stresses in the material compound, which cause the fragmentation preferentially at the inhomogeneities. In this way, fragmentation with a high degree of selectivity is achieved.

The breakdown through a solid body requires embedding in a *dielectrically strong liquid* to prevent breakdown in gas along the surface of the body to be fragmented. The breakdown strenght (*impulse voltage-time characteristic*) of many liquids increases with decreasing stress duration (i.e. increasing pulse rate of rise) more steeply than that of most of the solids, Figure 7.4.2-4. As a result, with rapidly rising impulses, breakdown of the solid body can be initiated prior to the breakdown of the insulating liquid. This is applicable even for **water**, Section 5.4.5, which is well suited on practical grounds and which even contributes to the displacement of the field in the solid body owing to its high permittivity. Since the voltage stress occurs only as a short impulse, the self-discharge time constants are not important here, Section 5.4.5.

This technology is now available even for industrial **applications** [354], such as for the recycling of *concrete* (breaking down into gravel, sand and cement powder), for the analysis of *steel fiber concrete*, for the analysis, metal separation and heavy metal immobilization of *slags* from waste incineration plants, for the removal of contaminated *concrete structures* as well as for low-contamination *milling* of various solids. Further, mono-mineral fractions can be obtained from crystalline multi-minerals such as feldspar, quartz and mica from *granite*, zircon from *tonalite* or

platinum minerals from *chromite ore*. This results in extensive applications for extraction of precious stones, for the analysis of stones and for the preparation of laboratory samples. When compared to conventional mechanical crushers, there are numerous *advantages*, for example, clean surfaces, high yield and low damage to the available target particles, dust-free production or detachment of morphologically intact fragments.

7.4.2.6 Electrohydraulic Fragmentation

In the case of slowly rising impulses, the liquid breaks down first, Figure 7.4.2-4. The energy must then be transferred to the material to be broken down by a hydraulic pressure surge. Therefore, this is known as electrohydraulic milling or electrohydraulic fragmentation.

7.4.2.7 Electroporation in Biological Cells

Pulsed electric field stresses of 1 to 100 kV/cm can lead to *irreversible pore openings* in the membrane of biological cells without the occurance of a breakdown. As a result of this so-called **electroporation,** *microorganisms* are killed or the *contents* of cells are released. Since the cells are always present in more or less conductive suspension, the field stress can be applied for only a very short period in the form of an impulse. The *energy requirement* for the opening of cells is at a minimum for pulse durations between 100 ns and 2 µs [360], [361].

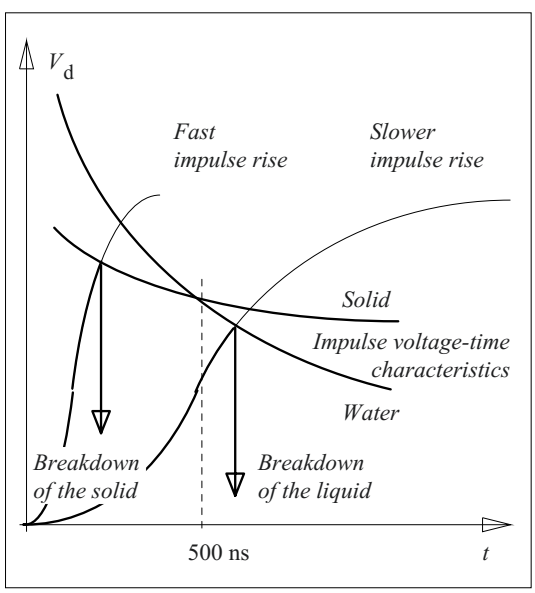

Figure 7.4.2-4: Different impulse voltage-time characteristics of solid and liquid media enable the impulse breakdown of the solid.

Note: The cell wall is generally made of so-called *lipid molecules*, which have a hydrophilic and a hydrophobic side.

It is assumed that *hydrophilic pores*, which are suitable for material exchange, at first develop as *hydrophobic pores* depending on temperature and membrane potential. If their radius attains a first critical value, they immediately transform into *hydrophilic pores*, whose radius increases further under the effect of the electric field stress. If the radius attains a second critical value r_{crit} under the effect of the pulsed field, the pore opening is *irreversible* and the cell dies.

Short term impulses have the potential for selective influencing of biological processes with different time constants and thereby even for *selective disruption of organelles* within the cell.

One application is the disruption of plant cells with low energy consumption, i.e. without conventional extraction at high temperatures, e.g. for the processing of *sugar beets*. Since heating is not necessary, *plant ingredients* can in principle be obtained with care and with high purity [361]. Making *fruit juice* or "pressing" *grapes* is feasible in this way. Further, methods have been developed for treating *waste water* contaminated with bacteria with the help of strong pulsed fields [354].

For the *purposeful opening of cell membranes*, the cells are brought into a spatially non-uniform electric field, in which the cell movement is controlled by *dielectrophoresis* (transport and spatial separation of different biological material components under the effect of electric field forces). The cell membrane is opened

by the application of a high voltage impulse in the microsecond range [384].

Example: For *pressing wine* by electroporation, a method was developed in which the mash between Rogowski-electrodes (with a largely homogeneous field) represents an electrolytic load for an impulse voltage generator. Breakdowns were largely prevented by a pressure of 3.4 bars. The impulse increases within about 0.5 µs to the peak value of 5.3 kV/mm, the wave tail half-value time is about 1.2 µs. For a repetition rate of 19 Hz and 5 impulses per filling of the reactor, a specific energy requirement of 89 kJ/kg and a temperature increase of 19 K resulted [473].

7.4.3 Light Technology and Laser Technology

Short-duration light impulses and laser impulses have an extensive technical *application spectrum*, for example, for photo flashes, hardening of resins, material processing, cutting, drilling, soldering, welding, inscribing or triggering of spark gaps. *Laser impulses of the highest power* up to the GW range and TW range, with short durations in the ns range, are necessary also for basic investigations on nonlinear optics, for testing matter in extreme states or for nuclear fusion experiments.

Flash units for short-duration photography and for the optical pumping of lasers include a *gas discharge lamp*, to which the voltage of a *capacitor bank* is applied, Figure 7.4.3-1. On closing the switch S, ignition takes place. The *charging* of the auxiliary capacitor generates a high voltage impulse via the ignition transformer, which leads to pre-discharges within the Xenon discharge pipe and triggers the main discharge [197].

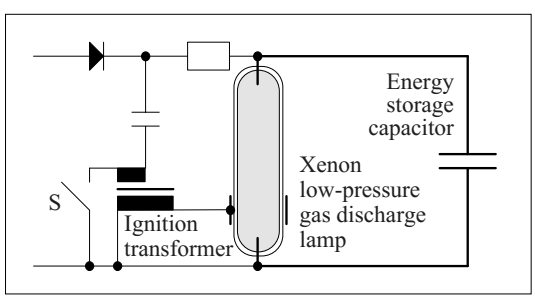

Figure 7.4.3-1: Flash unit with impulse lamp.

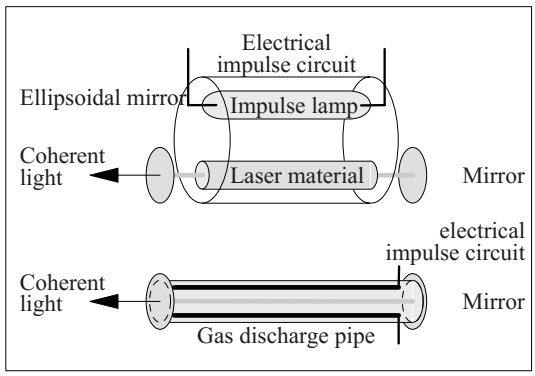

Figure 7.4.3-2: Optically pumped solid-state laser or liquid laser and gas-discharge laser for impulse operation (top and bottom, schematic).

Short flashes of high radiation power or temperature require large currents that are restricted by the inductance of the discharge circuit. If necessary, it must be designed with *low inductance*, e.g. as a coaxial construction.

Impulse lasers can generate coherent light of extreme power densities. The *principle of a laser* (**l**ight **a**mplification by **s**timulated **e**mission of **r**adiation) is based on the excitation of atoms in which higher energy levels are occupied by electrons and lower ones are left vacant *(population inversion).* The spontaneous transition of an electron to a lower energy level with the emission of a photon stimulates equivalent tranitions for other excited atoms resulting in *coherent* emission with equal wave length, equal phase and equal direction. For strengthening the stimulated emission, the laser medium is arranged between two mirrors in an *optical resonator,* from which only a small fraction of the coherent light is decoupled, Figure 7.4.3-2. As a result of the *impulse operation*, the population inversion and radiation power can be steeply increased.

Typical *laser materials* for high pulse powers are ruby crystals doped with chromium, Y-Al garnets (YAG laser), neodymium (Nd) glasses and CO_2 gas. In the case of CO_2 lasers with transversal electrical excitation, a pulsed high current discharge takes place in CO_2 gas under high pressure.

Here, the objective of *high voltage engineering* includes depositing the energy required for establishing population inversion in a laser medium in the shortest time possible. Since this relates to raising electrons to higher energy levels, it is referred to as "pumping" and "pumping energy" respectively. In extreme cases, pulse power generators are necessary as drivers.

Note: High powers and short impulses in the ns range (giant pulse laser) can even be achieved with *quality switching* (Q-switch). For this, the oscillation of the optical resonator is delayed up to very high population inversions by de-tuning the mirror. Q-switching of the resonator mirror takes place mechanically by rotation, electro-optically, electro-acoustically or chemically and releases the stored pump energy as a giant laser impulse [197].

7.4.4 X-ray Technology

X-rays result from the bombardment of a positive electrode (*anode*) with high-energy *electrons* in a vacuum tube (*X-ray tube*), Figure 7.4.4-1. During this, electrons from low energy states or from the inner atomic orbitals of the anode material are set free. Transitions of free electrons to unoccupied and *very low energy states* lead to the emission of *high-energy X-ray radiation quantums* according to a high energy difference [24], [25].

X-ray radiation is an indispensable aid for medical and technological diagnostics, for example, for computer tomography or for radiographical examination of welded seams. Depending on the energy of the radiation quantums, *accelerating DC voltages* of a few 10 kV up to several 100 kV are necessary.

Vacuum breakdown in the X-ray tubes must be prevented by high vacuum, adequately dimensioned insulator interfaces and smooth electrode surfaces, cf. Section 3.7. A *balanced-to-earth voltage* halves the voltage stress to ground, Figure 7.4.4-1. *Cathode heating* increases the number of emitted electrons. *Rotating anodes* help with a better heat dissipation [67].

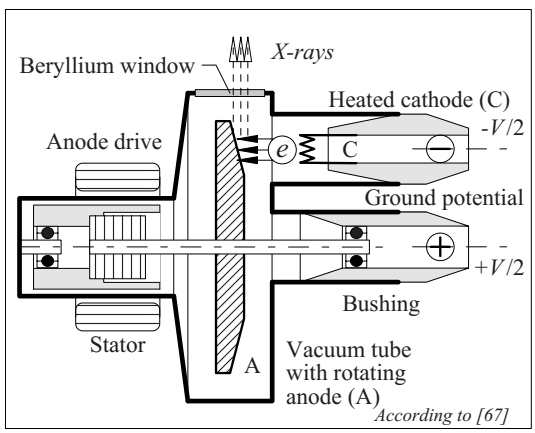

Figure 7.4.4-1: X-ray tube (example, schematic).

7.4.5 Electrostatic Particle Precipitation, Ionization

Electrostatic particle separation depends on the *charging* of insulating or conductive particles by *corona discharges* at an emission electrode. Under the effect of electric field *forces*, the particles (disregarding *fluid-dynamic processes*) approximately follow the field lines and deposit on a surface, Figure 7.4.5-1. Thus, defined layer thicknesses can be achieved by means of the electric field distribution. Typical operating voltages lie at a few 10 kV.

Important applications are the **vacuum metallizing** of glass and ceramics, **photocopiers**, electrostatic **powder coating** and **spraying**.

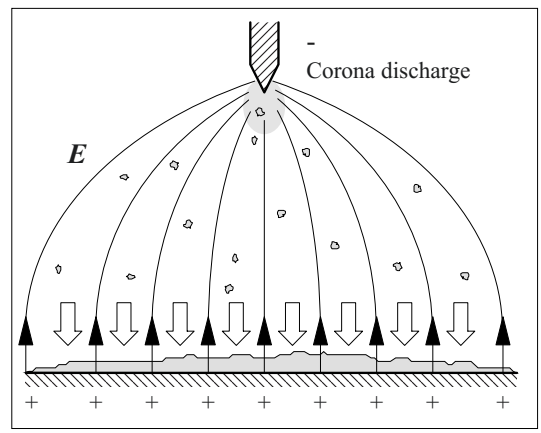

Figure 7.4.5-1: Deposition of charged particles.

For example, spray pistols with integrated DC voltage cascades are used for the specific coating of surfaces [16].

In **electrostatic precipitators**, *flue gas cleaning* is performed by precipitation of particles. The gas flows between grounded plates with a flow gap of approx. 20 to 40 cm. *Corona wires (barbed electrodes)* at a distance of about 10 to 20 cm are present in between. Because of the higher breakdown strength and in order to achieve a high efficiency, operation is generally with *negative DC voltage* and close to the breakdown limits. During operation, electrons and negative ions are attached to the particles and pull them by means of the electric field forces to the grounded plate electrode. Dusts deposited on the plates are regularly knocked off.

The degrees of separation of electrostatic precipitators are heavily dependent on the corona arrangement and on the voltage. Depending on the type of dust, a voltage with maximum *degree of separation* exists. Exceeding this leads to intensified *back coronas* of deposited dust in the flow gap, the degree of separation decreases and a breakdown can be initiated. Highly resistive dust layers, across which large voltage difference build up for DC voltage, are the cause. They lead to partial discharges and partial breakdowns in the dust layer.

Better separation results are possible with a *pulsed voltage supply* with pulse widths in the ms range, since particles can be charged higher at a given mean voltage value owing to a higher peak voltage magnitude [136], [198]. Additionally, short-duration voltage stress leads to a lower mean charging current. Owing to this, a smaller voltage drop in the highly resistive dust layer is built up and reduced back corona occurs.

Degrees of separation of electrostatic precipitators are in excess of 99% under optimal conditions and depending on the particle size. However, a separation minimum occurs for respirable *diameters* < 1 µm and further improvements are investigated [197]… [201].

Note: Corona discharges and surface discharges can be used even for the **ionization** of gases, e.g. in *ionizers* for ventilation system technology and for treating room air or for generation of *free radicals*, such as in chemical reactors for *generating ozone* or for the treatment of *waste water*.

7.4.6 Spark Plug

With the high voltage magnetic ignition (magneto), Robert Bosch solved “the problem of problems” in 1902 (quotation from Carl Benz) during the development of high-speed combustion engines. In the magneto, the current that is flowing through an inductance (ignition coil) is interrupted, owing to which a high switching overvoltage occurs, Figure 7.3-1 (right). Today, the impulse is generated electronically with the help of an ignition transformer.

The ignition impulse is passed through the grounded engine block via a suitably insulated **spark plug**, Figure 7.4.6-1. Therefore, inter alia it i*s* also a *bushing*.

In a *spark gap*, the ignition impulse leads to breakdown which is the ignition spark initiat-

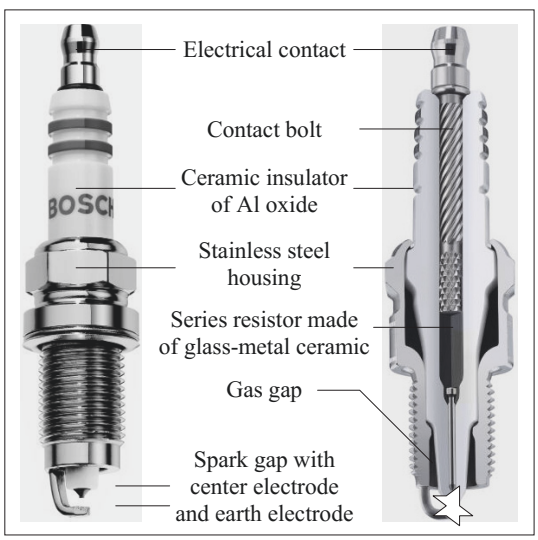

Figure 7.4.6-1: High-performance spark plug, photo Robert Bosch GmbH.

ing the ignition of the air-fuel mixtureat an exactly defined moment and at an exactly defined location. The energy dissipated in the spark and the associated electromagnetic disturbances are determined by an integrated series resistor and by the capacitances given by the geometry.

In the past years, the spark plug has developed from the classic standard product to a highly technological *system component*, which along with the ignition system must be aligned precisely with the thermodynamic processes in the combustion chamber of the respective motor [328], [329], [330]. Only in this way can the high electrical, thermal, and mechanical stresses occurring during operation be coped with and the high requirements for low emissions, economical operation as well as reliable and continuous operation over long periods are satisfied. This results in a steadily increasing number of different spark plugs.

The **construction of a spark plug** can be seen from Figure 7.4.6-1: the fundamental component is the ceramic *insulator* made of highly thermally-resistive aluminum oxide. It encloses a motor side *center electrode* made of a *contact pin* and an erosion-resistant *electrode* made of a nickel-yttrium alloy with a noble metal point (platinum or iridium). The center electrode, along with the earth electrode welded to the housing, which likewise carries an erosion-resistant noble metal inlay, forms the *ignition spark gap*.

Figure 7.4.6-2: Air spark gaps (bottom left) and creepage spark gaps (bottom right), Photo Robert Bosch GmbH.

Note: For a rapid and dependable ignition as well as for the maximum possible flammability range, a *spark position* extending deep into the combustion chamber (this refers to the position of the ignition spark gap in the combustion chamber) has proven advantageous [329]. The design of the spark plug must thus be suitable for the increased mechanical and thermal stresses that occur without any loss in durability. Therefore, an elongated housing is used against vibrations and *copper cores* are used in the electrodes against increased temperature.

The insulator body additionally encloses a special *resistor material mixture* made of glass particles, which are coated with conductive and non-conductive phases and are fused with the insulator body. This results in long-term stable resistance values, even for alternating thermal stresses during operation. The electrical contact to the contact pin (bottom of figure) and to the *contact bolt* (top of figure) is effected by a conductively set *contact material mixture*. The insulator body is clamped in a *housing* of stainless steel. The dimensions result from the threaded hole provided in the motor.

The **construction of the spark gap** is important for a reliable ignition, Figure 7.4.6-2. For pressures above 10 bars and temperatures at 1000 °C, the gas densities are multiple times the usual atmospheric values that are generally observed in air. Ignition voltages in the 30 kV range are therefore necessary for distances in the mm range, especially for a cold motor, cf. Section 3.2. After the electrodes are heated, the ignition delay is reduced owing to thermionic emission of electrons from the cathode.

Ignition delay can also be reduced by *creepage spark gaps*, Figure 7.4.6-2 (bottom right). This results in the additional advantage that *soot*

deposits on the insulator surface, such as those that can occur for short-trip operations in the partial load range of the combustion engine, are burnt away around the center electrode. Thus, the build-up of a surface shunt resistor, which could short circuit the ignition voltage, is avoided [329].

From the perspective of high voltage engineering, the **aluminum oxide insulator** forms a *creepage configuration*, Section 3.2.6. The *gas gap* between the insulator and the housing must be designed in such a way that for the pressures and temperatures that occur in the combustion chamber, the discharge inception voltage is higher than the breakdown voltage of the spark gap. Specific minimum diameters are necessary for this. At the *outdoor side*, flashovers can be prevented by adequately large insulator lengths and diameters.

In the radial direction, the *ceramic insulator* is stressed with very high field strengths. These stresses must be reduced by an appropriate geometrical design and must be withstood by especially developed *high-tech ceramics*. Parameters here are material composition, particle size, forming pressure and burning temperature.

The design of the spark plug is not only determined by electrical stresses but also by repetitive *thermal* and *mechanical* as well as by *oxidative* and *chemical* **stresses**. Temperature variations in the cylinder between 100 and 1000 °C, temperature gradients along the spark plug between 1000 and approx. 100 °C, as well as pressure surges up to 100 bars owing to the explosive combustion must be withstood over a long period of time. Additionally, erosion of electrodes and chemical changes of the surfaces owing to oxidation or fuel residues must be considered. Despite this, service lives of 60000 to 100000 km are possible today.

The thermal design of the spark plug must also ensure that the surface temperature is not too high, in order to prevent so-called *pre-ignitions*, i.e. untimely *self-ignitions* (*glow ignitions*), and self-ignition damage to the motor.

While **manufacturing** the spark plug, the insulator made of aluminum oxide mass is first pressed, polished and pre-heated. After installing the center electrode, the firing process takes place, during which the insulating material is sintered. Finally, the insulator is lettered and glazed. The contact pin, the contact element, the resistor element and the contact bolt are assembled and finally the insulator is fired. After the assembly of the insulator in the housing with the welded-on earth electrodes, the electrode distance is adjusted.

Spark plugs are manufactured in *large quantities* of millions per day using highly automated production processes. In this respect, spark plugs are different from so many other high voltage engineering products that are manufactured only as single units or only on a small scale.

7.5 Superconducting Equipment

7.5.1 Superconductivity

At very low temperatures, i.e. at the so-called *transition temperature* or at the *critical temperat*ure, many materials change to the **superconducting state**, i.e. they lose their electrical resistance, Figure 7.5.1-1. For a long time, only materials with transition temperatures T_C that were only slightly above the absolute zero of tempeerature were known, e.g. T_C is about 9 K for NbTi or approx. 18 K for Nb_3Sn (LTSC or LTS: **low-temperature superconductivity**).

Physically, superconductivity is described by the formation of so-called *Cooper pairs*, in which electrons with opposite spin and opposite impulse pair up via vibrations of the atomic lattice (phonons) and can be in motion together in the material in a *highly ordered state* of the electron gas without resistance.

However, on exceeding the critical temperature T_C, the critical magnetic flux density B_C

or the critical current density J_C, adequate energy for breaking the pairs is provided and the ordered state is destroyed. All these three parameters are dependent on each other, i.e. for high magnetic field strengths, the critical temperature and the critical current denstity reduce. The **existence range** of the superconducting state can therefore be specified by a three-dimensional state surface, Figure 7.5.1-2. Superconductors must be operated at an *operating point* below this transition surface. Loss of superconducting state is referred to as so-called "*quench*".

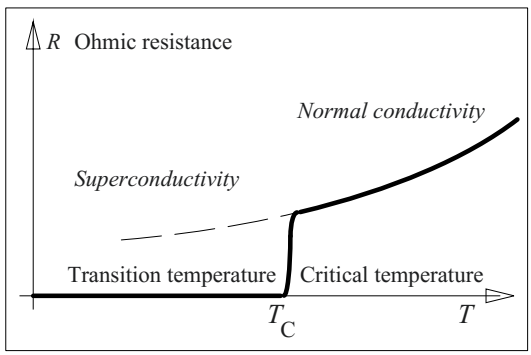

Figure 7.5.1-1: Superconductivity.

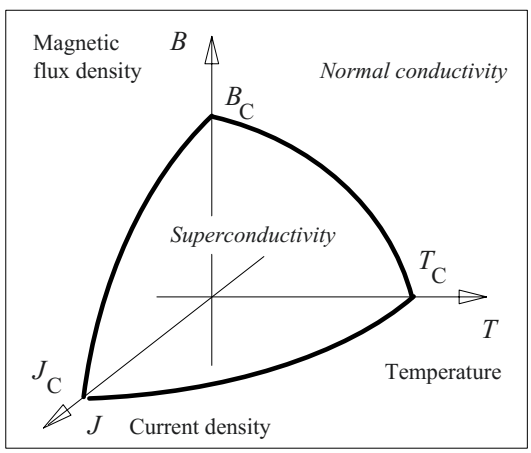

Figure 7.5.1-2: Existence range of superconducting state.

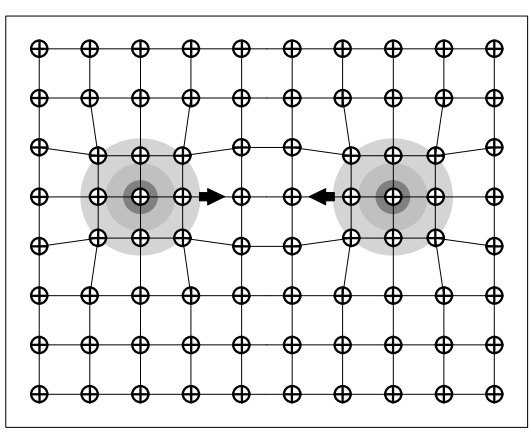

Figure 7.5.1-3: Formation of Cooper pairs through lattice deformation.

However, visions of no-loss energy transmission and energy storage were at first economical only in very few applications, since *liquid helium* with a boiling temperature of 4.2 K was necessary for the *cooling* of the superconductor, and this can be provided only with the expenditure of much energy and at the related costs. Nevertheless, the development of prototypes and niche applications has provided important technological experience.

The discovery of **high-temperature superconductivity** (HTSC or HTS) in the year 1986 was a decisive moment: new oxide ceramic materials with transition temperatures around 100 K now allow the utilization of *liquid nitrogen* LN_2 as the cooling medium with a boiling temperature of 77 K at drastically reduced energy requirement for cooling. Many new energy technology applications suddenly appear to be economically feasible in the foreseeable future. Superconductivity, therefore, is a *key technology* which requires special insulation systems.

Superconductivity results from the interaction of conduction electrons, grid structure and thermal agitation of the atomic lattice, Figure 7.5.1-3: While applying an electric field, not only a drift movement of individual electrons occurs, but also the fully ordered "electron grid" is set in motion in the direction of the field and effects an incomparably higher current [24]. The *lossless nature* of the current is explained by the fact that it is not possible to scatter out individual cooper pairs. Either all the pairs pass onto a new state or none do.

The magnetic field is completely displaced from an infinitely highly conductive material (Meißner-Ochsenfeld effect in so-called *type I superconductor*). So-called *type II superconductors,* which also include high-temperature superconductors, allow the penetration of the material by the magnetic field in the form of spatially delimited flux tubes (flow quantization). These flux tubes are areas with a normal-conducting state within the superconductor that are surrounded by superconducting ring currents. These ring currents limit the normal-conducting areas and shield them from the superconducting areas.

Note: Even *type I superconductors* show this effect, but to a distinctly lower extent, since this state is almost skipped during the increase in temperature before they become normal-conducting.

These *flux tubes* must be suitably anchored (e.g. at the grain boundaries of the material, lattice defects or foreign atoms) to avoid movement under the effect of the Lorentz force associated with energy dissipation.

Losses in superconductors occur not only owing to the *migration of the flux tubes*, but also owing to *hysteresis phenomena* and *eddy currents* in the surroundings of the superconductor for AC currents and for changing currents or magnetic fields respectively.

Furthermore, the superconducting filaments are stabilized with normal-conducting matrix material (generally, copper) on electrical and mechanical grounds. Superconductors and normal-conducting matrix material thus form *parallel current paths*. As a result of the voltage induction at the inductance of the conductor, a reactive voltage drop occurs (for example, for alternating current or while applying an external voltage with the objective of current variation or field variation in a superconducting coil), which also drives a current through the parallel normal-conducting current paths and causes *ohmic losses*.

Thus, only a pure *direct current* can be transmitted completely *free of loss*. The development of superconductors with low losses in alternating fields is therefore of great significance.

Table 7.5-1: Typical values of HTS according to [337].

Material	T_C	J_C	B_C	
	K	A/mm²	T	
Bi Bismuth				Wires,
Bi-2212	90	100	0.2	too high
Bi-2223	110	100	0.1	AC losses
Y Yttrium				Not available
Y-123	90	1000	20	in adeaquate
(YBCO)				size
Cu Copper		< 10		Normal conductor, for comparison

7.5.2 HTSC Conductor Materials

High temperature superconductors (HTS or HTSC) include a complex layering of insulating and superconducting layers based on bismuth compounds or yttrium compounds, Table 7.5-1. For high current carrying capacity, the transition at the crystal boundaries of the polycrystalline structure is important. Moreover, current carrying capacity is heavily anisotropic. During manufacture, an optimal orientation of crystals is achieved by texturing in order to avoid weak spots for current transport [336]. For operation close to the critical temperature, *critical current densities* of HTS are today even lower than those of LTS. However, for operation distinctly below the transition temperature, again higher current densities and flux densities (sometimes up to 200 T) are possible.

Ceramic HTS are non-conducting at higher temperatures. Therefore, they must be embedded in a **highly conductive matrix** (e.g. in silver), which includes approximately 70 to 75 % of the cross-section and which carries the current on losing the superconducting state.

Manufacturing technically applicable wires is possible by the **opit method** (oxide powder in

tube), Figure 7.5.2-1: the oxide powder is fused in silver tubes and drawn into wires. Several bundled wires are then drawn into a multifilament wire, rolled to a few mm broad tape conductor and finally annealed. The proportion of superconductor to the conductor cross-section today is up to 30%. Thus, *technical current densities* of about 80 A/mm^2 (in comparison to about 10 A/mm^2 for copper wires) are achieved. An increase in the current density by about one order of magnitude is the aim for economic reasons [336], [202].

Note: Very high current densities can be achieved with the **coating method**, whereby substantially mono-crystalline HTS films are deposited on previously texturized substrates. Owing to this, the occurrence of weak coupling points at the crystal boundaries is largely prevented. On including the base material, *technical current densities* of 100 A/mm² (Ibad method: ion beam assisted deposition) and 1000 A/mm² respectively (Rabits method: rolling-assisted biaxially- textured substrate) are achieved. The coating methods are, however, available only in *laboratory scale* and for small components [336].

For YBCO (yttrium-barium copper oxide), conductors have been manufactured until now only in small lengths and in linear form. For longer and more flexible conductors, therefore, the poorer properties of bismuth-based superconductors must be accepted or LTS conductors must be used and the temperatures must be reduced to a few K.

The HTS conductors are very brittle and must not be stretched (maximum about 0.1%). This results in increased **restrictions on processing**, i.e. twisting or transposing has until now only been possible on a laboratory scale.

Note: The aim are advanced YBCO tape conductors using a wet-chemical coating method on texturized substrate bands (Ni, NiW, Cu), so-called "coated conductor". Transposing was successfully achieved on a laboratory scale by punching out meandering single conductors from YBCO tape conductors and subsequent stranding [452].

A mechanically more robust design is obtained if the multifilament tape conductor is provided with a *covering* of silver-magnesium alloy.

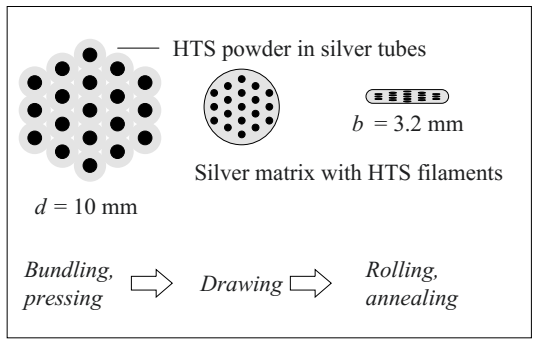

Figure 7.5.2-1: Manufacturing HTS tape conductors.

Also, *support structures* are necessary against magnetic forces.

Technological development is thus oriented towards the manufacture of HTS in longer lengths, with higher current carrying capacity, lower AC voltage losses and better processability.

7.5.3 Insulation and Cooling with LN_2

High temperature superconductors can be insulated and cooled with **liquid nitrogen LN_2** with a boiling point of 77 K. The *electric strength* of LN_2 is discussed in detail in Section 5.4.6. It is especially important that although LN_2 is an equally good insulation medium like insulating oil, the *formation* of thermal *gas bubbles* owing to alternating current losses or a quench cannot be ruled out.

Note: For *superconducting magnets*, high voltages occur especially in the event of a *rapid discharge* of the coil triggered by a quench. As a result of rapid current variations and field variations, also eddy currents are induced in the structural materials. The heat converted here, therefore generally requires re-cooling and stabilization over several hours for large coils.

A decrease in the strength resulting from bubble formation in LN_2 is more distinct for *impulse voltages* than for AC voltages and DC voltages, since the high impulse voltage strength of the liquid phase is lost, so that the impulse voltage strength and the AC voltage strength converge at the lower level. The loss

of strength owing to gas bubbles is, however, less dramatic as compared to insulating oil: Owing to lower permittivity $\varepsilon_r = 1.44$, the *field displacement* is weaker, and owing to low temperature, the *gas density and strength* are approximately increased by a factor of 3.8. Therefore, the *strength of the gaseous nitrogen* at 77 K should form the basis for dimensioning.

Note: Partial discharge inception field strengths for **solid insulating materials** under LN_2 are specified for *impregnable materials* as 7 to 10 kV/mm and for *GFK materials* (depending on the quality) as 2 kV/mm, 2 to 5 kV/mm (wound) and 4 to 7 kV/mm (impregnated) [350].

Cooling of superconducting components can take place as **bath cooling** in a *cryostat* with liquid cryogen. The *cooling medium* here is also the *insulating medium*. The cryostat is made of a thermally insulated *receptacle* (e.g. double-walled with vacuum insulation) and a thermally insulated *cover* with connections for the cooling circuit and *bushings* for the electrical connections, Figure 7.5.4-4. An alternative is **once-through cooling**, in which the conductor is cooled by the internal channels. In this case there is a vacuum outside the conductor for thermal insulation. Therefore, the electrical insulation must also be considered as *vacuum insulation*.

Note: The double-walled insulation receptacle has an *internal cold wall* and an *external hot wall* separated by the vacuum gap. Heat transmission by *radiation* is reduced by an additional insulation, the so-called *super insulation*.

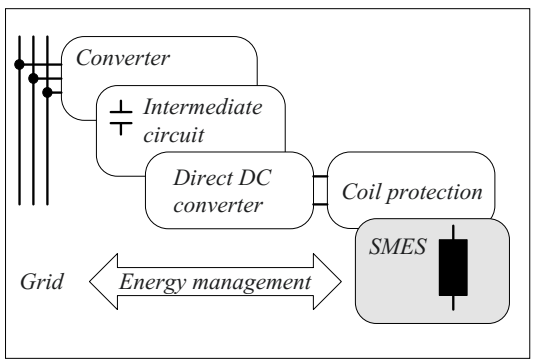

Figure 7.5.4-1: Principle of superconducting magnetic ernergy storage (SMES).

The cooling can take place *actively* by a suitable cooling unit (with LN_2 tank for buffering short-duration thermal output peaks) or *passively* by evaporation of an adequately large LN_2 supply that must be regularly supplemented. Even the second option can be economical, if the nitrogen used is prepared on a large scale.

Basically, it must be noted that the *thermal input power* occurring in the low temperature range remains small to the maximum possible extent, as the electrical *power of the cooling unit* necessary for the heat transport is greater by a factor of 20 to 25 at 77 K than the thermal input power, and increases more steeply than by $1/T$ (at 20 K by a factor of 100 and at 4.2 K by a factor of 500).

The thermal input power occurring at low temperatures results from the *AC conductor losses*, heat flux through the *thermal insulation* (can be kept comparatively small) and from heat flux through the conductors of the *electrical connections*.

7.5.4 Applications

Superconducting operating equipment, owing to still very high costs, will not replace the available equipment of electrical power engineering, but rather supplement them in the form of special applications, since partially they offer properties that cannot be achieved with conventional technologies. In the following section, some potential areas of application are described.

7.5.4.1 SMES Superconducting Magnetic Energy Storage

Magnetic energy storage allows much higher energy densities than capacitive storage. Ohmic heat losses in the coils, which until

now had complicated the practical application, can be avoided today by the use of superconductivity. Systems made of *He-cooled low-temperature superconductors* have already been in use since approximately 1990. They help in providing an active power **seconds reserve** and in the compensation of reactive power and can thereby protect sensitive loads for a short period against voltage dips or help in the equalization of network load of consumers with heavily fluctuating power consumption. The magnetic storage device is charged via rectifiers and supplies energy to the network via converters in series or parallel to the load [370], Figure 7.5.4-1. Mobile systems with rated power of 3 MW, which protect much larger drives by supplying inrush currents to them, are described as an example [338]. Studies have shown the feasibility of 50 MW to 100 MW SMES with an energy content of 2 to 3 MWh and access times in the ms range [202]. However, today's systems are still significantly smaller with energy contents of approximately 2 to 5 MJ or 0.5 to 1.5 kWh respectively. SMES can help to achieve or to improve the supply quality in networks, even without direct network extension. In the case of intermittent loads, the network is protected against undesirable system peturbations. The SMES is reloaded during the load-free pauses.

7.5.4.2 Fault Current Limiter, Switch

There are high expectations for the superconducting *fault current limiter* (FCL) that is already present in field tests. On exceeding a critical current, they change immediately from the superconducting to the normal-conducting state. Owing to this, a resistance is built up which restricts the critical value of the short-circuit current to an acceptable value within the ms range. The current can be interrupted by a weaker circuit-breaker. It is therefore possible to extend the networks and simultaneously prevent the rise in short-circuit currents. There are two basically different concepts for fault current limiters [339], [340], Figure 7.5.4-2:

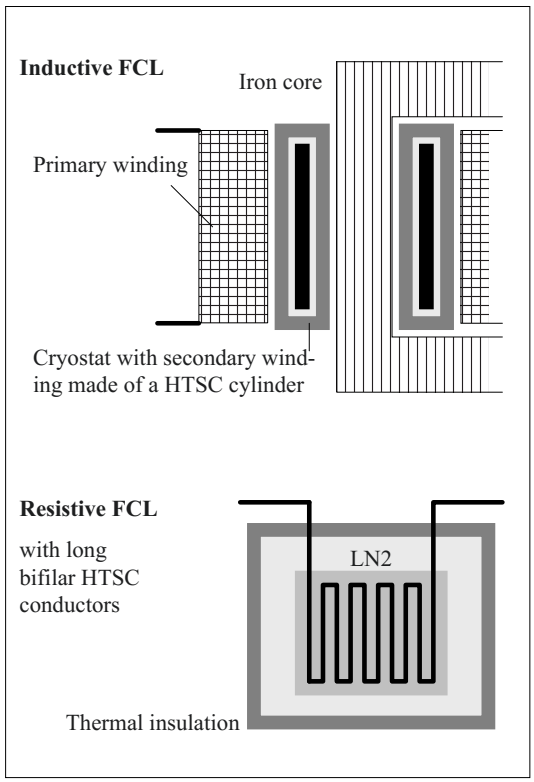

Figure 7.5.4-2: Superconducting fault current limter (FCL), inductive and resistive principles (top and bottom).

An **inductive FCL** consists of an iron core at ambient temperature, a normal-conducting primary winding that carries the current and a simple short-circuited *superconducting secondary winding* in its own cryostat [340]. In the case of a high fault current on the primary side, the high current that is transferred to the secondary winding causes a quench and the current limiting impedance is also transformed to the primary side. This principle could already be implemented with the available materials in 1996 as a 1.2 MVA/ 10.5 kV prototype [341]. The dimensions and weight as well as the cooling time until renewed operation readiness are problematic here.

A **resistive FCL** consists of a superconductor at high voltage potential carrying load current or short-circuit current directly [202]. A high short-circuit current leads to a quench and to a rise in resistance, whereby the current load of

the quenched superconductor can be reduced by a parallel resistor. Simple assembly, low reactance and the expected scalability for high powers are advantageous in this type of construction. However, until now sufficiently long superconductors have not been available. The worldwide first resistive current limiter (10 MVA/ 10 kV) was therefore put into operation only in 2004 [342]: The *superconducting elements* are made of BSCCO-2212 material, which was processed into melt-textured, approximately 30 cm long tubes by a centrifugal casting process. By cutting out a bifilar coil, a conductor length of 5.4 m is achieved. A Cu-Ni layer provides thermal and electrical stabilization and homogenization of the limitation effect for the whole conductor length. For each phase, 30 elements are connected in series. Tests have proven the reduction of the current peak value from 18 to 7.8 kA. As the next step, development of a FCL for the 110 kV level is planned.

Note: In principle, superconducting fault current limiters are switches which are actuated by the magnitude of the current. Switching between normal-conducting state and superconducting state is also possible by the magnitude of an external magnetic field, Figure 7.5.1-2. **Magnetically controlled superconducting switches were** used on an experimental scale for DC/AC converter, i.e. as a new kind of converter principle for *high voltage DC transmission HVDC* [343].

7.5.4.3 Cables

Superconducting cables play a key role in the original *vision of "lossless" energy transmission*. Therefore, they were implemented quite early as prototypes with classic *low-temperature superconductors* and He cooling/ insulation, but the high cooling requirements and the associated high costs led to a severe damping of expectations. When using *high-temperature superconductors*, the cooling requirements and costs are significantly lower. Despite this, their utilization is not viewed as a basic alternative but as a supplement to the existing network: they do not make the high voltage levels superfluous, but only *increase the power transmitted*.

Superconducting cables can transfer about four times **higher power** for a comparable space requirement than normal-conducting cables. Therefore, they are especially suitable for the *replacement of old cable sections* in case of increasing power requirement without the requirement for additional space. Owing to this, utilization of higher voltage levels with the corresponding transformation units can possibly be avoided. In a *demonstration experiment*, the option of a transmission of 100 MVA at 24 kV as an alternative to transmission at 120 kV will be shown. In this case, the dielectric is at ambient temperature and the conductors are internally cooled [344].

The first *HTSC cable system*, which transmits energy in a public network, was installed as three single-conductor cables (30 kV, 2 kA, 104 MVA) in 2001 in Copenhagen [383].

The single cable is made of flexible stainless steel supporting pipe, through which the LN_2 cooling medium flows. The HTSC bands are helically wound around the supporting pipe and they are *cooled only internally*. On the outside, there is thermal insulation by an internal and external steel pipe, both of which are at high voltage potential. In the intermediate space, a so-called *super insulation* is present, in which the convection, thermal conduction and thermal radiation are minimized by vacuum and by thin polymeric films with vapor deposited aluminum.

The *electrical insulation* is set up in a conventional manner with a conductor screen, dielectric and insulator screen and is at *ambient temperature*. Even the cable terminals correspond to the usual construction type. The

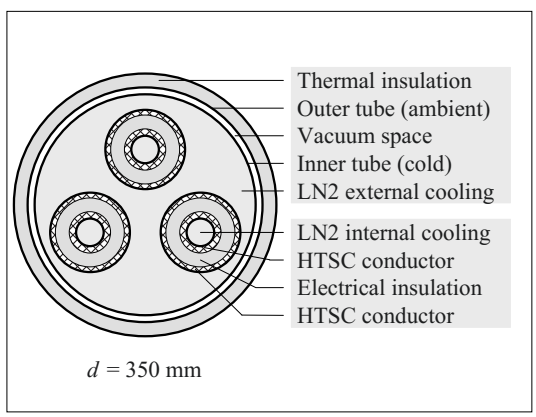

Figure 7.5.4-3: Concept of an 110 kV / 1000 MVA HTSC cable with LN2 cooling [202].

cooling medium is passed via insulation units (potential separators) into the high voltage conductor.

Studies deal with the transmission of 1000 MVA at 110 kV, Figure 7.5.4-3 [202]. The LN_2 cooling of three cables laid together in a tube takes place inside the inner conductor and outside the outer conductor. HTSC tape conductors are wound helically around the inner conductor supporting pipe and around the insulation.

Advantages of the concept here are a high *transmission capacity* at relatively low *voltage* and a small *space requirement*.

7.5.4.4 Motors, Generators

Synchronous generators and synchronous motors can already be implemented with low-temperature superconductors [345], [346]. For this, only the *DC excitation circuit* is implemented with *superconductors* on a cooled rotor. The *stator windings* are not (yet) designed to be superconducting owing to higher losses in the alternating field.

The high *magnetic flux densities* of about 5 T generated by the rotor as compared to approx. 1 to 2 T for conventional systems is a great advantage. It allows large reductions of **volume** and **weight**. Moreover, the **losses** fall from approximately 1% to about 0.5%. Further, the synchronous reactance of the generator can be reduced and this would have a positive effect on **power system stability**.

Note: Another aspect is the theoretical option to generate even **higher voltages** directly in the generator [345]: The high magnetic flux densities would lead to the saturation of the iron of the *stator teeth* between the conductor rods. The teeth can therefore be dispensed with and the space would be utilized for *other windings*. This means that, similar to a transformer, turn would be adjacent to turn and the *interturn insulation* could be weaker. Between the windings, however, the entire voltage must be insulated. Outside the windings, a frame of laminated magnetic material is present for closing the magnetic circuit. The turns must be adequately insulated against these frames. All the materials within this frame are non-magnetic (**air-core principle**).

7.5.4.5 Transformers

The design of superconducting transformers is generally similar to the design of conventional transformers. The *limb assemblies* are maintained in the *cryostats* at or below the boiling point of nitrogen (77 K). LN_2 thus acts as a cooling medium and an insulation medium. At least for large transformer ratings, it is useful to operate the *iron core* outside the cryostats at ambient temperature, in order to avoid that the iron losses must be removed via the cooling system with a high energy requirement, Figure 7.5.4-5.

Owing to higher current densities and smaller conductor volumes respectively, superconducting transformers can be designed with smaller windings and shorter iron cores, and thus can be of lighter construction. Owing to low temperatures, no **ageing** of the dielectric is to be expected, even for longer **overloads**. However, **drastically reduced losses** (about 30% of normal losses) and a **weight reduction** of approximately 50% are given priority, and cost advantages are expected for ratings above 40 MVA.

a) Traction transformers

A **conventional** single-phased traction transformer for 15 kV/ 16.7 Hz today contributes more than 10 % to the *total mass* of a railcar and is thereby a significant factor for acceleration capacity and for rail wear. Another factor is the frequent demand for a *space-saving underfloor construction*. The current densities and the magnetic flux are increased up to technically aceptable limits for space-saving and weight-saving reasons; therefore winding temperatures can be up to 175 °C. Here, the *ohmic heat losses and hysteresis losses* are so large that the *efficiency* of a traction transformer is of the order of 90%. As a result, it generates almost half the total losses of the train system. **Superconducting traction transformers** with almost halved volumes and weights, as well as efficiencies of more than 99%, are therefore particularly attractive.

The construction of a superconducting traction transformer corresponds to that of a conventional one: two parallel limb assemblies with parallel connected HV windings are arranged on a horizontal two-limb core, Figure 7.5.4-4. If requests are made for a special flat construction, e.g. for underfloor use in local rail systems, then it can be necessary to place the entire transformer including the core in a common cryostat ("*cold core*"), as e.g. in a 15 kV/ 1.1 MVA prototype [351]. Thereby, although the entire iron losses must be "pumped" with the help of LN_2 cooling plant to the ambient temperature level at the expense of energy, the total losses are lower by a factor of 12 than for the especially unfavorable conventional traction transformers. If the installation environment in the railcar permits, it is recommended, especially for high powers of 4.6 MVA for high-speed trains or 7.5 MVA for locomotives, to use "*hot core*" at ambient temperature and to operate the windings in separate cryostats [351].

It is proposed that windings are operated at 67K in a *sub-cooled* state, losses are removed via forced LN_2 cooling and gas bubble formation in the transformer is prevented. If there is a failure of the traction power supply and of the cooling system respectively, the readiness for operation must be maintained for a long period of time by the large *thermal time constants* of the cooled system. For a "hot core", shorter periods of 7 h are assumed than for a "cold core" with approximately 17 h [351].

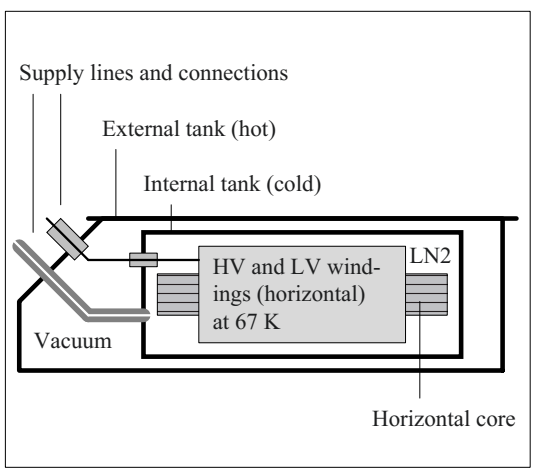

Figure 7.5.4-4: Superconducting traction transformer with cold core (schematic).

b) Line transformers

Line transformers can be designed in such a way that they remain in the superconducting state up to *twice the nominal power*. That is, even at high *overload*, superconducting operation is possible and *no thermal ageing* of the dielectric occurs. However, increased losses and cooling capacities must be accepted.

Note: While using a *hot core* according to Figure 7.5.4-5, the losses can still be approximately halved, compared to a conventional transformer which already has very low losses.

Inrush currents must be limited such that the superconductivity is preserved. In the case of *short-circuit currents*, the superconductor may indeed quench, but the thermal capacitance of the windings must be adequately dimensioned to prevent thermal damage. Unfortunately, there is no immediate *switch-on readiness* (as with a conventional transformer), as the windings must first be cooled down to the superconducting state, possibly even for hours. It is therefore recommended to operate a superconducting transformer in *parallel* with a *conventional transformer*: The former carries the usual operating currents and excess currents at lo loss and without ageing and the latter only preserves the immediate re-switching readiness in the event of a short circuit. It can thus be designed to be weaker.

Note: It is also conceivable to integrate the *current limiting effect* of a fault current limiter into the transformer, cf. Section 7.5.4.2.

Prototypes for **medium voltage distribution transformers** [349] are made of several single layered windings on *GRP cylinders* with different diameters, whereby the insulation is formed by LN_2-filled gaps. Studies are being carried out on **larger transformers**, e.g. 30 MVA/ 138 kV [347] and 240 MVA/ 400 kV [348].

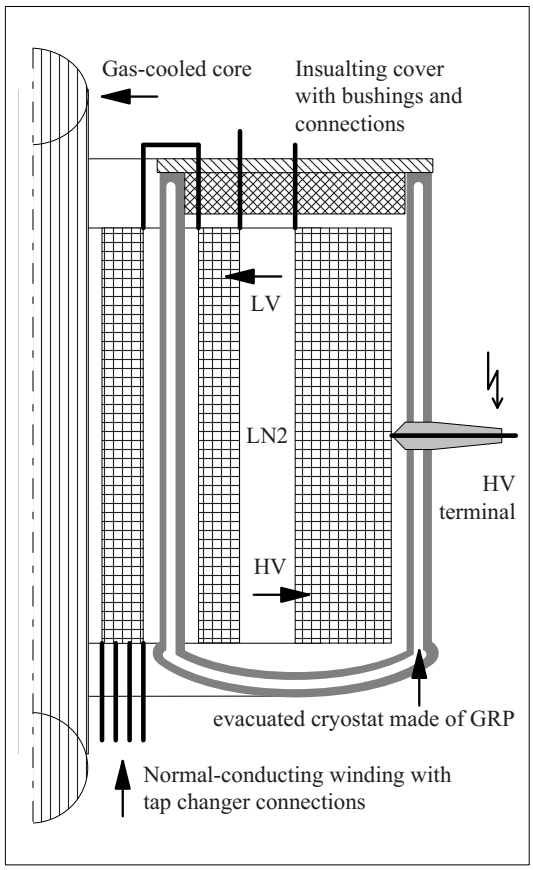

Figure 7.5.4-5: Concept of a superconducting high voltage transformer (schematic).

Example: For a *400 kV transformer*, it is proposed to design the high voltage winding as disc winding in which the spacers will receive the forces in the axial and radial direction [348], Figure 7.5.4-6. HTSC conductors allow very narrow windings of small radial extent be-

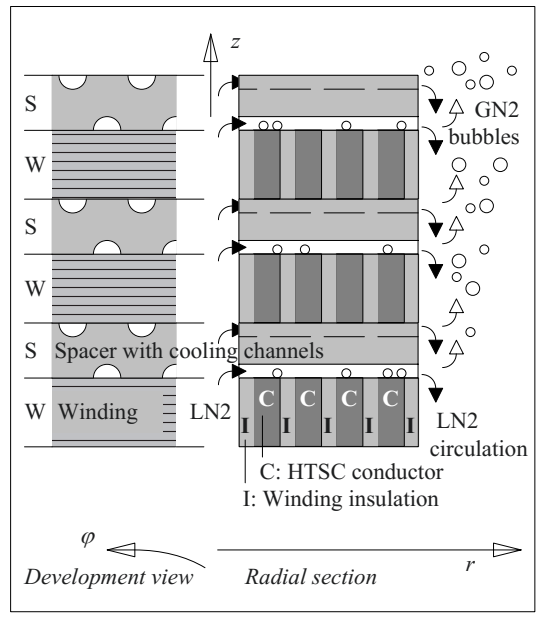

Figure 7.5.4-6: Superconnductig disc winding with spacers and LN2/ GN2 insulation (concept).

cause of the high current densities (up to 39 A/mm^2). Therefore, the conductors must be mechanically reinforced, e.g. by hard-soldered steel strips. The conductors remain in contact with the radial cooling channels on their upper side. LN_2 is passed in a circuit from inside to outside. Thermal gas-bubbles can be formed at the conductor surfaces and immediately rise upwards at the outer side. Insulation between the windings and to the outside is formed by adequately wide LN_2 gaps. The windings are supported in the radial direction against internal and external support tubes by radial ribs and clamped in the axial direction between pressure rings. For each limb assembly, a double-walled evacuated cryostat is provided, Figure 7.5.4-5.

8 REFERENCES

[1] H. Brumshagen, H.-J. Haubrich, D. Heinz, H. C. Müller; **Entwicklungen zum gesamteuropäischen Stromverbund;** GLOBAL LINK, VDI-GET-Tagung, Essen, 10/94

[2] K. Küpfmüller; **Einführung i. d. theoretische Elektrotechnik**; Springer, Berlin-Heidelberg- ..., 10. Aufl. 1973

[3] K. Simonyi; **Theoretische Elektrotechnik**; VEB Verl. d. dt. Wiss., Berlin, 7. Aufl. 1979

[4] H. Prinz; **Hochspannungsfelder**; Oldenbourg-Verlag, München, 1959

[5] A. Küchler; **Erfassung transienter elektromagnetischer Feldverteilungen mit konzentrierten und räumlich ausgedehnten Sensoren;** VDI-Fortschritt-Berichte 21/7, 1986

[6] I.N. Bronstein, K.A. Semendjajew; **Taschenbuch der Mathematik**; Verlag Harri Deutsch, Thun und Frankfurt/M., 1981

[7] F. Hammer, A. Küchler; **Insulating Systems for HVDC Power Apparatus;** IEEE Transactions on Electrical Insulation, Vol. 27, No. 3, 6/1992

[8] M.M. Rashwan, W. McDermid, F. Hammer, A. Küchler; **On the Design, Testing and Operating Experience of Composite Dry Bushings in HVDC;** 5th Int. Conf. on AC and DC Power Transmission, London 1991

[9] F. Hammer, A. Küchler, G. Mäueler**; Behaviour of Bushings with Silicone Rubber Sheds;** 6th ISH Int. Symp. on High Voltage Engineering, 47-38, New Orleans LA, USA, 1989

[10] F. Hammer, A. Küchler; **Insulating Systems for HVDC Power Apparatus;** 3rd Int. Conf. on Properties and Application of Dielectric Materials, Tokyo 1991, S. 965-968

[11] IEC 60071 **Insulation co-ordination** – Part 1: **Definitions, principles and rules;** Part 2: **Application guide**

DIN EN 60071 (VDE 0111); **Isolationskoordination** – Teil 1: **Begriffe, Grundsätze und Anforderungen;** Teil 2: **Anwendungsrichtlinie**

[12] D. Beste; **Impulse für Recycling;** VDI nachrichten fazit, Düsseldorf, 3/1995

[13] W. Boeck, R. Witzmann; **Main Influences on the Fast Transient Development in Gas-Insulated Substations (GIS);** 5th ISH Int. Symp. on High Voltage Eng., 12-01, Braunschweig, 1987

[14] J. Dams, Th. Dunz, A. Küchler, A. Schwab; **KAKTUS - A Flexible 24 MV / 240 TW Pulse Power Generation Concept;** 6th IEEE Pulse Power Conf., Arlington VA, USA, 1987

[15] J. Dams, Th. Dunz, A. Küchler, A. Schwab; **Design and Operation of a Tera-Watt Pulse-Power Generator;** 5th ISH Int. Symp. on High Voltage Eng., 61-02, Braunschweig, 1987

[16] M. Beyer,.W. Boeck, K. Möller, W. Zaengl; **Hochspannungstechnik;** Springer-Verlag, Berlin-Heidelberg- ..., 1986

[17] G. Strassacker, P. Strassacker; **Analytische und numerische Methoden der Feldberechnung;** B. G. Teubner, Stuttgart, 1993

[18] H. Bellm; **Übertragungseigenschaften von Stoßspannungsmeßkreisen unter Berücksichtigung des transienten Strahlungsfeldes;** Dissertation, Universität Karlsruhe, 1981

[19] R. Maier; **Näherungsweise Berechnung transienter Felder in Hochspannungsprüfkreisen;** Dissertation, Universität Karlsruhe, VDI-Fortschrittberichte, VDI Verlag, Düsseldorf, 1988

[20] K. Heuck, K.-D. Dettmann; **Elektrische Energieversorgung;** Vieweg, Braunschweig 4. Aufl. 1999

[21] A. Schwaiger; **Elektrische Festigkeitslehre;** Springer-Verlag, Berlin 1925

[22] E. Philippow u.a.; **Taschenbuch Elektrotechnik, Band 6: Systeme der Elektroenergietechnik; Hochspannungstechnik;** Carl Hanser Verl. München Wien, VEB Verl. Berlin 1982

[23] D. Kind, H. Kärner; **Hochspannungsisoliertechnik;** Vieweg-Verlag, Braunschweig 1982

[24] C. Gerthsen, H.O. Kneser, H. Vogel; **Physik;** Springer-Verl., Berlin-Heidelbg., 12. Aufl. 1974

[25] P. Schulz; **Elektronische Vorgänge in Gasen u. Festkörpern;** G. Braun, Karlsruhe, 2. Aufl. 1974

[26] A. Küchler; **Suppression of Surface Discharges and Flashover on Dielectric Surfaces;** 9th ISH Int. Symp. on High Voltage Engineering, No. 8032, Graz, Austria, 1995

[27] H.P. Moser; **Transformerboard;** H. Weidmann AG, Rapperswil 1979

[28] W. Boeck; **Isolationssysteme metallgekapselter SF_6-isolierter Schaltanlagen;** ETG-Fachber. 34, Gasisolierte Schaltanlagen im Mittel- u. Hochspannungsnetz, VDE-Verlag, 1991

[29] Maxwell Lab. Inc.; **Capacitor Selection Guide;** Maxwell Laboratories Inc., San Diego, 1994

[30] G. Doetsch; **Anleitung zum praktischen Gebrauch der Laplace-Transformation und der Z-Transformation;** R. Oldenbourg-Verl., München, 3. Aufl. 1967

[31] O. Föllinger; **Laplace- und Fourier-Transformation;** Elitera-Verlag, Berlin, 1978

A. Küchler, *High Voltage Engineering*, VDI-Buch,
DOI 10.1007/978-3-642-11993-4

[32] Bognár; G. Csépes, L. Kalocsai, I. Kispál; **Spectrum of Polarization Phenomena of Long Time-Constant as a Diagnostic Method of Oil Paper Insulating Systems;** 3rd Int. Conf. on Prop. and Appl. of Dielectric Mat., Tokyo 1991

[33] R. Porzel, M. Sturm; **Dielektrische Diagnostik von Hochspannungsisolierungen;** etz Elektrotechn. Zeitschrift, VDE-Verlag, Berlin, 10/1995

[34] H. Singer; **Present and Future Topics of HV Field Calculation and Measurement;** 9th ISH Int. Symp. on High Voltage Engineering, No. 9008, Graz, Austria, 1995

[35] Goering, Ross, Tobiska; **Finite-Elemente-Methode;** Harri Deutsch-Verl., Frankfurt/M., 1989

[36] Bathe; **Finite-Elemente-Methoden;** Springer-Verlag, Berlin-Heidelberg-New York, 1990

[37] Nasitta, Hagel; **Finite Elemente;** Springer-Verlag, Berlin-Heidelberg-New York, 1992

[38] Richter; **Numerische Lösung partieller Differentialgleichungen mit der Finite-Elemente Methode;** Vieweg-Verlag; Braunschweig, 1986

[39] G. Hilgarth; **Hochspannungstechnik;** B.G. Teubner, Stuttgart, 3. Aufl. 1997

[40] Th. Dunz, J. Dams, A. Küchler, A. Schwab; **Efficient Modeling of Transmission Lines for Traveling Wave Analysis with SCEPTRE;** 4th IEEE Pulse Power Conf., Albuquerque, 1983

[41] A. Schwab; **Elektromagnetische Verträglichkeit;** Springer-Verl., Berlin Heidelberg, 1991

[42] J. Dams, Th. Dunz, A. Küchler; **Hochspannungsgeneratoren großer Leistung zur Erzeugung gepulster Teilchenströme;** VDI-Seminar Beschleunigertechnik, Berlin 1982

[43] A. Küchler, Th. Dunz, J. Dams, A. Schwab; **Power and Voltage Gain of Pulse-Forming Lines with Double-Bounce Switching;** 4th IEEE Pulse Power Conf., Albuquerque NM, 1983

[44] W. Hauschild, W. Mosch; **Statistik für Elektrotechniker;** VEB Verlag Technik, Berlin 1984

[45] M. Minovic, P. Schulze; **Hochspannungstechnik;** VDE-Verlag, Berlin Offenbach, 1992

[46] B. Gänger; **Der elektrische Durchschlag von Gasen;** Springer-Verlag, Berlin Göttingen Heidelberg, 1953

[47] G. Lesch; **Lehrbuch der Hochspannungstechnik;** Springer-Verl., Berlin Göttingen Heidelberg, 1959

[48] E. Flegler; **Einführung in die Hochspannungstechnik;** Verlag G. Braun, Karlsruhe, 1964

[49] D. Flottmann, D. Forst, H. Roßwag; **Chemie für Ingenieure;** Springer Verlag, 2. Aufl. 2004

[50] K.-F. Geibig; **Ansprechverhalten von Edelgasfunkenstrecken bei kleinen pd-Werten;** Dissertation Univ. Karlsruhe, 1982

[51] Th. Dunz; **Zündverhalten heliumisolierter Funkenstrecken mit Gleitentladungszündhilfen;** Dissertation Univ. Karlsruhe, 1987

[52] IEC 60076-3; **Power transformers –** Part 3: **Insulation levels, dielectric tests and external clearances in air**

DIN EN 60076-3 (VDE 0532-76-3); **Leistungstransformatoren** – Teil 3: **Isolationspegel, Spannungsprüfungen und äußere Abstände in Luft**

[53] IEC 60060; **High-voltage test techniques**

DIN EN 60060 (VDE 0432); **Hochspannungs-Prüftechnik**

[54] H.H. Zimmer; **Gleich- und Wechselspannungskorona an technisch relevanten Elektrodengeometrien unter Berücksichtigung des Luftfeuchteeinflusses;** Diss. Univ. Karlsruhe, 1985

[55] W. Mosch, W. Hauschild; **Hochspannungsisolierungen mit Schwefelhexafluorid;** VEB Verlag Technik; Berlin, 1979

[56] IEC 60507; **Artificial pollution tests on higvoltage ceramic and glass insulators tob e used on a.c. systems**

DIN EN 60507 (VDE 0448-1); **Fremdschichtprüfungen an Hochspannungs-Isolatoren aus Keramik und Glas zur Anwendung in Wechselspannungssystemen**

[57] F. Hammer, A. Küchler; **Bewährte Silikonschirmdurchführungen für erhöhte Sicherheit und Verschmutzungsfestigkeit;** Elektrizitätswirtschaft Jg. 90 (1991), H. 11, S. 604-608

[58] H.M. Schneider, A.E. Lux; **Mechanism of HVDC Wall Bushing Flashover in Non-uniform Rain;** IEEE Trans. on Power Delivery, Vo. 6 No. 1 Jan. 1991 pp 448 - 455

[59] P.J. Sinz; **Der Einfluß von Feuchte und Partikeln auf die elektrische Festigkeit von Isolierölen;** Dissertation, Techn. Univ. Graz, 1990

[60] Badent, R.G.; **Untersuchung der Druckabhängigkeit des Öldurchschlags bei Beanspruchung mit Wechselspannung;** Jahresbericht IEH, Univ. Karlsuhe, 1991

[61] IEC 60243-1, -2, -3; **Electric strength of insulating materials – Test methods**

DIN EN 60243-1, 2, 3 (VDE 0303-21, 22, 23); **Elektrische Durchschlagsfestigkeit von isolierenden Werkstoffen – Prüfverfahren**

[62] IEC 60296; **Fluids for electrotechnical applications – Unused mineral inulating oils for transformers and switchgear**

DIN EN 60296 (VDE 0370-1); **Flüssigkeiten für elektrotechnische Anwendungen – Neue Isolieröle auf Mineralölbasis für Transformatoren und Schaltgeräte**

[63] UTE NF CIR C 163

[64] ASTM D 877; **Standard test method for dielectric breakdown voltage of insulating liquids using disc electrodes**

[65] D. Tschudi, V. Dahinden, F. Derler; **Dielectric Strength Assessment of Power Transformer Insulation;** 9th ISH Int. Symp. on High Voltage Engineering, No. 1081, Graz, Austria, 1995

[66] R. Badent, K. Kist; **Druckabhängigkeit des Durchschlags in Isolieröl bei Beanspruchung mit transienten Spannungen;** Jahresbericht IEH, Univ. Karlsuhe, 1992

[67] F.H. Kreuger; **Industrial High Voltage I and II;** Delft University Press, 1991 and 1992

[68] A. v. Hippel; **Der elektrische Durchschlag in Gasen und festen Isolatoren;** Ergebnisse der exakten Naturwiss., Bd. 14 (1935) S. 116 f

[69] F. Hammer; **Resin impregnated paper, a solid dry material for capacitance graded bushings;** Hochspannungsgeräte Porz GmbH, Köln, 1988

[70] P.K. Gmeiner; **Combi-LFH-Trocknung von Leistungstransformatoren im Felde;** Micafil-Symposium Stuttgart, 1996

[71] A. Küchler; **Messung und Interpretation von Teilentladungen in Folienisolierungen;** Studienarbeit Hochsp.institut Univ. Karlsruhe, 1979

[72] Th. Praehauser; **Lokalisierung von Teilentladungen in Hochspannungsapparaten;** Bull. SEV 63 (1972) Nr. 16 S. 893 - 905

[73] A. Küchler; **Diagnoseschema für die klassische Bewertung von Teilentladungsmessungen;** FH Würzburg-Schweinfurt-Aschaffenburg; 1995

[74] E. Gulski, F.H. Kreuger; **Recognition of Discharge Sources Using Statistical Tools;** Proc. 3rd Int. Conf. on Properties and Appl. of Dielectric Materials, Tokyo, 1991

[75] H. Suzuki, T. Endoh; **Pattern Recognition of Partial Discharge in XLPE Cables Using a Neural Network;** Proc. 3rd Int. Conf. on Prop. and Appl. of Dielectric Materials, Tokyo, 1991

[76] N. Hozumi, T. Okamoto, T. Imajo; **Discrimination of the Partial Discharge Patterns Using Neural Network;** Proc. 3rd Int. Conf. on Prop. and Appl. of Dielectric Materials, Tokyo, 1991

[77] A. Gross, H.G. Kranz; **Time resolved analysis of VHF (100 - 300 MHz) partial discharge measurements with neural networks;** 9th Int. Symp. on High Voltage Eng., 5611, Graz, 1995

[78] T. Hücker, H.G. Kranz, A. Lapp; **A partial discharge defect identification system with increased diagnosis reliability;** 9th ISH Int. Symp. on High Voltage Eng., 5612, Graz, 1995

[79] E. Gulski; **Application of modern PD detection techniques for fault recognition in the insulation of high voltage equipment;** 9th ISH Int. Symp. on High Voltage Eng., 5642, Graz, 1995

[80] T. Hücker, H.G. Kranz, T. Okamoto, P.G. von Glahn; **A standardised computer data file format for storage, transport, and off-line processing of partial discharge data;** 9th ISH Int. Symp. on High Voltage Engineering, No. 5613, Graz, 1995

[81] A. Roth; **Hochspannungstechnik;** Springer-Verlag, Wien, 3. Auflage 1950

[82] H.P. Moser, V. Dahinden; **Transformerboard II**; H. Weidmann AG, Rapperswil, 1987

[83] A.G. Schlag; **The Recovery Voltage Method for Transformer Diagnosis;** Tettex Instruments AG, Dietikon, 1995

[84] H. Lütke; **Heutige Methoden der off-line Diagnose;** Micafil-Symposium Stuttgart, 1996

[85] J. Fuhr; **Notwendigkeit der vor Ort Diagnose aus Sicht des Herstellers;** Micafil-Symposium Stuttgart, 1996

[86] A. Kachler; Diskussionsbeitrag Siemens AG; Micafil-Symposium Stuttgart, 1996

[87] W. Zaengl; Diskussionsbeitrag ETH Zürich; Micafil-Symposium Stuttgart, 1996

[88] C. Brinkmann; **Die Isolierstoffe der Elektrotechnik;** Springer-Verl., Berlin-Heidelbg; 1975

[89] M. Saure; **Kunststoffe in der Elektrotechnik;** AEG-Telefunken-Handbücher, Bd. 22, Berlin und Frankfurt a. M.; 1979

[90] J. Möckel, U. Fuhrmann; **Epoxidharze;** verlag moderne industrie; Landsberg/Lech; 1990

[91] M. Beyer u.a.; **Epoxidharze in der Elektrotechnik;** expert verlag; Grafenau/Württ.; 1983

[92] J. Kindersberger, M.Kuhl; **Effect of Hydrophobicity on Insulator Performance;** 6th ISH Int. Symp.on High Voltage Eng., New Orleans; 1989

[93] F. Hammer, A. Küchler; **Insulators with Silicone Rubber Sheds for Bushings in AC and DC Applications;** IEEE Power Eng. Society; Summer Meeting, Minneapolis, 1990

[94] D. Kind; **Hermetischer Luftabschluß ölisolierter Hochspannungsgeräte mittels Stickstoffpolster;** Elektrizitätswirtschaft, Band 58(1959) H. 5, S. 143 - 149

[95] R. Müller, H. Schliesing, K. Soldner; **Prüfung und Überwachung von Transformatoren durch Analyse der im Öl gelösten Gase;** Elektrizitätswirtschaft, Jg. 73 (1974), S. 683 - 687

[96] R. Müller; **Gasanalyse - Vorsorgeuntersuchung für Transformatoren;** Elektrizitätswirtschaft, Jg. 9 (1980) H. 10, S. 356 - 360

[97] W. Wohatschek; **Überwachung von Transformatoren, Meßwandlern und Koppelkondensatoren;** E und M, 1987, S. 406 - 412

[98] J.O. Church, T.J. Haupert, F. Jakob; **Analyze incipient faults with dissolved-gas nomograph;** Electrical World, October 1987, p. 40 - 44.

[99] IEC 60599; **Mineral oil-filled electrical equipment in service – Guidance on the interpretation of dissolved and free gases analysis**

DIN EN 60599 (VDE 0370-7); **In Betrieb befindliche, mit Mineralöl befüllte elektrische Geräte – Leitfaden zur Interpretation der Analyse gelöster und freier Gase**

[100] B. Fallou; **Detection of and Research for the Characteristics of an Incipient Fault from the Analysis of Dissolved Gases in the Oil of an Insulation;** Electra No. 42, p. 32 - 52

[101] H. Borsi; **Grundlagen der Flüssigkeit/Papierisolation und des Gasungsverhaltens von Isolierflüssigkeiten für Transformatoren;** Micafil-Symposium Stuttgart, 1996

[102] IEC 61099; **Insulating liquids – Specifications for unused synthetic organic esters for electrical purposes**

DIN EN 61099 (VDE 0375-1); **Isolierflüssigkeiten – Anforderungen an neue synthetische organische Ester für elektrotechnische Zwecke**

[103] H. Borsi, E. Gockenbach, K. Dumke; **A Synthetic Insulating Liquid for Application in Transformers;** 9th ISH Int. Symp. on High Voltage Engineering, No. 1025, Graz, 1995

[104] C. Brosseau; **Breakdown of a Thin Dielectric Liquid Layer and Interfacial Phenomena;** Proc. 3rd Int. Conf. on Properties and Appl. of Dielectric Materials, Tokyo, 1991

[105] N. Berger, P. Jay; **A New Impregnant for HV Power Capacitors;** IEEE Trans. on El. Insulation, vol. 21, 1986, p. 59

[106] C. Mazzetti, M. Pompili, E.O. Forster; **Electric Conduction, Breakdown and Partial Discharges in Dielectric Fluids;** 3rd Int. Conf. on Properties and Applications of Dielectric Materials, Tokyo, 1991

[107] C. Mazzetti, M. Pompili, R. Cercere, E.O. Forster; 10th Int. Conf. on Conduction and Breakdown in Dielectric Liquids, Grenoble, France, 1990, p. 557

[108] J. Dams, K.-F. Geibig, P. Osmokrovic, Th. Dunz, A. Küchler, A. Schwab; **Numerical Calculation of Breakdown-Voltages for Triggered Three-Electrode Spark Gaps;** 4th IEEE Pulse Power Conf., Albuquerque, 1983

[109] H. Okubo, H. Goshima, H. Sakakibara, N. Hayakawa, M. Hikita, K. Uchida; **Area and Volume Effects in Breakdown Strength in Liquid Helium and Liquid Nitrogen;** 9th ISH Int. Symp. on High Voltage Engineering, No. 7052, Graz, 1995

[110] Zhen-chao Wang, Hiroyasu Yoshizuka, Masanori Hara; **Electrical Breakdown of Liquid Helium Affected by Thermal Bubbles under D.C. Non-Uniform Electrical Fields**; 9th Int. Symp. on High Voltage Eng., 7875, Graz, 1995

[111] M. Hara, M. Miyama, F. Irie, K. Tsutsumi, K. Satow, J. Gerhold, E. Telser; **Insulation Design Philosophy of Superconducting Coils for Electric Power Apparatus and a Case Study for KEPCO's SMES;** 9th ISH Int. Symp. on High Voltage Eng., No. 7874, Graz, 1995

[112] U. Sundermann; **Vor Ort Diagnose an Transformatoren;** Micafil-Symp. Stuttgart, 1996

[113] A. Küchler; **Induktivität von Hochspannungskondensatoren;** etz Elektrotechnische Zeitschrift 109 (1988) 1070-1075

[114] C. Eberhard; **Neue Entwicklungen in der Vapour Phase Technologie;** Micafil-Symposium Stuttgart, 1996

[115] K.-H. Weck; **Akkreditierung von HS-Laboratorien und Kalibrieren der HS-Meßtechnik;** 7. Haefely-Trench-Symposium, Stuttgart, 1995

[116] K.-H. Weck; **Akkreditierung u. Zertifizierung v. Prüflaboratorien;** Micafil-Symp. Stgt. 1996

[117] H. Frohne, E. Ueckert; **Grundlagen der elektrischen Meßtechnik;** Teubner, Stuttgart, 1984

[118] DKD 3 - **Ermittlung von Meßunsicherheiten;** Physikalisch-Technische Bundesanstalt, Deutscher Kalibrierdienst, Braunschweig, 1991

[119] H.-R. Tränkler; **Taschenbuch der Meßtechnik;** R. Oldenbourg Verlag, München-Wien, 1989

[120] DKD 4 - **Rückführung von Prüfmitteln auf nationale Normale;** Phys.-Techn. Bundesanst., Deutscher Kalibrierdienst, Braunschweig, 1991

[121] IEC 60071-1; **Insulation co-ordination** – Part 1: **Definitions, principles and rules**

[122] DIN EN 60071-1 (VDE 0111-1); **Isolationskoordination** – Teil 1: **Begriffe, Grundsätze und Anforderungen**

[123] IEC 60071-2; **Insulation co-ordination –** Part 2: **Application guide**

DIN EN 60071-2 (VDE 0111-2); **Isolationskoordination** – Teil 2: **Anwendungsrichtlinie**

[124] IEC 60099-5; **Surge arresters** – Part 5: **Selection and application recommendations**

DIN EN 60099-5 (VDE 0675-5); **Überspannungsableiter** – Teil 5: **Anleitung für die Auswahl und die Anwendung**

[125] J. Schramm, U. Stietzel; **Wechselspannungsanlagen für Werks- und Vor-Ort-Prüfungen von SF_6-Anlagen;** 7. Haefely-Trench-Symposium, Stuttgart, 1995

[126] P. Mohaupt, M. Pasquier, R. Gleyvod, G. Voigt; **A 2100 kV - 90 MVA Resonant Test System - Design Criteria and Test Results;** 9th ISH Int. Symp. on High Voltage Eng., 4550, Graz, 1995

[127] A. Jenni, M. Pasquier, R. Gleyvod, P. Thommen; **Testing of high voltage power cables with series resonant systems and water terminations;** 7th ISH Int. Symp. on High Voltage Engineering, No. 53.02, Dresden, 1991

[128] R. Bach, W. Kalkner, H. Oldehoff; **Verlustfaktormesssung bei 0,1 Hz an betriebsgealterten PE/VPE-Kabelanlagen;** Elektrizitätswirtschaft, Jg. 92 (1993)

[129] K.-H. Krefter, **Erfahrungen mit Prüfverfahren für Kunststoffkabel in Mittelspannungsnetzen;** Elektrizitätswirtschaft, Jg. 92 (1993)

[130] K.-H. Weck; **Prüfung von Kabelanlagen vor Ort;** Elektrizitätswirtschaft, Jg. 92 (1993)

[131] IEC 60076-3; **Power transformers** – Part 3: **Insulation levels, dielectric tests and external clearances in air**

DIN EN 60076-3 (VDE 0532-76-3); **Leistungstransformatoren** – Teil 3: **Isolationspegel, Spannungsprüfungen und äußere Abstände in Luft**

[132] C. Neumann; **Dielektrische Prüfung und Überwachung von Betriebsmitteln vor Ort;** 7. Haefely-Trench-Symposium, Stuttgart 1995

[133] IEC 60060-1; **High-voltage test techniques** – Part 1: **General definitions and test requirements**

DIN EN 60060-1 (VDE 0432-1); **Hochspannungs-Prüftechnik** – Teil 1: **Allgemeine Begriffe und Prüfbedingungen**

[134] IEC 60060-2; **High-voltage test techniques** – Part 2: **Measuring systems**

DIN EN 60060-2 (VDE 0432-2); **Hochspannungs-Prüftechnik** – Teil 2: **Messsysteme**

[135] D. Kind; **Einführung in die Hochspannungsversuchstechnik;** Vieweg-Verl., Braunschweig, 4. Aufl. 1985

[136] A. Hinderer; **Einfluß gepulster Spannungsversorgung auf die Abscheidung hochohmiger Stäube in Elektrofiltern;** Dissertation, Univ. Karlsruhe; VDI-Fortschr.ber. R. 21 Nr. 92, 1991

[137] J. Dams, Th. Dunz, A. Küchler; **Tera-Watt-Impulsgenerator KIT;** Hochspannungsinstitut Univ. Karlsruhe, Jahresbericht 1984

[138] G. Yonas; **Fusion Power with Particle Beams;** Scientific American, Vol. 239, No. 5, Nov. 1978

[139] W. Frey, A.J. Schwab; **Performance of laser-triggered rail-gap switches using low-intensity UV laser-radiation;** 9th ISH Int. Symp. on High Voltage Eng., No. 7288, Graz, 1995

[140] W. Frey, A.J. Schwab; **Laser-triggered rail-gap switches with seed-electron generation by photoemission from metal aerosol particles;** 9th ISH Int. Symp. on High Voltage Engineering, No. 7931, Graz, 1995

[141] A.J. Schwab; **Hochspannungsmeßtechnik;** Springer-Verl., Berlin Heidelberg, 2. Aufl. 1981

[142] IEC 60052; **Voltage measurements by means of standard air gaps**

[143] DIN EN 60052 (VDE 0432-9); **Spannungsmessungen mit Standard-Luftfunkenstrecken**

[144] E. Peschke; **Der Durch- und Überschlag bei hoher Gleichspannung in Luft;** Dissertation TH München, 1968

[145] H. Bellm, A. Küchler, J. Herold, A. Schwab; **Rogowski-Spulen und Magnetfeldsensoren zur Messung transienter Ströme im Nanosekundenbereich, Teil 1;** Archiv für Elektrotechnik 68 (1985), S. 63 -68

[146] H. Bellm, A. Küchler, J. Herold, A. Schwab; **Rogowski-Spulen und Magnetfeldsensoren zur Messung transienter Ströme im Nanosekundenbereich, Teil 2;** Archiv für Elektrotechnik 68 (1985), S. 69 -74

[147] A. Küchler, J. Dams, Th. Dunz, A. Schwab; **Kapazitive Sensoren zur Messung transienter elektrischer Felder und Spannungen;** Archiv für Elektrotechnik 68 (1985) 335-344

[148] A. Küchler, J. Dams, Th. Dunz, A. Schwab; **Combined E- and H-Field Probe for Traveling Wave Analysis in Pulse Power Generators;** 5th IEEE Pulse Power Conf., Arlington VA, USA, 1985

[149] A. Küchler, Th. Dunz, A. Hinderer, A. Schwab; **Transient Field Distribution Measurements with "Electrically Long" Sensors;** 5th ISH Int. Symp. on High Voltage Engineering, 32-08, Braunschweig, 1987

[150] A. Küchler; A. Schwab; **Räumlich ausgedehnte Sensoren für transiente elektromagnetische Felder;** Archiv für Elektrotechnik 70 (1987)

[151] W.R. Pfaff; **Accuracy of a Spherical Sensor for the Measurement of Threedimensional Electric Fields;** 5th ISH Int. Symp. on High Voltage Eng., 32-05, Braunschweig, 1987

[152] W. Epping, A. Küchler, A. Schwab; **Elektrische Feldstärkemessung mit doppelbrechenden und optisch aktiven Kristallen;** Archiv für Elektrotechnik 67 (1984) 329-339

[153] A. Küchler, J. Dams, Th. Dunz, W. Epping, H. Kunz, A. Schwab; **Kerr-Effect Measurements of Pulsed Electric Fields in Water;** 5th IEEE Pulse Power Conf., Arlington VA, USA, 1985

[154] VDEW Vereinigung Deutscher Elektrizitätswerke; **Grundsätze für die Beurteilung von Netzrückwirkungen;** Verlags- und Wirtschaftsgesellschaft der Elektrizitätswerke VWEW, Frankfurt a.M., 2. Aufl. 1987

[155] A. Küchler; A. Schwab; **Zum Begriff der Netzfrequenz bei Netzstörungen;** Elektrizitätswirtschaft 86 (1987) 308-310

[156] K. Feser; **HS-Prüf- und Meßtechnik 2000;** 7. Haefely-Trench-Symposium, Stuttgart 1995

[157] IEC 60243-1, -2, -3; **Electric strength of insulating materials – Test methods**

DIN EN 60243-1, 2, 3 (VDE 0303-21, 22, 23); **Elektrische Durchschlagsfestigkeit von isolierenden Werkstoffen – Prüfverfahren**

[158] CISPR-Publ. No. 16; **Specifications for radio interference measuring apparatus and measurement methods;** Comité International Special des Perturbations Radiophoniques

[159] A.M. Ašner; **Stoßspannungsmeßtechnik;** Springer-Verl., Berlin-Heidelberg-New Y., 1974

[160] G. Hengge, P. Kemm, Th. Leibfried; **Anwendung von Transferfunktionen bei der Prüfung von Großtransformatoren;** 7. Haefely-Trench-Symposium, Stuttgart 1995

[161] Th. Leibfried; **Die Übertragungsfunktion als Methode zur Überwachung von Transformatoren im Betrieb;** Micafil-Symp. Stgt., 1996

[162] A. Claudi, R. Malewski, Ch. Josephy, St. Jud; **Checking electromagnetic compatibility of a HV impulse measuring circuit with coherence functions;** 7. Haefely-Trench-Symp., Stgt. 1995

[163] H. Schliesing, K. Soldner; **Die Technik der Analyse von Gasen, die im Transformatorenöl gelöst bzw. im Buchholzrelais angesammelt sind;** Elektrizitätswirtschaft, Jg. 75 (1976)

[164] E. Dörnenburg, W. Strittmatter; **Überwachung von Öltransformatoren durch Gasanalyse;** Brown Boveri Mitt. 5-74, S. 238 ff

[165] M. Duval; **Dissolved-Gas Analysis: New challenges and applications;** Electra No. 133, 1990

[166] Th. Miksa; **Online-Gas-in-Öl-Analyse;** Micafil-Symposium Stuttgart, 1996

[167] IEC 61198; **Mineral insulating oils – Methods for the determination of 2-furfural and related compounds**

DIN EN 61198 (VDE 0380-6); **Isolieröle auf Mineralölbasis – Prüfverfahren zur Bestimmung von Furfurol und verwandten Verbindungen**

[168] H.J. Knab; **Die Anwendung der Hochdruckflüssigkeitschromatographie zur Betriebsüberwachung von Transformatoren;** VGB Kraftwerkstechnik 71 (1991), H. 6, S. 594 - 597

[169] IEC 60112; **Method for the determination of the proof and the comparative tracking indices of solid insulating materials**

DIN EN 60112 (VDE 0303-11); **Verfahren zur Bestimmung der Prüfzahl und der Vergleichszahl der Kriechwegbildung von festen, isolierenden Werkstoffen**

[170] DIN VDE 0303- 5; **Prüfung von Isolierstoffen – Niederspannungs-Hochstrom-Lichtbogenprüfung**

[171] IEC 61621; **Dry solid insulating materials; Resistence test to high-voltage, low-current arc discharges;**

DIN EN 61621 (VDE 0303-71); **Trockene, feste Isolierstoffe – Prüfung der Lichtbogenbeständigkeit bei hoher Spannung und niedrigem Strom**

[172] IEC 60587; **Electrical insulating materials used under severe ambient conditions – Test method for evaluating resistance to tracking and erosion**

DIN EN 60587 (VDE 0303-10); **Elektroisolierstoffe, die unter erschwerten Bedingungen eingesetzt werden – Prüfverfahren zur Bestimmung der Beständigkeit gegen Kriechwegbildung und Erosion**

[173] IEC 60243-1; **Electric strength of insulating materials – Test methods** – Part 1: **Tests at power frequencies**

DIN EN 60243-1 (VDE 0303-21) **Elektrische Durchschlagfestigkeit von isolierenden Werkstoffen – Prüfverfahren**; Teil 1: **Prüfungen bei technischen Frequenzen**

[174] IEC 60243-2; **Electric strength of insulating materials – Test methods** – Part 2: **Additional requrements for tests using direct voltage**

DIN EN 60243-2 (VDE 0303-22) **Elektrische Durchschlagfestigkeit von isolierenden Werkstoffen – Prüfverfahren**; Teil 2: **Zusätzliche Anforderungen für Prüfungen mit Gleichspannung**

[175] IEC 60243-3; **Electric strength of insulating materials – Test methods** – Part 3: **Additional requirements for 1.2/50 µs impulse tests**

DIN EN 60243-3 (VDE 0303-23) **Elektrische Durchschlagfestigkeit von isolierenden Werk-**

stoffen – Prüfverfahren; Teil 3: **Zusätzliche Festlegungen für 1,2/50 µs Stoßspannungsprüfungen**

[176] IEC 60296; **Fluids for electrotechnical applications – Unused mineral inulating oils for transformers and switchgear**

DIN EN 60296 (VDE 0370-1); **Flüssigkeiten für elektrotechnische Anwendungen – Neue Isolieröle auf Mineralölbasis für Transformatoren und Schaltgeräte**

[177] IEC 60156, **Insulating liquids – Determiation oft he breakdown voltage at power frequency – Test method**

DIN EN 60156 (VDE 0370-5); **Isolierflüssigkeiten – Bestimmung der Durchschlagspannung bei Netzfrequenz - Prüfverfahren**

[178] DIN VDE 0303-4 (VDE 303-4); **Bestimmungen für elektrische Prüfungen von Isolierstoffen** – Teil 4: **Bestimmung der dielektrischen Eigenschaften**

[179] H.W. Lücking; **Energiekabeltechnik;** Viewег-Verlag, Braunschweig/Wiesbaden, 1981

[180] R. v. Olshausen; **Garnituren und Anlagentechnik; 110 kV-Kabelanlagen in der städtischen Stromversorgung;** ETG Fachbericht 44; VDE-Verlag, 1993

[181] A. Bachmeier, M. Schuster; **Vollisoliertes Kabelanschluß- und Verbindungssystem für Mittelspannungskabel 12 bis 36 kV;** Elektrizitätswirtschaft, Bd. 81 (1982) H. 20, S. 683 - 685

[182] A. Bachmeier, M. Schuster; **Kabelanschlußsysteme für metallgekapselte elektrische Betriebsmittel im Mittelspannungsbereich 7,2 bis 52 kV;** Elektrizitätswirtschaft, Bd. 87 (1988)

[183] R. Nagel; **Über eine Neuerung an Hochspannungstransformatoren der Siemens-Schukkertwerke G. m. b. H.;** Elektrische Bahnen u. Betriebe, Verl. R. Oldenbourg, München/Berlin, Jg. IV (1906) H. 15, S. 275 - 278

[184] R. Küchler; **Die Transformatoren;** Springer-Verlag, Berlin/Göttingen/Heidelberg, 1956

[185] J. Frost; **Wenn es durch Wände und Decken geht;** EV-Report, 2/95, S. 16 - 21

[186] R. Rüdenberg; **Elektrische Schaltvorgänge;** Springer-Verl., Berlin/Heidelbg./New Y.; 1974

[187] J. Reason; **SF_6: Revolution in switchgear;** Electrical World; Dec. 1989, S. 7 - 12.

[188] F. Hammer; **Design of Condenser Graded HVDC Bushings;** 4th Int. Conf. on AC and DC Power Transmission, IEE, London, 1985

[189] B.R. Hayworth, M.S. Hayworth; **The non-inductive myth;** IEEE Trns. on Electr. Insulation EI-18 (1983) H. 4, S. 390 – 395

[190] J. Dams; **Zur Stochastik des Impulsansprechverhaltens SF_6-isolierter Schaltfunkenstrekken;** Dissertation Univ. Karlsruhe, 1988

[191] M. Nothaft; **Untersuchung der Resonanzvorgänge in Wicklungen von Hochspannungsleistungstransformatoren mittels eines detaillierten Modells;** VDI-Fortschrittberichte, Reihe 21, Nr. 183, VDI-Verlag, Düsseldorf, 1995

[192] P. Hasse, J. Wiesinger; **Handbuch für Blitzschutz und Erdung;** Pflaum Verlag München, VDE-Verlag, 3. Aufl. 1989

[193] IEC 62305-1, 2; **Protection against lightning** – Part 1: **General principles**, Part 2: **Risk management**

DIN EN 62305-1, 2 (VDE 0185-305-1, 2); **Blitzschutz** – Teil 1: **Allgemeine Grundsätze**, Teil 2: **Risiko-Management**

[194] P. Hasse, K.-P. Müller; **EMV-Blitz-Schutzzonen-Konzept in seiner Anwendung**; Elektrotechnik, H. 6, 7/8 u. 9, 1992

[195] P. Hasse, J. Wiesinger, P. Zahlmann, W. Zischank; **EMV-gerechter Überspannungsschutz auch bei Blitzeinschlag;** etz Elektrotechnische Zeitschrift, H. 12/1993

[196] J. Birkl, P. Hasse, P. Zahlmann; **Systemgerechter Einsatz von Ableitern in Niederspannungsnetzen;** etz Elektrotechnische Zeitschrift, H. 17/1994

[197] E. Philippow u.a.; **Taschenbuch Elektrotechnik, Band 6: Systeme der Elektroenergietechnik; Lichttechnik;** Carl Hanser Verlag München Wien und VEB Verlag Berlin 1982

[198] J. Miller; **Trenngraduntersuchungen an einer Rohrelektrofilteranlage;** Jahresbericht IEH, Univ. Karlsruhe, 1992

[199] J. Miller; **Plattenelektrofilteranlage zur Untersuchung der Feinstaubabscheidung;** Jahresbericht IEH, Univ. Karlsruhe, 1993

[200] J. Miller; **Untersuchungen zum elektrischen Wind in Elektrofiltern;** Jahresbericht IEH, Univ. Karlsruhe, 1994

[201] J. Miller; **Rücksprühen im Elektrofilter;** Jahresbericht IEH, Univ. Karlsruhe, 1995

[202] F. Tannenberg, H. Schindler; **Hochtemperatur-Supraleitung - eine Herausforderung;** EV-Report 1/96

[203] H. Späth, P. Komarek, H.-J. Haubrich u.a.; **Supraleitender magnetischer Energiespeicher;** Projekt der Univ. Karlsruhe, des Forschungszentr. Karlsruhe und der RWTH Aachen, 1996

[204] H. Emanuel, M. Kuschel, C. Steineke, D. Pepper, R. Plath, W. Kalkner; **A new high voltage dielectric test system for insulation diagnosis and partial discharge measurements;** NORD-

IS 96, Bergen 1996, S. 283-290

[205] IEC 60076-3; **Power transformers –** Part 3: **Insulation levels, dielectric tests and external clearances in air**

DIN EN 60076-3 (VDE 0532-76-3); **Leistungstransformatoren** – Teil 3: **Isolationspegel, Spannungsprüfungen und äußere Abstände in Luft**

[206] IEEE Standard 62; **IEEE Guide for Diagnostic Field Testing of Electric Power Apparatus** – Part 1: Oil Filled Power Transformers, Regulators and Reactors

[207] F.H. Kreuger; **Industrial High DC Voltage;** Delft University Press, 1995

[208] H. Borsi, E. Gockenbach; **Partial Discharge Measurement and Evaluation Techniques for Transformers;** ISH 03 Int. Symp. on High Voltage Engineering, Delft, NL, 2003

[209] F. Gutfleisch, L. Niemeyer; **Measurement and Simulation of PD in Epoxy Voids;** IEEE Trans. on Dielectrics and El. Insulation, Vol 2 Nol 5, Oct. 1995, pp 729 - 743

[210] H. Frielingsdorf, P. Haberecht, R. Krump, W. Schütz; **Manufacturing and Testing of Modern Bushings;** transform 98, München, 1998

[211] R. Porzel, E. Neudert, M. Sturm; **Diagnostik der Elektrischen Energietechnik**; expert-verlag, Renningen, 1996

[212] H.-G. Kranz, R. Krump; **Partial Discharge Diagnosis using Statistical Optimization on a PC-based System**; IEEE Trans. on El. Insul. 1992

[213] E. Gulski; **Diagnosis of HV Components by Digital PD Analyzer;** IEEE Transactions on DEI, Vol. 2, No. 4 (1995)

[214] M. Hoof; **Impulsfolgen-Analyse: Ein neues Verfahren der Teilentladungsdiagnostik;** Diss. Univ.-GH Siegen, 1997

[215] M. Hartje; **Erfassung von Teilentladungen an Leistungstransformatoren im Netzbetrieb;** Diss. Uni Hannover, 1989

[216] A. Küchler, J. Frost, N. Koch, R. Krump; **Neue Diagnosegrößen für die Bewertung der TE-Alterung in hochbeanspruchten Isolationssystemen;** ETG-Fachtagung „Einfluß von Grenzflächen auf die Lebensdauer elektrischer Isolierungen“, Bad Nauheim, 1999

[217] K.-D. Plath, R. Plath, H. Emanuel, W. Kalkner; **Synchrone dreiphasige Teilentladungsmessung vor Ort und im Labor;** ETG-Fachtagung „Diagnostik elektr. Betriebsmittel“, Berlin 2002

[218] R. Pietsch; **Sinnvoller Einsatz von UHF-Teilentladungsmessungen bei Entwicklungs- und Vor-Ort-Prüfungen;** Symp. 2000, Hochspannungsprüf- u. Messtechnik, Stuttgart, 2000

[219] N. Leeners, K. Nembach; **Technische Funktionsweise und Anwendungsbeispiele der Tageslicht UV-Inspektionskamera DayCorll™;** 48. Int. wiss. Kolloquium, TU Ilmenau, 2003

[220] IEC 60814; **Insulating liquids – Oil-impregnated paper and pressboard – Determination of water by automatic coulometric Karl Fischer titration**

DIN EN 60814 (VDE 0370-20); **Isolierflüssigkeiten - Ölimprägniertes Papier und ölimprägnierter Pressspan – Bestimmung von Wasser mit automatischer Karl-Fischer-Titration**

[221] H. Hoffmann; **HYDRANAL®-Praktikum: Wasserreagenzien nach Eugen Scholz;** RdH Laborchemikalien GmbH & Co. KG, Seelze, 1999

[222] A. Kuechler, T. Bedel; **Dielectric Diagnosis of Water Content in Transformer Insulation Systems;** ETEP Vol. 11, No. 1, 2001

[223] M. Beigert; **Dielektrische Diagnoseverfahren im Zeitbereich;** 48. Int. wiss. Kolloquium, TU Ilmenau, 2003

[224] M. Beigert; **Mikrodielektrometrische zerstörungsfreie Alterungsdiagnostik von PE- und VPE-isolierten Mittelspannungskabeln;** Dissertation, Univ. Wuppertal, 1995

[225] R. Hofmann, H.G. Kranz; **The influence of the ambient temperature on IRC-analysis results of insulation material for epoxy insulated bushings;** ISH 03 Int. Symp. on High Voltage Engineering, Delft, NL, 2003

[226] A.J. Kachler, R. Baehr, W.S. Zaengl, B. Breitenbauch, U. Sundermann; **Kritische Anmerkung zur Feuchtigkeitsbestimmung von Transformatoren mit der „Recovery- Voltage- Methode“;** Elektriztätswirtschaft, Jg. 95 (1996), Heft 19 S. 1238 - 1245

[227] R. Patsch, O. Kouzmine, F. Berton; **Zum Einfluß der Jahreszeit bei der Kabeldiagnose;** ETG-Fachtagung „Diagnostik elektrischer Betriebsmittel“, Berlin 2002

[228] O. Kouzmine R. Patsch,; **Zustandsdiagnostik von Mittelspannungskabeln mit Rückkehrspannungsmessungen;** 48. Int. wiss. Kolloquium, TU Ilmenau, 2003

[229] V. Der Houhanessian; **Measurement and Analysis of Dielectric Response in Oil-Paper Insulation Systems.;** PhD Thesis, ETH Zuerich 1998

[230] J.J.Alff, V.Der Houhanessian, W.S Zaengl, A.J. Kachler; **A Novel, Compact Instrument for the Measurement and Evaluation of Relaxation Currents Conceived for On-Site Diagnosis on Electric Power App.;** IEEE Symp.on El. Insulation, Anaheim, USA, 2000

[231] A. Küchler, T. Leibfried; **Berücksichtigung geometrischer und parasitärer Einflüsse bei der Bestimmung des Wassergehaltes in Öl-Papier-Isolationen durch dielektrische Diagnose;** ETG-Fachtagung „Diagnostik elektrischer Betriebsmittel“, Köln 2004

[232] T. Leibfried, A.J. Kachler, W.S.Zaengl, V. Der Houhanessian, A. Küchler, B. Breitenbauch; **Ageing and Moisture Analysis of Power Transformer Insulation Systems;** CIGRÉ 2002, P. 12-101, Paris, Aug. 2002

[233] A. Küchler, B. Breitenbauch, W.S. Zaengl; **Zustandsbewertung von Transformator-Isolationen durch dielektrische Diagnose;** ETG-Fachtagung „Diagnostik elektrischer Betriebsmittel“, Berlin 2002

[234] A. Kuechler, T. Bedel, T. Haeusler, J.J. Alff; **Evaluation of Water Content in Transformer Insulation by Polarization and Depolarization Current Measurements;** Transformer 01, Bydgoszcz/ Poland, 2001

[235] T. Leibfried; **Zustandsdiagnose des Öl-Papier-Isolationssystems von Leistungstransformatoren mit Hilfe der Relaxationsstromanalyse;** ETG-Fachtagung „Diagnostik elektrischer Betriebsmittel“, Berlin 2002

[236] B. Breitenbauch, A. Kuechler, T. Leibfried, W.S. Zaengl; **Insulation Diagnosis by Polarisation and Depolarisation Current Measurements;** ISH 03 Int. Symp. on High Voltage Engineering, Delft, NL, 2003

[237] Z. T. Yao, **Analysis and Modelling of Dielectric Response in Power Transformer Insulation;** PhD Thesis, University of Queensland, Brisbane/ Australia, 2003

[238] T. K. Saha, J. H. Yew, P. Purkait; **Experience with Dielectric Response Measurement on Oil-Paper Insulated Cables;** ISH 03 Int. Symp. on High Voltage Engineering, Delft, NL, 2003

[239] W.S. Zaengl; **Dielectric Spectroscopy in Time and Frequency Domain for HV Power Equipment (Transformers, Cables etc.);** 12th ISH, Bangalore India, Aug. 2001

[240] S.M. Gubanski, P. Boss, G. Csépes, V. Der Houhanessian, J. Filippini, P. Guuinic, U. Gäfvert, V. Karius, J. Lapworth, G. Urbani, P. Werelius, W. Zaengl; **Dielectric Response Methods for Diagnostics of Power Transformers;** Electra No. 202, June 2002

[241] W.S. Zaengl; **Dielectric Spectroscopy in Time and Frequency Domain for HV Power Equipment, Part I;** IEEE El. Insul. Magazine, 2003

[242] T.K. Saha, **Review of Modern Diagnostic Techniques for Assessing Insulation Condition in Aged Transformers;** IEEE Trans. on Dielectrics and Electrical Insulation, 2003

[243] L. Pong; **Review Negative Power Factor Test Results and Case Study Analysis;** The 2002 Int. Conf. of Doble Clients; Boston/ USA, 2002

[244] A. Küchler, T. Leibfried, B. Breitenbauch, J.J. Alff, V. Der Houhanessian, W.S. Zaengl; **Transformer Insulation Diagnosis by Polarization and Depolarization Current Analysis;** 48. Int. wiss. Kolloquium, TU Ilmenau, 2003

[245] N. Koch; **Monitoring für kondensatorgesteuerte Durchführungen;** TRANSFORM 01, München, 2001

[246] IEC 60137; **Insulated bushings for alternating voltages above 1 000 V**

DIN EN 60137 (VDE 0674-5); **Isolierte Durchführungen für Wechselspannungen über 1 kV**

[247] M. F. Lachmann, W. Walter; **Experience with Application of Sum Current Method to On-Line Diagnostics of High-Voltage Bushings and Current Transformers;** International Conf. of Doble Clients; Boston, USA, 1998

[248] R. Henning; **Online-Feuchtemessung in Transformatorenöl;** Vaisala, Bremerhafen, 2002

[249] S. Happe, G. Kranz; **Ein realzeitfähiges Verfahren zur Unterdrückung von stochastischen TE-Störsignalen;** Highvolt Kolloquium 99, Cottbus 1999

[250] E. Bräsel, U. Sasum; **Die Einbeziehung ungelöster Transformatorgase in die Diagnostik;** ETG-Fachtagung „Diagnostik elektrischer Betriebsmittel“, Berlin 2002

[251] S. Tenbohlen, G. Pudlo, M. Linders, G. Krost; **Berechnung der Überlastbarkeit von Transformatoren in Energieversorgungsnetzen mit Monitoringsystemen;** ETG-Fachtagung „Diagnostik elektrischer Betriebsmittel“, Berlin 2002

[252] U. Sundermann, C. Neumann, C. Viereck, N. Koch; **Nutzung von Monitoringsystemen für den optimierten Betrieb von Transformatoren;** ETG-Fachtagung „Diagnostik elektrischer Betriebsmittel“, Berlin 2002

[253] R. Fuchs, J. Fries; **Umfassendes Generatormonitoring – Thermische Kühlluftanalyse;** ETG-Fachtagung „Diagnostik elektrischer Betriebsmittel“, Berlin 2002

[254] A. Bethge, M. Kaufhold; **Integrierte On-Line TE-Messung zur Vor-Ort-Diagnose rotierender elektrischer Maschinen;** ETG-Fachtagung „Diagnostik elektr. Betriebsmittel“, Berlin 2002

[255] H.J. van Breen, E. Gulski, J.J. Smit, H.F.A. Verhaart; **Interpretation of On-Line VHF PD Measurements on Turbo Generators;** ETG-

Fachtagung „Diagnostik elektrischer Betriebsmittel“, Berlin 2002

[256] R. Koch, J.R. Weidner; **Lokalisierung von Isolationsfehlern in Generatorwicklungen durch Laufzeitortung der Teilentladungen;** ETG-Fachtagung „Diagnostik elektrischer Betriebsmittel“, Berlin 2002

[257] H.J. van Breen, E. Gulski, M.G. Krieg-Wezelenburg; **PD Activity as a means to classify insulation degradation of large turbo generators;** ISH 03 Int. Symp. on High Voltage Engineering, Delft, NL, 2003

[258] M. Farahani, H. Borsi, E. Gockenbach, M. Kaufhold; **Partial discharge pattern recognition as a diagnostic tool for stator bar defects;** ISH 03 Int. Symp. on High Voltage Eng., Delft, 2003

[259] R. Heinrich, S. Schaper, W. Kalkner, R. Plath, A. Bethge; **Synchronous Three Phase Partial Discharge Detection on Rotating Machines;** ISH 03 Int. Symp. on High Voltage Eng., Delft, 2003

[260] B. Krampe, C. Neumann; **Betriebserfahrung mit der UHF-TE-Messung an gasisolierten metallgekapselten Schaltanlagen (GIS);** ETG-Fachtagung „Diagnostik elektrischer Betriebsmittel“, Berlin 2002

[261] A. Pharmatrisanti, S. Meijer; **VHF/UHF PD Detection on Aged GIS**; ISH 03 Int. Symp. on High Voltage Engineering, Delft, NL, 2003

[262] E. Lemke, H. Elze, W. Weissenberg; **Experience in PD diagnosis tests of HV cable terminations in service using an ultra-wide band probing in the real-time mode;** ISH 03 Int. Symp. on High Voltage Engineering, Delft, NL, 2003

[263] L. Yang, M.D. Judd; **Propagation characteristics of UHF signals in transformers for locating partial discharge sources;** ISH 03 Int. Symp. on High Voltage Eng., Delft, 2003

[264] L. Goehlich, F. Donazzi, R. Gaspari, L. Pax; **Monitoring von VPE-isolierten Hochspannungskabeln;** ETG-Fachtagung „Diagnostik elektrischer Betriebsmittel“, Berlin 2002

[265] R. Heinrich, W. Kalkner, R. Plath, D. Obst; **On-Site Application of Directional Coupler Sensors for Sensitive PD Measurement and Location on a 380 kV Cable Line;** ISH 01, Bangalore, India, 2001

[266] R.-D. Rogler, H. Löbl, D. Fricke; **Bestimmung der Restnutzungsdauer elektrotechnischer Verbindungen in Elektroenergieanlagen mit dem Diagnoseverfahren RELITE;** ETG-Fachtagung „Diagnostik elektrischer Betriebsmittel“, Berlin 2002

[267] J.M. Seifert; **Diagnose und Zustandsbewertung von Verbundlangstabisolatorketten in Anlagen und Freileitungen;** ETG-Fachtagung „Diagnostik elektrischer Betriebsmittel“, Berlin 2002

[268] D. Gebhardt, P. Kirchesch, A. Schiemann; **New Digital Control and Monitoring Devices for High Voltage Circuit Breakers;** ETG-Fachtagung „Diagnostik elektr. Betriebsmittel“, Berlin 2002

[269] A.K. Jonscher; **Dielectric relaxation in solids;** Chelsea Dielectric Press, London 1983

[270] R. Tobazéon, J.C. Filippini, C. Marteau; **On the Measurement of the Conductivity of Highly Insulating Liquids;** IEEE Trans. on DEIS, 1994

[271] A. Kuechler, F. Huellmandel, J. Hoppe, D. Jahnel, C. Krause, U. Piovan, N. Koch; **Impact of Dielectric Material Responses on the Performance of HVDC Power Transformer Insulations;** ISH 03 Int. Symp. on High Voltage Engineering, Delft, NL, 2003

[272] A. Bethge, M. Kaufhold, R. Plath, A. Obralic, W. Kalkner; **Neue Bewertungsverfahren für synchrone Mehrstellen-TE-Messung an rotierenden elektr. Maschinen;** ETG Fachtagung „Diagnostik elektr. Betriebsmittel“ Köln 2004

[273] S. Schaper, W. Kalkner, R. Plath; **Synchrone Mehrstellen-Teilentladungsmessung an Leistungstransformatoren bei variabler Mittenfrequenz;** ETG Fachtagung „Diagnostik elektr. Betriebsmittel“ Köln 2004

[274] V. Dahinden, K. Schultz, A. Küchler; **The Function of Solid Insulation in Transformers;** transform ‘98, München, 1998

[275] F. Elliott & B. Lavier, W. Kuehn, A. Kuechler; **FEM-study on converter transformer failures in the Celilo HVDC converter station;** IEEE PES winter power meeting, USA, 1999

[276] A. Küchler; **Isolationssysteme für die Hochspannungsgleichstromübertragung (HGÜ)**; XV. Wiss. Kolloq. „Science in Practice“ HS Bremen, 1999

[277] A. Küchler; **Dielektrische Beanspruchungen in HGÜ-Isolationssystemen**; IEH-Prüftechnik-Kolloquium, Universität Karlsruhe, 2000

[278] F.E. Elliott & B.E. Lavier, W. Kuehn, A. Kuechler; **DC-Voltage Grading in the Valve-Side-Bushing/Insulation Structure of the Celilo Converter Transformers**; 2000 NAPS North American Power Symp., Waterloo, Canada 2000

[279] F.E. Elliott & B.E. Lavier, W. Kuehn, A. Kuechler; **Relationship between temperature distribution and charge flow rate in the valve side bushings of Celilo HVDC converter transformers**; 4th Int. HVDC-Conf. China, 2001

[280] A. Kuechler, M. Siller, C. Krause, H. Hoffmann, N. Koch, J. Hoppe, P. Heinzig; **Transient Stress Management in HVDC Barrier-Oil Insulation**

Systems; ISH 03 Int. Symp. on High Voltage Engineering, Delft, NL, 2003

[281] A. Lindroth; **The Relationship between Test and Service Stresses as a Function of Resistivity Ratio for HVDC Converter Transformers and Smoothing Reactors**; ELECTRA 1994

[282] K.C. Wen, Y.B. Zhou, J. Fu, T. Jin; **A Calculation Method and some Features of Transient Field under Polarity Reversal Voltage in HVDC Insulation;** IEEE Transactions on Power Delivery; 1993

[283] IEC 61620; **Insulating liquids – Determination of the dielectric dissipation factor by measurement of the conductance and capacitance – Test method**

DIN EN 61620 (VDE 0370-16); **Isolierflüssigkeiten – Bestimmung des Permittivitäts-Verlustfaktors durch Messung der Konduktanz und Kapazität – Prüfverfahren**

[284] H. Böhme; **Welche Aufgaben stellt die zukünftige Entwicklung der Elektroenergieversorgung an die Hochspannungs.Prüftechnik?** Highvolt Kolloquium, Dresden, 2003

[285] Y. Julliard, R. Badent, A.J. Schwab; **Behaviour of Multiple Barrier Insulation Systems under Impulse Conditions;** IEEE 2001 Annual Report Conf. on Electrical Insulation and Dielectric Phenomena, 2001

[286] H.G. Fischer, V. Dahinden, R. Malewski; **New Components and Materials for a More Reliable Insulation of EHV Transformers**; CIGRE Symposium Montreal, 1991

[287] D.J. Tschudi, K. Schultz, T. Prevost, W. Ashton, M. Franchek; **Experimental Evidence of Transformer Insulation Design Methods**; 10th ISH Int.Symp. on High Voltage Eng., Montreal, 1997

[288] F. Derler, H.J. Kirch, Ch. Krause, E. Schneider; **Development of a Design Method for Insulating Structures exposed to Electric Stress in Long Oil Gaps and Along Oil Transformerboard Interfaces;** 9th CESPI Conf. on Electric Power Supply Industry, Hong Kong 1992

[289] D. Tschudi, V. Dahinden, F. Derler; **Dielectric Strength Assessment of Power Transformer Insulation;** 9th ISH Int. Symp. on High Voltage Engineering, Graz, Austria, 1995

[290] IEC 60076-1; **Power Transformers –** Part 1: **General**

DIN EN 60076-1 (VDE 0532-76-1); **Leistungstransformatoren** – Teil 1: **Allgemeines**

[291] IEC 60076-2, -3, -5; **Power Transformers** –Part 2: **Temperature rise for liquid-immersed transformers**, Part 3: **Insulation levels, dielectric tests and clearances in air**, Part 5: **Ability to withstand short-circuit**

DIN EN 60076-2, 3, 5 (VDE 0532-76-2, 3, 5); **Leistungstransformatoren** – Teil 2: **Übertemperaturen für flüssigkeitsgefüllte Transformatoren**, Teil 3: **Isolationspegel, Spannungsprüfungen und äußere Abstände in Luft**, Teil 5: **Kurzschlussfestigkeit**

[292] IEC 60076-4; **Power transformers** – Part 4: **Guide to the lightning impulse and switching impulse testing – Power transformers and reactors**

DIN EN 60076-4 (VDE 0532-76-4); **Leistungstransformatoren – Leitfaden zur Blitz- und Schaltstoßspannungsprüfung von Leistungstransformatoren und Drosselspulen**

[293] K. Hackemack, E. Gockenbach, H. Borsi, P. Werle, K. Scheil, M. Vogel; **Neues Verfahren zur Auswertung von Blitzstoßspannungsprüfungen an Transformatoren;** ETG Fachtagung „Diagnostik elektr. Betriebsmittel“ Köln 2004

[294] IEEE Standard 62; **IEEE Guide for Diagnostic Field Testing of Electric Power Apparatus** – Part 1: **Oil Filled Power Transformers, Regulators, and Reactors**

[295] IEC 60076-7; **Power transformers** – Part 7: **Loading guide for oil-immersed power transformers**

[296] DIN IEC 60076-7 (VDE 0532-76-7); **Leistungstransformatoren** – Teil 7: **Leitfaden für die Belastung von ölgefüllten Leistungstransformatoren**

[297] A. Krämer; **On-Load Tap-Changers for Power Transformers;** MR-Publ., Regensburg, 2000

[298] R.F. Cameron, T.B. Traub, B.H. Ward; **Update on EPRI Transformer Expert System (XVISOR);** EPRI 1999

[299] CIGRE SC A2; **Life Management Techniques for Power Transformers;** CIGRE Publication, SC A2 (12) WG 18, 2003

[300] I. Höhlein, A.J. Kachler u.a.; **Transformer Life Management, German Experience with Condition Assessmet;** ETG Fachtagung „Diagnostik elektrischer Betriebsmittel“ Köln 2004

[301] IEC 60296; **Fluids for electrotechnical applications – Unused mineral insulating oils for transformers and switchgear**

IEC 60422; **Mineral insulating oils in electrical equipment – Supervision and maintenance guidance**

DIN EN 60296 (VDE 0370-1); **Flüssigkeiten für elektrotechnische Anwendungen – Neue Isolieröle auf Mineralölbasis für Transformatoren und Schaltgeräte**

DIN EN 60422 (VDE 0370-2); **Isolieröle auf Mineralölbasis in elektrischen Betriebsmitteln**

– Leitlinie zur Überwachung und Wartung

[302] H. Strzala, A. Naundorf, B. Schmitz, K.-H. Häger; **Aufbereitung der Isolation von Leistungstransformatoren vor Ort durch Vapour-Phase-Trocknung;** ETG Fachtagung „Diagnostik elektrischer Betriebsmittel“ Köln 2004

[303] V. Wasserber, H. Borsi, E. Gockenbach, O. Schmidt, P. Hogrefe, J. Wohlfahrt, P. Werle; **Betriebserfahrungen mit einem neuen System zur kontinuierlichen Trocknung der Isolierung von Leistungstransformatoren ohne Beeinflussung der DGA;** ETG Fachtagung „Diagnostik elektr. Betriebsmittel“ Köln 2004

[304] T. Weekes, T. Molinski, G. Swift; **Transient Transformer Overload Ratings and Protection;** IEEE El. Insulation Magazine, 2004

[305] T. Weekes, T. Molinski, X. Li, G. Swift; **Risk Assessment Using Transformer Loss of Life Data;** IEEE El. Insulation Magazine, 2004

[306] I. Fofana, V. Wasserberg, H. Borsi, E. Gockenbach, M. Farzaneh; **Drying of Transformer Insulation using Zeolite;** IEEE Electrical Insulation Magazine, 2004, Vol. 20, No. 2

[307] S. Truant, T. Leibfried; **Vor-Ort-Trocknung von gealterten Transformatoren durch die Ölumlauftrocknung in Kombination mit der LFH-Technik;** Transformer Life Management Kolloq., Nürnberg, 2002

[308] T. Leibfried, U. Thieß, I. Höhlein-Atanasova, S. Truant, B. Heinrich, H.P. Gasser, B. Breitenbauch, T. Lainck, J. Leißner; **Profil von Wassergehalt und Polymerisationsgrad in der Feststoffisolation von Leistungstransformatoren;** ETG Fachtagung „Diagnostik elektr. Betriebsmittel“ Köln 2004

[309] IEC 60099-1; **Surge arresters** – Part 1: **Nonlinear resistor type gapped surge arresters for a.c. systerms**

DIN EN 60099-1 (VDE 0675-1); **Überspannungsableiter** – Teil 1: **Überspannungsableiter mit nichtlinearen Widerständen für Wechselspannungsnetz**e

[310] K. Kist; **Streamerausbreitung im Mischdielektrikum Isolieröl/ Transformerboard;** Dissertation Univ. Karlsruhe, 1999

[311] D. Meurer, M. Stürmer; **Kabelsysteme für Mittel- und Hochspannung, Alterungsdiagnose: notwendig und hilfreich?** ETG Fachtagung „Diagnostik elektr. Betriebsmittel“ Berlin 2002

[312] W.-D. Schuppe, W. Weißenberg; **Innere Grenzflächen in Kabeln und Garnituren;** ETG-Fachtagung „Einfluß von Grenzflächen auf die Lebensdauer elektrischer Isolierungen“, Bad Nauheim, 1999

[313] J. Alter, M. Ammann, W. Boeck, W. Degen, A. Diessner, H. Koch, F. Renaud, S. Poehler; **N_2/ SF_6 Gas-Insulated Line of a New GIL Generation in Service;** CIGRÉ Session Paris 2002

[314] H. J. Koch; **Magnetic fields of gas-insulated transmission lines –calculation and measurements;** ISH 03 Int. Symp. on High Voltage Engineering, Delft, NL, 2003

[315] Y. Maekawa, K. Watanabe, S. Maruyama, Y. Murata, H. Hirota; **Research and Development of DC +/- 500 kV Extruded Cables;** CIGRÉ Session 2002, P. 21-203, Paris 2002

[316] S. Giere; **Vakuumschalttechnik im Hochspannungseinsatz;** Diss. TU Braunschweig, 2003

[317] H. W. Klink; **Simulation der gasdynamischen Vorgänge in der Löschkammer eines SF_6-Blaskolben-Leistungsschalters;** Diss. Universität Karlsruhe, 1998

[318] T. Suwanasri, A. Schnettler, D. Fricke, A. Noack; **Untersuchung zur Zustandsüberwachung an Hochspannungsleistungsschaltern**; ETG Fachtagung „Diagnostik elektrischer Betriebsmittel“ Köln 2004

[319] E. A. Boulter, G. C. Stone; **Historical Development of Rotor and Stator Winding Insulation Materials and Systems;** IEEE El. Insulation Magazine, May/ June 2004

[320] A. Küchler; **Application of HV Test Methods to the Evaluation of LV Motor Insulation Quality;** optim ‘98, 6th Int. Conf. on Optimization of El. a. Electronic Equipment; Brasov, 1998

[321] M. Leijon, L. Gertmar, H. Frank, J. Martinsson, T. Karlsson, B. Johansson, K. Isaksson, U. Wollström; **Breaking Conventions in Electrical Power Plants;** CIGRÉ Sess. Paris, 11/37-03, 1998

[322] F. Owman, T. Sörqvist, A. Emlinger; **Ohne Transformator direkt ins Netz, Erstmaliger Einsatz eines Powerformers in einem Wärmekraftwerk;** Elektrizitätswirtschaft, H. 4, 1999

[323] A. Jaksts, M. Leijon, C. Sasse, H. Frank, T.H. Andersson, S. Forsmark, L. Nilsson, T. Fogelberg, A. Sjögren; **A Major Breakthrough in Transformer Technology;** CIGRÉ Sess. Paris, 12-101, 2000

[324] E. Peschke; R. Schroth, R. v. Olskausen; **Extension of XLPE cables to 500 kV based on progress in technology;** JICABLE 95, 4th Int. Conf. on Insulated Power Cables, Paris, 1995

[325] R. Maier, S. Pöhler, R. Schroth; **XLPE cable systems for 500 kV;** Elektrizitätswirtsch., 1998

[326] CIGRÉ Recommendation; **Recommendations for Electrical Tests, Prequalifications and Development on Extruded Cables and Accessoires at Voltages >150 (170) kV and < 400**

(420) kV; CIGRÉ WG 21-03, Electra No. 151, Paris, Dez. 1993

[327] **VPE-isolierte Hochspannungskabel**; Firmenschrift Pirelli Berlin

[328] **Zündkerzen;** Firmenschrift, R. Bosch GmbH, Stuttgart

[329] T. Kaiser, A. Hoffmann; **Einfluss der Zündkerzen auf das Entflammungsverhalten in modernen Motoren;** MTZ Motortechnische Zeitschrift, 2000

[330] T. Kaiser u.a.; **Erstes Zündungssymposium;** R. Bosch GmbH, Heilbronn, 2004

[331] J. Gerhold, M. Hara; **Insulation of high critical temperature superconducting power equipment with liquid nitrogen;** ISH 97 Int. Symp. on High Voltage Engineerig., Montreal, 1997

[332] K. Takano, J. Yan, S. Matsuura, M Hara; **Thermal Bubble-Triggered Breakdown of a Plane-to-Cylinder Electrode Partially Covered with thin Insulation Film in Liquid Nitrogen;** ISH 97 Int. Symp. on High Voltage Engineering, Montreal, 1997

[333] K. Takano, F. Shimokawa, M. Hara; **Thermal Bubble-Triggered Breakdown under DC, AC and Impulse Non-Uniform Electric Fields in Liquid Nitrogen**; ISH 99 Int. Symp. on High Voltage Engineering, London 1999

[334] J.K. Sykulski, C. Beduz, R.L. Stoll, M.R. Harris, K.F. Goddard, Y.Yang; **Prospects for large high-temperature superconducting power transformers: conclusions from a design study;** IEE Proc. Elect. Power Appl., Jan. 1999

[335] B.-Y. Seok, H. Komatsu, J. Suehiro, M. Hara; **Bubble Behavior and PBD Characteristics in the Simulated Electrode System of High Temperature Superconducting Coils;** ISH 99 Int. Symp. on High Voltage Engin., London 1999

[336] D. Schneider, S.. Köbel, L.J. Gauckler; **Hochtemperatur-Supraleiter vor der Anwendung;** Bulletin SEV/VSE 21/99

[337] J. Rhyner; **Hochtemperatur-Supraleitung im Energienetz;** SEV/ ETG-Bd. 70, Zürich, 2000

[338] R. Schöttler, G. Pailer, P. Wels; **Supraleiter optimiert Spannungsqualität;** El.wirtsch., 2000

[339] E. Baltzer, H. Schmitt, W. Schultz; **Kurzschlußstrombegrenzung mit HTSL**; etz Heft 12/97

[340] H.R. Ris, **Supraleitender Strombegrenzer**; Elektrotechnik 12/98

[341] D. Bonmann; **Supraleitende Betriebsmittel für die Energietechnik**; ETG-Fachtagung, Fachbericht 76, Bad Nauheim 1999

[342] M. Kleimaier; **Weltpremiere: Resistiver supraleitender Strombegrenzer im Feldtest bei RWE Energy;** ETG-Informationen, Juli 2004

[343] D.A. Barton, G.O. Zimmermann; **Superconducting AC/DC Power Conversion using High-Temperature Superconducting Components;** IEEE Trans. on Appl. Superconductivity, 1999

[344] NN (Detroit Edison); **Powering Up Superconducting Cable;** EPRI Journal 24, 1999

[345] M. Rabinowitz; **Superconducting Power Generation;** IEEE Power Eng. Review; May 2000

[346] D. Driscoll, V. Dombrovski, B. Zhang; **Development Status of Superconducting Motors;** IEEE Power Engineering Review, May 2000

[347] S.P.Mehta, N. Aversa, M.S.Walker; **Transforming transformers;** IEEE Spectrum, July 1997

[348] J. Sykulski, C. Beduz, R. Stoll, M. Harris, K. Goddard, Y. Yang; **Prospects for large high-temperature superconducting power transformers: conclusions from a design study;** IEE Proc.-Elect. Power Appl., Vol. 146, No. 1, 1999

[349] H.R. Ris; **Erster dreiphasiger Hochtemperatur-Supraleiter-Transformator am Netz;** Elektrotechnik Nr. 7/8 1997

[350] M. Lakner; **Supraleitender Transformator - Grundlagen;** SEV/ ETG-Band 70 (Anwendung der Supraleitung), Zürich, 2000

[351] R. Schlosser, U. Henning, M. Meinert; **HTSL-Bahntransformator;** Int. ETG-Kongress „Energietechnik der Zukunft“, Nürnberg 2001

[352] M. Hoof, C.-E. Stephan; **Diagnose des Isolationssystems elektrischer Maschinen, Aktueller Stand u. Entwicklungstendenzen;** ETG Fachtagung „Diagnostik elektrischer Betriebsmittel“ Köln 2004

[353] B. Dorra; **Stoßwellentherapie als Alternative zum künstlichen Hüftgelenk;** VDI-Nachrichten, Nr. 12/ 2004

[354] H. Bluhm, K. Baumung, R. Böhme, W. Frey, H. Giese, A. Heinzel, P. Hoppe, G. Link, G. Müller, C. Schultheiss, G. Schumacher, H. Strässner, D. Strauss, A. Weisenburger, F. Zimmermann; **Pulsed power science and technology at Forschungszentrum Karlsruhe;** PPA 2001: Int. Conf. on Pulsed Power Applications, Gelsenkirchen, 2001

[355] W. Schufft, P. Coors, J. Spiegelberg; **Resonanzprüfsysteme mit variabler Frequenz für die Prüfung und Diagnose an verlegten Kunststoffkabeln;** Highvolt Kolloq., Cottbus 1999

[356] D. Meurer; **Elektrische Prüfung von Mittel- und Hochspannungskabeln – Ziel, Stand und Ausblick;** Highvolt Kolloquium, Dresden 2003

[357] J.G. Head; **Use of Mobile Variable Fequency High Voltage Test Plant in the UK;** Highvolt Kolloquium, Dresden 2003

[358] H. Bluhm, W. An, W. Engelko, H. Giese, W. Frey, A. Heinzel, P. Hoppé, G. Mueller, Ch. Schultheiss, J. Singer, R. Strässner, D. Strauß, A. Weisenburger, F. Zimmermann; **High power particle beams and pulsed power for industrial applications**; Proc. 14th Int. Conf. on High-Power Particle Beams, Albuquerque 2002

[359] H. Bluhm, V. An, K. Baumung, P. Brenner, L. Buth, V. Engelko, W. Frey, H. Giese, C. Gusbeth, A. Heinzel, P. Hoppé, G. Müller, M. Sack, C. Schultheiß, J. Singer, R. Sträßner, A. Weisenburger; **Progress in High-Power-Particle Beams and Pulsed Power for Industrial Applications at Forschungszentrum Karlsruhe**; 15th Int. Conf. on High-Power Particle Beams, St. Petersburg, 2004

[360] H. Bluhm, C. Schultheiss, W. Frey, C. Gusbeth, M. Sack, R. Strässner; **Industrial scale treatment of biological cells with pulsed electric fields**; 26th Power Modulator Symp., San Francisco, 2004

[361] C. Schultheiss, H. Bluhm, H. Mayer, M. Kern, T. Michelberger, G. Witte; **Processing of sugar beets with pulsed electric fields**; IEEE Trans. on plasma science, 2002

[362] H. Bluhm, W. Frey, H. Giese, P. Hoppé, C. Schultheiß, R. Sträßner; **Application of pulsed HV discharges to material fragmentation and recycling**; IEEE Trans. on Dielectrics and Electrical Insulation 2000

[363] J. Ermisch, A. Georgi, A. Müller; **Ohmsche Spannungsteiler jetzt auch für Mittelspannung**; etz 15-16/1997

[364] F. Leitsch, C. Vetter; **Spannungsprüfsysteme – Sicherheit nach neuer Norm;** etz 6/ 1999

[365] T. Kohl, A. Müller, D. Scharnewski, S. Werner; **Meßwandler im Wandel;** etz 3/ 1997

[366] U. Gäfvert, A. Jaksts, C. Törnkvist, L. Walfridsson; **Electrical Field Distribution in Transformer Oil;** IEEE Trans. on Elec. Insulation, 1992

[367] M. Wakamatsu, K. Kato; N. Inoue, H. Koide, H. Okubo; **DC Field Measurement in Oil/Pressboard Composite Insulation System by Electro-Optic Kerr Effect;** IEEE Trans. on Dielectrics and El. Insulation, 2003

[368] P. Menke; **Optischer Präzisions-Stromsensor nach d. Faraday-Effekt**; Diss. Univ. Kiel, 1996

[369] Y. Du, M. Zahn, B.C. Lesieutre, A.V. Mamishev, S.R. Lindgren; **Moisture Equilibrium in Transformer Paper-Oil Systems;** IEEE Trans. on Dielectrics and Electrical Insulation, 1999

[370] O. Simon; **Einsatz eines Supraleitenden Magnetischen Energiespeichers zur Kompensation von Netzrückwirkungen;** Diss. Univ. Karlsruhe, 1998

[371] A. Kraetge, W. Kalkner, R. Plath, K.-D. Plath; **Transiente Öldruckmessung zur Diagnose der Kurzschlussfestigkeit von Leistungstransformatoren;** ETG Fachtagung „Diagnostik elektrischer Betriebsmittel“ Köln 2004

[372] J. Teunissen, D. Peier, B.M. Krijgsman, R. Verhoeven; **Prototype-integration of Fiber-Bragg-Sensors into high-voltage transformers for Online-Temperature-Monitoring;** ISH 03 Int. Symp. on High Voltage Engin., Delft, NL, 2003

[373] R. Schwarz, M. Muhr, S. Pack; **Partial discharge detection and localization for application in transformers;** ISH 03 Int. Symp. on High Voltage Engineering, Delft, NL, 2003

[374] R. Porzel; **Zustandsdiagnostik elektrotechnischer Betriebsmittel über bildgebende Verfahren – Visuelle Diagnostik der elektrischen Energietechnik am Beispiel des Hochspannungs-Leistungstransformators;** ETG Fachtagung „Diagnostik elektr. Betr.mitt.“ Berlin 2002

[375] W. Hauschild; **Der künftige IEC Standard 60 060-3 „Hochspannungsprüfungen vor Ort“ und seine Bedeutung für die off-line Diagnostik;** ETG Fachtagung „Diagnostik elektrischer Betriebsmittel“ Köln 2004

[376] G. Schiller; **Das Durchschlagverhalten von vernetztem Polyethylen (VPE) bei unterschiedlichen Spannungsformen und Vorbeanspruchungen;** Diss. Univ. Hannover, 1996

[377] E. Gockenbach, W. Hauschild; **The selection of the frequency range for HV on-site testing of extruded cable systems;** IEEE Insulation Magazine Vol. 16, No. 6, 2000

[378] M. Kuschel, R. Plath, W. Kalkner; **Dissipation Factor Measurement at 0,1 Hz as a Diagnostic Tool for Service Aged XLPE Insulated Medium Voltage Cables;** 9th ISH, Graz, 1995

[379] W. Hauschild, P. Coors, W. Schufft, R. Plath, U. Herrmann, K. Polster; **The Technique of AC On-Site Testing of HV Cables by Frequency-Tuned Resonant Test Systems**; CIGRÉ Session Paris 2002

[380] J. Vithayathil, M. Arunachalam, A.-A. Edris, B. Ekehov, Y. Fu, H. H. Lessmann-Mieske, M. Mohaddes, J. Pavelka, A. Phadke, K. Sadek, R. Shuttleworth, C. Taylor; **Thyristor Controlled Voltage Regulators, Part II: Static On-Load Transformer Tap Changers;** Electra, Apr.2004

[381] J. Kindersberger; **Stand und Tendenzen der Prüfung von Kunststoffen für Freiluftisolierungen;** Highvolt Kolloquium, Dresden 2003

[382] IEC 61302; **Electrical insulating materials – Method to evaluate the resistance to tracking and erosion – Rotating wheel dip test**

DIN EN 61302 (VDE 0303-12); **Elektroisolierstoffe – Prüfverfahren zur Beurteilung des Widerstandes gegen Kriechwegbildung und Erosion – Zyklische Prüfung**

[383] J. Ostergaard, O. Tonnesen; **Design, Installation and Operation of World's First High Temperature Superconducting Power Cable in a Utility Power Network;** CIGRÉ Session Paris 2002

[384] K.A. de Bruin, W. Krassowska; **Modeling Electroporation in a Single Cell; I. Effects of Field Strength and Rest Potential; II. Effects of Ionic Concentrations;** Biophys. 1999, 1213 ff

[385] IEC 61620; **Insulating liquids – Determination of the dielectric dissipation factor by measurement of the conductance and capacitance – Test method**

DIN EN 61620 (VDE 0370-16); **Isolierflüssigkeiten – Bestimmung des Permittivitäts-Verlustfaktors durch Messung der Konduktanz und Kapazität – Prüfverfahren**

[386] IEC 62631; **Dielectric and resistive properties of solid insulating materials**

DIN EN 62631 (VDE 0307); **Dielektrische und resistive Eigenschaften fester Isolierstoffe**

[387] K. Feser; **Die künftigen Aufgaben von IEC TC 42 „HV Test Technique";** Highvolt-Kolloquium, Dresden 2003

[388] ISO/IEC 17025; **Requirements on the competence of calibration and testing laboratories**

[389] K. Schon; **Der Deutsche Kalibrierdienst (DKD) auf dem Gebiet der Hochspannungs-Messgrößen;** Highvolt-Kolloquium, Dresden 2003

[390] IEC 60060-3; **High voltage test techniques** – Part 3: **Definitions and requirements for on-site tests**

DIN EN 60060-3 (VDE 0432-3); **Hochspannungs-Prüftechnik** – Teil 3: **Begriffe und Anforderungen für Vor-Ort-Prüfungen**

[391] R. Wimmer, K. Feser; **Berechnung der Übertragungsfunktion aus Online-Messdaten;** ETG Fachtagung „Diagnostik elektrischer Betriebsmittel" Köln 2004

[392] A. Küchler, F. Hüllmandel, K. Böhm, N. Koch, P. Brupbacher, C. Krause; **Das dielektrische Verhalten von Öl-Papier-Isolationen unter der Wirkung von Grenzflächen-, Material- u. Prüfparametern;** ETG-Fachtagung „Grenzflächen in elektr. Isoliersystemen", Hanau, 2005

[393] IEC 60599; **Mineral oil-filled electrical equipment in service – Guidance on the interpretation of dissolved and free gases analysis**

DIN EN 60599 (VDE 0370-7); **In Betrieb befindliche, mit Mineralöl befüllte elektrische Geräte – Leitfaden zur Interpretation der Analyse gelöster und freier Gase**

[394] A. J. Schwab; **Begriffswelt der Feldtheorie;** Springer-Verlag, Berlin, 5. Aufl. 1998

[395] G. Strassacker; **Rotation, Divergenz und das Drumherum – Eine Einführung in die elektromagnetische Feldtheorie;** Teubner, Stuttgart, 4. Aufl. 1999

[396] F. Beichelt; **Stochastik für Ingenieure;** B.G. Teubner, Stuttgart, 1995

[397] A. Küchler, F. Hüllmandel, J. Hoppe, C. Krause, N. Koch; **Transiente Belastungen durch Grenzflächen- und Materialpolarisation in HGÜ-Transformatoren;** angemeldet zur ETG-Fachtagung „Grenzflächen in elektrischen Isoliersystemen", Hanau, 2005

[398] A. Küchler, F. Hüllmandel, K. Böhm, N. Koch; **Einfluss äußerer Grenzflächen auf die dielektrische Diagnose betriebsgealterter Hochspannungsdurchführungen;** ETG-Fachtagung „Grenzflächen in elektrischen Isoliersystemen", Hanau, 2005

[399] R. Badent, M. Hemmer; **Eignung von Rapsöl als elektrischer Isolierstoff;** Jahresbericht des IEH, Univ. Karlsruhe, 2001

[400] M. Hemmer, R. Badent; **Probebetrieb eines rapsölisolierten Verteiltransformators;** Jahresbericht des IEH, Univ. Karlsruhe, 2002

[401] M. Hemmer, R. Badent; **Untersuchungen am Rapsöl-Transformerboard-Dielektrikum;** Jahresbericht des IEH, Univ. Karlsruhe, 2003

[402] T. J. Lewis; **Basic Dielectric Processes in Dielectric Liquids;** IEEE Trans. on DEI, Vol. 1 No.4, Aug. 1994

[403] R. Tobazéon; **Prebreakdown Phenomena in Dielectric Liquids;** IEEE Trans. on DIE, Vol. 1 No. 6, Dec. 1994, pp 1132-1147

[404] T.J. Lewis; **A New Model for the Primary Process of Electrical Breakdown in Liquids;** IEEE Trans. on DEI, Vol. 5 No.3, June 1998

[405] T.V. Top, G. Massala, O. Lesaint; **Streamer Propagation in Mineral Oil in Semi-Uniform Geometry;** IEEE Trans. on DIE, Vol. 9 No. 1, Feb. 2002, pp 76-83

[406] Yu. V. Torshin; **Prediction of Breakdown Voltage of Transformer Oil from Predischarge Phenomena;** IEEE Trans. on DIE, Vol. 10 No. 6, Dec. 2003, pp 933-941

[407] T. J. Lewis; **Breakdown Initiating Mechanisms at Electrode Interfaces in Liquids;** IEEE Trans. on DEI, Vol.10, No. 6, Dec. 2003

[408] W. R. Wilson; **A Fundamental Factor Controlling the Unit Dielectric Strength of Oil;** AIEE Transactions, vol 72, pt. III, Feb. 1953, pp. 68-74

[409] K. H. Weber, H. S. Endicott; **Area Effect and Its Extremal Basis for the Electrical Breakdown of Transformer Oil;** AIEE Trans. Vol. 75, June 1956

[410] K. H. Weber, H. S. Endicott; **Extremal Area Effect for Large Area Electrodes for the Electric Breakdown of Transformer Oil;** AIEE Trans. Vol. 76. Dec. 1957

[411] H. Kappeler; **Recent Forms of Execution of 380 kV Transformer Bushings;** CIGRÉ Session Paris, 1958

[412] N. G. Trinh, C. Vincent, J. Régis; **Statistical Dielectric Degradation of Large-Volume Oil-Insulation;** IEEE Trans. on PAS Vol. 101, No. 10, Oct. 1982

[413] O. Lesaint, T.V. Top; **Streamer Initiation in Mineral Oil Part I: Electrode Surface Effect Under Impulse Voltage;** IEEE Trans. on DEI, Vol. 9 No. 1, Feb. 2002, pp 84-91

[414] T.V. Top, O. Lesaint; **Streamer Initiation in Mineral Oil Part II: Influence of a Metallic Protrusion on a Flat Electrode;** IEEE Trans. on DEI, Vol. 9 No. 1, Feb. 2002, pp 92-96

[415] F. Carraz, P. Rain, R. Tobazéon; **Particle-initiated Breakdown in a Quasi-uniform Field in Transformer Oil;** IEEE Trans. on DEI, Vol. 2 No. 6, Dec. 1995, pp 1152-1163

[416] T. Tanaka; **Polymer Nanocomposistes as HV Insulation: Superiority and Expectation;** 15th ISH Int. Sympos. on High Voltage Engineering; Ljubljana, Aug. 2007

[417] E. Peschke, R. v. Olshausen; **Kabelanlagen für Hoch- und Höchstspannung;** Verlag Publicis MCD Verlag Erlangen – München, 1998

[418] D. Kind; **Die Aufbaufläche bei Stoßbeanspruchung technischer Elektrodenanordnungen in Luft;** Dissertation TU München, 1957

[419] M. Hahn, W. Sorgatz; **Möglichkeiten der Vor-Ort-Analyse der gelösten Gase nach DIN Norm;** ETG Fachtagung 104, Diagnostik elektrischer Betriebsmittel, Kassel 2006

[420] E. Bräsel; **Die Einbeziehung ungelöster Transformatorgase in die Diagnostik;** ETG Fachtagung 87, Diagnostik elektrischer Betriebsmittel, Berlin 2002

[421] G. Breitfelder, E. Buckow, W. Knorr, W. Peschke; **Dielectric strength of Transformer Oil under Impulse and High Frequency Voltage Stress;** 5th ISH Int. Symp. on High Voltage Engineering, paper 22.12, Braunschweig, 1987

[422] S. Schaper, A. Obralic, W. Kalkner, R. Plath; **Synchronous multi-terminal on-site PD measurements on power transformers with an enhanced time differential method;** 15th Int. Symp. on High Voltage Engineering ISH07, Ljulbljana, 2007

[423] R. Badent; **Modell der elektronendominanten Streamerentladung in Isolieröl;** Dissertation Univ. Karlsruhe, 1996

[424] S. Grimm; **Theoretische und praktische Untersuchungen zum Durchschlagsverhalten ölisolierter Elektrodenanordnungen;** Diplomarbeit Univ. Karlsruhe, 1992

[425] K. Kist, R. Badent; **Vorentladungsmechanismen in Isolieröl bei Elektrodenabständen bis 70 mm;** Jahresbericht des IEH, Univ. Karlsruhe, 1993

[426] W. Hauschild; **Eine Modellvorstellung vom Öldurchschlag im inhomogenen Feld bei Schaltspannungen;** Periodica Polytechnika, Budapest, Vol. 15, No. 2, 1971

[427] K. Böhm; **Dielektrische Diagnose von Hochspannungsisolierungen**; Masterarbeit FHWS Schweinfurt, 2005

[428] A. Küchler, F. Hüllmandel, K. Böhm, C. Neumann, N. Koch, K. Loppach, C. Krause, J.J. Alff; **Condition Assessment of Aged Transformer Bushing Insulations;** CIGRÉ Session 2006, Paper A2-104, Paris 2006

[429] A. Küchler, F. Hüllmandel, K. Böhm, C. Krause, B. Heinrich; **Dielektrische Eigenschaften von Öl-Board- und Öl-Papier-Isolierungen als Kenngrößen für die Diagnose von Transformatoren und Durchführungen;** ETG-Fachtagung „Diagnostik elektrischer Betriebsmittel“, Kassel, 2006

[430] A. Küchler, F. Hüllmandel, M. Appold, M. Liebschner, R. Krump, J. Titze; **Diagnose von Hochspannungsdurchführungen durch PDC-Analyse;** ETG-Fachtagung „Diagnostik elektrischer Betriebsmittel“, Kassel, 2006

[431] A. Kuechler, F. Huellmandel, K. Boehm, M. Liebschner, M. Appold, R. Krump, J. Titze; **Dielectric Diagnosis and Monitoring of High Voltage Bushings;** 51. IWK Int. Wissenschaftl. Kolloq., Technische Univ. Ilmenau, 2006

[432] R. Krump, P. Haberecht, J. Titze, A. Küchler, M. Liebschner; **Bushings for Highest Voltages - Development, Testing, Diagnostics and Monitoring;** Highvolt-Kolloq., Dresden, Mai 2007

[433] M. Liebschner; **Online-Monitoring von Hochspannungsdurchführungen;** Master Thesis, FHWS Schweinfurt, 2006

[434] Frank Huellmandel, Manuel Appold, Andreas Kuechler, Reiner Krump, Joachim Titze; **Condition Assessment of High Voltage Bushings by Means of Dielectric Diagnosis with PDC;** 15th ISH International Symposium on High Voltage Engineering, Ljubljana, 2007

[435] M. Liebschner, K. Boehm, A. Reumann, A. Kuechler, R. Krump, J. Titze; **Online-monitoring of Capacity and Dissipation Factor of High Voltage Bushings at Service Temperature;** 15th ISH International Symposium on High Voltage Engineering, Ljubljana, 2007

[436] A. Kuechler, F. Huellmandel, K. Boehm, M. Liebschner, C. Krause, B. Heinrich; **Parameters Determining the Dielectric Properties of Oil Impregnated Pressboard and Presspaper in AC and DC Power Transformer Applications;** 15th ISH International Symposium on High Voltage Engineering, Ljubljana, 2007

[437] A. Küchler, F. Hüllmandel, K. Böhm, M. Liebschner; **Charakterisierung von Isolierstoffen und Isoliersystemen durch Polarisations- und Depolarisationsstromanalysen (PDC-Analysen);** 1. Burghäuser Isolierstoffkolloq. 2007

[438] A.E.D. Heylen; **Sparking Formula for Very High-Voltage Paschen Characteristics of Gases;** IEEE Electrical Insulation Magazine, Vol. 22 No. 3, May/June 2006, pp. 25-35

[439] H. Bluhm; **Pulsed Power Systems – Principles and Applications;** Springer-Verlag, Berlin Heidelberg 2006

[440] A.I. Egorov, S.I. Stepanov; **Long-Lived Plasmoids Produced in Humid Air as Analogues of Ball Lightning;** Technical Physics. v. 47, pp. 1584-1586, 2002

[441] A. Versteegh, K. Behringer, U. Fantz, G. Fussmann, B. Jüttner, S. Noack; **Long-living plasmoids from an atmospheric water discharge**; Plasma Sources Science and Technology, vol. 17, 2008

[442] T. Bührke; **Kugelblitze aus dem Wasserbecher;** MaxPlanncKForschung, S. 34-38, 1/2008

[443] H. Moranda, K. Walczak, H. Moscicka-Grzesiak; **Dynamics of bridge creating in contaminated oil at AC voltage and analysis of accompanying partial discharges;** 13th Int. Symp. on High Voltage Engineering ISH, Delft, 2003

[444] M. Ossowski, J. Gielniak, H. Moranda, H. Moscicka-Grzesiak; **Oil resistance at different phases of bridge mechanism development at direct voltage;** 13th Int. Symp. on High Voltage Engineering ISH, Delft, 2003

[445] O. Lesaint; **„Streamers" in liquids: relation with practical high voltage insulation and testing of liquids;** Int. Conf. on Dielectric Liquids ICDL, Poitiers 7/ 2008, pp 120-125

[446] T.V. Oommen; **Bubble Evolution from Transformerboard Overload;** IEEE Insulation Life Subcommittee, Niagara Falls, Canada, Oct. 2000

[447] M. Koch, S. Tenbohlen; **Systematic Investigations on the Evolution of Water Vapour Bubbles in Oil-Paper-Insulations;** 15th ISH International Symposium on High Voltage Engineering, Ljubljana, 2007

[448] T.J. Lewis; **Nanometric Dielectrics**; IEEE Transactions on Dielectrics and Electrical Insulation; vol. 1, pp 812-825, 1994

[449] G. Green, A. Vaughan; **Nanodielectrics – How Much Do we Really Understand?**; IEEE Electical Insulation Magazine, July/August 2009

[450] M. Borlein; **Optimierung eines Quenchdetektionssystems für supraleitende Magnetspulen;** Wissenschaftliche Berichte FZKA 7076, Forschungszentrum Karlsruhe 2004

[451] H. Scheller, H.-P. Langenberg, M. Kuhnberg, J. Baldzuhn, B. Petersen-Zarling, D. Gustke, H. Fillunger; **Paschen Testing on W7-X Coils and Components in the BNN Test Facility**; IEEE Transactions on Applied Superconductivity, vol. 16, issue 2, pp 759-762, June 2006

[452] M. Noe u.a.; **Ergebnisbericht über Forschung und Entwicklung 2006;** Institut für Technische Physik, Forschungszentrum Karlsruhe, 2007

[453] B. Ehmann; **Stromrichtertransformatoren für die leistungsstärksten und längsten Energieübertragungsstrecken der Welt;** np netzpraxis, Jg. 47 (2008), Heft 12, S. 10-14

[454] K. Rethmeier, M. Krüger, A. Kraetge, A. Küchler; **Effective PD Measurements under DC Test Voltage by the Use of Synchroneous Measurement Methods;** NORD-IS09, Göteborg, 2009

[455] K. Rethmeier, A. Küchler, M. Liebschner, C. Krause, A. Kraetge, M. Krüger; **Enhanced Partial Discharge Evaluation Methods for DC PD Measurements Using Fully Digital PD Analysing Systems;** ISH09, Int. Sympos. on High Voltage Engineering, Cape Town, 2009

[456] M. Liebschner, A. Küchler, Ch. Krause, B. Heinrich, F. Berger; **Interaction of Oil Ducts and Solid Insulation in HVDC Barrier Systems;** ISH09, Int. Sympos. on High Voltage Engineering, Cape Town, 2009

[457] A. Reumann, M. Liebschner, K. Böhm, A. Küchler, A. Langens, J. Titze, B. Heil; **On-line Monitoring of Capacitance and Dissipation Factor of HV Bushings;** ISH09, Int. Sympos. on High Voltage Engineering, Cape Town, 2009

[458] A. Reumann, K. Böhm, A. Küchler, A. Langens, J. Titze, B. Heil; **Ageing of OIP Bushing Insulation at Very High Temperatures;** ISH09, Int. Sympos. on High Voltage Engineering, Cape Town, 2009

[459] N. Hayakawa, H. Okubo; **Lifetime Characteristics of Nanocomposite Enameled Wire Under Surge Voltage Application;** IEEE Electrical In-

sulation Magazine; Vol. 24, No. 2, pp 22-27, March/April 2008

[460] T. Tanaka, M. Frechette et al (CIGRÉ TF D1.16.03).; **Emerging Nanocomposite Dielectrics;** Electra, No. 226, June 2006, pp. 24-32

[461] K. Rethmeier, A. Obralic, A. Kraetge, M. Krüger, W. Kalkner, R. Plath; I**mproved Noise Suppression by Real-time Pulse-waveform Analysis of PD Pulses and Pulse-shaped Disturbances;** ISH09, Int. Sympos. on High Voltage Engineering, Cape Town, 2009

[462] K. Rethmeier, W. Weissenberg, R. Vogelsang, R. Plath, S. Hoeg, A. Kraetge, M. Krüger; **Benefits of Synchronous UHF and IEC-compliant PD Measurements for Effective Noise Suppression**; ISH09, Int. Sympos. on High Voltage Engineering, Cape Town, 2009

[463] W. Koltunowicz, R. Plath; **Synchronous Multichannel PD Measurements;** IEEE Transactions on Dielectrics and Electrical Insulation Vol. 15, No. 6; December 2008

[464] A. Eigner, S. Semino; **Feldsteuertechnologien bei Kabelgarnituren – Überblick und Stand der Technik**; ew Elektrizitätswirtschaft Jg. 107 (2008), Heft 15, S. 56-58

[465] U. Fromm; **Interpretation of Partial Discharges at dc Voltages**; IEEE Transactions on Dielectrics and Electrical Insulation, Vol. 2 No. 5, Oct. 1995

[466] M. Haeusler, H. Huang, K. Papp; **Design and Testeing of 800 kV HVDC Equipment;** CIGRÉ Session 2008, Paris, paper B4-115

[467] M. Koch, M. Krüger; **A Fast and Reliable Dielectric Diagnostic Method to Determine Moisture in Power Transformers**; 2008 Int. Conf. on Condition Monitoring and Diagnosis, Beijing, China, April 21-24, 2008

[468] M. Koch; **Reliable Moisture Determination in Power Transformers;** Dissertation Univ. Stuttgart, 2008

[469] S.M. Gubanski, P. Boss, G. Csépes, V. Der Houhanessian, J. Filippini, P. Guuinic, U. Gäfvert, V. Karius, J. Lapworth, G. Urbani, P. Werelius, W. S. Zaengl; **Dielectric Response Methods for Diagnostics of Power Transformers;** CIGRÉ Task Force D1.01.09, Technical Brochure 254, Paris 2004

[470] S.M. Gubanski, J. Blennow, B. Holmgren, M. Koch, A. Kuechler, R. Kutzner, J. Lapworth, D. Linhjell, S. Tenbohlen, P. Werelius; **Dielectric Response Diagnoses for Transformer Windings;** CIGRÉ Task Force D1.01.14 Technical Brochure, Paris 2009

[471] T. U. Braunsberger; **Verhalten zyklisch betauter Silikonoberflächen bei elektrischer Beanspruchung;** Dissertation, Technische Univ. Braunschweig, 2007

[472] G. Finis, O. Betz, A. Claudi; **Untersuchungen zur elektrischen Festigkeit von Silikongel im Bereich elektrisch belasteter Längsgrenzflächen;** ETG Fachtagung Grenzflchen in elektrischen Isoliersystemen, Würzburg, Sept. 2008

[473] M. Sack, G. Müller; **Optimisation of an Electroporation Device for Mash;** Optim 2008, Brasov, Romania, 2008

[474] P. Picher, J- Lapworth, T. Noonan, J. Christian u.a.; **Mechanical Condition Assessment of transformer windings using Frequency Response Analysis (FRA)**; Electra, No. 228, Oct. 2006

[475] J. Liu, X. Cheng, J. Pu, J. Zhang, J. Liu, X. Wang; **Experimental Study of the Electrical Characteristics of Ethylene Glycol/Water Mixtures in the Microsecond Regime;** IEEE Electrical Insulation Magazine, Vol. 23, No. 6, Nov./Dec. 2007

[476] IEC 60270; **High voltage test techniques - Partial discharge measurements**

DIN EN 60270 (VDE 0434); **Hochspannungs-Prüftechnik – Teilentladungsmessungen**

[477] E. Lemke u.a.; **Guide for Electrical Partial Discharge Measurements in compliance to IEC 60270**; Electra, No. 241, Dec. 2008

[478] P. Hasse, U. Landers, J. Wiesinger, P. Zahlmann; **EMV - Blitzschutz von elektrischen und elektronischen Systemen in baulichen Anlagen;** VDE-Verlag, Berlin Offenbach, 2. Aufl. 2007

[479] IEC 62305-1, 2, 3, 4; **Protection against lightning** – Part 1: **General principles**, Part 2: **Risk management**, Part 3**: Physical damage to structures and life hazard**, Part 4: **Electrical and electronic systems within structures**

DIN EN 62305-1, 2, 3, 4 (VDE 0185-305-1, 2, 3, 4); **Blitzschutz** – Teil 1: **Allgemeine Grundsätze**, Teil 2: **Risiko-Management**, Teil 3: **Schutz von baulichen Anlagen und Personen**, Teil 4: **Elektrische und elektronische Systeme in baulichen Anlagen**

[480] E. Kuffel, W.S. Zaengl, J. Kuffel; **High Voltage Engineering: Fundamentals**; Newnes, 2nd edition, 2000

[481] J. D. Kraus, D. A. Fleisch; **Electromagnetics with Applications**; McGraw-Hill, 5th ed. 1999

[482] H. Bluhm; **Pulsed Power Systems – Principles and Applications;** Springer Verlag, Berlin Heidelberg, 2006

[483] W. L. Boeck, O. H. Vaughan Jr., R. J. Blakeslee, B. Vonnegut, M. Brook; **The role of the space**

shuttle videotapes in the discovery of sprites, jets and elves; Journal of Atmospheric and Solar-Terrestrial Physics, 1998, Vol. 60, Issues 7-9, p. 669-677

[484] W. A. Lyons, T. E. Nelson, R. A. Armstrong, V. P. Pasko, M. A. Stanley; **Upward Electrical Discharges from Thunderstorm Tops;** 2003. Bull. Amer. Meteor. Soc., 2003, 84, 445-454.

[485] W.H. Bostick; **Experimental Study of Ionized Matter Projected across a Magnetic Field**; Physical Review, 1956, vol. 104, Issue 2, pp. 292-299

[486] M. Liebschner; **Interaktion von Ölspalten und fester Isolation in HVDC-Barrierensystemen;** Dissertation TU Ilmenau/FHWS Schweinfurt, VDI Verlag, Düsseldorf 2009

[487] A. Krivda, T. Tanaka, M. Frechette, J. Castellon, D. Fabiani, G.C. Montanari, R. Gorur, P. Morshuis, S. Gubanski, J. Kindersberger, A. Vaughn, S. Pelissou, Y. Tanaka, L.E. Schmidt, G. Iyer, T. Andritsch, J. Seiler, M. Anglhuber; **Characterization of Epoxy Microcomposite and Nanocomposite Materials for Power Engineering Applications;** IEEE Insulation Magazine, Vol. 28, No. 2, Mar./Apr. 2012, pp. 38 - 51

[488] A. Darwin, C. Perrier, P. Folliot; **The Use of Natural Ester Fluids in Transformers**; Mat-Post07, 3rd Europ. Conf. on HV & MV Substation Equipment, Lyon 2007

[489] C.P. McShane, J. Corkran, K. Rapp, J. Luksich; **Natural Ester Dielectric Fluid Development;** IEEE/PES Transmission & Distribution Conf., Dallas 2006

[490] K. Zafeiris, Y. Bertrand, G. Hipszki, M. Kuffel, C. Rehorek, S. Seidel, I. Atanasova-Hoehlein; **Investigation on Natural Ester Fluids concerning Gassing and Compatability with Transformer Materials;** ISH2011, XVII Int. Symp. on High Voltage Engineering, Hannover 2011

[491] X. Wang, Z.D. Wang; **Electrode Area Effect on Dielectric Breakdown Strengths of Mineral Oil and Esters;** ISH2011, XVII Int. Symp. on High Voltage Engineering, Hannover 2011

[492] M. Jovalekic, S. Tenbohlen, L. Bates, R. Szewczyk; **Water Saturation Limits and Moisture Equilibrium of Alternative Insulation Materials**; ISH2011, XVII Int. Symp. on High Voltage Engineering, Hannover 2011

[493] IEC 61198; **Mineral insulating oils – Methods for the determination of 2-furfural and related compounds**

DIN EN 61198 (VDE 0380-6); **Isolieröle auf Mineralölbasis – Prüfverfahren zur Bestimmung von Furfurol und verwandten Verbindungen**

[494] U. Gäfvert, A. Jaksts, C. Törnkvist, L. Walfridsson; **Electric Field Distribution in Transformer Oil;** IEEE Trans. El. Insulation, Vol. 27, No. 3, June 1992, pp. 647 - 660

[495] N. Inoue, M. Wakamatsu, K. Kato, H. Koide, H. Okubo; **Charge Accumulatioion Mechanism in Oil / Pressboard Composite Insulation System Based on Optical Measurement of Electric Field;** IEEE Trans. El. Insulation, Vol. 10, No. 3, June 2003, pp. 491 - 497

[496] M. Saltzer, Th. Christen, T. Sörqvist, M. Jeroense; **Electro-thermal simulations of HVDC cable joints;** ETG-Fachbericht 131, Feldsteuernde Isoliersysteme, VDE-Verlag, 2011

[497] R. Gaspari, P. Boffi; **FEM Electrical analysis and optimization of HVDC/HVAC sectionalized 300 kV joint;** ETG-Fachbericht 131, Feldsteuernde Isoliersysteme, VDE-Verlag, 2011

[498] W. Hauschild, E. Lemke; **High-Voltage Test and Measuring Techniques;** Springer-Verlag, Berlin Heidelberg, 2014

[499] D. Egger, U. Krüsi, A. Dais, Z. Zic, W. Odermatt, J. Czyzewski, J. Rocks; **New paper-free insulation technology for dry high-voltage condensor bushings;** CIGRÉ Session 2012, Paris, paper A2-211

[500] A. Küchler, U. Piovan, M. Berlund, G. Chen, A. Denat, J. Fabian, R. Fritsche, T. Grav, S. Gubanski, M. Kadowaki, Ch. Krause, A. Langens, S. Mori, B. Noirhomme, H. Okubo, M. Rösner, F. Scatiggio, J. Schiessling, F. Schober, P. Smith, P. Wedin, I. Atanasova-Höhlein, Ch. Perrier, S. Jaufer; **HVDC transformer insulation: Oil conductivity;** Joint Working Group A2/D1.41, CIGRÉ Technical Brochure No. 646, Paris 2016

[501] M.H. Zink; **Zustandsbewertung betriebsgealterter Hochspannungstransformatordurchführungen mit Öl-Papier-Dielektrikum mittels dielektrischer Diagnose;** Dissertation, TU Ilmenau, 2013

[502] G. Mazzanti, M. Marzinotto; **Extruded Cables for High Voltage Direct Current Transmission**; J. Wiley, Hoboken, 2013

[503] O. Hjortstam, J. Schiessling, Y.V. Serdyuk, S.M. Gubanski; **Measurements of ion mobility in transformer oil: Evaluation in terms of ion drift**; CEIDP-2012, 14-17 Oct, p496

[504] K. Backhaus; **Das dielektrische Verhalten der Öl-Papier-Isolierung bei Belastung mit hoher Gleichspannung**; Dissertation, Technische Universität Dresden, 2016

[505] A. Reumann, I. Wirth, A. Küchler, A. Langens, F. Berger; **Erfassung transienter elektrischer Potentialverteilungen in thermisch hoch belasteten Gleichspannungsdurchführungen;** ETG-Fachbericht 144, Diagnostik Elektrischer Betriebsmittel, VDE-Verlag, 2014

[506] I. Wirth, A. Reumann, M. H. Zink, A. Küchler, T. Schnitzler, A. Langens, F. Berger; **Steady-state and Transient Electrical Potential Distributions on HVDC Bushings Measured under Different Thermal Conditions;** 19th ISH Int. Sympos. on High Voltage Engineering; Pilsen, paper 189, 2015

[507] J. Kaumanns; **HVDC Cable Systems – State of the Art Technologies and Future Trends**; Int. High Voltage Direct Current 2015 Conference, Seoul, 18.-22.10.2015

[508] B. Sanden et a.l.; **Recommendations for Testing DC Extruded Cable Systems for Power Transmission at a Rated Voltage up to 500 kV;** CIGRÉ TB 496, Paris 2012

[509] Ch. Preve, R. Maladen, D. Piccoz, J.-M. Biasse; **Validation Method and Comparison of SF_6 Alternative Gases;** CIGRE Session 2016, Paper D1- 205, Paris 2016

[510] K. Pohlink, Y. Kieffel, J. Owens, F. Meyer, F. Biquez, Ph. Ponchon, R. van San; **Characteristics of a Fluoronitrile/CO_2 Mixture – An Alternative to SF_6;** CIGRE Session 2016, Paper D1- 204, Paris 2016

[511] F. Schober; **Elektrische Leitfähigkeit und dielektrisches Verhalten von Pressspan in HGÜ-Isoliersystemen;** Dissertation, TU Ilmenau, 2016

[512] Morshuis, P.; Jeroense, M.; Beyer, J.: **Partial Discharge Part XXIV: The Analysis Of PD In HVDC Equipment.** IEEE Electrical Insulation Magazine, Vol. 13, No. 2, March/April 1997

[513] Morshuis, P.H.M.; Smit, J.J.: **Partial Discharges at dc Voltage: Their Mechanism, Detection and Analysis**. IEEE Transactions on Dielectrics and Electrical Insulation, Vol. 12, No. 2; April 2005, pp 328 – 340

[514] T. Vogt; **Teilentladungsdiagnose bei Gleichspannung**; Dissertation, Univ. Dortmund, 2015

9 INDEX

A. Küchler, *High Voltage Engineering*, VDI-Buch,
DOI 10.1007/978-3-642-11993-4

D

E